

PROCEEDINGS

MEDSI
CHICAGO 2020

MEDSI2020

July 26-29, 2021
Virtual Format

**11TH INTERNATIONAL CONFERENCE ON
MECHANICAL ENGINEERING DESIGN
OF SYNCHROTRON RADIATION
EQUIPMENT AND INSTRUMENTATION**



Hosted by the Advanced Photon Source, Argonne National Laboratory



Preface

The 11th International Conference on Mechanical Engineering Design of Synchrotron Radiation Equipment and Instrumentation (MEDSI) took place from July 26-29, 2021, in virtual format on the Whova virtual conference platform. This conference, known as MEDSI2020, was originally scheduled as an in-person conference on July 13-17, 2020, in downtown Chicago. Due to the COVID-19 pandemic, the in-person conference was postponed a year to July 26-30, 2021. However, with the ongoing pandemic and travel restrictions, we finally had to change the conference to a virtual format. This important biennial conference was hosted by the Advanced Photon Source (APS), Argonne National Laboratory in the United States. MEDSI provides a forum for engineers from facilities around the world to meet and share their experience. The conference topics include insertion devices, storage rings, front ends, beamlines, optics, end station instrumentation, and core technology development in vacuum, cryogenic, optics, and precision mechanics.

This is the first ever MEDSI virtual conference. We tried hard to make the virtual conference as interactive as it can be. We retained all original in-person conference elements including the industrial exhibition. We had about 440 registered attendees, the highest in MEDSI history, and many of the attendees were college students. We had 169 submitted abstracts (talks + posters). The conference featured 4 keynotes, 4 invited talks, 24 contributed talks, and 8 poster sessions with 15-18 posters at each session. We also had 22 industrial exhibitors/sponsors, and many of them had a very well-designed virtual exhibition booth filled with product information, photos, and video. Some exhibitors hosted live-streamed events. We had a great conference, and we learned to interact with each other virtually during this trying time.

Finally, I want to take this opportunity to thank all the members of the Local Organizing Committee, the Local and International Scientific Program Committee, the International Organizing Committee, all session chairs and co-chairs, and, of course, the industrial exhibitors and participants for all of their work that made this conference a success.

A handwritten signature in black ink that reads 'Yifei Jaski'.

Yifei Jaski
MEDSI2020 Conference Chair
Advanced Photon Source
Argonne National Laboratory





International Organizing Committee

Brad Mountford (Chair)

Australian Synchrotron

Sushil Sharma

NSLS II/Brookhaven National Laboratory

Deming Shu

APS/Argonne National Laboratory

June-Rong Chen

National Synchrotron Radiation Research Center (NSRRC)

Ping He

Chinese Academy of Sciences

Will Hutcheson

ALS/Lawrence Berkeley National Laboratory

Sunao Takahashi

SPring-8/JASRI

Lin Zhang

LCLS/ SLAC National Accelerator Laboratory

Keihan Tavakoli

SOLEIL Synchrotron

Lixin Yin

Shanghai Synchrotron Radiation Facility (SSRF)

Regis T. Neuenschwander

Brazilian Synchrotron Light Laboratory

Carles Colldelram

ALBA Synchrotron

Martin Dommach

European XFEL

Gordon Barkway

Canadian Light Source

Karl Åhnberg

MAX-IV Laboratory

Ralph Döhrmann

PETRA

iv

Local Organizing Committee

Yifei Jaski (Chair)

Kelly Jaje (JACoW editor)

Lynnean Celmer

Patric Den Hartog

Constance Vanni

Christine McGhee

Marion White

Patty Cameli

Local Scientific Committee

Yifei Jaski (Chair)

Dana Capatina

Herman Cease

Patric Den Hartog

Mike Fisher

John Grimmer

Jie Liu

Gary Navrotski

Curt Preissner

Oliver Schmidt

Deming Shu

Kamlesh Suthar

International Scientific Committee

Keihan Tavakoli (Chair)

Will Hutcheson

Brad Mountford

Lixin Yin

Lin Zhang

JACoW Editorial Team

Catherine Eyberger

Kelly Jaje (Editor in Chief)

Maria Power

Volker RW Schaa (Technical Editor)

Contents

Preface	i
Preface	iii
Committees	iv
Contents	v
Papers	1
MOIO02 – BM18, the New ESRF-EBS Beamline for Hierarchical Phase-Contrast Tomography	1
MOOA01 – Overcoming Challenges during the Insertion Device Straight Section Component Production and Tuning Phase of the Advanced Photon Source Upgrade	6
MOOA02 – Experience with the Vacuum System for the First Fourth Generation Light Source: MAX IV	10
MOOB02 – ALBA BL20 New Monochromator Design	14
MOOB03 – Bendable KB Type Focusing Mirrors Designed for TPS IR Beamline	17
MOPB02 – Cryogenic Systems for Optical Elements Cooling at Sirius/LNLS	21
MOPB03 – Commissioning and Prospects of the High-Dynamic DCMs at Sirius/LNLS	25
MOPB04 – Four-Bounce Crystal Monochromators for the Sirius/LNLS Beamlines	29
MOPB06 – Installation and Commissioning of the Exactly-Constrained X-Ray Mirror Systems for Sirius/LNLS	33
MOPB08 – Vibration Assessment at the CARNAÚBA Beamline at Sirius/LNLS	37
MOPB09 – The Design and Manufacturing of Superconducting Undulator Magnets for the Advanced Photon Source Upgrade	41
MOPB10 – The Advanced Photon Source Upgrade (APSU) Superconducting Undulator (SCU) Component Database (CDB) Utilization	44
MOPB11 – The Advanced Photon Source Upgrade (APSU) Straight Section Vacuum Systems First Article Fabrication	47
MOPB13 – Automated Mechanical Inspection and Calibration of Insertion Devices in APS Storage Ring	50
MOPB15 – A Comparison of Front-End Design Requirements	53
MOPC01 – Mechanical Design of a Soft X-Ray Beam Position Monitor for the Coherent Soft X-Ray Scattering Beamline	56
MOPC03 – Diamond Refractive Optics Fabrication by Laser Ablation and at-Wavelength Testing	59
MOPC05 – Beamline Alignment and Characterization with an Autocollimator	62
MOPC07 – Weldable Copper Chromium Zirconium Mask	65
MOPC08 – Compact X-Ray and Bremsstrahlung Collimator for LCLS-II	68
MOPC10 – Mechanical Design Progress of the In Situ Nanoprobe Instrument for APS-U	71
MOPC11 – Discrete Photon Absorbers for the APS-Upgrade Storage Ring Vacuum System	75
MOPC12 – A New Magnetic Measurement System for the Future Low Emittance NSLS-II Storage Ring	78
MOPC13 – Recent Studies on the Vibration Response of NSLS-II Girder Support System	81
MOPC14 – Vacuum Pumping Crosses and Keyhole Vacuum Chambers for the APS-Upgrade Storage Ring Vacuum System	85
MOPC16 – Validation of APS-U Magnet Support Design Analysis and Prediction	89
TUIO02 – Mechatronics Approach for the Development of a Nano-Active-Stabilization-System	93
TUOA01 – Surface Twist Characterization and Compensation of an Elliptically Bent Hard X-Ray Mirror	99
TUOA02 – Conceptual Design of the Cavity Mechanical System for Cavity-Based X-Ray Free Electron Laser	103
TUOA03 – Zero-Length Conflat Fin-Type Nonevaporable Getter Pump Coated with Oxygen-Free Palladium/Titanium	107
TUOB01 – Exactly-constrained KB Mirrors for Sirius/LNLS Beamlines: Design and Commissioning of the TARUMÁ Station Nanofocusing Optics at CARNAÚBA Beamline	111
TUOB02 – Development of a Passive Tuned Mass Damper for Ultra-High Vacuum Beamline Optics	115
TUPA01 – Oxygen-Free Titanium Thin Film as a New Nonevaporable Getter with an Activation Temperature as Low as 185 �C	119
TUPA02 – Design of Remote Helium Mass Spectrometer Leak Detector	123
TUPA04 – Investigations on Stability Performance of Beamline Optics Supports at BSRF	125
TUPA05 – Research on Vibration Stability of SAPS Foundation	128
TUPA06 – Study the Active Vibration Control System of the Parallel 6-DOF Platform	131
TUPA08 – Performance of a Double Crystal Monochromator Prototype for HEPS under Water Cooling Condition at a Wiggler Beamline of BSRF	135

TUPA10 – Design of Magnet Girder System for Siam Photon Source II	138
TUPA12 – The Design and Prototype Test for the Tunnel Foundation of High Energy Photon Source . .	141
TUPA13 – Research of Bellow Shield Structure Applied to BPM	145
TUPA15 – Processing of HEPS Low Energy Transport Line Collimator	148
TUPA16 – Design and Development of the Advanced Diffraction and Scattering Beamlines at the Australian Synchrotron	150
TUPB05 – Investigation of Thermal Instabilities in the ALBA Cooling System, Based on Numerical Simulations and Experimental Measurements	153
TUPB06 – Design of Miniature Waveguides and Diamond Window Assembly for RF Extraction and Vacuum Isolation for the CWA	156
TUPB07 – Vacuum Analysis of a Corrugated Waveguide Wakefield Accelerator	160
TUPB08 – High-Precision Synchrotron Kappa Diffractometer	163
TUPB11 – Cryogenics Monitoring and Control System for EMBL Facilities at PETRA III	167
TUPB12 – Assessment of the Corrosion of Copper Components in the Water Cooling System of ALBA Synchrotron Light Source; Presentation of a Proposal to Mitigate the Corrosion Rate of Copper	171
TUPB15 – Fabrication of the Transition Section of a Corrugated Wakefield Accelerator via Laser Micro-machining	175
TUPC01 – Study of Copper Microstructure Produced by Electroforming for the 180-GHz Frequency Corrugated Waveguide	178
TUPC02 – Bringing the Ground Up (When Is Two Less Than One?)	182
TUPC06 – A Review of Ultrasonic Additive Manufacturing for Particle Accelerator Applications	185
TUPC07 – Utilizing Additive Manufacturing to Create Prototype and Functional Beamline Instrumentation and Support Components	189
TUPC08 – Design and Development of AI Augmented Robot for Surveillance of High Radiation Facilities	192
TUPC09 – Progress of Nano-Positioning Design for the Coherent Surface Scattering Imaging Instrument for the Advanced Photon Source Upgrade Project	196
TUPC10 – Modular Nanopositioning Flexure Stages Development for APS Upgrade K-B Mirror Nanofocusing Optics	199
TUPC11 – The HD-DCM-Lite: A High-Dynamic DCM with Extended Scanning Capabilities for Sirius/LNLS Beamlines	203
TUPC14 – Copper Braid Heat Conductors for Sirius Cryogenic X-Ray Optics	207
TUPC15 – A New Ultra-Stable Variable Projection Microscope for the APS Upgrade of 32-ID	211
WEOA01 – CAD Integration for PETRA-IV	215
WEOA02 – Design of Girders on the New Upgrade Lattice at Soleil	218
WEOA03 – Updated High Heat Load Front-Ends for SLS 2.0	221
WEOB01 – Engineering Challenges in BioSAXS for Australian Synchrotron	224
WEOB03 – Development of a Linear Fast Shutter for BM05 at ESRF and BEATS at SESAME	229
WEPA06 – The Beamline Motor Control System of Taiwan Photon Source	232
WEPA07 – The Fizeau System Instrument at ALBA Optics Laboratory	235
WEPA08 – Investigating of EBW Process Weldment Connections Stresses in ILSF 100 MHz Cavity by Simufact.äWelding Software	239
WEPA09 – A New Three-Signal 2D-Beam-Position-Monitor Based on a Segmented Ionization Chamber	243
WEPA10 – Design and Ray-Tracing of the BEATS Beamline of SESAME	246
WEPA11 – Design of Monochromatic and White Beam Fluorescence Screen Monitors for XAIRA Beamline at the ALBA Synchrotron	249
WEPA12 – X-Ray Facility for the Characterization of the ATHENA Mirror Modules at the ALBA Synchrotron	252
WEPA13 – Design of a High-Precision Lifting System for the HL-LHC Heavy Components in the Interaction Region	255
WEPA14 – All Applications of the ALBA Skin Concept	259
WEPA16 – Development and Applications of the White Beam Position Monitor for Bending Magnet Beamlines	263
WEPB01 – LINAC Section 3 and 4 Replacement at the Canadian Light Source	266
WEPB03 – Magnet Measurement Systems for the Advanced Photon Source Upgrade	269
WEPB04 – Design and Fabrication Challenges of Transition Section for the CWA Module	273
WEPB05 – Mechanical Design of a Compact Collinear Wakefield Accelerator	276
WEPB06 – Mechanical Design of the Booster to Storage Ring Transfer (BTS) Line for APS Upgrade	279

WEPB07 – Magnet Module Assembly for the APS Upgrade	283
WEPB08 – Multibody Simulations with Reduced Order Flexible Bodies Obtained by FEA	286
WEPB12 – ForMAX Endstation - a Novel Design Combining Full-Field Tomography with Small- and Wide-Angle X-Ray Scattering	289
WEPB13 – Design and Commissioning of the TARUMÃ Station at the CARNAÚBA Beamline at Sirius/LNLS	292
WEPB15 – A Novel Vacuum Chamber Design for the APS Upgrade of the 26-ID Nanoprobe	296
WEPB16 – CFD Predictions of Water Flow Through Impellers of the ALBA Centrifugal Pumps and Their Aspiration Zone. An Investigation of Fluid Dynamics Effects on Cavitation Problems	299
WEPB17 – A Fast Simulation Tool to Calculate Spectral Power Density Emitted by Wigglers and Short Insertion Devices	303
WEPC02 – A Cryogenic Sample Environment for the TARUMÃ Station at the CARNAÚBA Beamline at Sirius/LNLS	306
WEPC03 – Electrochemistry and Microfluidic Environments for the TARUMÃ Station at the CARNAÚBA Beamline at Sirius/LNLS	310
WEPC04 – A Compact X-Ray Emission (mini-XES) Spectrometer at CLS - Design and Fabrication Methods	314
WEPC05 – An Improved, Compact High Temperature Sample Furnace for X-Ray Powder Diffraction . .	317
WEPC07 – Thermal Model Validation for the Cryogenic Mirror Systems for Sirius/LNLS	320
WEPC09 – Temperature-Dependent Elastic Constants and Youngs Modulus of Silicon Single Crystal . .	324
WEPC10 – Design of Vacuum Chamber With Cryogenic Cooling of Samples for Bragg-Plane Slope Error Measurements	327
WEPC12 – A New Experimental Station for Liquid Interface X-Ray Scattering At NSLS-II Beamline 12-ID	330
WEPC13 – Sample and Detector Positioning Instruments for the Wide Angle XPCS End Station at 8-ID-E, a Feature Beamline for the APS Upgrade	333
THIO02 – Determination of Maximum Repetition Rate of a Corrugated-Waveguide-Based Wakefield Accelerator	336
THOA01 – A Family of High-Stability Granite Stages for Synchrotron Applications	341
THOA02 – A New Traveling Interferometric Scheme for the APS Upgrade of the 2-ID Bionanoprobe . .	345
THOA03 – Alignment Strategies and First Results on Sirius Beamlines	349
THOB01 – Thermal Contact Conductance in a Typical Silicon Crystal Assembly Found in Particle Accelerators	353
THOB02 – Heat Load Simulation of Optic Materials at European XFEL	357
THOB03 – Innovative and Biologically Inspired Petra IV Girder Design	360
Appendices	365
List of Authors	365
Institutes List	371
List of Attendees	379
Exhibitors	391

BM18, THE NEW ESRF-EBS BEAMLINE FOR HIERARCHICAL PHASE-CONTRAST TOMOGRAPHY

F. Cianciosi†, A.L. Buisson, P. Tafforeau, P. Van Vaerenbergh
European Synchrotron Radiation Facility (ESRF), Grenoble, France

Abstract

BM18 is an ESRF-EBS beamline for hierarchical tomography, it will combine sub-micron precision and the possibility to scan very large samples. The applications will include biomedical imaging, material sciences and cultural heritage. It will allow the complete scanning of a post-mortem human body at 25 μm , with the ability to zoom-in in any location to 0.7 μm .

BM18 is exploiting the high-energy-coherence beam of the new EBS storage ring. The X-ray source is a short tri-pole wiggler that gives a 300mm-wide beam at the sample position placed 172m away from the source. Due to this beam size, nearly all of the instruments are developed in-house. A new building was constructed to accommodate the largest synchrotron white-beam Experimental Hutch worldwide (42x5-6m). The main optical components are refractive lenses, slits, filters and a chopper. There is no crystal monochromator present but the combination of the optical elements will provide high quality filtered white beams, as well as an inline monochromator system. The energy will span from 25 to 350 keV.

The Experimental Hutch is connected by a 120m long UHV pipe with a large window at the end, followed by a last set of slits. The sample stage can position, rotate and monitor with sub-micron precision samples up to 2,5x0.6m (H x Diam.) and 300kg. The resulting machine is 4x3x5m and weighs 50 tons. The girder for detectors carries up to 9 detectors on individual 2-axis stages. It moves on air-pads on a precision marble floor up to 38m behind the sample stage to perform phase contrast imaging at a very high energy on large objects.

The commissioning is scheduled for the beginning of 2022; the first “friendly users” are expected in March 2022 and the full operation will start in September 2022.

BM18, HIERARCHICAL PHASE-CONTRAST TOMOGRAPHY

General Concept

BM18 is a project that developed within the ESRF-EBS project. It aims at benefiting from the new capabilities of the “bending magnet (BM)” X-ray sources from the new lattice. Indeed, the ESRF-EBS is reaching a new level in terms of X-ray coherence in a storage ring. The progress is impressive for undulators in the straight sections of the machine, but in fact, the smallest possible X-ray sources (and then the highest spatial coherence) are obtained using short

wigglers installed on the BM ports of the previous machine. As coherence depends on the X-ray source size and of the distance between the sample and the source, the BM18 concept has been developed to combine the smallest possible X-ray source with the longest possible beamline at the ESRF (220m in total).

The ESRF has a long tradition of X-ray full-field imaging at high energy, especially using propagation phase contrast. During the past two decades, important efforts have been made in order to increase the maximum size of the sample from a few mm up to about 20 cm in diameter and 50 cm vertically.

X-ray Source

This new beamline will allow a dramatic increase of sample sizes (up to 0.7m in diameter, 2.5m vertically and a total weight of 300 kg), while also increasing the sensitivity, especially at high energy. The source was then selected as a tri-pole wiggler with the central pole at 1.56T (the two lateral poles being at 0.85T) in order to produce a continuous X-ray spectrum optimized for very hard X-rays.

Optical Scheme

The beamline has been designed to be operated only in polychromatic mode in order to maximize the average usable energy, as well as to preserve the coherence as much as possible. The optical scheme is then based on mirror polished filters with different materials (C, SiO₂, Al₂O₃, Al, Ti, Cu, Mo, Ag, W, Au), with different thicknesses and shapes allowing the energy to be tuned from 25 keV to 350 keV. In addition, several systems of inline monochromators have been implemented using refractive lenses and high precision slits to be able to tune the bandwidth and beam geometry when needed. A chopper is integrated in order to fine tune the beam power without changing its spectrum. All in all, these optical combinations bring most of the functionalities from a classical insertion device beamline with a moveable gap, even if BM18 will be on a fixed gap system.

Experimental Hutch

Considering the large energy range and foreseen applications, the experimental hutch has been designed to be as long as possible (45m). This allows a propagation distance up to 38m between the centre of the sample and the most distant position of the detectors. The extremely small size of the X-ray source on this beamline makes it possible to exploit this long propagation distance for pixel size down to 13 μm . For smaller pixel sizes, the propagation distance can be reduced as required.

† ciancios@esrf.fr

Detectors and Automation

The main purpose of this new beamline is to offer a highly automated multi-resolution platform to investigate large samples through a hierarchical approach. The different detectors (up to 9 in total, covering from 100 μ m down to 0.7 μ m) will all be based on indirect detector principle. A scintillator screen is observed by CMOS sensors via different optical mounting systems (microscope, zoom, tandem optics, macro optics). These various optics will be installed on a large motorized detector stage that will be able to move along the entire hutch on a polished marble floor. The concept is to automatically change from one configuration to the next, without having to enter the hutch, making it possible to zoom-in anywhere on a sample via a graphical user interface.

Applications

BM18 will make hierarchical imaging possible in a large range of diverse samples, as well as high-throughput imaging of a large series of samples. The main scientific topics that motivated the construction of BM18 are material sciences (for both academic and industrial applications), cultural heritage (especially palaeontology which is a long standing tradition at the ESRF), as well as more recently geology, and biomedical imaging. This last topic emerged recently on BM18 following the covid-19 pandemic when it appeared that this beamline would have the capabilities to completely scan a human body (post-mortem), with an accuracy that's never been reached, and with the possibility to zoom-in down to the cellular level using the hierarchical imaging system.

The last important topic on BM18 is the industrial applications that span across many different fields, even if the material sciences remain the dominant topic.

BEAMLINE COMPONENTS

The components of the beamline are grouped into two zones, the ones located in the Optical Hutch (OH) and the ones in the Experimental Hutch (EH). They are connected by a 120m in-vacuum transfer pipe.

The first hutch is the OH (Fig. 1). It is a shielded hutch in the ESRF Experimental Hall, located in the vicinity of the storage ring and front-end wall. It contains 4 sets of slits, 15 axis of filters, 2 sets of lenses (1D and 2D respectively), a chopper, a beam enlarger and the safety and vacuum standard beamline equipment.

The second zone is the EH. It is placed in a new remote satellite building in order to put the sample at the maximum possible distance (172m) from the source on the ESRF site. It contains the final window, a last set of slits, two sample stages for tomography (the large one and a smaller one equivalent to the systems already installed on BM05, ID19 and ID17 at the ESRF) and the detectors on a movable girder (Fig. 2).

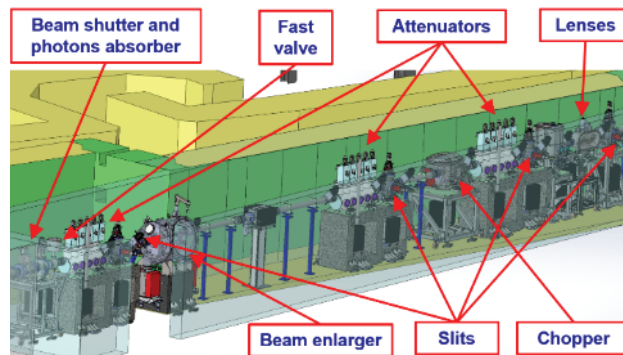


Figure 1: Optical hutch layout.

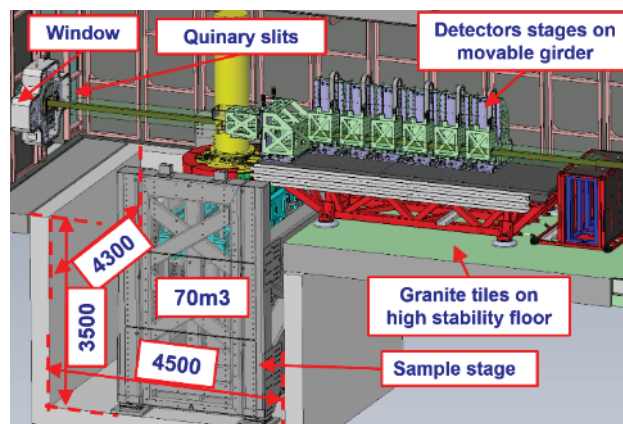


Figure 2: Experimental hutch layout.

Optical Hutch Slits

Four sets of identical slits are placed in the Optical Hutch. The design, including manufacturing drawings, was made by the ESRF. The construction was assigned to CINEL S.R.L. (Italy). The characteristics are listed in Table 1, and the design is shown in Fig. 3.

The main technical difficulty was to make a vertical scan with a minimum gap of 10 μ m. As the vertical blades are 100 mm wide, the wobbling around the beam axis shall be in the order of 10 μ rad. This result was obtained by: a) guiding the blades by precision rails put directly in vacuum and well-spaced carriages, b) careful cooling to reduce thermal deformation, c) actuating one of the blades with respect to the other, to have a motor to set the position and a second one to set the offset. This permits the beam to be scanned with nearly absolute constant aperture.

The motors (2-phase stepper) have very high reduction ratio gearboxes to ensure the irreversibility of the stages, leading to very high resolution (0.25 μ m/step horizontally, 0.15 μ m/step vertically) but relatively small maximum speed.

The test carried out by the supplier and repeated at the ESRF indicated that the maximum wobbling is about 20 μ rad. This value is slightly higher than expected but small enough to ensure the proper functioning. The lower than expected performance could be due to a relatively bad running parallelism of the guides.

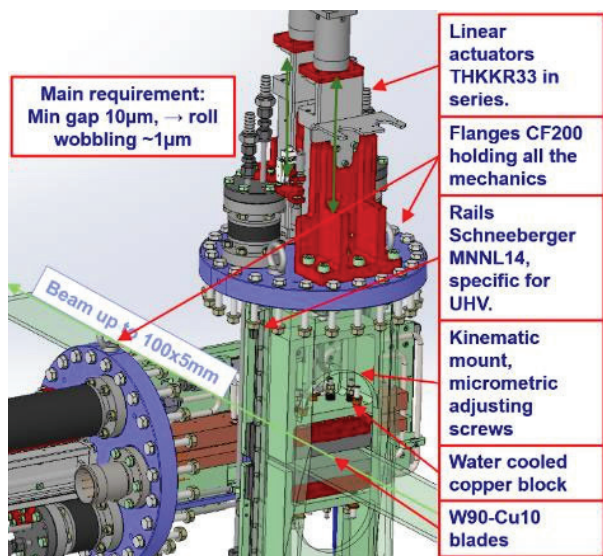


Figure 3: OH slits.

2D (2x1D) Cross-Lenses

The 2x1D Cross Lenses shown on Fig. 4 are composed of two sets of lenses: a horizontal block and a vertical block. Each of these blocks can hold two micro-lens chips intended to be made from sapphire, silicon or glassy carbon, with the dimensions: 100x50x2mm. The chips are clamped into water-cooled copper blocks and can be actuated along 5 degrees of freedom thanks to a stack of linear and rotary stages. To increase the thermal conductivity between the chip and the copper blocks, a pyrolytic graphite sheet is inserted (which can withstand a temperature of 400°C instead of the standard indium which would melt on the chip). The homogenous 2MPa pressure is obtained, over the whole chip, thanks to an assembly of 32 spring-pistons forming an elastic “bed”.

Each motor is linked via a copper thermal braid to a water-cooled loop to avoid a global heating of the positioning system.

The ESRF has made the design and carried out the assembly.

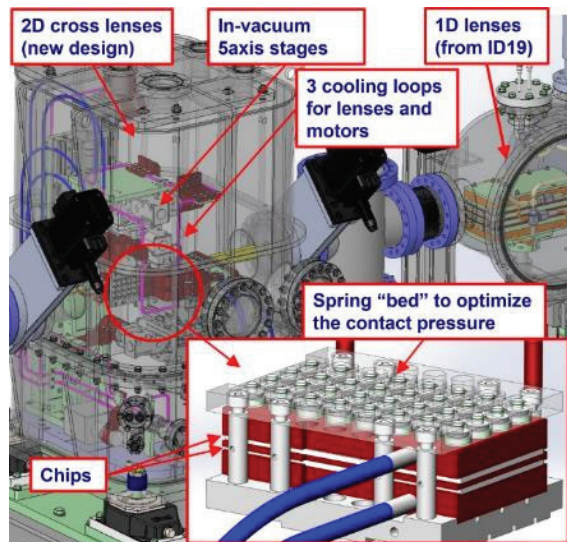


Figure 4: 2D Cross lenses – spring bed.

Attenuators

The attenuators system is composed of 5x3 movable axis (3 chambers with 5 axis each) carrying 3 types of filters of various materials. The filters have 3 possible shapes: a) thin sheet (up to 5mm thickness in the beam direction), b) blocks (from 5 to 100mm), c) rods (5mm diameter, with the cylinder axis placed horizontally, normal to the beam).

The conceptual design of the chamber and axis was made by the ESRF, while the detailed design and manufacturing was assigned to CINEL S.R.L.

The ESRF has made the detailed design of the brackets for the filters. The challenge was managing the cooling of different types of filters and many materials, keeping the design simple and affordable. The mechanical solution to hold thin filters is a simple copper bracket, cooled by water. For the other types (blocks and rods), a multilayer design was selected, alternating the filters with water cooled blocks of copper and uncooled intermediate plates (Fig. 5).

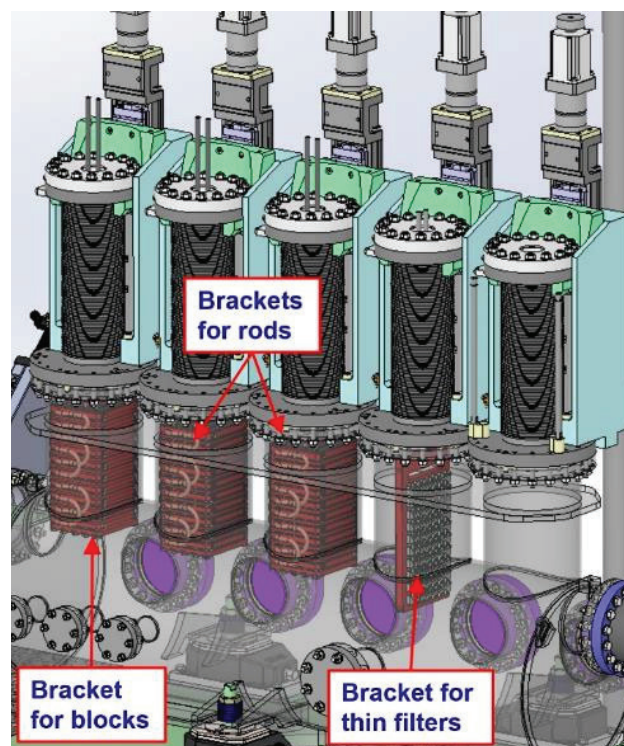


Figure 5: Attenuators.

Chopper

The aim of the chopper in BM18 is to reduce the average power of the beam without changing the beam characteristics, by cutting the beam temporally.

The design (Fig. 6) is based on 2 rotating wheels, in which radial slots reduce half of the total contact surface with the impinging beam. When the slots of the 2 wheels are aligned and are in rotation, 50% of the beam can pass through. When the phase difference is equal to the slot step, no beam is transmitted. The intermediate beam position allows the power to be adjusted between 0% and 50%. The entire beam can pass through when the wheels are aligned and stopped with a slot in the beam position. The requested

aperture frequency is 2 kHz. As the wheels have 100 slots, the angular velocity is 20rps -1200rpm.

The wheels are rotated together by a stepper motor. They are cooled by forced airflow, placed outside the vacuum chamber; a magnetic feedthrough transmits the torque. The phase is adjusted with a mechanism that transforms the axial movement of one-wheel in respect to the other to an angle, using the principle of a long pitch threading. The wheels are made in tungsten alloy. The cooling is secured only by radiating from a water-cooled cage located between the wheels and the chamber. As the temperature of the wheels can rise up to 200°C, ceramic bearings are used.

The complete design was made internally at the ESRF, including the manufacturing drawing. The instrument was produced and assembled by Alca Technology S.R.L. (Italy).

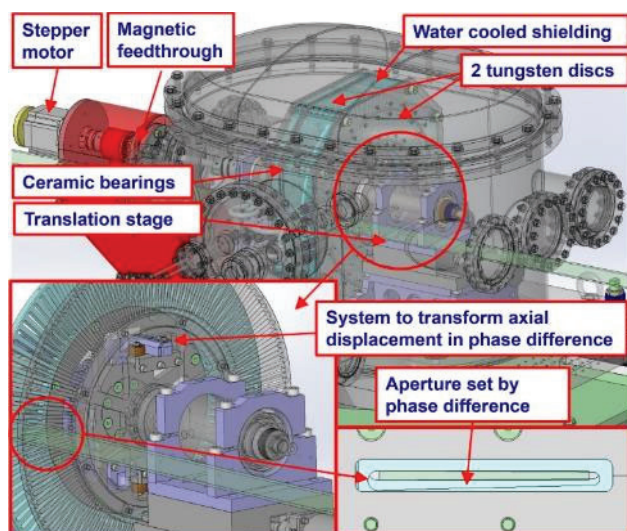


Figure 6: Chopper.

Window

A large window (in development) will be placed at the end of the transfer pipe in the OH. Its role is to separate the vacuum part of the beamline from the in-air part, with the minimum impact on beam quality and intensity. Table 1 contains the main requirements for the design of the window.

Several possible materials were investigated. Finding one with a high transparency to X-rays, low thickness and possibility of mirror polishing at a reasonable price is challenging. The best material candidate is 1050' series aluminium (even if reducing the thickness to a reasonable value in terms of X-ray absorption is challenging) and beryllium (for this material the challenges are the safety and cost). Vitreous Carbon was also studied and samples were tested however, this material was not available in the required dimensions.

In order to start the operation of the beamline as soon as possible, a preliminary smaller beryllium window (330x30x0.6mm), was installed.

Table 1: Window Specifications

Requirement	Dimension
Beam dimension	360×200mm
Max thickness (Z=13)	2 mm
Max thickness (Z=6)	6 mm
Mirror polishing	Ra min=0.1 μm
Homogeneity @ tomography resolution (0.5 μm)	
Radiation resistance	
Vacuum pressure mechanical resistance	
Low leak rate for UHV	
Safety (resistance to impacts...)	
Good thermal conductivity and high T resistance	

Experimental Hutch Slits

A large set of slits (Fig. 7) is settled at the very beginning of the EH. The whole assembly, and its nitrogen chamber (300kg total weight), are fixed on the concrete wall, to reserve space on the floor for the Sample Stage and its movable floor.

The main characteristic of this set of slits is its large dimensions, as the beam can have dimensions of 400x200mm. The minimum gap of 50 μm needs high precision guiding (max yaw error 12 μm), and fine resolution (0.5 μm/step). To reduce the thermal deformation on the edge of the slits the 20mm-thick tungsten blades have an inner cooling loop that should reduce the thermal bump to 5μm. All of the translated parts are lubricated with a special radiation-resistant grease (Lubcon - Turmotemp II/400 CL2).

The whole design is owned by the ESRF and produced by KINKELE GmbH & Co KG (Germany).

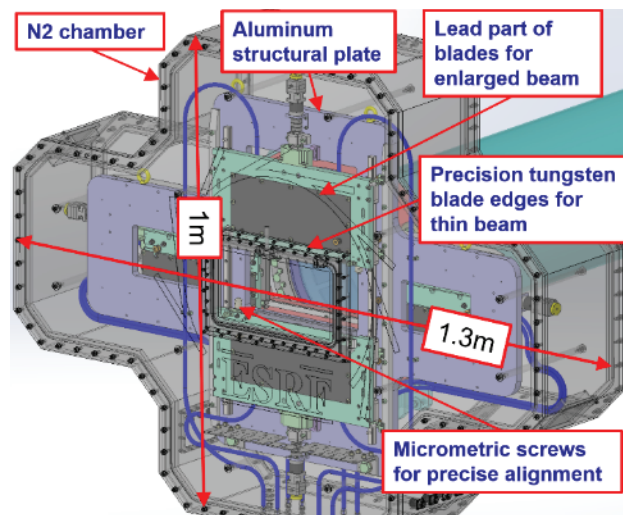


Figure 7: Experimental hutch slit.

Sample Stage

The Sample Stage is used to position and rotate a large sample in the beam in order to perform tomography. The combination of high precision and large (and heavy) samples is very challenging from a mechanical point of view (Table 2).

The ESRF made a call for tender to assign the supply of this machine to a single supplier, LAB Motion Systems (Belgium).

The proposed machine, currently in construction, (Fig. 8) weights approximately 50T and it will be placed in a 70m³ pit at the beginning of the EH. The main structure is made from steel, and the translation axes are obtained with balls linear rails and balls screws (Fig. 8).

The most innovative part is the air bearing spindle. It is based on 3 rotating air-pads on a granite table to hold the axial load (sample weight + magnetic preload). A central air bearing holds the axial load. A counterweight system is added to avoid static eccentricity, which can affect the sphere of confusion. The stage over the spindle is connected with a kinematic mount to avoid the propagation of deformations.

A metrology system was added to continuously monitor the sample error and use this information for data correction and to adjust the position of the counterweight. This system is composed of 8 capacitive sensors (6 axial and 2 radial, normal to the beam) mounted on a kinematic support, targeting a quasi-kinematic ring machined on the top plate of the spindle stage. The kinematic mounts should avoid transmitting the deformation of the spindle itself and provide the pure location of the rotation axis.

The Z stage is actuated by 4 vertical ball-screws, in order to finely level the Y stage and ensure verticality of the tomography axis.

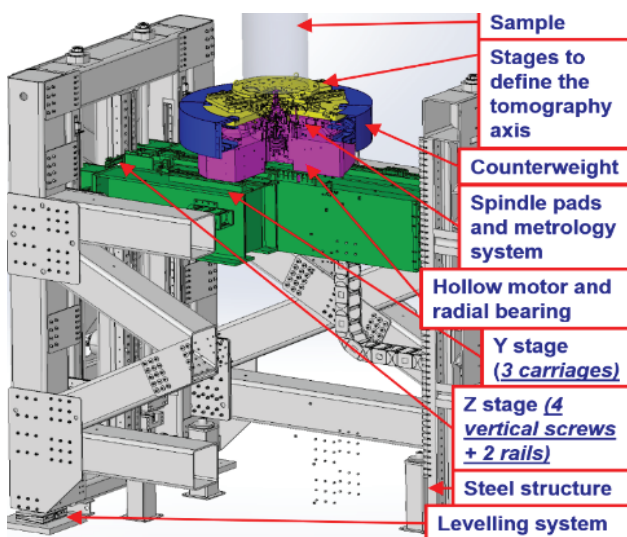


Figure 8: Sample stage.

Detector Supports

Each of the 6 “generic” detectors are placed on an individual 2 axis positioning stage. This allows the detector position to be adjusted laterally and vertically through the

Beamlines and front ends

Beamlines

Table 2: Sample Stage Specifications

Data	Dimension
Max sample weight	300 kg
Max sample dimensions	H=2.5 m, D=0.6 m
Z stage stroke	2.5 m
Y stage stroke	+/- 0.7 m
Z-Y stage precision	10 μ m
Sample positioning on spindle	+/- 0.3 m
Spindle sphere of confusion	0.5 μ m @ 2.5 m

beam and the removal from the beam when using the downstream detectors. All of the stages are mounted on a unique girder (5.5x1.9m) that moves 30m along the beam axis.

The girder was designed by the ESRF. It is composed of a granite table (produced by Zali S.R.L., Italy), supported by a steel structure (made by Nortemecanica, Spain [1]), sustained by precision air-pads on a stone tiled floor. A THK JR45 rail is used to guide the movement. The motion is driven by a friction wheel located between the structure and the floor (Fig. 9). The air-pad system is being studied.

The system is supplemented by an additional carriage on wheels for the electronics racks. This separation minimizes the thermal deformation of the girder and reduces the load on the precision air-pads.

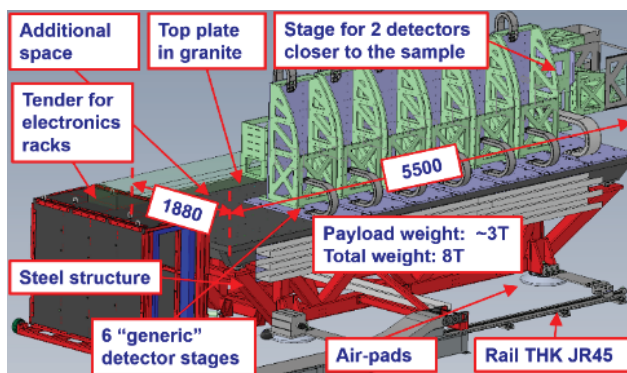


Figure 9: Detectors girders and stages.

ACKNOWLEDGEMENTS

The BM18 project is partially funded by the German Federal Ministry of Education and Research (BMBF), in collaboration with the Fraunhofer Gesellschaft, the Julius-Maximilians-Universität Würzburg, and the Universität Passau. The present presentation and paper has received funding from the European Union’s Horizon 2020 research and innovation program under grant agreement No 870313 (STREAMLINE).

REFERENCES

- [1] F. Cianciosi *et al.*, “The Girders System for the New ESRF Storage Ring”, in *Proc. 9th Mechanical Engineering Design of Synchrotron Radiation Equipment and Instrumentation Int. Conf. (MEDSI'16)*, Barcelona, Spain, Sep. 2016, pp. 147-151. doi:10.18429/JACoW-MEDSI2016-TUCA06

OVERCOMING CHALLENGES DURING THE INSERTION DEVICE STRAIGHT SECTION COMPONENT PRODUCTION AND TUNING PHASE OF THE ADVANCED PHOTON SOURCE UPGRADE*

J. Lerch[†], Argonne National Laboratory-Advanced Photon Source (APS), Lemont, IL 60439, USA

Abstract

The Advanced Photon Source Upgrade (APS-U) scope for insertion devices (IDs) and ID vacuum systems is extensive. Thirty-five of the 40 straight sections in the storage ring will be retrofitted with new 4.8-meter-long Superconducting Undulators (SCUs) or a mix of new and reused Hybrid-Permanent Magnet Undulators (HPMUs). All 35 ID straight sections will require new vacuum systems and new HPMU control systems. Production is well underway at multiple manufacturing sites around the world for these components. Simultaneously, ID assembly and HPMU tuning is occurring onsite at Argonne National Laboratory (ANL). In addition to component production and assembly/tuning activities, our team also started the ID swap out program at the Advanced Photon Source (APS) in late 2020. This program allows us to remove HPMUs intended for reuse from the APS storage ring and retune them to meet the APS-U magnetic specifications to reduce the tuning workload during the dark year. These activities have presented technical and logistical challenges that are as unique as the components themselves. Additionally, the ongoing Covid-19 pandemic presented unforeseen challenges that required new work processes to be created to sustain pace and quality of work while maintaining the high workplace safety standards required at Argonne. This paper will summarize the many challenges encountered during the project and how they were overcome.

INTRODUCTION

The APS-U Upgrade (APS-U) project plan calls for the current APS 40-sector storage ring (SR) to be retrofitted with a new 6 GeV, 200 mA storage ring optimized for brightness above 4 keV. 35 of the 40 sector straight sections will be dedicated to insertion devices (ID) which will produce photons at various energies to ID beamline users based on their needs. The APS-U ID group is responsible for upgrading equipment within the straight sections for the upgrade. The group's extensive scope can be broken up into three main technical areas: Hybrid Permanent Magnet Undulators (HPMUs), Superconducting Undulators (SCUs), and ID Vacuum systems (IDVS). The following sections will detail each areas scope, major challenges encountered during production, and solutions to those challenges.

*This research used resources of the Advanced Photon Source, a U.S. Department of Energy (DOE) Office of Science User Facility at Argonne National Laboratory and is based on research supported by the U.S. DOE Office of Science-Basic Energy Sciences, under Contract No. DE-AC02-06CH11357.

[†] jlerch@anl.gov

HPMU

Scope

HPMUs are the main type of ID utilized in the APS-U. 30 out of 35 straight sections will be equipped with at least one HPMU. This requires our group to deliver 55 HPMUs for which 12 are the revolving type. Of the 55 HPMUs required for the APS-U, 32 will be new period devices and 23 will be made from existing period magnet structures harvested from devices currently in use. The harvested devices will require retuning to meet APS-U magnetic specifications. All HPMUs require new motors and control system due to the obsolescence of the current motors and controls currently in use at the APS.

Challenges and Solutions

There have been many major challenges associated with the HPMU scope. Our group is required to deliver 55 HPMUs for installation to the Removal and Installation group (R&I) prior to the start of commissioning. We have also encountered issues during assembly of the HPMUs that occurred prior to sending the devices for tuning. Finally, our tuning facility has limited space for device tuning given the aggressive timetable required to meet our delivery schedule.

Schedule The APS-U ID group project schedule is one of our largest challenges. We are required to deliver all 55 HPMUs, canting and phase shifter magnets, and ID control system to the R&I group prior to the start of commissioning. We implemented two strategies to meet our schedule: pre-tune new period devices and swap out reused periods during maintenance periods.

Pre-tuning new period devices will allow our team to tune all new period magnet structure sets to the APS-U magnet requirements. New period devices represent the largest subset of HPMUs that need to be delivered. To accomplish this, our group has procured 6 additional gap separation mechanisms (GSM) from our central shops. After the magnetic structure set (MSS) is assembled onto one of the spare GSM, our tuning group tunes the MSS to meet APS-U magnetic requirements. The MSS is then removed from the GSM and stored until the start of dark time when it can be assembled onto the GSM that will be installed into the storage ring. The MSS cannot be considered "final tuned" until it has been installed onto the GSM it will be installed with due to minor variations in deflection that occur between different GSM. The exception to this is the revolver HPMUs, which our group redesigned the GSM as part of the design phase of the APS-U. This allows us to assemble the MSS onto the unique revolver GSM, which

in turn can be final tuned and then stored until R&I is ready to take possession for installation in the storage ring. The only additional tuning that will need to occur with this device, and this is true for non-revolving HPMUs as well, is to account for the center phase shifter for revolver HPMUs that will be installed in the inline configuration.

The strategy for the reused period devices is slightly different. Reused period devices represent a smaller subset of the overall quantity of HPMUs to be delivered prior to the start of commissioning. Our group is utilizing the remaining maintenance periods leading up to the dark year to swap out devices that are intended for reuse. Swap out is a logistically challenging exercise, as it requires coordination between APS operations (OPS) and the APS-U. The process begins with APS-U delivering a completed device to APS OPS prior to the start of a maintenance period. The device is an exact match to the device that will be swapped (i.e., same type of GSM and same MSS). APS OPS then remove the device that is installed in the storage ring and replaces the device with the exact match delivered by APS-U. The removed device has its MSS retuned to meet both APS and APS-U magnetic specifications. The retuned device is then delivered back to APS OPS for swap with a device in a different sector. This process is repeatable for most devices; however, a subset of swapped devices requires swapping of the MSS and GSM which can complicate the process. This challenge will be further described in the next section.

Assembly Assembly activities mainly involve assembling new period devices or reassembling reused devices removed during a maintenance period as part of the swap out program. Additionally, activities can require quality checks (QA) of manufactured assemblies upon delivery from the vendor as a pre-determined amount of time in the procurement contract. Challenges we have encountered during assembly activities are typically logistical or technical in nature.

Logistical issues arise due to late deliveries from manufacturers and sudden manpower needs by APS OPS. To try and mitigate this issue we require vendors to meet with the responsible technical team weekly. While this does not eliminate delays, we have found that it helps uncover delays sooner so that we can update our high-level schedule to accommodate the delays and reprioritize work accordingly. Unfortunately, this strategy does not work when sharing manpower with APS OPS. OPS require matrixed staff to support operations whenever an emergency arises that threatens the facilities ability to provide usable synchrotron radiation to users. Due to the nature of the need, notice is often extremely short or non-existent. To deal with this challenge, technicians and engineers were hired to specifically support the upgrade. These staff support OPS only during maintenance ID swaps. They maintain productivity when emergency situations occur that require OPS staff to support the current APS operations.

Technical issues arise when assembling multiple magnetic periods simultaneously. These issues can be in the assembly of the MSS or the GSM. For the MSS, the

challenge of assembling different periods simultaneously arises from the use of different fasteners and components for each MSS. For example, if the wrong fastener or torque is used, then the magnetic pole could be irreversibly damaged. To minimize the risk of error each MSS is documented in our Component Database (CDB) [1]. This allows our technicians and engineers the ability to identify what components, drawings, and specifications are required to assemble the MSS. We also prepare and stage components for each magnetic period near where the specific MSS is being assembled to avoid the risk that components for another magnetic period will be mixed in. For the GSM, the challenge is in identifying mechanical issues occurring within the GSM that are difficult to identify by eye or with conventional gauges. One example would be a gas spring that isn't providing the correct spring force. This can lead to an issue referred to as "clunk" where the MSS suddenly jolts during operation when the magnetic attractive force is overtaken by gravity while opening the magnetic gap. This leads to unreliable reads from the linear encoders which complicates user operation. To deal with this issue, the technical lead for APS-U ID controls has written a script that allows an engineer the ability to compare the rotary encoder output to the linear encoder output [2]. Although determining the specific mechanical cause (i.e., gas spring, lead screw misalignment, etc.) discovered by this script is still being developed, allows us to identify mechanical problems in the GSM before the device is tuned or installed in the storage ring.

Tuning Tuning represents a large challenge for the APS-U. For the APS-U, large volume of different period devices needs to be tuned in a short period of time. Most of these devices are new period devices which our team have little or no experience tuning. Additionally, our facility only has one 6- and 3-meter bench for tuning activities, limiting capacity for multiple measurements to occur at a single time. Our tuning team has implemented automatic tuning algorithms and phase error based tuning methods to overcome these issues. These techniques have been used on 24 devices thus far for APS-U with great success. More detailed information on these techniques can be found in the following [3-6].

SCUS

Scope

Eight SCUs are required to be delivered to R&I for installation, however, they must be delivered prior to the start of the dark year. Six of the eight SCUs have a magnetic period of 16.5 mm while the remaining two have a magnetic period length of 18.5 mm. Four of the SCUs are arranged in a colinear arrangement. The other four SCUs are canted devices. More information on details of the new design can be found in [7].

Challenges and Solutions

Although the SCUs represent a smaller part of the overall project scope, significant challenges are still present as we progress with production. Specifically, there are large

challenges in manufacturing the magnet cores to specification and challenges associated with assembling the device.

The new magnet cores in the colinear devices are each approximately 1.9 meters long. The flatness tolerance across the length of the cores is difficult for most vendors to hold. Additionally, footed poles are periodically required across the length of the core to help ensure pole contact with the impregnation mold guide plate. This is to give added confidence that epoxy will not build on the pole face, which could allow for contact conduction between the vacuum chamber operating at 20K and the 4K magnet cores.

The first attempt to solve these issues was to pursue two different magnet core designs with two different vendors. Both vendors had great difficulty in meeting the project schedule, and the cores ended up being delivered behind schedule. Additionally, once the cores were delivered, our team discovered that the areas near the footed poles on both designs were prone to shorts during winding. This had not been experienced on previous SCUs. The team quickly worked to solve both issues by coming up with a design that did not require footed poles. This required an alteration to the potting mold as well. This new design was used for canted SCU core periods. After award, the vendor for both sets of cores noted that the new design will be simpler to machine and that the simplicity of the design opened additional machines the vendor could use to manufacture the cores. More detailed information on the magnet core manufacturing can be found in [8].

ID VACUUM SYSTEM

Scope

35 IDVS require re-design and replacement. Separate vacuum systems are required for the HPMUs and SCUs due to the extreme difference in operating temperature. The small magnetic gap of the undulator and the minimum aperture allowed in the storage ring require extremely thin walls in both IDVS. The HPMU IDVS has a minimum wall thickness of 0.6 mm while the SCU IDVS has a minimum wall thickness of 0.4 mm. All IDVS are required to be fabricated and delivered before the start of the dark year.

Challenges and Solutions

One challenge both IDVS have in common is in performing the welding of aluminum joints to the labs strict weld standards. We require the welds meet spec AWS D17.1 class B or better standards. Given the thin wall of the joint being welded, this necessitates little to no porosity in the weld. The vendors awarded the contracts had great difficulty achieving these standards initially. The solution to this issue was to have our weld engineer become involved in our weekly vendor meetings. Our weld engineer was able to identify small details in the vendors weld process that was causing issues with minimizing porosity in the welds. We also worked with the vendor to provide additional resources so that they could produce additional weld samples and incorporate additional x-ray scans into their process. Both first article IDVS were delivered within

specification. The following will now describe challenges that were specific to each IDVS for the HPMUs and SCUs.

HPMU IDVS The main challenges that were present during the design and production of the new HPMU IDVS were mainly based around the manufacturing of the main vacuum chamber. Our physics requirements for the APS-U storage ring necessitated the minimization of welded joints. This required the design to be fabricated from a single extrusion. This included the aperture transitions that needed to occur at the ends of the chamber. To accomplish this, we worked with two vendors to develop multiple methods to machine and plunge electrical discharge machining (EDM) the cone into the ends of the extrusion. We then worked with our physics group to identify which solution presented the best environment for the stored beam. Our physics group selected the machined cone, and the group that produced the feature ended up being awarded the total manufacturing contract for the chamber. More information on the HPMU IDVS first article can be found in [9].

SCU IDVS The main challenge with the SCU IDVS was handling and integrating the chamber into the cold mass. The chamber arrives on a support structure due to its small cross section and thin wall. There is also a bimetal joint on each end that is very delicate. During assembly, our team discovered that the chamber would need to be removed from the support to assemble onto the cold mass. To solve this issue, a support beam was constructed to support the entirety of the chamber and end flanges during assembly. More information on the SCU IDVS first article can be found in [9].

COVID-19

Covid-19 shut down the laboratory at the end of March 2020. This time coincided with our ramp up in assembly and production. All work onsite was paused for a period of three weeks while procedures could be put in place so that work could be performed safely and minimize risk of transmission of the virus. We worked closely with our safety team to implement safety controls and were able to restart work a few weeks after work was halted. We updated procedures so that workers maximized social distancing. HPMU and SCU assembly work require workers to regularly be within 6 feet of one another. If social distancing was not possible, then we implemented moveable shields to separate workers. Using these controls, we were able to safely resume work and minimize the transmission of the virus within our group. No one in the APS-U ID group to date has contracted the virus from a coworker onsite.

SUMMARY

The APS-U ID group has an extensive scope that can be broken into three main technical areas: HPMUs, SCUs, and IDVS. Each area presented many challenges during production and ongoing assembly activities. The solutions we implemented were as unique as the challenges themselves.

ACKNOWLEDGEMENTS

The author would like to acknowledge the members of the APS-U ID group without whom our success to this point would not be possible.

REFERENCES

- [1] G. Avellar *et al.*, “Advanced Photon Source Upgrade (APS-U) Superconducting Undulator (SCU) Component Database (CDB) Utilization”, presented at the 11th Int. Conf. on Mechanical Engineering Design of Synchrotron Radiation Equipment and Instrumentation (MEDSI'20), Chicago, IL, July 26, 2021, paper MOPB10, this conference.
- [2] N. Weir, “Automated Mechanical Inspection and Calibration of Insertion Devices in APS Storage Ring”, presented at the 11th Int. Conf. on Mechanical Engineering Design of Synchrotron Radiation Equipment and Instrumentation (MEDSI'20), Chicago, IL, July 26, 2021, paper MOPB13, this conference.
- [3] M. Qian, R. Dejus, Y. Piao, I. Vasserman, and J. Xu, “A new method of undulator phase tuning with mechanical shimming”, presented the 12th Int. Particle Accelerator Conf. (IPAC'21), Campinas, Brazil, May 2021, paper WEPAB129, to be published.
- [4] M. Qian, R. Dejus, Y. Piao, I. Vasserman, and J. Xu, “Experience with algorithm-guided tuning of APS-U undulators”, presented at the 12th Int. Particle Accelerator Conf. (IPAC'21), Campinas, Brazil, May 2021, paper WEPAB130, to be published.
- [5] R. Dejus, Y. Piao, M. Qian, I. Vasserman, J. TerHAAR, and J. Xu, “Status of Insertion Device Tuning for The APS Upgrade”, presented at the 12th Intl. Particle Accelerator Conf. (IPAC'21), Campinas, Brazil, May 2021, paper THPAB085, to be published.
- [6] Y. Piao, R. Dejus, M. Qian, I. Vasserman, and J. Xu, “Magnetic shims studies for APS-U hybrid permanent magnet undulators”, presented at the 12th Int. Particle Accelerator Conf. (IPAC'21), Campinas, Brazil, May 2021, paper THPAB077, to be published.
- [7] Y. Ivanyushenkov *et al.*, “Status of development of superconducting undulators at the Advanced Photon Source”, presented at the 12th Int. Particle Accelerator Conf. (IPAC'21), Campinas, Brazil, May 2021, paper THPAB046, to be published.
- [8] E. Anliker *et al.*, “The Design and Manufacturing of Superconducting Undulator Magnets for the Advanced Photon Source Upgrade”, presented at the 11th Int. Conf. on Mechanical Engineering Design of Synchrotron Radiation Equipment and Instrumentation (MEDSI'20), Chicago, IL, July 26 2021, paper MOPB09, this conference.
- [9] M. Szubert *et al.*, “The Advanced Photon Source Upgrade (APS-U) Straight Section Vacuum Systems First Article Fabrication”, presented at the 11th Int. Conf. on Mechanical Engineering Design of Synchrotron Radiation Equipment and Instrumentation (MEDSI'20), Chicago, IL, July 26, 2021, paper MOPB11, this conference.

EXPERIENCE WITH THE VACUUM SYSTEM FOR THE FIRST FOURTH GENERATION LIGHT SOURCE: MAX IV

E. AL-Dmour[†], M. Grabski, K. Åhnberg, MAX IV Laboratory, Lund, Sweden

Abstract

The 3 GeV electron storage ring of the MAX IV laboratory is the first storage-ring-based synchrotron radiation facility with the vacuum system having small aperture and with the inner surface of almost all the vacuum chambers along its circumference coated with non-evaporable getter (NEG) thin film. This concept implies challenges during the whole project from design into operation.

The fast conditioning of the vacuum system and over five years of reliable accelerator operation have demonstrated that the chosen design proved to be good and does not impose limits on the operation. A summary of the vacuum system design, production, installation and performance is presented.

INTRODUCTION

The MAX IV facility in Lund-Sweden is composed of two storage rings with electron energies of 1.5 GeV and 3 GeV. A linear accelerator (LINAC) serves as the full energy injector to the two storage rings as well as a driver for a short pulse facility [1]. The MAX IV 3 GeV ring started delivering light to the users in April 2017.

3 GEV STORAGE RING

The 3 GeV storage ring is the world's first multibend achromat, ultra-low emittance light source. To achieve the low horizontal emittance, a 7 bend achromat lattice was chosen. The storage ring has a 20-fold symmetry and is 528 m in circumference [2].

Each achromat contains seven magnet blocks of two types: five unit cells (U) (with 3° bending magnets) and two matching cells (M) (with 1.5° bending magnets). Each achromat contains two short straight sections (S1 and S2). In addition 19 long straight sections (L) of 4.6 m length are used for the insertion devices (ID) and one long straight section is used as an injection straight. Figure 1 shows one standard 3 GeV ring achromat, including magnet blocks and the vacuum chambers of one achromat.

3 GEV STORAGE RING VACUUM SYSTEM DESIGN AND MANUFACTURING

The vacuum system of the 3 GeV ring is based on chambers which are made of copper and the chamber body is used as distributed absorbers. The inner surface of the vacuum chambers is NEG coated. Four ion pumps per achromat are installed in areas with high outgassing and provide pumping for noble gases (see Fig. 1).

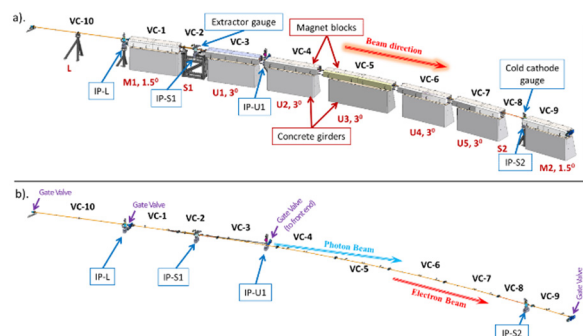


Figure 1: One standard 3 GeV storage ring achromat, a), with the magnet blocks and girders b), the vacuum chambers without the magnet blocks [3].

Vacuum Chamber Design

The vacuum chambers are made of oxygen-free silver-bearing (Ag 0.085%) copper (OFS-C10700). The internal diameter of the vacuum chambers inside the magnet blocks is 22 mm and the chambers have 1 mm wall thickness. The vast majority of the chambers have electron welded water cooling channels on one side.

Ten beam-position monitors (BPMs) per achromat are installed and mounted directly to the magnet blocks. Bellows with internal RF fingers are located at the extremities of the vacuum chambers, the main purpose of the bellows is to shield the BPM block from any deformation occurring in the vacuum chambers due to heating up from the synchrotron radiation.

Several design challenges were faced, some of which are listed below:

- Effectively extract the photon beam to the front end.
- Avoid interferences with the magnets.
- Provide cooling for the chambers in places with limited access and space.
- Guarantee the mechanical and thermal stability of the BPMs while vacuum chambers are allowed to expand.
- Provide a design that will allow successful implementation of NEG coating on the chamber's inner surface.
- Provide a design that allows easy installation.
- Keep standardization.

To assure the mechanical stability of the BPMs, the bellows' spacers were made from epoxy glass G10, with low thermal conductivity and high radiation resistance (see Fig. 2). The BPM blocks are shadowed by small absorbers at the end of each chamber body, just before the flange.

Finite element analysis (FEA) was performed during the design stage, to study several mechanical and thermal issues related to the vacuum chamber design, such as the deformation, stress and strain of the vacuum chambers, the deformation of the BPM during operation, the design of the

[†] eshraq.al-dmour@maxiv.lu.se

RF fingers and the insertion device power deposited on the vacuum chambers.

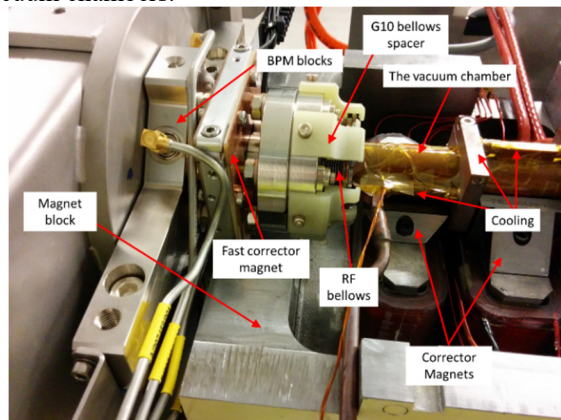


Figure 2: Location of BPM block and bellows.

An example of FEA results performed for the estimation of stress on the RF fingers is shown in Table 1. Such analysis was performed to optimize the shape of the RF fingers, the number of the RF fingers and effect of pre-stressing during assembly. The aim is to keep the stress and strain within the design criteria of the copper-beryllium (CuBe) RF fingers.

Table 1: Stress results for various RF fingers configuration and pre/stressing forces for MAX IV bellows.

Spring configuration	Pre-stress displacement [mm]	Pre-stress force [N/finger]	Stress [MPa]
30 spring finger	0.1	0.8-1	252
flat	0.25	2.0-2.7	630
	0.4	3.9-4.3	1000
30 spring finger	0.1	1.1-1.6	290
curved	0.25	2.7-4.0	730
	0.4	4.4-6.4	1170

The Vacuum Chambers Manufacturing

All the copper extruded tubes used for the production of the vacuum chambers were subjected to surface treatment at CERN [4]. Following this process, the tubes were sent to the manufacturer of the vacuum chambers.

Various manufacturing processes were needed for the production of the vacuum chambers:

- Machining of the chamber parts: flanges, bellows, bellows sleeves, ribs, BPM blocks, cooling tubes ...etc.
- Vacuum brazing of stainless steel flanges to transition copper sleeves of the bellows, brazing of the stainless steel ribs to copper transition...etc.
- TIG welding: flanges to the chamber body, ribs assembly to the chamber body...etc.
- Electron beam welding of the cooling tubes to the chamber body.
- Bending of chambers body to the correct radius of curvature.
- Vacuum cleaning.
- Testing: dimensional, vacuum, cooling...etc.

The main challenges during the production process were:

- Assure that the production processes proposed will not affect the NEG coating or its performance.
- Changes in the production that may cause interferences with other systems, e.g. magnets.
- Changes in other accelerator systems that may affect the vacuum system design and production.

NEG Coating

A collaboration between CERN and MAX IV Laboratory has been set up to address and validate challenges in coating long, small aperture, bent vacuum chambers manufactured with various methods [4-6].

The results of the R&D provided input for the series production of the chamber coating, with around 70% of the chambers coated at the manufacturer and the remaining coated at CERN and the ESRF.

THE VACUUM SYSTEM INSTALLATION AND OPERATION

Installation

From the very early stages of the design, it has been decided not to perform in-situ bakeout for the vacuum chambers, the decision was made due to the compactness of the lattice (small gap between the chambers and the magnets and very small space between the magnets for accommodating bellows) [6].

Prior to the start of the installation inside the 3 GeV tunnel, a mock-up was done to check the installation procedure and possible interferences

The installation of the vacuum chambers took place on the assembly tables which were placed over the open magnet blocks, this allowed accurate positioning of the BPM blocks relative to their final position in the achromat. The oven used for the bakeout has been placed over the concrete blocks.

The general installation procedure followed as described in [3].

The installation stage went smoothly, with minor issues being faced: rejection of few chambers due to peel off of the coating or partially uncoated area, damage of a chamber during the manipulation of an achromat and accidental venting of one full achromat after installation.

Operation

The vacuum conditioning is progressing well, this is evident by both the average pressure reduction and by the increase of the total beam lifetime as the accumulated beam dose has increased. Studies performed also indicated that the NEG coating performance after five years of operation is good, with no indication of saturation or peel off [3].

The average base pressure (without beam) before the start of commissioning with electron beam was $2 \cdot 10^{-10}$ mbar. When the first beam was stored, the pressure increased to the high 10^{-9} mbar range.

The average pressure rise normalized to beam current dP_{av}/I [mbar/mA] as a function of the accumulated beam

Content from this work may be used under the terms of the CC BY 3.0 licence (© 2021). Any distribution of this work must maintain attribution to the author(s), title of the work, publisher, and DOI

dose [Ah] is presented in Fig. 3. The slope of the conditioning curve is comparable to those of other similar machines, and slightly faster.

Figure 4 presents the increase of the normalized total beam lifetime $I\tau$ [A·h] versus accumulated beam dose [A·h]. The increase in the $I\tau$ product is an indication of the vacuum conditioning.

As of July 2021, the storage ring had an accumulated beam dose of 4620 Ah, and the maximum stored beam current was 500 mA. Standard delivery to beamlines is at 300 mA with top-up using multipole injection kicker (MIK) every 10 minutes.

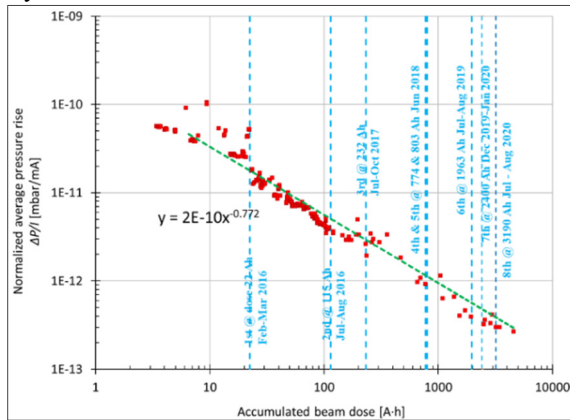


Figure 3: 3 GeV ring: normalized average pressure rise $\Delta P_{av}/I$ [mbar/mA] vs. beam dose [Ah].

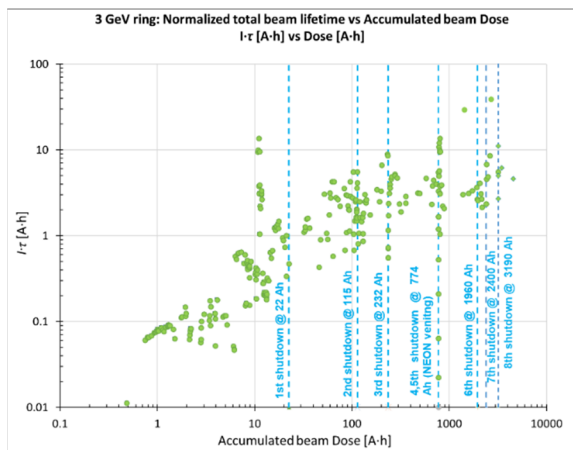


Figure 4: 3 GeV ring: normalized beam lifetime $I\tau$ [A·h] vs. beam dose [Ah] [3].

Operational Issues

Since the start of operation, the vacuum related failures were small. In 2020, there were seven vacuum alarms resulting in beam dumps, contributing 2.7 % of the total machine downtime. The main contributor to downtimes due to vacuum is alarms triggered by pressure spikes from ion pumps or vacuum gauges when a measured pressure reaches the interlock level and results in a beam dump.

With the help of around 30 thermocouples installed on the chamber of each achromat, it has been possible to identify few hot spots, where the readings from thermocouples did not correspond to the simulations done during the design stage. Investigation using FEA was done to identify the

causes and for trouble shooting. The causes of such problems are summarized below:

- Positioning of the vacuum chambers due to geometrical non-conformity, or deformation.
- Chamber non-conformities: crotch absorbers did not shield as per design, the straightness of the chambers and some tolerances did not meet the technical specifications defined on the drawings.
- Deformed chambers during installation: an example was that a thermocouple placed in the vicinity of the photon beam extraction was mispositioned and glued with an excessive amount of glue, when the magnet in that location was closed, it pressed the chamber through the glued thermocouple and caused deformation of the chamber.

As the production of new chambers would take a while, the hot spot issue was investigated, to verify what the damaged vacuum chamber can structurally withstand by limiting the beam current and the minimum gap of the insertion device. Due to this, FEA was performed, with the goal to match the temperature readings with the simulations results, and accordingly identify the allowed machine operational conditions (beam current, beam bumps minimum allowed insertion device gap).

Figure 5 shows the workflow being used for this analysis. The results from the analysis allowed MAX IV to decide on the allowed operational conditions until a new chamber being manufactured and installed.

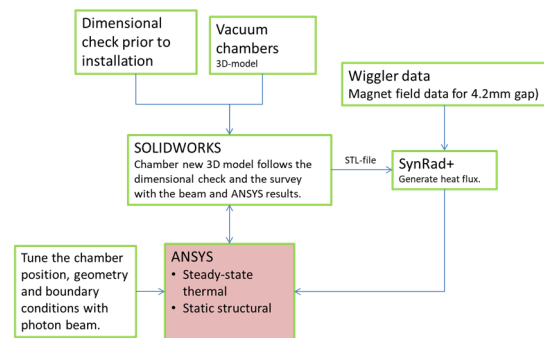


Figure 5: Workflow used to investigate hot spots and validate machine operational conditions.

CONCLUSION

During all the stages of the project, engineering studies, prototyping, mock up and FEA were crucial in validating solutions, investigation and troubleshooting, and provided the needed answers which were essential for the success of the project.

The use of the NEG coating on an unprecedented scale at MAX IV 3 GeV storage ring was a significant challenge. The goal of a simple and reliable ultra-high vacuum system was achieved thanks to careful design, NEG coating validation, appropriate production, installation, operation and precisely planned interventions optimized for the NEG coating. Furthermore, five years of operation ensures that the chosen design is a reliable solution for vacuum systems of new fourth generation, storage ring based light sources.

REFERENCES

- [1] P. F. Tavares *et al.*, “The MAX IV storage ring project”, *J. Synchrotron Radiat.*, vol. 21, pp. 862-877, Sep. 2014. doi.org/10.1107/S1600577514011503
- [2] M. Eriksson *et al.*, “The MAX IV facility”, *J. Phys. Conf. Ser.*, vol. 425, p. 072008, 2013. doi.org/10.1088/1742-6596/425/7/072008
- [3] M. Grabski and E. Al-Dmour, “Commissioning and operation status of the MAX IV 3 GeV storage ring vacuum system”, *J. Synchrotron Radiat.*, vol. 28, pp. 718-731, May 2021. doi.org/10.1107/S1600577521002599
- [4] M. Grabski *et al.*, “NEG thin film coating development for the MAX IV vacuum system”, in *Proc. 4th Int. Particle Accelerator Conf. (IPAC'13)*, Shanghai, China, May 2013, pp. 3385-3387. <https://accelconf.web.cern.ch/ipac2013/papers/thpfi044.pdf>
- [5] P. Costa Pinto *et al.*, “Development and production of non evaporable getter coatings for the vacuum chambers of the 3GeV storage ring of MAX IV”, in *Proc. 6th Int. Particle Accelerator Conf. (IPAC'15)*, Richmond, VA, USA, May 2015, pp. 3145-3147. <https://doi.org/10.18429/JACoW-IPAC2015-WEPHA019>
- [6] E. Al-Dmour *et al.*, “The vacuum system of MAX IV storage rings: installation and conditioning”, in *Proc. 8th Int. Particle Accelerator Conf. (IPAC'17)*, Copenhagen, Denmark, May 2017, pp. 3468-3470. <https://doi.org/10.18429/JACoW-IPAC2017-WEPVA090>

ALBA BL20 NEW MONOCHROMATOR DESIGN

A. Crisol*, F. Bisti, C. Colldelram, M. Llonch, B. Molas, R. Monge, J. Nicolàs, L. Nikitina,
 M. Quispe, L. Ribó, M. Tallarida, ALBA Synchrotron Light Source, Cerdanyola del Vallès, Spain

Abstract

LOREA Beamline (BL20) at ALBA Synchrotron is a new soft X-Ray Beamline dedicated to investigate electronic structure of solids by means ARPES technique. Optical design has been developed in-house so as most of beamline core opto-mechanics like monochromator. The design made for LOREA is based on a Hettrick-Underwood grating type that operates without entrance slit. Experience cumulated over years allowed to face the challenge of designing and building UHV Monochromator. The large energy range of LOREA (10-1000 eV) requires a device with 3 mirrors and 4 gratings with variable line spacing to reduce aberrations. Monochromator most important part, gratings system, has been carefully designed to be isolated from external disturbances as cooling water, and at the same time having high performances. Deep analytical calculations and FEA simulations have been carried out, as well as testing prototypes. The most innovative part of Monochromator is gratings cooling with no vacuum guards or double piping that are well-known source of troubles. Heat load is removed by cooper straps in contact with a temperature controller device connected to fixed water lines. In addition, motion mechanics and services (cabling, cooling) are independent systems. Designs involved give high stability (resonance modes over 60 Hz) and angular resolution below 0,1 μ Rad over 11 deg range. On mirrors side, it has been used gonio mechanics from MIRAS [1] plus an eutectic InGa interface between cooling and optics to decouple them. Grating and mirror holders are fully removable from main mechanics to be able to assembled at lab measuring to achieve the best fit. Instrument has been already assembled and motions characterization or stability measurements are giving expected results matching with specifications.

GENERAL DESCRIPTION

LOREA is a 10-1000 eV soft X-Ray beamline to study the electronic structure of solids by Angle Resolved Photo-Emission Spectroscopy (ARPES). Core level photoemission, resonant photoemission and X-Ray absorption spectroscopies are accessible in the entire energy range.

The whole design of the monochromator, which includes a novel cooling design of the gratings, has been fully developed at ALBA. The BL20 Monochromator is based on a Hettrick-Underwood geometry with 3 spherical mirrors (SM) and 4 plane varied line-spaced (VLS) gratings to cover the entire energy range of LOREA.

Optics and mechanics work at ultra-high vacuum (UHV) regime. It is considered a big circular vacuum chamber for gratings plus one of the mirrors and two additional

chambers for remaining two mirrors. An extra chamber contains part of the gratings pitch mechanism, Fig. 1.



Figure 1: External view of BL20 Monochromator.

GRATINGS MECHANISM

The gratings mechanics, which can locate up to five gratings, consists on a frame that can be moved transversally to the beam to select the suitable grating. This frame is mounted on an oscillating second frame that produces gratings pitch and it is commanded by a sine arm of 1 m long.

The entire mechanism is placed in vacuum, except the actuator of the sine arm. Two welded bellows, one of them connected to the support and thus standing all the force, compensate the vacuum force on the actuator. The vertical actuator, guided by cross roller linear guides consist on a preloaded satellite roller screw with roller recycling spindle that provides high stiffness and small pitch. Between the sine arm that describes an angular trajectory and the actuator that is lineal, there is a connecting rod with two doubled-ended flexural pivot bearings to reduce as much as possible rolling elements. Figure 2 shows full system.

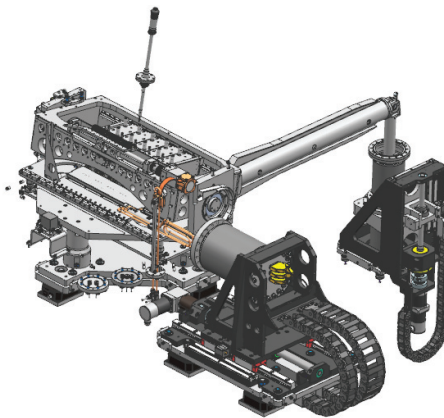


Figure 2: Gratings system design.

Regarding transversal motion, an UHV motor, vacuum adapted guides and spindle are installed, mounted directly on the pitch frame. As grating cooling lines are not linked

* acrisol@cells.es

directly to the optics, there is an extra actuator called services motion. This motion is in charge to move cooling fixed water circuit and the main cabling installed. Services motion is placed out of vacuum and has preload ball recirculating spindle and guides. It moves together with UHV grating exchange motion as a pseudo-motor. For the pitch motion, there are two angular absolute encoders to remove the residual eccentricity of mechanics.

Figure 3 shows the different motions that are involved at gratings mechanics. Grating holders are in the middle in grey color. Red colored parts are the pitch frame plus sine arm. In green color, the services motion fully decoupled, and in blue, the parts of pitch frame support.

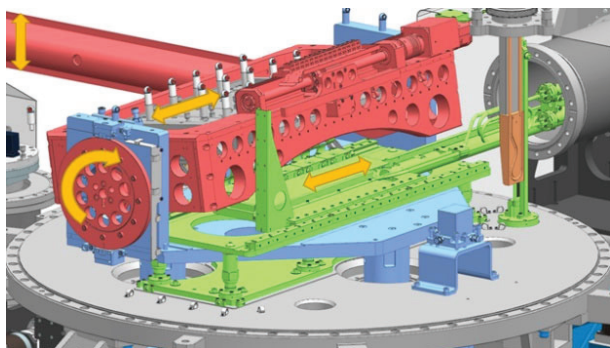


Figure 3: Motions involved at grating system.

The entire system rests on a big natural granite that is the support for all mechanics (seen at Fig. 1).

GRATINGS HOLDER

Each grating is mounted on an independent holder that can be disassembled from mechanics to be adjusted at lab (Fig. 4). It consists in two base plates. One is fixed to be connected on the frame. And the second, it is adjustable where the grating is clamped. There are three micrometer screws for the fine adjustment. Pitch and roll angles can be adjusted during operation through vacuum screwdriver. Also fixed to mobile base with the grating, there are three fiducial marks always accessible to have a reference of the mirror. The holder also supports two symmetric OFH cooper cooling pads. These pads, decoupled from the cooling pipes, also hold the protection chin guard.

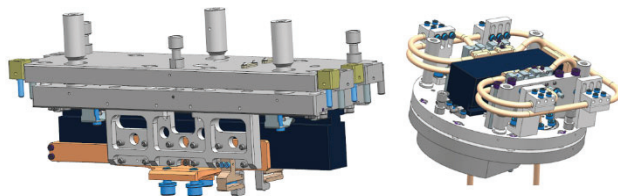


Figure 4: Gratings holder, left. Mirrors holder, right.

GRATINGS COOLING

In this design, doubled vacuum piping has been avoided. Cooling line is a single cooper pipe without any intermediate joint fixed at services actuator. Between pads placed at optics and cooling lines, flexible OHF Copper multi foil straps are used. Figure 5 shows final assembly of straps.

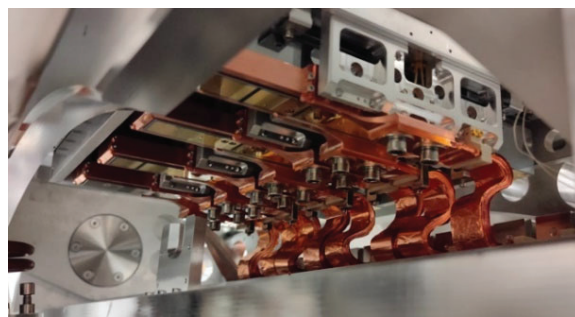


Figure 5: Cooling final design. Straps working “S” shape.

In order to avoid the rise of equilibrium temperature at optics caused by the distance between the heat source and the cooling pipes, a Peltier module is placed between water pipes and straps [2]. The Peltier module, applying an electrical current produces a ΔT between faces. The objective is to maintain the hot side of Peltier at 23 deg and adjust the temperature of the cold side in order to keep optics at a constant temperature also of 23 deg.

To prove this concept, a prototype was produced. It consisted on a silicon substrate including copper pads, straps and Peltier modules with cooling water lines, all in vacuum. A heater simulated the heat load and thermocouples were used as temperature sensors. One of them closed the control loop of Peltier current. Tests have been performed increasing the heat load at the silicon to see the thermal response of the system. The 400 mA corresponds to 4 W, maximum power expected. Figure 6 shows tests results.

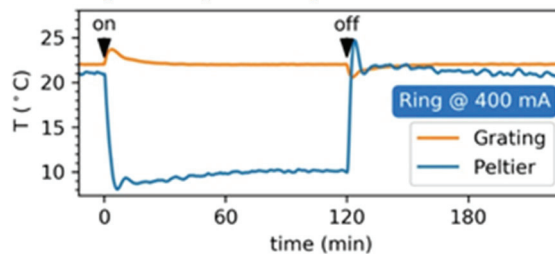


Figure 6: Gratings cooling prototype results.

Orange line corresponds to silicon temperature and blue line, the cold side of the Peltier. At ON point, heater starts to give power increasing temperature. Also, the control starts to put current to the Peltier drooping the temperature of the straps. The dynamic response is quite fast, the stabilization time is around 9 minutes with a ΔT of 1,7 deg. After set point is reached (23 deg), the temperature is maintained very stable via modulating the Peltier current. Once the load is removed, OFF point, the inertia of the system is continuing cooling down the mirror. Then, the polarity of Peltier is inverted acting as a heater to recover temperature.

The prototype validated the concept of Peltier modules and flexible cooper straps to allow the relative motion and also decouple from vibrations due to water-cooling flow.

MIRRORS MECHANISM

Mirror with holder are placed on a column mounted rigidly to a blank flange connected on a frame with curved linear guides to allow pitch motion. The center of these guides is pointing at the central axis of the mirror surface.

Externally there is an edge welded bellow to allow motion. This scheme was used also on MIRAS at ALBA [1].

The pitch stage is mounted on custom linear stages. Two verticals for SM173 and SM176, to put them at beam height or remove it. And one horizontal, transversal to the beam for SM162, that has two optical stripes. All moving elements, spindles and guides, have preload recirculated balls. Linear stages are mounted on small granites. Every mirror is a stand-alone system and can be aligned independently. Mirrors motions are shown at Fig. 7.

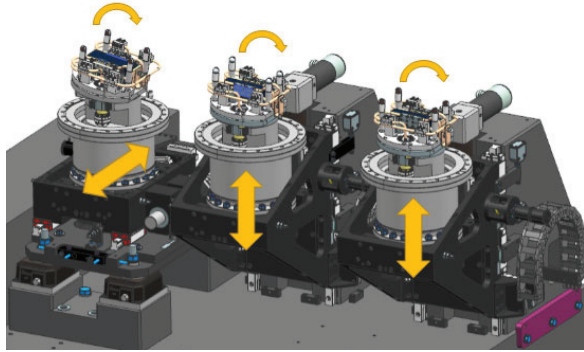


Figure 7: Mirrors motions. SM162, SM173 and SM176.

After that, the tree mirror systems are placed on the main granite support. SM162 mirror is placed at the same vacuum chamber that gratings and for SM173 and SM176 there are independent vacuum chambers.

MIRRORS HOLDER

As gratings, each mirror is mounted on independent holders that can be disassembled from motion actuators (Fig. 4). They consist on two base plates. One is fixed and connected at the main column, and the second, adjustable via three micrometer screws, and is where the mirror is clamped. Also fixed with the mirror, there are the fiducial marks. The holder also supports symmetric cooper cooling pads with fixed cooling circuit. The protection chin guard is also fixed at holder.

MIRRORS COOLING

The cooling water circuit is a continuous rigid cooper pipe that goes inside vacuum and it is fixed at internal mirror mechanics. The flexible lines out of vacuum absorb all the bending motion. The cooling circuit has two brazed cooper pads. There is an adjustable 0.1mm gap that is filled by a Eutectic InGa. Tests have been done to ensure a good behavior of the InGa, even during bake outs (80deg).

The solution, with no direct contact between the cooling pads and mirrors, reduces the deformations and stresses that might be introduced to the mirror when clamping. The assembly process is the following, half of the material is applied at the mirror on the surface contact and the other half is applied at copper pads. Notice that cooper pads must be nickel plated because eutectic InGa is very aggressive to cooper. After that, pads and optics must be mounted at final place controlling the gap between them. Once the gap is achieved, the cooling pad is fixed.

MECHANICS METROLOGY

Gratings and mirrors systems metrology have been done by Renishaw ML10 interferometer and autocollimator (Tables 1 and 2).

Table 1: Gratings Mechanism Measured Performances

Parameter	Pitch	Exchange
Total range	± 5.5 deg	± 150 mm
Resolution	0.085 μ rad/ 2 half steps	Not measured
Repeatability	0.77 μ rad	23.6 μ rad
1 st Resonance mode	56 Hz	

Table 2: Mirrors Mechanism Measured Performances

Parameter	Pitch (x3)	Z (x2), X
Total range	± 1 deg	+40 mm/ ± 10 mm
Resolution	0.232 μ rad/ 2 half steps	0.998 μ m/ half step
Repeatability	1.39 μ rad	0.18 μ m
1 st Resonance mode	74 Hz	

CONCLUSION

A high-performance soft x-ray monochromator has been designed and built at ALBA. Water circuit is mechanically decoupled from grating pitch mechanism and Peltier cooling allows for high cooling efficiency and active stabilization of gratings temperature. Regarding mirror system, it is a high stability system. Thermal contact between cooling and mirror is enhanced via a wet interface witch also minimizes mechanical deformations of the mirror. Finally, excellent results are confirmed by metrology and first commissioning results

ACKNOWLEDGEMENTS

The authors wish to acknowledge all those most involved in the project: Salvador Ferrer, Joan Casas, Nahikari Gonzalez, Gabriel Peña, Jon Ladrera, José Ferrer, Jordi Navarro, Karim Maimouni, Paco Trujillo, Raúl Lorenzo, Oscar Borrego, David Calderón, Lluís Ginés, Núria Martí, Igors Sics, Jordi Prat, Jose Avila, Bern Saló, Cristian Pérez, Sergio Astorga, Xavier Fariña, Fulvio Becherri, Jorge Villanueva, María José García and Arnaud Devienne.

This project is co-funded by the European Regional Development Fund (ERDF) within the Framework of the ERDF Operative Programme of Catalonia 2014-2020.

REFERENCES

- [1] L. Ribó *et al.*, “Mechanical Design of MIRAS, Infrared Microspectroscopy Beam Line at ALBA Synchrotron”, in *Proc. MEDSI'16*, Barcelona, Spain, Sep. 2016, pp. 403-408. doi:10.18429/JACoW-MEDSI2016-FRAA03
- [2] A. Crisol *et al.*, “Dispositivo de refrigeración para elementos ópticos en entornos de ultra alto vacío”, Oficina española de patentes y marcas U202131465, Jul. 15, 2021.

BENDABLE KB TYPE FOCUSING MIRRORS DESIGNED FOR TPS IR BEAMLINE

T.C. Tseng[†], H.S. Fung, H.C. Ho, K.H. Hsu, C.S. Huang, D.G. Huang, C.K. Kuan, W.Y. Lai,
 C.J. Lin, S.Y. Perng, H.S. Wang, National Synchrotron Radiation Research Center, Hsinchu, Taiwan

Abstract

A new IR beamline has been scheduled at TPS beam-line construction Phase III. The new beamline optical design is following the structure of the existed TLS IR beamline. However, the focusing mirrors has to be re-deign according to different situation. These KB type mirrors (HFM and VFM) are same thickness flat stainless plates assembled with bending arms and bended with single motor each to fit quintic polynomial surface profiles for focusing and also modifying arc source effect of bending section. For a same thickness plate in addition with the bending arms effect to form a desired polynomial surface profile, it demands specific width distribution. With the drawing method and FEM iteration simulation, the optimized surface polynomial equation and width distribution design of the mirror plates were defined. The detailed design sequences will be described in this paper.

INTRODUCTION

There is an IR microscopy beamline located at 14A branch in TLS NSRRC [1, 2]. However, the TLS is scheduled to be shut down after TPS phase III due to the budget consideration. A new IR beamline is therefore scheduled at phase III construction plane. With different conditions from TLS, The TPS IR beamline has to be re-design. The TPS IR beamline adopts the similar design as TLS by using K-B type focusing mirrors in the pre-focusing period. Two Stainless flat mirror plates are to be bended to the desired surface profile. In experience, a 5th order polynomial surface profile is enough and also for the manufacturing consideration [3].

With the frontend space consideration, HFM is located 2350mm from the light source point and 4150mm from the focus point. VFM is located 3900mm from the source point and 2600mm from the focus point respectively as in Fig. 1. The beam divergence angles of horizontal and vertical are 50mrad and 25mrad from the source point, respectively. The light-reflecting areas of HFM and VFM are about 166mm x 66mm (maximum) and 77mmx138mm respectively.

For an ideal point light source, by using an elliptical mirror, the light from one focus will be reflected and concentrated in another focus. This phenomenon is well adopted in VFM because it can be regard as from a point source without considering the electron beam size.

For HFM, the light source is an arc section from bending magnet, the light will not concentrate in another focus as in the Fig. 2 drawing and the profile should be modified.

In TLS HFM design, a fourth order RungeKutta numerical method was used to find out the coefficients of the

modified polynomial equation. This method is somewhat complicated to implement. A drawing method was adopted any try to easily find out the profile polynomial.

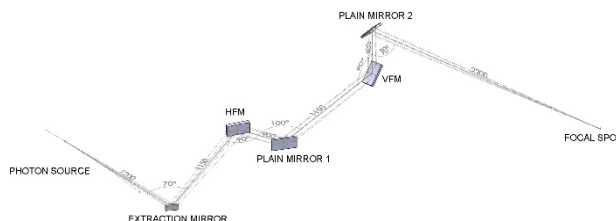


Figure 1: TPS IR beamline pre-focusing period mirror location scheme.

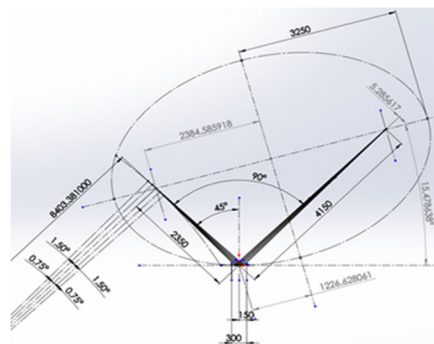


Figure 2: Drawing of light line from arc light source reflecting span on the focus point.

IDEAL KB TYPE MIRROR SURFACE PROFILE EQUATIONS DERIVED WITH DRAWING METHOD

Let the required 5th order profile polynomials equation is (HFM & VFM both):

$$y(x) = c_2x^2 + c_3x^3 + c_4x^4 + c_5x^5 \quad (1)$$

For HFM, at first, 5 ellipses were setup according to the arc divergence angle. The crossed sections were jointed to form a new profile and fitting to get a new polynomial as in Fig. 3.

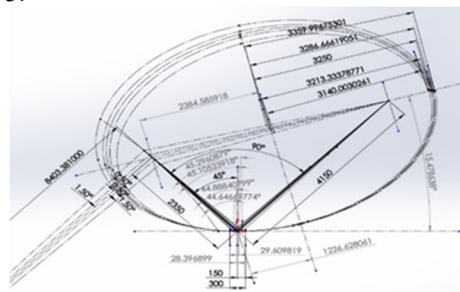


Figure 3: 5 ellipses setup according to the arc divergence angle.

[†] email address: tctsen@nsrrc.org.tw

The coefficients of the fitting polynomial are listed in Table 1. With this polynomial, the focusing area as in the Fig. 2 can be replot and focusing size is reduced to 0.5mm. It's better but still not good enough.

Fortunately, from the polynomial equation, it can be observed with magnifying the focusing area on the drawing. Coefficient of the 2nd order term control the 4 lines concentration and coefficient of the 4th order term enlarge the outside 2 lines concentration rate. Coefficient of the 3rd order term control 4 lines inclination and coefficient of the 5th order term enlarge the outside 2 lines inclining rate.

With these conditions, an ideal HFM surface profile polynomial can be obtained. The optimized coefficients are listed in Table 1 and a replot of Fig. 2 shows the focusing area size is only 0.15um.

While the VFM surface profile polynomial can be found from an ideal elliptical section fitting. The coefficients are also listed in Table 1 and a drawing shows focusing area size is 0.52um.

Table 1: The Coefficients of Surface Polynomial

Coef.	5 ellipse section HFM	Optimized HFM	Ellipse VFM
c ₂	1.179797E-04	1.178178E-04	1.133183E-04
c ₃	-3.20187E-08	-3.4673E-08	5.136405E-09
c ₄	2.45467E-11	3.953E-11	3.090696E-12
c ₅	-4.2178E-14	-4.92E-14	3.998784E-16

EQUATIONS DERIVED FOR BENDING FLAT MIRROR TO FIT IDEAL MIRROR SURFACE PROFILES

Although the ideal mirrors surface profile equations were obtained, the design requirement is to use a single force to bend a stainless flat mirror plate and to from the desired shape.

From the flexure equation:

$$\kappa(\text{curvature}) \approx \frac{d^2y}{dx^2} = \frac{M}{EI}$$

$$\Rightarrow M = EI(2c_2 + 6c_3x + 12c_4x^2 + 20c_5x^3) \quad (2)$$

Since the moment distributed of a same thickness plate from a single force is constant, a different width design is required to obtain the desired face shape. In principle, the flat plate with a 3rd order polynomial width distribution can get a surface profile polynomial of 5th order. But because the high order terms are not included in the calculation, to prevent the error accumulation, a 4th order polynomial width distribution can get a better approximation value.

Let the width distribution polynomial equation is:

$$b(x) = b_0 + b_1x + b_2x^2 + b_3x^3 + b_4x^4 \quad (3)$$

The moment of inertia is:

$$I_t(x) = \frac{b_t(x)h_0^3}{12}$$

$$= \frac{I_0}{b_0}(b_0 + b_1x + b_2x^2 + b_3x^3 + b_4x^4) \quad (4)$$

The bending moment is:

$$M = E \frac{I_0}{b_0} (b_0 + b_1x + b_2x^2 + b_3x^3 + b_4x^4)(2c_2 + 6c_3x + 12c_4x^2 + 20c_5x^3)$$

$$= E \frac{I_0}{b_0} [2c_2b_0 + (6c_3b_0 + 2c_2b_1)x + (12c_4b_0 + 6c_3b_1 + 2c_2b_2)x^2 + (20c_5b_0 + 12c_4b_1 + 6c_3b_2 + 2c_2b_3)x^3 + (20c_5b_1 + 12c_4b_2 + 6c_3b_3 + 2c_2b_4)x^4 + \dots] \quad (5)$$

The bending moment is constant, let the coefficient of the variable terms to zero and get the coefficients of width polynomial as following:

$$b_1 = -3c_{32}b_0(c_{32} = c_3/c_2)$$

$$b_2 = -3c_{32}b_1 - 6c_{42}b_0(c_{42} = c_4/c_2)$$

$$b_3 = -3c_{32}b_2 - 6c_{42}b_1 - 10c_{52}b_0(c_{52} = c_5/c_2)$$

$$b_4 = -3c_{32}b_3 - 6c_{42}b_2 - 10c_{52}b_1 \quad (6)$$

However, the above calculation is the ideal situation of a single flat mirror plate bended with equal moment. The real design of the focusing mirror needs to be assembled with bending arms to apply the torque, the actual inertial moment is complex and difficult for theoretical analysis.

A flexible way is to make the moment of inertia of the mirror structure same as a single plate, the mechanism of the bending arm is another pseudo bending moment. With the same applied force, the pseudo moment distribution will be the same, so the desired surface curve profile can be approached by the plate width modification iteration without to know the real pseudo moment distribution.

The mirror width curve parameters calculated from the above initial calculations can be used to establish a basic model for finite element analysis by using Solidworks and COSMOS software.

The surface center curve from the FEM simulation is polynomial fitting as:

$$y_s(x) = s_2x^2 + s_3x^3 + s_4x^4 + s_5x^5 \quad (7)$$

$$\kappa_s(\text{curvature}) \approx \frac{d^2y_s}{dx^2} = \frac{M_s}{EI_t}$$

$$= 2s_2 + 6s_3x + 12s_4x^2 + 20s_5x^3 \quad (8)$$

$$M_s(x) = E \frac{I_0}{b_0} (b_0 + b_1x + b_2x^2 + b_3x^3 + b_4x^4)$$

$$(2s_2 + 6s_3x + 12s_4x^2 + 20s_5x^3) \quad (9)$$

A single force only affects the 2nd order term, the desired surface polynomial is:

$$y_r(x) = s_2x^2 + c_3x^3 + c_4x^4 + c_5x^5 \quad (10)$$

The correction of other terms of the surface polynomial requires modifying the coefficient of the width curve polynomial so that the inertial moment of the new width curve polynomial becomes:

$$I_n(x) = \frac{b_n(x)h_0^3}{12}$$

$$= \frac{I_0}{b_0}(b_0 + b_{1n}x + b_{2n}x^2 + b_{3n}x^3 + b_{4n}x^4) \quad (11)$$

$$\kappa_r(\text{curvature}) \approx \frac{d^2 y_r}{dx^2} = \frac{M_s}{EI_n} = 2s_2 + 6c_3x + 12c_4x^2 + 20c_5x^3 \quad (12)$$

With the assumption of the same bending moment, then

$$\begin{pmatrix} b_0 + b_1x + b_2x^2 \\ +b_3x^3 + b_4x^4 \end{pmatrix} \begin{pmatrix} 2s_2 + 6s_3x \\ +12s_4x^2 + 20s_5x^3 \end{pmatrix} = \begin{pmatrix} b_0 + b_{1n}x + b_{2n}x^2 \\ +b_{3n}x^3 + b_{4n}x^4 \end{pmatrix} \begin{pmatrix} 2s_2 + 6c_3x \\ +12c_4x^2 + 20c_5x^3 \end{pmatrix} \quad (13)$$

The new coefficients of the width distribution can be obtained from the old ones combined with the data from the FEM simulation. (Skip the high order terms)

$$\begin{aligned} b_{1n} &= b_1 + 3b_0(s_3 - c_3)/s_2 \\ b_{2n} &= b_2 + 3(b_1s_3 - b_{1n}c_3)/s_2 + 6b_0(s_4 - c_4)/s_2 \\ b_{3n} &= b_3 + 3(b_2s_3 - b_{2n}c_3)/s_2 + 6(b_1s_4 - b_{1n}c_4)/s_2 \\ &\quad + 10b_0(s_5 - c_5)/s_2 \\ b_{4n} &= b_4 + 3(b_3s_3 - b_{3n}c_3)/s_2 + 6(b_2s_4 - b_{2n}c_4)/s_2 \\ &\quad + 10(b_1s_5 - b_{1n}c_5)/s_2 \end{aligned} \quad (14)$$

OPTIMIZED WIDTH PROFILE EQUATIONS WITH FEM ANALYSIS ITERATION

At first, a bending HFM model was built with the width coefficients derived from the single mirror plate Eq. (6) without bending arms and applied for FEM simulation as in Fig. 4. The initial polynomial equation applied to the drawing as in Fig. 2 shows a focus size is 5.7mm.

However, the HFM focus size down to 0.32mm with 1 iteration, and after 4 iterations, the focus size down to 0.0138mm and the optimized width distribution polynomial coefficients were obtained from Eq. (14) as shown in Table 2.

With the same procedures, the VFM focus size down to 0.0214mm after 3 iterations and the optimized width distribution polynomial coefficients were also listed in Table 2. The thickness of both mirror is 7mm.

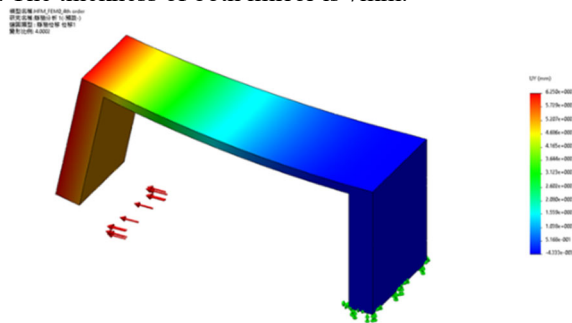


Figure 4: Initial HFM model for FEM simulation.

Table 2: The Coefficients of Width Profile Polynomial

Coef.	Bendable HFM	Bendable VFM
b_0	80	90
b_1	0.061754	-0.00753143
b_2	-6.527695E-04	-5.873345E-04
b_3	8.294557E-7	-1.679582E-6
b_4	4.173849E-9	1.080632E-10

From the Shadow simulation, the focusing point distribution plot of the bending mirrors is quite the same as the ideal profile. The size in horizontal direction is about only 1/5 of the vertical direction shows more better concentration. Compared to TLS IR, the situation is also the same as shown in Fig. 5.

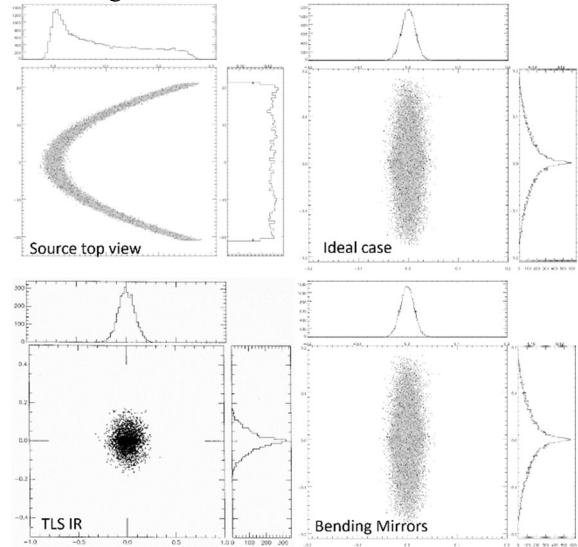


Figure 5: Shadow simulation of the bendable mirror.

ENGINEERING DESIGN

With the width profile equations derived. The engineering design can be carried out. One pair of focusing mirror prototype design was finished as in Fig. 6 and waiting for the budget to be fabricated.

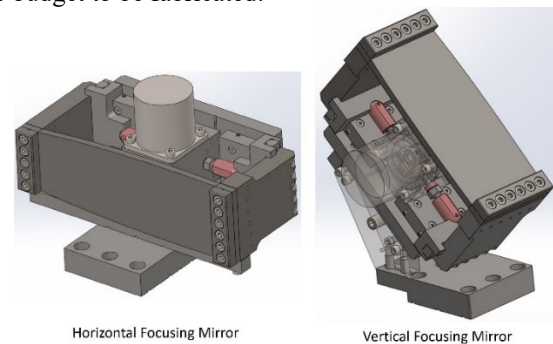


Figure 6: Prototype design of the two focusing mirror.

CONCLUSION

By using the drawing method, a fine way to define a correction polynomial equation for focusing arc source is identified. With the pseudo moment and FEM simulation iteration procedures, the width profile equation of a plane mirror can be found to define a desired mirror surface shape with pure bending moment (one single force). The shadow simulation result shows good condition.

With Exact beam size correction in the vertical direction, The VFM focusing might be further improved if demanded.

The Engineering design is on the way and waiting for the budget to be fabricated since the TPS IR beamline is still not into schedule.

REFERENCES

- [1] 14A1 BM - IR Microscopy - Taiwan Light Source Beamlines, http://tls.nsrcc.org.tw/bd_page.aspx?lang=en&port=14A1&pid=1287
- [2] C.-I. Chen, Y.-C. Lo, and K.-L. Tsang, "Optical Design and Construction of Mid-infrared beamline at SRRRC", NSRRC, Hsinchu City, Taiwan, SRRC/RBM/IM/99-06A, 1999.
- [3] S.-J. Chen, C.K. Kuan, S. Y. Perng, D. J. Wang, H. C. Ho, T. C. Tseng, Y.-C. Lo, C. T. Chen, "New focusing mirror system for synchrotron radiation infrared beamlines", *Opt. Eng.*, vol. 43, no. 12, Dec. 2004, pp. 3077~3082. <https://doi.org/10.1117/1.1813438>

CRYOGENIC SYSTEMS FOR OPTICAL ELEMENTS COOLING AT SIRIUS/LNLS

M. Saveri Silva[†], M. P. Calcanha, G.V. Claudiano, A. F. M. Fontoura, B. A. Francisco, L. M. Kofukuda, F. R. Lena, F. E. P. Meneau, G. B. Z. L. Moreno, J. H. Rezende, G. L. M. P. Rodrigues, L. Sanfelici, H. C. N. Tolentino, L. M. Volpe, LNLS, Campinas, Brazil

Abstract

This work presents the in-house solution for cryogenic cooling of beamline optics subject to low to moderate thermal loads at Sirius at the Brazilian Synchrotron Light Laboratory (LNLS). The main requirements regarding extracted power and coolant consumption are detailed. We also discuss discoveries and improvements deployed during the commissioning of the CATERETÊ and the CARNAÚBA beamlines, such as the prevention of ice formation, stabilization of both thermal load and flow-rate, and auto-filling parameters, among others.

INTRODUCTION

Sirius, the Brazilian 4th-generation light source at the Brazilian Synchrotron Light Laboratory (LNLS), presents high-performance requirements in terms of preserving photon-beam quality, particularly regarding wavefront integrity and position stability. In this context, it is imperative that many silicon optical elements are effectively cooled, so that temperatures and their control-related parameters can be precisely handled to the point in which thermal effects are acceptable concerning figure distortions and drifts at different timescales. Keeping in mind the class of precision equipment, the required performance can only be achieved with robust thermal modelling [1-3]. For this, relevant aspects related to the implementation of liquid nitrogen cooling systems need to be emphasized. Currently, two solutions are present in the first-phase beamlines, according to the component thermal load: (1) a commercial cryocooler for high-heat-load applications (50 – 3000 W), such as the double-crystal monochromators; and (2) an in-house low-cost system for components under moderate loads such as the mirror systems and the four-bounce monochromators (4CM). This work describes the in-house solution, with examples from the CARNAÚBA (CNB) and CATERETÊ (CAT) beamlines.

OPEN LN2 CRYOSTAT SYSTEMS

Figure 1 illustrates the cooling circuit of a 4CM at CNB. Inside the vacuum chamber (a), the crystals are connected through thermal braids [4] to a commercial cryostat (b), which is fed with liquid nitrogen (LN2) by an instrumented cylinder (c). Level and pressure are controlled by standard beamline automation system that automatically feed it from a dedicated transfer line (d) connected to a secondary service unit external to the hutch (e) or to the LN2 line of the building. Gaseous nitrogen leaves the first vessel by an

exhaust line (f) during filling, whereas the gas in the cryostat outlet is released inside the hutch at a significantly lower rate at normal operation. The LN2 flow in the cryostats is adjustable by regulating its flow regulating valve and the pressure of the liquid cylinder.

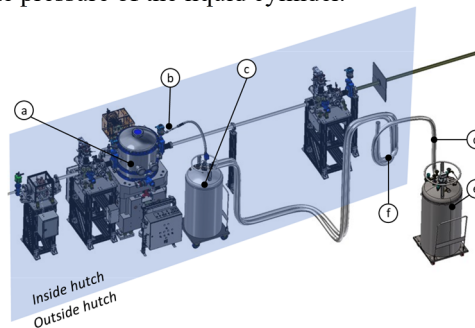


Figure 1: Third optical hutch of the CARNAÚBA beamline, highlighting the liquid nitrogen supply system of the 4CM, which comprises the vacuum chamber (a), the cryostat (b), the primary (c) and secondary (e) LN2 cylinders, the transfer line (d) and the exhaust line (f).

Figure 2 shows the top view of a primary vessel. Besides the standard items, custom stems were added to supply extra handles and solenoid valves for liquid and gas and to monitor pressure and level data.

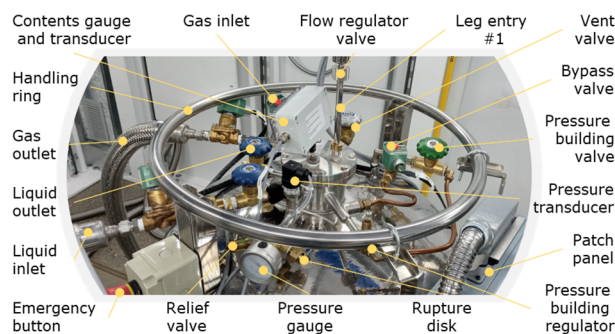


Figure 2: Top of primary LN2 cylinder and description of the connected elements.

The vessel inside the first optical hutch of CNB is connected to two cryostats, which cool the first mirror (M1) and an internal diagnostics (XDU), present in the same vacuum chamber. The same structure appears in its second optical hutch for the chamber enclosing the second mirror (M2) and the secondary source aperture (SSA). For all other optics, only one cryostat is assembled at each vessel.

[†] marlon.saveri@lnls.br

FILLING CONTROL

The PLC (Siemens S7-1512SP-1) was configured to keep the level of the primary LN2 cylinder between minimum and maximum setpoints by actuating the solenoid valves mounted at both ends of the transfer line. For CNB:4CM, for example, the setpoint was chosen as 80-95%, in which the temperature of the optics and the flow rate were considered stable even during filling. Those filling events took in average 18 minutes (2.5 L/min). During the offline tests, the speed for a 0-100% fill achieved 5.5 L/min with a 3 bar pressure gradient between vessels.

Figure 3 shows the history in the EPICS Archiver for the level of the primary and secondary LN2 cylinders of CNB and CAT during fifteen days. In average, the secondary cylinder is filled when its level decreases to 10%. The frequency of the filling events changes depending on the optics, since the theoretical heat load may vary from about 16 W (CAT: M1) to 60 W (CNB: M1+XDU). It can be used to estimate the consumption and, consequently, to calculate the losses of the systems.

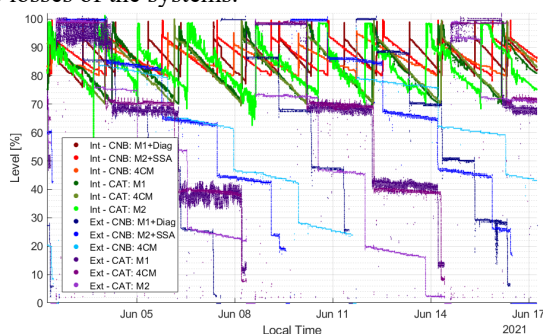


Figure 3: Levels of primary and secondary LN2 cylinders of CARNAÚBA and CATERETÊ beamlines.

Table 1 compares the consumption of the primary and secondary vessels to theoretical values, which are calculated from the estimated total heat load predicted in the thermal models. In addition, it is important to highlight that the cryostat consumes more nitrogen than the theoretical needs to avoid the drying of its internal reservoir in an event of power load increase or temporary liquid flow decrease (filling transfers). This event could lead to a binary gas-liquid flow with the increase of the cold finger temperature due to poor heat transfer or even increase the vibration disturbs, both noticed multiple times during the commissioning.

Table 1: Consumption of the Systems During Jun/2021

Optics	Load [W]	Consumption [L/h]		
		Theor.	Primary	Second.
CNB – M1+XDU	60	1.4	1.6	2.0
CNB – M2+SSA	20	0.5	1.1	1.4
CNB – 4CM	26	0.6	0.7	1.1
CAT – M1	16	0.4	1.55	1.64
CAT – 4CM	50	1.1	1.55	1.60
CAT – M2	20	0.5	1.66	1.71

In the considered time, the efficiency of the system oscillated between 22 and 73%. Furthermore, by comparing the contents of the primary and secondary vessels of CAT optics, it was verified that the losses during the transfer of the LN2 could be reduced to 3%. Investigations are being performed during the beamlines commissioning for optimizing the efficiencies by adjusting parameters such as level and pressure setpoints and opening of the flow regulator valves.

PRESSURE CONTROL

The pressure of the primary vessel is directly associated to the LN2 flow through the cryostat and, consequently to the temperature and dynamic stability of the optical elements. The pressure of the vessel naturally changes because of the outflow, the evaporation of LN2 inside it, and the filling process, which is accompanied by evaporation and the entrance of gas present in the transfer line. Thus, two methods (an active and a passive) were foreseen to keep the pressure of the receiver vessel constant and below the pressure of the provider vessel, which is also controlled.

In the active method, a solenoid valve is opened to vent gaseous nitrogen and decrease the pressure in the primary cylinder, while a second solenoid valve is opened to increase the pressure in the secondary cylinder by allowing a bypass of the vaporizer circuit. For high demanding systems, a third solenoid valve can be used to allow the entrance of gaseous nitrogen from a dedicated line. This solution should eliminate any possibility of condensate formation around the LN2 cylinder, which can occur in the traditional systems (pressure building valve) and would allow for a quick correction against filling events performed with a high gradient between the vessels. However, the on/off method was found to cause pressure variations as high as 0.2 bar in a 40-minute time span at the primary vessel. This variation is detrimental to the optical systems stability as it leads to a change in the LN2 flow, thus causing a change in the heat extraction capacity of the cryostats. For the so-far most sensitive system CNB:M1, considering the constant input power for the referred timespan, it generates a change in temperature as high as 0.42K at the mirror braids, leading to unacceptable thermal drifts. Furthermore, the pressure variation in the circuit was also found to actively move the cryostat, causing disturbances in a shorter timeframe as compared to thermal drifts. This could be solved with a proportional cryogenic gas flow valve for finer pressure control, but higher costs and integration complexity led to the search of a simpler passive solution.

As a simpler passive alternative, the use of the already built-in thermal relief valve was found to largely solve the pressure variation issues. At this operation mode, the solenoids of the PLC pressure control are turned off, thus making the pressure rise by passive evaporation until it hits the nominal relief valve rating of 3.6 bar. At this stage, the referred spring-loaded valve proportionally relieves the gas until the equilibrium is archived between evaporation and gas scape. Despite this method being prone to a pressure hysteresis of tenths of a bar, the long-term drift was found

to be as low as 18,3 mbar during a 12h test. Combined with the heaters PID control, this method led to a temperature variation of 50,2mK and 20,6mK in the M1 cooling braid and silicon substrate, respectively, Fig. 4. In this case, the solenoids are used during the transfer only when the primary vessel pressure is actively lowered back to 2.5 bar to generate the needed differential pressure for the liquid to flow.

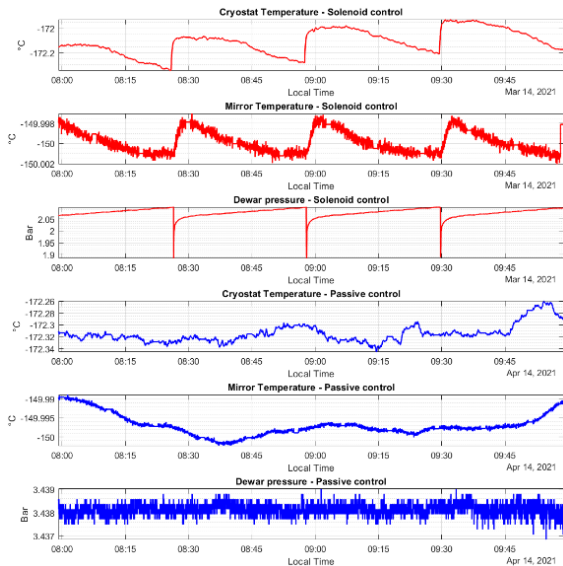


Figure 4: Temperature and vessel pressure when using the active solenoid control or the passive valve at the CNB:M1 systems.

EXHAUSTION

The gas released by the primary liquid cylinder during filling or automatic pressure control is directed out of the hutch through a vacuum-insulated exhaust line. However, the flow discharged by the cryostat is directly released into the hutches, since the flow rate is much lower. Indeed, Fig. 5 demonstrates that the oxygen ratio inside these hutches is comparable to those of the EMA beamline, in which there is no gaseous nitrogen release in the considered period, and even above the levels in experimental hutches of MANACÁ, CAT, and CNB beamlines, where cryojets for sample conditioning are commonly used.

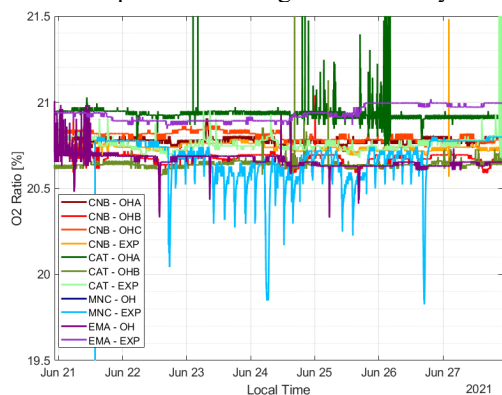


Figure 5: O2 ratio in several optical (OH) and experimental (EXP) hutches of CARNAÚBA, CATERETÊ, MANACÁ and EMA beamlines.

Beamlines and front ends
 Optics

Yet, in addition to occasional ejection of LN2 from the cryostat outlet, the output gas itself is frosty. Consequently, it's necessary to avoid the formation of ice and water around the cryostat outlets. Initially, it was observed that the use of an insulator would just offset the ice formation and that warming the residual gas required a noteworthy amount of energy, with additional safety concerns. Indeed, even when heating only the enclosure, significant power was also necessary, so that a fourth solution was developed. As shown in Fig. 6, it consists of a 3D printed PLA part in which the nitrogen flow is surrounded by a cylindrical channel through which there is a laminar flow of compressed air that act as an insulator.

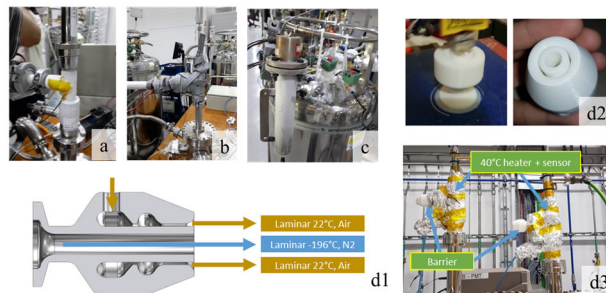


Figure 6: Options against condensate formation: nothing (a), blanket with heaters (b), gas heater (c), and custom part with air barrier (d).

INTERLOCK

The system is considered to have failed when the emergency button is pressed or when the control interface of the primary vessel is disconnected. It is also directly connected to the Equipment Protection System (EPS) such that unwanted events (as vacuum incident or overtemperature) trigger the actuation of valves and shutters as preventive measures.

CONCLUSION

A low-cost solution was developed for the cryogenic cooling of optics under moderate thermal loads at Sirius beamlines through the combination of commercial systems and ad hoc additions. The proposition aimed at solving the challenges associated with nitrogen supply and exhaust and to ensure temperature stability in the optics. Several systems are already operational while refined optimization proceeds. Performance limits could already be observed, and level and pressure controls have been effectively running for several months, endorsed by a robust interlock control.

ACKNOWLEDGEMENT

The authors would like to gratefully acknowledge the funding by the Brazilian Ministry of Science, Technology and Innovation and the contributions of the LNLS team, notably the CARNAUBA, CATERETE and Electronic Infrastructure and Automation (IEA) groups.

REFERENCES

- [1] L. M. Volpe *et al.*, “Thermal Model Validation for the Cryogenic Optical Systems for Sirius/LNLS”, presented at MEDSI 2020, Chicago, USA, July 2021, paper WEPC07, this conference.
- [2] M. Saveri Silva, R. R. Geraldes, A. Gilmour, T. A. M. Ruijl, and R. M. Schneider, “Thermal Management and Crystal Clamping Concepts for the New High-Dynamics DCM for Sirius”, in *Proc. 9th Mechanical Engineering Design of Synchrotron Radiation Equipment and Instrumentation Int. Conf. (MEDSI'16)*, Barcelona, Spain, Sep. 2016, pp. 194-197. doi:10.18429/JACoW-MEDSI2016-TUPE15
- [3] R. R. Geraldes *et al.*, “The Design of Exactly-Constrained X-Ray Mirror Systems for Sirius”, in *Proc. 10th Mechanical Engineering Design of Synchrotron Radiation Equipment and Instrumentation Int. Conf. (MEDSI'18)*, Paris, France, Jun. 2018, pp. 173-178. doi:10.18429/JACoW-MEDSI2018-WEOAMA04
- [4] F. Lena *et al.*, “Copper Braid Heat Conductors for Sirius/LNLS Cryogenic X-Ray Optics”, presented at MEDSI 2020, Chicago, USA, July 2021, paper TUPC14, this conference.

COMMISSIONING AND PROSPECTS OF THE HIGH-DYNAMIC DCMs AT SIRIUS/LNLS

R. R. Geraldes^{†1}, J. L. Brito Neto, R. M. Caliari, G. S. de Albuquerque, M. A. S. Eleotério,
S. A. L. Luiz, M. A. L. Moraes, A. V. Perna, M. Saveri Silva
Brazilian Synchrotron Light Laboratory (LNLS), 13083-970, Campinas, São Paulo, Brazil
¹also at the Eindhoven University of Technology (TUE), 5612AZ Eindhoven, The Netherlands

Abstract

The High-Dynamic Double-Crystal Monochromator (HD-DCM) is an opto-mechatronic system with unique architecture, and deep paradigm changes as compared to traditional beamline monochromators. Aiming at unmatched scanning possibilities and positioning stability in vertical-bounce DCMs, it has been developed since 2015 for hard X-ray beamlines of Sirius Light Source at the Brazilian Synchrotron Light Laboratory (LNLS). Two units are currently operational at the MANACÁ (macromolecular crystallography) and EMA (extreme conditions) undulator beamlines, whereas a model for extended scanning capabilities, the so-called HD-DCM-Lite, is in advanced development stage for forthcoming bending magnet and undulator beamlines. This work presents commissioning data related to the two HD-DCM units, together with the developed operation strategies and the overall control architecture, with emphasis on the 10 nrad RMS (1 Hz to 2.5 kHz) pitch parallelism performance, the calibration procedures and flyscan-related discussions.

INTRODUCTION

The High-Dynamic Double-Crystal Monochromator (HD-DCM) [1] has been developed by the Brazilian Synchrotron (LNLS) for Sirius [2] and the demanding new generation of X-ray beamlines. With a predictive design methodology [3] and original concepts for a DCM that are based on precision mechatronics [4], it has proven to meet the mark of 10 nrad RMS pitch parallelism performance, both in fixed-energy and scanning operation modes, over the broad frequency range from 1 Hz to 2.5 kHz, which is sui generis in vertical-bounce DCMs.

The system has already been described to the community in different aspects: the conceptual design, the mechatronic principles and thermal management solutions were presented in MEDSI 2016 [5–8]; results of in-air validation of the core, together with system identification and control techniques in the prototyping hardware, were shown in ICALEPCS 2017 [9, 10]; the offline performance of the full in-vacuum cryocooled system, including scans solutions were presented in MEDSI 2018 [11]; and the dynamic modelling work, together with updated control design and the FPGA implementation in the final NI CompactRIO (cRIO) hardware were discussed in the ASPE Topical Meeting 2020 [12–14]. Here, commissioning results of the two operational units at MANACÁ and EMA undulator

beamlines at Sirius are presented, together with procedures, strategies, and the related beamline architecture.

COMMISSIONING PROCEDURE

The commissioning procedure that has been developed for the HD-DCM follows the steps presented in Fig. 1 and described below:

1. *Beam through* consists of passing the first monochromatic beam of a given energy to downstream sensors or visualization elements after short scans in the Bragg angle, in the pitch angle of the 2nd crystal of the DCM and/or the undulator phase, which is a quick job if off-line fiducialization and laser-tracker-based alignment procedures at the beamline are properly realized.
2. *Preliminary DCM-undulator tuning* is meant as a coarse mapping between the Bragg angle and undulator phase for different harmonics, which relies on beam simulation and can be done in terms of output flux or image processing.
3. *Preliminary Rocking Curve analysis* is related to optimizing the roll parallelism and scanning the pitch of the 2nd crystal in the DCM for a few energy values of interest. Thus, the quality of the crystalline lattice –which depends on manufacturing, mounting and the cryogenic thermal management – can be verified, while the internal metrology feedback to keep the parallelism according to maximum flux is evaluated.
4. *Preliminary energy calibration* is dedicated to calibrating the Bragg angle encoder homing offset according to one or more absolute energy values provided absorption standards in spectroscopy measurements.
5. *Fine DCM-undulator tuning* is the refinement of the undulator energy-phase calibration with the calibrated Bragg angles over the whole operational energy range.
6. *Fine energy calibration* consists in optionally exploring multiple absorption edges over the full energy range to calibrate occasional repeatable non-linearities in the encoder of the Bragg angle.
7. *Fine parallelism calibration* is an optional flux-based step for repeatable non-linearities in pitch (in the piston-tip-tilt internal metrology of the crystal cage, as described in [5]) as the gap between crystals varies over the full energy range.
8. *Fixed-exit calibration* is the final step in which angular or translational deviations of the monochromatic beam are mapped over the complete energy range by image processing, quadrant sensors or knife-edge measurements, and compensated by the internal degrees-of-freedom in the crystal cage.

[†] renan.geraldes@lnls.br

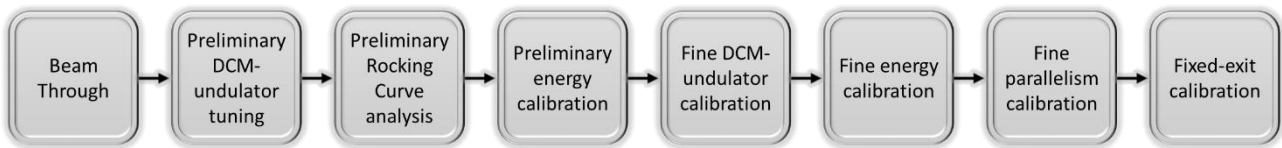


Figure 1: Commissioning procedure developed for the HD-DCM at MANACÁ and EMA undulator beamlines at Sirius.

Considering that ordinary calibration based on look-up tables would be incompatible with flyscan because of smoothness and differentiation issues, together with high-rate constraints, all the relations among quantities, i.e., energy, phase, angles and linear displacements, are defined according to polynomials, which are computed in real time at the FPGA level. Nominal, full-range calibration or short-range optimized polynomial sets can be defined. This process is repeated for both Si(111) and Si(311) crystal sets in the HD-DCM to provide a highly-stable monochromatic beam that can be explored in fixed-energy, step-scan and flyscan operation modes. The following section describes the integration architecture at MANACÁ as a case study.

INTEGRATION ARCHITECTURE

The HD-DCM has been designed not only to achieve position stability at fixed energy, but also to simultaneously enable high-performance spectroscopy in flyscan, which asks for consistent requirements for instrumentation and the control architecture at the beamline level.

Figure 2 depicts the integration diagram for MANACÁ. Information of the electron beam stability in the storage ring (SR) is made available to the beamline from two beam position monitors (BPMs), with synchronization triggers via an event handler hardware (EVE) developed in-house by the GCA group [15]. Regarding the undulator (UND) source, the options are still somewhat limited. Indeed, working in a coupled mode, the HD-DCM can currently only be used as the follower, receiving the quadrature signal that is derived from the undulator encoder. Furthermore, the trajectory generation in the Kyma commissioning undulator cannot be optimized for the best performance in flyscan with the existing firmware in its programmable

logic controller (PLC) either. With the installation of the Delta undulator that has been developed in-house, a more extensive integration will be possible.

In addition to the HD-DCM, two focalizing mirrors (M1 and M2) compose the beamline optics, currently delivering a monochromatic beam of about $10 \times 10 \mu\text{m}^2$ at the sample position. After the M1, there is a component for diagnostics that contains an AXUV36 photodiode (PD) and a CCD-based beam visualization system (BVS) with a resolution of about $10 \mu\text{m}$. The first is used for measurements of the Rocking Curves and for the *flux-based DCM-undulator tuning*. The latter is used for the *beam-through* step and visual inspection of the undulator emission profile when the M1 is removed from the beam path, but also to guide the alignment of the M1. After the M2, two Cividec diamond quadrant photon beam position monitors (XBPMs) are used for alignment, including the *fixed-energy calibration*, and beam stability measurements. A variety of in-vacuum filters are intended basically to control the flux at the sample, but have also been used as absorption standards for *energy calibration*. Finally, at the sample position the most common setup during commissioning consists in a YAG-Ce crystal and a high-resolution CCD-based optical microscope, which is used for the alignment of the mirrors, but also for *fixed-exit calibration* via image processing. Other items at the beamline are omitted in the diagram for clarity.

NI cRIO has been chosen as the standard controller for Sirius beamlines, being used not only to handle digital and analog signals of a variety of devices in rates up to 10 MHz, but also to host entire applications, as the HD-DCM itself, which runs at the control rate of 20 kHz. A special module, known as *time and trigger unit* (TATU), has been developed in-house by the SOL group for the NI-9401 board to work as a synchronization unit in the microsecond range.

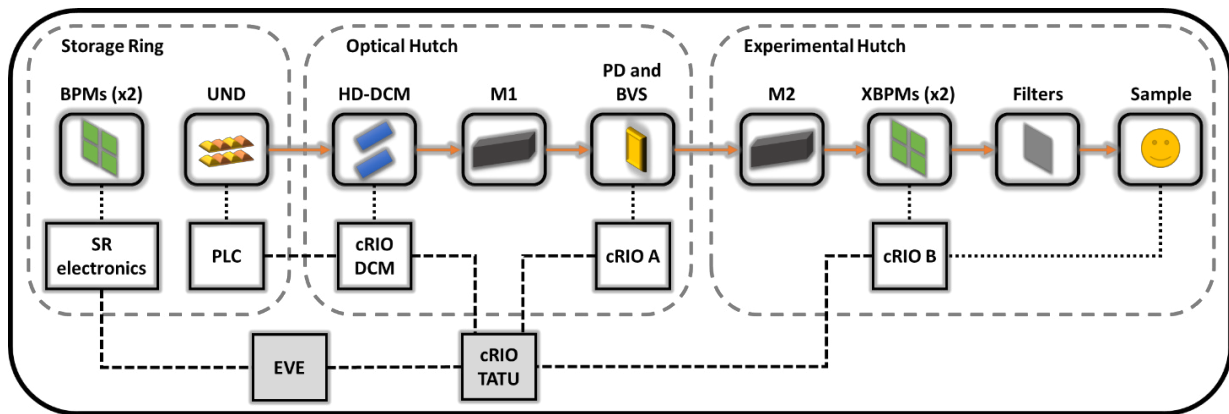


Figure 2: Integration diagram for the HD-DCM at MANACÁ beamline at Sirius. (Details in the text.)

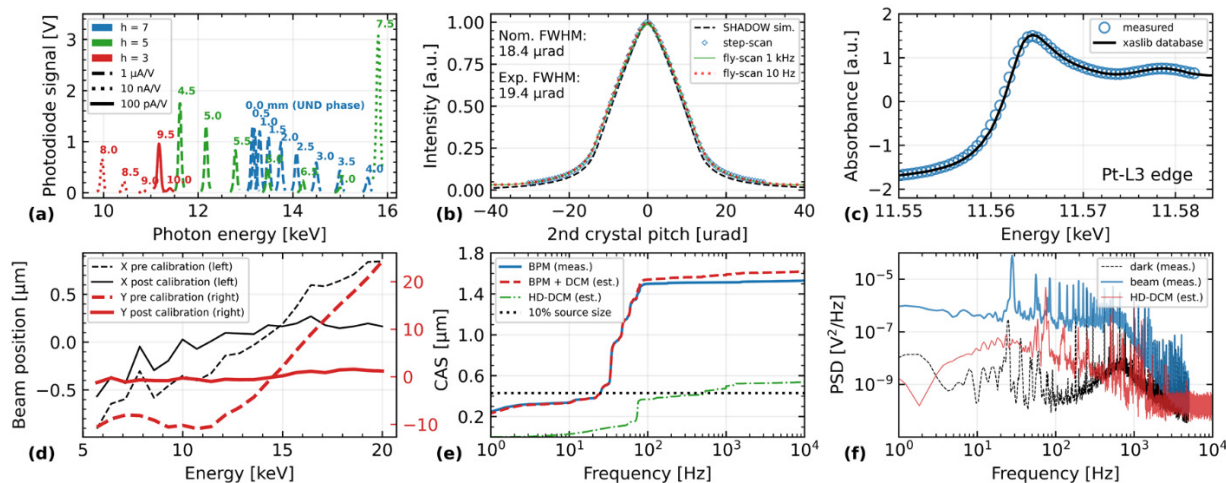


Figure 3: Commissioning results of the HD-DCM at MANACÁ and EMA beamlines at Sirius. (Details in the text.)

Thus, with the instruments relying on fast computing hardware and connected at the hardware level, commissioning and the experiments can be easily taken to the sub-millisecond range. Still at the FPGA level in cRIO, but with settings available to users at the EPICS level, averaging tools have been developed in-house to improve signal-to-noise ratio of digital and analog signals. The HD-DCM control itself is now fully available in EPICS via the Nheengatu solution developed by the SOL group to integrate EPICS with cRIO [16], and a library for the calibration procedures has been developed with Python scripts.

RESULTS

Figure 3 briefly illustrates some of the results obtained in the commissioning work of the HD-DCMs at MANACÁ and EMA beamlines. In (a), the photocurrent is measured (at different amplification gains) as a function of the photon energy for different undulator phases and harmonic tunings as the Bragg angle is scanned, such that the ideal tunings can be found and implemented a polynomial. In (b), measurements of the Rocking Curve for Si(111) at 20 keV are compared with theoretical simulated data, with agreement for the full width at half maximum within 5%. Step-scan data with detection averaging time of 1 s – and a total measurement time of about 5 minutes – is compared with flyscan data with detection averaging times of 1 ms (noisier) and 100 ms (smoother) – and total measurement time of 5 s each –, showing equivalent performance. In (c), the absorption edge for Pt at 11.56 keV is used for energy calibration at EMA. Although this measurement was done in step scan over a few minutes during calibration, up to 1 keV scans can also be realized in a few seconds in flyscan for spectroscopy experiments. In (d), the X and Y fixed-exit calibration via image processing at MANACÁ allowed the 10 μ m beam to have its vertical position dependence with energy reduced from more than 30 μ m to less than 1 μ m over the full energy range available at the beamline, which was at the resolution and stability limits of the experimental setup. Thus, concerning accurate flyscan spectroscopy measurements, the largest possible continuous scan is only limited by the undulator characteristics. In (e),

for stability evaluation, the estimated back-projected pitch stability of the HD-DCM at a given energy is compared via cumulative amplitude spectrum (CAS) with the vertical beam stability of the electron beam, as measured by the BPMs before the fast orbit feedback (FOFB) system is implemented in the SR. The DCM has a negligible impact in the vertical beam stability so far, which is confirmed in measurements with the XPBMs that are dominated by the source stability signature (not shown). Finally, in (f), a preliminary intensity measurement is shown also for stability evaluation. In this case, the 2nd crystal in the HD-DCM was intentionally detuned to the slope of the Rocking Curve for Si(333) at 20 keV, for the maximum flux-to-pitch sensitivity condition at MANACÁ. The power spectrum density (PSD) of the signal of the PD is shown in the dark condition for a noise background level and with beam on. The contribution of the HD-DCM could only be estimated from the internal metrology data, because over the whole range it would be partly noise-limited and partly overshadowed by the intensity variation of the source itself.

CONCLUSIONS

This work briefly summarizes the procedures, the integration architecture and some results in commissioning the HD-DCMs that at MANACÁ and EMA beamlines at Sirius. Thus, the innovative mechatronic architecture is now validated, allowing for superior beam position stability and enabling unmatched scanning possibilities, which can be explored both for higher throughput and new scientific opportunities. A new model for even faster scans, the so-called HD-DCM-Lite [17], is now in development.

ACKNOWLEDGEMENTS

The authors would like to gratefully acknowledge the funding by the Brazilian Ministry of Science, Technology and Innovation; the collaboration with Elina Kasman at APS for the silicon crystals; and the contributions of the LNL and the MI-Partners teams to the instrument. The HD-DCM is also a PhD project carried out with the CST group at TUE, with Marteen Steinbuch and Hans Vermeulen as promoters, and Gert Witvoet as co-promotor.

REFERENCES

- [1] R. R. Geraldes *et al.*, “Instrument for Moving and Positioning of Optical Elements with Nanometric Mechanical Stability and Resolution in Synchrotron Light Source Beamlines”, US Patent App. 16/331,925, July 4, 2019.
- [2] Sirius Project, <https://www.lnls.cnpem.br/sirius-en/>
- [3] L. Jabben, “Mechatronic design of a magnetically suspended rotating platform”, PhD Thesis, TU Delft, 2007.
- [4] A. Preumont, *Mechatronics*. Springer Netherlands, 2006.
- [5] R. R. Geraldes *et al.*, “The New High Dynamics DCM for Sirius”, in *Proc. MEDSI'16*, Barcelona, Spain, Sep. 2016, pp. 141-146. doi:10.18429/JACoW-MEDSI2016-TUCA05
- [6] R. R. Geraldes *et al.*, “Mechatronics Concepts for the New High-Dynamics DCM for Sirius”, in *Proc. MEDSI'16*, Barcelona, Spain, Sep. 2016, pp. 44-47. doi:10.18429/JACoW-MEDSI2016-MOPE19
- [7] M. Saveri Silva *et al.*, “Thermal Management and Crystal Clamping Concepts for the New High-Dynamics DCM for Sirius”, in *Proc. MEDSI'16*, Barcelona, Spain, Sep. 2016, pp. 194-197. doi:10.18429/JACoW-MEDSI2016-TUPE15
- [8] R. M. Caliarì *et al.*, “Studies on Flow-Induced Vibrations for the New High-Dynamics DCM for Sirius”, in *Proc. MEDSI'16*, Barcelona, Spain, Sep. 2016, pp. 8-11. doi:10.18429/JACoW-MEDSI2016-MOPE02
- [9] R. M. Caliarì *et al.*, “System Identification and Control for the Sirius High-Dynamic DCM”, in *Proc. ICALEPCS'17*, Barcelona, Spain, Oct. 2017, pp. 997-1002. doi:10.18429/JACoW-ICALEPCS2017-TUSH203
- [10] B. Z. L. Moreno *et al.*, “Rapid Control Prototyping Tool for the Sirius High-Dynamic DCM Control System”, in *Proc. ICALEPCS'17*, Barcelona, Spain, Oct. 2017, pp. 1941-1946. doi:10.18429/JACoW-ICALEPCS2017-THPHA214
- [11] R. R. Geraldes *et al.*, “The Status of the New High-Dynamic DCM for Sirius”, in *Proc. MEDSI'18*, Paris, France, Jun. 2018, pp. 147-152. doi:10.18429/JACoW-MEDSI2018-WEOAMA01
- [12] R. R. Geraldes *et al.*, “Dynamic error budgeting in the development of the High-Dynamic Double-Crystal Monochromator at Sirius Light Source,” presented at ASPE Topical Meeting 2020, Boston, USA, May 2020, unpublished.
- [13] R. M. Caliarì *et al.*, “Loop-shaping controller design in the development of the High-Dynamic Double-Crystal Monochromator at Sirius Light Source”, presented at ASPE Topical Meeting 2020, Boston, USA, May 2020, unpublished.
- [14] M. A. L. Moraes *et al.*, “The FPGA control implementation of the High-Dynamic Double-Crystal Monochromator at Sirius Light Source”, presented at ASPE Topical Meeting 2020, Boston, USA, May 2020, unpublished.
- [15] J. L. N. Brito *et al.*, “Development Status of the Sirius Timing System”, in *Proc. ICALEPCS'15*, Melbourne, Australia, Oct. 2015, pp. 1007-1010. doi:10.18429/JACoW-ICALEPCS2015-WEPGF128
- [16] D. A. D. Alnajjar *et al.*, “PROJECT Nheengatu: EPICS SUPPORT FOR CompactRIO FPGA AND LabVIEW-RT,” in *Proc. 17th Biennial International Conference on Accelerator and Large Experimental Physics Control Systems*, New York, USA, 2019.
- [17] A. V. Perna *et al.*, “The HD-DCM-Lite: a high-dynamic DCM with extended scanning capabilities for Sirius/LNLS beamlines,” presented at MEDSI 2020, Chicago, USA, Jul. 2021, paper TUPC11, this conference.

FOUR-BOUNCE CRYSTAL MONOCHROMATORS FOR THE SIRIUS/LNLS BEAMLINES

M. Saveri Silva[†], J. H. Rezende, L. M. Dos Santos, L. M. Kofukuda, A. P. S. Sotero
L. M. Volpe, G. S. de Albuquerque, S. A. L. Luiz, H. C. N. Tolentino
LNLS, Campinas, Brazil

Abstract

Beamlines of new 4th-generation machines present high-performance requirements in terms of preserving beam quality, in particular wavefront integrity and position stability at micro and nanoprobe stations. It brings about numerous efforts to cope with engineering challenges comprehending high thermal load, cooling strategy, crystal manufacturing, vibration sources, alignment and coupled motion control. This contribution presents the design and performance of four-bounce silicon-crystal monochromators for the Sirius beamlines at the Brazilian Synchrotron Light Laboratory (LNLS), which is basically composed of two channel-cut crystals mounted on two goniometers that counter-rotate synchronously. The mechanical design ascertained the demands for the nanoprobe and coherent scattering beamlines - namely, CARNAÚBA and CATERETÊ - focusing on solutions to minimize misalignments among the parts, to grant high stiffness and to ensure that the thermal performance would not impair beam characteristics. Hence, all parts were carefully simulated, machined, and measured before being assembled. The present work introduces mechanical, thermal, diagnostics, and dynamic aspects of the instruments, from the design phase to their installation and initial commissioning at the beamlines.

INTRODUCTION

Carnaúba (CNB) and Cateretê (CAT) are the longest Sirius beamlines. Their scientific programs bring several cutting edge contrasts and imaging techniques for research in numerous science fields. Carnaúba has a sub-microprobe (600-150 nm) and nanoprobe (120-40 nm) experimental stations and covers the energy range from 2.05 to 15 keV. Cateretê's experimental station is followed by a 30 m flight path in-vacuum detector and receives a 30 μm^2 beam in the energy range from 4 to 21 keV. In order to achieve such goals, the beamline instrumentation needs to present exceptional performance [1, 2]. Notably, such beamlines will use a four-bounce crystal monochromator (4CM) to select and scan X-rays with resolution of $\Delta E/E=10^{-4}$.

The main attributes of a 4CM are the high energy resolution and its independency from the beam divergence [3]. The first Sirius' 4CMs are based on cryogenically cooled Si crystals and it introduces a simple concept that prioritizes high mechanical stiffness associated to robust control.

[†] marlon.saveri@lnls.br

MECHANICAL DESIGN

The equipment comprises a pair of channel-cut silicon crystals in a horizontal +--+ configuration so that the parallelism between diffraction surfaces is inherently ensured, the downstream beam keeps the same direction of the upstream beam regardless of Bragg's angle, and higher resolution in the selection of X-ray energy is achieved when compared to double crystal monochromators [4]. Table 1 shows the 4CM specifications.

Table 1: Specifications of Carnaúba and Cateretê 4CMs

Parameter	CNB	CAT
Crystal Set	Si (111)	
Angular Range (°)	7-75	4.5-50
Encoder Resolution (urad)	<< 1	
Axes synchronization (urad)	< 10% D.W.	
Crystal Size (mm ³)	62x90x50	50x98x62
Channel-Cut gap (mm)	8.0	6.2
Crystal Temperature	125 K	
Beam Size (mm ²)	1.5x2.6	0.99 x 0.51
Heat Load from Beam (W)	7	17.4
Base Pressure	<5E-8 mbar	

The rotation of the crystals around Bragg angle is driven by a pair of high-resolution goniometers Aerotech APR-200. Naturally, both axes must rotate in opposite directions. Hard stops and limit switches confine the ranges to avoid damage.

The cooling source is a commercial ST-400 UHV cryostat (Janis) supplied by an open cycle liquid nitrogen flow, capable of dissipating 70 W and linked to the crystals by copper thermal straps (TS), which allows the rotations. Additional copper parts are used to fit the different geometries and follow the crystal rotation movement. The straps are also useful to attenuate vibrations from the cooling system, whereas the goniometers are rigidly fixed on a granite bench, which aims to minimize the amplification of vibrations from the ground, Figure 1.

Each channel-cut crystal is clamped to a titanium frame at three contact zones with flexible links designed to minimize deformation and maximize stiffness. The frame is kept in an intermediary temperature, while the rotary stage below it is kept at environmental temperature, Figure 2 zooms the previous figure, highlighting the crystal frame.

Content from this work may be used under the terms of the CC BY 3.0 licence (© 2021). Any distribution of this work must maintain attribution to the author(s), title of the work, publisher, and DOI

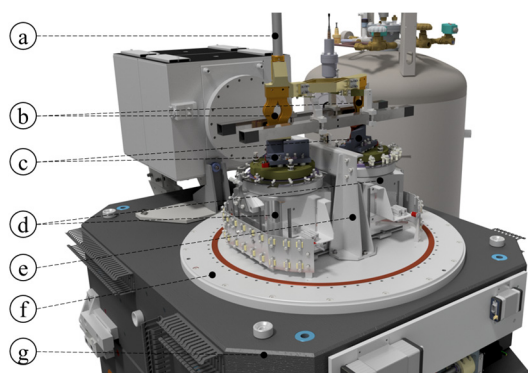


Figure 1: CAD representation of 4CM-CAT. Cryostat (a), copper straps (b), crystals (c), rotary stages (d), linear actuator module (e), vacuum chamber (f), granite bench (g).

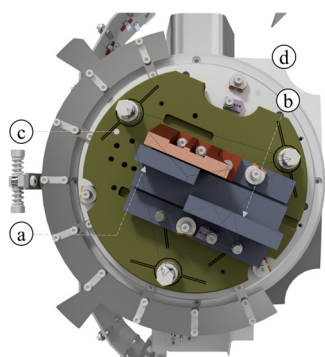


Figure 2: CAD representation of first channel-cut crystal module, containing the first (a) and second (b) diffraction surfaces and the crystal frame (c), which is clamped to the rotary stage (d) at three points 120° spaced.

A linear actuator assembled in a stainless-steel structure is used to move a slit between the two crystals. The slit supports beam diagnostics and acts as a mask to avoid diffractions from other lattice planes. The parts are mounted inside an ultra-high vacuum (UHV) stainless-steel chamber and a liquid nitrogen vessel is placed next to it in order to supply the fluid, Figure 3.

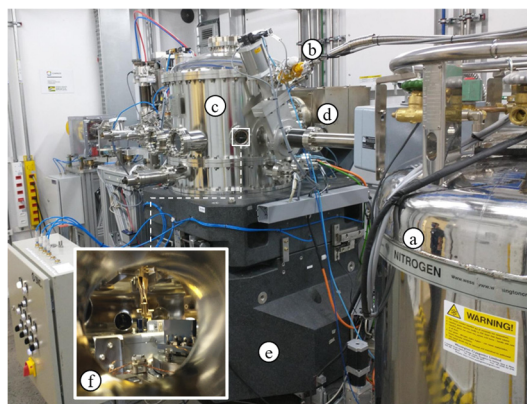


Figure 3: Photography of 4CM-CNB. Liquid nitrogen vessel (a), cryostat (b), vacuum chamber (c), ion pump (d), granite bench (e), and internal view (f).

Alignment

The number of degrees of freedom (DoF) is limited to enhance the stiffness of the system. The DoF for alignment of the entire equipment in relation to the beamline are entrusted to the granite bench (three rotations, Rx, Ry, Rz and two translations Tx, Ty) [5]. Inside the vacuum chamber, the only DoF are Bragg rotations delivered by the goniometers and the translation of the shielding. Therefore, the alignment of the parts, including the parallelism between axis and the positioning of the crystals in relation to Bragg axis, is defined by dowel pins, machining shims, control of screw tightening and metrology.

To ensure the perpendicularity between diffraction planes and rotation axis, with error below 100 μ rad, crystals were assembled on their goniometers and the crystallographic orientations were aligned by using an X-ray diffraction setup providing inputs for tailoring the shims among crystals and their frames.

The parallelism between the axis and the alignment of the entire equipment in the beamline is expected to be achieved with a precision better than $\pm 100 \mu\text{m}$ (Tx, Ty) and $\pm 500 \mu\text{rad}$ (Rx, Ry, Rz) (Fig. 4) when referencing via Laser Tracker.

A script was developed in Python to evaluate the effects of misalignments in the ray-tracing. Figure 4 shows the possible positions of the x-ray beam downstream 4CM-CAT along a full Bragg scan for 1×10^4 beams reflected by the four crystals subject to random misalignment conditions.

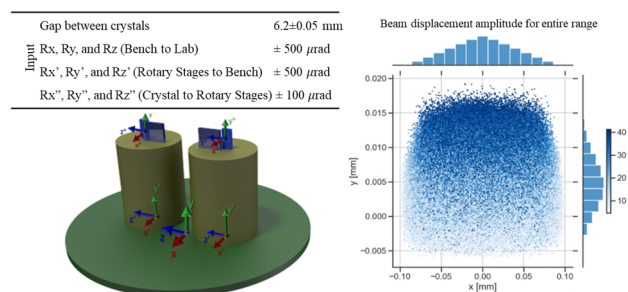


Figure 4: Variations of the virtual source due to random misalignments showed on top-left table. 1×10^4 cases were considered inside these ranges. The coordinate systems xyz, x'y'z' and x''y''z'' are fixed to bottom flange, bottom part of goniometers and center of rotation of crystals, respectively.

This study shows that the variations over the entire range according to the specified alignments values could achieve 20% of the beam size downstream the 4CM. Gap variations from machining process cause the major contribution for horizontal deviations whereas perpendicularity error among rotary stages and floor are dominant for vertical movements.

The offset calibration is achieved by matching reflections of the first and third surfaces to the white beam and by maximizing the intensity in the diagnostics between the channel-cuts and in the visualization device downstream.

Cooling

The high-power photon density from an X-ray synchrotron beam can deform the surfaces of the optical elements and affect the beam quality. The difference of temperature among the diffraction surfaces of the monochromator crystals leads to dissimilar distances between adjacent lattice planes (d-spacing), impairing the photon flux downstream. Moreover, the overall deformation on the footprint results in variations in terms of size and position of the focal point of the beamline, where the samples are usually placed [6, 7]. Such deformations are minimized when the crystals are maintained at cryogenic temperatures, where silicon has high thermal conductivity and low coefficient of thermal expansion (CTE). This effect is illustrated for 4CM-CNB by Figure 5. The smaller the crystal deformation the smaller the beam size at the focus and its position deviation along the X-Ray beam direction (Z)

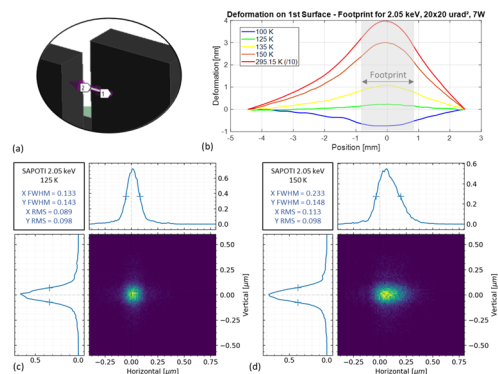


Figure 5: Deformation along the 1st crystal surface of 4CM-CNB (a) due to thermal effects for different bulk temperatures made on Ansys for a $1.6 \times 2.7 \text{ mm}^2$ 7W footprint at 2.05 keV (b). Values for 295.15 K are divided by 10. Raytracing of the diffracted X-Ray beam at experimental station downstream 4CM for crystals at 125 K (c) and 150 K (d) made on Shadow.

A lumped model was applied to design the parts to keep the crystals temperatures close to 125 K [8], which is expected to be achieved after the update of the thermal straps [9]. The cryostat and cryogenic infrastructure are analyzed in a dedicated work [10].

Control

The movements of all axes are controlled by a high-performance Delta Tau (Faraday) motion control solution. On the other hand, the temperature monitoring and control is overseen by a CompactRio (National Instruments) device. The position feedback system consists in a rotary scale TONIC Renishaw with resolution of 26.62 nrad. The control system used is the PowerBrickLV (Delta Tau) which allows kinematics transforms, thus being possible to control Bragg's angle with less than 50 nrad RMS positioning error (from 1 Hz to 2.5 kHz) and to maintain the synchronism of the stages during 600 eV/s movement within 3 urad RMS [11].

PRELIMINARY CHARACTERIZATION

Some preliminary characterizations were accomplished to evaluate the performance with beam. Figure 6 shows an experimental rocking curve obtained by fixing the first set at 9.75 keV and scanning the second set to calibrate small offset among the crystals at the CNB 4CM. The FWHM of the rocking curve matches the expected value, which is a convolution of the total intrinsic reflection width (~ 27 urad) and the small beam divergence (17 urad)

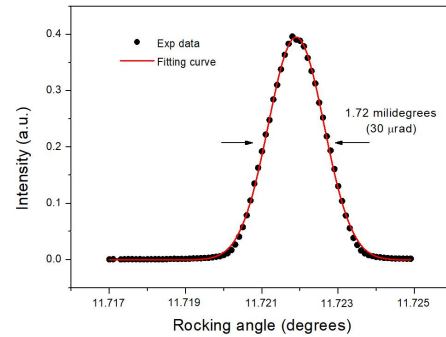


Figure 6: Rocking curve.

The energy resolution of the 4CM was analyzed in an X-ray absorption spectroscopy experiment at the CNB evaluating the sharp pre-edge peak in the Mn K-edge of KMnO_4 , Figure 7. The measured FWHM of 1.54 eV is consistent with the convolution of predicted 4CM resolution (0.65 eV) and the intrinsic core hole width of 1.3 eV [12].

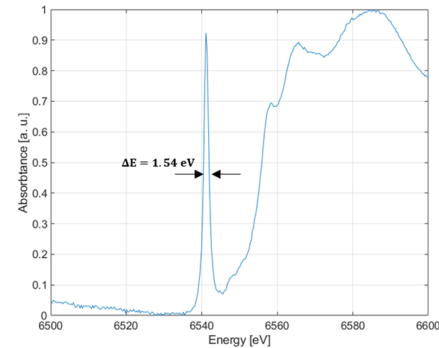


Figure 7: Beamline energy resolution measurement with KMnO_4 K edge.

FINAL REMARKS

Cryogenically cooled four-bounces monochromators were developed to meet the needs of Cateretê and Carnaúba beamlines. Preliminary analysis demonstrate reliability and that high resolution performances.

ACKNOWLEDGEMENTS

The authors would like to gratefully acknowledge the funding by the Brazilian Ministry of Science, Technology and Innovation and the contributions of the LNLS team. We also thankfully acknowledge Ms. Elina Kasman from the Optics Group of Advanced Photon Source of Argonne National Lab for manufacturing the channel-cut crystals in use at the Carnaúba beamline.

REFERENCES

- [1] H. C. N. Tolentino *et al.*, “Innovative instruments based on cryogenically cooled silicon crystals for the CARNAÚBA beamline at Sirius-LNLS”, *AIP Conf. Proc.*, vol. 2054, p. 060026, 2019. <https://doi.org/10.1063/1.5084657>
- [2] F. Meneau *et al.*, “Cateretê, the coherent scattering beamline at Sirius, 4th generation Brazilian synchrotron facility”, Coherence at ESRF-EBS, Grenoble, France, 2019.
- [3] S. Diaz-Moreno *et al.*, “I20; the versatile x-ray absorption spectroscopy beamline at Diamond Light Source”, *J. Phys. Conf. Ser.*, vol. 190, p. 012038, 2019.
- [4] J. W. M. DuMond, “Theory of the use of more than two successive x-ray crystal reflections to obtain increased resolving power”, *Phys. Rev.*, vol. 52, pp. 872-883, Oct. 1937. doi:10.1103/PhysRev.52.872
- [5] R. Geraldès *et al.*, “Granite benches for Sirius x-ray optical systems”, in *Proc. MEDSI'18*, Paris, France, June 2018. doi: 10.18429/JACoW-MEDSI2018-THPH12
- [6] M. Antimonov *et al.*, “On the influence of monochromator thermal deformations on X-ray focusing”, *Nucl. Instrum. Methods Phys. Res., Sect. A*, vol. 820, pp. 164-171, 2016. doi: 10.1016/j.nima.2016.02.103
- [7] J. Eckdahl, “Effects of lattice strain in silicon double crystal monochromators”, Department of Physics, MAX IV Laboratory, MAXM30, 20181, 2018.
- [8] M. Saveri Silva, “Thermal modeling for the development of a four-bounces crystal monochromator for the Sirius project”, University of Campinas, 2019.
- [9] F. R. Lena *et al.*, “Copper braid heat conductors for Sirius/LNLS cryogenic x-ray optics”, presented at the 11th Int. Conf. on Mechanical Engineering Design of Synchrotron Radiation Equipment and Instrumentation (MEDSI2020), Chicago, IL, USA, virtual conference, July 2021, paper TUPC14, this conference.
- [10] M. Saveri Silva *et al.*, “Cryogenic systems for optical elements cooling at Sirius/LNLS”, presented at the 11th Int. Conf. on Mechanical Engineering Design of Synchrotron Radiation Equipment and Instrumentation (MEDSI2020), Chicago, IL, USA, virtual conference, July 2021, paper MOPB02, this conference.
- [11] L. Martins dos Santos *et al.*, “The Control System of the Four-Bounce Crystal Monochromators for Sirius/LNLS Beamlines”, submitted to 18th International Conference on Accelerator and Large Experimental Physics Control Systems, Shanghai, 2021.
- [12] H. C. N. Tolentino *et al.*, “A 2.3 to 25 keV XAS beamline at LNLS”, *J. Synchrotron Radiat.*, vol. 8, pp. 1040-6, 2001. doi:10.1107/S0909049501005143

<http://lup.lub.lu.se/student-papers/record/8947155>

INSTALLATION AND COMMISSIONING OF THE EXACTLY-CONSTRAINED X-RAY MIRROR SYSTEMS FOR SIRIUS/LNLS

V.B. Zilli†, C.S.N.C. Bueno, G.V. Claudiano, R.R. Geraldés, G.N. Kontogiorgos, F.R. Lena, S.A.L. Luiz, G.B.Z.L. Moreno, A.C. Pinto, G.L.M.P. Rodrigues, M.S. Souza, L.M. Volpe
Brazilian Synchrotron Light Laboratory (LNLS), Brazilian Center for Research in Energy and Materials (CNPEM), 13083-970, Campinas, Sao Paulo, Brazil

Abstract

Innovative exactly-constrained thermo-mechanical designs for beamline X-ray mirrors have been developed since 2017 at the 4th-generation Sirius Light Source at the Brazilian Synchrotron Light Laboratory (LNLS). Due to the specific optical layouts of the beamlines, multiple systems cover a broad range of characteristics, including: power management from a few tens of mW to tens of W, via passive room-temperature operation, water cooling or indirect cryocooling using copper braids; mirror sizes ranging from 50 mm to more than 500 mm; mirrors with single or multiple optical stripes, with and without coatings; and internal mechanics with one or two degrees of freedom for optimized compromise between alignment features, with sub-100-nrad resolution, and high dynamic performance, with first resonances typically above 150 Hz. Currently, nearly a dozen of these in-house mirror systems is operational or in commissioning at 5 beamlines at Sirius: MANACÁ, CATERETÊ, CARNAÚBA, EMA and IPÊ, whereas a few more are expected by the end of 2021 with the next set of the forthcoming beamlines. This work highlights some of the design variations and describes in detail the workflow and the lessons learned in the installation of these systems, including: modal and motion validations, as well as cleaning, assembling, transportation, metrology, fiducialization, alignment, baking and cooling. Finally, commissioning results are shown for dynamic and thermal stabilities, and for optical performances.

INTRODUCTION

For the past couple of years many beamlines have passed from the design stage to assembly, installation, and commissioning at the 4th-generation Sirius Light Source at the Brazilian Synchrotron Light Laboratory (LNLS) [1]. Regarding the novel exactly-constrained X-ray mirrors for Sirius [2], during the design phase extra care was taken to ensure beam characteristics – i.e., acceptable nanometric deformation into the mirror’s optical faces –, and alignment capabilities at the beamline, with new procedures, tools, and manuals being developed to certify installations.

Five beamlines at Sirius, namely, MANACÁ (MAN), CATERETÊ (CAT), CARNAÚBA (CNB), EMA and IPÊ, summarized in Table 1, currently rely on these in-house solutions, and a few more are expected by 2021. Through the commissioning phase on the first three of them, some important results have been found regarding fine and coarse alignment, leading to some significant beam results. Ther-

mal management and cryogenics, modal and bench stability results are briefly presented. Some potential future improvements were found and are briefly discussed.

Table 1: First Beamlines Summary

Beam-line	Energy Range	Source	Status
CNB	2.05–15 keV	ID	Commissioning
MAN	5–20 keV	ID	Commissioning
CAT	5–20 keV	ID	Commissioning
IPÊ	100–2000 eV	ID	Installation
EMA	2.7-30 keV	ID	Assembling

ASSEMBLY AND INSTALLATION

Following standardized step-by-step guidelines, internal mechanisms pre-assembly, characterization and fiducialization ensures high-quality and repeatability to the assembly and installation processes. The main procedures steps are presented and discussed.

Assembly

A well-done cleaning certifies the removal of any contaminants into the ultra-high vacuum (UHV), to which most of the mirror systems are submitted. The main contaminants identified are machine oil used for lubrication, human skin oil, dust, and metal particles from machining which are mainly encountered on surface roughness and holes.

The first cleaning process is mechanically pre-cleaning the parts using the alkaline detergent IC115 which is followed by common water and demineralized water rinsing. To guarantee the part cleanliness, when necessary, an ultrasonic bath with the part submerged into a IC115 (10%) and water solution at ambient temperature is made for variable times, depending on the part size, geometrical complexity, and material.

A comprehensive and intuitive pre-assembly workflow has been developed ensuring quality and repeatability. The internal mechanism assembly method can be subcategorized into some main stages and were executed inside a controlled clean room [3]. Firstly, the mirror support is fixated, securing position, and favoring the precision mechanism fixation. Then, dowel pins and folded leaf-springs (FLS) fixation can be done (see [2]). The pins guarantee positions according to design. All FLS need to be screwed by hand before tightening, to prevent pre-tensioning, which might induce asymmetric stiffness into the system. Numer-

† vinicius.zilli@lnls.br

Content from this work may be used under the terms of the CC BY 3.0 licence (© 2021). Any distribution of this work must maintain attribution to the author(s), title of the work, publisher, and DOI

ous assembly tools have been developed to certify positioning and alignment of the stiffness components between the mirror and the mirror support. Lastly, sensors and actuators can be assembled, which include temperature sensors and heaters, for temperature measurement and control; linear encoders, for the support position measurements; and the piezo walker for fine movement actuation. All cables need to be divided, sorted, and routed on the top of the base frame. Figure 1 shows the CAT M2 mirror internal mechanism before the mirror was mounted to it.

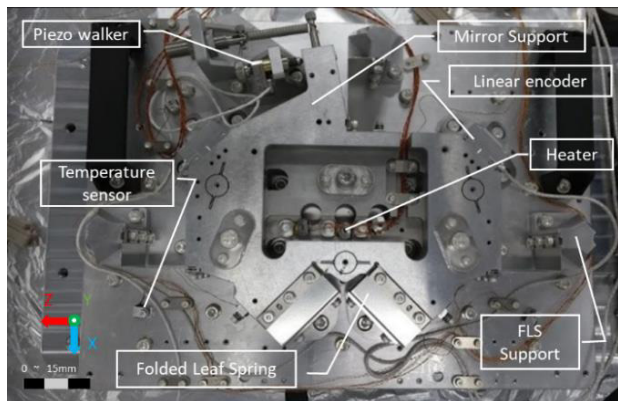


Figure 1: Fully assembled CAT M2 internal mechanism.

Fiducialization

An indirect fiducialization procedure has been developed to virtually match the components of interest from two independent measurement setups. The mirrors substrates are measured using a high-precision CMM (coordinate measuring machine) (Hexagon Global Performance). In turn, the assembled internal mechanics, that finally defines the mirrors positions, are measured using an articulated measuring arm (7-axis ROMER by Hexagon). The accuracy and repeatability of this procedure is below 0.1 mm, in average. As illustrated in Fig. 2, four fiducialization points outside the UHV chamber are also measured, to be related to the Sirius metrology network during the alignment campaigns with laser trackers [4].

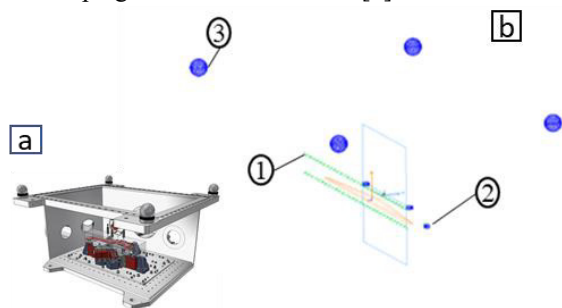


Figure 2: (a) CAT M2 CAD representation and (b) CAT M2 internal mechanism fiducialization measurements: (1) mirror optical face, (2) mirror internal mechanism, and (3) fiducialization points.

Installation

Following the offline internal mechanisms assembly, the installation procedure at the beamline starts by isolating the

optical hutch, installing an auxiliary portable laminar flow close to it, and iteratively cleaning both ambients until particle level measurements reach class ISO 5. First, the internal mechanisms without the mirrors are mounted to the vessels on the granite benches under the laminar flow, as depicted in Fig. 3. Then, the vessel is covered and transported with the laminar flow to inside the hutch, with controlled temperature of $24 \pm 0,1$ °C. Once everything is settled, the vessels are reopened, and the mirrors are mounted on the internal mechanisms.



Figure 3: CAT M2 granite bench and UHV chamber inside a portable cleanroom laminar flow ready for the installation procedure.

Due to higher thermal loads, some of the optical systems must be actively cooled. The strategy varies depending on beam aspects and deformation budgets [5], but all share the concept of flexible copper braids as heat conductors to couple the optics to the thermal sinks [6]. Depending on the constraints of the design, the fixation of the braid to the mirrors is done before or after the attachment of the mirror on the support (see Fig. 4). In the first case, the mirror is carefully manually hold, with its optical face facing slightly downwards for the braid attachment to avoid particles contamination on the optical face, then, the fixation on the supporting frame is performed. In the latter, the mirror is already safely mounted to its support when the braids are connected. The last step is the cryostats fixation and UHV chamber closure. The UHV chamber seal is certified doing a standard leak test using helium gas.

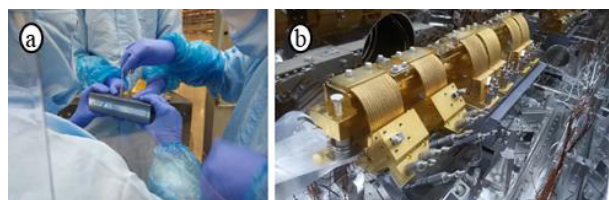


Figure 4: (a) CAT M1 flexible copper braid being fixed to the mirror and (b) the CAR M1 assembly installed inside the UHV chamber.

Baking

Depending on substrate, coating, and beam characteristics, as well as the operational energy range, X-ray mirrors may require UHV to XHV (ultra-high vacuum and extreme ultra-high vacuum) conditions to avoid the contamination and degradation of the optical surface. This is true especially for cryogenic systems, in which the gas molecules

become more strongly attached to the cold surfaces. To reach this environment, it is required to bake out the chamber with all the mechanics, motor, encoders, and X-ray mirror, such that desorbed water and other undesired elements can be pumped out.

Having the maximum baking temperature limited by the piezo actuators, all subsystems are baked at 80 ± 0.2 °C for about two weeks. Temperature homogeneity and stability is reached by using a "baking tent" with temperature control, as illustrated in Fig. 5. The final pressures of all systems are in the order of low 10^{-10} mbar.



Figure 5: Setup of the "baking tent" used at the beamline, developed to avoid high temperatures outside the tent.

COMMISSIONING

First results regarding alignment, vibrations, and thermal control have been obtained during commissioning of the first systems. Concerning the Sirius beamlines optical layout, the standard concept for high stability is the use of side-bounce sagittal cylindrical mirrors with fixed shape to deflect and focus the beam [7]. Figure 6 shows the beam focalized by the M1 mirror at the Secondary Source Aperture (SSA) at the CNB beamline, with a full width at half maximum (FWHM) value of about $45 \mu\text{m}$ [8].

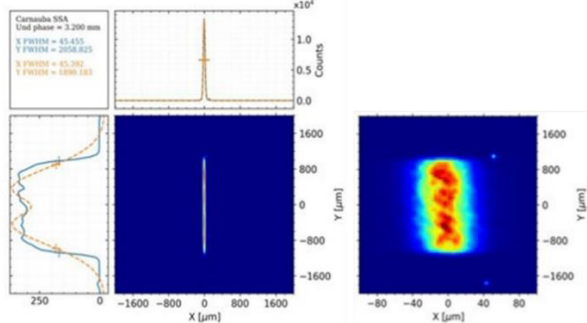


Figure 6: Measurement for the horizontally-focused beam at the CNB beamline, producing a vertical-line beam.

Regarding modal results, measurements performed on M1 and M2 CNB mirror systems have shown that first resonances in the bench are related to the ionic pump decoupling from the bench at approximately 42 Hz for both mirrors (see [2]). Yet, as these components represent only 10% of this systems mass, the granite modes are higher, and the vacuum chambers and mirrors have even higher suspension with respect to the bench (148Hz for M1 and 130Hz for M2), no amplification issues should occur. Stability on the benches and surrounding floor measurements have been done to complement the modal information [9]. An

example is given in Fig. 7 for the horizontal displacement of the granite benches of M1 and M2 at CNB, which can be integrated to find displacements in order of about 10 nm.

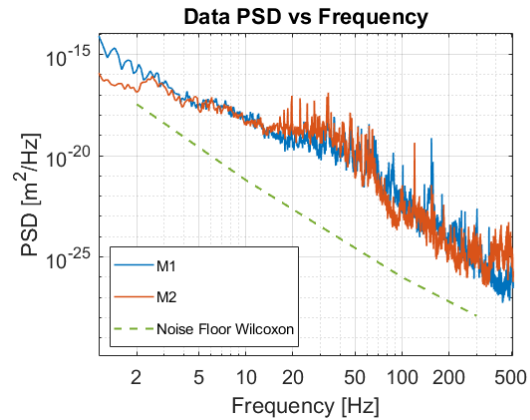


Figure 7: Horizontal displacement Power Spectrum Density measurements for CNB M1 and M2.

As for thermal management, the systems had been modeled using both FEA in ANSYS® and lumped mass in MATLAB®, in which PID control tuning could also be implemented [10]. In practice, to ensure temperature stability, minimizing deformation and drift in the optics, an in-house low-cost cryocooling solution was developed together with a high-performance temperature control architecture [11]. An example is given in Fig. 8 for the CAT M1, with temperature stability around 2 mK range over several hours.

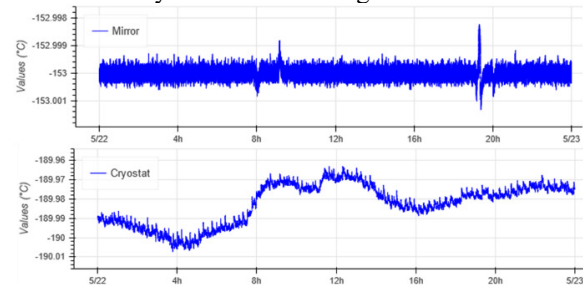


Figure 8: CAT M1 temperature deviation, with maximum values of about 2 mK.

CONCLUSION

The successful assembly, installation, and preliminary commissioning of the novel Sirius mirrors systems at the MANACÁ, CARNAÚBA and CATERETÊ beamline validated the proposed innovative concept and the required procedures. Indeed, specific tools and strategies have been developed for cleaning, baking, and assembly, according to the final alignment, dynamics, and figure preservation targets. These first results will feedback the design of the new systems to come, whereas more tests are planned for the granite benches ranges, repeatability, and accuracy.

ACKNOWLEDGEMENTS

The authors would like to gratefully acknowledge the funding by the Brazilian Ministry of Science, Technology, Innovation and Communication and the contribution of the LNLS team.

REFERENCES

- [1] Sirius Project, <https://www.lnls.cnpem.br/sirius-en/>.
- [2] R. R. Galdes *et al.*, “The design of exactly-constrained X-ray mirror systems for Sirius”, in *Proc. MEDSI'18*, Paris, France, Jun. 2018, paper WEOAMA04, pp. 173-178.
- [3] H. G. P. de Oliveira *et al.*, “The LNLS metrology building – environmental control results”, in *Proc. MEDSI'18*, Paris, France, Jun. 2018, paper TUPH43, pp. 143-146.
- [4] G. Rovigatti *et al.* “Status report on the Sirius beamlines alignment”, presented at MEDSI'20, Chicago, IL, USA, Jul. 2020, paper THOA03, this conference.
- [5] L. M. Volpe *et al.*, “Optimization method using thermal and mechanical simulations for Sirius high-stability mirrors”, in *Proc. MEDSI'18*, Paris, France, Jun. 2018, paper WEPH31, pp. 273-276.
- [6] F. Lena *et al.*, “Copper braid heat conductors for Sirius cryogenic X-ray optics”, presented at MEDSI'20, Chicago, IL, USA, Jul. 2020, paper TUPC14, this conference.
- [7] S. A. L. Luiz *et al.* “Flexible optical layouts based on cylindrical mirrors with sagittal curvature for high-stability beamlines”, in *Proc. SPIE 1193, Advances in Computational Methods for X-Ray Optics V*, p.1149305, Aug. 2020
- [8] H. C. N. Tolentino *et al.* “X-ray microscopy developments at Sirius-LNLS: First commissioning experiments at the Carnaúba beamline”, in *Proc. SPIE 11839, X-Ray Nanoimaging: Instruments and Methods V*, p. 1183904, Aug. 2021.
- [9] C. S. N. C. Bueno *et al.* “Vibration assessment at Carnaúba beamline at the Sirius/LNLS”, presented at MEDSI'20, Chicago, IL, USA, Jul. 2020, paper MOPB08, this conference.
- [10] L. M. Volpe *et al.* “Thermal model validation for the cryogenic mirror systems for Sirius/LNLS”, presented at MEDSI'20, Chicago, IL, USA, Jul. 2020, paper WEPC07, this conference.
- [11] M. Saveri Silva *et al.* “Cryogenic systems for optical elements cooling at Sirius/LNLS”, presented at MEDSI'20, Chicago, IL, USA, Jul. 2020, paper MOPB02, this conference.

VIBRATION ASSESSMENT AT THE CARNAUBA BEAMLINE AT THE SIRIUS/LNLS

C. S. N. C. Bueno†, F. A. Borges, G. S. de Albuquerque, G. R. B. Ferreira, R. R. Geraldés, L. M. Kofukuda, M. A. L. Moraes, G. B. Z. L. Moreno, D. V. Rocha e Silva, M. H. S. Silva, H. Tolentino, L.M. Volpe, V. B. Zilli, Brazilian Synchrotron Light Laboratory (LNLS), Brazilian Center for Research in Energy and Materials (CNPEM), 13083-970, Campinas, Sao Paulo, Brazil

Abstract

CARNAÚBA (Coherent X-Ray Nanoprobe Beam-line) is the longest beamline at Sirius Light Source at the Brazilian Synchrotron Light Laboratory (LNLS), working in the energy range between 2.05 and 15 keV and hosting two stations: the sub-microprobe TARUMÃ and the nanoprobe SAPOTI, with coherent beam size varying from 500 to 30 nm. Due to the long distances from the insertion device to the stations (135 and 143 m) and the extremely small beam sizes, the mechanical stability of all opto-mechanical systems along the facility is of paramount importance. In this work we present a comprehensive set of measurements of both floor stability and modal analyses for the main components, including: two side-bounce mirror systems; the four-crystal monochromator; the Kirkpatrick-Baez (KB) focalizing optics; and the station bench and the sample stage at TARUMÃ. To complement the components analyses, we also present synchronized long-distance floor acceleration measurements that make it possible to evaluate the relative stability through different floor slabs: the accelerator slab; experimental hall slab; and the slabs in the satellite building, consisting of three inertial blocks lying over a common roller-compacted concrete foundation, the first with the monochromator and the remaining ones with one station each. In addition to assessing the stability across this beamline, this study benchmarks the in-house design of the recently installed mirrors, monochromators, and end-station.

INTRODUCTION

CARNAÚBA's (Coherent X-Ray Nanoprobe Beamline) [1] sub-micron station TARUMÃ and nanoprobe SAPOTI are the two experimental station at Sirius Light Source with the largest distances to the source, namely, at 135 meters and 143 meters from the insertion device, respectively. Then, due to the long optical lever-arms, beam sizes at the sample between 30 and 500 nm, and strict stability requirements for coherent imaging techniques, all opto-mechanical systems in CARNAÚBA must be carefully designed [2], assembled, installed, and validated.

As shown in the simplified diagram of Fig. 1, CARNAÚBA relies on an undulator source, which is located inside the storage ring tunnel, lies on the storage ring especial floor [3], and serves as the origin for the CARNAÚBA coordinate system. At 27.4m, already outside the tunnel, but still on the storage ring special floor, the first main opto-mechanical system is the side-bounce elliptical mirror

(M1) [4], that focalizes the beam in the secondary source. Next, in the experimental hall, at about 54.3m from the source, the second main opto-mechanical system is composed of the secondary source mechanism and the planar mirror (M2), which finally directs the beam to the satellite building, where the monochromator (4CM) [5] and the experimental stations, TARUMÃ (TAR) [6] and SAPOTI (SAP), are found on special inertial blocks at 130m, 135m and 143m, respectively.

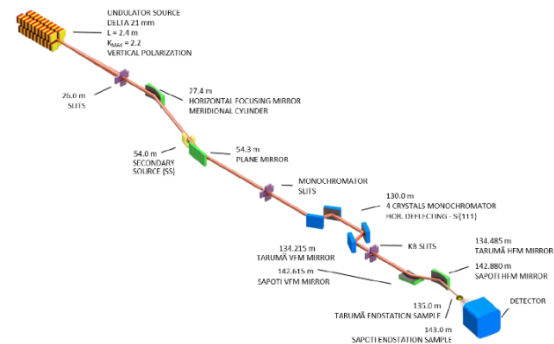


Figure 1: Simplified diagram of the CARNAUBA beamline.

METHODOLOGY

The different types of measurements relied on specific setups, hardware, and software. In the modal analyses, a triaxial modal accelerometer Kistler 8762A5, an instrumented impact hammer PCB Instruments 086C03, and a NI USB-4431 DAQ acquisition board with 24-bit resolution running with NI Signal Express at 10kHz, were used for the frequency response function characterizations. In a sequence of measurements for each component, by attaching the accelerometer to different points of the structure, while keeping the excitation with the impact hammer in a convenient point, animated mode shapes can be created using a software toolbox developed in-house. For each measurement point, a series of four impacts was repeated to maximize statistics for coherence and data quality. For each impact, the time signal was recorded for 2s, with a pre-trigger margin of 10% of this.

In the floor and component stability analyses two seismic accelerometers Wilcoxon 731 together with two power amplifiers P31 were used with the same acquisition board and rate mentioned above, but for a total of 60s. For the power spectrum density (PSD) calculations, it was used a window of 10s and 50% overlap. Then, for cumulative power spectrum (CPS) and cumulative amplitude spectrum (CAS) data, integration is made up to 450Hz, that is the maximum frequency for this seismic accelerometer.

† cassiano.bueno@lnls.br

Content from this work may be used under the terms of the CC BY 3.0 licence (© 2021). Any distribution of this work must maintain attribution to the author(s), title of the work, publisher, and DOI

Finally, in the long-distance measurements two Lennartz Eletronic LE-3Dlite geophones were used in parallel with the two seismic accelerometers to extend the measurement range in the lower frequency. The measured locations included distances from 28m (insertion device to M1) to 143m (insertion device to experimental station), such that overcoming the challenges regarding hardware and synchronization required the measurement setup to be carefully studied and planned. Eventually, the *White Rabbit* protocol, developed by CERN, was implemented and used to synchronize the data with nanosecond precision [7]. In our scenario, just two nodes of the White Rabbit were mounted in a custom application that was developed in Labview for NI CompactRIO (which has also been selected as the standard controller for Sirius beamlines). The first one stood at the insertion device location, whereas the second node moved from location to location. The station with the insertion device was the master, sending synchronization pulses to the traveling station via an optical fiber. Then, carefully considering the noise level limits in the sensors, the time signals were subtracted, so that just the relative vibration between both points would be analysed, using the same parameters as for the benches stabilities.

RESULTS

Modal Measurements

The modal measurements were taken in all of the granite benches of the main opto-mechanical systems at CAR-NAÚBA, with the objectives of studying the mechanical resonances and mode shapes of the structure and investigating possible influences in the optical elements and the sample. Figure 2 shows an example of the animated mode shapes of the 4CM structure, in which each relevant sub-component is displayed in a different color for clarity, and Table 1 summarizes the results.

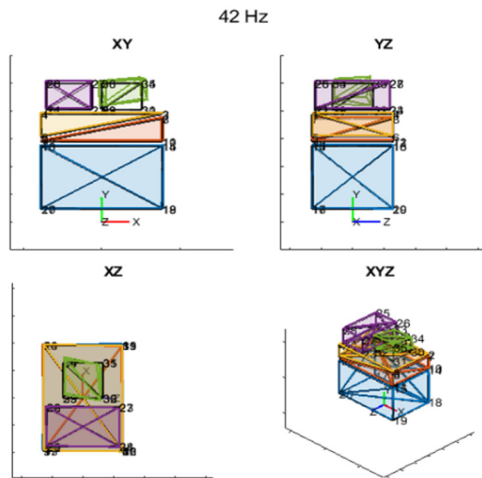


Figure 2: Representation of an animated mode shape for M1 modal Analysis. The components represented are bottom granite (purple), bottom granite wedge (red), top granite wedge (yellow), vacuum chamber (purple) and ionic pump (green).

Analysing the first modes, it can be seen that the fixation mechanisms of the ionic pumps are not fulfilling the de-

signed stiffness requirements, such that their first decoupling occurs in low frequencies, around 40 to 60Hz. Nonetheless, as the pump weighs less than 10% of the bench and the vacuum vessel is stiffly coupled to the granite bench [8], the amplification effects caused by these modes are not expected to significantly impact the optical elements and internal mechanisms of the M1, the M2 and the monochromator, as they are designed for resonances above 100 Hz. The horizontal and rotation modes, that can impact the in-position stability of internal mechanisms in mirrors are in frequencies above 100Hz, being 148Hz for M1 and 130Hz for M2.

Table 1: The seven first natural frequencies, in Hz, for all CAR-NAÚBA opto-mechanical system installed. The acronyms BG and AG stand for *Before grouting* and *After grouting*, respectively.

M1	M2	4CM	TAR BG.	TAR AG.
42	42	39	40	180
56	46	44	52	215
64	51	55	62	317
78	64	60	70	402
91	70	74	94	498
148	104	109	107	529
170	130	137	213	631

For TARUMÁ, two scenarios can be considered, namely: before grouting the bottom granite part, in early commissioning phase for alignment validation; and after the grouting work. *Before grouting* there was a critical 40Hz natural resonance due to the limited stiffness between the bench and the slab floor, resulting from the three simple aluminium supporting shims. Excited by disturbances in the floor, the in-position stability of the sample stage was limited to 50nm RMS in the horizontal axis, in a frequency range from 1Hz up to 500Hz. *After grouting*, another modal analysis was run to evaluate the changes in the natural frequencies and mode shapes. With the additional stiffness, the first natural frequency jumped to 180Hz, as depicted in Fig. 3, and the sample in-position stability could be improved 10nm RMS from 1Hz to 500Hz. The SAPOTI station is under construction and could not be evaluated yet.

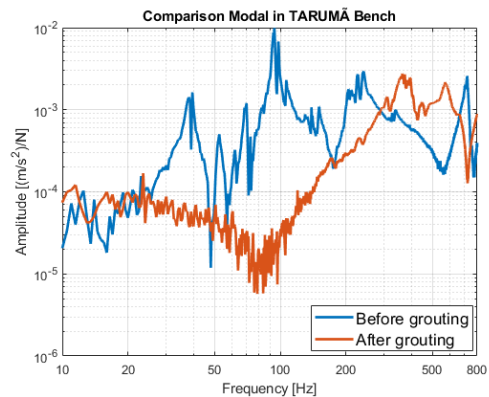


Figure 3: Comparison between the Frequency Response Function for the scenarios: *Before Grouting* and *After Grouting*.

Stability Measurements

To complement the modal measurements, stability measurements were made for the granite benches of all opto-

mechanical systems and the surrounding floors. As explained before, many components lie on different slabs, such that these measurements help understanding the different characteristics throughout the beamline. Table 2 summarizes the RMS cumulative spectra from 2 to 450Hz for each component and the floor, whereas Fig. 4 shows a comparison between the horizontal PSD for the different benches, from where it is possible to notice the resonances described in the last section, influence the final stability. Evaluating the one third octave velocity bands and comparing results with the Vibration Criteria curves (VC curves) [9], all points analysed in CARNAÚBA beamline meet standard VC H and NIST-A1.

Table 2: Cumulative amplitude spectrum from 2 to 450Hz, in nm, for 6DoF floor stability around opto-components and 3DoF translations in the granite benches.

	M1	M2	4CM	TAR	SAP
X floor	8.17	7.77	10.71	9.04	12.42
Y floor	7.2	7.69	7.53	5.34	5.67
Z floor	7.32	6.64	13.87	16.37	9.58
Rx floor	1.97	2.46	6.51	10.31	9.31
Ry floor	1.30	1.78	11.60	3.95	5.35
Rz floor	1.47	1.79	1.31	1.49	3.49
X bench	9.39	9.17	11.71	10.59	-
Y bench	7.58	8.07	8.06	7.33	-
Z bench	7.63	6.98	15.07	17.38	-

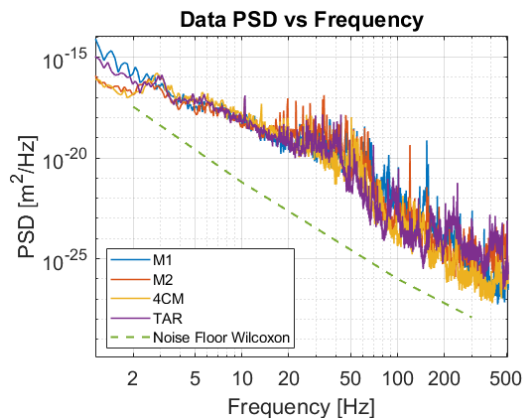


Figure 4: Horizontal Displacement Power Spectrum Density measurements for opto-mechanical system at CARNAÚBA and the seismometer noise floor to validate the measurements.

Long-Distance Stability Measurements

Finally, supplementing the local floor stability data, more information about correlation among the floor slabs was sought with measurements taken between the insertion device location and the opto-mechanical components locations: M1, M2, and both experimental stations. Table 3 summarizes the result for the 3 translational degrees of freedom that were measured, whereas Fig. 5 shows the three translational relative PSDs to the farthest measurement location, at the SAPOTI experimental station slab. The achievement of such high stability is extremely important since the beam stability in the experimental stations

has a direct dependence on the relative stability of the source and secondary source.

Table 3: Cumulative amplitude spectrum from 0.5 to 450Hz, in nm, for the three translational axes, for the long-distance measurements. The line “DI” inform the distance, in meters between the accelerometer in each setup.

	Und-M1	Und-M2	Und-Tar	Und-Sap	M1-M2	M1-TAR
X	1.9	2.1	10.7	10.1	1.1	3.2
Y	1.8	2.0	6.5	5.8	2.0	2.4
Z	2.8	2.5	10.7	10.3	1.2	3.5
Di.	28	58	136	143	29	118

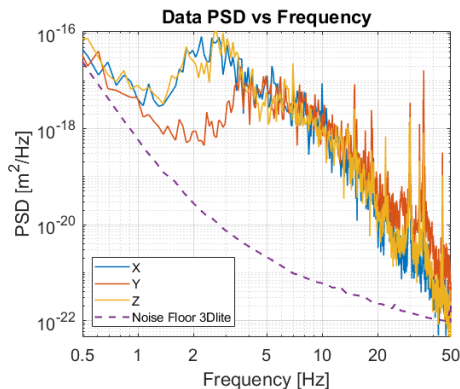


Figure 5: Relative displacement PSD for the long-distance measurement between the Undulator and the SAPOTI slab (143m) and the geophone noise floor.

It is possible to notice the good agreement between seismic accelerometer and geophone in both locations for the intermediary frequencies. For frequencies lower than 2Hz the data from the seismic accelerometer is dominated by noise, so that just de geophone can be considered. For frequencies higher than 50Hz the same occur with geophone data, such that just de seismic accelerometer can be used.

CONCLUSION

A full set of instruments and methods has been used for stability and dynamic analyses at CARNAÚBA, the longest beamline at Sirius that also hosts it’s the first nanoprobe TARUMÃ. The floor stability in all locations is remarkably well placed with respect to the common NIST-A and VC curves, with integrated displacement between 2 and 450 Hz below in the range from 5 to 15 nm RMS in XYZ. At the same time, the relative measurements over the long distances proved to be below 10 nm RMS, already partly limited by sensor noise. Finally, the granite benches of the opto-mechanical systems are validated, having achieved robust dynamic performances that do not amplify the cultural noise and providing suitable stands for the most sensitive beamline elements.

ACKNOWLEDGEMENTS

The authors would like to gratefully acknowledge the funding by the Brazilian Ministry of Science, Technology, Innovation and Communication and the contribution of the LNLS team.

REFERENCES

- [1] H.C.N. Tolentino *et al.*, “CARNAÚBA: the coherent x-ray nanoprobe beamline for the Brazilian Synchrotron SIRIUS/LNLS,” *J. Phys. Conf. Ser.*, vol. 849, p. 012057, 2017. <https://doi.org/10.1088/1742-6596/849/1/012057>
- [2] R. Geraldès *et al.*, “Granite benches for Sirius x-ray optical systems”, in *Proc. MEDSI 2018*, Paris, France, Jun. 2018, pp. 361-364. doi:10.18429/JACoW-MEDSI2018-THPH12
- [3] F. Rodrigues *et al.*, “Sirius stability: from foundation to girders”, *Synchrotron Radiat. News*, vol. 32, iss. 5, p. 20-26, 2019. <https://doi.org/10.1080/08940886.2019.1654828>
- [4] L. M. Volpe *et al.*, “Installation and commissioning of the exactly-constrained x-ray mirror systems for Sirius/LNLS”, presented at the 11th Int. Conf. on Mechanical Engineering Design of Synchrotron Radiation Equipment and Instrumentation (MEDSI2020), Chicago, IL, USA, virtual conference, July 2021, paper MOPB06, this conference.
- [5] M. Saveri Silva *et al.*, “Four-bounce crystal monochromators for the Sirius/LNLS beamlines”, presented at the 11th Int. Conf. on Mechanical Engineering Design of Synchrotron Radiation Equipment and Instrumentation (MEDSI2020), Chicago, IL, USA, virtual conference, July 2021, paper MOPB04, this conference.
- [6] R. Geraldès *et al.*, “Design and commissioning of the TARUMÃ station at the CARNAÚBA beamline at Sirius/LNLS”, presented at the 11th Int. Conf. on Mechanical Engineering Design of Synchrotron Radiation Equipment and Instrumentation (MEDSI2020), Chicago, IL, USA, virtual conference, July 2021, paper WEPB13, this conference.
- [7] The White Rabbit Project, <https://white-rabbit.web.cern.ch/>, accessed on July 19, 2021.
- [8] R. Geraldès *et al.*, “The design of exactly-constrained x-ray mirror system for Sirius”, in *Proc. MEDSI 2018*, Paris, France, Jun. 2018, pp. 173-178. doi:10.18429/JACoW-MEDSI2018-WEOAMA04
- [9] Vibration Criteria Standards, https://www.minusk.com/content/technology/vc_curves_minus_k_vibration_isolation.html, accessed on July 19, 2021.

THE DESIGN AND MANUFACTURING OF SUPERCONDUCTING UNDULATOR MAGNETS FOR THE ADVANCED PHOTON SOURCE UPGRADE*

E. Anliker†, Q. Hasse, Y. Ivanyushenkov, M. Kasa, Y. Shiroyanagi
Argonne National Laboratory, Lemont, Illinois, United States of America

Abstract

The Advanced Photon Source Upgrade (APS-U) will include 4 full length Superconducting Undulators (SCU). These SCUs require new undulator magnets to achieve the required performance of the new machine. The magnets are fabricated from low carbon steel and wound with NbTi superconductor. To meet the needs of the users, the magnets will be manufactured in different lengths and magnetic periods to accommodate SCUs in both inline and canted configurations. Because their operational conditions do not allow for shimming or other tuning adjustment, the magnets used in the APS-U SCUs require very tight tolerances for the poles and winding grooves that push the extents of their manufacturability. This paper will cover the design of the 1.9m long magnets for the inline SCUs, their measurement data, lessons learned from manufacturing, and an overview of design changes that were made for the magnets to be used in the canted SCU configurations.

INTRODUCTION

The Advanced Photon Source (APS) located at Argonne National Laboratory (ANL) is currently undergoing an upgrade (APS-U) including a new storage ring and new insertion devices (IDs). Among the new IDs are four new Superconducting Undulators (SCUs) that will occupy the entire space provided in a straight section (~5.3 m) of the new storage ring. The SCUs required new magnets to be designed and manufactured to fit inside the new devices while achieving the magnetic performance required by the new accelerator. The new magnet designs aim to preserve desired features and functionality from past magnet designs, while also integrating new features to make the design more universal and easier to manufacture.

INITIAL DESIGN

The APS-U SCU magnet designs are an evolution of previous magnet designs used in past SCUs [1]. The previous designs (Fig. 1) consisted of a low-carbon steel core with G-10 spacers on top that were held in place with spring pins and low carbon steel poles on the bottom held in place with screws. These spacers and poles created grooves that would be used to wind the conductor around the magnet. The magnets also included holes drilled into the top of the magnet core so turn-around pins could be inserted during the winding process.

* This research used resources of the Advanced Photon Source, a U.S. Department of Energy (DOE) Office of Science User Facility at Argonne National Laboratory and is based on research supported by the U.S. DOE Office of Science-Basic Energy Sciences, under Contract No. DE-AC02-06CH11357.

† eanliker@anl.gov

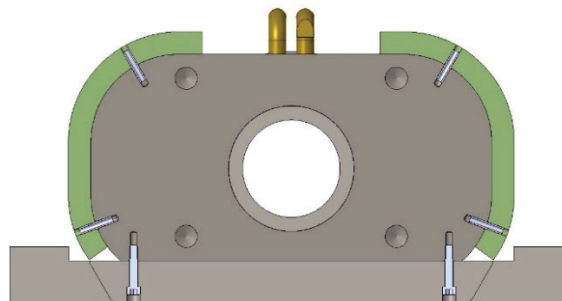


Figure 1: Previous SCU magnet core design that encompassed G-10 spacers and individual pole inserts.

The new SCU magnet designs for APS-U vary in length from 1.3 m - 1.9 m and have magnetic periods of 16.5 mm and 18.5 mm. This is the longest magnet that has been manufactured and wound by the SCU team at the APS. Features retained from previous designs include holes on top of the magnet core for the turn-around pins, helium channels that pass through the magnet, and a modified footed pole to be used during the resin impregnation (potting) process that extends out of the sides near the bottom of the magnet.

The magnets were modified from previous designs by changing the overall height and width of the magnet to have a better fit inside of the new cryostat [2]. Another benefit of a wider magnet is that the region of the magnet influencing the electron beam would be expanded and allow for a looser alignment tolerance of the magnets.

Other modifications include the removal of the G-10 spacers and individual poles on the magnet. The magnets now consist of a single piece with the grooves machined directly into the core, replacing the individual poles and spacers. This new magnet design can be seen in Fig. 2. This dramatically reduced the number of holes being drilled and tapped into the magnet core and reduced the overall number of pieces in the magnet assembly. The magnets still need to incorporate an extended pole insert at specific locations along the length of the core to be used in the potting process. Instead of using individual inserts like previous designs the inserts were changed to a single machined piece that included three poles and two grooves fastened by two 4-40 screws.

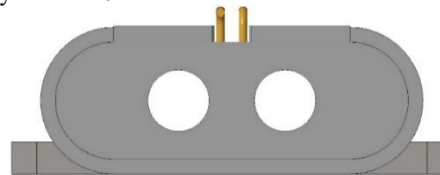


Figure 2: Magnet design used on the APS-U 1.9 m SCUs showing single piece core and footed poles.

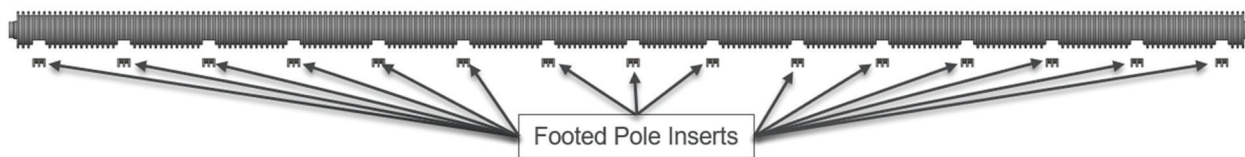


Figure 3: 1.9 m long magnet showing footed pole inserts and corresponding cutouts in the magnet core.

The inserts were machined to match the curvature of the grooves in the magnet core. The magnet core has corresponding pockets machined out to incorporate the inserts. The full-length magnet and insert locations can be seen in Fig. 3.

MANUFACTURING CHALLENGES

While the design was aimed at creating a more universal and straightforward approach for manufacturing, it did not eliminate all the challenges that come with fabricating magnets of this length to the level of precision required. Prior to fabrication, the initial design was finalized after consulting with reputable vendors and incorporating the inner cooling channels that run the entire length of the magnet; constructing the majority of the magnet out of a single piece of stock and with achievable tolerances for the grooves. The magnets operate at cryogenic temperatures in an insulating vacuum environment resulting in little to no accessibility for shims. The groove dimensions are thus critical dimensions that define the period of the magnet and require tight width and depth tolerances as small as ± 0.02 mm.

The magnets for the APS-U SCUs vary in length from 1.3 m to 1.9 m. The 1.9 m long magnets proved to be especially challenging for many manufacturers due to the difficulty holding the required tolerances of the grooves over that length. This limited the number of available vendors capable of producing the 1.9 m magnets whereas the fabrication of shorter magnets would be achievable by a wider range of manufacturers.

The inserts that were machined to fit in the corresponding cutouts on the bottom of the magnet also had to be machined to match the radius of the magnet core so that there was a seamless joint in each groove. A closer view of this joint can be seen in Fig. 4.

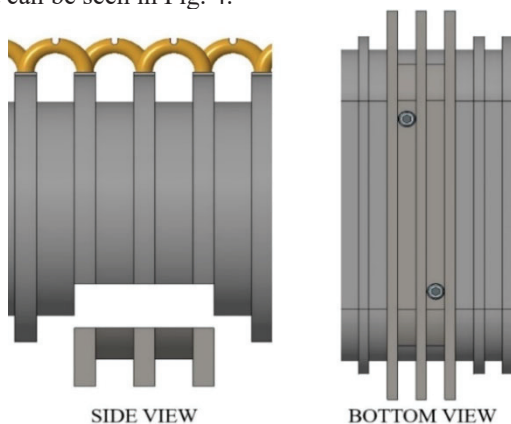


Figure 4: Side and bottom view of the footed pole insert and its 4-40 fasteners.

DATA AND PERFORMANCE

The magnets are required to pass a thorough measurement and inspection process completed by the vendor that consisted of measuring multiple points in every groove. This information was then tabulated into a report and required the approval by the technical representative before delivery. The points allow for the creation of virtual maps that could be used to determine the flatness of the pole face and the groove dimensions. The grooves are also verified with ceramic gauge blocks to ensure there is adequate space all around the core for the conductor winding. The measurements taken showed that there were inconsistencies in the flatness along the bottom pole surface of the assembled magnet located at each of the footed pole locations. The measurements that show this inconsistency are shown in Fig. 5.

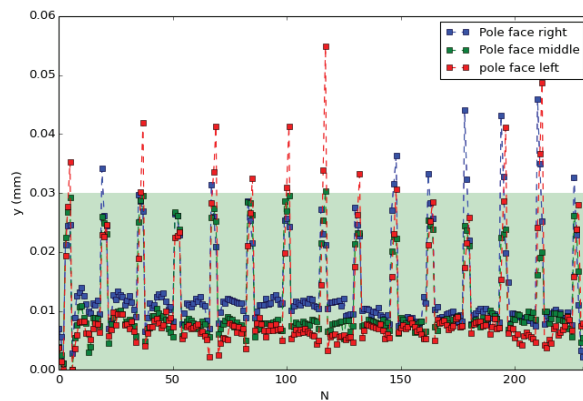


Figure 5: Plot of the pole face flatness along the bottom of the magnet core (number of measurements on X-axis) showing spikes out of the tolerance zone (green).

As shown in Fig. 5, the differences between poles largely fall within the required tolerances on the magnet yielding a minor impact on the periodicity of the magnet. However, the difference in pole height was a representation of the mismatch of the interfaces between the footed pole inserts and their cutouts in the magnet core.

During the potting process the magnets undergo a bakeout process where they are heated to 80 °C for 24 hours, then cured at 135 °C for 1.5 hours. Once potted the magnets are trained and tested in a liquid helium bath at an operating temperature of 4.2 K. The temperature differential was sufficient for the conductor to expand and contract enough that the protective layer around the conductor was penetrated or rubbed off at specific interfaces where the footed poles are attached to the magnet core. This created shorts to the magnet core which in turn created local hot spots where the conductor would burn up during coil training. The interface location where problems occurred, and

a cutout of the conductor damage can be seen in Figs. 6 and 7, respectively.



Figure 6: Interface where footed pole meets the magnet core where the conductor could potentially get pinched.

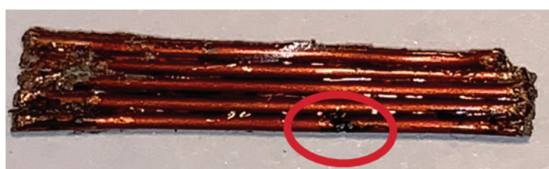


Figure 7: Conductor removed from a magnet after it had shorted to the core and caused a magnet failure. Red circle highlights the hot spot where the conductor burned.

FINAL DESIGN

Given that the interface between the footed pole inserts and magnet core exist in multiple locations along the length of each magnet, there was the possibility for failure on additional magnets on the remaining SCUs to be built. The design was modified to completely remove the footed poles. The magnet outer profile was changed to include a taper to the bottom pole surface to replace the footed poles and machining the entire magnet core out of a single piece of steel as shown in Fig. 8. The change was influenced by the single piece magnet cores manufactured for the Helical Superconducting Undulator (HSCU) built at Argonne in 2017 [3]. This would eliminate any interfaces where the conductor could potentially be damaged. The final design would retain the winding groove dimensions, turn around pins, helium channels, and tapered grooves on the top of the magnet, while removing the footed poles from the design, thus eliminating the interfaces that were causing the shorts to the magnet to occur. The final design also includes a new feature of channels machined down the sides of the magnet core to allow for epoxy to better flow through the magnet during the potting process. The final design also allows the magnet to maintain the same magnetic performance as the initial design and allows for the use of all the same components surrounding the magnet structure inside of the cryostat creating uniformity between all the magnets. The surrounding components are shown in Fig. 9.

As a result of removing the footed poles from the design, the potting molds for the magnets needed to be redesigned to fit the new magnet profile. The footed poles were an integral part of the potting mold, as they were used to fas-

ten the magnet onto a flat plate, ensuring a clean surface on the bottom of the magnet. A new method consisting of pressing the magnet down from the top was developed to retain the smooth surface on the bottom pole face.

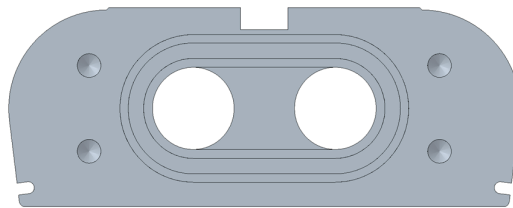


Figure 8: New single piece magnet design with tapered profile to be used on all future APS-U SCUs.

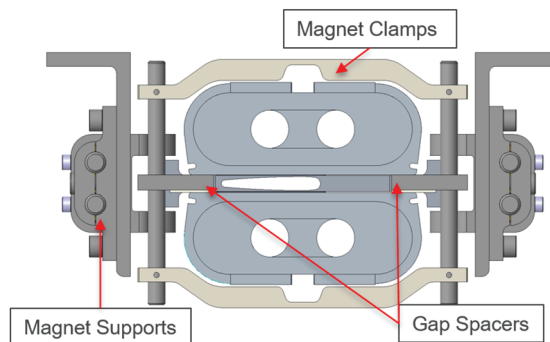


Figure 9: New single piece magnet design and corresponding components being reused inside of the SCU cryostat.

CONCLUSION

Following an extensive design, assembly, and testing process, the latest evolution of the superconducting magnet cores for the APS-U have been approved and are currently being manufactured with an anticipated arrival date of late 2021. After delivery, the magnets will be wound, potted, and tested before being installed into the new SCUs currently being assembled at the APS.

ACKNOWLEDGEMENTS

This research used resources of the Advanced Photon Source, a U.S. Department of Energy (DOE) Office of Science User Facility at Argonne National Laboratory and is based on research supported by the U.S. DOE Office of Science-Basic Energy Sciences, under Contract No. DE-AC02-06CH11357.

REFERENCES

- [1] E. Trakhtenberg, Y. Ivanyushenkov, and M. Kasa, "Evolution of the Design of the Magnet Structure for the APS Planar Superconducting Undulators", in *Proc. North American Particle Accelerator Conf. (NAPAC'16)*, Chicago, IL, USA, Oct. 2016, pp. 1245-1247. doi:10.18429/JACoW-NAPAC2016-THPOA69
- [2] E. Anliker *et al.*, "A New Superconducting Undulator Cryostat for the APS Upgrade", in *Proc. CEC-ICMC'19*, Hartford, CT, USA, July. 2019, doi:10.1088/1757-899X/755/1/012126
- [3] J. Fuerst *et al.*, "A second-generation superconducting undulator cryostat for the APS," *IOP Conf. Ser.: Mater. Sci. Eng.*, vol. 278, p. 012176, 2017. doi:10.1088/1757-899X/278/1/012176

THE ADVANCED PHOTON SOURCE UPGRADE (APSU) SUPERCONDUCTING UNDULATOR (SCU) COMPONENT DATABASE (CDB) UTILIZATION

G. Avellar[†], E. Anliker, J. Lerch, J. Saliba, M. Szubert
 Argonne National Laboratory, Advanced Photon Source-Upgrade, Lemont, USA

Abstract

The Component Database (CDB) is a document management platform created for the use of the Advanced Photon Source Upgrade (APSU) Project. It serves two major functions: (1) a centralized location to link all data relating to field-replaceable upgrade components, and (2) a way to track the components throughout the machine's 25-year lifetime. There are four (4) Superconducting Undulators (SCUs): two (2) Inline 16.5mm period devices, one (1) Canted 16.5mm period device, and one (1) Canted 18.5mm period device. Throughout the production process for these devices, tracking components between the different designs of SCU's has proven to be a logistical issue, as there are uniform components among all 4 devices, but many unique components as well. As the scope evolved from a Research and Development (R&D) activity to a production scope, the CDB has been critical in communicating with a growing team, allowing anyone to identify a part or assembly and access all its design and manufacturing data. The 4.8-meter long SCUs are the first of their kind, requiring thorough onsite inspections, intricate assembly procedural, and approved safety protocols. This is ideal information to document in an electronic traveler (e-traveler), which can then be attached to an item within the CDB. By providing a straightforward process for technicians to follow, the risk of miscommunication and unsafe practices are minimized. The CDB plays a vital role in simplifying and optimizing the transition of the SCU from an R&D unit to a production scope, from procurement to inspection, assembly and installation, and throughout the lifespan of machine maintenance.

INTRODUCTION

The Advanced Photon Source Upgrade (APSU) Project will replace the current storage ring with a combination of new and refurbished components. The result will be a new machine producing X-rays up to 500 times brighter than the current device. The design phase is complete, procurements are well underway, and the year-long shut down for installation is set to start in April 2023 [1]. Four of the Insertion Device (ID) straight sections will be equipped with new 4.8-meter long Superconducting Undulators (SCUs) of various magnetic periods, which accommodate canted and inline configurations. These complex devices produce photons at different energies to be used by the ID beamline users. A single cryostat and base assembly can house two undulator magnet pairs, the cryogenic cooling system, and vacuum chamber (Fig. 1) [2]. With the various designs for

the inline 16.5mm period device, canted 16.5mm period device, and canted 18.5mm period device, the need for a streamlined database to organize procurements and procedures, and to effectively communicate this information, was evident. The Component Database (CDB) has proven to be vital in the transition of SCUs from a Research and Development (R&D) scope to a production process. The defining feature of the CDB is that it is an integrated system that links many other databases and can pull data seamlessly from many sources.

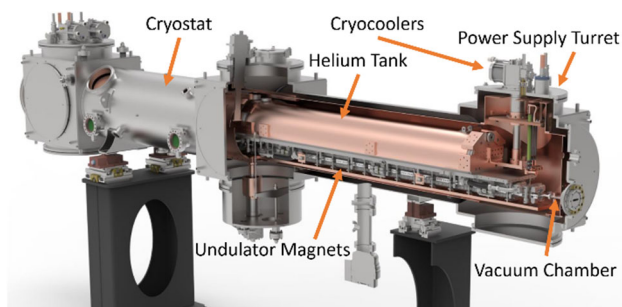


Figure 1: Cross-section rendering of the inline 16.5mm Superconducting Undulator, showing the cooling system, magnets, power supply turrets, and vacuum chamber.

OVERVIEW

The CDB is used Project wide and became increasingly more important as APSU procurements ramped up and the project transitioned into the production phase. The CDB is organized into two layers, the *Catalog* level and *Inventory* level. At the *Catalog* level, components are organized by Technical System and then by Function. Specifically, for SCU's, this path is *Insertion Devices* and then *Undulator-Superconducting*. Once here, a list of all components relating to the device are listed along with important information, such as model number, images, a description, and inventory information. There is also a search bar at the top of the CDB page allowing for ease of access if the model number or a key word is known. This allows anyone, project-wide, to quickly access information, even if they are not intimately familiar with the assembly and subassembly breakdown of an SCU. Selecting a part will redirect the page to that part's *Catalog* level where all general information on it can be found. Here, the *Inventory* sub-section is listed as one *Instance* entry for each item ordered, and if selected will display all the information collected for that item. This includes location, status, date received, the purchase requisition, links to vendor documentation and drawings, and an electronic traveler (e-traveler) that is filled out by the technicians and engineers after the part is inspected.

[†] Email: gavellar@anl.gov

The *Item Membership* and *Assembly Listing* sub-sections can organize CDB entries by assemblies and subassemblies. Within the top level SCU entry, there are many sub-assembled items. This helps to narrow one's search and focus on information about a particular system within the SCU. Starting at the Inline Top-Level Assembly and using this *Assembly Listing* feature, information can be found about a sub-assembly such as the Power Supply Turret as shown in Fig. 2. This breakdown of assemblies also correlates to the physical assembly process. A given subassembly of the SCU can be linked with a documented procedure and e-traveler to give instruction for assembly of a particular system before it is incorporated into the top-level SCU assembly. One can use the *Item Membership* function to navigate the CDB in the opposite direction, by seeing everywhere that a subassembly or component is used. In the case of the Power Supply Turret, it can be seen that it is used in all variations of the SCUs (Fig. 3).

Assembly Required	Name	Model Number
Yes	500A CURRENT LEAD ASSEMBLY	A182-TR0134
Yes	HTS CURRENT LEAD BUSHING	4101010601-700616
Yes	500A HTS INSULATING BUSHING	4101010601-700622
Yes	POWER SUPPLY TURRET FLANGE ASSEMBLY	A182-TR0151
Yes	FIRST STAGE ASSEMBLY	A182-TR0152
Yes	SECOND STAGE ASSEMBLY	A182-TR0153
Yes	CRYOCOOLER RDE-4180A PLATE NUT	A182-TR0155
Yes	CRYO-COOLER 1ST STAGE PLATE NUT	A182-TR0182
Yes	500A FIRST STAGE LINK ASSEMBLY	A182-TR0159

Figure 2: Component Database *Assembly Listing* feature for Power Supply Turret Assembly.

Part Of
Inline 16.5mm SCU Top Level Assembly
Canted 16.5mm SCU Top Level Assembly
Canted 18.5mm SCU Top Level Assembly

Figure 3: Component Database *Item Membership* feature for Power Supply Turret Assembly.

The CDB is a useful tool for the SCU group. With individual team members able to contribute in their various disciplines, the information is shared in a timely matter and is in an accessible space for all. There are three main pillars to the CDB utilization for SCU's: technical utilization, procurement tracking, and communication. A project of this size, duration, and cost needs a platform that can handle the significant quantity of information necessary for the upgrades design, installation, operation phases.

TECHNICAL UTILIZATION

The CDB has tools that allow for customization of information storage for the various component entries that come with varying types of data files. Inspection data, assembly and manufacturing notes, non-conformity tracking, and models are all linked to the CDB *Instance* level. Being able

[Accelerators](#)

[Insertion Devices](#)

to pinpoint a failure point is critical for a successful project, so the ability to reference this data in the future is essential.

Archives

Prior to the availability of the CDB, vendor-supplied documentation was sent as physical copies in the shipping crates during the delivery of the parts. These paper-copies were then stored in filing cabinets and there was no certainty that the vendor would save the information for their own records. Integrating this data was a major turning point in the SCU group's CDB utilization. This involved digitizing the information and organizing it accordingly with its *Instance* entry. Moving forward, vendor documentation is requested in an electronic format, for easier upload to the CDB. Loading this information in the CDB ensures that this information will be accessible for years to come. Throughout the lifetime of these components, this information will be available to new engineers and technicians.

New Component Deliverables

The APSU procurement process is well-defined and encourages obtaining as much information from the vendor as possible. By defining the contract deliverables in a clear way from the start, vendors are able to incorporate hold points into their schedules for APSU oversight and approval. The data requested is integral to the lifetime operation of these components.

An example of deliverable data for the SCU vacuum chambers (Fig. 4a) is the request for dimensional data verifying the thin wall, proof of thermal shock results of the bimetal component, and vacuum certification documentation. Throughout the contract, the vendor was able to supply pieces of this data, which was then stored at the *Instance* level. By the end of the contract for the first article, the vendor was able to tailor the deliverable information so that its integration with the developed e-traveler was seamless.

Another piece of information that was captured in the CDB was an approved non-conformity Supplier Disposition Request. The vendor produced a component that was out-of-spec according to the drawings but was acceptable for the form, fit, and function of the part. If the chamber is inspected in the future and does not match the drawings precisely, the justification is easy to find.

PROCUREMENT TRACKING

After a requisition is routed and assigned a req. number, this information is correlated with its CDB entry. Throughout the procurement process, more information can be added to the CDB from the contract paperwork. The technical advantages to using the CDB have been discussed, but the extension to the capability for onsite management is another major factor of using the CDB, especially for the SCU team.

When a component is received on site, it goes through a Quality Assurance (QA) process. This inspection information is input into the CDB in an e-traveler within that *Instance* part. The status, location, designation, and in-

tended use of each part is recorded to avoid duplicate purchases and inventory misplacement. This is particularly important for parts such as the SCU cryocoolers (Fig. 1) that will be rotated between devices, for maintenance purposes, and requires spares. SCU procurements are managed by multiple team members and the deliverables are stored in multiple buildings, so the CDB plays a vital role in the tracking of all the inventory.

The feature linking Argonne's Procurement And Requisition Integrated System (PARIS) to inventory items in the CDB allows employees to easily reference the requisition and contractual information. Often, the same vendor is working on multiple Purchase Orders for different components for the SCU's at the same time. An example is Anderson Dahlen, who is currently fabricating items for the inline and canted SCU scopes. They are producing the SCU vacuum chambers [3] (Fig. 4a), thermal shields (Fig. 4b), and cryostats (Fig. 4c). Tracking this work in the CDB allows the control account manager to access the information and determine priorities, notify the technical representative engineer of the work, and in turn convey this information to the vendor.



Figure 4: The SCU vacuum chamber (a), thermal shield (b), and cryostat (c) first articles onsite at APS.

COMMUNICATION

Efficient and effective communication is a critical component of a project of this scale and duration. It is equally important to leave information in an accessible and centralized database for future APSU team members to reference. Communication across different levels within the organization is vital to the success of the APSU.

Organization

Information is constantly uploaded to the CDB as it becomes available throughout the procurement and manufacturing process. Once the scope of work is defined for onsite inspection or assembly, the responsible engineers and technicians can review the data and component and create procedures for future work. These processes can be captured in Work Control Documents (WCDs) and e-travelers, which connect seamlessly with the CDB. The organizational value of the CDB allows for a centralized repository of information for the whole team.

In the future this repository will become increasingly important if an operational issue is detected. For example, if an SCU is in operation and it is experiencing unexpected quenching of the superconducting magnets, this is potentially caused by a head leak due to incidental contact with a system operating at a different temperature, such as the

vacuum chamber. Using the SCU vacuum chamber deliverables, a SCU team member can pull the dimensional data for information on any discrepancies and begin troubleshooting to find the root cause.

The link to procurement information also becomes important for project management reporting. Components can be located by requisition number and an algorithm can pull inventory status allowing for a high-level view of the project.

Safety

Hazards are identified while developing the WCDs, which is a collaborative effort of the engineers, technicians, and a safety representative. Safety concerns are made clear and each employee must review and sign before performing any work. APSU SCU assembly presents unfamiliar situations as the SCU group transitions from building an R&D unit to a production scope. As previously mentioned, e-travelers can be linked to *Inventory* items in the CDB and lay out procedures for authorized workers to follow. The process can be broken down to check points and can be organized for clear data entry of relevant information. Linking these documents to the associated component in the CDB will ensure that the technicians will have clear direction for the work at hand, lowering the potential for safety incidents and increasing efficiency, productivity, and quality of work.

CONCLUSIONS

The CDB plays a vital role in the success of the APSU SCU scope. The three most impactful aspects of the CDB are storing technical data, tracking procurements, and effectively communicating across all levels of the organization. An electronic platform ensures that this information will be accessible for years to come.

ACKNOWLEDGMENT

This research used resources of the Advanced Photon Source, a U.S. Department of Energy (DOE) Office of Science User Facility at Argonne National Laboratory and is based on research supported by the U.S. DOE Office of Science-Basic Energy Sciences, under Contract No. DE-AC02-06CH11357.

REFERENCES

- [1] APS-U *et al.*, "APS Upgrade Project Final Design Review Report," APS, Illinois, United States, Rep. APSU-2.01-RPT-003, May 2019.
- [2] E. Anliker *et al.*, "A new superconducting undulator cryostat for the APS Upgrade", presented at the 2019 Cryogenic Engineering Conference and International Cryogenic Materials Conference, Hartford, CT, July 2019. <https://doi.org/10.1088/1757-899X/755/1/012126>
- [3] M. Szubert *et al.*, "The Advanced Photon Source Upgrade (APSU) straight section vacuum systems first article fabrication", presented at the 11th Int. Conf. on Mechanical Engineering Design of Synchrotron Radiation Equipment and Instrumentation (MEDSI'20), Chicago, IL, USA, virtual conference, July 2021, paper MOPB11, this conference.

THE ADVANCED PHOTON SOURCE UPGRADE (APSU) STRAIGHT SECTION VACUUM SYSTEMS FIRST ARTICLE FABRICATION*

M. Szubert[†], E. Anliker, G. Avellar, J. Lerch

Argonne National Laboratory (ANL), Advanced Photon Source-Upgrade, Lemont, IL, USA

Abstract

The Advanced Photon Source Upgrade (APSU) includes 40 straight sections, 35 of which will be outfitted with Superconducting Undulators (SCUs) or Hybrid-Permanent Magnetic Undulators (HPMUs). The vacuum systems for these devices are primarily fabricated from aluminum extrusions and are required to provide Ultra-High Vacuum continuity between storage ring (SR) sectors for a nominal distance of ~5.4 meters. Each vacuum system has unique fabrication challenges, but all first article (FA) components have been produced successfully. The FAs arrived onsite at ANL installation-ready but have undergone functional testing activities to verify the production and vacuum certifications. The Insertion Device Vacuum Chamber (IDVC), used in HPMU sectors, is produced by SAES Rial Vacuum (Parma, Italy). The SCU vacuum system components are produced by two vendors, Cinel Instruments (Venice, Italy) and Anderson Dahlen (Ramsey, MN, USA). Based on the reliable outcomes and lessons learned from the FAs, production of the straight section vacuum systems is underway.

INTRODUCTION

The Advanced Photon Source Upgrade (APSU) project plan calls for the current APS 40 sector storage ring (SR) to be retrofitted with a new 6 GeV, 200 mA storage ring optimized for brightness above 4 keV [1]. Thirty-five straight sections produce photons at various energies to the Insertion Device (ID) beamline users, with 31 straight sections equipped with Hybrid Permanent Magnet Undulators (HPMUs) and 4 straight sections equipped with Superconducting Undulators (SCUs).

Each of these ID straight sections require a vacuum system to ensure Ultra-High Vacuum continuity between SR sector arcs. They both interface with the P0 Beam Position Monitor Bellows assembly at the upstream (US) and downstream (DS) locations. At these locations, the vacuum systems match the Ø22 mm SR aperture, but transition to various shapes at their thin-wall locations. In addition, both vacuum systems accommodate two configurations, i.e. canted and inline. While the HPMU ID Vacuum Chamber (IDVC) and SCU Vacuum System designs differ based on their operational and interface requirements, each vacuum system has been independently optimized to achieve a uniform design for both the canted and inline variants in their respective sectors [2, 3].

* This research used resources of the Advanced Photon Source, a U.S. Department of Energy (DOE) Office of Science User Facility at Argonne National Laboratory and is based on research supported by the U.S. DOE Office of Science-Basic Energy Sciences, under Contract No. DE-AC02-06CH11357.

[†] Corresponding Author's Email: mszubert@anl.gov

OVERVIEW

Procuring the ID straight section components included long lead items, sole-source awards, and best-value vendor evaluation. Each purchase order introduced its own unique challenges, both due to technical capabilities and aggressive scheduling. The first articles (FAs) are necessary to prove the design concept and uncover issues that would avoid future production complications that may incur a cost increase or add schedule delays.

The designs require the use of complex manufacturing processes, modified vacuum procedures, complicated weld joints, and off-site testing by the vendors. The FAs for the straight section vacuum system are critical hold points in the production process for these new vacuum designs.

ID VACUUM SYSTEM

The fabrication of the ID Vacuum System consists of 3 aluminum extrusions, each modified to create a vacuum chamber (VC) with an integrated aperture transition, a strongback (SB) spanning the length of the straight section (~5.4 meters), and an additional support bracket to satisfy the aperture alignment requirements. After competitively bidding the fabrication of the IDVC and supports, the scope was awarded to SAES Rial Vacuum (SRV) in Parma, Italy. The aluminum components, extrusions and flanges, were supplied to SRV at the beginning of the project, with the remaining material, components, and equipment acquired by the vendor.

Fabrication of the FA included procuring the aluminum extrusions and aluminum flanges early in the design process as they were long lead items. Fig. 1 shows the extrusions at various stages of manufacturing: preliminary material removal of the VC (Fig. 1a), the trapezoidal SB with a mounting plate prepared for shipping (Fig. 1b), and the l-brackets that support the chamber 5 places along its length, allowing for alignment (Fig. 1c).

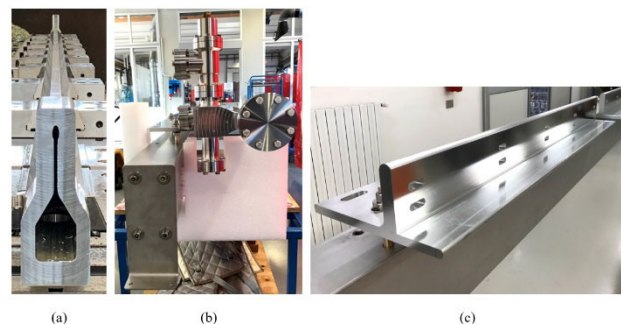


Figure 1: IDVC extrusion profiles throughout the fabrication process, 1a shows the VC, 1b shows a side view of the SB profile, and 1c shows the modified l-bracket profile.

The fabrication challenges included machining a thin wall feature (600 microns thick) for a length of 5+ meters, which allows for the IDs to operate at closed gap, integrating the aperture transition through conventional machining, and adhering to the AWS D17.1 weld specification [4].

Weld Development

The IDVC must operate for the lifetime of the APSU, or approximately 25 years. To ensure the success of these chambers, welds must adhere to class A or B welds, per AWS D17.1. While the design minimizes welds along the beam path, each weld is critical and most are thin wall connections, necessitating theoretically perfect welds with few-to-no porosities and inclusions. SRV worked to improve the weld quality, beginning with the weld sample deliverable, and continuing into the FA fabrication, including finding a vendor to perform the radiographic inspection. After radiographic inspection of the FA, many of the welds were class B but there were still non-conformities, with Class C welds present based on the tungsten inclusions and porosity size. The FA's intended use is for the installation mock-up, not for installation/operation, and therefore was acceptable, even with these discrepancies.

Re-evaluating the scope and deliverables, SRV agreed to produce a second article with installation-ready specifications, to be verified by x-ray inspection (Fig. 2). An additional weld sample was produced, and the process was vastly improved, producing all Class A or B welds. At the time of this publication, SRV has completed the 2nd article within specification and is confident in its welding capability. Production is underway [4]. APSU will randomly select 4 additional chambers to be x-ray inspected from the remaining 39 units, prior to shipment.



Figure 2: X-ray inspection of welds in the 2nd article, meeting Class A standard.

First Article Functional Testing

The scope of this award involved a thorough test plan for the FA. Due to COVID-19 international travel restrictions, the vendor performed the following tests for APSU remote approval of the FA: critical dimension verification, ultrasonic wall thickness measurement along the thin nose portion, vacuum certification producing a bake-out log and RGA scan, pumping slot deflection measurement, and aperture alignment [2, 4].

The vacuum certification is critical since the VCs will be stored under a nitrogen blanket for 2 years and need to be ready for installation during the dark time, beginning April

2023. While the vendor provides documentation for the proof of all these activities, the APS Mechanical Operations & Maintenance group verified the vacuum method by leak checking, pumping down, and baking out the chamber. (Fig. 3).



Figure 3: IDVC FA during bake-out at ANL.

Other components from this straight section vacuum system that have gone through similar test activities include: the photon absorber, ion pump, NEG cartridges, vacuum monitors, and installation cart. The IDVC fabrication and procurement process is estimated to be completed in December 2021.

SCU VACUUM SYSTEMS

The SCU Vacuum System consists of 3 assemblies: (1) US out-of-cryo vacuum assembly, (2) in-cryo vacuum assembly that resides inside the cryostat [5], and (3) DS out-of-cryo vacuum assembly (Fig. 4). The in-cryo chamber is supported as a part of the cold-mass inside the cryostat. The two out-of-cryo vacuum systems require supports external to the cryostat, using stand-offs and threaded rods.

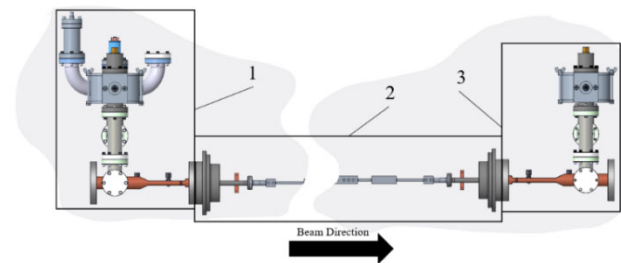


Figure 4: SCU VC assemblies, (1) US out-of-cryo VC, (2) in-cryo VC, and (3) DS out-of-cryo VC.

SCU In-Cryo Vacuum System

The FA in-cryo vacuum system has been produced by Anderson Dahlen (October 2020). This VC is a 4.8-meter long weldment spanning the length of the SCU cryostat. It is comprised of a machined aluminum extrusion, bi-metal joint, thermal insulation, and a flange/bellows assembly (Fig. 5).

The chamber's manufacturing challenges are the nominal wall thickness of 400 microns along the length of the extrusion, accommodating the small operating gap of the

SCU magnets, a brazing step for the chamber-end sub-assemblies, and the welding step of the aluminum from the bi-metal piece to the extrusion. Due to the specialized fabrication challenges, many vendors were vetted for their capabilities. Utilizing a domestic vendor was advantageous for oversight for the complex scope, although sample machining of the thin wall feature on a small length part was proven in past prototyping [3]. This resulted in the work being sole-sourced to Anderson Dahlen for the FA.

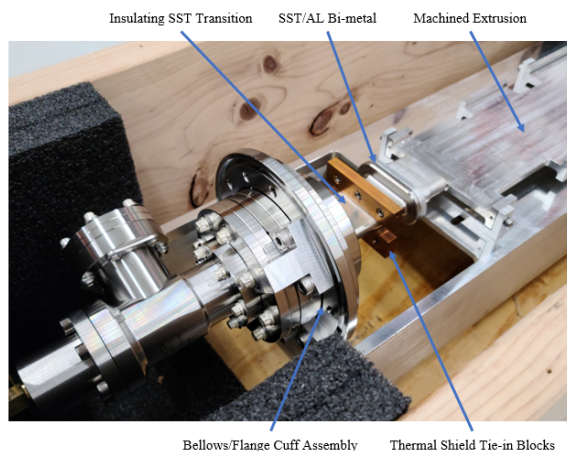


Figure 5: FA inline SCU VC weldment.

The FA fabrication was broken into three Purchase Orders for one vendor, (1) best effort machining of the thin wall of the extrusion, (2) brazing and welding the supplemental components at either end of the extrusion, and (3) welding the end sub-assemblies (copper blocks, stainless-steel (SST) insulator, and flange/bellows weldment). The FA weldment was completed in-spec and resulted in the remaining 3 weldments, with slightly modified geometry for the 2 canted chambers, to be awarded to Anderson Dahlen as well. While this is a significant amount of work for one vendor and leads to longer lead times, the quality and functionality of the end-product is the most critical factor.

SCU Out-of-Cryo Vacuum System

The FA out-of-cryo chambers have been produced by Cinel Instruments (June 2019) (Fig. 6). These are the smallest of the VCs in an ID straight section, but critical as they act as inline absorbers for synchrotron radiation, protecting the In-Cryo system and downstream equipment [3].

The vendor produced these components with minimal difficulty. The manufacturing process included preliminary machining of the copper, brazing SST collars to the copper, and welding SST flanges to these collars. Both US and DS require integrating a water-cooling channel to dissipate heat during operation. In addition to the vacuum processes previously discussed for the other systems, this feature required hydrostatic testing to 225 psi.

The scope of work also included producing the support assemblies that suspend from the cryostat and accommodate the VCs, vacuum equipment, and canting magnets (in canted configurations). The vendor delivered the FAs and production units fully assembled, ready for assembly to the cryostat [3].



Figure 6: DS VC undergoing inspection.

The fabrication processes for both the chambers and supports were straight forward and allowed the activities to remain on-schedule. The production units arrived at ANL in December of 2020. Even for simple components like these, the FAs allowed APSU to perform functional testing, resulting in support of the final design report analyses.

CONCLUSIONS

The APSU straight section vacuum systems have gone through the FA fabrication process, proving the validity of the designs, and allowing functional testing to be performed prior to full-scale production. Functional tests from each of the vendors, in addition to onsite testing, has resulted in confidence that the production units will arrive onsite, ready for installation.

ACKNOWLEDGMENT

This research used resources of the Advanced Photon Source, a U.S. Department of Energy (DOE) Office of Science User Facility at Argonne National Laboratory and is based on research supported by the U.S. DOE Office of Science-Basic Energy Sciences, under Contract No. DE-AC02-06CH11357.

REFERENCES

- [1] APSU *et al.*, “APS Upgrade Project Final Design Review Report,” APS, Illinois, United States, Rep. APSU-2.01-RPT-003, May 2019.
- [2] J. Lerch *et al.*, “APSU upgrade insertion device vacuum chamber design”, in *Proc. NAPAC2019*, Lansing, MI, USA, September 2019, pp. 450-452. <https://doi.org/10.18429/JACoW-NAPAC2019-TUPLS02>
- [3] M. Szubert *et al.*, “The design of the Advanced Photon Source upgrade superconducting undulator vacuum systems”, in *Proc. NAPAC2019*, Lansing, MI, USA, September 2019, pp. 453-455. <https://doi.org/10.18429/JACoW-NAPAC2019-TUPLS03>
- [4] J. Lerch *et al.*, “Overcoming Challenges during the Insertion Device Straight Section Component Production and Tuning Phase of the Advanced Photon Source Upgrade”, presented at the 11th Int. Conf. on Mechanical Engineering Design of Synchrotron Radiation Equipment and Instrumentation (MEDSI2020), Chicago, IL, USA, July 2021, paper MOOA01, this conference.
- [5] E. Anliker *et al.*, “A new superconducting undulator cryostat for the APS upgrade”, *IOP Conf. Ser.: Mater. Sci. Eng.*, vol. 755, p. 012126, 2020. <http://dx.doi.org/10.1088/1757-899X/755/1/012126>

AUTOMATED MECHANICAL INSPECTION AND CALIBRATION OF INSERTION DEVICES IN APS STORAGE RING*

N. Weir[†], E. Gubbels, Advanced Photon Source, Argonne National Laboratory, Lemont, IL, USA

Abstract

A novel technique has been developed to automatically inspect and calibrate the 53 permanent magnet insertion devices in the Advanced Photon Source (APS) storage ring. This technique employs standard frequency domain analysis to create easily identifiable signatures in an actionable format. We will discuss the mechanisms and actions taken behind various observed trends and its application for continuous monitoring and predictive maintenance of these devices. This technique has enabled predictive maintenance and provided new insights into optimizing device performance.

INTRODUCTION

Hybrid permanent magnet undulator (HPMU) insertion devices require reliable micron level accuracy and precision during operation [1]. Many of the devices have been in service for more than 25 years. Each of these devices have four or more drivetrains totalling to over 212 in operation. The continuous operation and radiation environment of the APS storage ring presents unique challenges for maintenance. To ensure the reliability of devices, manual measurements at common points of operation and regular preventative maintenance are performed during the available triannual “shutdowns”. While this provides a sanity check and adheres to manufacturers’ recommended maintenance schedule, it does not effectively prevent or provide insight to commonly occurring issues during operation. To enable a more efficient, comprehensive, and data-driven solution, a program to perform automated inspections was written.

Positioning of the upper and lower magnetic support structures (strongbacks) are each controlled by two individual drivetrains. Though they are controlled and operated individually, each of these two drivetrains are coupled through their shared connections with the upper or lower strongback. This coupling action can lead to a constructive amplification of errors in each drivetrain. Additionally, the drivetrain and feedback systems are inset from the end of the strongback. Small angular changes in the orientation of the strongback due to small errors in the drivetrain system will be magnified over the length of the strongback, leading to larger uncertainty in the exact position of the ends of the magnetic structures. These magnification effects make it crucial to identify and eliminate preventable errors in the drivetrain.

The most common faults during operations in order of occurrence is overtravel limit trip, extreme limit trip, motor stall, linear encoder failure, and rotary encoder failure. The overtravel switches are often set within 100 μm of the usable gap to balance machine safety and user reliability. Given that these switches are located at the ends of the strongback, the mechanical inaccuracies present are significantly amplified. Without quantitative characterization, reasons for the fault are difficult to troubleshoot due to the initial switch setting, start of travel position, and travel end positions all being factors in the diagnosis. The other faults can be equally difficult to diagnose due to the mechanical, electrical, and software components involved.

METHOD

Each HPMU contains a redundant set of feedback devices meant to maintain operation in case one fails; a rotary encoder directly coupled to the motor and a linear encoder directly coupled between the static frame and strongback. The rotary encoder uses a hard coded relationship between turns of the motor and physical position of the strongback to extrapolate its position. The linear encoder directly measures the position of the strongback. Errors in the drivetrain system (Fig. 1) that controls the strongback will therefore present themselves as an accumulated discrepancy between the rotary feedback and linear feedback. By analysing the discrepancy as a function of actual gap, a complete characterization of the drivetrain and crosschecking between the encoders can occur.

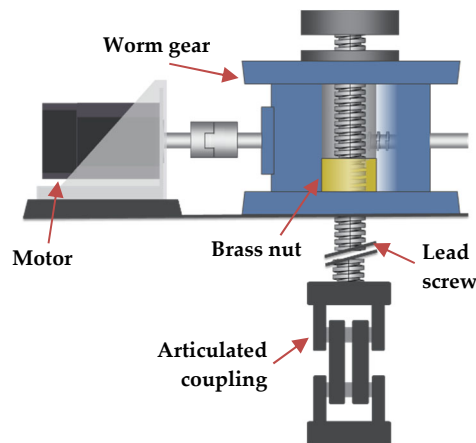


Figure 1: The drivetrain of an APS undulator device consists of a motor coupled to a 60:1 worm gear assembly. Motion is transferred to a lead screw, which is threaded through a bronze nut and connected directly to the strongback via an articulating coupling.

A python script sequentially commands each of the 53 insertion devices installed in the APS storage ring to move at a slow speed while oversampling the position readback

* This research used resources of the Advanced Photon Source, a U.S. Department of Energy (DOE) Office of Science User Facility at Argonne National Laboratory and is based on research supported by the U.S. DOE Office of Science-Basic Energy Sciences, under Contract No. DE-AC02-06CH11357.

[†] nweir@anl.gov

from each encoder. These data are collected using EPICS and device specific information needed for data processing is pulled from the Component Database (CDB) [2]. The oversampled position data from the rotary and linear encoders are subtracted from each other. Any mismatch due to the non-synchronicity of the data collection is accounted for by interpolation. The plot shown in Fig. 2 is then generated.

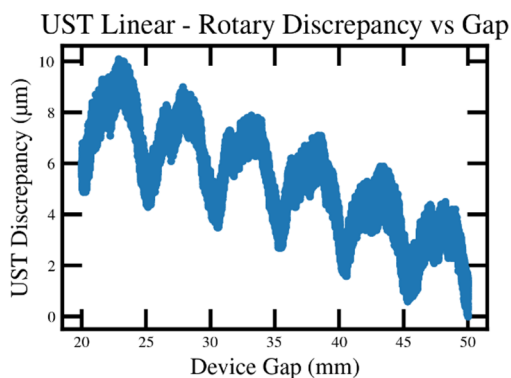


Figure 2: The discrepancy between linear and rotary encoder gap readings can illustrate mechanical error or defects in the system. Here, a repeating curve with a period of ~5 mm and an amplitude of ~6 µm.

The plot in Fig. 2 contains valuable information both at the 1 mm scale and the 1–10 µm scale. A standard fast Fourier transform (FFT) and power spectral density (PSD) analysis is performed to identify and extract meaningful signals in the discrepancy data shown in Fig. 3. Special attention is given to the frequencies that correspond to the characteristic periodicities of certain components in the drivetrain known to affect the accuracy of the positioning system. Table 1 lists the components in question along with their expected contribution to the accumulated drivetrain error when they are manufactured and installed within pre-defined tolerances.

Table 1: Expected contribution and repetition cycle of various drivetrain components based on manufacturing and installation tolerances.

Component	Repetition Distance [µm]	Amplitude [µm]
Rotary Feedback	84.67	<< 1
Motor Coupling	84.67	< 1
Worm Drive	5080	< 3
Leadscrew / Nut	5080	< 4
Linear Encoder SDE	64	< 4

One revolution of the components positioned before the worm gear corresponds to 1/60 of a revolution of the lead-screw. The magnitude of their expected errors should then be reduced by a factor of 60, making them a negligible contribution to the total error. Spectral analysis, therefore, concentrates on the frequencies $1/5080 \mu\text{m}^{-1}$ and $1/64 \mu\text{m}^{-1}$ and their related harmonics.

Accelerators

Insertion Devices

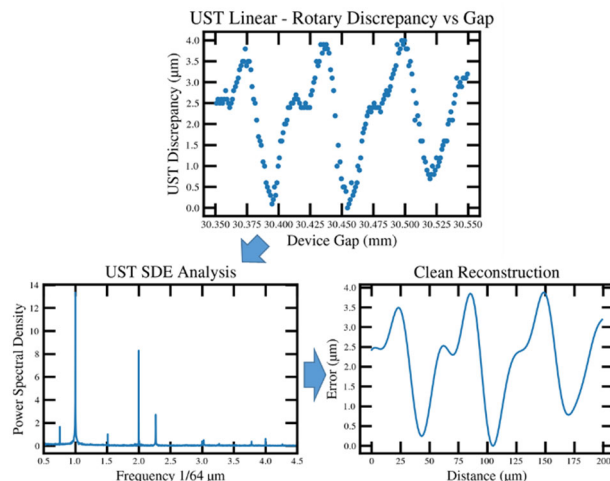


Figure 3: Frequency domain analysis can extract meaningful signals from the data and give information about the behaviour of components in the system. Signals can then be reconstructed from spectral information leading to a cleaned version of the original data. This cleaned data/fit can then be used for acceptance criteria and can automated acceptance testing. The plots shown are specifically looking at the SDE of the linear encoder which occurs every 64 µm.

The generated plots are consolidated on an easy to review report generated in HTML for each of the 53 devices. The use of HTML enables the ability for it to be hosted for others to view and makes it more intuitive to navigate. A summary is also included on the report of the settings used during data collection.

RESULTS

Over the past year this technique has enabled the finding of the following otherwise undetected issues: six devices with worn-out compensation springs, four preliminary rotary encoder failures, four linear encoder failures, and over 10 encoder alignment/tuning errors. Most importantly it provided a baseline expectation of dynamic device performance. This baseline led to quick pinpointing of mechanical errors in each device which has provided critical time savings for minimizing onsite personnel during the COVID-19 pandemic. In addition, it provided a baseline of comparison for the new construction of devices for APS-U catching manufacturing/assembly errors. Figure 4 shows two of the detected issues mentioned above.

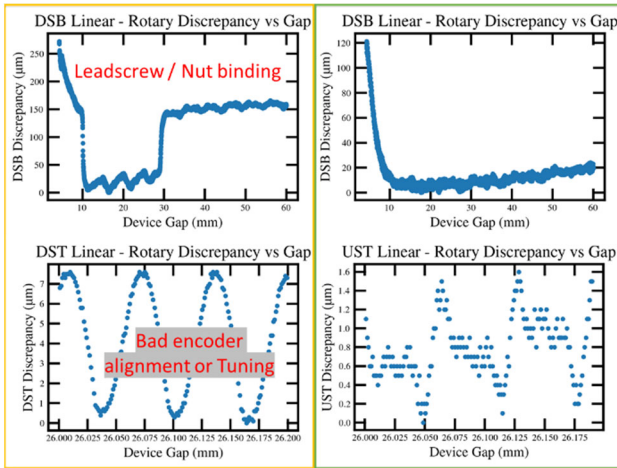


Figure 4: Plots on the left show devices out of tolerance with the cause in red. Plots on the right are for reference of what they should look like.

FUTURE WORK

Further improvements can be made by incorporating machine learning for anomaly detection and automatically classifying common defects. A more user-friendly version is currently in the works for use in other areas in the APS where insertion devices are being worked on. In addition, it is planned to incorporate the auto-calibration of linear

encoders into APSU ID motion control system to provide better gap accuracy for the users.

CONCLUSION

A new technique to better monitor and provide insight to the insertion devices installed in the APS storage ring has been developed and successfully tested. This technique has provided great value to operations enabling predictive maintenance and improved insight to device performance. This has been of great value during the COVID-19 pandemic as this enabled devices to be more efficiently diagnosed and be comprehensibly monitored remotely.

ACKNOWLEDGEMENTS

This research used resources of the Advanced Photon Source, a U.S. Department of Energy (DOE) Office of Science User Facility at Argonne National Laboratory and is based on research supported by the U.S. DOE Office of Science-Basic Energy Sciences, under Contract No. DE-AC02-06CH11357.

REFERENCES

- [1] E. M. Trakhtenberg *et al.*, “A new gap separation mechanism for APS insertion devices”, in *AIP Conference Proceedings* (521), 13 Mar. 2001, pp. 363. doi: 10.1063/1.1291816
- [2] S. Veseli *et al.*, “Component Database,” *APS Upgrade*, 2017, <https://cdb.aps.anl.gov/>.

A COMPARISON OF FRONT-END DESIGN REQUIREMENTS

S. Sharma[†], NSLS-II, Brookhaven National Laboratory, Upton, NY, USA

Abstract

Front ends of the NSLS-II storage ring have numerous design requirements to ensure equipment and personal safety aspects of their designs. These design requirements, especially many pertaining to raytracings, have gradually become overly stringent and a review is underway to simplify them for building future front ends. As a part of this effort, we have assembled the front-end design requirements used in several other light sources. In this paper the assembled design requirements are discussed in comparison with those currently in use at NSLS-II.

INTRODUCTION

Front ends are used to control the size of photon and gas bremsstrahlung beams traversing from the storage ring to the users' beamlines. At NSLS-II there are presently 17 front ends for insertion device (ID) beamlines and 6 front ends for BM (bending magnet or 3-pole wiggler) beamlines. A typical ID front end [1] is shown in Fig. 1. Its main components are, (1) XBPM, (2) fixed aperture mask (FM), (3) lead collimators (LCO), (4) a pair of XY slits, (5) photon shutter (PS), (6) safety shutters (SS), and (7) ratchet wall collimator (RCO). The components that trim or stop the bremsstrahlung beam, namely, LCO, SS and RCO, are classified as PSS (personnel safety system) components and the remaining as EPS (equipment protection system) components.

The design of NSLS-II front ends is deemed to be too conservative, in part due to a very stringent approach to raytracings involving PSS components, and to the requirement of minimizing the size of bremsstrahlung beam. For the new front ends, presently in the planning stage, some simplified design criteria are being evaluated. As a part of this evaluation, front end design criteria collected from several light source facilities (APS-U, ALS-U, CLS, DLS, ESRF(EBS), HEPS, SOLEIL, SSRF and TPS) are compared with those used at NSLS-II. The focus of this

comparison is on source definitions of photon and bremsstrahlung beams, and thermal fatigue design criteria.

FRONT END CONFIGURATIONS

Front-end configurations of different facilities mentioned above are quite similar except that XBPMs, XY slits and LCOs are not considered to be required components. XBPMs are not installed in ALS-U and most of the NSLS-II ID front ends to save space and/or cost. XY slits are not available in APS-U, ESRF(EBS) and SSRF front ends. In general, LCOs (to trim the bremsstrahlung beam) are not installed in the front ends of DLS, ESRF and TPS. A second SS for redundancy is used only at NSLS-II, APS-U, CLS and DLS. Vacuum pressure gages in the front ends of all facilities are interlocked to dump the stored beam. Thermal sensors are also used at ALS-U, HEPS, SSRF, Soleil, and DLS, although they are not interlocked in some cases. Trimming of un-interlocked photon beams by burn-through devices (explained below) is done only at NSLS-II and APS-U front ends. Only one of the facilities, (ALS-U), employs a sweeper magnet as safety against accidental entry of the injected e-beam into the front end.

RAYTRACINGS

Raytracings for both the photon and bremsstrahlung beams are critical part of the front-end design process at NSLS-II and a considerable design effort is devoted to generating formal raytracing drawings. The drawings are usually revised iteratively in order to optimize the apertures, lengths, and locations of the various front-end components.

Photon Beam Sources

Source definitions for raytracings consist of 3 parts, namely, (1) e-beam deviations, (2) location of the source in Z (along the beam) direction, and (3) fan angles of the device (defined by K and γ parameters) at the source point.

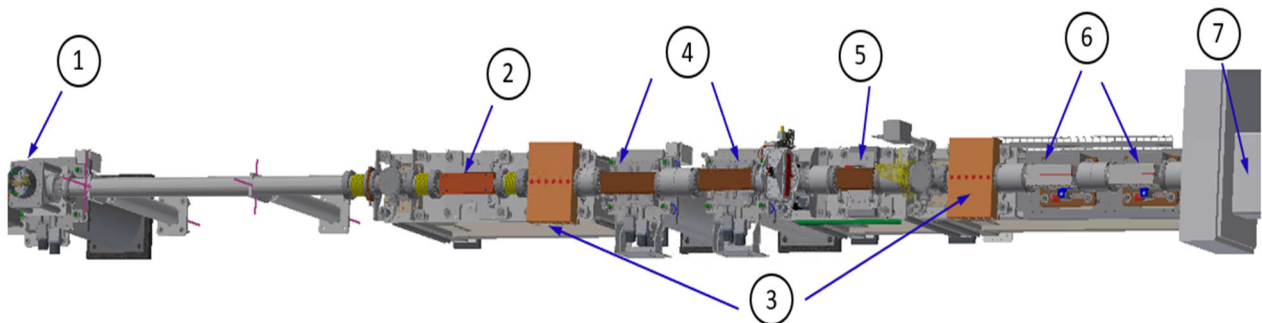


Figure 1: A typical NSLS-II ID front end; (1) XBPM, (2) fixed aperture mask (FM), (3) lead collimators (LCO), (4) XY slits, (5) photon shutter (PS), (6) safety shutters (SS), and (7) ratchet wall collimator (RCO).

[†] sharma@bnl.gov

E-beam deviations are controlled by active interlocks that use RF-BPMs installed at the upstream (US) and downstream (DS) ends of the ID straight sections. The displaced positions of the beam at the two ends determine its angle when it is not specified explicitly. Interlock specifications are carried over to BM source locations in some facilities whereas in other facilities, including NSLS-II, they are assumed to be inapplicable. In the latter case the beam is constrained by the geometry of the vacuum chamber (geometric envelope, GE). For photon beam raytracings the e-beam deviations used at different light sources are summarized in Table 1.

Table 1: E-beam Deviations for Photon Beam Raytracings

Facility	ID front end		BM front end	
	Position ± (mm)	Angle ± (mrad)	Position ± (mm)	Angle ± (mrad)
NSLS-II	0.5	0.25	GE	GE
ALS-U	1.0	0.2	1.0	0.2
APS-U	1.5 (H) 1.0 (V)		GE	GE
CLS	2.5 (H) 1.6 (V)		1.6 (H) 2.5 (V)	
DLS	1.0		2 (H) 4 (V)	3 (H) 0.5 V
ESRF	1.0		3 (H) 2 (V)	
HEPS		0.1		0.1
SOLEIL	0.8		0.5	0.5
SSRF		0.5 (H) 0.2 (V)	5 (H) 2 (V)	
TPS	1.0 (H) 0.2 (V)		GE	

For personnel safety components (vacuum chambers of LCO, SS and RCO), e-beam is assumed to be not interlocked at NSLS-II and APS-U in order to provide additional margin of safety. Geometric envelopes (GE) are then used to determine e-beam deviations. The resulting large angles are stopped by burn-through devices in the case of interlock failure. At NSLS-II burn-through flanges (BTF) are used upstream of LCOs and RCO. The basic concept is shown schematically in Fig. 2. The photon beam outside the interlock limits will first strike the thin wall of the BTF (in the case FM has failed) causing local melting and a beam dump due to air leak.

The source location for ID front ends is the center of ID straight. At NSLS-II and TPS, the ends (US and DS) of the ID straight are also used to determine the worst conditions of beam interception. For the BM frontends the source location is tangent intersect of the beamline to the e-beam trajectory, usually several mrad inside the dipole.

Source fan angles and mechanical tolerances are included in raytracing drawings at TPS and NSLS-II. Moreover, this is shown by separate rays in the NSLS-II drawings which, consequently, consist of a large number of lines.

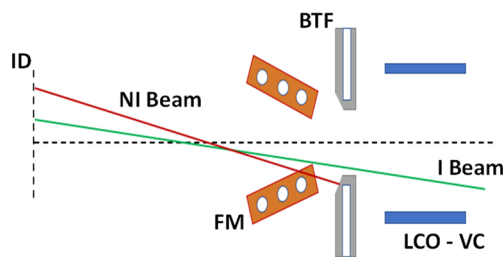


Figure 2: NSLS-II burn-through flange (BTF) concept. BTF stops photon beam outside the interlock limits (NI beam) to protect LCO vacuum chamber (VC). Upstream FM shadows BTF from interlocked beam (I beam).

Bremsstrahlung Radiation Sources

Transversely the entire cross-section of the storage ring vacuum chamber aperture (excluding antechamber) is specified to be the source size for gas bremsstrahlung. At NSLS-II and APS-U an exception to this source size is used in the radially inward direction in that the bremsstrahlung source is extended to the entire storage ring. In both the facilities LCOs (in addition to RCO) are then used to trim the resulting large angles of bremsstrahlung rays.

For ID front ends, the bremsstrahlung source is located at the center of the ID straight (APS-U, SSRF, Soleil, ESRF, DLS), or at the end of the ID straight (NSLS-II, HEPS), or at the US end of the first downstream bending magnet (ALS-U, CLS, DLS). For the BM front ends the bremsstrahlung source location is at the upstream end of the dipole with some exceptions, namely, at the BM source point (APS-U, CLS, DLS), and at the center of drift space after a specific magnet, DQ2 (ESRF).

The designs of SS are generally based on tungsten blocks, which are placed inside vacuum vessels (in-vacuum design), acting as bremsstrahlung beam stops. A second SS for redundancy is used at NSLS-II, APS-U, CLS and DLS. There are two exceptions to this common design: (1) lead bricks (instead of tungsten) are used at ESRF and NSLS-II as bremsstrahlung stops, (2) lead bricks are placed outside the vacuum chamber (out-of-vacuum design) in the NSLS-II design (Fig. 3). The NSLS-II design is passively safe in the sense that photon beam power cannot strike the lead block without first breaching upstream bellows which would result in a beam dump.

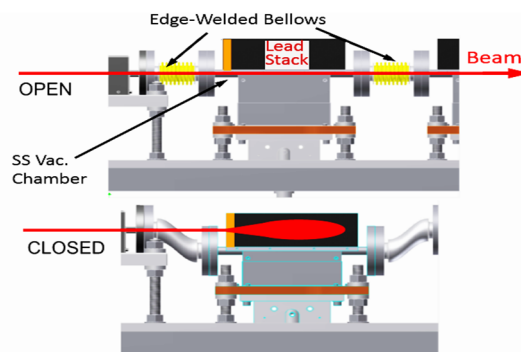


Figure 3: NSLS-II out-of-vacuum design of SS. In the closed position the bremsstrahlung beam is stopped by a stack of lead bricks.

DESIGN CRITERIA FOR FRONT-END EPS COMPONENTS

In some earlier designs [2], the EPS components (FM, and PS) were placed inside vacuum vessels. With some legacy exceptions (PS in the ID front ends of ALS and in the BM front ends of ESRF), all facilities are using out-vacuum designs for FM, PS and XY slits. Recently a new design was proposed [3, 4] based on CuCrZr flanges (or Conflat® knife-edges) integrated into the main body as shown in Fig. 4. Two of the main advantages of this design are: (1) elimination of the brazing step, and (2) wide availability of CuCrZr compared to GlidCop.

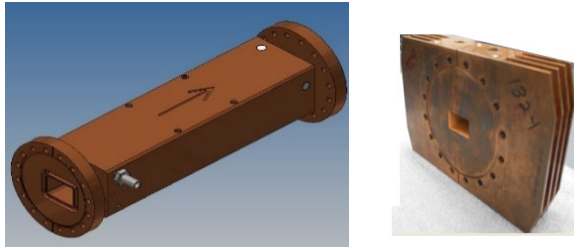


Figure 4: A high-power CuCrZr mask with integrated flanges (left), and an air-cooled, low-power, CuCrZr mask with integrated knife edges (right).

The new CuCrZr design is now used for essentially all new front ends at NSLS-II. GlidCop is used only for beryllium windows which require high-temperature diffusion brazing. CuCrZr has also been partially adopted at several other facilities, often with more conservative design criteria. In Table 2, design criteria for different Cu alloys, specified as maximum allowable values of temperature (T), von Mises stress (σ_y), or plastic strain (ϵ_p), are compared. The specified values differ significantly due in part to a lack of experimental data. Recently some thermal fatigue tests and analyses [5-7] have been performed to address this for GlidCop.

Table 2: Maximum Allowable Values of Temperature, von Mises Stress and Plastic Strain

Facility	Copper Alloys		
	OFHC Cu	GlidCop	CuCrZr
NSLS-II		300 °C + T_{amb}	300 °C + T_{amb}
ALS-U	300 °C 300 MPa	400 °C 430 MPa	
APS-U	200 °C	375 °C	250 °C
CLS	150 °C	300 °C	200 °C
DLS	400 °C $\epsilon_p < 0.5\%$	400 °C $\epsilon_p < 0.5\%$	
ESRF-EBS	200 °C	200 °C	250 °C 280 MPa
HEPS		400 °C	
SOLEIL	0.75 σ_{yield}	0.75 σ_{yield}	
SSRF	150 °C 340 MPa	300 °C 400 MPa	
TPS	150 °C	300 °C	200 °C

CONCLUSION

Front end design criteria for several light source facilities have been compared with those used at NSLS-II. Uninterlocked e-beam deviations for PPS components (LCO, SS and RCO), and expanded source locations for photon and bremsstrahlung fans have resulted in more conservative but elaborate designs at NSLS-II. The new design for EPS components (FM, PS and XY slits), based on CuCrZr bodies with integrated flanges, has been adopted at several facilities. A comparison of thermal design criteria for three copper alloys (OFHC Cu, GlidCop and CuCrZr) shows a wide range in maximum allowable values of temperature and stress.

ACKNOWLEDGEMENTS

This work was supported by the US Department of Energy under contact No. SC0012704.

The author gratefully acknowledges information provided by and discussions with the staff members of several facilities: ALS-U (I-C Sheng) APS-U (M. Ramanathan), CLS (C. Mullin), DLS (N. Hammond, X. Liu), ESRF (J-C Biasci), HEPS (P. He), Soleil (J. Castro, V. Leroux, K. Tavakoli), SSRF (Y. Li) and TPS (C-K Kuan). Thanks are also due to his colleagues at NSLS-II: M. Breittfeller, F. DePaola, L. Doom, M. Johanson and F. Lincoln.

REFERENCES

- [1] L. Doom *et al.*, "Front-end design of National Synchrotron Light Source II," *Diamond Light Source Proceedings*, vol. 1, p. e31, doi:10.1017/S2044820110000195
- [2] D. Shu *et al.*, "Front end designs for the 7-GeV Advanced Photon Source," *Nucl. Instrum. Methods Phys. Res., Sect. A*, vol. 319, pp. 63-70, 1992.
- [3] Sharma *et al.*, "A novel design of high-power masks and slits," in *Proc. MEDSI2014*, Melbourne, Australia, 2014.
- [4] M. Hussain, "Bending magnet and 3-pole wiggler frontend design," in *Proc. MEDSI2014*, Melbourne, Australia, 2014.
- [5] V. Ramanathan *et al.*, "Thermal fatigue life prediction of GlidCop Al-15," in *Proc. MEDSI2006*, Hyogo, Japan, 2006.
- [6] S. Takahashi *et al.*, "Fatigue life prediction for high-heat-load components made of GlidCop by elastic-plastic analysis," *J. Synchrotron Radiat.*, vol. 15, pp. 144-150, 2008.
- [7] J. Collins *et al.*, "Results from studies of thermomechanical-induced fatigue in GlidCop," in *Proc. MEDSI2014*, Melbourne, Australia, 2014.

MECHANICAL DESIGN OF A SOFT X-RAY BEAM POSITION MONITOR FOR THE COHERENT SOFT X-RAY SCATTERING BEAMLINE

C. Eng, D. Donetski¹, J. Liu¹, S. Hulbert, C. Mazzoli, B. Podobedov
 Brookhaven National Laboratory (BNL), ¹Stony Brook University (SBU)

Abstract

Achieving photon beam stability, a critical property of modern synchrotron beamlines, requires a means of high resolution, non-invasive photon beam position measurement. While such measurement techniques exist for hard x-ray beamlines, they have yet to be achieved for soft x-ray beamlines. A new soft X-ray beam position monitor (SXBPM) design based on GaAs detector arrays is being developed and will be installed in the first optical enclosure of the Coherent Soft X-ray Scattering (CSX) beamline at the National Synchrotron Light Source II (NSLS-II).

The SXBPM assembly contains four water-cooled blade assemblies, each of which will have a GaAs detector assembly mounted within it, that can be inserted into the outer edges of the CSX undulator beam with sub-micron accuracy and resolution. The primary challenges in design of the SXBPM include: 1) mechanical stability of the assembly, 2) management of the heat load from the undulator x-ray beam to protect GaAs detector assemblies from unwanted illumination, 3) assembly compactness to fit within the first optical enclosure (FOE) of the CSX beamline, and 4) accessibility for modifications. Balancing the unique design requirements of the SXBPM along with their associated constraints has resulted in the design of a non-invasive beam position monitor which will be installed in the CSX FOE as a prototype for testing and iterative improvement. The ultimate goal is development of a widely useful SXBPM instrument for soft X-ray beamlines at high brightness synchrotron storage ring facilities worldwide.

INTRODUCTION

Quality of data produced by the beamline is highly dependent on their soft x-ray beam control: both high positional beam stability and wavefront control are required at the sample position. In this respect, diagnostics such as Beam Position Monitors (BPMs) are a critical tool for evaluating and controlling photon beam delivered by modern highly coherent sources. Photoemission blade based BPMs work well for white beams of considerable power, while diamond x-ray BMS in transmissive geometry have proved effective for hard x-ray monochromatic beams. However, none of the above are ideal for soft coherent undulator sources, where a non-invasive device with high spatial resolution is needed. Stringent limitations come from intrinsic characteristics of the soft sources (halo extent, coherence of soft cone in the center of the undulator emission) and from the limited transmissive power of soft x-rays in materials.

Additionally, an optimal BPM design should permit positioning of the blades as far possible from the undulator central cone to preserve the wavefront coherence of the usable fraction of the beam. The BPM design described herein uses arrays of 1D strips of pixelated GaAs detectors mounted on adjustable blades that are inserted partially into the beam to intercept only the outer edge of the beam [1]. The SXBPM will be installed inside the FOE of the CSX beamline (Fig. 1) for ease of access to facilitate testing and development. Following commissioning and testing of this prototype, a subsequent “production” version is envisioned to be developed for placement in beamline front ends.

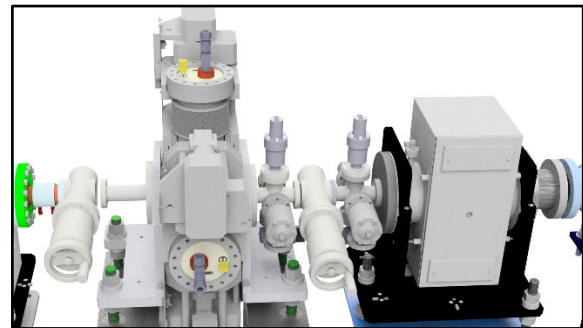


Figure 1: Rendering of the SXBPM installed in the CSX FOE as a separate section to facilitate replacement and reconfiguration of the detector assemblies.

DESIGN REQUIREMENTS

The SXBPM’s primary function is to non-invasively monitor the position of the soft x-ray beam upstream of the first optics element using novel GaAs detector arrays. As a beam position monitor, the device must be stable and support sub-micron scale resolution positioning of the detector arrays, while providing a stroke/travel range sufficient to remove the detector arrays completely from the photon beam. Additionally, the SXBPM requires accessibility in order to facilitate reconfiguration or replacement of the detector arrays for testing (Fig. 2). The selected location for the SXBPM is upstream of the first optics element of the CSX (23-ID) beamline, necessitating careful consideration for handling the heat load.

DESIGN OVERVIEW

The GaAs detector arrays will be mounted on the ends of 4 water-cooled blades consisting of OFHC copper. To protect the vulnerable parts of the detector arrays from excessive heating, a tungsten plate is mounted in front of each assembly. On the beam-facing edge of the tungsten plate, an array of laser-drilled 30 micron diameter holes

permit a limited amount of radiation to reach the detector (Fig. 3). A thermocouple will be affixed to the tungsten aperture plate to monitor the temperature of the device.

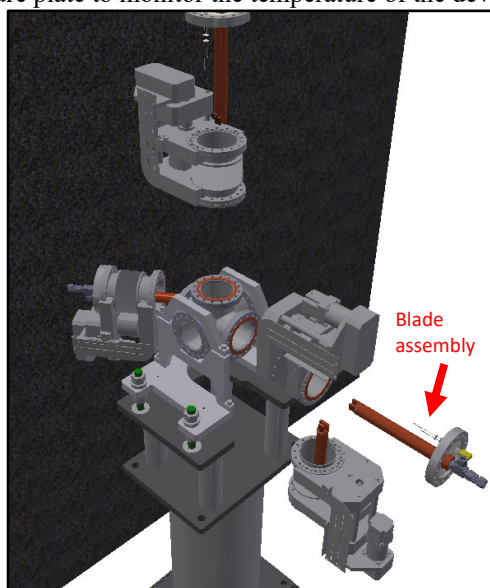


Figure 2: The SXBPM is designed to permit replacement, in-place, of each of the flange assemblies.

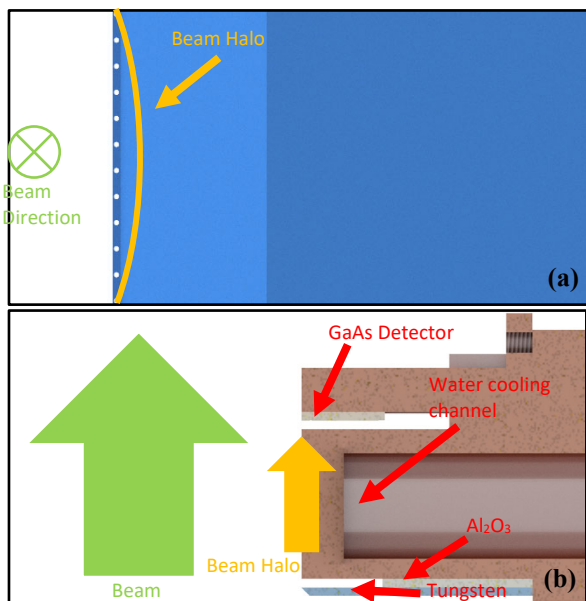


Figure 3: The tungsten heat shield, shown with the halo of the beam represented by the red line (a), is placed in front of an alumina (Al_2O_3) insulating element and the GaAs detector array (b).

The blade assembly is welded to a flange that also provides feedthroughs for cooling water and electrical connections for thermocouples and detector readout, forming a detector assembly. The four detector assemblies are mounted to bellows-coupled stepper-motor-driven linear manipulators, thus eliminating the need for relative motion of the components of each detector assembly internal to the vacuum vessel and obviating the need for any water connections in-vacuum. The linear manipulators enable sub-micron positioning of the detector arrays over a

Beamlines and front ends

Optics

25 mm travel range, permitting complete retraction of the detectors out of the beam (Fig. 4).

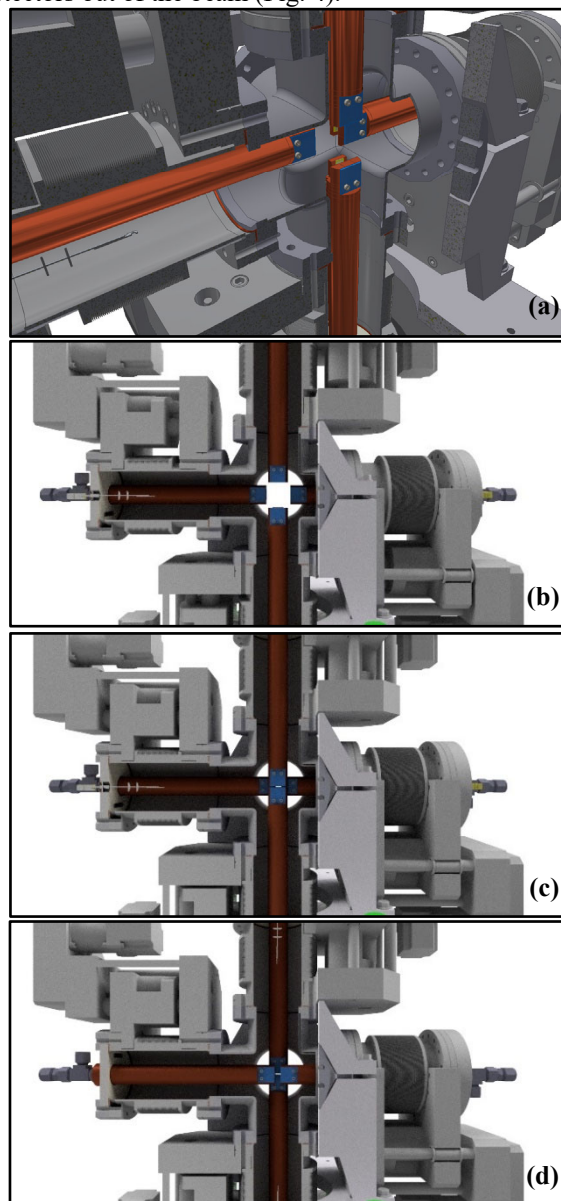


Figure 4: The SXBPM (a) consists of 4 separate blade flanges that can be extended into the beam and retracted out of the beam fully (viewed from the incoming beam direction) (b) and can be configured in either v-h configuration (vertical pair before horizontal pair) (c) or h-v configuration (d) by removing and repositioning the flange assemblies.

Simulations of the thermal load on the device are used to guide the design of the blade assemblies themselves (Fig. 5). Transient analysis is used to determine how quickly critical components of the detector, most notably the detector arrays themselves, reach maximum operating temperature under different conditions considering how much of the beam profile is intercepted. The maximum power density for the CSX undulator is approximately 20 W/mm^2 . However, the 23-ID canted straight section contains another identical undulator upstream. Therefore,

the worst-case scenario of approximately 35 W/mm² is achieved for the inline configuration of two undulators, each set at the minimum gap. In addition to the intended sampling of the extreme edges of the beam, the worst-case scenario in which the blade intercepts the full beam profile (error condition), has been considered.

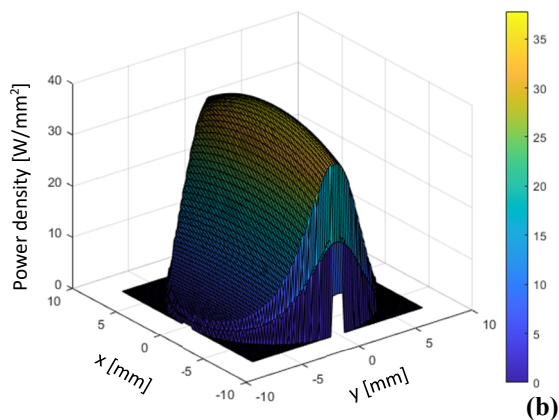
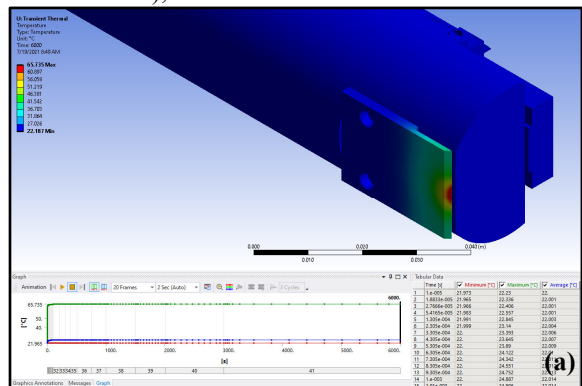


Figure 5: Design iterations are guided using thermal analysis (a) simulating thermal loading of the intercepted beam from the two undulators (b).

Operation of the SXBPM will consist of inserting the detector arrays into the halo of the beam while allowing unperturbed propagation of the soft part of the beam residing in the core, through to the beamline. The device will be integrated into the Equipment Protection System (EPS) to mitigate the possibility of intercepting full beam and consequent damage or destruction of the detector assembly via excessive thermal loading. Acceptable threshold values will be determined by thermal analysis which would trigger the retraction of the blade assemblies completely out of the beam. Additionally, a combination of mechanical hard stops, limits, and software controls will be used to monitor the position of the detector assemblies and prevent collisions.

CONCLUSION

A GaAs detector based, non-invasive, sub-micron resolution soft x-ray BPM has been developed and will be installed and tested at the CSX beamline. Successful demonstration of the SXBPMs capabilities will pave the way for future installations at new and existing soft x-ray beamlines, especially for coherent soft x-ray beamlines.

REFERENCES

- [1] J. Liu *et al.*, “Progress towards soft x-ray beam position monitor development”, in *Proc. IPAC’21*, Campinas, SP, Brazil, virtual conference, May 2021, paper MOPAB121, to be published.

DIAMOND REFRACTIVE OPTICS FABRICATION BY LASER ABLATION AND AT-WAVELENGTH TESTING

S. Antipov†, E. Gomez, Euclid Techlabs LLC, Bolingbrook, IL, USA
R. Celestre, T. Roth, European Synchrotron Radiation Facility, Grenoble, France

Abstract

The next generation light sources will require x-ray optical components capable of handling large instantaneous and average power densities while tailoring the properties of the x-ray beams for a variety of scientific experiments. Diamond being radiation hard, low Z material with outstanding thermal properties is proposed for front-end pre-focusing optics applications. Euclid Techlabs had been developing x-ray refractive diamond lens to meet this need. Standard deviation of lens shape error figure gradually was decreased to sub-micron values. Post-ablation polishing procedure yields $\sim 10\text{nm}$ surface roughness. In this paper we will report on recent developments towards beamline-ready lens including packaging and compound refractive lens stacking. Diamond lens fabrication is done by femto-second laser micromachining. We had been using this technology for customization of other beamline components.

INTRODUCTION

Significant increase in average synchrotron beam brightness is projected for numerous facilities as they upgrade to diffraction limited storage rings. For ultrafast experiments, x-ray free electron lasers produce 10 orders of magnitude larger peak brightness than storage rings. It is therefore extremely important to develop next generation x-ray optics for these new light sources. Diamond is a "go to" material for high heat load applications. Single crystal diamond is an excellent material for x-ray optics due to its high x-ray transmissivity and uniform index of refraction [1]. For compound refractive lens (CRL) application there is an additional benefit from the single crystal material of choice for the lens because small angle reflections on defects and voids, typical for polycrystalline materials, are minimized and the x-ray beam quality is preserved [2, 3].

It is, however, a challenging task to manufacture complex shapes out of diamond. We use femtosecond laser cutting technology to manufacture a compound refractive lens, the most popular x-ray optics element, from a single crystal diamond. A femtosecond laser pulse duration is extremely short: material is ablated while pulse heating effects are minimized. In the past 3 years we have developed a fs-laser ablation procedure that yields diamond refractive parabolic lenses with shape error of $0.8\ \mu\text{m}$ r.m.s. with surface roughness on the order of 200-300 nm Ra and polishing procedure that brings surface roughness into 10-20 nm Ra region but increases the figure error to $1.4\ \mu\text{m}$ r.m.s.

DIAMOND LENS FABRICATION

For diamond lens production we developed a femto-second laser ablation system. It consists of a fs-laser operating at the second harmonic (515 nm), a motorized lens that allows moving the position of the focal spot $\pm 2\ \text{mm}$ and a set of computer-controlled mirrors paired with a large aperture final-focus lens. Using this setup a laser beam can be steered at large speeds in the focal plane of the lens. The work surface is mounted on a linear stage for sample examination under a microscope for an in-line metrology.

We developed ablation scripting to minimize surface roughness and achieve high degree of shape fidelity. A typical lens parameters that we ablate is $450\ \mu\text{m}$ aperture with radius of curvature $100\ \mu\text{m}$. Given the difference in refractive decrement such lens is roughly equivalent to an industry standard beryllium lens of the same aperture and $R=50\ \mu\text{m}$.

As-ablated lenses have roughness on the order of 200-300 nm. For x-ray applications we are developing post-ablation chemical – mechanical polishing procedure. In this procedure a conformal bit is lowered into the diamond lens along with fine sub-micron diamond slurry and spun inside for anywhere from 4 to 8 hours. Large number of factors make this procedure quite complicated: uneven pressure distribution, not equal linear velocity at different parts of the polishing bit, different diamond crystal orientation along the paraboloid surface and some others. We are able to polish full lens surface to 10-20 nm Ra roughness. Figure 1 shows a comparison of polished and un-polished lens along with the residual plots of the paraboloid fit.

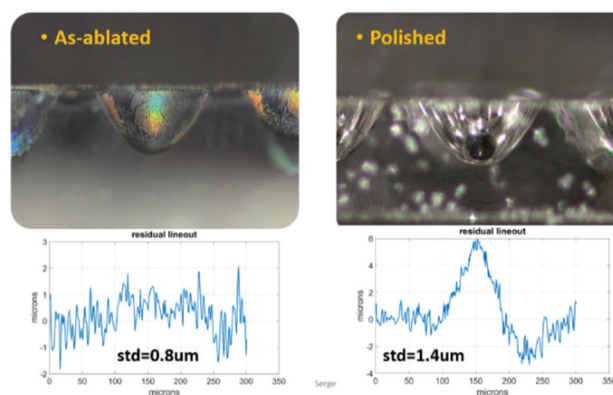


Figure 1: Top: Optical image through a polished side of the diamond plate. Left: as-ablated lens. Right: Polished lens. Bottom: corresponding lineouts of paraboloid fit residuals.

† s.antipov@euclidtechlabs.com

These lenses are packaged now into a tight tolerance aluminium-bronze disk for precision stacking (Fig. 2). Alternatively, an ultra-compact CRL can be produced by stacking individual diamond plates. This type of packaging does not require a heavy-load bearing stages for CRL alignment.



Figure 2: Top left: Side view of a double-sided lens. Bottom left: ultra-compact CRL made of diamond plate stack. Right: diamond lenses packaged in an aluminum-bronze holder.

AT-WAVELENGTH METROLOGY

Right after laser ablation we employ laser scanning confocal microscopy for metrology in-house. However visible light metrology does not give consistent results primarily due to the transparency of diamond samples and parabolic shape of the surface (these methods rely on light coming back to the sensor). Also, these methods do not probe the presence of any structural features inside the optical element that are sampled by x-rays.

X-ray metrology at the design operational energy (at-wavelength) is the best way to characterize diamond lenses. We had recently characterized a set of polished and un-polished lenses at the European Synchrotron Radiation Facility (ESRF) beamline BM05. At-wavelength metrology had been done using the x-ray speckle vectorial tracking (XSVT) technique at 17 keV. A speckle pattern is produced by inserting a membrane diffusor into the x-ray beam. When the lens is inserted after the diffusor the speckle pattern is changed due to x-rays refracting on the lens. Tracking these changes allows to reconstruct the lens profile. This technique is described in detail in [4, 5].

Ten polished and fourteen as-ablated lenses were characterized. Each measurement is fitted with a paraboloid of revolution, - a perfect lens shape. The residual of the fit is referred to as lens figure error (Fig. 3, Top). The goal of lens production is to minimize this figure error. The residual can be decomposed into Zernike polynomial to identify primary aberrations (Fig. 3, Bottom). This information can be used to improve fabrication process or plan correction optics for the diamond lens stack [6].

Average values for radius of curvature and figure errors are presented in the Table 1 along with other lens parameters.

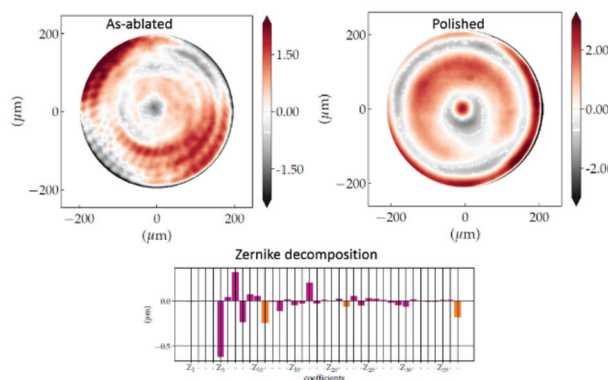


Figure 3: Top: Left: a typical figure error of as-ablated lens. Right: figure error of the polished lens. Bottom: Figure error decomposition into Zernike polynomials.

Table 1: Two-Sided Diamond Lens Metrology

Margin	Optical	17 keV
R(apex)	95.35 $\mu\text{m}/\text{side}$	48.1 μm , (96.2 $\mu\text{m}/\text{side}$)
Aperture, $2R_0$	420 μm	400 μm
Figure error for $A=350 \mu\text{m}$	0.64 $\mu\text{m}/\text{side}$	1.19 μm total
Figure error polished for $A=350 \mu\text{m}$	0.91 $\mu\text{m}/\text{side}$	1.09 μm total
d, neck	19.7 μm	
Roughness, S_a	300 nm	
Polished, S_a	20 nm	

CONCLUSION

Diamond refractive lenses have been systematically characterized at the ESRF by means of x-ray speckle vectorial tracking. These results show that figure errors achieved for diamond lenses are approaching beamline requirements and compatibility with industry standard lenses.

ACKNOWLEDGEMENTS

Diamond lens development had been supported by DOE SBIR grant #DE-SC0013129. The authors acknowledge the BM05 beamline staff for beamtime availability and technical support.

REFERENCES

- [1] S. Terentyev *et al.*, "Parabolic single-crystal diamond lenses for coherent x-ray imaging," *Appl. Phys. Lett.*, vol. 107, p. 111108, 2015.
- [2] M. Polikarpov *et al.*, "Spectral X-Ray Glitches in Monocrystalline Diamond Refractive Lenses," *Phys. Status Solidi B*, vol. 255, p. 1700229, 2017.
- [3] T. Roth *et al.*, "X-ray laminography and SAXS on beryllium grades and lenses and wavefront propagation through imperfect compound refractive lenses," in *Proc. SPIE 9207, Advances in X-Ray/EUV Optics and Components IX*, p. 920702, Sept. 2014. doi.org/10.1117/12.2061127

- [4] S. Berujon *et al.*, “X-ray optics and beam characterization using random modulation: theory,” *J. Synchrotron Rad.*, vol. 27, pp. 284-292, 2020.
<https://doi.org/10.1107/S1600577520000491>
- [5] S. Berujon *et al.*, “X-ray optics and beam characterization using random modulation: experiments,” *J. Synchrotron Rad.*, vol. 27, pp. 293-304, 2020.
<https://doi.org/10.1107/S1600577520000508>
- [6] R. Celestre, ‘Investigations of the effect of optical imperfections on partially coherent X-ray beam by combining optical simulations with wavefront sensing experiments’, PhD thesis, Université Grenoble Alpes, Grenoble, 2021.

BEAMLINE ALIGNMENT AND CHARACTERIZATION WITH AN AUTOCOLLIMATOR*

M. V. Fisher†, A. Khan, J. Knopp

Advanced Photon Source, Argonne National Laboratory, Argonne, IL, USA

Abstract

An electronic autocollimator is a valuable tool that can assist in the alignment of optical beamline components such as mirrors and monochromators. It is also a powerful tool for *in situ* diagnoses of the mechanical behavior of such components. This can include the repeatability of crystals, gratings, and mirrors as they are rotated; the parasitic errors of these same optical elements as they are rotated and/or translated; and the repeatability and parasitic errors as bendable mirrors are actuated. The autocollimator can even be used to establish a secondary reference if such components require servicing. This paper will provide examples of such alignments, diagnoses, and references that have been made with an autocollimator on existing and recently commissioned beamlines at the Advanced Photon Source (APS). In addition, this paper will discuss how this experience influenced the specifications and subsequent designs of the new primary high-heat-load mirror systems (PHHLMS) that are currently under fabrication for six of the APS Upgrade (APS-U) feature beamlines. Each mirror was specified to provide *in situ* line-of-sight access for an autocollimator to either the center of the mirror's optical surface or to a smaller polished surface centered on the backside of each mirror substrate. This line of sight will be used for initial alignment of the mirror and will be available for *in situ* diagnoses if required in the future.

INTRODUCTION

Many strategies can be employed in the alignment of optical beamline components such as mirrors and monochromators. One can reference the actual optical surfaces with classical optical tooling (white face scale, jig transit, etc.) or get more sophisticated and use a portable coordinating measuring machine that relates the measured position of the optical surface to an external reference. A mirror or monochromator can then be installed onto a beamline using these predetermined external references and these techniques have been employed at the Advanced Photon Source (APS). An electronic autocollimator offers an additional means of establishing such alignments as it can measure the pitch and roll of the optical surface assuming an appropriate line of sight is available. A vertical leveling mirror (VLM) [1] is useful optical tool that can be used in concert with an autocollimator to establish an absolute angular reference relative to gravity. This is especially helpful in setting the roll of horizontally defecting mirrors and

horizontally diffracting gratings and crystals. This paper begins with a discussion of how this technique was successfully used to align such a mirror system at the APS. This is followed by discussions of how an autocollimator was used to diagnose *in situ* the mechanical behavior of the motion systems on a couple of mirrors and one monochromator.

DUAL MIRROR SYSTEM AT 2-ID

The 2-ID beamline was converted from a colinear to a canted configuration [2] in late 2019. Part of that conversion involved installing two primary high-heat-load mirrors that share a common vacuum chamber into the upstream end of the first optical enclosure (FOE). The two mirrors increase the separation between the canted beams and focus these beams at slits located near the downstream end of the FOE. The upstream/inboard (us/in) mirror horizontally deflects the inboard canted beam outward. The downstream/outboard (ds/out) mirror horizontally deflects the outboard canted beam inward. The beams cross over each other about halfway along their path to their respective slits. The roll of these two mirrors was initially set using a jig transit lined up on the downstream end of each mirror. Each mirror was adjusted such that the top and bottom edges of each optical surface were aligned vertically. The holder and mechanism made it difficult to get a good line of sight to the mirror edges. Fortunately, the overall assembly was designed with an unobstructed line of sight to each optical surface. The process of setting up a VLM and auto-collimator was straightforward for the us/in mirror, which faces outward, but not as easy to implement for the ds/out mirror that faces inward. The setup for the ds/out mirror is complicated by its proximity to the inboard wall of the FOE. One can establish a line of sight to the mirror's optical surface using a VLM oriented at 45° to the mirror, but it is a two-stage process where the autocollimator is first leveled in roll by viewing the VLM straight on before rotating by 45°. The autocollimator indicated that the initial roll alignment on each mirror was in error by more than 1.0 mrad. The roll was eventually set to better than 100 μ rad and could have been set more accurately if needed.

Work continued into early 2020 on converting the 2-ID beamline to a canted configuration. That work came to a halt when the APS went into minimum safe operations during the early stages of the COVID pandemic. During that time a water leak developed on the us/in mirror. The leak was confined to a single air guard bellows that surrounded the leaking cooling line and the leak did not compromise the vacuum integrity of the mirror system. Fortunately, the leak was discovered, and the water turned off in a timely fashion, but the repair did not start until a few months later once COVID protocols were put in place. The repair

* This research used resources of the Advanced Photon Source, a U.S. Department of Energy (DOE) Office of Science User Facility at Argonne National Laboratory and is based on research supported by the U.S. DOE Office of Science-Basic Energy Sciences, under Contract No. DE-AC02-06CH11357.

† mfisher@anl.gov

required the removal of the vacuum chamber to access the internals. The existing position of the us/in mirror was documented prior to starting the repair. Survey and alignment documented the position of three of four extreme corners of the optical surface. An autocollimator was set up to measure the pitch and roll of the mirror. The autocollimator and VLM confirmed that the mirror's roll was very close to zero. A secondary reference mirror was then installed onto the vacuum chamber base flange and adjusted in pitch and roll such that the autocollimator read zero. A protective cover was placed around the reference mirror to prevent accidental bumping. This allowed the autocollimator to be removed during the actual leak repair. This is illustrated in Fig. 1.



Figure 1: Autocollimator was aligned to us/in mirror at 2-ID prior to addition of reference mirror.

The repair was further complicated when water left over from the original leak migrated into one of the welded bellows that is part of the mirror support. In the end, that bellows had to be removed and UHV cleaned. The repair activities were performed without disturbing the reference mirror. The autocollimator was set up and aligned (zeroed) to the reference mirror once repairs were complete. The reference mirror was then removed from the line of sight to the us/in mirror and the autocollimator revealed that the mirror was essentially in the same position as before the repair. The survey and alignment check of the optical surface confirmed a similar result.

The 2-ID beamline in its canted configuration began taking beam in late 2020. An autocollimator was set up to monitor the mechanical behavior of each mirror. The results of such a test on the us/in mirror are shown in Fig. 2

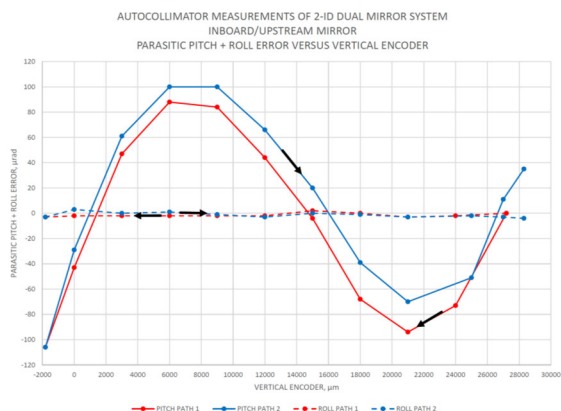


Figure 2: *In situ* autocollimator measurement of parasitic pitch and roll of the 2-ID us/in mirror.

where parasitic pitch and roll is plotted versus the full range of vertical stage travel. Similar tests were performed as part of the original factory acceptance testing (FAT), but these *in situ* tests are what really count as they are done as installed, under vacuum, and with cooling water flowing, and they can be repeated periodically to access whether the mechanical behavior has changed.

BENDABLE M5 MIRROR AT 4-ID XTIP

The 4-ID-XTIP branch beamline [3] was constructed in 2018-19 using the entrance slit, SGM, and exit slit that were part of the decommissioned 2-ID-B beamline. The exit slit has a long travel range to keep the slit at the grating focus as it is scanned in energy. That required that the final Kirkpatrick-Baez mirrors on the new XTIP branch have a horizontally focusing bendable mirror. The original plan was to specify and procure a new elliptically bent M5 Mirror. In the end, the decision was made to repurpose a cylindrically bent mirror system that was originally the 011 4m-NIM M0 Mirror [4] at the Synchrotron Radiation Center (SRC). That mirror system had been back filled, sealed up, crated, and moved to the APS when the SRC facility shutdown. It sat in storage for several years until consideration was given to using it for XTIP. The mirror was coated with hard carbon and would have to be stripped and recoated. In addition, the original welded steel support frame would have to be replaced with a granite base and kinematic mounts to more easily position the mirror. Before that work was performed, a simple *in situ* autocollimator test (see photo in Fig. 3) was performed to verify that the mirror bending mechanism was still able to operate in a smooth and repeatable fashion despite its age and having been mothballed and crated for some years. The autocollimator was deliberately aligned ~ 50-mm upstream of the mirror pole such that it could detect a change in pitch at a point on the mirror as the bending mechanism was actuated. The data from that test is provided in Fig. 4 and shows that the bending mechanism was very smooth and repeatable but had some hysteresis which is typical of mirror benders in general. Additional autocollimator measurements were made while lined up on the mirror pole and that data demonstrated that the pitch remained near zero over the same range of bender actuation.



Figure 3: *In situ* autocollimator measurement of former SRC mirror prior to refurbishment for use as XTIP.

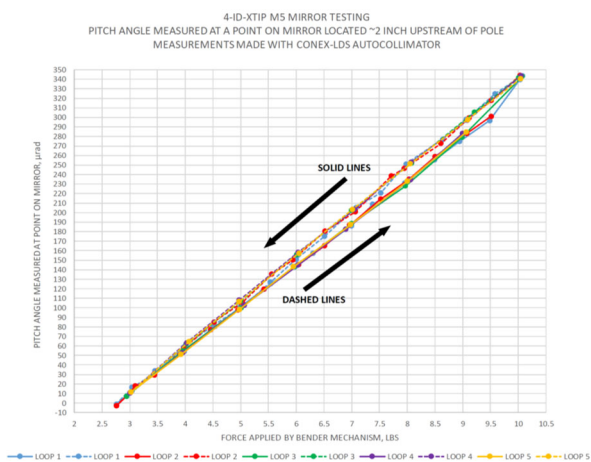


Figure 4: *In situ* autocollimator data of former SRC mirror prior to refurbishment for use at XTIP.

SGM SCAN DRIVE AT 4-ID-C

The SGM at 4-ID-C was procured in the mid-1990s. At that time most grating monochromators utilized linear encoders on an external sine drive that was calibrated to drive the energy scan. In later years, many monochromator designs adopted direct in-vacuum encoding of the scan axis rotation. A test was conducted with an autocollimator to see what improvement could be had if the SGM was retrofitted accordingly. An XPS measurement was made looking at the C 1s binding energy of HOPG, which has a sharp spectral feature. The autocollimator was aligned to the grating while set to an energy well above the binding energy. The SGM was then commanded to scan a large angular distance away and then return to the same energy according to the scan drive encoder. XPS measurements were repeatably made at this same energy reading according to the scan drive encoder. The graph in Fig. 5 shows a range of measured C1s binding energies that correlate linearly with the autocollimator reading. This data clearly shows that the scan drive encoder did not return the grating to the same position each time. Moreover, the correlation with the autocollimator indicated that the repeatability of the scan drive could be improved dramatically. This testing was

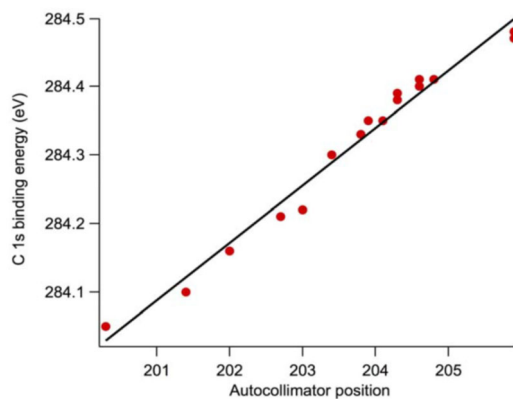


Figure 5: *In situ* autocollimator data from 4-ID-C SGM correlated with XPS measurements.

prompted by construction of the 4-ID-XTIP, which utilizes an almost identical SGM for which such an upgrade was being considered. The test proved the retrofit could improve the energy calibration, but in the end neither SGM was upgraded due to the complexity of the retrofit.

APS-U FEATURE BEAMLINE MIRRORS

The experiences gained at the APS from utilizing an autocollimator to align and diagnose the mechanical behavior of optical components drove the requirement that viewports, mounting hole patterns, and lines of sight be included on all the new primary high-heat-load mirror systems (PHLMS) for six APS Upgrade (APS-U) feature beamlines. There are at total of 13 mirrors that make up these primary mirrors: five inward facing, five outward facing, two downward facing, and one upward facing. A direct line of sight from a viewport to the mirror’s optical surface is ideal, but not very feasible on downward facing mirrors. In addition, it can be challenging to maintain lines of sight to the optical surface on the inward facing mirrors. In the end, a viewport and line of sight is still required for viewing the optical surface on all mirrors except for those that are downward facing. An additional requirement was made on inward and downward facing mirrors that a polished reference surface be centered on the backside of such mirrors and that corresponding lines of sight and viewports be provided for use with an autocollimator. These features will be used for initial alignment of the mirror and will be available for *in situ* diagnosing if required in the future.

CONCLUSIONS

An electronic autocollimator is a valuable tool for aligning beamline optical components and for *in situ* diagnoses of the mechanical behavior of such components. This has been a useful tool on many APS beamlines and that experience informed the specifications for the PHLMS for APS-U feature beamlines.

ACKNOWLEDGEMENTS

The author acknowledges Fabricio Marin for his collection of the parasitic pitch and roll data presented in Fig. 2 and Richard Rosenberg for the correlation of XPS to autocollimator data presented in Fig. 5.

REFERENCES

- [1] C. L. Farrand, “Vertical Leveling Mirror,” U.S. Patent No. 2907246, Oct. 6, 1959.
- [2] D. Capatina *et al.*, “APS 2-ID Beamline, Upgrade to Canted Configuration”, in *Proc. 9th Mechanical Engineering Design of Synchrotron Radiation Equipment and Instrumentation Int. Conf. (MEDSI’16)*, Barcelona, Spain, Sep. 2016, pp. 342-344. doi:10.18429/JACoW-MEDSI2016-WEPE18
- [3] V. Rose *et al.*, “XTIP – the world’s first beamline dedicated to the synchrotron X-ray scanning tunneling microscopy technique,” *J. Synchrotron Rad.*, vol. 27, pp. 836-843, 2020. doi:10.1107/S1600577520003689
- [4] T. Kubala, M. Fisher, R. Reininger, M. Severson, “New actively bent plane mirror at SRC,” *AIP Conference Proceedings 417*, p. 130, 1997. doi:10.1063/1.54610

WELDABLE COPPER CHROMIUM ZIRCONIUM MASK

T. J. Bender†, O. A. Schmidt, W. F. Toter, Argonne National Laboratory, Lemont, IL, USA

Abstract

A novel design for a weldable copper chromium zirconium (CuCrZr) mask is being developed for use in the Advanced Photon Source Upgrade (APSU) beamlines at the Argonne National Laboratory (ANL). This alternative attempts to drastically reduce cost and lead time over traditional brazed Glidcop® mask designs. Thermal analysis simulations of the mask have predicted that it will meet mechanical and thermal requirements, even when subjected to the intense white beam of the new superconducting undulators (SCU) of the APSU. As of the writing of this paper, a prototype is being fabricated for testing and eventual installation on the 28-ID Coherent High Energy X-ray (CHEX) beamline.

INTRODUCTION

Photon masks are radiation safety components meant to limit missteering of synchrotron radiation and protect downstream components in beamlines. They are also often used as in-vacuum beamstops and secondary apertures for controlling the size of the beam. Without photon masks, heat-sensitive radiation safety components like collimators would be exposed to the heat carried by the unattenuated beam.

The 28-ID CHEX beamline relies on two separate X-ray beams from the storage ring using a canted SCU configuration. One beam is multiplexed three times creating fixed discrete energy beamlines and one beamline is left fully tunable. This configuration will exploit the coherent flux enabled by APSU to advance the frontier for *in situ*, real-time studies of materials synthesis and chemical transformations in natural operating environments.

The proposed welded mask design will reside on the 5-60 keV tunable branch line, roughly 44 meters from the source in a lead-shielded mini-enclosure (Fig. 1). Its purpose is to protect downstream components from missteered synchrotron beam, define the size of the outboard canted beam, and prevent passage of the inboard canted beam to the 28-ID-B enclosure located downstream of the mini-enclosure.

CuCrZr masks are becoming widely used since it is affordable and simple to fabricate from a single piece of material, however more complicated absorber designs with overlapping internal features are difficult or impossible to machine [1, 2]. Also, brazing CuCrZr will anneal and negate useful properties of the beam intercepting surface and the hardened knife edge. Tests done by Bill Toter, ANL welding engineer show that gas tungsten arc welding (GTAW) is a viable strategy for joining CuCrZr bodies. The heat effective zone should be localized enough to not effect the knife edge and material properties.

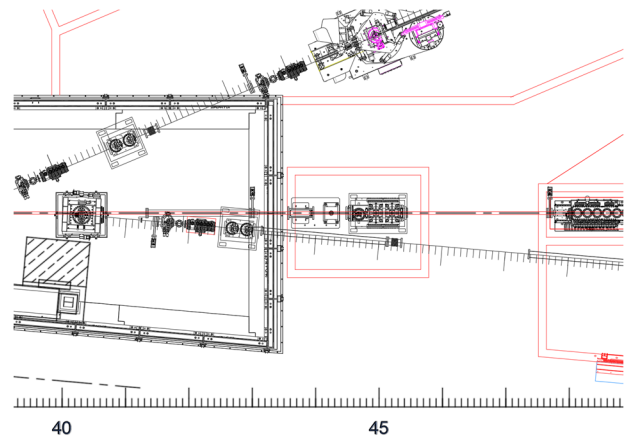


Figure 1: Location of mask in CHEX beamline.

MECHANICAL DESIGN

Absorbing Body

The main absorbing body of the mask consists of two CuCrZr top and bottom halves (Fig. 2). Both halves each contain five .375 in diameter water cooling channels with .25 in NPT threaded holes on either side to accept stainless steel compression fittings and return loops. The channels are drilled perpendicular to the beam direction to maximize the number of cooling channels present.

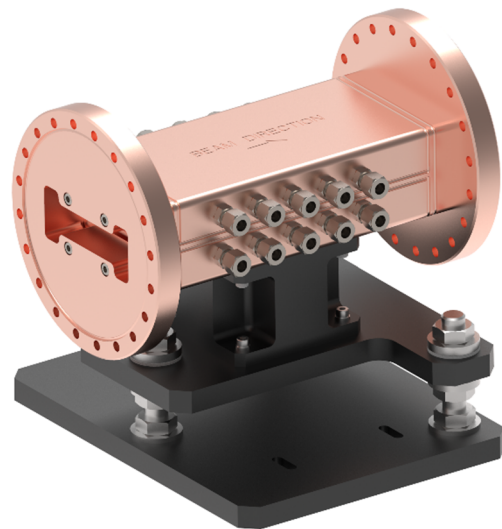


Figure 2: Welded mask assembly.

The top half contains the 2 mm horizontal x 10 mm vertical exit aperture meant to slit the outboard canted beam. The bottom half of the body contains the incident surface meant to absorb the extremal synchrotron rays as well as four M4 tapped holes for securing the assembly to an adjustable-height support table. Both halves also have inside surfaces angled in such a way as to block passage of the inboard canted beam. The inner angled surfaces on both halves are to be cut via wire EDM.

† tbender@anl.gov

Content from this work may be used under the terms of the CC BY 3.0 licence (© 2021). Any distribution of this work must maintain attribution to the author(s), title of the work, publisher, and DOI

Flanges

The design is noteworthy in that the flanges are also fabricated from CuCrZr and are bolted to the absorbing body before being welded in place. Four center-vented silver-plated M6 bolts are screwed into the absorbing body to hold the flanges in place during welding (Fig. 3). Each half of the absorbing body has two tapped holes on both the upstream and downstream ends to accommodate this mounting scheme. The bolts remain in place after welding to provide additional structural rigidity.

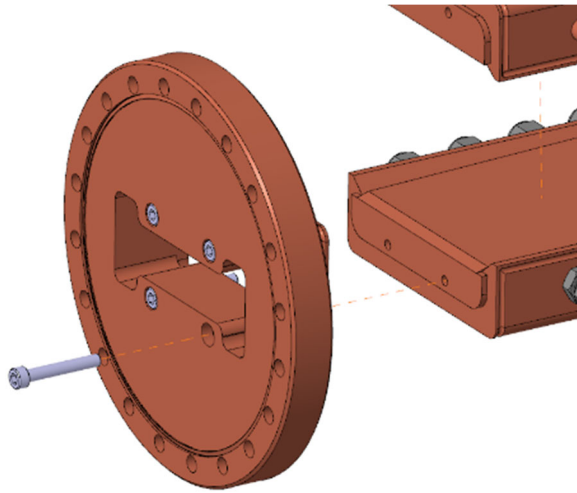


Figure 3: Exploded view showing center-vented bolts holding flanges to absorbing body.

Weld Reliefs

In order to allow both halves of the mask absorbing body and flanges to be united via welding, weld reliefs .125 in diameter are milled along the weld seams on each component (Fig. 4). These reliefs allow the formation of a continuous weld bead of sufficient size needed to provide strength, prevent virtual leaks, and ensure successful fusion of the halves.

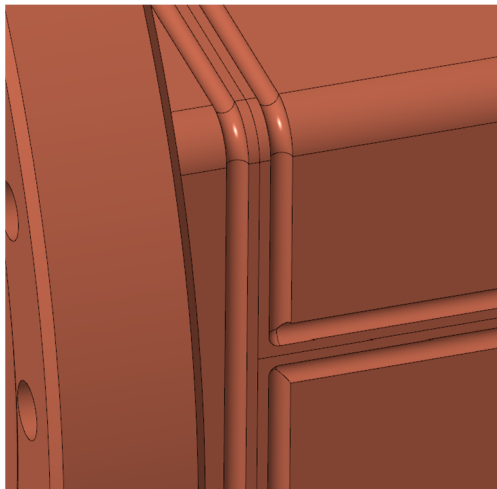


Figure 4: Image of reliefs surrounding the weld seams.

FINITE ELEMENT ANALYSIS

Thermal

The SCU insertion devices designed for the CHEX beamline have an 1.85 cm period and are 4.8 m in length. Calculations were performed when the undulators were tuned to emit the maximum photon energy corresponding to a total power of 1402.7 W at the front-end exit mask located 25.4 m from the source. The beam size at the welded mask was calculated by linearly interpolating the beam size present at the front-end exit mask aperture.

A program created in the Interface Description Language (IDL) development environment version 8.5, known as SRUFF, was used to calculate the undulator power density distribution. In order to perform these calculations, parameters such as the storage ring beam current of 220 mA, photon energy of 6 GeV, relativistic gamma, beam divergence, beam size, and the beam size at the welded mask were entered into SRUFF and the resulting undulator power density was fitted to a higher order Gaussian curve.

ANSYS Workbench 2020 R2 was used in the steady state thermal analysis of the mask. The power density curve was imported into ANSYS and applied as a heat flux evenly distributed between two canted beams projected onto the angled face of the bottom half of the mask body (Fig. 5). The film coefficient was calculated to be 10,000 W/m²K from the water channel diameter and the minimum water flow rate of 0.5 gpm, allowing a convection selection to be applied to the cooling channels (Fig. 6).

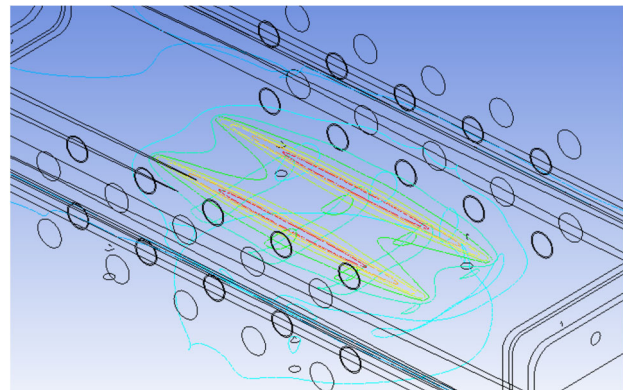


Figure 5: Result of thermal simulation showing canted beams heat deposited on mask interior surface.

The mesh size was set to 0.2 mm at the heat flux and convection selections, while the rest of the model was set to have a mesh size of 2 mm in order to reduce computation time. The beam envelope provided by the beamline ray tracing was used to determine the worst possible positioning of the canted beams and the analysis was run under that assumption. Several temperature and reaction probes were placed on the heat flux selections and cooling channels to measure the maximum temperature and the total dissipated power.

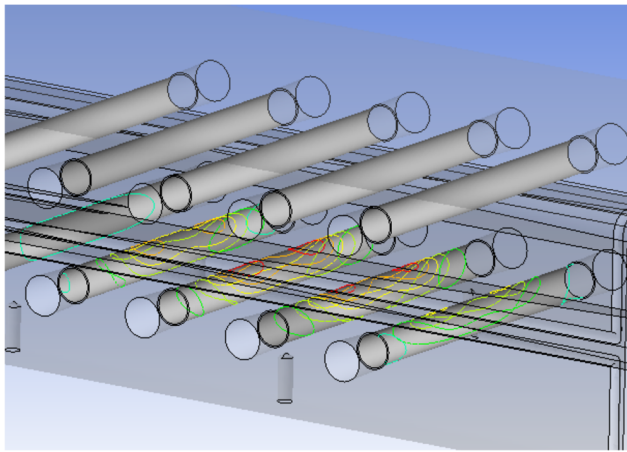


Figure 6: Heat dissipated due to convection in the water cooling channels.

The results of the analysis predict a maximum temperature at the incident surface of 53.1°C , which is far lower than the failure criterion of 250°C for CuCrZr. This provides a safety factor of nearly 4.7. The results also predict a maximum water temperature of 81.7°C , which is also far lower than the failure criterion of 153°C and offers a safety factor of about 1.7.

Several assumptions were made to simplify the analysis, including assuming that all materials were linear, elastic, isotropic, and homogenous, vibration induced by water cooling lines was negligible, the convection coefficient and supply water temperature were constant, and the water flow was laminar in nature.

CONCLUSION

Based on the positive results obtained from the thermal analysis, procurement and fabrication of the mask will commence and a prototype will be fabricated and tested. As this is an unproven design, there is likely to be further optimization to be realized after installation and testing. Assuming fabrication is successful, its installation into the CHEX beamline would introduce a new method for producing photon masks in an easier and more economical fashion when compared to traditional mask designs.

ACKNOWLEDGEMENTS

This research used resources of the Advanced Photon Source, a U.S. Department of Energy (DOE) Office of Science User Facility at Argonne National Laboratory and is based on research supported by the U.S. DOE Office of Science-Basic Energy Sciences, under Contract No. DE-AC02-06CH11357.

REFERENCES

- [1] C. Shueh, C.K. Chan, C.C. Chang, and I.C. Sheng, "Investigation of Vacuum Properties of CuCrZr Alloy for High-Heat-Load Absorber", *National Synchrotron Radiation Research Center A*, vol. 841, pp. 1-4, 2017.
- [2] S. Sharma *et al.*, "A Novel Design of High Power Masks and Slits", in *Proc. MEDSI'14*, Melbourne, Australia, October 2014, https://medsi.lbl.gov/SysIncludes/retrieve.php?url=https://medsi.lbl.gov/files/page_156/Presentations/A_Novel_Design_of_High_Power_Masks_and_Slits_Sushil_Sharma.pdf

COMPACT X-RAY AND BREMSSTRAHLUNG COLLIMATOR FOR LCLS-II

N. A. Boiadjieva[†] D. Fritz, T. Rabedeau
 SLAC National Accelerator Laboratory, Menlo Park, CA, USA

Abstract

Beam collimation is crucial to maintaining machine and personal safety during LCLS-II operation. This paper discusses a compact collimator consisting of an X-ray beam power collimator, a burn through monitor (BTM) designed to detect failure of the X-ray beam collimator, and a Bremsstrahlung collimator. The x-ray collimator body is a monolithic machined from CuCrZr that eliminates costly braze operations and reduces assembly time and complexity. Sintered high thermal conductivity SiC is employed as the X-ray absorber. The allowed beam power is limited to 100W and 50W/mm². Finite element analyses (FEA) ensure that the power absorber remains in safe temperature and stress regimes under the maximum power loading and smallest expected beam dimensions. Beam containment requirements stipulate the inclusion of a monitor to detect burn through events owing to absorber failure. The BTM is a gas-filled, thin wall vessel which, if illuminated by the beam, will burn through and release the contained gas and trip pressure switches that initiate beam shutdown. The beam absorber and BTM shadow the Bremsstrahlung collimator shielding after appropriate propagation of manufacturing, assembly, and installation tolerances. Tooling is developed to minimize assembly complexity and ensure minimal alignment errors.

INTRODUCTION

This presentation discusses a package consisting of photon collimator that intercepts and collimates the x-ray beam, Burn Through Monitor (BTM) that monitor for beam excursion from the design path, and Bremsstrahlung collimator which collimates high energy photons associated with electron beam interaction with residual gas and physical aperture. In general those three components are situated in sequence along a given beam line though in some cases not all three elements are required.

The key requirement for this design were:

- Design a compact and modular x-ray power and Bremsstrahlung collimators.
- X-ray collimator to handle allowed power of 100W.
- Come up with fixtures and locating features to minimize the relative alignment error on assembly and hence maximize allowed beam aperture while providing downstream beam containment.

DESIGN

X-ray Collimator

Previously designed collimator bodies have employed a vacuum nipple with welded flanges and braised copper elements that provide cooling for the beam intercepting disk. For this design the body is a monolithic machined Copper alloy CuCrZr (18150) that allows compact design with integrated conflat seal knife edges and eliminates the need for flanges welding [1]. See Fig. 1. In addition, the cooling channels are machined in the body which eliminates the brazing of an additional cooling block. The resulting mask body extends 72mm along the beam direction.

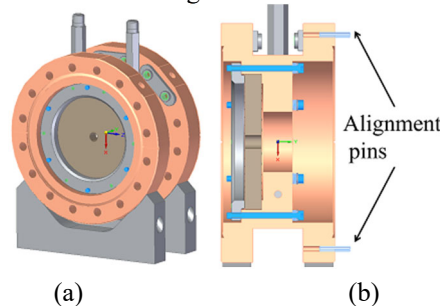


Figure 1: X-ray collimator. (a) CAD model, (b) cross section.

X-ray collimators are illuminated by x-ray beam power composed of high intensity, high frequency, short duration pulses. The collimator must not be damaged by the average beam power nor ablated through pulse by pulse energy deposition. Sintered high thermal conductivity SiC is employed as the x-ray absorber with design provisions incorporated to permit the inclusion of additional absorbers (e.g. diamond). The allowed beam power is limited to 100W.

The first beam intercepting element is cooled indirectly via indium mediated conduction cooling by the water-cooled collimator body. Figure 2 shows that the indium is positioned in the shadow of the beam intercepting element and maintained safely under the indium melting temperature at maximum power loading and maximum beam missteering.

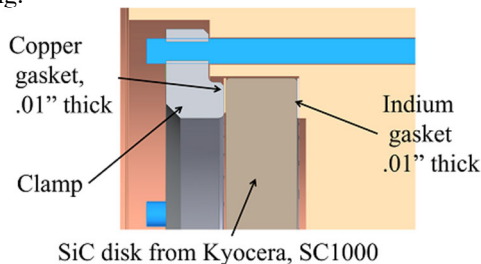


Figure 2: Design interface around SiC disk.

[†] ninab@slac.stanford.edu

The CuCrZr body is designed for reduced water consumption of 1.25 GPM relative to the LCLS-II photon collimator design. That flow is consistent with 15 ft/sec flow in a 0.186in ID tube (0.25in OD tube).

Finite Element Analysis of SiC

FEA are performed to ensure the components that intercept the free electron laser (FEL) beam shall remain in safe temperature and stress regimes under the maximum power loading and smallest expected beam dimensions. ANSYS workbench is used to perform the analysis. First, the thermal analysis is run to obtain the temperature field of the SiC disk. Second, the temperature profile is used as a thermal load in a structural analysis to determine the stresses in the disk. Figure 3 shows the three components that were analyzed and Table 1 provides the material properties. Bolt holes and small features were removed from the collimator housing with the goal of reducing analysis run time and mesh simplification. See [2] for Indium mechanical properties.

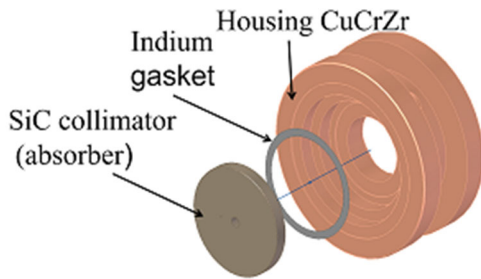


Figure 3: Exploded view of simplified geometry for FEA.

Table 1: Material Properties

Property	CuCrZr	SiC
Density, [g/mm ³]	8.91	3.16
Thermal Conductivity, [W/m-K]	323	f(temp)*
Coeff of Thermal Expansion, [10 ⁻⁶ x1/K]	18.6	3.9
Young's Modulus, [GPa]	128	430
Poisson Ratio	0.18	0.17

*f(temp) is given as: at room temperature, the thermal conductivity is 200W/m-K and at 600°C it is 82 W/m-K.

Thermal Conductance is applied at the interface between the SiC disk and Indium gasket. Indium foil interface conductance is modeled at 0.010W/mm²-K per A.M. Khounsary *et al.* [3].

The results of two cases, properly steered and significantly mis-steered beam, are shown in Table 2 and Table 3, respectively.

Table 2: Properly Steered 2.1mm Beam Diameter

Power	100W	50W
Max Temp, °C	845	323
Max Principal Stress, [MPa]	87	24
Min principal Stress, [MPa]	751	216

Table 3: Significantly Mis-Steered 2.1mm Beam Diameter

Power	100W	50W
Max Temp, °C	715	284
Max Principal Stress, [MPa]	26	10
Min principal Stress, [MPa]	675	208

The temperatures shown in Tables 2 and 3 are highly localized to the beam location. The peak temperatures at the indium interface are below the melting point of indium for all cases.

Flexural Strength of SiC from Kyocera (SC1000) is 480 MPa. Very conservatively, the tensile strength is 1/3 of the flexural strength. In this case the tensile strength will be 160 MPa. Results show maximum principal stress always below that level. Compressive strength of SiC varies between 3860 MPa and 4800 MPa. Results show minimum principal stress well below those values.

Burn Through Monitor

The BTM is a gas-filled, thin wall vessel which if illuminated by FEL beam will burn through thus releasing the contained gas (Fig. 4). Redundant gas channels communicate with the gas-filled vessel. The pressure in these gas channels is monitored by pressure switches which safely terminate the beam if rapid reduction of gas pressure indicates a burn through event. The BTM gas-filled cavity must shadow the Bremsstrahlung collimator shielding after appropriate propagation of manufacturing, assembly, and installation tolerances. Stresses in the edge weld are calculated using Roark, table 24, case 10b.

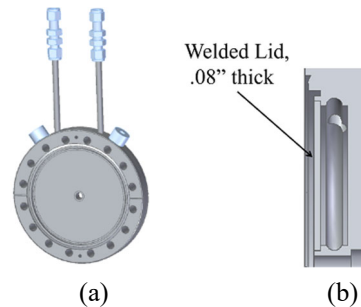


Figure 4: BTM, (a) CAD model, (b) cross section.

Bremsstrahlung Collimator

The Bremsstrahlung radiation is handled by a vacuum nipple and a block of tungsten alloy. The longitudinal length that intercepts the beam is $\geq 80\text{mm}$ and the beam aperture is completely shadowed by the x-ray collimator and BTM.

ASSEMBLY AND ALIGNMENT

The photon collimator aperture in conjunction with manufacturing, assembly, and installation tolerances define the cone transmitted to downstream components. The BTM and Bremsstrahlung collimator including the associated vacuum walls are not illuminated by the beam. Rather these components shall be safely shadowed by the photon collimator.

Holes for alignment pins have been incorporated in the flange of each component ensuring common reference and well defined flange position. Figure 5a shows alignment tool for different aperture sizes. The tool uses the pins as a reference and positions the SiC aperture. On Fig. 5b one can see how the BTM is mounted onto the collimator flange using the alignment pins and hence transferring relative alignment of SiC aperture to BTM and Bremsstrahlung collimator.

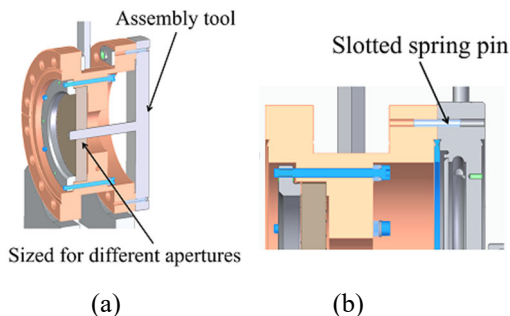


Figure 5: Assembly process. (a) Cross section of SiC disk installation, (b) cross section of collimator and BTM.

A list below shows an example of the diameter of the clear line of sight (CLS) for each component. Those values are calculated after taking into consideration the pin position tolerance, tooling tolerances and apertures dimensional tolerances and making sure each component shadows the next one downstream:

- SiC aperture: min CLS 7.48mm, max CLS 8.26mm.
- BTM aperture: min CLS 8.26mm, max CLS 9.1mm.
- BTM gas volume: min CLS 10.05mm, max CLS 11.14mm.
- Bremsstrahlung collimator aperture: min CLS 11.14, max CLS 12.03mm.

Figure 6 shows the clear line of sight for the whole assembly and Fig. 7 is a photograph of the final installed support structure and three components.

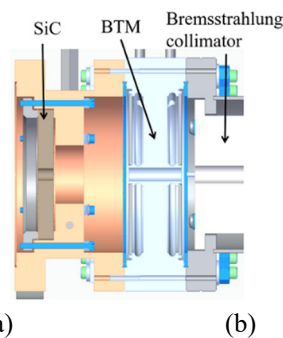


Figure 6: Cross section of a whole assembly.

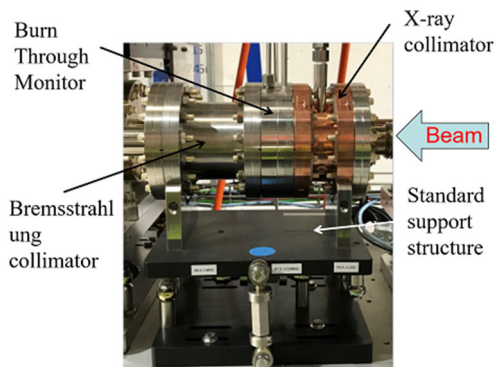


Figure 7: Final installed support structure with three components.

CONCLUSION

The design package is a compact, modular x-ray power and Bremsstrahlung collimator for beam containment. The FEA analysis of properly steered and significantly miss-steered beam confirmed the x-ray collimator (SiC) can handle up to 100W and 50W/mm².

The assembly tools and alignment pins ensure high relative alignment tolerance. Allowed beam is maximized and good downstream beam containment is provided.

Many packages with different sizes SiC disks, BTMs, and Bremsstrahlung collimators were installed in early 2019 and are operating successfully under the designed conditions.

ACKNOWLEDGMENTS

We are grateful for our colleagues at SLAC National Accelerator Laboratory who contributed to this project's success: C. Hardin, Frank O'Dowd – Mechanical engineering review and support; P. Grunow – *Assembly and alignment*; LCLS Designers - *Drafting Packages*.

REFERENCES

- [1] M. Li and S.J. Zinkle, "Physical and Mechanical Properties of Copper and Copper alloys," *Comprehensive Nuclear Materials*, vol. 4, pp. 667-690, 2012.
- [2] Indium Corporation, <http://www.indium.com/products/metals/indium/#documents>
- [3] A.M. Khounsary *et al.*, "Thermal contact resistance across a copper-silicon interface," in *Proc SPIE*, vol. 3151, pp, 45-51, 1997, doi:10.1117/12.294497

MECHANICAL DESIGN PROGRESS OF THE IN SITU NANOPROBE INSTRUMENT FOR APS-U*

Steven P. Kearney†, Deming Shu, Tim Mooney, Barry Lai, Si Chen, and Jörg Maser
Advanced Photon Source, Argonne National Laboratory, Lemont, IL 60439, U.S.A.

Abstract

The In Situ Nanoprobe (ISN, 19-ID) beamline will be a new best-in-class long beamline to be constructed as part of the Advanced Photon Source Upgrade (APS-U) project [1, 2]. To achieve long working distance at high spatial resolution, the ISN instrument will be positioned 210 m downstream of the x-ray source, in a dedicated satellite building, currently under construction [3]. The ISN instrument will use a nano-focusing Kirkpatrick-Baez (K-B) mirror system, which will focus hard x-rays to a focal spot as small as 20 nm, with a large working distance of 61 mm. The large working distance provides space for various *in situ* sample cells for x-ray fluorescence tomography and ptychographic 3D imaging, allows the use of a separate, independent vacuum chambers for the optics and sample, and provides the flexibility to run experiments in vacuum or at ambient pressure. A consequence of the small spot size and large working distance are stringent requirements for high angular stability of the K-B mirrors (5 nrad V-mirror and 16 nrad H-mirror) and high relative stability between focus spot and sample (4 nm_{RMS}). Additional features include fly-scanning up to 2 kg mass, sample plus *in situ* cell, at 1 mm/s in vertical and/or horizontal directions over an area of 10 mm x 10 mm. Environmental capabilities will include heating and cooling, flow of fluids and applied fields, as required for electrochemistry and flow of gases at high temperature for catalysis. To achieve these capabilities and precise requirements we have used precision engineering fundamentals to guide the design process.

INTRODUCTION

The advanced photon source (APS) at Argonne National Laboratory (ANL) is being upgraded with a new multi-bend achromat storage ring lattice and insertion devices that will provide increased brightness and coherence through reduced emittance of the stored electron beam [4]. To take full advantage of the new beam specifications, a new best-in-class In Situ Nanoprobe (ISN) instrument is being developed for the 19-ID beamline.

The ISN instrument will use a nano-focusing Kirkpatrick-Baez (K-B) mirror system to focus hard x-rays to a focal spot as small as 20 nm, with a large working distance of 61 mm. The large working distance provides space for various *in situ* sample cells for x-ray fluorescence tomography and ptychographic 3D imaging, allows the use of separate, independent vacuum chambers for the optics and

sample, and provides the flexibility to run experiments in vacuum or at ambient pressure.

Requirements of the ISN instrument that make it unique and a technically challenging design and allow it to support a broad range of *in situ* conditions are: high angular stability of the K-B mirrors (5 nrad V-mirror and 16 nrad H-mirror) and high relative stability between focus spot and sample (4 nm_{RMS}), fly-scanning a maximum of a 2 kg *in situ* cell at 1 mm/s in vertical and/or horizontal directions over an area of 10 mm x 10 mm, and separate vacuum chambers result in a metrology frame that needs to be transferred between two environments.

Achieving the requirements of ISN has required precision engineering of the entire instrument system from the soil up. All the components of the system need to work together, and any one component could push the instrument out of specification. In this paper we will discuss the design and state of the soil and foundation, enclosure environment, nanopositioning systems, and stable metrology frames. For details on the instrument support, which is a modification of granite stages developed by APS, see Preissner *et al.* [5].

INSTRUMENT DESIGN

Location

The ISN instrument will be positioned 210 m downstream of the x-ray source, in a dedicated satellite building, currently under construction. A sketch of the location of the new satellite building with respect to the main APS building and building schematic of the instrument control room and enclosure floor is shown in Fig. 1.

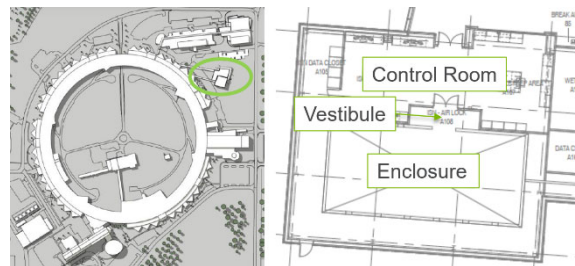


Figure 1: Left, circle is satellite building for ISN and High-Energy X-ray Microscope instruments. Right, floor plan of ISN showing control room, vestibule, and enclosure.

Foundation

We started the design process of the ISN with details of the foundation, which eventually included the soil underneath. To achieve a highly stable floor we measured the vibrations of other similar instrument foundations [3], and found a common successful strategy using slab isolation and 1 m thickness. With an isolated slab, there is a risk of

* This research used resources of the Advanced Photon Source, a U.S. Department of Energy (DOE) Office of Science User Facility at Argonne National Laboratory and is based on research supported by the U.S. DOE Office of Science-Basic Energy Sciences, under Contract No. DE-AC02-06CH11357.

†skearney@anl.gov

having too little mass and amplifying frequencies below 10 Hz, therefore we decided on a 1 m thick slab. Going further, we investigated whether the concrete enclosure should be placed on or off the isolated slab. Using lumped parameter models from soil dynamics that describe slab-on-grade vibrations [6], it was found that the added mass of the enclosure decreased the compliance in the vertical direction through increased coupling with the soil, and that it lowered the first natural frequency from 5 Hz to 3 Hz for vertical modes, with negligible impacts on tilt modes [7]. The soil in the calculations was assumed to be engineered fill, which was the replacement of the natural soil based on recommendations from the soil bore analysis.

Enclosure

Thermal stability is a major concern for the stability of the instrument. To deal with thermal drifts we have adopted a 2-stage thermal isolation method plus a separate requirement for the instrument surface temperature. Stage 1 is the control room (see Fig. 1) and is under the control of the main building HVAC system. It acts as the thermal barrier between the outside walls and the enclosure walls. Stage 2 is the instrument enclosure itself, which has two advantages for precise thermal stability. First, it is 12 in thick concrete and has a conductance of 5 W/K through a meter squared section of wall compared to 1791 W/K for our typical steel-lead-steel enclosure walls. For the concrete walls there is much less heat transfer for the same temperature difference compared to metal walls. Second, we will install a dedicated HVAC system for the instrument enclosure that uses low velocity duct socks to distribute laminar air flow evenly and control the air temperature to ± 0.05 °C for 1 hr. The final instrument surface temperature requirement, which is the most important as this is what causes the thermal drift, will be controlled to ± 0.01 °C for 1 hr.

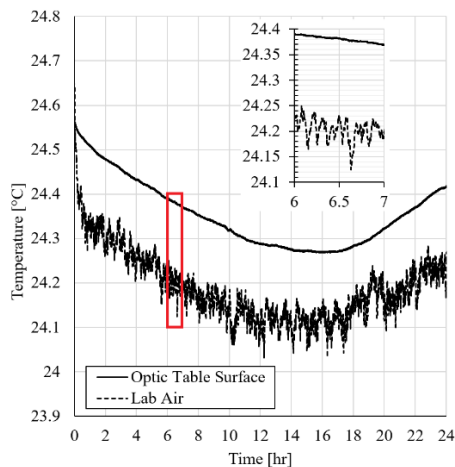


Figure 2: Comparison of air and surface temperatures over 24 hr, acquired with Omega™ precision thermistors.

Cooling using radiant water-cooled panels was implemented at Diamond Light Source and described by Cachon-Nerin *et al.* [8] achieved a 0.017 °C standard deviation stability over a longer period than our one-hour specification. However, we chose a conventional forced air system to avoid cooling pumps and water flow. In addition, a significant gain in stability due to the slow response of thermal masses is expected. An example of this is shown in Fig. 2, where the air temperature and surface temperature of an optics table in lab L1119 at APS was measured. In the inset, the pk-pk surface temperature is 6.5X less than the air.

Vacuum Chambers

Separate vacuum chambers will be used for the K-B optics and sample. The optics chamber will be at UHV pressures, while the sample chamber will be at HV pressures. Separating the environments helps to protect K-B mirror surface and maintain alignment by avoiding pressure cycles to atmosphere during sample changes. This method presents some difficulties in design, such as tight tolerances in assembly, extra windows, and the metrology frame. Accessibility, variability, and shorter sample change time outweighs these added difficulties. Figure 3 shows a cross-sectional view of the two chambers. Gaps between flanges are as small as 2 mm, and there are 2 additional x-ray windows needed to pass through two chamber walls.

The sample chamber is designed to operate with environments of both vacuum and at atmospheric pressure. In vacuum, the sample space available between the chamber wall and focus spot is 47 mm and increases to 55 mm when the top of the sample chamber is removed. Removing the top of the sample chamber is a delicate procedure because of the close tolerances, therefore special jigs and guides are being designed to make this process easier.

Various ports for detectors, sample access, cryostat, and windows can be seen in Fig. 4. Two ports are for SDD fluorescence detectors oriented at 15° and 0° from X. The port at 0° is for a back-scattering geometry detector, and the 15° port is being designed for a multi-element detector and to also accommodate a larger diameter confocal detector. The cryostat port is designed to come from above and slightly off-center from the sample to allow for a clear direct overhead port, which will be for optical or microscope access. Included are ports looking directly at the sample from the horizontal and sample access.

Figure 4 inset shows the details of the combined diffraction window and ptychography window. They are mounted together on the same hinged flange that can be opened for sample access. The flange is curved and will be sealed to the chamber flange using an o-ring seal held in a dovetail cut to keep it in place. The Be window gives a diffraction cone of 7°-60° in the vertical and -5°-60° in the horizontal and has a radius of 120 mm. Ideally, the Be window will be 0.5 mm thick, which does hold vacuum without breaking, however, from an operations point of view, it is risky for the window to be so thin. So, the thickness is still being optimized. The ptychography window will be Si3N4 and its dimensions are still being optimized as well.

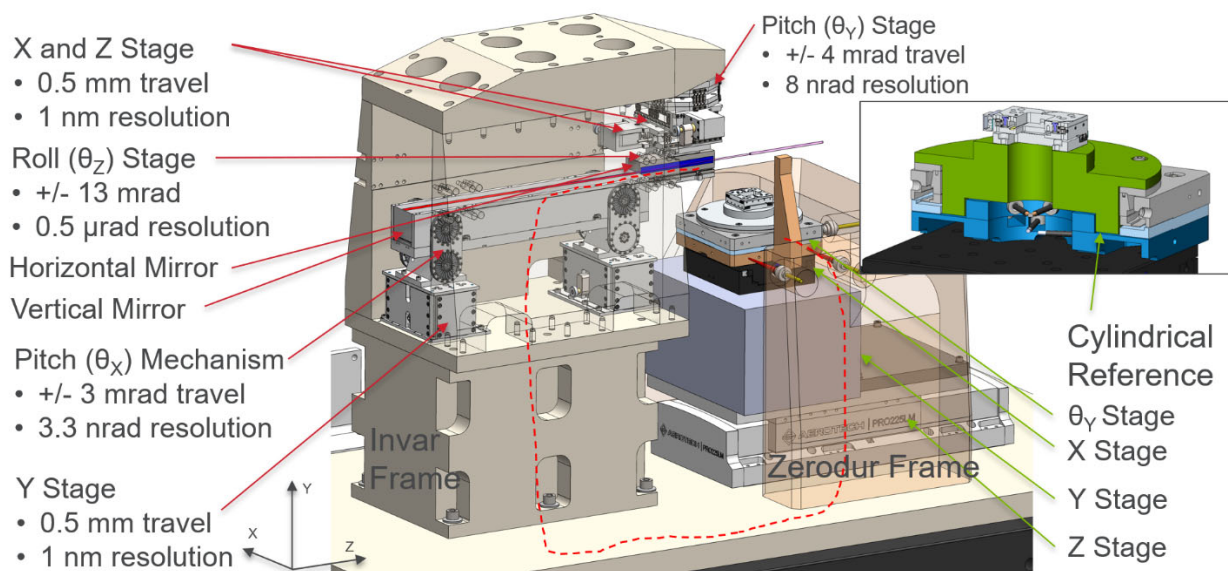


Figure 3: Details of the K-B optics system (left) and sample position stage system (right). The metrology loop is shown as a dashed line, and the inset shows the cylindrical reference mounted to the sample rotation stage.

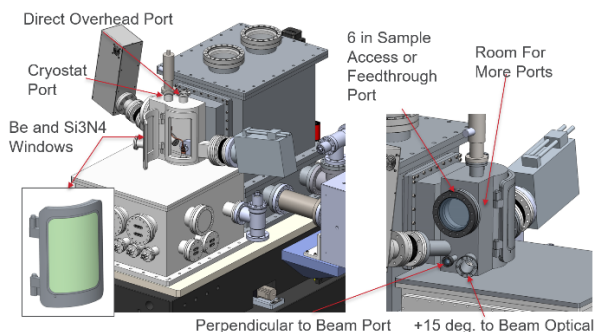


Figure 4: Model showing details of the ports and windows.

K-B System

The K-B optical system is shown in Fig. 3. The mirrors are positioned using nanopositioning flexure stages designed using Shu *et al.* [9] weak-link flexures. The vertical mirror is positioned vertically and pitched by differentially moving the vertical stages. A gantry type geometry is used for the horizontal mirror and stages to provide room for the sample chamber underneath. It is positioned in X, Z, pitch, and roll. More detail on the stages can be found in [10].

Sample Scanning System

A model of the sample scanning system is shown in Fig. 3. It is designed to handle up to a 2 kg load with 1 mm/s scan speed in X and Y over an area of 10 mm x 10 mm. A piezo rotation stage atop the XYZ stack is used for tomography and ptychography imaging. The last stage above the rotation stage is an XZ piezo linear stage to position the sample at the rotation center.

A direct drive stage will be used for scanning in the X direction and is sized so that, even at full speed and 5 Hz oscillation over a 100 μm scan, coil temperatures are expected to rise by 0.06 °C in vacuum. This is with the expectation that any external forces due to wires or tubing lines are negligible. Much care will be taken in the

finalizing of the design for strain relieving cables and tubes to provide enough slack for motion but not too much so that the stage is lifting cables.

Metrology

By separating the optics and sample environment the metrology frame to measure the relative position of the sample with respect to the optics becomes complicated. Fig. 3 shows the metrology loop with the vacuum chambers removed for clarity. The measurement loop must travel through 466 mm in the vertical direction down to the common Invar reference base. Then it is assumed that the Invar reference base is moving or deforming evenly across the plate. After the plate it then moves up through a Zerodur frame to the sample level. The Zerodur frame was chosen for the sample side since it does not have to support a load, as in the optics case, and it will be in the region with greatest heat load.

Errors from the rotation stage are corrected after each rotation step. The runout, wobble, and flatness errors are measured by capacitive sensors looking at a diamond turned reference cylinder. The errors will then be fed back to the XYZ stack to correct the errors.

CONCLUSION

The instrument design is close to completion, with procurement of components and system integration beginning in 2022.

ACKNOWLEDGEMENTS

We wish to thank S. Bean, from the APS, Y. Chu, H. Yan, and E. Nazaretski from the Hard X-ray Nanoprobe at the National Synchrotron Light Source II at Brookhaven National Laboratory, and N. Guisinger and J. Wen from Argonne's Center for Nanoscale Materials for help measuring foundation stability.

REFERENCES

- [1] J. Maser *et al.*, “A next-generation hard x-ray nanoprobe beamline for *in situ* studies of energy materials and devices,” *Metall. Mater. Trans. A*, vol. 45, no. 1, pp. 85-97, 2014. doi:<https://doi.org/10.1007/s11661-013-1901-x>
- [2] J. Maser *et al.*, “Design concept for the *in situ* nanoprobe beamline for the APS upgrade,” *Microsc. Microanal.*, vol. 24, suppl. S2, pp. 194-195, 2018. doi:[10.1017/S1431927618013314](https://doi.org/10.1017/S1431927618013314)
- [3] S. P. Kearney, S. Bean, and J. Maser, “Analysis of vibration isolated facilities for the *in situ* nanoprobe at the Advanced Photon Source,” *Synchrotron Radiat. News*, vol. 32, iss. 5, p. 13, 2019. doi:[10.1080/08940886.2019.1654827](https://doi.org/10.1080/08940886.2019.1654827)
- [4] <https://www.aps.anl.gov/APS-Upgrade>
- [5] C. Preissner *et al.*, “A family of high-stability granite stages for synchrotron applications,” presented at the 11th Int. Conf. on Mechanical Engineering Design of Synchrotron Radiation Equipment and Instrumentation (MEDSI2020), Chicago, IL, USA, virtual conference, July 2021, paper THOA01, this conference.
- [6] B. M. Das, *Fundamentals of Soil Dynamics*. New York, NY, USA: Elsevier Science Publishing Co., Inc., 1983.
- [7] S. P. Kearney *et al.*, “A comparison of isolated and monolithic foundation compliance and angular vibrations,” *APS/CNM Users Meeting*, Lemont, IL, USA, May 2019, poster abstract, <https://www.aps.anl.gov/Users-Information/User-Community/Users-Meetings/Program/Archive/2019/Program-Book>
- [8] F. Cacho-Nerin, J. E. Parker, P. D. Quinn, “A passive hutch-cooling system for achieving high thermal-stability operation at the nanoprobe beamline, Diamond Light Source,” *J. Synchrotron Radiat.*, vol. 27, Supporting information, 2020. doi:[10.1107/S1600577520004932](https://doi.org/10.1107/S1600577520004932)
- [9] D. Shu *et al.*, “Applications of laminar weak-link mechanisms for ultraprecision synchrotron radiation instruments,” *AIP Conf. Proc.*, vol. 879, iss. 1, pp. 1073-1076, 2007. <https://doi.org/10.1063/1.2436249>
- [10] D. Shu *et al.*, “Modular nanopositioning flexure stages development for APS upgrade K-B mirror nanofocusing optics,” presented at the 11th Int. Conf. on Mechanical Engineering Design of Synchrotron Radiation Equipment and Instrumentation (MEDSI2020), Chicago, IL, USA, virtual conference, July 2021, paper TUPC10, this conference.

DISCRETE PHOTON ABSORBERS FOR THE APS-UPGRADE STORAGE RING VACUUM SYSTEM*

O. K. Mulvany†, B. Billett, B. Brajuskovic, J. A. Carter, A. McElderry, R. Swanson
Advanced Photon Source, Argonne National Laboratory, Lemont, IL, USA

Abstract

The Advanced Photon Source Upgrade storage ring arc vacuum system features a diverse set of photon beam-intercepting components, including five discrete photon absorbers and a series of small-aperture vacuum chambers that shadow downstream components. The discrete photon absorbers—typically fabricated from electron beam-welded GlidCop® AL-15—are subject to heat loads ranging from approximately 170 to 3400 watts, with a peak power density up to approximately 610 W/mm² at normal incidence. Four of the five photon absorber designs are housed in vacuum chambers, including three that are mounted to the antechambers of curved aluminum extrusion-based L-bend vacuum chambers and one that is mounted to a stainless steel vacuum-pumping cross. Furthermore, two of the photon absorbers that are mounted to L-bend vacuum chambers are equipped with position-adjustment mechanisms, which are necessitated by the challenging design and fabrication of the curved vacuum chambers. The fifth photon absorber, unlike the rest, is a brazed design that is integral in sealing the vacuum system and intercepts approximately 170 watts. Each photon absorber design was optimized with thermal-structural finite element analyses while ensuring functional and spatial requirements were met. Some of these requirements include meeting internal high-heat-load component design criteria, respecting challenging component interfaces and alignment requirements, and minimizing impedance effects. Furthermore, photon beam scattering effects called for the use of scattering shields on three designs to minimize potential heating of vacuum chambers. This paper details the careful balance of functionality and manufacturability, and the overall design process followed to achieve the final designs.

INTRODUCTION

The Advanced Photon Source Upgrade (APS-U) project is building a storage ring upgrade that will be retrofitted to the current 1.1-km circumference APS storage ring. By utilizing narrow aperture magnets and thus a small-aperture vacuum system in a multi-bend achromat (MBA) lattice, the upgrade will produce a 6-GeV, 200-mA beam that is optimized for brightness above 4 keV [1].

Five GlidCop® AL-15 discrete photon absorbers (in addition to water-cooled, small-aperture vacuum chambers)

* This research used resources of the Advanced Photon Source, a U.S. Department of Energy (DOE) Office of Science User Facility at Argonne National Laboratory and is based on research supported by the U.S. DOE Office of Science-Basic Energy Sciences, under Contract No. DE-AC02-06CH11357.

† omulvany@anl.gov

were designed to shadow, or protect, neighboring electron and photon beam vacuum components in the APS-U MBA lattice. The final photon absorber designs were driven by several requirements, most notably including: protecting neighboring components in the storage ring vacuum system while safely handling the heat loads produced by the MBA lattice; achieving minimum vertical and horizontal apertures for the photon beams produced by the upstream straight sections and bending magnets; and finally, a need for seamless integration into the storage ring vacuum system.

Three of the five photon absorbers—A:CA1, A:CA2, and B:CA1—are considered “crotch” absorbers and thus permit photon extraction to the front ends while typically intercepting higher heat loads (Fig. 1a-1c). The final two photon absorbers include an “end” absorber, B:EA1 (Fig. 1d), and an “inline” absorber, B:FA1 (Fig. 1e), both of which strictly shadow uncooled downstream components from synchrotron radiation. The B:FA1 inline photon absorber, which is 60 mm in length, serves a dual purpose in that it is a vacuum chamber and also shadows downstream components. Each of the five photon absorber designs are required in the 40 repeating sector arcs of the APS-U storage ring vacuum system.

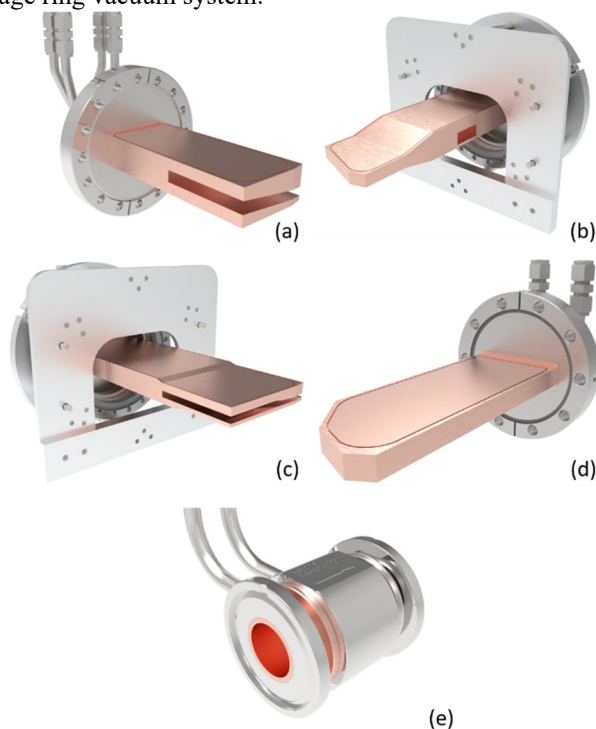


Figure 1: Discrete photon absorber designs, including crotch absorbers (a) A:CA1, (b) A:CA2, and (c) B:CA1, an end absorber (d) B:EA1, and an inline absorber (e) B:FA1.

INTERFACES

Each photon absorber design required a careful study of interfacing components to ensure a seamless integration into the storage ring vacuum system. The most prominent interfaces include the housing vacuum chamber, downstream vacuum components that must be shadowed, and a need to minimize impedance effects. Secondary interfaces include the water system, survey and alignment needs, and in some cases additional storage ring or front end equipment located outside of vacuum, which further constrained the designs.

Four of the five photon absorber designs are housed in vacuum chambers which, due to the tight confines of the overall storage ring vacuum system, typically meant strict spatial limitations. The A:CA2, B:CA1, and B:EA1 photon absorbers are mounted to the antechambers of stretch-formed aluminum L-bend vacuum chambers, while the A:CA1 photon absorber is mounted to a stainless steel vacuum-pumping cross as shown in Fig. 2.

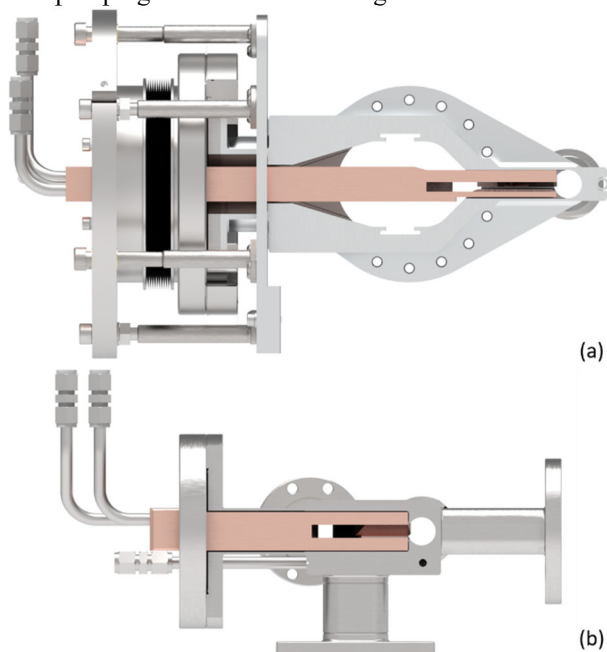


Figure 2: Cross-sectional view of (a) B:CA1 mounted to the B:M2 L-bend vacuum chamber and (b) A:CA1 mounted to the A:VC6 stainless steel vacuum cross.

The interface with the L-bend vacuum chambers was particularly challenging due to their narrow electron beam apertures and pumping slots, which typically limited water-cooling channel geometry to unique, non-circular shapes. Furthermore, nominal gaps of 1 mm to 1.25 mm were designed between the vacuum chambers (including the vacuum cross) and photon absorber surfaces, particularly in the regions closest to the electron beam. These gaps, in addition to beam-intercepting geometry of the photon absorbers, were negotiated with the accelerator physics group to minimize resulting impedance effects while ensuring adequate space for installation and alignment needs.

A skeleton-based CAD model was employed to design all custom vacuum components, which also permitted the creation of an integrated ray-trace model [2]. The ray-trace

model, built off the MBA lattice, allowed for subtle adjustments to vacuum component geometry and refinement of designs. Figure 3 portrays the B:CA1 crotch photon absorber mounted to its L-bend vacuum chamber and the components immediately downstream that it must shadow.

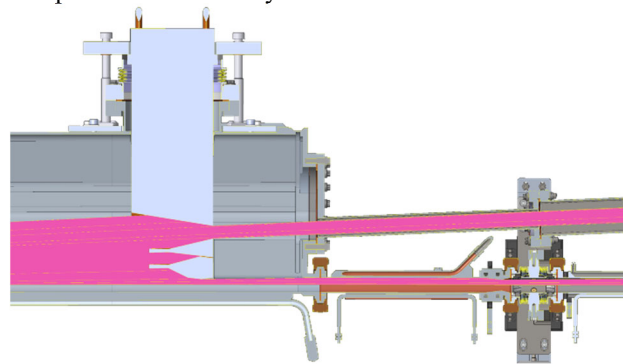


Figure 3: Example ray-trace driven by the skeleton CAD model, with the B:CA1 crotch photon absorber shown.

Using the 3D ray-trace model, beam footprints and corresponding heat loads were calculated for all beam-intercepting components; this data was then utilized as inputs for thermal-structural finite element analyses. From upstream to downstream in the sector arc, Table 1 lists the peak power density at normal incidence and total power for each of the five discrete photon absorbers. A maximum normal power density of 607 W/mm² occurs on the B:FA1 inline photon absorber and maximum total power of 3403 W occurs on the B:CA1 photon absorber.

Table 1: Discrete Photon Absorber Heat Loads

Photon Absorber	Normal Power Density (W/mm ²)	Total Power (W)
A:CA1	111	1064
A:CA2	226	581
B:CA1	251	3403
B:EA1	208	559
B:FA1	607	171

DESIGN AND FABRICATION

With the exception of B:FA1, and to maximize the heat removal capacity given the aforementioned strict interfaces, the photon absorbers were each originally conceived as a monoblock copper chromium zirconium (CuCrZr) design that relied primarily on sinker electrical discharge machining (EDM) to machine a “pocket” and electron-beam (e-beam) welding to weld a pocket “insert,” which together formed the water-cooling channel and avoided any water-to-vacuum joints, as depicted in Fig. 4a [2]. After consulting with reputable vendors, it was determined that this design would prove to be cost prohibitive and incur significant challenges during the manufacturing process, pushing the limits of today’s manufacturing capabilities. Consequently, the final discrete photon absorber designs kept the outer geometry of the CuCrZr variants, but primarily feature e-beam welded GlidCop instead. The primary joining

operation of the final designs was intended to be via brazing, however, the contracted vendor proposed e-beam welding in its place.

The change from the CuCrZr to GlidCop designs, in conjunction with strict spatial limitations, posed a new challenge in designing adequate water-cooling while avoiding water-to-vacuum joints. Fortunately (and historically implemented at the APS), adding another layer of material typically negates the concern with such a joint. Figure 4b depicts a cross-sectional schematic of the final design, wherein any potential breach in the water joint can be evacuated to the open air while preserving the vacuum joint.

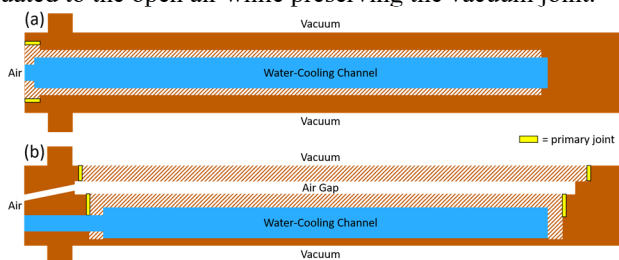


Figure 4: Illustration of a typical discrete photon absorber cross-section for (a) the CuCrZr design and (b) the final GlidCop design.

The production of the discrete photon absorbers will involve several planned manufacturing and incremental quality assurance (QA) steps, with B:CA1 being the most complex. Referring to Fig. 5, machining of the GlidCop B:CA1 photon absorber body—with the exception of the beam-defining edges—and other components such as the copper cover plates and flange components occurs first. The water and vacuum cover plates are then e-beam welded to the GlidCop body, followed by e-beam welding a pre-brazed cooling block and flange adapter disc to the body. The beam-defining edges are then machined via conventional machining and EDM after all e-beam welding to the photon absorber is completed. The bellows-flange assembly is then TIG welded to the photon absorber, followed by assembly of the position adjustment mechanism and water fittings. The B:FA1 photon absorber is a more straightforward brazed GlidCop assembly whose final design was based on that of the integrated photon absorbers that are common to most APS-U non-evaporable getter (NEG)-coated copper vacuum chambers [3]. All photon absorbers will undergo standard vacuum component QA processing, including dimensional evaluation, cleaning, bake-out, vacuum and hydrostatic leak testing, and a final residual gas analysis scan.

Two additional features required by some of the designs include the position-adjustment mechanisms and scattering shields. The A:CA2 and B:CA1 photon absorbers are equipped with position-adjustment mechanisms due to the challenging fabrication of the L-bend vacuum chambers. These mechanisms consist of bellows and supplemental hardware that permit the precise alignment required by the ray-trace. The remaining photon absorbers do not require this adjustable design due to the precise machining of the vacuum cross in the case of A:CA1, or more conservative shadowing incorporated into the nominal B:EA1 and

B:FA1 designs. The three crotch photon absorber designs also feature scattering shields, similar to those employed at the European Synchrotron Radiation Facility, whose sole purpose is to recapture power that is potentially scattered from the beam-intercepting surfaces [4]. Though the housing vacuum chambers are equipped with water cooling, the presence of a scattering shield further reduces any potential for overheating these components, particularly for the stainless steel vacuum-pumping cross due to its poor thermal conductivity.

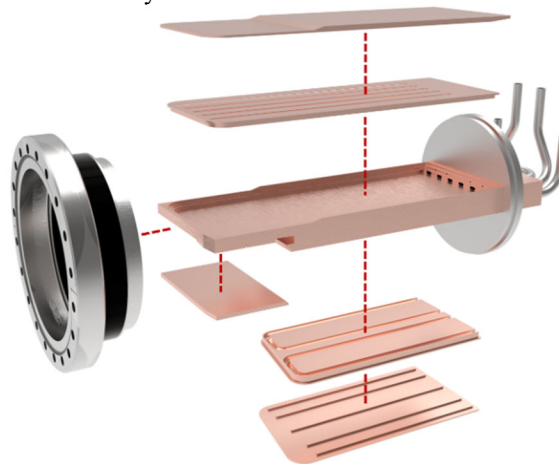


Figure 5: Simplified exploded view of B:CA1, with the major fabrication steps represented.

CONCLUSION

Following an intensive and well-scrutinized design process, the procurement of the discrete photon absorbers is underway with first articles expected in late 2021. Next steps include continued fabrication followed by testing and quality assurance steps, assembly onto the respective magnet modules, and finally, installation into the storage ring vacuum tunnel during the APS dark period.

ACKNOWLEDGEMENTS

The Advanced Photon Source is a U.S. Department of Energy (DOE) Office of Science User Facility operated for the DOE Office of Science by Argonne National Laboratory under Contract No. DE-AC02-06CH11357.

REFERENCES

- [1] APS-U *et al.*, “Advanced Photon Source Upgrade Project Final Design Report,” APS, Illinois, United States, Rep. APSU-2.01-RPT-003, May 2019.
- [2] J.A. Carter *et al.*, “Final Design of the APS-Upgrade Storage Ring Vacuum System”, in *Proc. NAPAC'19*, Lansing, MI, USA, Sep. 2019, pp. 315-317. doi:10.18429/JACoW-NAPAC2019-TUYBB3
- [3] O.K. Mulvany *et al.*, “NEG-Coated Copper Vacuum Chambers for the APS-Upgrade Storage Ring Vacuum System”, in *Proc. NAPAC'19*, Lansing, MI, USA, Sep. 2019, pp. 477-479. doi:10.18429/JACoW-NAPAC2019-TUPLS11
- [4] F. Thomas *et al.*, “X-Ray Absorber Design and Calculations for the EBS Storage Ring”, in *Proc. MEDSI'16*, Barcelona, Spain, Sep. 2016, pp. 257-261. doi:10.18429/JACoW-MEDSI2016-WEAA02

A NEW MAGNETIC MEASUREMENT SYSTEM FOR THE FUTURE LOW EMITTANCE NSLS-II STORAGE RING*

M. Musardo†, T. Corwin, F. DePaola, L. Doom, R. Faussete, D. Harder, S. Sharma, T. Tanabe
 Brookhaven National Laboratory, Upton, New York, USA
 C. L. Doose, A. K. Jain, Argonne National Laboratory, Lemont, Illinois, USA
 D. Assell, J. DiMarco, Fermilab, Batavia, Illinois, USA

Abstract

A new magnetic measurement system is under construction at BNL for accurate field harmonic measurements and fiducialization of magnets for a future upgrade of the NSLS-II storage ring. The entire storage ring is envisioned to be replaced with a new lattice concept, known as Complex Bend, which superimposes dipole and high-gradient quadrupole fields. The magnetic measurement system will use rotating wire and a PCB rotating coil specifically designed for small-aperture (< 15 mm) high gradient magnets. In this paper we describe in detail the mechanical design and the data acquisition hardware and software.

INTRODUCTION

Achieving a low-emittance ring design with high brightness is one of the most challenging aspects of advanced synchrotron light source projects. The major planned future improvement and upgrade of the National Synchrotron Light Source II (NSLS-IIU) at Brookhaven National Laboratory (BNL) is to replace the existing Double Bend Achromat lattice (DBA) with a new lattice element called “Complex Bend” [1-3], which consists of a combination of dipoles and high-gradient quadrupoles with superposing fields [4]. This approach provides reduction of the electron beam emittance to about 20 pm. Accurate and precise higher-order field harmonic measurements are essential to guarantee that the field performance of future magnets fulfills the demanding specifications.

MAGNETIC MEASUREMENT EQUIPMENT

The magnetic measurement system configured at NSLS-II is based on the measuring bench developed at Argonne National Lab (ANL) for the Advanced Photon Source (APS) upgrade project [5].

The new measuring bench consists of a Printed Circuit Board (PCB) rotating coil, designed for measuring field strength and field quality to a level of 0.1 units up to the 15th harmonic and a rotating wire system for determining the magnetic center and for fiducializing multipole magnets with an accuracy better than 10 μm using a Laser Tracker.

Rotating Wire System

Field integral measurement with continuously rotating wire loop was first tried at SPring-8 for the magnetic

measurement of an undulator with 3 mm gap [6]. Unlike a flip coil bench with finite rotation angle, continuously rotating system can use various techniques to improve a S/N ratio.

The measurement bench is assembled on a 2.75 m long granite block supported on 3 leveling jacks. The leveling jacks are JOYCE WJ123 with a 3 Ton capacity, 1 inch of screw travel and 12:1 ratio gearset. The granite block has machined T-slots and Survey & Alignment holes. Both the magnets and the stages are supported on three anodized aluminum plates affixed to the granite surface. Stop blocks on the center plate provide banking surfaces to align the magnet to the rotating wire. Other banking alignment features, such as magnet pushers and support assemblies, help to align the rotating wire and rotating coil to any type of magnet. Aluminum shims between the stop-blocks and the magnet reference surfaces are used depending on the geometry and dimensions of the magnet to be measured. The two outer aluminum plates are populated with Newport X,Y, Z and R stage assemblies as shown in Fig. 1. Thus there is independent X, Y, Z and R positioning at each end of the bench which can operate in tandem.

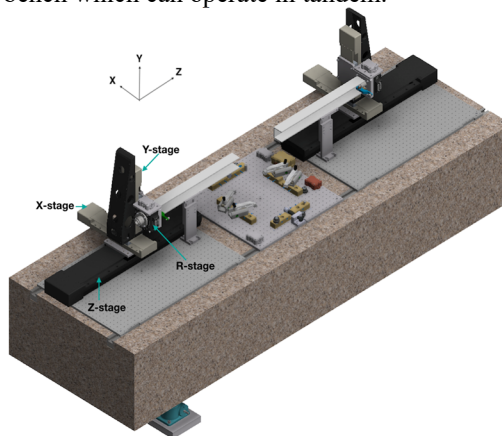


Figure 1: 3D rendering of the NSLS-II magnetic measurement system.

The longitudinal stages have a 600 mm travel range and a DC motor with a rotary encoder on the drive screw that provides 1.25 μm resolution and 2.5 μm bi-directional repeatability. The horizontal and vertical DC servo linear stages have a 200 mm and 100 mm travel range respectively. Both stages have a minimum incremental motion of 1 μm and a bi-directional repeatability of about ± 0.4 μm. A 4000 pts/rev. encoder is mounted directly on the screw in order to prevent screw/motor coupling errors consequently boosting stage motion accuracy. A compact rotation stage equipped with brushless direct drive technology

* Work supported by DOE under contract DE-SC0012704
 † Email address musardo@bnl.gov

provides fast rotation (maximum speed of 720°/s), with a resolution of 1.75 μ rad and an accuracy of $\pm 2.6 \mu$ rad. The rotary encoder, with 15,000 line pairs per revolution, is precisely aligned with the stage's rotation axis to minimize position errors induced by eccentricity, wobble and axial runout. The displacement of the geometric center of the rotation stage from the rotation axis is about $\pm 1 \mu$ m with a wobble error of $\pm 5 \mu$ rad. In order to reduce wire vibration induced by air flow in the Laboratory environment, two U-channel aluminum shields are used to cover the wire. An 8-axis Newport XPS-D integrated motion controller/driver provides coordinated motion of the upstream (US) and downstream (DS) stage assemblies. The motion controller is equipped with advanced compensation algorithms in the servo loop, for backlash and position error mapping. Four Digi-Pas inclinometers, with resolution less than 5 μ rad and accuracy of $\pm 5 \mu$ rad, are used for monitoring bench and stage angles.

A National Instrument (NI) PXI system is employed for trigger generation and data acquisition (DAQ). The NI-PXI (PCI eXtensions for Instrumentation) is composed of three main hardware subsystems: a PXIe-1078 9-slot chassis, a PXIe-8840 embedded controller and seven plug-in modules. The PXI modules and the DAQ system diagram is illustrated in Fig. 2.

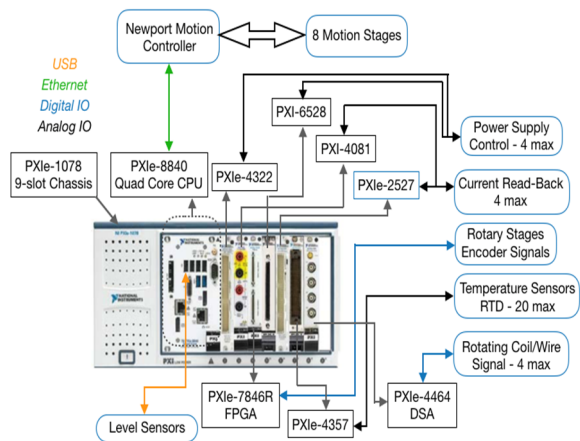


Figure 2: NI DAQ block diagram.

The PXI chassis provides power, cooling, and a 32-bit, 33 MHz communication bus to each hybrid slot, as well as timing and synchronization of the various hardware components with a mix of analog and digital I/O data transfer. The PXIe-8840 embedded controller, configured with LabView Real-Time software and NI drivers, eliminates the need for an external PC. The full control of the measuring bench, such as homing, multi-axis positioning and movement, as well as data acquisition and signal processing are driven by an APS custom-made LabView Virtual Instrument. The instrumentation modules that populate the PXI chassis are: a 24-bit Dynamic Signal Analyzer (DSA) for wire signal acquisition, a 7½-digit Digital Multi-meter for power supply (PS) current readback, a PXI 48-channel parallel digital I/O interface, a 16-Bit, 8-channel, 250 kS/s Ch-Ch isolated PXI Analog Output module for PS control, and a user-programmable FPGA I/O module for the rotary trigger generation. The PXIe-1078 chassis is also equipped

Accelerators

Storage Rings

with a 20-Channel, 24-Bit wire resistance temperature detector (RTD) and a 32-Channel, 300 V, 2-wire PXI Multiplexer switch module for PS DCCT current readback. Both the NI and the Newport equipment are housed in a UL listed NI equipment rack.

Rotating Wire Signal Acquisition

The voltage induced, as the wire rotates about the longitudinal magnet axis, is picked up by a Mercotac two conductor slip-ring and sent to the PXIe-4464 Dynamic Signal Analyzer module. The DSA module is set to 200 kS/s and acquires 10 revolutions of rotating wire signal. The acquired signal is 10 seconds long and contains 2 Msamples, as the rotary stages are set to spin at 1 rev/s. The 2 Msamples of data are integrated and interpolated at 1000 rotary positions per revolution and then averaged to obtain a flux vs rotary position signal.

The rotary data acquisition is triggered by a signal from the FPGA module after an index pulse from the downstream rotary stage is detected. The FPGA code counts the level-shifted and squared sin/cos rotary encoder signals generated by a comparator circuit and fed into the NI SCB-68A terminal box. Upon detection of the index pulse the DSA module promptly begins acquiring the rotating-wire signal. After acquisition, the voltage waveform is numerically integrated to obtain flux as a function of time. The rotary stage has 60k encoder counts per revolution and the time is captured for each 1/1000th of a revolution, therefore, 60 encoder counts is equivalent to 0.36 degrees. The FPGA code runs in a timed loop at 40 MHz, thus the time resolution is 25 ns. The loop index value is saved to memory every 60 encoder counts and the time for each position is equal to the loop index times 25 ns. The time values are used to interpolate the flux values at each 0.36 degree increment yielding a flux signal as a function of angular position.

PCB Rotating Coil

A 12 mm diameter PCB-based rotating coil is being developed under a BNL contract in which Fermilab will provide the conceptual design, prepare the engineering drawings, procure components, fabricate, and perform testing, assembly and commissioning.

The PCB coil design calls for a cylindrical sapphire support to ensure sufficient stiffness, thereby minimizing unwanted vibration and sag. The sapphire also curtails thermal expansion, with a coefficient of 4.3×10^{-6} units/°C. The sapphire support assembly design is similar to that of a small diameter probe built by CERN [7], which had a surface roughness on the bearing surfaces after polishing of 100 nm, and ends which were concentric with a straightness error between 1-3 μ m. The PCB structure outer diameter will be 12 mm and the ends will have 6 mm outer/ 3 mm inner diameter in order to accommodate the 1.8 mm thick printed circuit board, wiring, and ABEC 5 all-ceramic bearings. The active coil length is 270 mm, and the overall probe length is 390 mm. The main parameters of the PCB coil are shown in Table 1. In order to boost the signal amplitude, the probe is designed with a high density of turns

Content from this work may be used under the terms of the CC BY 3.0 licence (© 2021). Any distribution of this work must maintain attribution to the author(s), title of the work, publisher, and DOI

and multiple layers (75 μm wide traces with 75 μm space between them). The layers are very thin -- about 100 μm - and the connection 'vias' between the layers is small - 350 μm diameter. The PCB coil has the capability of providing un-bucked (UB), dipole bucked (DB), dipole-quad bucked (DQB) and dipole-quad-sextupole bucked (DQSB) signals, in order to ensure minimal spurious harmonics in measurements of both quadrupole and sextupole magnets. The coil will be suitable for measuring field quality to a level of 10 ppm of the main field (0.1 "units") up to the 15th harmonic with a sensitivity between 0.01 m^2 and 0.02 m^2 at the reference radius of 5 mm. The bucking factors are expected to be about 1000, therefore the DBuck signal should have a typical absolute measurement of the quadrupole field with an accuracy of about 0.15% (with no calibration).

Table 1: PCB Coil Parameters

Total PCB thickness	< 2 mm
Active coil length	270 mm
Length of each end stem	25 mm
Total probe length	390 mm
Reference radius	5 mm
Diameter	12 mm

For location and dimension control of the traces, a Laser Direct Imaging (LDI) process will be used, which is a precise means of fabrication that avoids physical contact effects, diffraction, temperature and humidity distortions, dimensional changes, etc. Therefore, the PCB coil should have traces with micron level control of both size and position. The PCB design cross-section is shown in Fig. 3. It will have a total of six windings, 16 layers and will be 1.8 mm thick.

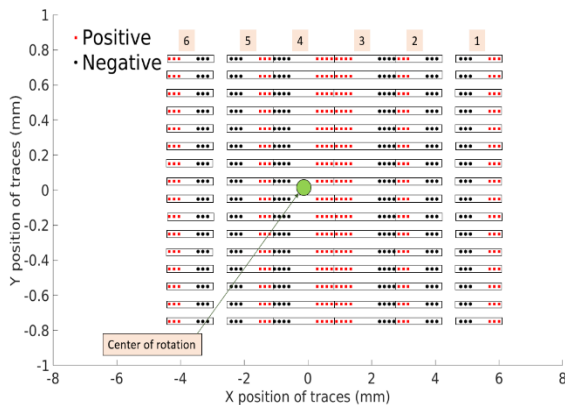


Figure 3: PCB design cross-section showing positive and negative wires of the 6 windings and the rotation center.

A high-accuracy calibration technique will be used to determine at the level of microns the radial and vertical offset of the PCB coil placement into the sapphire support structure, by using the bucked and un-bucked signals [8].

Measurement Plan

The rotating wire bench is currently under survey and alignment. The granite block, surface plates, stages, magnet mounting plate and the rotating wire holders will be aligned using a Laser Tracker. The alignment process will

ensure that the linear stages in each assembly are orthogonal to each other and that the upstream and downstream stage assemblies are parallel. Several small fiducial nests will provide the reference datum for the dimensional control and alignment of the stage assemblies, wire holder runout and for magnet fiducialization.

A 40 mm aperture quadrupole, previously measured at APS, will be used as a test magnet for calibration and comparative measurement of the harmonics in absolute strengths. Also, a set of nine Halbach-style permanent magnet quadrupoles (PMQ) with a bore diameter of 12.7 mm built by RadiaBeam, are planned to be measured using the new PCB coil. These PMQs are designed to produce the desired quadrupole strengths for a prototype Complex Bend application [9].

CONCLUSION

The rotating wire magnetic measurement bench is now fully assembled and nearly operational. The bench can also be used with a PCB coil for high precision harmonic field measurements. The NI hardware, the Newport stages and controller have been successfully tested and commissioned.

ACKNOWLEDGEMENTS

This work has been supported by the U.S. Department of Energy, Office of Science, under contract number DE-SC0012704.

REFERENCES

- [1] T. Shaftan *et al.*, "The Concept of Complex Bend", BNL tech note BNL-211211-2019-TECH, 2019.
- [2] V. V. Smaluk and T. V. Shaftan, "Realizing Low-Emittance Lattice Solutions With Complex Bends", in *Proc. 10th Int. Particle Accelerator Conf. (IPAC'19)*, Melbourne, Australia, May 2019, pp. 1906-1908. doi:10.18429/JACoW-IPAC2019-TUPRB105
- [3] G. Wang *et al.*, "Complex bend II: A new optics solution", *Phys. Rev. Accel. Beams*, vol. 22, p. 110703, 2019.
- [4] S. K. Sharma *et al.*, "High Gradient Quadrupoles for Low Emittance Synchrotrons", in *Proc. 10th Int. Particle Accelerator Conf. (IPAC'19)*, Melbourne, Australia, May 2019, pp. 4332-4334. doi:10.18429/JACoW-IPAC2019-THPTS094
- [5] S. J. Izzo *et al.*, "Magnet Measurement Systems for the Advanced Photon Source Upgrade", presented at MEDSI 2020, Chicago, Illinois, July 2021, paper WEPB03, this conference.
- [6] T. Tanabe *et al.*, "Rotating/Helmholtz Coil System Using a Lock-In Amplifier Method," *6th Int. Conf. on Synch. Rad. Inst. (SRI '97)*, Himeji, Japan, Aug. 1997, *J. Synchrotron Radiat.*, vol. 5, p. 475, 1998.
- [7] P. Arpaia *et al.*, "A high-precision miniaturized rotating coil transducer for magnetic measurements", *Sens. Actuators, A*, vol. 274, pp. 37-49, 2018.
- [8] J. DiMarco *et al.*, "Calibration technique for rotating PCB coil magnetic field sensors", *Sens. Actuators, A*, vol. 288, pp. 182-193, 2019.
- [9] G. M. Wang *et al.*, "CB-II Prototype Test Stand Design", presented at the 12th Int. Particle Accelerator Conf. (IPAC'21), Campinas, Brazil, May 2021, paper MOPAB078.

RECENT STUDIES ON THE VIBRATION RESPONSE OF NSLS-II GIRDER SUPPORT SYSTEM

S. Sharma[†] and C. Spataro, NSLS-II, Brookhaven National Laboratory, Upton, NY, USA

Abstract

The designs of various girder support systems were reviewed recently in a MEDSI School tutorial [1]. A comparison of their horizontal transmissibility values in (2-100 Hz) band showed that the NSLS-II girder support system had a lower transmissibility despite its first natural frequency being the lowest (~30 Hz). Detailed vibration tests and finite element (FE) analyses have been performed to understand this anomaly and to assess the role of viscoelastic damping pads underneath the NSLS-II girders. The analyses were extended to include harmonic response analysis to model viscoelastic properties, and to random vibration analysis to obtain uncorrelated motions between the magnets. The results of these new tests and FE analyses are discussed in this paper.

INTRODUCTION

Ambient floor motion is one of the major sources of beam stability perturbations in the storage rings. The floor motion is magnified by high transmissibility ratios of the girder-magnet assemblies at their natural frequencies. At higher frequencies, the floor motion reduces exponentially [2] as $1/f^n$ with exponent $n = 4$. Therefore, the girder support systems are usually designed with the requirement of high natural frequencies, specifically the 1st natural frequency of > 30 Hz. Girder support systems with higher 1st natural frequencies (see Table 1) are expected to have lower broadband (2 – 100 Hz) transmissibility ratios.

Table 1: Comparison of 1st Natural Frequencies and Transmissibility Ratios in (2 – 100 Hz) Band

Facility	1 st Nat. Freq.	Trans. (H)	Trans. (V)
NSLS-II	30 Hz	1.03*	1.01
APSU [†]	42 Hz	1.30	1.01
ESRF	42 Hz	1.24	1.21
TPS	44 Hz	1.20	1.01
SIRIUS	133 Hz	1.39	1.07

* Corrected to 1.07 [†] Estimated from FE Model

A low transmissivity ratio of 1.03 for NSLS-II girders in the horizontal direction appeared to be inconsistent with a lower 1st natural frequency, $f_{n,1}$, of 30 Hz. Additional vibrations tests were performed at NSLS-II in December 2019 and March 2020. The transmissibility ratio was corrected to 1.07 to account for a calibration difference between the seismometers in the very low frequency range of (2 – 4 Hz), but the apparent discrepancy was still significant.

The design of NSLS-II girder support system is unique in its use of viscoelastic pads for thermal stability. For any fluctuation in the tunnel-air temperature, or the floor

temperature, the viscoelastic pads allow the girders to expand or contract without bending, thereby minimizing magnet-to-magnet misalignment [3, 4]. Although not intended for vibration damping, they are expected to have some effect on reducing the transmissibility ratios. This was investigated by vibration tests and FE models as described in the following sections.

NSLS-II GIRDER-MAGNET ASSEMBLY

A typical NSLS-II multipole girder-magnet assembly is shown in Fig. 1(top). The girder is supported on 2-inch diameter threaded rods at 4 locations approximately 1.2 m apart. Multiple support points increase the stiffness of the girder and raise its natural frequencies. At the bottom, the threaded rods are bolted to a solid 2.5-inch steel plate at the 2nd location from the upstream end, and to viscoelastic pads (Fig. 1(bottom)) at the other locations.

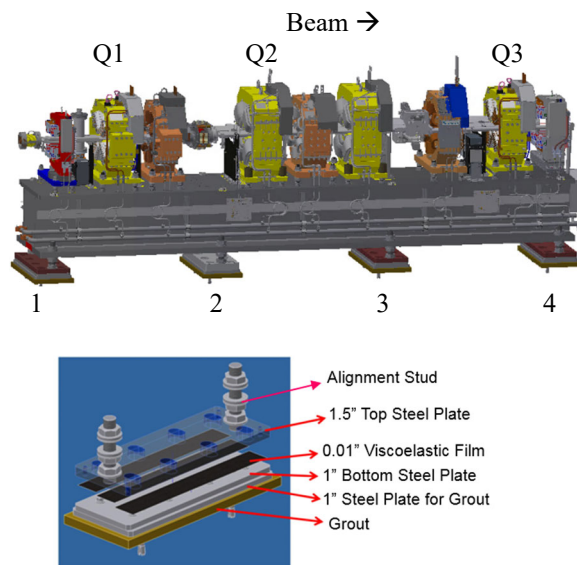


Figure 1: A typical NSLS-II girder (top) is supported at 4 locations. Viscoelastic pads (bottom) are used at locations 1, 3 and 4.

Viscoelastic pads consist of two steel plates, 1.5-inch thick (top) and 1.0-inch thick (bottom), joined by 0.01-inch thick viscoelastic films, brand-name VHB F9469PC, made by 3M[®]. Experimental data for the storage and loss moduli [5] for this film are plotted in Fig. 2.

FE MODELING OF VISCOELASTIC FILM

In Ansys FE models, viscoelastic properties can be expressed as shear and bulk relaxation moduli ($G(t)$ and $K(t)$) in Prony series:

$$G(t) = G_{\infty} + \sum_{i=1}^n G_i \exp\left(-\frac{t}{\tau_i^G}\right) \quad (1)$$

$$K(t) = K_{\infty} + \sum_{i=1}^n K_i \exp\left(-\frac{t}{\tau_i^K}\right) \quad (2)$$

[†] sharma@bnl.gov

where coefficients of the Prony series ($G(\infty), K(\infty), G_i, K_i, \tau_i^G, \tau_i^K$) are determined from experimental storage and loss moduli provided as input data.

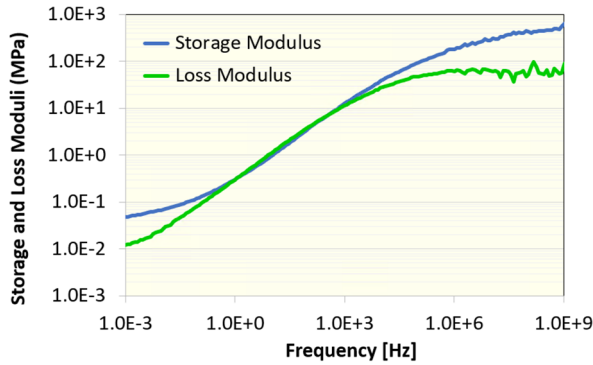


Figure 2: Storage and loss moduli of VHB F9469PC[®] viscoelastic film versus frequency [5].

Viscoelastic material models can be used in Ansys harmonic response analysis but not in random vibration analysis. Therefore, in random vibration analysis the effect of viscoelastic damping was included indirectly. The girder-magnet assembly was first modelled without the viscoelastic films with structural damping ratio decreasing with frequency. Based on past experimental data, the damping ratio was approximated as 0.01 (1 - 40 Hz), 0.005 (40 - 80 Hz) and 0.0025 (80 - 110 Hz). Harmonic response analyses with horizontal base excitation were then performed including viscoelastic films in the FE model. Finally, the damping contribution of the viscoelastic films was simulated by increasing the frequency dependent damping ratios while using only the elastic properties of the films. The resulting equivalent damping ratios were established as: 0.035 (1 - 40 Hz), 0.02 (40 - 80 Hz) and 0.0075 (80 - 110 Hz), representing a factor of ~ 3 increase over the initial damping ratios. Harmonic responses for the Q3 magnet (Fig. 1) for the three different cases of damping are compared in Fig. 3. Peak transmissibility values at the natural frequencies show that equivalent damping ratios can represent the viscoelastic damping effect reasonably well.

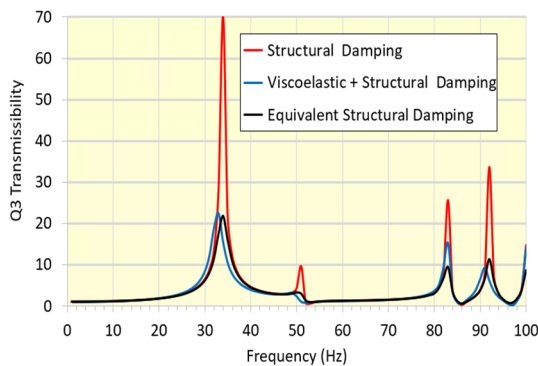


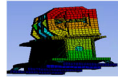
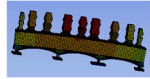
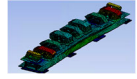
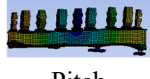
Figure 3: Horizontal transmissibility ratio of Q3 magnet for 3 different cases of damping, (1) structural, (2) structural + viscoelastic, and (3) equivalent structural.

RANDOM VIBRATION ANALYSIS

Natural frequencies of the girder-magnet assembly were first calculated as a prerequisite for the random vibration

analysis. The first five natural frequencies, $f_{n,1}$ to $f_{n,5}$, with their mode shapes are shown in Table 2. Higher modes ($f_n > 100$ Hz) are not included since the floor motion above 100 Hz is negligible.

Table 2: Natural Frequencies and Mode Shapes

$f_{n,i}$	FE Analysis (Hz)	Experimental (Hz)	Mode Shape (X, Y, Z: Hor., Ver., Beam)
1	30.4	30.0	 X-Translation – Roll
2	46.4	43.8	 Yaw
3	66.6	61.9	 Bend (Y-Z Plane)
4	81.3	77.5	 Bend (X-Z Plane)
5	84.1	89.1	 Pitch

The calculated natural frequencies and equivalent damping ratios were used in the random vibration FE model. Input motion at the base was applied as two separate PSDs at the support locations (1,2) and (3,4) because at NSLS-II the floor motion is not correlated above 10 Hz for a distance of > 2 m [6]. Experimental floor PSDs were obtained with Sercel (model L4-C) seismometers.

Measured and calculated PSDs in the horizontal direction for the Q3 magnet are plotted in Fig. 4 together with the floor PSD.

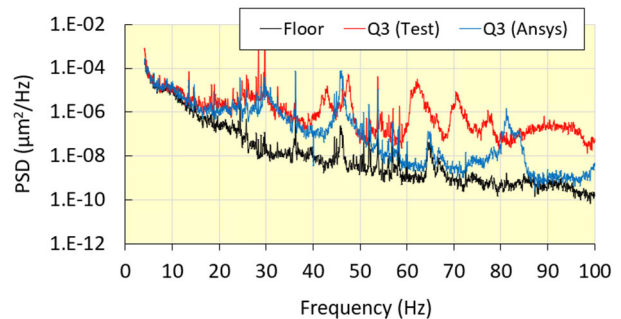


Figure 4: Measured (red) and calculated (blue) PSDs of Q3 magnet in the horizontal direction. PSD of the floor used as input in the FE analysis is also shown (black).

Figure 4 shows a good agreement between the experimental and FE analysis data for frequencies below 50 Hz. The agreement is poor above 60 Hz with more peaks in the test data. The floor motion above 50 Hz is small, 0.5 nm

rms compared to 13.3 nm rms in (4-50 Hz) band, and its effect on the integrated motion and transmissibility ratio is also comparatively small. The peaks at the first two natural frequencies, (30.4 Hz and 46.4 Hz) are damped substantially by the high equivalent damping ratios provided by the viscoelastic pads. This results in overall low transmissibility ratios of the NSLS-II girder-magnet assemblies (Table 1).

UNCORRELATED MOTION

At NSLS-II the vibration specification is given as uncorrelated motion between the end quadrupoles on the girder, Q1 and Q3, (Fig. 1). In the horizontal direction the rms value in (2–100 Hz) band is specified to be < 150 nm. For the upgrade of NSLS-II this value is expected to be an order of magnitude lower.

Uncorrelated rms motion between the quadrupoles can be readily measured on prototypes or in-service girder-magnet assemblies. However, in a random vibration FE analysis, the rms motions for the magnets contain no phase information. Uncorrelated motion between the magnets is, therefore, not available to evaluate different girder designs with respect to this specification. The following approach is being evaluated to address this for the future upgrade of NSLS-II.

Correlation coefficient between Q1 and Q3 is plotted in Fig. 5 from a recent (December 2019) set of test data. The correlation coefficient is ~ 1.0 up to the first natural frequency of 30 Hz. The girder can be assumed to be rigid in (2 - 30 Hz) band with no relative motion between Q1 and Q3. Above 30 Hz, the correlation coefficient drops sharply with its value fluctuating between roughly equal positive and negative values. Conservatively it can be assumed that the uncorrelated rms motion between the two magnets is the SRSS of their integrated rms motions in (30 – 100 Hz) band.

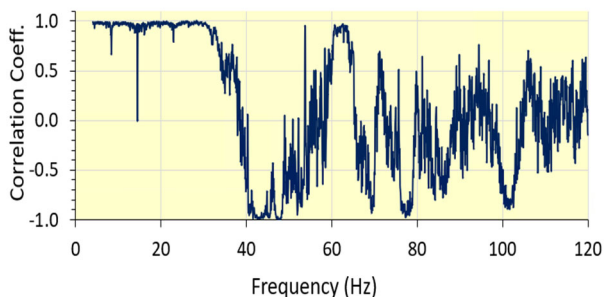


Figure 5: Correlation coefficient between Q1 and Q3 magnets.

FE analysis results for the integrated rms motions of Q1 and Q3 in the (30-100 Hz) band are plotted in Fig. 6. A large fraction of the motion occurs at 46.4 Hz in the yaw mode in which Q1 and Q3 move in the opposite directions. With integrated motions of 15.5 nm for Q1 and 7.5 nm for Q3, an uncorrelated motion of 17.2 nm is obtained. In comparison, the measured value of uncorrelated motion in the (4 - 100 Hz) band was 18.2 nm.

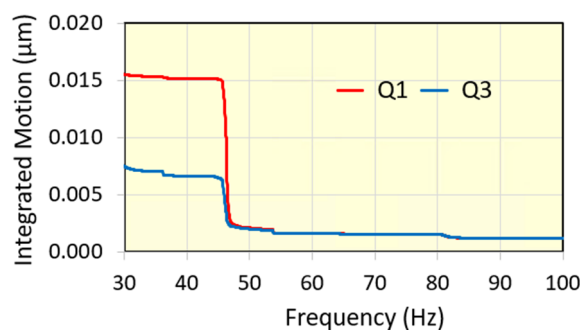


Figure 6: FE analysis results for the integrated rms motions of Q1 and Q3 in (30 - 100 Hz) band. A large fraction of the motion occurs in the yaw mode at 46.4 Hz.

CONCLUSION

FE analyses and experiments were performed to investigate the low transmissibility ratio of the NSLS-II girder support system. Viscoelastic films in the support pads were modelled using experimental storage and loss moduli. The results show that viscoelastic pads increase the effective damping ratio of the girder by a factor of ~ 3, thus lowering its transmissibility ratio. Relative motion between the quadrupole magnets was essentially uncorrelated above the 1st natural frequency (~ 30 Hz). From random vibration analysis the uncorrelated quadrupole motion was estimated as 17.2 nm.

ACKNOWLEDGEMENTS

This work has been supported by the U.S. Department of Energy, Office of Science, under contract number DE-SC0012704.

The authors thank Q. Yuan and A. Cotter of 3M[®] Corporation for providing technical data and guidance on VHB viscoelastic films. Many discussions with James Dymoke-Bradshaw of the Diamond Light Source were helpful in performing vibrations tests and interpreting the results.

REFERENCES

- [1] S. Sharma, “Storage ring issues for low-emittance storage rings,” presented at *MEDSI School 2*, Grenoble, France, 2019. https://medsi.lbl.gov/SysIncludes/retrieve.php?url=https://medsi.lbl.gov/files/page_164/Sharma_SupportSystem_Alignment_Stability_Oct18_2019.pdf
- [2] A. Seryi, “Ground motion and vibration issues for accelerators,” in *Proc. PAC2001*, Chicago, IL, USA, June 2001, paper WOAB009, pp. 364-368.
- [3] V. Ravindranath *et al.*, “Stability of NSLS-II girder-magnet assembly,” in *Proc. MEDSI2010*, Oxford, England, UK, October 2011. <http://dx.doi.org/10.1017/S2044820110000675>
- [4] S. Sharma *et al.*, “Optimization of magnet stability and alignment for NSLS-II,” in *Proc. PAC2011*, New York, NY, USA, March-Apr 2011, paper THOBS2, pp. 2082-2086.
- [5] Q. Yuan and A. Cotter, 3M[®] Corporation, Private Communication, March 2020.
- [6] C. Spataro *et al.*, “Recent site vibration studies at NSLS-II,” presented at *MEDSI2014*, Melbourne, Australia, October

Content from this work may be used under the terms of the CC BY 3.0 licence (© 2021). Any distribution of this work must maintain attribution to the author(s), title of the work, publisher, and DOI

2014. https://medsi.lbl.gov/SysIncludes/retrieve.php?url=https://medsi.lbl.gov/files/page_156/Presentations/Recent_Site_Vibration_Studies_at_NSLI_II_Sushil_Sharma

VACUUM PUMPING CROSSES AND KEYHOLE VACUUM CHAMBERS FOR THE APS-UPGRADE STORAGE RING VACUUM SYSTEM*

A. McElderry[†], B. Billett, J. Carter, O. Mulvany
Argonne National Laboratory, Lemont, Illinois, 60439 USA

Abstract

The Advanced Photon Source Upgrade (APS-U) storage ring arc consists of a diverse system of narrow-aperture chambers in compact magnet assemblies with gaps often less than 1 mm. The vacuum system contains two stainless steel pumping crosses and two keyhole-shaped vacuum chambers, as well as eight non-evaporative getter (NEG) coated aluminum chambers and crosses per sector (40 total sectors). Each chamber contains a 22 mm diameter electron beam aperture and the keyhole components also feature a photon extraction antechamber. Each design balances functionality, manufacturability, and installation needs.

The design process was aided by a flexible CAD skeleton model which allowed for easier adjustments. Synchrotron radiation heat loads applied to inline chamber photon absorbers and photon extraction beam envelopes were determined via a 3D ray tracing CAD model. The inline photon absorber and the keyhole shapes were optimized using iterative thermal-structural FEA. Focus was put on mesh quality to model the <0.5 mm tall synchrotron radiation heat load absorbed across the length of the chamber to verify cooling parameters. The design process also required careful routing of the water system and vacuum pumps. The designs incorporate beam physics constraints of the inline absorbers, cross-housed discrete absorbers, and pumping slots.

The group of chambers require complex manufacturing processes including explosion bonding, EDM, NEG and copper coating, extruded and drawn tubing, e-beam welding, challenging TIG welding, UHV cleaning, and critical dimensional measurements. The 528 chambers entered the production phase starting in 2019 with some design evolution reflecting the vendors' capabilities. This paper details the design, analysis, and manufacturing of these chambers.

INTRODUCTION

The APS-Upgrade (APS-U), when completed, will have a 6 GeV, 200 mA 1.1 km storage ring with a brightness greater than 4 keV. The storage ring consists of a diverse set of vacuum chambers including, but not limited to two stainless steel (SST) keyhole chambers, two specialty SST pumping crosses, and eight non-evaporative getter (NEG) coated aluminum vacuum chambers and crosses per sector (40 total sectors). The vacuum system also features NEG-coated copper and Inconel chambers, aluminum L-bend chambers, discrete photon absorbers, and beam position

monitors with RF-lined welded-on bellows [1, 2]. Generally, all chambers house the electron beam within a $\varnothing 22$ mm aperture, often with a minimum ~ 1 mm wall thickness and magnet gap <1 mm. An example of an aluminum cross is shown in Fig. 1.



Figure 1: Rendering of the NEG-coated aluminum pumping cross; chamber lengths range from 289 mm to 792 mm.

The SST keyhole chambers feature an extended outboard aperture to serve in the photon extraction scheme as shown in Fig. 2.



Figure 2: Rendering of a SST keyhole vacuum chamber; chambers lengths range from 305 mm to 350 mm.

The specialty SST crosses (Fig. 3) adapt similar concepts from the keyhole and aluminum chambers. The more complex A:VC6 cross houses a discrete crotch photon absorber and branches the photon extraction away from the electron beam.

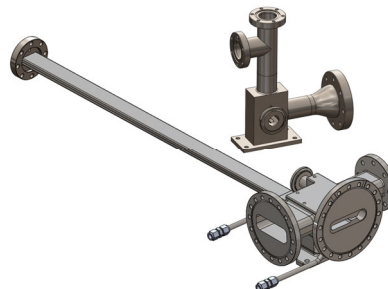


Figure 3: Rendering of the two specialty SST crosses (A:VC15 on top and A:VC6 on the bottom).

INTERFACES

All chambers interface with the following systems: magnets, water circuits, electrical bakeout system, and other vacuum components. The primary design constraint is the narrow space envelope allowed within the quadrupoles and sextupole magnet bores. Figure 4 and Fig. 5 highlight the common constraints.

* This research used resources of the Advanced Photon Source, a U.S. Department of Energy (DOE) Office of Science User Facility at Argonne National Laboratory and is based on research supported by the U.S. DOE Office of Science-Basic Energy Sciences, under Contract No. DE-AC02-06CH11357.

[†] amcelderry@anl.gov

Content from this work may be used under the terms of the CC BY 3.0 licence (© 2021). Any distribution of this work must maintain attribution to the author(s), title of the work, publisher, and DOI

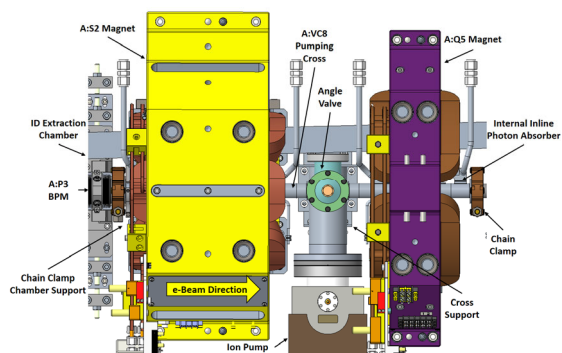


Figure 4: Top view of an aluminum pumping cross within a sextupole (left) and quadrupole (right) magnet.



Figure 5: Cross-sectional view of an aluminum chamber (left) and keyhole chamber (right) within a quadrupole magnet.

The second space constraint, especially for the keyhole chambers, is the stay clear space envelope designated for the electron and photon beams. A ray tracing layout was created in tandem with a CAD skeleton model as shown in Fig. 6. This allowed the ability to map heat load footprints of synchrotron radiation as well as have the flexibility to adjust design parameters while the ray tracing automatically updates. This system approach influenced the design of many storage ring components to carefully adjust heat loads and shadow sensitive components [3].

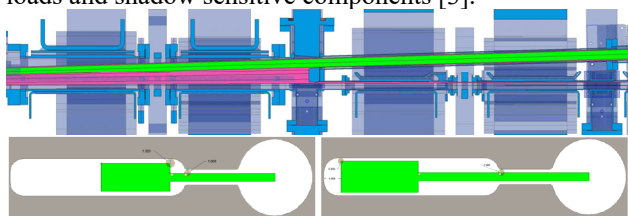


Figure 6: Top cross-sectional view of the ray trace through several chambers (top, beam direction from left to right), upstream (L) and downstream (R) cross-sectional view of the beam envelope (in green) within the keyhole chambers.

The A:VC6 cross houses a discrete crotch photon absorber within the main body as shown in Fig. 7. The pocket follows the contour of the absorber with a 1 mm gap to balance considerations for impedance and arcing concerns.

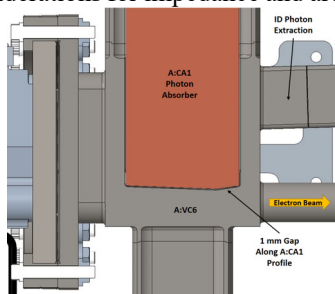


Figure 7: Top cross-sectional view of the discrete photon crotch absorber within the A:VC6 cross body.

DESIGN AND FABRICATION

The final design of the NEG-coated Al cross is shown in Fig. 8 after prototyping and consideration for manufacturability. The cross consists of a standard chamber on the upstream side, central body with venting slots, and a standard chamber with an inline photon absorber machined into the downstream flange. The chamber bodies are a three-cavity 6063 Al extrusion with the Ø22 mm beam aperture in the center and two flanking Ø5 mm channels for outboard water cooling and inboard in-situ bakeout heaters. All flanges are 316L SST/2219 Al bimetal. The flanges along the beam path are SST Quick ConFlat (QCF) which seal via space saving chain clamps and custom copper RF sealing gaskets common across the APS-U storage ring. The Al chambers are NEG coated after fabrication to reduce outgassing and add distributed pumping. Ion pumps and NEG-coated chambers provide the pumping for the conductance-limited vacuum system. Considerable effort was made to produce a compact water-cooling scheme to the inline absorber while fitting in the narrow space envelope and ensuring the parts could be welded [4].

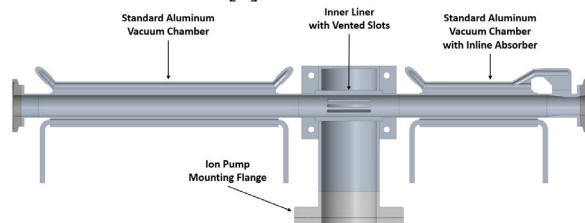


Figure 8: Top cross-sectional view of a NEG-coated Al cross.

A few minor design changes were implemented into the production parts after the completion of fabrication samples. The most considerable change was to the saddle weld joint between the cross body and vented tube. The joint was converted into a butt weld joint to achieve consistent full penetration welding, which eliminated the risk of trapped cleaning fluids compromising the NEG-coating process.

The design of the 316LN SST keyhole chamber is shown in Fig. 9. Generally, the design was driven by the tight interfaces with the magnets and beam envelope as well as mechanical stresses during operation [4]. Similar to many of the other vacuum chambers, it features outboard water cooling and a pair of bakeout heaters. Two heaters are necessary due to the poor thermal conductivity of SST.

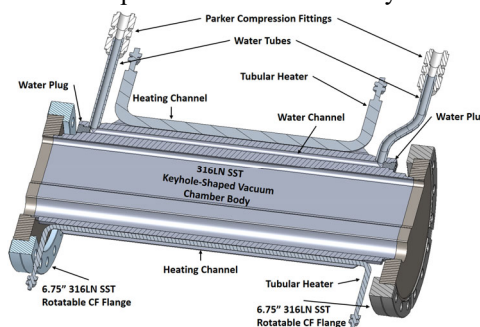


Figure 9: Top cross-sectional view of a SST keyhole chamber.

The final design required the chamber body to be fabricated via wire EDM and the flanges brazed to the ends. The chamber is completed after an electroplated copper finish is applied to the entirety of the aperture [4]. Since the start of production, the design has been updated to accommodate a vendor preferred fabrication approach. The chamber body exterior is milled and the interior is wire electrical discharge machined (EDM). The flanges are e-beam welded along a racetrack-shaped path perpendicular to the flange face. The flange is then machined flat. The A:VC6 cross utilizes this joint design for a nearly identical application. Thus far, this joint has been proven reliable from vendor performed leak tests and residual gas analysis.

The more complex A:VC6 specialty SST cross is shown in Fig. 10. The design shares a few aspects with the keyhole chambers (the aforementioned e-beam weld joint for one flange and copper electroplated interior). The cross body is the most complex component which requires careful EDM to produce the absorber pocket. The welded-on photon extraction chamber design originally consisted of two bent sheet metal halves with a longitudinal e-beam weld. Since production, most of the extraction chamber bodies are formed via drawn tubing. The SST A:VC15 cross (Fig. 3) shares many commonalities with the central body of the aluminum chambers.

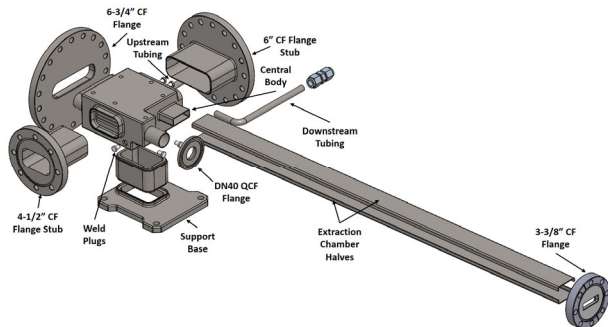


Figure 10: Exploded view of the A:VC6 cross design.

FINITE ELEMENT ANALYSIS

Finite element analysis (FEA) was extensively utilized to develop the final chambers designs. Chambers were analyzed under operating conditions, bakeout conditions, and tested for buckling. The overall strategy required model partitioning to optimize mesh quality for thin walls and beam heat load footprints. In the case for the larger crosses, submodeling was used to more efficiently analyze large models with sub-millimeter sized heat load applications. In the case of analyzing the chambers during operating conditions, a coupled thermal-structural set-up was used with a turbulent water-cooling convective heat transfer coefficient applied to the water channel and synchrotron heat loads applied on the beam footprint along the outboard surfaces. Figure 11 shows the hottest Al cross with 98 W and a max temperature of 83.7°C on the inline photon absorber. Atmospheric and water pressure as well as mechanical constraints were applied to the structural analysis. The resulting maximum stress (46.3 MPa) occurs on the aluminum part of the inline bimetal absorber as shown in Fig. 12.

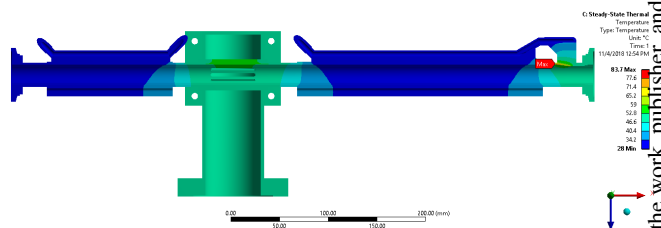


Figure 11: Top cross-sectional view of temperature results of the pumping cross FEA (max temperature of 83.7°C).

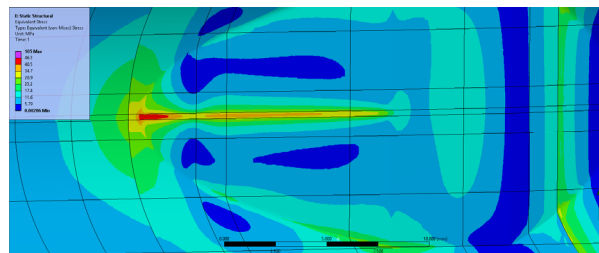


Figure 12: Von-Mises stress results on the inline photon absorber (maximum stress 46.3 MPa).

In addition to thermal-structural analysis, the thin-wall SST keyhole and rectangular extraction chambers were analyzed for buckling due to the wide non-circular aperture. An example shown in Fig. 13 demonstrates that the keyhole chambers' critical load is approximately 328 atm. The buckling model is kept simple with a 4 mm thick (in x) sliver since vertical collapse would be the most reasonable mode for buckling to occur.

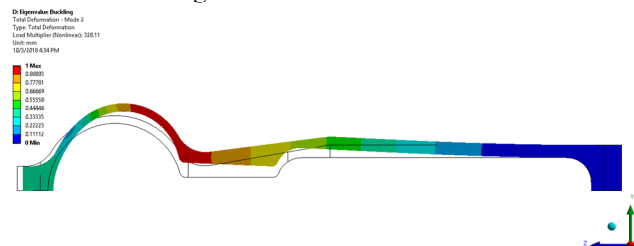


Figure 13: Critical load found to be 328 atm from buckling FEA for the keyhole chambers.

CONCLUSION

The APS-U is confident with the expected performance of the components presented in this paper. All components have been extensively designed, analyzed, and reviewed. At the time of this publication, most first article chambers have arrived at the APS with the production batches expected through 2022.

ACKNOWLEDGEMENT

The Advanced Photon Source is a U.S. Department of Energy (DOE) Office of Science User Facility operated for the DOE Office of Science by Argonne National Laboratory under Contract No. DE-AC02-06CH11357.

REFERENCES

- [1] J.A. Carter *et al.*, “Final Design of the APS-Upgrade Storage Ring Vacuum System”, in *Proc. NAPAC'19*, Lansing, MI, USA, Sep. 2019, pp. 315-317.
doi:10.18429/JACoW-NAPAC2019-TUYBB3
- [2] O.K. Mulvany *et al.*, “NEG-Coated Copper Vacuum Chambers for the APS-Upgrade Storage Ring Vacuum System”, in *Proc. NAPAC'19*, Lansing, MI, USA, Sep. 2019, pp. 477-479.
doi:10.18429/JACoW-NAPAC2019-TUPLS11
- [3] J.A. Carter, “3D Numerical Ray Tracing for the APS-Upgrade Storage Ring Vacuum System Design”, in *Proc. MEDSI'18*, Paris, France, Jun 2018, pp. 312-315.
doi:10.18429/JACoW-MEDSI2018-THOAMA05
- [4] A. McElderry *et al.*, “Final Design of NEG-Coated Aluminum Vacuum Chambers & Stainless Steel Keyhole Vacuum Chambers for the APS-U Storage Ring”, in *Proc. NAPAC'19*, Lansing, MI, USA, Sep. 2019, pp. 480-482.
doi:10.18429/JACoW-NAPAC2019-TUPLS12

VALIDATION OF APS-U MAGNET SUPPORT DESIGN ANALYSIS AND PREDICTION*

Z. Liu[†], W.G. Jansma, J. Nudell, C.A. Preissner
 Advanced Photon Source, Argonne National Laboratory, Lemont, IL 60439, USA

Abstract

The Advanced Photon Source Upgrade (APS-U) accelerator magnets have stringent stability requirements [1]. The project schedule and budget did not allow for full prototyping of the final design. Therefore, the engineers relied on accurate simulation to ensure that the design would meet the specifications. Recently, assembly and free-boundary vibration tests have been done on the first article of the upstream quadrupole Doublet, Longitudinal gradient dipole and Multipole module (DLM-A). The top surface flatness of the girder and the magnet alignment measurement results demonstrate the static positioning requirement of magnet-to-magnet is met. The free-boundary condition modal test results were used to validate dynamic performance of the FEA analysis used in the DLM-A design. These validations then confirm the predicted performance of the magnet support system design. Mode shapes and corresponding frequencies from the FEA modal analysis agree with the experimental modal analysis within an acceptable tolerance. The validation approves not only the procedure for accurate modelling of magnet support system that APS-U has developed, but also provides confidence in predicting the accelerator performance.

INTRODUCTION

The Advanced Photon Source Upgrade (APS-U) accelerator magnets have stringent stability requirement [1]. Some of the requirements are listed in Tables 1 and 2, which service as a guideline through all design phases.

Table 1: Positioning Tolerances

Elements within a girder		
Magnet to magnet (2 sigma cutoff)	30	$\mu\text{m rms}$
Dipole roll	0.4	mrad
Quadrupole roll	0.4	mrad
Sextupole roll	0.4	mrad

Table 2: Vibrational Tolerances

(1-100 Hz)	X (rms)	Y (rms)
Girder vibration	20 nm	20 nm
Quadrupole vibration	10 nm	10 nm
Dipole roll vibration	--	0.2 μrad

* This research used resources of the Advanced Photon Source, a U.S. Department of Energy (DOE) Office of Science User Facility at Argonne National Laboratory and is based on research supported by the U.S. DOE Office of Science-Basic Energy Sciences, under Contract No. DE-AC02-06CH11357.

[†] zpliu@anl.gov

The APS-U magnet support design has gone through phases of conceptual, preliminary, and final design. In preliminary design a prototype of FODO module assembly was reported [2-5]. The magnet grouping has been changed through the design phases [6]. Figure 1 shows APS-U magnet grouping of final design. The “QMQ” places a dipole magnet with its adjacent two quadrupoles on a common support (girder), while “A” and “B” imply upstream and downstream positions. Three plinths provide support to corresponding girders above each, while a QMQ girder is supported on adjacent plinths at each end.



Figure 1: APS-U magnet grouping of final design.

A testing and modelling process has been developed and established to close the loop on the design-analysis-testing workflow [4, 7]. This process provides confidence in simulation results and enables the exploration of many different design iterations using the same components.

These design iterations reflect updates of constraints, such as more stringent space limitations from interfacing systems. The support components between girder and plinth are also updated. Some constraints remained the same throughout the process, such as maximizing eigenvalues of low vibration modes of the system, whose mode shapes would cause dynamic deformation in a direction transverse to the beam path. For static deformation, minimizing the girder deformation improves alignment between magnets within a girder. One must also ensure that thermal fluctuations within the storage ring tunnel will not cause unacceptable changes in magnet alignment. Fabrication and material selection also constraint the design. All these constraints play roles in optimizing the design at each iteration.

Recently, the first article of the DLM-A module magnet support system arrived. Girder flatness was measured, both with and without magnets installed. Then, assembly of the DLM-A module without the APS-U vacuum system was completed. A free-boundary condition experimental modal analysis (EMA) was conducted using a Data Physics Abacus DAQ system [8] and Vibrant Technology MEScope [9] for modal property estimation. These results were used to validate the finite element (FE) analysis used in the DLM-A design.

This design-analysis-measurement chain for the DLM-A module validates the FEA prediction and modelling process. This validation provides confidence in predicting the accelerator performance.

Content from this work may be used under the terms of the CC BY 3.0 licence (© 2021). Any distribution of this work must maintain attribution to the author(s), title of the work, publisher, and DOI

VALIDATION: STATIC RESULTS

The girder was machined and measured with a Leica AT930 laser tracker while constrained by three vertical supports at the same locations used to support the girder in operation. The location of those three supports was chosen to minimize the girder static deflection.

In addition, mounting surface of magnets and stop blocks are precisely machined. Magnet alignment is achieved by precisely machining the girder reference surfaces, combined with shimming in the cases where it is necessary.

Surface Flatness and Deformation

The flatness of the girder prior to mounting magnets reflects machining accuracy. It's checked using the Leica AT930 laser tracker. The DLM-A girder is coated in a thin layer of Molykote Tecnite 3402 for rust prevention. The thickness of the coating varies from ~10 to 30 microns over the girder surface. The measurements include the effect of the coating. Many points on the top magnet-mounting surface of the 5.6m long girder were measured (Fig. 2). Flatness of the girder is ± 18 microns peak-peak [10]. After the magnets are positioned, the measured surface flatness of DLM-A girder is ± 23 microns (Fig. 3), while FEA predicted flatness is ± 29 microns in Fig. 4. Part of the magnet alignment survey data [10] are listed in Table 3, approving the magnet alignment in the critical X and Y directions meet the 30 microns RMS tolerance in Table 1.

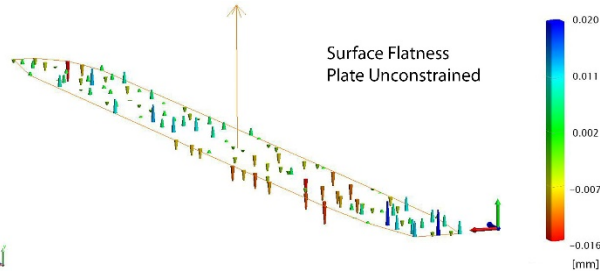


Figure 2: Measured flatness of DLMA girder, unconstrained and prior to mounting magnets.

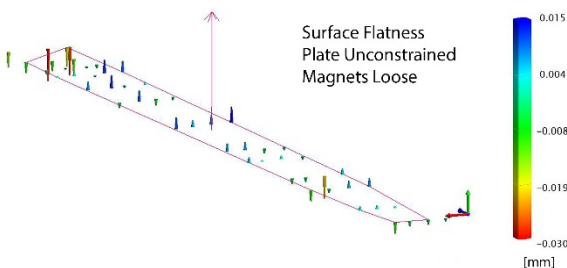


Figure 3: Measured flatness of DLMA girder, unconstrained and post mounting magnets.

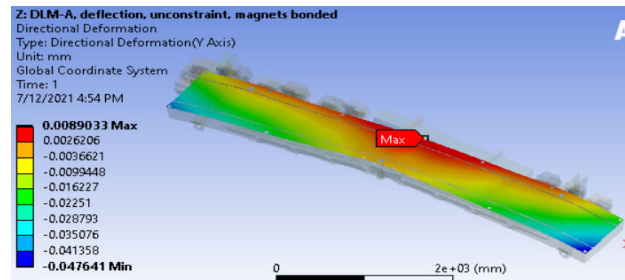


Figure 4: FEA simulated flatness of DLMA girder, unconstrained and post mounting magnets.

Table 3: Magnet Alignment Survey Results

	X offsets (μm)	Y offsets (μm)
Measurement	9, rms	13, rms
Uncertainty	7, rms (magnitude)	

VALIDATION: FODO PROTOTYPE

Previously, the FODO prototype provided validation to the design and analysis process for the support systems [7]. A full prototype was constructed, consisting of the girder, the plinth, and a set of support and alignment mechanisms. Analyses were carried out, along with EMA of both the components and the whole prototype FODO module, including both free and grouted boundary conditions. The results of all tests were found to compare well with the results from the analyses.

Girder

Ductile cast iron, A536, GR-60/40/18 was chosen as the girder material because of its design flexibility, low cost, and favourable vibration damping properties [3, 5]. Figure 5 shows the FODO prototype girder casting at the manufacturer, rigging for a free BC EMA [7]. The EMA and FEA results are compared in Table 4. It confirms the assumption that material properties of the cast iron in FEA are sufficient to predict its behaviour.



Figure 5: FODO prototype undergoing free BC EMA.

Table 4: Girder Modal Results (Avg. Difference 1.99%)

Mode	EMA (Hz)	FEA (Hz)	% Diff
1	106	104	1.89
2	157	154	1.91
3	232	227	2.16

Plinth

The prototype FODO plinth was a steel-reinforced concrete structure developed through a research and development collaboration with a university, concrete fabricator, steel fabricator, and ANL [5]. The steel-reinforced concrete structure was chosen for the favourable performance, cost, and convenience of local fabrication. As with the girder, a finite element modal analysis and EMA were performed. The results compared well and are shown in Table 5.

Table 5: Plinth Modal Results (Avg. Difference 5.4%)

Mode	EMA (Hz)	FEA (Hz)	% Diff
1	38	41	7.9
2	83	84	1.2
3	97	104	7.2

Support Components

Dynamic stiffness testing was conducted on the vertical and lateral support components. Linearized stiffness coefficients were determined for a variety of wedge jack adjusters, spherical bearings, metal-polymer bearings, and load conditions [7]. These components all have stiffnesses that are highly dependent on load. The experimentally measured values are the key information to be used with simplified geometry for accurate FEA.

Grouted FODO Prototype

After the subcomponent test the full FODO assembly was grouted to the floor and underwent EMA. The first three EMA modes are shown in Table 6 to match well with the first three FE modes, with an average error of 8.6%. With the models of the girder, plinth, previously validated, the experimentally measured support stiffnesses, and the assumed load on the supports, the close match confirms that the rigid ground assumption is valid. This also validated the whole design-modelling process, and this process was key for the final design.

Table 6: Grouted FODO Prototype Modal Results (Avg. Difference 8.6%)

Mode	EMA (Hz)	FEA (Hz)	% Diff
1	41	42	2.4
2	54	62	12.9
3	69	77	10.4

VALIDATION: DLM-A FIRST ARTICLE

Evolving accelerator design constraints meant the magnet support final design was quite different from that in preliminary design. For example, the girder width is 750 mm rather than 1 m, the wedge jack of vertical supports is Nivell DK-2/10 rather than Airloc 2012-KSKCV, and the plinth geometry is simplified. The previous validation of the process with the FODO prototype and its components provides confidence in the approach to final design. The stiffnesses of the support components was obtained through the same dynamic testing process. The girder and plinth properties did not change, only the geometry, so all

previous assumptions are still valid. As discussed in ref [7], the confidence leads to production of the final design.

Without prototyping and further validating individual components in the final design phase, the first article of DLM-A support system arrived. Figure 6 shows the first article DLM-A being lifted for a free BC EMA. Table 7 shows the good comparison between the EMA and FEA for first five modes. Note the good match for even the higher modes. Figure 7 shows match of the first natural frequency and mode shape as example.



Figure 6: DLM-A first article undergoing free BC EMA.

Table 7: DLM-A First Article Free BC EMA Modal Results (Avg. Difference 6.0%)

Mode	EMA (Hz)	FEA (Hz)	% Diff
1	68	74	8.8
2	71	76	7.0
3	85	88	3.5
4	91	83	8.8
5	101	103	2.0

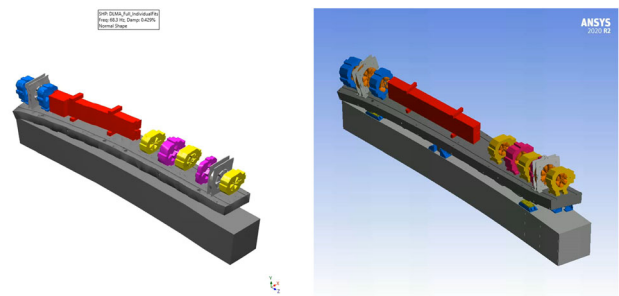


Figure 7: EMA (left) first mode shape at 68 Hz and FEA (right) first mode shape at 74 Hz.

CONCLUSION

The FEA prediction of the FODO prototype in preliminary design is validated by the free BC EMA results, which provide confidence to start designing the final magnet modules without further prototyping and validation. The DLM-A design has been shown to exceed the 30 microns rms magnet-to-magnet positioning tolerance through measurements on the first article [10]. The free BC EMA data of the DLM-A first article also confirm the confidence in design iterations. The validation confirms not only the procedure for accurate modeling of the magnet support

system that the APS-U has developed, but also provides confidence in predicting the accelerator performance. For example, a novel approach to estimating mechanical motion-related orbit distortions [6, 11] is based on FEA results of the modes of girders. The accuracy of FEA predictions is expected within 10 percent.

REFERENCES

- [1] T.E. Fornek, “Advanced Photon Source Upgrade project final design report”, APSU-2.01-RPT-003, 2019. <https://doi.org/10.2172/1543138>
- [2] J. Collins *et al.*, “Preliminary design of the magnet support and alignment system for the APS-U storage ring”, in *Proc. MEDSI2016*, Barcelona, Spain, September 2016, pp. 87-89. <https://doi.org/10.18429/JACoW-MEDSI2016-MOPE34>
- [3] Z. Liu *et al.*, “Optimization for the APS-U magnet support structure”, in *Proc. MEDSI2016*, Barcelona, Spain, September 2016, pp. 254-256. <https://doi.org/10.18429/JACoW-MEDSI2018-WEPH2210.18429/JACoW-MEDSI2016-TUPE44>
- [4] C. Preissner *et al.*, “Nostradamus and the synchrotron engineer: key aspects of predicting accelerator structural response”, in *Proc. MEDSI2016*, Barcelona, Spain, September 2016, pp. 272-276. <https://doi.org/10.18429/JACoW-MEDSI2018-WEPH2210.18429/JACoW-MEDSI2016-WEBA01>
- [5] J. Nudell *et al.*, “Preliminary design and analysis of the FODO module support system for the APS-U storage ring”, in *Proc. MEDSI2016*, Barcelona, Spain, September 2016, pp. 83-86. <https://doi.org/10.18429/JACoW-MEDSI2018-WEPH2210.18429/JACoW-MEDSI2016-MOPE32>
- [6] J. Nudell *et al.*, “Calculation of orbit distributions for the APS Upgrade due to girder resonances”, in *Proc. MEDSI2018*, Paris, France, June 2018, pp. 95-98. <https://doi.org/10.18429/JACoW-MEDSI2018-WEPH2210.18429/JACoW-MEDSI2018-TUPH28>
- [7] C. Preissner *et al.*, “Le guide for support: a cookbook for modeling of accelerator structures”, in *Proc. MEDSI2018*, Paris, France, June 2018, pp. 252-254. <https://doi.org/10.18429/JACoW-MEDSI2018-WEPH22>
- [8] Data Physics, <https://www.dataphysics.com/>
- [9] ME Scope, Vibrant Technology, <https://www.vibetech.com/>
- [10] K. Volin *et al.*, “Magnet module assembly for the APS Upgrade”, presented at the 11th Int. Conf. on Mechanical Engineering Design of Synchrotron Radiation Equipment and Instrumentation (MEDSI2020), Chicago, IL, USA, virtual conference, July 2021, paper WEPB07, this conference.
- [11] V. Sajaev *et al.*, “Calculation of expected orbit motion due to girder resonant vibration at the APS Upgrade”, in *Proc. IPAC'18*, Vancouver, BC, Canada, April-May 2018, pp. 1269-1271. <https://doi.org/10.18429/JACoW-MEDSI2018-WEPH2210.18429/JACoW-IPAC2018-TUPMF011>

MECHATRONICS APPROACH FOR THE DEVELOPMENT OF A NANO-ACTIVE-STABILIZATION-SYSTEM

T. Dehaeze^{1,†}, J. Bonnefoy, ESRF, Grenoble, France

C. Collette¹, Université Libre de Bruxelles, BEAMS department, Brussels, Belgium

¹also at Precision Mechatronics Laboratory, University of Liege, Belgium

Abstract

With the growing number of fourth generation light sources, there is an increased need of fast positioning end-stations with nanometric precision. Such systems are usually including dedicated control strategies, and many factors may limit their performances. In order to design such complex systems in a predictive way, a mechatronics design approach also known as “model based design”, may be utilized. In this paper, we present how this mechatronics design approach was used for the development of a nano-hexapod for the ESRF ID31 beamline. The chosen design approach consists of using models of the mechatronics system (including sensors, actuators and control strategies) to predict its behavior. Based on this behavior and closed-loop simulations, the elements that are limiting the performances can be identified and re-designed accordingly. This allows to make adequate choices regarding the design of the nano-hexapod and the overall mechatronics architecture early in the project and therefore save precious time and resources. Several test benches were used to validate the models and to gain confidence on the predictability of the final system’s performances. Measured nano-hexapod’s dynamics was shown to be in very good agreement with the models. Further tests should be done in order to confirm that the performances of the system match the predicted one. The presented development approach is foreseen to be applied more frequently to future mechatronics system design at the ESRF.

INTRODUCTION

With the new 4th generation machines, there is an increasing need of fast and accurate positioning systems [1]. These systems are usually including feedback control loops and therefore their performances are not only depending on the quality of the mechanical design, but also on its correct integration with the actuators, sensors and control system.

In order to optimize the performances of such system, it is essential to consider a design approach in which the structural design and the control design are integrated. This approach, also called the “mechatronics approach”, was shown to be very effective for the design many complex systems [2, 3]. Such design methodology was recently used for the development of several systems used by the synchrotron community [4–6].

The present paper presents how the “mechatronic approach” was used for the design of a Nano Active Stabilization System (NASS) for the ESRF ID31 beamline.

[†] thomas.dehaeze@esrf.fr

NASS - MECHATRONICS APPROACH

The ID31 Micro-Station

The ID31 micro-station is used to position samples along complex trajectories [7]. It is composed of several stacked stages (represented in yellow in Fig. 1) which allows an high mobility. This however limits the position accuracy to tens of micrometers.

The Nano Active Stabilization System

The NASS is a system whose goal is to improve the positioning accuracy of the micro-station. It is represented in Fig. 1 and consists of three main elements:

- A nano-hexapod located between the sample to be positioned and the micro-station
- An interferometric metrology system measuring the sample’s position with respect to the focusing optics
- A control system (not represented), which based on the measured position, properly actuates the nano-hexapod in order to stabilize the sample’s position.

This system should be able to actively stabilize the sample position down to tens of nanometers while the micro-station is performing complex trajectories.

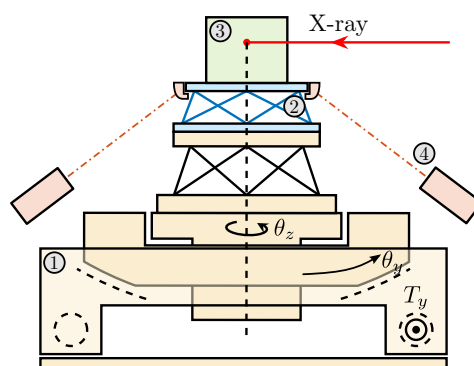


Figure 1: NASS - Schematic representation. 1) Micro-station, 2) Nano-hexapod, 3) Sample, 4) Metrology system.

Mechatronics Approach - Overview

In order to design the NASS in a predictive way, a mechatronics approach, schematically represented in Fig. 2, was used. It consists of three main phases:

1. *Conceptual phase*: Simple models of both the micro-station and the nano-hexapod are used to first evaluate the performances of several concepts. During this

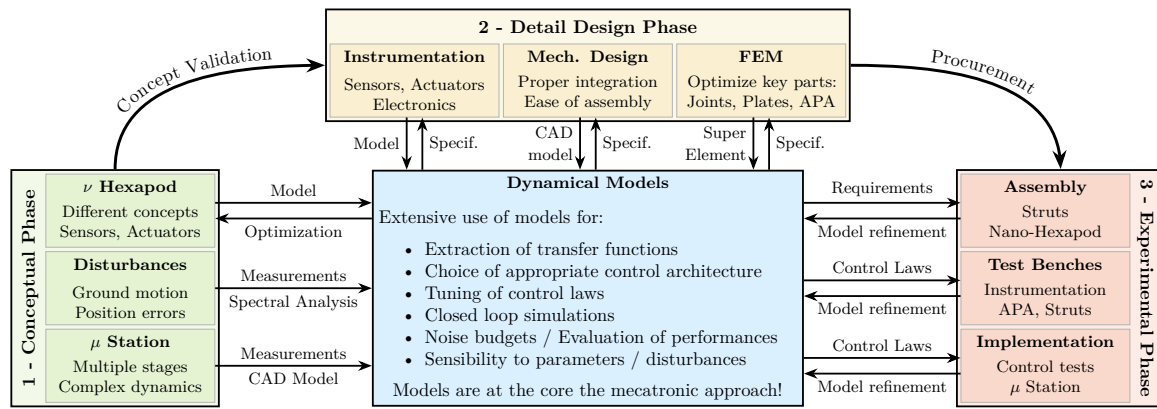


Figure 2: Overview of the mechatronics approach used for the design of the NASS.

phase, the type of sensors to use and the approximate required dynamical characteristics of the nano-hexapod are determined.

2. *Detail design phase*: Once the concept is validated, the models are used to list specifications both for the mechanics and the instrumentation. Each critical elements can then be properly designed. The models are updated as the design progresses.
3. *Experimental phase*: Once the design is completed and the parts received, several test benches are used to verify the properties of the key elements. Then the hexapod can be mounted and fully tested with the instrumentation and the control system.

Models

As shown in Fig. 2, the models are at the core of the mechatronics approach. Indeed, several models are used throughout the design with increasing level of complexity (Fig. 3).

At the beginning of the conceptual phase, simple “mass-spring-damper” models (Fig. 3a) were used in order to easily study multiple concepts. Noise budgeting and closed-loop simulations were performed, and it was concluded that a nano-hexapod with low frequency “suspension” modes would help both for the reduction of the effects of disturbances and for the decoupling between the nano-hexapod dynamics and the complex micro-station dynamics. I was found that by including a force sensor in series with the nano-hexapod’s actuators, “Integral Force Feedback” (IFF) strategy could be used to actively damp the nano hexapod’s resonances without impacting the high frequency disturbance rejection. The overall goal was to obtain a system dynamics which is easy to control in a robust way.

Rapidly, a more sophisticated and more realistic multi-body model (Fig. 3b) using Simscape [8] was used. This model was based on the 3D representation of the micro-station as well as on extensive dynamical measurements. Time domain simulations were performed with every stage of the micro-station moving and the nano hexapod actively stabilizing the sample against the many disturbances. The

multi-body model permitted to study effects such as the coupling between the actuators and the sensors as well as the effect of the spindle’s rotational speed on the nano-hexapod’s dynamics [9]. The multi-input multi-output control strategy could be developed and tested.

During the detail design phase, the nano-hexapod model was updated using 3D parts exported from the CAD software as the mechanical design progressed. The key elements of the nano-hexapod such as the flexible joints and the APA were optimized using a Finite Element Analysis (FEA) Software. As the flexible modes of the mechanics are what generally limit the controller bandwidth, they are important to model in order to understand which modes are problematic and should be addressed. To do so, a “super-element” can be exported using a FEA software and imported into the multi-body model (Fig. 3c). Such process is described in [10]. The multi-body model with included flexible elements can be used to very accurately estimate the dynamics of the system. However due to the large number of states included, it becomes unpractical to perform time domain simulations.

Finally, during the experimental phase, the models were refined using experimental system identification data. At this phase of the development, models are still useful. They can help with the controller optimization, to understand the measurements, the associated performance limitations and to gain insight on which measures to take in order to overcome these limitations.

For instance, it has been found that when fixing the encoders to the struts, as in Fig. 4a, several flexible modes of the APA were appearing in the dynamics which would render the control using the encoders very complex. Therefore, an alternative configuration with the encoders fixed to the plates was used instead.

NANO-HEXAPOD DESIGN

Nano-Hexapod Specifications

The nano-hexapod is a “Gough-Stewart platform”, which is a fully parallel manipulator composed of few parts as shown in Fig. 4a: only two plates linked by 6 active struts.

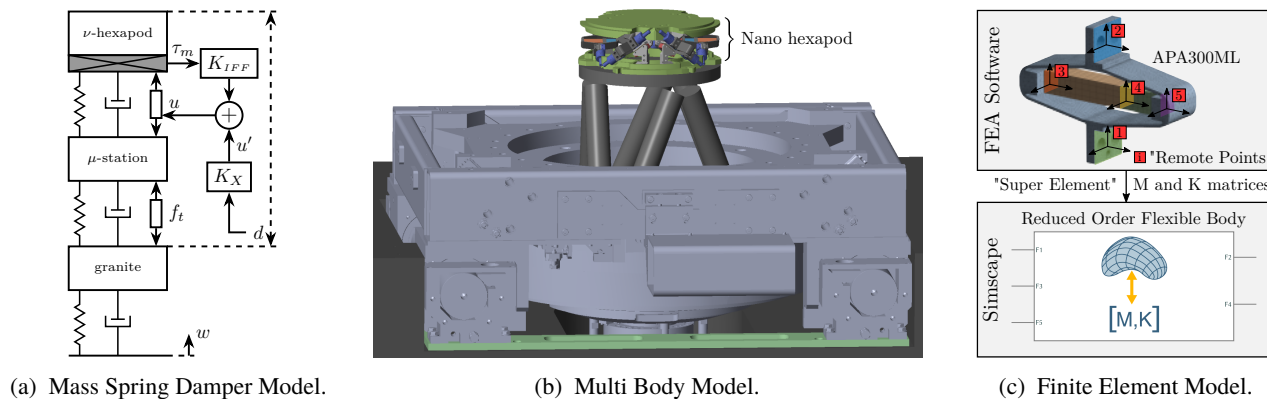


Figure 3: Schematic of several models used during all the mechatronics design process.

Each strut has one rotational joint at each end, and one actuator in between (Fig. 4b).

The main benefits of this architecture are its compact design, good dynamical properties, high load capability over weight ratio, and to possibility to control the motion in 6 degrees of freedom. The nano-hexapod should have a maximum height of 95 mm, support samples up to 50 kg, have a stroke of $\approx 100 \mu\text{m}$ and be fully compliant to avoid any wear, backlash, play and to have predictable dynamics.

Based on the models used throughout the mechatronics approach, several specifications were added in order to maximize the performances of the system:

- Actuator axial stiffness $\approx 2 \text{ N}/\mu\text{m}$ as it is a good trade-off between disturbance filtering, dynamic decoupling from the micro-station and insensibility to the spindle's rotational speed.
- Flexible joint bending stiffness $< 100 \text{ Nm}/\text{rad}$ as high bending stiffness can limit IFF performances [11].
- Flexible joint axial stiffness $> 100 \text{ N}/\mu\text{m}$ to maximize the frequency of spurious resonances.
- Precise positioning of the b_i and \hat{s}_i to accurately determine the hexapod's kinematics.
- Flexible modes of the top-plate as high as possible as it can limit the achievable controller bandwidth.
- Integration of a force sensor in series with each actuator for active damping purposes.

Parts Optimization

During the detail design phase, several parts were optimized to fit the above specifications.

The flexible joint geometry was optimized using a finite element software while the top plate geometry was manually optimized to maximize the frequency of its flexible modes.

Amplified Piezoelectric Actuators (APA) were found to be the most suitable actuator for the nano-hexapod due to its compact size, large stroke and adequate stiffness. The chosen model was the APA300ML from Cedrat Technologies (Fig. 4b). It is composed of three piezoelectric stacks, a lever mechanism increasing the stroke up to $\approx 300 \mu\text{m}$ and decreasing the axial stiffness down to $\approx 1.8 \text{ N}/\mu\text{m}$. One of the three stacks can be used as a force sensor, at the price of

losing 1/3 of the stroke. This has the benefits of providing good “collocation” between the sensor stack and the actuator stacks, meaning that the active damping controller will be robust [12].

Nano-Hexapod Mounting

Using the multi-body model of the nano-hexapod with the APA modeled as a flexible element, it was found that a misalignment between the APA and the two flexible joints was adding several resonances to the dynamics that were difficult to control. Therefore, a bench was developed to help the alignment the flexible joints and the APA during the mounting of the struts.

A second mounting tool was used to fix the six struts to the two plates without inducing too much strain in the flexible joints. The mounted nano-hexapod is shown in Fig. 5.

TEST-BENCHES

Flexible Joints and Instrumentation

Before mounting the nano-hexapod and performing control tests, several test benches were used to characterize the individual elements of the system.

The bending stiffness of the flexible joints was measured by applying a controlled force to one end of the joint while measuring its deflection at the same time. This helped exclude the ones that were not compliant with the requirement and pair the remaining ones.

The transfer function from the input to the output voltage of the voltage amplifier¹ as well as its output noise were measured. Similarly, the measurement noise of the encoders² was also measured.

These simple measurements on individual elements were useful to refine their models, to found any problem as early as possible, and to help analyzing the results obtained when the nano-hexapod is mounted and all the elements combined.

¹ PD200 from PiezoDrive

² Vionic from Renishaw

Content from this work may be used under the terms of the CC BY 3.0 licence (© 2021). Any distribution of this work must maintain attribution to the author(s), title of the work, publisher, and DOI

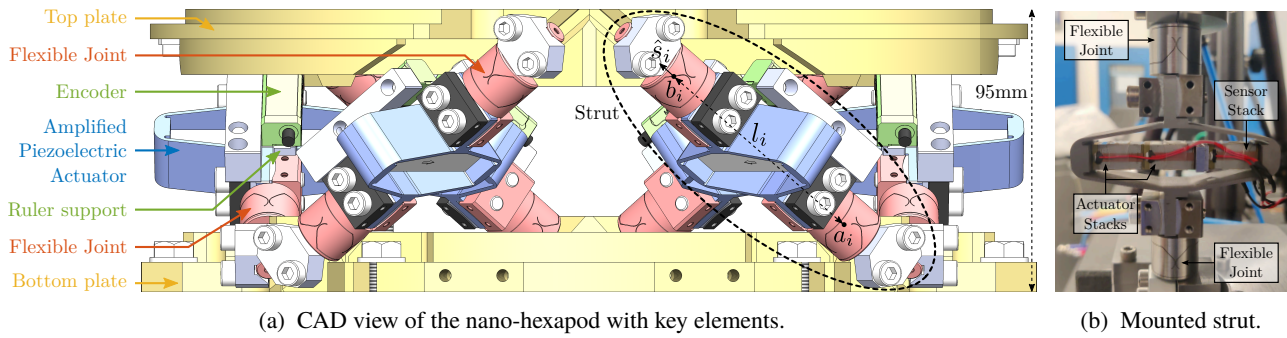


Figure 4: Nano-hexapod: A Stewart platform architecture.

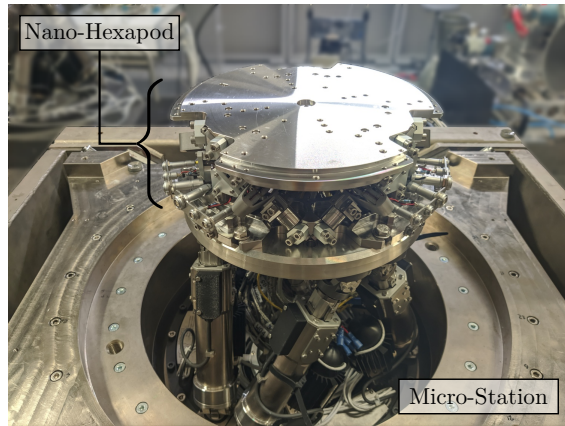


Figure 5: Nano-hexapod on top of the micro-station.

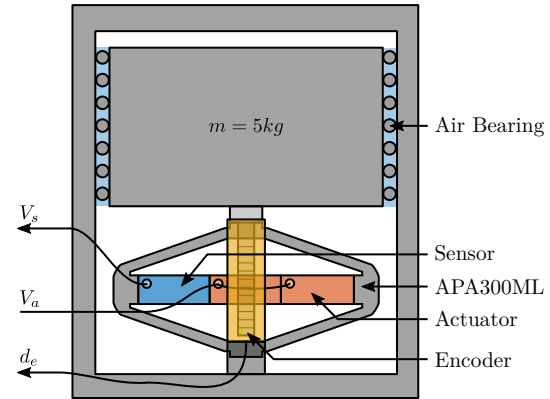


Figure 6: Schematic of the bench used to identify the APA dynamics.

APA and Struts Dynamics

A test bench schematically shown in Fig. 6 was used to identify the dynamics of the APA. It consist of a 5 kg granite fixed on top of the APA and vertical guided with an air bearing. An excitation signal (low pass filtered white noise) was generated and applied to two of the piezoelectric stacks. Both the voltage generated by the third piezoelectric stack and the displacement measured by the encoder were recorded. The two obtained frequency response functions (FRF) are compared with the model in Fig. 7.

The piezoelectric constants describing the conversion from the mechanical domain (force, strain), easily accessible on the model, to the electrical domain (voltages, charges) easily measured can be estimated. With these constants, the match between the measured FRF and the model dynamics is very good (Fig. 7).

The same bench was also used with the struts in order to study the added effects of the flexible joints.

Nano-Hexapod

After the nano-hexapod has been mounted, its dynamics was identified by individually exciting each of the actuators and simultaneously recording the six force sensors and six encoders signals. Two 6 by 6 FRF matrices were computed. Their diagonal elements are shown in Fig. 8 and compared with the model.

In Fig. 8a one can observe the following modes:

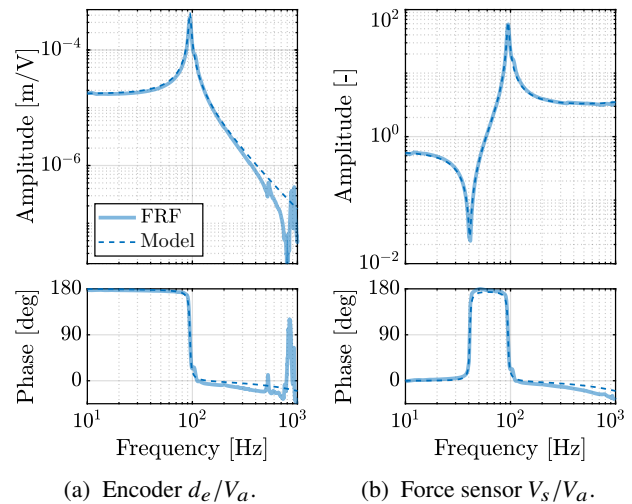


Figure 7: Measured Frequency Response functions compared with the Simscape model. From the actuator stacks voltage to the encoder (a) and to the force sensor stack (b).

- From 100 Hz to 200 Hz: six suspension modes.
- At 230 Hz and 340 Hz: flexible modes of the APA, also modeled thanks to the flexible model of the APA.
- At 700 Hz: flexible modes of the top plate. The model is not matching the FRF because a rigid body model was used for the top plate.

The transfer functions from the actuators to their “collocated” force sensors have alternating poles and zeros as expected (Fig. 8b). IFF was then applied individually on each pair of actuator/force sensor in order to actively damp the suspension modes. The optimal gain of the IFF controller was determined using the model. After applying the active damping technique, the 6 by 6 FRF matrix from the actuator to the encoders was identified again and shown in Fig. 9. It is shown that all the suspension modes are well damped, and that the model is able to predict the closed-loop behavior of the system. Even the off-diagonal elements (effect of one actuator on the encoder fixed in parallel to another strut) is very well modeled (Fig. 9b).

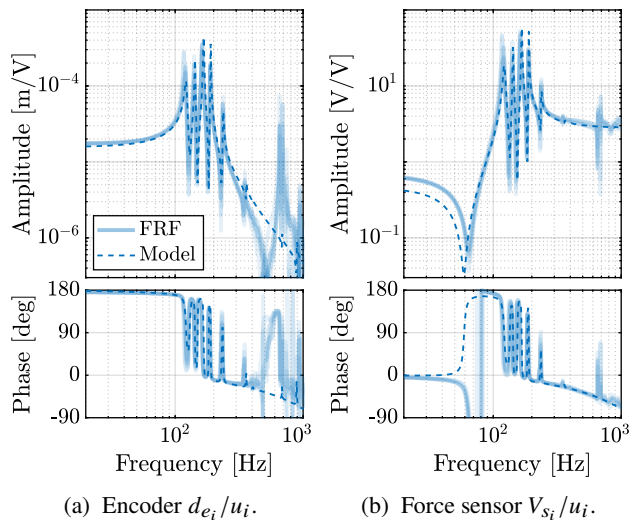


Figure 8: Comparison of the measured Frequency Response functions (FRF) with the Simscape model. From the excitation voltage to the associated encoder (a) and to the associated force sensor stack (b).

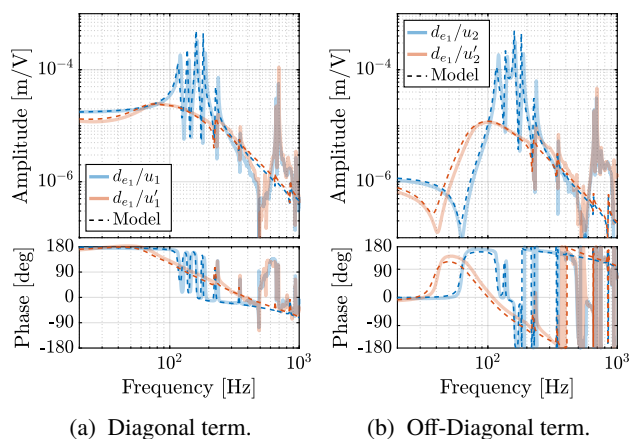


Figure 9: Transfer functions from actuator to encoder with (input u) and without (input u') IFF applied.

CONCLUSION

The mechatronics approach used for the development of a nano active stabilization system was presented. The ex-

tensive use of models allowed to design the system in a predictive way and to make reasonable design decisions early in the project.

Measurements made on the nano-hexapod were found to match very well with the models indicating that the final performances should match the predicted one. The current performance limitation is coming from the flexible modes of the top platform, so future work will focus on overcoming this limitation.

This design methodology can be easily transposed to other complex mechatronics systems and are foreseen to be applied for future mechatronics systems at the ESRF.

ACKNOWLEDGMENTS

This research was made possible by a grant from the FRIA. The authors wish to thank L. Ducotte, V. Honkimäki, D. Coulon, P. Brumund, M. Lesourd, P. Got, JM. Clement, K. Amraoui and Y. Benyakhlef for their help throughout the project.

REFERENCES

- [1] R. Dimper, H. Reichert, P. Raimondi, L. Ortiz, F. Sette, and J. Susini, “ESRF Upgrade Programme Phase II (2015-2022) - Technical Design Study”, ESRF, Tech. Rep., 2015, The Orange Book.
- [2] A. Rankers, “Machine Dynamics in Mechatronic Systems, an Engineering Approach”, English, Ph.D. dissertation, University of Twente, Jun. 1997, ISBN: 90-365-0957-2.
- [3] R. M. Schmidt, G. Schitter, A. Rankers, and J. Van Eijk, *The Design of High Performance Mechatronics: High-Tech Functionality by Multidisciplinary System Integration*, 3rd. IOS Press, 2020, ISBN: 161499367X.
- [4] R. Galdes, R. Caliani, G. Moreno, M. Ronde, T. Ruijl, and R. Schneider, “Mechatronics Concepts for the New High-Dynamics DCM for Sirius”, in *Proc. MEDSI'16*, Barcelona, Spain, Sep. 2016, pp. 44–47. doi: 10.18429/JACoW-MEDSI2016-MOPE19.
- [5] M. Holler *et al.*, “Omny-A Tomography Nano Cryo Stage”, *Review of Scientific Instruments*, vol. 89, no. 4, p. 043706, 2018. doi: 10.1063/1.5020247.
- [6] M. Brendike *et al.*, “ESRF-Double Crystal Monochromator Prototype - Control Concept”, in *Proc. 17th Int. Conf. on Accelerator and Large Experimental Physics Control Systems (ICALEPCS'19)*, New York, NY, USA, Oct. 2019, p. 777. doi: 10.18429/JACoW-ICALEPCS2019-TUCPL05.
- [7] T. Dehaeze, M. Magnin-Mattenet, and C. Collette, “Sample Stabilization for Tomography Experiments in Presence of Large Plant Uncertainty”, in *Proc. 10th Mechanical Engineering Design of Synchrotron Radiation Equipment and Instrumentation Int. Conf. (MEDSI'18)*, Paris, France, Jun. 2018, pp. 153–157. doi: 10.18429/JACoW-MEDSI2018-WEOAMA02.
- [8] MATLAB, *version 9.9.0 (R2020b)*. Natick, Massachusetts: The MathWorks Inc., 2020.
- [9] T. Dehaeze and C. Collette, “Active Damping of Rotating Platforms Using Integral Force Feedback”, *Engineering Research Express*, vol. 3, no. 1, p. 015036, Mar. 2021. doi: 10.1088/2631-8695/abe803.

- [10] P. Brumund and T. Dehaeze, "Multibody Simulations with Reduced Order Flexible Bodies Obtained by FEA", presented at MEDSI'20, Chicago, USA, Jul. 2021, paper WEPB08, this conference.
- [11] A. Preumont *et al.*, "A Six-Axis Single-Stage Active Vibration Isolator Based on Stewart Platform", *Journal of Sound and Vibration*, vol. 300, no. 3-5, pp. 644–661, 2007. doi: 10.1016/j.jsv.2006.07.050.
- [12] A. Souleille *et al.*, "A Concept of Active Mount for Space applications", *CEAS Space Journal*, vol. 10, no. 2, pp. 157–165, Jun. 2018. doi: 10.1007/s12567-017-0180-6.

SURFACE TWIST CHARACTERIZATION AND COMPENSATION OF AN ELLIPTICALLY BENT HARD X-RAY MIRROR*

Z. Qiao[†], J. Anton, L. Assoufid, S. Kearney, S. Mashrafi, J. Qian, X. Shi, D. Shu
 Advanced Photon Source, Argonne National Laboratory, Lemont, IL, USA

Abstract

Adaptive optics, including bendable and bimorph mirrors, have been widely used for hard X-ray dynamical focusing and wavefront correction. A recently developed elliptically bent mirror based on a laminar flexure bending mechanism has shown excellent performance. In this work, the mirror surface twist of the bent mirror was characterized using a Fizeau interferometer under different bending conditions. By applying a shimming correction, the surface twist was successfully reduced from 5.3 $\mu\text{rad}/\text{cm}$ to 0.09 $\mu\text{rad}/\text{cm}$. The twist angle variation from no bending to the maximum bending is about 0.05 $\mu\text{rad}/\text{cm}$. Simulation results show that these numbers are significantly lower than the required values to ensure optimum optical performance. The study helps confirm the bender design and guides the twist compensation procedures.

INTRODUCTION

The Advanced Photon Source (APS) at the Argonne National Laboratory (ANL) is under a major upgrade with more than two orders of magnitude increase in brightness [1]. The low emittance of the APS upgrade (APS-U) source will enable nanometer focused beam with high coherent flux, which requires optics with ultra-high quality. Many APS-U beamlines also demand variable focal spot sizes to adapt to different sample feature sizes. Such a zoomable beam can only be achieved by combining multiple optics [2] and using deformable optics, e.g., bendable mirrors and bimorph mirrors [3].

A high-precision compact flexure bending mechanism has been recently designed in-house at APS to provide elliptical (or hyperbolic) shaped mirror surfaces [4, 5]. A prototype bender mirror was fabricated and has demonstrated excellent performance in achieving variable shapes and focal spot sizes [3, 6]. In this paper, the surface twist of such a bender mirror is characterized using optical metrology. Then a practical twist compensation procedure is introduced and demonstrated.

BENDER MIRROR PROTOTYPE

A photograph of the bender mirror prototype is shown in Fig. 1. The mirror has a trapezoidal shape with a length of 300 mm, a narrow-end width of 19.32 mm, a wide-end width of 36.28 mm, and a thickness of 12 mm. It is a single-crystal silicon substrate coated with Pt on the optical surface. The bending moment is applied on each end of the

mirror by the flexure mechanism driven by a piezo linear actuator pushing a 65 mm long bending arm, the position of which is monitored by a capacitive sensor. There is also an array of capacitive sensors mounted underneath the mirror to record the surface profile of the bottom surface.

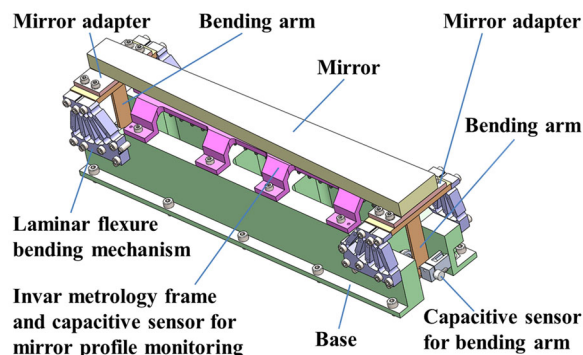


Figure 1: Photograph of the bender mirror prototype.

Although the mechanical design has shown excellent bending performance, a possible surface twist can exist due to the manufacture tolerance and the uniformity of the epoxy bonding the mirror to the adapter plates. There is no motorized or manual twist adjustment in the prototype design.

SURFACE TWIST TOLERANCE

Surface twist tolerance was studied for a typical bender mirror designed for focusing APS-U source as an example. The mirror can provide a minimum focal spot size of 200 nm. The effect of surface twist was simulated using ray-tracing software ShadowOui [7] and shown in Fig. 2.

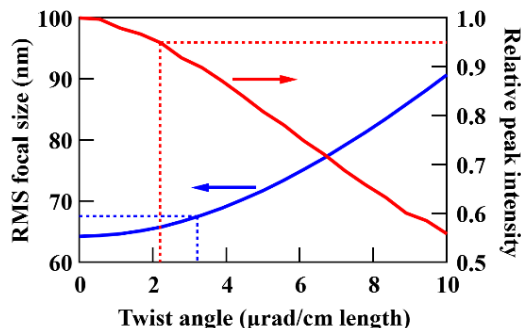


Figure 2: Simulated effects of mirror surface twist on the focal spot size and peak intensity.

As the twist angle increases, the focal spot size increases, while the relative peak intensity decrease. We specify the tolerance of the twist angle to ensure that both the focal size broadening and peak intensity reduction are less than 5%. Figure 2 shows that the twist angle needs to be smaller than 2 $\mu\text{rad}/\text{cm}$.

*This research used resources of the Advanced Photon Source, a U.S. Department of Energy (DOE) Office of Science User Facility at Argonne National Laboratory and is based on research supported by the U.S. DOE Office of Science-Basic Energy Sciences, under Contract No. DE-AC02-06CH11357.

[†] zqiao@anl.gov

Content from this work may be used under the terms of the CC BY 3.0 licence (© 2021). Any distribution of this work must maintain attribution to the author(s), title of the work, publisher, and DOI

METROLOGY SYSTEM

The mirror surface profile was measured using a Fizeau interferometer (AccuFiz[®], 4D Technology) in the APS Metrology Laboratory (Fig. 3), which has a 100 mm aperture and uses visible laser with a wavelength of 632.8 nm. The output images have 1200×1200 pixels with a pixel size of 91.1 μm.

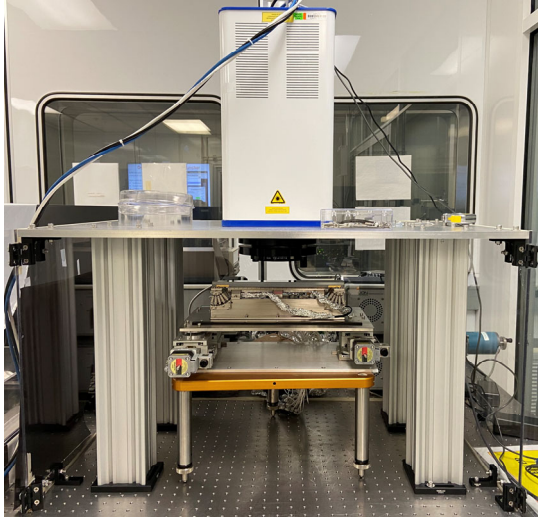


Figure 3: Photograph of the Fizeau interferometer set up to measure the bender mirror surface.

SURFACE TWIST CHARACTERIZATION

The surface profiles of the bender mirror at different bending settings were recorded, with two examples shown in Fig. 4(a) and 4(b). The bending surface curvatures of the surface were extracted by a circular fitting of centerline profiles along the mirror length [see Fig. 4(c)].

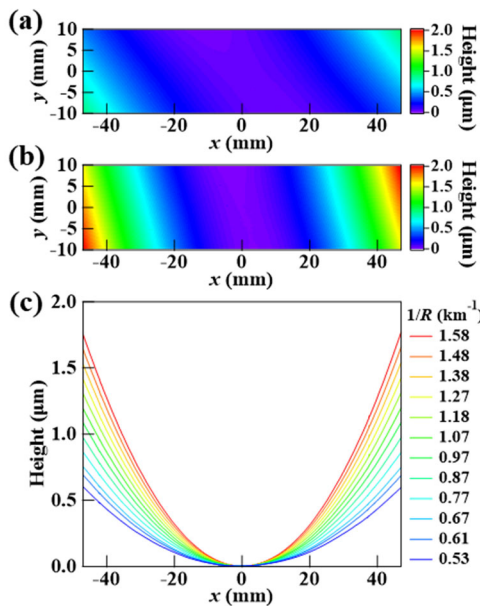


Figure 4: Mirror surface profiles with different bending surface curvatures of (a) $1/R = 0.53 \text{ km}^{-1}$ and (b) $1/R = 1.58 \text{ km}^{-1}$, and (c) extracted centerline profiles along mirror length.

Clear surface twists exist in all 2D surface profiles at different bending surface curvatures. To quantitatively analyze the results, we extracted the twist angle, defined as the relative angle between the two end edges of the mirror, shown as the two dashed lines in Fig. 5, and normalized to the mirror length.

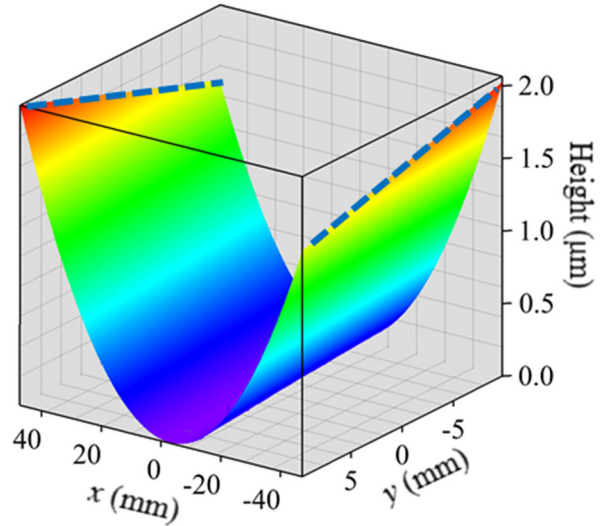


Figure 5: A 3D mirror profile with the twist angle defined as the angle between the two end edges (dashed lines).

The extracted twist angles at different bending surface curvatures are summarized in Fig. 6. The average twist angle is around $5.3 \mu\text{rad}/\text{cm}$. The twist angle deviation from the minimum to maximum bending is about $0.11 \mu\text{rad}/\text{cm}$. The measured twist angle is larger than the tolerance shown in Fig. 2. However, even as is, it will only reduce the peak intensity by 21% and broaden the focal size by 13%. The prototype bender mirror is already close to satisfactory, thanks to the state-of-the-art bender design and careful assembly. Further improvement can be achieved by twist compensation.

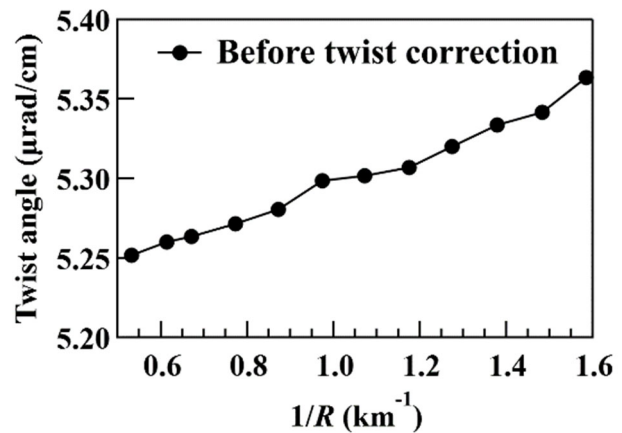


Figure 6: Extracted twist angles of the bender mirror at different bending surface curvatures before twist compensation.

SURFACE TWIST COMPENSATION

Twist compensation was studied by shimming the mirror bender in between the adapter plates near one end of the mirror, as shown in Fig. 7. Calculation shows that a few microns thick material is needed at the location of shimming. In this study, we used a 4 μm thick Ultralen film based on availability.

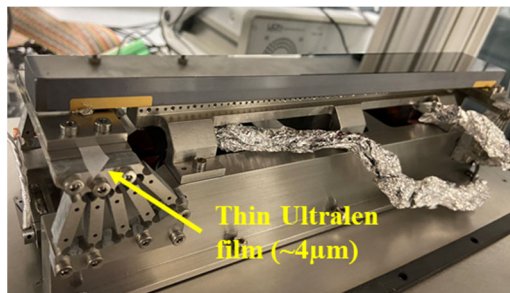


Figure 7: Photograph of the bender mirror with shimming applied for twist compensation.

The surface profiles after the twist compensation were measured and shown in Fig. 8, where the surface twist is not visible anymore. The extracted twist angles at different bending surface curvatures are summarized in Fig. 9. The average twist angle is now only $0.09 \mu\text{rad}/\text{cm}$, significantly better than the specified tolerance. The twist angle deviation from the minimum to maximum bending is about $0.05 \mu\text{rad}/\text{cm}$. If we simulate the mirror performance following Fig. 2, it will only affect the peak intensity and the focal size by a negligible amount ($< 0.05\%$).

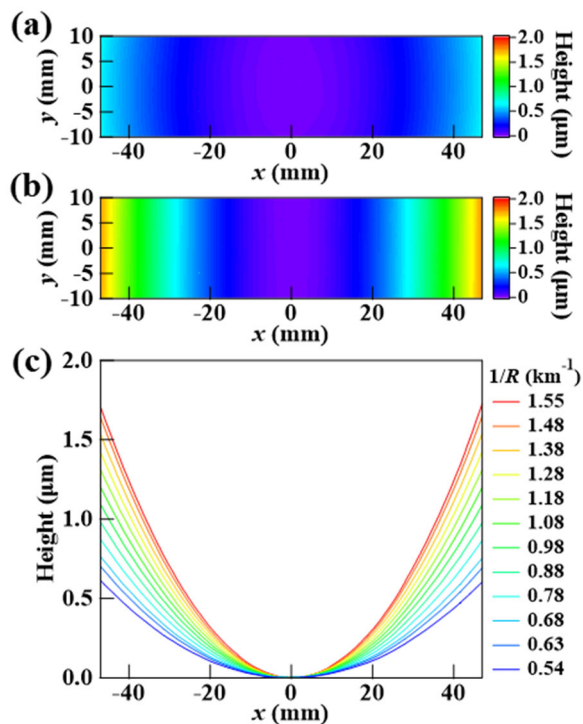


Figure 8: Mirror surface profiles after twist compensation with different bending surface curvatures of (a) $1/R = 0.54 \text{ km}^{-1}$ and (b) $1/R = 1.55 \text{ km}^{-1}$, and (c) extracted centerline profiles along mirror length.

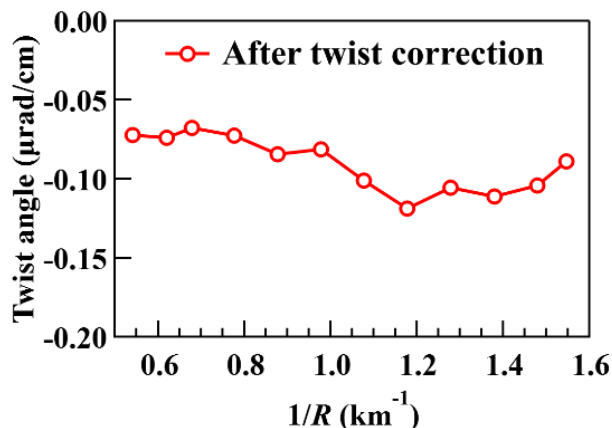


Figure 9: Extracted twist angles of the bender mirror at different bending surface curvatures after twist compensation.

CONCLUSION

The surface twist of a flexure-based bender mirror was evaluated using optical metrology. The mirror shows a slight but observable surface twist that could potentially affect the performance of APS-U nanofocusing beamlines. A practical shimming method is introduced to the current bender design for twist compensation. A final twist angle of less than $0.1 \mu\text{rad}/\text{cm}$ is demonstrated with negligible effects. The proposed method is proven to be adequate for all bender mirrors at APS-U. The study may also help the twist compensation design of future bender mirrors at other facilities.

ACKNOWLEDGEMENT

This research used resources of the Advanced Photon Source, a U.S. Department of Energy (DOE) Office of Science User Facility at Argonne National Laboratory and is based on research supported by the U.S. DOE Office of Science-Basic Energy Sciences, under Contract No. DE-AC02-06CH11357.

REFERENCES

- [1] M. Borland *et al.*, “The Upgrade of the Advanced Photon Source”, in *Proc. 9th Int. Particle Accelerator Conf. (IPAC'18)*, Vancouver, Canada, Apr.-May 2018, pp. 2872-2877. doi:10.18429/JACoW-IPAC2018-THXGBD1
- [2] X. Shi, R. Reininger, R. Harder, and D. Haefner, “X-ray optics simulation and beamline design for the APS upgrade,” *Proc. SPIE*, vol. 10388, p. 103880C, Aug. 2017, doi:10.1117/12.2274571
- [3] X. Shi *et al.*, “Prototype design and experimental tests of a zoom mirror system for the APS upgrade,” *Proc. SPIE*, vol. 11491, p. 1149110, 2020. doi:10.1117/12.2569129
- [4] D. Shu *et al.*, “Optomechanical design of compact laminar flexure bending mechanism for elliptically bent hard x-ray mirrors,” in *AIP Conference Proceedings*, vol. 2054, p. 060015, 2019. doi: 10.1063/1.5084646
- [5] J. W. J. Anton *et al.*, “Finite element modeling of a laminar flexure bending mechanism for elliptically bent hard x-ray mirror,” *Proc. SPIE*, vol. 11100, p. 111000B, 2019. doi: 10.1117/12.2529391

- [6] S. T. Mashrafi *et al.*, “Machine learning control of an elliptically bent hard X-ray mirror,” *Proc. SPIE*, vol. 11491, p. 114910T, Sep. 2020. doi: 10.1117/12.2567725
- [7] L. Rebuffi and M. Sánchez del Río, “ShadowOui: a new visual environment for X-ray optics and synchrotron beamline simulations,” *J. Synchrotron Radiat.*, vol. 23, no. 6, pp. 1357–1367, Nov. 2016.
doi: 10.1107/S1600577516013837

CONCEPTUAL DESIGN OF THE CAVITY MECHANICAL SYSTEM FOR CAVITY-BASED X-RAY FREE ELECTRON LASER*

D. Shu[†], S. Kearney, J. Anton, S. Mashrafi, Yu. Shvyd'ko, R. Lindberg, W. Jansma, W. Toter, X. Shi, L. Assoufid, M. White, K-J. Kim, Argonne National Laboratory, Lemont, IL 60439, USA
 T. Tan, D. Zhu, G. Gassner, F-J. Decker, H-D. Nuhn, H. Bassan, G. Marcus, Z. Huang, SLAC National Accelerator Laboratory, Menlo Park, CA 94025, USA

Abstract

The concept behind the cavity-based X-ray FELs (CBXFELs) such as the X-ray free-electron laser oscillator (XFEL) and the X-ray regenerative amplifier free-electron laser (XRAFEL) is to form an X-ray cavity with a set of narrow bandwidth diamond Bragg crystals. Storing and recirculating the output of an amplifier in an X-ray cavity so that the X-ray pulse can interact with following fresh electron bunches over many passes enables the development of full temporal coherence [1, 2]. One of the key challenges to forming the X-ray cavity is the precision of the cavity mechanical system design and construction. In this paper, we present conceptual design of the cavity mechanical system that is currently under development for use in a proof-of-principle cavity-based X-ray free electron laser experiment at the LCLS-II at SLAC.

INTRODUCTION

X-ray free electron lasers (XFELs) based on Self-Amplified Spontaneous Emission (SASE) [3] are demonstrated extremely bright, transversely coherent, ultrashort X-ray pulses for the investigation of ultrafast chemical and physical processes at the LCLS and other XFEL user facilities around world [4-6]. However, the single-pass SASE FEL amplifiers have poor longitudinal coherence.

Since 2019, collaboration between Argonne National Laboratory (ANL) and SLAC National Accelerator Laboratory has been established to design and construct a cavity mechanical system for use in a proof-of-principle cavity-based X-ray free electron laser experiment at the LCLS-II at SLAC. The experiment aim is to obtain temporally-coherent XFEL pulses by storing and recirculating the output of an amplifier in an X-ray cavity so that the X-ray pulse can interact with the following fresh electron bunches over many passes [1, 2].

A set of four diamond crystals with narrow Bragg bandwidth will provide high reflectivity and mono-chromatization to form a rectangular X-ray cavity around the first seven LCLS-II undulator units. The rectangular shape is chosen because of the constraints of the available space in the undulator hall. Two aspects of the cavity-based X-ray FELs (CBXFELs) are planned for this experiment: the X-ray free-electron laser oscillator (XFEL) [7] relies on a

low-loss cavity supporting a low-gain free-electron laser, and the X-ray regenerative amplifier free-electron laser (XRAFEL) [8, 9] leverages a high-gain FEL interaction. During the initial experiment, the LCLS-II Cu-linac will produce a pair of electron bunches separated by the cavity-round-trip distance during each linac cycle with a mean energy of 10.3 GeV. Figure 1 shows a schematic diagram of the CBXFEL experiment setup at the LCLS-II at SLAC.

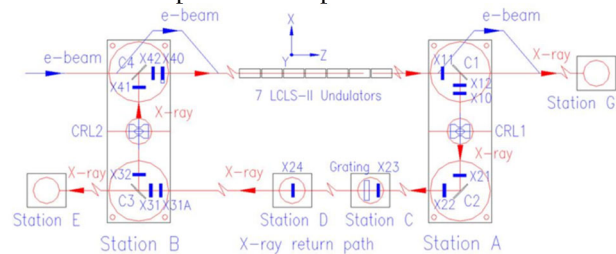


Figure 1: Schematic diagram of the CBXFEL experiment setup at the LCLS-II at SLAC.

EXPERIMENT STATIONS

The mechanical system for the rectangular x-ray cavity of the CBXFEL at LCLS-II includes four sets of diamond crystal holders (C1, C2, C3, and C4) with nanopositioning stages in UHV chambers, see Fig. 2. These nanopositioning stages and vacuum chambers are grouped into two crystal stations (stations A and B), and five diagnostic stations (stations C, D, E, F, and G). Each of the crystal stations shall be integrated with their associated chicane magnets and vacuum systems on the same girder to meet the requirement for LCLS-II e-beam-based alignment operation.

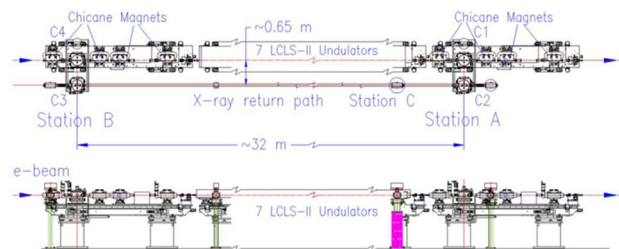


Figure 2: General layout of the cavity mechanical system for the CBXFEL at LCLS-II at SLAC.

The CBXFEL mechanical system also includes a vacuum pipe system as the cavity's X-ray return path. The X-ray diagnostic stations C, D, and E are located in the X-ray return path and its extension line. The X-ray diagnostic station G is located in the LCLS-II experimental station. Since it may not be in the same cavity vacuum system, the X-ray

* This research used resources of the Advanced Photon Source, a U.S. Department of Energy (DOE) Office of Science User Facility at Argonne National Laboratory and is based on research supported by the U.S. DOE Office of Science-Basic Energy Sciences, under Contract No. DE-AC02-06CH11357 (ANL) and DE-AC02-76SF00515 (SLAC).

[†]shud@anl.gov

diagnostic station E and G will be designed separately. Figure 2 shows the general layout of the cavity mechanical system for the ~ 32 m x ~0.65 m rectangular x-ray cavity of the CBXFEL experiment at LCLS-II.

UHV NANOPositioning DESIGN

One of the key challenges to forming the X-ray cavity is the precision of the cavity mechanical system design and construction. Nanopositioning techniques present a significant opportunity to support this state-of-the-art design with ultra-high-vacuum (UHV) compatibility.

Vacuum System Requirement

The LCLS-II undulator segment vacuum chamber needs to be operated at a pressure better than 10^{-6} torr in order to minimize bremsstrahlung and emittance growth. However, the design of vacuum system shall have highest priority on the operation reliability and maintainability to minimize any possible interference to the operations of the LCLS-II XFEL user facility. Similar to the design of the LCLS-I and LCLS-II self-seeding monochromators, the vacuum system of the CBXFEL optomechanical system need to meet typical UHV level cleanliness. Ion pumps are integrated with the CBXFEL vacuum chambers. All-metal manual isolation valves and welded bellows are the vacuum interfaces for the CBXFEL to the LCLS-II vacuum system.

Support and Metrology Reference Systems for Crystal Stations

Support System Based on the LCLS-II beam-based-alignment requirement, each of the diamond crystal station and its associated chicane dipole magnets are supported by a steel girder. As shown in Fig. 3, a special stiffener structure is designed to provide a stable interface between the girder and crystal station Invar base.

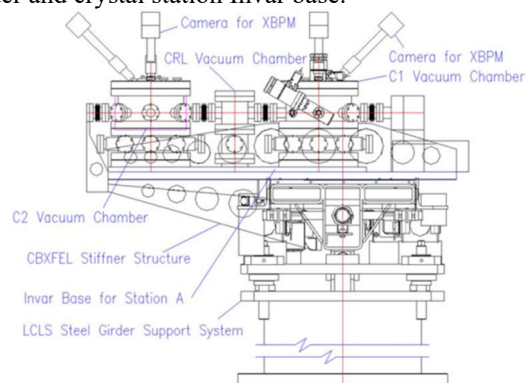


Figure 3: Rear view of the girder and stiffener structure for the CBXFEL diamond crystal station A.

Metrology Reference Base Each of the crystal stations has an Invar base with global survey/alignment fiducial holes outside the vacuum. Metrology reference frames are established inside the vacuum enclosure to mount the laser interferometer's fiber-optics frontends and the capacitive sensor's sensing heads.

To mount both C1 and C2 in-vacuum Invar metrology frames directly to a common Invar base in air with limited

space available for CBXFEL, a special flexure UHV interface has been developed for an Invar base near-zero-length feedthrough as shown in Fig. 4 [10]. The flexure interface structure is strong enough to hold the vacuum force and flexible enough to survive the thermal expansion stresses incurred during an 80 – 100 degree Celsius bakeout process for UHV preparation.

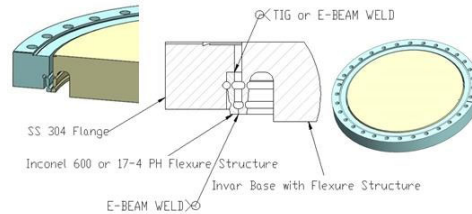


Figure 4: Invar base near-zero-length feedthrough for CBXFEL diamond crystal UHV Invar metrology frames.

Long Range Laser Interferometer

A customized commercial multichannel laser interferometer system is integrated as a part of the opto-mechanical system to monitor the cavity total length and XBPM locations during the system installation, commissioning and operation processes. With the laser interferometer's real-time measurements, the nanopositioning stages are able to compensate the thermal drifting of the mechanical system with a closed-loop feedback control.

The customized Hexagon™ Etalon™ absolute multiline laser interferometer system has a maximum measuring range larger than 32 meters with measurement uncertainty better than 0.4 micron/m [11, 12].

Capacitive Sensor

Commercial miniaturized capacitive sensors are applied in the CBXFEL mechanical system to provide repeatable absolute measurement in a short distance to ensure the traceability of the metrology structure during the CBXFEL mechanical system assembly, installation, commissioning and operation processes. A typical sensor has a measuring range ~ 2.0 mm with measurement resolution 5 - 10 nm.

Stages for Diamond Crystal Manipulation

As shown in Fig. 5, the nanopositioning stages group for diamond crystal manipulation includes four precision flexure stages and three commercial miniaturized PZT-motor-driven precision bearing stages [13].

The flexure linear and tip-tilting stages were designed based on the weak-link mechanism technique developed by Advanced Photon Source (APS) for synchrotron radiation applications [14-19]. The newly designed UHV-compatible tip-tilting weak-link stages for CBXFEL aim to have extended travel range up to 1.5 degree with 10 – 30 nrad resolution. With an end-target positioning closed-loop dynamic correction, the new linear flexure stages are designed to have maximum angular crosstalk below 100 nrad over $\pm 300 \mu\text{m}$ travel range. Design specifications are listed in Table 1.

A diamond crystal holder is mounted on the top of the stage group. The holder is similar to the APS designed

diamond crystal holder for European-XFEL self-seeding monochromator. A heater with thermostat is installed on the holder to keep an even temperature for all the diamond crystals in the cavity system.

To minimize the heat consumption of the stages in a vacuum environment, all of the nanositioning stages are driven by PZT-based motors or actuators.

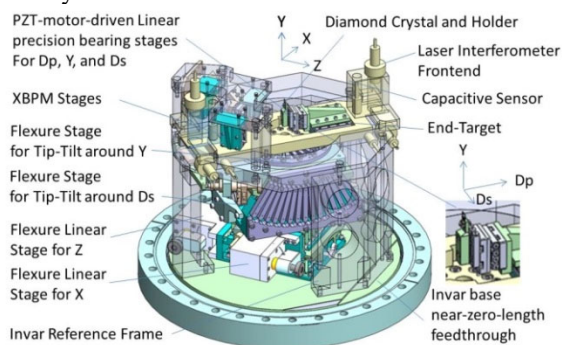


Figure 5: Nanositioning stages group for diamond crystal manipulation with in-vacuum Invar reference frame

Table 1: Design Specifications for Crystal Stages

Stage name	Travel Range	Resolution
Linear flexure stage for X and Z (coarse)	1000 micron	50 nm
Linear flexure stage for X and Z (fine, optional)	15 micron	5 nm
Tip-Tilt flexure stage for around Y and Ds (coarse)	26 mrad	350 nrad
Tip-Tilt flexure stage for around Y and Ds (fine)	0.1 mrad	20 nrad
Linear miniaturized stage for Dp, Y, and Ds	12 mm	50 nm

Stages for XBPMs and CRLs

The nanositioning stages group for X-ray beam position monitors (XBPMs) and compound refractive lenses (CRLs) includes two miniaturized PZT-motor-driven precision bearing stages.

Survey and Alignment of Stages

The home position of all stage groups is measured by CMM during the final assembly process with 3 μm uncertainty with respect to the reference base global survey/alignment fiducials. Positions are traceable using capacitive sensors for flexure stages and grating encoders for bearing stages.

Interface to the CBXFEL Control System

An integrated cavity optics dynamic positioning database (ICO-DPD) will be established as one of the interface between the CBXFEL mechanical and control system. The detailed ICO-DPD documentation will ensure uniformity and reduce system errors on the units, coordinates, names, tooling ball standards and etc. for cavity crystal motion control and beam diagnostics use.

The ICO-DPD will integrate the measurement results, including environment condition of the measurement, from digital measuring machine and digital microscope during the component manufacturing and sub-assembly process. With absolute and relative encoders mounted on the invar base and reference frame, the ICO-DPD will also record every movement of the cavity optical components

positions related to system fiducial positions on the invar base during the final assembly, installation, and survey/alignment process. The ICO-DPD could also be linked to the SLAC beam based alignment system.

SUMMARY

A cavity mechanical system that is currently under development for use in a proof-of-principle CBXFEL experiment at the LCLS-II is presented in this paper. As a part of the first article development activities, pilot flexure stages are designed, constructed, and started preliminary testing at the APS. Figure 6 shows a photograph of the pilot flexure stages group for diamond crystal manipulating. Figure 7 shows a preliminary test result for the tip-tilt flexure stage for the angular adjustment around the diamond crystal surface horizontal Axis Ds, which shows a 3-up and 3-down open-loop steps with resolution ~ 20 nrad. Further test is planned to demonstrate the stages' closed-loop dynamic correction capability with end-target laser interferometer and capacitive sensors. A final design review for the CBXFEL cavity mechanical system is scheduled at the end of August 2021.



Figure 6: A photograph of the pilot nanositioning stages for CBXFEL diamond crystal manipulation.

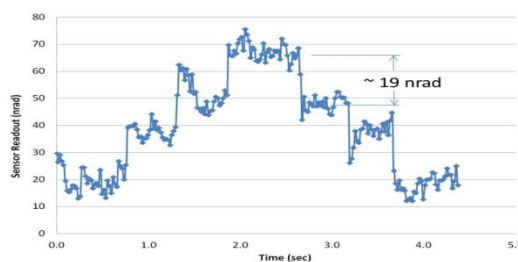


Figure 7: A preliminary open-loop test result for the tip-tilt flexure stage for the angular adjustment around the diamond crystal surface horizontal Axis Ds.

ACKNOWLEDGEMENTS

The authors would like to acknowledge the management support from Argonne National Laboratory and SLAC National Accelerator Laboratory.

REFERENCES

- [1] K-J. Kim *et al.*, "Test of an x-ray cavity with double bunches from the LSLC Cu-Linac," in *Proc. IPAC'19*, Melbourne, Australia, May 2019, pp. 1887-1890.

<https://doi.org/10.18429/JACoW-IPAC2019-TUPRB096>

[2] G. Marcus *et al.*, “Cavity-based free-electron laser research and development: a joint Argonne National Laboratory and SLAC National Laboratory collaboration.” in *Proc. FEL2019*, Hamburg, Germany, August 2019, pp. 282-287. <https://doi.org/10.18429/JACoW-FEL2019-TUD04>

[3] A. Kondratenko and E. Saldin, “Generation of coherent radiation by a relativistic electron beam in an undulator,” *Part. Accelerators*, vol. 10, pp. 207-216, 1980. <http://cds.cern.ch/record/1107977/files/p207.pdf>

[4] <https://www.xfel.eu>

[5] <https://pal.postech.ac.kr>

[6] <http://xfel.riken.jp>

[7] K.-J. Kim, Y. Shvyd'ko, and S. Reiche, “A proposal for an x-ray free-electron laser with an energy-recovery linac,” *Phys. Rev. Lett.*, vol. 100, p. 244802, 2008. doi:<https://doi.org/10.1103/PhysRevLett.100.244802>

[8] Z. Huang and R. D. Ruth, “Fully coherent x-ray pulses from a regenerative-amplifier free-electron laser,” *Phys. Rev. Lett.*, vol. 96, p. 144801, 2006. doi:<https://doi.org/10.1103/PhysRevLett.96.144801>

[9] G. Marcus *et al.*, “Refractive guide switching a regenerative amplifier free-electron laser for high peak and average power hard x rays,” *Phys. Rev. Lett.*, vol. 125, p. 254801, 2020. doi:<https://doi.org/10.1103/PhysRevLett.125.254801>

[10] D. Shu, S. Kearney, J. Anton, W. Toter, “Method and Mechanical Design of a Flexure Interface for Ultra-High-Vacuum Nanopositioning Invar Base Near-Zero-Length Feed-through,” U.S. Patent application #17/346537 for ANL-IN-20-092.

[11] John Dale *et al.*, “Multi-channel absolute distance measurement system with sub ppm-accuracy and 20 m range using frequency scanning interferometry and gas absorption cells,” *Opt. Express*, vol. 22, iss. 20, pp. 24869-24893, 2014. <https://doi.org/10.1364/OE.22.024869>

[12] <https://www.etalonproducts.com/en/products/lasertracer/>

[13] <http://www.smaract.com>

[14] D. Shu, T. S. Toellner, and E. E. Alp, “Modular overconstrained weak-link mechanism for ultraprecision motion control,” *Nucl. Instrum. Methods Phys. Res., Sect. A*, vols. 467-468, pt. 1, pp. 771-774, 2001. [https://doi.org/10.1016/S0168-9002\(01\)00499-5](https://doi.org/10.1016/S0168-9002(01)00499-5)

[15] D. Shu, T. S. Toellner, and E. E. Alp, “Redundantly constrained laminar structure as weak-link mechanisms,” U.S. Patent granted No. 6,607,840, 2003.

[16] D. Shu *et al.*, “Applications of laminar weak-link mechanisms for ultraprecision synchrotron radiation instruments,” *AIP Conf. Proc.*, vol. 879, pp. 1073-1076, 2007. <https://doi.org/10.1063/1.2436249>

[17] D. Shu *et al.*, “Mechanical design of a flexural nanopositioning stage system for hard x-ray nanofocusing at the Advanced Photon Source 32-ID-C station,” in *Proc. SPIE 11112, X-Ray Nanoimaging: Instruments and Methods IV*, San Diego, CA, USA, August 2019, p. 111120N. <https://doi.org/10.1117/12.2529384>

[18] S. Narayanan *et al.*, “Design and performance of an ultra-high-vacuum-compatible artificial channel-cut monochromator,” *J. Synchrotron Radiat.*, vol. 15, pp. 12-18, 2008. doi:10.1107/S090904950705340X

[19] X. Dong, D. Shu, and H. Sinn, “Design of a cryo-cooled artificial channel-cut crystal monochromator for the European XFEL,” *AIP Conf. Proc.*, vol. 1741, p. 040027, 2016. <https://doi.org/10.1063/1.4952899>

ZERO-LENGTH CONFLAT FIN-TYPE NONEVAPORABLE GETTER PUMP COATED WITH OXYGEN-FREE PALLADIUM/TITANIUM

K. Mase^{†,1}, T. Kikuchi, Institute of Materials Structure Science, KEK, 1-1 Oho, Tsukuba 305-0801, Japan

Y. Sato, S. Ohno, Graduate School of Engineering Science, Yokohama National University, 79-5 Tokiwadai, Hodogaya-ku, Yokohama 240-8501, Japan

A. Hashimoto², M. Yamanaka, National Institute for Materials Science, Tsukuba 305-0047, Japan
T. Miyazawa, Department of Materials Structure Science, SOKENDAI (The Graduate University for Advanced Studies), 1-1 Oho, Tsukuba 305-0801, Japan

¹also at Department of Materials Structure Science, SOKENDAI (The Graduate University for Advanced Studies), 1-1 Oho, Tsukuba 305-0801, Japan

²also at University of Tsukuba, Tsukuba 305-0047, Japan

Abstract

Nonevaporable getter (NEG) pumps are widely used in synchrotron radiation facilities because they are oil-free, vibration-free, space-saving, lightweight, and energy-saving. However, conventional NEG pumps have the following disadvantages: (1) a relatively high activation temperature (typically 300–450 °C for ZrVFe alloy); (2) the requirement for a dedicated power supply and electric feedthroughs; and (3) decreased pumping speeds after repeated cycles of activation and exposure to air. To overcome these disadvantages, we have developed a new zero-length conflat (CF) fin-type NEG pump with a DN 160 CF that uses oxygen-free Pd/Ti thin films as a new NEG material for evacuating residual H₂ and CO. The advantages of the new NEG pump are as follows: (1) it can be activated by baking at 150 °C; (2) no dedicated power supply or electric feedthrough is required; (3) pumping speeds do not degrade even after repeated cycles of activation and exposure to air; and (4) the unit is space-saving and lightweight.

INTRODUCTION

A nonevaporable getter (NEG) pump evacuates residual reactive gases at room temperature after it has been activated under clean ultrahigh vacuum (UHV) conditions [1-3]. However, the activation temperature of conventional NEG pumps is relatively high (typically 300-450 °C for ZrVFe alloy). In 1997, Benvenuti *et al.* proposed the idea of depositing a NEG thin film on the inner walls of a vacuum chamber to achieve a UHV after baking [4-6]. They named this method ‘NEG coating’. A thin film of TiZr, deposited by direct-current (DC) magnetron sputtering, with an activation temperature of 250 °C, was proposed for use as the NEG coating [4-6]. Shortly thereafter, it was reported that TiZrV thin films deposited by DC magnetron sputtering could be activated by baking at 180 °C for 24 hours [7, 8]. This TiZrV coating were used with great success at CERN and has now been adopted in accelerator facilities around the world [9].

Another disadvantage of a conventional NEG is that repeated activation and exposure to air results in oxidation of the surface, degrading its pumping performance. To overcome this disadvantage, a method was developed involving the sequential deposition of TiZr or TiZrV and Pd by DC magnetron sputtering (Pd/TiZr or Pd/TiZrV) [10-13]. Pd surface is capable of dissociating H₂ molecules into their constituent H atoms at room temperature, and the resulting H atoms diffuse into the bulk of the Pd [14]. Pd surface is also capable of chemisorbing CO at room temperature [15]. Consequently, Pd/TiZr and Pd/TiZrV can evacuate H₂ and CO at room temperature after activation. Because Pd surface does not readily oxidize, its pumping performance should not deteriorate after repeated activation and exposure to air. In fact, Mura, and Paolini reported that Pd/TiZrV is activated by baking at 150 °C and that it pumps H₂ and CO at room temperature; moreover, the pumping speed for H₂ does not decrease even after 30 cycles of activation and exposure to air [12].

Recently Mase *et al.* developed a new method for depositing a Pd-overcoated NEG thin film without using sputtering [16, 17]. Their NEG was fabricated by sequential sublimation of Ti and Pd under UHV at 10⁻⁷ to 10⁻⁸ Pa. This new NEG was named ‘oxygen-free Pd/Ti’ because its oxygen content was estimated to be less than 0.05% [17]. Kikuchi *et al.* developed a prototype of a NEG pump with a DN 160 conflat (CF) flange that used oxygen-free Pd/Ti (Fig. 1) [18]. Here, we report the development of a zero-length CF fin-type NEG pump [19]. This NEG pump can be easily fabricated by using a ring to which fins are attached. The pumping speeds of the NEG pump for H₂ and CO were measured by the orifice method [20].



Figure 1: Schematic showing the activation and pumping mechanisms of oxygen-free Pd/Ti deposited on stainless-steel SS304L. Reproduced from Ref. [18].

[†] mase@post.kek.jp

EXPERIMENTS

The vacuum vessel for the zero-length CF fin-type NEG pump (Fig. 2) consisted of a ring to which were attached 23 parallel fins (Fig. 3) and a DN 160 CF flange with a cylindrical space. Each fin was 0.2 mm thick and all the parts consisted of stainless steel 316L (SS316L). The vacuum vessel was placed on the side port of an apparatus for oxygen-free Pd/Ti deposition [18]. The Pd and Ti evaporator contained Pd and Ti filaments (Fig. 4). The fins were oriented perpendicularly to the Pd and Ti filaments, so that both sides of each fin were coated with oxygen-free Pd/Ti. H₂ and CO molecules entering between the fins are repeatedly adsorbed and desorbed in the spaces enclosed by the fins and the bottom, thereby increasing the probability of their sorption by the oxygen-free Pd/Ti thin film.

The oxygen-free Pd/Ti thin film was deposited on the vacuum vessel by the following procedure. The apparatus for oxygen-free Pd/Ti deposition was baked at 150 °C for 24 h. At the end of the baking period, the Ti and Pd filaments were degassed through heating by a direct current of 25 A for one hour for the former and at 19.5 A for 40 minutes for the latter. When the UHV chamber was cooled to room temperature, the pressure reached 1.7×10^{-8} Pa. The Ti filament was sublimated at about 47.5 A for three hours, and then the Pd filament was sublimated at about 33.0 A for five hours.

Pumping speeds of the NEG pump for H₂ and CO were measured by the orifice method [20]. Details of the pumping-speed measurements were similar to those reported in Ref. 18.



Figure 2: The vacuum vessel for the zero-length CF fin-type NEG pump before oxygen-free Pd/Ti deposition.

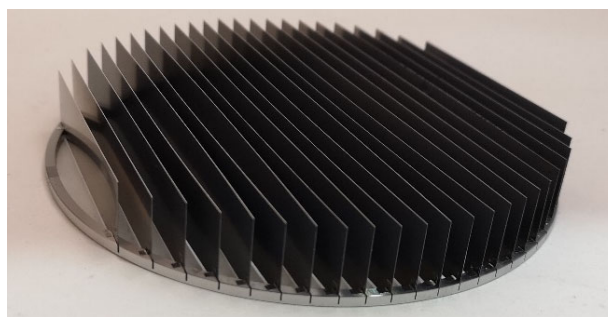


Figure 3: Ring with fins for the zero-length CF fin-type NEG pump before deposition of oxygen-free Pd/Ti. Reproduced from Ref. 19, with the permission of the Particle Accelerator Society of Japan (PASJ).



Figure 4: The Pd and Ti evaporator.

RESULTS AND DISCUSSION

The morphologies of oxygen-free Pd/Ti thin films on the fins and the bottom were examined by scanning electron microscopy, scanning transmission electron microscopy, and energy-dispersive X-ray spectroscopy. The Ti thin film was completely coated with Pd on the bottom, whereas the fins were covered by oxygen-free Pd/Ti nanostructures.

Figures 5 and 6 show the measured pumping speeds of the zero-length CF fin-type NEG pump for H₂ as a function of the pumped quantity after baking at 150 °C for 12 hours. The pumping speeds for H₂ were estimated to be about 2800, 1500, and 750 L s⁻¹ for pumped quantities of 3×10^{-4} , 3×10^{-3} , and 10 Pa L, respectively. The pumping speed for H₂ decreased rapidly at about 200 Pa L. This suggests that saturation of the oxygen-free Pd/Ti nanostructures on the fins as a result of H sorption occurred when 200 Pa L of H₂ was absorbed. Figure 7 shows the measured pumping speeds of the zero-length CF fin-type NEG pump for CO after baking at 150 °C for 12 hours. The pumping speed for CO at a pumped quantity of 1×10^{-3} Pa L was about 1550 L s⁻¹. The pumping speed for CO dropped to almost zero at 20 Pa L. This result

suggests that the oxygen-free Pd/Ti surface was almost completely covered with CO when 20 Pa L of CO was adsorbed.

This technology has been transferred to Baroque International Inc. and Irie Koken Co., Ltd.; as a result, more-sophisticated zero-length CF fin-type NEG pumps with superior pumping properties have become commercially available [21].

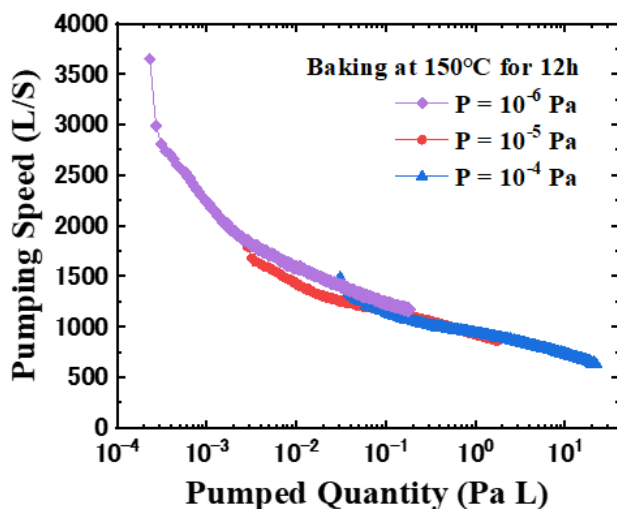


Figure 5: Pumping speeds of the zero-length CF fin-type NEG pump in various introduction pressures (P) of H_2 after baking at $150\text{ }^\circ\text{C}$ for 12 hours. Reproduced from Ref. 19, with the permission of the PASJ.

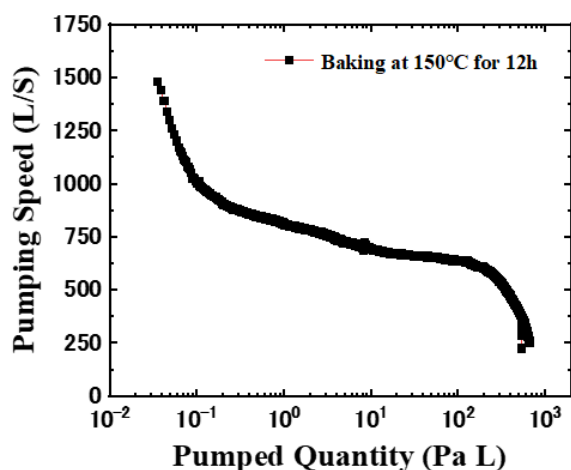


Figure 6: Pumping speeds of the zero-length CF fin-type NEG pump for H_2 after baking at $150\text{ }^\circ\text{C}$ for 12 h, when the H_2 introduction pressure was $1 \times 10^{-4}\text{ Pa}$.

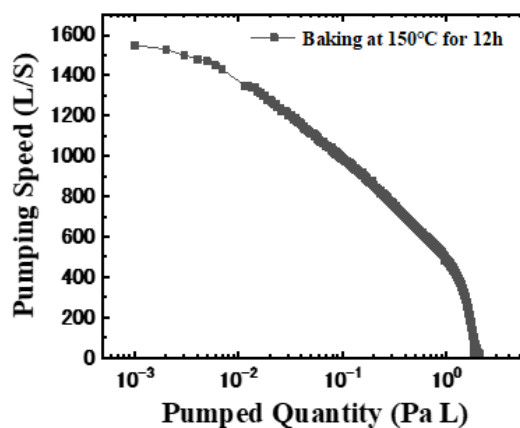


Figure 7: Pumping speeds of the zero-length CF fin-type NEG pump for CO after baking at $150\text{ }^\circ\text{C}$ for 12 h. The CO introduction pressure was $1 \times 10^{-4}\text{ Pa}$. Reproduced from Ref. 19 with the permission of the PASJ.

CONCLUSION

We have developed a zero-length CF flange fin-type NEG pump and have evaluated its pumping speeds for H_2 and CO. The pumping speed for H_2 at a pumped quantity of $3 \times 10^{-3}\text{ Pa L}$ was estimated to be about 1500 L s^{-1} , whereas the pumping speed for CO at a pumped quantity of $3 \times 10^{-3}\text{ Pa L}$ was estimated to be about 1550 L s^{-1} . This NEG pump can be used for accelerators, beamlines, and endstations in SR facilities because it can be activated by baking at $150\text{ }^\circ\text{C}$ for 12 hours. Research is being carried out to improve the pumping speeds further. More-sophisticated zero-length CF fin-type NEG pumps have since become commercially available [21].

ACKNOWLEDGEMENTS

This work was partly supported by the Matching Planner Program from the Japan Science and Technology Agency (JST) (VP29117940903), Grants-in-Aid for Scientific Research (JSPS KAKENHI Grant Nos. JP17K05067 and JP19K05280), TIA-Kakehashi grants (TK18-014 and TK19-035), joint research with Baroque International Inc. (18C208), joint research with Irie Koken Co., Ltd. (18C220), and a 2019 Takahashi Industrial Economic Research Foundation research grant (08-003-172). We would like to thank Mr. Tomohiro Okada (Tokyo Gakugei Univ.) and Mr. Hiromu Nishiguchi (Baroque International Inc.) for their invaluable advice and support.

REFERENCES

- [1] C. Boffito, B. Ferrario, P. della Porta, and L. Rosai, "A nonevaporable low temperature activatable getter material", *J. Vac. Sci. Technol.*, vol. 18, pp. 1117–1120, 1981. doi.org/10.1116/1.570852
- [2] C. Benvenuti and P. Chiggiato, "Pumping characteristics of the St707 nonevaporable getter (Zr 70 V 24.6–Fe 5.4 wt%)", *J. Vac. Sci. Technol. A.*, vol. 14, pp. 3278–3282, 1996. doi.org/10.1116/1.580226

- [3] P. Manini, “Non evaporable getter (NEG) pumps: A route to UHV-XHV”, *AIP Conf. Proc.*, vol. 1149, pp. 1138–1142, 2009. doi.org/10.1063/1.3215608
- [4] C. Benvenuti, “Pumping device by non-vaporisable getter and method for using this getter”, PCT Patent WO 1997/049109, Dec. 24, 1997.
- [5] C. Benvenuti, P. Chiggiato, F. Ciccoira, and Y. L’Aminot, “Nonevaporable getter films for ultrahigh vacuum applications”, *J. Vac. Sci. Technol. A*, vol. 16, pp. 148–154, 1998. doi.org/10.1116/1.580963
- [6] C. Benvenuti, P. Chiggiato, F. Ciccoira, and V. Ruzinov, “Decreasing surface outgassing by thin film getter coatings”, *Vacuum*, vol. 50, no. 1–2, pp. 57–63, May–June 1998. doi.org/10.1016/S0042-207X(98)00017-7
- [7] C. Benvenuti *et al.*, “Influence of the elemental composition and crystal structure on the vacuum properties of Ti–Zr–V nonevaporable getter films”, *J. Vac. Sci. Technol. A*, vol. 19, pp. 2925–2930, 2001. doi.org/10.1116/1.1414122
- [8] C. Benvenuti *et al.*, “Vacuum properties of TiZrV nonevaporable getter films”, *Vacuum*, vol. 60, no. 1–2, pp. 57–65, Jan. 2001. doi.org/10.1016/S0042-207X(00)00246-3
- [9] P. Chiggiato and P. C. Pinto, “Ti–Zr–V non-evaporable getter films: From development to large scale production for the Large Hadron Collider”, *Thin Solid Films*, vol. 515, no. 2, pp. 382–388, Oct. 2006. doi.org/10.1016/j.tsf.2005.12.218
- [10] C. Benvenuti, “Arrangement and method for improving vacuum in a very high vacuum system” PCT/EP 1998/000978, Feb. 20, 1998.
- [11] C. Benvenuti, P. Chiggiato, F. Ciccoira, Y. L’Aminot, and V. Ruzinov, “Vacuum properties of palladium thin film coatings”, *Vacuum*, vol. 73, pp. 139–144, 2004. doi.org/10.1016/j.vacuum.2003.12.022
- [12] M. Mura and C. Paolini, “Use of getter-catalyst thin films for enhancing ion pump vacuum performances.” *J. Vac. Sci. Technol. A*, vol. 25, pp. 1234–1239, 2007. doi.org/10.1116/1.2731348
- [13] C. Paolini, M. Mura, and F. Ravelli, “Efficient combining of ion pumps and getter-palladium thin films”, *J. Vac. Sci. Technol. A*, vol. 26, pp. 1037–1041, 2008. doi.org/10.1116/1.2834685
- [14] M. Wilde, M. Matsumoto, K. Fukutani, and T. Aruga, “Depth-resolved analysis of subsurface hydrogen absorbed by Pd(100)”, *Surf. Sci.* vol. 482–485, pp. 346–352, 2001. doi.org/10.1016/S0039-6028(01)00727-0
- [15] X. Guo and J. T. Yates, Jr., “Dependence of effective desorption kinetic parameters on surface coverage and adsorption temperature: CO on Pd(111)”, *J. Chem. Phys.*, vol. 90, pp. 6761–6766, 1989. doi.org/10.1063/1.456294
- [16] K. Mase and T. Kikuchi, “Non-evaporable getter coated component and chamber, manufacturing method and manufacturing apparatus, PCT/JP 2017/042682, Nov. 28, 2017.
- [17] T. Miyazawa *et al.*, “Oxygen-free palladium/titanium coating, a novel nonevaporable getter coating with an activation temperature of 133 °C”, *J. Vac. Sci. Technol. A*, vol. 36, p. 051601, 2018. doi.org/10.1116/1.5037023
- [18] T. Kikuchi, T. Miyazawa, H. Nishiguchi, and K. Mase, “Development of a new NEG pump using oxygen-free Pd/Ti thin film”, *AIP Conf. Proc.*, vol. 2054, p. 060046, 2019. doi.org/10.1063/1.5084677
- [19] Y. Sato, T. Kikuchi, T. Miyazawa, S. Ohno, and K. Mase, “Development of fin-type ICF zero-length nonevaporable getter (NEG) pump using oxygen-free Pd/Ti coating”, in *Proc. 16th Annu. Meet. Particle Accelerator Soc. Japan*, Kyoto, Jpn, July 31–Aug. 3, 2019, paper FRPH017 (in Japanese), pp. 907-910. https://www.pasj.jp/web_publish/pasj2019/proceedings/PDF/FRPH/FRPH017.pdf
- [20] M. H. Hablanian, “Recommended procedure for measuring pumping speeds”, *J. Vac. Sci. Technol. A*, vol. 5, pp. 2552–2557, 1987. doi.org/10.1116/1.574420
- [21] Baroque International Inc., “Oxygen-free Pd/Ti-coated nonevaporative getter (NEG) pump” (in Japanese), <https://www.baroque-inc.co.jp/custom.html>

EXACTLY-CONSTRAINED KB MIRRORS FOR SIRIUS/LNLS BEAMLINES: DESIGN AND COMMISSIONING OF THE TARUMÁ STATION NANOFOCUSING OPTICS AT CARNAÚBA BEAMLINE

G. B. Z. L. Moreno[†], R. R. Geraldés, C. S. N. C. Bueno, F. R. Lena, S. A. L. Luiz, Y. R. Tonin, E. O. Pereira, W. H. Wilendorf, H. C. N. Tolentino, Brazilian Synchrotron Light Laboratory (LNLS), Brazilian Centre for Research in Energy and Materials (CNPEM), Campinas, SP, Brazil

Abstract

Next-generation nanoprobe, empowered by diffraction-limited storage rings, as Sirius at the Brazilian Synchrotron Light Source (LNLS), present high-performance requirements aiming at high spatial resolution and throughput. For the focusing optics, this means assuring a small and non-astigmatic probe, high flux density, and remarkably high position stability, while simultaneously preserving beam wavefront. At stations further dedicated to spectromicroscopy and *in-situ* experiments, these requirements add up to having achromatic design and suitable working distance, respectively. In this way, Kirkpatrick-Baez (KB) mirrors have been chosen as an appropriate solution for many of Sirius focusing optics. Yet, the consequent requirements on mirror angular stability in less than 10 nrad RMS, surface quality in single-digit nanometers, and alignment tolerances in the range of hundreds of nanoradians, are particularly challenging regarding clamping, vibration, and thermal expansion budgets, even exceeding optical metrology limits. This work discusses the specifications, design concept, and assembly aspects of the new KB systems for Sirius, taking the TARUMÁ station from CARNAÚBA beamline as a case study with its early commissioning results.

INTRODUCTION

The design of efficient X-ray nanofocusing systems, with high mechanical stability and optimized compatibility with progressively ambitious experimental setups, is an investment of significant potential in spatial and temporal resolution, especially when fully utilizing the brightness and coherence of 4th-generation light sources [1]. Achromaticity, large working distances, and higher acceptance guided the choice for Kirkpatrick-Baez (KB) mirrors as the nanofocusing optics for many stations at Sirius [2].

TARUMÁ [3] is a sub-microprobe dedicated to multi-technique microscopy and spectroscopy experiments in the energy range of 2.05 to 15 keV in *in-situ* and *in-operando* conditions at CARNAÚBA (Coherent X-Ray Nanoprobe Beamline) [4, 5]. Starting commissioning in December 2020, it is the first nanoprobe at Sirius, where a KB focuses x-rays to 120 nm spot sizes (>8 keV) with 450 mm working distance and up to 1e11 ph/s/100mA on the sample.

Although very promising for scientific opportunities, this optical design brings remarkably strict requirements in manufacturing, installation, and positioning. This is clear from the short summary in Table 1, which includes the forthcoming station at MOGNO and the SAPOTI station at CARNAÚBA, with even tighter specifications. Hence, a high-stability KB system, built on precision engineering

Precision mechanics

Stability Issues & Vibration

concepts and following a predictive design approach, has been developed in-house. The first system, built for TARUMÁ, is also as a proof of concept for the next KB sets.

Table 1: Short Specifications for the First Sirius KB Sets

KB set	TARUMÁ	MOGNO	SAPOTI
Focus size	120 nm	100 nm	35 nm
Dep. of Focus	80 μm	20 μm	5 μm
Max. Mir. Len.	210 mm	450 mm	390 mm
Work. Distance	450 mm	175 mm	55 mm
Grazing Angle	3.9 mrad	4.0 mrad	3.9 mrad
Pitch stability	<10 nrad	< 10 nrad	< 4 nrad
Surface Error	< 1 nm	< 1 nm	< 1 nm

CONCEPT AND DESIGN

As compared with other X-ray focalizing elements, such as zone plates and refractive lenses, KB systems can be used in achromatic optical designs, reach larger working distances, and eventually allow for higher acceptance [6]. On the other hand, when also bounded to high numerical apertures and small grazing angles, mirrors are longer and heavier components, which are more difficult to handle and position, often resulting in limited dynamics. Moreover, apart from small focalizing elements, relative metrology over the extense mirror substrates and/or between the optics and the sample gets complicated. At TARUMÁ, for instance, where the KB set is in Ultra-High-Vacuum and the sample is in open-atmosphere, metrology with sufficient accuracy would be hardly even possible (see [7]).

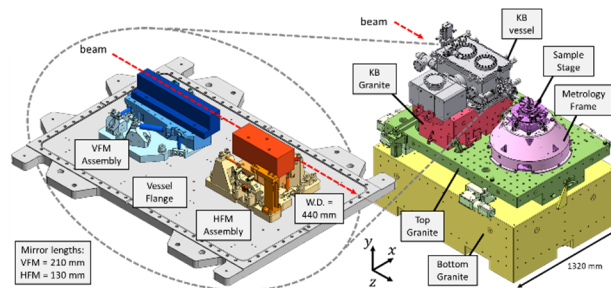


Figure 1: Reduced drawings of experimental bench and KB set with VFM and HFM assemblies in the vacuum vessel.

Building up from previous KB system and mirror base designs [8-12], and recent developments in primary optics for Sirius mirror systems [13], a deterministic design for passive high-stability performance was implemented for KB systems. The concept relies in maximizing the suspension frequency of both mirrors with respect to a single

TUOB01

111

reference frame, which can be directly shared with the sample stage or used as a metrology reference for it. With high suspension modes, the sensitivity to common mechanical disturbances is reduced, which, together with proper management of vibrational disturbances, allows for reducing displacement errors to a few nanometers. As illustrated in Fig. 1, for TARUMÃ this reference frame is the top granite of the experimental bench itself.

Sensitivity Analysis and Actuation Ranges

The design premise was to keep the internal mechanism as simple and stiff as possible. Thus, an error sensitivity analysis of each elliptical mirror permitted taking profit from the orthogonal nature of the KB set, and the fact that each mirror is shaped only in one direction. Error tolerances could be shared among both mirrors, and a better use of mounting tolerances, motion range, and actuator placement could be applied, avoiding unnecessary loss of support stiffness. Table 2 shows the alignment specs for each mirror regarding position tolerance for the focus: the maximum misalignment allowed in the transversal (Tx,Ty) and longitudinal (Z) axes was 10% of the focus size (σ) and depth (DF), respectively. Additionally, the last lines refer to the alignment and stability of the full set around each mirror reference point, considering that the sample and mirror move together on top of the same bench:

Table 2: Tarumã KB Alignment Specifications

Alignment specification	VFM	HFM
Pitch error tol. (mirror to sample)	4 μ rad	15 μ rad
Roll error tol. (mirror to mirror)	50 μ rad	50 μ rad
Yaw error tol. (mirror to mirror)	>1 mrad	>1 mrad
Pitch @ T=10% σ (stability)	7 nrad	10 nrad
Pitch @ Z=10% DF (astigmat.)	0.4 μ rad	0.7 μ rad
Pitch @ $\sigma=110\% \sigma_0$ (coma)	4 μ rad	15 μ rad
Focus Z @ max pitch allowed	~1 mm	~2 mm
KB set Pitch stability (to source)	14 nrad	20 nrad
KB set Tx/Ty stability (to source)	2 μ m	2 μ m
KB set Roll angle (to source)	>2 mrad	---

This way, only two actuation axes are implemented inside vacuum: the VFM pitch, for compensating possible mounting errors making the focus astigmatic, and the HFM roll, for correcting perpendicularity between the mirrors. All other actuation axes are covered by the 6-DoF granite bench that moves the entire KB set and the sample together.

Exactly-Constrained Design

To optimize vibration modes by reducing mass in the mirror frame, reinforced struts were used to exactly constrain each mirror frame instead of the folded leaf-springs used in [13]. This granted a significant size reduction since the mounting volumes for struts are far more compact. The center of gravity of the mirror-frame assembly was optimized to be as close as possible to the stiffness center of the struts, improving suspension frequencies to >450 Hz and the most sensitive mode to >1 kHz. Although this choice led to larger parasitic motion, from strut shortening

effects, and reduced range/stiffness ratio, both aspects were authorized by the sensitivity analysis mentioned in the previous section. For the in-vacuum actuation, an N-470 Piezo-Mike and a PiRest P-888.31 by PI were chosen for the HFM-roll and VFM-pitch actuation, respectively. For feedback, Lion Precision capacitive probes were used. The detailed design of the mirror mechanics is shown in Fig. 2.

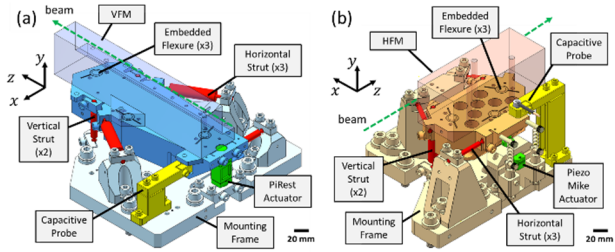


Figure 2: KB mechanisms for VFM (a) and HFM (b), highlighting embedded flexures in the frames reinforced flexural struts, piezo actuators and capacitive sensors.

As with the primary optics, deformations from thermal expansion mismatch are mitigated by having the mirrors fixed to three embedded flexures in the mirror frames, creating a thermal center. As an additional measure, the KB frames were made from a custom Invar alloy with a thermal expansion coefficient (CTE) closer to that of silicon at room temperature. The special Invar is a modified ASTM B743 Invar 37 re-forged with a Ni concentration of 37.5%, resulting in a tested CTE of 3.12 (μ m/m)/K at 35°C.

Next, ensuring high-stiffness links between the KB mirrors and their fixtures was mandatory to preserve the high suspension coupling to the granite bench and minimizing the errors in the passive stability or metrology. However, the common approach of bolting or clamping mirrors to their mounts would be impracticable for KB mirrors, as the required preload forces would introduce unacceptable deformations at the optical surfaces, affecting focus [14]. The solution consisted of epoxy-gluing the mirrors to the embedded flexures in the frames, such that, not only clamping forces are prevented, but also the hinges in [13] are expendable, with the interface stiffness becoming limited only by the adhesive elastic modulus, the bond layer thickness and interface area. A mixture of MasterBond 42HT-2LO epoxy adhesive with embedded 53 μ m glass microspheres (1% w.t.) is deposited over the three 8 mm diameter pads with a custom dispenser. The resulting bond layer has a reproducible 60 μ m interface thickness that is dominated by the spheres when preloaded by the mirrors weight.

To quantitatively evaluate the residual bond layer shear stresses from epoxy cure-induced contraction that could deform the mirror surface, deformations in 1mm thick glass slides glued to a metal substrate were measured during the curing process and fed to a custom material model in Ansys Mechanical. This model allowed some optimization of the interface area diameter by finding a suitable compromise between stiffness and adhesion strength in the point of maximum shear stresses. Figure 3 shows the simulated comparison between the deformation profiles of a 120N bolted solution and the glued interfaces (both with

estimated stiffness $> 1e9$ N/m), with the maximum values of 0.47 nm for the HFM and 2.3 nm for the VFM in the latter case, and the effects on the HFM focus profile.

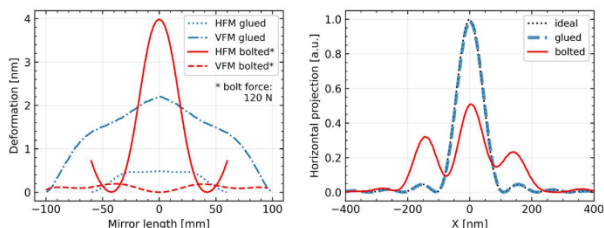


Figure 3: VFM and HFM surface deformations (left) and given HFM focus profiles (right) for different fixture types.

METROLOGY AND ASSEMBLY

Resulting from the design decisions stated previously, much engineering effort was transferred to the assembly phase, when the preliminary alignment of the KB set had to be done offline and with paramount precision. If the alignment between mirrors was to fall off the limits stated in Table 2, the specified in-vacuum motion ranges would become insufficient for an acceptable focus alignment in 2D. Therefore, in addition to confirming mirror figure, a proper fiducialization of such figure within space was mandatory for an adequate alignment of the KB set with regard to the sample at the experimental station.

A sequence of measurements with a Fizeau interferometer (FZI) setup was conducted to confirm figure error contributions from the gluing process. However, due to repeatability limits and height errors of the interferometric lens, the measurement error was limited to about 3 nm peak-to-valley, still above the expected surface deformations. Thus, ultimate validation remained for commissioning with the X-ray beam at the beamline.

Concerning alignment, the orientation of each mirror ellipse in their own substrate was estimated from fitting points at the side of the polished areas, measured with about 1 μ m resolution in a Zeiss coordinate measurement machine (CMM). The fitting algorithm used Python's *lmfit* library to perform a least-squares fit of the center and rotation angle of a fixed ellipse that generated from the p , q and θ design parameters obtained from the manufacturer's documentation. This assessment provided enough information to manufacture parts compensating deviations in the mirror substrate, allowing a more assertive assembly of the mechanics. The vacuum chamber was specially designed to fit within the CMM working volume, so the assembly could be metrology-assisted. A simultaneous setup with 6 length gauges provided a 6-DoF position-feedback of each mirror, mounted and adjusted with complementary structures. The VFM height and angle was aligned to the vessel base flange, whereas the HFM height and angle was aligned to the VFM axis. Lastly, the longitudinal position of the HFM was aligned to the VFM fitted focus.

To conclude, still in the CMM, the KB fitted focus was fiducialized to targets outside the vacuum chamber, used later for the experimental station laser tracker alignment. The final mounting errors for the KB are listed in Table 3.

Table 3: KB Set Assembly Uncertainties with the CMM

Mirror Axis	Ellipse Fit	CMM Uncertainty	HFM to VFM Mount Error*
Tx	50 μ m	1 μ m	15 \pm 50 μ m
Ty	70 μ m	1 μ m	15 \pm 70 μ m
Tz	164 μ m	1 μ m	8 \pm 164 μ m
Rx	3 μ rad	15 μ rad	40 \pm 15 μ rad
Ry	1 μ rad	15 μ rad	105 \pm 15 μ rad
Rz	---	67 μ rad	215 \pm 67 μ rad

COMMISSIONING

After the preliminary alignment campaign during installation, the alignment of the KB set with respect to the beam is done by jointly moving the experimental bench and searching for the focus with a reference sample, done at TARUMÁ via knife-edge fluorescence mapping or ptychographic reconstructions. The alignment strategy consists in firstly aligning the HFM and VFM to the source, correcting coma aberrations with the Ry and Rx DoFs in the KB granite and top granite, respectively. Next, the fine VFM coma, and astigmatism and trefoil aberrations between mirrors are corrected with the internal actuators. Figure 4 shows the preliminary results obtained with x-rays at TARUMÁ:

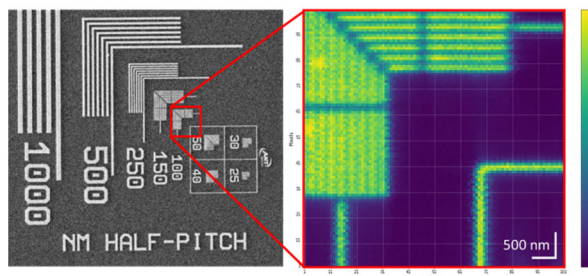


Figure 4: Applied Nanotools 100 nm calibration patterns (left) imaged by pink beam fluorescence mapping (right).

CONCLUSION

Although commissioning is still ongoing, the preliminary results of the first KB system following the innovative in-house design at TARUMÁ suggest that the ambitious design targets have been achieved. Although close to the limits of the instruments, the new dimensional metrology procedure proved successful. The optical metrology, however, needs even further improving, where a calibration of the lens and a more robust setup are underway, considering the validation of next KB systems. The sensitivity analysis paves the way to more optimized designs, considering not only better use of mounting and alignment tolerances, but also allowing high-dynamic realizations. The lessons learned at TARUMÁ already benefit the new designs with more challenging specs underway, including multiple coating stripes and even stricter stability tolerances.

ACKNOWLEDGEMENTS

The authors would like to gratefully acknowledge the funding by the Brazilian Ministry of Science, Technology

and Innovation, the contributions of the LNLS team and partners, and the participation of the MI-Partners in the SAPOTI project, with fruitful feedback to TARUMÃ.

REFERENCES

- [1] M. Eriksson, J. Friso, V. der Veen, and C. Quitmann, "Diffraction-limited storage rings – a window to the science of tomorrow," *J. Synchrotron Rad.*, vol. 21, pp. 837–842, 2014. doi: 10.1107/S1600577514019286
- [2] A. R. D. Rodrigues *et al.*, "Sirius Status Update," in *Proc. IPAC'19*, Melbourne, Australia, May 2019, pp. 1381–1384. doi:10.18429/JACoW-IPAC2019-TUPGW003
- [3] H. Tolentino *et al.*, "TARUMÃ station for the CARNAUBA beamline at SIRIUS/LNLS," in *Proc. SPIE Optical Engineering and Applications*, vol. 11112, X-Ray Nanoimaging: Instruments and Methods IV, p. 1111206, 2019. doi:10.1117/12.2531110
- [4] H. C. N. Tolentino *et al.*, "CARNAÚBA: the coherent x-ray nanoprobe beamline for the Brazilian synchrotron SIRIUS / LNLS," *IOP Conf. Ser.: J. Phys.*, vol. 849, no. 1, p. 012057, 2017. doi:10.1088/1742-6596/849/1/012057
- [5] H. C. N. Tolentino *et al.*, "X-ray microscopy developments at Sirius-LNLS: first commissioning experiments at the Carnaúba beamline," in *Proc. SPIE Optical Engineering and Applications*, vol. 11839, X-Ray Nanoimaging: Instruments and Methods V, p. 1183904, 2021. <https://doi.org/10.1117/12.2596496>
- [6] X. Shi, R. Reiningger, R. Harder, and D. Haeffner, "X-ray optics simulation and beamline design for the APS upgrade," in *Proc. SPIE Optical Engineering and Applications*, vol. 10388, Advances in Computational Methods for X-Ray Optics IV, p. 103880C, 2017. doi:10.1117/12.2274571
- [7] R. R. Galdes *et al.*, "Design and commissioning of the TARUMÃ station at the CARNAÚBA beamline at SIRIUS/LNLS" presented at the 11th Int. Conf. on Mechanical Engineering Design of Synchrotron Radiation Equipment and Instrumentation (MEDSI2020), Chicago, IL, USA, virtual conference, July 2021, paper WEPB13, this conference.
- [8] R. Barrett *et al.*, "Reflective optics for hard x-ray nanofocusing applications at the ESRF," *Synchrotron Radiat. News*, vol. 29, no. 4, pp. 10–15, 2016. doi:10.1080/08940886.2016.1198668
- [9] T. Goto *et al.*, "Hard X-ray nanofocusing using adaptive focusing optics based on piezoelectric deformable mirrors," *Rev. Sci. Instrum.*, vol. 86, no. 4, pp. 1–7, 2015. doi:10.1063/1.4916617
- [10] R. Baker *et al.*, "New generation mirror systems for ESRF upgrade beamlines," *J. Phys. Conf. Ser.*, vol. 425, no. 5, p. 052015, 2013. doi:10.1088/1742-6596/425/5/052015
- [11] C. Preissner *et al.*, "Earth, wind, and fire: the new fast scanning velociprobe," in *Proc. MEDSI'16*, Barcelona, Spain, Sep. 2016, pp. 112–115. doi:10.18429/JACoW-MEDSI2016-TUAA02
- [12] R. R. Galdes *et al.*, "Granite benches for SIRIUS x-ray optical systems," in *Proc. MEDSI'18*, Paris, France, Jun. 2018, pp. 361–364. doi:10.18429/JACoW-MEDSI2018-THPH12
- [13] R. R. Galdes *et al.*, "The design of exactly-constrained x-ray mirror systems for SIRIUS," in *Proc. MEDSI'18*, Paris, France, Jun. 2018, pp. 173–178. doi:10.18429/JACoW-MEDSI2018-WEOAMA04
- [14] L. M. Volpe *et al.*, "Optimization method using thermal and mechanical simulations for SIRIUS high-stability mirrors," in *Proc. MEDSI'18*, Paris, France, Jun. 2018, pp. 273–276. doi:10.18429/JACoW-MEDSI2018-WEPH31

DEVELOPMENT OF A PASSIVE TUNED MASS DAMPER FOR ULTRA-HIGH VACUUM BEAMLINE OPTICS

F. Khan, D. Crivelli, J. Kelly, A. Male, Diamond Light Source Ltd., Didcot, England

Abstract

Vibration in beamline optics can degrade the quality of experiments: the resulting movement of a mirror increases the X-ray beam position uncertainty and introduces flux variations at the sample. This is normally dealt with by averaging data collection over longer periods of time, by slowing down the data acquisition rates, or by accepting low-quality blurred images. With the development of faster camera technology and smaller beam sizes in next generation synchrotron upgrades, older optics designs can become less suitable, but still very expensive to redesign.

Mechanically, mirror actuation systems require a balance between repeatability of motion and stability. This leads to designs that are “soft” with resonant modes at a relatively low frequency, which can be easily excited by external disturbances such as ground vibration and local noise. In ultra-high vacuum applications, the damping is inherently low, and the vibration amplification at resonance tends to be very high.

At Diamond we designed a process for passively damping beamline mirror optics. First, we experimentally analyse the mirror’s vibration modes; we then determine the tuned mass damper (TMD) parameters using mathematical and dynamic models. Finally, we design a flexure-based metal TMD which relies on eddy current damping through magnets and a conductor plate. The TMD can be retrofitted using a clamping system that requires no modification to the existing optic. In this conference paper we show a case study on a mirror system on Diamond Light Source’s Small Molecule Single Crystal Diffraction Beamline, I19.

INTRODUCTION

The vibrational behaviour of the Horizontally Focusing Mirror (HFM) at I19 (Fig. 1) was evaluated upon witnessing low resonant signatures in the Fast Fourier Transform (FFT) of the X-ray beam positioning data. Figure 2 shows

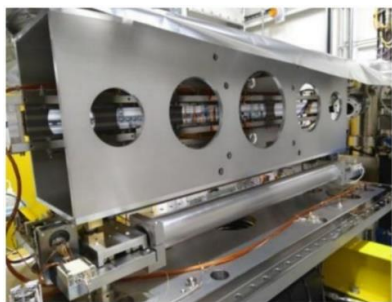


Figure 1: The HFM sitting on actuators is placed at the Small Molecule Single Crystal Diffraction Beamline, I19, at Diamond Light Source.

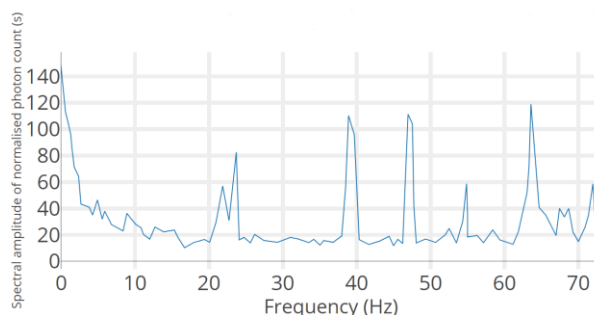


Figure 2: FFT plot of the HFM X-ray beam stability.

distinct peaks at 23, 40 and 47 Hz respectively. An experimental modal analysis characterised these natural frequencies with rocking and pitching modes in the actuators, which would magnify with distance from the centre of the mirror and affect beam positioning if left untreated.

A proposition was developed to house four retrofitted tuned mass dampers (TMDs) to effectively dampen the specific resonances. The TMDs would be installed and secured using slide-in trays and clamps, virtually leaving the expensive mirror system unchanged.

3D PRINTED TMD

An initial 3D printed TMD prototype was tuned to target the 23 Hz mode, as shown in Fig. 3. The monolithic design used calibrated double-hinged PLA flexures [1] (shown in purple) as a means of lateral motion and dissipation of energy through eddy current damping (ECD) (permanent magnets shown in yellow). The derived theory behind the flexure geometry is discussed under Design Process.

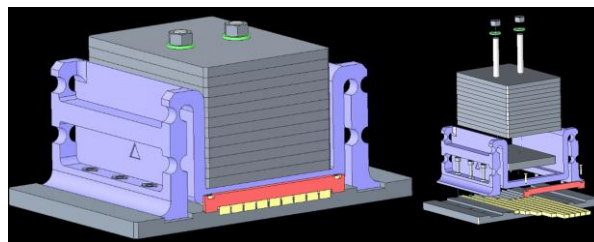


Figure 3: A representation of the 3D printed monolithic TMD prototype in a CAD assembly.

The passive vibration of the HFM was experimentally measured once more with the mounted TMD prototype. In the FFT plot (Fig. 4), the amplitude of the 23 Hz resonance visibly decreased with no additional parasitic motion introduced to the system. The 15 Hz peak, found to be a translation mode, was present during vibrational testing but was not registered by the beam positioning data seen in Fig. 2, hence it was disregarded.

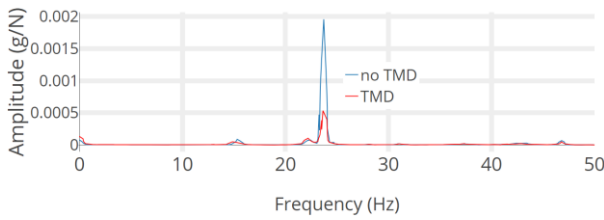


Figure 4: FFT plot showing a reduction in amplitude at 23.75 Hz in the presence of the TMD (red), measured using an accelerometer mounted on the optic.

Fundamentally, a TMD's effectiveness is controlled by material tolerances and manufacturing capabilities. Whilst 3D printing is recognised as the optimal solution for complex geometries, fabricating a printed flexure from ULTEM [2] revealed higher risk with little additional cost benefit. Most additive manufacturing operations, particularly using ULTEM, still experience limitations in repeatability and precision [3]. Although ULTEM is vacuum compatible, its performance and durability would require additional testing; dedicating time for such an inspection would have imposed extra delays on the beamline. Consequently, conventionally machined metallic flexures were opted as a reliable alternative which required a total redesign of the TMD.

DESIGN PROCESS

The redesign focussed on four key principles: compatibility with the ultra-high vacuum (UHV) environment, configurability, machinability, and precision. First the mass, stiffness and damping requirements were determined [4] (Table 1). The mass, limited to 4kg per TMD, was defined by the maximum weight the housing could support without compromising the mirror's performance.

Next the geometry of the flexure was configured to achieve the target stiffness, k_2 . Equation 1 was derived from first principles through likening the double-hinge stiffness to torsional springs [5] (Fig. 5).

$$k_{2_flexure} = \frac{16Ebt^5}{9\pi L_2^2 R^2} \quad (1)$$

The final model for the TMD is shown in Fig. 6. The values for b , t , R , and L_2 were chosen with spatial limitations in mind (Fig. 6a). Table 2 summarises the main design features and how they satisfy the four principles mentioned earlier.

Table 2: Main Design Attributes

	UHV	Configurability	Machinability	Precision
Flexures	Aluminium 6082-T6	Flexures can be swapped out.	Simultaneously cut two flexures per TMD to form matched pair.	Wire-EDM achieves 20-micron tolerance [6].
Mass	Stainless steel 304L	More/less mass plates can be suspended.	-	Smaller mass plates used for fine-tuning.
ECD	Can survive baking and cleaning prior to UHV insertion.	Adjustable distance between conductor/magnets. Magnets can be changed.	No viscoelastics.	Prototype testing determines optimal damping arrangement.

Table 1: Initial Parameters and Equations [4]

Parameter	Symbol	Equation	Units
Inertial Moment	J	From CAD Model	kgm ²
Inertial Radius	R	From CAD Model	m ²
Modal mass	m_1	$(Jr^2)/2$	kg
Frequency	f_1	Chosen	Hz
TMD Target			
Mass	m_2	Chosen	kg
Mass ratio	μ	m_2/m_1	-
Frequency	f_2	$(1/(1 + \mu))f_1$	Hz
Stiffness	k_2	$(2\pi f_2)^2 m_2$	N/m
Relative damping	ξ	$\sqrt{3\mu/(8(1 + \mu))}$	-
Absolute damping	c_2	$2\xi\sqrt{k_2 m_2}$	Ns/m

DESIGN ANALYSIS

Simscape

Before procurement and prototype testing, the suitability of the design was explored through simulations [7] and creating dynamic models [8]. A double-mass-spring system was set-up in MATLAB and Simscape using the initial inputs found from Table 1. The quick solving time allowed for "what-if" scenario iterations, hence establishing a desired tolerance for the flexure geometry which could be communicated to the manufacturers.

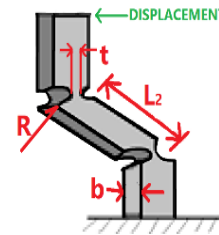


Figure 5: Dimensions of one double-hinge flexure column that support Eq. 1, with E = Young's Modulus

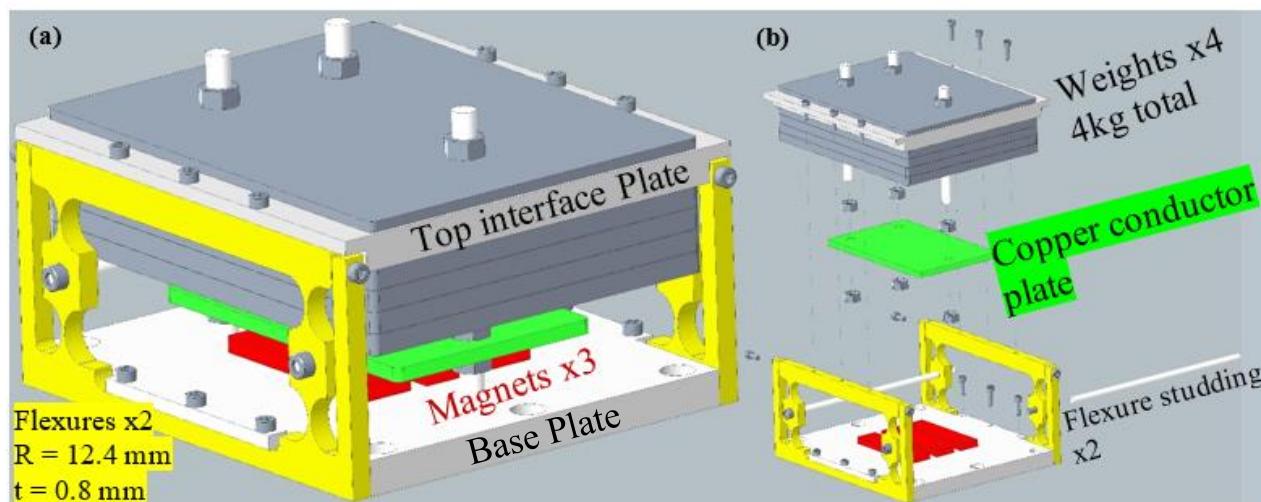


Figure 6: (a) A final CAD representation of the 23 Hz machined TMD prototype with annotations; (b) Exploded view showing how the mass component can be completely detached and reassembled with ease.

ANSYS

A buckling and stress analysis confirmed that the flexure would remain below yield stress when subjected to less than 0.4mm displacement during operation. A harmonic analysis predicted the natural frequency behaviour of the TMD. Any modes present after the expected resonance were critically required to be >100 Hz to prevent parasitic motion interfering with the HFM in operation. The ANSYS solution revealed a translational mode in the off-axis of the TMD at ~80Hz. Steel studding between the flexure pair (Fig. 6b) helped to increase this lateral stiffness, which seemed to be enough to shift the second mode above 80 Hz in the simulation.

PROTOTYPE TESTING

In-house experimental testing verified the modal behaviour of the machined TMD prototype in comparison to the ANSYS simulation. Simultaneously, the optimal ECD conditions were met by testing a combination of different strength magnets and polarity arrangements.

The time-based plot (Fig. 7a) shows a steep decay in oscillations with a damping ratio of 3.16%. The FFT plot (Fig. 7b) consistently displayed a sharp resonance at 15.5 Hz between repeats, but also an auxiliary peak at ~40-50 Hz. Hence, the TMD was performing as expected, but the real off-axis stiffness was at a resonance much lower than ANSYS predicted. This highlighted two design changes: (1) Accommodate up to 6 strong magnets to achieve higher damping, and (2) Machine a stainless-steel spacer block to replace the flexural studding and increase lateral stiffness further.

The final comparison between all the models can be summarised in Table 3. The prototype performed within ±0.5Hz of the target frequency with an error of 2.82%

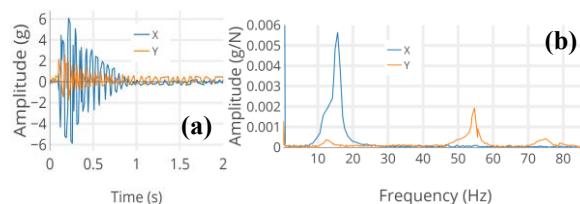


Figure 7: (a) Time-based plot showing a steep decay in oscillations during ECD; (b) FFT plot showing a distinct peak at 15.5Hz in the desired x-direction, and an orthogonal peak at 54 Hz in the y-direction as measured by an accelerometer.

Table 3: Model Parameter Value Comparison

	TARGET	Theory	ANSYS	Prototype
f_2 [Hz]	15.9	16.2	16.3	15.5
k_2 [N/m]	40202	40204	41755	36715
m_2 [kg]	4.00	3.94	3.99	3.87

CONCLUSION

This report outlined the justification and process behind designing and retrofitting machined TMDs to remove undesirable motion of the HFM in I19. Once the mirror is open for installation later in the year, all four TMDs will be fitted and tuned; the optic stability will be remeasured with an accelerometer and validated with X-ray data. This in-house design procedure utilises the best engineering practises whilst emphasising the importance of conscientious modelling before procurement, which will lead to optimised damping designs that will work first time. The end-product is entirely passive and undistruptive, which will allow beamline users to continue invaluable research at the facility.

REFERENCES

- [1] A. H. Slocum, "Precision Machine Design," United States, Society of Manufacturing Engineers, 1993, Topic 17, pp. 1-20.
- [2] StrataSys, "ULTEM™ 1010 Resin Data Sheet," <https://info.stratasysdirect.com/rs/626-SBR-192/images/Data%20Sheet%20-%20%20EN%20ULT-EM%201010.pdf>
- [3] Formlabs, "Understanding Accuracy, Precision, and Tolerance in 3D Printing," <https://formlabs.com/blog/understanding-accuracy-precision-tolerance-in-3d-printing>
- [4] J. Vink, "Flexure hinges: theory and practice," Vink System Design & Analysis, <https://www.vinksda.com/flexure-hinges-theory-and-practice/?web=1&wdLOR=cF383EDB8-0AEF-45A7-83C0-0735E2E062BE>
- [5] J. Paros and L. Weisbord, "How to design flexure hinges," *Machine Design*, vol. 37, pp. 151–156, 1965.
- [6] "Electrical discharge machining," Wikipedia, The Free Encyclopedia, https://en.wikipedia.org/w/index.php?title=Electrical_discharge_machining&oldid=1029272834
- [7] I. Hussain *et al.*, "Multi-Physical Design and Resonant Controller Based Trajectory Tracking of the Electromagnetically Driven Fast Tool Servo," *Actuators*, vol. 9, no. 2, p. 28, 2020. <https://doi.org/10.3390/act9020028h>
- [8] X. Chen, "Optimization and estimation routine for tuned mass damper," Blekinge Institute of Technology, Karlskrona, Sweden, 2010.

OXYGEN-FREE TITANIUM THIN FILM AS A NEW NONEVAPORABLE GETTER WITH AN ACTIVATION TEMPERATURE AS LOW AS 185 °C

Kazuhiko Mase^{†,1}, Takashi Kikuchi, Institute of Materials Structure Science, KEK, 1-1 Oho, Tsukuba 305-0801, Japan

Masato Ono, Kazuo Yoshioka, Ichiro Yoshikawa, Department of Complexity Science and Engineering, University of Tokyo, 5-1-5 Kashiwanoha, Kashiwa 277-0882, Japan

Kenichi Ozawa², Department of Chemistry, Tokyo Institute of Technology, Meguro, Tokyo 152-8551, Japan

Yusuke Masuda, Yasuo Nakayama, Department of Pure and Applied Chemistry, Tokyo University of Science, 2641 Yamazaki, Noda, Chiba 278-8510, Japan

Yuta Sato, Shinya Ohno, Graduate School of Engineering Science, Yokohama National University, 79-5 Tokiwadai, Hodogaya-ku, Yokohama 240-8501, Japan

¹also at Department of Materials Structure Science, SOKENDAI (The Graduate University for Advanced Studies), 1-1 Oho, Tsukuba 305-0801, Japan

²also at Institute of Materials Structure Science, KEK, 1-1 Oho, Tsukuba 305-0801, Japan

Abstract

Although nonevaporable getter (NEG) pumps are widely used in synchrotron-radiation facilities, unalloyed titanium (Ti) has rarely been used as a NEG. It has been previously shown that high-purity Ti deposited under an ultrahigh vacuum, followed by introduction of N₂, operated as a NEG with an activation temperature of 185 °C. This Ti thin film contained a concentration of oxygen and related impurities of 0.05% or less. In the present study, we used synchrotron-radiation X-ray photoelectron spectroscopy to analyze the oxygen-free Ti thin films after the introduction of high-purity N₂ or air. After the deposition of oxygen-free Ti, more surface TiN was formed by the introduction of high-purity N₂ than by introduction of air. We also evaluated the pumping properties of the oxygen-free Ti thin films treated with high-purity N₂ by means of total and partial pressure measurements. A vacuum vessel with oxygen-free Ti deposited on its inner walls was found to pump H₂, H₂O, O₂, and CO even after 30 cycles of pumping, baking at 185 °C for 6 hours, cooling to room temperature, introduction of high-purity N₂, and exposure to air. The high purity of the Ti thin film and the formation of TiN on its surface appear to be responsible for the reduced activation temperature of 185 °C.

INTRODUCTION

A nonevaporable getter (NEG) is a material that evacuates residual reactive gases at room temperature after it has been activated under clean ultrahigh-vacuum (UHV) conditions (Fig. 1) [1–3]. In 1997, Benvenuti *et al.* proposed the idea of depositing NEG thin films on the inner walls of vacuum chambers to achieve an UHV after baking [4–6]. They named this method ‘NEG coating’. Soon afterward, they reported that thin films of TiZrV deposited by direct-current magnetron sputtering can be activated by baking at 180–250 °C for 24 hours [7, 8]. This TiZrV coating was used with great success at the European

Organization for Nuclear Research (CERN) and has now been adopted in accelerator facilities around the world [9, 10].

Although a single-metal Ti deposition is widely used in Ti sublimation pumps [11], it has rarely been used as a NEG coating because its activation temperature has been reported to be as high as 350–400 °C [4–6]. However, Miyazawa *et al.* found that a thin film of high-purity Ti deposited by sublimation of Ti metal under UHV followed by introduction of N₂ can work as a NEG with an activation temperature of 185 °C [12, 13]. Because the concentration of oxygen and related impurities in the Ti thin film was 0.05% or less, we refer to it as ‘oxygen-free Ti’ hereafter. Here, we present the results of our study by synchrotron-radiation X-ray photoelectron spectroscopy (SR-XPS) of oxygen-free Ti thin films treated with high-purity N₂, together with measurements of total and partial pressures to verify their NEG properties [14].

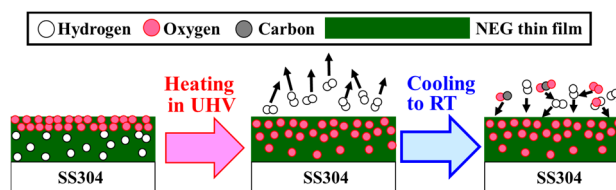


Figure 1: Schematic showing the activation and pumping mechanisms of a NEG thin film deposited on an SS304 stainless-steel substrate.

EXPERIMENTS

Thin films of oxygen-free Ti were deposited on silicon wafers or the inner surfaces of a vacuum vessel by means of Ti sublimation under UHV in the range 10⁻⁷ to 10⁻⁸ Pa. N₂ with a purity of more than 99.9% was then introduced (Figs. 2-4). The purity of the oxygen-free Ti thin films was estimated to be more than 99.995% from the pressure and the Ti deposition rate. The oxygen-free Ti thin films were analyzed by SR-XPS at BL-13B of the Photon Factory

[†] mase@post.kek.jp

[15]. The total-pressure curves and mass spectra of residual gases in the vacuum vessel were measured by using the apparatus shown in Fig. 5. The procedure for repeatedly measuring the total pressure curves and the mass spectra of residual gases is outlined in Fig. 6.

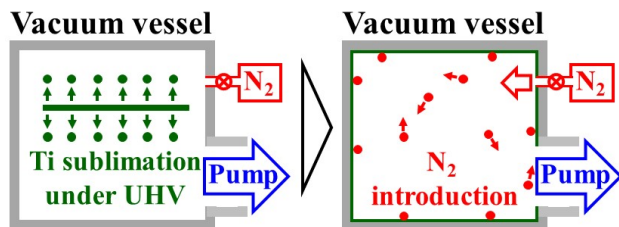


Figure 2: Schematic showing the procedure for deposition of the oxygen-free Ti thin film followed by introduction of high-purity N₂.

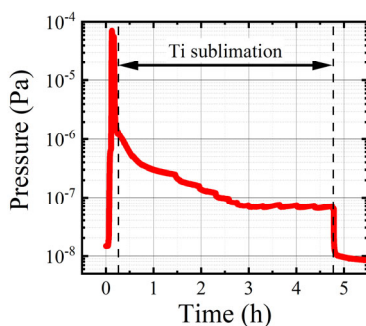


Figure 3: Total pressure curve in the chamber during deposition of the oxygen-free Ti thin film.

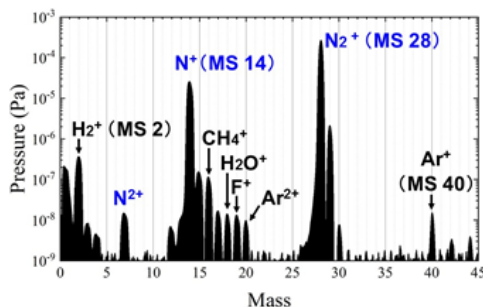


Figure 4: Mass spectrum of introduced high-purity N₂. The quadrupole mass spectrometer used was uncalibrated.

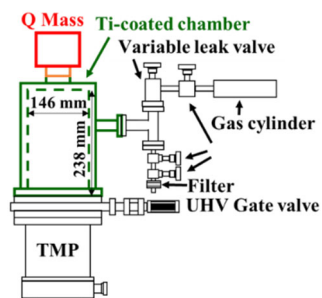


Figure 5: Apparatus for measurements of the total and partial pressures, and mass spectra of residual gases.

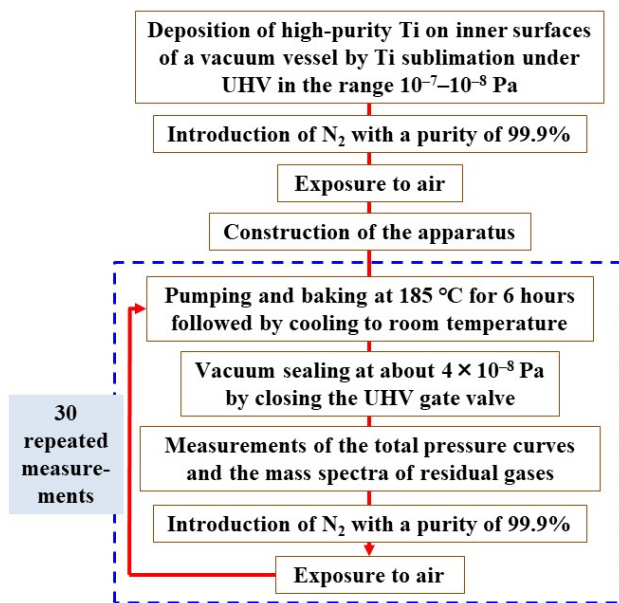


Figure 6: The procedure for 30 repeated measurements of the total pressure curves and the mass spectra of residual gases.

SR-XPS SPECTRA

SR-XPS spectra in the N 1s core-level region showed that the N 1s peaks consisted of multiple components from nitride species (396.6 eV) and adsorbates with nitrogen-containing functional groups, such as cyanides or anilines (399 eV) or nitroxides (400.5 eV) (Fig. 7). The greater height of the nitride peak of the oxygen-free Ti film after introduction of high-purity N₂ (N₂ vent) was much higher than that of the air-introduced sample (air vent), showing that the surface of the N₂ vent sample surface was nitrified to a greater extent than the air vent sample [14]. Wide-scan, Ti 2p region, and O 1s region SR-XPS spectra were almost identical for the N₂ vent and air vent samples [14]. These results showed that the surfaces of the oxygen-free Ti thin films were highly nitrified when high-purity N₂ was introduced before exposure to air, whereas they were less nitrified when air was introduced first.

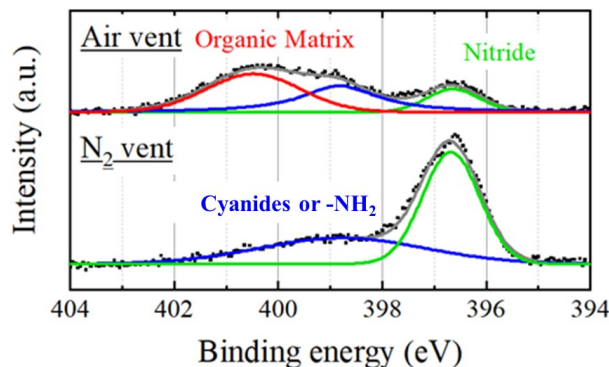


Figure 7: Enlarged SR-XPS spectra in the region of N 1s peaks. Reproduced from Ref. 14, with the permission of Particle Accelerator Society of Japan (PASJ).

TOTAL PRESSURE CURVES AND MASS SPECTRA

Figure 8 shows total-pressure curves for a vessel coated with oxygen-free Ti as a function of the number of cycles of pumping, baking at 185 °C for 6 hours, cooling to room temperature (RT), closure of the UHV gate valve, introduction of high-purity N₂, and exposure to air. The pressures in the oxygen-free Ti coated vessel after closure of the UHV gate valve were found to be more than two orders of magnitude smaller than those in the uncoated vacuum vessel. Figure 9 shows total and partial pressure curves of the oxygen-free Ti coated vessel for the first cycle of pumping, baking at 185 °C for 6 hours, cooling to RT, and closure of the UHV gate valve. Figure 10 shows mass spectra of the residual gases after five hours of vacuum sealing of the vacuum vessel coated with oxygen-free Ti. The main components of the residual gas were Ar and CH₄. This result is reasonable because clean Ti thin films do not pump Ar or CH₄ [11]. Under vacuum

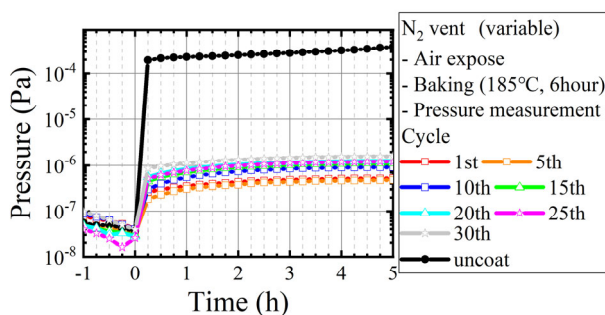


Figure 8: Total pressure curves of the oxygen-free Ti coated vessel as a function of cycles of pumping, baking at 185 °C for 6 hours, cooling to RT, closure of the UHV gate valve, introduction of high-purity N₂, and exposure to air. Reproduced from Ref. 14, with the permission of PASJ. The quadrupole mass spectrometer used was uncalibrated.

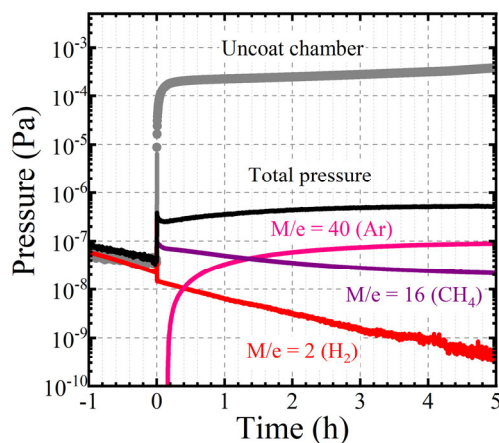


Figure 9: Total and partial pressure curves of the oxygen-free Ti coated vessel for the first cycle of pumping, baking at 185 °C for 6 hours, cooling to RT, and closure of the UHV gate valve. The quadrupole mass spectrometer used was uncalibrated.

sealing after 30 cycles of baking and exposure to air, the partial pressure of H₂ was less than 5×10^{-7} Pa, and the partial pressures of H₂O, O₂, and CO were all less than 1×10^{-8} Pa. These results show that the vacuum vessel onto which oxygen-free Ti was deposited and into which high-purity N₂ was introduced continued to evacuate various reactive residual gases, such as H₂O, H₂, O₂, and CO, even after 30 cycles of baking and exposure to air.

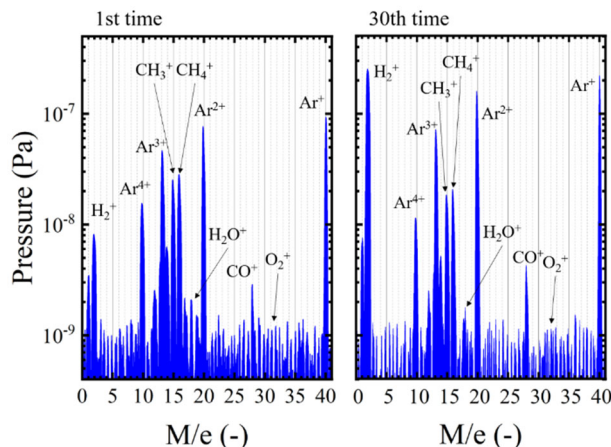


Figure 10: Mass spectra of residual gases after 5 hours of vacuum sealing of the oxygen-free Ti coated vessel for the first and 30th cycles of pumping, baking at 185 °C for 6 hours, cooling to RT, closure of the UHV gate valve, introduction of high-purity N₂, and exposure to air. The quadrupole mass spectrometer used was uncalibrated.

CONCLUSION

The SR-XPS spectra showed that the surfaces of the oxygen-free Ti thin films were highly nitrided when high-purity N₂ was introduced before exposure to air, whereas they were less nitrided when air was introduced first. Furthermore, the vacuum vessel onto which oxygen-free Ti was deposited and high-purity N₂ was introduced was found to evacuate H₂O, H₂, O₂, and CO, even after 30 cycles of pumping, baking and exposure to air. This oxygen-free Ti deposition technology can be applied to accelerators, beamlines, or endstations in SR facilities. The high purity of the Ti thin film and the formation of TiN on its surface appear to be responsible for the reduced activation temperature, which is as low as 185 °C.

ACKNOWLEDGEMENTS

This work was partly supported by Grants-in-Aid for Scientific Research (JSPS KAKENHI Grant Nos. JP17K05067 and JP19K05280) and TIA-Kakehashi grants (TK19-035, TK20-026, and TK21-046), and by joint research with Irie Koken Co., Ltd. (18C220 and 2020C216). We would like to thank Dr. Yoshihiro Aiura (AIST) and Mr. Hiromu Nishiguchi (Baroque International Inc.) for their invaluable advice and support. We are grateful to Dr. Haruo Ohkuma (Osaka Univ.) for his invaluable advice.

REFERENCES

- [1] C. Boffito, B. Ferrario, P. della Porta, and L. Rosai, "A nonevaporable low temperature activatable getter material", *J. Vac. Sci. Technol.*, vol. 18, pp. 1117–1120, 1981. <https://doi.org/10.1116/1.570852>
- [2] C. Benvenuti and P. Chiggiato, "Pumping characteristics of the St707 nonevaporable getter (Zr 70 V 24.6–Fe 5.4 wt %)", *J. Vac. Sci. Technol., A.*, vol. 14, pp. 3278–3282, 1996. <https://doi.org/10.1116/1.580226>
- [3] P. Manini, "Non evaporable getter (NEG) pumps: A route to UHV-XHV", *AIP Conf. Proc.* vol. 1149, pp. 1138–1142 2009. <https://doi.org/10.1063/1.3215608>.
- [4] C. Benvenuti, "Pumping device by non-vaporisable getter and method for using this getter", PCT Patent WO 1997/049109, Dec. 24, 1997.
- [5] C. Benvenuti, P. Chiggiato, F. Ciccoira, and Y. L'Aminot, "Nonevaporable getter films for ultrahigh vacuum applications", *J. Vac. Sci. Technol., A*, vol. 16, pp. 148–154, 1998. <https://doi.org/10.1116/1.580963>
- [6] C. Benvenuti, P. Chiggiato, F. Ciccoira, and V. Ruzinov, "Decreasing surface outgassing by thin film getter coatings", *Vacuum*, vol. 50, no. 1–2, pp. 57–63, May–June 1998. [https://doi.org/10.1016/S0042-207X\(98\)00017-7](https://doi.org/10.1016/S0042-207X(98)00017-7)
- [7] C. Benvenuti *et al.*, "Influence of the elemental composition and crystal structure on the vacuum properties of Ti–Zr–V nonevaporable getter films", *J. Vac. Sci. Technol., A.*, vol. 19, pp. 2925–2930, 2001. <https://doi.org/10.1116/1.1414122>
- [8] C. Benvenuti *et al.*, "Vacuum properties of TiZrV non-evaporable getter films", *Vacuum*, vol. 60, no. 1–2, pp. 57–65, Jan. 2001. [https://doi.org/10.1016/S0042-207X\(00\)00246-3](https://doi.org/10.1016/S0042-207X(00)00246-3)
- [9] P. Chiggiato and P. C. Pinto, "Ti–Zr–V non-evaporable getter films: From development to large scale production for the Large Hadron Collider", *Thin Solid Films*, vol. 515, no. 2, pp. 382–388, Oct. 2006. <https://doi.org/10.1016/j.tsf.2005.12.218>
- [10] M. L. Stutzman, P. A. Adderley, M. A. A. Mamun, and M. Poelker, "Nonevaporable getter coating chambers for extreme high vacuum", *J. Vac. Sci. Technol., A*, vol. 36, p. 031603. <https://doi.org/10.1116/1.5010154>
- [11] D. J. Harra, "Review of sticking coefficients and sorption capacities of gases on titanium films", *J. Vac. Sci. Technol.*, vol. 13, pp. 471–474, 1976. <https://doi.org/10.1116/1.568900>
- [12] T. Miyazawa *et al.*, "Non-evaporable getter (NEG) coating using titanium and palladium vacuum sublimation", *Vac. Surf. Sci.* vol. 61, no. 4, pp. 227–235, 2018. <https://doi.org/10.1380/vss.61.227>
- [13] K. Mase and T. Kikuchi, "Non-evaporable getter coated component and chamber, manufacturing method and manufacturing apparatus", PCT/JP 2017/042682, Nov. 28, 2017.
- [14] M. Ono *et al.*, "Preparation and performance evaluation of oxygen-free Ti thin film as a new nonevaporable getter", *Proc. 17th Annu. Meeting Particle Accelerator Soc. Japan* (September 2–4, 2020; Online), WEPP42 (in Japanese). https://www.pasj.jp/web_publish/pasj2020/proceedings/PDF/WEPP/WEPP42.pdf
- [15] A. Toyoshima, T. Kikuchi, H. Tanaka, K. Mase, K. Amemiya, and K. Ozawa, "Performance of PF BL-13A, a vacuum ultraviolet and soft X-ray undulator beamline for studying organic thin films adsorbed on surfaces", *J. Phys.: Conf. Ser.*, vol. 425, p. 152019, 2013. <https://doi.org/10.1088/1742-6596/425/15/152019>

DESIGN OF REMOTE HELIUM MASS SPECTROMETER LEAK DETECTOR*

H. Y. He[†], J.M. Liu, R.H. Liu, H. Song, G.Y. Wang, Spallation Neutron Source Science Centre,
Dongguan, China

Abstract

Leak detection is the key to get a good vacuum system. For the dangerous areas, or facility with complicit structure required to be detect online, it is a hard mask to seek for the suspected leaks one after another. After studying the basic principle of helium mass leak detection, design a remote leak detector based on the PLC, as well as multi monitoring cameras, which can achieve successfully injection and sniffer probe leak detection during the range of 270 degree. Compared with the manual operation, this device aims at accurately and reliably detecting leak rate, which can greatly provide technique support of online leak detection. And it can bring the value of reducing the labour intensity and ensuring personal safety.

INTRODUCTION

Vacuum With the continuous development of science and technology and industrial production, the requirements of vacuum equipment are higher and higher, and vacuum leak detection technology is also playing a more and more important role. The injection method and the inhalation method can be used to determine the location of the leak, and the helium mass spectrometry method is the most commonly used. In the process of leak detection, controlling the leak detector and auxiliary spray gun at the same time, observing the change of leak rate, data analysis and feedback operation in time, often requires multiple operators to work together, which greatly reduces the efficiency and accuracy of measurement. The development of computer technology leads the development of measuring instruments to automation and intelligence. At present, the helium mass spectrometer leak detector is controlled by microcomputer, but the intelligent leak detection and defect diagnosis still have a long way to go.

Based on PLC (programmable logic controller) and camera monitoring, helium injection method and positive pressure suction gun leak detection are carried out to realize remote online intelligent detection of vacuum system in high-risk environment

BASIC PRINCIPLES AND METHOD FOR HELIUM MASS SPECTROMETRY LEAK DETECTION

With vacuum leak detection technology is a technology to determine whether there is air leakage in the vacuum system and to determine the location and size of the leakage. Helium mass spectrometer leak detection is to add helium to one side of the workpiece to be tested by certain

means, and then use helium mass spectrometer leak detector to detect the helium overflowing through the leak hole by appropriate methods on the other side to achieve the purpose of detection. Helium injection method and positive pressure method are two basic methods of helium mass spectrometry leak detection [1].

Helium injection leak detection is to vacuum the inner cavity of the tested part, and use the gun to inject helium with a certain pressure on the surface of the tested part, to detect the helium leakage into the tested part. Helium injection method takes a lot of time, but it can determine the location of the leak, and has the advantages of high sensitivity and low cost. It is a common qualitative leak detection method.

OVERALL DESIGN OF THE DEVICE

The remote vacuum leak detector consists of two main modules: the control and adjustment module of the probe and helium mass spectrometer leak detector, and the identification and monitoring module of the camera. The core function is to realize the remote control of the helium mass spectrometer leak detector and its accessory spray gun based on the auxiliary identification and real-time monitoring of the camera to complete the leak detection operation of the vacuum specimen [2]. The overall block diagram of the remote helium mass spectrometer leak detector is shown in Fig. 1 [3].

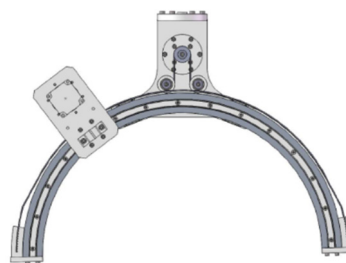


Figure 1: Structure of mobile prob for remote helium mass leak detector.

Helium injection leak test and result analysis

With The test is divided into two parts: helium injection method and positive pressure suction gun. During the test, the ambient temperature is about 24 °C. Firstly, the leakage rate of different positions is detected by the conventional manual method as the benchmark, and then the leakage rate data of each position is detected by the remote controlling mobile probe. To eliminate the accidental error, repeated tests were carried out and the average value was taken as the last result [4].

* Work supported by Institute of High Energy Physics

[†] hehy@ihep.ac.cn.

Content from this work may be used under the terms of the CC BY 3.0 licence (© 2021). Any distribution of this work must maintain attribution to the author(s), title of the work, publisher, and DOI

Add 0.5m long inner diameter $\Phi 250$ mm round vacuum box is used as the tested device. The kf250 quick release flange and blind plate are sealed by quick release chain, and then connected with vspd03 helium mass spectrometer leak detector to form a vacuum system. After confirming that the sealing state of the test vacuum system meets the test requirements, a leakage point is artificially made at the joint of the flange. After the leakage rate at each position of the joint is detected by the manual helium injection method, the helium cylinder is connected to the probe spray gun, and the remote control of the spray gun movement detection is carried out. When helium is sprayed into the leak area, it will be immediately inhaled into the mass spectrometer chamber of the leak detector, and the leak rate change response of the leak detector will be output. The connection of helium injection leak test is shown in Fig. 2.

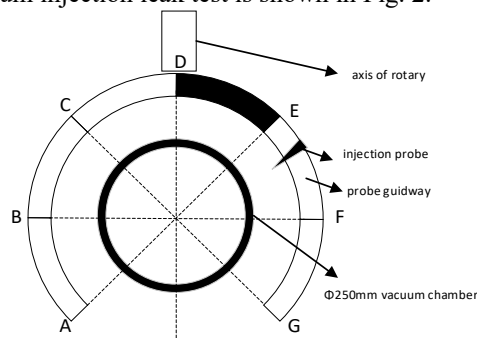


Figure 2: Layout of detection points for remote injection leak detection.

The spray gun probe detects and records the position of 7 vacuum box flange joints. During the test, the background leakage rate of the vacuum system gradually improved, and the average value was $9.0E-11 \text{ Pa} \cdot \text{m}^3 / \text{s}$, and the pressure was $5.3E-1 \text{ Pa}$. The final leakage rate after repeated helium injection is shown in Fig. 3 [5].

In the helium injection leak detection test, the leakage rate difference of 7 points detected by manual and device is less than 1 order of magnitude, which indicates that the remote helium injection leak detection is effective and reliable. Compared with the background value, the leakage rate of re-mote detection points a, B, C and D of the device changes little, close to the order of $1E-10 \text{ Pa} \cdot \text{m}^3 / \text{s}$; Point e began to increase significantly compared with the background, and the leakage rate was in the order of $10^{-7} \text{ Pa} \cdot \text{m}^3 / \text{s}$; The maximum leakage rate at point F is $4.88E-7 \text{ Pa} \cdot \text{m}^3 / \text{s}$, while the leakage rate at point G is smaller but remains at the order of $10^{-7} \text{ Pa} \cdot \text{m}^3 / \text{s}$. Through the test results of the device, it can be judged that the leakage position of the test system should be in the range of radian DF.

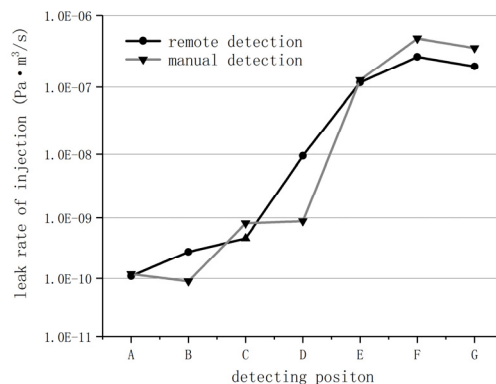


Figure 3: Leak rate of injection detection.

The average leakage rate of point d manual method is $8.8 \times 10^{-10} \text{ Pa} \cdot \text{m}^3 / \text{s}$, while the leakage rate of remote detection of the device is $9.44 \times 10^{-9} \text{ Pa} \cdot \text{m}^3 / \text{s}$, which is relatively different from the other two methods. The helium injection method relies on the artificial control of helium duration and pressure, and the helium rapidly diffuses around to the adjacent leak hole, which leads to low detection repeatability. The same reason also leads to the device unable to further confirm the exact position of the leakage in the arc DF range [6]. Although the helium injection method is qualitative, it is very positive to control the duration and pressure value of helium accurately. The equipment should be further studied and upgraded.

REFERENCES

- [1] SU Lin, "Application of smart ball leakage detection technology in long distance pipeline," *Pipeline Technique and Equipment*, vol. 1, pp. 30-31, 2017.
- [2] H. Zhang, "The application analysis of the seal ability experiment of pressure vessel of helium mass spectrometer technology," *Welding Technology*, vol. 39, pp. 61-64, 2010.
- [3] H.Y. He *et al.*, "Design of Remote Helium Mass-Spectrometer Leak-Detector," *Chinese Journal of Vacuum Science and Technology*, vol. 40, no. 2, pp. 128-131, 2020.
- [4] L. Fan, "Design of the Monitoring System for Helium Mass-Spectrometer Leakage Detector Based on Virtual Instrument," *Vacuum Electronics*, vol. 3, pp. 20-22, 2007.
- [5] S.S. Mahler, Hans-Christoph *et al.*, "Comparing physical continuer closure integrity test methods and artificial leak methodologies," *PDA J. Pharm. Sci. Technol.*, vol.73, no. 3, pp. 220-234, 2019.
- [6] J.W. Wang, "Current situation of helium mass spectrometer leak detector at home and abroad," in *Proc. The 16th Annual Meeting of Mass Spectrum Analysis and Leak Detection Special Committee of China Vacuum Society and the 11th Annual Meeting of Vacuum Measurement Special Committee of China Metrology and Testing Society*, 2011, pp. 39-45.

INVESTIGATIONS ON STABILITY PERFORMANCE OF BEAMLINE OPTICS SUPPORTS AT BSRF

W.F. Sheng¹ H. Liang^{†,1} Y.S. Lu, Z. Zhang

Institute of High Energy Physics, [100049] Beijing, P. R. China

¹also at University of Chinese Academy of Sciences, School of Physics, [100049] Beijing, China

Abstract

The stability of beamline optics directly affects the beamline's performances, such as coherence, focal size, position stability of the beam and so on, it has become a serious issue for a low emittance 4th generation light source. The vibration transmitting function of supports plays a big role in the stability performance of the optics. In order to design better supporting structure, several types of support structures were tested, and the transfer ratio were studied. The result shows that wedge structures generally have a lower transfer ratio, and point contact support structures should be avoided.

INTRODUCTION

HEPS is a new generation light source which aims to reach emittance as low as 60 pmrad with a circumference of about 1360 m. [1] It started construction in 2019 and will be finished in 2025. With the new light source there will be very small sized source, vibration will be a big challenge for HEPS. The beam position, intensity and focal size are often affected by stability of beamline optics such as monochromators, mirrors, sample stages, optical tables, etc. Those instruments are usually very sensitive to ground vibration, the vibration transfer ratio, or transfer function of their supporting structure, plays a big role in the performance of optics under ground motion and vibration. In order to build better optics for the HEPS project, also to get a better understanding of the issue of stability, investigations were carried out to find out what the common performances are, and provide some basic guidelines regarding design of stable supports.

The following sections will introduce the test conditions, and some results of different optics support.

TEST CONDITIONS AND METHODS

Most of the tests were carried out at BSRF, a first generation light source with about 3 months of dedicated synchrotron mode every year. The ground vibration level is about 18 nm RMS in the range of 1 Hz to 100Hz.

The vibration data was acquired by a DEWESOFT SIRIUSi 8xACC ADC [2], with DYTRAN 3192A and 3191A1 accelerometers [3]. The accelerometers were attached to different layers of optics support and on the ground. Sampling rate is usually set at 2000 Hz or 3000 Hz. The acceleration data then was integrated into RMS displacement. Then by comparing the RMS displacement of upper layer to lower layer, or to the ground, the transfer ratio, or transfer function of the RMS vibration displacement can be obtained. The eigenfrequencies are deduced

by the peaks of amplification curve. Due to the noise of the accelerometers at low frequency ($<5\text{Hz}$), the analysis frequency range is defined between 5 Hz to 1000 Hz.

TEST RESULTS

DCM Support

A DCM prototype shown in Fig. 1 was designed to verify technologies to be used for HEPS [4]. When it was designed, not much consideration in support stability was taken other than a granite table. The support of this DCM granite table are 6 wedges. A steel frame sits on those wedges, supporting a granite table with 6 screw levellers, which has ball bearings to make the adjustment easier. It is not good for high stability, because the ball bearings provide small area of contact, also screw levellers are not strong enough.

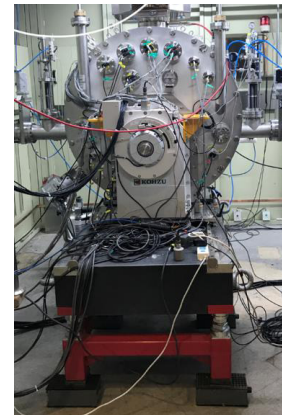


Figure 1: DCM under test.

The integrated RMS vibration of different layers are shown in Fig. 2. It shows that vibration level increase at 8 Hz and 31 Hz for the granite table (line 3, line 4 in the graph). With an eigenfrequency of 8 and 31 Hz, it has an overall transfer ratio of 3 from granite table to ground.

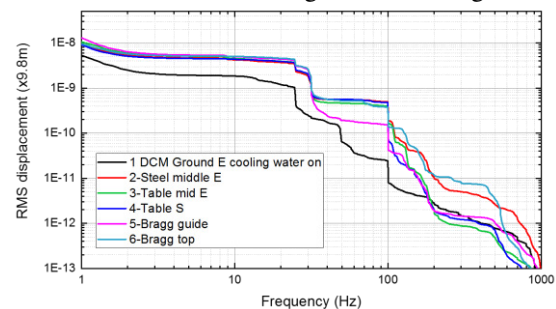


Figure 2: Integrated RMS vibration of DCM.

[†] Email address: lianghao@ihep.ac.cn

Content from this work may be used under the terms of the CC BY 3.0 licence (© 2021). Any distribution of this work must maintain attribution to the author(s), title of the work, publisher, and DOI

Mirror Support

This mirror support provides 5 DOF adjustment capability of a bending mirror is shown in Fig. 3. The bottom level is directly put on the floor, the second layer provide horizontal adjustment, supported and guided by 2 ball linear guide ways. The third layer provide yaw adjustment, supported on 2 sliding bearings. The fourth layer provide roll adjustment, supported on 2 arc shaped ball guide ways in a cantilever way. The mirror installation base is the fifth layer, sitting on 2 roller bearings arm, with the capability of pitch and vertical adjustments.



Figure 3: Test of a mirror support.

The integrated RMS displacement is shown in Fig. 4. It shows that vibration level increase at 8 Hz, which indicates it to be an eigenfrequency, it has a total transfer ratio of 1.76. With no increase at 8Hz on the third layer, it can be concluded that the fourth layer should claim this eigenfrequency. The contact of cantilever ball bearing support may be not perfect and resulted in this behaviour.

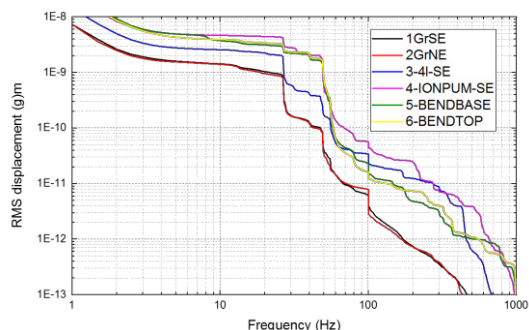


Figure 4: Integrated RMS displacement.

LAUE Monochromator Support

The double Laue crystal monochromator shown in Fig. 5 support provides 6 DOF adjustment capability of 2 crystal assemblies. The bottom layer sits on 4 screw levelers, providing height, roll and pitch of the whole monochromator. The second layer is supported by 2 sliding bearing and confined in horizontal movements in the middle, providing the yaw adjustment capability. The third layer also supported by 2 v-grooves, driven by a stepper motor, providing the horizontal adjustment capability. The fourth layer is supported by 2 levering arms with sliding bearings, which is driven by screw-nut mechanism. The vacuum chamber sits on the fourth layer, supported by 4 screw levers, with point contact at the bottom end of those drivers. And the crystal assembly is put on the bottom plate of the vacuum chamber.

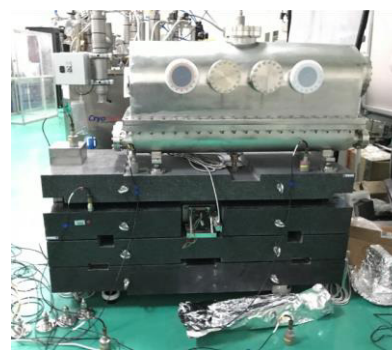


Figure 5: Test of a LAUE mono support.

The integrated RMS displacement is shown in Fig. 6. It shows a sudden increase at 8 Hz on the fourth layer, which could be the lowest eigenfrequency for this layer. The fourth layer has an overall transfer ratio of 6.5 to the ground. It also shows that on top of the chamber the vibration level is lower than that of the fourth layer, which shows vibration isolation behaviour on this layer. This means that the eigenfrequency of the vacuum chamber is so low that most of the vibration is above 1.41 times of its eigen frequency.

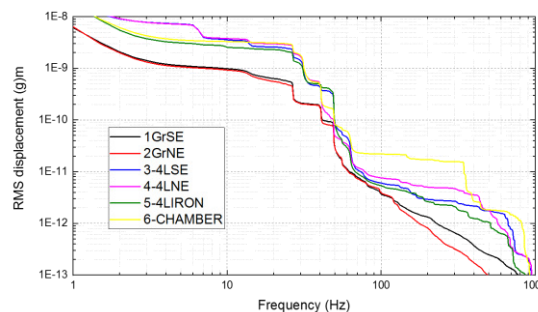


Figure 6: Integrated RMS displacement.

Vertical Direct Drive Spindle

The direct drive spindle shown in Fig. 7 was built for future monochromator, the support of its granite table are 4 wedges. The integrated RMS displacement is shown in Fig. 8. Due to the simplicity of this support and good contact of those wedges, it shows some increase at 66Hz, which should be the eigenfrequency, it has an overall transfer ratio of 1.12 from granite table to ground. The air bearing support is very stable, with an transfer ratio of 1.04 without air flow is the lowest of all.

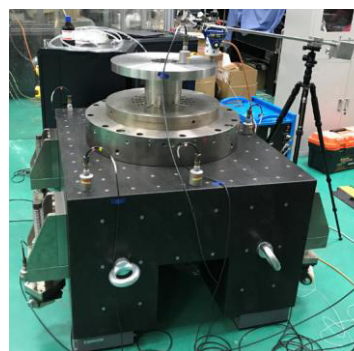


Figure 7: Vertical direct drive spindle.

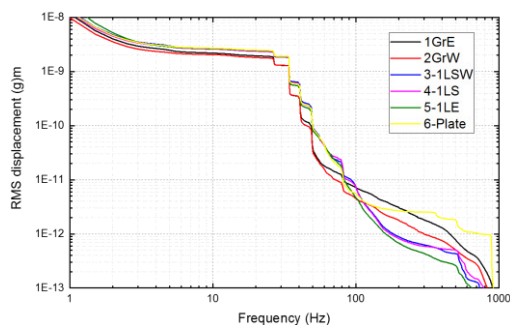


Figure 8: Integrated RMS displacement.

Horizontal Direct Drive Spindle

The horizontal direct drive spindle is shown in Fig. 9. The support of this massive granite table are 4 wedges. The integrated RMS displacement is shown in Fig. 10. The support and granite layout is the same as those of the vertical direct drive spindle, but it's significantly heavier (5 tons vs 3 tones). With an eigenfrequency of 56 Hz, it has an overall transfer ratio of 1.21 from granite table to ground. This is due to the added mass to those wedges thus lowering the eigenfrequency.



Figure 9: Horizontal direct drive spindle.

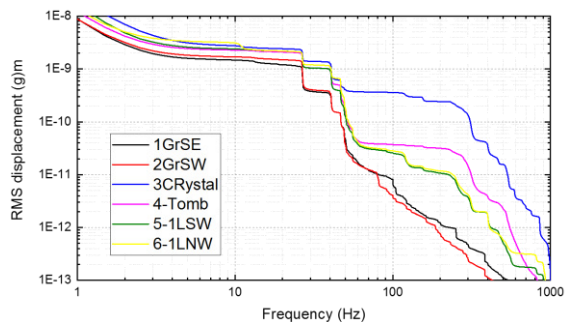


Figure 10: Integrated RMS displacement.

Summary of Relationship Between Amplification Ratio and Eigenfrequencies

Other than those results discussed above, a lot of other supports were also tested. With the eigenfrequency and transfer ratio calculated, plotted in Fig. 11. It shows that with an eigenfrequency above 50 Hz, a transfer ratio around or below 1.2 could be expected.

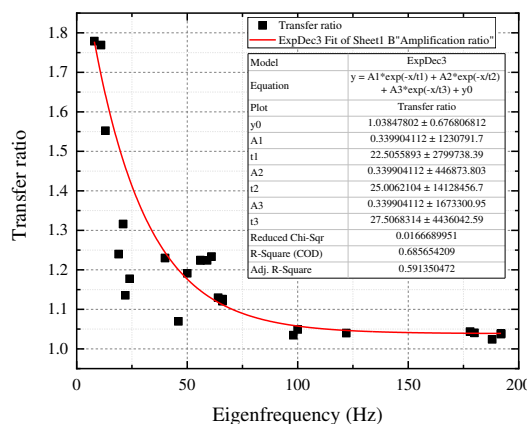


Figure 11: A summary of relationship between eigenfrequency and vibration transfer function.

CONCLUSION

A lot of optics support were tested and the relationships between eigenfrequency and transfer ratio were tested and studied. It can be concluded that wedges combined with granite tables could be a good combination, such as the supports of those two direct drive spindle. Also screw type levelers such as the DCM and the Laue monochromator support, does not perform well. Point support like those of the vacuum chamber of Laue mono is so low that they are isolating vibration, which is not recommended.

Another thing we noticed is that even on the same layer, the vibration level depends on where the sensors were put. Geometry plays a big role in the final vibration level. For a more thorough study, more sensors should be added and the modal shapes should be considered.

In general, a first eigenfrequency above 50Hz will provide a transfer ratio around or below 1.2 for the BSRF site. For future HEPS optics supports, those results will be taken into consideration.

ACKNOWLEDGEMENTS

We thank Brian Norsk Jensen for advice and help of building the vibration measurement system. And a lot of help from BSRF colleagues are also appreciated.

This research is supported by National Natural Science Foundation of China (NSFC) (No.11905243).

REFERENCES

- [1] Yi Jiao *et al.*, "Progress in the Design and Related Studies on the High Energy Photon Source", *Physics Procedia*, vol. 84, pp. 40-46, 2016. doi:https://doi.org/10.1016/j.phpro.2016.11.008
- [2] DEWESoft website, <https://dewesoft.com>
- [3] DYTRAN website, <https://www.dytran.com/>
- [4] Hao Liang *et al.*, "A high heat load double crystal monochromator and its cryo cooling system for HEPS", in *Proc. MEDSI'18*, Paris, France, June 2018, pp. 430-434. <https://doi.org/10.18429/JACoW-MEDSI2018-FROAMA02>

RESEARCH ON VIBRATION STABILITY OF SAPS FOUNDATION

G. Y. Wang[†], J. X. Chen, H. Y. He, L. Kang, L. Liu, R. H. Liu, X. J. Nie, C. J. Ning,
 A. X. Wang, J. B. Yu, Y. J. Yu, J. S. Zhang, L.Q. Zhao, D. H. Zhu
 Institute of High Energy Physics, Chinese Academy of Sciences, Beijing, China
 Spallation Neutron Source Science Center, Dongguan, China

Abstract

With the development of science and technology, the technology of synchrotron radiation light source is further developed. As the fourth generation synchrotron radiation light source, Southern advanced photon source forward more stringent requirements on the beam stability. The foundation vibration is the main factor affecting the beam stability. In this paper, the foundation vibration characteristics of the proposed site of Southern advanced photon source are studied, and the foundation vibration test is carried out. The data analysis is carried out from the aspects of different locations, day - night vibration variation characteristics, vibration source frequency, vibration attenuation, and the influence of Expressway on the foundation vibration. This paper provides guidance for the follow-up construction and anti micro vibration foundation vibration treatment of Southern advanced photon source

PREFACE

With the improvement of science and technology, the performance of large scientific devices is constantly developing towards higher requirements. Southern advanced photon source (SAPS) is the fourth generation synchrotron radiation light source to meet the new development requirements. As the fourth generation synchrotron radiation source, South light source needs higher performance, and beam stability is a very important index. Beam stability needs a stable and non-interference equipment environment. The settlement of the ground, the movement of the surrounding ground, the vibration caused by the fluid and the change of the ambient temperature will affect the mechanical stability of the equipment itself. The foundation vibration is transmitted to the magnet, BPM and other beam equipment through the equipment girder, which eventually leads to the degradation of beam stability. In order to meet the requirements of beam stability, it is necessary to carry out a detailed study on the foundation vibration of the proposed site of the South light source, and clarify the characteristics of the foundation vibration, so as to lay the foundation for the subsequent construction of the light source.

MEASUREMENT CONTENT AND ANALYSIS METHOD

Southern advanced photon source is located on the west side of China spallation neutron source. The experimental measurement system uses 3ESPCDE seismograph to obtain the velocity signal of foundation vibration. In order to

[†] gywang@ihep.ac.cn.

grasp the overall foundation vibration situation of Southern advanced photon source, the vibration measurement is divided into six areas, each area is arranged with 5 measuring points, and the 24-hour vibration measurement is carried out in three directions of east-west, north-south and elevation. The layout of each point is shown in Fig. 1. Because the survey area is mountain forest area, the surface layer is soft soil, and the bottom layer is hard rock. In order to get the ground vibration results more accurately, each measuring point is dug to remove the loose soil on the surface, and the concrete with the thickness of 100 mm is poured to make the measured value of the seismograph closer to the real situation of the foundation, as shown in Fig. 2.



Figure 1: Distribution points of vibration measurement.

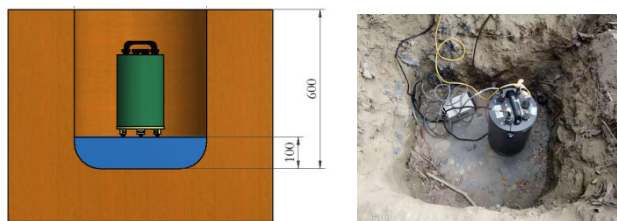


Figure 2: Installation method of seismograph.

Time domain analysis, frequency domain analysis and wavelet analysis are often used in vibration data analysis [1]. In this study, the vibration data are analyzed and evaluated by root mean square (RMS) and power spectral density (PSD), and the time domain RMS value is used to evaluate the energy of foundation vibration signal. The calculation formula of RMS value is shown in Formula 1, In frequency domain, the power spectral density is taken as the evaluation standard, and the calculation formula is formula 2. Considering the measurement accuracy of the seismograph, and the artificial vibration interference in the environment is mainly within 1-100hz. For the evaluation of foundation vibration, the RMS value of 1-100hz is taken as the evaluation standard, and formula 3 is used for calculation [2].

$$RMS = \sqrt{\frac{1}{k+1} \sum_{i=0}^k Y_i^2} \quad (1)$$

$$PSD = \frac{\Delta t}{N} \left| \sum_{n=0}^{N-1} u(n) e^{-i2\pi kn/N} \right|^2 \quad (2)$$

$$RMS = \sqrt{\frac{A_0 \Delta f}{2} + \sum_{i=1}^{k-1} A_i \Delta f + \frac{A_k \Delta f}{2}} \quad (3)$$

ANALYSIS OF VIBRATION MEASUREMENT RESULTS

In order to simulate the vibration of the storage ring of Southern advanced photon source, the vibration measuring points are distributed in six areas, each of which has five measuring points. Among them, the vibration of Z3 and Z4 area is affected by the traffic flow of forest path, and the vibration of Z1 and Z2 area is affected by the traffic flow near the expressway. Z5 and Z6 areas are deep in the forest, and are less disturbed by the outside, which can better reflect the vibration of the whole mountain forest. Taking the average RMS value of 1-100 Hz amplitude as the vibration measurement index, the vibration analysis results of daytime and late night are counted respectively, and the RMS values of each measuring point in vertical, east-west, north-south directions are listed. The results are shown in the Fig. 3 below. The influence of traffic flow on foundation vibration is obvious. Zone Z1 and zone Z2 area are close to the expressway, and the vibration value is significantly higher than that of other areas, The RMS value of vibration is 100-200nm. The vibration values of Z3 and Z4 area affected by forest mountain road are 15-70nm. The vibration of Z5 and Z6 area is the lowest, and the RMS value is 20-40nm.



Figure 3: RMS value of the proposed site.

The measuring points of area Z5 and area Z6 are perpendicular to the expressway, and the vibration value distribution of the measuring points reflects the vibration attenuation from near to far away from the expressway, as shown in Fig. 4. From the change of measuring point 21 to 30, it can be seen that the vibration increases gradually, and the vibration amplitude increases gradually. At the same time, the vibration of the whole area at night is slightly lower than that during the day, as shown in Fig. 5.

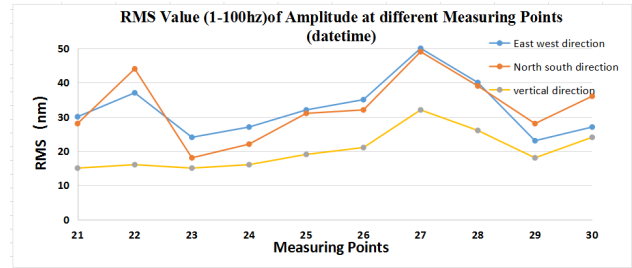


Figure 4: RMS value of different Measuring Points (datetime).

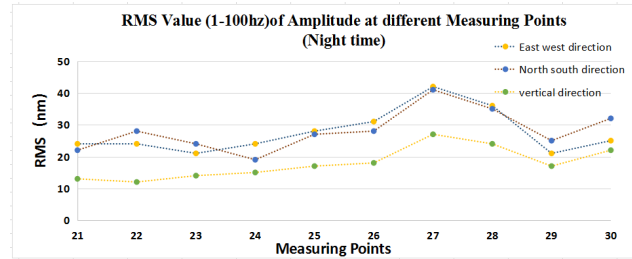


Figure 5: RMS value of different Measuring Points (nighttime).

The RMS values of the above measuring points are the average values of 12 hours in day and night respectively. In order to better grasp the variation trend of the foundation vibration of Southern advanced photon source with time, the RMS statistical values of each measuring point per minute are carried out, and the scatter diagram of 24-hour vibration measurement is drawn. Take No. 17 measuring point as an example, as shown in Fig. 6. Under the influence of traffic flow in the daytime, the RMS value of foundation vibration can reach more than 500 nm, while in the case of less human activity at night, most of the vibration value is less than 30 nm. The large-scale change of the vibration reflects the influence of Road on the foundation vibration. The subsequent treatment of the foundation of Southern advanced photon source should consider the isolation of the surrounding human activities (the vibration value of 500nm), rather than reduce the vibration of the whole foundation plate itself (the vibration value of 30nm). It can be seen from the figure that the RMS value in the vertical direction of the three directions is smaller than that in the east-west direction and north-south direction, so the vibration isolation needs to consider the horizontal vibration more seriously.

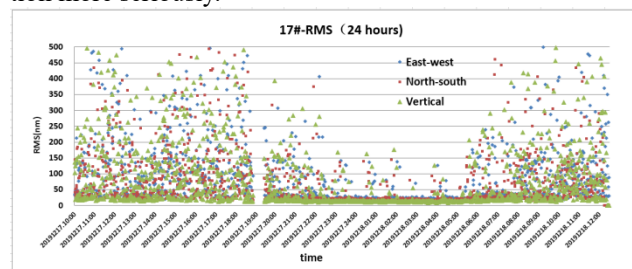


Figure 6: RMS value of 24-hour vibration.

The vibration frequency of traffic and industrial production activities is mainly in 1hz-100hz. In order to study the RMS contribution value of different frequency bands, the RMS value statistics of four frequency bands are carried out, as shown in Fig. 7, the RMS value of 1-100hz frequency band is close to that of 4-100hz, and the RMS value contribution value of 15-100hz frequency band is very low, which indicates that the foundation vibration mainly comes from the low frequency band of 4-15hz. As the high-frequency vibration decays rapidly in the stratum, the low-frequency vibration signal is mainly felt on the surface [3]. This conclusion is also obtained from the power spectral density analysis of the measuring points, as shown in Fig. 8.

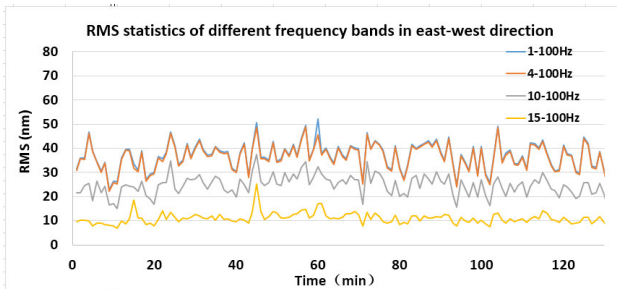


Figure 7: RMS statistics of different frequency bands.

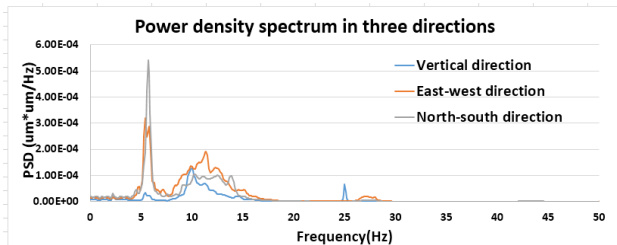


Figure 8: Rower density spectrum in three directions.

Analyze the power density spectrum change of a measuring point for 24 hours, as shown in Fig. 9. The frequency below 15Hz is the main frequency component, and the frequency band with 5Hz highlight has the largest contribution, which runs through the whole day of measurement, indicating that there is still a high traffic flow on the expressway at night. 60Hz frequency is the frequency of industrial machinery, which only appears in the daytime and disappears at night.

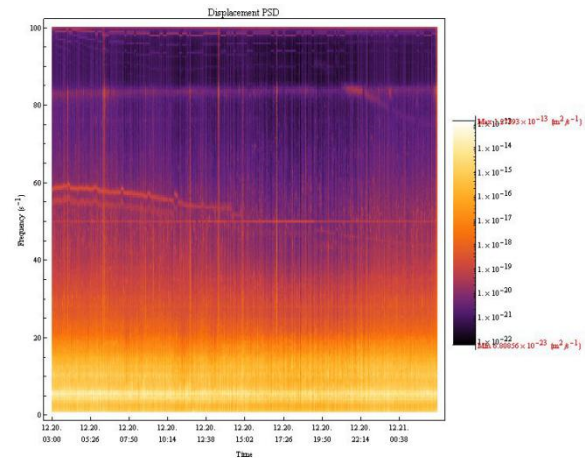


Figure 9: Power Spectral Density in 24-hour.

CONCLUSION

Through the above analysis, we can draw the following conclusions: (1) the foundation of the South light source is located in the mountains and forests, and the RMS is mainly within 30nm, but some areas are affected by the high speed, reaching more than 200nm.(2)The vibration value in horizontal direction is greater than that in vertical direction, and the horizontal vibration isolation measures should be considered in later engineering.(3)The main part of foundation vibration is the low frequency part of 1-15Hz, and the influence of 5Hz expressway is the most obvious. Isolating the influence of Expressway vibration is helpful to reduce the RMS value of the whole area.

REFERENCES

- [1] X.F. Wang *et al.*, “Analysis of Flight Vibration Data for an Airplane”, *Metrology & Measurement Technology*, vol. 39, no. 3, p. 73-77, 2019. doi:10.11823/j.issn.1674-5795.2019.03.14
- [2] R.Z. Zhang *et al.*, “Numerical Method of the Power Spectral Density”, *High power laser and particle beams*, vol. 12, no. 6, pp. 661-664, 2000.
- [3] M. Yu *et al.*, “Research review on measurement and evaluation methods of environmental vibration for precision instruments”, *Journal of vibration and shock*, vol. 29, no. 8, pp. 214-216, 2010. doi:10.3969/j.issn.1000-3835.2010.08.048

STUDY THE ACTIVE VIBRATION CONTROL SYSTEM OF THE PARALLEL 6-DOF PLATFORM*

R.H. Liu †, H.Y. He, L. Kang, Z. Y. Ke, L. Liu, X.J. Nie, C.J. Ning, A.X. Wang, G.Y. Wang, Y.J. Yu, J.S. Zhang, D.H. Zhu, CSNS/IHEP, CAS, Dongguan, 523803, China

Abstract

With the development of high-energy synchrotron radiation light source with high energy, high brightness, low emittance and nano-scale light spot, accelerators and beamline stations have higher requirements for the stability of the system, and active vibration isolation technology has been paid more and more attention. It has become the key technology for the development of major scientific devices (such as high-energy synchrotron radiation light source, free electron laser, etc.) in the future. In this paper, an active vibration control system driven by piezoelectric ceramic actuator with strong adaptability is designed. NI CompactRIO real-time control system and Fx-LMS adaptive filter control algorithm are used for the active vibration control system. The identification method of input and output channels and the active control module are simulated by MATLAB. And an active vibration control system based on a parallel 6-DOF platform was built for experimental verification. The experimental results show that the designed active vibration control system has a good control effect for low-frequency micro-vibration.

INTRODUCTION

The micro-vibration of synchrotron radiation light sources such as ESRF, APS and SSRF etc. shows that the low-frequency micro-vibration below 20Hz contributes significantly to the overall vibration in the frequency domain, which will cause micro-displacement and micro-deformation between pose-sensitive equipment and various parts of the optical system, thus affecting the performance of various precision components. Therefore, the control of low-frequency micro-vibration interference has become one of the factors that cannot be ignored in the development of advanced light source technology [1]. Low-frequency micro-vibration has the characteristics of miniature, inherent and difficult to control, which makes the micro-vibration dynamic environment become extremely complex and special, and the analysis and vibration control are very difficult, so it is urgent to restrain and control the micro-vibration [2]. Active vibration control has the advantages of good low frequency damping performance, high reliability, easy expansion and easy to realize multi-machine distributed parallel processing due to the existence of actuators [3]. It has been more and more widely used in large scientific devices such as synchrotron radiation light source, aerospace, industrial control, communication and scientific research.

THE ACTIVE CONTROL PRINCIPLE OF MICRO-VIBRATION

In the actual control engineering, the mathematical models of the actual controlled systems are difficult to be identified in advance through mechanism modeling or off-line system identification, or some parameters or structures of their mathematical models are in change. In the face of the situation that the characteristics of these systems are unknown or often changing and can't be completely determined in advance, how to design a satisfactory control system that can actively adapt to the unknown or changing characteristics is the problem to be solved by the adaptive control algorithm.

Principles of the FX-LMS Active Control

In practical application, the error signal (vibration response signal) $e(n)$ is not a simple superposition of the filter output $y(n)$ and the desired signal $d(n)$. There is a transfer function of a secondary channel between $y(n)$ and $e(n)$. $S(z)$ is the transfer function from the control input of the actuator to the load response, which represents the dynamic characteristic of the actuator, as shown in Fig. 1. Morgan proposed Fx-LMS algorithm to eliminate the influence of secondary channel [4]. The identification process of secondary channels can be carried out by online or offline. The implementation of online identification is relatively complex, so the $S(z)$ is usually identified by offline [5]. According to the derivation process of the standard LMS algorithm, a similar result can be obtained. The whole filtered Fx-LMS algorithm can be simply summarized as follows:

$$\left\{ \begin{array}{l} y(n) = \sum_{l=0}^{L-1} w_l x(n-l) \\ e(n) = d(n) - S^T Y(n) \\ w(n+1) = w(n) + \frac{\tilde{\mu} e(n) X'(n)}{\gamma + X'^T(n) X'(n)} \\ X'(n) = [x'(n) \quad x'(n-1) \quad \dots \quad x'(n-L+1)] \\ x'(n) = \sum_{h=0}^{H-1} s_h x(n-h) \end{array} \right. \quad (1)$$

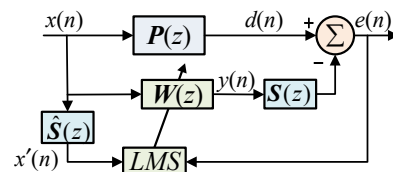


Figure 1: The principle of FX-LMS algorithm.

* Work supported by NNSF of China: N0. 11905231

† liurh@ihep.ac.cn

Content from this work may be used under the terms of the CC BY 3.0 licence (© 2021). Any distribution of this work must maintain attribution to the author(s), title of the work, publisher, and DOI

Simulation of the Secondary Channel Identification Algorithm

In order to simulate and verify the system identification algorithm, it is necessary to assume the channel model to be identified. This paper assumes that the channel model to be identified is $S(z) = [0.038, 0.0875, -0.175, 0.035, -0.175, 0.0875, 0.21, 0.0385, 0.084, -0.105]$. The excitation signal $x(n)$ is taken as the order of Gaussian white noise. The order of $w(z)$ is set as order 14, the convergence factor $\mu=0.1$. The number of identification times are 2000. Through simulation, the secondary channel model parameters of the system can be effectively identified by using Fx-LMS adaptive algorithm, which was shown in Fig. 2.

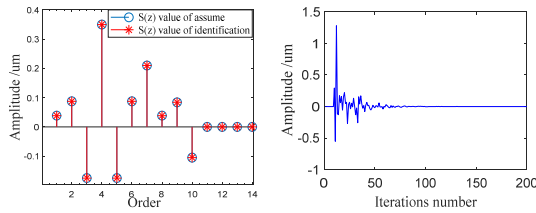


Figure 2: The secondary channel identification results(left) and the error of the simulation(right).

Simulation of Active Vibration Control Algorithm

In this paper, the MATLAB is used to simulate and verify the algorithm of the active vibration control module. The excitation source set here is a square sinusoidal wave with amplitude of 2mm at 5Hz, 15Hz and 20Hz, and the multi-frequency interference signal with white Gaussian noise of 0.1um is superimposed. The order of the weight $w(z)$ is 16, and the convergence factor $\mu=0.005$. The results in the above identification algorithm test is shown in Fig. 3. By calculation, the vibration amplitude of the system is reduced from 4.96um to 0.15um. The system has a good isolation effect in theory.

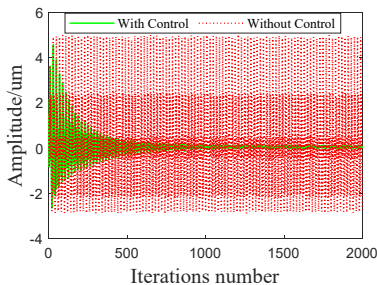


Figure 3: Simulation of active vibration control.

DESIGN OF ACTIVE VIBRATION CONTROL SYSTEM

The control process of the active vibration control system designed in this paper mainly includes two parts: the secondary channel identification process and the active vibration control process. The process of estimating the transfer function of the secondary channel is called the secondary channel modeling process. In practical

application, firstly, the external interference source of the system should be turned off, and the FPGA controller generates the Gaussian white noise voltage signal and outputs it to the piezoelectric ceramic controller, which is used as the excitation source signal of the secondary channel modeling. Then turn to the active control process, and realizes the adaptive active vibration control function through the vibration signal acquisition and the iterative calculation control of the active control algorithm. The whole control process is shown in Fig. 4.

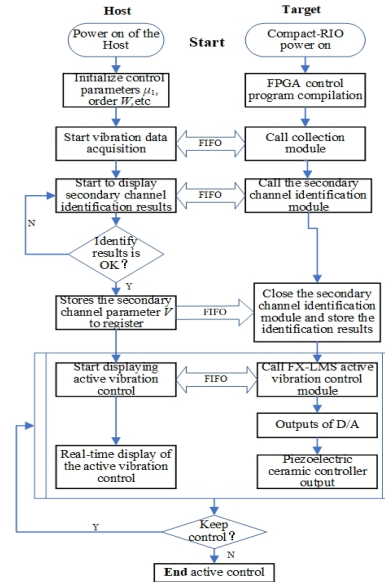


Figure 4: Flow block of the active control system.

The software architecture of the active vibration control system is shown in Fig. 5. The system software is mainly composed of the host RT software and the target FPGA software. The host computer software is mainly composed of vibration data display interface, secondary channel identification interface and active vibration control interface. The target computer software is mainly composed of vibration data acquisition module, secondary channel identification algorithm module, Fx-LMS active vibration control algorithm module and 6-channel piezoelectric ceramic drive control module, which mainly realizes the functions of vibration data acquisition and transmission, closed-loop control signal output control and active vibration control during the operation of the system.

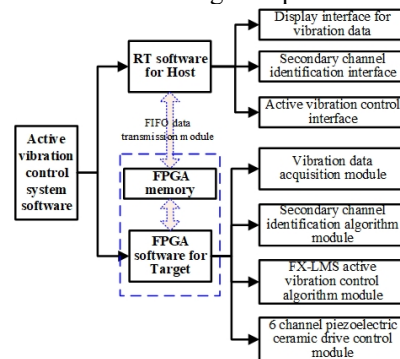


Figure 5: Software architecture of the active vibration control system.

EXPERIMENTAL STUDY ON ACTIVE VIBRATION CONTROL

This paper presents a single direction active vibration control system based on a parallel 6-DOF platform is shown in Fig. 6. It is mainly used to control the low frequency micro-vibration in the vertical Z direction of the platform [6]. The vibration acquisition module in the control system collects the vibration signal in the Z direction of the upper and lower plane of the parallel platform in real time. The signals are amplified and adjusted by Compact-RIO charge, and then the system excitation signals and the platform response signals are transmitted to the FPGA processor in real time. The Fx-LMS module in FPGA analyzes and processes the control target signal, obtains the real-time feedback control quantity, and sends out the control signal through the output module. The piezoelectric ceramic actuator driven by the piezoelectric controller produces a reaction force acting on the plane of the parallel platform to achieve the effect of vibration reduction.

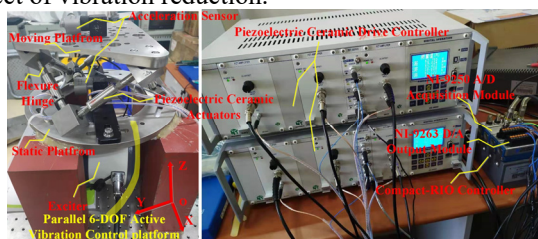


Figure 6: Photograph of the active vibration control system.

In the secondary channel Parameter identification experiment, the identification results of the Z direction of the platform is shown in left Fig. 7, which shows that the channel parameters of the system are mainly concentrated in the first 80 orders. At the same time, five groups of white noise signals of different sizes are used to drive piezoelectric ceramic actuators, and the standard deviation distribution of secondary channel parameters is shown in right Fig. 7. The maximum standard deviation of secondary channel parameters is 0.175. Different sizes of white noise signals have little influence on the identification of the secondary channel parameters.

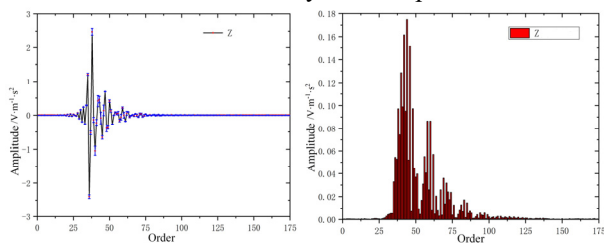


Figure 7: Secondary channel identification result of active vibration control system (left), and Standard deviation distribution of secondary channel parameters (right).

In the active vibration control experiment, different frequency excitation and vibration control experiments on the Z direction of the platform are carried out to test the low frequency damping effect of the control system. The

vibration damping effect under different excitation frequencies are listed in Table 1.

Table 1: Vibration Reduction Results under Different Frequency Exciting Conditions

exciting frequency /Hz	with control / μm	without control / μm	vibration reduction rate /%	vibration attenuation /dB
7	9.179	2.247	75.52	14.66
10	9.475	1.017	89.27	23.89
15	9.955	0.512	94.85	52.04
20	9.634	0.554	94.24	43.41
25	7.234	0.412	94.31	70.21
30	6.165	0.561	90.91	58.16
40	4.924	0.943	80.84	64.23
50	4.493	0.834	81.43	71.82

Figure 8 shows the experimental results of active vibration reduction, it can be seen that under the action of sinusoidal interference signal of vibration exciter at 7Hz, the amplitude of displacement vibration is reduced from 9.179 μm to 2.247 μm , which is reduced by 75.52%, the vibration amplitude of the platform attenuates to 14.665dB. With the increase of the excitation frequency, the active damping efficiency and attenuation of the active damping control system increase obviously, and the vibration damping effect is better.

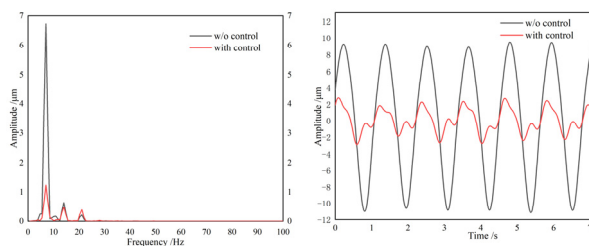


Figure 8: Experimental results of active vibration control.

CONCLUSION

In this paper, an active vibration control system is designed on a parallel 6-DOF platform driven by a piezoelectric actuator. The Fx-LMS adaptive control algorithm is used as the system control method. The medium and low frequency excitation test of 7Hz to 50Hz was carried out on the platform, and the low-frequency micro-vibration control in vertical Z direction was realized, especially the upper platform achieved a good vibration reduction effect of 75.52% in the vertical Z direction under the low frequency excitation interference of 7 Hz which verifies that the active vibration control system designed in this paper is feasible. The system can lay a foundation for low-frequency micro-vibration control system and multi-directional adaptive active control of southern advanced synchrotron radiation light source precision equipment in the future.

REFERENCES

- [1] P. Kristiansen *et al.*, “Vibration measurements of high heat-load monochromators for DESY PETRA III extension,” *J. Synchrotron Radiat.*, vol. 22, pp. 879-885, 2015. doi: 10.1107/S1600577515005664
- [2] C. Doose, S. Sharma, “Investigation of Passive Vibration Damping Methods for the Advanced Photon Source Storage Ring Girders,” in *Proc. MEDSI’02*, Chicago, IL, USA, 2002, pp 133-139.
- [3] R. L. Breton, G. Deleglise, J. Allibe *et al.*, “Nanometer Scale Active Ground Motion Isolator,” *Sens. Actuators, A*, vol. 204, pp. 97-106, 2013. doi: 10.1016/j.sna.2013.09.020
- [4] D.R. Morgan, C. Sanford, “A control theory approach to the stability and transient analysis of the filtered- xLMS adaptive notch filter”, *IEEE Transactions on Signal Processing*, vol. 40, no. 9, pp. 2341-346, 1992. doi: 10.1109/78.157237
- [5] Yixin Chen and J. E. McInroy, “Decoupled control of flexure-jointed hexapods using estimated joint-space mass-inertia matrix,” *IEEE Transactions on Control Systems Technology*, vol. 12, no. 3, pp. 413-421, May 2004, doi: 10.1109/TCST.2004.824339
- [6] Liu Ren-hong *et al.*, “Study of Micro-vibration Active Control System Base on Piezoelectric Driver,” *Atomic Energy Science and Technology*, vol. 54, no. 10, pp. 1940-1946, 2020. doi: 10.7538/yzk.2019.youxian.0757

PERFORMANCE OF A DOUBLE CRYSTAL MONOCHROMATOR PROTOTYPE FOR HEPS UNDER WATER COOLING CONDITION AT A WIGGLER BEAMLINE OF BSRF

Hao Liang^{†,1}, Weifan Sheng¹, Hong Shi, Yiming Yang, Lirong Zheng¹
 Institute of High Energy Physics, 100049 Beijing, P. R. China

¹also at University of Chinese Academy of Sciences, School of Physics, 100049 Beijing, China

Abstract

The performance of monochromator is crucial to the performance of a beamline, especially for a 4th generation synchrotron light source. To find out the performance of the monochromator prototype built for the HEPS project, it was tested at a wiggler beamline of BSRF with water cooling. The cooling of the crystals was measured by rocking curve broadening at different energy and cooling seems to be not enough due to indium foils. The repeatability in 1 hour was about 0.1 eV. The energy drift in 9 hours after the beam hit the beamline was 0.4 eV at the Cu K edge. The short-term stability was tested with synchrotron beam under various cooling condition, and results between 4.4 nrad to around 400 nrad were observed. In conclusion, some performances are satisfying, but further improvements should be carried out in the future.

INTRODUCTION

HEPS is a new generation light source which employs multi-bend achromat lattices and aims to reach emittance as low as $60 \text{ pm} \cdot \text{rad}$ with a circumference of about 1360 m [1]. A double crystal monochromator prototype was built for the HEPS project, as shown in Fig 1. It went through a series of offline and online test with LN2 cooling during 2016~2019, some key performances were tested. The prototype has a stability of 40 nrad RMS with a LN2 flow rate of about 4.5 L/min. The LN2 cooling works fine under 800 watts of heat load provided by a heater. Other performances such as mechanical resolution, repeatability, vacuum, motion functions are all up to design requirements. Details can be found in [2].

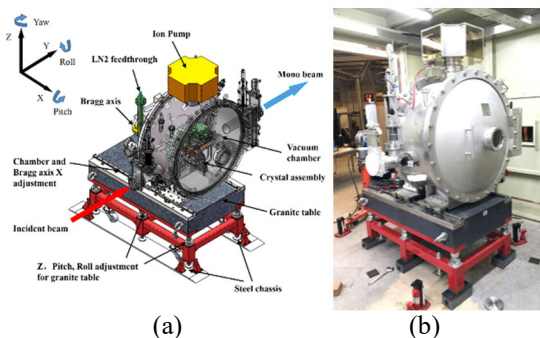


Figure 1: DCM design model (a) and prototype (b).

However, it's still not guaranteed that it will really work for demanding experiments such as XAFS. In order to find out its reliability, it was installed in 3W1 of BSRF, a

wiggler beamline. It was tested only under water cooling condition, since BSRF does not have dedicated LN2 distribution lines. XAFS experiments requires good repeatability of the energy, and good energy stability. Test methods were also developed for such kinds of requirements.

The following sections will share the test conditions, methods and results.

TEST CONDITIONS

The new 3W1 test beamline layout is shown in Fig. 2. The original 3W1 was dismantled for optics testing. The DCM is 20.8 meters from the source, before the DCM is a collimating mirror, which will reduce the heat load irradiated to the monochromator. By measurement of cooling water temperature rise, the heat load is about 35W. After the DCM is a toroidal mirror at 23 meter. The focal point is 32 meter from the source. The monochromator was cooled by a water chiller made in China, LX series from Coolium Instruments [3], which has a cooling capability of 1000 watts.

Most of the tests and experiments were done under XAFS mode, as shown in Fig. 3. Two Ion Chambers and diamond XBPM were used to measure intensity before and after sample. An ADC [4] were used to take data at high speed in order to measure vibration level.

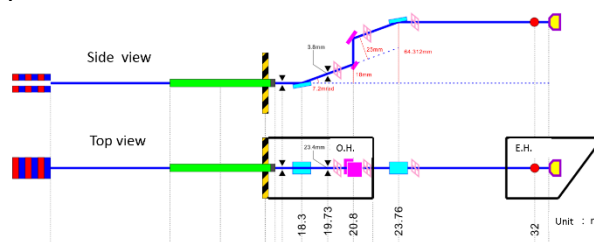


Figure 2: Test beamline layout.

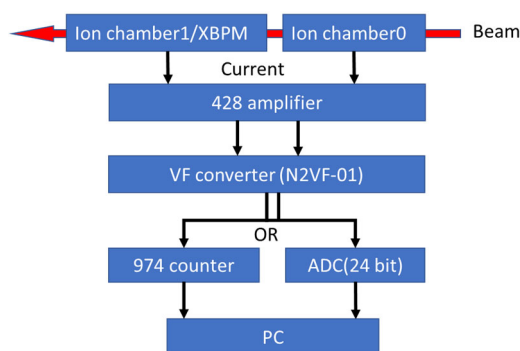


Figure 3: Data acquisition equipment.

[†]lianghao@ihep.ac.cn

TEST RESULTS

Cooling Performance

The cooling performance was measured by rocking curves. Figure 4 shows that intensity drops when flow rate drops from 4 L/min to 2 L/min. At flow rate of 0.3 L/min the intensity drops further. Also there are shifts of peaks, indicating insufficient cooling of crystals and further thermal deformation has taken place. Figure 5 Compares all results with theory calculation, it shows that FWHM of rocking curve is slightly larger than theory calculation at higher energies, with a flow rate of 4 L/min. At lower energies the difference is not that obvious, but still larger than LN2 cooling. The results may indicate that thermal contact resistance of indium foils is too high for water cooling. A contact interface made of indium-gallium eutectic is better for water cooling.

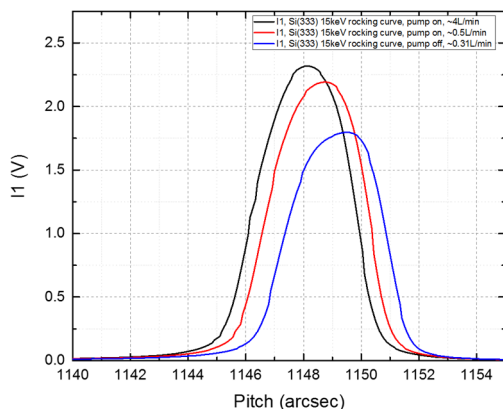


Figure 4: Rocking curves.

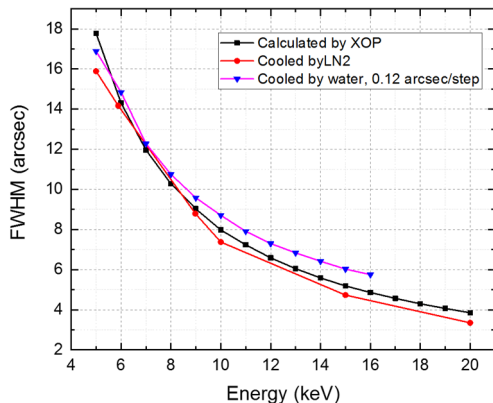


Figure 5: FWHM of rocking curves.

Short-Term Repeatability

The repeatability of a monochromator is very important for XAFS application, good repeatability leads to better data quality. Repeatability is determined by the mechanical repeatability of the Bragg goniometer and thermal deformation, if any. The short-term repeatability was measured by non-stop Cu K edge scans. It is about 0.1 eV for a period of 1 hour.

Long-Term Stability

The long-term energy stability is crucial for XAFS application. The overall repeatability of a long period can be estimated by adding up the short-term repeatability and energy drift. By using 2 ion chambers we can easily get the absorption ratio for a Copper foil under different energy. Fix the energy at one point where the relationship between absorption ratio and energy is known, energy drift can be calculated by measuring the absorption ratio. Test result in Fig. 6 shows that a 0.4eV drift from a “cold state” beamline to 9 hours after beam on, this is mainly due to the thermal deformation of the whole beamline and monochromator. Another reason maybe the surrounding temperature variation during this period, which is about 0.1°C in the hutch as shown in Fig. 7, could lead to a thermal deformation both in the support of mirror and the monochromator, possibly also the source. At the final stage the drift speed is less than 0.013eV/hour. Another thing to be noticed is that the hutch temperature is passively controlled without any ventilation or air conditioning.

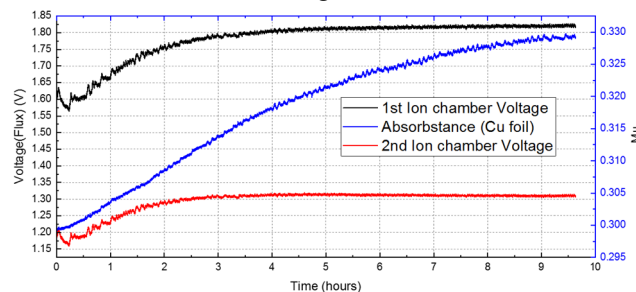


Figure 6: Cu K edge flux and absorption ratio for 9 hours.

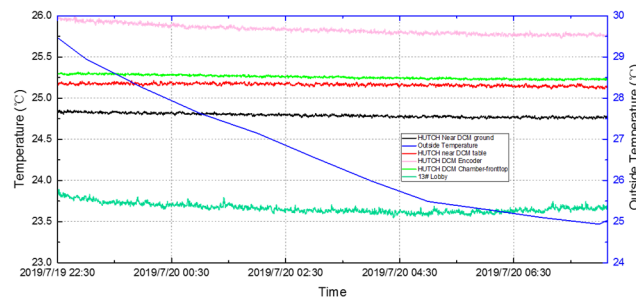


Figure 7: Temperature recordings during long-term stability test.

Short-Term Stability

The short-term stability is crucial to position sensitive experiments, also influencing the intensity and coherence of the beam. To measure the stability, intensity data of ion chamber 0 was acquired by an ADC with a sampling rate of 2kHz, then converted to rocking angle of the second crystal [5, 6]. Figure 8 shows ion chamber readings under different cooling conditions. The black curve stands for intensity cooled by chiller at a flow rate of 4 L/min, in the middle section of the black curve the pump for cooling circuit was turned off, but the refrigerant pump is still on, the intensity fluctuation quickly drops to a much lower level. When the pump was turned on again, the intensity fluctuation resumed to its previous level. The red curve stands for

intensity cooled by chiller at a flow rate of 0.5 L/min, the intensity fluctuation is much smaller than that of 4 L/min, which agrees well with prediction. The bottom line in blue stands for gravity cooling with a flow rate about 0.31 L/min. The intensity fluctuation can barely be observed, indicating very good stability.

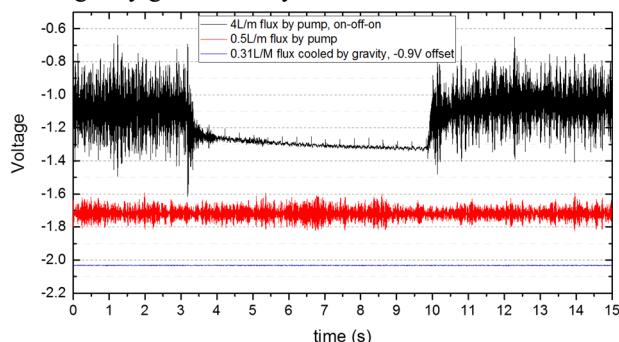


Figure 8: Ion chamber readings under different conditions.

After converting the intensity to angular vibration, then by data processing using FFT, the integrated angular displacement is shown in Fig. 9. Total RMS vibration with chiller ranging from 100 to 500 nrad. The main cause is the vibration from the chiller's motor, which can be observed at 100 and 200 Hz. Flow induced vibration contributed around 90 Hz and around 120 Hz. Comparing this result to previous LN2 cooling result, the resonance peaks slightly moves to lower frequency. The cause of this might be the difference of density between water and liquid nitrogen, or due to structural change we made to the support of liquid nitrogen lines.

With gravity cooling, best result is about 4 nrad. Explanation on this could be that without the disturbance from the pump the system performs better. Another way to look at this is that the flow state has changed from turbulence flow to laminar flow. The main cause of vibration at 50 Hz comes from a vacuum pump transmitted by the floor. It shows great potentials for gravity cooling. As introduced before, cooling efficiency is not enough for gravity cooling due to the low flow rate and high thermal contact resistance of indium foils. Solutions could be a bigger difference in height of the inlet and outlet of the cooling circuit and indium-gallium eutectic thermal conducting material between cooling blocks and crystal.

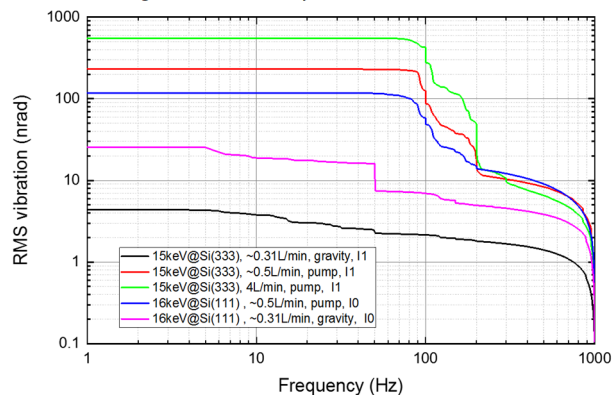


Figure 9: Integrated RMS displacement.

One thing to be noticed is that the data acquisition system seems have a lot of noise above 200Hz, this could be the limit of the hardware such as ion chamber or ADC. Higher energy could also be a cause for higher noise level. However, 200 Hz is enough for vibration measurement of a monochromator.

CONCLUSION

A series of tests were carried out for the DCM, all results seems to satisfy XAFS requirements. The test equipment served all tests well, with some difficulty above 200 Hz of vibration due to hardware limits, but served all tests well. The repeatability and energy stability should be carefully looked after in the future. Water cooling seems not enough for this beamline, due to the thermal contact resistance of indium foils. Cooling by the chiller induced a high level of vibration for the monochromator, the main cause is the pump. Future work could focus on how to reduce the fluctuation induced by the pump, such as vibration absorption techniques. Gravity cooling turns out to have great benefit for stability since it does not involve pumping in the cooling circuit. The cooling capability of gravity cooling is determined by height difference between inlet and outlet of cooling circuit. For high heat load condition, the flow rate must be raised and thermal contact resistance reduced. These tests provided useful information for future development of monochromators or other beamline instruments, such as cooling methods or temperature control level in order to get desired stability.

ACKNOWLEDGEMENTS

We thank all BSRF colleagues for their support during the test.

This research is supported by National Natural Science Foundation of China (NSFC) (No.11905243).

REFERENCES

- [1] Y. Jiao *et al.*, "Progress in the Design and Related Studies on the High Energy Photon Source," *Physics Procedia*, vol. 84, pp 40-46, 2016. <https://doi.org/10.1016/j.phpro.2016.11.008>
- [2] H. Liang *et al.*, "A High Heat Load Double Crystal Monochromator and Its Cryo Cooling System for HEPS," in *Proc. MEDSI'18*, Paris, France, Jun. 2018, pp. 430-434. doi:10.18429/JACoW-MEDSI2018-FROAMA02
- [3] Coolium Instruments, <http://www.ykky.com/>
- [4] MCC DAQ, <https://www.mccdaq.com/sound-vibration-daq>
- [5] A.I. Chumakov *et al.*, "Performance of a silicon monochromator under high heat load," *J. Synchrotron Radiat.*, vol. 21, pp. 315-324, 2014. doi: 10.1107/S1600577513033158
- [6] I. Sergueev *et al.*, "Angular vibrations of cryogenically cooled double-crystal monochromators," *J. Synchrotron Radiat.*, vol. 23, no. 5, pp. 1097-1103, 2016. <https://doi.org/10.1107/S1600577516011188>

DESIGN OF MAGNET GIRDER SYSTEM FOR SIAM PHOTON SOURCE II

O. Utke[†], S. Chaichuay, S. Klinkhieo, S. Pongampai, K. Sittisard, S. Srichan
Synchrotron Light Research Institute, Nakhon Ratchasima, Thailand

Abstract

The new Siam Photon Source II (SPS-II) storage ring is designed with a circumference of 327.502 m. It consists of 14 DTBA cells, where each cell requires six magnet girders. For the storage ring of SPS-II we developed a magnet girder system which uses wedgemounts for the precision alignment. The girder alignment is based on a 3-2-1 alignment method and requires three wedgemounts to control Z direction, two wedgemounts to control Y-direction and one wedgemount for the X-direction. The magnet alignment is based on mechanical tolerances. Therefore, the girders top plate is designed with precision surfaces with a flatness tolerance of 30 μm . Regarding low girder deformation (from magnet load) and gaining a high mechanical natural frequency to reduce the amplitude of vibrations, FEM simulations were carried out. In this paper simulation results are presented as well as the design of the girder, pedestal and its wedgemount based alignment system.

INTRODUCTION

The existing storage ring of Siam Photon Source (SPS) has 1.2 GeV beam energy and ~ 41 nm·rad beam emittance. The new Siam Photon Source II (SPS-II) has to provide better parameters to stay competitive for the user community in the South-East Asian region. Therefore, a new machine is being designed with a storage ring circumference of 327.502 meters, a beam energy of 3 GeV and a beam current of 300 mA. The beam emittance should be lower than 1.0 nm·rad. For the lattice design a Double Triple Bend Achromat (DTBA) lattice was chosen. The storage ring consists of 14 DTBA cells where each cell requires six girders to provide a stable platform for the magnets of the storage ring.

Since the DTBA cell consists of two mirrored halves only three different girders have to be designed (Fig. 1). The girders are 2240 mm, 2750 mm and 2870 mm long. All of them have a width of 750 mm. The beam height was set to 1.2 meters. For all three girders a 3-2-1 alignment system was developed where wedgemounts are being used.

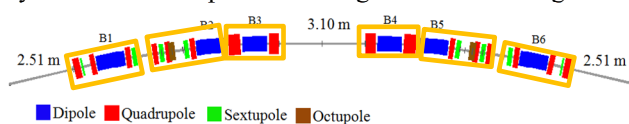


Figure 1: DTBA cell divided into girder sections.

The girder structure was developed focusing on low deformation and high vibration stability. Simulation software was used to design girders with less than 20 μm deformation under full magnet load. Also, modal simulation

software was used to optimize the girder structure in terms of pushing the natural frequency as high as possible.

GIRDER DESIGN

The designed girder structure is a box-type structure with a thick top plate and seven internal enforcement ribs (Fig. 2). The steel plates thicknesses are between 30 to 70 mm. There are three 80 mm thick support beams welded transversal to the top plate and they provide a basis for three vertical girder support points.

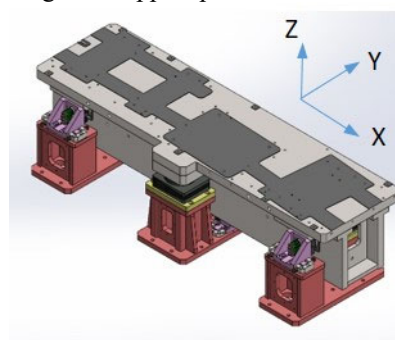


Figure 2: Girder system with three vertical support points.

The top plate of the girder requires high precision surfaces for the magnets. These surfaces as well as surfaces for fiducial marks will be machined with a flatness of 30 μm .

The pedestals are the connection between girder and the ground/concrete floor. The pedestals carry the weight of the girder and magnets. They transfer vibration into the girder which is caused by the ground itself (low frequencies) or from machines such as water-/vacuum pumps, air conditions, etc. installed nearby. Therefore, it is planned to install a damping layer (e.g. epoxy concrete) between concrete floor and pedestal base plate to improve the vibration stability.

The pedestals carry not only the weight of the girder and magnets but also they accommodate the adjustment components for horizontal girder alignment. The material for the pedestals is the same as for the girder structure which is a structural steel S355JR (or A572 Grade 50). This steel shows a good strength, durability and weld ability. The pedestals as well as the girder structure are put together by full penetration welding (wherever its possible). The pedestal deformation was decreased by increasing the steel plate thickness at high load areas. Also, an exchangeable “height compensation plate” was added between pedestal and each vertical wedgemount in case of large floor settlement.

[†]utke@slri.or.th

ADJUSTMENT SYSTEM

For the adjustment system six wedgemounts manufactured by AirLoc AG will be used (Fig. 3). It is planned to motorize the Y- and Z-direction for girder alignment in the future. For the Z-direction wedgemount model 414-KSKC was chosen since it was already successfully installed and used (with motorization) at ESRF [1]. For the Y-direction wedgemount 2130-KSKCV with modifications to allow motorization will be used. The X-direction will be adjusted manually with wedgemount model 2012-KSKCV. The horizontal (X and Y) fine adjustment range is +/- 6 mm while the vertical range is +/- 9 mm.

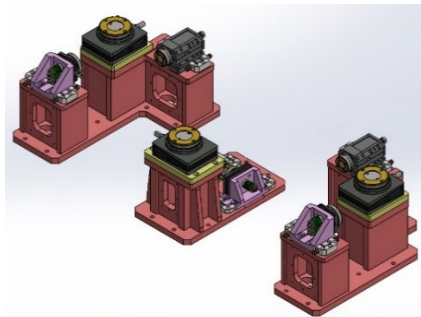


Figure 3: Wedgemounts for girder alignment on pedestals.

All adjustment components are equipped with oil-free sliding washers which contact the girder. The vertical Z-adjustment is realized by three large wedgemounts (414-KSKC) because having three support points is the easiest way to level a girder and no over-determination occurs. The center of mass of girder structure including magnet load stays within the triangle of the three support points.

All wedgemounts are equipped with spherical seat which follows the movement directions of the girder during the alignment process (Fig. 4).

On top of the spherical seat is a plate that houses an oil-free washer. Two long studs with coil springs at their end induce a preload between plate and seat. The coil springs are pushed onto a pair of spherical and conical seat as well which should allow the springs to follow the same movement as the girder respectively the oil-free washer.

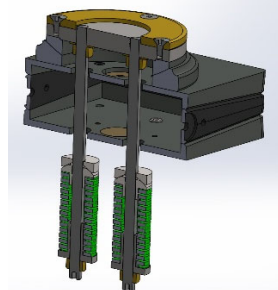


Figure 4: Section view of Z-align wedgemount.

For the horizontal adjustment the wedgemount had to be rotated by 90° so that the wedgemount position is vertical which it is not designed for. The wedgemount had to be modified to allow this installation position (Fig. 5). Two sets of coil springs with spherical/conical seat induce a pretension between the plate that accommodates the oil-

free sliding washer and the wedgemount (same method as described before).

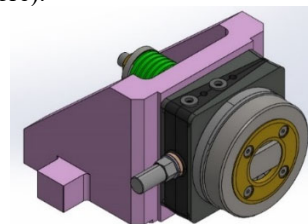


Figure 5: Vertically installed wedgemount for horizontal girder alignment.

Since a wedgemount can push the girder only in one direction a mechanism had to be designed which is installed opposing to each wedgemount and enables the girder to be moved back. In case of the Y-direction a push back spring assembly and for the X-direction a push-push screw is being used.

In Fig. 6 the push-back spring assembly is shown. Inside the push back spring assembly are two strong coil springs which have a maximal load of 18.4 kN each, which means a maximum push-back force of 3.75 t can be generated. The maximum deflection of the coil springs is 13 mm. The springs are pushing against a cylinder which is supported by an oil-free bushing. Inside the cylinder is a set of radial spherical and thrust spherical plain bearings. The bearings allow a shaft with attached oil-free washer to swivel and thereby follow the movement of the girder. A large screw at the end cover plate of the housing is used for adjusting the spring load respectively the deflection.

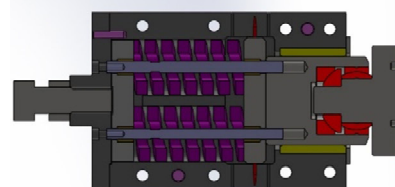


Figure 6: Push-back spring assembly.

The adjustment components for X-direction were placed on the base plate of the center pedestal and they contact the girder in its center (Fig. 7).

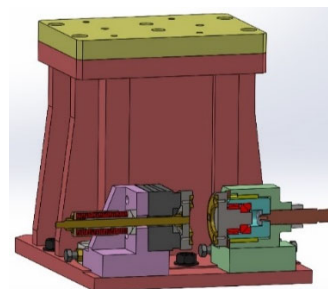


Figure 7: Section view of center pedestal and X-adjustment components.

All components for the horizontal (X and Y) adjustment can be pre-adjusted by push-push screws with a range of

+/- 12.5 mm. For the girder fine alignment only the wedgemounts will be used. The sensitivity of the fine alignment is specified by the leveling distance per turn of the wedgemounts, e.g. for 2130-KSKCV (Y-direction) 0.3 mm distance is specified. When it is assumed that by manual adjustment with a key wrench a rotation of the leveling screw of 5° is easily possible, then the alignment precision can be given with approximately 4 µm.

STRUCTURAL FEM ANALYSIS

The simulation software ANSYS was used to optimize the girder geometry regarding an as low as possible girder deformation and a high first natural frequency. A simplified CAD model of girder with magnets was used for the simulations. The design goal was a total deformation of less than 20 µm and a frequency for the 1st mode of higher than 35Hz. The girder design was step by step improved by changing geometry parameters such as varying the thickness of all used steel plates as well as the length of the girder flanks. Also the width of the girder box and the number of internal ribs was varied. The arrangement and location of the three support points was also essential for the deformation and vibration behaviour. So, the location of all three support points was varied until a satisfying solution was found. Finally, three girder models were prepared each carrying a magnet load according to the half-DTBA cell design. All three girders (all with different length and load) were investigated separately to analyse the effect of the magnet load on each girder.

The results of the analysis (Table 1 and Fig. 8) were focused on “total deformation” and all “directional deformations” in X, Y and Z. The reaction forces at the three large wedgemounts and the spherical bearing forces were taken into account. These forces indicate the weight distribution on each girder.

Table 1: Girder Deformation Results

Deformation	Girder 1 (L2.75m)	Girder 2 (L2.87m)	Girder 3 (L2.24m)
at magnet top [mm]	0.013	0.017	0.014
at girder top plate [mm]	0.010	0.012	0.009

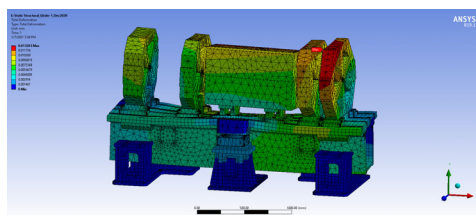


Figure 8: Girder 1 deformation simulation.

The results of the structural analysis were used further to perform the modal analysis. Environment vibrations for the existing machine SPS were measured between 20 to 30 Hz. We assume at this point the vibration level will be comparable for SPS-II as well which leads us to a first

natural frequency that should be above the measured level. The simulation results for the modal analysis for all three girders are shown below in Table 2 and Fig. 9.

Table 2: Modal Analysis Results

Mode	Girder 1 Freq. [Hz]	Girder 2 Freq. [Hz]	Girder 3 Freq. [Hz]
1	72.7	54.9	69.4
2	86.4	63.8	83.6
3	94.8	67.3	100.4
4	107.7	70.6	116.9
5	110.4	72.3	136.7
6	112.7	83.4	146.6

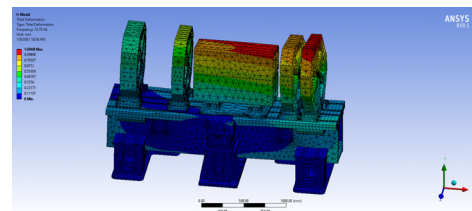


Figure 9: Girder 1, 1st mode modal analysis.

The frequencies for all three girders are above the design frequency of 35Hz. The high frequencies of more than 70 Hz can be explained by the strong structure of the girder but especially it is due to the short girder length of less than 3 meters. The frequencies for girder 2 (1st mode: 54 Hz) are lower due to a thin and tall structure of an octupole magnet.

CONCLUSION

A magnet girder system for the new SPS-II synchrotron with DTBA cell structure was developed. Three girders of different lengths were designed which share the same type of pedestals and adjustment components. It is explained how all components are designed and how the alignment system using wedgemount works. FEM simulation was used to investigate the deformation and vibration behavior of the girder system under full magnet load. The results of the simulations are presented.

ACKNOWLEDGEMENTS

The author would like to thank Prof. J. R. Chen (NSRRC, Taiwan) and F. Cianciosi (ESRF, France) for their useful suggestions and good collaboration. Furthermore, the author would like to thank the SLRI 3GeV team for their support and help with the girder project.

REFERENCES

- [1] F. Cianciosi *et al.*, “The Girders System for the New ESRF Storage Ring”, in *Proc. 9th Mechanical Engineering Design of Synchrotron Radiation Equipment and Instrumentation Int. Conf. (MEDSI'16)*, Barcelona, Spain, Sep. 2016, pp. 147-151. doi:10.18429/JACoW-MEDSI2016-TUCA06

THE DESIGN AND PROTOTYPE TEST FOR THE TUNNEL FOUNDATION OF HIGH ENERGY PHOTON SOURCE

F. Yan¹, G. Xu^{1†}, G.P. Lin¹, N.C. Zhou¹, X.P. Jing¹, J. Qiu¹
Y.L. Xing², Z.G. Xu², A.Z. Lu², Y.S. Zhang²

¹Key Laboratory of Particle Acceleration Physics and Technology, Institute of High Energy Physics (IHEP), Chinese Academy of Sciences 100049, Beijing, China

²China Electronic Engineering Design Institute (CEEDI), Beijing 100142, China

Abstract

High Energy Photon Source (HEPS) is being built in China with challenging beam stability requirements. To fulfil the 25 nm ground motion restriction on the storage ring tunnel slab, two prototype slabs with different design schemes were constructed on the HEPS site. The first scheme adopted a 1 m reinforced concrete with replacement layer of a 1 m sand & stone underneath. The second scheme employed an extra 5 m grouting layer below the previously mentioned two layers. A series of tests had been carried out. The prototype slab with grouting layer is testified to have comparable vibration level with the bare ground, which is under 25 nm without traffic inside the HEPS campus, while the vibration level is amplified a lot on the other prototype slab. However, it is hard to make the grouting layer homogeneously under the kilometre-scale tunnel and besides the cost is unacceptable for 5 m grouting with such a large scale. The finalized design is fixed to be a 1 m reinforced concrete slab and 3 m replacement layer underneath using plain concrete. In this paper, the details of the prototype slab test results will be presented.

INTRODUCTION

Currently, the low emittance storage ring has considered being future development direction of the photo sources. However, with the decreasing of the designed emittance of the ring, the problems caused by the ambient ground motion have been increasingly highlighted. High Energy Photon Source (HEPS) is a 6 GeV, 1.3 km, ultralow-emittance storage ring light source to be built in Beijing, China [1]. The designed natural emittance is about 35 pm [2]. To ensure the stability of the beam on experimental station, the RMS displacement integration of vibrations on the slab has to be kept smaller than 25 nm over frequency range of 1 Hz up to 100 Hz [3]. In order to fulfil this requirement, three more specifications are set up according to the ground motion level of HEPS site:

- 1) Ambient motions on the slab caused by internal and external vibration sources have to be smaller than 1 nm in all three directions;
- 2) No vibration amplification by the slab of the storage ring (RMS integral over frequency of 1-100Hz);
- 3) No vibration amplification by the pedestal-girder-magnet assembling.

The first one will be realized by setting regulation plan to the transportation inside the HEPS campus and taking damping measures for the vibration utilities. And the Egan

frequency of the pedestal-girder-magnet assembling is specified to be not smaller than 54 Hz for achieving amplification factor closing to one [3]. A well designed and made slab has no vibration magnification to the ground motions [4]. To construct such a slab and finalize the slab design, two prototype slabs with different design schemes were constructed on the HEPS site. The test results will be introduced in this paper.

PROTOTYPE SLABS

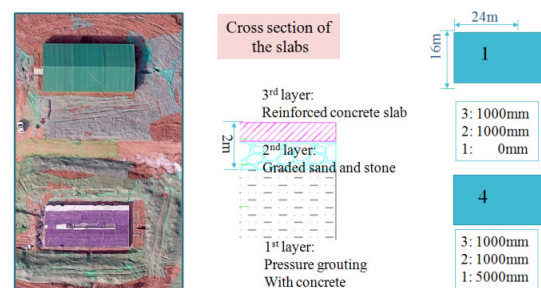


Figure 1: The schematic design of the two prototype slabs.



Figure 2: The prototype #4 slab: after grouting.

As shown in Fig. 1, the dimension of the prototype slab is 16×24 m. To construct slab #1, the soil from 2 m underground to the top were taken out and backfilled with one meter of "graded sand and stone" and one meter of "reinforced concrete slab". For the 2th slab (slab #4), there is an extra grouting layer from -2 m (underground) to -7m.

For constructing the grouting layer, as shown in Fig. 2, steel pipes (about 8 m long) were inserted in the ground using boring machine. The pipes are placed at the intervals of 1 m (0.8 m for the outermost two rows). There are some small holes regularly distributed on the pipe from depth of -2 m to -7 m. Mixture of cement and water were grouted through the pipe for reinforcement of the underground layer (-2 m to -7 m). The maintenance time for the grouting layer is ~28 days, all the other steps are the same with slab #1 hereafter.

† email address: xug@ihep.ac.cn

Vibration Response on Prototype Slab #1



Figure 3: Graded sand and stone layer of slab #1.

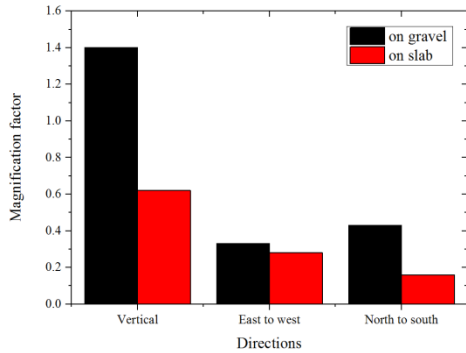


Figure 4: Vibration magnification factor of each layer for #1 slab.

During construction of slab #1, to evaluate the damping effect of "graded sand and stone" layer (the 2nd layer) and the "reinforced concrete slab" (the 3rd layer), an excavator was used to generate noises by hitting the ground as shown in Fig. 3. Vibration data was taken before and after pavement of each layer. The ratio between the noise level on each layer to the noise level 2 m underground gives the magnification factor. As shown in Fig. 4, the magnification factor of the 2nd layer (black bar) is bigger than one for vertical plane and smaller than one for the other two planes. While for the 3rd layer, the magnification factor (red bar) is smaller than one for all three planes. We can conclude that the performance of the 3rd layer is good, but the 2nd layer is not as good as expected. Figure 3 shows what the 2nd layer looks like. We suspect that the bad performance of the 2nd layer might be caused by not even enough stones, and not compact enough pavement.

Vibration Response on Prototype Slab #4

Slab #4 has an extra grouting layer of 5 m. After finished grouting and taking out soils with thickness of 2 m, vibration data were taken in the #4 pit (-2 m: on the grouting layer) and compared with the noise level on slab #1. A vibration exciter placed in middle of the two prototype slab positions, was used for generating 1 Hz~100 Hz vibrations. Besides the sensors on slab #1 and on grouting layer of #4 pit, an extra one with the same distance to the vibration exciter is placed on the ground as a reference. As shown in Figs. 5 and 6, the noise level on grouting layer (before pavement of the other two layers on top) is already smaller than slab #1 (both at 3 m away from the prototype margin).

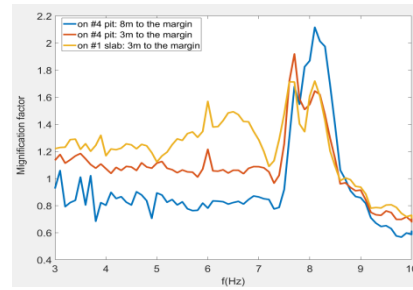


Figure 5: Magnification factor for slab #1 and 4# pit with grouting layer for frequency range of 1-10Hz.

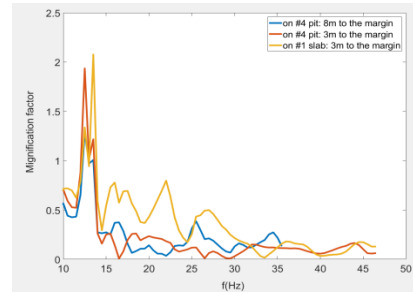


Figure 6: Magnification factor for slab #1 and 4# pit with grouting layer for frequency range of 10-50Hz.

And the further the sensor from the vibration source, the smaller the noise level will be. For the noise level 8 meters away from the margin of grouting layer, the magnification factor is smaller than one for 1 Hz~50 Hz, except 7-9 Hz and 10-15 Hz. The ground is sensitive to the vibrations of these frequencies, and grouting could not solve this problem either.

After finished the pavement of the other two layers. Long time vibration monitoring on the two prototype slabs were carried out for about one week.

Long-Time Motion Monitoring on Prototype Slabs & on Ground

As shown in Fig. 7, vibrations on four positions were monitored, two seismographs on two prototype slabs and one sensor on ground close to slab #4. The vibration source is the traffic noises on a municipal road (labeled in Fig. 7 as blue arrows, closed now) of HEPS site, which has approximately same distance to the above mentioned three sensors. As the prototypes are located at the position where the outdoor cryogenic storage tank farm is, which is about 100 m away from the storage ring. One extra sensor is placed on the ground of the storage ring close by. As shown in Fig. 8, the measurement results of two sensors on ground show clearly day and night shift. Horizontal vibrations are bigger than vertical directions. During night, the motion on ground is about 4 nm and 10 nm vertical and horizontal respectively. During day time, it is about 10 and 20 nm. Most of the time, the green field vibration is smaller than 25 nm, the sparks might be caused by cars with higher speed or trucks with heavier load, which is under control. For the vibrations on the slabs, as shown in Fig. 9, during the weekend, when there is not so much traffic, the vibration level is almost the same on the two prototype slabs & the ground. During the weekdays, when the traffic is

heavier, the vibration is amplified a lot on slab #1, while the prototype slab #4 with extra 5 m grouting layer has comparable vibration level with green field. Although the

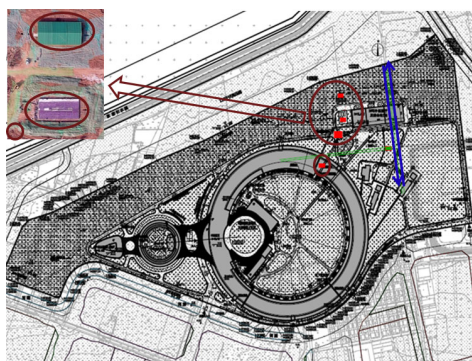


Figure 7: Long-time motion monitoring on prototype slabs & on ground: the four red squares are four monitor positions, the street where the blue arrows are is a municipal road inside the HEPS campus (it is closed now).

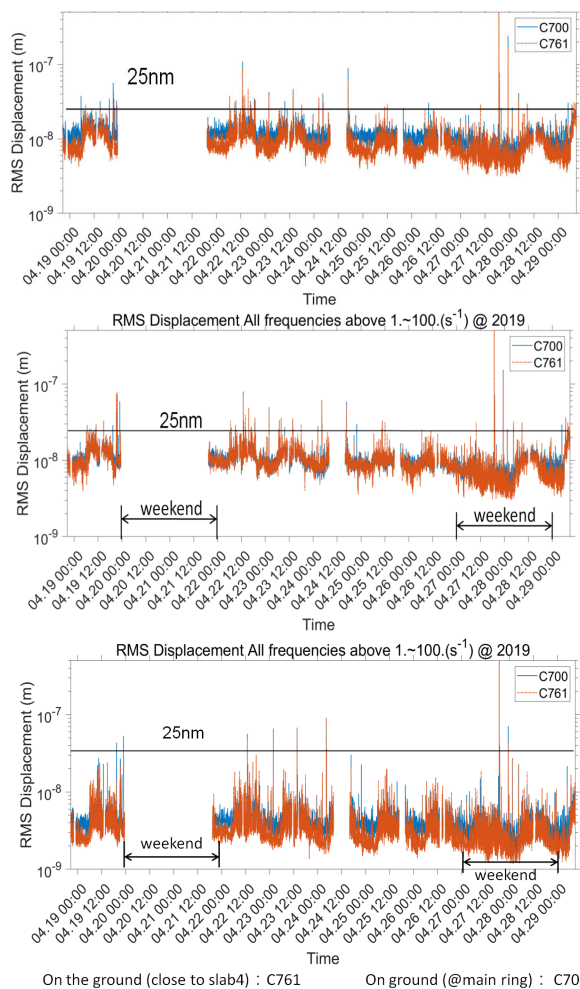


Figure 8: The red curve (C761) is the vibration RMS displacement on the ground nearby slab #4, north & south (above figure), east & west (middle figure) and vertical direction (the figure below); the blue curve (C700) is RMS displacement on ground of storage ring for the three directions respectively.

performance of the grouting scheme can fulfill the requirement pretty well, it is not adopted for the foundation design finally. As it is hard to make the grouting layer homogeneously under the kilometer-scale tunnel and besides the cost is unacceptable for 5 m grouting layer with such a large scale too. The finalized foundation design for the storage ring and experimental hall is fixed to be a 1 m reinforced concrete slab & 3 m replacement layer underneath using plain concrete which is verified by simulation to be having equivalent effect as the grouting scheme.

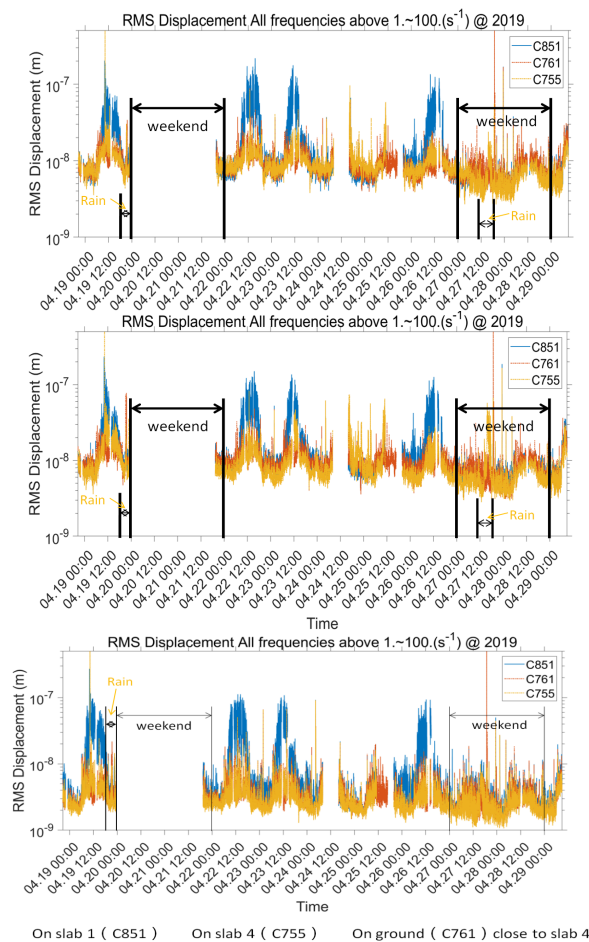


Figure 9: The red curve (C761) is vibration RMS displacement on ground close to slab #4, the yellow curve (C755) is vibration RMS displacement on slab #4, and the blue curve is the measurement data on slab #1.

CONCLUSION

In order to define the tunnel foundation of HEPS. Two prototypes of different design were constructed. The one with extra grouting layer has comparable noise with bare ground. Considering the cost and construction difficulty, the finalized design is fixed to be a 1 m reinforced concrete slab & 3 m replacement layer underneath using plain concrete which is verified by finite element analysis to be having equivalent effect as the grouting scheme.

REFERENCES

- [1] Y. Jiao *et al.*, “Progress of Lattice Design and Physics Studies on the High Energy Photon Source”, in *Proc. IPAC’19*, Melbourne, Australia, May 2019, pp. 1510-1513. doi:10.18429/JACoW-IPAC2019-TUPGW046
- [2] Y. Jiao, IAC (International Advisory Committee) 2019 report, Dec. 16th, 2019, Beijing, China
- [3] Fang Yan, IAC (International Advisory Committee) 2019 report, Dec. 17th, 2019, Beijing, China
- [4] Lin Zhang, GM2017 report, Dec. 10th, 2017, Beijing, China.

RESEARCH OF BELLOW SHIELD STRUCTURE APPLIED TO BPM

X.J. Nie*, L. Kang, R. Liu, S.K. Tian

Institute of High Energy Physics (IHEP) Accelerator Center, Dongguan, China

J.X. Chen, H.Y. He, L. Liu, C.J. Ning, A.X. Wang,

G.Y. Wang, J.B. Yu, Y.J. Yu, J.S. Zhang, D.H. Zhu

Institute of High Energy Physics (IHEP CSNS) China Spallation Neutron Source, Dongguan, China

Abstract

The design of shield structure for bellow is an important content for the research of beam position monitor (BPM). The bellow shield structure consists of contact fingers and spring fingers. Several alternative schemes for bellow shield were achieved based on BPM detailed structure. The optimal scheme was achieved by the impedance simulation analysis with CST. The dimension of the contact finger was decided based on the length of BPM with the stress condition. The C-type string was manufactured, and the spring force was measured as well.

INSTRUCTIONS

Beam position monitor (BPM) is an important diagnostic equipment of beam position. It is widely applied on accelerator. Normally, four electrodes are applied to get the beam signal and the beam position is calculated by the signal contrast. To decrease the effect of near equipment to BPM, the bellows are applied to the two ends of BPM [1, 2]. But they will lead to a discontinuous surface inside the vacuum chamber and thus the impedance will increase accordingly. So, it is necessary to design the shield structure to reduce the impedance of the bellows.

DESIGN OF BELLOW SHIELD STRUCTURE FOR BPM

The shielding principle is stated as the following. Some mental wires or strips are used to contact the two ends of the bellows to form a smooth transition. This can eliminate the cavity structure inside the vacuum chamber, decrease the impedance and the HOM leakage [3, 4].

Design of Shield Plan

According to some related references and the overall structure of BPM, several alternative shielding structures were achieved as Fig. 1. Model 1 was the C type shielding structure in which the C type string was used to press the contact fingers. Model 2 was the double fingers in which the contact fingers touch the vacuum chamber and spring fingers pressed on them. Model 3 had a simple structure which just had contact fingers to touch a cone-shaped sleeve. An insert block was used in model 4 to touch the spring finger, which could get a small step with big gaps. Model 5 had a net type shield structure to touch the vacuum chamber.

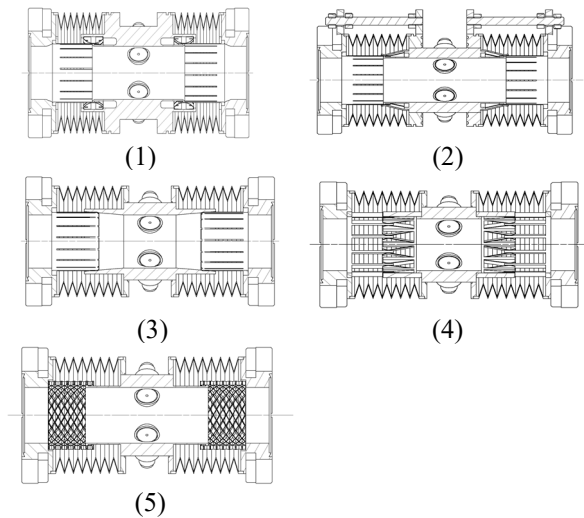


Figure 1: Shield plans of BPM bellow.

To understand the impedance characteristic for above shield structures, the simulation of impedance was done for them. The result showed as Figs. 2 and 3.

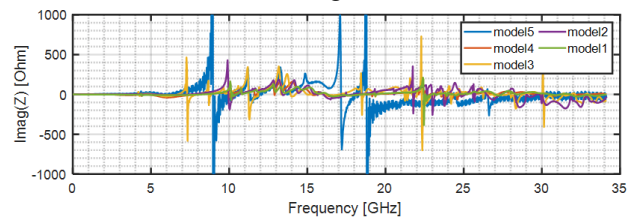


Figure 2: Imaginary part of impedance for the shield structures.

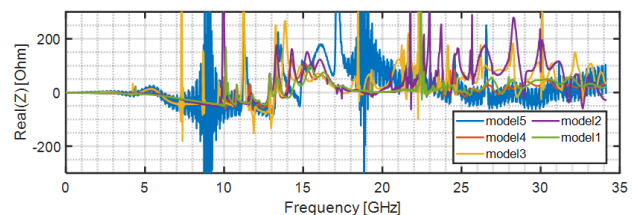


Figure 3: Real part of impedance for the shield structures.

It seemed that model 1 had the best impedance characteristic. So, the further study was focused on it. The main structure of the final shield plan showed as Fig. 4.

* niexj@ihep.ac.cn

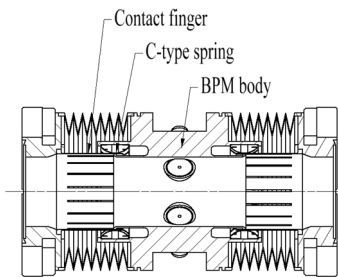


Figure 4: Final BPM bellow shield structure.

Design of Contact Fingers

Contact finger touches vacuum chamber directly. It's easy to make offset with the bellow when making vacuum connection. Simulative computation of stress was done for different length contact finger under 1mm offset. The result showed as Fig. 5, which illustrated that the longer contact finger would get better stress. Based on some related reference, beryllium Copper C17200 was selected to make contact finger, which had about 1000MPa yield limit [5]. Thus, the minimum length was set as 8mm according to the chart and BPM structure.

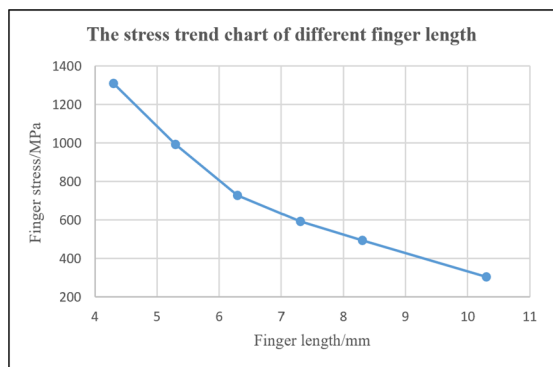


Figure 5: Stress trend chart of different finger length.

Meanwhile, the stress with different contact finger width was simulated. The result showed as Fig. 6. According to the chart, we can conclude that the narrower width of the contact finger can achieve better stress. But there are not significant difference among them. So, the final width of contact finger was set as 4mm.

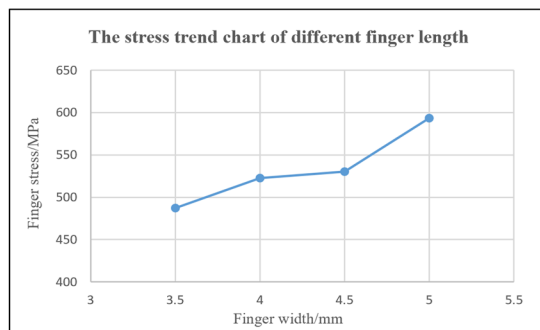


Figure 6: Stress trend chart of different finger width.

Analogized to shanghai synchrotron radiation facility (SSRF), the thickness of the contact finger was set as 0.2mm according to some references. And the gap between two fingers was set as 0.5mm [3].

Design and Trial Manufacture for C-Type Spring

C-type spring was a critical component for the shield of BPM bellow, which presses on the contact fingers to keep them touching with the vacuum chamber. According to some references, when the elastic force reaches 125g, the contact fingers can touch the vacuum chamber well with flexible adjustment. The C-type model was designed based on BPM contact finger. Then the trial-manufacture and the measurement of elastic force were made to verify the technology and elastic force. The result showed that about 0.19mm deformation can obtain about 125g elastic force. Figure 7 showed the model and result.

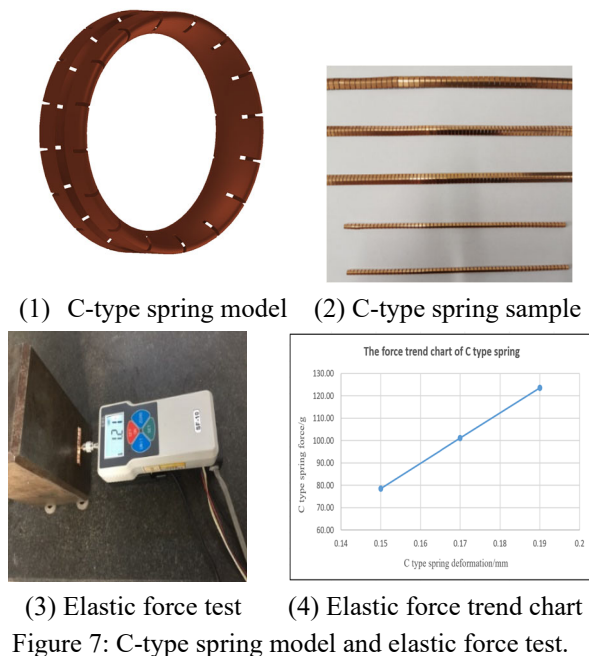


Figure 7: C-type spring model and elastic force test.

SUMMARY

The shield plan of BPM bellow was decided by BPM structure and impedance characteristic. The structural dimensions of contact fingers such as the length and width were achieved by the stress trend chart. Finally, the C-type spring was manufactured by trial and the elastic force was measured accordingly.

ACKNOWLEDGEMENTS

The authors would like to express their appreciation to all the colleagues who have contributed to this project.

REFERENCES

[1] J. He, H. Ma, Z. Wang *et al.*, "Simulation of BEPCII beam position monitor with CST", *Nuclear Techniques*, vol. 40, no. 10, pp. 100401-1~100401-8, 2017. <http://dx.doi.org/10.11889/j.0253-3219.2017.hjs.40.100401>

- [2] Zhao Guobi, “Beam Signal Detection & Transmission Technology Research for Button-type pickup”, Ph.D. thesis, Beijing: University of Chinese Academy of Sciences, May 2014, pp. 1-16.
- [3] J. Dikui, J. Xiaoli, “Research of bellows with RF shield for SSRF storage ring”, *Nuclear Techniques*, vol. 28, no. 2, pp. 93-97, 2005.
- [4] Z. Lijuan, “Heating test of RF-shield bellows for BEPC II storage ring”, *Vacuum*, vol. 42, no.2, pp. 49-52, 2005.
- [5] [https://baike.baidu.com/item/beryllium copper](https://baike.baidu.com/item/beryllium%20copper)

PROCESSING OF HEPS LOW ENERGY TRANSPORT LINE COLLIMATOR*

J. B. Yu^{1†}, J. X. Chen¹, H.Y. He¹, L. Kang¹, L. Liu¹, R. H. Liu¹, X. J. Nie¹, C. J. Ning¹, A. X. Wang¹,
G. Y. Wang¹, Y. J. Yu¹, J. S. Zhang¹, D. H. Zhu¹

Institute of High Energy Physics, Chinese Academy of Sciences, Beijing, China
¹also at Spallation Neutron Source Science Center, Dongguan, China

Abstract

In order to protect the equipment such as BPM at low energy transport line (LB), a momentum collimator is designed with one movable absorber. This paper will show the mechanical design and manufacturing of the collimator.

DESIGN OF THE LB MOMENTUM COLLIMATOR

HEPS is an ultra-low emittance synchrotron light source will be constructed in Beijing. Its injector consists of a 500MeV linac with a thermionic gun, a 500MeV low energy transport line, a full energy booster which ramping the beam energy from 500MeV to 6 GeV and two high energy transport lines [1]. LB is a transport line connecting the linac and the booster [2].

With the distance of 700mm away from the LBQ4, a momentum collimator with one movable absorber is designed to protect the downstream equipment, the layout is shown in Fig. 1.

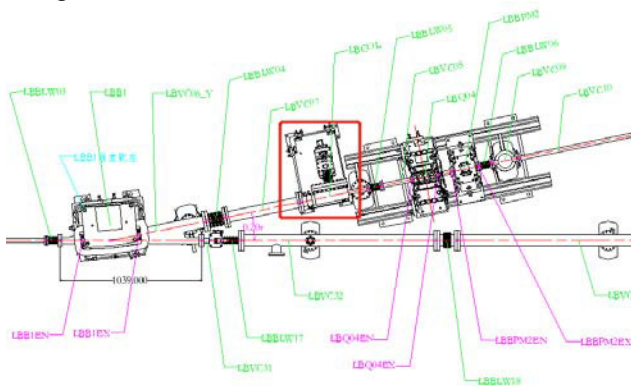


Figure 1: Position of the collimator at the LB layout.

According to the physical requirements, the absorber should be designed with the material of copper, and the profile is shown in Fig. 2, the maximum energy deposited on it is 20J. In order to make sure the thermal structure of the absorber, thermal analysis with different power deposition have been done, and the analysis results are shown in Fig. 3, the maximum temperature on the absorber is 134.5°C with the load of 20W, and the maximum temperature is 30.5°C when the load is 1W. Figure 4 shows the stress distribution of the absorber.

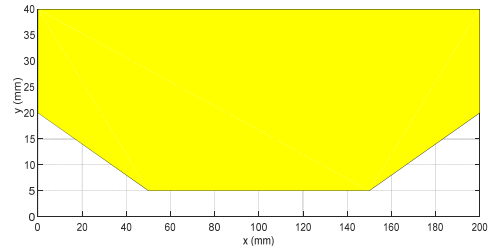
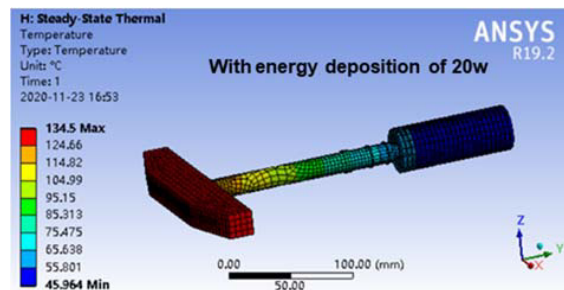
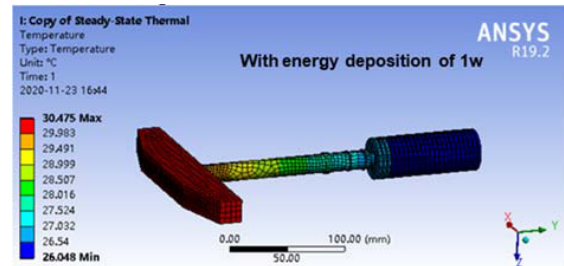


Figure 2: Profile of the absorber.



(a) Temperature distribution with 20W load



(b) Temperature distribution with 1W load

Figure 3: Temperature distribution of absorber component with different energy deposition.

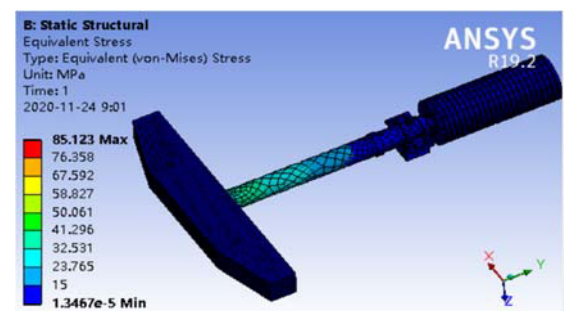


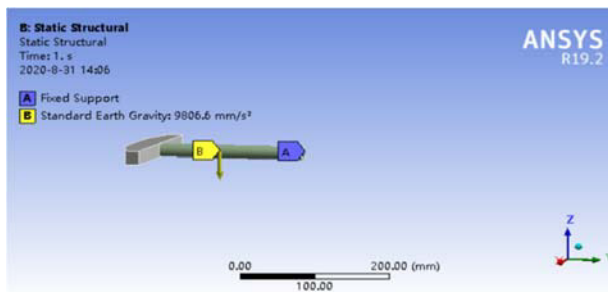
Figure 4: Stress distribution of absorber component with load of 20W.

The support structure of the absorber is designed far from the absorber and it is similar to cantilever structure, in order to ensure the straightness of the trajectory while

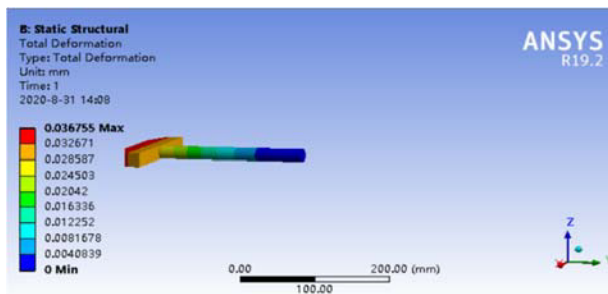
*Work supported by Natural Science Foundation of Guangdong Province (No. 2018A030313959)
†email address yuib@ihep.ac.cn.

Content from this work may be used under the terms of the CC BY 3.0 licence (© 2021). Any distribution of this work must maintain attribution to the author(s), title of the work, publisher, and DOI

moving, structure analysis of the absorber has been done, the boundary conditions and results are shown in Fig. 5.



(a) Boundary conditions of absorber



(b) Stress distribution of absorber

Figure 5: Boundary conditions and stress distribution of the absorber.

The vacuum chamber should be designed with the size of 70mmx30mm at the upstream of the absorber, and the size of $\Phi 30$ mm at the downstream. Structure analysis of the vacuum chamber has been done. Figure 6 shows the stress distribution of the vacuum chamber.

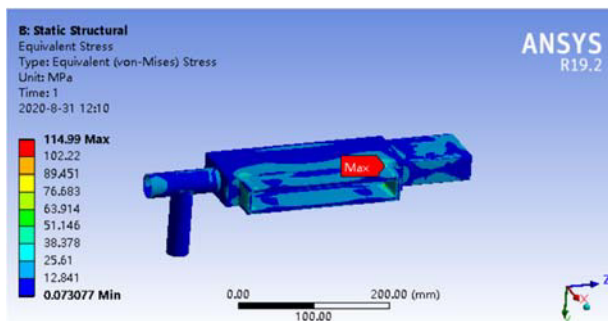


Figure 6: Stress distribution of vacuum chamber.

Based on the design and analysis of absorber and vacuum chamber, the structure of the collimator is designed as shown in Fig. 7.

MANUFACTURE STATUS OF THE LB COLLIMATOR

Most parts of the collimator have been manufactured, which include vacuum chamber, support, and the absorber component. Straightness of the absorber while moving has been measured, it's within 0.1mm, and the flatness of the absorber has been controlled within 0.05mm. Figure 8 shows some pictures of the collimator while processing.

Beamlines and front ends

Front Ends



Figure 7: Structure of LB collimator.



Figure 8: Processing pictures of the collimator.

CONCLUSION

After the collimator reaching the ultimate vacuum, the collimator will complete acceptance, and it will be installed on LB next year.

REFERENCES

- [1] Y. M. Peng *et al.*, "Status of HEPS Booster Lattice Design and Physics Studies", in *Proc. 9th Int. Particle Accelerator Conf. (IPAC'18)*, Vancouver, Canada, Apr.-May 2018, pp. 1407-1410. doi:10.18429/JACoW-IPAC2018-TUPMF062
- [2] Y. M. Peng, C. Meng, and H. S. Xu, "Physical Design of HEPS Low Energy Transport Line", in *Proc. 10th Int. Particle Accelerator Conf. (IPAC'19)*, Melbourne, Australia, May 2019, pp. 2349-2352. doi:10.18429/JACoW-IPAC2019-WEPMP019

TUPA15

149

DESIGN AND DEVELOPMENT OF THE ADVANCED DIFFRACTION AND SCATTERING BEAMLINES AT THE AUSTRALIAN SYNCHROTRON

B.J. McMahon[†], J. Auckett, M. Fenwick, R. Hogan, J.A Kimpton, R. Lippi, S. Porsa
 ANSTO, Australian Synchrotron, Melbourne, Australia

Abstract

The Advanced Diffraction and Scattering (ADS) beamlines will provide high energy synchrotron X-rays for a variety of different diffraction- and imaging-based experiments at the Australian Synchrotron. A 4.5 T superconducting multipole wiggler will be used to provide X-rays in the range 50-150 keV, to two experimental endstations. The high power density of the beam requires significant thermal management through the whole beamline from the front end to the endstation. Flexible endstation designs have been developed to facilitate X-ray diffraction experiments on a range of sample types and environments (up to 300 kg). Detector positioning systems have been developed from industrial CNC robots to provide high speed, precise motion over large spatial envelopes.

SOURCE & BEAM CONDITIONING

The SCMPW source for the beamline produces a beam with a central power density of 33 kW/mrad², a total power of 45 kW and divergence of 7×1 mrad². The final beam size required in the beamline is 0.3×0.3 mrad². The heat load from reducing the beam size this amount was difficult to achieve in the storage ring for the compact front ends at the Australia Synchrotron.

Due to space constraints in the storage ring the beam conditioning was split between the front end and the beamline. Inside the front end a crotch absorber, mask and a diamond filter reduce the beam to 0.85×0.75 mrad² and absorb 40 kW, as shown Fig. 1. Inside the beamline a secondary mask trims the beam to the final size of 0.3×0.3 mrad² and a SiC filter absorbs another 0.8 kW of low energy photons. A summary of the beam conditioning is shown Table 1.

The front end mask was designed to absorb only the horizontal fan, to decrease the thermal strain and thereby increase the power absorption capability of the front end mask. A design consisting of 2×800 mm flat cooled plates eliminates the need for an aperture throat and reduces the peak strain on the absorber. The mask absorbs a total power of 35 kW with a central power density up to 460 W/mm². Figure 2 shows the layout of the mask and the thermal stress under a missteer event.



Figure 1: Front end and source in ADS beamlines.

[†] mcmahonb@ansto.gov.au

Table 1: Beam Conditioning in ADS Beamlines

Element	Divergence		Power	
	Vert. (mrad)	Horiz. (mrad)	Absorbed (kW)	Transmitted (kW)
Source	1	7	–	45
CA	0.85	6	2.5	42.5
FE Mask	0.85	0.75	35.4	7.1
Diamond Filter (1.2mm)	0.85	0.75	2.0	5.1
PDS Mask	0.3	0.3	3.5	1.6
SiC Filter (2mm)	0.3	0.3	0.8	0.8

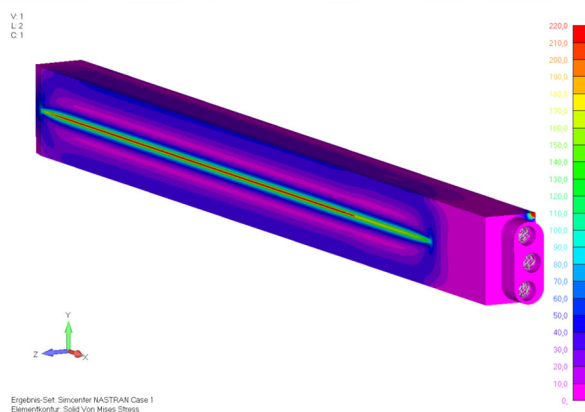


Figure 2: Front end mask (top showing assembly design, lower showing FEA of stress in beam missteer loading (22kW on one half of mask). Images courtesy of FMB-Berlin.

ADS-1 BEAMLINE

The primary beamline, ADS-1, will provide white, pink and monochromatic beam (50-150 keV) to a large end-station located outside the main synchrotron building.

For monochromatic beam modes a Transfocator is used to input a tunable collimating beam to a cryogenically-cooled double crystal Laue monochromator (DCLM),

The Transfocator has water cooled lenses with a copper mask and integrated aluminium filter. The Transfocator consists of Al and Be lenses arranged in pneumatically actuated cassettes. The cassettes shall have 1, 2, 4, 8, 16 & 32 Be lenses and 32 and 64 Al lenses. The lens material is polycrystalline Be or Al and each lens has a radius of curvature of 200 μm , a web thickness of <50 μm and an aperture size of 0.8 mm. With the expected lens layout the Transfocator can collimate photons up to 110 keV and produce low divergent beam up to 150 keV.

A cryogenically cooled DCLM (shown in-situ in Fig. 3) is utilised in the ADS-1 beamline to select energies. The DCLM shall be a bent vertical fixed exit double Si 111 crystal Laue system and cover the energy range 50 keV to 150 keV with an energy resolution within $1 \times 10^{-2} < \Delta E/E < 2 \times 10^{-4}$. Each crystal shall be capable of being spherically bent using a bender mechanism. The beam shall be incident on the concave side of the bent crystals and both the (111), (220) and (113) planes shall be accessible. The first and second crystals shall be asymmetrically cut at $\chi = -35^\circ \pm 0.02^\circ$ and the V_{perp} directions shall be (110) to ensure that the (113) planes can be accessed by a 29.2° pitch rotation of the crystals.

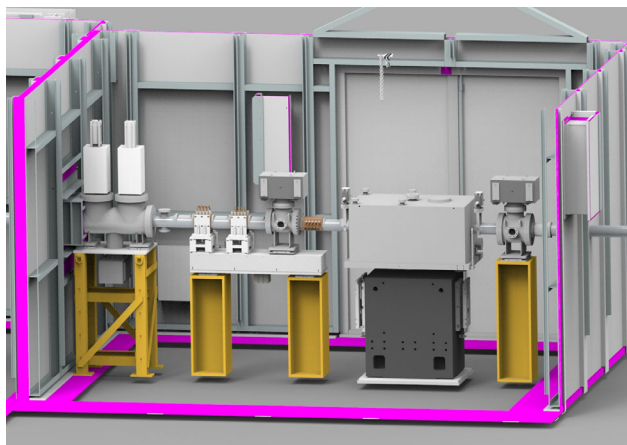


Figure 3: Second optics hutch showing DCLM, slits and shutters.

The endstation of ADS-1 is designed to be flexible and will enable; rapid powder diffraction, energy dispersive diffraction, white/pink beam Laue diffraction, high speed imaging and combined imaging and diffraction. The ADS-1 endstation will have the full experimental capabilities and flexibility, and accommodate both small and large samples up to 300 kg.

A large gantry robot (shown in Fig. 4) will position up to 4 detectors on 2 arms in a spatial envelope of $2.5 \times 0.3 \times 6 \text{ m}^3$ with 20 μm precision. The gantry robot has been adapted from a CNC machine application and allows for high speed operation (>1000 mm/s) with payload masses up to 250 kg. The detector housing in this design will incorporate radiation shielding to protect the detectors during operation and when not in use.

The detectors will be interchangeable and will allow for future expansion of detector types available for experiments. The initial detector types will be; hybrid pixel and amorphous silicon detectors for monochromatic diffraction; indirect scintillator-based CCD imaging detectors and novel, state-of-the art Energy Dispersive detectors. The high speed and dual arm positioning system allows for quick transitions between different detector types and sample to detector distances for multi modal experiments.

The sample goniometer has a modular configuration and will allow small and large samples and environments up to 300 kg, to be positioned in the beam. A tomography stage will be available to users for samples up to 50 kg. The travel range of the sample goniometer is shown in Table 2.

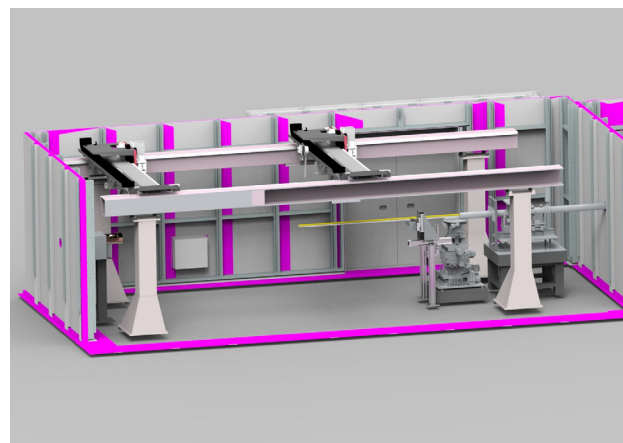


Figure 4: ADS-1 endstation.

Table 2: ADS-1 Goniometer Motion Envelope

Subassemblies	Axes	Range	Repeatability
Tomography	X	$\pm 25 \text{ mm}$	0.002mm
	Z	$\pm 25 \text{ mm}$	0.002mm
	RY	∞	10 μrad
Intermediate	Y_{fine}	20 mm	0.002 mm
	Y_{coarse}	100 mm	0.01 mm
	X	$\pm 50 \text{ mm}$	0.002mm
Permanent	Z	$\pm 50 \text{ mm}$	0.002mm
	RZ	$\pm 5^\circ$	20 μrad
	RX	$\pm 5^\circ$	20 μrad
	RY	0-360°	20 μrad
	X	100 mm	0.01mm
Y	30 mm	0.01mm	

ADS-2 BEAMLINE

The second ADS beamline, ADS-2, will take a 5° deflected beam from a cryogenically-cooled side-bounce Laue monochromator (SBM) (shown in Fig. 5). The deflected beam is focussed using a mirror and delivered to the endstation.

The monochromator houses 3 crystals operating in Laue geometry that vertically translate into the beam. The silicon crystals in the monochromator have a triangular form factor with an optical thickness of 3mm. The crystals select the energies 45.3, 74.0 and 86.8 keV with a bandwidth of 2.9×10^{-3} using reflection from the 111, 220 and 311 planes respectively. The heat load on the SBM crystals is the most significant driver of beam size and filtration due to their upstream location. A set of SiC filters is immediately upstream of the SBM with multiple filter thicknesses to manage power. A high efficiency cooling design enables the SBM crystals to absorb up to 300 W of power with a power density of 110 W/mm².

A vertical focussing mirror is used on ADS-2 to focus the beam and reduce the intensity of higher order harmonics. The multilayer mirror has 3 stripes of (Ni/B₄C, Au/B₄C & Pt/B₄C) suitable for the monochromated beam generated by the SBM (45.3 keV to 86.8 keV) with each stripe 10 mm wide. The substrate is 1100 × 50 × 40 mm with stripes that translate laterally into the beam.

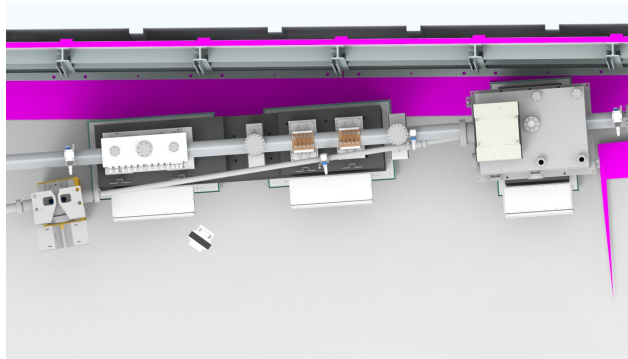


Figure 5: Branchline from SBM.

The monochromatic ADS-2 endstation utilises a modular sample goniometer and another high travel range detector positioning system to enable in-situ, high throughput powder & single crystal diffraction.

The sample goniometer has a modular construction with a permanent alignment base upon which different experiment specific goniometers may be mounted. The alignment base can translate vertically 20 mm with +/- 25 mm horizontal travel across the beam axis. 600 mm travel along the beam axis will allow access to the varying focal points from the upstream mirror. A capillary spinner and single-crystal kappa goniometer will be available for users and will mount to the alignment base.

A gantry style robot (shown in Fig. 6) will position 2 detectors in a 0.6 x 0.3 x 4 m³ spatial envelope with 20 μm precision. Incorporating a similar concept to the motion system in ADS-1 endstation, the gantry robot has been adapted from a CNC machine application and allows for high-speed operation (>1000 mm/s) with payload masses up to 250 kg

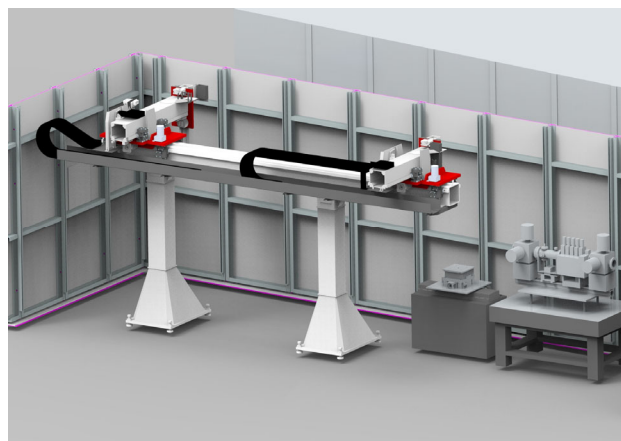


Figure 6: ADS-2 endstation.

CONCLUSION

The ADS beamlines are the fifth and sixth beamlines being built within the Australian Synchrotron/ANSTO BR-GHT program. The Australian Synchrotron is a 3 GeV machine designed to operate continuously 24 hours per day, 7 days per week, providing ≥ 5000 user-beam hours annually. The ADS beamlines project encompasses design, procurement, build/installation and commissioning phases. The beamline will commence user operations in July 2023.

The Advanced Diffraction and Scattering (ADS) beamlines will provide high energy X-rays to the Australian and New Zealand synchrotron User communities for dedicated diffraction and imaging experiments. A range of new and traditional white and monochromatic beam techniques will fulfil an important role for the materials, engineering, energy and Earth science communities particularly when coupled to a broad range of sample stages and environments. The resulting in-situ capability will be a powerful feature of the ADS beamlines.

INVESTIGATION OF THERMAL INSTABILITIES IN THE ALBA COOLING SYSTEM, BASED ON NUMERICAL SIMULATIONS AND EXPERIMENTAL MEASUREMENTS

F. Hernández[†], Universitat Politècnica de Catalunya, Barcelona, Spain
M. Quispe*, E. Ayas, J.J. Casas, C. Colldelram, M.Ll. Fuentes, J. Iglesias
ALBA – CELLS Synchrotron, Cerdanyola del Vallès, Spain

Abstract

This paper presents an investigation into the thermal instability problems that currently affect the ALBA Cooling System. During these periods of instabilities, which occur for a few hours every week of operation, there are deviations up to +1.5 °C, concerning the nominal temperature of 23 ± 0.2 °C in the four rings of ALBA: Service Area, Booster, Storage and Experimental Hall. This problem has a direct impact on the quality of the beam of the Accelerator. Previous studies have preliminarily concluded that the causes of this problem are due to (1) thermohydraulic anomalies in the operation of the external cogeneration plant, which supplies cold water to ALBA, and (2) cavitation problems in the pumping system (the water mass flow has been reduced to 67% of its nominal value to temporarily mitigate the cavitation). In order to confirm these hypotheses and propose solutions to the problem, an investigation has been developed making use of one-dimensional thermo-hydraulic simulations, performing Computational Fluid Dynamic (CFD) studies, statistical evaluations of data taken from our control system, and systematic flow measurements in critical areas, with ultrasonic flowmeters. As a result of this research, a set of solutions and recommendations are finally proposed to solve this problem.

BACKGROUND

ALBA is a third-generation synchrotron light source facility located in Cerdanyola del Vallès, Spain, with more than eleven years of operation and eight operating beamlines. Over the last years, the water-cooling system of ALBA has been under thermal instability problems, which affect the control of the inlet temperature in its four main rings: Service Area (SA), Booster (BO), Storage (SR) and Experimental Hall (EH).

These anomalies appear during changes in the operating modes of the external cogeneration plant, called ST4, which supplies cold water to ALBA. An increment of the ST4 water temperature rises the in-tank temperature of D02, which is a high-capacity tank of 40 m³ [1].

Otherwise, the volumetric flow circulating through the ALBA's circuit, where heat is exchanged with ST4, is reduced from the design value of 645 m³/h to 430 m³/h, to mitigate unexpected cavitation problems that affect the performance of the principal recirculation pump in ALBA, called P11. One possible cause of this cavitation

problem is an inappropriate sizing of the manifold located in the suction zone of the P11 pumps.

This is an utmost magnitude issue, insofar there is a direct linkage between the electron beam stability and the thermal stability of the water-cooling circuit. Moreover, this behaviour restricts ALBA's expansion capability in terms of machine current: whereas its design current is 400 mA, ALBA operates at 250 mA. Furthermore, this would affect the growth plan of ALBA II [2].

ALBA'S THERMOHYDRAULIC CIRCUIT

The ALBA's thermohydraulic cooling system in nominal conditions is described in a simplified scheme in Fig. 1. The circuit begins with the hot deionized water returning from the machine headed to the P11 pump, which should move 645 m³/h at 26.8 °C after a filtering process. The water circulates through E01 heat exchangers, where heat is partially exchanged with the Cooling Towers. In real operation, all the flow circulates through E01B and steers to heat exchangers E07, where each exchanger takes 156 m³/h and transfers 1815 kW of heat to ST4 water, aiming to decrease the water temperature to 22 °C. After that, the water is stored in tank D02.

The circuit ends with the 3-way valve and the P7-P10 pumps, which allow the impulsion of the water from D02 to the machine. The function of the bidirectional tube is to maintain the hydraulic balance in the system.

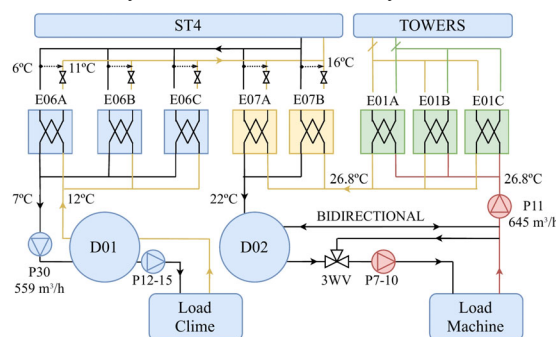


Figure 1: Simplified scheme of the ALBA's thermohydraulic cooling system.

The HVAC applications use water from the D01 tank employing P12-P15 pumps. The water from D01 is cooled with the E06 heat exchangers, each one taking 187 m³/h and transferring 1080 kW of heat to ST4 water. Once cooled, the flow returns to D01 circulating through the P30 pumps, which move 559 m³/h. Two-way mixing valves and differential pressure valves regulate the flow that circulates through E06 and E07 exchangers.

[†] fran.14hg@gmail.com
* mquispe@cells.es

Content from this work may be used under the terms of the CC BY 3.0 licence (© 2021). Any distribution of this work must maintain attribution to the author(s), title of the work, publisher, and DOI

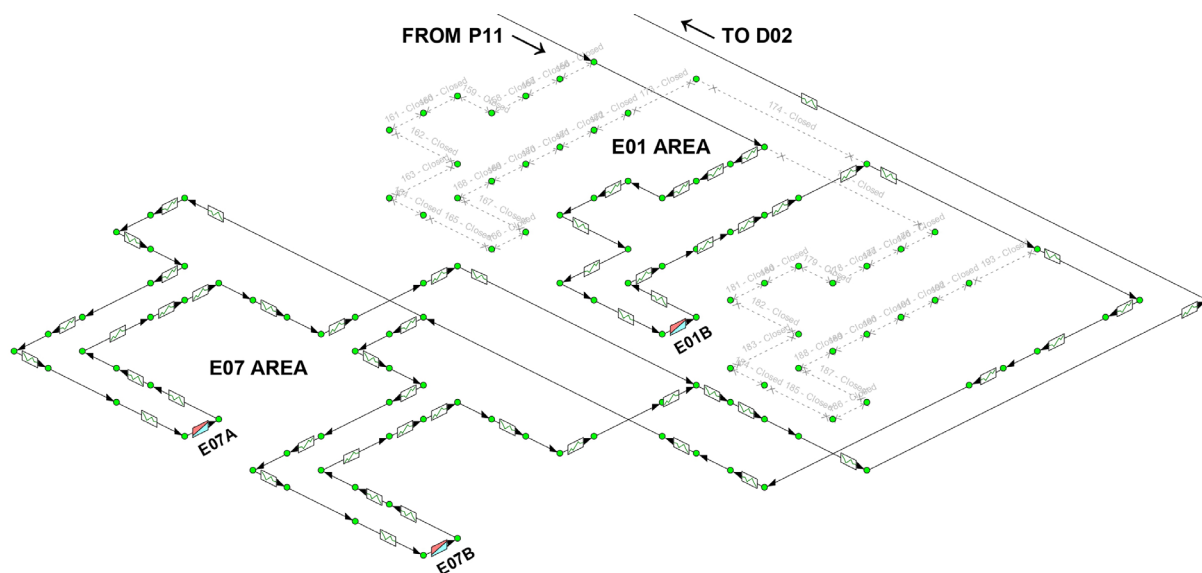


Figure 3: Fragment of the geometry modelled with Pipe Flow Expert, including E01 and E07 heat exchanger zones.

Thermal Instabilities

The thermal instabilities tend to appear in the first hours of the morning, causing a maximum increase of 1.5 °C above the inlet temperature (23 ± 0.2 °C) of the four main rings. For each week, it has been quantified that these instabilities have a total duration of 10 hours.

Figure 2 shows the thermal instabilities in the morning of the 28th of April of 2021. The continuous lines correspond to polynomial regressions of the points, while the scattering corresponds to real data extracted from historical records. For this example, the mean amplitudes of the rings EH, SR, BO, and SA are 0.59°C, 0.05°C, 0.57°C, and 0.70°C, respectively.

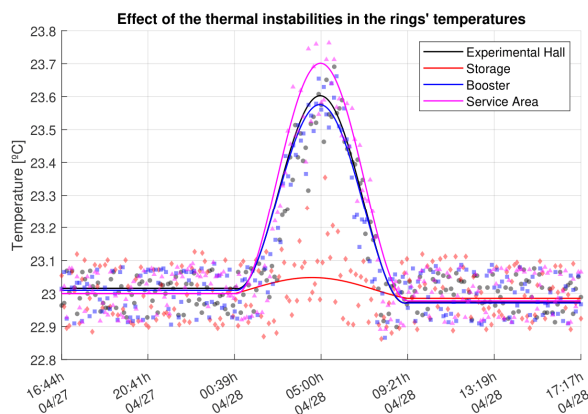


Figure 2: Inlet temperature of the EA, SR, BO and SA rings. Date 28th of April of 2021.

EXPERIMENTAL STUDIES AND THERMAL HYDRAULIC SIMULATIONS

One-Dimensional Simulations

The hydraulic behaviour of the circuit is studied by the use of one-dimensional simulations implemented in the software Pipe Flow Expert (PFE) [3]. Figure 3 shows the part of the hydraulic circuit corresponding to areas E01

and E07. The simulation describes the mass flow and pressure distributions along the circuit. Based on the one-dimensional model, the existence of an irregular flow distribution has been detected in the three branches of the manifold in the suction zone of the pump P11.

The thermal performance of the circuit has been simulated employing a self-made Matlab code, based on the hydraulic results given by PFE and solving energy balance equations over the circuit. The E07 heat power has been statistically modelled with more than 500,000 values from historical records. The results have been compared with real data, obtaining errors of less than 2%.

CFD Calculations

In particular, the E07 exchanger zone has been studied with three-dimensional CFD simulations due to its great importance in the heat exchange.

The SimsScale software [4] has been used for the simulations. For the model, a laminar flow condition with more than 4,5M elements is considered for both ST4 and ALBA flows. In regard to the pressure distribution of ST4 water in the E07 inlet, an example of this simulation is shown in Fig. 4.

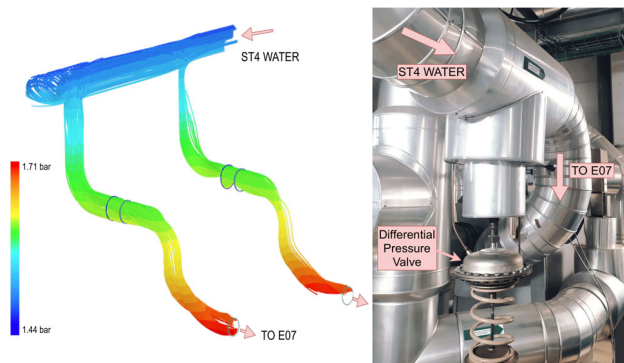


Figure 4: CFD of the ST4 water circuit. Details of pressure distribution in E07 inlet.

These simulations permitted to obtain a detailed description of the temperature, pressure and mass flow distribution in the pipes close to E07. Integrating on the different branches, it is observed that, due to the geometry of the pipes, 48.65% of the secondary flow is distributed by E07A and 51.35% by E07B. These CFD results differ from the experimental ones, 44% and 56%, obtained employing ultrasonic flowmeter equipment. The causes of these differences are attributed to (1) low precision measurements due to the lack of space when installing the ultrasonic equipment and (2) geometric limits imposed in the CFD model.

CONCLUSIONS AND RECOMMENDATIONS

A) In the current operating conditions, it is not possible to increase the ST4 mass flow in the E07 circuit due to a full opening condition of the two-way mixing valves. It is recommended to increase the setpoint of the differential pressure valves, located on the ST4 circuit of E06 and E07, from 0.5 bar to 1.5 bar. By changing this, a reduction in the opening condition of the two-way mixing valves from 100% to a new working regime between 50% and 70% is expected.

B) Lack of instrumentation for the pressure and mass flow measurements has been evidenced in the E06 and E07 zones. It is strongly recommended the installation of ultrasonic flowmeters located in the pipes of the ST4 circuit, pressure sensors near the differential pressure valves, and an intensive calibration of the temperature sensors along the circuit.

C) The one-dimensional model detected an irregular distribution of the flow in the suction zone of the P11 pump, which has been confirmed by the use of ultrasonic equipment measurements. Moreover, the flow has an oscillatory behaviour, with an average oscillation amplitude of $\pm 2.7 \text{ m}^3/\text{h}$ in this zone, which is counterproductive in connection to the occurrence of cavitation problems. A deeper investigation into the fluid dynamics in the aspiration zone of the P11 is strongly recommended in order to dim or remove the mentioned anomalies [5].

D) The Matlab simulation concludes that, by maintaining the current mass flow condition of the ST4 water and recovering the nominal mass flow in the ALBA's circuit (from 430 to 645 m^3/h), it would not be possible to improve the tank temperature condition. This is described in Fig. 5, which compares the D02 tank temperature against the return water temperature at the nominal ST4 working regime. As it is possible to see, an increase of the P11 volumetric flow (Q_{P11}) would only increase the in-tank temperature. This hypothesis has been confirmed with several experimental tests, by changing the duty point of the P11. Although a favourable thermal effect has not been observed, increasing the mass flow rate in the P11 pump is recommended in order to increase the mass flow in the bidirectional tube, currently low.

E) Simulations show that the temperature variation in the tank, relative to the variation of ST4 temperature, would be reduced by more than 50% when recovering the

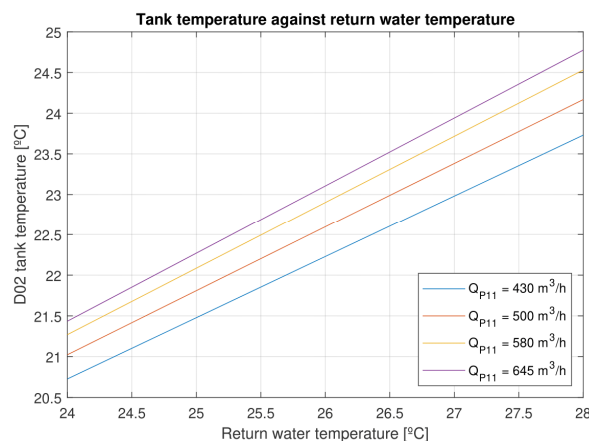


Figure 5: D02 temperature against return water temperature at ST4 nominal conditions.

nominal mass flow conditions in the ALBA's circuit. Thus, temperature deviations in the rings due to the thermal instabilities, currently up to 1.50 °C, would be mitigated to 0.75 °C.

F) Putting together the ultrasonic measurements with the results of the simulations, it is estimated that to achieve a desired stable temperature of 21°C in-tank, 25 m^3/h of additional cold water are needed in each E07 for the current regime, and 65 m^3/h for the nominal regime.

G) According to the thermal calculations, there are no significant changes in the D02 tank temperature between summer and winter. Table 1 shows the tank's temperature increment between summer and winter (ΔT_{D02}), taking into account the heat transfer throughout the entire circuit for an extreme scenario, with an outdoor temperature of 14°C in winter and 28°C in summer. The results are given for different volumetric flow conditions of the P11 pump.

The low values show that it is not necessary to insulate the pipes of the system since it would not have a relevant effect on the temperature of the tank.

Table 1: Estimation of the D02 Temperature Increment Between Winter and Summer

Q_{P11} [m^3/h]	380	430	500	580	645
ΔT_{D02} [°C]	0.096	0.087	0.076	0.067	0.061

REFERENCES

- [1] M. Quispe, "Cooling Water System in the Field of Accelerators", Open SESAME Project, Barcelona, Spain, October 2018.
- [2] C. Biscari, "ALBA towards ALBA II: Introduction and Institutional Background", ALBA II Day Virtual Event, Barcelona, Spain, June 2021.
- [3] Pipe Flow Expert, <https://www.pipeflow.co.uk/>
- [4] SimScale, <https://www.simscale.com/>
- [5] A. González, "CFD Predictions of Water Flow Through Impellers of the ALBA Centrifugal Pumps and Their Aspiration Zone. An Investigation of Fluid Dynamics Effects on Cavitation Problems", presented at MEDSI2020, Chicago, United States, July 2021, paper WEPB16, this conference.

DESIGN OF MINIATURE WAVEGUIDES AND DIAMOND WINDOW ASSEMBLY FOR RF EXTRACTION AND VACUUM ISOLATION FOR THE CWA *

B. Popovic[†], S. Lee, E. Trakhtenberg, K. Suthar, A. Siy¹,
 G. J. Waldschmidt, S. Sorsher, A. Zholents, Argonne National Laboratory, Lemont, IL, USA
¹also at University of Wisconsin, Madison, WI, USA

Abstract

This paper outlines the design of a diamond vacuum window and a millimeter wavelength (mmWave) waveguide assembly that will hold vacuum but still allow the mmWaves to propagate out of the structure for diagnosis and thermal management purposes. Currently under development at Argonne is a corrugated wakefield accelerator (CWA) that will operate at mmWave frequencies, with its fundamental mode of operation at 180 GHz and relatively high power levels up to 600 W. The fundamental mode needs to be extracted from the accelerator at approximately every 0.5 m to prevent the unwanted heating of the accelerator structure. Therefore, the structure is intentionally designed so this fundamental mode does not propagate further; instead it is transmitted through the waveguide assembly under vacuum and out via the vacuum window. As a result of the relatively high mmWave power densities, CVD diamond was chosen as the vacuum window material due to its low electromagnetic losses, mechanical strength, and superior thermophysical properties. Mechanically it is necessary to be able to hold the tight tolerances necessary for window performance at millimeter wavelengths. Other mechanical difficulties involve assembly of the window due to the CVD diamond material and preservation of ultra-high vacuum even if the integrity of the CVD diamond window is somehow compromised.

INTRODUCTION

Under development at Argonne National Laboratory (ANL) is a miniature accelerator that utilizes Čerenkov radiation to generate an accelerating electromagnetic (EM) mode at 180 GHz. The structure facilitates this Čerenkov radiation due to its corrugated waveguide structure and high-charge electron bunches [1]. After the accelerating structure ends, it is necessary to extract this accelerating mode using a fundamental coupler. This coupler is designed to couple only to the accelerating mode and transport it out of the main section via four rectangular waveguides. These waveguides then transport the mode out via the vacuum windows to RF loads. The fundamental coupler is shown in Fig. 1, along with a portion of the accelerating structure.

* This research used resources of the Advanced Photon Source, a U.S. Department of Energy (DOE) Office of Science User Facility and is based on work supported by Laboratory Directed Research and Development (LDRD) funding from Argonne National Laboratory, provided by the Director, Office of Science, of the U.S. DOE under Contract No. DE-AC02-06CH11357.

[†] bpopovic@anl.gov

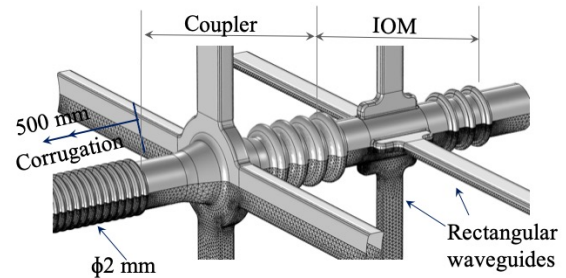


Figure 1: The corrugated waveguide and fundamental coupler followed by the IOM.

First and foremost, the vacuum window must perform adequately electromagnetically, with minimal losses and reflection of the extracted electromagnetic (EM) wave, thereby maximizing transmission out of the structure via the window. Any reflection off the window or its structure could return to the accelerator and disrupt its operation, potentially heating or, even worse, destabilizing the beam. Minimizing EM losses is vital since it is necessary to transport as much of the wave's energy as possible to a location outside of the accelerator vacuum where it can be properly cooled. The main basis of the design is the window material; specifically, chemical vapor deposition (CVD) diamond was chosen for its thermal and electrical properties. Currently CVD diamond windows are used extensively in mmWave gyrotrons operating at megawatt power levels [2, 3].

It is also necessary to keep in mind that this accelerator is operating at a much shorter wavelength than a typical accelerator, these mmWaves having a freespace wavelength of 1.7 mm at 180 GHz. Thus, all the design parameters that are on the EM side must have submillimeter tolerances to ensure EM performance. There are additional issues relating to machining finishes.

As mentioned previously, the outputs of the fundamental coupler are rectangular waveguides but for structural and vacuum reasons, windows at these frequencies are typically circular. A rectangular window is not as structurally strong and is more difficult to fabricate, more difficult to braze, and more prone to vacuum leaks in the corners. Thus, it is necessary to transition from a rectangular waveguide to a circular one, and then uptaper to a larger diameter waveguide. A larger diameter window is preferable for heating concerns along with ease of manufacturing and assembly, though it introduces more potentially disruptive resonances within the window itself.

This design employs a double-window structure to protect the accelerator from a catastrophic failure of one of the windows. Even though a window failure will still bring the system offline, having a second window will allow the system to maintain its vacuum levels and prevent contamination. The system would be brought offline since a damaged window would have extremely poor EM performance and result in poor transmission and high levels of reflected power.

Thus, the design consists of a rectangular-to-circular waveguide transition section leading to a circular waveguide with two mounted circular diamond windows in series. The rectangular waveguide is connected to one of the fundamental coupler's rectangular waveguide arms, which is under vacuum. The other side of the window section is at atmosphere, either radiating into a load via free-space or directly into a waveguide load. Figure 2 shows the entire window structure.

FABRICATION CONCERNS AT mmWAVE FREQUENCIES

Two major fabrication concerns at these frequencies are surface roughness and dimensional accuracy. Poor surface roughness results in increased ohmic losses; this is due to the effect of the skin depth of EM waves. The skin depth is how deeply the wall currents of the EM wave mode penetrate into the conductor. It is inversely dependent on the conductivity and magnetic permeability of the material but, most importantly, inversely proportional to the operating frequency. Thus, the higher the frequency, the smaller the skin depth and the greater the need for reduced surface roughness. Having the surface roughness greater than the skin depth at the operating frequency causes discontinuities in the conductor of the wall currents, effectively increasing the ohmic wall losses. The surface roughness referred to is the roughness average (R_a) of a surface. At 180 GHz, with annealed copper's conductivity of 5.8×10^7 S/m, the skin depth is 155 nm. Ideally the skin depth should be a number of times higher than the surface roughness [4].

Regarding dimensional accuracy, at 180 GHz the wavelength is 1.66 mm. Thus, a variance of ± 50 μ m would result in a frequency deviation of ± 5 GHz in vacuum, while it would be even greater within the diamond window material due to its relative permittivity value. Potential effects on EM performance due to dimensional variance on window performance is discussed in a later section alongside a tolerance study done in simulation.

WAVEGUIDE AND WINDOW STRUCTURE

Rectangular-to-Circular Transition

The element consists of a transition from a standard rectangular WR5.1 waveguide to a circular waveguide of 1.5-mm radius. A smooth taper is necessary to provide good mode conversion from the rectangular fundamental waveguide mode (TE_{10}) to the circular fundamental waveguide mode (TE_{11}); ideally all the EM energy is converted from

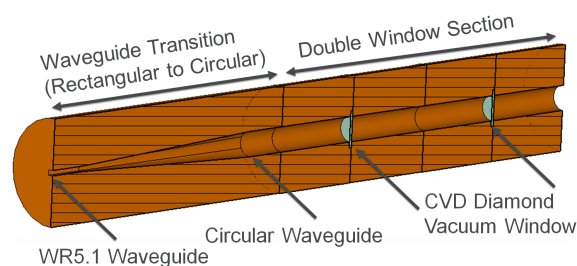


Figure 2: The entire window structure is shown. On the left is the rectangular-to-circular transition. In the center is the diamond window section, with the two windows shown.

one mode to the other. An abrupt or poorly fabricated taper would lead to reflections and, potentially, mode conversion to undesirable waveguide modes. Converting to modes other than the desired circular TE_{11} mode would significantly reduce the EM performance of the structure and increase reflections and conductive losses.

The length of the uptaper is 32 mm, with 5 mm of straight WR5.1 and 5 mm of straight circular waveguide on either side. It is necessary to have at least a few wavelengths on either end of the taper to ensure the mode is stable before any attempt is made to add a bend, window, or other transition, otherwise there is a risk of mode conversion or reflections.

Window Materials

The material properties of various materials traditionally used for RF vacuum windows are listed in Table 1. Note the far superior thermal conductivity of CVD diamond and lower loss tangent. The higher the relative permittivity, the thicker the window design, since the window is typically an integer number of the half wavelength within the window.

Table 1: Typical RF Vacuum Window Material Properties

Material	Relative Permittivity	Loss Tangent	Thermal Conductivity W/(m K)
Diamond	5.68	2×10^{-5}	2000
Alumina	9.9	0.001	30
BeO	6.5	0.004	330
Quartz	3.75	0.0004	5

Diamond Window

The window's thickness is determined by the EM wavelength at the operating frequency of 180 GHz within the material, dependent on its relative permittivity (ϵ), 5.68 for CVD diamond. The ideal thickness is an integer of the half wavelength, which at 180 GHz is 0.35 mm. A thicker window would function equally well in reflection performance but would result in greater transmission losses within the window itself due to the longer signal path length.

The design choice of the maximum diameter of the circular waveguide is constrained by the need to transition from

Table 2: Tolerance analysis of the CVD diamond window's thickness and radius with the resulting insertion loss (S_{21}) (dB) at 180 GHz. In bold is the nominal insertion loss value.

S_{21} (dB)		Window Thickness		
180 GHz		-50 μm	0.35 mm	+50 μm
Radius	-50 μm	-0.70	-0.090	-0.64
	2.2 mm	-0.90	-0.015	-0.66
	+50 μm	-0.815	-0.014	-0.77

a rectangular waveguide to a circular one. A larger diameter waveguide would be preferable, since it would result in a larger diameter window that would be easier to fabricate and mount, and have improved thermal handling. However, a larger diameter window could also potentially have more resonance modes within, and would also require a longer transition piece to ensure adequate EM performance. A longer transition piece would be more difficult to fabricate and would increase costs.

The double-window design presents the potential issue of a standing wave developing between the two windows if they are not spaced apart adequately. This standing wave is generated and trapped by reflections off the windows. If a standing wave were to build up, it would cause an EM wave mismatch in the window structure, resulting in further reflections back to the accelerator structure. Additionally, this standing mode would introduce further thermal losses in the structure. This risk is mitigated by the spacing between the windows being at least a few wavelengths, chosen here as 24 mm, so any trapped standing waves would be attenuated away. The overall length of the double window section is 54 mm, bringing the total length of the structure to 86 mm.

SIMULATION RESULTS

The entire design (shown in Fig. 2) was simulated in CST Microwave Studio in the frequency domain, with the scattering parameter results shown in Fig. 3. At the mode of operation, 180 GHz, the insertion loss (S_{21}) is -0.015 dB, which is the amount of signal that is not transmitted thru the structure, either from conductive losses or reflection back. The return loss (S_{11}), the amount of signal reflected back to the fundamental mode, is -25 dB, and the passband is 7.5 GHz. This design allows a substantial frequency deviation from the designed frequency of 180 GHz. Note that this passband has two sharp dips on either end. These are resonance modes that occur within the diamond window and are a function of the window's material properties, thickness, and radius. These resonance modes are unavoidable and can only be shifted up or down in frequency by changing the thickness or radius of the window. During the design process these parameters were chosen to provide a large enough passband between resonances and ideally place the mode of operation in the center of the passband.

A tolerance analysis was done of a single CVD diamond window and compared to the design parameters, as shown in Table 2. The major degradation in performance was due to

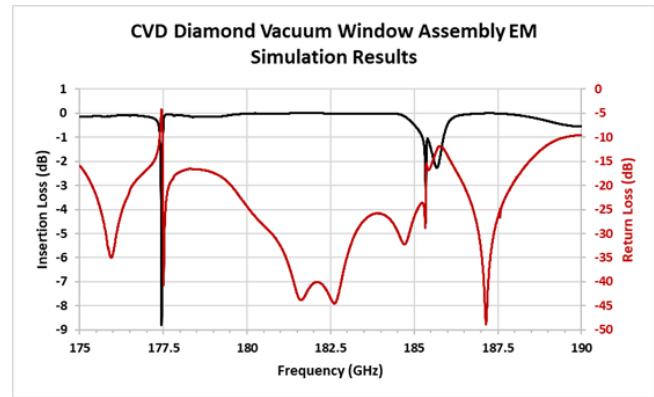


Figure 3: Electromagnetic simulation results from CST Microwave Studio of the entire vacuum window assembly, as shown in Fig. 2.

the window thickness being out of specification. Simulations show that a ± 50 μm difference in thickness increases the transmission loss (S_{21}) at 180 GHz by 0.55 dB and 0.89 dB, respectively. Since ± 50 μm would be equivalent to a half wavelength at 207 and 177 GHz, respectively, the degradation in performance with respect to a variance in the window's radius was not significant.

As a result of this analysis, when the windows are delivered and before they are inserted into the assembly, they will be characterized electromagnetically using a vector network analyzer (VNA) to determine if their EM performance will suffice at 180 GHz. A window that is at the upper or lower bounds of the tolerance would be identified via the EM measurements and rejected for use in the vacuum window system.

SUMMARY

An EM design at these millimeter wavelengths presents numerous issues from a fabrication and assembly standpoint. Issues such as surface roughness and dimensional tolerances are crucial for adequate EM performance. The window system presented focuses on a simple design to minimize these difficulties. The selection of CVD diamond as the window material is based on its electrical properties, low loss, and low relative permittivity, along with its superior thermal properties compared to other traditional vacuum window materials. The choice to use a circular window presents the need for a rectangular-to-circular waveguide transition, though this trade-off allows for a more mechanically robust circular window. Finally, a double-window design introduces a safety redundancy such that if one window fails, the vacuum of the entire accelerator is not compromised.

FUTURE WORK

With the EM design complete, the mechanical and vacuum design and sourcing of parts are the next steps. Once the parts have been fabricated, EM testing of the windows, the elements of the structure, and the fully assembled structure will be done using the new mmWave test lab at Argonne.

Finally, assembly and vacuum testing will be done at ANL before the window system is deployed on ANL's corrugated wakefield accelerator.

REFERENCES

- [1] A. Zholents *et al.*, "A conceptual design of a compact wake-field accelerator for a high repetition rate multi user x-ray free-electron laser facility," in *Proc. IPAC'18*, Vancouver, BC, Canada, Jun. 2018, pp. 1266–1268. doi: 10.18429/JACoW-IPAC2018-TUPMF010
- [2] G. Gantenbein *et al.*, "First operation of a step-frequency tunable 1-MW gyrotron with a diamond brewster angle output window," *IEEE Trans. Electron Devices*, vol. 61, no. 6, pp. 1806–1811, 2014. doi: 10.1109/TED.2013.2294739
- [3] Y. Gorelov, J. Lohr, P. Borchard, R. Callis, and D. Ponce, "Characteristics of diamond windows on the 1 MW, 110 GHz gyrotron systems on the DIII-D tokamak," in *Proc. Twenty Seventh International Conference on Infrared and Millimeter Waves*, 2002, pp. 161–162. doi: 10.1109/ICIMW.2002.1076134
- [4] D. Gamzina *et al.*, "Nanoscale surface roughness effects on THz vacuum electron device performance," *IEEE Trans. Nanotechnol.*, vol. 15, no. 1, pp. 85–93, 2016. doi: 10.1109/TNANO.2015.2503984

VACUUM ANALYSIS OF A CORRUGATED WAVEGUIDE WAKEFIELD ACCELERATOR

K. Suthar*, E. Trakhtenberg, S. Sorsher, and A. Zholents
 Argonne National Laboratory, Lemont, IL, USA

Abstract

The vacuum level in a 2-mm-diameter, 0.5-m-long copper corrugated waveguide tube proposed for a compact high repetition rate wakefield accelerator has been investigated. The analytical calculations have been found to be in good agreement with the result of computer modeling using the finite element method. A representative experiment has been conducted using a smooth copper tube with the same inner diameter as the corrugated tube. The vacuum level calculated for this experiment agrees well with the measurement.

INTRODUCTION

The sustainable operation of all accelerators requires high vacuum within the vacuum chamber [1], which is very challenging for the long tubular chamber with a small-diameter opening that is employed in a miniature collinear wakefield accelerator (CWA)—A-STAR—under development at Argonne National Laboratory. This accelerator uses a corrugated waveguide and sub-terahertz Čerenkov radiation produced by an electron bunch traveling longitudinally on the centerline of the waveguide [2].

This paper focuses on vacuum analysis of the accelerator. The 2-mm-inner-diameter, 0.517-m-long corrugated vacuum chamber of the accelerator module will be assembled from five 100-mm-long, thin-wall corrugated tubes. It will operate with 1-GeV, 10-nC electron bunches that will be coming to the accelerator with a 15-kHz repetition rate, producing Čerenkov radiation, inducing surface currents on the corrugation, and depositing about 800 W of heat distributed over the entire accelerator module [3]. As a result, the chamber will heat up from room temperature to ~50 °C [4]. The heat load increases along the length of the structure, causing a progressively higher thermal outgassing in the downstream direction. Additionally, an electroforming fabrication technique will be used to produce the corrugated waveguide [5]; therefore, due to hydrogen trapping [6], a higher outgassing rate is expected in the electroformed copper compared to the oxygen-free copper used in the accelerator applications.

While the accelerator chamber fabrication concept is still being developed [7], we performed a preliminary vacuum analysis using the chamber dimensions presented in [7] and report it here in the first section.

A major concern for the accelerator module fabrication is the integrity of the brazed joints between the adjacent corrugated waveguide sections. Therefore, we fabricated a 152-mm-long mock-up vacuum chamber containing three 2.1-mm-inner-diameter, 50-mm-long oxygen-free copper tubes without corrugation and measured vacuum in two

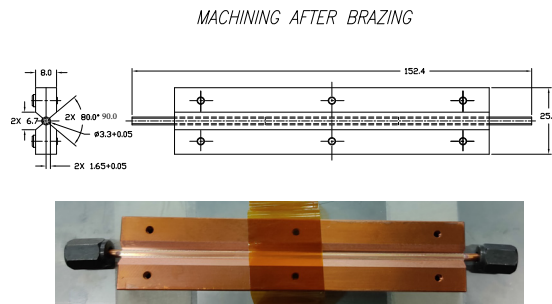


Figure 1: Test piece of the vacuum chamber showing dimensions (top) and the machined chamber (bottom).

setups: a) with these joints enclosed and brazed inside the copper block, and b) after machining the copper block to obtain a vacuum chamber profile. The machined chamber has a thin (<0.9-mm-thick) section exposed to atmospheric pressure, as seen in Fig. 1. The result of this experiment is reported in the second section.

VACUUM CALCULATIONS

Analytical Estimation

For vacuum calculations we modeled the corrugated waveguide as a smooth tube with an effective diameter $d=2.26$ mm and an effective length $\ell=0.95$ m that has the same surface area as a 2-mm-diameter, 0.517-m-long tube with corrugations. We calculated the tube's molecular flow using the engineering formula [8]

$$C(x) = 12.1 \frac{d^3}{x} \quad (1)$$

that defines the conductance C in liter/sec for a tube with an internal diameter d and length x in cm. Expecting pumping efficiency to be limited by the tube's conductance, and assuming use of pumps on both sides of the vacuum chamber, we obtained a result for the vacuum pressure as a function of the relative distance along the tube length $\xi = x/\ell$:

$$P(\xi) = \pi R \frac{\ell^2}{12.1 d^2} \xi(1 - \xi), \quad (2)$$

where R is the outgassing coefficient, and we ignore here a small variation of this coefficient with the temperature. Using $R=3.6 \times 10^{-11} \frac{\text{torr L}}{\text{cm}^2 \text{ s}}$ for copper after backing [6, 9], we calculated the vacuum pressure at the center of the tube as $P(1/2) \approx 1.5 \times 10^{-6}$ torr.

* suthar@anl.gov

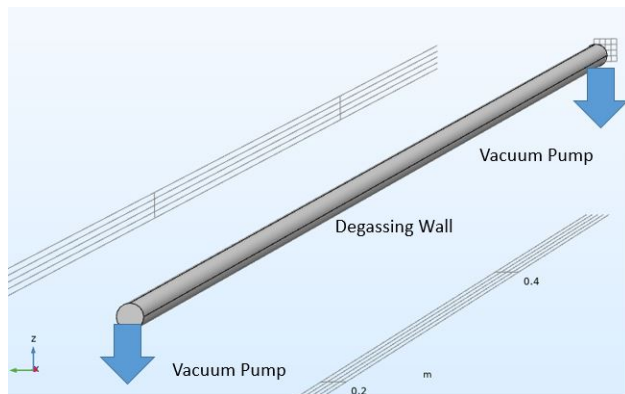


Figure 2: The 517-mm-long, 2-mm-inner-diameter corrugated copper tube with corrugation depth of 0.26 mm modeled as a 950-mm-long, 2.26-mm-inner-diameter smooth copper tube.

Simulation Result

The simulation was performed using the COMSOL multi-physics molecular flow module with the parameters listed in Table 1. The model geometry is shown in Fig. 2. Two pumps were attached to the system on either end. Both pumps operated at a pump speed of 1 liter/sec. A constant outgassing

Table 1: Parameters used in Simulation

Parameter	Value
Temperature	293.15 K
Molar mass	0.028/kmol
Pump speed	1 liter/sec
Outgassing rate	$3.6 \times 10^{-11} \frac{\text{torr L}}{\text{cm}^2 \text{ s}}$

flux was assumed to be emitted from the walls of the tube with an outgassing coefficient of $3.6 \times 10^{-11} \frac{\text{torr L}}{\text{cm}^2 \text{ s}}$ [6, 9].

The maximum pressure of 7×10^{-7} torr occurred at the center of the tube since the vacuum pumps were allocated at both ends. The simulation result is shown in Fig. 3. We note that the analytical estimation agreed with this result within a factor of 2.

The long, smooth tube may not perfectly represent the practical case of a corrugated tube, however, since it only accommodates the total surface area of the corrugations in the simulation.

EXPERIMENT

The prime focus of the experiment was investigation of the brazed joints between adjacent corrugated waveguide sections as discussed in the introduction. However, instead of the 100-mm-long corrugated tubes produced via the electroforming process, we used 2.1-mm-diameter, 50-mm-long oxygen-free copper tubes without corrugation, but with a similar wall thickness of 0.9 mm. This is about the same thickness as the wall of the corrugated tube in the middle of the ridge in the corrugation profile. We also benchmarked

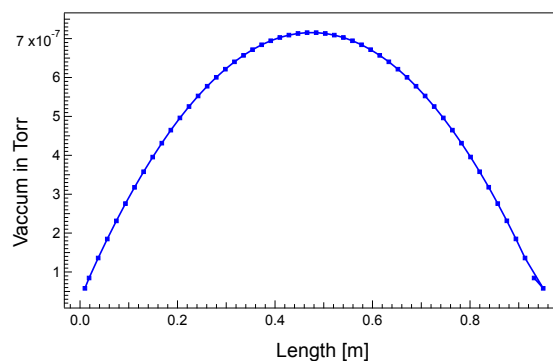


Figure 3: Molecular flow simulation result of the total pressure for an equivalent 0.95-m-long copper tube.

our vacuum simulation. Specifically, we used vacuum measurements to find the outgassing coefficient that would produce the best fit of simulations to the experiment.

Figure 4 shows the fabrication steps of the 0.95-m-long copper mock-up chamber. Figure 4e shows the vacuum testing setup before machining the designed profile of the chamber. The vacuum pumps is located on one side of the chamber, and the vacuum gauge is located on the opposite side of the chamber.

The system was pumped down for 48 hours, and the base pressure at room temperature before baking was 4.5×10^{-7} torr. Figure 5 shows two graphs. The blue line is the vacuum pressure versus time, and the red line is the ramp-up and ramp-down of the baking temperature versus time. After the ramp-down process, the system was brought down to room temperature, and the vacuum pressure was 1×10^{-7} torr. The final pressure after baking improved over 24 hours to 8.5×10^{-8} torr. To obtain this vacuum pressure in simulation, we had to use $R = 7 \times 10^{-11} \frac{\text{torr L}}{\text{cm}^2 \text{ s}}$, which is not surprising considering the typical uncertainty for the outgassing coefficient in the literature [6, 9].

After machining the mock-up vacuum chamber to the required shape shown in Fig. 1 and, thus, exposing the brazed tubes to atmospheric pressure over a large fraction of the circumference and length, the second vacuum test was performed. Figure 6 shows this measurement. The final vacuum pressure degraded to 2.1×10^{-7} torr, which can be attributed to a thin section of the tube, but the integrity of the brazed joints was not compromised in the fabrication process.

SUMMARY

The steady state molecular flow simulation was performed based on the outgassing condition that develops due to heat load. The simulation with boundary conditions shown in Fig. 2 was performed on a 2-mm-diameter, 0.95-m-long copper tube without corrugation representing the actual surface area of the 0.517-m-long vacuum chamber with corrugation. The outgassing coefficient for the oxygen-free copper after backing was used to simulate the gas load. In the

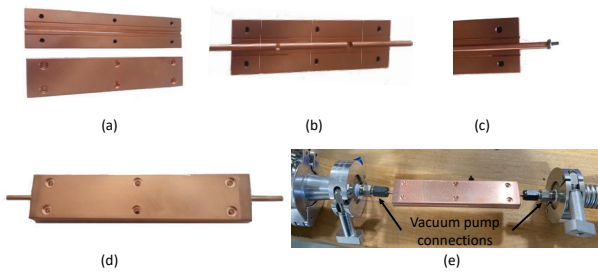


Figure 4: Fabrication process for a mock-up vacuum chamber. (a) Preparation of two halves before brazing, (b) three 50-mm tubes assembled in the channel, (c) assembled vacuum chamber with titanium rod inserted for clamping via application of spring force, (d) brazed chamber without machining operation, and (e) vacuum chamber on testing rig attached with vacuum pumps.

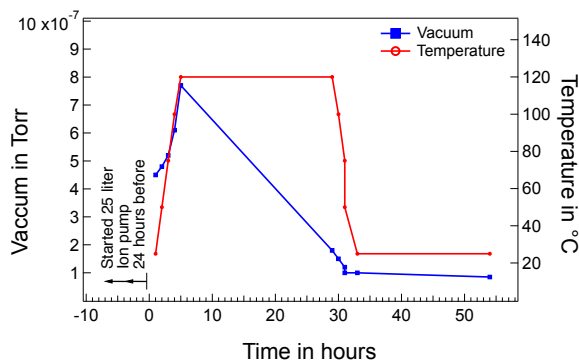


Figure 5: Vacuum testing with baking out process.

result shown in Fig. 3 we predict a maximum pressure of 7×10^{-7} torr and a line average pressure of 5.6×10^{-7} torr.

However, the long, smooth tube may not perfectly represent the practical case of the corrugated tube and, thus, our next goal is to fabricate and study the vacuum holding capacity of the 0.3-m-long vacuum chamber with three 0.1-m-long corrugated tubes.

The vacuum testing results shown in Figs. 5 and 6 using a mock-up vacuum chamber are in good agreement with each other. In both cases, the vacuum level improved after baking and sustained an equilibrium between outgassing and pumping that confirms the successful brazing process. Exposing the brazed tubes to atmospheric pressure over a large fraction of the circumference and length slightly degraded the vacuum pressure, which can be attributed to the thin section of the tube.

ACKNOWLEDGMENTS

The authors would like to thank Mark Martens and Leonard Morrison of the Mechanical Maintenance group for conducting vacuum experiments, Nemanja Kuzmanovic for machining the chamber after vacuum testing, and Gary Navrotski for conducting metallurgical studies before and after vacuum testing. This research used resources of the Advanced Photon Source, a U.S. Department of Energy (DOE) Office of Science User Facility and is based on work sup-

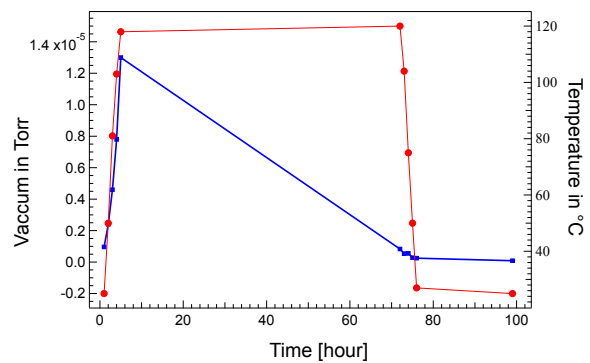


Figure 6: Vacuum testing with baking out process after machining the chamber.

ported by Laboratory Directed Research and Development (LDRD) funding from Argonne National Laboratory, provided by the Director, Office of Science, of the U.S. DOE under Contract No. DE-AC02-06CH11357.

REFERENCES

- [1] O. B. Malyshev, "Vacuum requirements," in *Vacuum in Particle Accelerators*. John Wiley & Sons, Ltd, 2019, ch. 1, pp. 1–23. doi: <https://doi.org/10.1002/9783527809134.ch1>.
- [2] A. Zholents *et al.*, "A conceptual design of a compact wakefield accelerator for a high repetition rate multi user x-ray free-electron laser facility," in *Proc. IPAC'18*, Vancouver, BC, Canada, Jun. 2018, pp. 1266–1268. doi: 10.18429/JACoW-IPAC2018-TUPMF010.
- [3] A. Siy *et al.*, "Design of a compact wakefield accelerator based on a corrugated waveguide," in *Proc. NAPAC'19*, Lansing, MI, USA, Oct. 2019, pp. 232–235. doi: 10.18429/JACoW-NAPAC2019-MOPLH26.
- [4] K. Suthar *et al.*, "Determination of maximum repetition rate of a corrugated-waveguide-based wakefield accelerator," in *Proc. 11th Mechanical Engineering Design of Synchrotron Radiation Equipment and Instrumentation*, Chicago, IL, USA, virtual conference, Jul. 2021, paper THIO02.
- [5] K. Suthar *et al.*, "Study of copper microstructure produced by electroforming for the 180GHz frequency corrugated waveguide," in *Proc. 11th Mechanical Engineering Design of Synchrotron Radiation Equipment and Instrumentation*, Chicago, IL, USA, virtual conference, Jul. 2021, paper TUPC01.
- [6] P. Massuti Ballester, "Outgassing analysis of different copper materials for ultra-high vacuum by thermal desorption spectroscopy," Ph.D. dissertation, Saarland University, Saarbrücken, Germany, 2017.
- [7] S. Lee *et al.*, "Mechanical design of a compact collinear wakefield accelerator," in *Proc. 11th Mechanical Engineering Design of Synchrotron Radiation Equipment and Instrumentation*, Chicago, IL, USA, virtual conference, Jul. 2021, paper WEPB05.
- [8] D. Hoffman, B. Singh, and J. Thomas III, *Handbook of Vacuum Science and Technology*. 1998. doi: <https://doi.org/10.1016/B978-0-12-352065-4.X5040-8>.
- [9] T. Abe *et al.*, "Outgassing rate of highly pure copper electroplating applied to rf cavities," in *Proc. EPAC2006*, Edinburgh, Scotland, UK, Jun. 2006, pp. 1307–1309.

HIGH-PRECISION SYNCHROTRON KAPPA DIFFRACTOMETER

G. Olea[†], N. Huber, J. Zeeb, HUBER Diffraction GmbH & Co.KG, Rimsting, Germany

Abstract

A new research product aiming to work in a 3rd generation synchrotron facility has been developed. Based on increased energy X-ray synchrotron radiation tool and well-known Kappa geometry, the product is expected that will investigate atomic and molecular structures of materials at nanoscale level using X-ray diffraction (XRD) technique. The Kappa Diffractometer (KDm) machine is maintaining the common structural principle of its family, but working with an extreme precision, which is far of the competition. The main body is consisting of a customized Kappa goniometer (KGm) device with vertical axis of rotation for high-precision sample (cryostat) manipulation, versatile detector arm (Da) for manipulating in horizontal plan different detectors (optics, slits, etc.) after X-ray beam is scattered and stable alignment base (Ab) for roughly adjusting the product towards the X-ray beam. In addition, a new XYZ cryo-carrier inside of the KGm is included for fine(submicron) sample adjustments. The kinematic, design and precision concepts applied, together with the obtained test results are all in detail presented.

INTRODUCTION

Synchrotron radiation is one of the most powerful investigative tools available today for exploring internal structure of the matter. Last generation (4th) synchrotrons are being currently on the way to be built and several other (3rdgeneration) took a modernization process. However, advanced investigations are requiring not only new modern techniques [1], but dedicated instruments adapted to the specificity of the applications, as well.

Korean Pohang Accelerator Laboratory (PAL) research facility is managing the 3th generation accelerator, which was under an upgradation process (2009-2012). In the actual configuration (PLS II) it is including a portfolio of 40 beamlines [2] from which an appreciable number are dedicated to X-ray diffraction (XRD). 1C beam line is managed by Institute of Basic Science (IBS) being currently under the development. After its completion, it will investigate the properties of advanced functional materials lattices dynamics using time-resolved scattering technique (TR-XRS).

A growing interest is seen today to discover new materials with improved quantum features. A research centre at IBS (CALDES) is focusing on investigating such properties based on untapped potential of low-dimensional electronic materials [3]. An international request to develop a specific diffractometer has been launched [4] and attracted several proposals. In one of them [5], the intention was to use a four-circle diffractometer with Kappa geometry (horizontal), to provides a better access and large Bragg diffraction angles for preferred crystallographic orientations. However, after the proposal was accepted, based on a more detail analysis of required precision and load - sample and

specific instruments manipulation, it has been concluded that a new solution must be adopted to cope with all the specifications. The proposed diffractometer hoping to offer not only an improved manipulation capability, maintain at the same time the intrinsic advantages of the architecture, but an increased precision, as well.

The main features of the first product (prototype) are described below, including most important aspects related with kinematics, design and precision concepts.

DIFFRACTOMETER

Generally, diffractometers have been conceived till now based on two type of architectures- Eulerian (E) and Kappa (K), respectively. These are deriving from the way a sample is manipulated; specifically, the working principle chosen for the manipulation mechanisms. There are several well-known companies producing both of such machines (HUBER, NEWPORT, KOHZU).

Euler Diffractometer (EDm) is using a combination of three orthogonal gonio (G) stages, forming Euler goniometer (EGm) device. It delivers high precision positions, able to carry instruments with appreciable weight and size because of its intrinsic high stiffness of the mechanism (closed loop). However, it is providing a limited access of X-ray (incident, scattered) to the sample, and to operator (setup, maintenance). On contrary, Kappa diffractometers (KDm) are based on an open loop angular device to manipulate the sample, called Kappa goniometer (KGm). By this, the access at the sample is almost entirely free. However, the precision of the manipulated load and size are limited, because of intrinsic flexible (open loop) working principle of the mechanism. A good overview of Kappa diffractometer capabilities is given in [6].

Requirements

One of the express requirements for the new Kappa Diffractometer (KDm) was to manipulate a specific atmosphere & temperature-controlled instrument (cryostat) having a maximum - weight (20kg) and size (500mm) with highest possible accuracy (SoC<30 μ m). In addition, the orthogonality of the last rotation axis has to be less than a maximum value (20"). It should accommodate the use of several type of detectors - in-line and area, weighing a value of about (40kg) for related processes use. An overview of the most important motion parameters and their values for precision are included in Table 1.

Table 1: Motion Parameters (Sample)

Range (°/mm)	Acc. ("/ μ m)	Rep. ("/ μ m)	Res. ("/ μ m)
$\varphi=\kappa=\theta=\pm 180$	20	1	0.36
X,Y,Z= $\pm 5,5,3$	2,2,2	1	<1

Content from this work may be used under the terms of the CC BY 3.0 licence (© 2021). Any distribution of this work must maintain attribution to the author(s), title of the work, publisher, and DOI

Kinematics

From kinematic point of view, the new diffractometer is based on a classical four-circle (4C) geometry using Kappa concept with vertical axis of motion [7]. It can be seen as a well-established combination of two independent manipulators – sample(S) and detector(D), each of them being composed from joints and links, forming distinct kinematics chains (K_i , $i=1,2$), involving a basic set of rotative actuation called circles (C_i , $i=1,\dots,4$), Fig. 1.

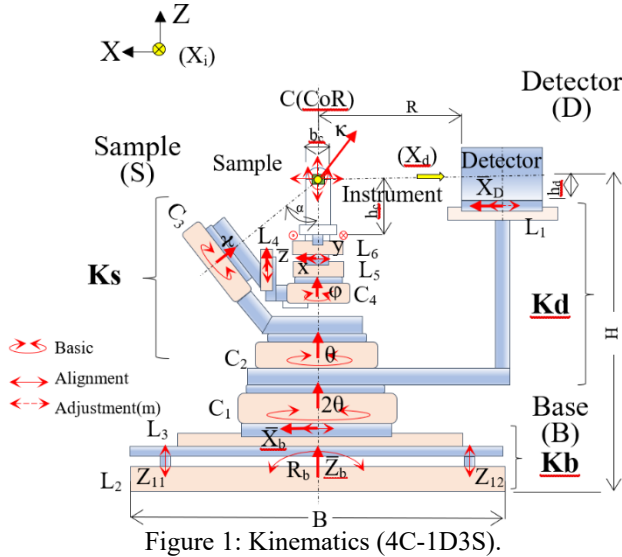


Figure 1: Kinematics (4C-1D3S).

All the experimental investigations are based on above corelated motions(positioning) relative to X-ray (fixed) beam, respecting the diffraction law (Bragg) and specific procedures.

The detector manipulator (D) is based on a simple kinematic chain (K_d) mechanism, consisting of an active rotational joint $C_1(2\theta)$ and an arm, supporting linear sliding guides (L_1), accommodating the use of different detectors, covering a large region in the reciprocal space (time-resolved), catching the scattered X-rays. A detector is performing a plan-parallel circular motion ($R=1000\text{mm}$, $X_d=\pm 150\text{mm}$). The corresponding (pseudo) vector of rotation (2θ) is vertical with positive direction upwards and null position when D is in the YZ plan (-Y). The angular motion range ($\pm 160^\circ$) has the same precision parameters as in Table 1.

The sample manipulator (S) is an open loop kinematic chain (K_s) mechanism, consisting of three actuation circles (C_i , $i=2,\dots,4$) linked together at a fixed angle ($\alpha=50^\circ$). $C_2(\theta)$ is supporting the two others - $C_3(\kappa)$ and $C_4(\varphi)$; last one holding the sample. It performs spherical motions around a fixed point (C), called centre of rotation (CoR).

As the specific instrument (cryostat) is with an appreciable weight and size and the final precision was always related before with Z carrier stage source of errors, a new carrier mechanism has been included for fine adjustments, between the circles, instead of the classical one at the end (XYZ). By this solution, is providing not only an increased access to easily mount and operate (setups, maintenance) the afferent instruments, but is opening the way for an

increased weight (load) manipulation. However, attention must be paid to the stiffness of the arm.

The nominal position of the mechanism is defined by $\theta_0=\kappa_0=\varphi_0=0^\circ$ and $2\theta_0=0^\circ$ angles. Then, θ and φ (pseudo) vectors coincide (support, direction), and κ lies in XZ plane (second quadrant); φ direction can be arbitrary chosen, often null coinciding with OX(-X) axis. Positive rotations for 2θ , θ and φ are consisting in moving X towards Y (right hand rule), and for κ to be always out(upper)side of horizontal plane (XY); K resultant orientation vector being upside, as well. All vectors must intersect in C point. Generally, the convention follows the basic rules included in [8].

Note: The OXYZ reference system is a right-handed set of orthogonal axes. It has OY axis against the incoming X-ray beam.

Design

A modular approach has been applied in the design process [9], consisting of adopting the detector, sample and base manipulation subsystems, as the main positioning modules (Pm_i , $i=1,2,3$), Fig. 2.

The core of sample module (Pm)s is a modified standard Kappa goniometer (KGm) TS70712. It is based on a combination of two active positioning units (Pu_i , $i=1,2$) called Goniometers (Gm) or simply gonio(G) linked together in an angular way, as described before. The first one is a precision gonio (G430/X2W2) able to carry the second one (G420/X2W2) and the linear in-parallel redundant actuated unit Z (Z_1, Z_2) located in-between; both gonios being integrated in the supporting arms (θ_a, κ_a) for increasing stiffness. This solution is coping not only an increased load manipulation but could eventually solve the arm deflection error compensation.

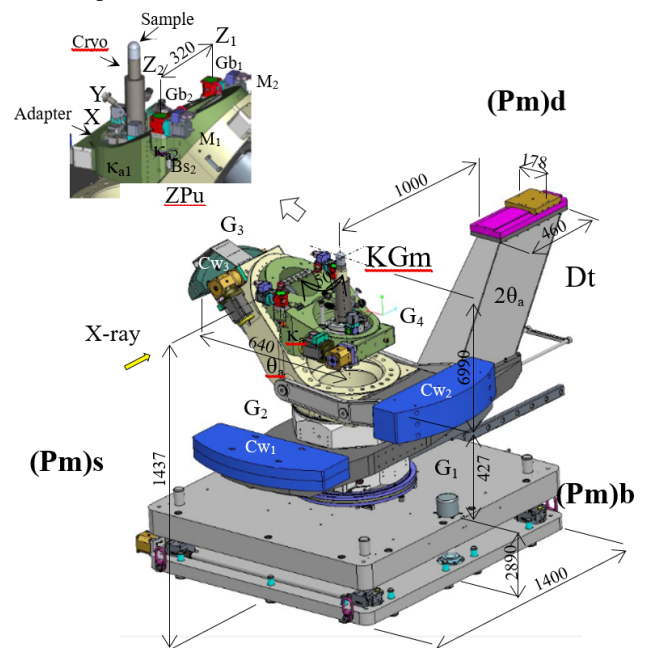


Figure 2: CAD layout (ZPu).

The whole device is being carried by a precision (G440/X2W2) gonio for which a compact solution has been applied for its static balance (CW2-counterweight). On top (and, inside) of the last gonio, a cryostat (CS202SK) is being held through a dedicated interface. It is a relatively simple (reliable) and efficient (economical) instrument for low temperatures (4.2K ÷325K) experiments [10].

(Pm)d was built on precision gonio (G440/X2W1), having a very light (welded) arm, but with stiff structure. The detector is manually moved and fixed (dovetail slide).

The alignment base module (Pm)b was designed based on the existent table type (6204), providing stiff (1000kg) and short motions (Z, X, Rx) support for roughly alignment against the X-ray beam.

For the whole KDM design, different types of materials (e.g. steel, Al) has been carefully chosen as to be a compromise between own weight and stiffness

As precision was the main concern, modelling and simulations using Finite Element Analysis (FEA) have been performed iteratively to estimate the deflections and by this reducing (or, eliminating) them. Kappa arm being one of the critical components, simulations have been performed for both parts (κ_1, κ_2) in several critical configurations (0° - 120°). Figure 3 is showing von Mises stress distribution for second part(a2) in nominal position (0°), with maximal value (ϵ_{κ_2}) $_{max}$ =12.5 μ m occurring on the upper site of the surface adjacent to the rails. The variation across of the rail width (l) is given in a diagram (b).

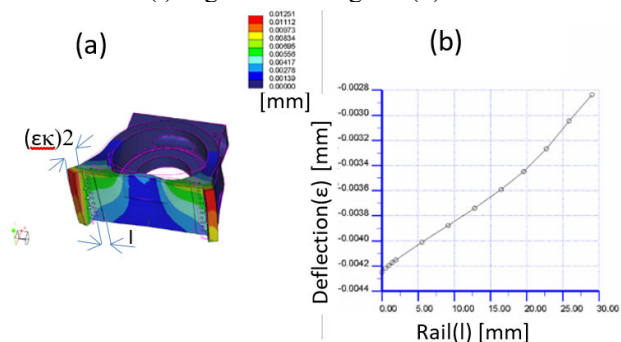


Figure 3: κ_2 deflection-a) distribution & b) variation.

Prototype

A first product based on above design considerations has been manufactured. Attention was given in the machining process for obtaining high quality of functional surfaces, respecting geometrical tolerances, as those in contact with important components (e.g. gonio, rails, etc). Then, in the assembly process care has been taken to mounting the components with highest precision, from earlier to the final stage, by performing fine adjustments. The control of the system with eleven (11) motorized axes has been realized using closed loop method (motors, gears, mechanism, encoder) based on a dedicated programmable hardware (SMC9300) with Ethernet interface and a PC with a pre-installed operation system (LINUX) and specific software (SPEC/C-PLOT).

The prototype was tested at factory site from functional and precision point of view. A factory acceptance test

(FAT) report was issued before the installation at the indicated premise. An overview of the set-up(a) and obtained results(b) are given in Fig. 4. The main source of runout errors values (negative) is coming along Z axis (14 μ m) when rotation angle is between (190° - 210°); the smallest ones (positive) encountered along X axis (3 μ m) is corresponding to 180° . As errors are with substantially increased values (negative) along Y axis around (150° - 240°) interval, we suspect that the effect is coming from a combined deformation result of components under an increased moment of own weight(s), especially in the maximum extension (180°). Runout errors for theta (ϵ_θ) and 2theta ($\epsilon_{2\theta}$) rotations have been around one ($\epsilon_\theta = \pm 1 \mu$ m) and few micrometres ($\epsilon_{2\theta} = \pm 2.5 \mu$ m) and, for phi (ϵ_ϕ) below 3 μ m ($\epsilon_\phi < 3 \mu$ m). The above values conducted us to consider a maximal value for the (sample) sphere of confusion (SoC=15 μ m) which is well behind the specification (SoC=30 μ m). In addition, precision measurements have been performed in relation with the geometry of axes. The orthogonality of (ϕ) vector was inside of eight arcsec interval ($\epsilon_{\phi \perp} = \pm 8''$, $\epsilon_{(\phi \perp) \min} = -8''/90^\circ$, $\epsilon_{(\phi \perp) \max} = 8''/270^\circ$) being below the requested value ($\epsilon_{\phi \perp} = 20''$). All values included the motion of a dummy cryostat (10kg) and the measurements have been performed with an electronic dial gage instrument (TT60/TESA/1 μ m) and a calibration ball (\varnothing 14mm). In addition, an electronic autocollimator (ELCOMAT 3000 / MÖLLER/ 0.01'') with plan-parallel mirror was used.

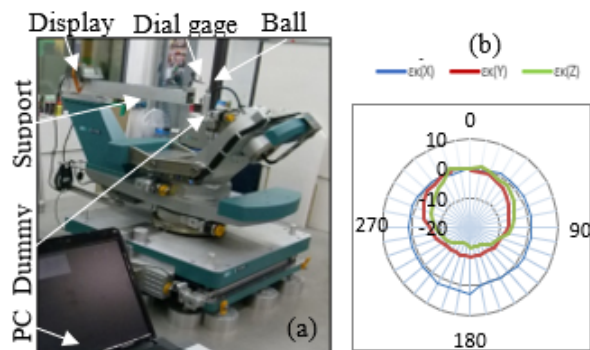


Figure 4: Measurements a) set-up and b) errors (ϵ_{Xmax} =4 μ m, ϵ_{Ymax} =10 μ m, ϵ_{Zmax} =15 μ m, $\kappa = \pm 180^\circ$).

CONCLUSION

A new kappa diffractometer (KDM) with improved precision capabilities for X-ray scattering investigations (XRS) of materials, to work in a 3rd generation upgraded synchrotron has been developed. Built on a classical four-circle (4C) concept, it has resulted as a fine balance between robustness and manipulability, including an innovative concept for fine alignments (Z) and compact (integrated) design solutions (Gonio, CW) for Kapa goniometer (KGM). Mainly, it offers an improved solution to manipulate instruments specific to cryo-conditions (4K) with appreciable load (20kg) and size (500mm) with highest available precision (SoC=15 μ m), using several types of detectors (1D/2D). Due to its modular design is prone to be adapted at other similar applications.

REFERENCES

- [1] C. Battocchio (Ed.), *Advanced Synchrotron Radiation Techniques for Nanostructured Materials*, MDPI, 2019, <https://doi.org/10.3390/books978-3-03921-681-9>
- [2] “Annual Report,” Pohang Accelerator Laboratory, PAL, 2019.
- [3] IBS(CALDES), 2020, www.ibs.re.kr
- [4] 4-Circle Kappa Diffractometer, Bid, IBS, 2017, www.ibs.re.kr/cop/bbs
- [5] “4-Circle Kappa Diffractometer, Draft-Proposal,” HUBER GmbH & Co. KG, 2017.
- [6] D. E. Nowack *et al.*, “Six-circle diffractometer with atmosphere- and temperature-controlled sample stage and area and line detectors for use in the G2 experimental station at CHESS”, *Rev. Sci. Instrum.*, vol. 77, p. 113301, 2006. <https://doi.org/10.1063/1.2372730>
- [7] HUBER Diffractionstechnik GmbH&Co.KG, 2020, www.xhuber.com
- [8] *NONIUS CAD4/MACH3 User Manual*, Nonius, 2000.
- [9] CREO 5, Design Package, <https://www.ptc.com/en/products/creo/packages>
- [10] CS202-DMX-2, <https://www.arscryo.com/cs202-dmx-2>

CRYOGENICS MONITORING AND CONTROL SYSTEM FOR EMBL FACILITIES AT PETRA III

Moises Bueno¹, Liliana Kolwicz-Chodak, Jochen Meyer, Uwe Ristau and Stefan Fiedler²
European Molecular Laboratory (EMBL), Hamburg, Germany

Abstract

At the integrated facility for structural biology of the EMBL at PETRA III on the DESY campus in Hamburg, several devices require cryogenic cooling with liquid nitrogen (LN₂). For the cryogenic devices local servers and clients have been created to monitor and operate the corresponding sensors, actuators and provide the safety logic. In addition, the local cryo-clients are integrated in a cryogenics supervision interface. The supervision client allows password protected access to three levels: monitoring, operator and expert. The monitoring level offers an overview of the status of all EMBL cryogenic sub-systems. At the higher access levels, cryogenic components can be also controlled. The application can be used from remote via a VPN connection or the TeamViewer software or a web client (in preparation). Because of the heterogeneity of the cryogenic devices different protocols for interfacing had to be applied.

INTRODUCTION

Cryogenic installations and their controls are key components of the infrastructure for many large research facilities [1-3]. This is also valid for smaller size structural biology facilities like the EMBL beamlines at PETRA III on the DESY campus in Hamburg where EMBL is operating a small angle scattering beamline for proteins in solution and two macromolecular crystallography beamlines. Cryogenic cooling with liquid nitrogen (LN₂) is needed for commercial or in-house built instruments like cryo-coolers to stabilize the temperature of the Double Crystal Monochromators (DCMs) under thermal load, cold gas stream units for cryo-protection of protein crystals during the different phases of an experiment and cryogenic sample dewars for robotic sample handling under LN₂. In order to communicate with the controllers of each device, servers and clients based on the TINE control system (Three-fold Integrated Networking Environment) developed by DESY [4] and the LabVIEW software suite [5] have been created, that monitor and operate the corresponding sensors, actuators and provide the safety logic. Depending on the options offered by the different controllers, the servers had to be interfaced with several other communication protocols such as EtherCAT [6], ADS-OCX [7] and EPICS [8]. The wide variety of instruments that have to be monitored and controlled, with single clients for each element, distributed over several computers on different beamlines, called for centralizing

the cryogenic information. For every beamline and/or laboratory, a central client has been written and an overarching cryo-client in which all cryogenic devices are combined that are operated at the EMBL PETRA III facilities.

MATERIAL AND METHODS

Hardware Components

LN₂ is supplied by central storage tanks managed by DESY to all consumers in the Max-von-Laue Hall where also the EMBL beamlines are situated. The EMBL installations comprise (see Fig. 1):

- three cryo-coolers for the DCMs (from FMB Oxford) [9] of the P12, P13 (type D cryo-coolers) and P14 beamlines (type XV cryo-cooler);
- four cold gas stream units for cryo-crystallography, ('cryostream 800' series by Oxford Cryosystems [10]);
- three LN₂ sample storage dewars for robotic protein crystal mounting, the in-house built MARVIN systems [11] at the P13 and P14 beamlines respectively and for the automatic Crystal Direct Harvester (CDH) system [12].

Hardware:

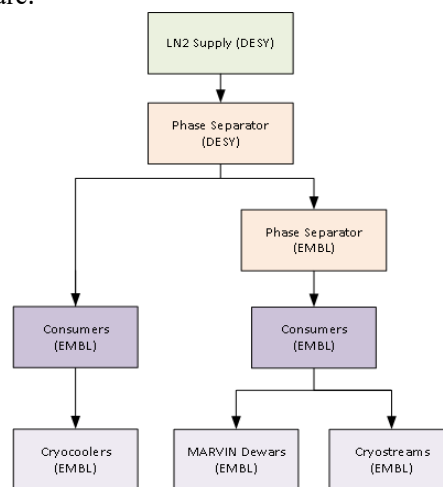


Figure 1: Cryogenics system: layered structure of hardware.

An additional 100 liter (Cryotherm [13]) phase separator has been installed on top of the macromolecular crystallography beamlines in sector-9 of the Max-von-Laue hall in order to achieve an efficient filling of the different LN₂ reservoirs (with exception of the ones for the DCM cryo-coolers).

The LN₂ consumers are connected by super insulated LN₂ transfer lines equipped with remotely controllable

¹m.bueno@embl-hamburg.de

²stefan.fiedler@embl-hamburg.de

valves. Signals from valves, from several different LN2 level sensor systems, temperature sensors, pressure gauges and from oxygen content monitors are fed into PLCs respectively PCs depending on the device.

PLC/PC Software and Interfaces

Due to the variety of systems by different suppliers, the data has to be read out using different protocols and technology. The general structure of the controls of the cryogenic system is depicted in Fig. 2.

a) The control server for the central LN2 supply under DESY responsibility, is based on EPICS (Experimental Physics and Industrial Control Systems) and is a read-only server for EMBL. This is achieved by using a gateway from where the relevant values can be transferred with the standard EPICS commands for 'Channel Access'. On the EMBL side, the data is distributed through TINE. For this, a TINE server has been created in order to handle the signals from the central LN2 tanks, the main phase separator, the sector-9 phase separator and its valves and pressure gauges. All signals are available in the entirely separate EMBL network.

The workflow of the server comprises only a few steps:

1. Initialization upon start of the program (in case of an error during initialization, the subsequent commands will not be executed).
2. Requesting data from DESY server using the EPICS command 'caget'.
3. Parsing of the string returned by the DESY server and pushing it to the TINE server.
4. Repetition of steps 2 and 3 to read more data.

b) The cryo-cooler at the P14 beamline was the first upgraded to the FMB Oxford XV type, equipped with a controller using EPICS. Therefore, a new program has been written using LabVIEW. This piece of software is at the same time an EPICS client and a TINE server. Its main function is to read out the data from the EPICS server and push it into the TINE server.

For the older type D cryo-coolers installed at the P12 and P13 beamlines, the standard TINE installation could not be used because of superseded hard- and software. Therefore, the readout has been achieved using an ADS-OCX API running on a BC9100 bus controller module by Beckhoff. Readouts have to be converted afterwards on the server side by a LabVIEW-TINE server. Depending on the nature of the signals (current, voltage, frequency etc.) different conversions of the raw data have to be applied before making them available on the entire network.

c) The cryostream 800 controller uses a firmware called *cryoconnector*. Once the controller is connected to a computer through USB, the software creates three XML files (Connection.xml, Commands.xml, Status.xml) containing the ID of the device, status variables and commands for execution.

The XML files are accessed using LabVIEW for reading out the information or sending a command. Four LabVIEW routines verify the connection and data path, read or send information (ReadConnections.vi, ReadStatus.vi, ReadInfo.vi and SetTemp.vi).

Software:

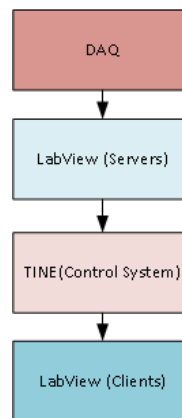


Figure 2: Cryogenics system: layered structure of software.

d) Most of the instruments at the EMBL PETRA III beamlines are controlled by Beckhoff PLCs [13]. In this manner are handled also:

- the automatic filling/refilling with LN2 of the MARVIN sample changer dewars,
- the monitoring and control of valves in the LN2 transfer lines of the EMBL LN2-subnet,
- the cryogenic gas streams at the beamlines and the CDH,
- different LN2 level sensors systems with analog and digital outputs [14, 15],
- personnel and instrument safety logic related to LN2 usage.

A server based on the powerful Common Device Interface (CDI) offered by TINE can be created by simply preparing a configuration file. It allows linking the variables in the PLC with the properties of the TINE server pushing the data to the server as soon as the values change in the PLC. As this type of server has no graphical user interface (GUI), but instead uses a prompt window of the operating system only, it calls for a generic client (see next paragraph).

Software Clients

Depending on the purpose and on the target group, three types of clients have been developed to monitor and control the cryogenic devices.

Initially, individual clients have been provided to configure and control single devices on an expert level.

Another type of client has been created in order to provide to a beamline operator an overview of all devices in one of the beamlines or in the laboratory at one glance (for an example see Fig. 3).

A third interface called 'Cryogenic Supervision System' gives access to all information shown in the clients described above, i.e. all cryogenic installations of EMBL at PETRA III to a cryogenic expert (see Fig. 4). This client can be accessed remotely using VPN connection, TeamViewer software [16] or a web client. This increases the versatility of the system, especially in situations when errors occur and the expert in charge is not on site, such as

- [8] EPICS, <https://epics.anl.gov/>
- [9] FMB Oxford, <https://fmb-oxford.com>
- [10] Oxford Cryosystems, <http://oxcryo.com>
- [11] U. Ristau *et al.*, “MARVIN Update - the Robotic Sample Mounting System at the EMBL-Hamburg”, in *Proc. PCaPAC2018*, Hsinchu, Taiwan, October 2018, pp. 163-166. DOI: 10.18429/JACoW-PCaPAC2018-THP03
- [12] F. Cipriani *et al.*, “CrystalDirect: a new method for automated crystal harvesting based on laser-induced photoablation of thin films”, *Acta Crystallogr., Sect. D: Biol. Crystallogr.*, vol. 68, pp. 1393-1399, 2012. DOI: 10.1107/s0907444912031459
- [13] U. Ristau, A. Kolozhvari and S. Fiedler, “The EMBL beamline control framework BICFROK”, in *Proc. PCaPAC2014*, Karlsruhe, Germany, October 2014, paper pp. 60-62. <https://accelconf.web.cern.ch/PCaPAC2014/papers/wpo012.pdf>
- [14] Cryotherm, www.cryotherm.de
- [15] American Magnetics, Inc., <http://www.americanmagnetics.com>
- [16] TeamViewer, <https://www.teamviewer.com>

ASSESSMENT OF THE CORROSION OF COPPER COMPONENTS IN THE WATER COOLING SYSTEM OF ALBA SYNCHROTRON LIGHT SOURCE; PRESENTATION OF A PROPOSAL TO MITTIGATE THE CORROSION RATE OF COPPER

M. Quispe[†], E. Ayas, J.J. Casas, C. Colldelram, M.Ll. Fuentes, J.C. Giraldo, J. Iglesias, M. Pont
ALBA – CELLS Synchrotron, Cerdanyola del Vallès, Spain
J. Buxadera, M. Punset, Universitat Politècnica de Catalunya, Barcelona, Spain

Abstract

This paper presents the most recent results on the corrosion of copper components in ALBA water cooling system. The studies have been carried out using a variety of techniques: Scanning Electron Microscopy (SEM), Energy-Dispersive X-Ray Spectroscopy (EDS) and X-Ray Diffraction (XRD).

Representative samples of the Accelerator Facility were examined: Storage Ring Absorbers, Front End Masks, Radio Frequency Cavity Pipes, Experimental Line Mask, Radio Frequency Plant Pipes at Service Area and Booster Quadrupole.

The studies show the presence of intergranular, pitting and generalized corrosion. The presence of Copper Oxide is confirmed, as well as other elements such as Aluminum, Carbon, Sulfur, Silver, Calcium, Silicon, Titanium and Iron in some regions of the samples. Likewise, other elements from circulating water such as Potassium and Chlorine have also been detected. The depth of pitting corrosion is less than 119.4 μm for the samples studied, after 10 years of operation.

To minimize the corrosion problem, an upgrade of the ALBA cooling system is under study. The objective is to reduce the current corrosion rate by a conservative factor of 5. This change is possible by modifying the characteristics of the cooling water, reducing the dissolved oxygen content to values below 10 ppb and increasing the pH above 7.5. Technical aspects of this upgrade are discussed in this paper.

BACKGROUND

The phenomenon of copper corrosion has been studied with special interest in the field of accelerators, due to its impact on the equipment life of the installation, and on the efficient and continuous operation of the deionized water cooling system. Specifically, corrosion can cause an increase in the pressure drop of the components and hydraulic interfaces, loss of thermal dissipation capacity, clogging in water cooling circuit resulting from the deposition of corrosion products, and in a worst scenario crack of the absorbers located inside the vacuum chambers.

At ALBA, after 10 years in operation, there are some indications may be attributed to corrosion, such as: (i) agglomeration of oxide particles in some small cavities of regulation valves that cause a localized decrease in water

flow and (ii) malfunction of flow switches due to accumulation of oxide particles in its orifice plate geometry. In order to understand and mitigate these effects, we are investigating the state of corrosion of copper components and planning preventive actions.

THE ALBA WATER COOLING SYSTEM

By design, the ALBA cooling system is a hydraulic closed loop [1]. It consists of four main rings which feed the local consumption of the Service Area (SA), Booster (BO), Storage Ring (SR) and Experimental Area (EA) (see Fig. 1). The water is heated through all the rings and it is collected in a common return. The total water flow for the accelerator is approximately 525 m^3/h .

By means of a reverse osmosis plant, the conductivity of water is controlled at 0.2 $\mu\text{S}/\text{cm}$. The average values of pH and dissolved oxygen (DO) content are 7 and 6500 ppb, respectively, both properties are not actively controlled.

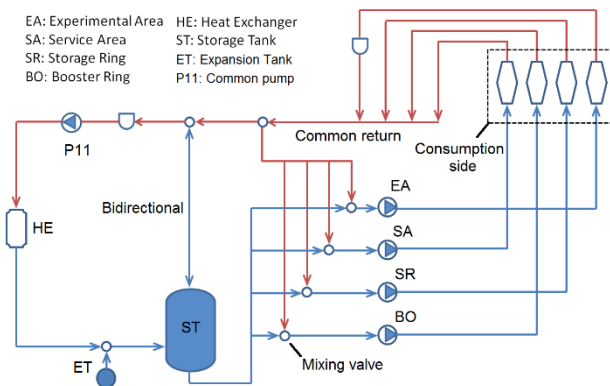


Figure 1: ALBA cooling system scheme.

Antecedent: Irregular pH Evolution

The pH is one of the main parameters involved in copper corrosion. As a practical number, it is recommended to have the water with a pH above 7.5. In Fig. 2 the evolution of the pH in ALBA is represented for the last 9 years. According to this result, most of the time the average pH value has been 7, but irregular values of 5.5 to 6.5 are reported for the years 2013 and 2014. Very high pH values (between 8 and 8.5) have also been found during the year 2012. It is assumed as a hypothesis that the pH data in the first years have been affected by problems in the instrumentation.

[†]mquispe@cells.es

Content from this work may be used under the terms of the CC BY 3.0 licence (© 2021). Any distribution of this work must maintain attribution to the author(s), title of the work, publisher, and DOI

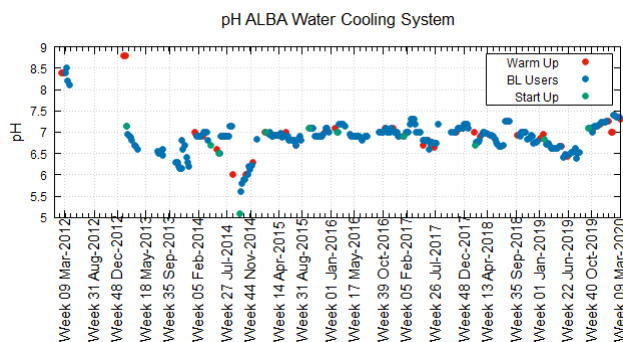


Figure 2: PH values in the ALBA deionized water cooling system, for the period 2012 to 2020. The data are weekly average values.

CORROSION STUDIES OF COPPER COMPONENTS

Nine representative samples of the ALBA deionized water cooling system were analyzed: Glidcop Al-15 Crotch Absorber (S1), OFHC Copper Crotch Absorber (S2), Copper Masks of the Front Ends BL11 (S3) and BL13 (S4), Copper Radio Frequency Cavity (S5), Copper Mask in Beam Line BOREAS (S6), Copper Circulator in Service Area (S7), and Copper straight (S8) and bent (S9) pipes of a Quadrupole of the Booster.

Naked-Eye Detection of Corrosion-Erosion

In the first visual analysis, high roughness was observed on the internal surfaces of the samples, such as the example in Fig. 3a, 3b and 3c, corresponding to samples S4, S3 and S5. In other cases, such as in Fig. 3d, the surfaces were characterized by having a smooth morphology, with a brown dark colour, indicative of the formation of oxide layers. In various parts of the system, deposits of oxide particles have been found, presumably they are copper oxide particles.

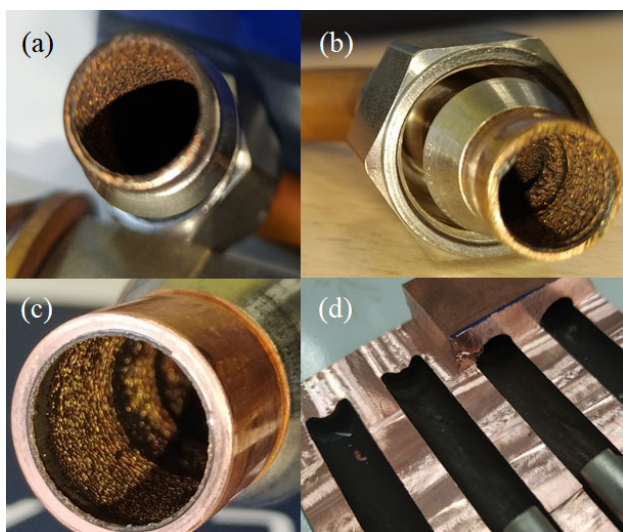


Figure 3: Images of four samples under study: Copper Masks of the Front Ends (a) BL13 and (b) BL11, (c) Copper Radio Frequency Cavity and (d) Glidcop Al-15 Crotch Absorber.

Corrosion Studies Based on SEM, EDS and XRD

We set a cooperation agreement with the Polytechnic University of Catalonia (UPC) [2] for the study of corrosion, by means of superficial observation by Scanning Electron Microscopy (SEM), Energy-Dispersive X-Ray Spectroscopy (EDS) and X-Ray Diffraction (XRD).

The samples S1, S2, S3, S4 and S5 show pitting corrosion on their surfaces (see example of Fig. 4b, sample S1). In addition, the samples S1, S2, S3 and S4 show generalized corrosion. As a particular case, the sample S5 exhibits intergranular corrosion. In some regions of samples S1, S2, S3, S4 and S5 the EDS analysis has confirmed the presence of Copper, Oxygen, as well as other elements such as Sulfur, Silver, Chlorine and Calcium (see example of Fig. 4c, sample S1). The cross-sectional analysis of samples S1, S2, S3, S4 and S5 has determined the pit depth, with values between 3.84 and 101.5 μm . The XRD analysis has confirmed the presence of copper oxide on the inner surface of samples S1, S2, S3, S4 and S5.

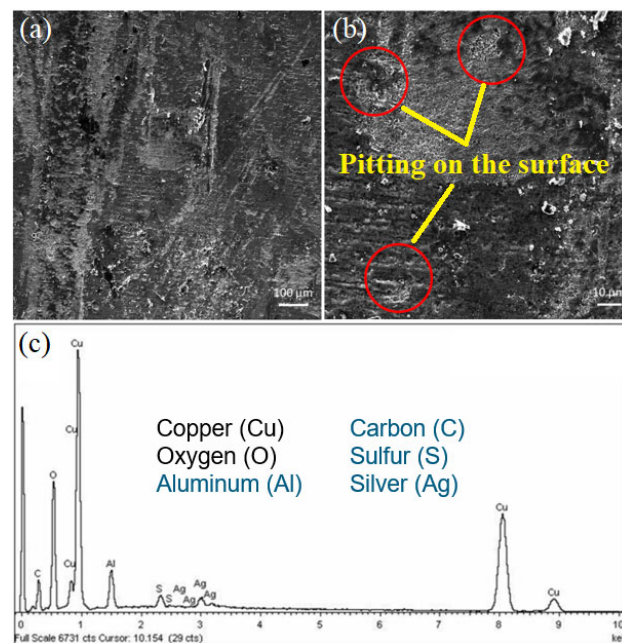


Figure 4: Study of sample Glidcop Al-15 Crotch Absorber. SEM images, (a) and (b): internal surface with detail of pitting. (c) EDS results reveals Copper, Oxygen and Aluminium as original components; also, Sulfur in the corroded areas is observed, as well as Carbon and Silver in some regions.

The samples S6, S7, S8 and S9 show pitting corrosion on their interior surfaces, with the presence of Cl⁻ ions in some of their semi-quantitative EDS composition spectra. The samples S6 and S7 show generalized corrosion on their inner surface, in the form of a dark-colored oxide layer. The samples S8 and S9 did not show the presence of a homogeneous oxide layer, but rather signs of pitting and crevice corrosion, respectively (see example of Fig. 5a and 5b, sample S9). In some regions of samples S6, S7, S8 and S9 the EDS analysis has confirmed the presence of Copper

and Oxygen, as well as other minor elements of the different base metal compositions such as Sulfur, Silver, Carbon, Silicon and Iron (see example of Fig. 5c, sample S9). Likewise, other elements from circulating water such as Potassium and Chlorine have also been detected. The recurrent presence of Chlorine in the EDS spectra carried out on the corrosion oxides present in the samples S6, S7, S8 and S9, would establish a cause-effect relationship between the presence of chlorides in the circulating water and the action of pitting and crevice corrosion. The pit depth present in samples S6, S7, S8 and S9 is in the range between 1.82 and 119.4 μm and the XRD analysis of the oxidized surfaces has confirmed the presence of two crystalline copper oxide phases on the inner surfaces, a first phase corresponding to metallic copper (JCPDS 85-1326) and the second corresponding to standard copper oxide (JCPDS 48-1548).

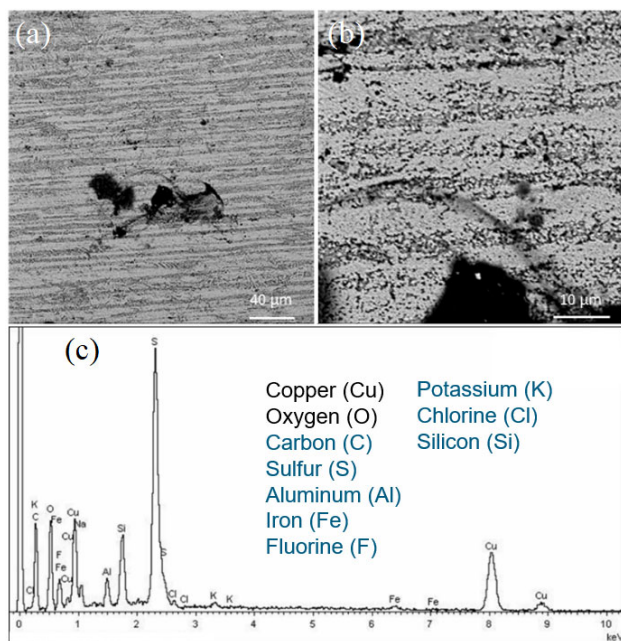


Figure 5: Quadrupole sample (bent pipe). SEM results, (a) and (b): not generalized corrosion with presence of pits. (c) EDS spectra: presence of Copper, Oxygen, Potassium, Aluminium, Silicon, Iron, Carbon, Fluorine, Sulfur and Chlorine.

CONCLUSIONS

This work shows that generalized, pitting and intergranular corrosion are present in the studied samples.

The depth values in the pits are less than 119.4 μm . From the point of view of mass loss, this value is not critical for masks and crotch absorbers, but pits are the sources for crack initiation.

Corrosion products, in the form of copper oxide, tend to accumulate in cavities with complex geometries such as regulating valves. This fact explains the flow reduction that appears occasionally in local components, especially after periods of shutdown.

The agglomeration of corrosion products in the flow switches, around their orifice plate, is an explanation of the

malfunction of this equipment, problem that occurs sometimes in ALBA.

To minimise the effects of corrosion, there is a consensus solution applied by complex facilities: improve the quality of deionized water [3–9]. This alternative is represented in the experimental curve in Fig. 6. Depending on the combination of pH versus (DO) content, the copper components have different corrosion rates (regimes 1, 2, 3, 4 and 5). Regime 1 is the preferred option, where the water is characterized by having (DO) content values < 10 ppb and pH > 7.5. In the case of ALBA, due to the fact that the pH has varied irregularly during the last 10 years, is assumed the hydraulic system has operated in regimes 3, 4 and 5.

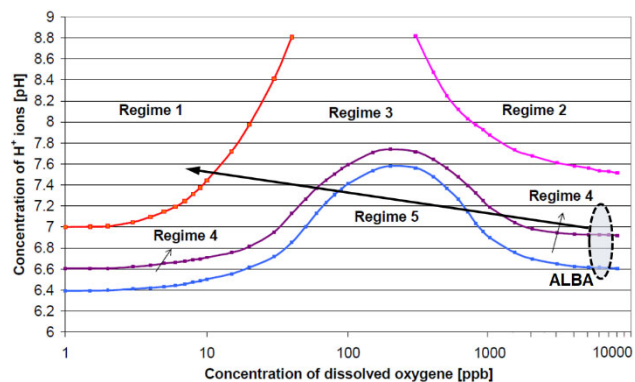


Figure 6: Copper corrosion rates. Regimes 1 and 2: < 0.1 $\mu\text{g}/(\text{cm}^2\text{y})$, regime 3: 0.1-0.4 $\mu\text{g}/(\text{cm}^2\text{y})$, regime 4: 0.4-1 $\mu\text{g}/(\text{cm}^2\text{y})$ and regime 5: > 1.0 $\mu\text{g}/(\text{cm}^2\text{y})$. According to historical data, ALBA has operated in regimes 3, 4 and 5. The optimization objective is to operate in regime 1.

For the future, the ALBA's objective is to operate in regime 1. It is planning to have an Oxygen Degassing Plant to reduce the current (DO) content from 6500 ppb to values below 10 ppb. This means an average reduction of corrosion rate by a factor of 5. But prior to this step we are investigating the causes of the very high values in (DO) content that we have, considering that by design our circuit is a hydraulic closed loop. For a closed system (assuming negligible oxygen ingress), the concentration of DO will approach zero because all DO will be consumed by the corrosion process. This does not occur at ALBA.

It is known that a high velocity between a corrosive fluid and a metallic surface tends to accelerate the corrosion. The modification of the criteria of the maximum velocity for the design of components in ALBA, from 3 to 2.5 m/s, is under discussion.

As part of the optimization task, the instrumentation for the control and monitoring of pH, Conductivity and (DO) content will be expanded. The monitoring of rings EA, SR, BO and SA is of special interest.

REFERENCES

- [1] M. Quispe, "Cooling Water System in the Field of Accelerators", Open SESAME Project, Barcelona, Spain, October 2018.
- [2] Biomaterials, Biomechanics and Tissue Engineering BBT, <https://biomaterials.upc.edu/ca>

- [3] D. Katonak *et al.*, “Water Purity Development for the Coupled Cavity LINAL (CCL) and Drift Tube LINAC (DTL) Structures of the Spallation Neutron Source (SNS) LINAC”, in *Proc. 2001 Particle Accelerator Conference*, Chicago, IL, USA, June 2001, paper TPAH097, pp. 1432-1434.
- [4] J.C. Chang *et al.*, “Current Status of the De-Ionized Cooling Water System and Improvement at TLS”, in *Proc. MEDSI04*, ESRF, Grenoble, France, May 2002.
- [5] R. Dortwegt *et al.*, “Mitigation of Copper Corrosion and Agglomeration in APS Process Water Systems”, in *Proc. MEDSI02*, APS, Argonne, Illinois U.S.A, September 2002, pp. 462-468.
- [6] S. Suhring, “Accelerator Availability and Reliability Issues”, in *Proc. 2003 Particle Accelerator Conference*, Portland, OR, USA, May 2003, paper ROPB007, pp. 625-629.
- [7] B. Adak, “Copper Corrosion and Clogging in APS Deionized Water Cooling System”, Doctoral Thesis, Illinois Institute of Technology, Chicago, Illinois, May 2009.
- [8] N. Hammond, “Cooling Water Chemistry, Corrosion Products and their effect on Accelerator Operation at the Diamond Light Source”, in *Proc. MEDSI 2012*, SSRF, Shanghai, China, October 2012.
- [9] P. Czernecki *et al.*, “Technical Overview of the SOLARIS Low-Conductivity Water Cooling System”, in *Proc. IPAC2017*, Copenhagen, Denmark, May 2017, paper WEPVA082, pp. 3449-3451.
<http://dx.doi.org/10.18429/JACoW-IPAC2017-WEPVA082>

FABRICATION OF THE TRANSITION SECTION OF A CORRUGATED WAKEFIELD ACCELERATOR VIA LASER MICROMACHINING*

P. Bado†, M. A. Dugan, and A. A. Said, Translume, Inc., Ann Arbor, MI, 48108, USA
S. Siy, K. Suthar, A. Zholents, Argonne National Laboratory, Lemont, IL, 60439, USA

Abstract

A wakefield accelerating structure is being designed to facilitate sub-terahertz Čerenkov radiation. This accelerating structure consists of several sections of internally corrugated tubes, that are coupled together using transition sections. The fabrication of these transition sections is presented. Modelling of various fabrication errors was undertaken to understand their effect and to determine fabrication tolerances. Source of machining imperfections are reviewed and their impact compared to the modelling results.

INTRODUCTION

A cylindrical, corrugated wakefield accelerating (CWA) structure [1] is being developed to create sub-terahertz Čerenkov radiation produced by an electron bunch. The accelerating structure consists of several copper-based, 50-cm long, sections of internally corrugated tubes with a 1-mm inner-radius. These elements are coupled together using ultra-compact transition sections, as shown in Fig. 1, which are also copper-based.

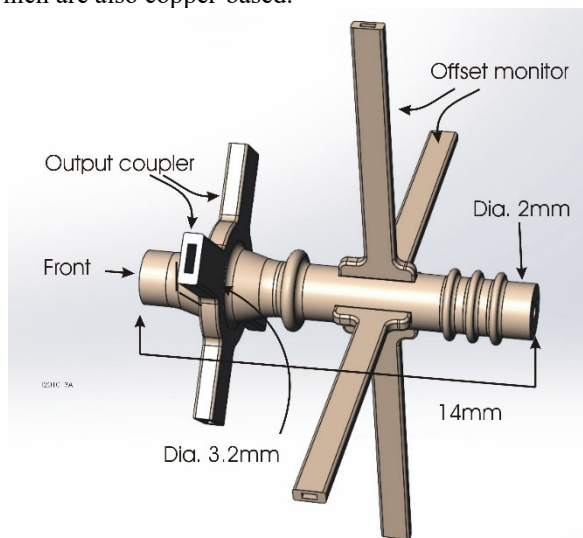


Figure 1: Model of the inner volume of a transition section, with main dimensions.

Beside their mechanical and vacuum coupling functions, these transition sections provide a means to monitor the centering of the electron bunch, and to couple out unused energy in the TM01 accelerating mode from the corrugated

waveguide while allowing the TE11 transverse mode to pass through. The output coupler is expected to extract on the order of a kilowatt of power.

FABRICATION APPROACH

The fabrication is divided into four main steps: First, a fused silica glass mandrel is fabricated. Its external shape corresponds to the internal volume of the transition section. Second, a thin layer of Gold is sputtered onto the surface of this glass mandrel, and subsequently a thick copper layer is electro-deposited on top of the gold. Third, the glass mandrel that is at the core of this assembly is etched away, leaving a hollowed copper shell with the desired internal geometry; and finally secondary machining operations, such as milling and drilling, generate the external end faces and other reference surfaces required for the integration of the transition section into the general CWA structure.

The first step – the fabrication of the sacrificial fused silica glass mandrel- is based on a sequential combination of laser irradiation and chemical etching [2], as illustrated in Fig. 2. Shape-contouring is introduced by illuminating a defined pattern with a laser generating ultrashort pulses. The pulse energy is set sufficiently low to avoid ablation, yet high enough to locally modify the short-range ordered fused silica molecular matrix.

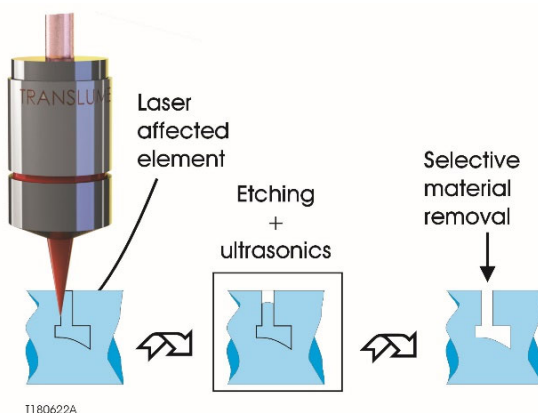


Figure 2: The two-step glass shaping process - Laser direct write, followed by selective etching.

With the proper processing parameters, the laser-exposed volume elements (*i.e.* voxels) etching susceptibility is greatly increased. This localized enhanced etching is used to shape the desired glass part geometry. One of the key metrics associated with this part of the fabrication process is the ratio of the etching rate of the laser-exposed voxels versus the etching rate of the virgin fused silica glass. Under optimized conditions this etching ratio can exceed 100:1, but it degrades rapidly with the depth of the laser processing.

* This manuscript is based upon work supported by the Director, Office of Science, Office of Basic Energy Sciences, of the U.S. Department of Energy under Contract No. DE-AC02-06CH11357; and by the Office of Science, SC-1, U.S. Department of Energy under Award No. DE-SC0019677.

† pbado@translume.com

FABRICATION DETAILS

The transition section has a central body with a rotational geometry, and two sets of four waveguides that are perpendicular to the main axis. The main body diameter ranges from 2 mm to 3.2 mm (not including the two sets of orthogonal waveguides) and the length is approximately 14 mm. These various dimensions correspond to the inner geometry of the final copper interface section. Due to spatial and temporal aberrations, the intensity and the shape of the laser focal spot change drastically with the depth of the laser processing. This limits the depth of the laser writing to approximately 3.5 mm. The transition section has dimensions that exceed this limit. To address this issue, the transition section is divided into several sub-units that independently fit in the machinable volume.

Initially the transition section was divided in a main cylindrical section, to which lateral waveguides were subsequently attached (either in group or separately) using an epoxy, as illustrated in Fig. 3. With this fabrication approach, the cylindrical section main axis rested perpendicular to the laser writing beam. The lateral waveguides were written separately, and they were subsequently epoxied to the main body. This approach resulted in relatively large errors exceeding the maximum allowable tolerances, as defined from simulations. Several sources of errors were identified: The epoxy thickness could not be reproducibly controlled; the etching ratio was poor (this is indirectly related to the cylindrical section main axis being perpendicular to the laser axis); and the lateral waveguides could not be aligned accurately with the device main axis.

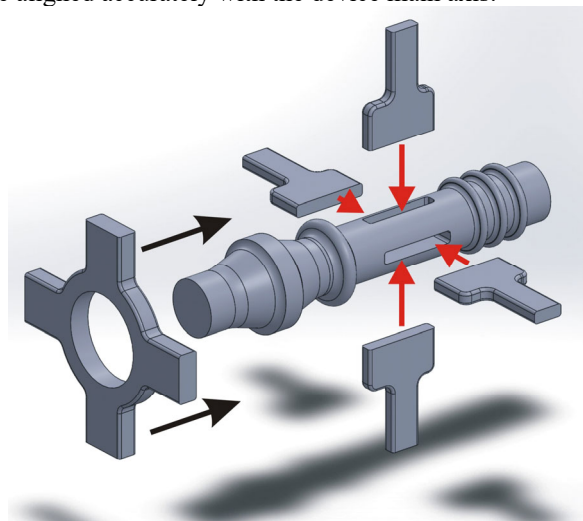


Figure 3: Exploded schematic view of a transition unit consisting of a central cylindrical into which waveguides are attached.

The division of the transition section into sub-elements was modified to address these issues. Shorter sections that can be fabricated with the laser axis parallel to the sub-elements central axis are now used. The various elements are no longer epoxied. Rather they are mechanically held together during the sputtering and the electroforming. The lateral waveguides are fabricated as stand-alone units comprising all four arms.

This approach offers a fair amount of flexibility as to where the divisions between the various subunits are located. However, due to the height restrictions discussed above, numerous sub-elements are required. Several configurations are being explored. In one configuration, the transition element is divided into twelve main elements, some of which have identical geometry but different lengths, as shown in Fig. 4. Once the various fused silica glass sub-elements have been fabricated, the transition section is assembled by sliding them onto a precision-machined stainless steel pin. This master pin forms the backbone of the assembly. It provides the main mechanism to insure concentricity between the sub-elements. During the ensuing fabrication steps, the sub-elements are held tightly together using jigs with compression springs.

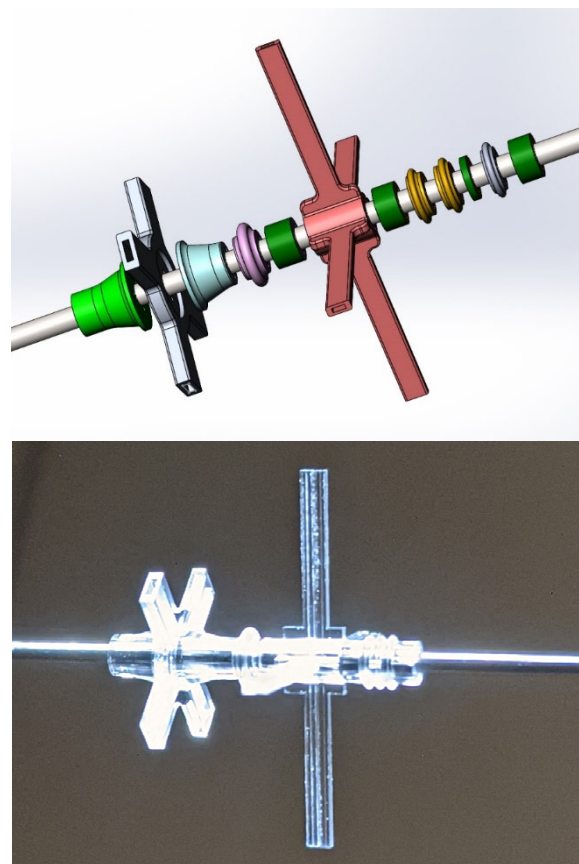


Figure 4: (Top) Exploded schematic view of a transition unit consisting of twelve glass elements and one metal pin. (Bottom) Corresponding assembled glass demonstrator.

Modelling of the transition section was used to determine the maximum acceptable fabrication deviations from the design intent. The impact of any waveguide offsetting was studied for both the TM01 coupler and the beam offset monitor. Based on this simulation, it is estimated that the maximum acceptable TM01 coupler lateral offset is $50\mu\text{m}$. The system is more susceptible to offsets along the main (Z-) axis.

The impact of concentric misalignments (radial shift) between adjacent elements forming the transition section was also modelled, as shown in Fig. 5.

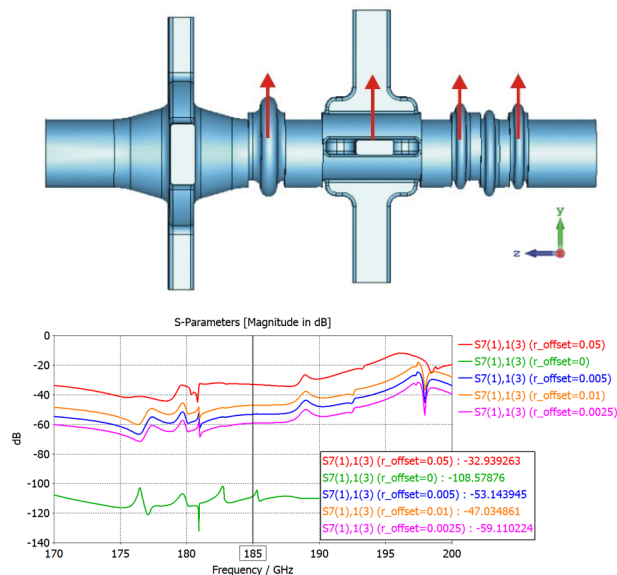


Figure 5: (Top) Schematic view showing radial offsets between adjacent elements of the transition section. (Bottom) TE11 Isolation from TM01 as function of radial offset.

The total radial offset between adjacent sections should not exceed 10 microns.

Deviations from the design intent are associated with various parts of the fused silica glass elements: While the stages moving the substrate have a positioning accuracy that is better than 1 micron, the change of the laser spot shape with the depth of the laser processing results in larger dimensional nonconformities. The etching process introduces further divergences from the design intent. These are related to the time it takes for the etchant to reach a given voxel. This is a strong function of the depth of the feature and the local geometry. However, these etching and focal spot deviations are reproducible, and through trial and error can be mostly compensated, as illustrated in Fig. 6. We project that the residual errors due to the laser writing and the etching will be less than 10 microns for any critical dimensions of any given sub-element.

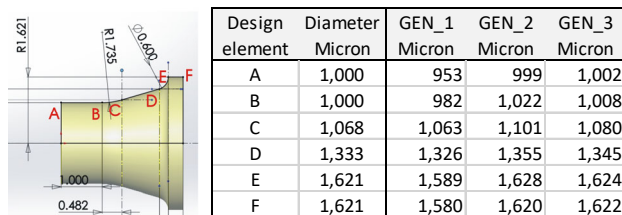


Figure 6: (Left) Drawing of one of the transition section's elements. (Right) Metrology data from successive device.

The diameter of the central hole (used for the alignment pin) is the most critical dimension, and the etching is stopped once this diameter reaches a predetermined value. The associated dimensional error is less than 3 microns. Radial offsets (Fig. 7) are held below the 10- μ m limit established from simulations.

The length of each element (along the central axis) is presently adjusted by selecting a fused silica substrate of

the proper thickness. This introduces another source of error. To minimize its impact, the number of glass elements is being reduced through the combination of shorter adjacent ones. This part reduction effort will also eliminate other imperfections.

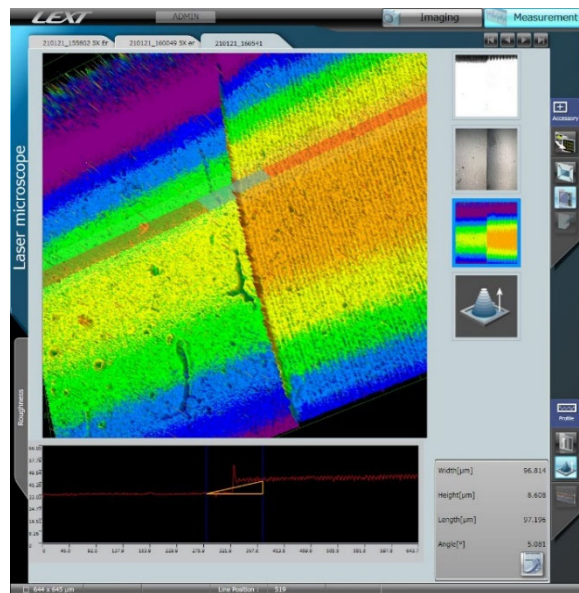


Figure 7: Radial offsets between adjacent sub-elements.

Subsequently a thin layer of Gold is sputtered onto the mandrel. This layer serves as a conductive seed for the copper electroforming. The copper is electrodeposited using a recipe optimized to minimize electric breakdown [3].

CONCLUSION

An ultra-compact transition section of a corrugated wakefield accelerator is fabricated by electro-depositing copper onto a sacrificial fused silica glass mandrel. While a full copper demonstrator has yet to be produced, it appears that the deviations from the design intent associated with the glass mandrel fabrication are within the range established through simulations.

REFERENCES

- [1] A. A. Zholents and W. M. Fawley, "Proposal for intense attosecond radiation from an X-ray free-electron laser," *Phys. Rev. Lett.*, vol. 92, no. 22, p. 224, 2004. doi:10.1103/PhysRevLett.92.224801
- [2] Y. Bellouard, A. Said, M. Dugan, and P. Bado "Fabrication of high-aspect ratio, micro-fluidic channels and tunnels using femtosecond laser pulses and chemical etching", *Opt. Express*, vol. 12, pp. 2120-2129, 2004. doi.org/10.1364/OPEX.12.002120
- [3] S. Kobayashi *et al.*, "Electrical breakdown characteristics of electroformed copper electrodes in vacuum", in *Proc. ISDEIV. 19th International Symposium on Discharges and Electrical Insulation in Vacuum* (Cat. No.00CH37041), pp. 41-44 vol.1, 2000. doi: 10.1109/DEIV.2000.877247

STUDY OF COPPER MICROSTRUCTURE PRODUCED BY ELECTROFORMING FOR THE 180-GHz FREQUENCY CORRUGATED WAVEGUIDE*

K. Suthar[†], G. Navrotski, P. Carriere¹, and A. Zholents
Argonne National Laboratory, Lemont, IL, USA
¹RadiaBeam Inc., Santa Monica, CA, USA

Abstract

Fabrication of the corrugated structure that generates a field gradient of 100 MV m^{-1} at 180 GHz is a challenge, requiring unconventional manufacturing methods. The corrugated waveguide with 2-mm-inner-diameter will be produced by electroplating copper on the aluminum mandrel as proposed in [1]. A thin seed layer is usually applied to achieve uniform wetting of the plated copper on the aluminum mandrel. The copper waveguide is retrieved by removing the mandrel. Uniform copper plating and etching of the aluminum are crucial steps to keep the surface uniformly smooth and free of impurities that are especially necessary for the vacuum RF application. Previous studies suggest that electroplated copper has variations in both electrical and mechanical properties compared with those of bulk copper from batch production. In this paper we discuss the copper microstructure produced by the electroforming method and a literature study on variations, which can be attributed to disparity in the crystalline grain structure of the plated material.

INTRODUCTION

A 0.5-m-long, 1 mm internal radius, miniature cylindrical corrugated waveguide accelerator (CWA) is being proposed [2] and designed to create sub-terahertz Čerenkov radiation produced by an electron bunch traveling longitudinally on the centerline of the corrugated waveguide [1]. The dimensions of the corrugated structure are shown in Fig. 1. While the RF design [3] and prototype fabrication efforts are under development [4], we are investigating the limits of operating conditions based on the heat transfer and mechanical robustness of the structure during operation via fully coupled multiphysics finite element analyses.

The corrugated structure operates at 180 GHz with a transformer ratio of 5 that can deposit about 600 W of heat load at 10 kHz repetition rate on the inner surface of the corrugation and the transition section. The RF-heat-load deposition increases along the length of the structure producing a temperature gradient that can generate progressively higher thermal expansion in the downstream direction. Estima-

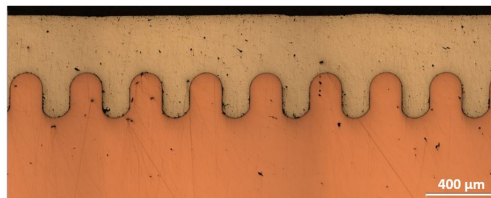


Figure 1: A micrograph of a section of the copper corrugated waveguide on an aluminum forming mandrel.

tion of unavoidable fabrication errors and the differential dimensional changes due to thermal expansion are crucial for achieving the required performance from the corrugated waveguide. The resulting thermal stress from the differential thermal expansion can lead to tensile-yield failure. Such failure can generate arcing due to surface cracking that ultimately causes loss of the beam. Operating parameters, such as energy and repetition rate, are the deciding factors for how much energy and how fast heat will be deposited on the structure. Therefore, fabrication acceptance criteria are also critical in reducing the beam instabilities that are potentially caused by fabrication errors. To quantify such behavior and to evaluate the mitigation scheme in the high-frequency structure, we are investigating the thermal budget for the structure via careful and detailed finite element analyses [1].

ANALYSIS

The Geometry

The corrugated waveguide geometry is shown in Fig. 1, and further details can be found in [4]. The CWA length with the corrugated waveguide is 0.5 m.

Table 1: Dimensions of Corrugation

Dimension	Value
a - Waveguide inner radius)	1 mm
d - Corrugation depth	263 μm
t - Corrugation tooth width	160 μm
v - Corrugation spacing	340 μm
r - Corrugation corner radius	80 μm

Fabrication Considerations

The corrugated waveguide is produced by electroplating copper on an aluminum mandrel. A thin seed layer of copper, measuring $2.0 \pm 0.5 \mu\text{m}$ in thickness is usually applied

* This research used resources of the Advanced Photon Source, a U.S. Department of Energy (DOE) Office of Science User Facility and is based on work supported by Laboratory Directed Research and Development (LDRD) funding from Argonne National Laboratory, provided by the Director, Office of Science, of the U.S. DOE under Contract No. DE-AC02-06CH11357.

[†] suthar@anl.gov

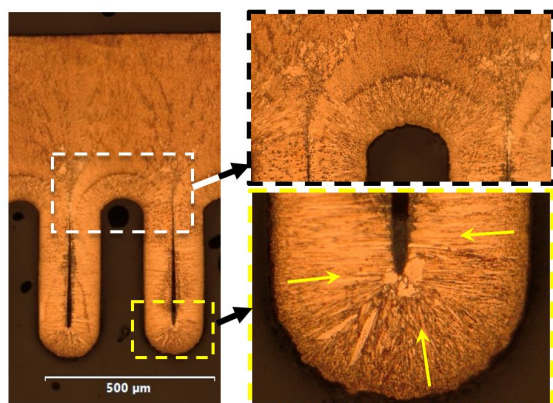


Figure 2: Cross section of an early prototype of an electroformed copper waveguide. (left) Etched microstructure of two corrugations. (top right) Magnified view of the corrugation root radius showing the dramatic change in crystalline morphology at the ‘pinch point’ where copper grains from adjacent corrugations collide, resulting in the creation of a central void along the convolution axis. (bottom right) Magnified view of the waveguide inner diameter corrugation radius with highly directional, acicular crystalline growth highlighted by yellow arrows.

to achieve uniform wetting of the aluminum mandrel. Bulk copper is subsequently layered by electroplating until the full thickness of the component has been achieved. The completed copper waveguide is retrieved by chemical dissolution of the aluminum mandrel. Preparation of the mandrel, uniform copper plating of the seed layer, electrodeposited growth of the bulk component, and the subsequent removal of the aluminum mandrel are all crucial steps to produce a waveguide with vacuum-side surfaces that are smooth, uniform, and free of impurities, which are especially necessary for corrugated waveguide accelerators. In addition, previous studies suggest that electroplated copper has variations in both electrical and mechanical properties compared with those of bulk copper from batch production. These variations can be attributed to disparities of the crystalline grain structure in plated material [5].

In an electroplating bath the deposition of copper atoms follows the lines of electrical potential. As a result, the grain growth direction is perpendicular to the surface being plated, in this case, an aluminum mandrel surface. The dynamic growth process can be impeded by changes in the geometry and flow of electrolytes. This leads to variation in growth rate, size, and orientation of the grain structure as can be seen in Fig. 2.

Porous or sparse grain boundaries can decrease thermal conductivity, increase electrical resistivity, and produce variations in mechanical strength at various locations. Defects on the mandrel surface act as templates for future copper electroformation. These mandrel defects imprint into the structure as shown in Fig. 3. Small machining marks on the aluminum mandrel surface, inadvertent scratches from handling, or shallow pitting created during cleaning form

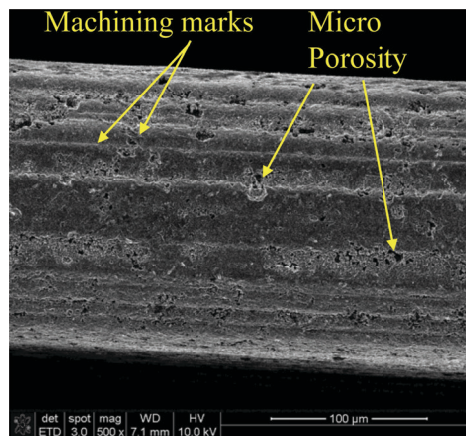


Figure 3: Defects in electroplated copper.

a template that is duplicated in the electroforming process. Combining material history, achievable fabrication tolerances, and electromagnetic heating lead to dimension uncertainty to a high level of concern that necessitates rigorous investigation into the thermal stress and resulting expansion.

RESULTS

Microstructural Observations

Building upon experience gained with initial prototypes, the current waveguide design is shown in cross section in Fig. 4 with the geometry outlined in Table 1. The microstructure shows natural variations in color highlighted by etching with a ferric nitrate and nitric acid solution. A magnified image highlighting the fine structure of one corrugation is shown in the upper right. Following the crystal morphology from bottom to top in the image: each corrugation begins with a 3-µm seed crystal skin followed by (1) a small cluster of large, equiaxed grains at the apex of each corrugation. This grouping represents the lightest colored and lowest strength material in the composite system. Following in conformation to the seed layer is (2), a layer composed of highly elongated, single-crystal grains aligned with their long axes oriented perpendicular to the growth mandrel interface. Regions (3) and (4) complete the distinct interior core of the electroformed waveguide with region (3) having a more amorphous character and region (4) exhibiting a degree of recrystallization preferentially oriented out and away from layer (2). Region (5), the darkest, most amorphous, and hardest region of the component, may be the byproduct of a planned change in chemical electrodeposition conditions to increase the growth rate of the component. Region (6) is farthest removed from the initial electroplating template and exhibits the same nascent recrystallization characteristics as region (4), except that the nucleation source of region (6)’s recrystallization process started at the outer surface of the waveguide. Unlike the interface between regions (4) and (5), there is no distinct change in mechanical properties (microhardness) between regions (5) and (6).

The microstructure of electrodeposited copper is unique due to the assembly of atoms at room temperature via chem-

Content from this work may be used under the terms of the CC BY 3.0 licence (© 2021). Any distribution of this work must maintain attribution to the author(s), title of the work, publisher, and DOI

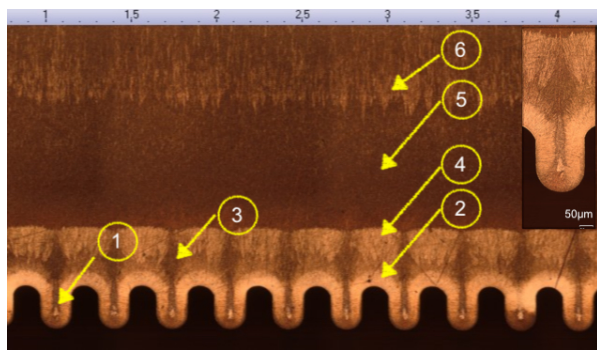


Figure 4: Cross section of an electroformed copper waveguide tube with improved geometry. See text for a detailed explanation of the numbered regions.

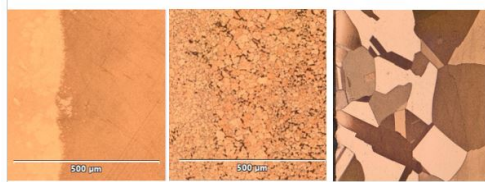


Figure 5: Comparison of microstructures: (left) As fabricated electrodeposit, (center) fully annealed microstructure, and (right) typical high conductivity copper.

ical methods that hinder the growth of crystallites and thus produce an atypical grain structure in the metal (see Fig. 5). Even at highest practical optical magnification, the electroformed copper remains uniform and featureless except for the distinct interface between dark and light regions that indicates a material change [noted as region (4) in Fig. 4]. When fully annealed, the microstructure recrystallizes, and grains grow to roughly $8\ \mu\text{m}$ in diameter (Fig. 5, center image) with void coalescence at the grain boundaries. For comparison, a typical microstructure of oxygen-free copper (UNS C10100) is shown in the right image.

Microhardness Measurements

Average microhardness measured across this waveguide was Vickers $\text{HV} = 170 \pm 25\ \text{kgf/mm}^2$, which is equivalent to an ultimate tensile strength (UTS) of approximately 500 MPa. This surpasses the strength of GlidCop® (UNS C15715) [6] and copper-chromium-zirconium (UNS C18150) at the expense of being brittle and highly sensitive to fracture at stress concentrations [7]. At the other extreme, this component material can be fully annealed to $\text{HV} 29\ \text{kgf/mm}^2$, equivalent to a UTS near 90 MPa with recovery of maximum ductility.

Microroughness Measurements

These convolutions interact with the wakefield of the electron bunch being accelerated along the central axis of the device. The quality of the electroformed interior surface duplicates the quality of the aluminum mandrel template at sub-micrometer scales. For this prototype, average surface roughness of the interior convolutions is measured $R_A =$

$6\ \mu\text{m}$. A high temperature anneal, equivalent to subjecting the waveguide to a brazing cycle, reduces the average roughness by 30% by smoothing the highest roughness peaks at the expense of coarsening the overall roughness profile.

Electrical Conductivity Measurements

The transport properties, i.e., electrical and thermal conductivity, are crucial in defining the performance of the wakefield accelerator. Four witness coupons, 10 mm in diameter and $500\ \mu\text{m}$ thick, were included in the waveguide plating bath. The electrical conductivity was measured using a 480 kHz SigmaScope SMP10 eddy current probe according to ASTM E1004 [8]. The electrical conductivity of the electroplated copper is equal to about $88 \pm 2\%$ of the International Annealed Copper Standard (IACS), wherein 100% IACS is $58.108\ \text{MS/m}$ at $20\ ^\circ\text{C}$. The corresponding skin depth is estimated to be $88\ \mu\text{m}$, which is much smaller than the sample thickness. The 2% uncertainty is derived from prior benchmarking tests performed on various copper grades, wherein the SMP10 eddy current results were compared against more accurate 4-probe measurements performed according to ASTM B193 [9]. Further through-thickness validation is required, as the eddy current method only samples the uppermost layer of the copper.

SUMMARY

Electroforming of components can be a high-precision and cost-effective method of producing complex parts. This study has examined the underlying material properties that affect component physical and mechanical performance in a unique accelerator application. The electroplated copper showed directional growth of grains. After annealing, it was observed that the grains grew in size, leaving large void spaces between clusters of grains. While the surface roughness study inferred that the peaks formed due to smaller grains after the electroplating process, they were modulated after annealing at $750\ ^\circ\text{C}$ for 30 minutes. Therefore, the average surface roughness has not improved significantly. Moreover, the mechanical hardness property measurements showed a higher hardness value for the electroplated copper; however, that reduced significantly after annealing the same sample. Similarly, the electrical conductivity measurement showed about 12% reduction compared to the IACS standard. We conclude that the researcher should exercise great care using electroformed components in applications using high vacuum and high frequency electromagnetic fields.

FUTURE WORK

We are planning to conduct a thorough investigation to study the electroformed waveguide for the A-STAR project at Argonne National Laboratory. An investigation is in progress to determine how to improve the metallurgy to increase thermal and electrical conductivity and achieve better dimensional tolerances. One of the main goals of our research is to decrease surface roughness. Researchers are

welcome to send their comments and suggestions regarding this topic to the authors of the paper.

REFERENCES

- [1] A. Zholents *et al.*, “A conceptual design of a compact wake-field accelerator for a high repetition rate multi user x-ray free-electron laser facility,” in *Proc. IPAC’18*, Vancouver, BC, Canada, Jun. 2018, pp. 1266–1268. doi: 10.18429/JACoW-IPAC2018-TUPMF010.
- [2] A. A. Zholents and W. M. Fawley, “Proposal for intense attosecond radiation from an X-ray free-electron laser,” *Phys. Rev. Lett.*, vol. 92, no. 22, p. 224 801, Jul. 2004. doi: 10.1103/PhysRevLett.92.224801.
- [3] G. Waldschmidt *et al.*, “Design and test plan for a prototype corrugated waveguide,” in *Proc. IPAC’18*, Vancouver, BC, Canada, Jun. 2018, pp. 1550–1552. doi: 10.18429/JACoW-IPAC2018-TUPML009.
- [4] K. Suthar *et al.*, “Investigation of various fabrication methods to produce a 180GHz corrugated waveguide structure in 2mm-diameter 0.5m-long copper tube for the compact wakefield accelerator for FEL facility,” in *Proc. NAPAC’19*, Lansing, MI, USA, Oct. 2019, pp. 286–289. doi: 10.18429/JACoW-NAPAC2019-MOPL023.
- [5] N. Murata *et al.*, “Micro texture dependence of the mechanical and electrical reliability of electroplated copper thin film interconnections,” in *Proc. 2011 IEEE 61st Electronic Components and Technology Conference (ECTC)*, May 2011, pp. 2119–2125. doi: 10.1109/ECTC.2011.5898811.
- [6] “GLIDCOP AL-15: dispersion-strengthened copper,” *Alloy Digest*, vol. 45, no. 5, 1996. doi: 10.31399/asm.ad.cu0603.
- [7] G. Navrotski, internal communication, 2019.
- [8] ASTM, “Standard test method for determining electrical conductivity using the electromagnetic (eddy current) method,” ASTM International, Tech. Rep. E1004-17, 2017. doi: 10.1520/E1004-17.
- [9] ASTM, “Standard test method for resistivity of electrical conductor materials,” ASTM International, Tech. Rep. B193-19, 2019. doi: 10.1520/B0193-19.

BRINGING THE GROUND UP (WHEN IS TWO LESS THAN ONE?)

A. A. Khan, C. A. Preissner, Argonne National Laboratory, Lemont, Illinois, USA

Abstract

The Advanced Photon Source Upgrade (APSU) project has employed the use of high-heat-load dual-mirror systems in the new feature beamlines being built. Due to the shallow operating angles of the mirrors at a particular beamline, XPCS, the two mirrors needed to be approximately 2.5 m apart to create a distinct offset. Two separate mirror tanks are used for this system. However, it is unclear if the vibrational performance of these tanks would be better if they were both mounted on one large plinth or each mounted on a small plinth. Using accelerometers at the installation location, the floor vibrations were measured. The resulting frequency response function was then imported into a finite element analysis software to generate a harmonic response analysis. The two different plinth schemes were modeled, and the floor vibration was introduced as an excitation to the analysis. The relative pitch angle (θ_Y) between the mirrors was evaluated as well as the relative gap between the mirrors (X_{MAG}). Results showed that a single plinth reduces the relative X_{MAG} (RMS) compared to two plinths by approximately 25%. However, the relative θ_Y (RMS), which is arguably more critical, is significantly lower by approximately 99.7% in two plinths when compared to a single plinth. Therefore, it is more effective to use two separate plinths over a longer distance as opposed to a single longer granite plinth.

INTRODUCTION

Floor and support vibrations can introduce unwanted motion in a beamline. Optics, such as mirrors, are especially sensitive to these vibrations as they operate at small angles. Small variations in the angle can propagate into large errors over a distance of several meters. Therefore, it is important to design support structures that minimize these vibrations.

In the case of the XPCS beamline at APSU, the high-heat-load dual-mirror system operates at a shallow angle, and to create a distinct offset, the mirrors must be separated by 2.5 m along the beam direction. The question arose whether having the mirror tanks share one large granite plinth as a base would be better to minimize vibrations or would it be better to use two smaller granite plinths, one for each mirror tank.

Definition of Parameters

Two important parameters affect the beam position and energy range. To better illustrate, a top-down view of the mirrors is shown in Fig. 1.



Figure 1: Top-down view of mirrors showing 0° angle with respect to the beam (dotted line). Beam travels left to right. The first mirror is called M1 and the second mirror is M2.

The first parameter of interest is the relative gap between the mirrors (X_{MAG}). X_{MAG} can affect the offset beam position downstream of the mirror system as it may cause the beam to wander along the X direction. Ideally the X_{MAG} should be zero.

Using the absolute motion of each mirror as shown in Fig. 2, the relative gap can be calculated:

$$X_{MAG} = X_1 - X_2 .$$



Figure 2: Top-down view of the mirror system showing absolute motion of each mirror with respect to the beam in the X direction.

The second parameter of interest is the relative pitch angle between the mirrors (θ_Y). The relative pitch angle is more critical as it can affect the energy range of the beam passing through the mirror system as well as reduce its effectiveness at absorbing high heat load from the white beam. Ideally θ_Y should be zero.

Using the absolute pitch angle of each mirror as shown in Fig. 3, the relative pitch angle can be calculated:

$$\theta_Y = \theta_1 - \theta_2 .$$

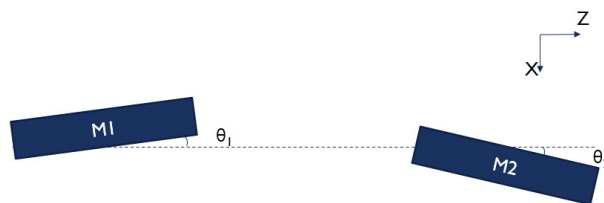


Figure 3: Top-down view of the mirror system showing the absolute pitch angle of each mirror with respect to the beam. Pitch angle is considered rotation about the Y axis coming out of the page.

METHODOLOGY

Floor Vibration Measurements

To best model these parameters, accelerometers were used at the installation location to measure floor vibrations. Two sets of tri-axial accelerometers were used for these measurements. Each set was oriented to measure vibrations in the beam coordinate system, where Z is along the beam, X is orthogonal to the beam and parallel to the ground, and Y is orthogonal to the beam and the ground as shown in Fig. 4.

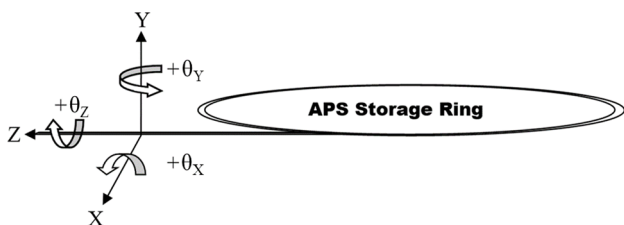


Figure 4: APSU beamline coordinate system.

One set of accelerometers was placed at 28 meters and the second set was placed at 30.4 meters, each with respect to the beam source as shown in Fig. 5. Existing installed components prevented the placement of the accelerometers at exactly 2.5 m apart, but the small error does not impact the overall measurements.



Figure 5: Placement of tri-axial accelerometers on the installation site with respect to the beam source.

The accelerometers measured vibrations from 1.5 Hz to 200 Hz. At the APS, floor vibrations beyond 100 Hz are negligible in amplitude and are therefore not a concern. However, for the purpose of the study, the bandwidth goes up to 200 Hz.

Finite Element Analysis

Once the measurements were taken, two finite element analysis studies were generated using ANSYS to measure the effects of the floor vibrations on the two parameters. The first study used the case of a single large granite plinth while the second used two smaller granite plinths.

For the first study, three steel plates were bonded to the base of the granite, which were then subsequently bounded to a grout material. The frequency response function (FRF) from each accelerometer was applied to the grouted plates at either end of the granite plinth. An average of the FRF data was applied to the center grouted plate. A point mass distributed the weight of two mirror tanks across the top surface of the granite plinth as shown in Fig. 6.

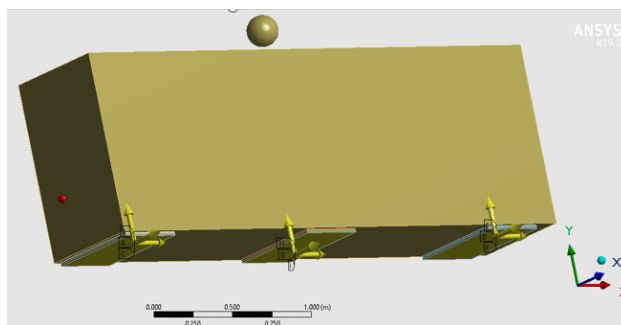


Figure 6: First study, single large granite plinth showing three grouted plates along the bottom and a point mass distributing mass across the top surface.

For the second study, each smaller granite plinth had two grouted plates (same as the first study) on either end of the plinth base. The individual mirror tank mass was applied as a point mass on each granite plinth surface as shown in Fig. 7. The FRF data from one set of accelerometers was applied to both grouted plates on one granite plinth and the other data set was applied to the second granite plinth.

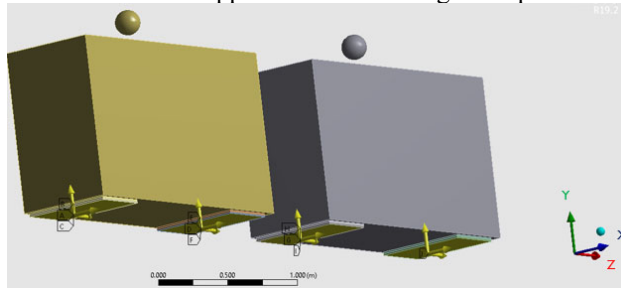


Figure 7: Second study, two smaller granite plinths showing four grouted plates along the bottom and a point mass distributing mass across each granite top surface.

The displacement of the mirror centers along the X direction was extracted, along with the rotation of the mirror centers about the Y direction. They were then used to calculate the RMS values of X_{MAG} and θ_Y .

RESULTS

The ANSYS data was processed using a custom MATLAB script. The relative pitch angle and relative gap were processed for each study and graphs were plotted in Fig. 8 along with their RMS values across the frequency bandwidth. The values are summarized in Table 1.

Table 1: Summary of Relative Stability

Study	θ_Y (RMS)	X_{MAG} (RMS)
One Plinth	1.2 nrad	2.6 nm
Two Plinths	0.0042 nrad	3.4 nm

The results showed that using a single plinth reduced X_{MAG} by 25% compared to the two plinths case. However, θ_Y was reduced by three orders of magnitude in the two plinths case when compared to the single plinth case. As this is the more critical parameter, the results show that two smaller plinths are the better option to reduce vibration motion.

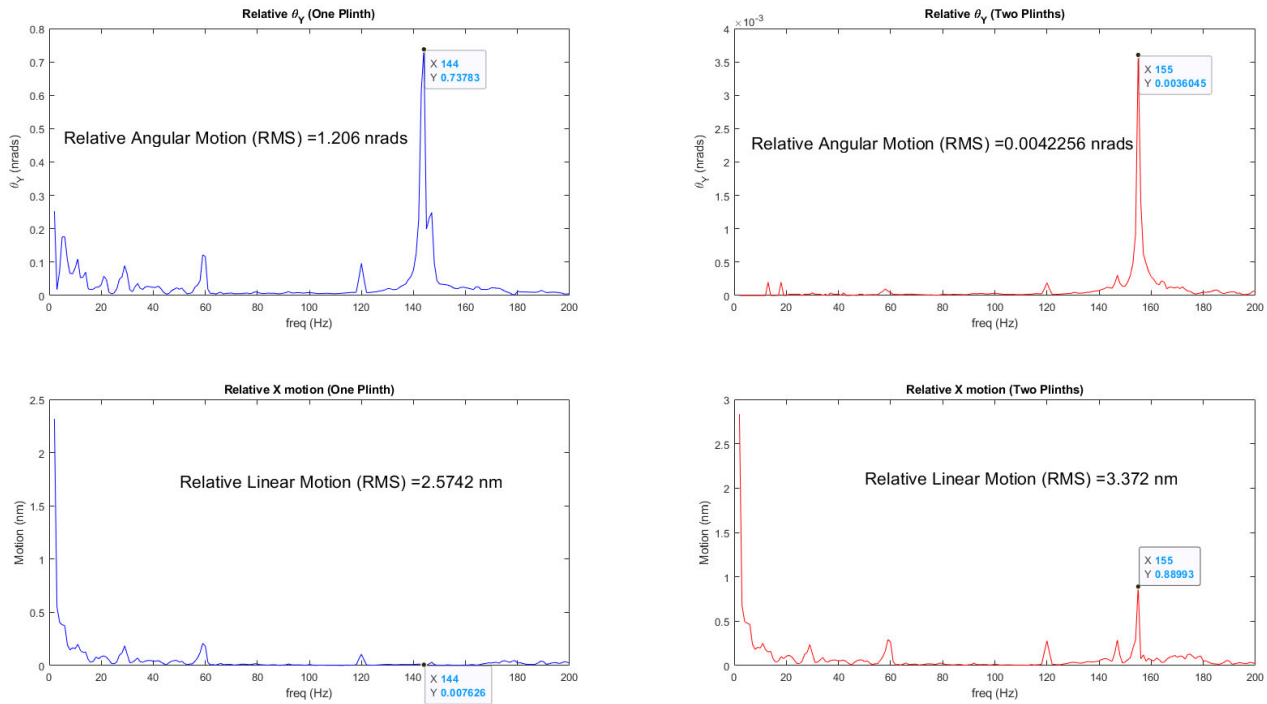


Figure 8: Plots of X_{MAG} and θ_Y in both studies across the frequency bandwidth.

CONCLUSION

The results in this paper show a clear distinction between using two smaller granite plinths versus one large granite plinth. This was contrary to the initial assumption that using a single large base would move the mirror optics uniformly. The improved performance for X_{MAG} shows that a single granite plinth does move the mirrors together better. However, due to the large distance between the mirrors, their relative pitch errors can add up to yield much larger values. As this is the critical dimension, it is more effective to use two smaller granite plinths. The smaller granite

plinths also aid in the ease of installation when maneuvering around the installation site compared to moving one larger and heavier piece.

ACKNOWLEDGEMENTS

This research used resources of the Advanced Photon Source, a U.S. Department of Energy (DOE) Office of Science User Facility at Argonne National Laboratory and is based on research supported by the U.S. DOE Office of Science-Basic Energy Sciences, under Contract No. DE-AC02-06CH11357.

A REVIEW OF ULTRASONIC ADDITIVE MANUFACTURING FOR PARTICLE ACCELERATOR APPLICATIONS

J. Brandt*, Enrico Fermi Institute - University of Chicago, Chicago, IL 60637, USA

Abstract

Additive manufacturing (AM) technologies have been used for prototyping and production parts in many industries. However, due to process limitations and the unknown material properties of AM parts, there has been limited adoption of the technology in accelerator and light-source facilities.

Ultrasonic Additive Manufacturing (UAM) is a hybrid additive-subtractive manufacturing process that uses a solid-state ultrasonic bonding mechanism attached to a CNC mill to join and machine metal parts in a layer-by-layer manner. The solid-state and hybrid nature of UAM ensures base material properties are retained and mitigates process limitations which traditionally inhibit integration of parts produced by other AM processes.

This paper presents a review of the UAM process and its potential application to accelerator and beamline needs. Several specific areas are discussed including: replacement of traditional manufacturing approaches, such as explosion bonding to join dissimilar metals; improved internal cooling channel fabrication for thermal management; and imbedding of electronics and materials for more accurate remote sensing and radiation shielding.

INTRODUCTION

Components used in accelerators and beamlines operate in demanding environments which often require specialized and difficult fabrication processes to manufacture. Ultra-high vacuum (UHV) chambers may require explosion welding and beam stops and collimators utilize electrical discharge machining (EDM), both of which can be time consuming, costly, and are limited in their application.

As a hybrid, additive-subtractive manufacturing process, ultrasonic additive manufacturing (UAM) possesses unique capabilities which could make explosion welding or EDM options instead of necessities. The solid-state additive welding stage operates well below the melting temperature of the substrate materials, which ensures bulk material properties are largely retained.

Subtractive machining is completed by a computerized numerical control (CNC) mill to which the ultrasonic transducer and sonotrode are also mounted. This allows for both three and five-axis milling operations of complex geometries and retains the tolerances, surface finish, stability, and repeatability inherent to milling processes. In turn, parts printed using UAM can be more rapidly integrated without the need for time-consuming and costly post-processing operations that can include finish machining and surface finishing. A schematic depiction of both additive and subtractive stages of UAM is shown in Fig. 1.

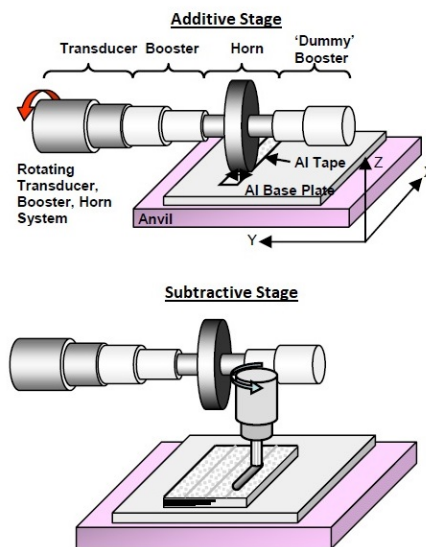


Figure 1: UAM process schematic showing additive and subtractive stages [1].

APPLICATIONS FOR ACCELERATORS

Accelerator facility adoption of parts printed with other metal additive manufacturing (AM) processes like selective laser melting (SLM), or electron beam melting (EBM) has been slow in part due to the uncertainty of printed parts' material properties. However, with the advantages of UAM, more rapid adoption of metal AM parts could occur for certain application areas.

Dissimilar Metal Welding

Bi-metallic joints are widely used for accelerator vacuum systems, thermal management components, and instrument feedthroughs with explosion welding serving as a common method of fabrication. Explosion welded joints are formed when a controlled explosion shockwave accelerates one material of the joint into the other [2]. The process is limited to simplistic geometries, which in turn limits the parts that can be fabricated.

The mechanisms for successful bonding during the UAM process are similar and generally believed to be shear deformation, inter-diffusion, and sometimes mechanical interlocking. The applied normal force from the sonotrode head compresses the foils ensuring good contact of the asperities which are subsequently sheared by the ultrasonic oscillations. Both the down force and ultrasonic oscillations also contribute to plastic flow of the material and breakdown and redistribution of surface oxide layers and impurities to promote a clean mating surface for solid joints [3]. Figure 2 shows several UAM welded dissimilar metal interfaces with varying bond topographies.

*brandtj@uchicago.edu

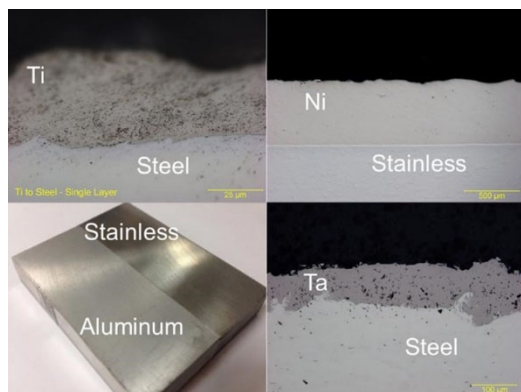


Figure 2: Example UAM dissimilar metal interfaces showing (a) titanium and steel (b) nickel and stainless steel (c) aluminum and stainless steel (d) tantalum and steel [4].

Explosion welding and UAM both form welds with comparable strengths and qualities due to their similar low-temperature, plastic deformation bonding mechanisms. What sets UAM apart is greater flexibility and control afforded by the integrated precision machinery. More complex geometries that could feature many multi-layered dissimilar metal interfaces are achievable and with greater speed and accuracy. Features normally requiring post-machining when using explosion welding, such as holes and knife edges, would be completed in-situ.

Another possible application is the manufacture of custom beryllium x-ray windows and vacuum flanges. As there exist a very limited number of beryllium window manufacturers, having the means to produce custom windows on demand could be incredibly valuable, especially for time-constrained projects.

Research examining beryllium window manufacture using ultrasonic welding was completed by NASA researchers in 1963 using 0.001" thick beryllium foil and an ultrasonic ring welder. Though the weld joint design and beryllium quality were called into question, the report ultimately determined that ultrasonic welding was feasible for obtaining vacuum-tight joints between thin beryllium disks and stainless steel rings [5]. With advances made in beryllium foil manufacture and quality since the 1960s, the chances of success using UAM for x-ray window fabrication seem plausible. However, little documentation exists on the generation of particulate during UAM, which would need to be investigated further to ensure beryllium could safely be processed.

Internal Features

The most common application for UAM is the optimization of heat exchangers. As radiation shielding component designs continue to evolve to meet the demands of greater beam energies, UAM could increase thermal efficiencies while decreasing weight and providing another avenue for fabricating critical components. Additionally, the footprint of UAM machines, that of a standard CNC machining center, could allow for easy integration into existing machine shop facilities and contribute to more rapid prototyping and production.

Traditionally, parts requiring internal features also require assembly of multiple constituents with welding or brazing to join them together. Water cooling channels or tubing in beam stops use machined channels in a block of copper which are then sealed using a brazed-on jacket or directly brazed to the copper to ensure water tightness and good heat transfer.

UAM can combine these two processes to create internal geometry without the need for extra assembly steps. Figure 3 shows UAM fabricated aluminum heat exchangers with internal cooling channels and machined recesses to reduce weight. Combining both dissimilar metal welding and internal feature integration, UAM could produce more thermally efficient beam stops and collimators or unique instrument feedthroughs tailored to better shield or route electronics.

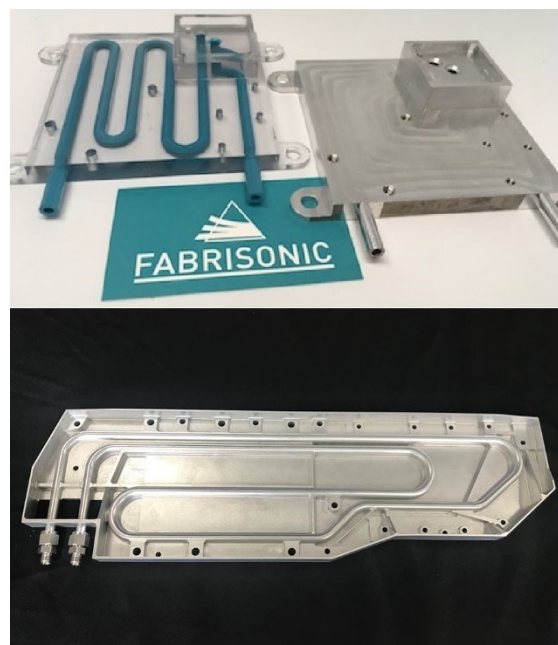


Figure 3: Aluminum heat exchangers showing complex internal geometry capabilities of UAM [4].

Embedded Electronics and Materials

Due to the lack of melting in the UAM process, materials which would otherwise be damaged by the heat of a traditional fusion welding or brazing application can be imbedded directly into UAM parts. Electronic sensors, such as thermocouples or strain gauges, can be strategically located closer to their points of interest enabling higher accuracy data acquisition.

An additional benefit of embedding electronics inside metal parts is the shielding that metal encasement affords. Electronics could potentially be shielded from beam or thermal radiation by clever layering of high-Z or less thermally conductive materials. Figure 4 shows the interface between an aluminum coated fiber optic cable embedded in an aluminum 6061 fatigue specimen. The metallized coating serves to promote a more homogenous bond and improve strength by reducing the possibility of defects at the weld interface.

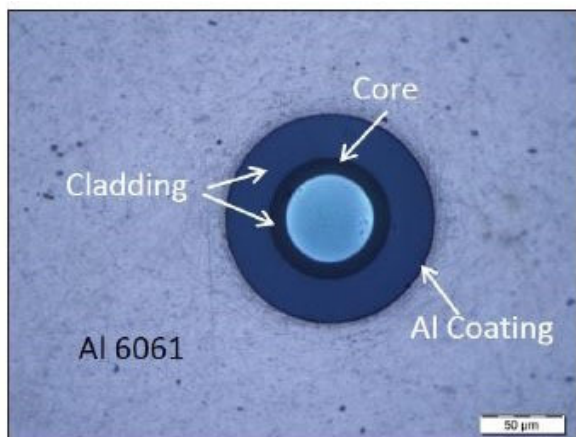


Figure 4: Metallized fiber optic cable embedded in aluminum 6061 fatigue specimen [6].

Materials not conducive to welding or that require precision placement within a part can also be embedded using UAM. Oak Ridge National Laboratory (ORNL) partnered with Fabrisonic, the primary manufacturer of UAM machinery, to fabricate control elements for use in the High Flux Isotope Reactor (HFIR). These control elements are curved and contain particles of Eu_2O_3 and Ta dispersed along their axis for neutron absorption. As such, they are costly to manufacture using traditional processes.

Using a 5-axis CNC mill with an attached UAM system, features were machined along a curved substrate plate. The neutron absorbing materials were then embedded in the machined holes and sealed by further layers of aluminum tapes. Figure 5 shows the layout of the neutron-absorbing disks just before they are further embedded underneath the remaining layers of aluminum required to complete the part.



Figure 5: Eu_2O_3 and Ta neutron absorbers embedded in a control panel used in a high-flux isotope reactor at ORNL [4,7].

A similar approach could be carried out for radiation shielding materials in accelerator systems. Tungsten or lead could be strategically added to locations in parts or used to encase sensitive electronics that would otherwise experience faster degradation from radiation damage.

PROCESS LIMITATIONS

Material Incompatibilities

As plastic deformation of asperities is one of the main mechanisms of the UAM process, harder materials are more difficult to process as they require greater energy to deform and collapse surface asperities. In order to achieve a high bonding density, high oscillation amplitude and/or high normal force will be required [3].

Additionally, some material combinations, particularly pure metals, are impeded by oxide layer interference. Pure titanium, for example, will gall during processing as the ductility of the titanium oxide layer tends to cause smearing at the sonotrode contact area and weld interface. Interlayers of softer materials, e.g. aluminum, may be required in these cases.

Post-Processing

UAM does suffer from mechanical strength anisotropy depending on the build direction and consequent layer orientation, which is a common feature of most AM processes. Anisotropies can be mitigated by post-process heat treatments which have been shown to increase bonding strength through controlled generation of intermetallics or relaxation of residual stress and promotion of inter-diffusion [3]. Hot isostatic pressing (HIP) is one heat treatment process that produces significant improvements in the density and mechanical strength of most AM parts.

Bi-metallic parts produced by UAM may require tailored heat treatments based upon the chemistry of the materials used. More complex, multi-metallic parts would thus require more extensive post-processing prior to integration.

CONCLUSION

UAM technology could provide multiple avenues for optimization of parts in accelerator applications. New and unique material constructions, more accurate thermal management, and improved sensing and data acquisition capabilities are some of the areas UAM welding could immediately affect. As with any new technology, further applications would only increase as more experience and familiarity are gained.

The Engineering and Technical Support Group (ETSG), part of the Enrico Fermi Institute at the University of Chicago, recently received funding to purchase a Fabrisonic SonicLayer1200 UAM machine. Due to the relationships ETSG has built with groups at both Argonne National Laboratory and Fermilab, future ETSG projects could enable testing of UAM parts to qualify the process for use in accelerator applications in the future.

REFERENCES

- [1] A. Hehr *et al.*, "A comprehensive review of ultrasonic additive manufacturing," *Rapid Prototyp. J.*, vol. 26, no. 3, p. 445-458, Apr. 2020. doi:10.1108/RPJ-03-2019-0056
- [2] E. Huttel, "Materials for accelerator vacuum systems," in *Proc. CAS-CERN Accelerator School: Vacuum Technology*, Snekersten, Denmark, Jun. 1999, p. 237-253.

- [3] D. Li, "A review of microstructure evolution during ultrasonic additive manufacturing," *Int. J. Adv. Manuf. Technol.*, vol. 113, pp. 1-19, Jan, 2021. doi:10.1007/s00170-020-06439-8
- [4] *Industrial Heating*, Dec 5, 2019, <http://industrialheating.com/articles/95338-metal-additive-manufacturing-without-melting>
- [5] B. R. Cantor, J. A. Munford, and A. Piltch, *Ultrasonic Welding of a Beryllium Window Assembly*, Greenbelt, MA, USA: NASA Technical Memorandum, 1963.
- [6] A. Hehr, "Integrating fiber optic strain sensors into metal using ultrasonic additive manufacturing," *JOM*, vol. 70, no. 3, pp. 315-320, Dec. 2017. doi:10.1007/s11837-017-2709-8
- [7] A. Hehr *et al.*, "Five-axis ultrasonic additive manufacturing for nuclear component manufacture," *JOM*, vol. 69, pp. 485-490, Mar. 2017. doi:10.1007/s11837-016-2205-6

UTILIZING ADDITIVE MANUFACTURING TO CREATE PROTOTYPE AND FUNCTIONAL BEAMLINE INSTRUMENTATION AND SUPPORT COMPONENTS

D. Jensen[†], Argonne National Laboratory, Lemont, Illinois, USA

Abstract

The world of beamline science is often fast-paced and dynamic. One of the major challenges in this environment is to be able to design, manufacture and then implement new items for use on the beamlines in a fast and accurate manner. Many times, this involves iterating the design to address unknown or new variables which were not present at the beginning of the project planning task. Through the use of additive manufacturing, I have been able to support the user programs of various (APS) Advanced Photon Source beamlines* across multiple scientific disciplines. I will provide a few detailed examples of Items that were created for specific beamline applications and discuss what benefits they provided to the pertinent project. I will also talk about why choosing consumer-level printer options to produce the parts has been the direction I went and the pros and cons of this decision. Primarily, this choice allowed for quicker turnaround times and the ability to make more frequent changes in an efficient manner. Currently, we are utilizing only the fused deposition modelling (FDM) type printers but I am exploring the addition of UV-activated resin printing, exotic materials that can be utilized using the current toolset, and the possibility of commercial metal printing systems. This technology has been a game-changer for the implementation of new support items and instrumentation over the last couple of years for the different disciplines I am supporting. I will discuss how the roadmap ahead and what the evolving technologies could potentially allow us to do.

INTRODUCTION

The Advanced Photon Source (APS) located at Argonne National Laboratory (ANL) has many user programs. In my daily function I am supporting a variety of these groups. Time is something that is very limited and budgetary constraints are always in the backs of our minds. With the adoption of Additive manufacturing (AM) I have been able to provide a cost effective and timely way in which to produce instrumentation and beamline support components. The approach I have taken is to utilize a consumer-grade machine, which allows me to support the devices, and run it at very low cost without the need for lengthy licensing agreements.

EXAMPLES OF USE CASES

Use case example one, as shown in Fig. 1, is a collimator holder for use on the 11-ID-D beam line at the APS. This is a Time Resolved Research (TRR) Group [1] Project. The scientist approached me as the existing holder was not

functioning in a manner that was still optimal. The experiment was going to be happening in the following week. The task was design and print a holder for the collimator. Using Fused deposition modelling (FDM) I was able to produce the part from a 3d CAD model to finished fixture in about 3 days. Average turn around for an item such as this is around 2 to 4 weeks utilizing a traditional manufacturing route. There was also issues as the current collimator had taken on a non-cylindrical shape on the outer surface from the normal use by the staff over the years. The benefit of a printed part was I could then install the collimator in a semi clamped manner and hone it into a good fit using the rough surface of the outer diameter of the collimator. The fact that I could turn this around in about 3 days with a material cost of around ten Us Dollars (USD) was a huge benefit. It was also found that the stability was good enough that we did not see the immediate need to move forward with a traditionally manufactured setup.

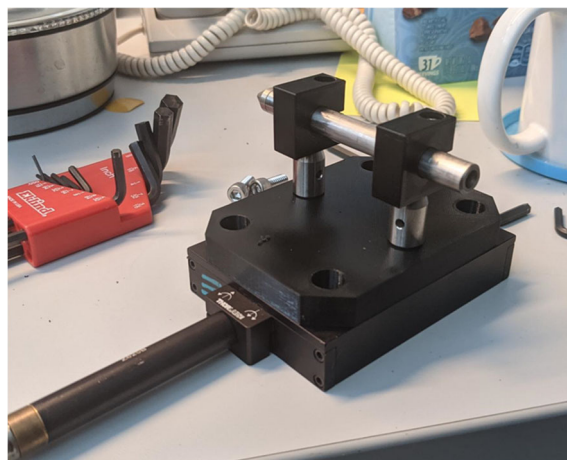


Figure 1: Collimator Mounting setup 11-ID-D.

Use case example two, as shown in Fig. 2, is a flight path to keep the beam scatter coming off the sample and directed to the detector in a vacuum or gas environment. The set up was done for 6-ID-B for the Magnetic Materials (MM) Group [2], the item was originally quoted at twelve hundred USD and a 8 to 12 week lead time through a tradition manufacturing method. The Support staff at this beamline approached me and asked if it would be possible to create this using AM. We decided it was worth a try. The challenge on this is that it is about a meter long. The limitations of the tools I have at my disposal are about 9 inches of print height in the vertical. What this led me to do was to break the piece up into multiple segments and then epoxy them together. I used key features to help with alignment and the 5-minute epoxy which is readily available created the equivalent of a plastic seam weld. The total cost material wise was around fifteen to twenty dollars out

[†] dpjensen@anl.gov

side of the NW-40 flange which was purchased and epoxied in place, and the Newport clamps which were used to mount it to the rail on the device at the hutch. There were also two Kapton windows which were epoxied to either end of the flightpath to allow it to hold vacuum. The print time for all parts was under 24 hours total and glue up took roughly one to two hours. This allowed me to have the item in the support staff's hands and installed in under a weeks' time. The item was able to be pumped down with a vacuum pump and was in service for the experiment without issue.



Figure 2: Flightpath 6-ID-B.

Use case three was a mount for microscope which needed to assemble into an existing diffractometer. The assembly area was constrained and there was a desire for motion so that a range of the magnifications could be used. The setup, as shown in Fig. 3, was printed on once setup with a total time of 8 hours to print. The item in which clamped the microscope into place was reprinted multiple times to adjust the feel to the liking of the support staff. The cost of this was around ten USD with the multiple iterations of the once clamping piece. The final result was able to adjust the microscope to utilize a 70X to 40X range. Time from initial design to parts ready for installation one week. This item also used some salvaged threaded rod to allow the vertical motion by driving a threaded feature in the one part.

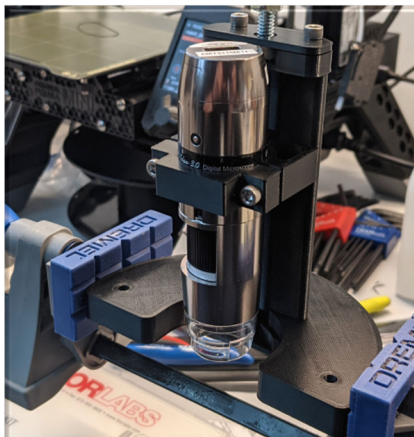


Figure 3: Microscope mount 6-ID-B.

Use case four was a prototype sample holder and sample holder mount for 8-ID-E Dynamic Structures group (DYS) [3]. With the implementation of remote user support Division wide the exploration of use for robots and automating sample exchange has become a more looked at option. There is currently a project underway to implement this at 8-ID-E. The Wheel (Fig. 4) will in the end be made of metal but the intended final design for the sample holding cubes, which are the grey parts in Fig. 4, would be that of

a AM made part. Where AM became valuable here was that we could iterate wheel and sample holder designs to find the desired fit very quickly and at a low cost. After the fit we desired was found we then created a functional prototype and mounting assembly's so that the items could be tested in a real-world environment. This allowed the support staff to program the robot and then test the integration with a real-world object to see how it would act. These prototypes were and mounting fixtures were all printed a cost of under one hundred USD and has provided a vast amount of hands on feedback. The design also is utilizing an off the shelf isometric magnetic mount so do all the precision locating of the sample holder. it also provides the mechanical mount for the sample wheel once installed. An example of this set up can be seen in Fig. 5.



Figure 4: Sample wheel with Robot Gripper interacting 8-ID Lab test area.

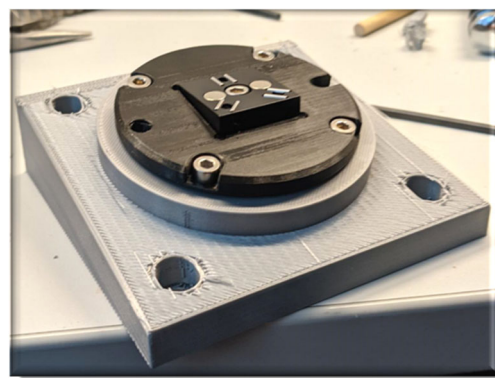


Figure 5: Sample wheel mount 8-ID Lab test area.

MANUFACTURING CHALLENGES

Because of the process of laying layers of material down upon each other design for manufacturing (DFM) should be considered. When wanting to place treads for example if the height between layers is set to large this can case the tap to wander well hand taping. Hand taping, I have found is also a must. Power taping has in my experience lead to the material building up to much head and gumming up the tap or turn the tap into a drill and boring out the hole. I have

also found that doing 100% infill which can be time consuming is the best route for parts both tapped and untapped as this provides better stability to the part. One other challenge is utilizing this in the right way. It can be very easy to say I will print everything from now on. The application must be looked at in some cases a hightbred between AM and tradition manufacturing will work, and in other only traditional manufacturing will work.

CONCLUSION

Following the testing and implementation which I have been able to do over the following year I can see many more use cases for these lower cost FDM printers and the parts they create. The support staff in the groups I am working with has started to inquire about possible future uses and have become much more receptive to the suggestions of just printing many of the items they need. The road map ahead would be to start looking into possible creating some AM FDM metal parts and then moving towards some of the more commercial grade AM Metal printing process. The need and use for the consumer grade printer will be

there but there are many other possibility's that these new tools could provide for our use.

ACKNOWLEDGEMENTS

This research used resources of the Advanced Photon Source, a U.S. Department of Energy (DOE) Office of Science User Facility at Argonne National Laboratory and is based on research supported by the U.S. DOE Office of Science-Basic Energy Sciences, under Contract No. DE-AC02-06CH11357.

REFERENCES

- [1] Time-Resolved Research Group,
<https://www.aps.anl.gov/Time-Resolved-Research>
- [2] Magnetic Materials Group,
<https://www.aps.anl.gov/Magnetic-Materials>
- [3] Dynamics and Structure (DYS) group,
<https://www.aps.anl.gov/Dynamics-and-Structure>

DESIGN AND DEVELOPMENT OF AI AUGMENTED ROBOT FOR SURVEILLANCE OF HIGH RADIATION FACILITIES

K. Suthar*, M. White

Argonne National Laboratory, Lemont, IL, USA

A. Suthar¹, S. Suthar¹, G. Mistri, mySTEMbuddy Robotics, Naperville, IL, USA

¹also at Neuqua Valley High School, Naperville, IL, USA

Abstract

Scientific instruments and utility equipment at high-radiation facilities such as the Advanced Photon Source at Argonne National Laboratory are often challenging to monitor during actual operation. To help augment monitoring capabilities, we are developing an instrumented robot that uses artificial intelligence (AI) to create a thermal and spatial 3D map of its surroundings. The robot can be self-driven or controlled remotely. The robotic vehicle—whose overall dimensions are 50 cm in length, 20 cm in width, and 20 cm in height—carries a depth perception camera to guide itself on a predetermined path; an IR camera for thermal imaging; dosimeters to measure stray radiation; and a cluster of other sensors to assist in communications and navigation, as well as measuring noise, vibration, temperature, and humidity of the surrounding space. This inexpensive robot is operated and controlled by NVIDIA’s Jetson Nano™ development board, one brushless DC motor, and one servomotor that controls the movement of the robot. All control and data acquisition programs are written in Python for ease of integration with institution-specific operating systems such as EPICS. The AI robot was trained using machine learning followed by the application of a trained algorithm for navigation. This paper discusses our preliminary development of the robot.

INTRODUCTION

Synchrotron radiation facilities such as the Advanced Photon Source, and nuclear radiation facilities—e.g., nuclear power plants, isotope fabrication plants, and nuclear material handling plants—often require continuous monitoring to ensure the safety of radiation workers, existing infrastructure, and the environment [1]. The existing practice for radiological monitoring uses static devices during operation or intervention using human operators. These methods are often costly, time-consuming, and challenging when intervention is necessary or unavoidable. In a radiation facility, the radiation decay and heat immediately after a shutdown due to routine maintenance or due to failure needs to be quantified quickly [2]. To assess the damage or contain/collect contamination is very difficult if human intervention is required [3]. In all such events, a robotic system can be beneficial to assess the condition of the instruments, collect any samples, and monitor the radiation [4]. Moreover, due to recent developments in robotics and artificial intelligence, it

is easier to develop a robotic system that can be utilized for this purpose.

The challenge of monitoring scientific instruments in radiation facilities can be solved through this self-guided robot. Equipped with various sensors and artificial intelligence, the robot can successfully and autonomously navigate through facilities while acquiring thermal environmental data and images essential to monitoring scientific instruments, equipment, and the environment. The lead case around the robot protects its various electronic components from damage while navigating through a facility.

In this paper, we discuss our preliminary design of an AI-driven autonomous robot. The robot uses a ready-made radio-controlled car chassis that is equipped with an open-source software platform called Donkey Car [5] installed on a NVIDIA Jetson Nano board [6]. The robot was manually trained on a convoluted path using machine learning [7] and used its very own AI algorithm to select parameters to control the brushless DC motor and servomotor with help from processing the images that it acquired during its travels. The FLIR Lepton camera [8] was used to identify temperature anomalies in the acquired thermal images/video. The robot was trained to identify its travel boundaries via blue tape placed on the floor.

ROBOT DESIGN

The current design of the robot is a WiFi operated, front-wheel controlled, all-wheel-drive vehicle, as shown in Fig. 1. The textured wheels grip smooth surfaces and prove efficient traction over various other types of surfaces. The 3D-printed outer shell combined with lead plates protects the internal hardware from becoming damaged in high radiation conditions. The internal mounting structure allows for seamless cable management through routing slots between the NVIDIA Jetson Nano™ and the motor controller. The slightly raised structure provides room for the batteries needed by the NVIDIA Jetson Nano™, the FLIR Lepton camera, the Intel RealSense camera, and the motors. The Intel RealSense mount maintains a consistent view of the robot’s surroundings, while the FLIR Lepton mount is strategically raised to procure more useful thermography. The on-board NVIDIA Jetson Nano™ acquires images and sensor data to control the robot. The robot can also be remotely controlled using SSH to acquire the navigation panel and access the robot’s camera view. A brushless motor is used as a drive, while a servomotor attached to an Ackerman’s steering trapezium is used for turning the vehicle. The controlling

* suthar@anl.gov

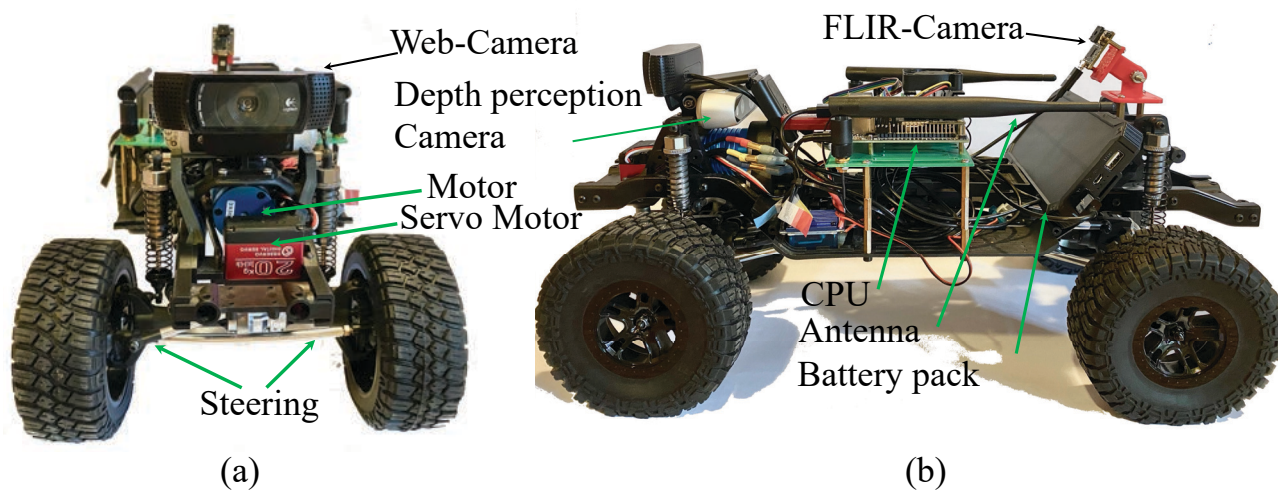


Figure 1: Images showing various parts of the robot using (a) front view and (b) side view.

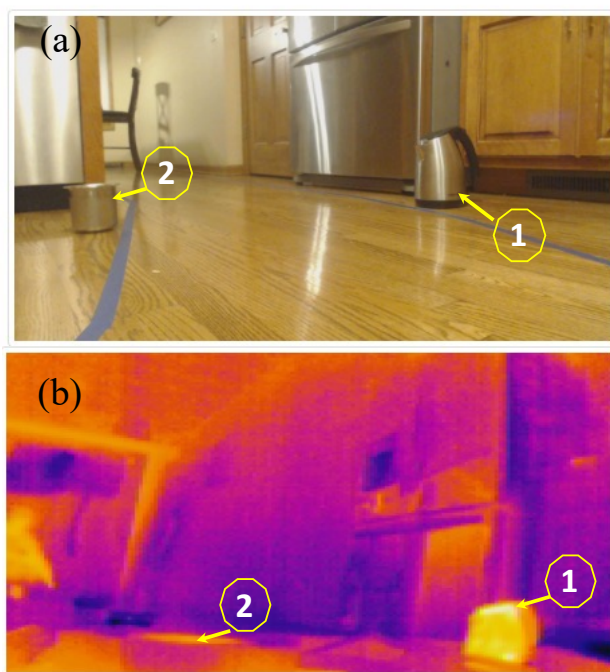


Figure 2: Computer interface images taken (a) by webcam and (b) by FLIR thermal imaging camera. Object 1 is a warm kettle and object 2 is a cold water container.

parameters for speed and steering angle were decided by image processing using machine-learned algorithms while acquiring the images during travel. It can autonomously navigate given areas while effectively avoiding virtual collisions by identifying the path boundaries with colored tape. The current design uses simple images acquired from the webcam, processes those images on board, identifies the boundaries, and avoids them by changing the motor speed and servomotor lever angle attached to the trapezium. The FLIR Lepton (thermographic camera) allows the robot to

take thermal images periodically to monitor temperature and possibly identify unwanted hot spots within scientific instruments and utility equipment. The onboard sensors for temperature, humidity, and radiation, as well as noise and vibration sensors will acquire and relay this information to the control station. The final design will be able to avoid the obstacles by identifying them by depth perception camera and plotting the open area using artificial intelligence handled by the NVIDIA Jetson Nano™.

Mechanical and Electronics Hardware

The chassis is a ready-made radio-controlled toy car frame equipped with a singular brushless motor, a four-wheel drive transmission, and a servo for steering.

Various hardware works in conjunction to provide streamlined navigation using artificial intelligence. The Intel RealSense camera, which captures depth, and the FLIR Lepton, an IR thermal camera, connect to the NVIDIA Jetson Nano™, a powerful yet small computer capable of AI. The 16-channel PWM/servo driver, an I2C interface, provides the necessary infrastructure to steer and drive the robot (combining a 20-kg servomotor and a brushless motor). WiFi connectivity is necessary in order for the NVIDIA Jetson Nano™ to access the internet; it also provides a solution to remote control and image acquisition during the early stages of development. The DHT11 temperature and humidity sensor updates the robot with both these data periodically. A more minor yet essential hardware component is the battery temperature sensor, strapped around the battery, that is used to operate the 16-channel PWM/servo driver; this sensor triggers a stop to all motor functions when the maximum temperature threshold is reached.

Intel RealSense D435i Depth Camera Equipped with a bmi055 inertial measurement unit, the Intel RealSense D435i Depth Camera provides depth and time-stamped data. When required, the inertial measurement data can be asso-

Content from this work may be used under the terms of the CC BY 3.0 licence (© 2021). Any distribution of this work must maintain attribution to the author(s), title of the work, publisher, and DOI

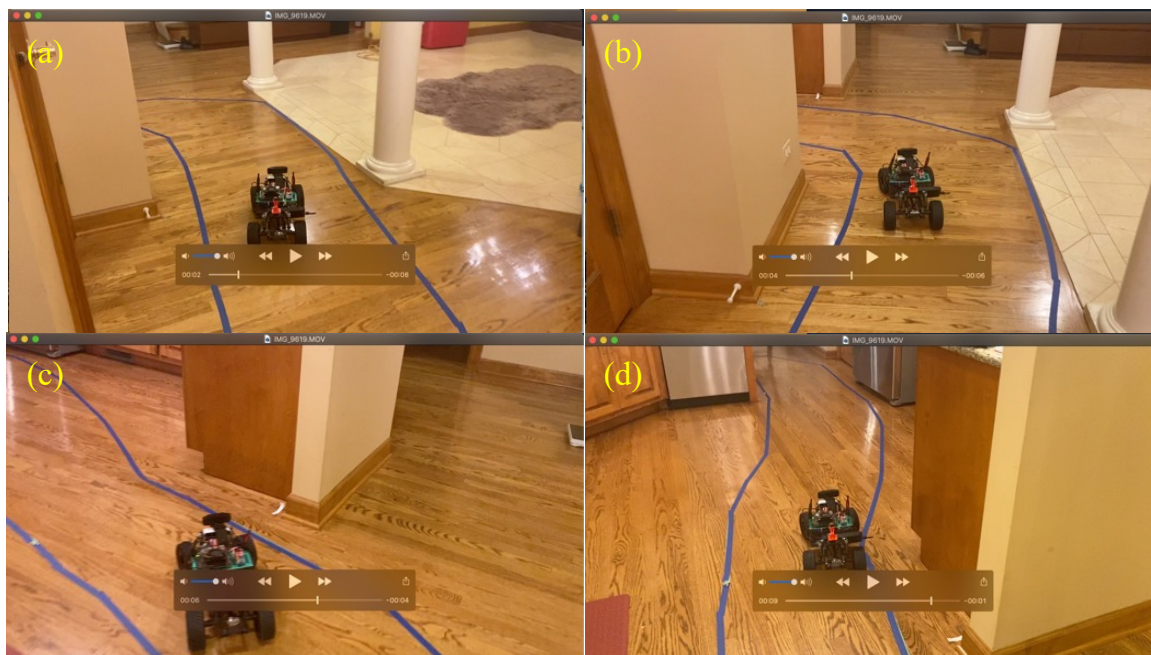


Figure 3: Still video images showing the robot self-navigating the path at intervals of (a) 2 s, (b) 4 s, (c) 6 s, and (d) 9 s.

ciated to detect changes in terrain via measurements of the rate of change of acceleration.

FLIR Lepton The FLIR Lepton is a micro thermal camera module that allows for contactless temperature acquisition and provides a thermal color grade picture of the acquired surroundings.

Programming and Operation

Figure 2(a) shows an image taken by the webcam attached to the front of the robot, and Fig. 2(b) is a thermal image taken by the FLIR camera located at a height at the back of the robot. The robot was trained on a 10-turn closed-loop path using the computer-controlled remote. Nine training sessions were conducted to create the required epoch for machine learning. Donkeycar [5] was utilized to acquire a large number of images by controlling the robot to travel on a simple track. After acquisition of approximately 5000 images, a model was trained on a separate computer. After 25 hours of computing time on a computer, the final metrics were copied back to the robot's CPU. The configuration of the computer that trained the model runs an AMD Radeon 5700XT, an AMD Ryzen 5 5600x, with 16 GB of 3600 mHz RAM at CL16, and a NVME solid state drive. Figure 3 shows time-lapse images of the robot moving on the track. The FLIR Lepton takes pictures using Python software. We integrated this into our Python code to simplify image acquisition.

NEXT STEPS

The team is implementing plans to navigate the robot solely using its depth-perception camera to avoid moving and non-moving hindrances. Incorporating an inertial unit will help us detect slippage and changes in terrain such as

bumps. The sensor network will be programmed to acquire surrounding information. The authors plan to incorporate a microphone and speaker for communication purposes. After construction and testing of this first prototype, it was decided that a second camera may be necessary to provide for more efficient and accurate navigation and data acquisition, further straining the already-limited memory. The NVIDIA Jetson Nano™ has 2 GB RAM on-board, a limiting factor for the AI process; additional memory would be required to process the increased amount of data.

CONCLUSION

The robot was successfully trained and navigated its way through a prescribed path bounded by blue tape. The thermal images acquired during the run show the capabilities of inexpensive hardware. This economical approach to monitoring can help operators quickly assess the state of the scientific instruments and utility equipment during operation or during decay time after a shutdown. The capabilities of this robot can be enhanced and used to find trends and indications of equipment problems well before failure leading to improved availability of the facility.

ACKNOWLEDGMENTS

Special thanks to Evan Johns and Steve Spreitzer for help in troubleshooting the camera communication with the robot. This research used resources of the Advanced Photon Source, a U.S. Department of Energy (DOE) Office of Science User Facility at Argonne National Laboratory and is based on research supported by the U.S. DOE Office of Science-Basic Energy Sciences, under Contract No. DE-AC02-06CH11357.

REFERENCES

- [1] B. Bird *et al.*, “A robot to monitor nuclear facilities: Using autonomous radiation-monitoring assistance to reduce risk and cost,” *IEEE Robotics Automation Magazine*, vol. 26, no. 1, pp. 35–43, 2019. doi: 10.1109/MRA.2018.2879755.
- [2] A. Tobias, “Decay heat,” *Prog. Nucl. Energy*, vol. 5, no. 1, pp. 1–93, 1980. doi: [https://doi.org/10.1016/0149-1970\(80\)90002-5](https://doi.org/10.1016/0149-1970(80)90002-5).
- [3] S. Kawatsuma, M. Fukushima, and T. Okada, “Emergency response by robots to Fukushima-Daiichi accident: summary and lessons learned,” *Industrial Robot*, vol. 39, no. 5, pp. 428–435, Jan. 2012. doi: 10.1108/01439911211249715.
- [4] K. Ohno, S. Kawatsuma, T. Okada, E. Takeuchi, K. Higashi, and S. Tadokoro, “Robotic control vehicle for measuring radiation in Fukushima Daiichi nuclear power plant,” in *Proc. 2011 IEEE International Symposium on Safety, Security, and Rescue Robotics*, 2011, pp. 38–43. doi: 10.1109/SSRR.2011.6106792.
- [5] *Donkey Car*, Jun. 2021, <https://docs.donkeycar.com/>
- [6] *Jetson Nano Developer Kit*, Apr. 2021, <https://developer.nvidia.com/embedded/jetson-nano-developer-kit>
- [7] I. Orsolc, “Izgradnja modela autonomnog vozila,” Ph.D. dissertation, University of Zagreb, 2020.
- [8] MyzharBot, *Thermal Images on Jetson™ Nano with FLIR Lepton3 - Myzhar's MyzharBot and more*, Jul 2021 [Online], <https://www.myzhar.com/blog/jetson-nano-with-flir-lepton3/>

PROGRESS OF NANO-POSITIONING DESIGN FOR THE COHERENT SURFACE SCATTERING IMAGING INSTRUMENT

J.W.J. Anton[†], M. Chu, Z. Jiang, S. Narayanan, D. Shu, J. Strzalka, J. Wang
 Advanced Photon Source, Argonne National Laboratory, Lemont, IL 60439, USA

Abstract

As part of the Advanced Photon Source Upgrade (APS-U) project, the Coherent Surface Scattering Imaging (CSSI) [1] instrument is currently being developed. One of the most important components of the CSSI instrument at the 9-ID beamline of the APS-U, the Kirkpatrick-Baez (K-B) mirror system, will focus hard X-rays to a diffraction-limited size of 500 nanometers at a working distance of 550 mm. High angular stability (19 nrad for the horizontal mirror and 14 nrad for the vertical mirror) is specified not just for the focused beamsizes but, more importantly, to ensure the beam stability at the detector position that is up to 24 m from the K-B mirrors. A large sample-to-detector distance (up to 23 m), one of the beamline's unique features for achieving a sufficient coherent-imaging spatial oversampling, requires sample angular stability of 50 nrad. In CSSI scattering geometry, the vertically placed sample reflects X-rays in the horizontal direction at an extremely shallow angle. The design includes two high-precision rotary stages for sample pitch (vertical axis) and yaw (horizontal axis). The current design of instrument's nano-positioning stages [2] and metrology required to satisfy the stability and positioning requirements are discussed in this paper.

INTRODUCTION

Motivation

The instrument will use coherent X-ray scattering for non-destructive, in-situ structure characterization with high three-dimensional resolution and high temporal resolution. This will allow for the investigation of self-assembly of mesoscale structures at surfaces at interfaces, as well as three-dimensional surface nano-patterning and nano-fabrication.

Large Sample to detector distance (up to 23m) is needed to achieve speckle oversampling. Figure 1 shows a schematic of the instrument, K-B mirrors, and the detector. The X-ray beam is shown in red and the horizontally scattered beam as it travels to the detector is in orange.

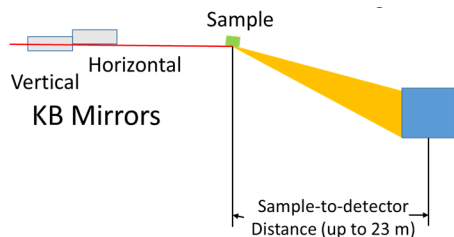


Figure 1: Instrument schematic: Not to scale.

Samples must be scanned with five (5) degrees of freedom (3 linear directions and 2 rotary directions: sample pitch and sample yaw [axis normal to sample surface]).

Technical Approach

To meet the stability and positioning requirements the design makes use of precision commercial stages, custom weak-link laminar flexure stages, and a metrology systems.

Weak-link laminar flexures are used to overcome limitations of ball-/cross-roller bearing stages. Resulting in minimal motion error and high repeatability of motion [2].

Four (4) different metrology frames using capacitive sensors and laser interferometers to achieve positioning and stability requirements. The KB mirror nanopositioning stages measured by a metrology frame with four (4) laser interferometers. The sample nanopositioning stages have three (3) metrology frames. One (1) capacitive sensor based metrology for both rotation scanning stages. The other frame with both capacitive sensors and laser interferometers is used to measure linear scanning stage motion errors.

INSTRUMENT LAYOUT

The CSSI Instrument consists of five (5) major components as shown in Fig. 2:

- Granite air-bearing stages for aligning K-B mirrors and sample to the Beam
- Ultra-high Vacuum Chambers for K-B mirrors
- High vacuum chamber for samples
- Kirkpatrick-Baez mirrors with alignment apparatuses and laser interferometer metrology.
- Sample nanopositioning stages and metrology frames

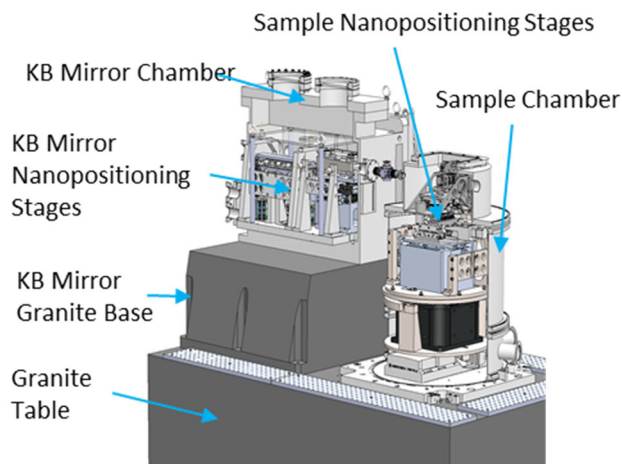


Figure 2: 3D model of the APS CSSI instrument.

[†]anton@anl.gov

FLEXURE STAGES FOR K-B MIRROR SYSTEM

The K-B mirror components are shown in Fig. 3. Two (2) bendable mirrors are used for nanofocusing. One reflecting the beam vertically and the other for horizontally. As seen in Fig. 4 the bending mechanism consists of a lever arms driven by a piezo actuators. Laminar weak-link flexure guided are used for precision bending.

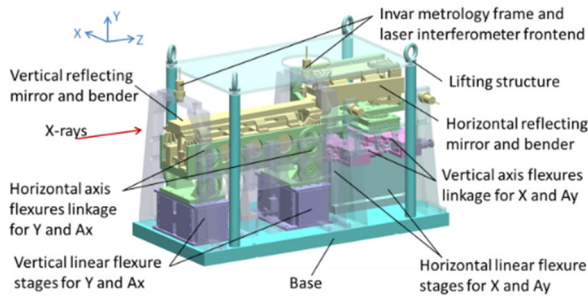


Figure 3: 3D model of the flexure stages system for K-B mirror alignment.

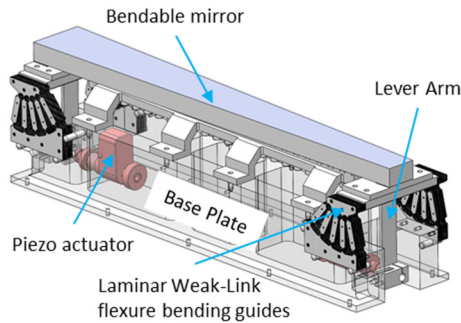


Figure 4: 3D model of KB mirror flexure bending mechanism.

The vertical and horizontal mirrors each utilize weak-link flexures are utilized for aligning the mirrors. The alignment apparatuses consist of two (2) linear weak-link flexure stages and passive weak-link flexures allowing for linear and angular adjustments (see Fig. 5):

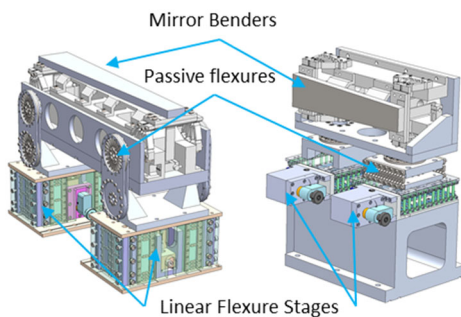


Figure 5: 3D model of horizontal and vertical KB alignment apparatuses.

STAGE SYSTEM FOR SAMPLE MANIPULATION AND SCANNING

The sample manipulation and scanning stages are shown in schematic form in Fig. 6. The Sample motion is divided into 5 groups. Group 0 is the granite support table for the instrument. Group 1 is for sample alignment and positioning. Group 2 are the sample scanning stages. Group 3 are stages to correct sample orientation errors. Group 4 are stages to position a point of interest on the sample with respect to the scanning stages.

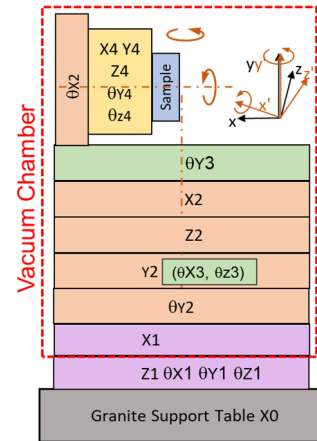


Figure 6: Schematic view of sample stages.

Figure 7 shows a cutout 3D view of the all the sample stages and metrology frames. The sample scanning, correction, and point of interest positioning stages will be discussed further in this section.

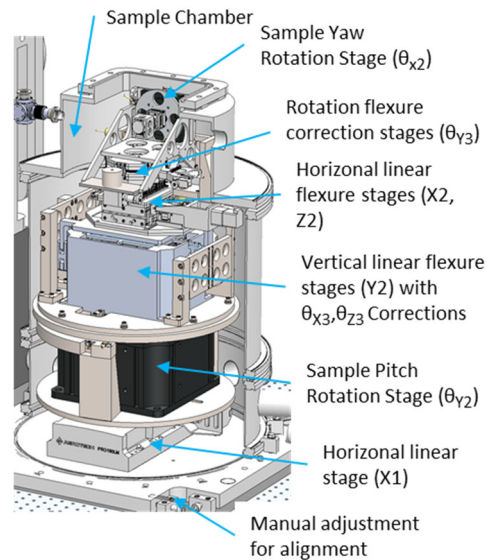


Figure 7: 3D model of the sample stages system.

Sample Scanning and Correcting Stages

The custom flexure stages for scanning and correction are shown in Fig. 8:

1. horizontal stage: flexure bearing stage with centimeter-level travel range with nanometer minimum incremental motion (MIM) [3].
2. Horizontal stage: Piezo driven flexure stage with travel range of 1 mm and nanometer-level MIM [4].
3. Vertical stage: flexure bearing stage with centimeter-level travel range and nanometer level MIM. With piezo actuators to correct any tilt errors.
4. Rotation Correction: flexure stage sample pitch with a travel range $< 1^\circ$ and MIM of tens of nano-radians [2].

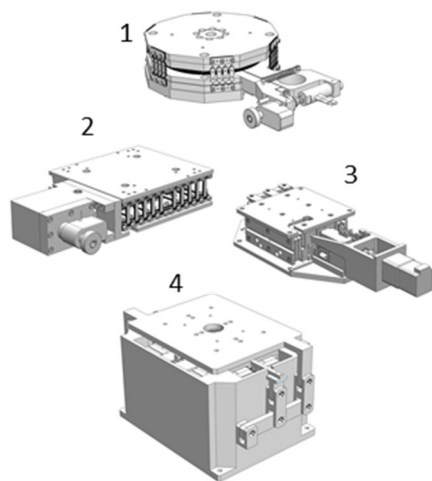


Figure 8: Custom flexure stages for sample scanning and sample.

SAMPLE METROLOGY SYSTEMS

The rotation metrology (shown in Fig. 9) use six (6) channels each of capacitive sensors. The sensors are mounted to an Invar® frame and target a polished aluminum disc. By calibrating the system [5] axial and radial errors can be measured on the nanometer level and tilt errors in the 10s of nanoradians.

The linear stage metrology (Fig. 9) consists of an Invar® frame and three (3) collimated laser interferometers heads with mirrored targets and three (3) capacitive sensors. Linear errors measured at 10s of nanometers and angular errors to 100-200 nanoradians.

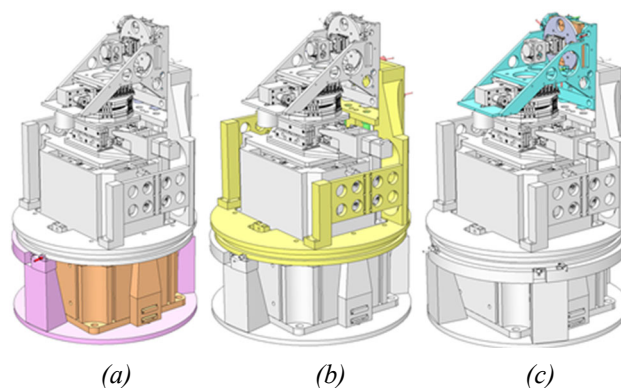


Figure 9: 3D model of the capacitive sensor metrology for scanning rotation stages (a) sample pitch stage metrology (b) linear sample scanning stages (c) sample yaw stage metrology.

SUMMARY

Nanopositioning stages for KB focusing and aligning and for sample scanning and orientation correction. Most of these stages are laminar weak-leak flexure stages allowing the design to meet the stability and poisoning requirements of the APS Upgrade project featured CSSI beamline.

ACKNOWLEDGEMENTS

This research used resources of the Advanced Photon Source, a U.S. Department of Energy (DOE) Office of Science User Facility at Argonne National Laboratory and is based on research supported by the U.S. DOE Office of Science-Basic Energy Sciences, under Contract No. DE-AC02-06CH11357.

REFERENCES

- [1] T. Sun *et al.*, “Three-dimensional coherent X-ray surface scattering imaging near total external reflection,” *Nat. Photonics*, vol. 6, p. 586, 2012. <https://doi.org/10.1038/nphoton.2012.178>
- [2] D. Shu *et al.*, “Modular Nanopositioning Flexure Stages Development for APS Upgrade K-B Mirror Nanofocusing Optics,” presented at MEDSI'20, Chicago, USA, Jul. 2021, paper TUPC10, this conference.
- [3] D. Shu *et al.*, “Mechanical Design of Compact Vertical and Horizontal Linear Nanopositioning Flexure Stages With Centimeter-Level Travel Range for X-Ray Beamline Instrumentation,” in *Proc. IPAC'17*, Copenhagen, Denmark, May 2017, pp. 4096-4099. [doi:10.18429/JACoW-IPAC2017-THPAB154](https://doi.org/10.18429/JACoW-IPAC2017-THPAB154)
- [4] D. Shu *et al.*, “Nanopositioning flexure stages development for synchrotron radiation instrumentation at the advanced photon source,” *AIP Conference Proceedings*, vol. 2054, p. 060025, 2019. <https://doi.org/10.1063/1.5084656>
- [5] R. Grejda *et al.*, “Techniques for calibrating spindles with nanometer error motion,” *Precis. Eng.*, vol. 29, no. 1, pp. 113-123, 2005. <http://dx.doi.org/10.1016/j.precisioneng.2004.05.003>

MODULAR NANOPositionING FLEXURE STAGES DEVELOPMENT FOR APS UPGRADE K-B MIRROR NANOFOCUSING OPTICS*

D. Shu[†], J. Anton, L. Assoufid, S. Bean, D. Capatina, V. De Andrade, E. Dufresne, T. Graber, R. Harder, D. Haskel, K. Jasionowski, S. Kearney, A. Khan, B. Lai, W. Liu, J. Maser, S. Mashrafi, G. Mistri, S. Narayanan, C. Preissner, M. Ramanathan L. Rebuffi, R. Reininger, O. Schmidt, X. Shi, J. Tischler, K. Wakefield, D. Walko, J. Wang, X. Zhang,

Advanced Photon Source, Argonne National Laboratory, Lemont, IL 60439, USA

Abstract

Kirkpatrick and Baez (K-B) mirror-based nanofocusing optics [1] will be applied to many beamlines endstation instruments for the APS-Upgrade (APS-U) project. Precision nanopositioning stages with nanometer-scale linear positioning resolution and nanoradian-scale angular stability are needed as alignment apparatuses for the K-B mirror hard X-ray nanofocusing optics. For instance, at the APS-U 19-ID-E In Situ Nanoprobe beamline endstation [2], to maintain stability of a 20-nm focal spot on the sample, nanofocusing K-B mirror system with 5-nrad angular stability is required. Similar angular resolution and stability are also required for APS-U 9-ID CSSI, APS-U 34-ID ATOMIC and other beamline endstation instruments [3, 4]. Modular nanopositioning flexure stages have been developed for the K-B mirror nanofocusing optics, which includes: linear vertical and horizontal flexure stages, tip-tilting flexure stages, and flexure mirror benders for bendable nanofocusing K-B mirrors, to overcome the performance limitations of precision ball-bearing-based or roller-bearing-based stage systems. The mechanical design and applications are described in this paper.

INTRODUCTION

The Advanced Photon Source (APS) at Argonne National Laboratory (ANL) is scheduled to undergo a massive upgrade that will replace the current electron storage ring with a new Multi-Bend-Achromat (MBA) reverse bent lattice model. X-rays generated by the upgraded APS will be up to 500 times brighter than those created by the current APS. Nine new feature beamlines and enhancements to many existing beamlines will be completed to enable many new exciting scientific research and development capabilities. A total of 12 pairs of K-B nanofocusing mirror systems, including 8 pairs of prefigured mirrors and 4 pairs of bendable mirrors, will be designed and constructed for the APS-U project.

To overcome the performance limitations of precision ball-bearing-based or roller-bearing-based stage systems, precision flexure nanopositioning stages with nanometer-scale linear positioning resolution and nanoradian-scale angular stability are developed at the APS to use as

alignment apparatuses for the K-B mirror hard X-ray nanofocusing optics [5]. These modular stages are designed based on the experiences gained from the flexure stages APS developed for high resolution monochromators [6-10], and especially, for the K-B mirror alignment apparatus for APS 34-ID-E sub-micron 3-D Diffraction experimental station [11, 12]. Lamina weak-link mechanisms [13-15] are applied as a motion guiding structure for the flexure stages. The planar-shape weak-link lamina structure is configured and manufactured by chemical etching and lithography techniques with high-stiffness and high-precision.

As shown in Fig. 1, a typical K-B mirror optics for hard x-ray micro- or nano- focusing is a two-mirror system. Placed orthogonal to each other, each mirror is responsible for a single direction focusing and focused to the same focal spot [5]. With assistance of manual alignment processes prior to the x-ray alignment, the motorized manipulations for the K-B mirrors alignment can be minimized for the linear motion axes X_h , Y_v , and angular tilting motion axes A_{xv} , A_{yh} . In many in-vacuum setup, the orthogonality and distance between the two mirrors are also need to be aligned under X-ray.

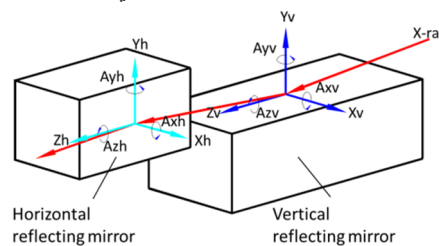


Figure 1: Schematic diagram of the K-B mirror hard X-ray nanofocusing optics.

STAGES DESIGN ENHANCEMENT

Several design enhancements are made for the modular K-B mirror stages for the APS-Upgrade project, which include:

- Designed linear flexure stages with optional extended travel range.
- Designed flexures linkage mechanisms with two vertical or horizontal linear flexure stages to perform linear and angular adjustment for longer mirrors.
- Designed motorized flexure stages for orthogonality adjustment.
- Equipped capacitive sensor for all linear and tip-tilt flexure stages as an option.

* This research used resources of the Advanced Photon Source, a U.S. Department of Energy (DOE) Office of Science User Facility at Argonne National Laboratory and is based on research supported by the U.S. DOE Office of Science-Basic Energy Sciences, under Contract No. DE-AC02-06CH11357.

[†]shud@anl.gov

Content from this work may be used under the terms of the CC BY 3.0 licence (© 2021). Any distribution of this work must maintain attribution to the author(s), title of the work, publisher, and DOI

- Ultra-High-Vacuum (UHV) compatibility option is available for both linear and tip-tilt flexure stages.
- Options for bendable K-B mirrors.

Figure 2 shows a photograph of the new laminar weak-link linear motion guiding mechanisms for APS T8-49v02 UHV-compatible vertical flexure stage with 1-nm positioning resolution and 1-mm travel range. The load capacity of the Picomotor™/PZT-driven stage is 10-kg. As shown in Fig. 3, the new T8-48v04 horizontal flexure stage is UHV-compatible with 1-nm positioning resolution, 1-mm travel range, and 4-kg load capacity. A 3D model is shown in Fig. 4 to illustrate a flexures linkage mechanism for a 400-mm-long vertical reflecting mirror alignment apparatus. With two vertical linear flexure stages, it can perform a minimum vertical displacement of 1 nm, and a pitch adjustment in nanoradian scale.



Figure 2: Photograph of the APS T8-49v02 vertical flexure stage weak-link guiding mechanisms.



Figure 3: Photograph of the APS T8-48v04 UHV-compatible horizontal flexure stage.

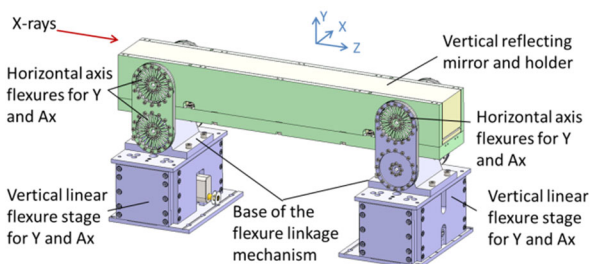


Figure 4: 3D model of the APS UHV-compatible flexures linkage mechanism for a 400-mm-long vertical reflecting mirror alignment apparatus.

APPLICATION CONFIGURATIONS

Short K-B Mirrors in a Mini-UHV-Chamber

A Mini-UHV-Chamber has been developed at the APS 34-ID-E for nanofocusing K-B mirrors with vertical reflecting mirror length of 65 – 100 mm, and horizontal reflecting mirror length of 25 – 40 mm. The Mini-UHV-Chamber is mounted on the top of a multidimensional flexure stage system with four flexure stages for x-ray nanofocusing with focal spot in the sub-50-nanometer scale as shown in Fig. 5 [5].

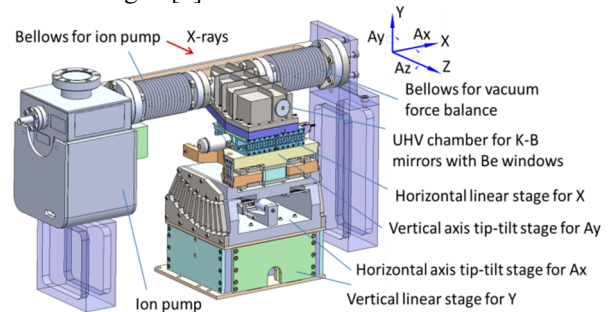


Figure 5: 3D model of the 34-ID-E Mini-UHV-Chamber with multidimensional flexure stage system.

Short or Medium K-B Mirrors in Helium

As a compact/cost-effective solution, nanofocusing K-B mirrors with vertical reflecting mirror length of 65 – 200 mm, and horizontal reflecting mirror length of 45 – 100 mm can be mounted on separate flexure stage groups on a base with gantry structure as shown in Fig. 6 [16].

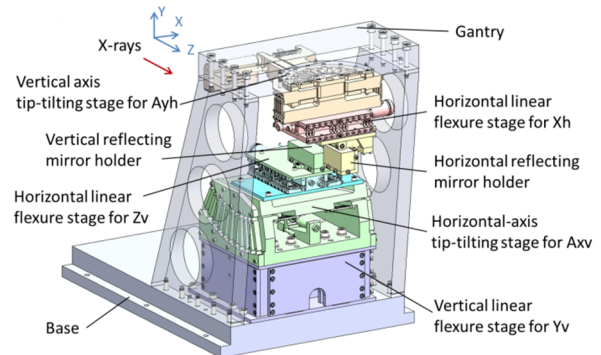


Figure 6: 3D model of the 32-ID nanofocusing K-B mirrors with separate flexure stage groups on a base with gantry structure.

Short or Medium K-B Mirrors in UHV

Short or medium K-B mirrors can also be mounted on separate flexure stage groups in a UHV chamber with or without gantry structure to fit with the instrument space. Figure 7 shows a pair of nanofocusing K-B mirrors with a vertical reflecting mirror length of 150 mm, and a horizontal reflecting mirror length of 100 mm for the APS-U 7-ID-D Multi Modal Imaging and Diffraction (MMID) instrument. Both stage groups for vertical and horizontal mirrors are mounted on the same base in UHV.

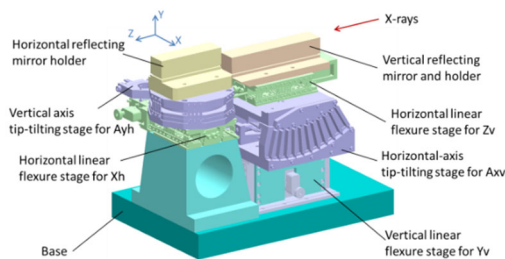


Figure 7: 3D model of the 7-ID-D nanofocusing K-B mirrors with flexure stage groups on same base in UHV.

Long Prefigured K-B Mirrors in UHV

For a nanofocusing K-B mirror with length longer than 200 mm, flexures linkage mechanism driven differentially by two linear flexure stages can perform better angular positioning resolution and stability. Figure 8 shows the design of K-B mirror stage system for APS-U 19-ID-E In-Situ Nanoprobe (ISN) instrument [2] with vertical reflecting mirror length of 404 mm, and horizontal reflecting mirror length of 129 mm. The design aim is to achieve 1 nm and 5 nrad positioning resolution for x-ray nanofocusing with focal spot ~ 20 nm with integrated laser interferometer and capacitive sensors. Figure 9 shows the design of K-B mirror stage system for APS-U 4-ID-G Polarization Modulation Spectroscopy (POLAR) instrument with vertical reflecting mirror length of 328 mm, and horizontal reflecting mirror length of 147 mm. Commercial motorized coarse stages are used to switch between multiple mirror coating strips.

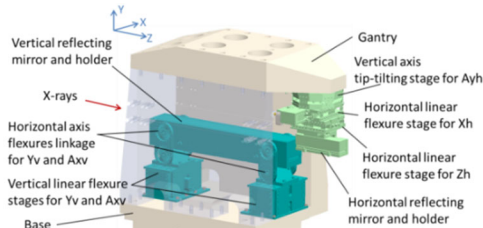


Figure 8: 3D model of the 19-ID-E ISN K-B mirrors with stage groups on a base with gantry structure in UHV.

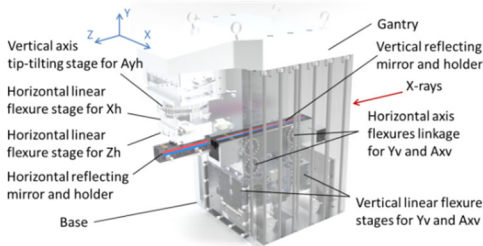


Figure 9: 3D model of the 4-ID-G ISN K-B mirrors with stage groups on a base with gantry structure in UHV.

Long Bendable K-B Mirrors in UHV

The APS modular nanositioning flexure stages also support the applications with APS bendable K-B mirrors [17, 18]. As shown in Fig. 10, the K-B mirror stage system for APS-U 9-ID-D Coherent Surface Scattering (CSSI) instrument [3] includes two APS developed flexure mirror benders with vertical reflecting mirror length of 300 mm, and horizontal reflecting mirror length of 180 mm.

Precision mechanics

Nano-Positioning

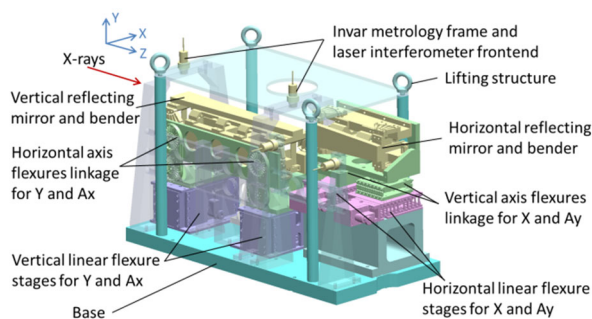


Figure 10: 3D model of the 9-ID-D nanofocusing K-B mirrors with flexure stage groups on the same UHV base.

The flexure stage group for both vertical and horizontal mirror benders are mounted on the same Invar base with Invar metrology frames for laser interferometer fiber optics frontends in UHV. The design goal of this bendable K-B mirror stage system is to provide variable x-ray focal spot with angular beam stability better than 20 nrad.

SUMMARY

Modular nanositioning stages with nanometer-scale linear positioning resolution and nanoradian-scale angular stability are developed for the K-B mirror hard X-ray nanofocusing optics. Preliminary test results for the APS 32-ID flexure stages showed nanometer-scale linear positioning resolution with nanoradian-scale angular stability [16]. Table 1 summarized UHV-compatible modular nanositioning stages to be applied for the K-B mirror hard X-ray nanofocusing optics for APS-U project.

Table 1: Applications of the UHV-Compatible Modular Nanositioning Flexure Stages for APS-U Project

UHV Flexure Stages Linkages Benders					
	H Stage T8-48v04	V Stage T8-49v02	Ay Stage T7-52	Linkage Z7-61	Bender Z7-70
APS-U 4-ID-G POLAR	Qty. 2	Qty. 2	Qty. 1	Qty. 1 With adj.	
APS-U 4-ID-H POLAR	Qty. 2	Qty. 2	Qty. 1	Qty. 1 With adj.	
APS-U 7-ID-D MMID	Qty. 1	Qty. 1	Qty. 1		
APS-U 8-ID-E XPCS	Qty. 2	Qty. 2		Qty. 1 With adj.	Qty. 2 With adj.
APS-U 9-ID-D CSSI	Qty. 2	Qty. 2		Qty. 1 With adj.	Qty. 2 With adj.
APS-U 19-ID-E ISN	Qty. 2	Qty. 2	Qty. 1	Qty. 1 With adj.	
APS-U 34-ID-F ATOMIC	Qty. 2	Qty. 2		Qty. 1 With adj.	Qty. 2 With adj.

ACKNOWLEDGEMENTS

The authors would like to acknowledge the management support from Advanced Photon Source, Argonne National Laboratory.

REFERENCES

- [1] P. Kirkpatrick, and A. V. Baez, "Formation of Optical Images by X-Rays," *J. Opt. Soc. Am.*, vol. 38, no. 9, pp. 766-774, 1948.
<https://doi.org/10.1364/JOSA.38.000766>
- [2] S. Kearney *et al.*, "Mechanical Design Progress of the In Situ Nanoprobe Instrument for APS-U," presented at MEDSI2010, Chicago, IL, USA, July 2021, paper MOPC10, this conference.
- [3] J. Anton *et al.*, "Progress of Nano-Positioning Design for the Coherent Surface Scattering Imaging Instrument for the Advanced Photon Source Upgrade Project," presented at MEDSI2010, Chicago, IL, USA, July 2021, paper TUPC09, this conference.
- [4] C. Preissner, private communications.
- [5] D. Shu, W. Liu, J. Maser, B. Lai, Z. Cai, R. Harder, R. Xu, L. Assoufid, S. Vogt, and J. Z. Tischler, "Design of Multi-dimensional Flexure Stage System for Hard X-ray Mirror Focusing at Sub-50-Nanometer Scale," in *Proc. 2013 ASPE Annual Meeting*, St. Paul, MN, USA, October 2013, pp. 182-185.
- [6] D. Shu, S. Kearney, J. Anton, "Nanopositioning Flexure Stages Development for Synchrotron Radiation Instrumentation at the Advanced Photon Source," *AIP Conference Proceedings 2054*, p. 060025, 2019.
<https://doi.org/10.1063/1.5084656>
- [7] S. Narayanan, A.R. Sandy, M. Sprung, J. Sullivan, C. Preissner, and D. Shu, "Initial Characterization and Design of an UHV-Compatible Artificial Channel-Cut Monochromator," *AIP Conference Proceedings 879*, pp. 911-914, 2007.
<https://doi.org/10.1063/1.2436209>
- [8] S. Narayanan, A. Sandy, D. Shu, M. Sprung, C. Preissner and J. Sullivan, "Design and performance of an ultra-high-vacuum-compatible artificial channel-cut monochromator," *J. Synchrotron Radiat.*, vol. 15, pp. 12-18, 2008.
 doi:10.1107/S090904950705340X
- [9] D. Shu, S. Narayanan, A. Sandy, M. Sprung, C. Preissner, and J. Sullivan, "Precision Mechanical Design of an UHV-Compatible Artificial Channel-Cut X-ray Monochromator," *Proc. SPIE Vol. 6665*, p. 666500, 2007.
<https://doi.org/10.1117/12.733101>
- [10] X. Dong, D. Shu, and H. Sinn, "Design of a cryo-cooled artificial channel-cut crystal monochromator for the European XFEL," *AIP Conference Proceedings*, vol. 1741, p. 040027, 2016. <https://doi.org/10.1063/1.4952899>
- [11] D. Shu, W-K. Lee, W. Liu, G. E. Ice, Y. Shvyd'ko, K-J. Kim, "Development and Applications of a Two-Dimensional Tip-Tilting Stage System with Nanoradian-Level Positioning Resolution," *Nucl. Instrum. Methods Phys. Res., Sect. A*, vol. 649, pp. 114-117, 2011.
 doi:10.1016/j.nima.2011.01.039
- [12] D. Shu, J. Maser, W. Liu, B. Lai, and L. Assoufid, "Nanopositioning Design for X-ray Nanofocusing with K-B Mirrors and MLLs at the APS", in *Proc. MEDSI-2012*, Shanghai, China, Oct. 2012, <http://medsi2012.csp.science.cndct/page/65624>
- [13] D. Shu, T. S. Toellner, and E. E. Alp, "Modular Overconstrained Weak-Link Mechanism for Ultraprecision Motion Control," *Nucl. Instrum. Methods Phys. Res., Sect. A*, vol. 467-468, pp. 771-774. 2001.
[https://doi.org/10.1016/S0168-9002\(01\)00499-5](https://doi.org/10.1016/S0168-9002(01)00499-5)
- [14] D. Shu, T. S. Toellner, and E. E. Alp, "Redundantly constrained laminar structure as weak-link mechanisms," U.S. Patent granted No. 6,607,840, 2003.
- [15] D. Shu, T. S. Toellner, E. E. Alp, J. Maser, J. Ilavsky, S. D. Shastri, P. L. Lee, S. Narayanan, and G. G. Long, "Applications of Laminar Weak-Link Mechanisms for Ultraprecision Synchrotron Radiation Instruments," *AIP Conference Proceedings 879*, pp. 1073-1076, 2007.
<https://doi.org/10.1063/1.2436249>
- [16] D. Shu, V. De Andrade, J. Anton, S. Kearney, K. Fezzaa, S. Bean, A. Deriy, "Mechanical design of a flexural nanopositioning stage system for hard x-ray nanofocusing at the Advanced Photon Source 32-ID-C station," in *Proc. SPIE 11112, X-Ray Nanoimaging: Instruments and Methods IV*, vol. 11112, San Diego, CA, USA, August 2019, p. 111120N.
<https://doi.org/10.1117/12.2529384>
- [17] D. Shu, A. Li, S. P. Kearney, C. Mao, J. Anton, R. Harder, X. Shi, T. Mooney, and L. Assoufid, "Optomechanical Design of Compact Laminar Flexure Bending Mechanism for Elliptically Bent Hard X-ray Mirrors," *AIP Conference Proceedings 2054*, p. 060015, 2019.
<https://doi.org/10.1063/1.5084646>
- [18] D. Shu, J. Anton, S. Kearney, R. Harder, X. Shi, T. Mooney, S. Mashrafi, J. Qian, B. Shi, and L. Assoufid, "Design of a capacitive-sensor-array-based real-time mirror profiler for elliptically dynamic bent mirror for hard x-ray zoom optics," in *Proc. ASPE 2019 Annual Meeting*, vol. 71, Pittsburgh, PA, USA, 2019, pp. 111-114.

THE HD-DCM-Lite: A HIGH-DYNAMIC DCM WITH EXTENDED SCANNING CAPABILITIES FOR SIRIUS/LNLS BEAMLINES

A. V. Perna[†], G. S. de Albuquerque, H. O. C. Duarte, R. R. Gerald¹, M. A. L. Moraes,
M. Saveri Silva, M. S. Souza, LNLS, Campinas, Brazil

¹also at the Eindhoven University of Technology (TUE), 5612AZ Eindhoven, The Netherlands

Abstract

After successfully designing, installing, and commissioning two units of the High-Dynamic Double-Crystal Monochromator (HD-DCM) at the Brazilian Synchrotron Light Laboratory (LNLS) - Sirius, two more units are now required. Since they demand only a smaller energy range (5 to 35 keV), the total gap stroke of the new instruments can be significantly reduced, creating an opportunity to adapt the existing design towards the so-called HD-DCM-Lite. Removing the large gap adjustment mechanism allows a reduction of the main inertia by a factor of 5, enabling the HD-DCM-Lite to deliver energy flyscans of hundreds of eV reaching 20 cycles per second while keeping fixed exit and the pitch stability in the range of 10 nrad RMS (1 Hz - 2.5 kHz). Hence, an unparallel bridge between slow step-scan DCMs and fast channel-cut monochromators is created. This work presents the in-house development of the HD-DCM-Lite, focusing on its mechanical design, discussions on the ultimate scanning constraints (rotary stage torque, voice-coil forces, interferometers, and encoders readout speed limits and subdivisional errors), and thermal management.

INTRODUCTION

A lighter version of the High-Dynamic Double-Crystal Monochromator (HD-DCM) [1-3] has been designed for two of the new Sirius beamlines at the Brazilian Synchrotron Light Laboratory (LNLS): the QUATI (quick absorption spectroscopy) and the SAPUCAIA (small-angle scattering) beamline. Differently from the two first beamlines that required larger angular (3° to 60°) and energy range (2.3 to 35 keV), these two forthcoming beamlines have smaller energy range requirements – namely, 5 to 35 keV for QUATI and 5 to 18 keV for SAPUCAIA –, allowing a design with an angular range from 5° to 40° . In addition, QUATI also adds the challenge of time-resolved analysis, benefiting from quick energy scans. The new design focus on extending its scan capabilities while preserving stability creating a solution between the current HD-DCM (limited in speed but with fixed-offset and extremely stable) and fast channel-cut monochromators [4], which suffer from offset variation. This work will present the main topics considered during the design of the HD-DCM-Lite.

MECHANICAL DESIGN

The current HD-DCM design was used as starting point for the HD-DCM-Lite because it is an extensively optimized and tested system, proven to reach 10 nrad RMS

(root mean square) of pitch parallelism performance (within 1 Hz to 2.5 kHz) [2]. Nevertheless, the design had to be adapted to become capable of meeting the fast energy scan requirements for quick-EXAFS (Extended X-ray Absorption Fine-Structure) experiments. Since only the design variations can be discussed here for conciseness, [1] may be consulted for the full set of specifications.

The total gap range between crystals could be reduced from 9 mm to 2.75 mm, such that the long-stroke (LOS) mechanism (see [1]) could be eliminated, enabling a more compact, easier to assemble and cheaper system. Consequently, the moment of inertia was reduced from 13.5 kg.m² to 2.7 kg.m², allowing higher accelerations, an important upgrade towards fast scan capability.

Another essential step was doubling the torque capability, now reaching 58.2 N.m after substituting the passive bearing by another Aerotech's APR-260DR-180 rotary stage, thus increasing the scanning capabilities. To handle the power dissipation of the two rotary stages in demanding long-term scan trajectories, a water-cooling circuit has been implemented on the stages. The HD-DCM-Lite is shown in Fig. 1 in comparison to the original HD-DCM.

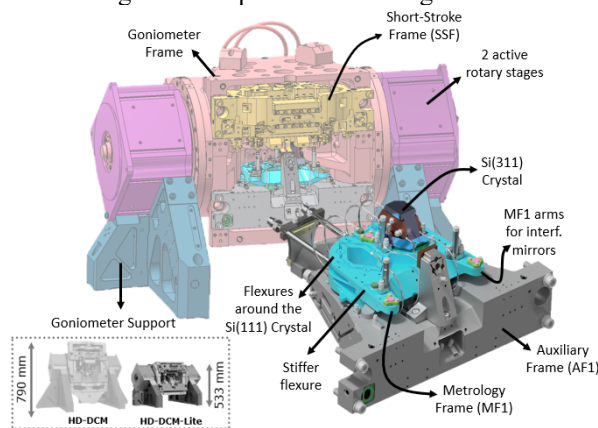


Figure 1: Highlights of the main mechanical design changes and improvements in the HD-DCM-Lite.

From lessons learned [5], this designing opportunity is also taken for improvements in the dynamics of the metrology frame (MF1) supporting the first crystals (CR1s). Increasing its mounting stiffness – by removing the zirconia spacers between MF1 and Auxiliary Frame (AF1) and stiffening the flexures between them – and shortening its “arms” for the interferometer mirrors, the first eigenfrequency should increase from 500 to 800 Hz, reducing the sensitivity to disturbances. Then, to recover the required thermal resistance between the CR1s and the AF1, a complementary set of flexures is added around the CR1s.

[†] alain.perna@lnls.br

SCANNING CONSTRAINTS

For time-resolved experiments, faster energy scans may enable scientific opportunities in analyzing quick chemical reactions or material phase variations, for example. Therefore, every design decision in the HD-DCM-Lite must consider its impact on pushing the scanning speed to its limits. The following discussion presents the main factors that constrain the scanning capabilities, also predicting how fast the system will be able to go.

Torque and Sensors Constraints

Regarding the rotary stages, scanning speeds can be limited by torque and sensor readout rate for quadrature signals, which, assuming sinusoidal trajectories, can be evaluated according to:

$$f_{\max_T} = \frac{1}{2\pi} \sqrt{\frac{T_{\max}}{AI_{xx}}} \quad (1)$$

$$f_{\max_e} = \frac{res_e f_r}{2\pi A} \quad (2)$$

In (1), knowing the system moment of inertia I_{xx} and given a desired angular amplitude A , the maximum frequency f_{\max_T} that the system can develop is bounded by the maximum torque T_{\max} in the rotary stages. This maximum frequency will be different for: the Si(111) and Si(311) crystal sets; the absolute energy values; and the scanning energy amplitude, because they change the amplitude A according to Bragg's law of diffraction.

In (2), the maximum scanning frequency f_{\max_e} due to the encoder readout speed depends on its resolution res_e , the angular amplitude A , and the acquisition rate f_r for the quadrature signal. With the current control solution for the HD-DCM using NI's CompactRIO (cRIO) [6], f_r is limited to 10 MHz. Among the options given by the stage manufacturer, two encoders with resolutions of 191 nrad and 19.1 nrad were compared. For some range of energies, it was observed that the encoder with the best resolution would dominate the scanning frequency limits over the torque boundaries, whereas the encoder with 191 nrad of resolution will not add new limits - while preserving acceptable energy resolution - becoming the one selected.

Yet, a sinusoidal trajectory is never completely smooth in real world. For example, when using optical encoders, there are errors within the scale pitch length called Sub-Divisional Errors (SDE). This noise added to the smooth position trajectory creates regions with higher derivative, resulting in an increment of the speed read by the encoder. In this case, the calculations show that this contribution is not more than 1% of the total speed. Still, these accelerations do have some impact in the control dynamics and final stability.

Now, concerning the control of the gap between crystals made by the short-stroke (SHS) (see [1]), its built-in SmarAct's Picoscale interferometer is also currently read as a quadrature signal limited at 10 MHz in cRIO, such that the target speed is limited to 1 mm/s for the current resolution of 0.1 nm. Therefore, the speed in the gap adjustment

(following the rotary stages angle to keep the fixed beam offset) cannot exceed this limit. This sensor also has SDE, but its amplitude is negligible. If required in the short term, the resolution can be worsened, at the cost of some loss in stability performance, to increase speeds. For the long term, work is in progress to handle the PicoScale data as an absolute measurement, without speed limits.

Uniting the torque, encoder and current interferometer limitations, Fig. 2 was constructed to show the first prediction for the HD-DCM-Lite scanning boundaries (the horizontal boundary is related to the balance-mass (BMS) [1] displacement limits, which will be presented later). For low energies, the interferometer is the main constraint (non-linear in energy), whereas torque (linear in energy) limits the higher frequencies. Scanning frequencies above the curves cannot be performed.

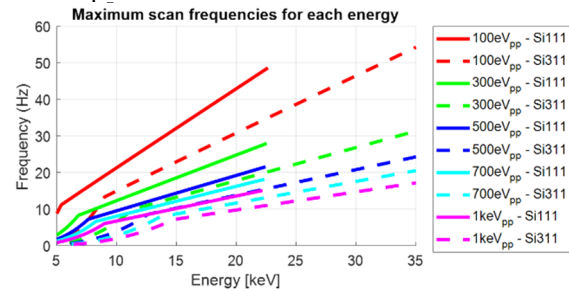


Figure 2: Maximum scanning frequencies constrained by torque, encoder, and interferometer limitations for each crystal set, central energy, and amplitude (peak-to-peak).

Voice-Coil Effort Constraints

In the field of possible trajectories constrained as previously discussed, some representative options were simulated (using a MATLAB® toolbox developed for Dynamic Error Budgeting [5]) to predict the resulting effort at each of the three voice-coil (VC) actuators of the SHS (see [1]), checking for their operational limits and verifying if their dissipated power could compromise the thermal management (detailed in the next session). The worst-case scenario happens for the trajectory with highest possible frequency, i.e., 54 Hz and 0.2 mrad of amplitude for Si(311), resulting in RMS forces of 0.3 N in the upstream (VC1) and 3.1 N in the downstream VCs (VC2 and VC3).

These RMS forces do not include the offset effort necessary to have the SHS at the exact nominal gap value to start scanning, which is a crucial aspect in the HD-DCM-Lite, since there is no compensation by the LOS module. Considering the limits at 5° and 40°, with gap values of 9.03 mm and 11.75 mm, and the natural sag variation related to the SHS weight, up to more 3.1 N is required for each VC. Finally, these effort contributions must be added to a final one: the force necessary to correct angular misalignments and parasitic torques (passively introduced after baking and cryocooling procedures) between the SHS and the MF1. With the experience gathered with the existing HD-DCMs and considering a safety factor, the resulting worst-case misalignment correction could reach 3 mrad, demanding additional 1.3 N for VC1 and 1.8 N for VC2 and VC3.

Uniting all contributions, maximum values of 4.7 N for VC1 and 8.0 N for VC2 and VC3 are obtained, which, according to Akribis' AVM-40-HF-6.5 datasheet [7], is still within 50% of the maximum continuous force specification (at 100°C). Thus, using the force sensitivity constant of 20.7 N/A and the resistance of 11.31 Ω, the power consumption for VC1 could reach 0.6 W, and 1.7 W for VC2 and VC3 individually, totalling 4.0 W.

Balance-Mass Displacement Constraints

The last factor to be considered is the balance-mass (BMS) displacement. As the VCs act to position the SHS with respect to the MF1, the reaction forces are directed to the BMS, which responds passively over its mounting stiffnesses, with the possibility of collisions against the mechanical hard-stops, creating disturbances and stopping the system. The solution was to increase the stiffness of the folded leaf-springs that constrain the BMS. Yet, although smaller displacements now occur for the same reaction forces and higher forces are allowed, the consequence in dynamics is shifting the eigenfrequencies from 6.1 Hz to 25.8 Hz and from 9.0 Hz to 38.0 Hz for the gap and pitch/roll degrees of freedom (DoFs), respectively. This means that the BMS is now slightly less efficient as a dynamic filter, but still compatible with the overall mechatronic architecture, as verified in the dynamic models.

Then, still using the same model and following the analyses of the VC efforts, i.e., considering offset, scanning and misalignment-related effects, a few representative cases were selected to investigate the displacement of the BMS in all three DoFs with respect to both its mounting frame and the SHS. As the BMS is now relatively stiffer, for the lower scanning frequencies its displacements remain within only a small fraction of the tolerable ranges of a few millimeters and milliradians. As it might be expected, the limits are found as the displacements quickly increase near the BMS resonances. Thus, respecting the constraints in Fig. 2, a new constraint of at least 24 Hz must be considered, with simulation results suggesting that even higher frequencies still below 38 Hz may become feasible.

To conclude, with simplified mechanics, the predictions for the HD-DCM-Lite pitch stability show the even better static performance of 5 nrad RMS (1 Hz - 2.5 kHz), which may be maintained even for some scanning conditions with appropriate control strategies, but also leaves some margin for occasional scanning disturbances.

THERMAL MANAGEMENT

As in the mechanical design, the thermal management of the HD-DCM-Lite was also based on the HD-DCM [8]. Here, the beam power load inputs are 54 W for QUATI and 80 W for SAPUCAIA. Aside from keeping all components functioning within nominal temperatures, the main objective is to keep the CR1s cryogenically cooled at 78 K – as not to damage them with the high-power densities –, and the lattice parameter of the 2nd crystals (CR2s) close to that of the hotspot in the CR1s, to prevent energy mismatching. For modelling purposes, the ideal temperature

was considered as 155 K as a mean value for different operating conditions or modes of the system.

A lumped-mass thermal model was developed in Simulink®. The conductances were simulated via Ansys® for each connection separately as a geometric factor to include non-linear temperature effects. The model also included radiation, which was obtained using Gebhart factors [9] from a view factor matrix simulated in Ansys Fluent® from a simplified model. The contact resistances were estimated according to [10, 11]. The Simulink® model was a time-domain transient solution for the system, using look-up tables to get the temperature-dependent conductivity for the nodes, and an algebraic thermal radiative heat flux output at each time step, from the Gebhart factors. With this model, it was possible to obtain the desired high-conductivity braid specifications [12] for the CR2s. Only one braid was necessary in this design, resulting in less contact resistances and better cooling performance.

Then, a sensitivity study for the voice-coils was made, to analyse its power output influence on the CR2s working temperature, in addition to its own. The results can be seen in Fig. 3. As the expected power output is less than 4 W total, this should not impose an additional constraint on the design.

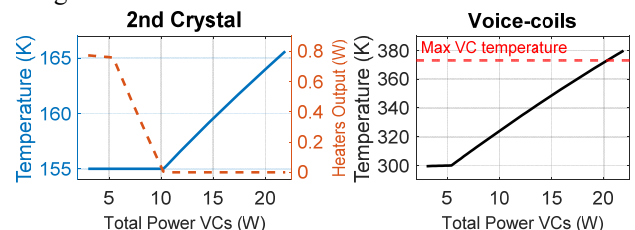


Figure 3: Simulated temperatures of the active 2nd crystal and mean VCs temperature as a function of the VCs power.

CONCLUSION

The predictive design methodology that successfully conceived the HD-DCM is now applied in the development of the HD-DCM-Lite for extended scanning capabilities while maintaining ultra-high stability performance. The competences in design and control, together with toolboxes and libraries, that were developed over the first project have allowed the new machine to be completely designed in-house at LNLS in a short time scale. The prototype is expected to start to be tested still in 2021.

ACKNOWLEDGEMENTS

The authors would like to gratefully acknowledge the funding by the Brazilian Ministry of Science, Technology and Innovation and the contributions of the LNLS team. They also recognize the essential role of MI-Partners in the development of the original HD-DCM and in the workflow adopted here, and the discussions that allowed for the development of many of the tools used in this work as part of a PhD project carried out with the CST group at TUE, with Marteen Steinbuch and Hans Vermeulen as promoters, and Gert Witvoet as co-promotor.

REFERENCES

- [1] R. R. Geraldès *et al.*, “The New High Dynamics DCM for Sirius,” in *Proc. 9th Mechanical Engineering Design of Synchrotron Radiation Equipment and Instrumentation Int. Conf. (MEDSI'16)*, Barcelona, Spain, Sep. 2016, pp. 141-146. doi:10.18429/JACoW-MEDSI2016-TUCA05
- [2] R. R. Geraldès *et al.*, “The Status of the New High-Dynamic DCM for Sirius,” in *Proc. 10th Mechanical Engineering Design of Synchrotron Radiation Equipment and Instrumentation Int. Conf. (MEDSI'18)*, Paris, France, Jun. 2018, pp. 147-152. doi:10.18429/JACoW-MEDSI2018-WE-OAMA01
- [3] R. R. Geraldès *et al.*, “Commissioning and prospects of the High-dynamic DCMs at Sirius/LNLS,” presented at MEDSI 2020, Chicago, USA, Jul. 2021, paper MOPB03, this conference.
- [4] O. Müller *et al.*, “Quick scanning monochromator for millisecond in situ and in operando X-ray absorption spectroscopy,” *Rev. Sci. Instrum.*, vol. 86, no. 9, p. 093905, 2015. doi.org/10.1063/1.4929866
- [5] R. R. Geraldès *et al.*, “Dynamic error budgeting in the development of the High-Dynamic Double-Crystal Monochromator at Sirius Light Source,” in *Proc. ASPE Topical Meeting 2020*, Boston, USA, May 2020.
- [6] M. A. L. Moraes *et al.*, “The FPGA control implementation of the High-Dynamic Double-Crystal Monochromator at Sirius Light Source,” presented at ASPE Topical Meeting 2020, Boston, USA, May 2020, unpublished.
- [7] Akribis Systems, “AVM Series,” AVM-40-HF-6.5 datasheet, https://www.micromech.co.uk/uploads/assets/pdf/akribis/voice_coil_motors/akribis_avm_series_datasheet.pdf
- [8] M. Saveri Silva, R. R. Geraldès, A. Gilmour, T. A. M. Ruijl, and R. M. Schneider, “Thermal Management and Crystal Clamping Concepts for the New High-Dynamics DCM for Sirius,” in *Proc. 9th Mechanical Engineering Design of Synchrotron Radiation Equipment and Instrumentation Int. Conf. (MEDSI'16)*, Barcelona, Spain, Sep. 2016, pp. 194-197. doi:10.18429/JACoW-MEDSI2016-TUPE15
- [9] B. Gebhart, “Surface temperature calculations in radiant surroundings of arbitrary complexity—for gray, diffuse radiation,” *Int. J. Heat Mass Transfer*, vol. 3, no. 4, pp. 341–346, 1961. doi.org/10.1016/0017-9310(61)90048-5
- [10] P. Marion, L. Zhang, L. Goirand, M. Rossat, and K. Martel, “Cryogenic cooling of monochromator crystals: indirect or direct cooling?”, in *Proc. MEDSI 2006*, Hyogo, Japan, May 2006.
- [11] M. S. Silva, “Thermal modelling for the development of a four-bounces crystal monochromator for the Sirius project”, University of Campinas, 2019.
- [12] F. R. Lena *et al.*, “Copper Braid Heat Conductors for Sirius Cryogenic X-Ray Optics,” presented at MEDSI 2020, Chicago, USA, Jul. 2021, paper TUPC14, this conference.

COPPER BRAID HEAT CONDUCTORS FOR SIRIUS CRYOGENIC X-RAY OPTICS

F. R. Lena[†], G. V. Claudiano, J. C. Corsaletti, R. R. Geraldes, D. Y. Kakizaki, R. L. Parise,
M. Saveri Silva, M. S. Souza, L. M. Volpe, LNLS, Campinas, Brazil

Abstract

The low emittance and high photon flux beam present at the 4th-generation Sirius synchrotron light source beamlines result in high energy densities and high heat loads at some specific X-ray optics such as monochromators and white beam mirrors. This challenges the design of such systems since the introduction of thermal stresses may lead to optical surface deformation and beam degradation. Thus, to keep the systems within acceptable deformations some of the optical elements are cryogenically cooled. However, this poses the requirements of decoupling the thermal sinks (cryostats) from the optics and the mechanisms to maintain their desired degrees of freedom for alignment and dynamic operation. In this context we present the development of low-stiffness copper-braid-based heat conductors, summarizing the motivation and main aspects regarding their fabrication and application at the beamlines.

INTRODUCTION

For high heat-loads monocrystalline silicon optics at Sirius beamlines, one of the standard design concepts for beam-load deformation suppression is the use of liquid nitrogen (LN₂) cryostats for cooling the elements down to near 125K, where their coefficient of thermal expansion is virtually zero and deformations due to thermal gradients are minimized [1]. In this context, low-stiffness copper braids are widely used to thermally couple the optics to the cryostats while limiting the mechanical coupling between them, such that external vibration disturbances are avoided and kinematic is preserved. Even though commercial solutions for cryogenic, ultra-high vacuum (UHV) compatible copper braids exist worldwide, the high costs, long lead time and customization limitations stimulated the development of an in-house solution with local partners. For special applications, either because of complex geometry or heat extraction capacity, smaller braided modules can be soldered into larger systems using low temperature fillers.

COPPER BRAID MANUFACTURE

The basic manufacturing process consists in cold forging (ambient temperature), or *pressing*, copper ropes inside bulky copper terminals. The copper ropes are usually made from cold-drawn thin wires stranded together to form a small braid with the diameter in the millimeter range. This results in an all-copper, weld free braid system with solid ends that can be machined for different geometries. As there is no metallurgical joint between the wires themselves and the end-blocks, the heat must be carried across multiple contact interfaces, making the correct design of these interfaces a point of attention. Furthermore, the

copper thermal conduction at low temperatures has a strong correlation with its electrical conductivity [2] and is heavily affected by impurities as oxygen and sulphur, leading to the correct material selection [3].

Commercial and 1st-Generation In-House Braids

An initial effort of in-house development of copper braids for mirrors and monochromators was made between the years of 2017 and 2019. The first systems were designed by the LNLS team and manufactures by a local partner (Barbanera Qualità) and consisted of pressing multiple braids of 2.5mm in diameter inside electrical-discharge-machined (EDM) cavities in the electrolytic copper end-blocks. The braids were made of 588 40 AWG stranded electrolytic-tough-pitch (ETP) copper wires by the national manufacturer Indel LTDA. The pressing was performed with a 100-ton hydraulic press in an open-die fashion, i.e. without any mold. The compaction criteria were visual, with the pressing process being stopped when there were no visible gaps between the wires and the block. The large end-blocks were then machined, and the entire braid system gold plated to reduce radiation heat transfer.

Despite the good geometry and low-stiffness results, they presented much lower thermal conductivity when compared to commercial systems that were already in use. In fact, some of the braided systems had a tested performance as low as 57% of the theoretical calculated thermal conductivity (CATERETÉ beamline M2 braid). Initial investigations performed via microscopy, after cutting both a commercial braid and an in-house one (Fig. 1), highlighted the potential culprit, namely: the poor wire compaction inside the end blocks. It was found that the cross section of the first one had an average void density of 4.2%, whereas the problematic one had 24.1% (ImageJ). Also, the wires were much less deformed, leading to limited contact area between them due to insufficient pressing forces. This resulted in a poor thermal coupling among both the wires themselves and the end-blocks.

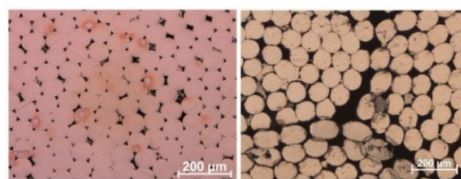


Figure 1: Micrographies of the commercial (left) and the 1st-generation in-house (right) solutions from section-cut of the braids inside the end-blocks.

The hypotheses for the bad pressing consisted of a combination of insufficient hydraulic pressing forces and excessively large and stiff end-blocks, resulting in low plastic

[†] francesco.lena@lnls.br

deformation. These results led to new efforts being made towards improving the manufacturing process, focusing on better compaction and deformation of the wires.

2nd-Generation In-House Braids

To reduce the end-block stiffness for better pressing, we abandoned the concept of starting from the large copper blocks for subsequent machining. Instead, those terminations were standardized as 1x1x1/4" (LxWxH) for systems with a single row of 9 of the same 2.5mm ETP braids, and 1x2x1/4" for the single-row 18-braid ones. In this manner, most of the termination internal volume was comprised by the wires. After the pressing, the blocks were fine machined to remove the extra material (approx. 1 mm) and for hole drilling. Also, the blocks were manufactured out of completely annealed OFHC copper, increasing the load transfer to the wires due to their low yield strength. The pressing strategy and load were varied aiming the lowest void density among wires.

Open Versus Closed Die Pressing

Initial tests with the new 9 braids, 1x1" geometry was performed without any die and a pressing load of 30 Ton (456 MPa). While already achieving a better pressing performance, as compared to the 1st-generation systems, the open fashion resulted in an anisotropic wire load distributions and highly deformed end-block, making it difficult to machine the final form. Also, the load could not be further increased without breaking the blocks.

To better distribute the pressing loads to the wires and blocks, a U-shaped, 2-part die was machined out of high-speed steel (HSS) with the exact final geometry of the desired end-blocks. Then, new tests were performed with the same load. The void densities achieved were 6.6 and 6.8% for the open and closed die, respectively.

Pressing Load

A new U-shaped HSS closed die was made to admit the larger 1x2", 18-braid system. The pressing was then redone with the same 456 MPa compression load (60 tons scaled total force), reaching a slight higher void density of 8.2%. Following this, an even higher load of 570 MPa (75 tons total force) was used to press another 18-braid system. This time, the final average void density was of only 1.7% and was considered enough as it was already better than the well performing commercial braids (4.2%) (see Fig. 2).

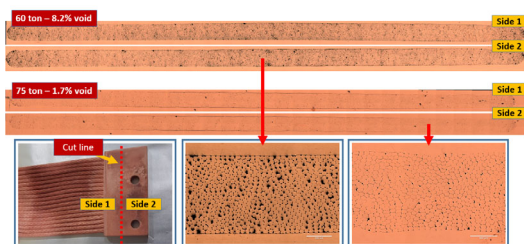


Figure 2: Closed die pressing with different loads.

Conditioning for UHV

To remove contaminants introduced during manufacturing for the UHV application compatibility, the systems

were sonicated with: IC115 + deionized (DI) water solution (1:4, volume); then, pure DI water; and, finally, pure isopropanol, 30 minutes each. After that, cleansing was made in a sulphuric acid and hydrogen peroxide (1:1, volume) bath, aka. *Piranha* solution, for approximately 2 minutes, followed by DI water rinse and isopropanol sonication for 15 minutes. The braids were, then, vacuum backed at 120°C for 24h, and stored in vacuum until assembled or gold plated. Residual gas analyses (RGA) were performed with a Stanford SRS RGA200 up to 200 Da in a ~1e-6 mbar vacuum, with no specific contaminants detected. Indeed, some systems are currently working at < 5e-10 mbar. In the cases of gold plating, the braids were still re-cleaned with the same IC115/DI water solution, followed by isopropanol sonication for 30 minutes and the same baking procedure.

THERMAL CONDUCTION TESTS

To validate the thermal conductivity of the braids, a dedicated setup was developed (Fig. 3). It consisted of an aluminium machined bar coupled to a Janis ST400 LN₂ cryostat, to which one of the end-blocks of the braids was coupled. 2k Ohm IST resistive temperature detectors (RTD) were attached to both braid end-blocks and read by a NI cRIO 9226 card. Thin film Kapton heaters were attached to the other extremity and driven by a Keithley controller. Indium foil was used in all interfaces. The entire system was kept under high vacuum (< 1e-6 mbar).

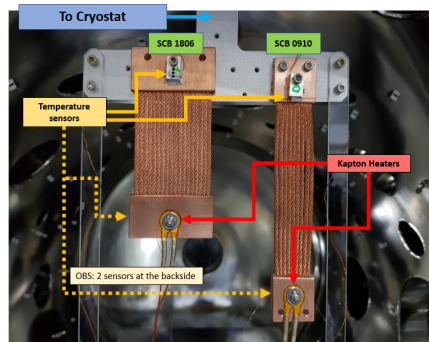


Figure 3: In-vacuum cryogenic thermal test setup.

After cooling, the temperature offset of both terminations caused by the radiation heat transfer was normalized and power was delivered to the heaters in controlled steps. The thermal conductivity was then calculated by the simple division of the total power delivered to the heaters by the temperature difference of both end-blocks, with corrections for cable losses and radiation heat transfer. Some of the results are shown at Table 1. For all tests, the determined conduction efficiency varied between 82 and 91% of the theoretical values.

Table 1: Thermal Conduction Test Results

Braid ID	Braid n#	Length (mm)	Mean Temp. (K)	Power (W)	Conductivity (W/K)
SCB1806	18	60	111.4	5.55	0.314
SCB1806	18	60	131.0	9.78	0.293
SCB0910	9	100	111.0	2.35	0.101
SCB0910	9	100	139.6	5.25	0.094

SOLDERING AND BRAZING

A common fashion for thermally coupling solid bodies consists in layering a soft, good conductor interface material and compressing it with a static load. Due to the need for UHV compatibility and cryogenic properties, annealed indium foil (0.2 mm, Goodfellow) is usually employed between the conduction blocks, mirrors, and cryostats at Sirius. An acceptable thermal conductivity value for this solution currently used in many Sirius thermal models is 3 kW/m²K, based on [4]. Nevertheless, since the new developed braids end-block geometries are standardized, they often must be coupled to intermediary parts to form the thermal links, but any new interface may lead to a loss in thermal efficiency. To improve the interface conductivity in relation to the pressed indium, soldering and brazing tests were performed in vacuum (<1e-5 mbar) with multiple fillers (Table 2).

Table 2: Brazing and Soldering Tests

Filler Material	Filler Thickness (mm)	Temp. (°C)	Time (min)	Category
Palcusil 10	0,1	885	5	Brazing
Cusil	0,1	780	5	Brazing
Sn100C	0,3	227	30	Soldering
Sn100CV	0,3	227	30	Soldering
Indium	0,5	157	30	Soldering

Figure 4 shows the micrographies for the several cases. Despite both Cusil and Palcusil resulted in thinner, metallurgically bonded interfaces, the high temperatures employed during the process caused an undesired adhesion of the copper wires among themselves by diffusion bonding, as well as strong annealing. This led to a completely loss of flexibility in the braids, as the wires could no longer slip among themselves, invalidating the application. Thus, new efforts for low temperature bonding (soldering) using tin based fillers, namely, Sn100C and Sn100CV, and pure indium were made.

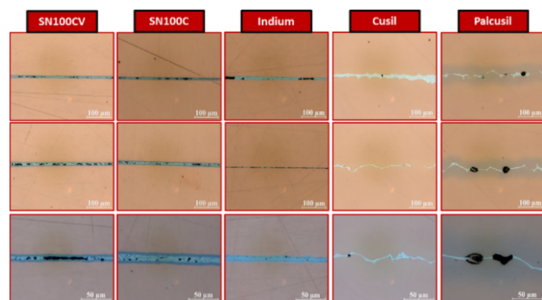


Figure 4: Different brazing and soldering interfaces between copper end-blocks.

Although the Sn100C and Sn100CV fillers resulted in even, reproducible interfaces, it was later found that both alloys contained a considerable amount of phosphorus (0.73 and 0.68% w.t. respectively, measured by inductively coupled plasma mass spectrometry), being unsuitable for vacuum applications near optical surfaces. Therefore, the pure indium soldering method was chosen, having an expected conductivity near 400 kW/m²K [5].

Core technology developments

Cryogenics

BEAMLINE SYSTEMS

The CARNAÚBA beamline M1 mirror along with an associated diffraction beam diagnostic is currently the cryogenic system relying on copper braids with the highest power load at Sirius [6]. Indeed, the total power in the commissioning phase of the storage ring is approximately 77 W [7], but it should reach 100 W in the near future.

To solve the needed cooling requirements, while preserving the optics alignment and motion, a set of 12x 18-rope braids were used to couple a cryostat-cooled copper block to the optics interface sets (Fig. 5). All copper surfaces were gold plated to reduce radiation heat exchange. Solid indium foil was used as interface material in all cases but will be indium-soldered soon. The system has been proven fully functional during the beamline commissioning.



Figure 5: Braided system at the CARNAÚBA beamline M1 mirror and diagnostic system.

Also, both the M2 mirror and SSA (secondary source aperture [8]) at CARNAÚBA use the same developed braids, but have already indium-soldered interfaces, as they were used as experimental systems, having the best performance so far. Other systems, as the CARNAÚBA 4CM monochromator [9] and IPÉ M4 and M5 mirrors, also use these braids, and many others are on the way.

CONCLUSION

A manufacturing process for fabricating weld-free, low-cost, high-efficiency flexible copper braids for cryogenic applications was developed in-house with the help of a local partner. The main challenge of achieving a high compaction at the braids solid blocks was solved with: a closed die pressing process, optimized end-block geometries, and copper annealing for lower yield strength, resulting in a void density as low as 1.7% when cold pressed with 570 MPa. Both the vacuum and thermal performances were tested with successful results, with systems working down to < 5e-10 mbar and conduction efficiency between 82 and 91% of the theoretical values. Large optical systems currently use the developed systems at Sirius up to 100 W.

ACKNOWLEDGEMENTS

The authors would like to gratefully acknowledge the Brazilian Ministry of Science and Technology for the funding, as well as all the engineering and science team members working for the Sirius project. A special thanks also goes to the people from Barbanera Qualità for all the shared efforts towards developing the braids solution.

TUPC14

209

REFERENCES

- [1] R. R. Geraldès *et al.*, “The Design of Exactly-Constrained X-Ray Mirror Systems for Sirius”, in *Proc. 10th Mechanical Engineering Design of Synchrotron Radiation Equipment and Instrumentation Int. Conf. (MEDSI'18)*, Paris, France, Jun. 2018, pp. 173-178. doi:10.18429/JACoW-MEDSI2018-WE0AMA04
- [2] G. White, “The Thermal and Electrical Conductivity of Copper at Low Temperatures,” *Aust. J. Phys.*, vol. 6, no. 4, 1953. doi:10.1071/ph530397
- [3] S. S. Rosenblum, W. A. Steyert, and F. R. Fickett, “A simple method for producing high conductivity copper for low temperature applications,” *Cryogenics*, vol. 17, no. 11, 1977. doi:10.1016/0011-2275(77)90123-0
- [4] D. A. Schneider, “Thermal Contact Resistances in a Thermal Conductivity Test System”, Master Thesis, Oregon State University, 1998.
- [5] R. Radebaugh, “Thermal conductance of indium solder joints at low temperatures,” *Rev. Sci. Instrum.*, vol. 48, no. 1, 1977. doi:10.1063/1.1134856
- [6] V.B. Zilli *et al.*, “Installation and Commissioning of the Exactly-constrained X-ray Mirror Systems for Sirius/LNLS,” presented at MEDSI 2020, Chicago, USA, July 2021, paper MOPB06, this conference.
- [7] L. M. Volpe, B. A. Francisco, S. M. Saveri Silva, J. C. Corsaletti, R. R. Geraldès, “Thermal Model Validation for the Cryogenic Optical Systems for Sirius/LNLS,” presented at MEDSI 2020, Chicago, USA, July 2021, paper WEPC07, this conference.
- [8] H. C. N. Tolentino *et al.*, “Innovative instruments based on cryogenically cooled silicon crystals for the CARNAÚBA beamline at Sirius-LNLS,” in *AIP Conference Proceedings*, vol. 2054, p. 060026, 2019. doi: 10.1063/1.5084657
- [9] M. Saveri Silva *et al.*, “Four-Bounce Crystal Monochromators for the Sirius/LNLS beamlines,” presented at MEDSI 2020, Chicago, USA, July 201, paper MOPB04, this conference.

A NEW ULTRA-STABLE VARIABLE PROJECTION MICROSCOPE FOR THE APS UPGRADE OF 32-ID*

S. Bean, V. De Andrade, A. Deriy, K. Fezzaa, T. Graber[†], J. Matus, C. Preissner, D. Shu
Advanced Photon Source, Argonne National Laboratory, Lemont, IL 60439, USA

[†]Deceased April 29, 2021

Abstract

A new nano-computed tomography projection microscope (n-CT) is being designed as part the Advanced Photon Source Upgrade (APS-U) beamline enhancement at sector 32-ID. The n-CT will take advantage of the APS-U source and provide new capabilities to the imaging program at 32-ID. A Kirkpatrick and Baez (KB) mirror-based nanofocusing optics [1, 2] will be implemented in this design. To meet the n-CT imaging goals, it is the desire to have sub 10 nanometer vibrational and thermal drift stability over 10-minute measurement durations between the optic and the sample. In addition to the stability requirements, it is desired to have a variable length sample projection axis of up to 450 mm. Such stability and motion requirements are challenging to accomplish simultaneously due to performance limitations of traditional motion mechanics and present a significant engineering challenge. To overcome these limitations, the proposed n-CT design incorporates granite air bearing concepts initially used in the Velociprobe [3]. These types of granite stages have been incorporated into many designs at APS [4] and at other synchrotron facilities [5]. Utilizing the granite air bearing concept, in tandem with other design aspects in the instrument, the requirements become reachable. A novel multi-degree of freedom wedge configuration is also incorporated to overcome space limitations. The design of this instrument is described in this paper.

INTRODUCTION

The new n-CT instrument will exploit the new APS-U source characteristics by implementing projection x-ray imaging for the high-speed imaging program at APS. A throughput gain is achieved as the temporal resolution of the nano-imaging tomography instrument goes from 500 ms to tens of μ s. A unique advantage of the instrument geometry allows zooming capability that fills the gap in terms of resolution and field of view between the currently available μ -computed tomography (μ -CT) and the transmission x-ray microscopy (TXM) based nano-computed tomography (n-CT). Another unique advantage of the instrument geometry allows the multi-modality measurement capability coming from the simplicity of using the focused beam as a probe for XRF measurement.

* This research used resources of the Advanced Photon Source, a U.S. Department of Energy (DOE) Office of Science User Facility at Argonne National Laboratory and is based on research supported by the U.S. DOE Office of Science-Basic Energy Sciences, under Contract No. DE-AC02-06CH11357.

The variable projection microscope at 32-ID will be a combination of a KB mirror system and a high precision sample rotation and nano positioning stack on a common support structure with separate granite air bearing coarse positioning axes. A separate camera and detector system will be integrated just downstream of the instrument. A visualization of the instrument is shown in Fig. 1.

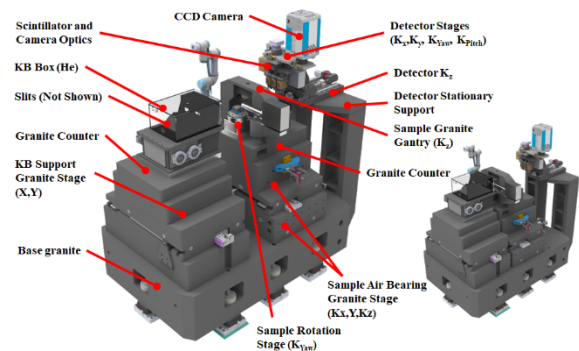


Figure 1: Rendering [6] of the n-CT instrument design, labeling major components. Largest working distance (left) and probing stage (bottom right).

It is the desire to have sub 10 nm vibration and thermal drift stability over the course of 10-minute measurements. Because of the long variable zoom axis of this instrument, it is difficult to implement relative optic to sample metrology to correct thermal drifts. It is the design of the coarse granite stage positioning system and support that enables this relative stability. The instrument design and these details are discussed in subsequent sections.

N-CT CONFIGURATION METHODOLOGY

The following numbered items represent the most critical requirements of design and configuration for this instrument:

1. A stable, helium isolated KB optics environment is required to achieve the nanofocusing of the KB's along with extending their lifetime.
2. Optics to sample stability is required. This is both when considering contributions of vibrations and thermal drifts.
3. Variable projection zoom axis of 450 mm must be implemented in the design. Stability cannot be compromised with variable zoom.
4. Various sample environments must be accommodated with >360 rotation capability. Voltage biasing and fluid feedthroughs must be integrated into the design

- The ability to mount multimodal detection strategies must be facilitated by the design. An example is the ability to mount a fluorescence detector in the future.

N-CT CONFIGURATION AND PARAMETERS

Figure 2 depicts the optical configuration of the n-CT instrument. The defining characteristic of this instrument is the variable projection zoom axis K, which moves along the kicked beam of the KB mirror to change magnification. The key performance parameters of the instrument are shown Table 1.

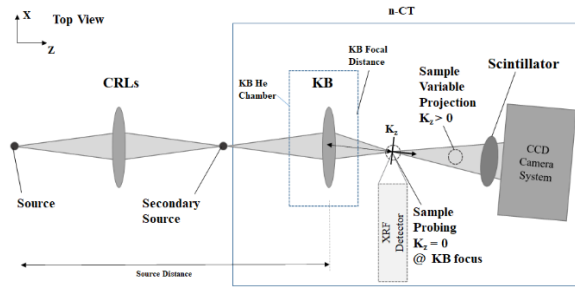


Figure 2: Schematic showing the optical layout and detection of the n-CT instrument. The n-CT works with a secondary source created by a CRL system upstream in the beamline. The new directions KX, KY, and KZ are noted as the “kicked” axes of the beam by the KB mirror pair.

Table 1: Characteristic Parameters of the n-CT Instrument

Specification	Value	Unit
n-CT Characteristic Parameters Specifications		
Simultaneous Measurement Methods	FFnCT, XRFnCT*	
Variable Projection Zoom (K_z) Total Range	450	mm
Selectable Scan Axis	Sample X, Y, Sample θ_y	
Rotational Scan Range	>360	deg
MIM for rotation step	150	μ rad
Sample K_y Scan Range	≥ 50	μ m
Sample K_x Scan Range	≥ 100	μ m
MIM for planar scan	≤ 2	μ m
Relative Sample to Optic Positioning Resolution	≤ 10	nm
Relative Sample to Optic Stability	$\leq 10, 10$ minutes	nm
Optic Focal Spot Size (KB)	20	nm
Optical Working Distance	60	mm
Working Energy	25	keV
Detector Pixels	4000 x 4000	
Largest Volume of Interest	80 x 80 x 80	μ m
Target Imaging Resolution	15	nm

GRANITE SUPPORT AND MOTION DESIGN

The granite air bearing concept is to float and position dynamic pieces of granite with air pressure and then to set them back down (air off) thus again creating a monolithic structure.

The n-CT incorporates 6 such dynamic granite pieces, resulting in 4 degrees of freedom (DOF) for the sample stack, and 2 for the KB system. The sample stack granite configuration is shown in Fig. 3. The KB has almost identical form factor and components, however just X and Y motions. The KB motions are expected to only be used

during initial commissioning, while the sample motions are expected to be used frequently during user experiments. A new 2 DOF wedge design has been incorporated in this instrument such that pieces 2 and 3 of Fig. 3 provide both X and Y motion with two independent drives. The drive for the following wedge is shown in Fig. 4. By incorporating transverse motion in the follower, one less air bearing interface is needed in the motion stack.

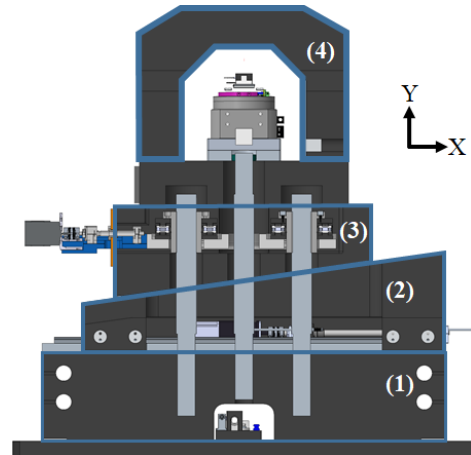


Figure 3: n-CT granite stage stack with motion granite components highlighted. 1- granite Z motion (KZ for sample), 2- X driving wedge that creates Y follower motion, 3- Two degree of freedom Y follower wedge with X motion, 4-Z motion granite gantry for sample environments and detector mounting. Pieces 1, 2 and 3 are nearly identical for supporting the KB system.

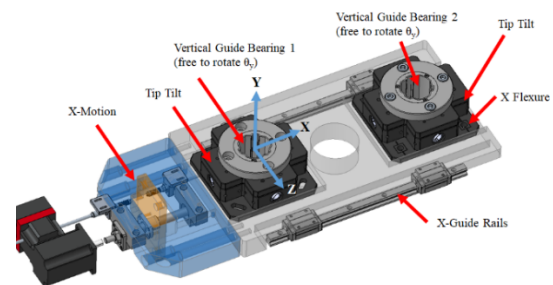


Figure 4: n-CT following wedge guide/drive design. This drive allows the follower wedge to be guided vertically by two posts but be driven transversely.

KB SYSTEM

A set of KB mirrors and stages are configured inside a helium enclosure, shown in Fig. 5. A set of highly stable and repeatable nanopositioning stages are configured to give all the DOF required to align the system to the beam. The specification of the KB mirrors is given in Table 2. The performance of the KB system is not discussed in this paper, but the reader is encouraged to read the referenced papers pertaining to the KB nanopositioning system [1, 2].

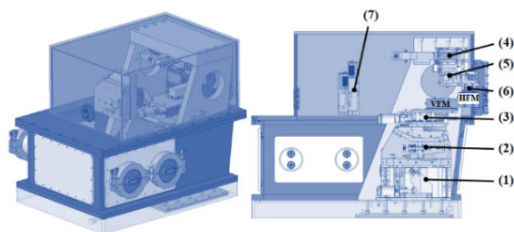


Figure 5: n-CT KB system. VFM – vertically focusing mirror, HFM – horizontally focusing mirror, 1- Vertical stage, 2-Rotation X stage, 3- Translation Z stage, 4- Rotation stage Y, 5-Translation X stage, 6- Rotation Z stage (manual), 7-Clean up slits upstream of the KB mirror.

Table 2: Characteristic Parameters of n-CT KB Mirrors

KB Mirror Specification Table				
Specification	VFM	HFM	Unit	Comment
Substrate material	Silicon	Silicon		
Mirror Shape	Elliptic	Elliptic		
Useful length	60	40	mm	
Useful width	3	3	mm	
Mirror Length	65	45	mm	
Roughness (at 50x)	0.2	0.2	nm rms	
Tangential Slope error	0.1	0.1	μrad rms	
Tangential figure error (PV)	1	1	nm	
Incidence angle	20	20	mrاد	at mirror center
Object distance	33	33.057	m	at mirror center. Secondary source (BDA) is at 41 m.
Image distance	0.13950	0.08250	m	at mirror center
Gap between mirrors		2	mm	
Working Distance		60	mm	
Coating	None	None		Multilayer coating will be deposited in-house

SAMPLE STACK

A compact continuous rotation samples stack has been designed for the n-CT and is shown in Fig. 6. The union and slip ring are buried in the granite plate this stage stack is interfaced with. The option to choose piezo scanning (load limited) or a kinematic mounting interface has been incorporated to increase user flexibility.

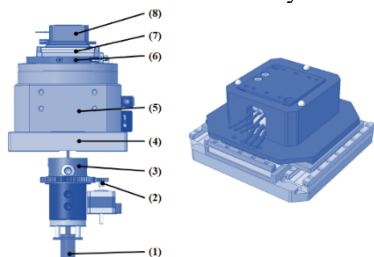


Figure 6: n-CT sample stack. 1-Electrical slip ring, 2- Rotary union separate rotation mechanics, 3- rotary union, 4- base plate, 5-rotation stage, 6- feedthrough manifold, 7- XZ nanopositioner, 8- optional scanning mount or stationary kinematic mount (right picture).

DETUNING CONSIDERATIONS

The worst parasitic error for this instrument is rotational detuning of the sample rotation axis about the X direction of the kicked KB beam (K_x). In relation to the pixel size and working distance, it is desired to keep this number below 1000 μrad. Parasitic errors are contributed to by granite guiding mechanics and form for positional

repeatability. Considering all the errors it is expected a worst-case detuning of 173 μrad can occur (non-quadrature).

MODAL ANALYSIS

A modal analysis was performed on the instrument support and staging to determine the natural frequency is sufficiently above the cultural noise floor of 30Hz at APS [7]. The n-CT preloaded jack stiffness used to define the 8 floor interfaces is given in Table 3. Modal analysis results are shown in Fig. 7. The supporting structure and granite stages are sufficiently stiff to not amplify vibrations.

Table 3: Jack stiffness matrix. Z – beam direction, Y – vertical direction. Empirical tested values obtained at APS.

n-CT Jack Stiffness						
Load (N)	K_{xx} (N/m)	K_{yy} (N/m)	K_{zz} (N/m)	K_{gx} (Nm/rad)	K_{gy} (Nm/rad)	K_{gz} (Nm/rad)
60,000	1.14E9	2.31E9	1.15E9	2.32E6	4.79E6	5.42E6

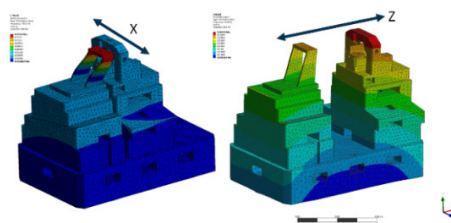


Figure 7: Modal analysis [8] results. The first mode is a KB frame motion (~158 HZ) and is not a rigid body motion of the support structure or granite stages. In the probing (left) and farthest projection position (right), the second natural frequency is ~179 Hz and ~172 Hz respectively for rigid body the rigid body modes. The direction of rigid body motion induced by rocking is shown in the figure.

THERMAL CONSIDERATIONS

The KB optics and sample stack are mounted on nearly identical granite stage platforms. Both granite stage stacks should respond the same to environmental change. The KB system is inside a helium enclosure. The sample environment is exposed to air. It is expected that the largest thermal drift is the relative response of these two systems, where the KB tank is more invariant to temperature change. It is estimated currently that the thermal response time of the sample stack given a 0.2 degC change to respond 10 nm is ~6 minutes from simplified lumped thermal calculations. It is expected after incorporating more resistance to convection to the sample stack exposed areas (Lexan panels) that this instrument will not respond more than 10 nm over 10-minute timescales.

CONCLUSIONS

The stability requirements for this instrument are very demanding. By incorporating a granite coarse positioning design along with stiff KB nanopositioning, the stability goals at both projection extremes can be met. This instrument provides the right combination of flexibility and motion for user experiments, without sacrificing stability performance.

REFERENCES

- [1] D. Shu *et al.*, “Modular nanopositioning flexure stages development for APS upgrade K-B mirror nanofocusing optics,” presented at MEDSI’20, Chicago, USA, July 2021, paper TUPC10, this conference.
- [2] D. Shu, V. De Andrade, J. Anton, S. Kearney, K. Fezzaa, S. Bean, A. Deriy, “Mechanical design of a flexural nanopositioning stage system for hard x-ray nanofocusing at the Advanced Photon Source 32-ID-C station,” *Proc. SPIE 11112, X-Ray Nanoimaging: Instruments and Methods IV*, p. 111120N, September 2019.
<https://doi.org/10.1117/12.2529384>
- [3] C. A. Preissner *et al.*, “Earth, Wind, and Fire: The New Fast Scanning Velociprobe”, in *Proc. 9th Mechanical Engineering Design of Synchrotron Radiation Equipment and Instrumentation Int. Conf. (MEDSI’16)*, Barcelona, Spain, Sep. 2016, pp. 112-115. doi:10.18429/JACoW-MEDSI2016-TUAA02
- [4] C. A. Preissner, S. J. Bean, M. Erdmann, M. Bergeret, and J. R. Nasiatka, “A Family of High-Stability Granite Stages for Synchrotron Applications”, presented at MEDSI’20, Chicago, USA, Jul. 2021, paper THOA01, this conference.
- [5] R. R. Geraldès *et al.*, “Granite Benches for Sirius X-ray Optical Systems”, in *Proc. 10th Mechanical Engineering Design of Synchrotron Radiation Equipment and Instrumentation Int. Conf. (MEDSI’18)*, Paris, France, Jun. 2018, pp. 361-364. doi:10.18429/JACoW-MEDSI2018-THPH12
- [6] Keyshot 8 – 3D rendering software (2019), www.keyshot.com
- [7] S. Kearney, D. Shu., “A Survey of Floor Vibration Noise at all Sectors in the APS Experiment Hall,” Argonne National Laboratory, ANL/APS/LS-344, 2016.
- [8] ANSYS Engineering simulations and 3D design software (2018), www.ansys.com.

CAD INTEGRATION FOR PETRA-IV

B. List*, L. Hagge, M. Hüning, D. Miller, P.-O. Petersen
Deutsches Elektronen-Synchrotron DESY, Hamburg, Germany

Abstract

The PETRA-IV next-generation synchrotron radiation source at DESY is currently in preparation with a completely new accelerator and a new experimental hall, retaining as much of the existing PETRA-III buildings, tunnels and experimental beamlines as possible.

We have set up a CAD integration model for the complete accelerator and photon science complex. The model hierarchy has levels reflecting decisions on project organisation, project phases, design process, and overall product structure. Modularisation and designing in three levels of detail help to manage the complexity and keep the model performant. Placement of accelerator components is determined by the lattice through direct access to spreadsheet data, allowing fast design changes after a lattice update and ensuring consistency between mechanical and lattice design. The resulting model will support engineering processes over the complete facility lifecycle.

INTRODUCTION

Lifecycles of accelerator facilities extend over decades, spanning a number of phases from concept over design, construction, and operation to dismantling. Computer Aided Design (CAD) is an essential tool for supporting the engineering in the various stages of the lifecycle. CAD applications include space allocation, basic and detailed engineering, matching of interfaces, clash checks, technical documentation for installation, operation, and maintenance. Figure 1 shows a simplified lifecycle of an accelerator facility and highlights phases with important CAD contributions. The CAD integration model accumulates and conserves all mechanical engineering designs, decisions, and knowledge throughout the entire lifecycle. It is implemented and maintained in the CAD software Siemens NX and the PLM system Teamcenter.

OBJECTIVES

The integrated CAD model of PETRA-IV [1] is intended to serve as a comprehensive mechanical model of the entire system: the accelerators with all their components, photon beamlines with optics and experiments, supporting infrastructure such as water, electricity, ventilation, and buildings. It will be maintained throughout the project life span and remain usable during its whole life cycle for all stakeholders with their differing needs. The overarching objectives of the model are to establish vision sharing, support interface management, enable early detection of potential clashes, foster design collaboration, and to support better and faster decision making

* Benno.List@desy.de

REQUIREMENTS

Performance is a major requirement: the model has to provide the means to efficiently edit the data and provide the necessary design context. Collaboration across different trades and organisational units needs to be supported with minimal side effects from changes in one trade to other parts of the model and with data protection against unwanted changes from third-party groups.

Collaboration with external groups and suppliers, who do not have access to the integration model, demands support for work with minimal context: clearly defined interfaces and space reservations for import of the contributed data, are required.

Accelerator design starts from a mathematical model of the components governing the beam dynamics (the so-called lattice). An associative relation between the CAD model components and their lattice representations and the ability of automatic geometry updates are needed for fast design iterations.

Collaboration with civil engineering requires the import of the building and tunnel CAD models from dedicated architectural CAD systems into the integration model, with accurate placement of the buildings and an exchange of space reservations as input for the civil engineering design process. Infrastructure, such as water and electricity supplies and heating and ventilation, has interfaces to the buildings and the accelerator and experimental facilities that need to be present in the model.

METHODS

In the following, we describe briefly some of the methods we have employed in response to the CAD model objectives and requirements.

Model Structure

CAD models are typically structured according to a spatial and functional decomposition of the product. A close correspondence between CAD model structure and the product breakdown structure (PBS) supports processes that are closely linked to the PBS such as verification of requirements, validation, and testing.

The structure has a consistent set of levels corresponding to a logical hierarchy, namely program, complex, facility, area, and unit, inspired by the physical model of the ISA-106 set of standards, as illustrated in Fig. 3. Additional interim levels (not shown in the figure) implement different levels of detail, organize responsibilities and access rights of the different trades and work packages, and manage different configurations.

We find that the CAD model structure reflects, and often necessitates, project decisions on topics such as responsibil-

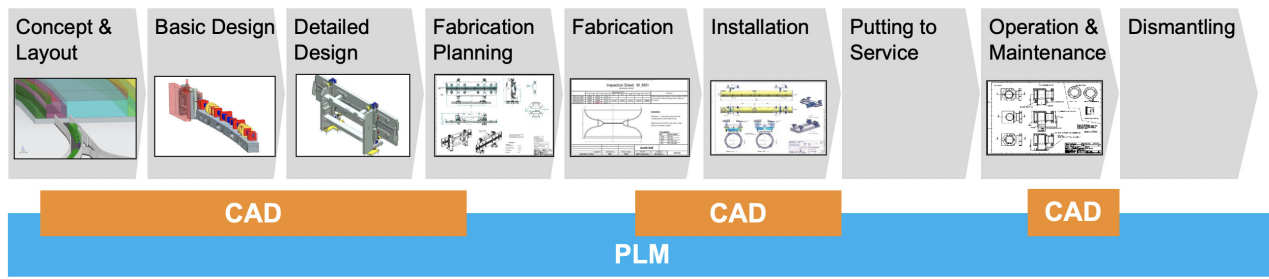


Figure 1: Accelerator lifecycle. The orange boxes indicate which phases update the CAD integration model. The PLM system ensures data management throughout the entire lifetime of the facility.

ities (connected to different trades), work package organisation (reflected in the PBS and functional decomposition), design process (levels of detail), and project phases (configurations).

Modularisation

Modules are functionally and spatially coherent subsystems that occupy a specific space and have a defined interface to their surroundings. In the PETRA-IV integration model modularisation is used extensively and recursively at different levels. Examples for modules are an arc cell of the accelerator, the optics of a photon beamline, an experiment, a section of the water supply system, or a section of free space for transport, escape routes etc.

Levels of Detail

We represent elements in the CAD models at different levels of detail (DG “detail grade”), which can be switched according to purpose:

- DG1: This coarsest level of detail indicates the space required for the module, typically as a box.
- DG2: The required space required is modelled precisely enough for collision checks and external interfaces modelled.
- DG3: A fully detailed model with the full internal structure of the module, suitable for tendering, production and installation.

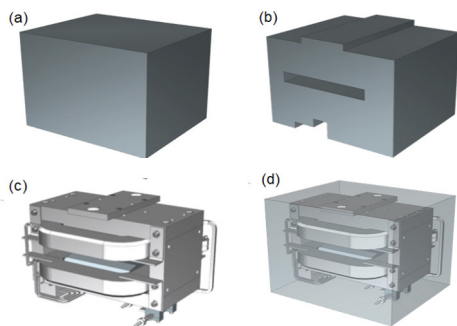


Figure 2: Example of a magnet model in three levels of detail: (a) DG1, (b) DG2, (c) DG3, (d) DG1 and DG3 overlaid.

Fig. 2, illustrates the DG mechanism for a component such as a magnet. Figure 3 illustrates the application of the DG mechanism, where a unit is represented in DG1 for studying its placement in an area and in DG3 for assembly and installation (right, top and bottom).

The DG approach was extensively used at the European XFEL (E–XFEL) project [2]; it was applied in NX for the ARES project [3], where the concept of a DG master was introduced: an assembly that combines the different DG1/2/3 models, each a separate CAD item, into a single assembly. We use the NX “reference set” mechanism to select dynamically at which level of detail a module should be shown. NX provides assembly load options to define rules which reference sets shall be loaded preferentially; loading only DG1 or DG2 models initially and selectively loading DG3 models in regions of interest ensures that even a model of the complete PETRA-IV program can be opened and manipulated.

With modularisation comes a design process that proceeds from coarse layout with space allocation (DG1) go conceptual design with interface definition (DG2) to a full engineering design (DG3). Where this approach is followed, integration of higher-level systems can be performed based on DG2 models. Particularly collision checks, which are invaluable in detecting and removing overlaps between components at an early stage, can be performed efficiently at DG2 level, which was extensively done at E-XFEL [2]. Providing a well-defined interface to the outside world ensures that results of collision checks remain valid as long as the DG2 space allocation does not change. This interface can even be frozen by releasing the DG2 model, while work on the DG3 engineering design continues or even before it has started. In addition, separation of DG2 and DG3 offers to protect proprietary or confidential design details by restricting access to DG3 models without compromising the ability to integrate the full system.

Placement of Components from Lattice Files

The number, size, and placement of accelerator components, such as magnets, RF cavities, and instrumentation, is designed with dedicated programs such as MAD-X [4]. It is of highest importance to faithfully implement the placement of all these components in the engineering model and support design iterations with a fast and efficient turn-around, so

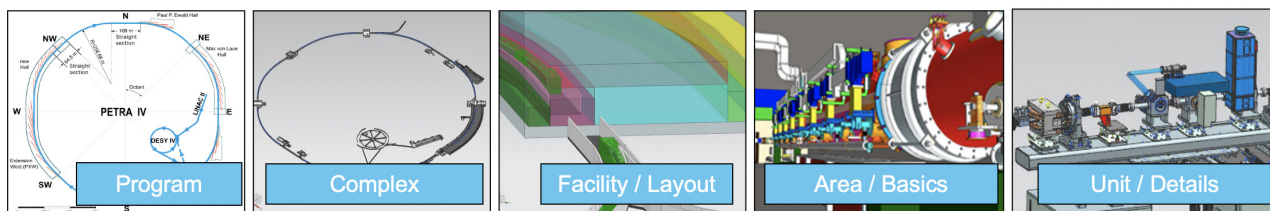


Figure 3: Hierarchical structure of CAD integration model: Top-level summarizes the entire PETRA IV program; complex separates accelerators, experiments and civil infrastructure facility defines major functional installations like (pre-) accelerators and beamlines, which are sub-divided into spatial and technical areas, which in turn are made from assembly and installation units.

that the lattice can be promptly updated and validated when additional components such as absorbers, pumps, shutters etc. are added to the design.

In our approach, special parts are employed that contain only coordinate systems at the calculated positions of components; these coordinate systems serve as anchors for constraints that position all lattice components such as magnets, RF cavities, or beam instrumentation. Because these parts contain no geometric volumes that represent tangible components, they may be included in the CAD model wherever necessary and do not lead to double-counting of components. These lattice parts are also used to position support structures, reducing the need for constraints on geometric features such as surfaces or bores that depend on the detailed design of the components and may change as the design evolves.

The coordinate systems are generated automatically with a set of Python scripts in NX. Their placement is parametrised by expressions which read their values from spreadsheets that are directly generated from the lattice program. Also, placing components into the assembly and constraining them to the coordinate systems has been automated. This offers a reliable and rapid way to generate realistic CAD geometries from lattice files already in early design stages and helps to adapt the lattice to space constraints. This is of particular importance in the PETRA-IV project, where existing tunnels and experimental halls pose stringent constraints on the geometry of the new accelerator.

CONFIGURATION MANAGEMENT

An accelerator facility undergoes constant change, ranging from adaption of specimen holders to the installation of whole new photon beamlines or the complete refurbishment of an accelerator. Representing the exact configuration of the whole facility for every given time is next to impossible, but also unnecessary, when changes remain local and do not affect the space requirements or interfaces to the surroundings. Nonetheless, at each level of the model, configuration changes need to be tracked and modeled.

We use configurations to represent an entity in a specific constellation, e.g. at a specific point in time, or a design variant. Distinct configurations are modelled by one assembly per configuration, such that the assembly represents the entity's state completely, without double counting, observing

a 100%–rule. All configurations are combined in a configuration master assembly that collects all states of the given entity that are present in the model.

RESULTS AND BENEFITS

Based on the techniques discussed above, we have set up an integration model of the PETRA-IV program, with a spatial extent of 1 km². The model comprises more than 70 buildings relevant for the construction project. The model includes configurations for the present (PETRA-III) state as well as design variants for PETRA-IV based on several lattice variants currently under study.

Using different levels of detail at several levels, we ensure that even the top level assembly encompassing the complete model can still be opened efficiently, with the possibility to successively load more and more details where needed. These levels of detail support a design process based on a progression from layout via concept to detailed design, decoupling these design phases to a large extent.

Alignment of the model structure with the product breakdown structure facilitates review and sign-off processes, with a product item that has a well-defined scope, purpose and requirements. Teams from separate groups or project work packages have assemblies that they own exclusively, ensuring clear responsibilities and preventing unauthorised or accidental changes by others.

Automation tools that generate geometry from accelerator lattice calculations enables fast and efficient design iterations, such that the accelerator makes optimal use of the scarce available space.

REFERENCES

- [1] C. G. Schroer *et al.*, “PETRA IV: upgrade of PETRA III to the Ultimate 3D X-ray microscope,” Conceptual Design Report, Hamburg Deutsches Elektronen-Synchrotron (DESY) 2019, doi:10.3204/PUBDB-2019-03613
- [2] L. Hagge *et al.*, “Examples for 3D CAD models at the European XFEL,” in *Proc. IPAC2012*, New Orleans, LA, USA, May 2012, paper THEPPB015, pp. 3266.
- [3] F. Burkart *et al.*, “The experimental area at the ARES linac,” in *Proc. IPA C19*, paper MOPTS014, pp. 867, doi:10.18429/JACoW-IPAC2019-MOPTS014
- [4] <http://madx.web.cern.ch/madx/>

DESIGN OF GIRDERS ON THE NEW UPGRADE LATTICE AT SOLEIL

J-L Giorgetta[†], A. Lestrade, A. Mary, K. Tavakoli, Synchrotron SOLEIL, Paris, France

Abstract

The current girder set of SOLEIL features 4 girder types weighing from 1.85 t to 3 t, with a respective mass payload varying from 4.1 t to 8 t and lengths from 2.4 m to 4.8 m. The smaller size of magnets used for the present version of the SOLEIL upgrade allows a dramatic size and weight reduction of the magnet-girder assemblies (Fig. 1). On the other hand, the number of magnets has increased by a factor of 3, implying longer alignment and installation operations. Several setups involving 116 to 212 girders with various magnet layouts and binding systems have been studied. Dynamic and thermal performances have been evaluated by FEA analysis. This approach gives to accelerator physicists the performance of each solution, and thus a great versatility in the choice of the best setup in terms of dynamic and thermal stability.

DESIGN BASELINE

The design of the new magnet-girder assemblies considers experience gained from the existing installation, using concepts with proven efficiency and good performance in terms of stability. However, some other features are not optimized for the new storage ring and had to be adapted or totally redesigned. The large number of girders and magnets in the new lattice leads to a need to reduce unit cost and alignment time.

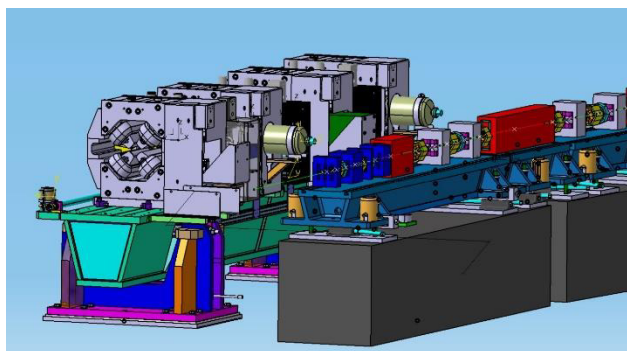


Figure 1 : SOLEIL vs Upgrade magnet girder assembly.

The small size of magnets makes possible to reduce the distance between beam axis and the upper face of girders to 240 mm, improving overall stability. However, the girder position is then higher with respect to the ground, imposing increased stability requirements on the girder support structures. Both granite and welded steel plinths have been considered as girder supports. These plinths are aligned, in all directions, with an accuracy of ± 1 mm and grouted to the ground. The new lattice features 4 or 6 fixing

point girders depending on the length. Due to the high long-term stability of the SOLEIL slab, motorization of the positioning system is not envisaged, particularly when considering its extra cost and complexity. In the same way, the current lock/release system is replaced by high stiffness wedges for vertical adjustment and push-pull screws for horizontal position. Stiffness is improved by applying a permanent vertical preload on wedges.

Girders are equipped with a HLS (Hydrostatic Leveling System) used during alignment operations. The new design implements a tooling referenced on the girder side face to set magnets on the beam axis with the requested accuracy.

MAIN SPECIFICATIONS

- Dynamic sensitivity of beam towards magnet position: lowest frequency > 70 Hz
- Sensitivity of beam towards magnet alignment:
 - girder to girder $30 \mu\text{m}$ vertical and $50 \mu\text{m}$ horizontal
- $100 \mu\text{m}$ RMS in both planes for all girders
- Thermal stability based upon BPM specification:
 - 50 nm a couple of minutes
 - 500 nm on one day
 - $\sim 1 \mu\text{m}$ on a week
- Ex-situ bake-out of vacuum chambers:
 - C-shape dipoles and transverse motion mandatory

GENERAL LAYOUT

SOLEIL Upgrade features 2 basic cells: 7 BA* and 4 BA* 3 configurations have been studied:

- 212 girders with 1.80 m max length (Fig. 2).
- 116 girders with 3.60 m max length (Fig. 3).
- 176 girders with 3.20 m max length (Fig. 4).

In the 2 first layouts, long dipoles share the plinth with adjacent girders, the third layout features standalone dipole stands. Using a girder as a dipole support allows for fine setting and avoids the low resonance frequency of dipoles encountered on the present SOLEIL setup. Dipoles are fixed on an air bearing cradle which can be removed from beam axis for vacuum chamber installation (Fig. 5).



Figure 2: Configuration 1 (7BA segment).

*BA: Bending Achromat

[†] jean-luc.giorgetta@synchrotron-soleil.fr.

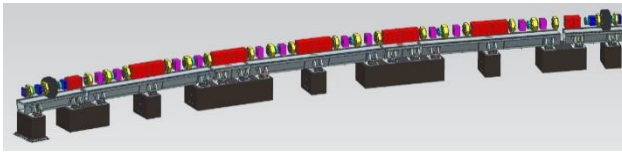


Figure 3: Configuration 2 (7BA segment).

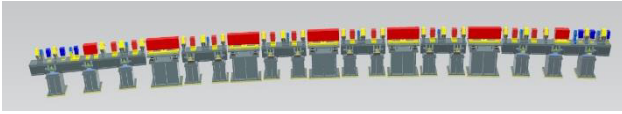


Figure 4: Configuration 3 (7BA segment).

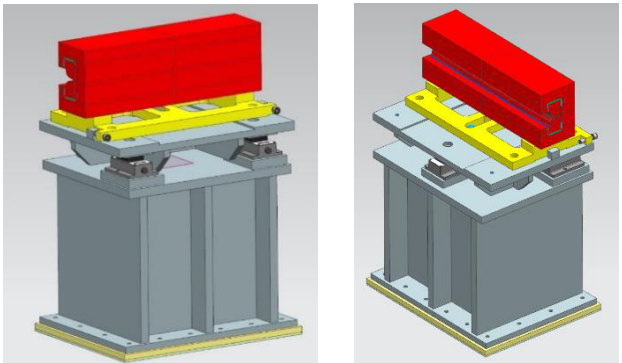


Figure 5: Dipole in operating and off beam position.

GIRDER CONSTRUCTION

The construction of the girders uses welded steel plates associated with cast steel parts common to all types. The length and fixation position are defined by the welded plates which are adapted to the different types (Figs. 6 and 7). The cast steel parts integrate fixation, setting, HLS support and lifting points. In addition to cost reduction, casting allows realization of continuous internal stiffeners and limits stress caused by welding. Functional surfaces of girders are machined after welding and stress relief treatment.

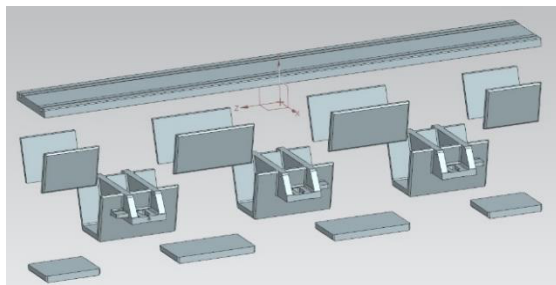


Figure 6: Configuration of 6 point girder.

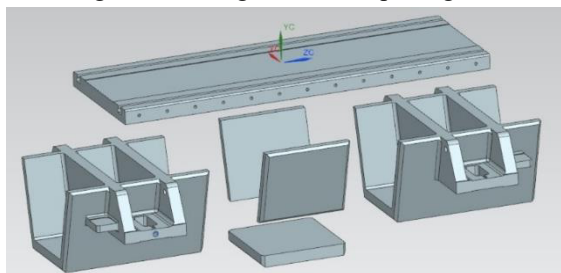


Figure 7: Configuration of 4 point girder.

FASTENING AND ADJUSTMENTS

The setting and fastening systems are located as high as possible with respect to the ground. Each girder is placed on commercial NIVELL® DK3 jacks (featuring 7 mm set-ting range and 25 t load capacity). Girder position along the beam axis is referenced by a spherical link aligned be-fore installing the girder. Horizontal adjustment is achieved using push-pull screws located on the inner side of girder (Fig. 8). A set of removable sensors monitor the position of the girder and controls the twist during align-ment. Fastening is achieved using vertical rods and a 5 t preload is applied at each point using a stack of elastic washers. Each girder is equipped with 3 HLS sensors used as reference during alignment operations.

Magnet alignment is achieved using a tooling refer-enced to the top and side surfaces of the girder machined with a $\pm 15 \mu\text{m}$ flatness tolerance. Magnets are fastened us-ing the T-slots of the top plate.

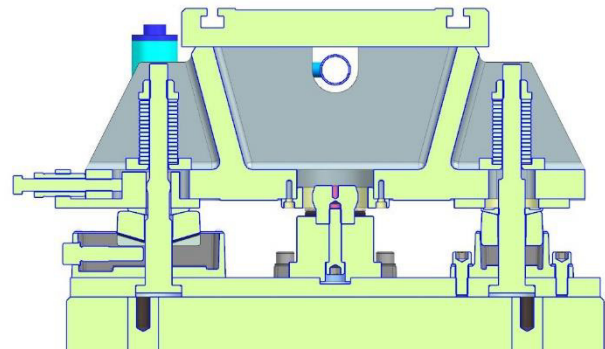


Figure 8: Section of girder setting system.

DYNAMIC SIMULATION

Simulation by Finite Element Analysis (FEA) has been carried out for the most critical magnet-girder types. Mag-nets are simulated by their 3D models, defined by a prelim-inary design. Jacks are modelled with their real shape and materials in order to accurately estimate stiffness. However non-linear effects are not yet been considered, so the effect of preload does not appear in the results. As an example, the calculated lowest resonance frequency (yaw mode) of the 3.60 m girder fixed on 6 points is 77 Hz (Fig. 9) which is higher than the current SOLEIL girders (47 Hz).

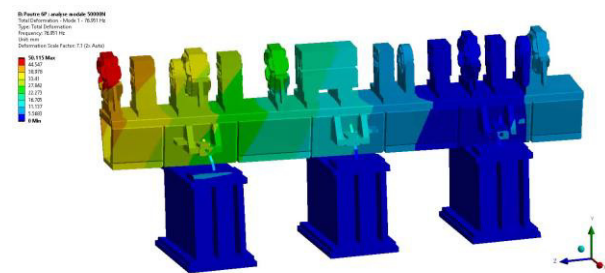


Figure 9: Dynamic simulation on a 3.60 m girder.

THERMAL SIMULATION

Thermal stability specifications are critical for the Upgrade machine, in particular long-term drift. Granite and steel have been studied as a material for girder stands. Data for both materials are summarized in Table 1. Although volume heat capacity of granite is lower, stands are massive blocks and yield a better thermal inertia than welded steel plate stands. In the same way, considering stiffness, low Young modulus of granite is compensated by greater inertia of granite stands. Steel allows more complex shapes than natural granite, and the final cost depends on design and manufacturing process for both materials.

Table 1: Steel and Granite Characteristics

Material	Steel	Granite
CTE	11×10^{-6}	6.4×10^{-6}
Density	7.8 Kg.m^{-3}	2.7 Kg.m^{-3}
Thermal capacity	$435 \text{ J.Kg}^{-1}.\text{K}^{-1}$	$837 \text{ J.Kg}^{-1}.\text{K}^{-1}$
Volume thermal capacity	$3393 \text{ J.m}^{-3}.\text{K}^{-1}$	$2260 \text{ J.m}^{-3}.\text{K}^{-1}$
Young modulus	210 GPa	60 GPa

FEA simulations have been carried out to evaluate the thermal sensitivity of girders standing on two plinths (Figs. 10 and 11). Ground temperature is assumed to be 20°C and air temperature 23°C with a convection exchange factor of $10 \text{ W.m}^{-2}.\text{C}^{-1}$. Temperature effect in these conditions is a deflection along vertical axis of -7.2 and $+4.2 \mu\text{m}$ on extreme points. If we consider that alignment is made in these steady conditions, stress will only result of air temperature variation in the tunnel, i.e $\pm 0.1^\circ\text{C}$.

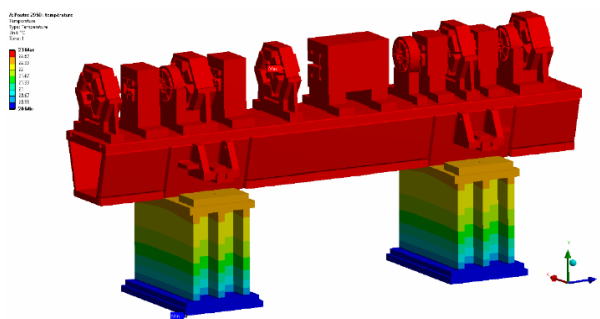


Figure 10: Temperature gradient.

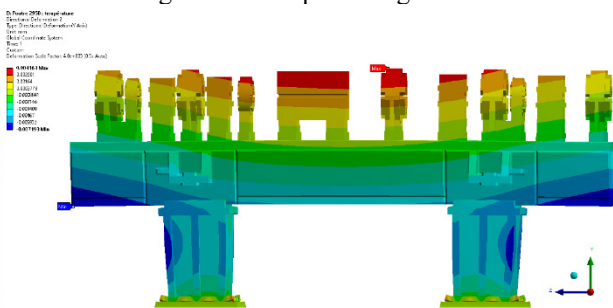


Figure 11: Thermal stress.

R&D PROGRAM

Vibration tests involving velocimeter sensors on the machine slab (Fig. 12) have been carried out in June 2021, and spectrum results will be used to evaluate vibrations on the FEA models. Measurements on NIVELL jacks using a test bench (Fig. 13) will give a real stiffness evaluation for preloads from 2 t to 5 t.



Figure 12: Velocimeters implementation on slab.



Figure 13: NIVELL jack on test bench.

Tests on prototypes will validate design features of the magnet-girder and FEA calculation. A steel plinth will be realized to perform thermal tests such as transient temperature measurements, and a long girder prototype loaded with dummy magnets will be used to carry out vibration response tests. If necessary, improvements will be made on the girder design. This prototype will also permit to validate alignment procedures for the girder itself and the magnets, and to improve the mounting process.

CONCLUSION

- Several setups have been evaluated, choice will be made considering stability, alignment and dark time reduction.
- Magnets are still in design phase, but the models of girders using modular elements can be easily changed to meet the final requirements.
- Further experimental measurements will be carried out to get realistic data for dynamic and thermal FEA simulation.
- The prototype of a complete girder is planned for 2022.

UPDATED HIGH HEAT LOAD FRONT-ENDS FOR SLS 2.0

D.M. Just†, C. Pradervand, Paul Scherrer Institute, 5232 Villigen, Switzerland

Abstract

The Swiss Light Source (SLS) at the Paul Scherrer Institute (PSI) in Switzerland undergoes from 2021 to 2024 an upgrade named SLS 2.0 to increase brightness and coherence. This upgrade will have a significant impact on the existing front-ends. Due to the proven reliability and good concept, we plan a refurbishment strategy for all front-end (FE) components where possible. New source points for all beam-lines – resulting in shifts both lateral and tangential, newly developed insertion devices and bending magnets as well as spatial restrictions due to the multi bend achromat (MBA) design challenges this strategy. We demonstrate how we plan to deal with these challenges for the case of high heat load FEs. We discuss the design and thermal analysis of a novel primary aperture and high heat load slits, the adaptations that will be made to the tungsten blade x-ray beam positioning monitors (XBPM) and the modifications on the photon shutter will be discussed

PURPOSE OF A FRONT-END

A front-end delivers a synchrotron radiation beam, through the tunnel wall, to the beamlines and end stations in order to perform experiments using said beam. Another important task of the front-end is to securely shut the radiation to allow people to work in downstream areas even if the rest of the beamlines is in operation mode.

Additionally the front-end performs some first beam conditioning. Most importantly the maximum beam size is defined by a diaphragm (or fixed aperture). This helps to reduce the heat load on all downstream elements. Additionally slits define the beam size according to the need of the beamline and downstream optical elements.

FRONT-END STRATEGY FOR SLS 2.0

The front-ends at SLS have proven to be very reliable and low-maintenance during the last two decades. Therefore we plan to reuse some of the existing components after refurbishment for SLS 2.0. All elements will be updated to state of the art motion control and safety standards [1]. However some FE elements need to be completely redesigned. The primary reason for this is the increased heat load on the exposed elements. For hard x-ray FEs, generally associated with high power loads, the power has increased by a factor of three coming from SLS going to SLS 2.0. This is due to the increase in storage ring energy from 2.4 GeV to 2.7 GeV and more powerful insertion devices.

Due to the new lattice all beamlines shift in lateral and longitudinal direction and available FE floor space has been reduced due to the more round storage ring with MBAs (see Fig. 1).

Because of these reasons all FEs need to be completely removed from the storage ring tunnel and carefully reassembled in dedicated areas during the SLS 2.0 dark time.

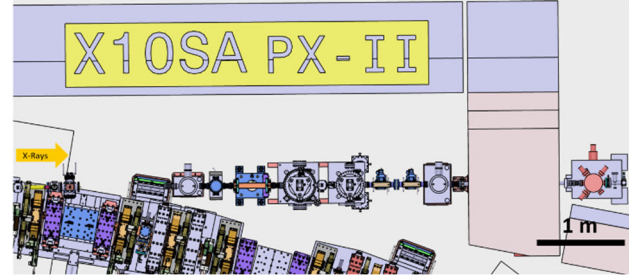


Figure 1: The PX-III front-end in its SLS 2.0 confines.

HIGH HEAT LOAD FRONT END COMPONENTS

The most demanding FEs in terms of thermal management are the hard x-ray FEs (see Fig. 2). In the most extreme case a cryogenically cooled U16 undulator produces up to 10 kW and 56 kW/mrad². But also some soft x-ray front ends are equipped with very powerful undulators producing comparable amounts of heat load which needs to be dealt with.

This is why our novel high heat load components are designed for versatility: by adapting only a few computer-aided design (CAD) parameters the same design can be used for different beam sizes to suit the diversity between the different FEs.

Following the most important components of a high heat load FE are outlined.

Tungsten Blade XBPM

Tungsten blade XBPMs (Pos. 1, Fig. 2) will be used to provide a feedback of the beam position to the machine and the beamline. This feedback will be used to optimize the electron-beam stability and serves as a reference for the beamline.

For SLS 2.0 we will reuse the existing tungsten blade monitors (W-XBPM). In order to use the W-XBPMs with the new beam parameters we developed a python script to calculate the response function of tungsten i.e. the probability of a photon emitting an electron from a tungsten blade and thus generating a signal using Eq. (1).

$$Y = \int_{30 \text{ eV}}^{30 \text{ keV}} F'(E) \cdot BW \cdot \sigma_{ph}(E) dE \quad (1)$$

Where Y is the tungsten response function $F'(E)$ is the flux density per energy [ph/s/mrad²/0.1BW], BW the band width and $\sigma_{ph}(E)$ the photoelectric cross section.

The result is then plotted together with the power density and the blades are then manually adjusted in order to maximize the signal and minimize the heat exposure (see Fig. 3). We will then physically adapt the position of each blade for SLS 2.0 according to these findings.

Content from this work may be used under the terms of the CC BY 3.0 licence (© 2021). Any distribution of this work must maintain attribution to the author(s), title of the work, publisher, and DOI

† david.just@psi.ch

Content from this work may be used under the terms of the CC BY 3.0 licence (© 2021). Any distribution of this work must maintain attribution to the author(s), title of the work, publisher, and DOI

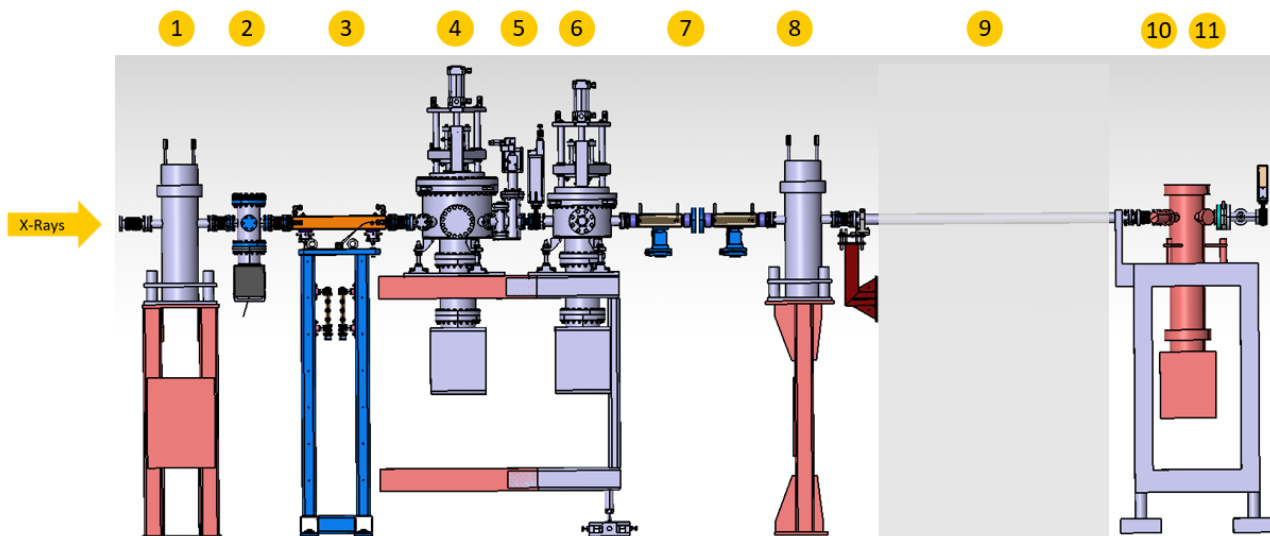


Figure 2: Typical component layout of a hard x-ray front-end at SLS 2.0. Labels: 1. 1st XBPM, 2. pump stand, 3. high-power diaphragm, 4. photon shutter, 5. fast- and gate valve, 6. beam stopper, 7. high power slits, 8. 2nd XBPM, 9. tunnel wall, 10. pump stand, 11. CVD window, arrow labelled X-Rays: propagation direction of the synchrotron radiation.

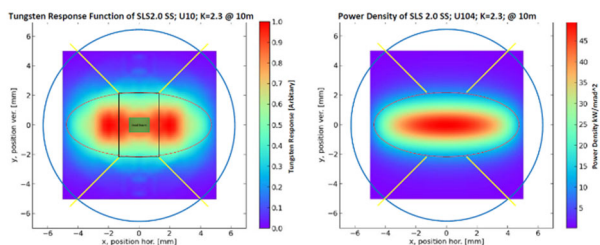


Figure 3: Example of the plots used to adjust the positions of the tungsten blades in the W-XBPMs. Left: tungsten response function plot. Right: power density plot.

New High Power Diaphragm

The new high power diaphragm (Pos. 3, Fig. 2) is a heavily water cooled (18 l/min) beam-defining fixed aperture. It will be completely rebuilt for most beamlines and consist of two copper parts brazed together (see Fig. 4).

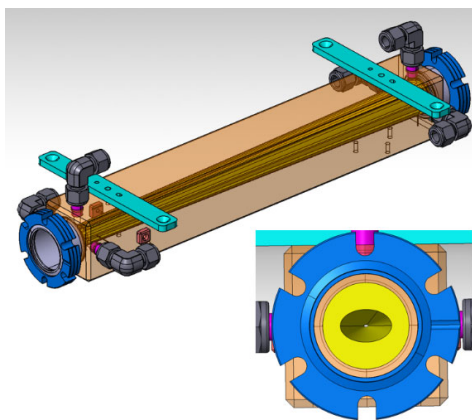


Figure 4: High power diaphragm. Insert bottom: cornerless entrance and exit window.

This innovative design allows us to optimize the cooling to deal with the increased power load of SLS 2.0. The inner

part, exposed to the heat load, forms 12 coaxial cooling channels. These cooling channels follow the tapering of the exposed surfaces to minimize the distance between the heat and the water and therefore optimize the heat flow from the exposed surface to the cooling water over the whole length of the device. Additionally the water inlet, with the coolest water, is at the narrowest part of the diaphragm i.e. the part where the most heat is absorbed. The outer part of the diaphragm closes the cooling channels as a sleeve and holds all the connectors, flanges et cetera.

The surface which is directly exposed to the synchrotron beam, formed by wire erosion, is designed in such a way that no corners are directly exposed to the beam in order to avoid corner stresses.

We performed finite element analyses FEA using ANSYS CFX in combination with ANSYS Mechanical and found that we are well below our design criteria even with a safety margin of 40 %.

Photon Shutter and Beam Stopper

The primary safety element in an insertion device FE is a combination of a photon shutter and beam stopper (see Fig. 5). The photon shutter (Pos. 4, Fig. 2) is water cooled and absorbs the synchrotron radiation whereas the beam stopper (Pos. 6, Fig. 2) consist of a 180 mm long Inermet-IT180 block and stops the high power radiation such as the gas Bremsstrahlung.

For SLS 2.0 we plan to reuse the existing components. We will replace the bellows with new ones, the end switches will be replaced with new and certified safety end switches and we will install a fall through protection i.e. if any of the mechanical supports would beak the photon shutter and the beam stopper will remain inside the beam. Additionally we will replace the pneumatic components with the latest versions and we will generally refurbish the devices thoroughly.

We also performed FEA for the photon shutter and found that we are below our design criteria.

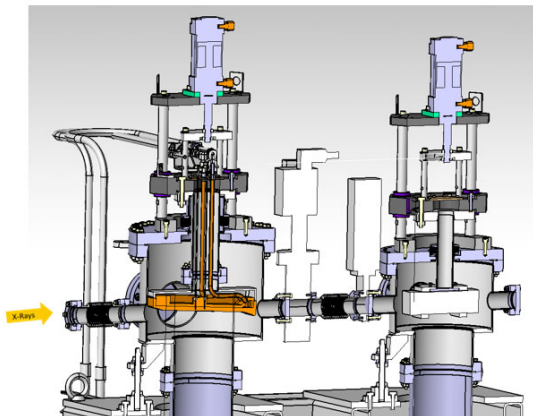


Figure 5: Cut through photon shutter (left) and beam stopper (right) with fast- and gate valve in between.

New High Power Slits

The purpose of the FE slits (Pos. 7, Fig. 2) is to reduce the beam size and to scan the beam with a small aperture to obtain the beam position.

At SLS most slits were built in the blade or shovel style i.e. four different blades were independently moved in and out of the beam. This design requires a vacuum chamber and occupies a lot of floor space. For SLS 2.0 we designed a new set of slits (see Fig. 6) which uses the L-Slit principle where each of the two elements is able to cut the beam in horizontal and vertical direction. The first element cuts the Down and Ring part of the beam while the second element cuts the Up and Wall part.

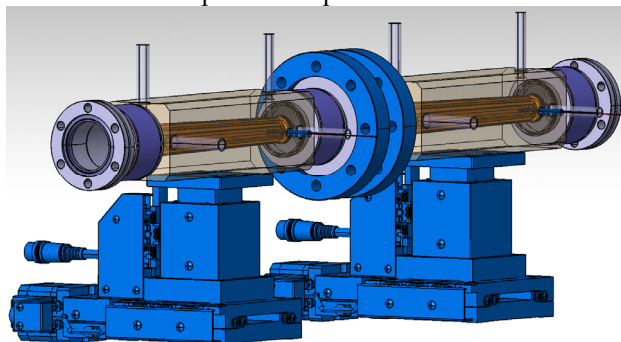


Figure 6: Draft of the new high power slits (design to be finished).

The new design has several advantages over the old blade slits design. Since the vacuum chamber is an integral part of the slits, the design is more compact and occupies less floor space.

In the conventional design the motors were placed outside of the vacuum chamber guiding the motion through a

set of bellows and linkages over several dozens of centimetres to the beam cutting surface. This reduces the mechanical stability of the blade. With the new design we can apply the motion more direct and design for stiffness.

In the case of high power slits an additional advantage comes to play: using the design principle of the high power diaphragm we can build slits with small tapering angles at the beam exposed surfaces and with excellent cooling. This allows to deal with the high power and high power densities at SLS 2.0 and improves the thermal stability of the slits.

Tunnel Wall Break Through

Due to the shifts of the source points and the beam lines it will no longer be possible to reuse the existing filler elements of the tunnel wall break through.

We therefore plan to cast the tunnel wall break through in a single concrete block of the same density as the surrounding concrete (4.5 t/m³) (see Fig. 7).

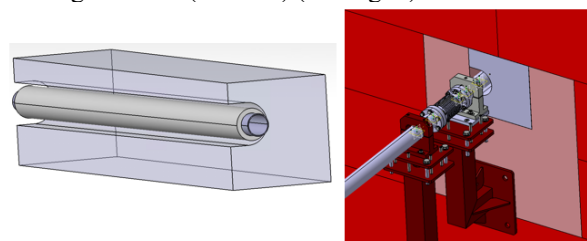


Figure 7: Tunnel wall break through. Left: casted mono block concrete filler with beam tube (surrounded with insulation for bake out). Right: Situation.

ACKNOWLEDGEMENTS

We are very thankful for the help and support our colleagues P. Willmott, H. Siebold, K. Bühlmann, M. Brüstle, S. Guntli, A. Bischofsberger, L. Day, R. Oeschger, B. Zumsteg, A. Stoyanov, A. Keller, B. Rösner, A. Weber, C. Schmid, C. Hess, D. Meister, D. Hauenstein, E. Zehnder, G. Käslin, I. Besana, J. Wickström, J. Buchmann, J. Honegger, L. Schultz, N. Gaiffi, P. Wiegand, P. Huber, R. Widmer, R. Ganter, R. Scheibl, Th. Schmidt, U. Frommherz, U. Flechsig at PSI as well as our colleagues at the beam lines and from the SLS 2.0 project. Special thanks also to Y. Jaski from APS and X. Liu and C. Bloomer from DLS.

REFERENCES

- [1] D. M. Just, C. Pradervand, P. Willmott, "Front-Ends", in SLS 2.0 Technical Design Report TDR, to be published.

ENGINEERING CHALLENGES IN BIOSAXS FOR AUSTRALIAN SYNCHROTRON

S. Venkatesan, C. Kamma-Lorger, L. Barnsley, A. Clulow, G. Conesa-Zamora, R. Grubb, B. Jensen,
 N. Hamed, V. Samardzic-Boban, C. Roy, T. Mazonowicz
 Australian Synchrotron, ANSTO, Melbourne, Australia

Abstract

The Biological Small Angle X-Ray Scattering (BioSAXS) beamline is the third beamline designed, developed and soon to be installed as part of the BRIGHT Program at the Australian Synchrotron. The BioSAXS beamline will deliver a high flux beam at sample position and will be optimised for time resolved experiments and low concentration/low scattering samples. This paper presents the various engineering challenges in this high flux design, including thermal management of critical components, design developments to accommodate the various operational modes and various stages of the Photon Delivery System and Experimental Station components. The paper aims to present details of design, Finite Element Analysis results and approaches taken to solve problems.

INTRODUCTION

The Biological Small Angle X-Ray Scattering (BioSAXS) beamline is the third beamline designed, developed and soon to be installed as part of the BRIGHT Program at the Australian Synchrotron. The BioSAXS beamline will deliver a high flux beam at sample position and will be optimised for time resolved experiments and low concentration/low scattering samples. The beamline will offer increased efficiency, and data quality, for all liquid phase scattering experiments, allowing measurement of new and novel samples, and experiments, that otherwise would not be possible. The BioSAXS beamline will accommodate a wide range of experiments by offering a q-range of $\sim 0.001 - 4 \text{ \AA}^{-1}$ and an optical design optimized for high flux ($\sim 5 \times 10^{14} \text{ ph/s}$) x-rays. At this flux rate, BioSAXS will offer users one of the highest flux beamlines in the world.

To achieve this, the beamline will use a superconducting undulator insertion device, double multilayer

monochromator, and vertical and horizontal bending mirrors, providing flexibility in optical configurations. The beamline will primarily collect data in a vertically unfocused mode. BioSAXS will also be able to achieve a fully focused and a fully unfocused beam.

The beamline is designed in 8 vacuum sections. The first contains a fixed mask, a bremsstrahlung collimator, cooled filter rack and a fluorescence screen. Vacuum section 2 is designed for the Double Multilayer Monochromator, two bremsstrahlung elements in each of the ports and a QBPM. The third vacuum section houses diagnostics and the attenuators. These are used to determine any shift in the beam location and enable correction for the beamline. The fourth vacuum section is design for the KB mirror system with horizontal and vertical focussing mirrors. This is followed by another group of diagnostics, formed by a grouping of QBPM and Fluorescence screens for real time analysis and correction, when combined with F460 electronics and in-flange slits, as well as a fast closing valve in the fifth vacuum section and the safety shutter in the sixth vacuum sections respectively. A beam conditioning table to manipulate the beam to sample is designed in vacuum section 7 and the end station as vacuum section 8. The beam conditioning table consists of a NanoBPM, two guard slits, XBPM and a Sample Camera for the visualisation of the sample at 29 m from the source and a mica exit window. The end station is formed by a sample table to carry samples in various environments, a vacuum vessel to house the in-vacuum Dectris detector, a detector actuation system for in-vacuum manipulation of detector position, the Beam-stops and the vacuum vessel actuation.

The design of the beamline is shown in Fig 1.

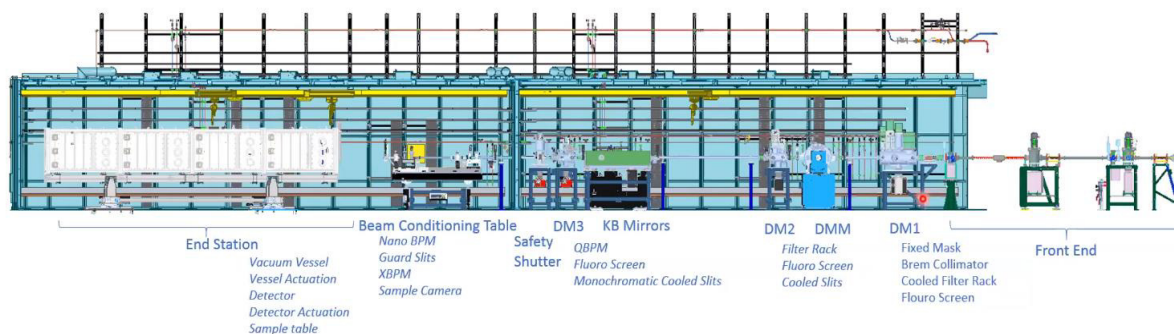


Figure 1: BioSAXS beamline schematic.

KEY TECHNICAL CHALLENGES

BioSAXS Beamline had a preliminary design to deliver a flux of 1.8×10^{14} photons/sec. The source for BioSAXS is a Super Conducting Undulator (SCU) with period length of 16mm, 98 full periods and magnetic field strength of 1.084 T (on axis). Constrained by the length of the straight in the storage ring, the design of the SCU was adapted to suit, leading to a drop in performance. With design changes in the SCU, BioSAXS Beamline needed to adapt to deliver a high performance. In order to accommodate this, changes were initiated in the design of the beamline.

The key change initiated into the beamline design to adapt to the source, were an increase in the aperture of the fixed mask to allow for more photons entering the beamline. The change to a 3.5 mm (H) x 2 mm (V) aperture allowed for a higher than anticipated performance, albeit with some challenges.

The Key challenges in the beamline and end station design were

1. Thermal load management from the increased flux
2. Management and mitigation of Bremsstrahlung radiation, and
3. Design flexibility in end station components to allow for three key operational modes in the beamline.

APPROACH TO PROBLEM

Thermal Management

The design change of increasing the aperture of the fixed mask still allowed for the capture and management of this thermal load with water cooling. Using a flow rate of 5 L/minute, a total power load of 1.98 KW. This was verified through FEA.

However, there was still a high amount of heat going through to the beamline. In order to offer an added layer of protection for the optics, a cooled CVD diamond filter rack was added to the beamline design. CVD diamond allows for the reduction of heat while remaining transparent to the Xray going through to the monochromator, in the energy range that BioSAXS is aiming to work in.

While this reduced the thermal load on the first crystal of the monochromator, there was still a need to manage, up to 400 W of thermal loads in this area. The approach taken by the design team at the Australian Synchrotron and FMBO, our design partners, was to increase the footprint of the beam on the substrate. While this meant a larger substrate, the design of the monochromator would be simpler, with the need for a translation stage removed. This thereby, reduces the size of the vacuum vessel and directly reducing the cost of the device. In addition to the change in size of the substrate, the method to manage the thermal loads was to reduce the offset of the crystals in the crystal cage. The initial offset of 15 mm between the crystal was changed to 10 mm to allow for the spread of the incoming beam, thereby increasing the beam footprint. In addition to increasing the surface area on the substrate, this also enabled

the design team to increase the performance of the beam at sample position.

For the thermal management at the monochromator, the options available for the team included water cooling and cryo-cooling. Cryo-cooled multilayer monochromators have been built and tested in the recent past by several synchrotron facilities. However, the long-term impact on the multilayers from thermal loads and the lack of long-term performance data presented a risk to the project. The design team undertook the option of pursuing water cooling, to minimise the risk and also generate cost savings.

Finite Element Analysis of the crystal substrate was undertaken to ensure that the requirements of slope errors could be met. With the addition of the cooled filters, upstream of the monochromator, the power load on the first crystal substrate was reduced to a maximum of 402 W. With a beam footprint of 4.3 mm x 121 mm, the results from the analysis showed that there was a maximum deformation of 1.8 μm , on axis. With the correction from the mirrors, further downstream, the slope errors were then maintainable within an acceptable limit. The results for the deformation from the analysis are given in Fig. 2 and Fig. 3 shows the slope errors from the monochromator.

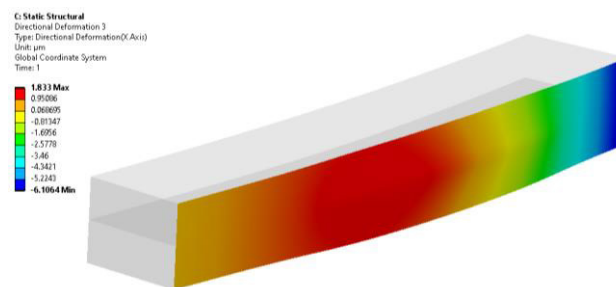


Figure 2: Deformation on the first crystal substrate of the DMM.

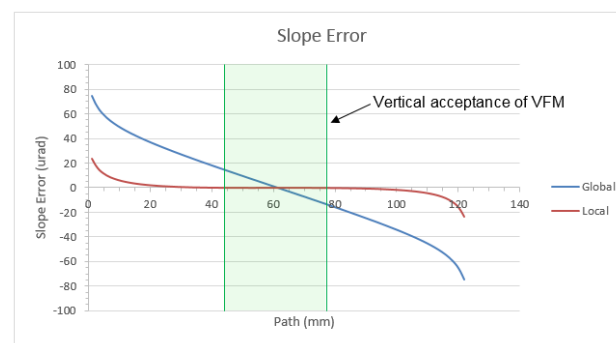


Figure 3: Slope error resulting from water cooling of the first crystal in DMM.

Bremsstrahlung Radiation Management

One of the challenges arising from a low-offset monochromator design is the subsequent radiation issues arising from the close distance of the optical aperture to the Bremsstrahlung rays. The guidelines at the Australian Synchrotron recommend a minimum of 3 Moliere radii from the edge of the optical ray to the edges of the Bremsstrahlung

components or in the presence of an optical aperture in the component, a minimum of 1 Moliere radius to the optical aperture, followed by 2 Moliere radii after the optical aperture. This has shown to reduce the scatter of the radiation going downstream from the component, by up to 95%. Since the Moliere radius for the materials vary, Tungsten was selected as the suitable material, providing a needed clearance of ≈ 8 mm. The low offset design in the monochromator allowed for a clearance of 1.9mm to start with. One new Bremsstrahlung collimator was included in the beam in-port of the DMM and the downstream stop was relocated to the beam out-port of the DMM to create an increased distance. With the design changes, a maximum aperture-to-aperture clearance of 6.5 mm was achieved (0.7 Moliere Radius). A Montecarlo analysis was performed by B. Bewer of the Canadian Light Source to investigate the effect of this clearance not meeting the required guidelines. The results from the analysis showed that the radiation dose rates on the outside hutch walls were able to meet the required specification of $<0.5\text{mSv/hr}$. This was achieved through ray tracing and identifying the scatter directions through the optical aperture. By increasing the need from a minimum of 20 radiation lengths (3.5 mm for Tungsten/ length) to a total of 200 mm thickness, there was sufficient material through the aperture to absorb the scatter through the optical aperture. This enabled the team to meet the radiation dose rate requirements. Typical results, for this general arrangement in BioSAXS beamline, is show in Fig. 4.

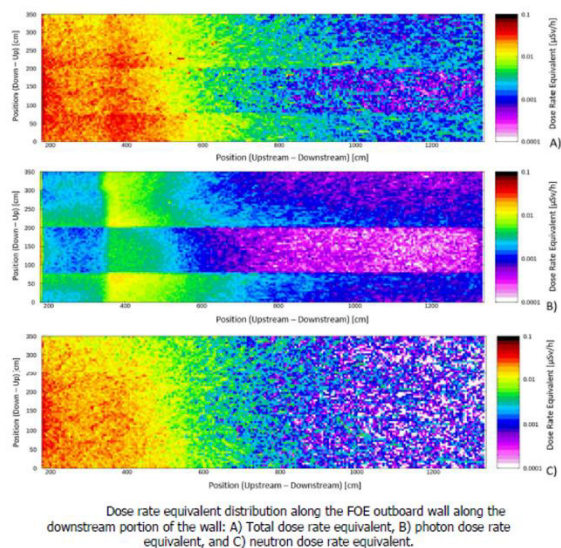


Figure 4: Results from Montecarlo analysis for Bremsstrahlung radiation dose rates.

Design Flexibility

The BioSAXS beamline aims to provide users three main modes of operation, enabled by design flexibility provided through the optics. The modes are

1. Fully focussed
2. Vertically unfocussed
3. Fully unfocussed

While the beamline anticipates the majority of users would prefer the vertically unfocussed mode, the option of having

all three modes of operation addresses the needs for future users, expanding the outreach of the beamline. In order to enable experiments in these modes, the end station of the beamline had to adapt to the beam positions in all the three modes, while also accommodating a variety of sample environment. To achieve this, the BioSAXS end station is designed as two major components. The beam conditioning table, as part of the photon delivery system, provides five axes of movement. This includes vertical, transverse, pitch, roll and yaw motions. The end station aimed to accommodate the beam through these different positions.

The detector is housed in a rectangular vacuum vessel with a cross section of 1.1 m (H) x 1 m (V) and a length of 8 m. With a three degree of freedom actuation system for the detector, the detector stage can transverse the entire length of the vessel, allowing for fast change of the focal lengths of the camera for imaging. The detector stage, in vacuum, allows for transverse and vertical movements, driven on stages powered by stepper motors. The beamstops are also built on the same stage and allow for the positioning of four photodiodes built on a rotary stage to change between the diodes. This is then mounted on two translation stages allowing any of the diodes to be placed anywhere on the detector surface. A coarse beamstop is also included in the design to allow the users to stop the beam while the diodes are being positioned. The design of the detector stage was first built and used in the SAXS/WAXS beamline at the Australian Synchrotron by L. Adamson and N. Kirby. The design of the detector stage is shown in Fig. 5.

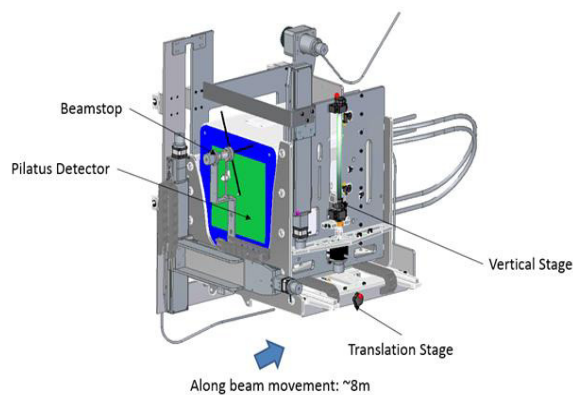


Figure 5: Detector stage.

The vacuum vessel table, carries the vacuum vessel and allows for the positioning of the vessel, depending on the beam operational mode and also accommodating differences in the sample table dimensions. To meet this positioning requirement, the table is equipped with four different axes of movement. This includes a total range of ± 150 mm in the vertical axes, ± 150 mm in transverse and a total range of 600 mm along the beam in the downstream direction. The travel requirements are met with an upgrade to the motions but following the same design principle of the vacuum vessel table in the SAXS/WAXS beamline. The vertical motion of the vessel is achieved four vertical jacks, powered in pairs through two high power motors, generating the capability to move the upstream and downstream

ends of the vessel independently. A shoulder joint installed on the upstream side, in conjunction with linear slides on the downstream end, enable pitching motion of the vessel. The transverse and longitudinal motions are powered using a combination of stepper motors and air bearings. Eight, 300 mm air bearings support a total load of 5.57 tons, including the vessel and the table components. The design of the vacuum vessel table is shown in Fig. 6.



Figure 6: Design of vacuum vessel table.

The sample table, which accommodates samples in various sample environments is also designed to suit the motion ranges in the beam conditioning table and the vacuum vessel table. The sample table is designed over a granite block and carries an optical breadboard 450 mm x 750 mm. Similar to the vacuum vessel table, two vertical stages, on the upstream and downstream ends, provide vertical and pitch motions. The pitch motions are enabled through double flexures on the downstream side and single flexures on the upstream side. Two additional stages provide the transverse and longitudinal motion. The longitudinal motion is a total of 50 mm. Transverse motion for the breadboard is a total of 600 mm. To achieve this challenging range, a double rail, telescopic arrangement has been developed driven by a rack and pinion, with adjustments to minimise backlash. The double rail enables the moment and load management, with a total payload capability of 100 Kgs. The design of the double rail system is shown in Fig. 7 and the sample table at the extremities of the vertical motion is shown in Fig. 8.

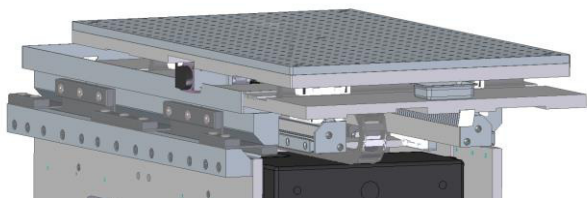


Figure 7: Sample table double rail motion arrangement.

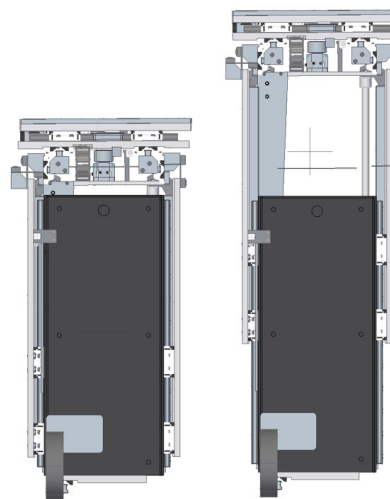


Figure 8: Sample table at high extremities.

In addition to the motion range requirements, the same table design is also covered by specifications for stability. In order to achieve this, the design of the upstream and downstream vertical plates was optimised for the loads and free vibration requirements. FEA was applied to analyse the deformation in a static environment and for modal analysis. The results from the analysis showed a maximum deformation of 9 μm at the breadboard. This result is shown in Fig. 9. Figure 10 shows a typical result from the modal analysis. The first Eigen frequency was calculated to be 137.3 Hz while the vertical axes was at the lowest position and 78.1 Hz at the highest position.

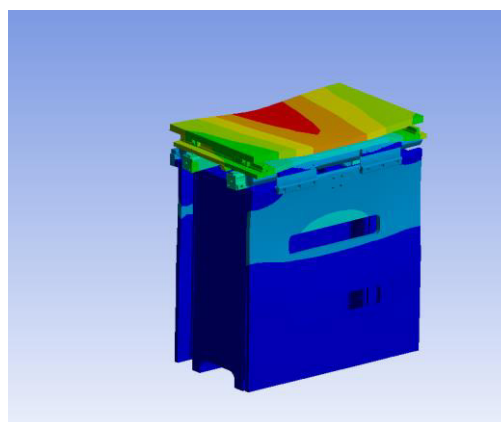


Figure 9: FEA static deflection analysis results.

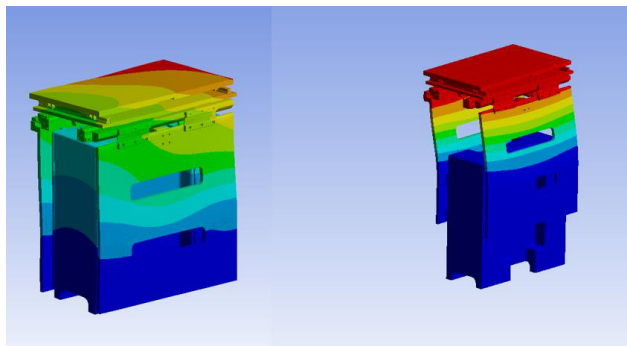


Figure 10: Typical results from modal analysis.

The complete results from the modal analysis are shown in Table 1. The results show a good stability in the design and the first Eigen Frequency falls within the specification.

Table 1: Results from Modal Analysis for Sample Table

Mode	Lowest Vertical Height	Highest Vertical Height
1	137.3 Hz	78.1 Hz
2	167.4 Hz	128.6 Hz
3	169.9 Hz	132.3 Hz
4	174.3 Hz	166.6 Hz
5	207.8 Hz	185.5 Hz
6	228.9 Hz	205.9 Hz

The results of the engineering undertaken in this beamline and end station design has delivered the needs to achieve a high flux beam at sample. With the design flexibility and effective management of thermal loads in the beamline components has kept slope errors to a minimum and achieving a flux of 8.07×10^{14} photons/sec with a beam size of 2.38 mm x 1.23 mm.

CONCLUSION

The BioSAXS beamline is currently being manufactured and installation is slated to commence for the photon delivery system in January 2022. The design of the end station components is in various stages of final design, with the vacuum vessel table currently being built for testing and the sample table in advanced final design phase. The engineering effort have achieved the goals of the beamline science requirements and it is expected that the results from the commissioning activities will be presented in upcoming conferences.

ACKNOWLEDGEMENTS

The authors of this paper would like to acknowledge the efforts and assistance from FMB Oxford in relation to the design of the photon delivery system. The authors would also like to acknowledge and thank B. Bewer from Canadian Light Source for assistance in completion of the

Radiation Shielding Analysis for BioSAXS and Brad Mountford, Luke Adamson and Nigel Kirby for end station design contribution

DEVELOPMENT OF A LINEAR FAST SHUTTER FOR BM05 AT ESRF AND BEATS AT SESAME

C. Muñoz Pequeño [†], J. M. Clement, P. Thevenau, P. Van Vaerenbergh
 European Synchrotron Radiation Facility, 38043 Grenoble, France

Abstract

A new linear fast shutter for X-ray topography and tomography is currently under development. This first prototype will be assembled and tested on the BM05 beamline at the ESRF, and another unit will be installed in the future BEATS beamline at SESAME. The new shutter aims to overcome the stability, control and thermal issues reported with previous versions. This versatile design can be used with monochromatic and white-beam, reaching minimum exposure times of 50 ms for a beam size of $H 80 \text{ mm} \times V 20 \text{ mm}$.

Powered by two linear brushless DC motors, the exposure sequence is achieved through the synchronization of two tantalum blades. This concept has been tested in a dedicated bench to characterize the sequence produced by the linear motors, and exposure times of 50 ms with a maximum error of 1.5 ms have been measured. This article describes the main features of the shutter prototype design and its associated motion control system. The main results of the measurements with the test bench are discussed as well.

INTRODUCTION

Fast shutters are widely used in synchrotron beamlines for applications in X-ray topography and tomography. Topography typically requires exposure times ranging from milliseconds to hundreds of seconds. Due to its low signal-to-noise ratio, it is essential to shield the CCD detector during readout to avoid added noise [1]. In addition, shutters are of special relevance when performing white beam tomography in delicate samples that are easily degraded when exposed to high photon flux. The use of a shutter allows for sample repositioning and prevents sample irradiation when data is not being recorded. This highlights the importance of the control in the exposure time and its uniformity to guarantee an adequate image quality.

In the context of the refurbishment of the BM05 instrumentation beamline at the ESRF, an old shutter was installed in the tunnel located before the experimental hutch EH2. In this model, the exposure sequence was achieved through the synchronization of two stainless steel blades powered by electromagnets. However, in addition to the tremendous vibrations and the limited duration of the exposure cycle due to the electromagnets overheating, their control system was obsolete. The main motivation of this project was to develop a new shutter that can overcome these issues with up-to-date controls to replace the prototype installed at BM05. Another prototype is being developed for installation in the experimental hutch of the BEATS tomography beamline currently under construction at SESAME [2].

[†] munozpeq@esrf.fr

DESIGN

The main advantage of the proposed concept is its suitability for larger beams thanks to the use of linear brush-less DC motors featuring high dynamics and precision. Other technologies often employed in the synchrotron community, such as rotary and piezoelectric shutters [3], can achieve very small exposure times as well, but over much smaller beam apertures.

Table 1: Fast Shutter Specifications

Parameter	Value
Beam size [mm × mm]	80 × 20
Exposure time [ms]	< 100
Repetition rate [Hz]	> 1
Maximum beam power [W]	380
Blade material	Tantalum
Blade thickness [mm]	4

The motors have been selected to fulfil the specifications listed in Table 1. The objective is to achieve a reproducible and uniform exposure time over the beam window. The exposure cycle is achieved through the synchronization of two blades so that the exposure time depends on the delay between their opening and closing trajectories. Therefore, it is crucial that the trajectories of the blades are identical, i.e. to ensure the delay between the opening and closing of the blades, Δt_1 and Δt_2 , is the same for all the points of the window (see Fig. 1).

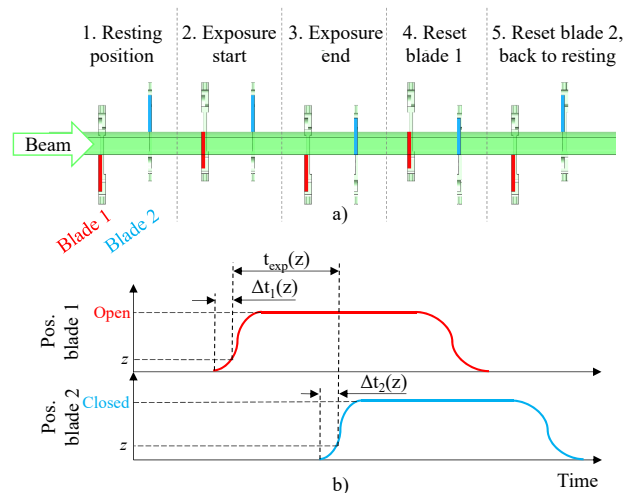


Figure 1: Exposure sequence, a) schematic of the phases of the exposure cycle b) diagram of the blades trajectories.

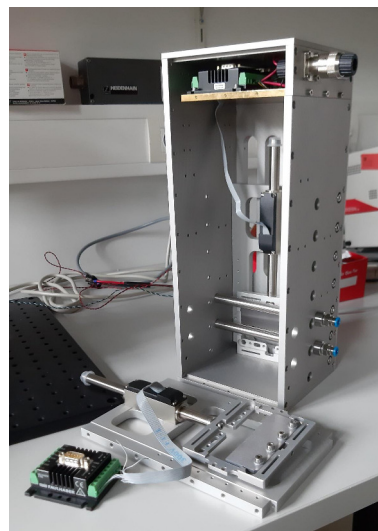
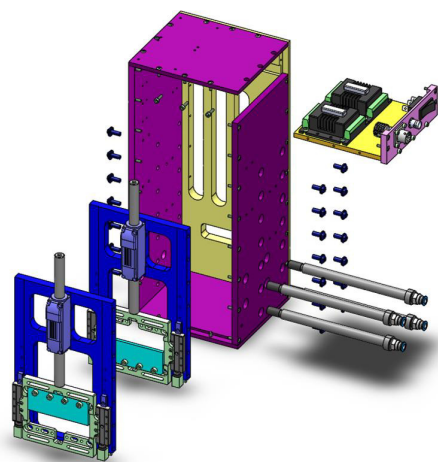


Figure 2: 3D model and picture of the prototype in construction.

The proposed sequence is schematized in Figure 1. When the exposure starts, the first blade is opened, allowing for beam exposure. Once the desired exposure time is reached, the second blade is closed, stopping the beam irradiation. Then, the first blade and the second blade are reset to their original position one after the other.

Linear Motors and Control

The chosen solution for the blades motion are brushless DC linear motors from Faulhaber. The main parameters of the employed model LM2070-80-11 are listed on Table 2. They feature high compactness, easy installation, and a good dynamic performance that allows for the rapid timing required for short exposures. These motors consist of a 3-phase coil housed in a non-magnetic steel stator. The high-power magnets drive a magnetic multi-pole rod, and Hall-sensors are integrated in the stator housing for positioning control.

Table 2: Linear Motor Specifications

Parameter	Value
Stroke [mm]	80
Continuous force [N]	9.2
Peak force [N]	27
Continuous current [A]	0.79
Peak current [A]	2.4
Accuracy [μm]	300
Repeatability [μm]	80
Temperature range [$^{\circ}\text{C}$]	-20 – 150

Each motor is actuated by a controller MCLM3006 S with interface RS232, which is programmed independently to follow a sequence that can be triggered by a TTL signal. The two positions of the blade are pre-programmed, and to switch between them, a basic triangular profile of velocity is implemented, i.e. the blade is accelerated up to the mid-

point of the movement with the maximum acceleration, then it brakes with the maximum deceleration.

The sequence is programmed as it follows:

- Power ON: the blades go to their resting position.
- Control signal transition from 0 to 1: the first blade moves to the open position.
- Control signal transition from 1 to 0: the second blade moves to the closed position. The first blade waits for a delay and returns to its original position. After another delay, the second blade returns to its original position.

Mechanics

Figure 2 shows the general overview of the shutter. The blades are installed in two identical aluminium frames optimized to avoid stress concentrators while keeping a light mass. The assembly blade-motor is attached to a support with two ball bearing guideways Schneeberger of the MSQ line. These can work at velocities and accelerations up to 3 m/s and 300 m/s², while withstanding temperatures up to 150 °C.

These supports are assembled onto a protective cage of dimensions 15 × 15 × 40 cm, which has been carefully designed to respect the distances between the motors and the rest of the elements to avoid magnetic forces that would compromise their performance. The controllers are assembled onto a 5 mm thick lead plate to shield the electronics from radiation. Each blade is cooled by two buffers that ensure continuous nitrogen flow at the two blade positions.

Thermo-mechanical Analysis

A thermo-mechanical FEA analysis has been implemented with Ansys to determine if nitrogen cooling is enough to guarantee the safe operation of the shutter. The convection coefficient has been estimated at 300 W/m²°C through empirical correlations [4] with an inlet pressure of 1.4 bar.

The results are shown in Fig. 3, which depicts a maximum temperature of 218 °C and a maximum stress of 173 MPa in the aluminium frames, well below its maximum working temperature and elastic limit.

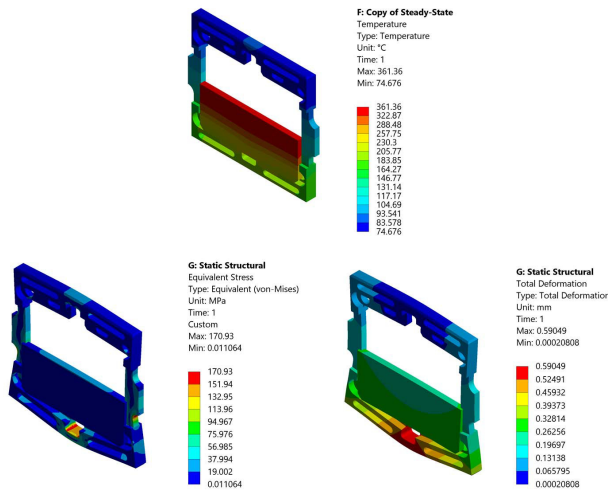


Figure 3: FEA analysis results of the shutter blade and frame.

TEST MEASUREMENTS AND RESULTS

The synchronization of the motors has been tested in a dedicated bench to recreate their working conditions and characterize the blades trajectories. The goal of this setup was to reconstruct these trajectories by measuring the delay the blades take to reach different positions of the window.

To do so, a movable frame containing a laser and a photodiode is fixed at different heights to perform the measurements (see Fig. 4). The photodiode detects the laser beam passing through the shutter, and its output is connected to an oscilloscope to analyse the resulting signal.

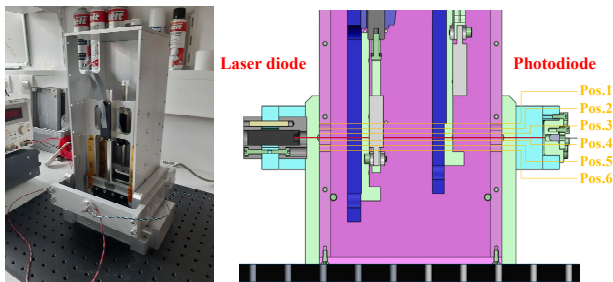


Figure 4: Picture and 3D model of the test bench setup.

When the laser-photodiode is fixed at a position, the time elapsed between the opening order for the first blade and the detection of light by the photodiode is the time taken by the first blade to reach position, $\Delta t_1()$. Analogously, the time elapsed between the closing order for the second blade until light is no longer detected corresponds to the time taken by the second blade to reach position, $\Delta t_2()$.

40 cycles have been measured at 6 different heights with an exposure time of 100 ms, as shown in Figure 4. The average trajectories reconstructed through these measurements are shown in Fig. 5, revealing that the maximum deviation in the exposure and reaction times is 1.5 ms. The reaction time ranges between 6 -7 ms, while the rising times for rearming are between 62-70 ms. Time between exposures down to 300 ms can be used, but the system becomes unstable if values lower than this threshold are used.

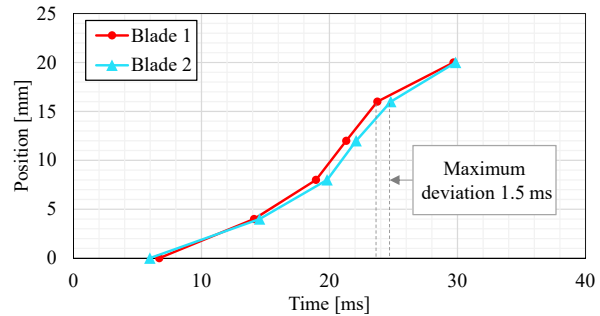


Figure 5: Measured blade trajectories.

CONCLUSION

A versatile design for a linear fast shutter based on linear brushless DC motors has been presented. The feasibility of this concept has been proved through a series of tests, which show that short exposures of 50 ms can be reached with a maximum error of 1.5 ms and time between expositions down to 300 ms. The prototypes for BM05 and BEATS are almost ready for commissioning, and in later stages, the thermal and fatigue behaviour of the system under white beam will be analysed. This design can be adapted to other shutters with different strokes and blade materials if the timing of the motors is optimized.

ACKNOWLEDGEMENTS

The authors would like to thank T. Durand for the drafting works, C. Ravary for the electronics and cabling work, and the staff of BM05 for their input to complete this project.

REFERENCES

- [1] S. Bérújon, "At-Wavelength Metrology of Hard X-Ray Synchrotron Beams and Optics", Ph.D. Thesis, Université de Grenoble, France, 2013.
- [2] G. Iori *et al.*, "Design and Ray-Tracing of the Beats Beamline of SESAME", presented at MEDSI 2020, Chicago, IL, USA, July 2021, paper WEPA10, this conference.
- [3] B. Laluc, T. Maillard and A. Riquer, "Piezo Technology in Synchrotron", in *Proc. MEDSI 2018*, Paris, France, pp. 321-323, 2018. doi: 10.18429/JACoW-MEDSI2018-THOPMA01
- [4] F. P. Incropera, D. P. DeWitt, T. L. Bergman and A. S. Levine, "External flow", in *Fundamentals of Heat and Mass Transfer*, 6th ed., Hoboken, NJ: John Wiley & Sons, 2007, pp. 447-452.

THE BEAMLINE MOTOR CONTROL SYSTEM OF TAIWAN PHOTON SOURCE

C.F. Chang[†], C.Y. Liu
 National Synchrotron Radiation Research Center, Hsinchu, Taiwan

Abstract

Different experiments have different features, so does the optical design; however, all of them are necessary to be adjusted according to mechanism. For example, adjusting mechanism of optical element is often based on stepper motor, for stepper motor possesses high resolution ability, which can adjust mechanism to precise location. This study illustrates how motor system of our Taiwan Photon Source integrates adjusting mechanisms of stepper motor on beamline. In addition, the firmware of close-loop system is cooperated to further improve veracity of location.

INTRODUCTION

When using the beamline, in order to be able to adjust the light source to the required environment of the experiment, the optical system on the beamline is designed to be adjustable. The types of mechanisms on the beamline are divided into two categories. The first is the optical path adjustment mechanism used to adjust the position of the light source; the second is the light path diagnosis mechanism, used to check the condition of the light source when it is in use. Most of the mechanisms are designed with stepper motors. This article explains how the TPS beamline motor control system control various movable mechanisms on the beamline.

SYSTEM STRUCTURE

The movable components on the beamline use the eight-axis motor controller as the control core and can be moved after being equipped with a suitable driver, so the user can freely match according to the needs of use, and the controller adopts an independent. In addition, the TPS beamline has improved position accuracy, so all the motor control components on the beamline are equipped with various optical scales to obtain the actual position signal, and the TPS beamline the motor controller of the beamline selection can read the encoder, allowing the control system to fine-tune the mechanism, so that the position accuracy is improved [1-2]. (See Fig. 1.)

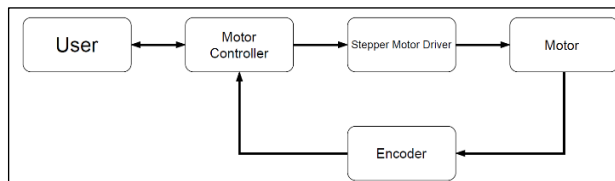


Figure 1: System architecture of Beamline Motor Control System.

[†] donnychang@nsrrc.org.tw

HARDWARE DESCRIPTION

The DMC-40x0 motion controller is Galil's highest performance, stand-alone motion controller packaged with optional multi-axis drives in a compact, metal enclosure. The unit operates stand-alone or interfaces to a PC with Ethernet 10/100Base-T or RS232 [3]. (See Fig. 2.)



Figure 2: The picture of DMC-40x0 motion controller.

CONTROL HARDWARE

TPS motor control system is based on the eight-axis motor controller DMC-4080 manufactured by GALIL, and the peripheral hardware is different due to the experimental characteristics of the beamline, and the stepping motor selected for the optical system will be different, but most of them are divided into Two types, one is a 5-phase stepper motor, the number of divisions is more than 500 (0.72°/Step), and the other is a 2-phase stepper motor, the number of divisions is more than 200 (1.8°/Step), the difference is the smallest part The difference in resolution is set by 5-phase stepper motor 1000 (0.36°/Step) and 2-phase stepper motor 400 (0.9°/Step) in TPS. As for the actual resolution, it is set by stepping motor. The ratio between the motor and the mechanical structure is determined. (See Fig. 3.)

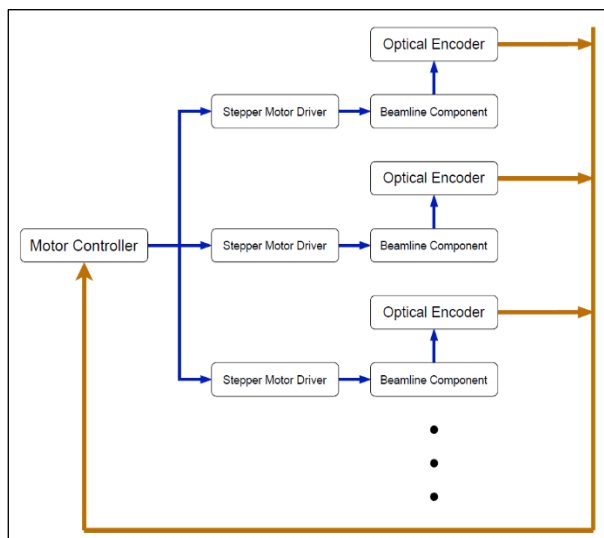


Figure 3: System architecture of Hardware.

In addition, many mirror chamber in the TPS beamline are equipped with vacuum motors to move the platform in the vacuum, but the vacuum cannot rely on convection to dissipate heat, and can only be carried out by conduction, but in order to protect the motor in the vacuum Overheating will cause damage, so a temperature controller is installed to monitor the motor in the vacuum. When the temperature is too high, the motor driver will be turned off, interrupting the current to the motor, and when the temperature is low, it will start, so that the vacuum can be extended. The life of the motor [4]. (See Figs. 4 and 5.)

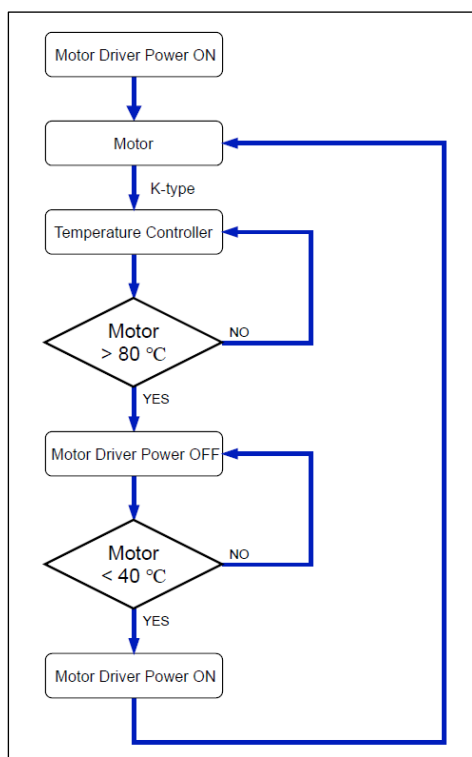


Figure 4: The temperature protection flow chart of the vacuum motor.

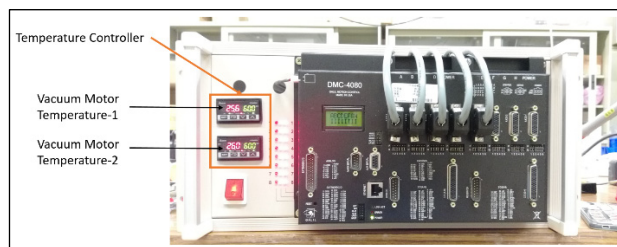


Figure 5: Temperature Controller & Motor Controller.

CONTROL FIRMWARE

Because the computer sends commands to the motor controller, it will take a lot of time to complete certain modes (such as closed-loop mode and searching for reference points... etc.). If you must increase the speed of its operation, you can use firmware Way to speed up its operation. (See Fig. 6.)

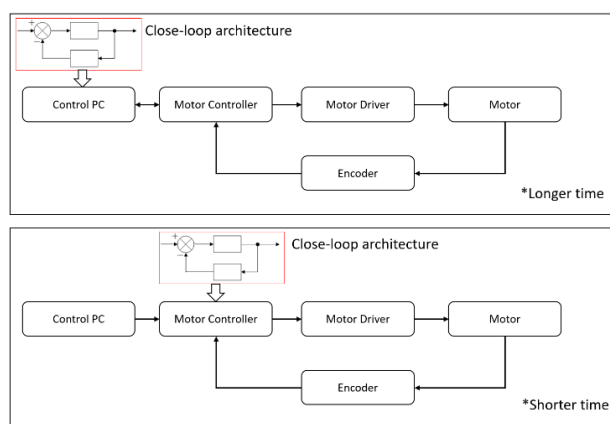


Figure 6: Close-loop diagram of software and firmware operation.

APPLICATION

At present, most of the beamline control systems that have been completed in TPS are built with GALIL controller as the core. Although the mechanical structure of the following purchased equipment is designed and manufactured by an external manufacturer, the motor control system that can be executed is designed and manufactured in the NSRRC, such as various optical mirror chamber on the TPS beamline(TPS 21A 4BCM, TPS 23A HDCM, TPS 09A End-Station, TPS 44A CM...) (See Fig. 7.)

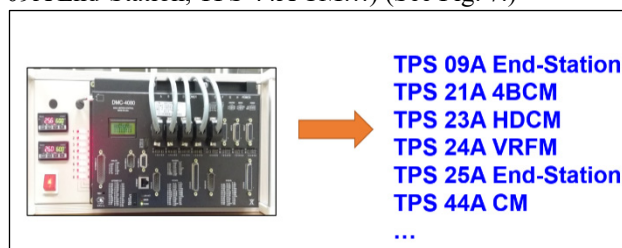


Figure 7: Motor control system application.

CONTROL SOFTWARE

Because the motor controller on the TPS beamline uses the network to operate, any software that can control the network can operate the beamline control system, but for the control software on the beamline, the operation and compatibility are considered at present, EPICS is used for the control operation of the control system. As for the part of the experimental station, it is designed according to the needs of the experimental station personnel. Currently, the software in use includes CSS, LabVIEW [5] and SPEC. (See Figs. 8 and 9.)

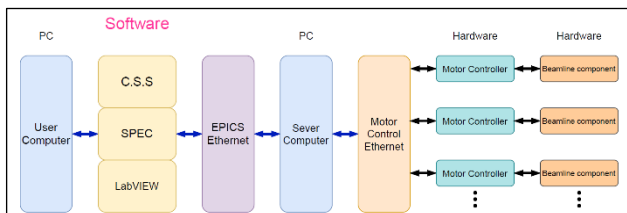


Figure 8: Software architecture diagram.

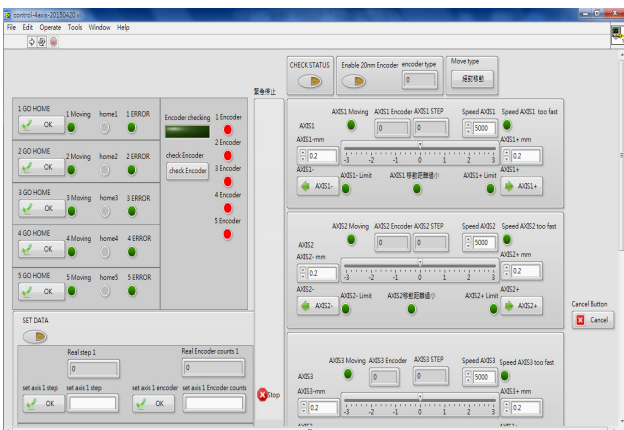


Figure 9: The visual Control interface.

CONCLUSION

The motor control system on the TPS beamline is designed and manufactured internally by NSRRC. Therefore, the mastery of the technology is quite mature. When an abnormality or malfunction occurs in the system, it can be quickly eliminated, which greatly improves the efficiency of use.

ACKNOWLEDGEMENT

We would like to thank the staffs at NSRRC, especially those in the Beamline Group, for assistance in this project.

REFERENCES

- [1] C. F. Chang, "An FPGA-based feedback control system that suppresses the nanoscale resonance", in *Proc. MEDSI'14*, Melbourne Victoria, Australia, 2014.
- [2] C. F. Chang, "Real-Time Motor Control System for Beamlines", in *Proc. 9th Mechanical Engineering Design of Synchrotron Radiation Equipment and Instrumentation Int. Conf. (MEDSI'16)*, Barcelona, Spain, Sep. 2016, pp. 41-43. doi:10.18429/JACoW-MEDSI2016-MOPE18
- [3] GALIL, <https://www.galil.com/>
- [4] DELTA, <https://www.deltaww.com/zh-TW/index>
- [5] NI, <https://www.ni.com/zh-tw.html>

THE FIZEAU SYSTEM INSTRUMENT AT ALBA OPTICS LABORATORY

Llibert Ribó†, Igors Sics, Domingo Alloza, Carles Colldelram, Josep Nicolas
ALBA Synchrotron, Carrer de la Llum 2 26, 08290 Cerdanyola del Vallès, Spain

Abstract

The ALBA optics laboratory has recently acquired a new Zygo Verifire HD Fizeau interferometer. The instrument has been integrated into a positioning stage to allow stitching of long x-ray optical elements. The mechanical set up, with four axes, allows for automatic positioning and alignment of the interferometer aperture to the surface under test. The longitudinal movement allows for scan of X-ray mirrors up to 1500 m long. The positioning platform includes two angles, roll and yaw, and two translations, vertical and longitudinal translations. The longitudinal translation is a custom designed linear stage. The yaw rotation is based on a sine arm mechanism. The vertical and roll motions are combined in a single stage, closely integrated around the main linear stage. The system reaches repeatability better than 1 μm or 1 μrad for all axes. The system is mounted on top of a vibration isolated bench in the clean room of the laboratory. The control software of the instrument allows direct control of every individual axis, and allows selecting the centre of rotation for both roll and yaw. The system includes inclinometers and autocollimators to control the relative orientation between the interferometer and the mirror under test. The system is integrated to the software of the interferometer, and includes features for automatic alignment of the interferometer to the mirror, or for automatic stitching acquisition, with selectable parameters. The system allows for full three-dimensional characterization of the optical surface of mirrors and gratings, and provides height map reconstructions with accuracy in the order of 1 nm, for flat or curved surfaces with lengths up to 1500 mm.

POSITIONING STAGE

The positioning stage consists on an integration of 5 motorized actuators for the positioning of the Fizeau interferometer. It has been designed to achieve the maximum compactness to give versatility to all possible measurements set ups. The stage has to operate on top of an antivibration system, thus the design included the weight as a requirement.

Design Description

The specifications for the positioning of the interferometer are listed below in Table 1 and Fig. 1.

The longitudinal actuator has a range of 1500 mm. The guides are mounted on the sides of an aluminum standard profile but on precise machined intermediate plates. The carriage is positioned by a ball spindle driven by a stepper motor. In order to avoid stresses caused by guidance errors between the spindle and the guides, a flexible nut support has been included. The system has been designed to reach

a speed of 25 mm/s and a theoretical resolution of 8,3 μm at full step. The resolution is achieved by means of micro stepping down to 1/8 of step.

Table 1: Specifications Table

Axis	Specification	Value
X	Longitudinal Stroke	1500 mm
	Resolution	5 μm
	Guidance Flatness	<50 μm
Z	Vertical stroke	$\pm 10\text{mm}$
Roll	Angular Range	20 mrad
	Resolution	1 μrad
Yaw	Angular Range	50 mrad
	Resolution	1 μrad

The vertical stage is mounted around the longitudinal one and it is based on the design of a double flexure that compacts the vertical movement and the rotation in a single following the concept *ALBA XALOC Beamline diffractometer table skin concept* [1, 2]. The angular resolution of the system is 5 μrad /full step, while the system is operated at 1/8-step.

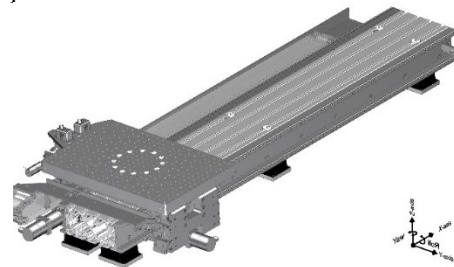


Figure 1: Representation of the axis.

The yaw actuator is the last stage mounted on the top of the vertical stage, and is the mechanical interface with the interferometer. The rotation is driven by means a sine arm. The mechanical architecture, allows for a fine yaw positioning resolution of 0,26 μrad /full step.

All axes include absolute encoders for positioning feedback and dynamic close-loop motion.

FEA Analysis

The design has been validated with simulation to check its stability (see Fig. 2). The lowest resonance modes, (at 49 Hz and 56 Hz) are related to the displacement of the full system due to the spindles compliance, although they but are within tolerance, particularly considering the weight of the system.

The skin concept flexures have been also calculated and optimized simulating the differential displacement between both plates for maximum Roll. The maximum stress is 198 MPa and in this case a high strength aluminium from serial 7000 has been chosen with a yield stress beyond

† lribo@cells.es

500 MPa. With these values the maximum of 40% of the yield stress as a generic fatigue limit is assured.

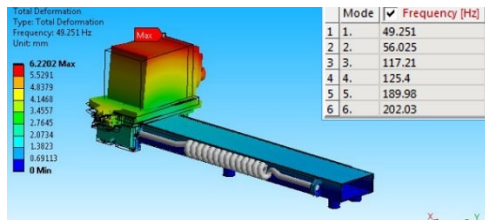


Figure 2: First eigen modes of the positioning platform.

Performances

Several tests have been done to check the motion performances. These tests have been done by means optical metrology, an interferometer and encoders. The results show that the longitudinal axis has a good resolution, well below 1 μm, see this results in following graphs Fig. 3.

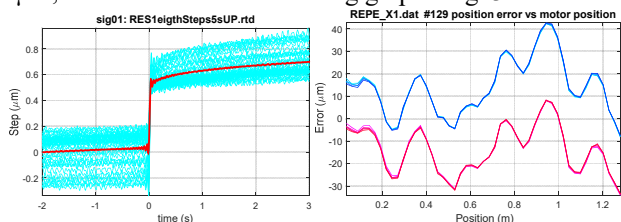


Figure 3: a) Longitudinal axis motion tests, resolution. b) Motion error.

Nevertheless, the system has poor guidance performance. Straightness and flatness are about 150 μrad, and in fact, positioning errors (Figure 3b) are partially caused by them. This is caused by the aluminium profile beam flatness as well as by the difficulty to align properly the two pairs sets of guides at opposite sides of the beam. This is one of the improvements to be done in a future upgrade. On the other hand, the yaw rotation has a good resolution as expected about 0,16 μrad per half step. Vibration tests have been also done and it is possible to see quite good response, there are not relevant resonance peaks below 150 Hz, the resonance modes are shown in next Fig. 4.

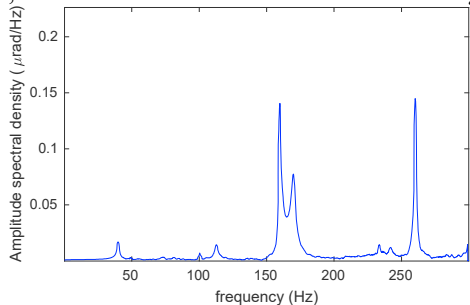


Figure 4: Stage resonance modes.

FIZEAU SYSTEM INSTRUMENT

The measurement system is based on the integration of several elements. The whole environment and tools give to the instrument system the capability to perform functional and accurate measurements. The stable environment of the optical laboratory stabilizes the temperature within

±around 0.1°C. The set-up is installed on a vibration isolation bench. The described mechanical setup allows taking stitching measurements for optical elements up to 1.5 m long. Next picture, Fig. 5. shows the interferometer integrated at the ALBA Optics laboratory.

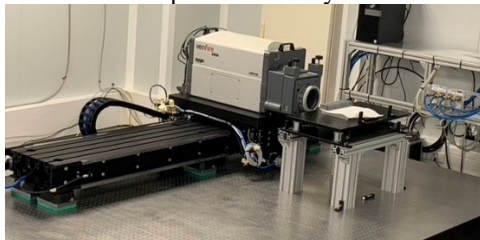


Figure 5: Picture of the Fizeau system at ALBA optics laboratory.

This mechanics, and Fizeau interferometer and its control are integrated into ALBA control system allowing interactive operation of the complete instrument. This allows for user friendly operation, with features like, for instance, automatic alignment of the interferometer optical axis to the surface under test. In addition, the measurement processing algorithms [3, 4] give automated functional data analysis allowing for easy determination of the main optical parameters of the optics under tests, as well as a high-resolution map reconstruction of its surface.

RESULTS

The new ALBA Fizeau Stitching Instrument allows for easy and quick measurements. This enables the full characterization of optics in short time and boosts the works on the optical set ups.

In the following Fig. 6, we give an example of a 1.4 m long flat mirror surface reconstruction obtained with this system. It is a 2D reconstruction with a spatial resolution of 0.09 mm, showing topography details at the nanometre level. It is perfectly visible the separation between the mirror stripes. In addition, the high-resolution performance allows even distinguishing coating defects on some of the mirror lanes.

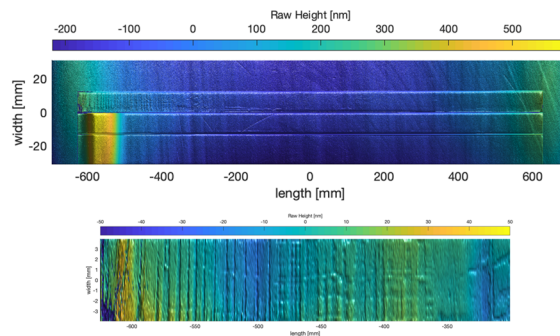


Figure 6: 1.4m long mirror surface map reconstruction.

Very similarly, Fig. 7 shows how the system reveals some characteristic features from traditional polished mirrors. Polishing passes are accurately distinguishable on the surface remodelling.

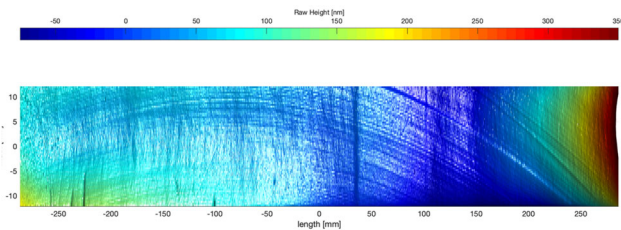


Figure 7: Example of map reconstruction.

Figure 8 shows some errors induced by IBF polishing, which are perfectly visible as a periodic pattern of square points.

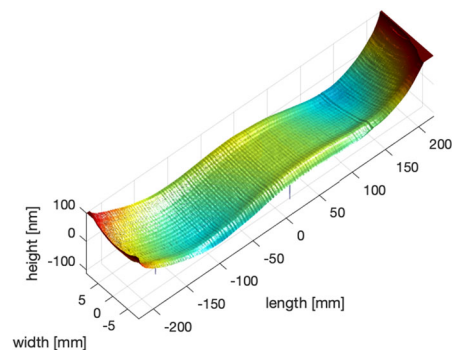


Figure 8: Example of map reconstruction.

The measurement is fast enough to allow to work on the optics setups. Next figures show examples of this, Fig. 9. First a 500 mm long mirror twist correction using the Fizeau system by monitoring the evolution of the adjustment. The two graphs show the surface mapping before and after the correction respectively.

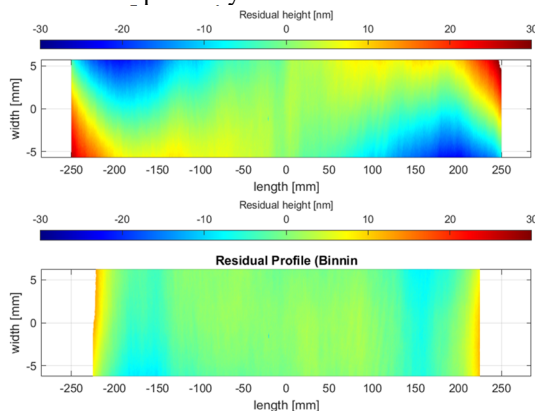


Figure 9: Mirror twist correction example.

Figure 10 shows a measurement result of a mirror with its bender. This is the surface reconstruction of an 800 mm flat mirror after the best fit meridional cylinder subtraction. The measurement provides a clear assessment of the sagittal radius of curvature and of the sagittal slope error. Also it is possible to find out the separation between stripes.

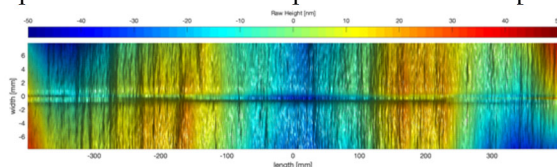


Figure 10: Mirror with bender metrology example.

It is possible to figure out the effect of the mirror holders clamping's. Below Fig. 11 is an example of the characterization of a mirror where it is clearly visible the local deformations of the contacts at the extremes of the mirror.

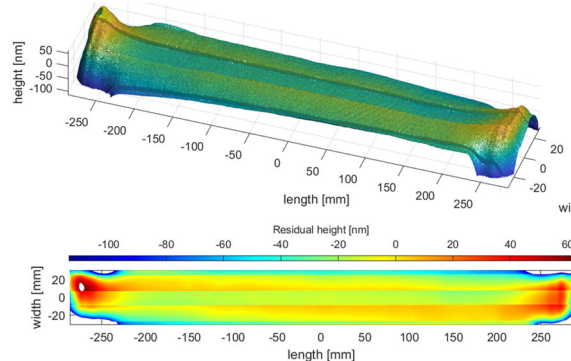


Figure 11: Clamps effect on a mirror.

CONCLUSION

The ALBA optics laboratory has been upgraded with a new Fizeau Interferometer. This instrument has been integrated mechanically with a long linear stage that allows for characterization of optical lengths up to 1,5 m. This mechanics also includes several linear and angular movements allowing for the automatic alignment of the Fizeau to the optics being tested. The system has been installed on a vibration isolation table in a temperature controlled clean room. The mechanics, the instrument and its control software have been integrated to ALBA control system providing an interactive interface of the whole system. In addition, an in-house developed data analysis software and algorithms, allow for automated quick extraction of the main optical parameters of the surface under test becoming very fast and easy to operate. All this combination together makes the Fizeau interferometer system at ALBA a very reliable instrument, accurate and with a sharp resolution. With this system it is possible to quickly extract optical surface map reconstruction, highly detailed and resolute. The measurement and analysis are quick, easy and with enough resolution to allow distinguishing tiny features on the surfaces, like polishing patterns or other defects, as well as, clamp-induced deformations. This makes possible to work with the optics being tested, allowing to adjust holders and benders, for instance, on a straightforward and brief iterative process.

ACKNOWLEDGEMENTS

The authors wish to acknowledge all those most involved in the design, construction, testing the Fizeau Instrument System at ALBA; Technical Office Gabriel Peña, Liudmila Nikitina, workshop Jose Ferrer, Karim Maimouni; Electronics Cristian Pérez; Controls Systems Guifré Cuní; Engineering Alignment Group, Jon Ladrera, Marta Llonch.

This Project is partly funded by the Spanish Ministry of Science, Innovation and Universities, under contract RTI2018-097107-B-C32.

REFERENCES

- [1] C. Colldelram, C. Ruget, and L. Nikitina, "ALBA XALOC beamline diffractometer table skin concept design", *Diamond Light Source Proceedings*, vol. 1, Issue MEDSI-6, October 2010, E44. doi:10.1017/S2044820110000754
- [2] C. Colldelram, A. Crisol, A. Carballado *et al.*, "All Applications of the ALBA Skin Concept", presented at MEDSI'20, Chicago, USA, Jul. 2021, paper WEPA14, this conference.
- [3] J. Nicolas *et al.*, "Completeness condition for unambiguous profile reconstruction by sub-aperture stitching", *Opt. Express*, vol. 26, no. 21, pp. 27212-27220, 2018. <https://doi.org/10.1364/OE.26.027212>
- [4] L. Huang *et al.*, "Two-dimensional stitching interferometry for self-calibration of high-order additive systematic errors", *Opt. Express*, vol. 27, no 19, pp. 26940-26956, 2019. <https://doi.org/10.1364/OE.27.026940>

INVESTIGATING OF EBW PROCESS WELDMENT CONNECTIONS STRESSES IN ILSF 100 MHz CAVITY BY Simufact.Welding SOFTWARE*

V. Moradi[†], Department of Mechanical Engineering, ILSF, Tehran, Iran

A. Adamian, N. B. Arab, Dept. of Mechanical Engineering, Tehran Central Azad Univ., Tehran, Iran

Abstract

The cavity is one of the main components of all accelerators, which is used to increase the energy level of charged particles (electrons, protons, etc.). The cavities increase the energy level of the charged particle by providing a suitable electric field to accelerate the charged particle. Here, information about electron beam welding analysis in 100 MHz cavities of ILSF design will be explained. According to studies performed in most accelerators in the world, connections in cavities are made by various methods such as explosive welding, brazing, electron beam welding, etc. Many articles on large cavities state that the connection of the side doors must be done by the electron beam welding process. However, in the present paper, the three-dimensional model of the cavity is imported into Simufact.Welding software after simplification and mesh process was done, then the heat source of electron beam welding and other welding factors such as beam power, Gaussian distribution, etc. are applied in the software. The purpose of this study is the number of residual stresses during the EBW process in the 100 MHz cavity of ILSF.

INTRODUCTION

Since the early 1970s, finite element modelling has been used to simulate mechanical problems in welding. Some popular sources up to the 1990s are the works of Ueda and Yamakawa [1], Goldak [2] and Radaj [3]. Finite element codes have been described to address these issues among numerous articles such as Dexter [4] and Karlsson [5]. In most finite element models, it is common to assume a number of simplifications. The reason for this simplification is the high computational cost of 3D models (which, of course, is not always approved). However, Duranton et al. [6] showed that when the heat flux in the welding direction is ignored, shortcomings in the two-dimensional method in longitudinal welding will occur.

According to the mechanical explanations of the problem, in some articles such as Song et al. [7] and several other articles, it is assumed that the material acts as a viscous elastoplasty pattern, and in others such as Branza et al. [8], Duranton et al. [6] The assumption of hard isotropic materials, or in other articles such as Nandan et al. [9], has considered the material as an elasto-viscoplastic material. Alberg and Berglund [10] compare the plastic and viscoelastic models used to simulate welding and recommend that a simple plastic model be used in the early stages of the study. However, the viscosity effects of materials at high temperatures cannot be ignored, as they have a

significant effect on the behaviour of metals. Also, welding generally involves cooling cycles whose effect on the mechanical behaviour of the material will only be considered if the material is in a state of kinematic hardening. Therefore, the justification for using simpler models such as plastic elastic, without considering the hardening of the material or just the isotropic hardening (which has been the most widely used to date) is only to reduce computational costs. In this paper, the analysis of welding joint calculations in ILSF 100 MHz cavity will be investigated. According to studies performed in most accelerators in the world, the welding connections of the cavities have been done by electron beam. Therefore, in the forthcoming research, the three-dimensional cavity model after simplification and meshing was entered into Simufact.Welding software and then the heat source of electron beam welding and other welding factors such as beam power, Gaussian distribution amount, and etc. Finally, in the software, the simulation of the beam welding process will be done. The purpose of this study is to determine the number of residual stresses in the cavity after the EBW process.

NUMERICAL MODEL OF HEAT SOURCE

The heat source model in the EBW process is combined in such a way that the thermal effect of the key hole in the penetration depth is modelled with a three-dimensional conical heat source and also the molten metal vapor at the weld surface which has its own local thermodynamic equations of the surface heat source. Used by a Gaussian heat source model to simulate the effect of surface heat.

The formula for the distribution of Gaussian heat source is as follows [11]:

$$q_s(x, y) = \frac{3Q_s}{\pi R^2} \times \exp\left[-\frac{3(x^2+y^2)}{R^2}\right] \quad (1)$$

Where, (q_s) is the heat flux in the Cartesian coordinates, (Q_s) is the Gaussian heat source power, and (R) is the effective radius of the electron beam. Of course, assuming that (r) is the distance of each point from the heat source to its center, the relation $x^2 + y^2 = r^2$ holds. Also, by moving the welding heat source, the inlet heat flux changes in different positions along the direction of the welding speed. The relationship between moving coordinates and static coordinates is defined as follows:

$$u = y + v(\tau - t) \quad (2)$$

Where, (t) is the welding time, (v) the welding speed and (τ) the time delay factor. After converting the static coordinates to motion coordinates in Eq. (1) we will have:

$$q_s(x, y) = \frac{3Q_s}{\pi R^2} \times \exp\left[-\frac{3(x^2 + y + v(\tau - t)^2)}{R^2}\right] \quad (3)$$

* Work supported by Iranian Light Source Facility (ILSF)

[†] v.moradi1985@gmail.com

Content from this work may be used under the terms of the CC BY 3.0 licence (© 2021). Any distribution of this work must maintain attribution to the author(s), title of the work, publisher, and DOI

Where, the relation $x^2 + u^2 = r^2$ is assumed. And the distribution of heat flux from the conical heat source in the kinetic coordinates is as follows:

$$q_v(x, y, z) = \frac{9Q_v}{\pi h v_0^2} \times \exp \left[-\frac{h^2}{(h-z)^2} \cdot \frac{3(x^2 + y + v(\tau-t)^2)}{r_0^2} \right] \quad (4)$$

Where, $q_v(x, y, z)$ is the heat flux within the welding heat source range effective in Cartesian coordinates. (Q_v) The power of the conical heat source and (h) the depth of the electron beam heat source is effective and (z) vary from "0" to "h". The total power of the two welding heat sources (q_s) and (q_v) is equal to the effective input power during the welding process, i.e.:

$$Q_s + Q_v = Q \quad (5)$$

Where, (Q) is the effective input power which can be expressed as:

$$Q = C U_a I_b \quad (6)$$

Where, (C) is the effective power factor for the electron beam heat source, (U_a) is the accelerator voltage and (I_b) is the beam current.

If the energy distribution coefficient of the Gaussian surface source is the effective input power (γ_s) and the ratio of the power distribution of the conical heat source to the effective input power (γ_v) and the relation $\gamma_s + \gamma_v = 1$ is established, then we have:

$$Q_s = \gamma_s Q \quad (7)$$

$$Q_v = \gamma_v Q \quad (8)$$

RESULTS

There is the ability to create tracking points in the Simufact.Welding software. Figure 1 (left) shows these points in two paths, 1 and 2, both on the side door. Path 1 passes where the welding line have overlap, but Path 2 is not.

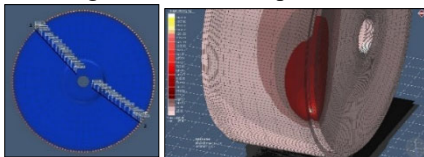


Figure 1: Trace points created on the side door of the cavity (left) Perform the electron beam welding process of the cavity (right).

A view of the cavity electron beam welding process is shown in Fig. 1 (right). In this figure, it is possible to see the key hole effect that exists in the heat source sequence. Figure 2 (left) shows the heat distribution in the parts per 604 seconds of the welding process. According to it, it can be seen that during welding, the areas close to the welding site are heated to about 650 degrees and a little further away to about 400 degrees Celsius. But other parts of the body and side door will be between 100 and 200 degrees Celsius. Figure 2 (right) shows well the HAZ area in this welding process. Due to the expected high penetration depth (18 mm) as well as the high percentage of volumetric heat fraction, the thickness of the HAZ area seems a little bit high.

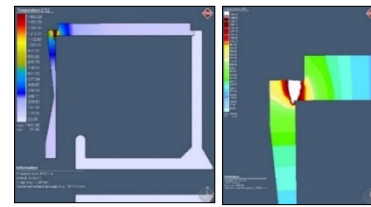


Figure 2: Thermal distribution in parts (left) of heat affected zone (HAZ) in copper cavity analysis (right).

Figure 3 (left) shows the total displacement value at the tracking all points of Route 2. The largest amount of displacement occurred at point 36, as shown in the figure (right), which is about 3.2 mm. This is due to the thinning on the side door to perform the cavity tuning process.

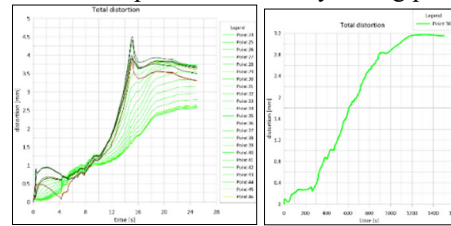


Figure 3: Total deformation value at tracking all points of Route 2 (left) Total deformation value at tracking point 36 from track 2 (right).

In Fig. 4 (left) it can be seen that in 418th seconds of calculations, the heat source passes through the outer edge (point 25) and at this time the stress at the outer edge is zero. Before the heat source reaches this point, the stress is positive (compressive) and then negative (tensile). The outer edge will experience the most negative stress at 473th seconds (55 seconds after the heat source passes through this point), which is about 42 MPa. The stress will then move in the positive direction until the maximum amount of stress is generated at this point, which is equal to about 18 MPa at this point. After that, the tension will decrease but will remain positive. Therefore, the maximum amount of stress remaining at the outer edge at the point where the heat source has passed once will be about 10 MPa. According to Fig. 4, in path 2 and at points that are far from the path of the heat source, about 20 MPa of negative stress will remain.

On other hand, we can compare the outer edges of path 1 and path 2. In Fig. 4 (right) difference between the stress of the outer edge of path 1 (point 04) and the outer edge of path 2 (point 27) is shown, and the point is the amount of residual stress of two edges are too close together.

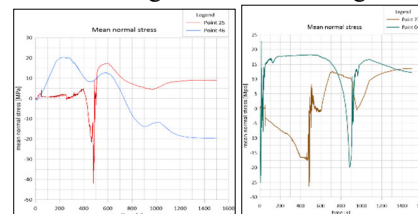


Figure 4: Stress changes in the tracking points of the outer edge (25) and inner edge (46) of the side door of the cavity in path 2 (left) Stress changes in the tracking points of outer edges of path 1 and path 2 (right).

But the most critical point in terms of residual stresses in route 2 is the thinning point on the side door. In Fig. 5 (right) the amount of residual stress at this point can be found, which is equal to 27 MPa. Also, the amount of deformation of this point in the Y direction (the direction of movement of the beam through the cavity) will be equal to -2.3 mm. According to Fig. 5 (left) and comparing the tracking points of Route 1 (where the heat source has twice affected the outer edge areas of this route) with Route 2, it can be seen that the most critical point in terms of residual stress in the whole outer edge of the door The side is on path 1. However, the greatest amount of total deformation in path 1 also belongs to the thinning part of the side door and its value will be equal to 3.7 mm, the share of this value in the Y direction is about -2.8 mm.

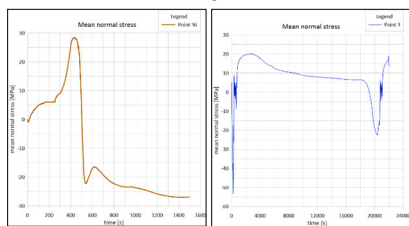


Figure 5: Stress changes in the tracking at point 36 - Side door thinning part - from path 2 (right) The maximum amount of stress remaining in path 1 (left).

VALIDATION OF CALCULATION

In order to improve the production process of a product, some reputable companies in the world raise the existing problems in the form of student and research projects, either within the company itself or in prestigious universities around the world. An example of this is an article by Michael Chiumenti et al. [12] at the Polytechnic University of Catalonia for Airbus.

In this paper, entitled “Numerical analysis of electron beam welding and its practical validation” presented in the journal Finite Elements in Analysis and Design in 2016, a simple model is considered to numerical calculations and practical validation. The numerical calculations were done by COMET code. The dimensions of this model are $290 \times 52 \times 10.5$ mm. To ensure the calculation, this model has been tested in two situations. The difference between the first case and the second case is the location of the thermal sensors during the welding process, as well as the location of the parts by the clamp. Figure 6 shows the studied states. The material intended for calculations is titanium alloy Ti6Al4V.

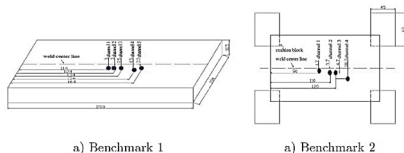


Figure 6: Location of thermocouples in position 1 and 2.

Table 1 shows the parameters of the EBW process for welding sample parts. This process is very expensive, so to reduce costs, the EBW of these samples has been done in China “BAMTRI” research laboratory.

Table 1: Electron Beam Welding Parameters of Both Case

Voltage 150 [kV]
Current Intensity 100 [mA]
Speed 25 [mm/s]
Spot Size 1 [mm]
Penetration 10 [mm]

Figure 7 shows a comparison of temperature changes at four similar points from Benchmark 2 analysis in Simufact.welding and COMET software. As can be seen, the consistency of the performed analyses can be seen well. On the other hand, by comparing the HAZ region in the two analyses in Fig. 8, we will find that the calculations performed for welding 100 MHz ILSF cavity with Simufact.Welding software are reliable.

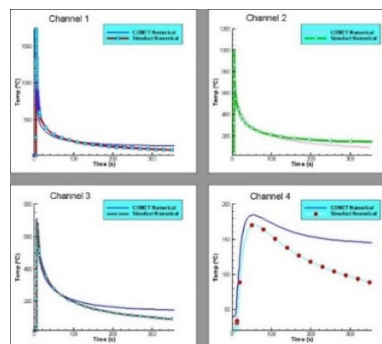


Figure 7: Comparison of temperature changes at four different points of the Benchmark 2 model. Comparison of numerical computing temperatures with COMET software and Simufact.Welding software.

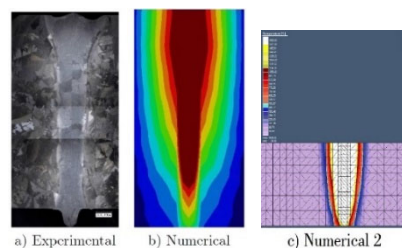


Figure 8: Comparison of HAZ region in empirical evidence (a) and numerical analysis in COMET (b) and numerical analysis in Simufact.welding (c).

CONCLUSION

According to the obtained results and validation, it can be concluded that the boundary conditions defined in the software are correct and appropriate. The amount of heat generated in the weld seam is slightly high, so we can increase the speed of the heat source or reduce the inlet power. In the analysis, the amount of residual stress in the parts is not so high, therefore, there is not a serious need for stress release operation after the EBW process in the 100 MHz ILSF cavity. The amount of deformation in the side doors and especially in the thinning part in this analysis is very high and the side door must be machined to the thin part of it, after the welding process. It is suggested that different methods of mounting to improve the amount of deformation is considered in the next analysis in the future.

REFERENCES

- [1] Y. Ueda and T. Yamakawa, “Analysis of thermal elastic–plastic stress and strain during welding by finite element method”, *Transactions of the Japan Welding Society Transactions*, vol. 2, pp. 186–196, 1971.
- [2] J Goldak *et al.*, “Coupling Heat Transfer, Microstructure Evolution and Thermal Stress Analysis in Weld Mechanics”, in *Mechanical Effects of Welding*, L Karlsson, L-E Lindgren, M, Jonsson, Eds., Berlin, Heidelberg: Springer, 1992, pp. 1–30.
- [3] R. Radaj, “Finite element analysis of welding residual stresses”, in *2nd International Conference on Residual Stresses*, Springer, Dordrecht, 1989, pp. 510–516. doi:10.1007/978-94-009-1143-7_85
- [4] R. Dexter *et al.*, “Residual Stress Analysis in Reactor Pressure Vessel Attachments – Review of Available Software”, Southwest Research Institute, San Antonio, TX, Rep. NP-7469, Sep.1991.
- [5] L. Karlsson, “Modeling in Welding, Hot Powder Forming, and Casting”, ASM International, Ohio, Rep. 0871706164, Dec. 1997.
- [6] P. Duranton *et al.*, “3D modeling of multipass welding of a 316L stainless steel pipe”, *Journal of Materials Processing*, vol. 153–154, pp. 457–463, Nov. 2004. doi:10.1016/j.jmatprotec.2004.04.128
- [7] J. Song *et al.*, “Sensitivity analysis of the thermomechanical response of welded joints”, *Int. J. Solids Struct.*, vol. 40, pp. 4167–4180, Aug. 2003. [https://doi.org/10.1016/S0020-7683\(03\)00223-3](https://doi.org/10.1016/S0020-7683(03)00223-3)
- [8] T. Branza *et al.*, “Experimental and numerical investigation of the weld repair of superplastic forming dies”, *J. Mater. Process. Technol.*, vol. 155–156, p. 1673–1680, Nov. 2004. doi:10.1016/j.jmatprotec.2004.04.388
- [9] R. Nandan *et al.*, “Numerical modelling of 3D plastic flow and heat transfer during friction stir welding of stainless steel”, *Sci. Technol. Weld. Joining*, vol. 11, p. 526–537, Dec. 2006. doi:10.1179/174329306X107692
- [10] H. Alberg and D. Berglund, “Comparison of plastic, viscoplastic, and creep models when modelling welding and stress relief heat treatment”, *Comput. Methods Appl. Mech. Eng.*, vol. 192, pp. 5189–5208, Sep. 2003. doi:10.1016/J.CMA.2003.07.010
- [11] Y. Luo *et al.*, “Simulation on welding thermal effect of AZ61 magnesium alloy based on three-dimensional modeling of vacuum electron beam welding heat source”, *Vacuum*, vol. 84 p. 890–895, Mar. 2010. doi:10.1016/j.vacuum.2009.12.005
- [12] M. Chiumenti *et al.*, “Numerical modeling of the electron beam welding and its experimental validation”, *Finite Elem. Anal. Des.*, vol. 121, pp. 118–133, Nov. 2016. doi:10.1016/j.finel.2016.07.003

A NEW THREE-SIGNAL 2D-BEAM-POSITION-MONITOR BASED ON A SEGMENTED IONIZATION CHAMBER

M. Goerlitz*, W. A. Caliebe, DESY, Hamburg, Germany

Abstract

At DESY in 2020 a three-signal beam position monitor (BPM) was constructed, which is based on a Ionization Chamber design with split up electrodes. It is using three signals to determinate horizontal and vertical positions of a x-ray beam. The relation between signals and position can be described by a multiple linear regression (MLR). The calibration is done by linear optimization algorithms, which are described in detail, especially to give an engineering-based resume, which can easily applied to other systems. The results of the solution will be compared and discussed.

INTRODUCTION AND MOTIVATION

Due to the facts that synchrotron x-ray beam sizes are getting smaller and more experiments demand a focussed beam, the necessity of a controlled stable beam increases. Some demands of monitoring devices are, that they should not absorb significantly x-ray intensity, do not lead to bragg peaks on x-ray cameras, nor have a large signal to noise ratio. Most available transmissive BPMs are based on: (1) deposited segmented diamond windows [1,2] with measurement ranges in the μm -region and fast acquisition times. (2) two 90°-turned ionization chambers with split up electrodes [3,4], wherefore the measuring range is in the mm-range. They have in common that they need four raw signals to calculate a 2D-position xy -location. A conventional ionization chamber at a synchrotron beamline consists of two plates, which are arranged parallel to each other and give one signal. They have the advantage to measure at low as well as high energies, whereas the absorption can be adjusted by using heavier gas like Krypton for higher energies or Nitrogen for lower energies [5].

The new evaluated design of a beam position ionization chamber is based on three signals.

MATERIAL AND METHODS

Design and FEM

Figure 1 shows the design of the electrodes: two small electrodes on the front and back, which are connected to the same signal wire; two bigger measuring electrodes, which are each connected to a single signal wire; one large high voltage electrode. The highest density of the electric field is reached in between the parallel 6 mm gap (see Fig. 1b).

Signal Evaluation

The three raw signals can be used to calculate the xy -coordinates. The transformation (Eq. 1) can be written within a matrix quite similar to the Clarke-transformation [6],

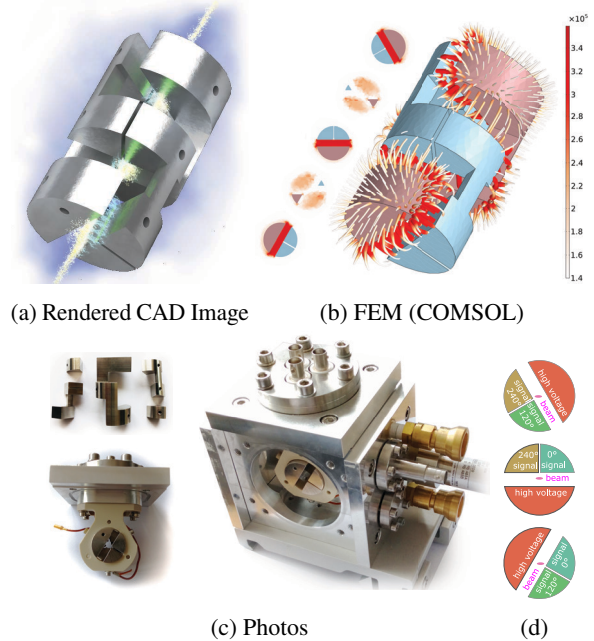


Figure 1: (a) expected location of gas-ions (*light-yellow*), trajectory of free electrons (*lightblue*) (b) electrostatic: measuring electrodes (blue), HV electrode (red), tube-thickness and color: electric field strength [V m^{-1}] (d) signal and HV connections.

which is well-known in electromechanical theory. The values of u, v and w are normalized, taking into account the sum of all intensities. The values c_i are fixed calibration parameters. They can be obtained by linear optimization using measured data.

$$\begin{bmatrix} x \\ y \end{bmatrix} = \begin{bmatrix} c_{x0} & c_{x1} & c_{x2} & c_{x3} \\ c_{y0} & c_{y1} & c_{y2} & c_{y3} \end{bmatrix} \cdot \begin{bmatrix} 1 \\ u \\ v \\ w \end{bmatrix} \quad (1a)$$

$$u = \frac{I_A}{I_A + I_B + I_C} \quad v = \frac{I_B}{I_A + I_B + I_C} \quad w = \frac{I_C}{I_A + I_B + I_C} \quad (1b)$$

Signal-Position Calibration

For the calibration several tuples $\langle u_i, v_i, w_i, x_i, y_i, p_i \rangle$ are needed. They have to include the three measure signal values and the corresponding true real x and y positions. Weighting or proportional factors $p_i(x, y)$ assure that some regions will be taken more into account than others. For both algorithms five or more linear independent point assignments are needed. More values will improve the precision of calibration.

Calibration Method I: Simplex-algorithm including weighted residuals To calculate the different coefficients c_* , a Simplex-algorithm was applied. All examples are shown for the y -axis. x -coordinate will be calculated similar to the procedure shown in that chapter. The expression x in

* marcel.goerlitz@desy.de

this part corresponds to a vector containing the calibration-coefficients. Calculation can be done by available programs like *Matlab*, where the minimization problem is described as in Eq. (2) [7].

$$\min_x (f^T \cdot x) \quad \left\{ \begin{array}{l} \mathbf{x} \mid \mathbf{A}_{con} \cdot \mathbf{x} \leq \mathbf{b}_{con} \\ \mathbf{A}_{eq} \cdot \mathbf{x} = \mathbf{b}_{eq} \end{array} \right\} \quad (2)$$

Note: Column-vectors: bold lowercase letters; matrices: bold capital letters

In order to use the linear optimization the corresponding fixed matrices \mathbf{A}_{con} , \mathbf{b}_{con} , \mathbf{A}_{eq} and \mathbf{b}_{eq} have to be expressed in the right way, as it is shown in the following. First of all, new variables will be introduced in Eq. (3).

$$\mathbf{T} = \begin{bmatrix} 1 & u_1 & v_1 & w_1 \\ 1 & u_2 & v_2 & w_2 \\ \vdots & \vdots & \vdots & \vdots \\ 1 & u_k & v_k & w_k \end{bmatrix} \quad \mathbf{y}_{pos} = \begin{bmatrix} y_{pos0} \\ y_{pos1} \\ \vdots \\ y_{posk} \end{bmatrix} \quad \mathbf{c} = \begin{bmatrix} c_{y0} \\ c_{y1} \\ c_{y2} \\ c_{y3} \end{bmatrix} \quad \mathbf{p} = \begin{bmatrix} p_1 \\ p_2 \\ \vdots \\ p_k \end{bmatrix} \quad (3)$$

The vector \mathbf{y}_{pos} contains the expected y-Positions. The vector \mathbf{p} comprises weight factors for each residuum Δy_i . The calibration coefficients in the vector \mathbf{c} are unknown and have to be calculated. The standard problem would be solved like in Eq. (4a). Due to the fact that the right inner part can contain positive as well as negative errors the problem has to be extended by a trick: $\Delta \mathbf{y}$ will be replaced by a difference expression, in Eq. (4b), such that errors reached from positive and negative sites are taken into consideration. The constraint in Eq. (4a) implicates that the offset c_0 is taken into account, in a way that the optimum will be found where signal values u , v and w have almost the same value.

$$\Delta \mathbf{y} = |\mathbf{T} \cdot \mathbf{c} - \mathbf{y}| \quad \text{with } \Delta \mathbf{y} > 0 \quad (4a)$$

$$(\Delta \mathbf{y}_+ - \Delta \mathbf{y}_-) = \mathbf{T} \cdot \mathbf{c} - \mathbf{y}_{pos} \quad (4b)$$

$$\Leftrightarrow \mathbf{y}_{pos} = \mathbf{T} \mathbf{c} - \Delta \mathbf{y}_+ + \Delta \mathbf{y}_- \quad (4c)$$

$$\mathbf{b}_{eq} = \mathbf{A}_{eq} \mathbf{x} \quad (4d)$$

$$\text{Further constraints (con):} \quad \Delta \mathbf{y}_+, \Delta \mathbf{y}_- \geq 0 \quad (4e)$$

$$c_0 = c_1 + c_2 + c_3 \quad (4f)$$

To express Eq. (4c) in the form of Eq. (4d), the vectors and matrices will be described as in Eq. (5). The constraints-Eq. (4f) is expressed in Eq. (5b). The transposed vector of weight factors \mathbf{p}^T emphasizes the most significant data point errors. To calculate x the simplex algorithm is used and calculated like it is described in Eq. (2).

$$\mathbf{A}_{eq} = \begin{bmatrix} \mathbf{T} & -\mathbf{I} & \mathbf{I} \\ \mathbf{C}_{con} & 0 & 0 \end{bmatrix} \quad \mathbf{b}_{eq} = \begin{bmatrix} \mathbf{y}_{pos} \\ 0 \end{bmatrix} \quad (5a)$$

$$\text{with } \mathbf{C}_{con} = \begin{bmatrix} -1 & 1 & 1 & 1 \end{bmatrix} \quad (5b)$$

$$\mathbf{A}_{con} = \begin{bmatrix} 0 & 0 & 0 \\ 0 & -\mathbf{I} & 0 \\ 0 & 0 & -\mathbf{I} \end{bmatrix} \quad \mathbf{b}_{con} = \begin{bmatrix} 0 \\ 0 \\ 0 \end{bmatrix} \quad \mathbf{x} = \begin{bmatrix} \mathbf{c} \\ \Delta \mathbf{y}_+ \\ \Delta \mathbf{y}_- \end{bmatrix} \quad (5c)$$

$$\mathbf{f}^T = \begin{bmatrix} 0 & \mathbf{p}^T & \mathbf{p}^T \end{bmatrix} \quad (5d)$$

Calibration Method II: the pseudo-inverse including weighted residuals An alternative solution for the calculation is to use a approximative solution with help of a pseudo-inverse. The Moore-Penrose pseudoinverse notation has to be taken into account to solve a non-quadratic matrix, which will result in a problem like it is described in (6d).

The description of the matrix \mathbf{A} and the vector \mathbf{b} is as shown in Eq. (6d). The inner matrices \mathbf{T} , \mathbf{y}_{pos} and \mathbf{c} are described in Eq. (3). The diagonal matrix \mathbf{D} contains the weighting coefficients p_i on the diagonal. The inner product of the hermetic matrix $\mathbf{A}^T \mathbf{A}$ could be calculated manually by Singular Value Decomposition. Software like Matlab calculate the pseudoinverse directly [8]. After the successful calculation of the pseudo-inverse \mathbf{A}^+ , it just has to be multiplied by \mathbf{b} to obtain the vector \mathbf{x} [Eq. (6b)], which contains the sought coefficients.

$$\mathbf{A} \mathbf{x} = \mathbf{b} \quad (6a)$$

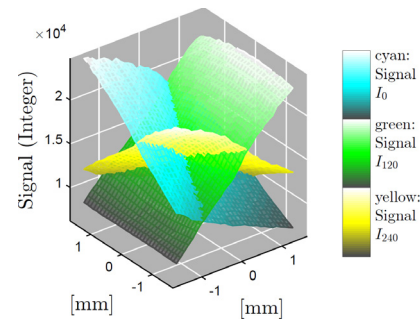
$$\mathbf{x} \approx \mathbf{A}^+ \cdot \mathbf{b} \quad (6b)$$

$$\mathbf{x} \approx (\mathbf{A}^T \mathbf{A})^{-1} \mathbf{A}^T \cdot \mathbf{b} \quad (6c)$$

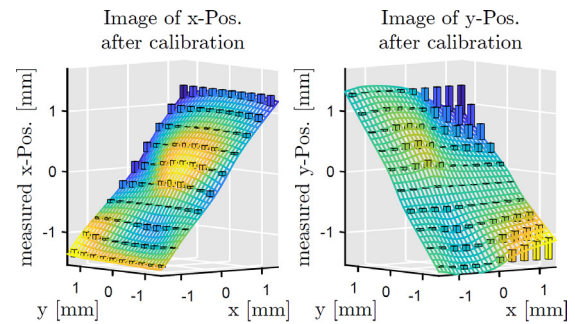
$$\mathbf{A} = \begin{bmatrix} \mathbf{T} & -\mathbf{I} \\ 0 & \mathbf{D} \end{bmatrix} \quad \mathbf{b} = \begin{bmatrix} \mathbf{y}_{pos} \\ 0 \end{bmatrix} \quad \mathbf{x} = \begin{bmatrix} \mathbf{c} \\ \Delta \mathbf{y} \end{bmatrix} \quad (6d)$$

RESULTS

First measurements were taken at the DESY-beamline P64 [9] at 20 keV, the chamber was filled with 100 % Nitrogen at atmospheric pressure. Figure 2a shows the measured raw signals, which were obtained by moving the BPM with xz-linear-stage in front of a stable beam. Calibration coefficients were computed by using a mesh of 31x30 different support



(a) raw signals of the current amplifier:
 xy-beam position \mapsto electrode raw signals



(b) xy-beam position \mapsto measured (calibrated) value
 bar/color: difference to the calibration function

Figure 2: Plots: a N_2 -filled chamber was moved along x and y in front of a $0.5 \times 0.5 \text{ mm}^2$ small 20 keV x-ray beam, 31x30 points were taken.

Table 1: Calibration Coefficients of Different Beam Sizes - 31x30 datapoints have been used, beamsize was defined by slits alignment. Beamsize before slits was approximately 0.7 mmx1.5 mm

Coefficients	Beamsize [mm]											
	0.5 x 0.5		0.5 x 1.0		0.5 x 1.5		0.5 x 2.0		1.0 x 2.0		1.0 x 0.5	
	Method I	Method II	Method I	Method II	Method I	Method II	Method I	Method II	Method I	Method II	Method I	Method II
c_{x0}	-0.18	-0.19	-0.16	-0.17	-0.17	-0.18	-0.17	-0.18	-0.25	-0.26	-0.27	-0.27
c_{x1}	-2.73	-2.71	-2.75	-2.74	-2.79	-2.78	-2.79	-2.78	-2.82	-2.81	-2.78	-2.77
c_{x2}	5.07	4.97	5.14	5.06	5.19	5.11	5.22	5.15	5.22	5.16	5.10	5.01
c_{x3}	-2.52	-2.45	-2.55	-2.49	-2.58	-2.52	-2.60	-2.55	-2.65	-2.60	-2.58	-2.51
c_{y0}	-0.17	-0.18	-0.17	-0.18	-0.18	-0.18	-0.15	-0.16	-0.15	-0.15	-0.17	-0.17
c_{y1}	-5.89	-5.96	-5.96	-6.04	-5.99	-6.10	-6.00	-6.14	-6.05	-6.19	-5.92	-6.01
c_{y2}	-0.09	-0.07	-0.11	-0.08	-0.11	-0.07	-0.11	-0.10	-0.11	-0.10	-0.09	-0.07
c_{y3}	5.81	5.85	5.89	5.94	5.92	5.99	5.96	6.08	6.00	6.14	5.84	5.90

points, and a 2d-Gauss weighting. They are shown in Table 1 for different slits openings. One can see that the ratio of coefficients stay almost constant even with different beam sizes. Nevertheless there is a small upscaling, as when the beam-size gets larger. Values show a strictly monotonic behaviour in both directions. For this reason the chamber can be used for position control in further steps.

DISCUSSION

Using one single high voltage electrode and only three signals instead of four might reduce noise failures, particularly because the measured current of an ionization chamber is in the μA to nA-range. Moreover, the design and distribution of electric stray field might be improved by different gap ratios or by redesigning the electrodes gap with an acute instead of a right angle.

Concerning the calibration: The errors between measurement and calibration function are around 0.15 mm in an area $1 \times 1 \text{ mm}^2$ and 0.40 mm in an area of $3 \times 3 \text{ mm}^2$. Improvements can be reached by a higher-order polynomial regression. In addition, there exist other methods, like least-square-optimization or gradient-based optimization. However, the shown methods do not require start parameters and is well suited for small problems. On the contrary data points have to be injective [10] and the problem has to be linear.

CONCLUSION

A new concept of a beam position monitor using three signals to determine a 2d-position has been presented. After the calibration, position data shows a linear behaviour. The basic idea opens possibilities for new types of beam position monitors. The chamber can find application at beamlines, where BPM diffraction peaks have to be avoided or absorption behaviour need to be changed easily.

The calibration was validated by the comparison of two different methods, which lead to similar results. These methods have been explained in detail to give a comprehensive overview. They can be applied to other unknown linear

systems as well, like mechanical multi-sensor-positioning systems, mixed signal measurements etc.

ACKNOWLEDGEMENTS

Special acknowledge goes to the DESY-workshop, the CNC preparation group and to the P64 staff: Akhil Tayal, Vadim Murzin, Maria Naumova, Aleksandr Kalinko.

REFERENCES

- [1] E. Griesmayer, P. Kavrigin, Ch. Weiss, and C. Bloomer, "The Use of Single-crystal CVD Diamond as a Position Sensitive X-ray Detector", in *Proc. 5th Int. Beam Instrum. Conf. (IBIC'16)*, Barcelona, Spain, Sep. 2016, pp. 71–74. doi:10.18429/JACoW-IBIC2016-MOPG14
- [2] M. Marinelli, E. Milani, *et al.*, "X-ray beam monitor made by thin-film CVD single-crystal diamond", *J. Synchrotron Rad.*, vol. 19, pp. 1015–1020, Nov. 2012. doi:10.1107/S0909049512038186
- [3] A.N. Fisenkoa, A.V. Kosova, *et al.*, "Coordinate-sensitive ionization chamber with highspatial resolution", *Nucl. Instrum. Methods A*, vol. 543, no. 1, pp. 361–364, May 2005. doi:10.1016/j.nima.2005.01.256
- [4] K. Sato, "A position-sensitive ionization chamber for XAFS studies at synchrotron sources", *J. Synchr. Radiat.*, vol. 8, pp. 378-80, 2001. doi:10.1107/s0909049500015855
- [5] K. Sato, H. Toyowaka *et al.*, "The Behavior of Ionization Chambers under the Irradiation of High Flux X-Ray Beam", SPring-8, Hyogo, Japan, 1998.
- [6] Edith Clarke, *Circuit Analysis of AC Power Systems. Vol. I*. New York, NY, USA: J. Wiley & sons, 1943.
- [7] <https://www.mathworks.com/help/optim/ug/linear-programming-algorithms.html>
- [8] <https://de.mathworks.com/help/matlab/ref/pinv.html>
- [9] W.A. Caliebe, V. Murzin, A. Kalinko, and M. Görlitz, "High-flux XAFS-beamline P64 at PETRA III", *AIP Conference Proceedings*, vol. 2054, p. 060031, 2019. doi:10.1063/1.5084662
- [10] <https://mathworld.wolfram.com/Injection.html>

DESIGN AND RAY-TRACING OF THE BEATS BEAMLINE OF SESAME*

G. Iori[†], M. Al’Najdawi¹, M. Al Shehab, A. Lausi, SESAME, Allan, Jordan
 I. Cudin, M. Altissimo, Elettra-Sincrotrone Trieste, Basovizza, Trieste, Italy
 T. Kołodziej, NSRC SOLARIS, Jagiellonian University, Krakow, Poland
 P. Van Vaerenbergh, J. Reyes-Herrera, A. Kaprolat, ESRF, Grenoble, France
¹also at MAX IV Laboratory, Lund University, Sweden

Abstract

The European Horizon 2020 project BEAmline for Tomography at SESAME (BEATS) has the objective to design, procure, construct and commission a beamline for hard X-ray full-field tomography at the SESAME synchrotron in Jordan. In this paper we present the raytracing simulations performed to quantify the performance and verify the optical design of the beamline. The specifications of a vertically-deflecting double multilayer monochromator are investigated comparing multilayer mirrors with different meridional slope error. The use of a pinhole in the beamline Front-End (FE) acting as a secondary source with enhanced spatial coherence is discussed for phase-contrast applications. We anticipate that the BEATS beamline will fulfill the needs of a heterogeneous community of users of X-ray tomography at SESAME.

INTRODUCTION

The BEATS beamline will operate an X-ray micro tomography station serving a broad user community. The scientific case of the BEATS beamline is the result of close interactions with the scientific communities of current and potential synchrotron users in the SESAME region. Special emphasis is given to the regional aspect, taking stock of existing research contributions from the region. Four key areas for the scientific case for BEATS in the SESAME landscape are identified:

- Archaeology and Cultural Heritage – This includes the study of archaeological materials such as human, plant or animal remains and artefacts of animal bone, antler and teeth.
- Health, Biology and Food – Research in bone and dentistry; in vitro imaging of the brain vascular and neuronal network and of other organs such as the eye, heart, lung and liver; musculoskeletal and soft tissue imaging; bio mineralisation; entomology; food science.
- Material science and Engineering – Study and development of light and composite materials for construction and transport engineering; energy materials research
- Geology and Environment – Research in soil and rock characterization.

Applications within other domains as well as the possibility to provide services to industrial and private sector users are also envisaged.

* BEATS project has received funding from the EU’s H2020 framework programme for research and innovation under grant agreement n°822535.

[†] gianluca.iori@sesame.org.jo

BEAMLINE DESIGN

The design of the beamline allows for a variety of operation modes and ensures sufficient photon flux density in filtered white beam or monochromatic beam from 8 keV and up to 50 keV. The broad energy range and required high photon flux is achieved by a 3 T wavelength shifter insertion device (ID) installed on one of SESAME’s short straight sections. The beamline can work with either monochromatic or filtered white beam, with minimum energy tunable by absorbers in the FE. The beam size at the sample position and the propagation distance between sample and detector can be varied displacing the rotation and detector stages along the beam path. For measurements requiring high sensitivity and spatial coherence of the beam (e.g., for phase-contrast tomography), the beamline FE slits are partly closed to define a smaller, secondary source with higher spatial coherence.

Layout

The beamline FE comprises photon absorbers and stoppers, a mask defining a useful beamline aperture of 1.8 mrad (h) by 0.36 mrad (v), a CVD diamond window separating the machine and the beamline vacuum, filters and primary slits. The main optical component is a Double Multilayer Monochromator (DMM) placed outside of the SESAME storage ring tunnel in a dedicated optics hutch. The experimental station is located approximately 45 m from the photon source and comprises secondary slits, a linear fast shutter allowing to reduce exposure of delicate samples [1], a high precision sample positioning and rotation stage, and two full-field detectors based on scintillating screens and sCMOS sensor cameras mounted on a common granite stage [2].

Raytracing

The BEATS optical design is verified with simulation tools included in the OASYS suite [3]. Raytracing calculations are performed in ShadowOui, while power profiles are computed using XOPPY. Software and notebooks for the reproduction of this work are available on Zenodo [4].

Heat Load

The beam power density is calculated for each beamline component sustaining the white beam during operation or possibly in direct sight of the white beam with the OASYS Wiggler Radiation widget [5]. The power density profile of the incoming or absorbed beam is used as input for thermal verification with commercial Finite-Element software. Due to the position of absorbers and apertures in the storage ring

and beamline FE, a portion of dipole emission can enter the beamline. Therefore, for the calculation of the power density profiles on the first two beamline apertures (crotch absorber and fixed mask) the contribution from the upstream and downstream bending magnets is considered in addition to the emission of the BEATS wavelength shifter. For simulations in XOPPY, the magnetic field profile of the BEATS ID is modified to include part of the dipole field as shown in Fig. 1. For all components after the fixed mask, only the ID contribution is considered. The heat load expected on the main beamline components is reported in Table 1.

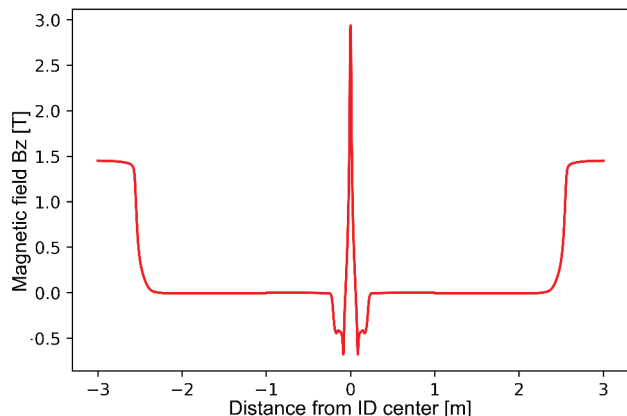


Figure 1: Magnetic field profile modified for simulation in XOPPY considering the BEATS wavelength shifter and the upstream and downstream dipoles.

Table 1: Maximum Power and Power Density on Beamline Components Illuminated by the White Beam

Component	Position [m]	P [W]	P density [W/mm ²]
ID	0.0	857	
Absorber	4.1	4300	20.4
Fixed mask	5.9	271	9.7
Photon shutter	7.6	134	5.2
Window 1	9.0	134	3.7
Filters	11.0	94	1.9
DMM M1	15.1	94	1.0
Combined stopper	94.0	271	0.6
Window 2	37.9	94	0.2

Double Multilayer Monochromator Design

A double-bounce, vertically-deflecting DMM is modelled as a series of two Shadow *Plane Mirror* widgets. The surface and reflectivity of each multilayer is modelled with the Shadow *PreMLayer* PreProcessor. Discrete multilayer surface errors are simulated by external splines with slope error along the beam axis varying between 0.1 and 0.5 μrad (RMS). Modified surfaces are generated with the Shadow PreProcessor - *Height Profile Simulator* widget. The slope error perpendicular to the beam axis is kept constant at 20

μrad RMS, and fractal profiles are chosen (Fig. 2). Plots of the positions of both multilayer mirrors at different working energies are generated for varying bilayer composition and d-spacing. DMM configurations with independent pitch cradles or a common, pseudo-channel-cut layout are investigated.

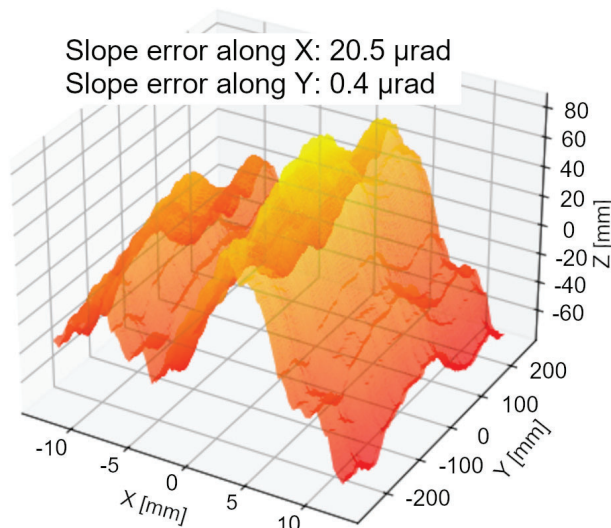


Figure 2: Example of modified multilayer surface: the Y-axis corresponds to the beam path and the X-axis is perpendicular to the beam.

Secondary Source and Coherence Length

Owing to the electron optics of the SESAME storage ring, the BEATS ID generates an X-ray source almost 2 mm in width. Consequently, the beam spatial coherence is limited. To allow for propagation-based phase contrast tomography requiring a certain degree of spatial coherence, the FE slits can be closed to generate a horizontal aperture acting as a smaller and coherent secondary photon source. A comparison of the transverse coherence length at 20 keV with that of other tomography beamlines is shown in Table 2. The transverse coherence length is calculated as:

$$l_{coherence} = \frac{2\lambda d}{\sigma_x} \quad (1)$$

where d is the distance between source and sample, λ is the wavelength (0.62 Å) and σ_x is the FWHM horizontal photon source size [6].

The reduced beam size available with FE slits closed can be calculated as $2\eta_x d$ where η_x is the effective beam half-divergence behind an aperture of size a :

$$\eta_x = \frac{\sqrt{(\frac{\sigma_x}{2})^2 + (\frac{a}{2})^2}}{d} \quad (2)$$

The effect of closing the FE slits on both the available white beam size and flux for experiments is investigated through raytracing simulations.

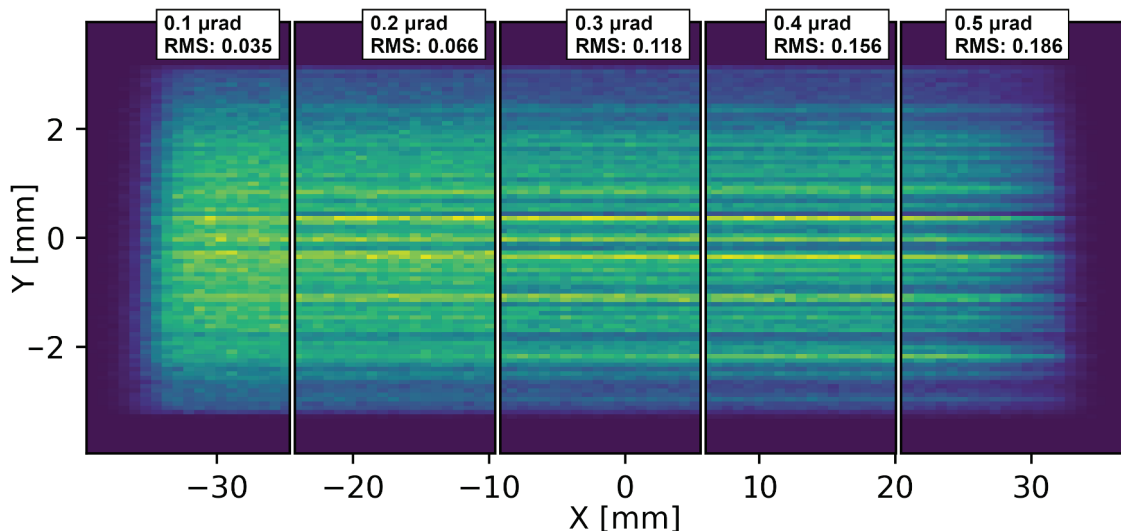


Figure 3: Monochromatic beam flat field snapshots at the sample position (43 m from source) for different multilayer mirrors slope errors. $[W/B_4C]_{100}$ bilayers with a d-spacing of 3.0 nm coated on $500 \times 25 \text{ mm}^2$ mirror surfaces are considered. The grazing angle is optimized for an energy of 45 keV ($\theta = 0.274^\circ$). 16×10^6 rays are used for Monte Carlo simulations.

Table 2: Transverse Coherence Length at 20 keV; Comparison of BEATS with other Beamlines

Beamline	d [m]	σ_x [μm]	$l_{\text{coherence}}$ [μm]
ID19@ESRF	145.0	25	720.0
TOMCAT@SLS	34.0	140	30.2
SYRMEP@Elettra	23.0	197	14.5
BEATS	43.0	1978	2.7
BEATS - Slits @ 0.5 mm	34.6	500	8.6

RESULTS

The expected white beam flux delivered through a square millimeter at the sample position is as high as $1 \times 10^{10} \text{ Ph/s/mm}^2$ in 0.1 % of the source bandwidth, for a maximum usable beam size of $72 \times 15 \text{ mm}^2$. With both multilayers, the expected energy resolution of the monochromatic beam is 3 %, for a total monochromatic photon flux at 20 keV of $3 \times 10^{11} \text{ Ph/s/mm}^2$ through one square millimeter at the sample. Simulated monochromatic beam profiles at the sample are shown in Fig. 3 after double reflection by two multilayers with varying mirror surface slope error. The quality of the flat field deteriorates for mirror slope errors $> 0.2 \mu\text{rad}$. When the FE slits are closed to produce a secondary photon source, the beam size is also reduced, limiting the horizontal field of view for phase contrast imaging to 10 mm or less (Fig. 4). The reduction in photon flux density at the sample position when the FE slits are closed to 500 μm is estimated to be of the order of 70 %.

ACKNOWLEDGEMENTS

We thank C. Morawe and R. Barrett of the ESRF X-ray optics group for the support on multilayer design.

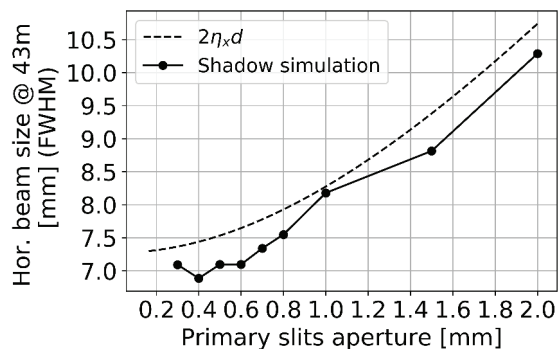


Figure 4: Horizontal beam size at the sample position when the FE slits aperture is reduced.

REFERENCES

- [1] C. Muñoz Pequeño *et al.*, “Development of a Linear Fast Shutter for BM05 at ESRF and BEATS at SESAME”, presented at MEDSI’20, Chicago, IL, USA, July 2021, paper WEOB03, this conference.
- [2] F. Mokoena *et al.*, “An FEA Investigation of the Vibration Response of the BEATS Detector Stage”, presented at MEDSI’20, Chicago, IL, USA, July 2021, paper WEPB09, this conference.
- [3] L. Rebuffi and M. S. del Rio, “OASYS: an open-source graphical environment for x-ray virtual experiments”, in *Proc. SPIE 10388*, Aug. 2017, pp. 103880S, doi:10.1117/12.2274263.
- [4] BEATS TDR - raytracing, doi:10.5281/zenodo.3988604.
- [5] J. Reyes Herrera *et al.*, “A Fast Simulation Tool to Calculate Spectral Power Density Emitted by Wigglers and Short Insertion Devices”, presented at MEDSI’20, Chicago, IL, USA, July 2021, paper WEPB17, this conference.
- [6] A. Pogany *et al.*, “Contrast and resolution in imaging with a microfocus x-ray source”, *Rev. Sci. Instrum.*, vol. 68, no. 7, pp. 2774–2782, Jul. 1997. doi:10.1063/1.1148194

DESIGN OF MONOCHROMATIC AND WHITE BEAM FLUORESCENCE SCREEN MONITORS FOR XAIRA BEAMLINE AT THE ALBA SYNCHROTRON

J.M. Álvarez[†], C. Colldelram, N. González, J. Juanhuix, J. Nicolas, I. Šics
ALBA Synchrotron Light Source, Cerdanyola del Vallès, Spain

Abstract

XAIRA, the hard X-ray microfocus beamline at ALBA, includes three monochromatic fluorescence screens and one water cooled white beam monitor in its layout, mounting respectively YAG:Ce and polycrystalline CVD diamond as scintillator screens. All monitors share the same design scheme, with a re-entrant viewport for the visualization system that allows reducing the working distance, as required for high magnification imaging. The scintillator screen assembly is held by the same CF63 flange, making the whole system very compact and stable. The re-entrant flange is driven by a stepper motor actuated linear stage that positions or retracts the screen with respect to the beam path.

To cope with high power density (18,6 W/m²) on the white beam monitor 100 μm-thick diamond screen, an InGa-based cooling system has been developed. The general design of the new fluorescence screens, to be used also in other ALBA's upcoming beamlines, with particular detail on the water-cooled white beam monitor, is described here.

INTRODUCTION

This paper reviews the design of the Fluorescence Screen Monitors (FSM) of XAIRA, the microfocus Macromolecular Crystallography (MX) beamline at ALBA. Two types of FSM have been developed: the water-cooled White Beam Fluorescence Screen (FSWB) and the Monochromatic Fluorescence Screen Monitor (FSM1 and FSM2), which mount respectively as scintillator screen polycrystalline CVD and YAG:Ce.

Due to the high heat flux deposition (18,6 W/m²) on the FSWB screen, FEM analysis has been performed to optimize the cooling design, adopting InGa contact interface to enhance heat transmission.

The design has been conceived to produce a compact and stable instrument to be used as a standard FSM in future beamlines.

TECHNICAL SPECIFICATIONS

From an optical point of view the design of the FSM must comply with the following specifications:

- Beam envelope in each FSM should represent ~25% field of view (FOV) to allow severe beam misalignment.
- Partial beam transmission through diagnostic device is not required.

- Each beam dimension should be made at least of 100-200 pixels to allow identification of beam shape pathologies.
- Two different configurations of screen-imaging system are proposed for FSWB or FSM1 and FSM2 (Fig. 1).

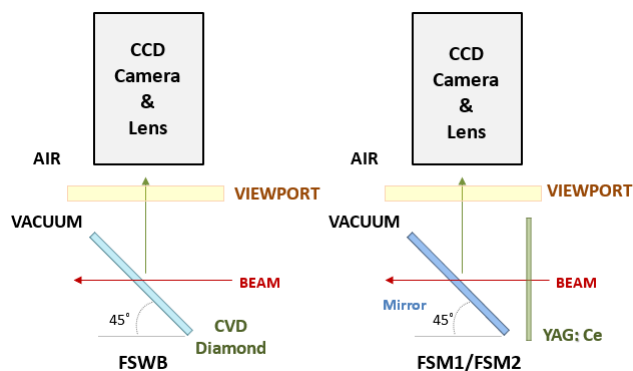


Figure 1: Geometrical configurations of the FSMs.

Both camera-lens system and fluorescence screen support should be mounted on the same moving DN63 CF flange, maximizing compactness and imaging system stability.

SYSTEM DESCRIPTION

General Description

The camera-lens system and the sensible scintillator screen are mounted on a common moving re-entrant flange. This flange is assembled on a DN63 CF welded bellow that is actuated by a linear moving stage consisting on a high precision ball screw, high precision linear guideways and low backlash stepper motor. Finally, the system is controlled with absolute encoder feedback. (Fig. 2).

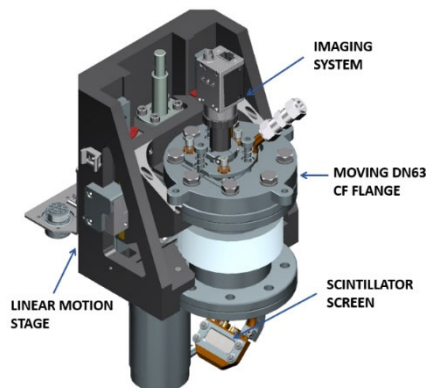


Figure 2: FSWB assembly.

[†] jalvarez@cells.es

Content from this work may be used under the terms of the CC BY 3.0 licence (© 2021). Any distribution of this work must maintain attribution to the author(s), title of the work, publisher, and DOI

Motion Stage

The conceptual design of motion stage is shared among the different monitors, existing only small differences to adapt different ranges and, in the case of FSM1, to comply with the tight geometrical constraints at the beamline. All the standard components (high precision ball screw, recirculating linear guideways, low backlash stepper motors, absolute encoder and limit switches) are common (Fig. 3).

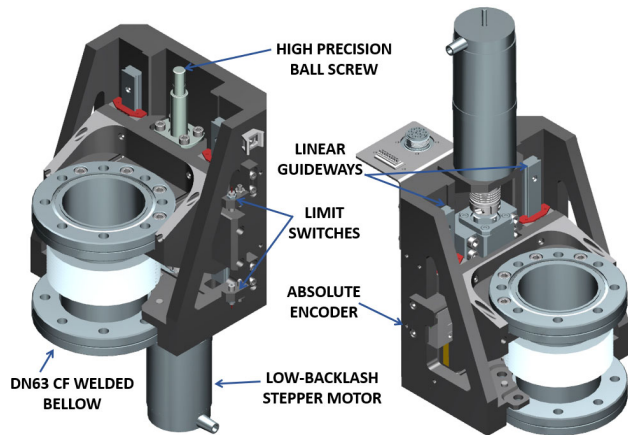


Figure 3: Motion stage assembly. FSM2 and FSM1 arrangement (left), FSM1 arrangement (right).

Scintillator Screen and Imaging System

As previously commented, the optical arrangement of the scintillator screen (direct incidence or mirrored) depends on the X-ray beam monitor type (white or monochromatic) (Fig. 1). Apart from this, all the monitors share the same design scheme, with a re-entrant viewport for the visualization system, which allows reducing the working distance (WD) to the minimum.

The imaging system is equipped with a manual tilt alignment stage that allows correcting small angular deviations between the scintillator screen and lens (Figs. 4 and 5). In addition, the assembly of the imaging system the tilt alignment stage is accurately mounted on the moving flange by means of kinematical mount arrangement.

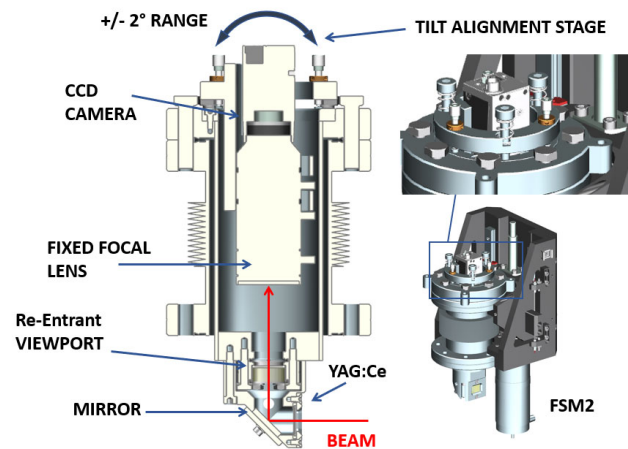


Figure 4: Imaging system and scintillator screen arrangement for monochromatic FSM2.

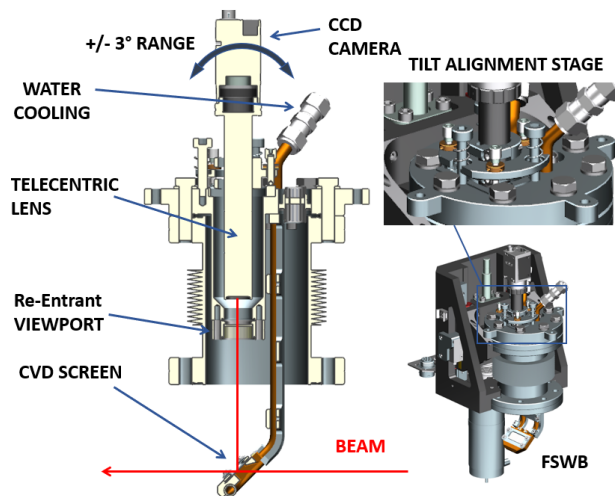


Figure 5: Imaging system and scintillator screen arrangement for monochromatic FSWB.

FSWB Cooling Design

For the FSWB monitor, a water-cooling system has been designed to cope with the power and power density of the pink beam at the exit of the first mirror. With a thin 100 μm thick CVD diamond screen, total absorbed power is 116.8 W while the peak power density is 18.56 W/mm^2 .

The conventional election of Indium foil as thermal interface layer between CVD screen and copper substrate was quickly discarded due to its insufficient thermal performance. Instead, a more efficient InGa cooling system has been developed to manage these demanding heat conditions (Fig. 6).

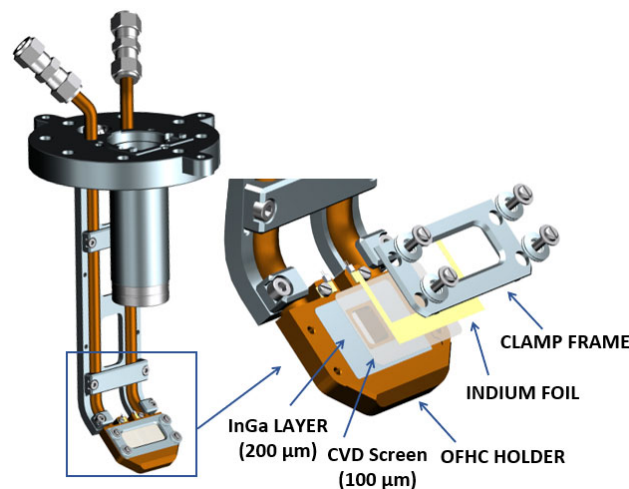


Figure 6: FSWB Cooling Flange and detail of the CVD diamond screen clamping design.

SIMULATIONS

A coupled thermal and mechanical FEA calculation has been conducted with ANSYS Workbench software to assess the temperature distribution and maximum induced stresses and deformations (Figs. 7 and 8). In addition to the more standard simulation assumptions the following criteria has been considered:

- The thermal Contact Conductance (TCC) between CVD Screen-InGa-Copper substrate is assumed to be 10^5 W/mm².
- Contact between CVD screen, copper substrate and clamp are considered to be sliding with 0.2 of friction coefficient [1].
- For 35x21x0.1 mm CVD polycrystalline screen a value of 350 MPa has been adopted as fracture stress after conservative evaluation of data available in bibliography [2].
- Principal stress will be used as failure criteria for CVD polycrystalline screen since diamond is a brittle material [1].

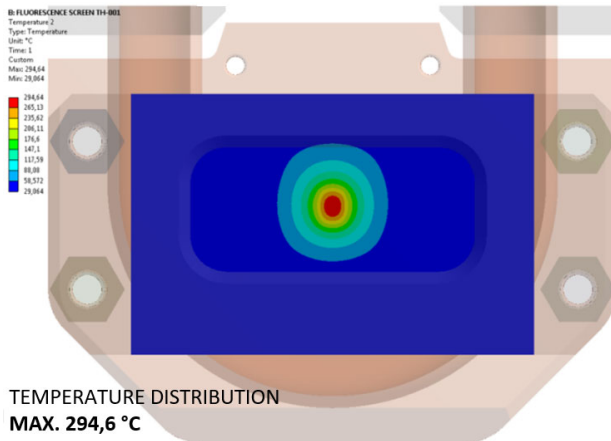


Figure 7: Temperature distribution on diamond screen.

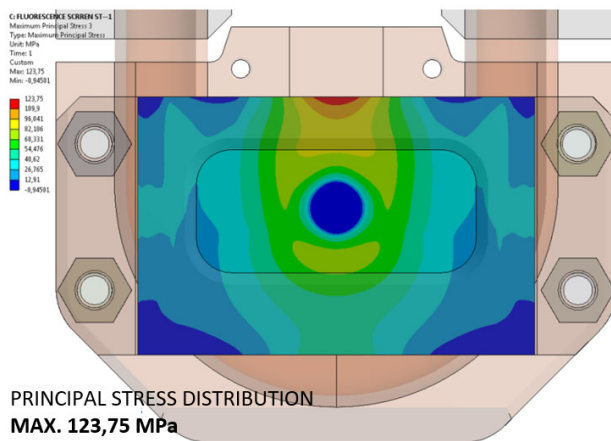


Figure 8: 1st principal stress on diamond screen.

CONCLUSIONS

Two types of Fluorescence Screen Monitors have been developed for XAIRA, the microfocus MX beamline at ALBA, currently under construction. The beam monitors have a compact design that aims to be adaptable to a wide range of X-ray beamlines and become standard at ALBA light source facility.

The Fluorescence Screens are currently being assembled and tested, their installation at XAIRA beamline is being scheduled during forthcoming months.

ACKNOWLEDGEMENTS

The authors wish to acknowledge all the ALBA staff involved in the design of XAIRA Fluorescence Screen Monitors, in particular, Marta Llonch, Jon Ladrera, Liudmila Nikitina, Marcos Quispe, Gabriel Peña and Bernat Molas.

REFERENCES

- [1] D. M. Smith, M. J. P. Adam, G. R. Barkway, and A. J. Janis, "Finite Element Analysis of a Combined White Beam Filter and Visual Screen Using CVD Diamond for the BXDS Beamline", in *Proc. MEDSI'18*, Paris, France, Jun. 2018, pp. 208-210. doi:10.18429/JACoW-MEDSI2018-WEPH04
- [2] V.G. Ralchenkoa, E. Pleilerb, D.N. Sovyka, and V.I. Konova, "Strength of Optically Quality Polycrystalline CVD Diamond", *Inorg. Mater. Appl. Res.*, vol. 2, pp. 439-444. 2011. doi.org/10.1134/S2075113311050273

X-RAY FACILITY FOR THE CHARACTERIZATION OF THE ATHENA MIRROR MODULES AT THE ALBA SYNCHROTRON

A. Carballedo[†], D. Heinis, C. Colldelram, C. Cuní, N. Valls Vidal, O. Matilla, J. Marcos,
 A. Sánchez, J. Casas, J. Nicolàs, ALBA Synchrotron, Cerdanyola del Vallès, Spain
 N. Barrière, M. J. Collon, G. Vacanti, Cosine Measurement Systems, Warmond, The Netherlands
 E. Handick, P. Müller, M. Krumrey
 Physikalisch-Technische Bundesanstalt (PTB), Berlin, Germany
 I. Ferreira, M. Bavdaz, European Space Agency (ESA), Noordwijk, The Netherlands

Abstract

MINERVA is a new X-ray facility under construction at the ALBA synchrotron specially designed to support the development of the ATHENA (Advanced Telescope for High Energy Astrophysics) mission [1]. The beamline design is originally based on the monochromatic pencil beam XPBF 2.0 from the Physikalisch-Technische Bundesanstalt (PTB), at BESSY II already in use at this effect [2]. MINERVA will host the necessary metrology equipment to integrate the stacks produced by the cosine company in a mirror module (MM) and characterize their optical performances. From the opto-mechanical point of view, the beamline is made up of three main subsystems. First of all, a water-cooled multilayer toroidal mirror based on a high precision mechanical goniometer, then a sample manipulator constituted by a combination of linear stages and in-vacuum hexapod and finally an X-ray detector which trajectory follows a cylinder of about 12 m radius away from the MM. MINERVA is funded by the European Space Agency (ESA) and the Spanish Ministry of Science and Innovation. MINERVA is today under construction and will be completed to operate in 2022.

INTRODUCTION

The ATHENA telescope is a space observatory that will address fundamental questions about energetic objects (accretion disk around black holes, large-scale structure, etc...). One of the key elements of the telescope is the innovative modular architecture of its optics subdivided by 15 concentric rings and filed by about 600 sub-systems called mirror modules (MMs). The technology used to manufacture the MM is based on the Silicon Pore Optics technology developed at cosine. At XPBF 2.0, cosine is currently optimizing the method to produce MMs at large scale [3] and today MINERVA is built to strengthen and boost their production and characterization while preserving the interoperability with XPBF 2.0. The final angular resolution of ATHENA strongly depends on the alignment accuracy between the 4 stacks constituting a singular MM. It is why stability, accuracy and repeatability are crucial parameters for the opto-mechanical components specifications.

GENERAL BEAMLINE DESCRIPTION

MINERVA takes port 25 at the ALBA experimental hall. This port is fed by a bending magnet source and provides optimal spatial distribution to allow future upgrades of the components. The beamline will operate under Ultra High Vacuum conditions (UHV) from the source to the exit of the photon shutter, where a vacuum window (Silicon Nitride) will separate them from the rest of the beamline. Downstream the vacuum window, the beamline will operate under High Vacuum conditions (HV, 10-5 mbar). The beamline will assess the absolute distance between the end detector and the MM origin with the adequate accuracy needed by the data analysis. This measurement is performed by the combination of laser tracking technology and high positioning repeatability of the mechanics. The whole beamline will be controlled using the Tango control system, standard at ALBA. MINERVA follows the optical layout sketched in Fig. 1. In there are presented the following components:

- A bending magnet of the ALBA storage ring as the X-ray source and the front-end elements.
- A toroidal mirror (M1) with a multilayer coating. The mirror deflects the beam inboard, with a total deflection angle of 14 degrees. It collimates the beam in both the horizontal and vertical planes. Its reflective surface selects a narrow bandwidth at the nominal energy of 1.0 keV. This element is enclosed in the optics hutch.
- A filter unit consisting of one Si3N4 membrane coated with a thin Al deposition. This filter removes the visible light reflected by the M1 mirror.
- A set of pinholes ranging from 10 μm to 500 μm in diameter.
- A photon beam shutter which includes a fluorescent screen beam diagnostic unit.
- A Si3N4 window, which separates the upstream UHV section from the downstream HV.
- A four-blade slit system that allow for apertures from fully closed to more than 10 mm in aperture.

[†] acarballedo@cells.es

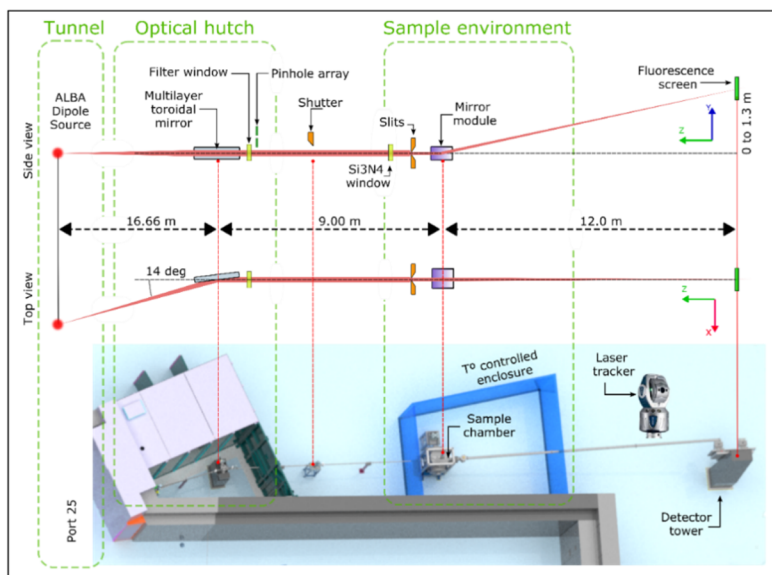


Figure 1: MINERVA layout presenting the main components of the beamline. Side view in a), top view in b) and 3D view in c).

- The sample station, which includes an in-vacuum hexapod and 2 linear stages for vertical and horizontal linear translations. The sample chamber seats inside a temperature-controlled enclosure.
- A flight-tube, which links the sample station to the detector. The flight-tube preserves the vacuum along the 12 meters long beam path between the MM and the detection system.
- The imaging detector, which consists on a fluorescent screen coated at a viewport at the downstream flange of the flight-tube, and imaged by a visible light 2D visible camera. The detector is mounted on a support tower that allows changing its height from 1.4 m from the floor to about 2.7 m. Also, for calibration purpose, the direct beam (not deflected by any MM) can be accessed.

MECHANICAL SPECIFICATIONS

Minerva beamline three main mechanical components are now detailed as follow:

Monochromator

The mirror substrate holder and surrounding elements are shown in Fig. 2. They are mounted on a single column as has been done before for MIRAS and LOREA beamline [4], with a proven outstanding resolution and stability, reaching up to 192 Hz for the first resonance mode. The column is decoupled from the vacuum chamber thanks to a large bellow and acts as a standalone insert that constitutes the base for the mirror holder, the cooling pipes and electrical feedthroughs. The column motion mechanics are based on a high precision goniometer that adjusts the angular X-ray beam incidence angle with a sub-micro-radian angular resolution and a horizontal translation stage that move the substrate perpendicular to its surface.

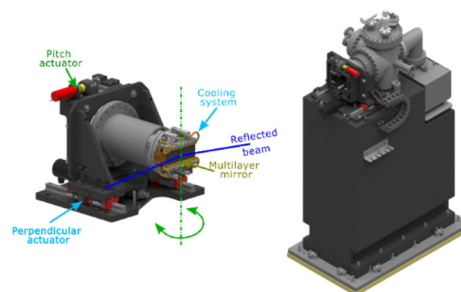


Figure 2: Monochromator mechanics description.

Sample Environment

For the characterization of each MM, the four stacks are inserted into a jig. The MM optical entrance is scanned both vertically and horizontally in front of the fixed incident beam keeping its orientation within 1.0 arcsec. The main components used to fulfill those requirements are shown in Fig. 3. The jig is mounted on top of two high precision linear stages and an in vacuum hexapod. The vertical stage takes place in air and is particularly designed to keep constant the orientation of the MM during a vertical scan. It is based on the ALBA skin concept [5] that includes two precisions synchronized actuators mounted at both sides of the granite for better mechanical and thermal stability. Combination of ball spindles and ball linear guides accurately move a thick horizontal platform with two flexures joints on its sides. The displacement range of this motion is enough to scan the height of a complete MM. The horizontal linear stage work under vacuum and consists in a ball spindle and cross roller linear bearings actuated by a stepper motor. Both vertical and horizontal stages are provided by optical encoders.

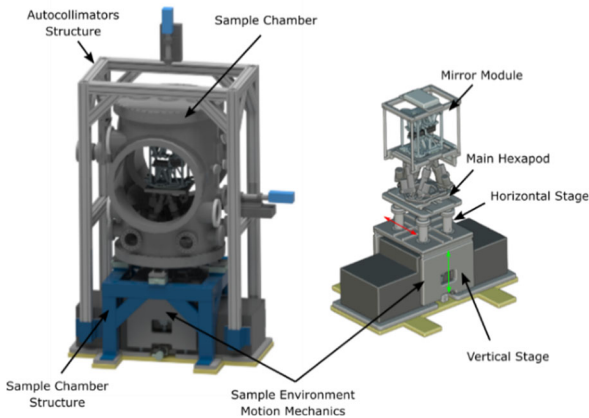


Figure 3: Sample environment.

The vacuum chamber is fully decoupled of the sample positioning stages by means welded bellows with robust columns holding the in-vacuum base plate. A metallic frame around the chamber includes two autocollimators that measure the 3 orientation angles MM respect of the incident beam which signal is re-used to act on the main hexapod for orientation correction.

Detector Tower

The beam deflected by the MM is then sent to a 2- dimensional array detector. To fully characterize a MM, the detector has to move on the portion of a cylinder surface with radius between 11.5 and 12.5 m. This trajectory is performed by using a 4-axis positioning combination, as is shown in Fig. 4. The height and the orientation of the detector are achieved by a twin vertical linear stages placed side by side. The detector can also follow the line of sight of the deflected beam and be adjusted to find the focus of the optics. The mechanics of all the stages are based on precision ball spindles and ball linear guides, all actuated by stepper motors. Each stage position feedback is given by optical encoders. The position of the detector is accurately measured and related with the MM position by a permanent laser tracker.

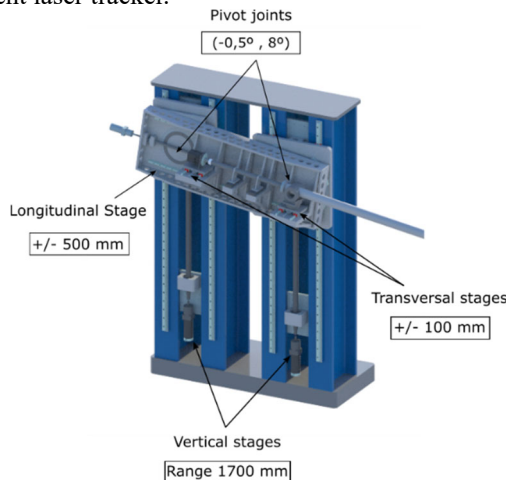


Figure 4: Detector tower.

CONCLUSIONS

MINERVA, a new beamline under construction at the ALBA synchrotron, has been described. The optical layout is a replica of XPBF 2.0, however, MINERVA will bring some innovation by trying to reduce the MM characterization time with a different scanning scheme. Also, more stability and repeatability are expected with the innovative sample environment and detector tower design, bringing improved mechanical performances.

The beamline, which is currently finishing the detailed design phase, will move into the production phase during the following months until 1st semester 2022, aiming to receive first synchrotron light by the end of 2022.

ACKNOWLEDGEMENTS

The authors wish to acknowledge all the ALBA staff involved in several aspects of the design, in particular, Alejandro Crisol, Marta Llonch, Jon Ladrera, Liudmila Nikitina, Marcos Quispe, Gabriel Peña, Núria Martí, Cristina Orozco and Domingo Alloza.

REFERENCES

- [1] D. Heinis *et al.*, “X-ray facility for the characterization of the Athena mirror modules at the ALBA synchrotron”, in *Proc. SPIE 11852, International Conference on Space Optics — ICSO 2020*, p. 1185222, 2021.
doi.org/10.1117/12.2599350
- [2] E. Handick *et al.*, “Upgrade of the x-ray parallel beam facility XPBF 2.0 for characterization of silicon pore optics”, in *Proc. SPIE 11444 Space Telescopes and Instrumentation 2020: Ultraviolet to Gamma Ray*, p. 114444G, 2020.
doi.org/10.1117/12.2561236
- [3] Nicolas M. Barrière *et al.*, “Assembly of confocal silicon pore optic mirror modules for Athena”, in *Proc. SPIE 11119, Optics for EUV, X-Ray, and Gamma-Ray Astronomy IX*, San Diego, California, p. 111190J, 2019.
doi.org/10.1117/12.2530706
- [4] Llibert Ribó *et al.*, “Mechanical design of MIRAS, Infrared Microspectroscopy beam line at ALBA Synchrotron”, in *Proc. MEDSI'16*, Barcelona, Spain, Sep. 2016, pp. 403-408.
doi.org/10.18429/JACoW-MEDSI2016-FRAA03
- [5] C. Colldelram *et al.*, “ALBA XALOC beamline diffractometer table skin concept design,” *Diamond Light Source Proceedings*, vol. 1, issue MEDSI-6, p. e44, 2011.
doi:10.1017/S2044820110000754

DESIGN OF A HIGH-PRECISION LIFTING SYSTEM FOR THE HL-LHC HEAVY COMPONENTS IN THE INTERACTION REGION

F. Micolon, M. Sosin, CERN, 1211 Geneva 23, Switzerland

Abstract

Given the high radiation level and the tight alignment tolerances, the HL-LHC interaction region components are designed to be realigned remotely using motorized supporting jacks, as human interventions in these zones must be limited to the strict minimum.

A position adjustment system will allow a vertical and horizontal displacement of each jack support by at least +/- 2.5 mm with a resolution of less than 10 μm. The weight of the supported elements, up to 170 kN and transverse loads reaching 30 kN, will have to be remotely moved by means of mechanical actuators. The system will be exposed to a cumulated radiation dose of up to 2 MGy during the 15 years of lifetime [1].

To comply with these requirements, an extensive design effort has been initiated at CERN to study the possible system layouts. This includes the prototyping of various solutions, studying subsystems through dedicated test setups and using simulations to obtain a clear understanding of the mechanical principles at play.

This paper reports on the work undertaken to design the high-precision lifting system, the various mechanical analysis carried out, and their main outcome. It reviews the proposed solutions and their expected alignment performance.

SYSTEM INTEGRATION REQUIREMENT

The heavy components of the HL-LHC interaction region are designed to be supported on standardized HL-LHC jacks, closely derived from the original design of the LHC supporting jacks [2].

These jacks are based on the concept of a tilting-column with two bearings on each end (see Fig. 1). They allow the accurate positioning within a range of +/-10 mm of the top bearing in one direction of the horizontal plane, while the other horizontal position is left free to move.

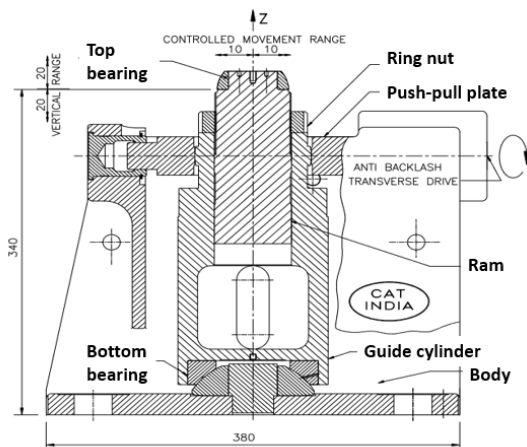


Figure 1: Transverse cross section of the LHC jack [2].

Like in the LHC, the heavy accelerator components are designed to be supported on three jacks located on two support planes on both ends of the component (see Fig. 2).

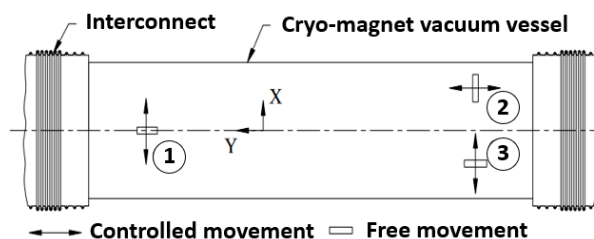


Figure 2: Top view of a cryomagnet - supporting jacks at position 1, 2 and 3 – adapted from [1].

Jacks 1 and 3 will permit the accurate positioning of the component in the radial (X) direction while jack 2 will determine the position in the longitudinal direction (Y).

The height (Z) of the component can be controlled on each jack by lifting the ram inside the guide cylinder, following which the ring nut is adjusted to retain the chosen height (see Fig. 1).

In the HL-LHC interaction region, the ram will be permanently supported by the motorized lifting system. Thanks to this, the height can be adjusted remotely without a manual intervention underground. Consequently, the lifting system must fit inside the bottom cavity of the guide cylinder to allow actuation of the ram from below.

STICK SLIP AND SYSTEM STIFFNESS REQUIREMENTS

The Principle of Frictional Stick-Slip

The so-called « stick-slip » describes the oscillatory motion affecting most common materials when they are sliding. For example it commonly occurs when rubbing a wet finger on the edge of a crystal glass or when dragging a chair on the floor. The amplitude of the sliding motion is directly dependent on the materials in contact and the system stiffness. With a simple demonstration, based on the conservation of energy [3], it can be shown that the stick slip amplitude for a sliding system is:

$$d = \frac{2.N.(\mu_s - \mu_d)}{k} = \frac{N.(\mu_s - \mu_{stop})}{k} \quad (1)$$

With N being the normal force at the sliding interface, μ_s , μ_d , μ_{stop} respectively the static, dynamic and rest friction coefficient, and k the system stiffness along the sliding direction. In our case, this amplitude defines the alignment resolution of the system. This highlights the importance of good material selection for loaded sliding surfaces and the need for sufficient system stiffness along the alignment direction.

Material Friction Testing

To select suitable interface materials and to define the required system stiffness accordingly, a friction testing campaign has been conducted at CERN in early 2021 to quantify the static and rest friction coefficients for selected materials [4]. This setup was based on the friction of two disk samples and the measurement of the friction load before and after the sliding occurred (see Fig. 3).

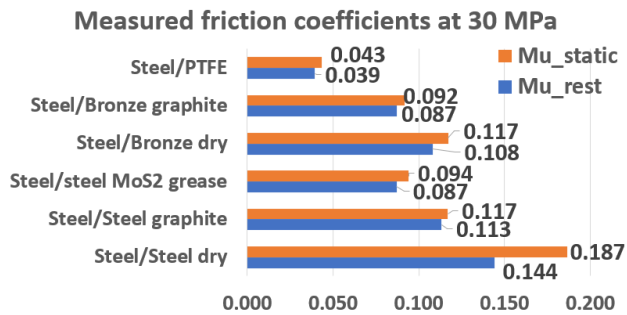


Figure 3: Measured friction coefficients at 30 MPa interface pressure for selected materials.

While the absolute value of friction coefficients is important to determine the system actuation load, it is the scatter between the static and rest friction coefficient that defines if the system is sensitive to stick slip.

Among the candidate materials tested, PTFE has the lowest friction coefficients and lowest friction coefficient scatter. It is however notoriously subject to radiation degradation and creep and so it cannot be used for our application. The steel/bronze couple, even at dry state, shows an interestingly low scatter of friction coefficients while being less susceptible to galling. So whenever possible, we will use this material combination lubricated with graphite for sliding interfaces.

System Stiffness Requirement

The supporting jacks will be subjected to transverse loads coming from the LHC operational conditions (vacuum, cryogenics) and neighbouring accelerator components. For the superconducting magnets of HL-LHC, this transverse force was evaluated to be up to 27 kN [5]. At this transverse load, a static friction force of 6 kN is expected at the ram/guide cylinder interface [6]. Considering the friction test results (Fig. 3) the residual force after sliding is expected around 4.5 kN. From Eq. (1) we can then compute that the required vertical stiffness must be at least 150 kN/mm to get a resolution below 0.01 mm.

THE LIFTING LEVER DESIGN

Lever System Design

A first design was conceived on the principle of a simple lever system. By carefully choosing the position of the fulcrum, this principle allows both a good control over the displacement and a low actuation force.

The design solution is based on a lever resting on a cylindrical bearing. The distance between the bearing centre and the lifting point is 40 mm, respectively 280 mm to the

application point of the actuation load, thus giving a displacement reduction ratio of 7:1 (see Fig. 4).

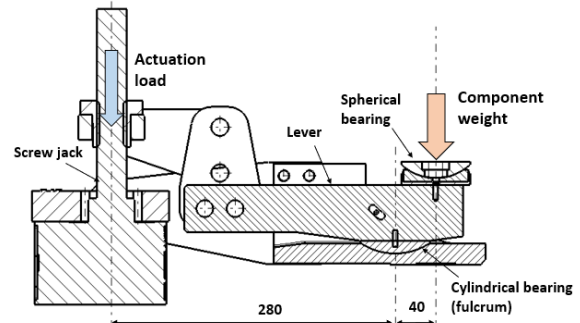


Figure 4: Cross section of the lifting lever solution.

The lever is actuated by a commercial worm gear jack with a maximum actuation load of 30 kN which results in a maximum actuation load of 210 kN at the component level. The component weight is supported on a bronze spherical bearing. Both, the cylindrical and spherical bronze bearings are lubricated with dry graphite to limit the stick-slip on these highly loaded interfaces. Finite element simulations show a vertical system stiffness of 600 kN/mm, and a maximum Von-Mises equivalent stress on the lever of 270 MPa under a load of 200 kN.

Lever Prototype Testing

A prototype for this lever-based solution has been produced and tested (see Fig. 5).

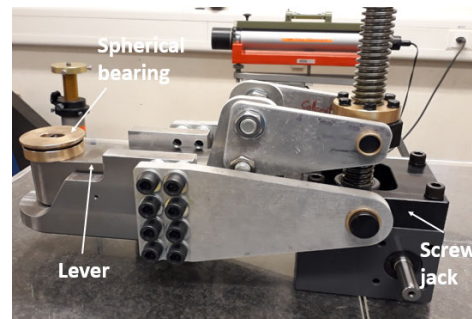


Figure 5: Prototype of the lifting lever design.

A 200 kN magnet was used for the purpose of testing (Fig. 6). Actuation loads of up to 100 kN were possible within the alignment range with a measured alignment resolution of about 5 μm .



Figure 6: Prototype lever inserted in the magnet jack.

HYDROSTATIC ELASTOMER DESIGN

Based on the extensive operational experience with the LHC design [7], a solution using the hydrostatic deformation of an elastomer body was also proposed. Among the possible elastomers, thermoplastic polyurethane (TPU) has shown to be radiation resistant, while it is being considered incompressible since it allows very big elastic deformation while having a low shear modulus. These materials have been used successfully within the LHC alignment systems, with the advantage over fluids of limiting the risk of hydraulic leaks which would eventually lead to a loss of control over the components vertical position.

The TPU cylinder pad ($\phi 50$ mm – 30 mm high) is enclosed within a cavity with the component load applied from the top through a vertical piston. A pushing finger ($\phi 25$ mm) is then gradually inserted horizontally inside the cavity and deforms the TPU pad which in turn pushes the vertical piston in a controlled way. Given the large alignment range requested, a test bench was setup at CERN to measure the ability of the TPU pad to allow alignment within a wide range of deformation and to measure the required actuation force (see Fig. 7).

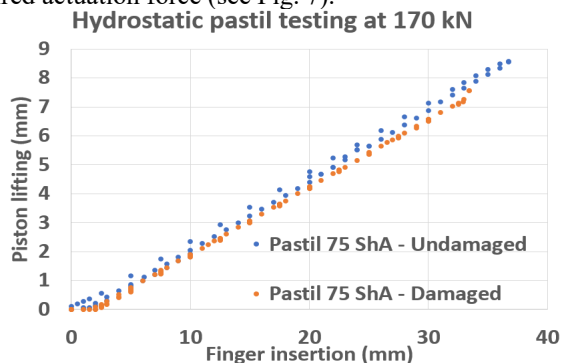


Figure 7: Testing of the 75 ShA TPU pad at deep finger insertion and high loads.

The test was conducted with increasing loads of up to 250 kN of vertical force on the pad (hydrostatic pressure of 127 MPa) with satisfactory results. As shown in Fig. 7, the piston lift is both very linear with respect to the finger insertion and reproducible upon loading and unloading. A TPU pad was purposefully damaged to simulate crack due to ageing and was re-tested with similar results (orange points in Fig. 7).

At ultimate finger insertion, the finger actuation force is 58 kN. This exceeds the theoretical hydrostatic force of 42 kN by 16 kN and shows that pushing the pad to big deformations requires a pushing force larger than the hydrostatic force. This is typically not the case for conventional fluid-based hydraulic systems where the actuation force is constant and always equal to the hydrostatic pressure. A uniaxial compressibility test was carried out on the TPU pad and the bulk modulus was measured in the order of 2.4 GPa for a 75 ShA TPU and 2.9 GPa for a 90 ShA TPU. This was confirmed by the measured linear slope of the piston-to-finger displacement of 0.23 mm/mm instead of 0.25 mm/mm if the pad was strictly incompressible (Fig. 7).

This compressibility adds however an additional vertical system flexibility in the order of 160 kN/mm. This is above the required stiffness necessary to comply with the resolution requirement (150 kN/mm). However, the actual resolution in extreme loading conditions with the full system should be assessed by further dedicated tests.

Since the TPU pad is enclosed in a cavity, any thermal expansion can only translate into a vertical piston translation. For TPU, thermal expansion coefficients up to $200 \mu\text{m}/\text{m}/\text{K}^{-1}$ were reported. With the current TPU pad dimensions of this would amount to $18 \mu\text{m}/\text{K}$.

A prototype was designed based on a worm gear principle with a reduction ratio of 107:1 (Fig. 8). It will actuate an M18 screw to produce the required pushing force on the finger of 60 kN. The system transfer function is then $35 \mu\text{m}$ of vertical piston displacement per input shaft turn.

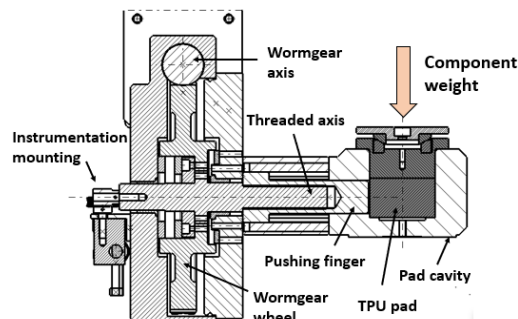


Figure 8: Cross-section of the prototype TPU pad design.

A prototype has been assembled (see Fig. 9) and has been tested on the test magnet (Fig. 4) with positive results. Loads up to 100 kN were successfully lifted with a resolution inferior to $5 \mu\text{m}$

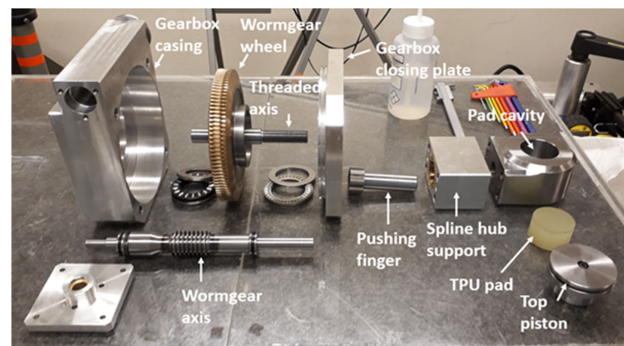


Figure 9: TPU pad prototype upon assembly.

CONCLUSION

The need for a lifting solution allowing the positioning of heavy elements with a $10 \mu\text{m}$ resolution has driven an extensive design and validation effort at CERN. Among the numerous alignment solutions considered, the lever and hydrostatic elastomer pad have been prototyped and tested with positive results. Further testing should now aim at validating the system's radiation and ageing resistance before choosing the most appropriate design for series production.

REFERENCES

- [1] P. Fessia, H. Mainaud Durand, “Full Remote Alignment Specification”, CERN, Geneva, Switzerland, Rep. EDMS 2166298 v1.0, Sept. 2019.
- [2] J. Dwivedi, S. G. Goswami, A. Kumar, V. Madhumurthy, V. Parma, and H. C. Soni, “The Alignment Jacks of the LHC Cryomagnets”, in *Proc. 9th European Particle Accelerator Conf. (EPAC'04)*, Lucerne, Switzerland, Jul. 2004, paper WEPKF038, pp. 1687-1689.
- [3] F. Micolon, “Evaluation of HL-LHC Jacks stiffness requirements for the FRAS alignment resolution”, CERN, Geneva, Switzerland, Rep. EDMS 2581596, May 2021.
- [4] F. Micolon, “Friction coefficient evaluation for HL-LHC alignment systems”, CERN, Geneva, Switzerland, Rep. EDMS 2581593, July 2021.
- [5] D. Duarte Ramos, “LOADS ON THE JACKS OF THE HL-LHC WP3 CRYO-MAGNETS. Functional Specification”, CERN, Geneva, Switzerland, Rep. EDMS 2278680 v1.0, Sept. 2020.
- [6] F. Micolon *et al.*, “Mechanical Consolidation of the LHC Inner Triplet Magnet Supporting System for Remote Alignment”, presented at the 12th Int. Particle Accelerator Conf. (IPAC'21), Campinas, Brazil, May 2021, paper TUPAB308.
- [7] J. Dwivedi *et al.*, “The Motorized Alignment Jacks for the LHC Low-Beta Quadrupoles”, in *Proc. International Workshop on Accelerator Alignment (IWAA'06)*, Stanford, United States, Sept. 2006, paper WEPO15.

ALL APPLICATIONS OF THE ALBA SKIN CONCEPT

Llibert Ribó†, Nahikari Gonzalez¹, Joaquín González², Alejandro Crisol¹,
Antonio Carballo¹, Luke Adamson³, Elliot Reece Jane⁴, Claude Ruget¹,
Judith Juanhuix¹, Josep Nicolas¹, Carles Colldelram¹,

¹ALBA Synchrotron, Carrer de la Llum 2 26, 08290 Cerdanyola del Vallès, Spain

²MAX IV Laboratory, Lund University, Box 188, SE 221 00 Lund, Sweden

³Australian Synchrotron, 800 Blackburn Rd, Clayton VIC 3168, Melbourne, Australia

⁴FMB Oxford, Ltd. Units 1 4 Ferry Mills, Osney Mead, Oxford, OX2 0ES, United Kingdom

Abstract

During the ALBA design phase, the protein macromolecular protein crystallography beamline, XALOC, required several in-house developments. The major part of these designs was at the end station where the necessity of customization is always much higher. The most relevant of these instruments was the beam conditioning elements table [1]. This accurate stage, which supports the diffractometer as well, includes the four movements required to align the components to the nominal beam as well as position the diffractometer. This design compacts, especially the vertical and pitch movements, both in a single stage, with a couple of stages for all four excursions. The solution maximises the stiffness and preserves at the same time the resolution close to $0.1\mu\text{m}$ while being able to withstand a half tone of payload. Thanks this compactness and performances this design concept, the vertical and pitch combined stage, was not only applied at XALOC for its diffractometer and detector table, but it has been widely adapted at several ALBA beamlines: at NCD-SWEET [2] as a detector table, a beam conditioning elements table [3] and sample table, at MSPD beamline as the KB table, at NOTOS beamline as metrology table, and also at the new ESA MINERVA beamline [4] for their sample mirror modules positioning. Beamlines have not been the only beneficiaries of this design, also different kind of instrumentation like an hall probe measuring bench [5], and even a stitching platform for the ALBA optics laboratory [6]. Moreover, the concept has outreach ALBA and has been adopted also at other facilities worldwide, synchrotrons and also scientific instrumentation suppliers around Europe. This poster presents most of the applications of the skin concept and their variations and main measured performances.

INTRODUCTION

The original design of the ALBA Skin Concept Design [1] was the diffractometer and beam conditioning elements table for the protein macromolecular protein crystallography beamline, BL13 XALOC [7]. The beamline has a simple optical lay-out based in three main instruments a S111 channel-cut DCM monochromator and a Kirkpatrick-Baez (KB) mirrors pair. The different beamline configurations, vertically and horizontally mirrors focus or unfocused, divert the beam at sample position. The diffractometer, the sample, has to follow the beam excursions.

† lribo@cells.es

Moreover, the previous beam conditioning elements have to be aligned jointly with the diffractometer, to the beam. All this system has to be positioned not only on position but also colinear with the beam path. These requires for this positioning system four axis (vertical, transversal, pitch and yaw), with resolutions well below $1\mu\text{m}$ and $1\mu\text{rad}$ for ranges up to 70 mm for the translations and 15 mrad for the rotations. In addition, these specifications have to be met still being able to withstand heavy load capacity, up to half a tone, and at the same time being accurate and stable.

ORIGINAL DESIGN

High payload, accuracy, resolution and stability are requirements that are very difficult to achieve all together. Moreover, the diffractometer and beam conditioning elements define an elongated shape. In order to achieve proper performance for all characteristics at the same time it was proposed the skin concept [1] where vertical translation and pitch were compact in a single stage as well as for the transversal and yaw movements.

While accuracy and resolution, but also the payload, are assured by means the quality of the mechanical elements the stability is achieved by several different strategies. The quality of the mechanical elements is guaranteed selecting the proper supplier's: high precision preloaded linear guides and oversized balls grind spindles for instance. In the other hand the stability approach is based on a design architecture intrinsically stable: using a big granite reference base, compacting movements by pairs: a translation and a rotation in a single stage, placing these stages surrounding the granite base (skin concept), with approach the loads are as close as possible to the granite minimizing the mass level arms, etc... With this configuration, especially for the combined vertical and pitch movements, the stage is placed like an inverted U shape along the granite with a vertical motion at each of the longitudinal extremes of the granite, light grey at Fig. 1a. A motor synchronized motion

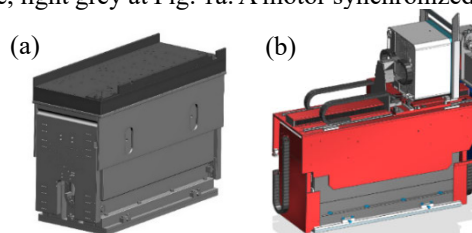


Figure 1: a) ALBA BL13 Diffractometer table. b) 3D model of the BL13 XALOC detector table.

delivers the vertical translation while a differential motion the pitch. This layout takes advantage of the elongated shape to place the two motions as separate as possible, longitudinally, maximizing the counter-level arm supporting the mass and thus the maximizing stability but also contributing to a smoother angular resolution thanks again to the long level arm. The transversal movement and the yaw pair have a similar concept and they are described the original design paper [1].

APPLICATIONS

The solution has demonstrated a proper performance on resolution, accuracy and stability. For all these reasons this design has been adopted in many applications at ALBA. Some of these applications almost exactly copied the full concept and in others partially and/or with some adaptations. In specific applications the solution needs larger angular ranges, beyond the limits of a flexure option for the pitch. In other applications the pitch solution has been rotated to work as a Roll angle. Also, different flexure approaches have been developed improving further the range and stability. It has been adapted mainly for beamline End Station, but also for beam line optics, Insertion Devices hall probe measurement benches, optical set ups, at ALBA but also at other facilities like the Australian Synchrotron, MAXIV and also suppliers like FMB Oxford.

In the following list there is the known applications:

- The Diffractometer and beam conditioning elements table [1] at BL 13 XALOC beamline, ALBA.
- The Detector table at BL 13 XALOC beamline, ALBA.
- The KB and beam conditioning element table at BL04 MSPD beamline, ALBA.
- The detector table at NCD-SWEET Beamline, ALBA.
- The sample table [2] at NCD-SWEET Beamline, ALBA.
- The beam conditioning element table [3] at NCD-SWEET Beamline, ALBA.
- The KB Table at XFM [8] beamline at the Australian Synchrotron.
- The Closed Gap Hall Probe Bench [5] for the Insertion Device laboratory at ALBA.
- The Lorea M3 & M1 mirror mechanics at ALBA by FMB Oxford.
- The Fizeau System Instrument [6] at ALBA optics laboratory.
- The Sample Table at ForMAX beamline at MAXIV.
- The Sample Chamber at the BL25 MINERVA beamline for ESA at ALBA
- The Metrology Table at BL16 NOTOS beamline, ALBA.

Different Adaptations

Following are described the most relevant variants of the skin concept. The NCD Sample Table, Fig. 2a, requires an extended Pitch angular range up to $\pm 10^\circ$. The design has been modified including a roller, bearing, articulation to allow this range instead of a flexure. As the angular range is

large it is needed a distance relieve guide, passive, to compensate the length variation. The bearing articulation allows large angular movements thus this now is not the limitation for the angular range it become limited only by the vertical stages ranges. The articulated solution introduces much less stresses to the parts and loads to the motion, but it becomes a much noisy movement as it can be seen in the following chapter of comparison results, Fig. 5.

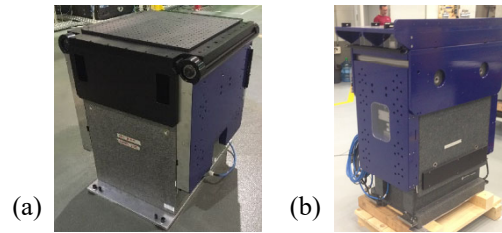


Figure 2: a) Sample Table for BL11 NCD-SWEET beamline with bearing articulated pitch. b) Beam conditioning elements table for BL11 NCD-SWEET beamline.

Another evolution of the table it is an optimization of the pitch flexure made at Australian Synchrotron [8]. Four possible improved flexures, Figs. 3a and 3b, were analysed and the better results were for 90° Cross Hinge.

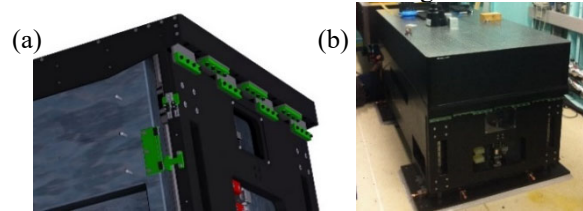


Figure 3: The KB Table at XFM beamline, Australian Synchrotron. a) Detailed view of the 90° Cross flexure hinge. b) picture of the KB table.

The conventional flexures are designed with high elastic limit steels, for the first design 1.2738 with an elastic limit about 780 MPa. This material is treated, hardened, material that does not need further process to reach its final characteristics and the treatment reaches the full bulk of the material, thus keeping these properties for the flexure slots. Despite these properties it still maintains a friendly machineability. The final calculated stress on the flexure was about 270 MPa which is about 35% of the yield stress, thus well below the 40% taken as a reference for generic fatigue limit. Moreover, from the material supplier the raw material has to be cut with steel fibber placed properly oriented vertically to ensure the material works properly. In addition, for each project a material test probe is done to verify the offered yield stress. The 90° cross flexure hinges solution simplifies the design and production and give an improved stability up to 85 Hz for the first resonance mode.

RESULTS

Most of the projects have been measured by means optical metrology. The original paper [1] shows the results for the first table. The several applications of this concept allow for very reliable comparison of different mechanical solutions as all them are very similar. One important point to evaluate is the effect of the table length on the Pitch, not

only level arm resolution conversion but mainly on the quality of this parameter. One of the longest applications is the BL13 XALOC detector table, Fig. 1b, with a granite length about 1,5 m and one of the shortest that can be compared is the beam conditioning elements table for BL11 NCD-SWEET beamline with a 650 mm granite length, Fig 2b.

Figure 4 shows the resolution graphs for both applications, both for 1 full step. Taken in account the reduction ratio, the length of the granite, the resolution of the beam conditioning table has to be twice(half) of the detector table and considering this, the major difference is the level arm. Both graphs show a clean resolution and show clearly one is twice the other for a full step motion, but it is possible to see a cleanest resolution for the longer table solution. Thus the level arm contributes to refine the resolution better than use mechanical elements like the reducer. Another relevant comparison is the flexure vs bearing articulation solution. Other comparable projects which there are metrology measurements are the Sample Table, Fig. 2a, and beam conditioning element table, Fig 2b, both at BL11 NCD-SWEET beamline. Motors and spindles are equivalent. The motor reduction ratio is 64 and 100 respectively. And the granite length is rather similar 605 and 648 mm.

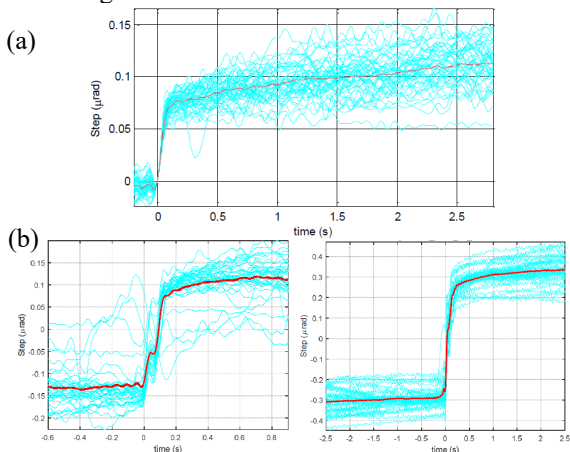


Figure 4: a) Resolution at 1 full step of the BL13 XALOC detector table. b) Resolution at 1 & 2 full steps (Figure b1 & b2) of the beam conditioning elements table for BL11 NCD-SWEET beamline.

As the reduction ratio is close to be one the double of the other it can be compared by 1 full motor step graphs Fig. 4b1 vs Fig. 5b, or by equivalent resolution steps Fig. 4b2 vs Fig. 5b and Fig. 4b1 vs Fig. 5a. It is clearly

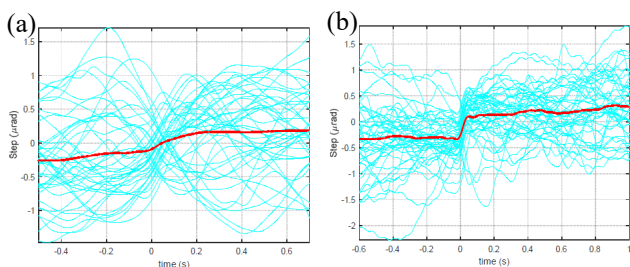


Figure 5: Resolution at 1 and 2 half steps (5a & 5b) of the sample table for BL11 NCD-SWEET beamline.

visible that the resolution of the bearing articulation is much more noisy, non-uniform, than the flexure. In addition, the repeatability is much better for the flexure solution 0,7 μrad vs 2 μrad of the bearing articulated table.

CONCLUSION

The skin concept table is a very good solution reaching at the same time performances that are very difficult to meet with the same mechanics: high payload, accuracy and resolution, and stability. The solution has successfully been adopted for many other applications successfully: for other similar end station applications, for optics mechanics, for measurement benches at ALBA and other synchrotrons and even their suppliers. New solution has further improve the stability and in other cases increase the functional range but relaxing the motion performances. It gives the opportunity to test the same conceptual solution in different adaptations but allowing a very reliable comparison between different mechanical approaches. The skin concept design strategies are: chose a stable reference (a granite for instance), place the masses close to this reference, reducing payload and mass level arms, compacting: two movement in a single stage, but increase the motion level arm for angular movement like the pitch solution. The results could give some design principles guides for better motion and stability performances. These performances can be easier achieved by the mechanical architecture design, mechanical configuration and shape, rather than charge on the components (linear guides, spindles). This means: placing the supporting components, the spindles for this case, as separated as possible, maximizing the counter-level arm to support the weights (the masses) rather than increase this spindle size; this geometry also maximize the pitch resolution by, in this case, maximizing the length, but in general maximize the angular motions level arms than rely on increasing the motor reducers ratio. And finally, when possible, include flexure hinges, when the range allow for it, instead of placing ball bearings articulations in general than roller components for articulations despite its fine movement.

ACKNOWLEDGEMENTS

The authors wish to acknowledge all those most involved in the design, construction, testing or applying this solution and share the results of all this projects ALBA beamlines staff Marc Malfois, François Fauth, Dominique Heinis; Insertion Device Laboratory Josep Campmany; Management Joan Casas; Workshop Jose Ferrer, Jordi Navarro, Karim Maimouni, Raúl Lorenzo, Oscar Borrego, Electronics Section, Alberto Ruz, Bern Saló, Bernat Molas, Cristian Pérez, Joan Pagès, Jose Avila, Sergio Astorga, Xavier Serra, Óscar Matilla, Antonio Camps, Manel Baena, Domingo Alloza and Roberto Petrocelli; Control Systems, Alberto Rubio, Guifré Cuní; Engineering Alignment Group, Jon Ladrera, Marta Llonch; Vacuum Group, Raquel Monge, David Calderón, and Lluís Ginés; Optics, Development & Innovation Section, Pablo Pedreira and Igors Sics; Australian Synchrotron Brad Mountford; FMB Oxford Scott Mowat and Luis Mateos.

REFERENCES

- [1] C. Colldelram and Claude Ruget, “ALBA XALOC Beamline diffractometer table skin concept”, in *Proc. MEDSI’10*, Oxford, UK, Oct. 2011, Diamond Light Source Proceedings, vol. 1, e44. doi:10.1017/S2044820110000754
- [2] J. B. González *et al.*, “NCD-SWEET Beamline Upgrade”, in *Proc. MEDSI’18*, Paris, France, Jun. 2018, pp. 314-376. doi:10.18429/JACoW-MEDSI2018-THPH17
- [3] N. González *et al.*, “Beam Conditioning Optics at the ALBA NCD-SWEET Beamline”, in *Proc. MEDSI’18*, Paris, France, Jun. 2018, pp. 365-367. doi:10.18429/JACoW-MEDSI2018-THPH14
- [4] A. Carballedo *et al.*, “X-Ray Facility for the Characterization of the ATHENA Mirror Modules at the ALBA Synchrotron”, presented at MEDSI’20, Chicago, USA, Jul. 2021, paper WEPA12, this conference.
- [5] L. Ribó and C. Colldelram., “Hall probe bench prototype for closed magnetic structures”, in *Proc. MEDSI’14*, Melbourne, Australia, Oct. 2014.
- [6] L. Ribó and C. Colldelram., “The Fizeau System Instrument at ALBA Optics Laboratory”, presented at MEDSI’20, Chicago, USA, Jul. 2021, paper WEPA07, this conference.
- [7] J. Juanhuix *et al.*, “Developments in optics and performance at BL13-XALOC, the macromolecular crystallography beamline at the Alba Synchrotron”, *J. Synchrotron Radiat.*, vol. 21, p. 4, Jul. 2014, pp. 679-689. <https://doi.org/10.1107/S160057751400825X>.
- [8] L. Adamson and Adam Walsh, “X-ray Fluorescence Microscopy End Station Upgrade”, presented at MEDSI’14, Melbourne, Australia, Oct. 2014, unpublished.

DEVELOPMENT AND APPLICATIONS OF THE WHITE BEAM POSITION MONITOR FOR BENDING MAGNET BEAMLINES

Chao-Yu Chang[†], Chia-Feng Chang, Chien-Hung Chang, Shih-Hung Chang,
Liang-Chih Chiang, Robert Lee, Bo-Yi Liao, Chin-Yen Liu,
National Synchrotron Radiation Research Center (NSRRC), Hsinchu, Taiwan

Abstract

We developed a white beam position monitor to be applied in beamlines with bending magnets. By 0.1 mm light-receiving opening, the beam is split and converted to a photocurrent intensity which can be used to detect the size and position of the beam ≤ 50 mm, and to align the locations of beamline components. A stop-beam measurement method is utilized, so it cannot monitor the beam in real time.

The motorized stage of the monitor has a range of motion up to ± 25 mm with position accuracy of ≤ 1 μm and vacuum capability of $\leq 5 \times 10^{-10}$ Torr, which is compatible with ultra-high vacuum environments. In addition, taking the thermal load 62.89 W of the TPS 02A beamline as an example, the thermal deformation of the analog monitor opening lead to a result that the measured value will have a maximum of 2 μm from the center of the beam.

The monitor is equipped with other components designed by NSRRC colleagues, including a motor control system, a four-channel current amplifier, an EPICS control system, and a GDA data acquisition and analysis software. The whole system has been successfully applied in the TPS 02A beamline. All features are verified and the performance meets the requirements. Besides, the positioning tasks of Slits1 was accomplished and the position variation of the light source was detected by this beam position monitor.

INTRODUCTION

When it comes to monitoring light source and calibration of beamline components, the size and position of the beam are extremely important information, so a beam position monitor with good performance is a necessity. The design of a white beam position monitor is more difficult than a mono beam position monitor, because the thermal load of white light will cause thermal deformation of the material such that the accuracy becomes worse. Moreover, there is more scattered stray light in the white light region than that in the mono beam region. The background value of the white light area is higher, and the scattered stray light passing through different structures may also have an asymmetric spatial distribution. Therefore, a white beam position monitor needs to be designed with an appropriate structure to accurately interpret the beam position signal while limiting the proportion of external stray light entering the detector. These are the key points that must be achieved in the design of the mechanical structure.

The white beam position monitor described in this report is based on various measurement requirements proposed by users, such as calculating the center position of the beam, obtaining the overall beam imaging distribution, analyzing the quality and stability of the beam, and calibrating the zero position of beamline components, and other functions. Because the above requirements are suitable for light-blocking measurement methods, the beam will be completely shielded during measuring. Therefore sample measurements in the experimental station and real-time feedback adjustments of beam position cannot be performed at the same time.

MECHANICAL DESIGN

The white beam position monitor for the beamlines of deflection magnet is shown in Fig. 1. The internal mechanism and accessory design [1] is consisted of (1) cooling water inner and outer pipes (cooling water flows from the outside to the inside of the pipe), (2) fixture (fixing the temperature and electrical current measuring circuits to avoid direct radiation exposure during operation), (3) sapphire sheet (resistivity of $1 \times 10^{11} \Omega\text{-cm}$, excellent electrical insulation property, and good thermal conductivity and mechanical strength performance), (4) tungsten alloy plate (high melting point and good conductivity, as a metal substrate for receiving electron flow), (5) oxygen-free copper (C10100) cover (fixed on the body with a screw lock and ceramic gasket, and insulated from the ground), (6) oxygen-free copper cooling seat body, (7) composed of components such as the lower cover of the oxygen-free copper cooling seat [2].

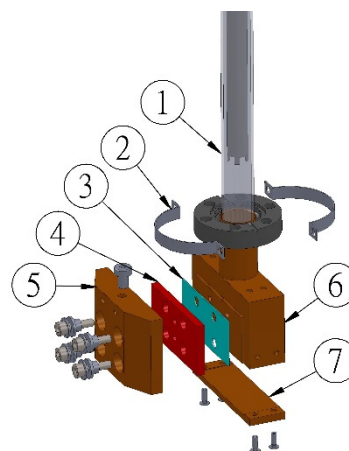


Figure 1: Internal mechanism and accessories of white beam position monitor.

[†]chang.cy@nsrrc.org.tw

Content from this work may be used under the terms of the CC BY 3.0 licence (© 2021). Any distribution of this work must maintain attribution to the author(s), title of the work, publisher, and DOI

The white beam position monitor is coated with a light-receiving tungsten alloy plate with oxygen-free copper, as shown in Fig. 2. In order to make the current signal measurement spectrum show the beam distribution as accurately as possible, we need to effectively reduce the luminous flux of scattered stray light and reduce the influence of circuit noise. The size of the light inlet is measured after the current intensity of the TLS beamline is known as a reference. As shown in Fig. 2, the design uses 1/20 of the vertical size of the beam as the short side size of the light inlet. At present the short side size of the beam entrance is 0.1 mm, but this size is extremely difficult to be manufactured. Therefore, two accurate-sized oxygen-free copper blocks are designed, and then the assembled opening is confirmed with a thickness gauge.

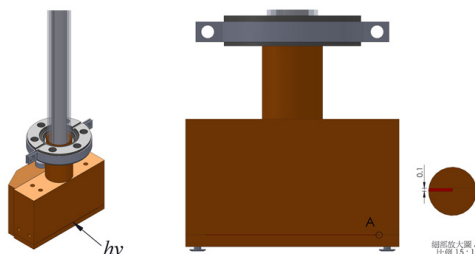


Figure 2: White beam position monitor measurement and beam light entrance size.

THERMAL DESIGN

Simulation is performed to calculate the expansion and deformation of the light inlet due to thermal load [3] and the position error value caused by the deformation. As shown in Fig. 3, the cooling seat bears the temperature distribution of 62.89 W heat load. Due to the cooling water circulation of the main body copper block, the temperature difference on the upper side of the light inlet has a small variation. The lower cover copper block can only transfer heat by the contact area of 5 mm × 15 mm on both sides, so the temperature variation of the lower side of the light inlet is relatively large. In the entire cooling seat, the highest temperature appears at the copper block middle position of the lower cover.

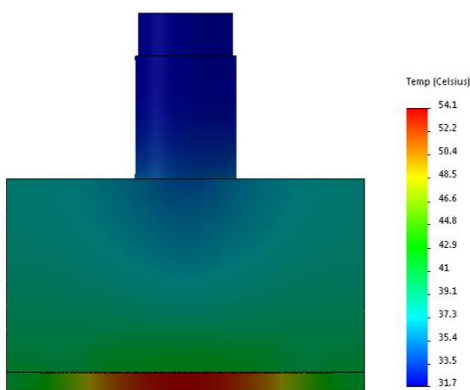


Figure 3: Temperature distribution diagram of the cooling seat under 62.89 W heat load.

As shown in Fig. 4, when the cooling seat is subjected to a 62.89 W thermal load, the maximum stress appears at the ends of the two oxygen-free copper openings. The analysis result shows that the maximum stress is 125 MPa, which is still less than the yield stress of the material itself which is 195 MPa.

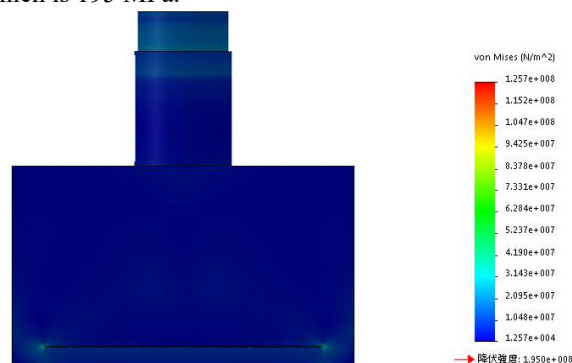


Figure 4: The cooling seat bears the stress distribution of 62.89 W thermal load.

Figure 5 shows that the deformation distribution of the cooling seat in the vertical direction under the heat load of 62.89 W. First, the deformation of the body will also affect the position of the lower cover. Then, the deformation of the cover under the same heating condition is more serious than the body, so the overall The deformation takes on the shape of an open mouth. As shown in Fig. 5 and Fig. 6, the opening-shaped deformation data of the cooling seat in the vertical direction under a heat load of 62.89 W is further captured. The upper side of the light inlet expands downward by 0.0005 mm, the lower side of the light inlet expands downward by 0.004 mm, and the center is calculated. The maximum offset is 0.00175 mm and the full width at half maximum relative to the vertical direction of the beam is 7.25 mm, so its deformation is still within an acceptable range.

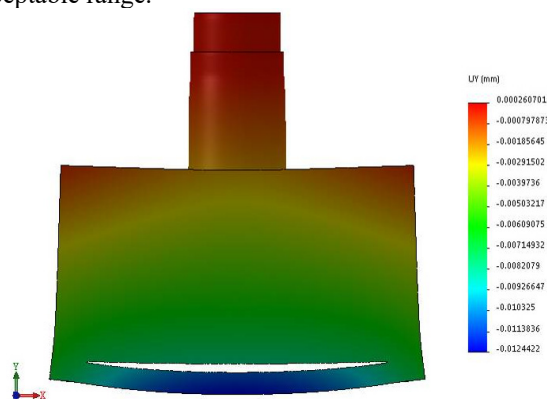


Figure 5: Deformation distribution diagram of the cooling seat in the vertical direction with a heat load of 62.89 W.

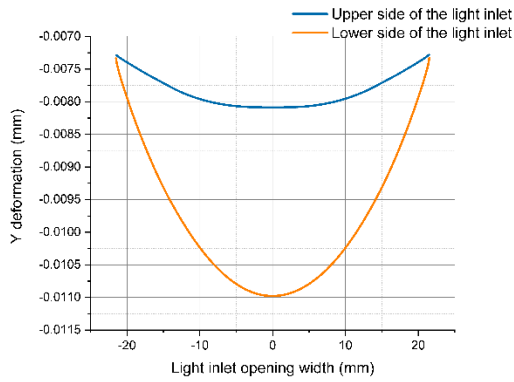


Figure 6: The data graph of the opening deformation of the cooling seat in the vertical direction under the heat load of 62.89 W.

APPLICATIONS

The electric meter used in this report is an integral four-channel current amplifier with a detection current range of 1 nA-100 μ A. It can be used with various types of X-ray position monitor to measure the spot position. It also has versatile features such as providing positive or negative bias voltage, RS-232 and Ethernet dual communication interfaces, as well as SD card for data logging and reading data via FTP. The communication specifications include TCP/IP, UDP, and EPICS, which can be easily connected to existing beamline control systems.

This white beam position monitor system has been applied to the commissioning of the TPS 02A beamline, and the simulation results are compared with the measured data to verify the actual performance. After the white beam of the bending magnet interacting with a beamline component, the component motorized stage can be moved and the BPM image can be measured at the same time. When the center of the component and the center of the beam coincide with each other, the calibration is completed.

In addition to directly scanning to observe the distribution of light, it can also be applied to, for example, the calibration of the zero point of each blade in Slits 1. The bpm_x detector is placed in the center of the beam, and the s1t scan data is differentiated and smoothed as shown in Fig. 7. Figure 8 shows that the overall spectrum is approximately Gaussian distribution, and finally s1t is reset to 0 at the above position.

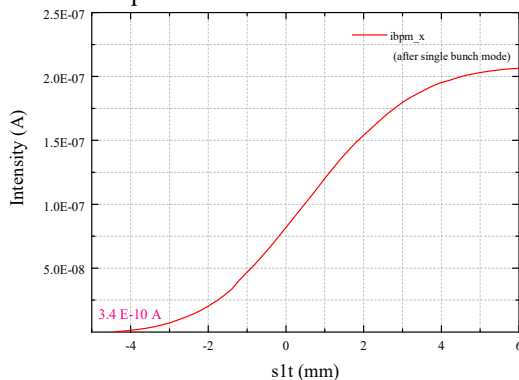


Figure 7: s1t measurement result.

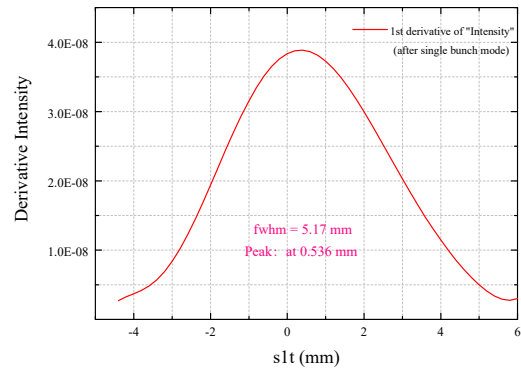


Figure 8: First differential and smoothing of s1t measurement results.

CONCLUSION

A white beam position monitor suitable for bending magnet beamlines is successfully developed. Being equipped with a four-channel current amplifier, the system can calculate the center position of the white beam during the test run period of the beamline, and obtain the overall imaging distribution of the white light beam. Furthermore, it provides a complete solution to the needs of analyzing the quality and stability of the beam, and calibrating the zero positions of the beamline components. After the measurement results during the TPS 02A beamline test run was obtained, the data is compared with the theoretical simulation results to verify the accuracy degree. In the future, the composition structure of the white beam position monitor system will be modified based on the above measurement results. The primary goal is to improve the position inaccuracy caused by the asymmetry of the cooling water circuit, clarify the actual impact of various other noises, and seek better solutions.

ACKNOWLEDGEMENT

We would like to thank the staffs at NSRRC, especially those in the Beamline Group, for assistance in this project.

REFERENCES

- [1] P. Berkvens *et al.*, "Radiation safety around the ESRF beamlines", in *Proc. 5th European Particle Accelerator Conf (EPAC'96)*, Sitges, Spain, Jun. 1996, paper THP028L, pp. 2618-2620.
- [2] A. Ferrari, P. R. Sala, A. Fassò, and J. Ranft, "FLUKA: a Multi-particle Transport Code", SLAC National Accelerator Lab., Menlo Park, CA, U.S.A., SLAC-R-773, Dec. 2005. doi:10.2172/877507
- [3] Y. Asano and N. Sasamoto, "Development of Shielding Design Code of Synchrotron Radiation Beamline", *Radiat. Phys. Chem.* vol. 44, pp. 133-137, Jul. 1994. doi:10.1016/0969-806X(94)90119-8

LINAC SECTION 3 AND 4 REPLACEMENT AT THE CANADIAN LIGHT SOURCE

E. X. Li*, X. Shen†, R. Zwarich*, Canadian Light Source, Saskatoon, Saskatchewan, Canada

Abstract

The Canadian Light Source Inc. (CLSI), opened in 2004 and located in Saskatoon, Saskatchewan, Canada, is a third-generation synchrotron light source facility with a 2.9 GeV storage ring. CLSI was built based on the Saskatchewan Accelerator Laboratory (SAL) with its LINAC. The SAL LINAC was built in 1960s and refurbished to operate at 250 MeV in 2002. It was also designed at an average beam power up to 46KW. To be used by CLS, the LINAC was modified for operation at pulse power levels of 25 MW with the current 100 mA. The modified LINAC consists of an electron gun and section 0 to 6 (Fig. 1), Energy Compression System (ECS) and Section 7.

The LINAC has kept a steady performance throughout the years, along with many repairs and replacements – most of which are preventative. The original Varian type accelerating Sections are planned to be replaced gradually by SLAC type Sections. Section 3 and 4 are two of the original 3 Varian type sections left in CLS - with over 55 years of service, they were accumulating vacuum leak problems from time to time. The replacement of Section 3 and 4 was completed in 2020. The mechanical consideration of the Section 3 and 4 replacement mainly includes upgrading supporting structures, designing Waveguides, modifying LCW systems, getting solution to move the sections around in the LINAC tunnel, etc.

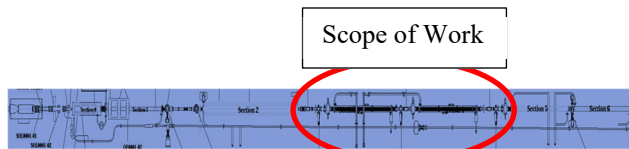


Figure 1: CLS gun and section 0-6.

BACKGROUND

CLS has encountered gun failure in 2018, and the repairing of the device took quite a long time. The old Varian Section was discontinued and no spare could be available. We have been experiencing some vacuum leaks from the old Sections over time. It is a huge risk to run the old Varian Sections that were built at the same time as the electron gun. The old Varian Sections in CLS had been planned to be replaced gradually.

The goal this time was to replace the Section 3 and 4 and add more components together with the new Sections in between Section 2 and 5 (Fig. 2). New added components include Ion pumps, View Screens, Vacuum Valves, Steer Magnets, FCT's, CCG's, TCG's and BPM's. As well, RF Loads were replaced and Waveguides were redesigned.

* CLS Engineering group
 † CLS AOD group



Figure 2: Overview of the new installation.

OLD VARIAN SECTION VS. NEW SLAC SECTION

The old Varian Section (Fig. 3a) in CLS weighs around 2 tons; its outside diameter is close to 400mm and the total length is around 5 meters. Solenoids are located surrounding outside of the Varian Section and need separate cooling.

The new SLAC Sections (Fig. 3b) are quite small compare to the old Varian ones: each one weighs around 400 kg, the contour diameter is about 145mm, and the length is around 3.1 meters. The SLAC Sections do not have solenoids.



Figure 3a: An old Varian section.



Figure 3b: A new SLAC section.

DESIGN OF NEW STRUCTURES

Three types of structures (Figs. 4a-c) were added to meet the supporting requirements.

Structure Assembly Type A

This type of structure assemblies supports the groups of new components, features bolted connections completed with side reinforcements and is adjustable from all directions (Fig. 4a).



Figure 4a: Structure type A.

Structure Assembly Type B

This type of structure assemblies supports the new Sections, features bolted connections and is adjustable from all directions (Fig. 4b).



Figure 4b: Structure type B.

Structure Assembly Type C

This type of structure assemblies supports the new Waveguides, features bolted connections and is adjustable from all directions (Fig. 4c).

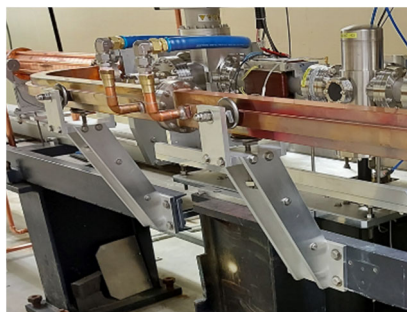


Figure 4c: Structure type C.

FEA ASSISTING DESIGN OF NEW COMPONENTS' SUPPORTING ASSEMBLIES

Three different new structure assemblies were designed to carry the three groups of new components added between Section 2 and 5 (Fig. 4a).

To meet the original beam height, it is critical to support all of the new equipment without any deflections caused by any source such as heat, unbalanced weight and misalignment. Ansys analysis (Fig. 5) was performed to optimize the design of the new added supporting structures by comparing the results of the stresses and the deflections of the different designs. Deflections on the base plates of all the fully loaded new structures were optimized to minimal.

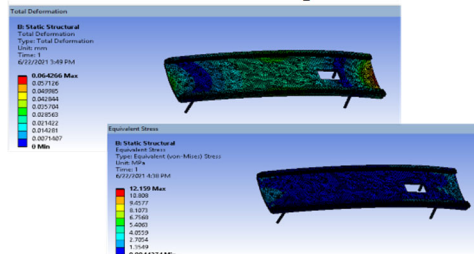


Figure 5: Typical FEA simulation of a components' supporting assembly.

REPURPOSING THE EXISTING SUPPORTS

With the new components added in between the new shorter sections, the weight distribution is not even on the reused girders (Fig. 6). New supporting structures should be designed to be capable of maintaining the expected beam position by considering possible adjustments from all directions.

Force distribution on each girder has been carefully analysed and proper reinforcements were applied to limit deflections. FEA simulations (Fig. 7) has been performed to help prove the estimations.

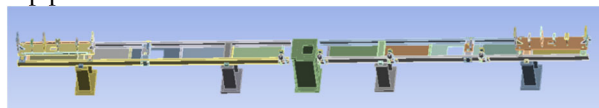


Figure 6: Overview of the existing supports.

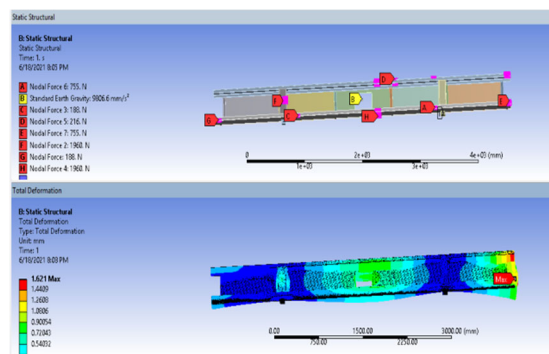


Figure 7: FEA simulation for one girder.

DESIGN OF WAVEGUIDES

The existing CLS LINAC Section 3 and 4 Waveguides were installed in the 1960s. With years of operation, dust and stains have accumulated throughout the full length of the Waveguides (Fig. 8). In addition, the placements of the RF inputs/ outputs on the new LINAC Section 3 and 4 were

opposite from the old Sections (Fig. 9). Thus, the waveguides had to be replaced with the Sections.



Figure 8: Stain at the WG bend/ bottom.



Figure 9: Old (left)/ new (right) waveguides.

The two new Waveguides route from the ceiling of the LINAC tunnel down to the RF inputs of the new Section 3 and 4. Multiple identical Waveguide segments were adapted for easy installation and utmost interchangeability.

The positions of the new Waveguides were constrained by the locations of the tie-in flanges which were not movable and were precisely surveyed (Fig. 10). Any deviation caused by the manufacturing processes of the Waveguide segments could lead to unacceptable results.

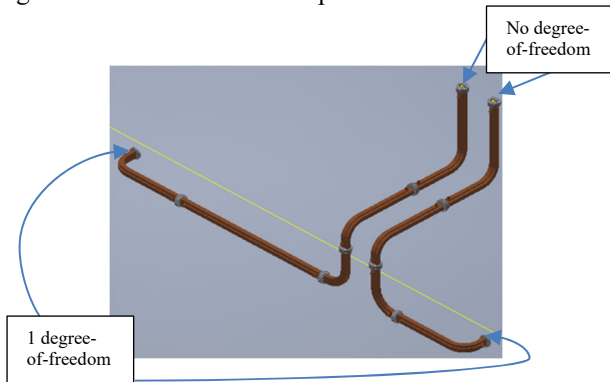


Figure 10: Constraints of the new waveguides.

MODIFICATION OF LCW SYSTEMS

Each of the old Varian Sections has separated cooling systems for solenoids and Section/RF Load. Thus, the pump of the Low Energy LCW system (which supplies cooling LCW to the solenoids) was resized.

Section 3 LCW system and Section 4 LCW system were modified and optimized to cool each Section and its RF Load in series instead of parallel. Auto and manual Vents were installed to eliminate air clogging in each system (Fig. 11).



Figure 11: Vents installed on top of the RF load.

MOVING THE SECTIONS AROUND INSIDE THE LINAC TUNNEL

The space in the LINAC tunnel was carefully measured. Special tools were designed to support the old Sections during its moving and storage (Fig. 12). By using the special tools and the heavy-duty scissor lifts, the old and new Sections were able to be successfully moved around in the tunnel.



Figure 12: Disassembled old sections.

CONCLUSION AND FUTURE WORK

The Section 3 and 4 replacement was engineered and executed in 2019-2020. We have been observing good performance of the LINAC ever since. We look forward to the continued beam quality improvements this will bring.

In the future, we are going to replace the RF Loads of Section 5 and 6, and Section 2 will be the last Varian Section to be replaced.

ACKNOWLEDGEMENTS

Thank you to CLS Engineering, OTS, CID and HSE groups.

MAGNET MEASUREMENT SYSTEMS FOR THE ADVANCED PHOTON SOURCE UPGRADE*

Scott Izzo†, Animesh Jain, Charles Doose, William Jansma
Argonne National Laboratory, Lemont, IL 60439, USA

Abstract

The present storage ring at the Advanced Photon Source will be replaced with a new ring based on a Multi-Bend Achromat (MBA) design as part of an upgrade currently in construction. The new ring will require about 1320 new magnets which need to be measured and fiducialized to ensure field quality and alignment requirements are met. Seven test benches were designed and built to meet these measurement requirements. Field quality in the multipole magnets is measured using four rotating coil benches, whereas the longitudinal gradient dipoles are mapped using a Hall probe system. Two rotating wire benches are used to find the magnetic centers of multipoles and relate them to magnet fiducials using laser trackers. Mechanical designs of the measurement benches are presented.

INTRODUCTION

The Advanced Photon Source-Upgrade (APS-U) project [1] is under construction at Argonne National Laboratory. As part of this upgrade the present storage ring will be replaced with a new ring based on a Multi-Bend Achromat design. The new storage ring will require about 1320 new magnets and magnetic measurements are needed to characterize and fiducialize all these magnets to ensure field quality and alignment requirements are met.

Seven specialized test benches, as listed in Table 1, were designed and built to meet the measurement requirements for the APS-U project. Four of these benches are rotating coil benches for measuring field harmonics in multipole magnets (quadrupoles Q1-Q3, Q6 and Q7, sextupoles S1-S3, fast correctors FC, and combined dipole-quadrupole magnets Q4, Q5, Q8, M3 and M4). Two rotating wire benches were setup to fiducialize all the multipole magnets. The longitudinal gradient dipoles (M1, M2) are mapped using a Hall probe system which is also designed and built in-house. The salient mechanical features of these benches are described in the following sections.

COMMON FEATURES

All the rotating coil and rotating wire benches employ similar design features and use standardized commercial hardware to the extent possible. All benches use a block of granite supported by a custom steel stand as the base on which the measurement equipment is mounted. The stand has six adjustable feet for levelling and to distribute the load. The magnet under test (MUT) is placed near the

center of the granite on a 1.0-inch-thick ground steel plate. All APS-U magnets have built-in side and bottom reference surfaces and the benches make use of these same surfaces to quickly align the magnets to the rotating coil axis by banking against stop blocks fixed on the magnet support plate. Magnets of different sizes are accommodated on the same bench by changing aluminum shims between the stop blocks and the magnet reference surfaces.

Table 1: Magnetic Measurement Benches for APS-U

Bench	Magnet Types	Quantity
Rotating Coil (RC1)	Q1-Q6	492
Rotating Coil (RC2)	S1-S3, FC	411
Rotating Coil (RC3)	M3, M4	123
Rotating Coil (RC4)	Q7, Q8	164
Rotating Wire (RW1)	Q1-Q5, S1-S3	656
Rotating Wire (RW2)	Q6-Q8, M3, M4	369
Hall Probe (HP1)	M1, M2	164

The rotating coil and rotating wire systems have gravity sensors on the rotary encoders and magnet support plate to allow measurement of the magnetic roll angle in a frame where the bottom reference surface of the magnets is level. The measurement resolution is ~ 0.010 mrad and the absolute angle measurement is calibrated to better than 0.1 mrad.

ROTATING COIL SYSTEMS

A total of four rotating coil measurement benches (RC1-RC4) were designed and built to accommodate the large variety and quantity of magnets needed for the APS-U project (see Table 1). A typical rotating coil bench is shown in Fig. 1.

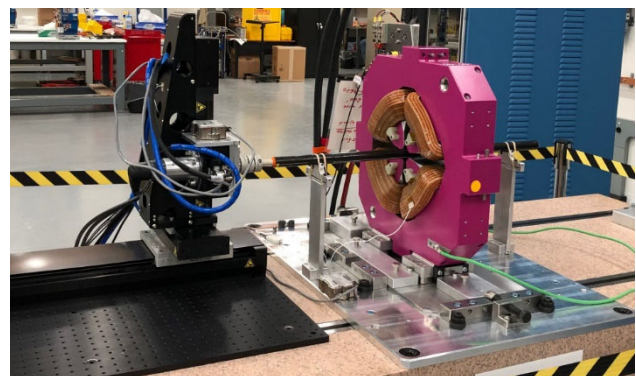


Figure 1: One of the rotating coil benches showing the granite block, XYZ- θ stages, magnet support plate, stop blocks and customized shim plates for alignment in X, Z.

* This research used resources of the Advanced Photon Source, a U.S. Department of Energy (DOE) Office of Science User Facility at Argonne National Laboratory and is based on research supported by the U.S. DOE Office of Science-Basic Energy Sciences, under Contract No. DE-AC02-06CH11357.

† email address: sizzo@anl.gov

The RC1 and RC2 benches are functionally the same and were designed to measure the smaller quadrupole, sextupole and fast corrector magnets (Q1-Q6, S1-S3 and FC). Both RC1 and RC2 use the same 0.481 m long printed circuit (PCB) coil [2] built by Fermilab. The PCB coil design offers unbuckled (UB) and suitably bucked signals for accurate measurement of field harmonics in dipoles, quadrupoles and sextupoles. The PCB coil is mounted on a 3-D printed coil support and rotates inside a carbon fiber cylindrical housing. The coil shaft is attached to a Newport rotary stage (θ -stage), which is mounted on Newport X-Y-Z linear translation stages. The transverse (X) and vertical (Y) stages have a travel of 100 mm in most benches. The Z-stages in these two benches have a travel of 0.6 m used to place the coil into and out of the magnet. Both benches have performed flawlessly over the course of more than 850 magnets measured so far.

The RC3 and RC4 benches are functionally similar and were designed to measure the larger combined function transverse gradient dipoles (M3, M4 and Q8) and the larger quadrupoles (Q7). The two PCB coil-probe supports in these two benches are attached to two X-stages which allow programmable X-motion of the coil-probes. The three X-stages (two coil probe supports, and the coil drive system) move in unison to allow placing the coil-probe at a desired X-offset from the magnet's geometric center during measurements. The coil support assemblies have a custom designed set of concave rollers which constrain the coil probe in X and Y but allow the coil to move freely in the Z-direction. The Z-stages have a travel of 1.2 m. The coil-probe housings have a physical length of 2.5 m and are designed in two sections which can be easily separated using a custom screw joint. During magnet installation and removal, the section of the coil probe not connected to the rotary stage is removed and the remaining section is retracted from the magnet bore using the Z-stage. Without this removable section, one would need a much longer travel on the Z-stages, and nearly twice the space in the measurement laboratory.

The RC3 bench, designed for measurements of the M3 and M4 transverse gradient dipole magnets, utilizes a PCB which is 400 mm in length. These magnets are essentially offset quadrupoles, with curved poles to follow the curvature of the beam. In order to measure the field harmonics integrated along the curved beam path using straight rotating coils, a method was developed [3] where the field is measured in three axial segments with suitable X-offsets at each position to follow the beam path. The results of these three measurements are combined mathematically and post-processed to determine the field strength and harmonics integrated on the curved path.

The RC4 bench is designed for the Q7 and Q8 magnets and utilizes a 1-m long PCB coil for integral measurements. Although the Q8 magnet is also a combined function magnet with slightly curved poles, the sagitta is very small (0.433 mm). Analysis of field maps computed using Opera-3D simulations showed that it is sufficient to measure the integral field using a single long rotating coil. The supports for the coil-probe and the motion control

configuration is identical to the RC3 system, so these two systems can serve as a backup for each other if such a need arises.

ROTATING WIRE SYSTEMS

The RW1 and RW2 rotating-wire systems were designed to locate the magnetic center of the multipole magnets and relate it to fiducials which are accessible on the magnet exterior. The uncertainty in determining the magnet center with this method has been shown to be better than 10 microns [4]. The main difference between the two benches is that the RW1 utilizes one granite base with 600-mm Z-stages and RW2 uses two granite bases with 1.2-m Z-stages to accommodate the large Q7, Q8, M3 and M4 magnets.

Each rotating-wire bench utilizes two XYZ- θ stage assemblies facing each other on each end of the MUT, as shown in Fig. 2. These stages allow programmable X and Y linear motion of a one-turn loop of 0.100 mm diameter Cu-Be wire which is stretched between the two sets of θ -stages. The width of the wire-loop, 8-mm for RW1 and 10 mm for RW2, is determined by precision-ground pulleys which are attached to the θ -stages. During magnetic measurements the wire-loop is rotated at 1 Hz via the two synchronized θ -stages. The offset from the wire-loop rotation center to the magnetic center is determined by analyzing the induced signal on the wire-loop.

The average wire sag over the magnet length is determined by measuring the resonant frequency and the wire length. The X-Y stages are placed such that the rotation axis of the wire-loop *at the magnet location* is at the magnetic center in X and is below the magnetic center in Y by the value of the wire-sag. The wire *ends* are thus aligned to the magnetic axis, compensating for wire sag.

The wire holders have a nest to affix a spherically mounted retroreflector (SMR) for laser tracker measurement of the wire rotation centers. The circular path of each wire-loop holder is measured, and the center of rotation is then fitted for each. A line constructed between the two end points defines the magnetic axis. Knowing the measured magnetic axis and surveying the magnet fiducials and other alignment features on the magnet, the magnetic center is related to externally accessible features. This relationship is used to align magnets to each other on module assemblies.

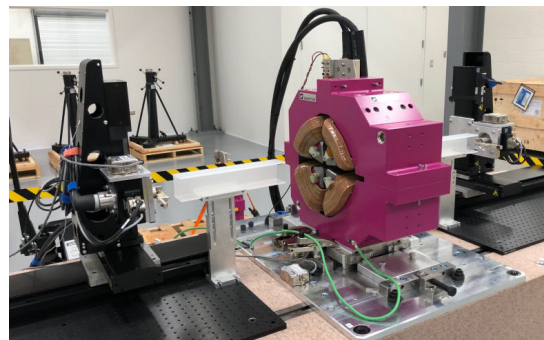


Figure 2: One of the two rotating wire benches showing motion stages and wire holders on both ends. Most of other mechanical features are similar to the rotating coil benches.

HALL PROBE FIELD MAPPING BENCH

The M1 and M2 longitudinal gradient dipole magnets are magnetically measured with a Hall probe-based system (HP1). This system includes a Hall probe sensor translation bench (HP1-A), and a magnet support bench (HP1-B) as shown in Fig. 3.

The magnets are pre-surveyed on a separate bench (HP1-PS) with a laser-tracker by measuring the top and bottom pole profiles and magnet fiducials. This bench is a precision granite surface plate used to support one M1 or M2 dipole magnet at a time. The goal of the pre-survey is to define the local “Magnet Coordinate System” (MCS) based on the as-built geometry for each magnet and relate this to the magnet fiducials.

The HP1-A and HP1-B benches are located in a temperature-controlled room and are aligned laterally to one another, with approximately 100 mm gap between them. The HP1-B supports the MUT and is decoupled from the HP1-A bench which supports the motion control stages and the Hall probe assembly. The HP1-A bench is a unique profiled granite bench that supports the three independent linear motion stages used to position a 3-axis Hall probe. The profile is designed to facilitate mounting of the long Z-stage which needs to be bolted from below. Due to a very high aspect ratio of length-to-width of the granite, a unique support system for the granite was employed. Two independent leg support assemblies were designed to not only support the granite, but to allow for the granite to be levelled without imposing a longitudinal torsional moment load onto the granite.

The top surface of HP1-A supports a 3-m-long linear THK Z-stage. The carriage of the Z-stage supports an X-Y- θ stage assembly with Newport motion control stages. The θ -stage supports a cantilevered Hall probe holder assembly. The probe holder assembly contains a 3-axis F3 type Senis Hall probe and two Metrolab NMR probes used to calibrate the Hall probe in-situ in the MUT.

A “Stage Coordinate system” (SCS) was defined based on fiducials on the HP1-A granite bench. The motion of the XYZ stages was measured with a laser tracker over the range of the stages and “motion vectors” relative to the SCS were derived. It should be noted that while these motion vectors are nearly orthogonal, they do not constitute a true Cartesian coordinate system.

A permanent-magnet-based skew-quadrupole “Reference Magnet” (RM) is used to relate the sensitive area of the Hall probe elements in the SCS coordinates. A virtual magnetic center of the RM is determined and related to fiducials on its yoke.

Once a MUT is placed on the HP1-B bench, the MUT, HP1-A and RM fiducials are measured using a laser tracker. Using the pre-survey data, the MCS is related to the SCS. The required motion of the XYZ stages can then be computed such that the field map is measured on a rectangular grid aligned to the MCS. This procedure eliminates the need to precisely align the MUT to the SCS. Use of motion vectors also eases the requirement to precisely align the motion stages orthogonal to each other. Typically,

field measurements are performed as a set of line scans along the magnet Z-axis at fixed X and Y positions. The Hall probe data are acquired on-the-fly at 1-mm increments in Z with a velocity of 27 mm/s. A zero-Gauss chamber is used to measure and record the Hall probe offset voltages which are later subtracted from the raw Hall voltages.



Figure 3: Hall probe field mapping system showing the HP1-A bench with a custom profiled granite block and support stand, the HP-1B bench used to support the magnet under test (MUT) and the reference magnet (RM).

ACKNOWLEDGEMENTS

The authors would like to thank J. DiMarco of Fermilab for the design and fabrication of the PCB coils, and M. Jaski for the design of the Reference Magnet. Careful assembly and efficient operation of all benches by G. Curescu, T. Malas, S. Skiadopoulou and R. Lopez is deeply appreciated.

REFERENCES

- [1] T. E. Fornek, Advanced Photon Source Upgrade Project Final Design Report, APSU-2.01-RPT-003, 2019. <https://doi.org/10.2172/1543138>
- [2] J. DiMarco *et al.*, “Application of PCB and FDM technologies to magnetic measurement probe system development,” *IEEE Trans. Appl. Supercond.*, vol. 23, no. 3, p. 9000505, 2013. doi:<https://doi.org/10.1109/TASC.2012.2236596>
- [3] A. Jain, “Overview of magnetic measurements for the Advanced Photon Source upgrade,” presented at 20th International Magnetic Measurement Workshop (IMMW20), Didcot, U.K., June 2017. <https://www.diamond.ac.uk/dam/jcr:e8ca5fa8-9630-401d-958f-eef13d832123/A%20Jain.pdf>

- [4] C. Doose, "Performance of rotating wire magnetic alignment systems for the Advanced Photon Source upgrade," presented at 20th International Magnetic Measurement Workshop

(IMMW20), Didcot, U.K., June 2017. <https://www.diamond.ac.uk/dam/jcr:a5ee8973-587f-4a27-891b-002f9de6b5c2/C%20Doose.pdf>

DESIGN AND FABRICATION CHALLENGES OF TRANSITION SECTION FOR THE CWA MODULE*

S. Lee†, W. Jansma, A. Siy¹, S. Sorsher, K. Suthar, E. Trakhtenberg, G. Waldschmidt, A. Zholents
 Argonne National Laboratory, Lemont, IL 60439, USA
¹ also at University of Wisconsin, Madison, WI 53715, USA

Abstract

An effort to build Argonne’s Sub-THz Accelerator (A-STAR) for a future multiuser x-ray free-electron laser facility proposed in [1] is underway at Argonne National Laboratory. The A-STAR machine will utilize a compact collinear wakefield accelerator (CWA) assembled in modules. To extract the wakefield and monitor beam position downstream of each module, a 45-mm-long transition section (TS) has been proposed and designed. This paper will discuss the design and fabrication challenges for production of the TS.

INTRODUCTION

The CWA TS consists of multiple miniature components that must be brazed or TIG welded vacuum leak-tight using a multi-step brazing processes with filler material of successively lower temperature to maintain the integrity of previously brazed joints. The internal vacuum surface geometry of the TS will be fabricated by electroforming copper (Cu) on an aluminum (Al) mandrel and chemically dissolving the Al mandrel to create the structure. Micro-manufacturing processes such as high-precision milling and wire electric discharge machining (EDM) will be utilized to produce the TS Cu base. A cold drawing process will be considered to produce flexible waveguide tubes. The CWA vacuum chamber module is comprised of a corrugated tubing/strongback (CTS) unit, a bi-metal vacuum flange, and a TS unit with a bellows as shown in Fig. 1. The following sections will focus on the design and fabrication challenges of the TS unit for the CWA vacuum chamber module.

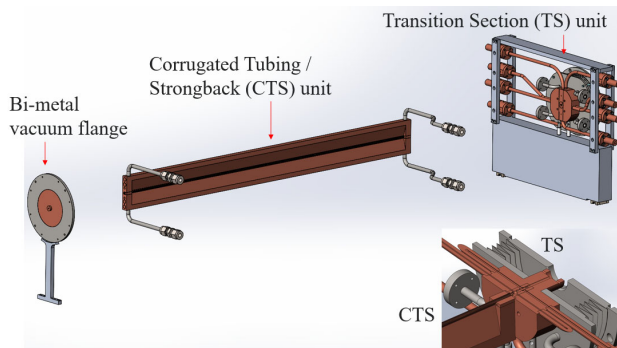


Figure 1: CWA vacuum chamber module and its components for the compact collinear wakefield accelerator.

* This research used resources of the Advanced Photon Source, a U.S. Department of Energy (DOE) Office of Science User Facility and is based on work supported by Laboratory Directed Research and Development (LDRD) funding from Argonne National Laboratory, provided by the Director, Office of Science, of the U.S. DOE under Contract No. DE-AC02-06CH11357.

† shlee@anl.gov

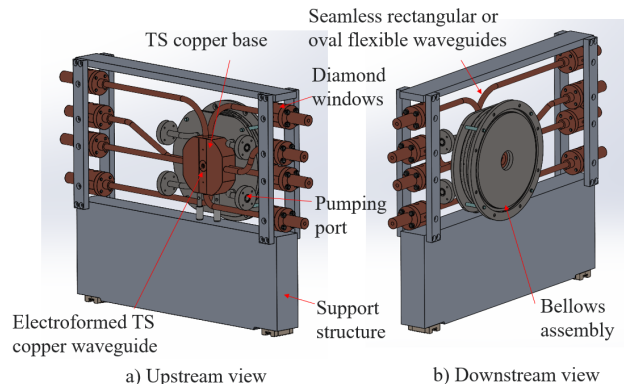


Figure 2: Transition section and its components for the compact collinear wakefield accelerator.

DESIGN OF TRANSITION SECTION

The TS unit is comprised of an electroformed Cu waveguide, a machined Cu base, eight seamless flexible rectangular or oval waveguides, diamond windows, and a stainless-steel bellows assembly with vacuum ports (see Fig. 2). The eight waveguides are utilized to extract unused TM01 accelerating mode from the output coupler of the corrugated waveguide while allowing the TE11 transverse mode to pass through to the integrated offset monitor (IOM) for beam offset measurements [2]. As shown in Fig. 3, its design consists of a four-way rectangular waveguide cross, which interfaces to the circular waveguide via tapers and a circular cavity. Immediately following the output coupler cross is a notch filter, designed to reflect the TM01 mode. Then, the IOM is located downstream to couple the transverse TE11 modes for beam offset measurements.

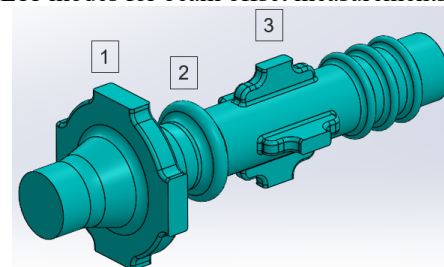


Figure 3: Geometry of the mandrel: (1) TM01 output coupler, (2) notch filter, and (3) integrated offset monitor.

Electroforming is utilized to fabricate complex features of the output coupler, notch filter and IOM in the TS. A negative form of the internal TS features is machined on an Al mandrel, and reference holes are added for alignment during future brazing and micro-machining steps. The mandrel is electroplated with Cu, and Al is then chemically dissolved, leaving behind the TS Cu structure. Finally,

Content from this work may be used under the terms of the CC BY 3.0 licence (© 2021). Any distribution of this work must maintain attribution to the author(s), title of the work, publisher, and DOI

external micro-machining of the TS Cu waveguide for future brazing joints to the TS Cu base can be performed as shown in Fig. 4.

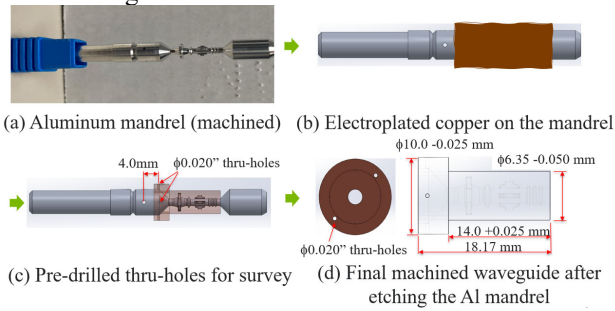


Figure 4: Schematic of the electroforming and micro-machining process of the electroformed TS Cu waveguide.

TS Waveguide-Base Unit

The electroformed TS Cu waveguide will be embedded into a pre-machined TS Cu base by a high-temperature brazing process as shown in Figs. 5(a-b). This TS waveguide-base unit will be vacuum leak-tested with two connectors as shown in Fig. 5(c). After the unit is leak-tested, holes (ϕ 0.30–0.50 mm) will be drilled for threading of thin wire rods into the unit for profiling of the rectangular waveguide, shown in Fig. 5(d). Finally, the unit will be machined to create the brazing joints for eight flexible waveguides and the CTS unit as shown in Figs. 5(e–f).

Flexible Waveguides and Diamond Windows

Custom-sized waveguide tubing will be used to extract unused RF power and for beam offset measurements. The waveguide is a non-standard size with an internal cross-section of 1.78 mm x 0.723 mm and can be produced by either extrusion or cold drawing. In the extrusion process, the temperature change can cause deformation with

shrinkage of the inner walls. Cold drawing pulls the tubing through hardened steel die at room temperature, holding the shape and the tolerance of the waveguide and producing a fine grain structure. Cold drawing is our preferred method to make our custom-made waveguide tubing. As shown in Fig. 6, we plan to use double diamond windows to isolate the CWA system vacuum. After brazing a diamond and a Cu flange, the diamond window unit will be bolted to a flexible waveguide. The 2nd diamond window will be bolted to the 1st diamond window with two O-rings.

Bellows Assembly

A bellows assembly will be utilized to pump out the CWA vacuum chamber module and for proper installation and handling during installation and maintenance. The concept selected utilizes off-the-shelf thin-wall edge-welded bellows allowing a ± 2.4 -mm translational stroke with four pumping ports, made of stainless-steel 304L or 316L as shown in Fig. 7. We also consider formed metal bellows to compensate for manufacturing and installation misalignment errors.

Transition Section Unit

As shown in Fig. 8, all the components listed above will be brazed together to produce the TS unit for the CWA vacuum chamber module.

FABRICATION CHALLENGES

Successful fabrication of the CWA vacuum chamber module relies on proper brazing and machining techniques [3]. We anticipate several technical challenges in developing the TS unit during brazing of dissimilar or similar metals, micro-machining of the electroformed TS Cu waveguide, and wire-EDM of the TS Cu base, etc.

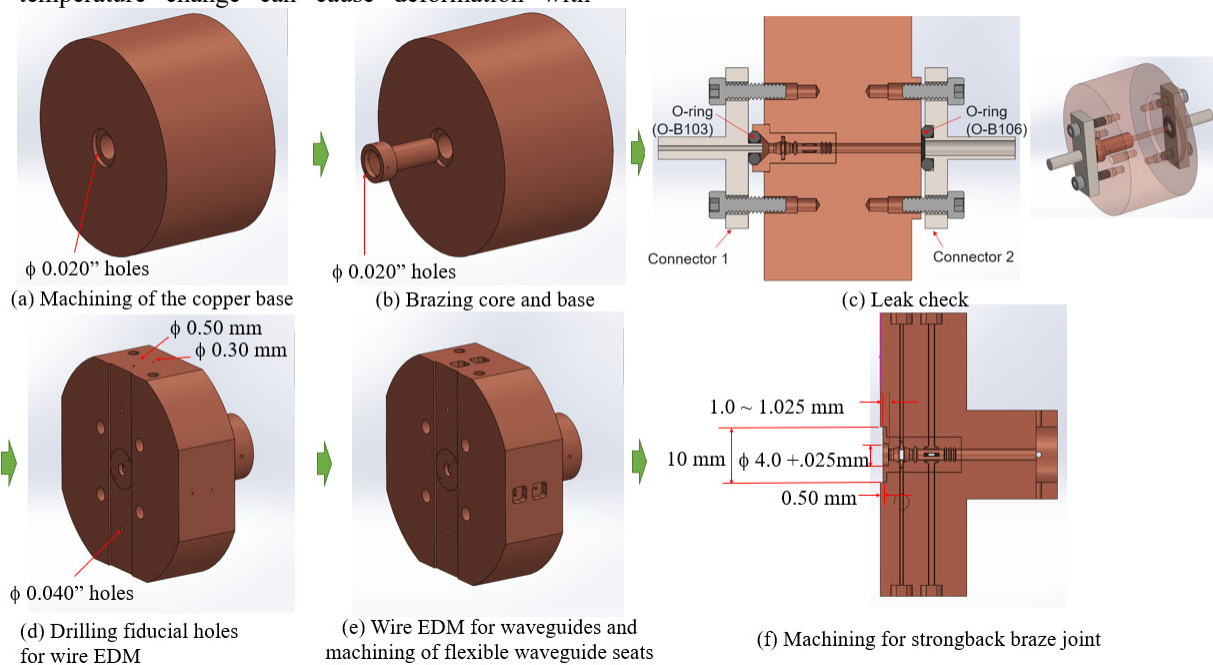


Figure 5: Figures show manufacturing process of the transition section core-base braze assembly.

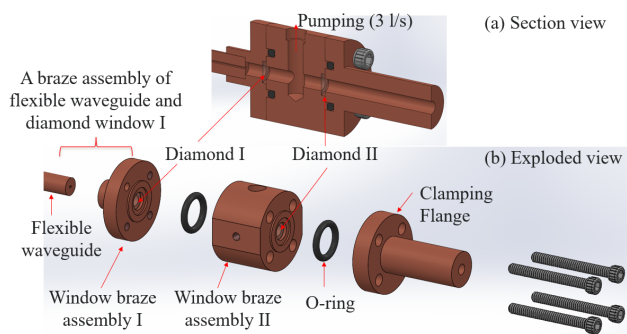


Figure 6: Flexible waveguides and double diamond window assembly.

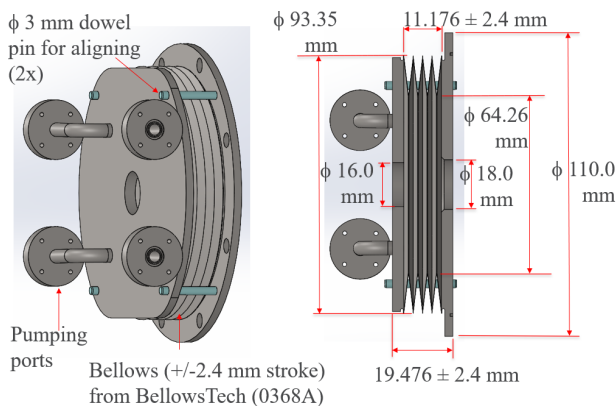


Figure 7: TIG welded stainless steel bellows assembly.

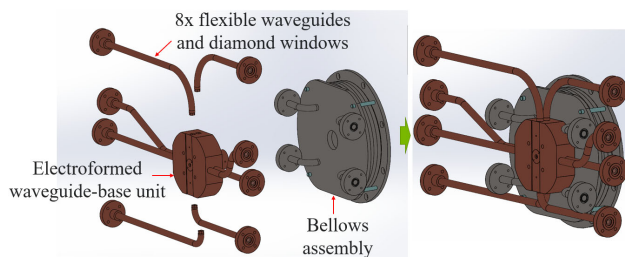


Figure 8: Transition section unit.

Currently, the 35/65 Au/Cu (BVAu-9) brazing filler metal is chosen to braze the TS waveguide-base unit and diamond window flange or assembly. For brazing of the flexible waveguide and the diamond window flange, BVAu-4 is considered as a filler metal to maintain the integrity of previously brazed joints. Then, BVAg-8, having a relatively low melting temperature, is considered as a filler metal to braze the TS waveguide-base unit with eight flexible waveguides. Finally, BAg-7 is considered in brazing of the TS unit, the CTS module, and the bi-metal vacuum flange for the CWA vacuum chamber module.

For successful braze joints, the part must be cleaned appropriately to remove oxides before and after brazing and the joints to be brazed must be designed to have a proper gap clearance for capillary attraction. When we braze, a clearance of 0.038-0.050 mm between the joining surfaces will be maintained. All brazing will be performed in a vacuum furnace that can decompose oxide layers to enhance the base metal wetting properties and reduce metal distortions due to precisely controlled heating and cooling rates [4]. Micro-EDM technology will be utilized to

produce micro-features of the internal rectangular waveguide profiles including internal round corners. For achieving high-aspect-ratio micro-features, wire with a diameter as small as 0.020 mm can be utilized, but manipulating and handling wire rods with small diameters is difficult because frequent wire breaks require manual intervention, even tungsten or tungsten carbide rods with diameters in the range of 0.10 - 0.40 mm [5]. Furthermore, the small holes for threading such thin wire rods must be placed in the TS Cu base by drilling or EDM drilling process, as they are in the range of 0.30-0.50 mm diameter with a very high-aspect-ratio as shown in Fig. 5(d). It also requires accurate positioning from fiducial holes in a mandrel and in an electroformed TS Cu waveguide. Common sources of errors include machine positioning, temperature instability, spark gaps, and electrode wear. Thus, care should be taken to keep the permissible tolerances of the wire-EDM process by avoiding any activities that can accumulate machining errors.

CONCLUSION

In this paper, the design and fabrication strategies of the transition section unit and technical challenges anticipated in the fabrication process are discussed. The transition section unit requires multi-step brazing of subsequent lower temperature, micro-drilling, and wire-EDM processes. Future work includes further optimization of the joint geometries, machining tolerances, and machining process through a step-by-step process evaluation in fabricating a transition section prototype.

ACKNOWLEDGEMENTS

We thank Gary Navrotski for assistance with metrological analysis of the transition section mandrel.

REFERENCES

- [1] A. Zholents *et al.*, "A conceptual design of a Compact Wakefield Accelerator for a high repetition rate multi user X-ray Free-Electron Laser Facility," in *Proc. IPAC2018*, Vancouver, BC, Canada, Apr.-May 2018, pp. 1266-1268. doi:10.18429/JACoW-IPAC2018-TUPMF010
- [2] A.E. Siy *et al.*, "Design of a compact wakefield accelerator based on a corrugated waveguide," in *Proc. NAPAC2019*, Lansing, MI, USA, September 2019, pp. 232-234. doi:10.18429/JACoW-NAPAC2019-MOPLH26
- [3] S. Lee *et al.*, "Mechanical design of a compact collinear wakefield accelerator," presented at MEDSI'20, Chicago, IL, USA, virtual conference, July 2021, paper WEPB05, this conference.
- [4] J. Kowalewski *et al.*, "Issues in vacuum brazing," *Heat Treating Progress*, vol. 6, May 2006. ASM International, <https://www.asminternational.org/>
- [5] D.T. Pham *et al.*, "Micro-EDM – Recent developments and research issues," *Jour. of Mat. Proc. Tech.*, vol. 149, pp. 50-57, 2004. doi:10.1016/j.jmatprotec.2004.02.008

MECHANICAL DESIGN OF A COMPACT COLLINEAR WAKEFIELD ACCELERATOR*

S. Lee[†], S. Doran, W. Jansma, A. Siy¹, S. Sorsher, K. Suthar, E. Trakhtenberg, G. Waldschmidt,
 and A. Zholents, Argonne National Laboratory, Lemont, IL 60439, USA
¹ also at University of Wisconsin, Madison, WI 53715, USA

Abstract

Argonne National Laboratory is developing a Sub-THz AcceleRator (A-STAR) for a future multiuser x-ray free electron laser facility. The A-STAR machine will utilize a compact collinear wakefield accelerator (CWA) based on a miniature copper (Cu) corrugated waveguide as proposed in [1]. The accelerator is designed to operate at a 20-kHz bunch repetition rate and will utilize the 180-GHz wakefield of a 10-nC electron drive bunch with a field gradient of 100 MVm⁻¹ to accelerate a 0.3-nC electron witness bunch to 5 GeV. In this paper, we discuss specific challenges in the mechanical design of the CWA vacuum chamber module. The module consists of series of small quadrupole magnets with a high magnetic field gradient that houses a 2-mm diameter and 0.5-m-long corrugated tubing with brazed water-cooling channels and a transition section. The 45-mm-long transition section is used to extract the wakefield and to house a beam position monitor, a bellows assembly and a port to connect a vacuum pump. The CWA vacuum chamber module requires four to five brazing steps with filler metals of successively lower temperatures to maintain the integrity of previously brazed joints.

INTRODUCTION

Development of a CWA accelerator presents significant engineering challenges due to the miniature scale of the components. The CWA vacuum chamber module is comprised of a corrugated tubing-strongback (CTS) unit, a bi-metal vacuum flange, and a transition section (TS) unit with a bellows as shown in Fig. 1. The CTS will be fabricated from cylindrical corrugated waveguide tubes with a 2-mm ID that will be electroformed from aluminum (Al) mandrels. It will generate ~100 MV/m accelerating fields during operation, and its overall length will be about 0.5 meter long. The bi-metallic flange will be brazed to the upstream end of the CTS. The TS unit consists of an electroformed TS Cu waveguide, a TS Cu base, a stainless steel welded bellows assembly, eight flexible Cu waveguides, and diamond window assemblies. The CTS, bimetal flange, and TS units will be brazed together, then machined to be embedded into the quadrupole wiggler with alternating focusing and defocusing quadrupoles. Figure 2 shows two CWA vacuum chamber modules and one quadrupole wiggler assembly to reveal the structural clarity of the

CWA vacuum chamber module. This paper will focus on the design of the CWA vacuum chamber module and its fabrication challenges.

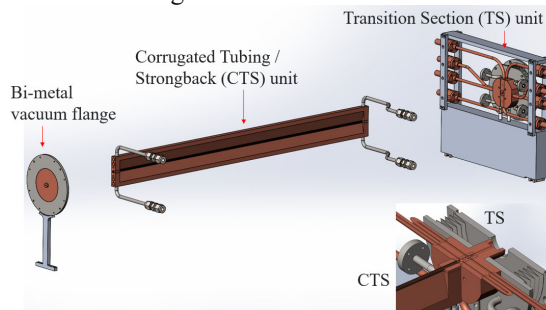


Figure 1: A vacuum chamber module and its components for the compact collinear wakefield accelerator.

DESIGN OF A CWA VACUUM CHAMBER MODULE

Various fabrication techniques to create a corrugated waveguide structure were investigated. Based on our previous study [2, 3], electroforming was selected to produce internally corrugated tube segments for the CWA vacuum chamber module. The corrugated waveguide tubes are created by electroplating Cu on an Al mandrel [3]. The Al mandrel is then chemically dissolved, leaving behind the internally corrugated Cu structure. The internal Cu surface reflects the shape and finish of the Al mandrel surface. A micro-turning process is utilized to meet the dimensional and surface quality tolerances of the mandrels. The internal dimensions of the corrugated waveguide structure are shown in Fig. 3. The maximum length of the Al mandrel is ~100 mm; therefore, several corrugated waveguide segments must be brazed together to fabricate the 0.5-m-long vacuum chamber. The waveguide segments will be inserted into a channel-cut machined Cu strongback plate, then secured by a machined Cu bar with braze filler metal spreading adequately over the tubing surfaces or using wire rods as shown in Fig. 4. If needed, all parts will be secured by jigs and fixtures, then carefully held in position for brazing in a vacuum furnace to produce a 0.5-m-long CTS unit.

During the brazing process, compression force will be applied inwards along the length using spring sheets and spacers at both ends to maintain tight surface contact of the corrugated tubes. This will help to prevent filler metal from flowing inside the inner corrugation surface area. After the post-braze cleaning process, both end surfaces of the CTS unit are milled for vacuum leak testing (see Fig. 5). The strongback sides will be milled to produce tapered surfaces to fit within the quadrupole wiggler magnet assembly as shown in Fig. 6. The strongback end surfaces will then be

* This research used resources of the Advanced Photon Source, a U.S. Department of Energy (DOE) Office of Science User Facility and is based on work supported by Laboratory Directed Research and Development (LDRD) funding from Argonne National Laboratory, provided by the Director, Office of Science, of the U.S. DOE under Contract No. DE-AC02-06CH11357.

[†] shlee@anl.gov

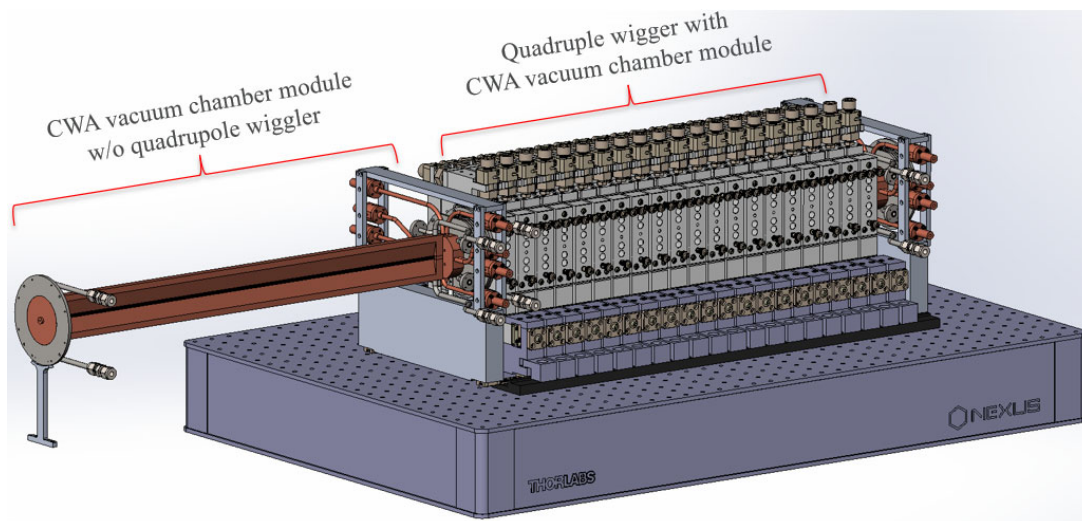


Figure 2: Two CWA vacuum chamber modules and a permanent magnet quadrupole wiggler on the optical breadboard.

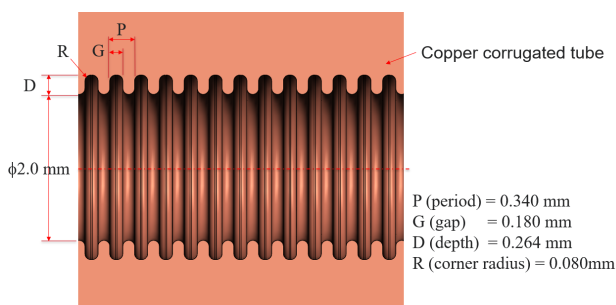


Figure 3: Schematic of corrugation inside of the copper tube.

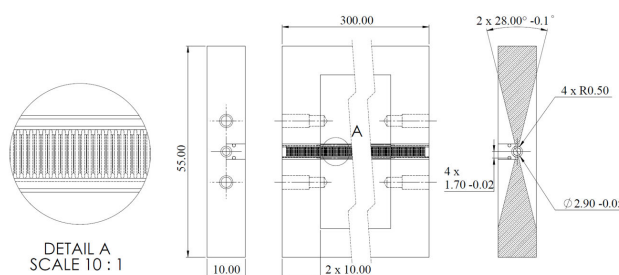


Figure 6: Machining of the corrugated tubing-strongback prototype for the quadrupole wiggler magnet (unit: mm).

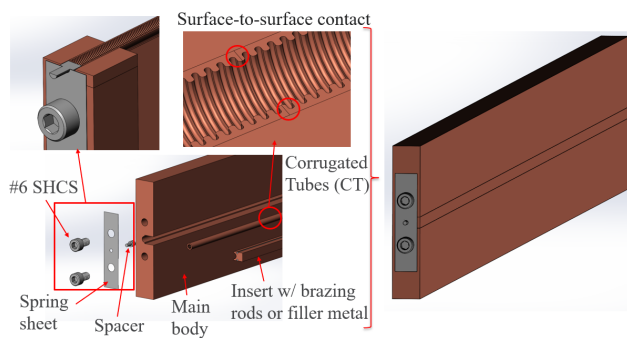


Figure 4: The components of a corrugated tubing-strongback (CTS) unit.

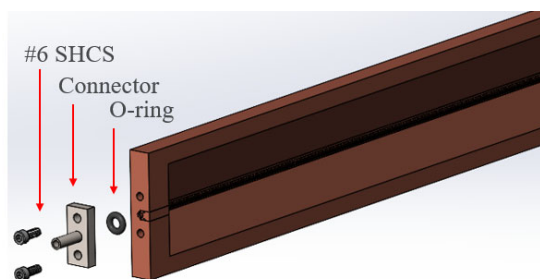


Figure 5: Schematic of leak check after brazing or machining the corrugated tubing-strongback (CTS) unit.

further machined as shown in Fig. 7(d) to prepare for the final brazing process at a lower temperature for connection to the bi-metallic flange and a 45-mm-long TS unit. The TS unit has many braze joints such as a braze joint between an electroformed TS waveguide and a TS body, eight braze joints between the TS body and eight flexible waveguides, eight brazing joints between the flexible waveguides and diamond flanges, and a joint between the TS body and the bellows assembly [4]. The CWA vacuum chamber module requires a total of 22 brazed joints that will be achieved via four to five brazing steps with filler metals (paste or wire rods) at successively lower temperatures to maintain the integrity of previously brazed joints.

FABRICATION CHALLENGES OF THE CWA VACUUM CHAMBER MODULE

Successful fabrication of the CWA vacuum chamber module relies on proper brazing and machining techniques. We expect several technical challenges in the brazing and micro-machining process during fabrication of each brazement and the final CWA vacuum chamber module, such as tolerance stack-up; base material condition; design variables including compression force along the corrugated tubes; process parameters during brazing, testing, and inspection of finished brazed assemblies, etc. In the brazing process, the following are challenges for producing a successful vacuum chamber module:

1. Braze joint design for proper gap clearance: when we braze, a clearance of 0.038~0.050 mm will be maintained between the two joining surfaces. But a close press-fit or contact between the corrugated tubes along the length must be considered to eliminate excessive braze filler flow into the corrugated surfaces by use of compression force.
2. Surface finish on the joints to be brazed will be 32~64 RMS for drawing the filler metal into the joint and getting better capillary action.
3. Vacuum cleaning to remove oxides from stainless steel and Cu materials for better surface conditioning before brazing and post brazing.
4. Suitable brazing filler metals of successively lower temperatures to maintain the integrity of previously brazed joints. For the brazing of successive joints in the CWA vacuum chamber module, the following are recommended as filler metals (Solidus, liquidus, brazing temperature range low-high).
 - a) BV Au-9, 35/65 Au/Cu (988, 1010, 1038-1066°C)
 - b) BV Au-4 (949, 949, 977-1004 °C)
 - c) BV Ag-8 (779, 779, 779-835°C)
 - d) BAg-7 (618, 651, 679-707°C)
5. Fixturing during brazing: Self-fixturing and self-aligning where possible. The use of fixture increases the cost and adds distortions to the braze assembly. To maintain a proper gap clearance, the fixture must be properly designed and used during brazing.

The standard CNC milling process can produce shapes with rounded corners of the CTS unit, but a micro-machining process, such as diamond-turning or micro-milling, can be considered due to tolerances as tight as 0.001" or less. Therefore, care must be taken during the micro-machining process of the exterior round surfaces of the CTS unit,

especially braze joints between the corrugated tubes. Undercut of the corrugated tubes can develop vacuum leaks under high-vacuum operation.

CONCLUSION

In this paper, we proposed design parameters such as braze joint geometries, clearance gap, surface roughness, and brazing filler metals of successively lower brazing temperature and technical challenges in the brazing and micro-machining of the CWA vacuum chamber module. Future work will focus on further optimization of the joint geometries, brazing filler metals, process parameters, and machining tolerances and techniques in detail to produce the CWA vacuum chamber module prototype.

REFERENCES

- [1] A. Zholents *et al.*, "A conceptual design of a Compact Wakefield Accelerator for a high repetition rate multi user X-ray Free-Electron Laser Facility," in *Proc. IPAC2018*, Vancouver, BC, Canada, Apr.-May 2018, pp. 1266-1268. doi:10.18429/JACoW-IPAC2018-TUPMF010
- [2] A.E. Siy *et al.*, "Design of a compact wakefield accelerator based on a corrugated waveguide," in *Proc. NAPAC2019* Lansing, MI, USA, September 2019, pp. 232-234. doi:10.18429/JACoW-NAPAC2019-MOPLH26
- [3] K. J. Suthar *et al.*, "Investigation of various fabrication methods to produce a 180GHz corrugated waveguide structure in 2mm Diameter 0.5m long copper Tube for the compact wakefield accelerator for FEL facility," in *Proc. NAPAC2019* Lansing, MI, USA, 1-6 September 2019, pp. 286-289. doi:10.18429/JACoW-NAPAC2019-MOPL023
- [4] S. Lee *et al.*, "Design and fabrication challenges of transition section for the CWA module," presented at MEDSI'20, Chicago, USA, virtual conference, July 2021, paper WEPB04, this conference.

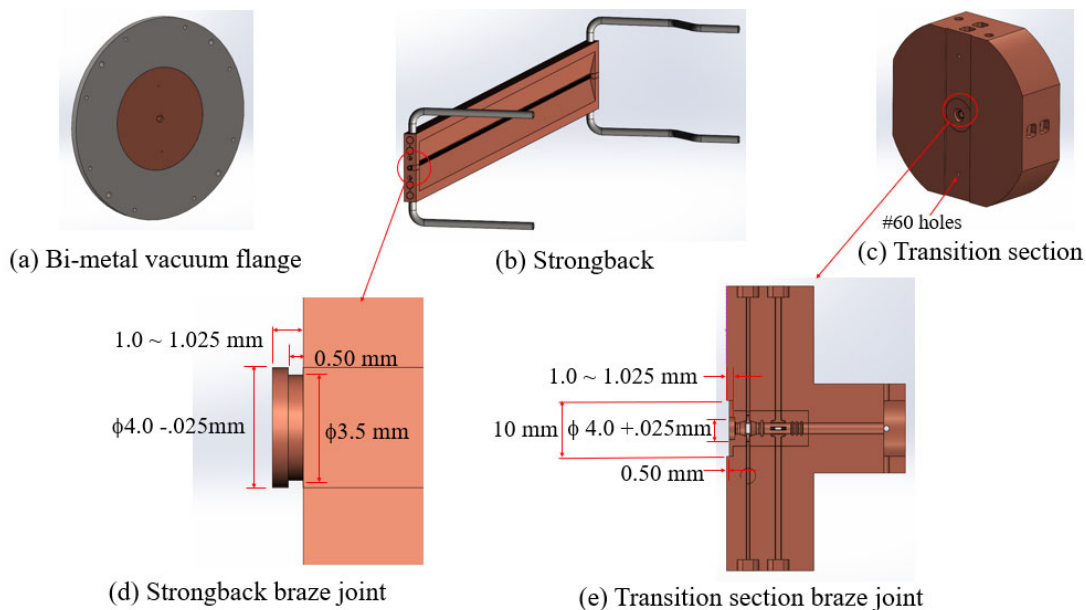


Figure 7: CWA module components and braze joints for strongback and transition section.

MECHANICAL DESIGN OF THE BOOSTER TO STORAGE RING TRANSFER (BTS) LINE FOR APS UPGRADE*

J. Liu[†], M. Borland, T. Clute, J. Downey, M. Jaski, U. Wienands
Argonne National Laboratory, Argonne, USA

Abstract

The APS Upgrade selected the horizontal injection scheme which requires exchanging the x and y emittances in the BTS transport line through a series of six skew quadrupoles, as well as matching the beam parameters to the APS Upgrade storage ring through two dipoles and a conventional pulsed septum. This paper presents the layout of this BTS line section in the storage ring tunnel and key components in this section including the mechanical design of dipole magnet, quadrupole and skew quad magnets, the vacuum system, the diagnostics system, and the supports. Finally, detailed mechanical design of this BTS line section in modules and some consideration for fabrication and installation are addressed.

INTRODUCTION

The Advanced Photon Source Upgrade Project (APS-U) is planning a storage-ring upgrade that will reduce the electron-beam emittance by a factor of ~ 75 [1]. This ultra-low emittance is achieved by replacing the present storage ring lattice with a hybrid multi-bend achromat (MBA) lattice [2, 3]. The MBA lattice will increase the x-ray coherent fraction by two orders of magnitude and decrease the horizontal source size by a factor of ~ 20 . The upgrade project adopts a horizontal injection scheme using a pulsed septum and fast stripline kickers for swap out injection and extraction [4]. The horizontal injection requires exchanging the x and y emittances in the BTS transport line [5]. To minimize change to the booster side of the BTS line, the section of BTS line on the SR side is redesigned and will be replaced with new a layout and components.

The scope of this paper mainly focuses on the mechanical design of the section of BTS transfer line located in the SR tunnel, including Lattice design, magnets design, vacuum system design, diagnostics design, and modular design of the whole section. Details of the designs are described in the following sections.

DESIGNS

The mechanical design of the BTS section is based on a beam physics design. The beam physics design developed for the APS-U is a horizontal injection scheme. The scheme requires exchanging the x and y emittances using six skew quadrupoles, as well as matching the beam

parameters to the APS-U storage ring. After iterative processes of lattice and magnetic designs, the parameters were finalized for the dipole, quadrupole, and skew quadrupole magnetic designs. The mechanical design was conducted from magnetic design according to the magnetic model. All new magnet designs are consistent with the SR magnet designs to take advantage of the work and experience with the SR magnets.

Lattice of BTS Section

Figure 1 shows the final layout of the BTS section. This section includes a total of 16 quadrupoles, 2 dipoles, 3 vertical correctors and 2 horizontal correctors. Of the 16 quadrupoles, 5 of them - BTS:BQ1 to BTS:BQ5 - are existing APS BTS magnets that will be reused. BTS:EXQs are skew quadrupoles and BTS:CQ1-3 and BTS:DQ1,2 are new quadrupole magnets. Skew and normal quadrupole magnets are of the same geometry but oriented in normal and skew orientation to reduce engineering work. All the new normal and skew quadrupoles include horizontal and vertical corrector trims. They will be operated at different parameters. BTS:BB1 and BTS:CB1 are new dipoles, but identical dipoles. BV1-3 are vertical correctors and BH1-2 are horizontal correctors. All the correctors are existing APS BTS magnets that will be reused. The locations of BPMs and Flags are also identified in Fig. 1. Between sections BTS:EXQ1B and BTS:BV3 will be the duck-under to allow passage across the BTS section.

Magnet Design

Table 1 lists the parameters of the BB1/CB1 dipoles in the BTS section on the SR side. Table 2 lists the parameters of the new skew and normal quadrupoles.

The mechanical design of the dipole magnet is shown in Fig. 2. The dipole yoke takes a three-piece design. Four taper dowel pins holes are drilled and reamed on pilot holes after aligning and clamping the yokes to the backplate. This method gives cost effective control of pole gap tolerance with high repeatability. It has been tested successfully on our SR dipole magnets.

Dipole coils are made of water-cooled hollow copper conductor of $SQ 6 \pm 0.1$ mm with 3.5 ± 0.1 mm I.D. Each coil is made of 5 pancakes, with each pancake having two five-turn layers.

* This research used resources of the Advanced Photon Source, a U.S. Department of Energy (DOE) Office of Science User Facility at Argonne National Laboratory and is based on research supported by the U.S. DOE Office of Science-Basic Energy Sciences, under Contract No. DE-AC02-06CH11357.

[†] jliu@aps.anl.gov

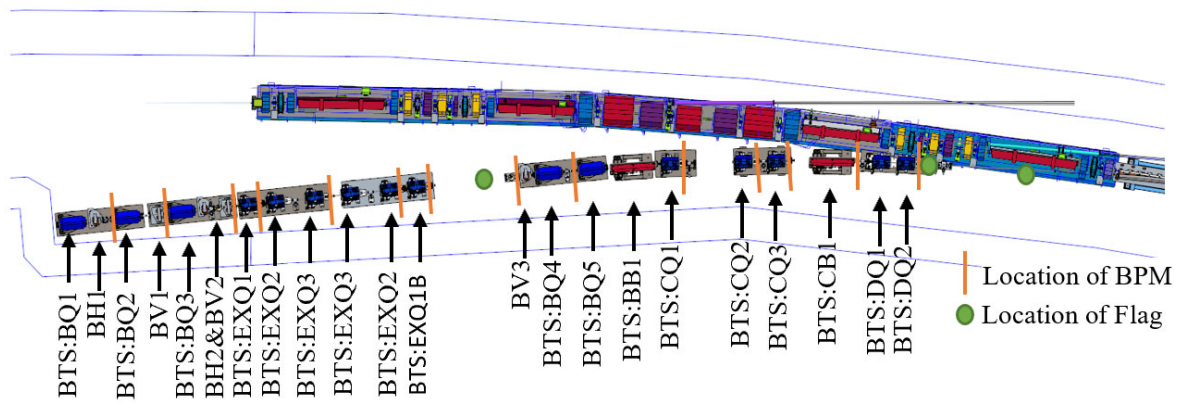


Figure 1: Layout of the BTS section in SR tunnel.

Table 1: BB1/CB1 Dipole Parameters

Parameter	Value	Unit
Length	1.18	m
Angle	0.07846	radian
B	-1.4	T
Critical energy	33.9	keV
SR Power	0.002023	W

Table 2: Normal and Skew Quadrupole Parameters

Parameter	Value	Unit
Length	0.482	m
Aperture	26	mm
Max required integrated gradient	27.9	T
Min required integrated gradient	7.8	T
Max integrated corrector	0.0077	T-m

within 25 μm . Coils are made of water-cooled hollow copper conductor of $\text{SQ } 6 \pm 0.1 \text{ mm}$ with $4 \pm 0.1 \text{ mm}$ I.D.

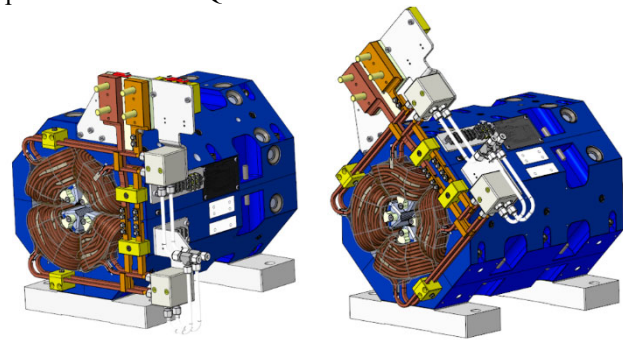


Figure 3: Mechanical design of the normal/skew quads.

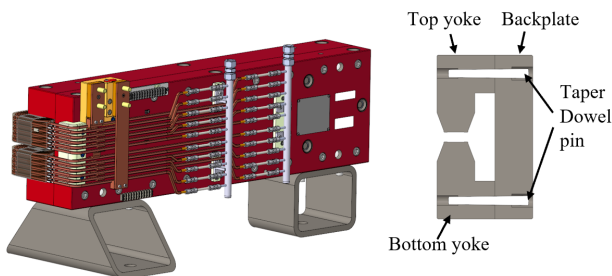


Figure 2: Mechanical design of the BB1/CB1 dipole.

Vacuum Systems

The BTS line overall length is 27.4 m. All the vacuum chambers are made of electro-polished stainless steel with CF flanges. The chamber ID is 22 mm in the quadrupole sections, 12 mm from before DLMB: BM1 to the septum magnet. Target pressure is lower than 5×10^{-9} Torr as read at the ion pumps. There will be one gate valve installed at each end of the section and a gauge tree near the connection of the BTS line to the storage ring. Gate valves are of the All-Metal variety to avoid radiation damage to a Viton/buton seal. The gauges are hardened against radiation with remote electronics and are capable of measuring into the 10^{-13} torr range. A total of seven pumps of 45 l/s will be installed at various sections to achieve the desired pressure.

Diagnostics

Three type of Diagnostics will be installed in this BTS section: Beam Position Monitor (BPM), beam profile monitor (Flag), and Fast Beam Loss Monitor (BLM). The locations of BPMs and Flags are shown in Fig. 1.

There is a total of 14 4-button BPMs. The mechanical design of the BPM is shown in Fig. 4. The BPM is made of four welded electrode feedthroughs in a SS holder. The electrode feedthroughs are the same as the standard BPMs used in the storage ring vacuum system of APS-U [7]. There is one welded bellow connected to one side of the BPM to accommodate thermal expansion. There are three survey cups on the feedthrough holder to allow proper alignment of the BPMs.

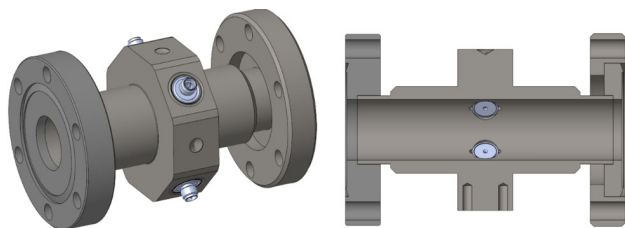


Figure 4: Mechanical design of BPM.

There will be one Flag in the zero-dispersion regions after the emittance-exchange section. There will be two Flags near the very end of the BTS line between the septum and the BTS: CB1 dipoles. The Flags will be reused from the existing BTS.

There will be a fast, fiber-based BLM installed in the BTS for localizing losses as well as measuring loss levels along the BTS line. The fiber bundle will run the length of the transport line, ending just upstream of the S39B:Q2 magnet. The fiber bundle will be as close to the beam pipe as possible, ideally being attached directly to the vacuum chamber. A photomultiplier tube at the upstream end of the fiber bundle will be used to establish the loss location by timing the arrival of pulses using an oscilloscope. Integration of the signal will allow determining total losses. The primary use of the BLM is to diagnose issues with poor transfer efficiency during commissioning and operations and to assist in BTS steering and optimization.

Support Tables

All support tables are designed to allow ± 12 mm component adjustment in x, y, and z directions. The rms vibration for frequencies above 0.1 Hz is less than 1 μm to keep the effective emittance of the injected beam from being inflated by more than a negligible 1 nm.

Module Assembly

BTS components are grouped into 12 modules for effective module assembly and installation, as shown in Fig. 5. All components will be pre-assembled into modules. The magnets will be aligned to each other within each module. The modules will then be fiducialized and delivered to the installation team to be installed. Table 3 lists the alignment requirements. Fig. 6 shows module 3 with all components in the module. Each module begins or ends with a bellows to facilitate easy connection of the vacuum chamber after installation.

Prior to shipment and storage, the vacuum system of each module will be blanked off and backfilled with $\frac{1}{2}$ psig dry nitrogen. All water-cooling lines will be blown dry and capped off. All components at risk of damage due to

vibration or shocks less than 3g will be supported and protected for transportation.

Power Supply and Control Systems

All power supply systems, diagnostics electronic systems, and control systems will be installed at the dedicated places close to sector 38 and 39. All cables will drop from an overhead cable tray to the components below. All magnet cooling water lines will connect with headers overhead.

CONCLUSION

The APS BTS transfer line section in the SR tunnel needs to be replaced to facilitate horizontal injection. All design work and the final design review have been completed. The APS-U BTS section is now proceeding through the procurement and fabrication phases. With all the experience gained from SR magnets and other components, this work on the BTS does not pose much risk to the project.

Table 3: Alignment Requirements

Parameter	Value	Unit
Fiducialization uncertainty for each magnet module, transverse	50 rms	μm
Align magnet-to-reference line within a module, transverse	100 rms	μm
Module fiducials to reference line, transverse	100 rms	μm
Module alignment to adjacent modules, transverse	100 rms	μm
Alignment magnet to magnet within a module, longitudinal	0.5 rms	mm
Alignment module to adjacent magnet modules, longitudinal	0.5 rms	mm

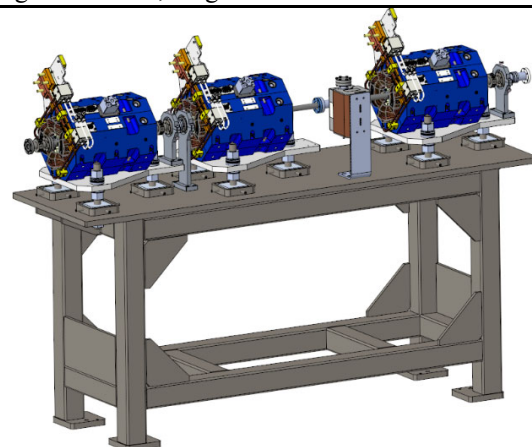


Figure 6: Mechanical design of the module 3.

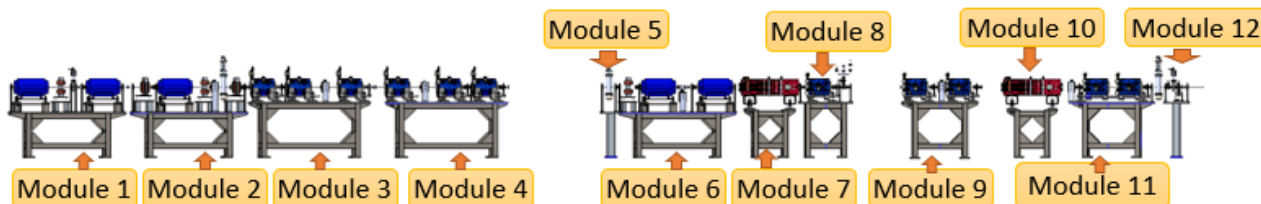


Figure 5: Modular layout of the BTS section.

REFERENCES

- [1] T. Fornek, "Advanced Photon Source Upgrade Project Final Design Report," APSU-2.01-RPT-003, 2019.
<https://doi.org/10.2172/1543138>
- [2] L. Farvacque *et al.*, "A low-emittance lattice for the ESRF," in *Proc. IPAC'13*, Shanghai, China, May 2013, paper MOPEA008, pp. 79-81.
- [3] M. Borland *et al.*, "Lower Emittance Lattice for the Advanced Photon Source Upgrade Using Reverse Bending Magnets," in *Proc NAPAC'16*, Chicago, USA, October 2016, pp. 877-880. doi:10.18429/JACoW-NAPAC2016-WEPOB01
- [4] L. Emery, M. Borland, "Possible long-term improvements to the Advanced Photon Source," in *Proc. PAC'03*, Portland, OR, USA, May 2003, paper TOPA014, pp. 256-258.
- [5] P. Kuske and F. Kramer, "Transverse emittance exchange for improved injection efficiency," in *Proc. IPAC'16*, Busan, Korea, May 2016, pp. 2028-2031. doi:10.18429/JACoW-IPAC2016-WE0AA01
- [6] M. Jaski, J. Liu, A. Donnelly, J. Downey, J. Nudell, J. Animesh, "Eight piece quadrupole magnet, method for aligning quadrupole magnet pole tips," United States: N.p, No. 9,881,723, 2018.
<https://www.osti.gov/servlets/purl/1418829>
- [7] J.A. Carter *et al.*, "Final Design of the APS-Upgrade Storage Ring Vacuum System," in *Proc. NAPAC2019*, Lansing, MI, USA, Sep. 2019, paper TUYBB3, pp. 315-317.
 doi:10.18429/JACoW-NAPAC2019-TUYBB3

MAGNET MODULE ASSEMBLY FOR THE APS UPGRADE*

K. J. Volin[†], R. R. Bechtold, A. Jain, W. G. Jansma, Z. Liu, J. J. Nudell, and Curt Preissner
Advanced Photon Source Upgrade Project, Argonne National Laboratory (ANL), Lemont, IL, USA

Abstract

With the Advanced Photon Source Upgrade (APSU) well into the procurement phase of the project, the APSU assembly team has completed a “DLMA Practice Assembly”, comprised of the support system and all magnets required to complete a module. The purpose of this test was to verify assembly and documentation procedures, ensure proper fit between mating components, and verify that alignment specifications can be met. The results of this exercise are presented. This test was completed on the ANL site and work continues in the APSU offsite warehouse where our first production plinths and girders have been shipped and where production modules are assembled. This space has been outfitted by ANL contractors and APSU assembly technicians with 1) five parallel DLM/FODO module assembly stations, each outfitted with a 3-ton overhead crane, retractable cleanroom, staging tables, and tools, and 2) two QMQ module assembly stations each outfitted with a 5-ton gantry crane, assembly support stands, staging tables, and tools. An overview of this production assembly space is also presented.

INTRODUCTION

A major part of the APS Upgrade [1] is the installation of a new Multi-Bend Achromat (MBA) storage ring. The MBA storage ring is comprised of 40 sectors. Each sector is approximately 27.6 meters long (path length) with mirror symmetry about the central Q-bend (transverse-gradient dipole) magnet. There are a total of 1320 magnets comprising the new MBA storage ring. Each storage ring sector consists of three large modules with two support plates, supporting three magnets each (QMQ), bridging between them. Figure 1 shows one of the 40 sectors of the storage ring. The upstream Doublet-L-bend-Multiplet (DLM) module A supports a quadrupole doublet, an L-bend, and a multiplet array of magnets. In the center of the sector is the curved Focusing-Defocusing (FODO) module which supports five large bending/focusing magnets. The down-stream DLM module B is a mirror image of the upstream DLM module A. Each module contains a concrete plinth grouted to the floor with an alignable support girder mounted on top, which in turn supports the individual magnet strings, vacuum system, and auxiliary hardware. In addition to the 200 magnet modules comprising the storage ring, a full sector mockup

of 5 modules will be assembled and used for storage ring installation training.

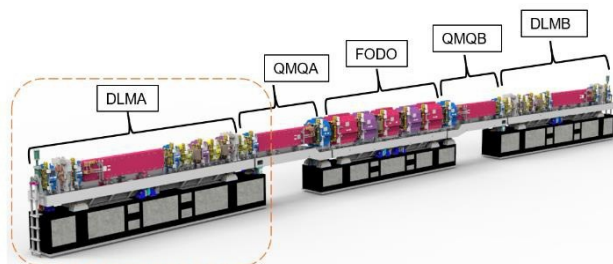


Figure 1: Typical APSU arc sector. DLMA Module (circled above) used for the first practice assembly.

MODULE ASSEMBLY OVERVIEW

To assemble the 123 DLMA, DLMB, and FODO magnet modules, 5 assembly stations were each outfitted with a 3-ton overhead crane, steel weldment tables for staging the magnets, stainless steel (SS) tables for staging the vacuum strings, and an ISO7 (Class 10,000) retractable clean room for installing the particle-sensitive open vacuum chambers. To assemble the 82 QMQA and QMQB magnet modules, two assembly stations were each outfitted with a 5-ton gantry crane, steel weldment assembly stands for mocking up the support ends of the DLMA/B and FODO plinths, steel weldment tables for staging the magnets, and SS tables for staging the vacuum strings. The QMQ magnet modules are assembled with complete, sealed, nitrogen backfilled, vacuum chambers. There is no need for a clean room environment for the QMQ.

DLMA Practice Assembly

With the arrival of the APSU vacuum system later than the bulk of the accelerator components, a first “practice assembly” was planned to use all magnets and support system components required to complete a DLMA assembly (see Fig. 1). The purpose of this activity was to verify assembly and documentation procedures, ensure proper fit between mating components, and verify that alignment specifications can be met.

Magnet Installation Extremely precise alignment of magnets within a module is necessary for achieving key performance parameters in the new machine. To achieve alignment specifications, we rely on precise machining of the girder and magnets, in conjunction with shimming.

Each magnet is fiducialized on a rotating wire bench before it is installed on a module [2]. This relates the magnet’s magnetic center to its fiducials, as well as documenting offsets from the magnetic center to its X, Y, and Z reference

* This research used resources of the Advanced Photon Source, a U.S. Department of Energy (DOE) Office of Science User Facility, operated for the DOE Office of Science by Argonne National Laboratory under Contract No. DE-AC02-06CH11357. Extraordinary facility operations were supported in part by the DOE Office of Science through the National Virtual Biotechnology Laboratory, a consortium of DOE national laboratories focused on the response to COVID-19, with funding provided by the Coronavirus CARES Act.

[†] kjvolin@anl.gov



Figure 2: Quadrupole magnet enroute via overhead crane to its final location in the DLMA module (Image by JJ Starr/Argonne National Laboratory).

mounting surfaces. Typical X and Y errors of a magnet's reference surfaces are less than 50 microns.

Prior to mounting magnets on the first article, shims for each magnet were chosen based on magnetic measurements and placed on the girder mounting surfaces to account for the slight errors in position of the magnet's X and Y reference mounting surfaces. Then, each magnet was lifted into position using an overhead crane and bolted into place on the girder (Fig. 2).

Survey Results Fiducials on 9 out of 11 magnets of the DLMA array (excluding Fast Correctors) were measured from 5 stations using a Leica AT930 laser tracker [3]. Data was analysed using the Spatial Analyzer software package. Temperature was not controlled during the ~2 hour measurement.

A Spatial Analyzer file was developed which contains the ideal locations of each magnet center or vertex point in the DLMA array [3], based on the Lattice File. Once the measurement of each magnet fiducial in the array is complete, the individual magnet fiducialization data is imported and fitted using Least Squares to the new measured fiducial locations of that magnet in the array. Then, the X, Y, and Z offsets (difference in location between the ideal magnet center points and measured magnet center points) may be extracted and plotted.

The magnet alignment specifications and results in the X and Y directions are shown below in Table 1 and Figs. 3 and 4. The magnet alignment in the critical X and Y directions far surpasses the 30 microns RMS tolerance.

Table 1: DLMA Practice Assembly Survey Results

	X-Offsets	Y-Offsets
Specification	30 μ m, RMS	30 μ m, RMS
Measurement	9 μ m, RMS	13 μ m, RMS

The magnitude of measurement error is estimated to be 7 μ m RMS. The magnitude of the alignment error in X and Y is 16 μ m RMS. RMS error is derived using a best-fit line

through the measured magnet center offsets from ideal position in X and Y. Overall, the alignment is exceptionally good on the DLMA practice assembly, and the magnet positioning scheme is deemed a success. The completed practice assembly in ANL Building 375 is shown in Fig. 5.

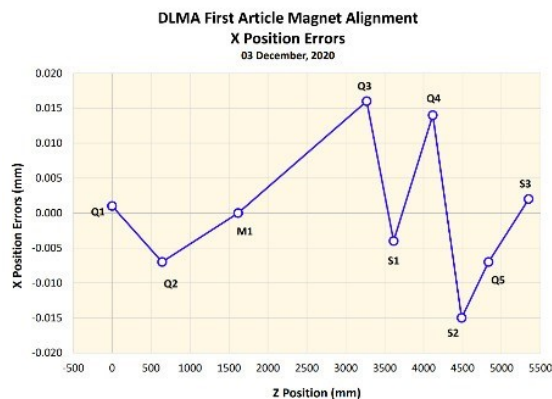


Figure 3: DLMA first article, magnet X-position errors.

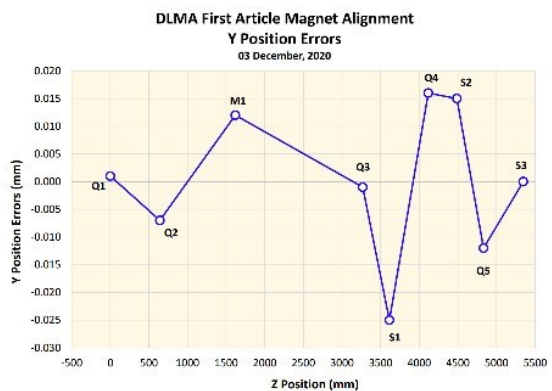


Figure 4: DLMA first article, magnet Y-position errors.

Assembly Update

Outfitting of the off-site Assembly Area is complete. As of this writing, twenty-one (21) production support systems

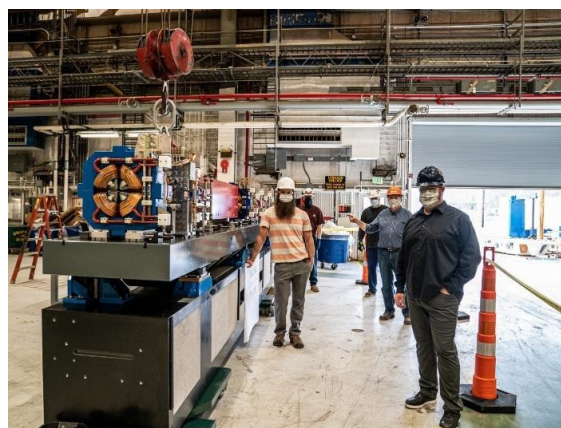


Figure 5: The completed DLMA practice assembly.



Figure 6: Picture showing the off-site Module Assembly Area including overhead cranes, retracted cleanrooms, and several modules in the magnet mounting process.

have arrived, and fiducialized magnets are available to complete the magnet portion of Module Assembly. Thus, production work has begun on training technicians, and mounting and aligning magnets on Support Systems (see Fig. 6).

CONCLUSION

The preparation for the assembly and testing of the accelerator magnet modules is nearly complete. A first article practice assembly involving the mounting of all magnets onto a DLMA support system showed achievement of magnet alignment goals stated in the APSU Functional Requirements Document. The APSU Project has begun building partial production storage ring modules as we await arrival of the vacuum systems.

REFERENCES

- [1] "APS Upgrade Project Final Design Report," APSU-2.01-RPT-003, 2019. doi:10.2172/1543138
- [2] S. Izzo, A. Jain, C. Doose, and W. Jansma, "Magnet measurement systems for the Advanced Photon Source Upgrade," presented at the 11th Int. Conf. on Mechanical Eng. Design of Synchr. Rad. Equipment and Instrum. (MEDSI'20), Chicago, USA, Jul. 2021, paper WEPB03, this conference.
- [3] W. Jansma, J. Nudell, and A. Jain, "APS Upgrade Girder Alignment," presented at 2021 Virtual Mini-Workshop on Girders and Alignment, Hamburg, DE, May 10-11, 2021.

MULTIBODY SIMULATIONS WITH REDUCED ORDER FLEXIBLE BODIES OBTAINED BY FEA

P. Brumund*, T. Dehaeze¹, ESRF, Grenoble, France

¹also at Precision Mechatronics Laboratory / A&M department, Liege, Belgium

Abstract

Tighter specifications in synchrotron instrumentation development force the design engineers more and more often to choose a mechatronics design approach. This includes actively controlled systems that need to be properly designed. The new Nano Active Stabilization System (NASS) for the ESRF beamline ID31 was designed with such an approach.

We chose a multi-body design modelling approach for the development of the NASS end-station. Significance of such models depend strongly on its input and consideration of the right stiffness of the system's components and sub-systems. For that matter, we considered sub-components in the multi-body model as *reduced order flexible bodies* representing the component's modal behaviour with reduced mass and stiffness matrices obtained from finite element analysis (FEA) models. These matrices were created from FEA models via modal reduction techniques, more specifically the component mode synthesis (CMS). This makes this design approach a combined multibody-FEA technique.

We validated the technique with a test bench that confirmed the good modelling capabilities using reduced order flexible body models obtained from FEA for an amplified piezoelectric actuator (APA).

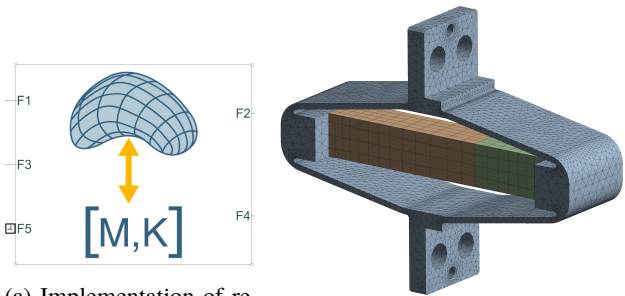
INTRODUCTION

To meet its tight requirements in terms of precision and stability, a “model based design” approach was chosen for the development of the new ID31 end-station [1]. This type of design approach joins the need for dynamical models to test control architectures and to help specifying the requirements in the detail design stage.

We used a *MATLAB Simscape* multibody model for the detailed modular based design which is used to simulate the dynamical behaviour of the system. These models consist of *SIMULINK*-typical blocks, each representing one body or link. Such models were formerly limited to simple rigid bodies linked by “weak” links. They can be used as a first approximation. However, performances are often limited by resonances of flexible elements, i.e. the approximation by multiple solid bodies is not valid anymore.

Since recently, such *Simscape* models can be extended by a block named “Reduced Order Flexible Solid” (see Fig. 1a). This body consists of several interface points (here 5 points) and reduced FEA stiffness \hat{K} and mass matrices \hat{M} that describe its dynamical characteristics. This extends the body's represented behaviour in the simulations from pure inertial rigid-body representation to elastically deformable behaviour.

* brumund@esrf.fr



(a) Implementation of reduced order model in *Simscape* multibody simulation block [2].

(b) Meshed FEA model of an amplified piezoelectric actuator. Number of nodes: $\approx 130\,000$.

Figure 1: Flexible body used in a *Simscape* model as a reduced model from a fully meshed FEA model.

Application: Amplified Piezo Actuator

For the ID31 nano-end-station development we applied the FEA modal reduction technique to obtain reduced stiffness \hat{K} and mass matrices \hat{M} of key flexible components. This enables us to accurately model the dynamic behaviour of the end-station's nano-active-stabilization-system (NASS) hexapod. We applied the method on the hexapod struts containing amplified piezo actuators (type APA300ML, [3]) and flexible joints. We model the APAs as reduced order flexible bodies, which is explained in this paper. Figure 1b shows the fully meshed FEA model of the APA that we used for that matter. For the modal reduction of these APAs we used the commercial FEA software *ANSYS*. The resulting data was used as input in the *Simscape* multibody analysis.

REDUCTION OF AMPLIFIED PIEZO

We applied the modal reduction technique from FEA (also called component mode synthesis) for the reduction of the high number of FEA degrees of freedom (DoF) to a smaller number of retained degrees of freedom¹. For the example of the APA in Fig. 1b this results in a reduction from about $130\,000 \times 3 = 390k$ DoF of the 3D FEA model down to only tens of DoFs, as explained in the next section. This reduced amount of DoF makes the model easy to integrate in a multibody simulation.

FEA Modal Reduction Model

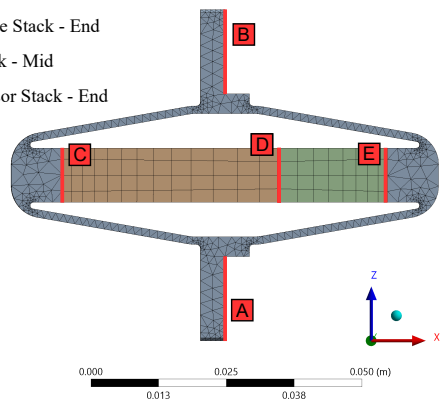
The *ANSYS* FEA model used for the modal reduction is shown with the used meshed in Fig. 2a. The points A to E mark the interfaces that were linked via a multi-point-

¹ Additional info on our applied procedure can be found in: <http://doi.org/10.5281/zenodo.5094419>

constraint to a pilot node (called remote points in ANSYS) on respective reference locations, as explained in the provided appendices. This couples the movement of the chosen interfaces to the pilot nodes.

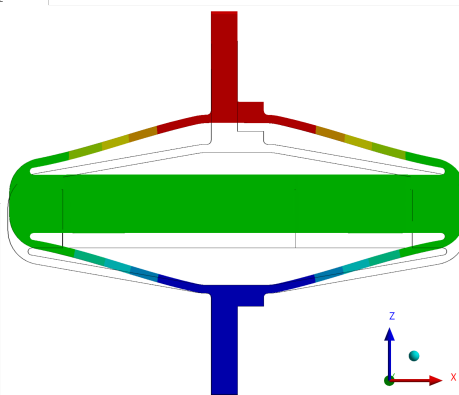
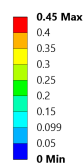
Remote Points

- A Bottom
- B Top
- C Piezo Force Stack - End
- D Piezo Stack - Mid
- E Piezo Sensor Stack - End



(a) ANSYS modal reduction model with labeled retained interface “remote points” (A to E).

E: fixed-freeZ, 5kg
 Total Deformation - Mode 1
 Type: Total Deformation
 Frequency: 95.9 Hz
 Unit: m
 26/03/2021 10:16



(b) Modal analysis total deformation results. The plot shows the first mode at $f_1 = 95.9$ Hz from FEA with 5 kg point mass attached to top node. Bottom node fixed and top node only free in z-direction.

Figure 2: Super element generation model and first mode from FEA.

The modal reduction was then performed retaining only the 6 DoFs of each of the 5 shown points, thus resulting in $m = 6 \times 5 = 30$ retained physical DoFs. In addition, $p = 6$ additional Eigenmodes were retained, creating 6 additional generalized coordinates. This procedure results in the reduced mass \hat{M} and stiffness matrices \hat{K} to be both square-matrices of length size $(m + p) \times (m + p) = 36 \times 36$. Thus the whole flexible behaviour of the reduced APA is now represented by these 36 DoFs. We used the “fixed-interface method”, also called “Craig-Bampton-method” for the reduction [4, 5].

Simulation

Structural Statics And Dynamics

Table 1: Material Properties used for the FEA Modal Reduction Model in Fig. 2a; Stated data: Young’s Modulus E , Poisson Ratio ν and Density ρ .

	E GPa	ν -	ρ kg/m ³
Stainless Steel	190		
Piezoelectric Ceramics (PZT)	49.5	0.31	7800

Table 1 lists the material properties used for the reduction model. The stainless steel properties were fixed for the frame, whereas the Young’s modulus E for the piezo-electric material PZT was obtained by matching the vendors specifications² in terms of linear static stiffness ($k_s = 1.79 \text{ N } \mu\text{m}^{-1}$) free-free Eigenfrequency and blocked-free Eigenfrequency as good as possible. The result is typical for PZT data.

We confirmed the model by verifying also the first Eigenfrequency for the blocked-free condition and an added load of $m = 5$ kg to the top. The result is shown in Fig. 2b. From the vendors specifications for stiffness and given load this should result in

$$f_1 = \frac{1}{2\pi} \sqrt{\frac{k_s}{m}} = 95.3 \text{ Hz}, \quad (1)$$

which is very close the calculated FEA result for the discrete model of $f_{1,FEA} = 95.9$ Hz.

Test-Bench for Model Validation

A test bench shown in Fig. 3 was used to identify the dynamical behavior of the APA and to validate the reduced order model of the APA. To do so, a *Simscape* model of this bench was developed with the APA being modeled with the reduced order model. Both measured dynamics can then be compared.

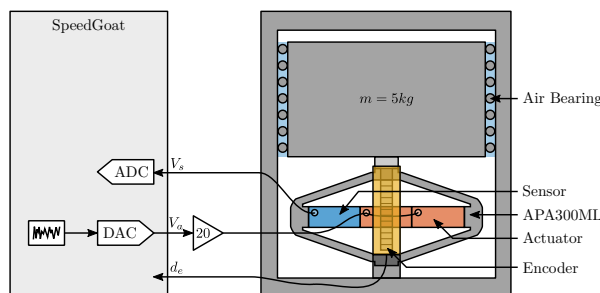


Figure 3: Schematic of the test bench used.

Depending on the application, one can draw advantage of the fact that the APAs (the trapezoid in Fig. 3) consist of 3 piezoelectric stacks in series. To obtain information on the compression/extension of the whole APA, one piezo stack is used as a force sensor, and 2 stacks as force actuator by wiring them separately (cf. Fig. 3 and technique from [6]).

² Specifications APA300ML: <https://www.cedrat-technologies.com/fileadmin/datasheets/APA300ML.pdf> (last accessed 26/3/2021)

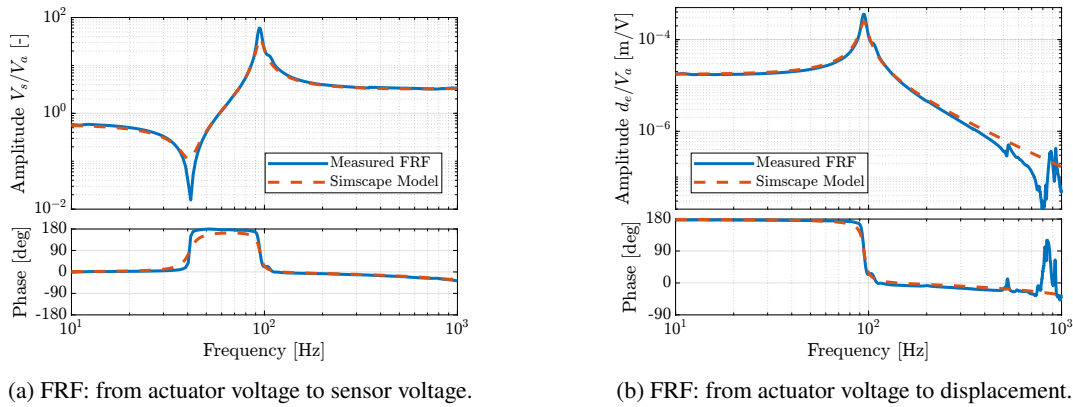


Figure 4: Frequency response functions (FRF) of experimental results in comparison with simulations using reduced order model from FEA.

In order to measure the dynamics of the APA, a digital to analog converter is used to generate a low pass filtered excitation signal V_a which is applied to the two actuator stacks. The voltage generated by the force sensor stack V_s as well as the vertical displacement d_e measured by the encoder are recorded simultaneously.

Then, two Frequency response Functions (FRF) can be computed:

1. actuator voltage to sensor voltage (Fig. 4a) $V_s/V_a(s)$,
2. actuator voltage to displacement (Fig. 4b) $d_e/V_a(s)$.

The comparison of experimental data (blue line) with the simulation (red dashed line) using the reduced order model reveals sufficient agreement for both FRFs to confirm the use of the model for further dynamical analysis using this procedure.

It is found that the open-loop transfer function from V_a to V_s is very typical for APA [6, Fig. 3]. Therefore, the force sensor stack can be used to actively damp the resonance of the APA at around $f_1 \approx 95$ Hz using a technique called “Integral Force Feedback”. This technique does not compromise the high-frequency isolation as compared with passive damping techniques and is used in the concerned project’s nano-hexapod [7].

CONCLUSION

Modal reduction of finite element models to a more practical reduced number of DoFs make implementation of flexible bodies of any geometry in multibody models possible. The user can decide to perform the modal reduction to include a desired number of Eigenmodes and frequencies in the reduced order model. The application of this technique for the design of the nano-endstation project was very promising and validated on a test bench.

One limitation regarding the response of the reduced model is the unknown damping. Such damping can however be experimentally estimated if the parts are previously

available. Also, the reduction procedure is limited to linear behaviour of FEA models due to the reduction procedure via linear modal analysis.

ACKNOWLEDGEMENTS

We thank the precision electronics lab (PEL) team (L. Ducotte and H.-P. Van der Kleij) for providing us with the necessary space and equipment to perform the model tests.

REFERENCES

- [1] T. Dehaeze, C. Collette, and M. Magnin-Mattenet, “Sample Stabilization for Tomography Experiments in Presence of Large Plant Uncertainty,” in *Proc. MEDSI’18*, Paris, France, Jun. 2018, pp. 153–157. doi: 10.18429/JACoW-MEDSKI2018-WEOAMA02.
- [2] *MATLAB documentation, Reduced Order Flexible Solid - Flexible body based on a reduced-order model*, 2021, <https://www.mathworks.com/help/physmod/sm/ref/reducedorderflexiblesolid.html> MATLAB, version 9.10.0 (R2021a).
- [3] B. Laluc, T. Maillard, and A. Riquer, “Piezo Technology in Synchrotron,” in *Proc. of MEDSI’18*, Paris, France, Jun. 2018, pp. 321–323. doi: 10.18429/JACoW-MEDSI2018-THOPMA01.
- [4] *Ansys® Academic Research Mechanical APDL, Release 2020 R2, Help System, Theory reference*, 15.6. Substructuring Analysis, 2020, ANSYS Inc.
- [5] R. R. Craig and M. C. C. Bampton, “Coupling of substructures for dynamic analyses,” *AIAA Journal*, vol. 6, no. 7, pp. 1313–1319, Jul. 1968, issn: 0001-1452, 1533-385X. doi: 10.2514/3.4741.
- [6] A. Souleille *et al.*, “A concept of active mount for space applications,” *CEAS Space Journal*, vol. 10, no. 2, pp. 157–165, Jun. 2018, issn: 1868-2502, 1868-2510. doi: 10.1007/s12567-017-0180-6. <http://link.springer.com/10.1007/s12567-017-0180-6>
- [7] T. Dehaeze, J. Bonnefoy, and C. Collette, “Mechatronics Approach for the Development of a Nano-Active-Stabilization-System,” presented at MEDSI’20, Chicago, IL, USA, Jul., 2021, paper TUIO02, this conference.

ForMAX ENDSTATION – A NOVEL DESIGN COMBINING FULL-FIELD TOMOGRAPHY WITH SMALL- AND WIDE-ANGLE X-RAY SCATTERING

J. B. González[†], S. A. McDonald, K. Nygård, L. Roslund, MAX IV Laboratory, Lund, Sweden

Abstract

ForMAX is a new beamline at the MAX IV Laboratory for multi-scale structural characterization of hierarchical materials from nm to mm length scales with high temporal resolution. This is achieved by combining full-field microtomography with small- and wide-angle x-ray scattering (SWAXS) in a novel manner. The principal components of the endstation consist of two units of beam conditioning elements, a sample table, an evacuated flight tube and a detector gantry. The beam conditioning units include a diamond vacuum window, an attenuator system, a fast shutter, a slit collimation system, two sets of compound refractive lenses, three x-ray beam intensity monitors, a beam viewer and a telescopic vacuum tube. The sample table has been optimized with respect to flexibility and load capacity, while retaining sub-micron resolution of motion and high stability performance. The nine metre long and one metre diameter evacuated flight tube contains a motorised detector trolley, enabling the sample-detector position for small-angle x-ray scattering (SAXS) to be easily adjusted under vacuum conditions. Finally, a two metre high and two metre wide granite gantry permits independent and easy movement of the tomography microscope and wide-angle x-ray (WAXS) detector in and out of the x-ray beam. To facilitate propagation-based phase-contrast imaging and mounting of bulky sample environments, the gantry is mounted on motorized floor rails. All these characteristics will allow to combine multiple complementary techniques sequentially in the same experiment with fast efficient switching between setups. The ForMAX endstation is presently in the design and construction phase, with commissioning expected to commence early 2022.

INTRODUCTION

Many natural and man-made materials are hierarchical, exhibiting important structure at several different length scales. In order to understand the structure-function relationship in such materials, one needs to characterise the structure at all these different length scales with sufficient temporal resolution to follow processes *in situ*. The versatile ForMAX instrument will address this problem by combining two complementary techniques – full-field tomographic imaging on μm to mm and SWAXS on nm length scales.

The main technical challenge when combining full-field tomography and SAXS stems from space constraints behind the sample; in full-field tomography one monitors the x-ray beam transmitted through the sample in forward di-

rection, while in SAXS one records the x-ray beam scattered at small angles $\leq 3^\circ$, i.e., in nearly forward direction. The novel approach at ForMAX is sequential tomography and SWAXS experiments, based on a motorized detector gantry that allows the tomography microscope (and WAXS detector) to be readily translated in and out of the x-ray beam, thereby allowing a fast and efficient switch of modes of operation.

In this conference paper, we outline the design of the ForMAX endstation. For an overview of the main components, see Fig. 1.

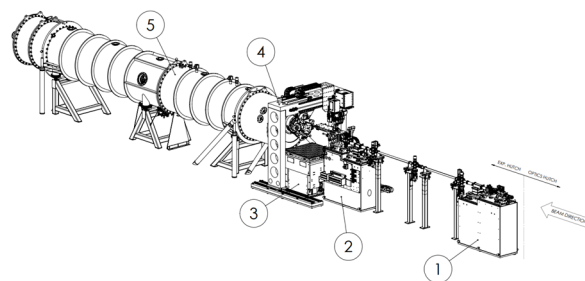


Figure 1: Main components of the endstation: (1) BCU I, (2) BCU II, (3) sample table, (4) detector gantry, and (5) flight tube.

BEAM CONDITIONING UNITS

Two beam conditioning units (hereafter BCU I and BCU II), located upstream of the sample table, include elements and equipment needed for fine-tuning the beam characteristics (final size, microfocus, beam positioning, attenuation, etc.) for each experiment performed in the endstation. Both units consist of two independent granite blocks grouted to the floor and with the different elements mounted on the top surfaces, facilitating alignment with the beam.

BCU I is located 5 metres upstream of the sample table and includes a diamond vacuum window, an attenuator system, a fast shutter, horizontal and vertical slits and a set of beryllium compound refractive lenses (CRLs). The CRLs permit expansion of the beam during tomography experiments and their position is motorized in order to facilitate alignment in the beam.

BCU II is located directly upstream of the sample table and includes a motorized set of CRLs for microfocusing during SWAXS experiments, a beam diagnostic module, horizontal and vertical slits and a telescopic vacuum tube, permitting the users to minimize the x-ray beam path in air. The beam diagnostic module includes three x-ray beam intensity monitors and a YAG crystal screen.

[†] joaquin.gonzalez@maxiv.lu.se

All the elements of the BCUs are designed for operation under high vacuum. Table 1 shows the respective position of the elements from the beam source.

Table 1: BCU Elements and Their Distance From Source

BCU elements	Distance from source (mm)
Diamond window	35750
Attenuator system	35900
Fast shutter	36100
Slits (BCU I)	36300
Tomography CRLs	36500
μ focus CRLs	40500
Beam diagnostic module	40700
Slits (BCU II)	41500
Telescopic vacuum tube	41600-42000

SAMPLE TABLE

The sample table, centred at 42 metres downstream of the source, will support the sample environments, sample manipulation stages and other equipment needed to perform SWAXS and tomography experiments. It has an available top surface of 800 × 800 mm and permits positioning of the sample environment in vertical, lateral and pitch. It is based on the “skin” concept design developed at the ALBA Synchrotron, which provides high stability and excellent resolution performances [1].

It consists of a granite block base grouted to the floor with two movable lateral plates driven by ball screws with linear guides actuated by stepper motors. Lateral plates are linked together by a top plate articulated by flexure hinges, providing vertical and pitch motions. The lateral motion stage, also driven by a ball screw with linear guides, is added on top of the previously described assembly. The granite block functions as a stable and stiff reference for the whole system. The ball screws have low axial clearance in order to assure good repeatability, while the linear guides are slightly preloaded for stiffness. Finite element analysis (FEA) shows the first mode of vibration to be above 65 Hz.

Table 2 shows the range and resolution for the respective motions of the sample table. The load capacity of the table is 200 kg.

Table 2: Ranges and Resolutions of Sample Table Motions

Axis ¹	Range	Resolution ²
X	±100 mm	0.3125 μ m
Y	±105 mm	0.3125 μ m
Pitch	±10 mrad	0.42 μ rad

DETECTOR GANTRY

The granite detector gantry is located around the sample position, 42 metres from the source. The tomography microscope and the WAXS detector, both commercial but specifically designed for the ForMAX beamline, will be mounted on the gantry. Two independent linear stages, installed on the gantry lintel, permit easy and independent lateral movement of microscope and detector, in and out of the beam. Additionally, two independent vertical stages permit vertical adjustment of the microscope and the detector. The whole system is mounted on motorized floor rails. All the stages consist of low axial clearance ball screws and preloaded linear guides driven by stepper motors.

The motorized floor rails along the beam (between 41 and 42.5 metres from the source) facilitate propagation-based phase-contrast imaging and mounting of bulky sample environments on top of the sample table. Furthermore, the two independent lateral linear stages allow users to combine multiple complementary techniques sequentially in the same experiment, with fast efficient switching between modes of operation. The range and resolution for the respective motions of the detector gantry are shown in Table 3.

Table 3: Ranges and Resolutions of Detector Gantry Motions

Axis ¹	Range	Resolution ²
Gantry Z	1500 mm	10 μ m
WAXS X	670 mm	10 μ m
WAXS Y	±10 mm	10 μ m
Microscope X	670 mm	1 μ m
Microscope Y	±15 mm	1 μ m

The overall design is optimized to permit free access for users to the sample table from the outboard side of the end-station.

The system includes three modes of operation. First, a parking mode where the gantry is in an upstream position with the microscope and detector out of the beam and their lateral motions are disabled, thus avoiding collisions with BCU I. Second, a microscope operation mode with the WAXS detector in parking position. In this case only the lateral motion of the detector is disabled and any collision with the flight tube is avoided. Third, an operation mode where the microscope and the WAXS detector are free to move in and out of the beam. Detector gantry is shown in Fig. 2.

¹ With Z axis following beam direction, Y axis vertical direction and X axis perpendicular to both.

² Resolution defined as minimum incremental motion per full step.

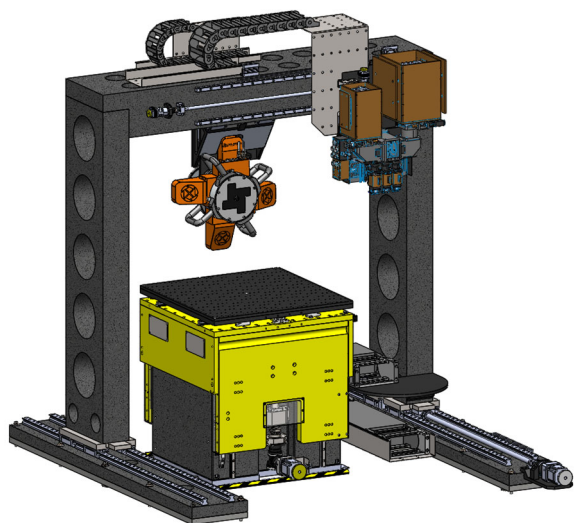


Figure 2: Sample table, detector gantry, tomography microscope and WAXS detector.

FLIGHT TUBE

A critical component of the endstation is the evacuated flight tube between the sample and the SAXS detector, which minimizes parasitic scattering and absorption of the x-ray beam between the sample and the detector. The flight tube consists of a stationary, eight metre long and one metre diameter vacuum chamber, with the SAXS detector installed inside it on motorized rails.

Similar flight tube concepts have been developed at other SAXS beamlines [2]. The vessel is built up of five sections: a 1 metre long upstream end section, two 0.5 metre long downstream end sections, and two long middle sections with a combined length of 6 metres. The two downstream end sections can be easily removed for maintenance tasks. Additionally, the flight tube is equipped with a quick release door in the upstream and inboard side. For an overview of the flight tube, see Fig. 3.

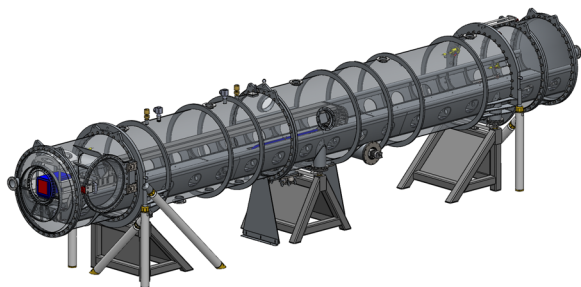


Figure 3: Flight Tube and SAXS detector.

The motorized rails along the beam are driven by a belt system and a servo motor located outside of the vacuum chamber by means of a rotary feed-through. The whole system is supported by a rigid girder mechanically decoupled from the vacuum chamber through vacuum bellows. This characteristic keeps the girder isolated from the vibration behaviour of the vacuum chamber. Moreover, the SAXS detector is equipped with two additional motions, vertical and lateral, for adjusting position in the beam.

Personal safety is guaranteed by the MAX IV Personal Safety Systems. A search procedure and emergency pull-wire switches inside of the chamber guarantee no personnel can be trapped inside. The flight tube is designed for operation under rough vacuum.

CONCLUSIONS

We have presented the ForMAX endstation, with a focus on the novel design for multi-scale structural characterization by combined full-field tomography and SWAXS. The versatile sample table and flight tube designs will permit state of the art SWAXS experiments to be performed with a wide range of different sample environments. The detector gantry will allow full-field tomography and SWAXS experiments to be combined sequentially in the same experiment with fast and efficient switching between setups. The ForMAX endstation is presently in the design and construction phase. Commissioning and user operation is expected to commence early and autumn 2022, respectively.

ACKNOWLEDGEMENTS

The construction of the ForMAX beamline is funded by the Knut and Alice Wallenberg Foundation, while the operation costs are covered by industry via Treesearch (www.treesearch.se), a national platform for research on new materials and speciality chemicals from forest raw material.

The authors wish to acknowledge all those most involved in the design: Jörgen Hellborg, Karl Åhnberg, El Sayed El Afifi, Mohammad Al-Najdawi, Suleyman Malki, Julio Lidon, Hussein Al-Sallami, Keyu Zhou, Alina Andersson, Behrouz Afzali, Magnus Malmgren, Albert Torrente, Gábor Felesuti, Marek Grabski, Byungnam Ahn, Hasse Andersson, Joakim Edlund, Niklas Jönsson, Tobias Jeppsson, and Silvia Forcat.

REFERENCES

- [1] C. Colldelram, C. Ruget, and L. Nikitina, "ALBA XALOC Beamline diffractometer table skin concept", in *Proc. MEDSI'10*, Oxfordshire, UK, July 2010, Vol 1, paper e44. doi:10.1017/S2044820110000754
- [2] J. Léonardon *et al.*, "Design of a new detector tube for wide, small and ultra small-angle X-ray scattering", in *Proc. MEDSI'14*, Melbourne, Australia, October 2014, online.

DESIGN AND COMMISSIONING OF THE TARUMÃ STATION AT THE CARNAÚBA BEAMLINE AT SIRIUS/LNLS

R. R. Galdes^{†1}, C. S. N. C. Bueno, L. G. Capovilla, F. R. Lena, D. Galante, L. C. Guedes, L. M. Kofukuda, G. N. Kontogiorgos, S. A. L. Luiz, G. B. Z. L. Moreno, I. T. Neckel, C. A. Pérez, A. C. Piccino Neto, A. C. Pinto, C. Sato, J. L. Silva, A. P. S. Sotero, V. C. Teixeira, H. C. N. Tolentino, W. H. Wilendorf, Brazilian Synchrotron Light Laboratory (LNLS), Brazilian Center for Research in Energy and Materials (CNPEM), 13083-970, Campinas, São Paulo, Brazil
¹also at the Eindhoven University of Technology (TUe), 5612AZ Eindhoven, The Netherlands

Abstract

TARUMÃ, the sub-microprobe station at CARNAÚBA (Coherent X-Ray Nanoprobe Beamline) at Sirius at the Brazilian Synchrotron Light Laboratory (LNLS), has been designed to allow for simultaneous multi-analytical X-ray techniques both in 2D and 3D. A systemic approach, heavily based on precision engineering concepts and predictive design, has been adopted for first-time-right development, effectively achieving all-together: the alignment and stability requirements of the large KB mirrors with respect to the beam and to the sample; and the nanometer-level positioning, flyscan, tomographic and setup modularity requirements of the samples. This work presents the overall station architecture, the key aspects of its main components, and the first commissioning results.

INTRODUCTION

CARNAÚBA (Coherent X-Ray Nanoprobe Beamline) [1] belongs to the first set of beamlines of Sirius [2], the 4th-generation synchrotron light source at the Brazilian Synchrotron Light Laboratory (LNLS). It is meant for simultaneous multi-analytical X-ray techniques in 2D and 3D, with diffraction (XRD), spectroscopy (XAS), fluorescence (XRF), luminescence (XEOL) and ptychographic coherent diffractive imaging (ptycho-CDI). It is based on an all-achromatic optical design for the energy range from 2.05 to 15 keV, granting a flux up to $1e11$ ph/s/100mA at the probe for high-throughput experiments with flyscans.

TARUMÃ is its sub-microprobe station, located at 136 m from the undulator source, in a satellite building, and reaching fully-coherent monochromatic beam sizes from 550 to 120 nm after the achromatic KB (Kirkpatrick-Baez) focusing optics. In addition to the multiple techniques available at TARUMÃ, a large working distance of 440 mm after the ultra-high vacuum (UHV) KB system allows for another key aspect of this station, namely, a broad range of decoupled and independent sample environments. Indeed, modular setups outside vacuum allow for *in situ*, *in operando*, cryogenic and/or *in vivo* experiments, covering research areas in biology, chemistry, physics, geophysics, agriculture, environment and energy.

SAPOTI will be the in-vacuum nanoprobe station at CARNAÚBA, located at 145 m from the undulator source. With an innovative manipulator developed in collaboration with MI-Partners, operation is expected by 2022.

[†] renan.galdes@lnls.br

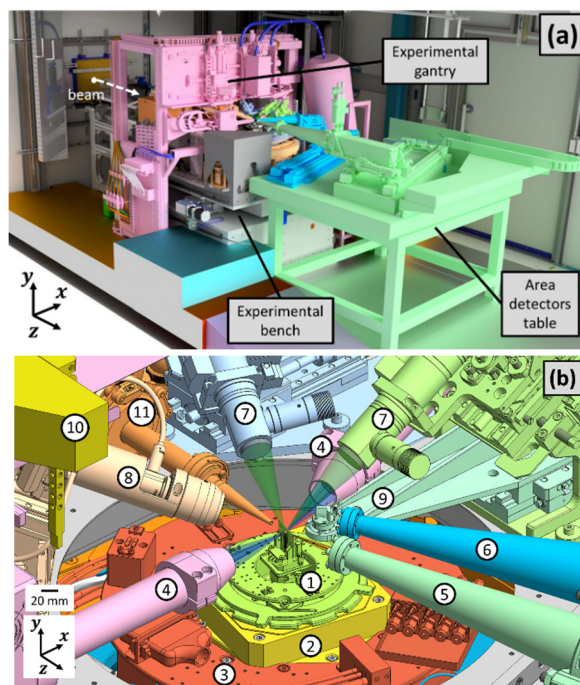


Figure 1: (a) TARUMÃ station at the experimental hutch. (b) Drawing of the region surrounding the sample, detailing: the sample setup (1), the sample stage (2 and 3), the fluorescence detectors (4), the flying paths for the transmission (5) and the diffraction (6) area detectors, the optical microscopes (7), the XEOL optics (8), a crystal analyzer spectrometer (9), the pick-and-place gripper (10), and the KB vessel exit port (11).

OVERVIEW

Figure 1 shows an overview of the TARUMÃ station. The experimental bench hosts: the high sensitivity elements, i.e., the KB vessel and the sample stage; and essential auxiliary elements, such as a complementary metrology frame and an auxiliary rotary stage for cable management (see Fig. 3), and an auxiliary table holding two optical microscopes, the XEOL lenses and a crystal analyzer. A separate table is used for two Medipix-based area detectors with pixel size of $55 \times 55 \mu\text{m}^2$: a PiMEGA, with 1536×1536 pixels at the working distance of 1.1 m, and a MobiPix, with 512×512 pixels at 0.44 m. These detectors can be alternated between transmission and diffraction positions, and the MobiPix can still be oriented towards the crystal analyzer at the distance of 0.42 m to work as a spectrometer

for higher-resolution fluorescence data. Finally, an experimental gantry is placed over the experimental bench, holding heavier or noisier instrumentation, and allowing for additional accessibility. Among these items are two fluorescence detectors, which have fan-based cooling systems, a cryojet system, and a pick-and-place gripper.

In addition to multiple techniques, TARUM \tilde{A} is open to a variety of setups on the sample stage, ranging from macroscopic holders for fossils and plants to microscopy holders, such as grids, silicon nitrite membranes and chips. Many of these setups bring embedded functionalities, such as infrastructure for liquids, gases or vacuum, as well as heating and cooling. More details on an open-atmosphere cryogenic setup can be found in [3], whereas the setups developed for microfluidics and electrochemistry in [4].

SYSTEM ARCHITECTURE

TARUM \tilde{A} specifications had the ambitious target of offering a rich infrastructure for multiple techniques and scientific cases, together with tomography and fast positioning for flyscan, while preserving the stability levels within a few tens of nanometers. Thus, the project has been fully developed in-house, according to a systemic perspective for the broadest possible range of present and future experiments, while following a predictive design approach in applying precision engineering mechatronic solutions.

The core concepts in TARUM \tilde{A} can be extracted from the schematic of its experimental bench in Fig. 2. The main aspect driving its mechanical architecture is the position sensitivity of the components in multiple degrees of freedom (DoFs) regarding keeping the beam variation at the sample within a fraction of its size, or better, for ptychography. Indeed, as detailed in [5], the numbers between the KB mirrors and both the source and the sample are in the order of 10 nm and 10 nrad only. On the one hand, part of the relative stability between the KB mirrors and the source (or virtual source) depends both on the motion of the floor along the multiple slabs in such a long beamline and on the stability of the intermediate optical components. All these aspects are carefully assessed in [6]. On the other, in what concerns the station itself, the critical stability of the KB mirrors with respect both to the floor in the station and to the sample is addressed precisely within the experimental bench, while complementary components are pushed as much as possible to the auxiliary separate structures, i.e., the experimental gantry and the area detectors table.

Firstly, the design of bench followed the concepts developed for Sirius optical systems [7]. The *bottom granite* is directly grouted to the floor, reaching measured suspension frequencies beyond 300 Hz. Above it, a *top granite* sits on four high-stiffness levellers for positioning in the y , R_x and R_z axes with respect to the beam. Its measured suspension frequencies exceed 150 Hz, which is sufficient to prevent the amplification of most of the content of floor vibrations. Moreover, considering that direct metrology between the KB mirrors in-vacuum and the sample in its complex setups would be practically impossible, the top granite effectively works as a sturdy common reference frame between the mirrors and the sample.

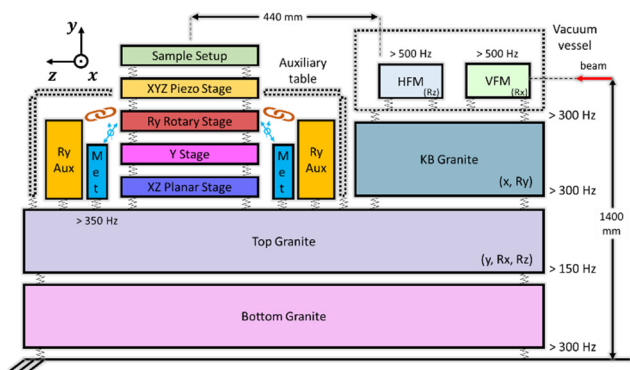


Figure 2: Schematic of experimental bench of TARUM \tilde{A} , highlighting some of the links and the dynamic characteristics of the main components, including: the granite parts, the KB mirrors (VFM and HFM), the sample stage, the auxiliary rotary stage and the metrology frame.

Regarding the KB mirrors, the *KB granite* is moveable in the x and R_y axes with respect to the top granite to provide the remaining DoFs for positioning the mirrors with respect to the beam. This follows a combination of embedded and commercial air-bearing [7], such that suspension above 300 Hz is also obtained once the air is off. Finally, the mirror mechanics is stiffly connected to the vacuum vessel bottom, which, in turn, is stiffly mounted to the KB granite, concluding the stiffness chain for the optics.

As described in [5], the design of Sirius mirror systems [8] has been further improved for the KB mirrors, such that the extreme figure quality can be preserved together with mechanical resonances beyond 500 Hz to reduce the sensitivity to disturbance sources. A minimum set of alignment fixtures, namely, one DoF in pitch (R_x) in the *vertical-focusing mirror* (VFM) and one DoF in roll (R_z) in the *horizontal-focusing mirror* (HFM), is implemented for fine tuning at the beamline. The remaining alignment targets between mirrors are achieved with novel offline alignment strategies (see [5]). With this concept, the dynamics of the mirrors with respect to the floor and, particularly, to the top granite can be kept within a few nanometers, whereas thermal drifts are minimized due to the thermal properties of granite, thermal management in vacuum, and the temperature stability of the air-conditioning system in the hutch.

Regarding the *sample stage*, shown in Fig. 3, it consists of a stack of commercial stages in air to position the sample with respect to the focal spot. It is formed by: an Aerotech's PlanarDL300XY with linear motors for the x and z ; a Newport's IDL280-Z20 wedge stage with a DC motor for y ; an Aerotech's ABRS-250MP air-bearing rotary stage with a direct drive for R_y ; and a PI's P-563 piezo stage for fast and fine position in the x , y and z . Optionally, for ptycho-Bragg-CDI, Attocube's ANGp101 and ANGt101 piezo cradles can be mounted to the XYZ stage. The dynamics of the commercial stages have been measured and modelled to validate their consonance with the application, whereas all the interfaces were carefully designed. Moreover, except for the cradles, all the driving systems were selected for smooth actuation, i.e., preventing steppers, to minimize disturbances in flyscan operation.

Content from this work may be used under the terms of the CC BY 3.0 licence (© 2021). Any distribution of this work must maintain attribution to the author(s), title of the work, publisher, and DOI

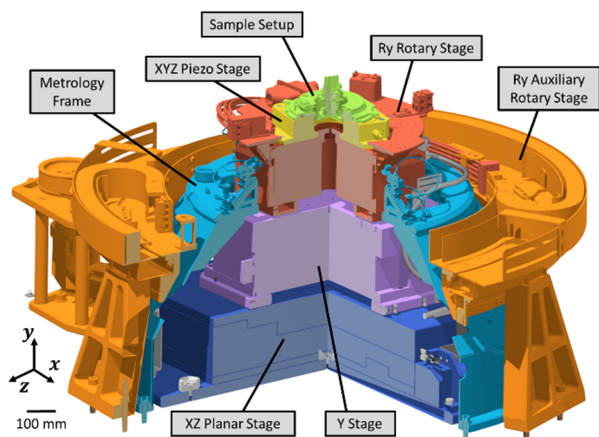


Figure 3: Quarter section view with the sample stage, the metrology frame and the auxiliary rotary stage in the experimental bench of TARUMÃ.

Still, as the position accuracy of the sample with respect to the top granite is limited to the basic metrology in the stages and the passive stability of the non-controlled DoFs over a large stiffness chain, a complementary metrology frame was implemented. With measured dynamics above 350 Hz, it has capacitive probes pointing to the nominal sample position in Abbé, over a conical target fixed to the rotor of the rotary stage, such that information in the nanometer level in the low- and mid-frequency ranges can be used in post-processing algorithms if desired. The sample setups must be designed for maximum dynamics.

Finally, to preserve the accuracy of the stages and the dynamics of the sample, while allowing for the infrastructure of electrical signals and fluids to the sample setups, an auxiliary rotary stage is electronically coupled with the air-bearing rotary stage over a functional range of $\pm 110^\circ$. Thus, the auxiliary stage takes the burden of carrying the cables and tubes, whereas only a pre-determined compliant link exists between the stages. At the top of the rotary stage, electrical panels and manifolds are used for distribution.

Naturally, the dynamics of the auxiliary table, with the microscopes, the XEOL set and the crystal analyzer, are also of concern. Yet, this partly filtered by the inertia of granite bench, with negligible expected impact in the sample position. Due to the limited space here, more details on the gantry, the detector table and complementary resources will be left for a future publication. Similarly, the control architecture that allows for the integration and synchronization of the several stages and detectors in the sub-millisecond range and the strategies for efficient flyscan experiments will be addressed in [9].

COMMISSIONING

Since first light, commissioning at CARNAÚBA has been ongoing for about six months. In addition to the TARUMÃ station, this includes first use, validation and optimization of several instruments that were designed by Sirius engineering teams and built in collaboration with partners, including: the cryogenic mirror systems [8,10], a four-bounce monochromator [11], innovative instruments for diagnostics [12], and even the area detectors.

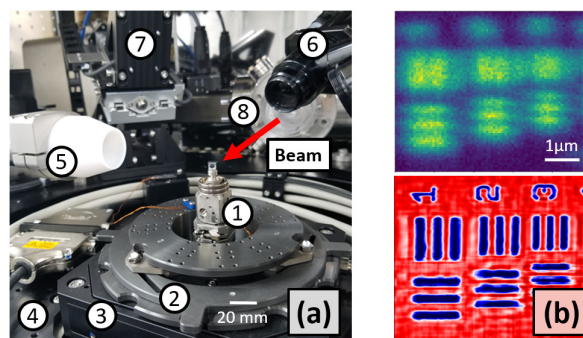


Figure 4: (a) Sample region at TARUMÃ, with: sample holder (1); interface plate (2) on the XYZ stage (3), rotary stage with electrical and fluid lines (4); fluorescence detector (5); optical microscope (6); luminescence stage (7); and KB vessel (8). (b) Simultaneous 3-minute $5 \times 5 \mu\text{m}^2$ flyscan measurements of X-ray fluorescence (top) and ptychography (bottom).

At TARUMÃ, all the functionalities have been gradually implemented and validated. There are more than 50 motion axes and a dozen detectors. They are integrated in EPICS, but many also linked via hardware for flyscans. Figure 4 shows the setup and preliminary 3-minute flyscan results for $5 \times 5 \mu\text{m}^2$ of a standard sample, comparing Au fluorescence and ptychography, with spatial resolutions around $800 \times 300 \text{ nm}^2$ and $200 \times 70 \text{ nm}^2$, respectively. Now, significant improvements are still expected for the near future, once: the fast orbit feedback correction is implemented in the storage ring; further optimization in alignment and residual instabilities in the primary optics is achieved; and the control in the station and the reconstruction algorithms reach maturity. Finally, preliminary tomography experiments have already been realized, and most of the special environments and sample setups are in commissioning.

CONCLUSIONS

TARUMÃ has been fully designed and built in-house, according to the same precision engineering concepts and predictive design principles that have led to a whole series of innovative instruments for Sirius beamlines. A complex scenario results from the achromatic optics, with large KB mirrors and working distances, vacuum-air separation, and multiple techniques and setups, but the successful initial results build confidence in the current workflow, at the same time that bring valuable lessons for the ongoing and forthcoming projects. The unique features of TARUMÃ are expected to be open for users in the second half of 2021.

ACKNOWLEDGEMENTS

The authors would like to gratefully acknowledge the funding by the Brazilian Ministry of Science, Technology and Innovation, the contributions of the LNLS team and partners, and the participation of the MI-Partners in the SAPOTI project, with fruitful feedback to TARUMÃ.

REFERENCES

- [1] H.C.N. Tolentino *et al.*, “CARNAÚBA: The coherent x-ray nanoprobe beamline for the Brazilian Synchrotron SIRIUS/LNLS”, *J. Phys. Conf. Ser.*, vol. 849, p. 012057, 2017. <https://doi.org/10.1088/1742-6596/849/1/012057>
- [2] Sirius Project, <https://www.lnls.cnpem.br/sirius-en/>
- [3] F.R. Lena *et al.*, “A cryogenic sample environment for the TARUMÃ station at the CARNAÚBA beamline at Sirius/LNLS”, presented at the 11th Int. Conf. on Mechanical Engineering Design of Synchrotron Radiation Equipment and Instrumentation (MEDSI2020), Chicago, IL, USA, virtual conference, July 2021, paper WEPC02, this conference.
- [4] W.H. Wilendorf *et al.*, “Electrochemistry and microfluidic environments for the TARUMÃ station at the CARNAÚBA beamline at Sirius/LNLS”, presented at the 11th Int. Conf. on Mechanical Engineering Design of Synchrotron Radiation Equipment and Instrumentation (MEDSI2020), Chicago, IL, USA, virtual conference, July 2021, paper WEPC03, this conference.
- [5] G.B.Z.L. Moreno *et al.*, “Exactly-constrained KB mirrors for Sirius/LNLS beamlines: design and commissioning of the TARUMÃ station nanofocusing optics at CARNAÚBA beamline”, presented at the 11th Int. Conf. on Mechanical Engineering Design of Synchrotron Radiation Equipment and Instrumentation (MEDSI2020), Chicago, IL, USA, virtual conference, July 2021, paper TUOB01, this conference.
- [6] C.S.N.C. Bueno *et al.*, “Vibration assessment at the CARNAÚBA beamline at Sirius/LNLS”, presented at the 11th Int. Conf. on Mechanical Engineering Design of Synchrotron Radiation Equipment and Instrumentation (MEDSI2020), Chicago, IL, USA, virtual conference, July 2021, paper MOPB08, this conference.
- [7] R.R. Geraldès *et al.*, “Granite benches for Sirius x-ray optical systems”, in *Proc. of MEDSI'18*, Paris, France, Jun. 2018, pp. 361-364. doi:10.18429/JACoW-MEDSI2018-THPH12
- [8] R.R. Geraldès, *et al.*, “The design of exactly-constrained x-ray mirrors systems for Sirius”, in *Proc. of MEDSI'18*, Paris, France, Jun. 2018, pp. 173-178. doi:10.18429/JACoW-MEDSI2018-WE0AMA04
- [9] C.S.N.C. Bueno *et al.*, “Positioning Scanning Solutions at the TARUMÃ Station at the CARNAÚBA Beamline at Sirius/LNLS,” to be presented at ICALEPCS 2021, Shanghai, China, 2021.
- [10] L.M. Volpe *et al.*, “Installation and commissioning of the exactly-constrained x-ray mirror systems for Sirius/LNLS,” presented at the 11th Int. Conf. on Mechanical Engineering Design of Synchrotron Radiation Equipment and Instrumentation (MEDSI2020), Chicago, IL, USA, virtual conference, July 2021, paper MOPB06, this conference.
- [11] M. Saveri Silve *et al.*, “Four-bounce crystal monochromators for the Sirius/LNLS beamlines,” presented at the 11th Int. Conf. on Mechanical Engineering Design of Synchrotron Radiation Equipment and Instrumentation (MEDSI2020), Chicago, IL, USA, virtual conference, July 2021, paper MOPB04, this conference.
- [12] H.C.N. Tolentino *et al.*, “Innovative instruments based on cryogenically cooled silicon crystals for the CARNAÚBA beamline at Sirius-LNLS,” *AIP Conf. Proc.*, vol. 2054, p. 060026, 2019. <https://doi.org/10.1063/1.5084657>

A NOVEL VACUUM CHAMBER DESIGN FOR THE APS UPGRADE OF THE 26-ID NANOPROBE

S. Bean, M. Holt¹, P. Amann, M. Bartlein, Z. Cai, T. Graber[†], D. Shu

Advanced Photon Source, Argonne National Laboratory, Lemont, IL 60439, USA

¹also at Center for Nanoscale Materials, Argonne National Laboratory, Lemont, IL 60439, USA

[†]Deceased April 29, 2021

Abstract

An enhancement design of an existing 26-ID nanoprobe [1] instrument (NPI) at APS is being completed as part of work for the APS-Upgrade (APS-U) project. As part of this enhancement design, a new vacuum chamber geometry configuration has been implemented that balances the desired simultaneous x-ray measurement methods with accessibility and serviceability of the nanoprobe. The main enabling feature on the vacuum chamber is a slanted mid-level vacuum sealing plane. The new chamber design geometrically optimizes the ability to perform simultaneous diffraction, fluorescence and optical or laser pump probe measurements on the sample. A large diffraction door geometry is strategically placed near the sample for ease of access. The newly designed chamber can be readily serviced by removal of the upper chamber section, on which most larger instrument assemblies or beamline attachments are not interfaced. The mechanical design intent and geometry of this chamber concept is described in this paper.

INTRODUCTION

The upgrade of the 26-ID NPI will enable the observation of samples with x-ray diffraction, fluorescence, and photoluminescence while also allowing for the ability to manipulate the sample with laser or electronic stimulation and its environment with heating and cooling. This combination of measurement and sample manipulation enables world class operando studies.

The scope and breadth of the science to be performed by the upgraded 26-ID NPI are enabled by several technologies. Area and fluorescence detectors and manipulations, vacuum design, windowing, nanopositioning mechanics [2], and high resolution optics all need to be thoughtfully integrated to create an effective nanoprobe. Although trivial in technical merit compared to the other aspects and technologies of the, the vacuum chamber geometry imposes fundamental limitation on measurement capability, flexibility, and adaptability of the instrument. The limitations that can come with a vacuum chamber design may present challenges to scientific staff that could detract from their mission.

The prior nanoprobe vacuum chamber had desirable features, such as a large diffraction window, cable management that is incorporated into a lower section of the chamber, and adequate space inside the chamber for routing wiring and accessing equipment. However, this prior iteration presented challenges for adding more modalities of measurement, and also has some non-ideal

servicing steps, such as removing the x-ray fluorescence detector to take the upper portion of the chamber off.

To optimize the capabilities of the upgraded nanoprobe, the proposed vacuum chamber design incorporates a new angled sealing plane. The sealing plane is strategically positioned to enable simultaneous measurement techniques, while also balancing other serviceability and accessibility. For the upgrade door solution, inspiration was drawn from the existing NPI and the hard x-ray nanoprobe (HXN) at NSLS-II [3, 4]. An image of the entire new instrument is shown in Fig. 1.

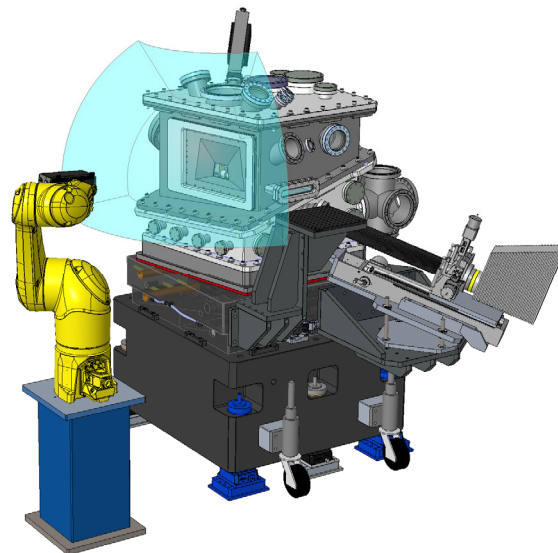


Figure 1: The new 26-ID nanoprobe enhancement as part of the advanced photon source upgrade.

NANOPROBE CONFIGURATION METHODOLOGY

The following numbered items represent the most critical requirements of design and configuration for this instrument:

1. The design must maximize the diffraction envelope downstream of the instrument for area detection over the original design.
2. A Be window must be used for the downstream window.
3. A wide-angle range (>25deg) for optical configurations or laser pump probe measurements must be implemented on the outboard side of the chamber in the horizontal sample plane.

4. A fluorescence detector must be able to approach the sample. It is acceptable for this to approach the sample from below the horizontal plane.
5. The ability to have simultaneous diffraction, optical, and fluorescence detection should be implemented in the design.
6. The sample region must be accessible for exchange.
7. It is desirable to be able to service the instrument without having to remove the fluorescence detector, beamline connection, or wiring feedthrough for all internal components.

VACUUM CHAMBER DESIGN

In order to optimize the requirements, a slanted mid-level sealing plane is implemented. A render of the design can be seen in Fig. 2. The vacuum chamber is to be made of 304L stainless steel, with half inch wall and four inch base plate thicknesses. There are o-ring gaskets incorporated in each major chamber joint. Custom optical viewports are integrated to meet the needs of the optical and fluorescence measurements. A custom Be window and door design is on the downstream side of the chamber. The XRF detector, beamline connection, electrical feedthroughs, and turbo pump are all mounted to the lower chamber section below the slanted sealing plane. This allows for easier removal of the top chamber section.

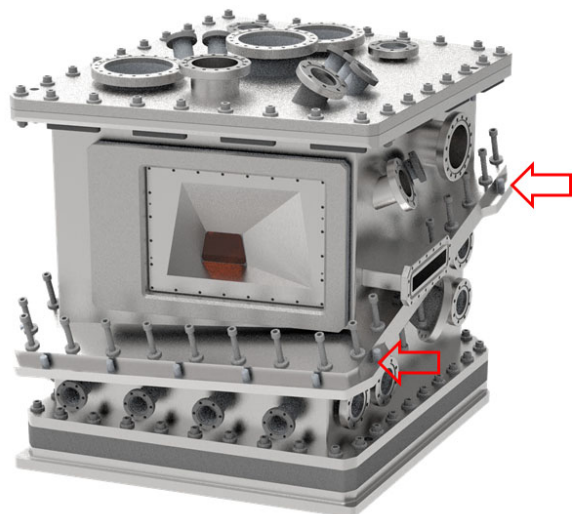


Figure 2: Rendering [5] of the nanprobe vacuum chamber design. The slanted mid sealing plane is pointed to in two locations upstream and downstream.

SIMULTANEOUS METHODS

Figures 3 and 4 depict how the simultaneous methods are achieved with the chamber design.

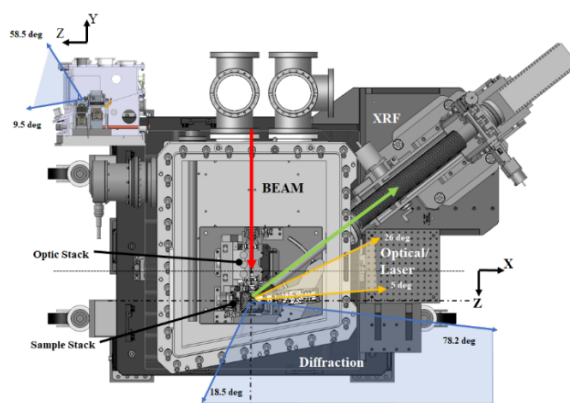


Figure 3: Schematic showing how the simultaneous methods of the NPI are carried out with cross section in the XZ plane. The fluorescence detector is 18° below the XZ plane. The beam (red), diffraction range (blue), optical or laser (gold), and fluorescence (green).

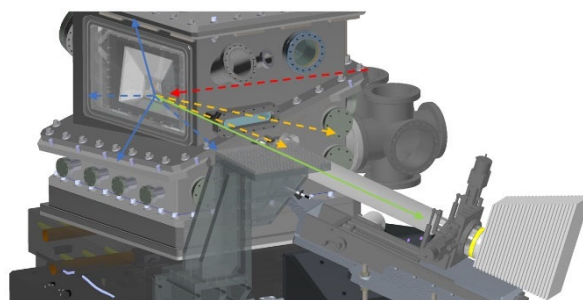


Figure 4: Schematic showing how the simultaneous methods of the NPI are carried out. The fluorescence detector is 18° below the XZ plane. The beam (red), diffraction range (blue), optical or laser (gold), and fluorescence (green).

Be WINDOW UPGRADE

The beryllium window is a cartridge brazed design that gets brazed into a weldment. The Be window design is depicted in Fig. 5. The weldment is mounted on the downstream chamber door onto an O-ring joint. The Be window design was made to have higher angular diffraction range than the historic design using less area by carefully choosing its proximity to the sample. The door feature allows for ease of sample or optic change.

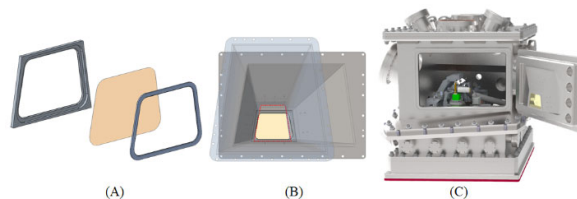


Figure 5: Schematic showing the beryllium window (A), The old (blue transparent) and new (gray) NPI window weldment design (B), and the open door of the NPI with the beryllium weldment loaded (C).

ACCESSIBILITY

In addition to the door of the prior section, the new chamber was designed to allow for accessibility to service items when the upper chamber is removed. The slanting of the sealing plane allows for more access to internal components. This is depicted in Fig. 6, along with the modular instrumentation bench that can be removed.

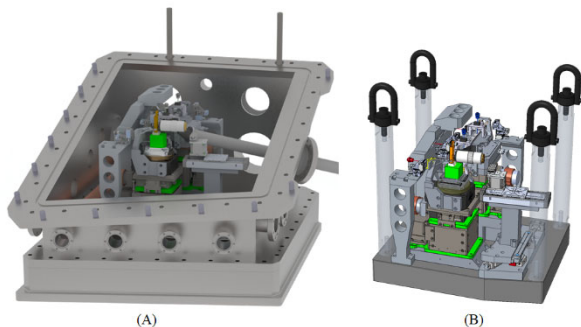


Figure 6: Schematic showing the NPI chamber with the upper portion removed (A) and the modular instrumentation bench that can be removed (B).

VACUUM CHAMBER FEA

FEA [6] was performed to determine sufficient stresses in the chamber concept. The results are shown in Fig. 7. Displacements are also used to inform design tradeoffs. A thicker base plate reduces the shifting of internal components when going from atmosphere to vacuum.

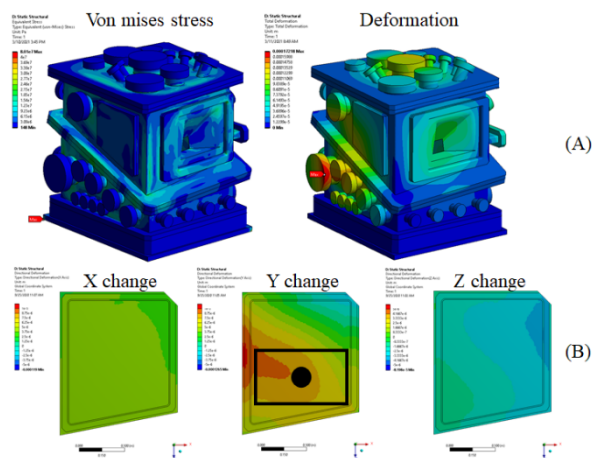


Figure 7: FEA Results. Stress and deformation of the chamber (A) and the base plate deformation (B). These results were used to inform design decisions, including the shifting of components mounted to the chamber externally or internally.

CONCLUSIONS

The novel slanted sealing plane vacuum chamber design meets the multimodality requirements of this instrument while also enabling accessibility, serviceability, and forward looking flexibility.

AKNOWLEDGEMENTS

This research used resources of the Advanced Photon Source and the Center for Nanoscale Materials, U.S. Department of Energy (DOE) Office of Science User Facilities at Argonne National Laboratory and is based on research supported by the U.S. DOE Office of Science-Basic Energy Sciences, under Contract No. DE-AC02-06CH11357.

REFERENCES

- [1] R.P. Winarski *et al.*, “A hard X-ray nanoprobe beamline for nanoscale microscopy,” *J. Synchrotron Radiat.*, vol. 19, no. 6, pp. 1056-1060, 2012.
 DOI:10.1107/S09090049512036783
- [2] D. Shu *et al.*, “Modular Nanopositioning Flexure Stages Development for APS Upgrade K-B Mirror Nanofocusing Optics”, presented at the 11th Mechanical Engineering Design of Synchrotron Radiation Equipment and Instrumentation Int. Conf. (MEDSI'20), Chicago, USA, Jul. 2021, paper TUPC10, this conference.
- [3] E. Nazaretski, K. Lauer, H. Yan, N. Bouet, J. Zhou, R. Conley, X. Huang *et al.*, “Pushing the limits: an instrument for hard x-ray imaging below 20 nm,” *J. Synchrotron Radiat.*, vol. 22, pp. 336-341, 2015.
<https://doi.org/10.1107/S1600577514025715>
- [4] Hard X-ray Nanoprobe Beamline at NSLS-II, <https://www.bnl.gov/nsls2/beamlines/beamline.php?r=3-ID>
- [5] Keyshot 8 – 3D rendering software, www.keyshot.com
- [6] ANSYS engineering simulations and 3D design software, www.ansys.com

CFD PREDICTIONS OF WATER FLOW THROUGH IMPELLERS OF THE ALBA CENTRIFUGAL PUMPS AND THEIR ASPIRATION ZONE. AN INVESTIGATION OF FLUID DYNAMICS EFFECTS ON CAVITATION PROBLEMS

A. González Romero*, ESEIAAT-UPC, Terrassa, Spain

J. J. Casas, C. Colldelram, M. Quispe†, ALBA-CELLS Synchrotron, Cerdanyola del Vallès, Spain

Abstract

Currently, the ALBA refrigeration system pumps present cavitation when operating at their nominal regime. To alleviate this phenomenon temporarily until a definitive solution was found, the water flow was reduced to 67% of its nominal value. As this flow exchanges heat with the cooling water produced in an external cogeneration plant, modifying the working point of the pumps resulted in a reduction of the Accelerator cooling capacity. However, even at such low flow conditions, the flow has an anomalous oscillatory behaviour in the distributor of the aspiration zone, implying that the cause may be in a bad dimensioning of the manifold.

This paper presents a study of Computational Fluid Dynamics (CFD) applied to the aspiration zones of the pumps, to investigate the effects of fluid dynamics on cavitation problems and understand what may be happening in the system. The need for such research arises from the urge to recover the accelerator cooling capacity and the constant pursuit for the improvement of the system. The geometries for this study include the general manifold in the aspiration zone and a simplified model of the pump impeller. The simulations have been carried out with the ANSYS-FLUENT software.

Studies performed include considering the total water flow in nominal and under current operating conditions. In addition, the cases in which the flow is distributed through the manifold tubes in uniform and non-uniform ways have been treated separately. Pressure and velocity fields are analysed for various turbulence models. Finally, conclusions and recommendations to the problem are presented.

INTRODUCTION

During the last years, ALBA's operation has been affected by general thermal stability problems that prevent the correct performance of the system.

The cooling capacity of the facilities, which depends on the cold water supply from an external cogeneration plant (ST4), is affected by irregularities in the supplier's operation. The cogeneration plant changes its operating mode for a few hours each weekend, producing losses in the stability of the cold water supply (both in temperature and flow).

Moreover, from the ALBA side, the thermohydraulic system, described in [1], cannot move the required design flow in the heat exchange zone due to cavitation problems, which arise when the pump system (called P11) operates on design

conditions. For this reason, the operating flow was reduced by 33% to protect the pumps from such phenomenon, worsening the heat transfer efficiency between ALBA and ST4 (see detailed description in [2]).

The thermal instability promoted by these factors affects the stability of the photons generated in the synchrotron's ring and, therefore, the quality of the experiments performed by scientists.

Seeking to solve the local problem, this study focuses on investigating whether the cause of cavitation in P11 pumps is a bad configuration of the distribution panel in the suction zone or a bad dimensioning of the aspiration zone.

For this research, CFD (Computational Fluid Dynamics) systematic studies, global calculations and flow measurements are applied.

MAIN PUMPING SYSTEM: P11 PUMPS

Operation

P11 is the main pumping system of ALBA, composed by a couple of pumps which intersperse every 6 months their operation to avoid excessive wear or overload.

The pumps are fed by the hot water from the accelerator, after passing through filters and the three pipes connected to them (see Fig. 1). The flow is then redirected towards a group of heat exchangers before reaching the storage tank, where the water is cooled with the incoming flow from ST4.

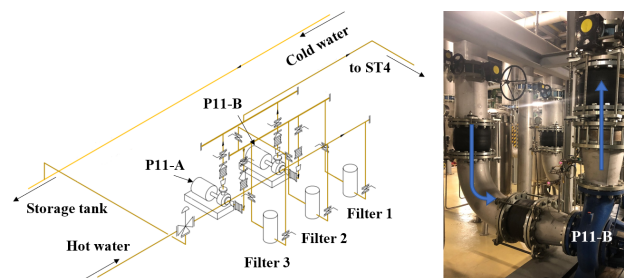


Figure 1: Schematic of the overall circuit studied (left) and photography of the P11 pumps (right).

Encountered Problems

Different problems have been detected in the P11 system during its operation in recent years:

- Reduced flow rate to avoid cavitation problems at nominal value.

* andreagonrom@gmail.com

† mquispe@cells.es

- Non-uniform geometry of the suction zone, distribution panel, which produces a flow imbalance detected with ultrasound reading.
- Oscillatory behaviour measured with ultrasound in the suction branches, which could be due the pump or the geometry of the suction zone.
- Anti-vibration effect of expansion sleeves cancelled when connecting pressure gauges with rigid tubes.
- Possible presence of foreign bodies as sponges trapped in the distribution zone from past experiences [3].

Cavitation

The NPSH required by the manufacturer is 2.42 m for 647 m³/h. Under current operating conditions at 430 m³/h, the pressure gauge reading in the suction zone is 1.6 bar, value over the NPSH limit taking 23 °C water conditions.

However, there are still exploding bubbles noises which indicate cavitation. Therefore, the conclusion that the NPSH complies may be questioned by a possible malfunction of the pressure gauge, and/or a high pressure gradient in the suction zone.

On the other hand, a poorly designed aspiration zone could promote high speeds and/or a complex, unstable distribution, which is also a source of cavitation. A situation expected to worsen with flow rate increases from 430 to the nominal value of 645 m³/h.

A high-level CFD study has been conducted, as it is the only engineering tool that allows to confirm whether there are high pressure gradients and/or complex velocity distributions in the suction zone.

CFD MODEL

Geometry

The geometry used includes the general manifold in the aspiration zone and a simplified model of the pump impeller (see Fig. 2), as confidentiality prevents access to its drawings.

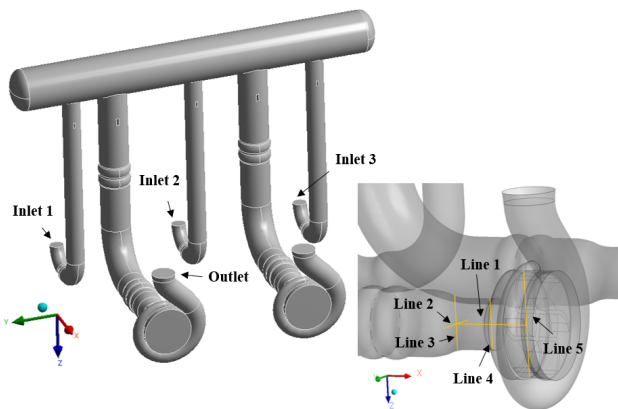


Figure 2: Boundary conditions and lines set to extract data from the 3D model of the system.

The mesh used has 3,570,085 elements. Moreover, an ideal setup of the pump together with a 6 m straight pipe was simulated with a mesh of 1,825,999 elements. For both

cases, the lines depicted at Fig. 2 have been used to extract the data presented on the following section, being lines 2 and 3 at the current pressure gauge location.

Boundary Conditions

At the inlets, the velocities obtained from uniformly distributing the current and nominal flow rates (see Table 1) and the current non-uniform distribution (see Table 2) as measured by ultrasound were applied.

Table 1: Current and Nominal Flow Regimes

Case	Flow rate [m ³ /h]	Angular velocity [rpm]
CURRENT	430	1372
NOMINAL	645	1475

Table 2: Current Distribution of the Total Water Flow (referred as **non-uniform conditions** hereinafter)

Inlet 1	Inlet 2	Inlet 3
36.441%	33.377%	30.182%

In the simulations, the movement of the pump blades has been implemented in the rotor area following the real behaviour of the system.

A zero value has been set as the reference pressure at the pump outlet. Water at 23 °C is considered, together with steady, isothermal and no-slip walls conditions.

RESULTS & DISCUSSION

Experimental Measurements

As part of the research, a hydraulic test on the system was performed, forcing a flow increment on the P11 from 430 to 585 m³/h. As observed in Table 3, aspiration pressure tends to decrease up to 1.24 bar, a value which would leave the system far below the NPSH limitation given by the manufacturer. The precision of the pressure gauges remains to be investigated to confirm the validity of the measurements.

Table 3: Pump P11-B Aspiration Zone System's Total Flow and Average Pressure Measurements

Flow [m ³ /h]	430	450	505	548	585
Pressure [bar]	1.59	1.55	1.45	1.35	1.24

Convergence Results

According to the reference variables defined in ANSYS Workbench as residuals, asymptotic results were obtained in all simulated cases for an average of 800 iterations with a trend below 10⁻² in continuity, and 10⁻³ in the velocity field (see Fig. 3).

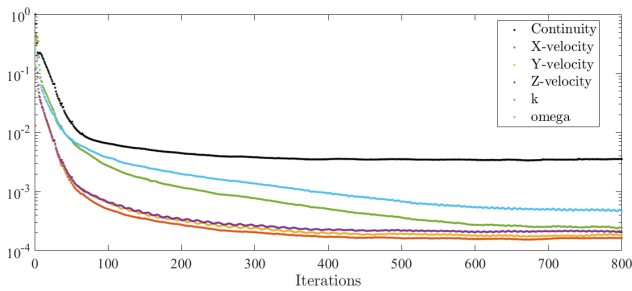


Figure 3: Residuals of continuity, velocity field, k and ω in a reference case ($430 \text{ m}^3/\text{h}$, $k-\omega$ SST model at uniform conditions).

Laminar and Turbulent Models

In order to validate the conditions set, a study was initially carried out without the pump to later add its geometry together with its dynamics. For both situations at $430 \text{ m}^3/\text{h}$, a comparison of the velocity and pressure distributions obtained in the lines defined in Fig. 2 for different models was performed: laminar, $k-\epsilon$, $k-\omega$ and $k-\omega$ SST.

The results show matching velocity distributions between models at all the lines considered (see Fig. 4). As for pressure, differences of maximum 4% between turbulent models with equal trend distributions were obtained, allowing the use of the $k-\omega$ SST model in the rest of analysis. The laminar model is not valid as the flow's Reynolds value of 762,000 indicates for an average velocity of 3 m/s and water at 23 °C.

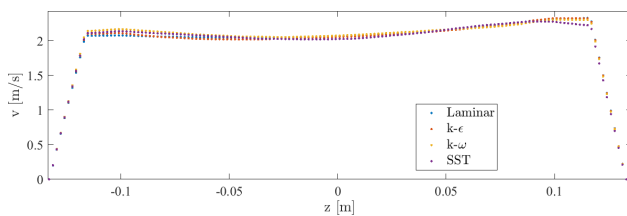


Figure 4: Comparison of velocity distributions at line 4. Case with uniform inlet distribution at $430 \text{ m}^3/\text{h}$.

Comparison of Flow Conditions

First, the uniform and non-uniform flow conditions were compared with the ideal setup results for each regime considered (see Table 1). As Fig. 5 clearly shows, the uniform and non-uniform velocity distributions are similar, differentiating from the ideal distribution in the centre of the pipe. Such behaviour is repeated with both flows. Figure 6 allows to appreciate the velocity distribution in the gauge section.

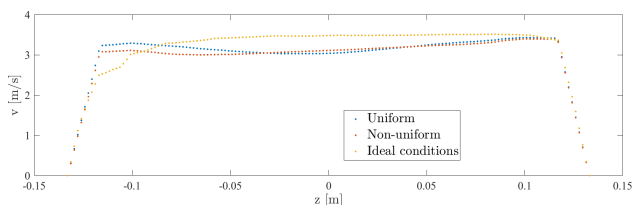


Figure 5: Velocity distributions at line 4 for $645 \text{ m}^3/\text{h}$.

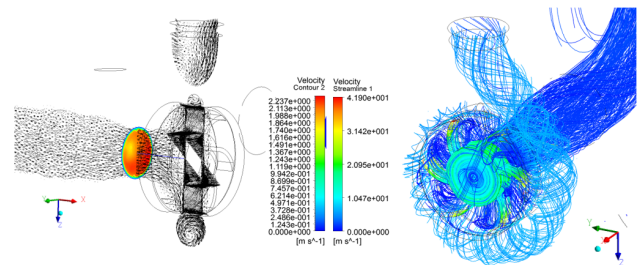


Figure 6: Flow at $430 \text{ m}^3/\text{h}$ (a) left: velocity distribution at the gauge section; (b) right: streamlines around P11-B.

Regarding the pressures, an approximately constant distribution is obtained in all directions. The uniformity in the suction inlet tube allows to conclude that the readings of the pressure gauge installed in the area of lines 2 and 3 (see Fig. 2) is representative.

The main difference between regimes is given in the order of magnitude of the velocity as it can be observed in Fig. 7, going from a maximum of 2.12 to 3.2 m/s. However, such values fall above the limits established by the literature regarding adequate velocities in the suction zone of centrifugal pumps, becoming a problem to be solved [4, 5].

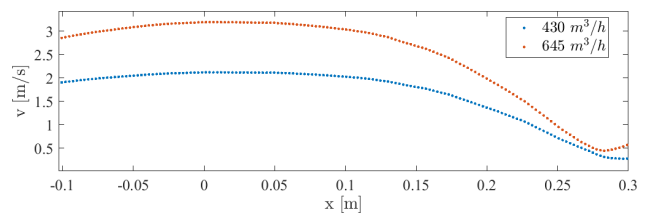


Figure 7: Velocity distributions at line 1 for both flow regimes. Case with uniform inlet distribution.

The study carried out has allowed to verify that the manometer readings are representative, although to work at nominal flow the pressure value in the suction zone should increase to comply with the NPSH limit. Moreover, the velocities reached by the fluid in the aspiration zone must be reduced to enter the recommended limits.

On the other hand, the existing rigid tubes must be changed to avoid vibrations transmission. Moreover, the manifold must be redesigned and the pumps must be changed or a third must be added to distribute the flow between two and keep another one as backup.

Finally, this research has been dedicated to the aspiration zone, but the impulsion zone immediately after the pump remains to be investigated.

REFERENCES

- [1] M. Quispe, "Cooling Water System in the Field of Accelerators", ALBA, Cerdanyola del Vallès, Spain, Open Sesame Project, Oct. 2018.
- [2] F. Hernández *et al.*, "Investigation of Thermal Instabilities in the ALBA Cooling System, Based on Numerical Simulations and Experimental Measurements", presented at the MEDSI 2020, Chicago, USA, July 2021, paper TUPB05, this conference.

- [3] M. Quispe, "Cooling System Operation", ALBA-CELLS, Cerdanyola del Vallès, Spain, ALBA Cooling Project Upgrade Team, 10 Dec. 2015.
- [4] Considerations for Designing Piping Adjacent to a Centrifugal Pump, <https://www.waterworld.com/technologies/pipes/article/16190795/>
- [5] Engineering Toolbox, https://www.engineeringtoolbox.com/pump-suction-flow-velocity-water-d_228.html

A FAST SIMULATION TOOL TO CALCULATE SPECTRAL POWER DENSITY EMITTED BY WIGGLERS AND SHORT INSERTION DEVICES

J. Reyes-Herrera* and M. Sanchez del Rio
European Synchrotron Radiation Facility, 38000 Grenoble, France

Abstract

The analysis of thermal stress of beamline components requires a comprehensive determination of the absorbed power profile. Consequently, accurate calculations of beam power density and its dependency on the photon energy are required. There exist precise tools to perform these calculations for undulator sources, like several methods available in the OASYS toolbox [1] considering, for example, the contribution of the different harmonics of the undulator radiation or using ray-tracing algorithms [2]. This is not the case for wiggler sources, in particular for short insertion devices that are used as source for the bending magnet beamlines in some upgraded storage rings like the ESRF-EBS. Wiggler radiation is incoherent and although it is possible the use of undulator methods for calculating it, this is very inefficient. In this work, we describe a tool that performs fast calculations of spectral power density from a wiggler source. The emission is calculated starting from a tabulated magnetic field and computes the power spatial and spectral density. It uses concepts inspired from Tanaka's work [3]. It is implemented in a user-friendly widget in OASYS and can be connected to widgets to calculate absorbed and transmitted power density along the beamline components. The accuracy of the method is verified by calculating three examples and comparing the results with ray-tracing. The three insertion devices simulated are: the EBS-ESRF-3PW (see results in Figure 1), the ESRF W150 (a high power wiggler) and the 3PW for the BEATS project [4] at the SESAME synchrotron source.

INTRODUCTION

Currently, there are some synchrotron facilities that are implementing short insertion devices (IDs) as suitable photon sources that fits the demands of different beamlines. For example, in the new ESRF-EBS storage ring, all the 16 bending magnet beamlines have been upgraded with 3-pole wigglers, 2-pole wigglers or short bending magnets [5]. Another example is at SESAME, where a 3-pole wiggler is planned to be used at the BEAmline for Tomography at SESAME (BEATS) [4]. Therefore, in order to perform analysis of thermal stress of components of beamlines with this kind of sources, there is a demand of accurate and efficient tools to calculate the spectra power density distribution of these type of IDs. In this work, a new fast algorithm implemented as a user-friendly widget in OASYS [1] is presented.

* juan.reyes-herrera@esrf.eu

CALCULATION METHOD

The goal is to calculate the emitted flux by a wiggler F as a function of the horizontal and vertical coordinates (x, y) of a screen plane perpendicular to the propagation direction (optical axis) and located at a distance D from the center of the wiggler. The flux distribution is calculated for a grid of photon energies E , therefore $F(x, y, E)$.

We do not restrict to conventional wigglers with sinusoidal field, but use a numerical map of the magnetic field in the vertical direction $B_y(z)$. This allows us to simulate short IDs like the ones used at EBS-ESRF in the bending magnet photon sources, namely 3-pole wigglers (3PWs), 2-pole wigglers and 1-pole wigglers (or superbendings).

Contrary to the conventional method to calculate the differential emission at any coordinate point (x, y) for then averaging to the pixel size, we use a top-to-bottom method, first calculating the emission spectrum (integrated over an infinite size) for then distributing each integrated intensity for a given photon energy $F(E)$ over its spatial distribution calculated ad-hoc. This method is explained in this section.

We assume (like in [3]) that i) the wiggler emission is fully incoherent (emission at every position of the electron trajectory are superimposed incoherently); ii) the electron emittances (finite size and divergence of the electron beam) are neglected, because they are usually smaller than the average sizes and divergences of the photon beam emitted by a single electron (or filament beam); and iii) the emission at a given point of the electron trajectory is the same as the Bending Magnet emission.

The calculation of the electron trajectory and emission spectrum follows the model implemented in SHADOW ([2]) and XOPPY ([1]).

Calculation of Electron Trajectory Under a Magnetic Field

Let us start with the wiggler magnetic field, that for a conventional wiggler has only a vertical component ($\vec{B} = (0, B_y, 0)$) and is given by tabulated values $B_y(z)$, with z the wiggler direction centered at the middle of the wiggler. An electron entering in this magnetic field will have a transversal velocity β_y (in c units) given by the integral of the magnetic field

$$\beta_y(z) = -\frac{c10^{-9}}{E_e[GeV]} \int_{z_1}^z B_y(s) ds. \quad (1)$$

The electron trajectory is in the horizontal plane and is given by the integral of the velocity,

$$x(z) = \int_{z_1}^z \beta_y(s) ds. \quad (2)$$

The local curvature (or inverse of the local radius) is also calculated, because the local emission corresponds to that of a bending magnet of that curvature. It is proportional to the second derivative of the trajectory, therefore proportional to B_y

$$R^{-1}(z) = \frac{e}{\gamma m_e c} B_y(z), \quad (3)$$

with e the electron charge, m_e the electron mass and γ the electron energy in units of $m_e c^2$. Each curvature has associated a bending magnet critical energy given by

$$E_c(z) = \frac{3}{4\pi} \lambda \gamma^3 R^{-1}(z), \quad (4)$$

with λ the photon wavelength.

Calculation of Spectrum of the Wiggler Full Emission

Once calculated $E_c(z)$ we compute the number of photons emitted per mrad at each z point (using the equations of the bending magnet). This result is multiplied by $(R(z)10^{-3})^{-1}$ to get the number of photons emitted along each trajectory arc step, and then multiplied by $\sqrt{1 + (\beta_x(z)/\beta_z(z))^2}$ to account for the projection of the arc on the axial length Δz . A final integration in z results in the total number of photons at that photon energy.

Calculation of Screen Illumination at a Given Photon Energy

Consider a plane at a distance D from the center of the ID. We want to determine the flux as a function of the coordinates (x, y) and energy E . A first step is to define automatically the window that will receive the full radiation. For that, we consider $\sigma' \approx (0.597/\gamma)\sqrt{\max(E_c)/\min(E)}$ the maximum angular deviation of the emitted photons in a bending magnet approximation (after first equation in page 43 of [3]). The angular interval to be considered in horizontal is $\Delta x' = 2n_p\sigma' - \min(\beta_x) + \max(\beta_x)$ with n_p a "passepartout" coefficient to enlarge the window (by default $n_p = 3$). In vertical, $\Delta y' = 2n_p\sigma'$. The spatial points (x, y) at a distance D from the source are in the window $(D\Delta x', D\Delta y')$. Each point (x, y) subtend angles $(x/D, y/D)$ with the center of the ID.

For each photon energy E , we calculate the 1D intensity profiles $I_x = I(x, 0)$ and $I_y = I(0, y)$. The 2D map is constructed making the outer product of I_x and I_y . The vertical profile I_y corresponds to the bending magnet emission with an averaged critical energy \bar{E}_c . We recall that each point of the trajectory has a different curvature and therefore a different critical energy. We compute

$$\bar{E}_c = \frac{\int E_c(z)I(z)dz}{\int I(z)dz}, \quad (5)$$

where $I(z)$ is the local intensity emitted at the z coordinate. In vertical, each point y sees the emission with an approximated angle y/D as there the electron trajectory is in the

(x, y) plane. However, in horizontal the situation is different, as each trajectory point emits with an angle $\beta_x(z)$. The function $I(\beta_x)$ is multivalued, therefore intensity at a given coordinate angle x/D is originated from different trajectory points with $\beta_x \approx x/D$. By doing a multivalued interpolation we can obtain the intensity at coordinate x/D . It has then to be convolved with the bending magnet emission (using here critical energy $\max(E_c(z))$ as suggested in [3]) to obtain the profile I_x .

Evaluation of the $F(x, y, E)$ Stack

Having the intensity distribution $I(x, y)$ (normalized such as $\int dx \int dy I(x, y) = 1$) for each photon energy E , the spectral flux $F(E)$ is then multiplied by I to obtain the spectral flux density $F(x, y, E)$.

EXAMPLES

SHADOW ray tracing and the new OASYS widget Wiggler Radiation have been used to get the power density distribution at 30 m from the source. Calculations were done using 100 eV steps withing 0.1 keV to 100 keV photon energy range. ESRF-3PW are shown in Fig. 1, ESRF high power wiggler W150 in Fig. 2 and BEATS source in Fig. 3.

CONCLUSION

A new algorithm has been developed that allows a fast and accurate calculation of the spectral power density emission of Wigglers, with particular application on short wigglers and not periodical magnetic fields wigglers. It is implemented as an OASYS widget, representing an useful tool for heat-load calculations in beamline components, especially those found in the beamline front end. For that purpose, the new widget can be connected to the beamline elements (slits, mirrors, crystals) under study.

REFERENCES

- [1] L. Rebuffi and M. Sanchez del Rio, "OASYS (OrAnge SYnchrotron Suite): an open-source graphical environment for x-ray virtual experiments," *Proc. SPIE*, vol. 10388, no. 103880S, pp. 169–177, 2017, doi:10.1117/12.2274263
- [2] M. Sanchez del Rio, N. Canestrari, F. Jiang, and F. Cerrina, "Shadow3: A new version of the synchrotron x-ray optics modelling package," *Journal of Synchrotron Radiation*, vol. 18, no. 5, pp. 708–716, 2011, doi:10.1117/12.893433
- [3] T. Tanaka and H. Kitamura, "Source size and angular divergence of wiggler radiation," *AIP Conference Proceedings*, vol. 705, no. 1, pp. 41–44, 2004, doi:10.1063/1.1757729
- [4] G. Iori *et al.*, "Design and Ray-Tracing of the BEATS Beamline of SESAME," presented at MEDSI'20, Chicago, IL, USA, Jul. 2021, paper WEPB10, this conference.
- [5] S. Liuzzo, N. Carmignani, J. Chavanne, L. Farvacque, B. Nash, and P. Raimondi, "Optics Adaptations for Bending Magnet Beam Lines at ESRF: Short Bend, 2-Pole Wiggler, 3-Pole Wiggler," in *Proc. IPAC'17*, Copenhagen, Denmark, Geneva, Switzerland, May 2017, pp. 666–669, doi:10.18429/JACoW-IPAC2017-MOPIK062

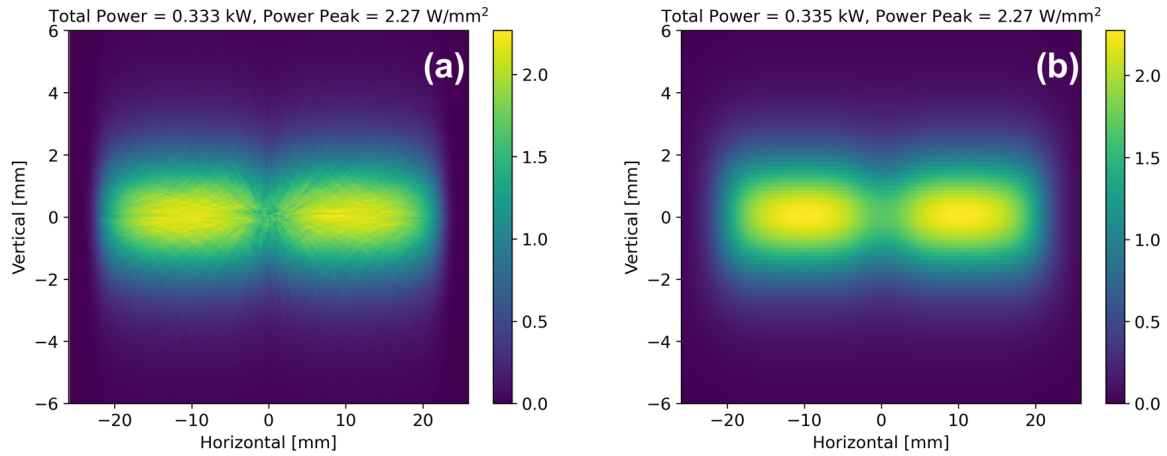


Figure 1: Power density distribution of ESRF-3PW: (a) Using ray-tracing and (b) New OASYS widget Wiggler Radiation.

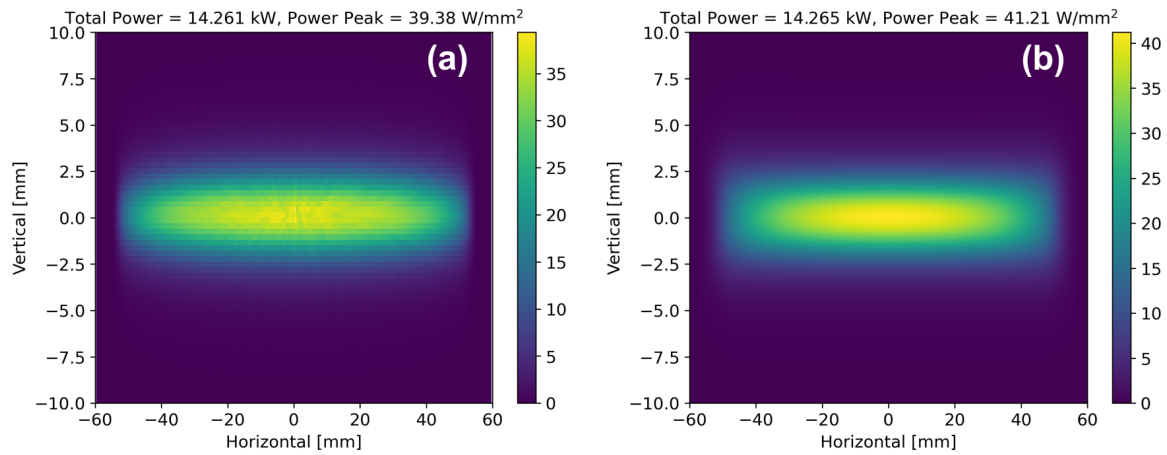


Figure 2: Power density distribution of ESRF-W150: (a) Using ray-tracing and (b) New OASYS widget Wiggler Radiation.

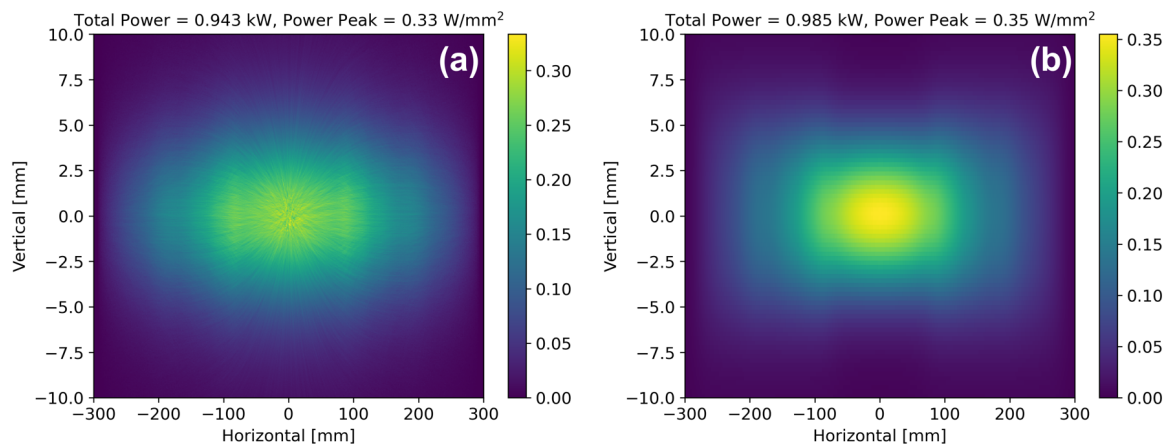


Figure 3: Power density distribution of BEATS project source: (a) Using ray-tracing and (b) New OASYS widget Wiggler Radiation.

A CRYOGENIC SAMPLE ENVIRONMENT FOR THE TARUMÃ STATION AT THE CARNAÚBA BEAMLINE AT SIRIUS/LNLS

F.R. Lena[†], C.S.N.C. Bueno, F.H. Cardoso, J.C. Carvalho, M.M. Donatti, R.R. Geraldés, L.M. Kofukuda, L.S. Perissinotto, E. Piragibe, C. Sato, H.C.N. Tolentino, W.H. Wilendorf, Brazilian Synchrotron Light Laboratory (LNLS), Campinas, Brazil

Abstract

TARUMÃ is the sub-microprobe station of CARNAÚBA (Coherent X-Ray Nanoprobe Beamline) at Sirius at the Brazilian Synchrotron Light Laboratory (LNLS). Covering the tender-to-hard energy range from 2.05 to 15 keV with achromatic fixed-shape optics, the fully coherent submicron focused beam can be used for multiple simultaneous advanced micro and nanoscale X-ray techniques that include ptychography coherent diffraction imaging (ptycho-CDI), absorption spectroscopy (XAS), diffraction (XRD), fluorescence (XRF) and luminescence (XEOL). Among the broad range of materials of interest, studies of light elements present in soft tissues and other biological systems put TARUMÃ in a unique position in the Life and Environmental Sciences program at LNLS. Yet, to mitigate the detrimental effect of the high photon flux of the focused beam due to radiation damage, cryocooling may be required. Here we present the design and first results of a novel open-atmosphere cryogenic system for online sample conditioning down to 110 K. The high-stiffness and thermally-stable sample holder follows the predictive design approach based on precision engineering principles to preserve the nanometer-level positioning requirements, whereas a commercial nitrogen blower is used with a cold gas flow exhaustion system that has been developed in order to avoid unwanted cooling of surrounding parts and water condensation or icing.

INTRODUCTION

With the advancements of low-emittance 4th-generation synchrotron light sources, small X-ray probes with higher photon flux are made possible [1]. Here we bring the case of the TARUMÃ station [2, 3] at the CARNAÚBA (Coherent X-ray Nanoprobe Beamline) [3, 4] beamline at Sirius at the Brazilian Synchrotron Light Laboratory (LNLS), where the ultra-high vacuum (UHV) KB optics is capable of delivering the submicrometric focus of 550 to 120 nm while yielding a high photon flux of up to $1e11$ ph/s/100mA [4]. In addition, the large working distance of 440 mm after the KB set allows a broad range of sample environments outside vacuum (see [2]).

Working in the tender X-ray region, the station can be used for soft tissue and light elements multi-instrumentation probing. One of the most appealing techniques is the nano ptycho-CDI, in which the referred probe, combined with the beamline optics and the characteristics of the PiMEGA or MobiPix Medipix-based area detectors [5], can result in spatial resolution in the nanometer range [2].

Yet, this resolution limit is directly impacted not only by the relative position stability between the sample and the probe, bringing the TARUMÃ stability requirements down to the same order, but also by the characteristics of the sample itself over time. This results in two main challenges: ensuring the sample-to-probe spatial stability, that is mostly addressed by the high-stiffness and exactly-constrained optics [6]; best effort over the commercial stages composing the sample manipulator (with a complementary metrology frame) [2] and sample setups based on precision engineering principles; and mitigating the dose-induced sample degradation due to the high photon density and absorption in the tender energy range, especially in biological samples. For the latter, cryocooling the sample has been proved very effective, greatly reducing the dose damage, and improving temporal preservation during long scanning times [7]. In the following sections we present the in-house development and pre-commissioning tests of the TARUMÃ cryogenic sample environment.

SYSTEM OVERVIEW

Aiming at implementing the needed sample cryocooling functionality for the tender X-ray TARUMÃ station and unlocking the possibility of studying soft organic and other dose-sensitive materials, a commercial liquid nitrogen (LN₂) based Cryojet-5 from Oxford Cryogenics system was chosen as the cooling instrument. This choice was made because of the open-atmosphere condition of the sample stage and space constraints limiting other conductive options. Yet, despite the simplicity of the system and easily achievable gas temperatures as low as 80K, the high density of instruments around the sample (see [3]) made its integration at the station a challenging task.

Firstly, the open-atmosphere concept of the commercial cryojet might lead to thermal drift, condensation and/or icing issues in the sample or in sensitive nearby instruments, if the cold gas outflow would not be properly managed. At TARUMÃ, this is prevented with the implementation of an exhaustion system. Then, the open flow nature of this solution might be conflicting with the nanometric sample positioning requirements. This is addressed by a thermo-mechanical design that decouples the high-stiffness sample holder assembly from an auxiliary gas shield with optimized aerodynamics to minimize flow-induced disturbances. In addition to the cryojet and the sample itself, the TARUMÃ cryogenic setup (Fig. 1) is composed of three main subsystems: the *sample holder*, the *holder shield* and the *exhaustion system*.

[†] francesco.lena@lnls.br

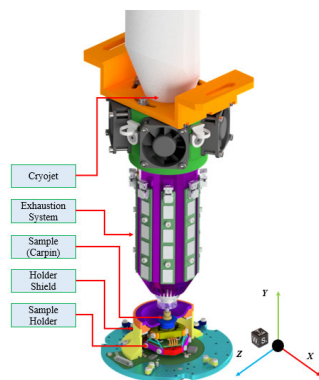


Figure 1: TARUMÃ cryogenic setup main subsystems.

As TARUMÃ is a scanning station that may take experiments reaching several hours, the thermal drift must be minimized. Moreover, to archive a high throughput of the beamline with fast sample exchange, the cooldown and heat up times must be limited to few minutes. These aspects are addressed via embedded thermal management.

SAMPLE HOLDER

The sample holder system (Fig. 2) comprises the CARNAÚBA standard sample pin (Carpin), a magnetic coupling system for an aerodynamic bridge to the shield, two frames (SSTop and SSBot), a set of thermal decoupling flexures (A-struts), and temperature sensors and heaters on printed circuit boards (PCBs). To speed up setup time by making it as modular and easily exchangeable as possible, the standard mounting plate for the holder was made compatible with the TARUMÃ standard interface plate that lies on the PI P-563 XYZ piezo scanning stage.

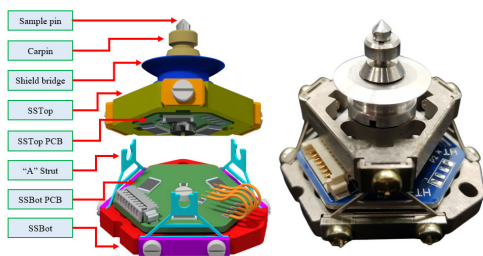


Figure 2: Left: overview of the sample holder with its main subcomponents. Right: picture of the assembly.

Alternatively, the holder was also designed to be compatible with the ptycho-Bragg-CDI setup, in which it is instead fixed to a tip-tilt Attocube piezo assembly (ANGt101 and ANGp101) on a different mounting plate. This sets an additional requirement that the sample holder accepts rotations of about $\pm 4^\circ$ in the Rx and Rz axes with respect to the holder shield around the sample nominal position.

In addition to low position drift in the sample, low thermal conductivity is required between the sample and the room-temperature (RT) parts, so that sufficiently low temperatures can be achieved with a given heat exchange with the cold air. Thus, the main material in the holder (SSTop, SSBot and "A" Struts) is Invar 36. In spite of not being the most refractory metal available, analytical models and finite element (FE) simulations resulted in

minimum sample temperature around 110 K, whereas the maximum vertical position sensitivity should be in the range of 41 nm/K for constant variation either in the temperature of the cold gas or the RT base (SSBot). Other options, such as Ti6Al4V might reach even lower temperatures, but showed higher sensitivity. All the Invar parts were nickel plated to mitigate corrosion and will be gold-plated to reduce radiation heat exchange.

Both SSTop and SSBot are equipped with custom aluminum metalcore PCBs with Riedon 1kOhm RTD (Resistance Temperature Detector) temperature sensors and Susumu 2512 SMD (Surface Mounted Device) power resistors acting as heaters. Each PCB can then deliver up to 4 W to the Invar parts. This is needed to control the cold SSTop temperature few degrees above the minimum achievable temperature to reduce thermalization times (220 s for 150 K, estimated) and drifts, and to maintain the SSBot at RT. Keeping both referred parts under control also allow the Invar A-struts internal gradient to be constant, as convection heat exchange is minimum, greatly reducing position drifts. The SSTop PCB can also be used to heat all the cold parts for faster sample exchange.

HOLDER SHIELD

The sample holder shield (Fig. 3) has two main functions: guiding the cryojet cold gas back to the exhaustion system in a controlled way, thus, minimizing flow-induced disturbances in the holder and preventing nearby components from being cooled; and providing a dry environment to avoid icing on the sample holder cold parts.

The first is achieved by the appropriate design of a concave aluminum gas guide that forces the incoming cryojet flow back upwards, to where the low differential pressure of the exhaustion system can draw it, according to CFD simulations. Yet, as the shield is cooled by the cold gas in forced convection, an embedded heating system was designed to avoid unwanted icing by controlling it slightly above RT. 10x Susumu 2512 SMD power resistors connected in series in a circular aluminum metalcore PCB can deliver up to 40 W to the shield. For temperature feedback for a PID control loop, two 1 kΩ Riedon platinum RTD sensors are again used.

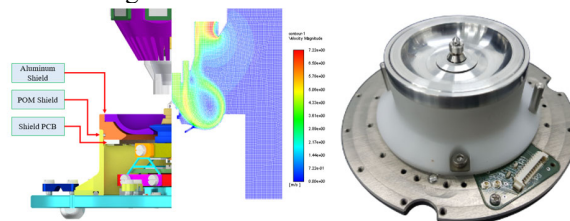


Figure 3: Overview of the Holder Shield including a CFD velocity plot example and the final assembly.

Next, the dry environment for the Sample Holder by is achieved by purging dry nitrogen gas into the Holder Shield. Sealing at the base is made via o-rings, whereas there is a small the gap of a few tenths of a millimeter between the holder and the shield, with unimportant leakage. This assures the mechanical decoupling between both parts and complies with the tip-tilt requirements for the holder.

An analog pressure transducer KP216H1416XTMA1 by Infineon Technologies is used to ensure a minimum of 20 Pa of relative pressure is always kept, while an analog HIH-4031-001 air humidity sensor by Honeywell is used to constantly monitor if the internal atmosphere water content is below dew point. Both sensors are assembled in a FR4 PCB and used in an interlock system for the cryojet.

EXHAUSTION SYSTEM

The exhaustion system (Fig. 4) was design to create a negative pressure zone as close to the cryojet nozzle as possible, collecting the cold gas around the nozzle itself after cooling the sample to preserve the surroundings. The system also acts as a gas heater by exchanging heat through internal fins. A total heating power of 190 W can be used to rise the cold gas temperature back to RT. This is especially important to avoid further condensation inside the exhaustion channels and to mitigate any undesired cooling of secondary nearby instrumentation.

The module main frame is an aluminum heatsink machined via EDM (Electrical Discharge Machining) for the internal fins, which is equipped with 8 custom aluminum metalcore PCBs with four 100 Ω Ohmite D-Pack power resistors acting as heaters. The temperature control feedback is provided by two 1 kΩ Riedon RTD sensors assembled in aluminum PCBs. The negative differential pressure is achieved by a set of 4 Sanyo commercial cooling fans controlled by the same driver that is used for the heaters. According to CFD simulations, the fans can reach the needed static pressure of 36 Pa and flow of 113 l/min.

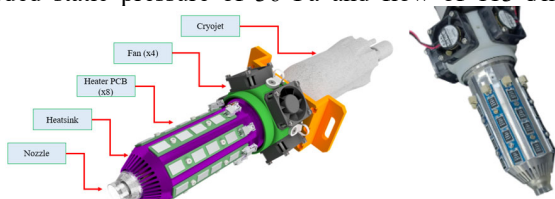


Figure 4: Exhaustion system render and final assembly.

FIRST RESULTS

To validate the system shield flow and induced disturbances before the final commissioning at the beamline, a mockup of the system was 3D printed and a parallel flexure-based precision load cell (< 0.6 μN resolution with first mode at 102 Hz) with a Lion Instruments capacitive probe was made (Fig. 5). Both the in-plane and vertical force disturbances were measured for multiple sample configurations and flow conditions: for the cold flow rates of 7 and 21 l/min, and the RT flow rates of 5.7 and 18.9 l/min.

The results suggest that the low-frequency contribution (< 10 Hz) dominates the disturbances for all flow rates and sample conditions. With the nominal sample holder position, the average 0-90 Hz RMS in-plane force level with the maximum cryojet flow was 2.2 ± 0.7 mN, whereas the vertical was 4.1 ± 2.1 mN. The force data from two X and Y average test runs (Fig. 6) was used to feed a dynamic model of the TARUMÃ sample stages to calculate the expected position disturbances at the sample position in with respect to the experimental bench (see [3]).

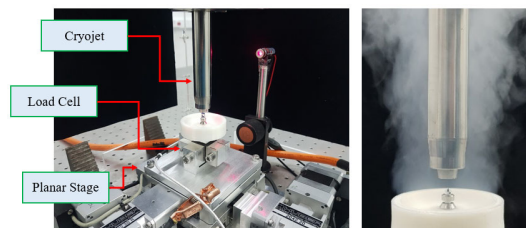


Figure 5: Test setup and mockup shield flow.

The resulting X position RMS value from 0 to 90 Hz was 3.6 nm, whereas the Y was 6.7 nm, which is acceptable within the design budget, as a fraction of the beam size and reasonable for ptychography.

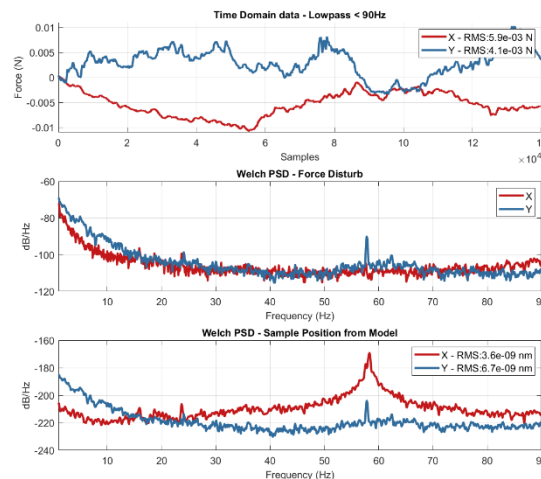


Figure 6: X and Y force time plot and PSD with the referred sample position PSD from the dynamic model.

CONCLUSION

We present the main design remarks regarding the integration of a commercial cryojet into a cryogenic sample setup for cooling sensitive samples at the TARUMÃ station, with focus on position stability, and condensation/icing and thermal managements. Although the final assembly has not yet been fully commissioned due to delays related to the COVID19 pandemic, the first force disturbance results with a mock-up system endorse the correct use of design-for-stability concepts resulting in acceptable predicted disturbances within the design budgets. It's also important to highlight the extensive use of SMD components with metalcore PCBs as heating elements and temperature sensors as well as ordinary (FR4) PCB with SMD pressure and humidity sensors for control and interlocking purposes, leading to the needed setup compactness for the strict space-constraints in the station.

ACKNOWLEDGEMENTS

The authors would like to gratefully acknowledge the Brazilian Ministry of Science and Technology for the funding, as well as all the engineering and science team members working for the Sirius project, and the Microfabrication Laboratory (LMF) at LNNano/CNPEM.

REFERENCES

- [1] D. Einfeld, "Performance and Perspective of Modern Synchrotron Light Sources", in *Proc. 58th ICFA Advanced Beam Dynamics Workshop on High Luminosity Circular e+e- Colliders (eeFACT'16)*, Daresbury, UK, Oct. 2016, pp. 17-24. doi:10.18429/JACoW-eeFACT2016-M00TH4
- [2] H. Tolentino, R. R. Geraldès, G. Moreno, C. S. B. Dias, C. Perez, and M. M. Soares, "TARUMÃ station for the CARNAUBA beamline at SIRIUS/LNLS," *X-Ray Nanoimaging: Instruments and Methods IV*, vol. 11112, Sep. 2019, p. 5. doi: 10.1117/12.2531110
- [3] R. R. Geraldès *et al.*, "Design and Commissioning of the TARUMÃ Station at the CARNAUBA Beamline at Sirius/LNLS," presented at MEDSI2020, Chicago, IL, USA, Jul. 2021, paper WEPB13, this conference.
- [4] H. C. N. Tolentino *et al.*, "CARNAUBA: The Coherent X-Ray Nanoprobe Beamline for the Brazilian Synchrotron SIRIUS/LNLS," in *Journal of Physics: Conference Series*, vol. 849, no. 1, p. 012057, 2017. doi:10.1088/1742-6596/849/1/012057
- [5] L. Sanfelici *et al.*, "Solutions for the SIRIUS' beamlines in a nutshell," *AIP Conference Proceedings*, vol. 2054, p. 030033, 2019. doi:10.1063/1.5084596
- [6] G. B. Z. L. Moreno *et al.*, "Exactly-constrained KB Mirrors for Sirius/LNLS Beamlines: Design and Commissioning of the TARUMÃ Station Nanofocusing Optics at CARNAUBA Beamline," presented at MEDSI2020, Chicago, IL, USA, Jul. 2021, paper TUOB01, this conference.
- [7] M. Odstrcil *et al.*, "Ab initio nonrigid X-ray nanotomography," *Nat. Commun.*, vol. 10, no. 1, p. 2600, 2019. doi:10.1038/s41467-019-10670-7

ELECTROCHEMISTRY AND MICROFLUIDIC ENVIRONMENTS FOR THE TARUMÃ STATION AT THE CARNAÚBA BEAMLINE AT SIRIUS/LNLS

W. H. Wilendorf[†], R. R. Gerales, L. M. Kofukuda, I. T. Neckel, H. C. N. Tolentino,
Brazilian Synchrotron Light Laboratory (LNLS), Campinas, São Paulo, Brazil

P. S. Fernandez, Chemistry Institute, State University of Campinas, Campinas, São Paulo, Brazil

Abstract

TARUMÃ is a multi-technique sub-microprobe experimental station of the CARNAÚBA (Coherent X-Ray Nanoprobe Beamline) beamline at Sirius, the 4th-generation synchrotron light source at the Brazilian Synchrotron Light Laboratory (LNLS). This work describes two related setups that have been developed in-house for TARUMÃ: a small-volume electrochemical cell, and another multifunctional liquid environment that can be used both as a microfluidic device and as an electrochemistry cell that allows for fluid control over electrodes. The mechanical design of the devices, as well as the architecture for the fluid and electrical supply systems are described in detail.

INTRODUCTION

CARNAÚBA (Coherent X-Ray Nanoprobe Beamline) [1] is a state-of-the-art multi-technique beamline of Sirius [2], the 4th-generation Light Source at the Brazilian Synchrotron Light Laboratory (LNLS) at the Brazilian Center for Research in Energy and Materials (CNPEM), with achromatic optics and fully-coherent X-ray beam in the energy range between 2.05 and 15 keV. It is equipped with two in-line experimental stations, namely: TARUMÃ [3], a sub-microprobe station in an advanced commissioning phase, for which the sample environments presented here were specially designed; and SAPOTI, a nanoprobe station still in design phase.

At the TARUMÃ station, the in-vacuum KB focusing system has been designed with a large working distance of 440 mm, allowing for a broad range of independent sample environments to be developed in open atmosphere to benefit from the spot size between 550 and 120 nm, with a flux in the order of $1e11$ ph/s/100mA. Hence, together with a number of detectors that can be simultaneously used, as shown in Fig. 1, a wide variety of studies of organic and inorganic materials and systems are possible using cutting-edge X-ray-based techniques in the micro and nanoscale, including: coherent diffractive imaging (CDI), fluorescence (XRF), optical luminescence (XEOL), absorption spectroscopy (XAS), and diffraction (XRD). Even though samples over the centimeter range can be taken at TARUMÃ, the small beam and relatively low energies point towards optimized and small sample setups for in situ experiments. Indeed, reduced-size geometry and light materials allow lighter sample environments, helping with fast flyscan mapping and the final stability of the sample positioning system, which is composed of commercial stages for up to 6 degrees of freedom (DoF) (see [3]).

[†] willian.wilendorf@lnls.br

To explore the resolution and the multi-techniques available at TARUMÃ for studies in the fields of electro-chemistry (electrocatalysis) [4] and microfluidic (in situ reactions and in vivo studies) [5], two sample environments for *in situ* experiments were especially designed following the precision engineering concepts required for nanopositioning performance. The first setup is a small-volume electrochemical cell with working, counter and reference electrodes, and the machined parts made of light and non-reactive polymeric materials. The second one is a multifunctional glass-based device that can be used both as a microfluidic device only, or an electrochemical cell, by controlling fluids over embedded electrodes. This work presents the details of the mechanical designs of the two sample environments developed in-house, and the architecture for the electrical and hydraulic supply system.

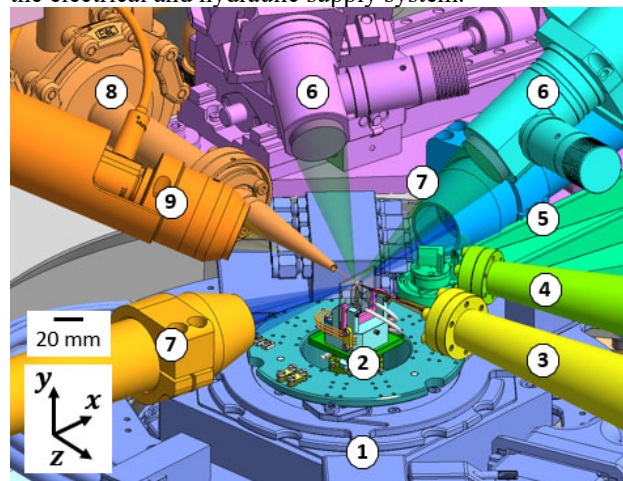


Figure 1: Sample region at TARUMÃ, with the several detectors that allow for multi-technique experiments: sample positioning stages (1), sample environment setup (2), flying paths for transmission (3) and diffraction (4) area detectors, crystal analyser spectrometer (5), optical microscopes (6), fluorescence detectors (7), exit vacuum nipple of KB chamber (8) and luminescence detector (9).

ELECTROCHEMICAL SETUP

The setup depicted in Fig. 2 was designed for in situ experiments in electrochemistry and electrocatalysis at TARUMÃ, according to the infrastructure capabilities and interfaces at the station. It is a versatile small-volume oxidation-reduction reaction cell with external dimensions of $45 \times 33 \times 45$ mm³. The electrolyte, with a static volume of 1 ml, as well as the working, counter and reference electrodes, may be suitably selected according to the scientific

cases. The parts in contact with the electrolyte are manufactured in PEEK, due to its inert condition and chemical resistance, whereas the remaining parts can be manufactured of a more cost-effective polymer, such as POM (Polyoxymethylene), which still has some resistance to reactions. The cell main elements are detailed below:

Main frame (1) – it is the main structural part of the cell, with the electrolyte container and the fittings for coupling the electrodes. Two auxiliary access points (2) at the top are used to manage the electrolyte and two nuts at the rear (3) allow for fine position adjustment and locking of the working and counter electrodes. The sealing of the electrolyte container is made with a 12.5 μm thick Mylar® film (4) (for about 50% beam transmission at 2.05 keV), which is clamped via a Viton® o’ring (5) that is fitted into a groove on the outer cylindrical surface.

Working electrode (6) – it consists of a solid cylinder, typically of gold or platinum, with diameter of 1 mm and length of 15 mm, that is hermetically inserted into a PEEK threaded housing, which is sealed via a double layer of Viton o’rings and has an opening for the electrical connector (detailed below). Only the reaction surface of the electrode, with 0.785 mm², is exposed to the electrolyte, while facing the film for the X-ray probing in reflection mode.

Counter electrode (7) – it is a disk with an outside diameter of 17 mm and thickness of 0.5 mm that fixed to the bottom of the electrolyte container by a nut (8). A gold-plated stainless-steel cylinder hermetically fitted into another PEEK threaded housing, also with a complementary double-layered Viton o’ring sealing and an opening for the electrical connector, is put in contact with the electrode disc to for electrical connection.

Reference electrode (9) – as the working electrode, it is also a solid cylinder with diameter of 1mm and length of 15mm, inserted in a polymeric housing that allows the coupling of the electrical connector. Yet, as it currently implemented as a commercial silver chloride (Ag/AgCl) electrode [6], which is fragile and prone to damage, a clamping system with manual force control was designed, in which two Viton o’rings are compressed by a nut (10) to make pressure on the cylindrical surface of the electrode.

Electrical connectors (11) – they are customized parts that electrically connect the solid electrodes to the control hardware. They consist essentially of a cylindrical piece of copper that is soldered to a 24-AWG cable at one side and fitted with a spring-loaded probe [7] making contact with the electrode at the other. This set is inserted into a POM housing with a pin (12), for a locking mechanism.

Interface frame (13) – it is the part responsible for the interface with the TARUMÃ sample positioning system, which is achieved via a magnetically-preloaded kinematic mount. Since it is made of POM, three stainless steel spheres are glued in recesses in the bottom face for Hertz contact with three V-grooves in the coupling part, whereas a magnetic piece in the center of the contact triangle is used to increase the preloading loading force and, thus, the contact stiffness for superior dynamic performance. Also regarding dynamics, the wider footprint was made to increase the mounting lever-arms as much as possible and to

shift the center of mass of the assembly, both downwards and to the center of the kinematic mount in the xz plane. Finally, to passively minimize drifts in the region of interest in the sample due to thermal expansion effects, the reaction surface of the working electrode was aligned over the thermal center of the assembly, lying on the center of the kinematic mount in the xz plane. Anticipating that sealing failures could occur, the interface base has high borders to contain the leaked solution before it reaches (and possibly damages) the stages located just below the cell.

To conclude, some clamps are fixed to the sides of the main and interface frames for routing and fixing the cables according to predictable dynamic links with respect to the sample stage, both preventing tensions forces and/or fatigue from damaging the connectors, and managing disturbance forces in the cell due to sample positioning.

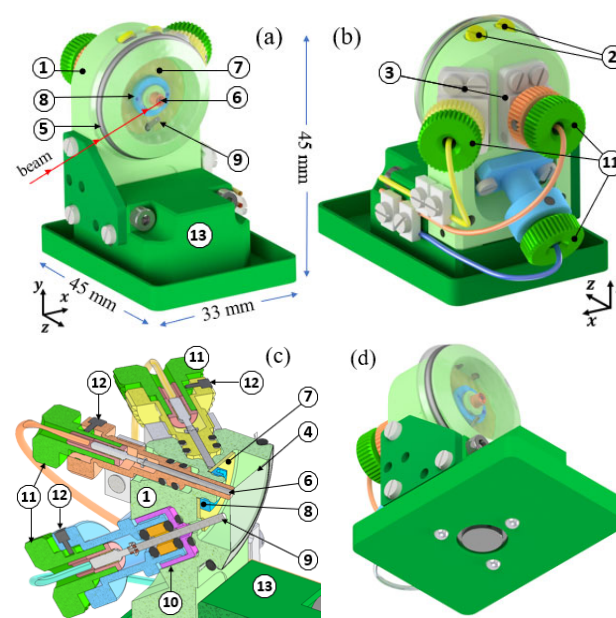


Figure 2: The electrochemical setup seen from the front (a) and back (b) sides, in quarter-section view (c) and also from below (d) (with the kinematic mount).

MICROFLUIDIC SETUP

The setup shown in Fig. 3 has been designed to be the microfluidics platform at TARUMÃ, with volumes in the order of μl and a precise flow control. Optionally, embedded metallic electrodes can be prepared via photolithography and deposition processes to allow for in situ experiments of electrochemistry [8], as in the previous cell, but at a different scale. It can be broken down into 3 main parts, as described below:

Microfluidic device (1) – it is the core component in the setup, manufactured with in-house technology in the Microfabrication Laboratory (LMF) at LNNano/CNPem. Although different geometries and features may be considered in the future, the first device (see [8]) consists of a 30 x 26 x 1 mm³ glass substrate with a micro-reservoir connected to one inlet and one outlet microchannels. Bridging from the micro-reservoir to a macroscopic connection re-

gion, three 100 μ m-thick gold electrodes are deposited on the glass via a lithographic process. Finally, two small flexible silicone tubes (6) are connected to the microchannels via a PDMS (5) pad. In this case, the regions of interest for the sub-micrometer X-ray probe are the electrodes within the micro-reservoir volume, where the reaction occurs.

Main frame (2) – made of aluminum, it is the part responsible for holding the microfluidic device in place via fastening screws (9) and making the interface with the TARUMÃ sample positioning system. As in the interface frame of the electrochemical cell, coupling is made via a magnetically-preloaded kinematic mount. Also, equivalently to the interface frame, a complementary tray (4) is included to contain any leaks and prevent damage to the stages. The same care regarding precision engineering concepts for dynamics, thermal drift and cable/tubing management with clamps (7 e 8) are applied here.

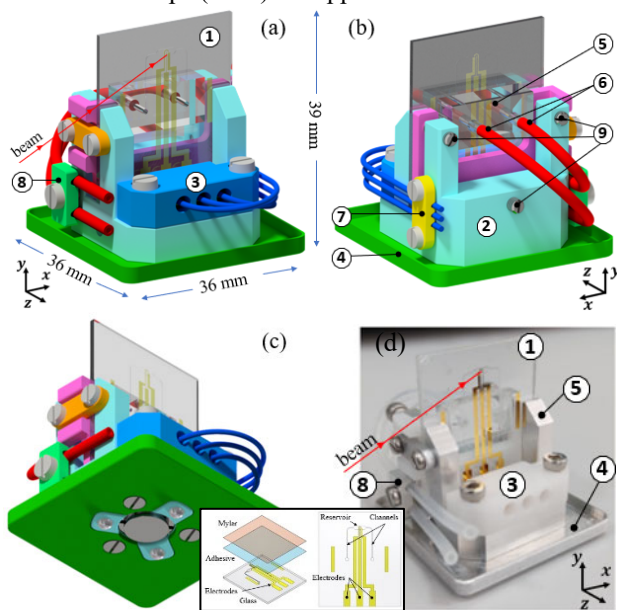


Figure 3: Drawing of the microfluidic setup seen from the front (a) and back (b) sides, and the bottom view, with of the kinematic mount (c). Prototype fully made in house (d).

Electrical connector (3) – for devices with electrodes, it is used to connect them to the control hardware. It consists of an insulating housing made of POM with contact sets based on spring-loaded probes, as in the connectors of the electrochemical cell. Here the spring probes help compensating small dimensional variations in the glass or assembly errors, ensuring electrical contact while preserving the glass substrate.

SUPPLY SYSTEM

Both special sample setups require complementary functional resources, i.e., either a control hardware for current/voltage, or pumps for the fluids. Due to the tight volume constraints in the surroundings of the sample and the dynamic-oriented architecture of the station, the standard solution is installing the large pieces of equipment on auxiliary stands around the station. Hence, a permanent set of cables and tube guides – with deterministic links between

the precise air-bearing rotary stage of sample stack and a synchronized auxiliary rotary stage dedicated to cable management – should be used. Indeed, as illustrated in Fig. 4, this concept allows for rotations of $\pm 110^\circ$ for tomography experiments, while preventing unknown and uncontrolled force disturbances at the sample.

Thus, the electrodes of the cells can conected via a short cable to an electrical patch panel on the top frame of the sample stage, while the cables exiting the cable chain are connected to the control hardware, such as the SRS EC301 potentiostat, to be used in day 1 at TARUMÃ. Similarly, short tubes leaving the microfluid cell can be connected to a manifold on the sample stage, while independent tubes are connected to a syringe pump, for example. Still, for small volumes, a local embedded reservoir for the outlet fluid can also be considered.

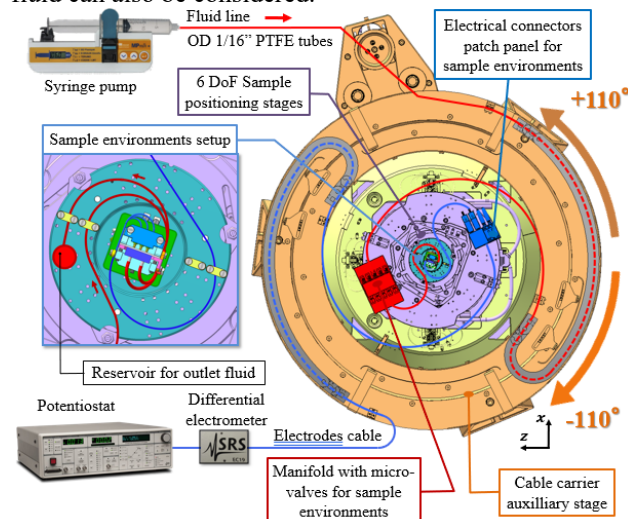


Figure 4: The supply system architecture at TARUMÃ.

CONCLUSION

Two sample environments for in situ experiments in electrochemistry with static fluid and microfluidics have been designed in-house for compatibility with the multiple X-ray techniques at the TARUMÃ station. They are based on previous experience in the field and follow precision engineering concepts, not only for stability with respect to the nanometric beam and but also for flyscan compatibility. After validating assembling and sealing concepts via preliminary prototypes, the microfluidic cell has just been manufactured and the electrochemical cell is in procurement. They are expected to be finalized and fully commissioned soon, becoming part of the station experiments portfolio in the second half of 2021.

ACKNOWLEDGEMENTS

The authors would like to gratefully acknowledge the funding by the Brazilian Ministry of Science, Technology and Innovation, the contributions of the LNLS team and partners, and the collaboration with the Microfabrication Laboratory (LMF) at LNNano/CNPEN.

REFERENCES

- [1] H. C. N. Tolentino *et al.*, “CARNAÚBA: The Coherent X-Ray Nanoprobe Beamline for the Brazilian Synchrotron SIRIUS/LNLS,” *J. Physics: Conf. Series*, vol. 849, no. 1, p. 012057, 2017.
<http://dx.doi.org/10.1088/1742-6596/849/1/012057>
- [2] Sirius Project, <https://www.lnls.cnpem.br/sirius-en/>
- [3] R. R. Geraldes *et al.*, “Design and Commissioning of the TARUMÁ Station at the CARNAÚBA Beamline at Sirius/LNLS”, presented at MEDSI 2020, Chicago, USA, July 2021, paper WEPB13, this conference.
- [4] R. A. Vicente *et al.*, “Bragg Coherent Diffraction Imaging for In Situ Studies in Electrocatalysis,” *ACS Nano*, vol. 15, no. 4, pp. 6129-6146, 2021.
<https://doi.org/10.1021/acsnano.1c01080>
- [5] A. Ghazal *et al.*, “Recent advances in X-ray compatible microfluidics for applications in soft materials and life sciences,” *Lab Chip*, vol. 16, no. 22, pp. 4263-4295, 2016.
<https://doi.org/10.1039/C6LC00888G>
- [6] Innovative Instruments, <https://www.2in.com/products/reference/reference.html>
- [7] Feinmetall, <https://www.feinmetall.com/product-finder/contact-probes/contact-probes/?kid=F704&filter1=&filter2=&filter3=&filter4=&tags=>
- [8] I. T., Neckel *et al.*, “Dispositivo microfluídico selado com película de polyester,” Patent App. BR 10 2020 020040 2, September 30, 2020.

A COMPACT X-RAY EMISSION (mini-XES) SPECTROMETER AT CLS - DESIGN AND FABRICATION METHODS

T. W. Wysokinski[†], M. Button, A. F. G. Leontowich, B. D. Moreno, CLS, Saskatoon, Canada

Abstract

A compact X-ray emission spectrometer (mini-XES) has been designed and fabricated for use at the Brockhouse undulator beamline. The mini-XES design was developed to be as simple to fabricate and as easy to operate as possible. We tried to minimize the number of parts. From the beginning, the design was trying to achieve no tools assembly, alignment, and operation. The first tests of the spectrometer were completed and were successful.

INTRODUCTION

A compact X-ray emission spectrometer (mini-XES) has been designed and fabricated for use at the Brockhouse undulator beamline [1]. The mini-XES uses cylindrical von Hamos geometry tuned for Fe K-edge and uses a Pilatus 100K area detector from Dectris [2]. It is based on a general design implemented at the APS [3].

The mini-XES design was developed to be as simple to fabricate and as easy to operate as possible. We tried to minimize the number of components, so there are only two main parts that create a chamber. Those two components are joined and aligned by a NW-80 flange. From the start, the design was trying to achieve no tools assembly, alignment, and operation. For lower precision alignment we decided to use the centering ring of the NW-80 flange which, together with two posts integrated with the chamber, provides an adequate method for joining the two parts of the enclosure. We use level vials for horizontal adjustment of the holder for the 10 crystals. For high precision alignment of the crystal holder, we use the Thorlab KC1/M kinematic mount, which have the adjustment screws accessible from outside of the chamber. The fabrication was done in-house using uPrint SE Plus 3D Printer [4].

The first tests of the spectrometer were completed in the Brockhouse wiggler beamline [5] and were successful. Future improvements will aim to reduce the background scatter and better position the detector, to improve the fill. Now that the relatively inexpensive design was tested and tried, there is an option to upgrade it to 3D printed tungsten or steel version that would intrinsically provide the required shielding.

MAIN COMPONENTS

The spectrometer consists of:

- Top Chamber
- Bottom Chamber
- Crystal Holder with crystals
- Apertures

The estimates for the model material used and the print time are included in Table 1.

[†] wysokinski@alumni.sfu.ca

Main Printed Components

The top chamber (Fig. 1), attaches to the detector and the design protects the sensitive part of the detector. It assures that there is no possibility of contact with the focal plane once the detector is ready to use. The other end of the chamber mates to the NW-80 flange.

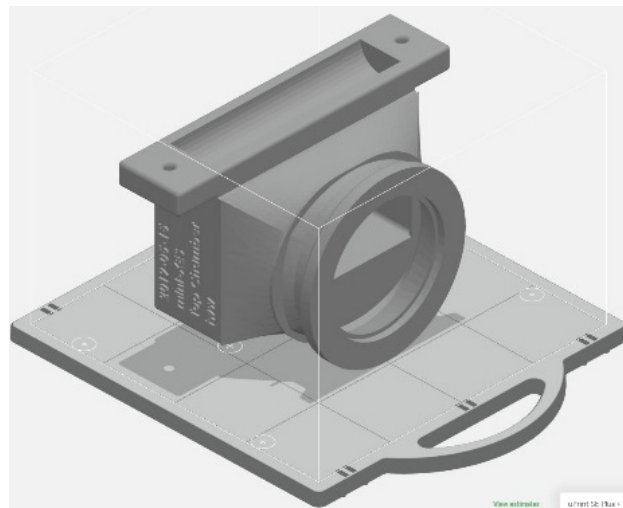


Figure 1: Top chamber model.

The bottom chamber is more complex (Fig. 2). It starts with NW-80 flange at the top that connects to the top chamber. The centering ring provides axial alignment. Two horizontal arms, that contact the backplate, provide the rotational alignment.

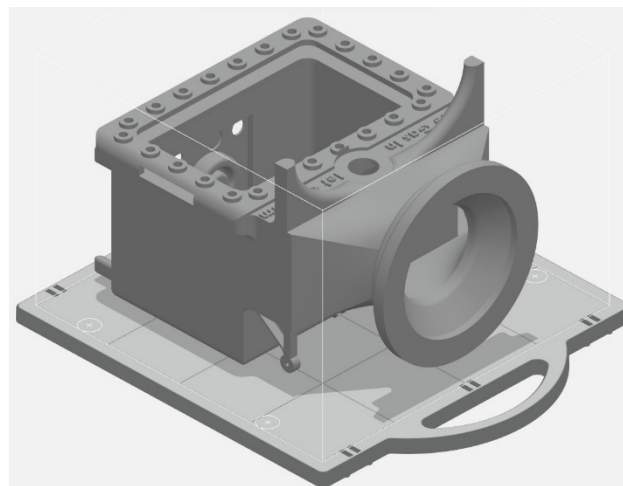


Figure 2: Bottom chamber model.

The chamber has several slots for apertures, a slot for the back door, support legs and alignment posts which combined with the alignment lines help to position the sample at the right location.

As can be seen, the parts were very close to the maximum part size that the uPrint SE Plus 3D printer could fabricate: 203x203x152 mm³ (8x8x6 in³).

Table 1: Model Material and Print Time Estimates

Part name	Model Material [cm ³ /in ³]	Print Time [hours]
Top Chamber	226/13.8	24
Bottom Chamber	389/23.7	42
Crystal Holder	46.2/2.8	5
TOTAL	661.2/40.3	71

Additional Parts

For alignment between the top and bottom chambers, we decided to use the centering ring of the NW-80 flange which, together with two horizontal posts integrated with the bottom chamber provide an adequate method for joining the two parts of the enclosure. NW-80 flange was chosen as it provides the minimum window opening required for the design. We use three level vials for initial horizontal adjustment of the crystal holder (Fig. 3).



Figure 3: A photograph of the crystal holder with Ge (620) crystals installed with small dabs of Apiezon M vacuum grease. At the bottom, press-fit posts are visible, which are used to attach the holder firmly to the kinematic top plate.

For higher precision alignment of the crystal holder, we use the Thorlabs KC1/M kinematic mount (Fig. 4). We use a press-fit geometry to anchor the rear plate to the floor of the bottom chamber from inside and to anchor the front plate to the crystal holder. The adjustment screws are accessible from outside of the chamber and the legs on the bottom chamber protect them from contacting any surface.

The back door was made out of Lucite (PMMA) plate (0.25" thick). The door has an O-ring installed into the machined groove and it is pressed against the chamber wall using M-6 Thumbscrews from Thorlabs (TS6H/M-p5).

The chamber has threaded holes that provide enough accuracy for the thumbscrews to work. As a redundancy, in case of thread failure, 24 threaded holes are provided. A backup option would be to install metal inserts into failed plastic threads if needed.

We also integrated a quick disconnect port for the He supply line above the door (Fig. 4). There is no exhaust port as the flow out is provided by diffusion thru the walls, and

by small openings in the chamber around the kinematic mount adjusters and back door.

Figure 5 shows a closeup of the bottom chamber. The crystal holder and its alignment system are visible thru the Lucite back door. Several of the thumbscrews pressing the back door to the chamber are visible.

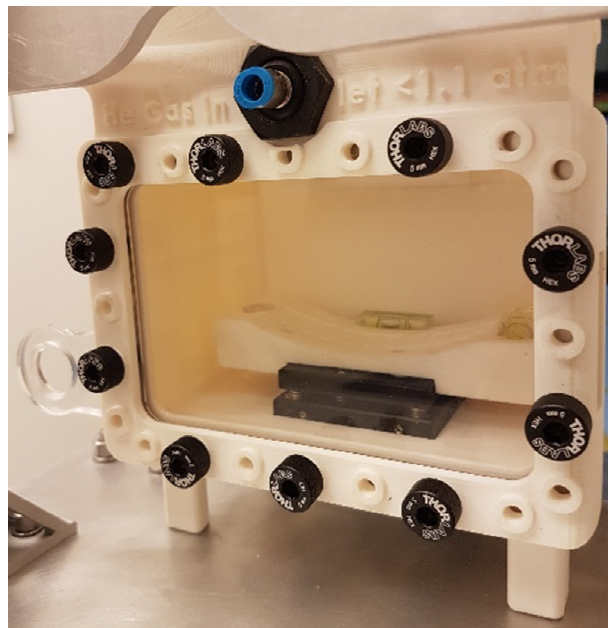


Figure 4: Close-up of the bottom chamber with crystal holder, back door, and He supply port.

Figure 5 shows the same bottom chamber from the user access side. Alignment posts help to align the complete assembly with the beam and the sample. Aperture holders are designed to easily slide in/out from the chamber housing.

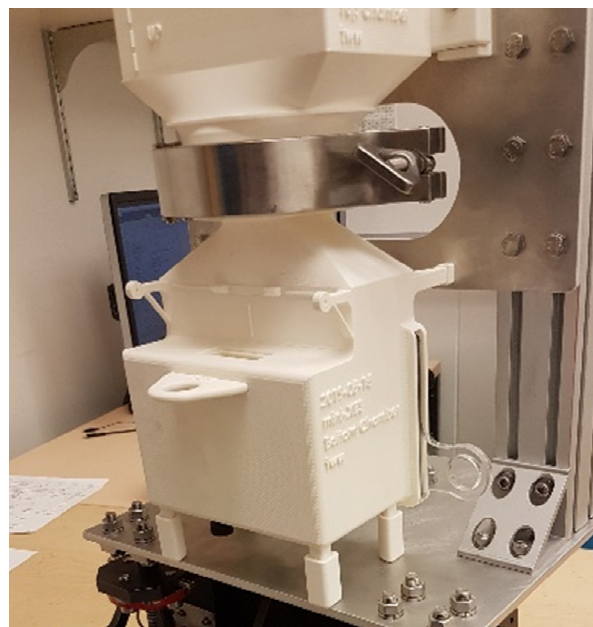


Figure 5: User side view of the completed assembly attached to the positioning table.

Sealing the Chamber

We applied several coats of Woods™ Waterproof Silicone Spray to seal the plastic walls as much as possible. We used a Kapton window to close the top of the chamber, next to the area detector. The top chamber design has an internal horizontal flat with a window cut-out for that purpose.

COMPLETED ASSEMBLY

The mini-XES is attached to an external aluminium plate and frame structure that provides required support and has additional motorized jacks for alignment (Fig. 6). Additional shielding was added to minimise external scatter and to improve S/N ratio.

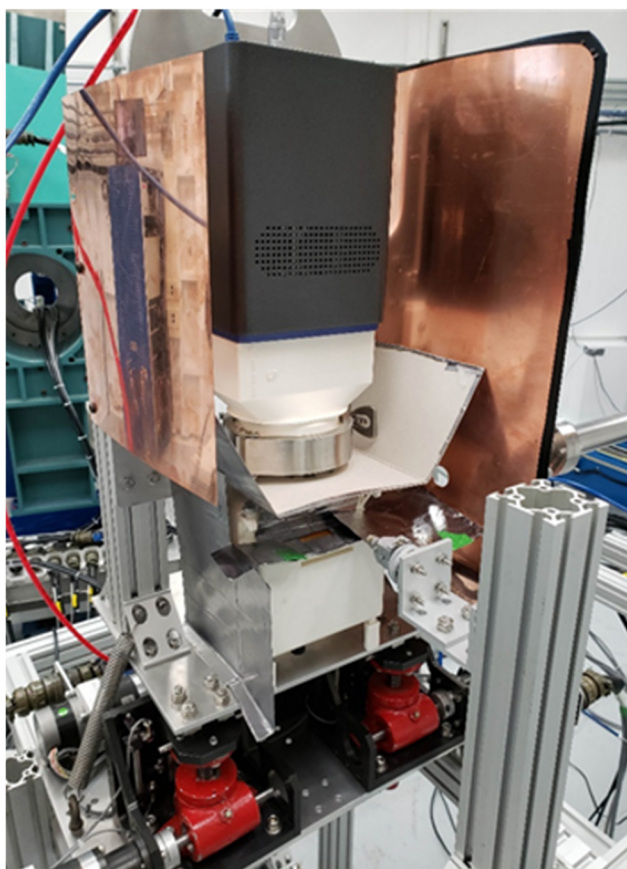


Figure 6: A photograph of the experimental setup with outside shielding in place.

FIRST TESTS

The device works! (Fig. 7). Our observations compare well against the APS paper [3]. The jacks work well with good motion, but they must be spaced out further to provide more stability. Positioning of the sample is manual, tedious, and time-consuming. A 3-axis motorized sample positioning system is required.

To better fill the detector, the top chamber should be optimized by a few mm. It would be helpful if the detector had some vertical adjustment.

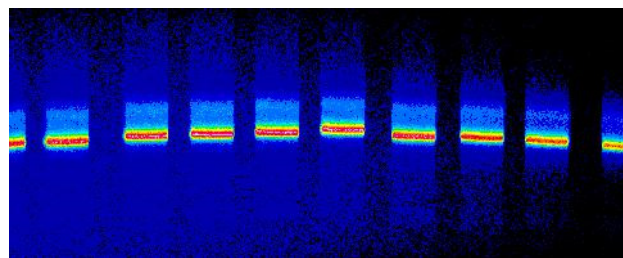


Figure 7: Recorded fluorescence of the Fe₂O₃ nanoparticles, 20-50 nm diameter.

CONCLUSION

A compact X-ray emission spectrometer (mini-XES) has been designed and fabricated for use at the Brockhouse undulator beamline. The mini-XES uses cylindrical von Hamos geometry tuned for Fe K-edge and uses a Pilatus 100K area detector from Dectris.

The mini-XES design was developed to be as simple to fabricate and as easy to operate as possible. We tried to minimize the number of components so there are only two main parts that create a chamber, which are joined by NW-80 flange. The design was trying to achieve no tools assembly, alignment, and operation.

The first tests of the spectrometer were completed and were successful. Future improvements will aim to reduce the background scatter and to provide better positioning of the detector, to improve the focal plane fill.

Now, that the relatively inexpensive design was fabricated, tested, and tried, there is an option to upgrade to 3D printed tungsten or steel version that would intrinsically provide the required shielding. Likewise, the Lucite back door could be replaced with lead glass or lead acrylic material to further reduce the scatter.

ACKNOWLEDGEMENTS

Part or all of the research described in this paper was performed at the Canadian Light Source, which is supported by the Canada Foundation for Innovation (CFI) and others agencies.

REFERENCES

- [1] B. Diaz *et al.*, “Undulator beamline of the Brockhouse sector at the Canadian Light Source,” *Rev. Sci. Instrum.*, vol. 85, p. 085104, 2014. doi: 10.1063/1.4890815085104
- [2] DECTRIS, <https://www.dectris.com>
- [3] B. A. Mattern *et al.*, “A plastic miniature x-ray emission spectrometer based on the cylindrical von Hamos geometry,” *Rev. Sci. Instrum.*, vol. 83, p. 023901, 2012. doi: 10.1063/1.3680598
- [4] STRATASYS, <https://support.stratasys.com>
- [5] A. F. G., Leontowich *et al.*, “The lower energy diffraction and scattering side-bounce beamline for materials science at the Canadian Light Source.” *J. Synchrotron Rad.*, vol. 28, no. 3, pp. 961-969, 2021. doi: 10.1107/S1600577521002496

AN IMPROVED, COMPACT HIGH TEMPERATURE SAMPLE FURNACE FOR X-RAY POWDER DIFFRACTION

E. Haas, E. Cardenas, A.P. Sirna

National Synchrotron Light Source II, Brookhaven National Laboratory,
Upton, NY 11973-5000, USA

Abstract

A compact sample furnace was designed to heat samples to temperatures of 2000 - 2300°C at the X-ray Powder Diffraction (XPD) beamline at NSLS-II. This furnace allows the XPD photon beam to pass through with adequate downstream opening to collect diffraction data for high-temperature materials research. Since the XPD samples did not reach the desired temperatures, engineering studies, tests, and incremental improvements were undertaken to improve performance. Several approaches were considered, and the sample holder design was improved, and high-temperature coatings were used. The engineering work undertaken to improve furnace performance is included herein.

INTRODUCTION

The XPD Beamline at NSLS-II does materials research at temperatures ranging from cryogenic to ~1700°C, and efforts to conduct materials research at higher temperatures are ongoing. The present XPD sample furnace uses infrared lamps with ellipsoidal reflectors to focus infrared rays at a single sample. This furnace has been operating in air, and high-temperature oxidation has been destroying thermocouples. A plan therefore was developed to investigate potential areas of improvement:

- The use of IR lenses to focus forward-directed IR rays otherwise lost as halo.
- Improved sample tube holders.
- The use of inert gas shielding to prevent oxidation.
- The use of high-temperature coatings.
- The use of a custom-designed secondary reflector to redirect forward-directed IR halo.
- The use of a CO₂ laser as a supplementary (or primary) sample heat source
- Optimization of heat lamps and focal distance.

This paper briefly discusses each of the above options and explains why some of the above items were pursued further and others rejected. Considerations of material properties at high temperatures are also included.

SAMPLE AND FURNACE CONDITIONS

Powder samples contained in sapphire tubes are held by ceramic holders for X-Ray Powder Diffraction research in air at atmospheric pressure. Sapphire is used for its' high-temperature and optical properties. A computer graphic (CG) image and photo of a sapphire tube in its' ceramic tube holder is shown in Fig. 1 along with an image of one infrared heat flux pattern. This heat flux for a single ellipsoidal reflector indicates loss of some flux past the sample holder tube. Infrared lamps direct 150W each of heat flux at a ceramic sample tube holder in the bandwidth

shown in Fig. 2. Six infrared lamps each have ellipsoidal reflectors and water-cooled jackets to minimize external temperatures for safety and to extend lamp life. Cooling water at 17-20°C from a chiller is circulated in parallel paths through all lamp cooling jackets and through two water-cooled outer shells.

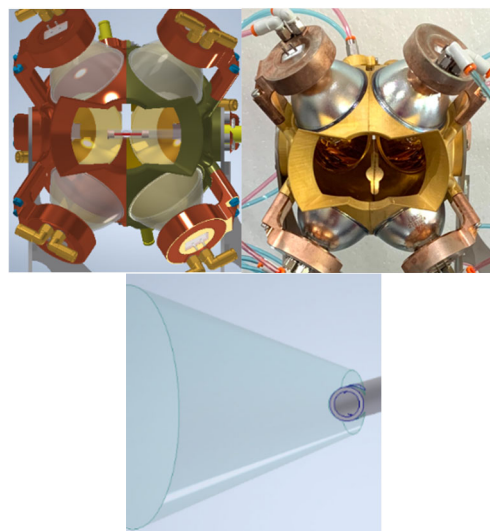


Figure 1: XPD Sample Furnace looking upstream: (a) CG image, (b) photo, and (c) heat flux pattern.

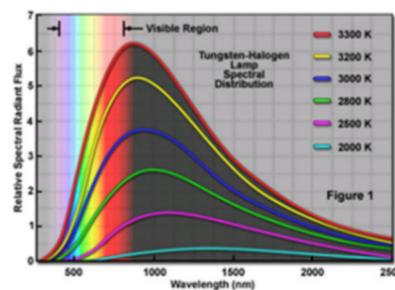


Figure 2: IR lamp flux spectrum.

ENGINEERING INVESTIGATIONS

- The use of plano-convex infrared lenses as a primary means to focus forward-directed rays was considered, but not pursued as available infrared lens geometries and IR source distance limitations meant only a small portion of forward-directed rays were properly focused. When IR lenses were used to supplement ellipsoidal reflectors, too many reflected rays that would have been focused at the sample center were misdirected. IR lenses therefore were ruled out as a viable solution. Two IR lens configurations are shown in Fig. 3.

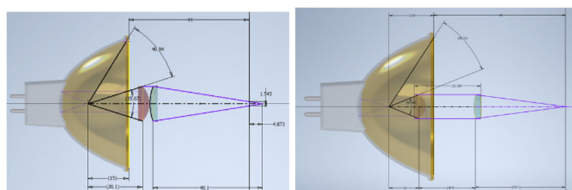


Figure 3: IR lens designs; focal point (a) behind sample, and (b) at sample center

- b. Iterative design and thermal analyses were used to optimize the design of the sample tube holder. The external surface area was increased to capture more infrared rays while eliminating an internal cavity, thus convective cooling was reduced, and the conduction path to the sample itself shortened to transfer more heat to the sample by direct conduction to the sapphire tube. Figure 4 below shows the improved sample tube holder. Its features include a small hole in the front to allow the XPD beamline in, and a $\pm 45^\circ$ downstream opening to allow X-ray diffraction data to be collected.

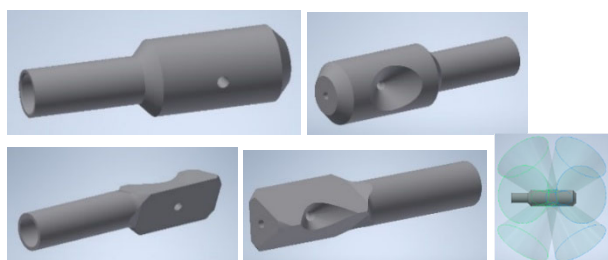


Figure 4: New sample holder designs and heat flux pattern impinging on a redesigned sample holder

- c. Inert gas shielding - oxidation within the furnace increases non-linearly as the temperature inside the furnace increases. This may be mitigated by introducing an inert gas to shield materials from oxidation. Three inert gases and their specific heat capacities are shown in Table 1. The lowest specific heat will absorb the least amount of heat. This concept is demonstrated in the equation below. Based on gas specific heat capacity and cost effectiveness, Argon is the best inert gas for this application as it will carry away the least heat via convection.

$$Q = mc\Delta T \quad (1)$$

Table 1: Specific Heat Capacities for Helium Argon, and Nitrogen Gases [1]

Gas	Specific Heat Capacity (KJ/kg K)
Helium	5.1926
Argon	0.5203
Nitrogen	1.039
Air	1.005

- d. Two high-temperature coatings were tested to improve heat transfer to high heat-flux areas of the sample holder and insulate areas outside the heat flux area. Important properties include coating adherence and high-temperature resistance in air. YSZ coating from Zypcoatings is a zirconia-based coating that can reach temperatures $>2000^\circ\text{C}$ without oxidizing per the manufacturer's specifications. This coating reduced the maximum internal temperature in initial tests and is being considered as an insulator outside the sample holder high-heat flux area. In other tests, a silicon carbide high-temperature coating significantly increased heat transfer to increase heat absorption are ongoing. Thermal properties of three sample holder materials are presented in Table 2.

Table 2: Thermal Properties of Tubing Materials [2, 3]

Properties	Alumina	Zirconia	Sapphire
Thermal Conductivity (W/m K)	2.2-4.3	14-30	34.6
Thermal Expansion ($\mu\text{m/m K}$)	8.8-9.5	6.7-8.2	4.5
Max. Temp ($^\circ\text{C}$)	1330	1730	2053
Specific Heat Capacity	400-510	870-940	750

- e. The use of a custom designed secondary reflector was investigated to recover some of the forward directed IR rays otherwise lost as halo. The shape and overall design of the reflector is shown in the Fig. 5. This shape and location were determined by radiation heat transfer view-factor calculations. The reflector needs the lowest view factor possible to reduce the number of rays blocked. Fig. 5 (a) represents the View Factor Geometry. Spherical reflectors were not pursued further due to decreased lamp life and loss of flux reflected by the ellipsoidal reflector.

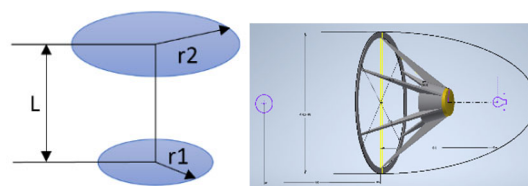


Figure 5: (a) Reflector View Factor Geometry and (b) Proposed Spherical Reflector Design

- f. Small cross-sectional beam (i.e., ≤ 1.5 mm diameter) CO₂ lasers operating at a wavelength between 9.5 and 10.5 μm can apply IR heat energy directly to the sample at a wavelength where the heat energy will be absorbed more efficiently by the sapphire sample tube. Due to a limited budget, this area was not pursued yet, but future laser power versus sample temperature tests are being considered.
- g. IR heat lamps tests indicated as much as 28 $^\circ\text{C}$ difference when moving a single heat lamp 1 mm away from its' maximum temperature point. Further tests

using shims to optimize the focus of heat lamps are ongoing.

RESULTS

The following two graphs (Figs. 6 and 7) were produced by focusing an ILT (model L6409G) lamp at 1/4" diameter Alumina and Zirconia ceramic tubes with, and without silicon carbide and type YSZ high-temperature coatings. In all tests, lamp voltage, tube position, and thermocouple position were held constant, and the same size tube was used. The heating and cooling curves in Fig. 7 show the results of the tube materials and the effects of the coatings. The highest temperature was reached by a silicon carbide coated zirconium tube, and the YSZ coating showed some value as an insulator. The effects of various gases were also explored and tabulated in Table 3. It was found that the use of an inert gas can improve the efficiency of radiation transfer from lamp to inside ceramic tubing with Argon gas proving the best performance.

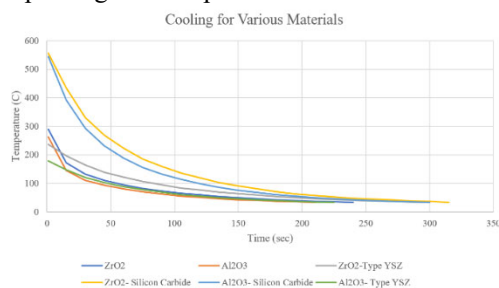


Figure 6: Cooling rate for selected ceramic materials and coatings.

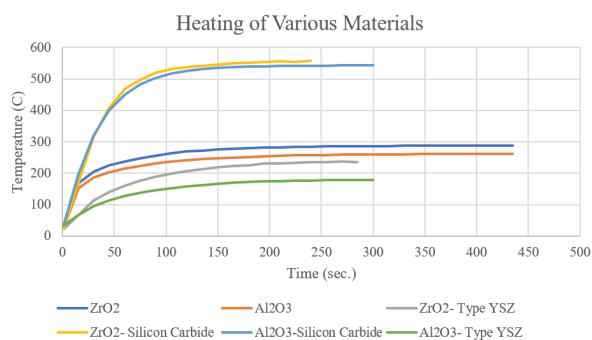


Figure 7: Heating rate for selected ceramic materials and coatings.

Table 3: Single Lamp Max Temps for Noble Gases

Gas	Max Temp Achieved (°C)
Helium	185
Argon	258
Air	242
Nitrogen	243

CONCLUSIONS

Materials research at temperatures above 1750°C in air requires careful sample holder material selection and an understanding of material properties at high temperatures. Refractory metals undergo oxidation, and high-

temperature ceramics are very difficult to machine. Additionally, thermal absorptivity and emissivity are wavelength dependent when using infrared heat sources. Some materials (e.g., sapphire) are mostly transparent to near infrared rays, and many ceramics are poor heat conductors. Cost is also a consideration. The solutions chosen to improve the performance of the XPD Infrared Sample Furnace include the selective use of infrared lamp position adjustments and an improved sample holder. The new sample holder maximizes heat absorption, provides a short heat conduction path to samples, and optimizes external size to reduce convective heat transfer losses. The use of high-temperature coatings is promising, but coating adherence and maximum coating temperature need further improvement. The authors were not able to improve performance with infrared lenses, and secondary reflectors will diminish lamp life with insufficient thermal gain. Lastly, CO₂ lasers (~10µm wavelength) hold significant promise as a primary or secondary heat source, but tests were not undertaken in time for publication of this paper.

ACKNOWLEDGEMENTS

The authors thank Jianming Bai, PhD (XPD scientist and project leader) and Sanjit Ghose, PhD (XPD Lead Beamline Scientist) for project guidance, Hui Zhong (SUNY SB liaison engineer) for thermal data, G. Lawrence ('Larry') Carr, PhD (FIS/MET Lead Beamline Scientist) for infrared guidance, Leo Reffi for design drawings, and John Trunk (HXSS program chief technician) for thermal experiment support. Also, thanks go to Eric Dooryhee, PhD (HXSS program manager), Lisa Miller, PhD (NLS-II educational program coordinator), and Noel Blackburn (BNL SULI program coordinator); without their support (and DOE-SULI program funding), this work would not have been possible.

REFERENCES

- [1] Properties of Various Ideal Gases (at 300 K), www.ohio.edu/mechanical/thermo/property_tables/gas/idealGas.html
- [2] Oxide-Based Engineering Ceramic, MakeItFrom.com, www.makeitfrom.com/compare/Alumina-Aluminum-Oxide-Al2O3/Zirconia-Zirconium-Dioxide-ZrO2
- [3] Supplier Data - Sapphire Single Crystal (Alumina 99.9%) - (Goodfellow), www.azom.com/properties.aspx?ArticleID=1721

THERMAL MODEL VALIDATION FOR THE CRYOGENIC MIRROR SYSTEMS FOR SIRIUS/LNLS

L.M. Volpe*, B.A. Francisco†, J.C. Corsaletti, R.R. Gerales, M. Saveri Silva
 Brazilian Synchrotron Light Laboratory (LNLS), Brazilian Center for Research in Energy and Materials
 CNPEM, Campinas, São Paulo, Brazil

Abstract

One of the challenges of fourth-generation synchrotron light sources as Sirius at the Brazilian Synchrotron Light Laboratory (LNLS) is the high power density that may affect the beamline optical elements by causing figure deformations that deteriorate the quality of the beam. Indeed, surface specifications for height errors of X-ray mirrors are often within a few nanometers. To deal with these thermal management challenges, thermo-mechanical designs based on cryogenic silicon have been developed, taking advantage of its high thermal conductance and low thermal expansion in temperatures of about 125 K. A liquid nitrogen (LN2) cryostat connected to the optics by copper braids has been used to handle moderate power loads, reducing costs when compared to closed-circuit LN2 cryocoolers and mechanically decoupling flow-induced vibrations from the optics. To guarantee the functionality of such systems, lumped mass thermal models were implemented together with auxiliary finite elements analyses. With the first systems in operation, it has been possible to compare and validate the developed models, and to carry out optimizations to improve them for future projects, by adjusting parameters such as emissivity, thermal contact resistance, and copper braid conductance. This work presents the updated models for CARNAÚBA and CATERETÊ beamlines as reference cases.

INTRODUCTION

The analysis of thermal deformation in synchrotron mirrors is a well known research field due to the impacts in the final shape of the beam [1]. At Sirius, the 4th-generation light source at the Brazilian Synchrotron Light Laboratory (LNLS), this issue has been addressed with an innovative thermo-mechanical concept for exactly-constrained cryocooled mirrors, as detailed in [2]. Indeed, given the high conductivity and the quasi-zero-expansion properties of silicon around 125 K, detrimental thermal effects can be minimized. Here, the methodology and latest developments in thermal models for Sirius mirrors are presented, with the CARNAÚBA and CATERETÊ beamlines taken as study cases due to their demanding requirements concerning small beam sizes and high coherence [3,4]. With lower modeling effort and computational cost for the complex mirror systems, lumped mass models in MATLAB Simscape® have been preferred over finite element analyses (FEA), which are then used mainly as complementary tools as to define con-

trol parameters temperature PID, power heater and diagnosis fails in the system.

METHODOLOGY

In lumped mass models, bodies and assemblies in complex geometries can be reduced as nodes with thermal resistances and thermal masses, which are combined according to parameters such as Biot and Fourier number [5]. The example of a node in Simscape is shown in Fig. 1.

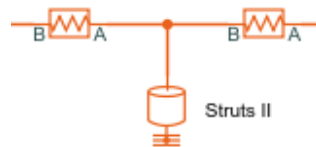


Figure 1: The center block represent the mass of the “struts II” and others are two resistances that represents the conductances between the center of the body and their extremes wich are in contact with other bodies. The central point represent the middle temperature.

Thermal Conduction Resistance

For an 1D solid between two nodes of interest, for example, the conduction thermal resistance may be derived from Fourier’s law in Eq. (1), where: Q is the heat flow; ΔT the temperature gradient between the ends of the body; A the cross section; k the thermal conductivity and Δx the solid length. Then, according to Eq. (2), the resistance R is often defined as the inverse of the conductance g , given by the ratio between Q and ΔT . For more complex bodies, the conductances can be calculated after splitting them into simpler bodies or by FEA.

$$Q = \frac{kA\Delta T}{\Delta x} \tag{1}$$

$$g = \frac{Q}{\Delta T} = \frac{kA}{\Delta x} \longrightarrow R = \frac{1}{g} = \frac{\Delta x}{kA} \tag{2}$$

Thermal Contact Resistance

The interfaces between bodies are also modelled as resistances and then associated with the node resistances. As shown in Eq. (3), the contact resistance R_c can be written as a function of the heat flux Q and the temperature difference between surfaces ΔT , being typically extracted from experimental results and/or literature estimates [6, 7].

$$Q = \frac{1}{R_c} \Delta T = g_c \Delta T \tag{3}$$

* lucas.volpe@lnls.br
 † barbara.francisco@lnls.br

Thermal Convection Resistance

The convection heat exchange with fluids can also be modelled using the concept of resistance, being derived from Newton’s law in Eq. (4), where: h is the average convection coefficient; A , the contact surface area between the fluid and the solid; T_∞ , the temperature of the far fluid; and T_s the surface temperature. As shown in Eq. (5), the convective resistance R_{conv} can be written as a function of the heat flux Q and the temperature difference, being extracted from FEA simulations, experimental results and/or literature.

$$Q = (T_\infty - T_s) \int_A h(A)dA = (T_\infty - T_s)hA \quad (4)$$

$$g_{conv} = \frac{Q}{(T_\infty - T_s)} \rightarrow R_{conv} = \frac{1}{g_{conv}} \quad (5)$$

Thermal Radiation Resistance

The radiative heat exchange from a body i to a body j can be calculated using Eq. (6), where $\sigma = 5.67 \times 10^{-8} \text{ W m}^{-2} \text{ K}^{-4}$ is the Stefan-Boltzmann constant; T_i and T_j are the temperatures of the bodies; ϵ_i is the emissivity of body i as compared with an ideal blackbody; and B_{ij} is the Gebhart factor, calculated by solving Eq. (7). The view factor F_{ij} is defined “as the part of the radiation emitted by surface i and directly incident on surface j ” [5]. The emissivity can be taken from experimental data and/or literature references, whereas the view factors can be conveniently extracted from FEA tools.

$$Q = \epsilon_i A_i B_{ij} \sigma (T_i^4 - T_j^4) \quad (6)$$

$$B_{ij} = F_{ij} \epsilon_j + \sum_k F_{ik} (1 - \epsilon_k) B_{kj} \quad (7)$$

Another possibility for radiative heat transfer is the net radiation method [8], in which the heat transfer between two bodies is not directly calculated, but the total heat flux among the surfaces can be described.

Lumped Mass Design

Figure 2 shows the steps for a Simscape model. Firstly, a FEA model is implemented in Ansys® assuming constant conductivities and then reproduced in Simscape. After this, upgrades including variable conductivity and radiative heat transfer are included.

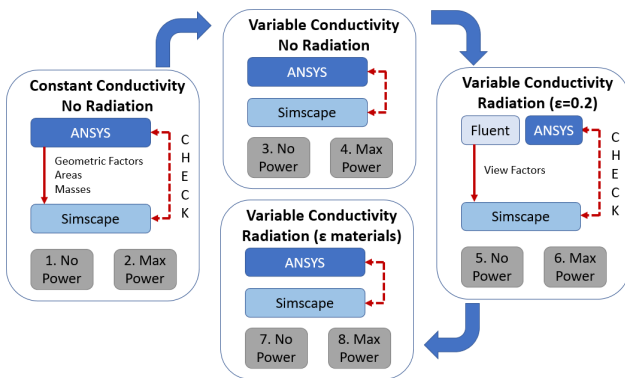


Figure 2: Steps to develop the lumped mass models.

RESULTS

Comparison Between the Models

Figure 3 shows the comparison between Simscape and FEA models for the temperature of the components in the first mirror of CATERETÊ (M1 CAT). The enumerated cases correspond to those in Fig. 2 and the major differences occur when the heat exchange by radiation (cases 5–8) is considered, reaching a maximum of about 17 K in the mirror support.

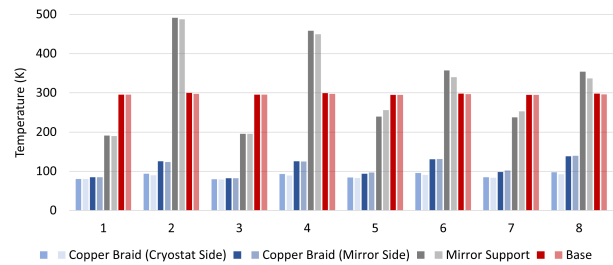


Figure 3: Comparison between FEA (dark) and lumped mass (light) models with temperatures for the CATERETÊ M1 mirror. Numbers in the x-axis are the cases in Fig. 2.

When reviewed the design that we used to FEA simulation, we observed that leaf springs that were in contact with the mirror support presented gradient around 52 K. We modeled these bodies in Simscape as a single part. We suspect that when applied to the radiative heat exchange model, the radiative heat exchanges across the entire piece were not considered, but everything was simplified by considering only the temperatures of the body borders. We will further investigate this question in the development of next models.

Comparison Between the Models and Real Systems

After commissioning the first beamlines, lumped mass models can be compared with the real systems. The first mirrors at CATERETÊ and CARNAÚBA (M1 CAT and M1 CNB) (Fig. 4) are discussed considering their specificities.

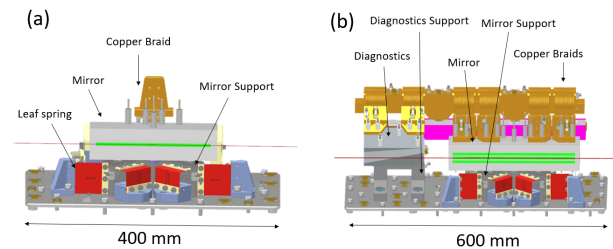


Figure 4: Drawings of Sirius mirror systems: (a) M1 CAT and (b) M1 CNB.

M1 CAT: To create evaluation cases, heat loads were experimentally applied to the mirror and its support frame according to Fig. 5, and also simulated in lumped mass and FEA models.

Initially, significant differences were found between experimental and simulated data, and the cause could be eventually associated to the efficiency of the cooling copper braids. As shown in Fig. 6, a better agreement has been achieved by reducing the nominal efficiency by 50%, with closer agreement in the FEA simulations.

The limited performance of the first-generation copper braids made in house led to the developed of a new version, with superior performance [9]. Finally, the major difference between measured and modeled temperatures happens in the mirror support as discussed in the previous section.

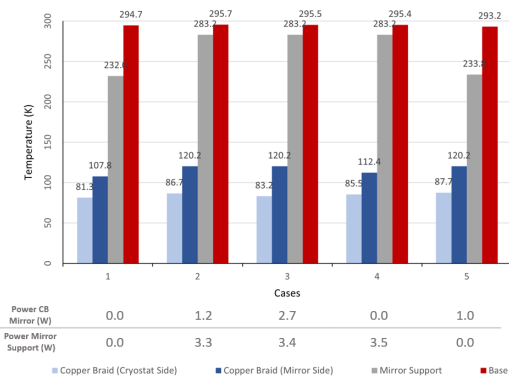


Figure 5: Temperatures in M1 CAT for different power loads.

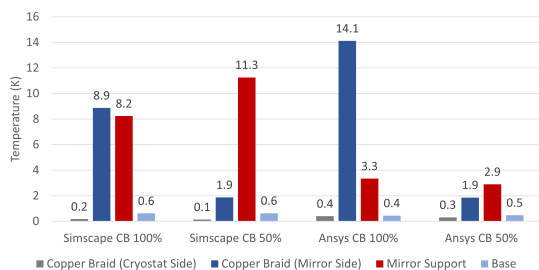


Figure 6: Average of the absolute temperature errors obtained for the five cases presented in Fig. 5 for M1 CAT in comparison with FEA and lumped mass models considering different copper braid efficiencies.

M1 CNB: As in the previous system, different heat loads were applied on the M1 CNB system, as shown in Table 1. Such system is composed of two optics (the mirror M1 and a silicon diagnostic) assembled on independent supports and mounted to a copper rod clamped to two cryostats [10]. In addition, the new-generation braids were already used in this design. The variation of the lumped mass model compared with the measurement is shown in Fig. 7. The divergence found in the mirror support pointed out in Fig. 3 and Fig. 6 was also found here. As previously, each leaf spring had been modelled as a single part, which adds to the hypothesis of they being responsible for the differences.

Other variations observed were the model that we designed to represent both cryostats of this system did not consider the flux variation of the LN2 seen during the operation. The flux variation happens specially during the filling

Table 1: Power (W) Applying in Three Different Measurements in Different Bodies in the M1 of the Carnaubá's Beam-line

Bodies	Case 1	Case 2	Case 3	Case 4
Diag.	0	0.4	2.9	16.9
Diag. Support	0	0.4	6.9	1.1
M1	0	5.2	10.9	35.8
M1 Support	0	1.5	5.0	3.7

of the liquid nitrogen cylinders that feed the system [11] and are distinct between one cryostat and the other since it is not directly controlled and it is subject to obstruction, level, and pressure fluctuations.

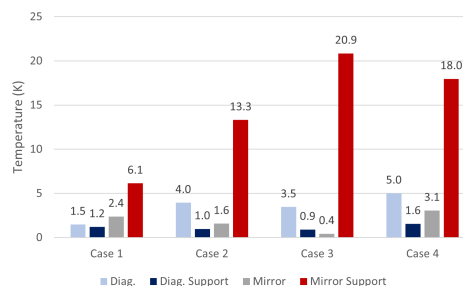


Figure 7: Temperature differences between measurements and simulated by lumped mass model in Simscape.

CONCLUSION

The updated lumped mass models have contributed to validate and improve thermal modeling of the first mirror systems, not only defining power requirements for control heaters and PID control parameters under variable operational conditions. Also diagnosing system issues, as the manufacturing limitations of the first copper braids. Furthermore, a trustful Simscape model makes the dimension of the parts during the design phase faster than by using FEA, since it is necessary only changing numbers instead of redraw pieces.

The differences founded between models and measurements were below 10 K and in the non critics elements. Apart from refinement of model bodies with high gradients (52 K), we are currently optimizing the nitrogen flux system.

Although the mentioned divergences, this modelling technique proves to be enough to the application, keeping the mirror deformation within the requirements and has been also used in other mirrors and monochromator projects on Sirius.

ACKNOWLEDGEMENTS

The authors would like to gratefully acknowledge the funding by the Brazilian Ministry of Science, Technology and Innovation and the contributions of the LNLS team.

REFERENCES

- [1] Z. Xu *et al.*, “Study on cooling for optical parts with high heat loads at the SSRF”, *J. Phys. Conf. Ser.*, vol. 425, no. 5, p. 052011, 2013. doi:10.1088/1742-6596/425/5/052011
- [2] R.R. Geraldès *et al.*, “The Design of Exactly-Constrained X-Ray Mirror Systems for Sirius”, in *Proc. MEDSI'18*, Paris, France, Jun 2018, pp. 173–178. doi:10.18429/JACoW-MEDSI2018-WEOAMA04
- [3] H. C. N. Tolentino *et al.*, “Innovative instruments based on cryogenically cooled silicon crystals for the CARNAÚBA beamline at Sirius-LNLS”, *AIP Conference Proceedings*, vol. 2054, p. 060026, 2019. doi:10.1063/1.5084657
- [4] F. Meneau *et al.*, “Cateretê, the Coherent Scattering Beamline at Sirius, 4th Generation Brazilian Synchrotron Facility”, presented at Workshop on Coherence at ESRF-EBS, Grenoble, France, 2019.
- [5] Dutch Society for Precision Engineering (DSPE), <https://www.dspe.nl/knowledge/thermomechanics/chapter-2-in-depth/2-4-thermal-radiation/2-4-3-gebhard-method/>
- [6] S. Scott, “Thermal contact between Silicon and Copper”, MEDSI Design Guidelines, pp. 1-4, 2016. https://medsi.lbl.gov/files/page_159/Thermal_contact_between_silicon_and_copper.doc
- [7] F.P. Incropera *et al.*, *Fundamentals of Heat and Mass Transfer*, 7. ed. Hoboken, NJ: John Wiley, 2011.
- [8] J. H. Lienhard IV and J. H. Lienhard V, *A Heat Transfer Textbook*. 4th. ed. Cambridge, MA, USA: Phlogiston Press, 2018.
- [9] F.R. Lena *et al.*, “Copper braid heat conductors for Sirius Cryogenic X-ray Optics”, presented at MEDSI'20, Chicago, USA, Jul 2021, paper TUPC14, this conference.
- [10] H. C. N. Tolentino *et al.*, “X-ray microscopy developments at Sirius-LNLS: first commissioning experiments at the Carnauba beamline”, *Proc. SPIE 11839, X-Ray Nanoimaging: Instruments and Methods V*, p. 83904, Aug. 2021. doi:10.1117/12.2596496
- [11] M. Saveri Silva *et al.*, “Cryogenic Systems for Optical Elements Cooling at Sirius/LNLS”, presented at MEDSI'20, Chicago, USA, Jul 2021, paper MOPB02, this conference.

TEMPERATURE-DEPENDENT ELASTIC CONSTANTS AND YOUNG'S MODULUS OF SILICON SINGLE CRYSTAL*

Zunping Liu[†], Advanced Photon Source, Argonne National Laboratory, Lemont, IL 60439, USA

Abstract

Silicon crystals have been widely used for x-ray monochromators. It is an anisotropic material with temperature-dependent properties. Values of its thermal properties from cryogenic to high temperature are available in the literature for expansion, conductivity, diffusivity, heat capacity, but neither elastic constants nor Young's modulus. X-ray monochromators may be liquid-nitrogen cooled or water cooled. Finite Element Analysis (FEA) is commonly used to predict thermal performance of monochromators. The elastic constants and Young's modulus over cryogenic and high temperature are now collected and derived from literature, with the purpose of assisting in providing accurate FEA predictions.

INTRODUCTION

Silicon single crystals have been widely used for x-ray monochromators [1], in addition to application in MEMS fabrication, both as a substrate for compatibility with semiconductor processing equipment and as a structural material for MEMS devices [2-4]. It is an anisotropic material with temperature-dependent properties, such as thermal conductivity [5, 6], thermal expansion coefficients [7-9], and elastic constants [10] or Young's modulus [11, 12]. At room temperature, Young's modulus varies from 130 GPa in the <100> directions to 190 GPa in the <111> directions.

Burenkov *et al.* [13] and Kury *et al.* [14] studied the temperature dependence of Young's modulus $E_{\langle ijk \rangle}$ for Si and Ge. Polynomial expressions for the dependence on temperature between room temperature and 1000°C of the bi-axial Young's modulus $E_{\langle ijk \rangle} / (1 - \nu)$, with ν the Poisson's ratio, were developed. Vanhellefont *et al.* reported temperature-dependent Young's modulus of silicon by means of impulse excitation technique [12]. The data $E_{\langle ijk \rangle}$ along <100>, <110>, and <111> directions are available from room temperature to 1400°C.

McSkimin measured elastic constants C_{11} , C_{12} , C_{44} of silicon single crystal at low temperatures by means of ultrasonic waves [10]. The data are valid from 78 K to 300 K.

This report derives Young's modulus at low temperatures from elastic constants C_{11} , C_{12} , C_{44} of silicon single crystal in ref. [10], and elastic constants at high temperatures from Young's modulus in ref. [12]. Therefore, complete sets of Young's modulus and elastic constants are provided from -196°C up to 1400°C, or ~78 K to ~1673 K. Further, users may derive temperature-dependent Young's modulus or elastic constants at any arbitrary orientations.

* This research used resources of the Advanced Photon Source, a U.S. Department of Energy (DOE) Office of Science User Facility at Argonne National Laboratory and is based on research supported by the U.S. DOE Office of Science-Basic Energy Sciences, under Contract No. DE-AC02-06CH11357.

[†] zpliu@anl.gov

ELASTIC CONSTANTS

The stiffness coefficients C_{ijkl} and the compliance coefficients S_{ijkl} are defined as the proportionality constants between stress σ and strain ϵ tensors in the form of generalized Hooke's law:

$$\sigma_{ij} = C_{ijkl}\epsilon_{kl}, \text{ and } \epsilon_{ij} = S_{ijkl}\sigma_{kl}. \quad (1)$$

In the Coordinate System of a Cubic Crystal

Figure 1 shows the coordinate system with "X,Y,Z"-axes in the <100>, <010>, and <001> directions of a cubic structure. Because of its orthogonality, this coordinate system is actually a Cartesian coordinate system. An arbitrary orientation <hkl> rotating with respect to those three directions is also illustrated.

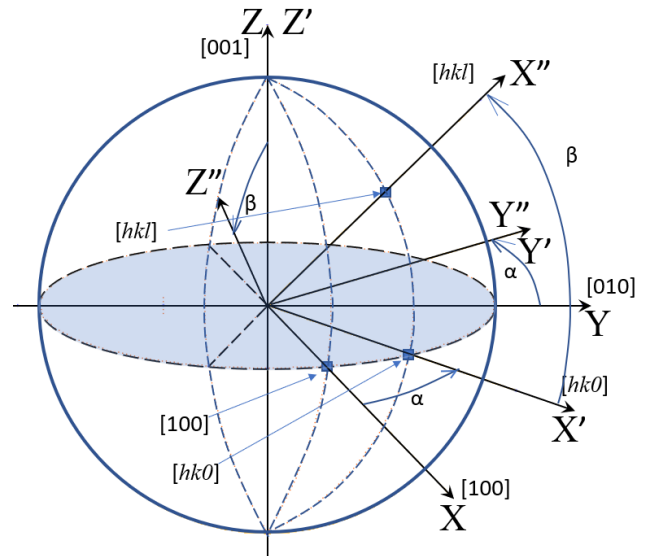


Figure 1: Illustration of coordinate system transformation with respect to the primary directions of a cubic structure.

For a cubic crystal such as silicon, the combination of cubic symmetry and the equivalence of the shear conditions enables specifying the fourth rank tensor with only three independent elastic constants. With respect to a specific basis that is commonly given for the <100> directions of the cubic structure, these tensors are given as [15, 16]:

$$\sigma_{ii} = C_{11}\epsilon_{ii} + C_{12}(\epsilon_{jj} + \epsilon_{kk}), \text{ and } \sigma_{ij} = C_{44}\epsilon_{ij}. \quad (2)$$

The stiffness matrix can be shortened as C_{pq} or:

$$C = \begin{bmatrix} C_{11} & C_{12} & C_{12} & & & \\ C_{12} & C_{11} & C_{12} & & & \\ C_{12} & C_{12} & C_{11} & & & \\ & & & C_{44} & & \\ & & & & C_{44} & \\ & & & & & C_{44} \end{bmatrix}. \quad (3)$$

The compliance matrix can be written in a similar form, which is the inverse of the stiffness matrix. The second-order elastic compliances S_{pq} can be expressed as:

$$\begin{aligned} S_{11} &= (C_{11} + C_{12}) / [(C_{11} - C_{12})(C_{11} + 2C_{12})], \\ S_{12} &= -C_{12} / [(C_{11} - C_{12})(C_{11} + 2C_{12})], \\ S_{44} &= 1/C_{44}. \end{aligned} \quad (4)$$

To obtain Eq. (4), the following relation is applied [17]:

$$2C_{11}(C_{11} + C_{12}) = (C_{11} - C_{12})(C_{11} + 3C_{12}) \quad (5)$$

In an Arbitrary Orientation of a Cubic Crystal

In an arbitrary orientation $\langle hkl \rangle$ as shown in Fig. 1, the corresponding elastic constants C_{pq}' and S_{pq}' can be calculated through a transformation [11, 18]. The results of such a transformation are listed in Table 1. The transformation from the crystal axes x_i (unprimed) to the arbitrary system x_i'' (primed) is expressed by:

$$x_i'' = l_i x_1 + m_i x_2 + n_i x_3, \quad i = 1, 2, 3 \quad (6)$$

with l, m, n being the direction cosines of the rotational transformation.

Table 1: Stiffness and Compliance Coefficients of Transformation for Rotated Axes in Cubic Crystals

Coefficient transformation ¹	Analogous ² coefficients
$C_{11}' = C_{11} + C_c(l_1^4 + m_1^4 + n_1^4 - 1)$	C_{22}', C_{33}'
$C_{12}' = C_{12} + C_c(l_1^2 l_2^2 + m_1^2 m_2^2 + n_1^2 n_2^2)$	C_{13}', C_{23}'
$C_{14}' = C_c(l_1^2 l_2 l_3 + m_1^2 m_2 m_3 + n_1^2 n_2 n_3)$	$C_{15}', C_{16}', C_{24}', C_{25}', C_{26}', C_{34}', C_{35}', C_{36}', C_{45}', C_{46}', C_{56}'$
$C_{44}' = C_{44} + C_c(l_2^2 l_3^2 + m_2^2 m_3^2 + n_2^2 n_3^2)$	C_{55}', C_{66}'
$S_{22}' = S_{11} + S_c(l_2^4 + m_2^4 + n_2^4 - 1)$	S_{11}', S_{33}'
$S_{13}' = S_{12} + S_c(l_1^2 l_3^2 + m_1^2 m_3^2 + n_1^2 n_3^2)$	S_{12}', S_{23}'
$S_{14}' = 2S_c(l_1^2 l_2 l_3 + m_1^2 m_2 m_3 + n_1^2 n_2 n_3)$	$S_{15}', S_{16}', S_{24}', S_{25}', S_{26}', S_{34}', S_{35}', S_{36}'$
$S_{56}' = 4S_c(l_1^2 l_2 l_3 + m_1^2 m_2 m_3 + n_1^2 n_2 n_3)$	S_{45}', S_{46}'
$S_{55}' = S_{44} + 4S_c(l_1^2 l_3^2 + m_1^2 m_3^2 + n_1^2 n_3^2)$	S_{44}', S_{66}'

Note:
1. $C_{ij}' = C_{ji}'$, $S_{ij}' = S_{ji}'$;
 $C_c = C_{11} - C_{12} - 2C_{44}$, $S_c = S_{11} - S_{12} - \frac{1}{2}S_{44}$
2. The subscript on a direction cosine, as well as on a coefficient, represents two subscripts: (1→11, 2→22, 3→33, 6→12, 5→13, 4→23).

YOUNG'S MODULUS, SHEAR MODULUS, AND POISSON'S RATIO

Young's modulus is defined as a proportional constant of stress over its corresponding strain of a normal deformation, while the shear modulus is defined as stress over the corresponding strain of a transverse deformation:

$$\begin{aligned} E_i &= \sigma_i / \varepsilon_i, \quad i = 1, 2, 3 \\ G_i &= \sigma_i / \varepsilon_i, \quad i = 4, 5, 6. \end{aligned} \quad (7)$$

The Poisson's ratio is defined as

$$v_{ij} = -\varepsilon_j / \varepsilon_i, \quad i, j = 1, 2, 3, i \neq j. \quad (8)$$

By comparing the definitions of these moduli and stiffness, it can readily be shown that

$$E_i \text{ (or } G_i) = 1/S_{ii}, \text{ and } v_{ij} = -S_{ji}/S_{ii}. \quad (9)$$

The Young's modulus E_{hkl} can be calculated from the general formulae for cubic crystal as [15, 16, 19]:

$$\frac{1}{E_{hkl}} = S_{11} - 2 \left(S_{11} - S_{12} - \frac{1}{2S_{44}} \right) (l^2 m^2 + m^2 n^2 + l^2 n^2). \quad (10)$$

The corresponding Poisson's ratio and shear modulus in the cubic configuration can be expressed as:

$$v_{\alpha\beta} = \frac{S_{12} + (S_{11} - S_{12} - \frac{1}{2S_{44}})(l_\alpha^2 l_\beta^2 + m_\alpha^2 m_\beta^2 + n_\alpha^2 n_\beta^2)}{S_{11} - 2(S_{11} - S_{12} - \frac{1}{2S_{44}})(l_\alpha^2 m_\alpha^2 + m_\alpha^2 n_\alpha^2 + l_\alpha^2 n_\alpha^2)} \quad (11)$$

$$G_{ij} = 1/S_{ij}', \quad (S_{ij}' \text{ as shown in Table 1}) \quad (12)$$

with α and β being the two orthogonal directions, and $l_\gamma, m_\gamma, n_\gamma$ are the directional cosines of the angles between the γ direction and basis axes.

By substituting Eq. (4) into Eq. (10), one obtains

$$\frac{1}{E_{hkl}} = \frac{C_{11} + C_{12}}{(C_{11} - C_{12})(C_{11} + 2C_{12})} - 2 \left(\frac{C_{11} + C_{12}}{C_{11} - C_{12}} - \frac{C_{44}}{2} \right) (l^2 m^2 + m^2 n^2 + l^2 n^2). \quad (13)$$

Young's moduli in the $\langle 100 \rangle$, $\langle 110 \rangle$, and $\langle 111 \rangle$ crystallographic directions can be derived as [20]:

$$\begin{aligned} E_{[100]} &= (C_{11} - C_{12})(C_{11} + 2C_{12}) / (C_{11} + C_{12}), \\ E_{[110]} &= 2 / \left\{ \frac{C_{11}}{(C_{11} - C_{12})(C_{11} + 2C_{12})} + \frac{1}{2C_{44}} \right\}, \\ E_{[111]} &= 3 / \left(\frac{1}{C_{11} + 2C_{12}} + \frac{1}{C_{44}} \right). \end{aligned} \quad (14)$$

Inversely stiffness coefficients C_{11} , C_{12} , and C_{44} can be obtained from Eq. (14).

TEMPERATURE-DEPENDENT ELASTIC CONSTANTS AND YOUNG'S MODULUS

The temperature-dependent Young's modulus of silicon $E_{\langle 100 \rangle}$, $E_{\langle 110 \rangle}$, and $E_{\langle 111 \rangle}$ are available from room temperature to 1400°C [12]. The corresponding stiffness coefficients C_{11} , C_{12} , and C_{44} can be calculated with Eq. (14) if one is interested in the coefficients at high temperature.

Data of measured stiffness coefficients C_{11} , C_{12} , and C_{44} of silicon single crystal are valid from 78 K to 300 K [10]. The data can be converted to the Young's modulus, Poisson's ratio, and shear modulus by using Eqs. (4, 10-12) when needed. For example, ANSYS Workbench takes temperature dependent data of orthogonal elasticity in terms of Young's modulus, Poisson's ratio, and shear modulus.

By combining data at low and high temperatures, Fig. 2 shows Young's modulus $E_{\langle 100 \rangle}$, $E_{\langle 110 \rangle}$, and $E_{\langle 111 \rangle}$ from 4 to 1400 K, and Fig. 3 shows stiffness coefficients C_{11} , C_{12} , and C_{44} from 4 to 1400 K. The data below 80 K are artificial for curve fitting purposes.

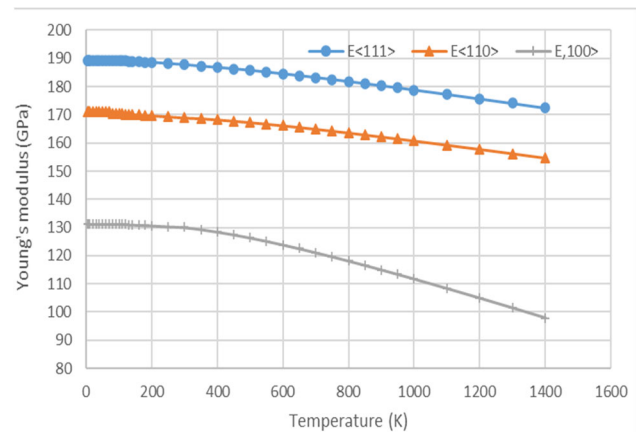


Figure 2: Young's modulus of silicon single crystal.

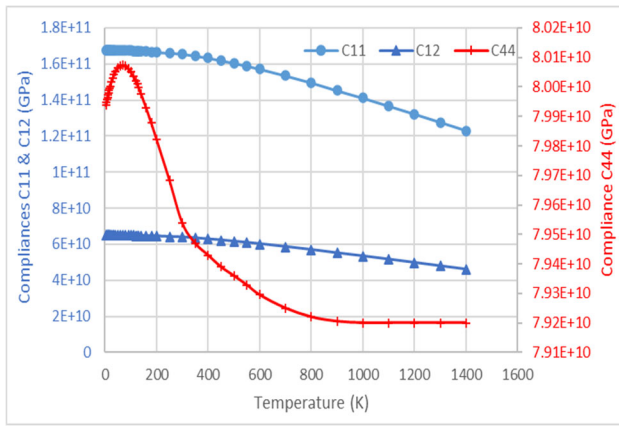


Figure 3: Stiffness coefficients of silicon single crystal.

CONCLUSION

For cubic crystals such as silicon, conversion equations between elastic constants and Young’s modulus along crystallography axes are summarized. Based on the available amount of measured data of Young’s modulus from room temperature to melting temperature and stiffness coefficients from room temperature to cryogenic temperature, complete sets of data of both Young’s modulus and stiffness coefficients from cryogenic temperature to 1400 K are presented.

ACKNOWLEDGEMENTS

Thanks to Xianbo Shi for his advisory assistance with information on the coordinate transformation for silicon crystals.

REFERENCES

[1] D.H. Bilderback *et al.*, “The historical development of cryogenically cooled monochromators for third-generation synchrotron radiation sources”, *J. Synchrotron Radiat.*, vol. 7, iss. 2, pp. 53-60, 2000.
<https://doi.org/10.1107/S0909049500000650>

[2] K.E. Petersen, “Silicon as a mechanical material”, in *Proc. IEEE*, vol. 70, no. 5, pp. 420-456, May 1982.
 doi:10.1109/PROC.1982.12331

[3] M.A. Hopcroft *et al.*, “What is the Young’s modulus of silicon?”, *J. Microelectromech. Syst.*, vol. 19, iss. 2, pp. 229-238, April 2010. doi:10.1109/JMEMS.2009.2039697

[4] D.V. Dao *et al.*, “Micro/nano-mechanical sensors and actuators based on SOI-MEMS technology”, *Adv. Nat. Sci: Nanosci. Nanotechnol.*, vol. 1, iss. 1, p. 013001, 2010.
 doi:10.1088/2043-6254/1/1/013001

[5] C.J. Glassbrenner and G.A. Slack, “Thermal conductivity of silicon and germanium from 3°K to the melting point”, *Phys. Rev.*, vol. 134, no. 4A, May 1964.
<https://doi.org/10.1103/PhysRev.134.A1058>

[6] A.C. Sparavigna, “Thermal conductivity of the crystalline silicon”, *Philica*, Philica, p.1143, 2017. hal-01626126

[7] Y. Okada and Y. Tokumaru, “Precise determination of lattice parameter and thermal expansion coefficient of silicon between 300 and 1500 K”, *J. Appl. Phys.*, vol. 56, no. 2, p. 314, 1984. <https://doi.org/10.1063/1.333965>

[8] K. G. Lyon *et al.*, “Linear thermal expansion measurements on silicon from 6 to 340 K”, *J. Appl. Phys.*, vol. 48, no. 3, p. 865, 1977.
<https://doi.org/10.1063/1.323747>

[9] V. M. Glazov and A.S. Pashinkin, “The thermophysical properties (heat capacity and thermal expansion) of single-crystal silicon”, *High Temp.*, vol. 39, no. 3, pp. 413-419, 2001. <https://doi.org/10.1023/A:1017562709942>

[10] H.J. McSkimin, “Measurement of elastic constants at low temperatures by means of ultrasonic waves – data for silicon and germanium single crystals, and for fused silica”, *J. Appl. Phys.*, vol. 24, no. 8, p. 988, 1953.
 doi:10.1063/1.1721449

[11] J.J. Wortman and R.A. Evans, “Young’s modulus, shear modulus, and Poisson’s ratio in silicon and germanium”, *J. Appl. Phys.*, vol. 36, no. 1, p. 153, 1965.
<https://doi.org/10.1063/1.1713863>

[12] J. Vanhellemeont *et al.*, “Temperature Dependent Young’s Modulus of Si and Ge”, *ECS Trans.*, vol. 64, iss. 11, pp. 283-292, 2014. doi:10.1149/06411.0283ecst

[13] Yu.A. Burenkov, S.P. Nikanorov and A.V. Stepanov, *Soviet Physics - Solid State*, vol. 12, p. 1940, 1971.

[14] P. Kury and M. Horn-von Hoegen, “Impact of thermal dependence of elastic constants on surface stress measurements”, *Rev. Sci. Instrum.*, vol. 75, iss. 5, p. 1357, 2004.
 doi:10.1063/1.1711151

[15] A. Masolin *et al.*, “Thermo-mechanical and fracture properties in single-crystal silicon”, *J. Mater. Sci.*, vol. 48, no. 2, pp. 979-988, 2013. doi:10.1007/s10853-012-6713-7

[16] J.F. Nye, *Physical Properties of Crystals*, Oxford University Press, London, 1957.

[17] P.N. Keating, “Effect of invariance requirements on the elastic strain energy of crystals with application to the diamond structure”, *Phys. Rev.*, vol. 145, iss. 2, pp. 637-645, 1966.
<https://doi.org/10.1103/PhysRev.145.637>

[18] W. P. Mason, *Physical Acoustics and the Properties of Solids*, D. Van Nostrand Company, Inc., Princeton, New Jersey, 1958.

[19] W.A. Brantley, “Calculated elastic constants for stress problems associated with semiconductor devices”, *J. Appl. Phys.*, vol. 44, iss. 1, pp. 534-535, 1973.
 doi:10.1063/1.1661935

[20] W.W. Zhang *et al.*, “Modelling of the elastic properties of crystalline silicon using lattice dynamics”, *J. Phys. D: Appl. Phys.*, vol. 44, iss. 33, p. 335401, 2011.
 doi:10.1088/0022-3727/44/33/335401

DESIGN OF VACUUM CHAMBER WITH CRYOGENIC COOLING OF SAMPLES FOR BRAGG-PLANE SLOPE ERROR MEASUREMENTS*

J.W.J. Anton[†], P. Pradhan, D. Shu, Yu. Shvyd'ko
Advanced Photon Source, Argonne National Laboratory, Lemont, IL 60439, USA

Abstract

Wavefront preservation is essential for numerous X-ray science applications. Research is currently underway at the Advanced Photon Source to characterize and minimize Bragg-plane slope errors in diamond crystal optics [1]. Understanding the effect of cooling the optics to cryogenic temperatures on Bragg-plane slope errors is of interest to this research. Through the use of a finite element model a custom, compact vacuum chamber with liquid nitrogen cooling of samples was designed and is being manufactured. The design process and initial results are discussed in this paper.

INTRODUCTION

Wavefront-preserving X-ray diamond crystal optics are essential for numerous applications in X-ray science [1, 2]. Perfect crystals with flat Bragg planes are a prerequisite for wavefront preservation in Bragg diffraction. However, this condition is difficult to realize in practice because of inevitable crystal imperfections. Even for practically flawless diamond crystals, internal strain of various origins, such as mounting and low-temperature cooling, can give rise to Bragg planes slope errors and significant wavefront distortions. Research is currently underway at the Advanced Photon Source to characterize and minimize Bragg-plane slope errors in diamond crystal optics [3].

One of present major goals is to develop and test schemes for mechanically-stable strain-free diamond crystal mounting with excellent heat transport to heat sinks at room and liquid nitrogen (LN) temperatures. Use of wavefront-preserving diamond crystals in x-ray Bragg diffraction at low temperatures is essential in particular for the realization of the next generation light sources of highest brilliance such as x-ray free-electron laser oscillator (XFEL) [4].

For this purpose a low-temperature compact vibration-free diamond crystal chamber is required, which could be mounted on high-precision angular goniometers in the rocking curve imaging (RCI) [3] and wavefront imaging (WFI) setups [5]. Commercially available cryostats are too bulky for this purpose.

Through the use of a finite element model a custom, compact vacuum chamber with liquid nitrogen cooling of diamond crystal samples for RCI and WFI was designed and is being manufactured. The design process and initial results are discussed in this paper.

* This research used resources of the Advanced Photon Source, a U.S. Department of Energy (DOE) Office of Science User Facility at Argonne National Laboratory and is based on research supported by the U.S. DOE Office of Science-Basic Energy Sciences, under Contract No. DE-AC02-06CH11357.

[†]anton@anl.gov

DESIGN REQUIREMENTS

To complete the the RCI and WFI studies the following design requirements were decided on:

- Rotate crystal surface $\pm 45^\circ$
- Keep sample temp. $< -185^\circ\text{C}$ long enough to conduct X-ray experiment (approx. 20 min.)
- Operate in high-vacuum environment
- Size: Compact and light as possible so it can be installed on current beamline stages

Figure 1 shows a schematic view of the chamber design. Materials with low thermal conductivity are used to mount the crystal holder and the N2 reservoir. Oxygen-free copper is used to conduct heat away from the crystal and cooled by the liquid nitrogen. Mylar sheeting was used to shield the N2 Reservoir from radiation heat loads.

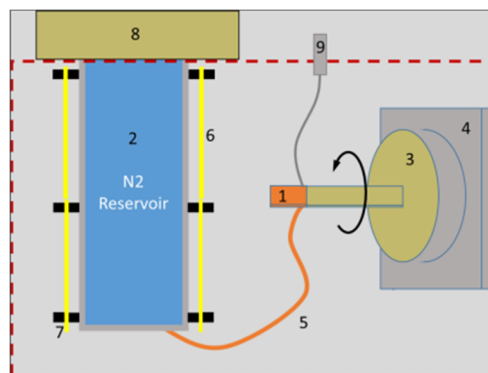


Figure 1: Schematic diagram of the sample cryogenic cooling: 1. Crystal sample (diamond), 2. N2 reservoir, 3. crystal mount (PEEK), 4. rotation stage, 4. thermal conductor (OFHC), 5. rad. shielding (Mylar), 6. Spacer/clamps (PEEK), 7. reservoir flange (PEEK), 8. temp. sensor (RT100).

VACUUM SEAL AT CRYOGENIC TEMPERATURES

Vacuum seal at cryogenic temperatures: Relatively large thermal contraction will happen between the N2 Reservoir (AL-6061) and the Reservoir Flange (PEEK). A vacuum seal using an indium wire allows the seal to hold even at very low temperatures. Figure 2 shows the flange mating with the N2 reservoir.

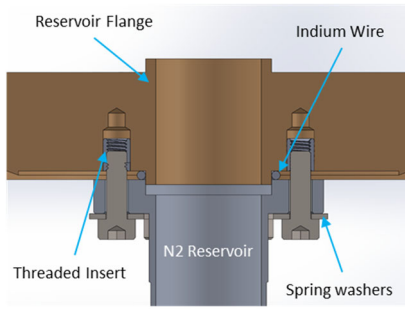


Figure 2: Reservoir flange and N2 reservoir mating with indium wire vacuum seal.

THERMAL FINITE ELEMENT ANALYSIS

A Finite Element Model was created in SolidWorks® Simulation software and a Steady State Thermal analysis was run. Conduction and Radiation heat transfer were of primary concern for this analysis. Shell elements were used for the N2 Reservoir, the Mylar Radiation Shielding, and a section of the vacuum chamber to reduce the overall number of elements in the model and thus the run time (see Fig. 3).

At the sample location the steady state temperature measured from the model is -189 °C.

The power into the system was measured from the FE model. Length of time for all the liquid nitrogen to evaporate and the model is no longer in steady state. time the sample will stay at that this temperature (-189°C) would be constant for approximately 16 minutes.

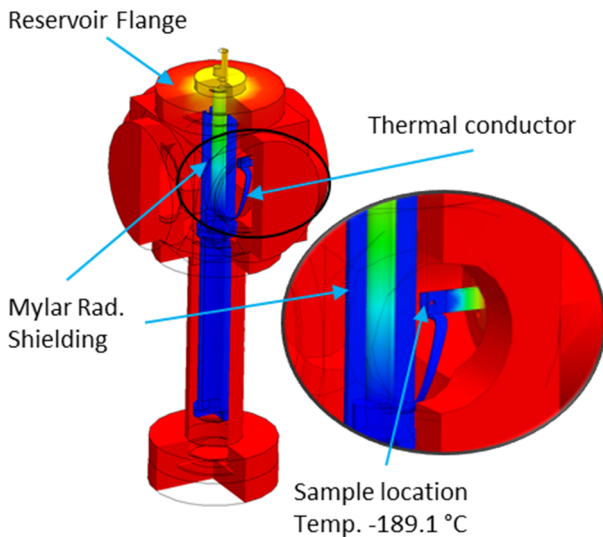


Figure 3: 3D model for thermal finite element analysis.

PROTOTYPE TESTING

From the Finite Element Analysis (FEA) results a prototype chamber was designed and built to test the coolmechanism. The prototype is shown mostly assembled in Fig. 4. An RT100 thermal sensor was fastened to the sample location to measure temperature. The chamber vacuum and cooling capabilities being tested is shown in Fig. 5.

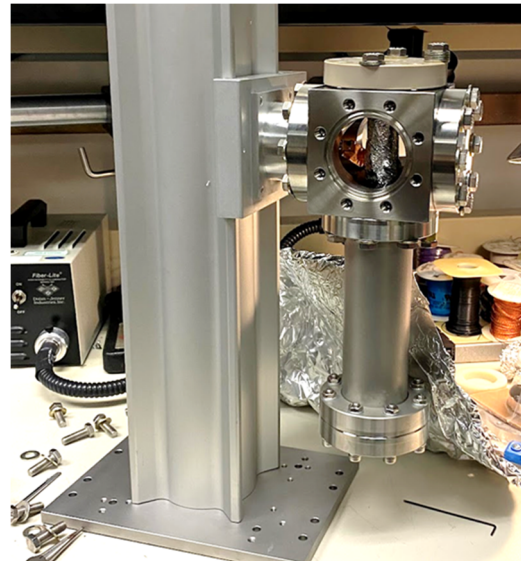


Figure 4: Photograph of the prototype sample cryogenic cooling chamber during assembly.



Figure 5: Photograph of the prototype sample cryogenic cooling chamber test setup.

As seen in Fig. 6, the prototype chamber test results were remarkably similar to the FEA results. The sample location was cooled to about -180 °C for about 15 minutes before starting to warm. The roughly 10 °C discrepancy between finite element analysis and prototype results is due to the thermal conductor needing to be lengthen for manufacturability of the prototype.

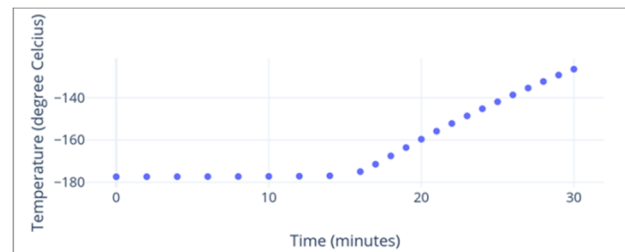


Figure 6: Preliminary test result of the prototype sample cryogenic cooling chamber.

SUMMARY

- Using finite element analysis a compact, [approximately 120 mm x 170 mm x 300 mm] cryo-cooling vacuum chamber was designed, built, and tested.
- The sample location was cooled to near about -180 °C for 15 minutes and -160°C for more 20 minutes.
- A high vacuum environment was achieved utilizing an indium wire seal at low temperature joints high-vacuum was achieved.

These positive result lead to a final design for the chamber has being completed. The design includes a rotation stage and beryllium windows to allow the X-ray beam through to the sample. The final design is currently being manufactured. Figure 7 is a solid model of the final cryogenic cooling chamber.

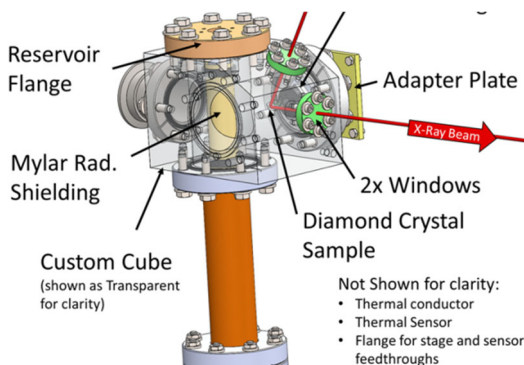


Figure 7: 3D model of the sample cryogenic cooling chamber (now being built) for Bragg-plane slope errors measurements.

ACKNOWLEDGEMENTS

This research used resources of the Advanced Photon Source, a U.S. Department of Energy (DOE) Office of Science User Facility at Argonne National Laboratory and is based on research supported by the U.S. DOE Office of Science-Basic Energy Sciences, under Contract No. DE-AC02-06CH11357.

REFERENCES

- [1] Yu. Shvyd'ko, S. Stoupin, V. Blank, and S. Terentyev, "Near 100% Bragg Reflectivity of X-rays," *Nat. Photonics*, vol. 5 pp. 539-542, 2011. <https://doi.org/10.1038/nphoton.2011.197>
- [2] Yu. Shvyd'ko, V. Blank, and S. Terentyev, "Diamond x-ray optics: Transparent, resilient, high-resolution, and wavefront preserving," *MRS Bulletin*, vol. 42, issue 6, pp. 437-444, June 2017. doi:10.1557/mrs.2017.119
- [3] P. Pradhan, M. Wojcik, X. Huang, E. Kasman, L. Assoufid, J. Anton, D. Shu, S. Terentyev, V. Blank, K.-J. Kim, and Yu. Shvyd'ko, "Small Bragg-plane slope errors revealed in synthetic diamond crystals," *J. Synchrotron Radiat.*, vol. 27 pp. 1553-1563, 2020. <https://doi.org/10.1107/S1600577520012746>
- [4] K.-J. Kim, Yu. Shvyd'ko, and S. Reiche, "A Proposal for an X-Ray Free-Electron Laser Oscillator with an Energy-Recovery Linac," *Phys. Rev. Lett.*, vol. 100, p. 244802, 2008. doi.org/10.1103/PhysRevLett.100.244802
- [5] Z. Qiao, X. Shi, M.J. Wojcik, L. Rebuffi, and L. Assoufid, "Single-shot x-ray phase-contrast and dark-field imaging based on coded binary phase mask," *Appl. Phys. Lett.*, vol. 119, p. 011105, 2021. doi: 10.1063/5.0053553

A NEW EXPERIMENTAL STATION FOR LIQUID INTERFACE X-RAY SCATTERING AT NSLS-II BEAMLINE 12-ID

D. M. Bacescu[†], L. E. Berman, S. L. Hulbert, B. M. Ocko, Z. Yin, National Synchrotron Light Source II (NSLS-II), Brookhaven National Laboratory, Upton, New York 11973, USA

Abstract

Open Platform and Liquids Scattering (OPLS) is a new experimental station recently built and currently being commissioned at the Soft Matter Interfaces (SMI) beamline 12-ID at NSLS-II. The new instrument expands SMI's beamline scientific capabilities via the addition of X-ray scattering techniques from liquid surfaces and for measurements that require an open platform.

The design of this new instrument, located inside the 12-ID-B beamline shielding enclosure, uses a single Ge (111) crystal deflector to bounce the incident x-ray beam by a variable angle α downwards away from the horizontal by rotating the large Huber Eulerian cradle χ stage. Tilting the beam is essential for liquid samples where gravity dictates the sample normal.

The OPLS instrument has a variable deflector-to-sample distance ranging from 0.6 m to 1.5 m where the larger distances are preferred for large processing chambers. Up to three X-ray detectors are mounted on a 2-theta scattering arm located downstream of the sample location. These detectors support a variety of X-ray techniques including X-ray reflectivity (XR), Grazing Incidence (GI) Small-Angle X-ray Scattering (SAXS) and Wide-Angle X-ray Scattering (WAXS), and grazing-incidence angle X-ray fluorescence.

Currently, the OPLS experimental station intercepts the 12-ID beam that otherwise propagates to the SMI experimental station located in hutch 12-ID-C and can be retracted to a "parking" position laterally out of this beam to allow installation of a removable shielded beam pipe that is needed to support operations in hutch 12-ID-C.

The design of OPLS is flexible enough to adapt to a planned future configuration of the SMI beamline in which OPLS is illuminated independently of SMI via a second, canted undulator source and a separate photon delivery system. In this future configuration, both branches will be able to operate independently and simultaneously.

INTRODUCTION

SMI beamline is one of the five beamlines of the Complex Scattering Program at NSLS-II. The beamline is served by a 2.8m long, 23mm period length, in-vacuum undulator (IVU23) generating x-rays with energy ranging from 2.05 – 24 keV. OPLS, one of the two experimental stations of the 12-ID (SMI) beamline, is located at approx. 51m from the source, inside shielded hutch enclosure, 12-ID-B (see Fig. 1). The OPLS uses the same photon delivery system as the SMI branch. The bimorph optical mirrors of

the SMI beamline can focus the beam at one of the two end station or at a secondary source aperture.

The OPLS experimental station is a liquid surface spectrometer designed with an open sample platform, which is a unique feature which offers high versatility, and allows X-ray scattering studies from liquid surfaces and interfaces, as well from different processing environments (e.g., roll-to-roll processing). The OPLS experimental station is designed to operate from 8 – 24 keV, with a beam spot size of approx. 20 μm vertically and 400 μm horizontally, and a photon flux of approx. 10^{12} ph./sec. [1].

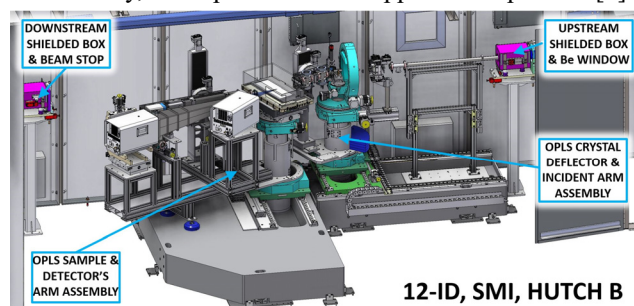


Figure 1: OPLS instrument (shown in operation mode).

THE OPLS DESIGN OVERVIEW

To illuminate the rear hutch (12-ID-C) the SMI X-ray beam propagates through a removable and interlocked shielded beam transport pipe (approx. 4.5 m long), located in hutch 12-ID-B. For OPLS operation, this beam pipe is removed, the upstream vacuum section is terminated by a Beryllium (Be) window and a removable lead beam stop is mounted at the downstream end, thereby defining the space available for OPLS experimental station.

The Crystal Deflector Assembly

The crystal deflector assembly (see Fig. 2) has a granite base (0.89m×1.85m×0.30m) with sufficient length to allow the motion along Z-axis, to accommodate a variable deflector-to-sample distance ranging from 0.6 m to 1.5 m.

The Z-axis translation stage ($\pm 650\text{mm}$) is actuated by a stepper motor and rack and pinion mechanism. To overcome the pinion backlash, the motion control system uses feedback from an incremental encoder. To lock the stage into position, an air-actuated clutch-brake module is used on the inboard guide rail. The brake module uses spring energy to clamp onto the guide rail and air pressure to overcome the spring force and release it [2].

The X-axis translation stage ($\pm 150\text{mm}$), actuated by a stepper motor and a preloaded ball screw assembly (NSK PSS25-05-N1-D-0499), is used to center the crystal deflector into the beam using the cross-hair alignment

[†] dbacescu@bnl.gov

target, or to move it out of the beam, to the retracted position, when OPLS is not operated. Both Z and X axes translation stages are based on pairs of linear roller guides (NSK RA30 series), incremental encoders and limit switches.

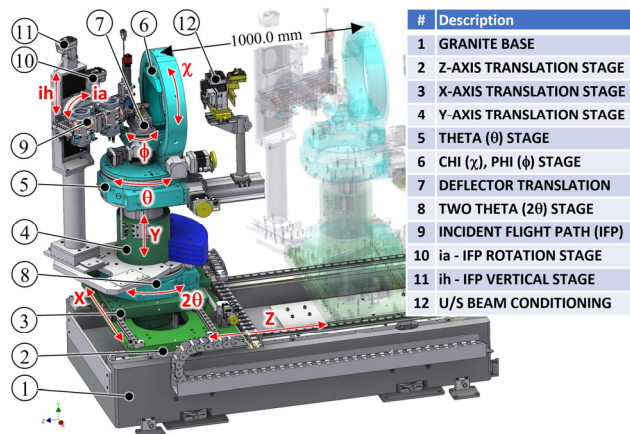


Figure 2: Deflector crystal and incident arm assemblies.

The Y-axis vertical stage with vertical stroke of ± 75 mm, is a recycled component from a former instrument. It consists of two concentric and guided cylinders and is actuated by motorized a screw jack assembly. Mounted on top of the Y-axis translation stage is a 3-circle goniometer consisting of a θ -stage (Huber 430) and an Eulerian cradle (Huber 512.1). The θ -stage is used to position the χ -stage perpendicular to the incoming beam. The χ -stage is used to rotate the crystal and bounce the incident X-ray beam downwards by a variable angle α from horizontal. The ϕ -stage is used to set the Bragg angle [3]. Above the ϕ -stage, there is an additional crystal translation stage which positions the crystal or a cross-hair alignment target at the Eulerian cradle's center. On top of the X-axis translation stage, a 2θ -stage (Huber 430) provides rotation of the incident arm. The arm is holding a vertical ih-translation stage (Daedal 406004LN) on which the ia-goniometer (Huber 411) is mounted, where the ia-rotation axis orientation is horizontal. All these motions allow the alignment of the incident flight path with the deflecting beam angle α . A beam conditioning module is located upstream of the χ -stage, attached to the base θ -stage, consisting of an absorber bar, beam slits, photon shutter, and an ion chamber (see Fig. 2).

The Incident Flight Path (IFP)

The compact incident flight path was designed to fit within the specified minimum deflector-to-sample distance. All components of the IFP are mounted on an extruded aluminum rail. The IFP (see Fig. 3) consists of a vacuum section with in-vacuum slits centered on the ia-axis and vacuum crosses at the upstream and downstream ends, each equipped with end flanges holding Kapton® windows. Also, ion chambers are attached at each end of the vacuum section. The upstream vacuum cross house a vertically retractable Diamond Beam Position Monitor (DBPM) and a filter selector (see Fig. 3b).

The downstream vacuum cross is used for pumping and can house an optional secondary DBPM. A beam visualization module is located upstream of the IFP (see Fig. 3c), consisting of a 100 μ m thick Cadmium Tungstate (CdWO₄) polished crystal scintillator plate, a 30 mm cage cube-mounted silver-coated turning mirror, a 5X Mitutoyo objective lens, a 152.5mm-long extension tube, and a CMOS monochrome camera (Allied Vision Mako G-419B). An in-air attenuator translator bar is mounted downstream of the IFP, (see Fig. 3a).

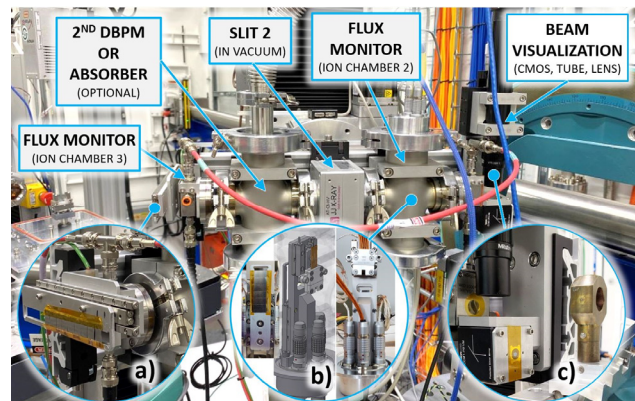


Figure 3: Incident flight path assembly. a) in-air attenuator translator bar; b) DBPM & absorber; c) beam visualization scintillator, mirror, and objective lens.

The Sample and Detector Arm Assemblies

The sample and detector arm assemblies (see Fig. 4) are mounted on a granite base (1.62m \times 2.43m \times 0.30m) with sufficient length and width to allow the sample assembly, together with the detector arms, to translate along the X-axis. In addition, the detector arms are rotated by the 2θ -stage (Huber 440) about an axis concentric with sample vertical translation.

The geometry code translates in X-axis and Y-axis so that the downward deflected beam intercepts the center of the sample. The detector arms are supported by a pair of flat and round air bearings that ride on the top surface of the granite base and can rotate from $2\theta=0^\circ$ position (parallel with Z-axis) to $2\theta=90^\circ$ (perpendicular to Z-axis) for any X-axis position in operation mode.

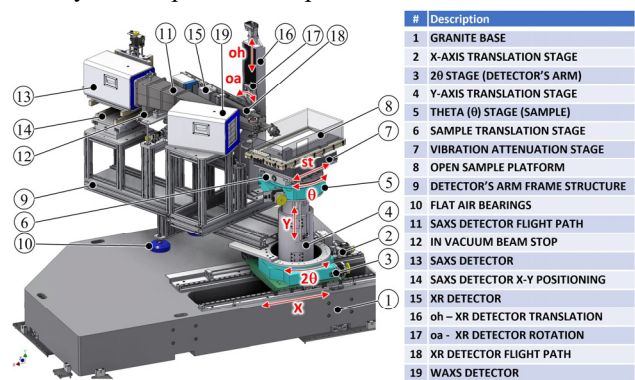


Figure 4: The OPLS sample and detector arm assemblies.

The detectors arms are constructed from extruded aluminum structural framing, designed to hold up to three

detectors located downstream of the sample, with fixed 20° angular offsets, each dedicated to a different technique.

The XR detector assembly is supported on the inboard side of the detector's frame structure, with 11° inboard angular offset. The XR detector uses a Lambda 250k GaAs detector (55 μm pixel size) interchangeable with a Dectris Pilatus 100K detector. The XR detector is located 1.0 m downstream from the sample, mounted downstream of a rectangular cross-section flight tube. Both detectors are mounted on extruded aluminum rail which can be rotated horizontally by the ϕ -axis stage (Huber 411) and translated vertically by the z -axis stage. All these motions allow the XR detector to be positioned at an angle β with respect to the horizontal whose height is arranged to intercept the reflected beam from the sample.

The SAXS detector assembly (see Fig. 5) consists of a detector flight path and is equipped with an in-vacuum beam stop (with x and y translations, see Fig. 5b) and a flight path motion system. The flight path motion system is based on two custom-designed vertical translation stages, located at the end, each actuated by a motorized screw jack. The downstream end has a hinge that is coupled with the corresponding vertical translation stage (Fig. 5c).

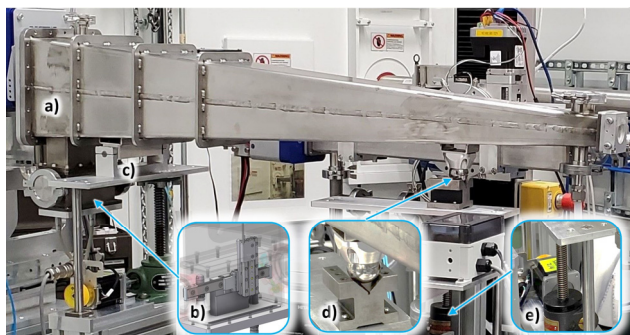


Figure 5: The SAXS detector flight path assembly. a) Flight path; b) in-vacuum beam stop; c) hinge; d) upstream pivot; e) upstream vertical stage.

The upstream end has a spherical pivot which sits on a “V” groove (Fig. 5d) located above the upstream vertical stage. By moving the two vertical stages, the flight path can be adjusted in height or inclined (moving differentially, with the downstream end higher than upstream one) around a virtual axis located at the sample position. The current setup locates the SAXS detector at 1.5m from the sample. The detector is not coupled to the flight path and can be positioned by a set of X-Y custom-made translation stage modules. The setup is compatible with either a Dectris Pilatus 300K or 1M detectors. The WAXS detector is supported on the outboard side of the on same frame structure, with 20° outboard angular offset and at a distance between 0.3-0.5 m from the sample. The WAXS detector is designed for a Dectris Pilatus 1M.

The sample positioning mechanism design is similar to the one described for the crystal deflector assembly except that there is no Z-axis translation (not required). The sample X-axis translation stage has stroke of ±435mm and the sample Y-axis vertical stage has a stroke of ±125mm. The sample rotates using a θ -stage (Huber 430) on top of

which there is a custom-made sample translation stage (stroke ±180mm). An active vibration isolation table (Herzan TS-150), mounted on top of the sample translation stage, can support a maximum load of 150 kg and maximizes the instrument resolution by removing the ambient vibration noise (less than 5 Hz).

Commissioning Results

This Fig. 6 shows the ϕ rocking scan profiles at 16.1 keV, for various downward projected angles α from 0° to 4° deg. The rocking curve width are dominated by the Ge (111) deflection crystal's Darwin width. The deviation in the centroid of these rocking curves varies by about +/- 0.0002°, more than adequate for a single χ motion to deflect the beam downwards and much less than the Darwin width.

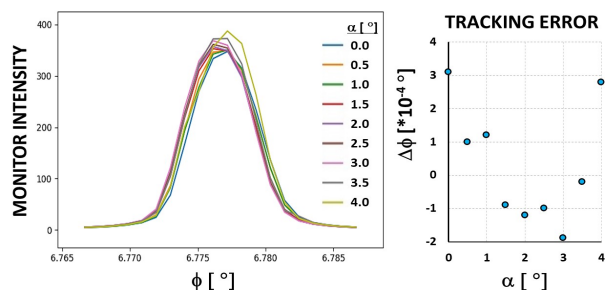


Figure 6: Instrument tracking @ 16.1 keV.

CONCLUSIONS

The OPLS is fully assembled and functional. The experimental station was recently successfully commissioned, and soon will start the general user operation.

ACKNOWLEDGEMENTS

The authors would like to extend their gratitude to the entire beamline support team, especially to Rick Greene and Leo Reffi for their technical support and Chris Stebbins for his project coordination. The Work was supported by the National Synchrotron Light Source II, a U.S. Department of Energy (DOE) Office of Science User Facility operated for the DOE Office of Science by Brookhaven National Laboratory under Contract No. DE-SC0012704.

REFERENCES

- [1] Mikhail Zhernenkov, Niccolo Canestrari, Oleg Chubar, Elaine DiMasi, “Soft matter interfaces beamline at NSLS-II: geometrical ray-tracing vs. wavefront propagation simulations,” in *Advances in Computational Methods for X-Ray Optics III, Proc. SPIE*, vol. 9209, p. 92090G, 2014.
- [2] Nexen Group, <https://www.nexengroup.com/>
- [3] Peter S. Pershan, Mark Schlossman, *Liquid Surfaces and Interfaces: Synchrotron X-Ray Methods*. Cambridge: Cambridge University Press, 2012

SAMPLE AND DETECTOR POSITIONING INSTRUMENTS FOR THE WIDE ANGLE XPCS END STATION AT 8-ID-E, A FEATURE BEAMLINE FOR THE APS UPGRADE*

K. Wakefield†, S. Bean, D. Capatina, E. M. Dufresne, M. Fisher,
M. J. Highland, S. Narayanan, A. Sandy, R. Ziegler
Advanced Photon Source, Argonne National Laboratory, Lemont, Illinois, USA

Abstract

The X-ray Photon Correlation Spectroscopy (XPCS) beamline at the Advanced Photon Source (APS) has been selected as one of the nine feature beamlines being designed to take advantage of the increase in coherent flux provided by the APS Upgrade. The 8-ID-E enclosure at the beamline will have a dedicated instrument for performing Wide Angle XPCS (WA-XPCS) measurements across a range of length and time scales. The instrument will feature a high-stability 6-circle diffractometer, a moveable Long Distance Detector Positioner (LDDP) for positioning a large pixel array detector, and a removable flight path assembly. For intermediate sample to detector distances of 1.5 to 2 meters, a large pixel array detector will be positioned on the diffractometer detector arm. For longer sample to detector distances up to 4 meters, an horizontal scattering geometry will be utilized based on the LDDP to position a second large pixel array detector. The LDDP will consist of a large granite base on which sits a combination of motorized stages. The base will sit on air casters that allow the LDDP to be coarsely positioned manually within the enclosure. Final positioning of the detector will be achieved with the mounted stages. The spatial relationship between the sample and the free moving LDDP will be monitored using a laser tracking system. A moveable flight path will be supported by the diffractometer arm and a mobile floor support to minimize air scattering while using the LDDP. The WA-XPCS instrument has been designed with users and beamline staff in mind and will allow them to efficiently utilize the highly enhanced coherent beam provided by the APS Upgrade.

INTRODUCTION

The Advanced Photon Source Upgrade Project (APS-U) is planning a storage-ring upgrade that will reduce the electron-beam emittance by a factor of ~ 75 . This ultra-low emittance is achieved by replacing the present storage ring lattice with a multi-bend achromat (MBA) lattice. The MBA lattice will increase the x-ray coherent fraction by two orders of magnitude and decrease the horizontal source size by a factor of ~ 20 . In addition, the APS-U is planning to build nine new featured beamlines and make optics upgrades to many others.

* This research used resources of the Advanced Photon Source, a U.S. Department of Energy (DOE) Office of Science User Facility at Argonne National Laboratory and is based on research supported by the U.S. DOE Office of Science-Basic Energy Sciences, under Contract No. DE-AC02-06CH11357.

† kwakefield@anl.gov

One of the feature beamlines built as part of the APS-U will be dedicated to X-ray Photon Correlation Spectroscopy (XPCS) studies at sector 8ID of the APS. The 8-ID-E enclosure of the XPCS beamline will primarily perform Wide Angle XPCS (WA-XPCS) measurements and occasionally be used for positioning samples during Ultra-Small Angle XPCS measurements. Two key elements to the instrumentation required to perform these measurements are a large 6-circle diffractometer for precise positioning of samples in 3 spatial and 3 angular co-ordinates, detectors, and a Long Distance Detector Positioner (LDDP) that will allow x-ray detectors to be positioned up to 4 m away from the sample location and will span an angular range of 3-55 degrees. These instruments are shown in Fig. 1 below.

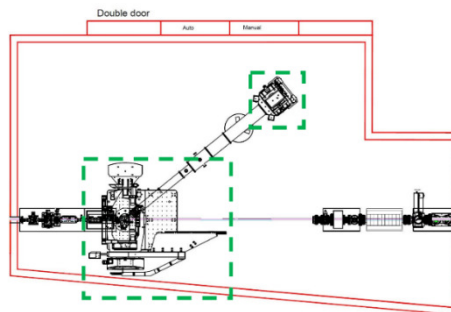


Figure 1: 8-ID-E enclosure layout with WA-XPCS instruments, diffractometer and LDDP outlined in green.

SCIENCE DRIVER

Photon correlation spectroscopy (PCS) provides information about dynamic heterogeneity in complex systems by characterizing fluctuations in condensed matter across a broad range of length and time scales while x-ray scattering provides sensitivity to order and motion at scales spanning the mesoscale to the atomic scale. A general subset of the areas of scientific investigation that will be pursued at the beamline include the role of fluctuations and dynamic heterogeneity in the properties of phase-change materials, understanding structural relaxations in supercooled liquids and their connection to glass formation, the effect of interfaces and confinement on nanoparticle dynamics, and the connection between dynamics and relaxation of shearthinned and shear thickened states. To perform successful WA-XPCS measurements requires, the formation of a small coherent x-ray spot, accurate and stable positioning of a sample, and the ability to resolve coherent x-ray speckles with an area detector. These requirements have driven the overall design of the WA-XPCS instrument.

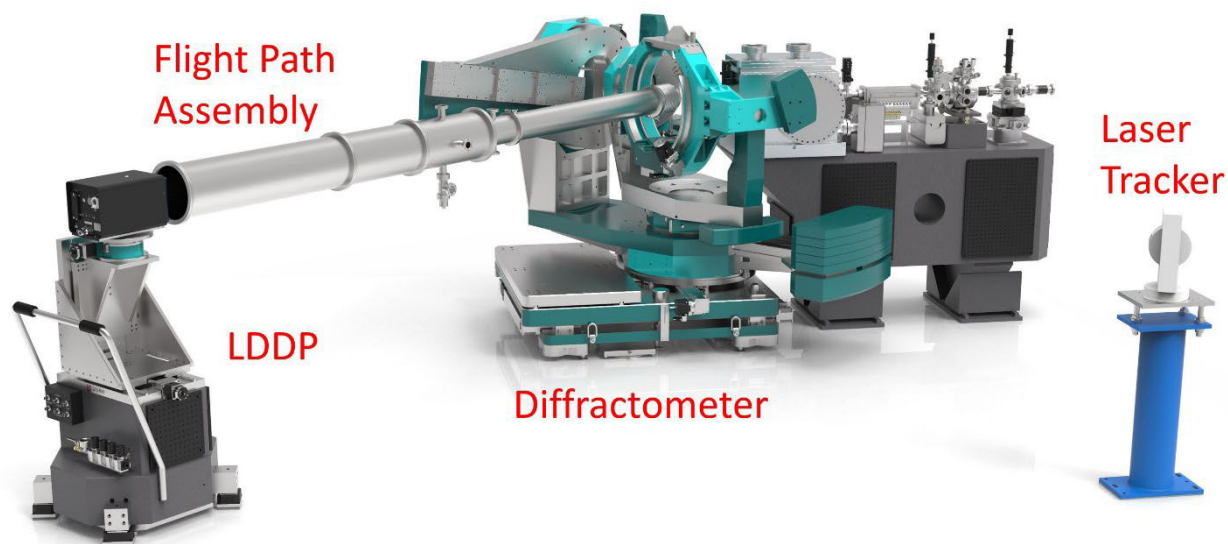


Figure 2: 8-ID-E instrument with the detector located 4 m from the sample on the LDDP. A laser tracking system positioned on a pedestal is also shown. Flight path support and window are not shown.

WIDE ANGLE INSTRUMENT OVERVIEW

The WA-XPCS instrument at 8-ID-E facilitates a variety of operating modes and experimental methods. The combination of the 6-circle diffractometer and the mobile LDDP creates a highly versatile instrument capable of positioning state-of-the-art pixel array detectors at a variety of locations throughout the enclosure. The 3 primary configurations of the instrument will be the following:

1. **Short sample-to-detector WA-XPCS (vertical scattering geometry):** In this configuration, a pixel array detector will be positioned on the diffractometer detector arm at a sample-to-detector distance of 1.5-2 m.
2. **Long sample to detector WA-XPCS (horizontal scattering geometry):** In this configuration, a second large area detector will be positioned using the LDDP at a sample-to-detector distance of up to 4 m, spanning an angular range of 3-55 degrees. Figure 2 shows the instrument in this configuration.
3. **Pinhole Ultra-Small XPCS (US-XPCS):** In this configuration the sample will be mounted on the WA-XPCS diffractometer and the detector will be positioned in the 8-ID-I shielded enclosure with a sample to detector distance of up to ~22 m.

6-CIRCLE DIFFRACTOMETER

The WA-XPCS diffractometer will be a large 6-circle diffractometer for accommodating a wide range of samples in a variety of scattering geometries. The diffractometer will have a “split” detector arm with two mounting rails for mounting detectors near the sample as well as supporting flight paths for use with the LDDP. The base positioning table of the diffractometer will have an extension in the downstream direction for mounting large additional pieces of instrumentation, which can be seen in Fig. 3 below.

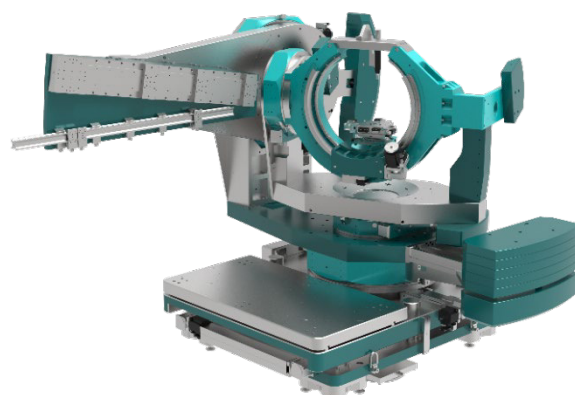


Figure 3: 6-circle diffractometer. Design and 3D model of the diffractometer provided by Huber Diffractionstechnik GmbH & Co. KG.

LONG DISTANCE DETECTOR POSITIONER (LDDP)

The LDDP provides a versatile platform for mounting detectors up to 4 m away from sample. The LDDP will consist of a large granite base on which sits a combination of motorized stages. The granite base will sit on air casters that allow the LDDP to be coarsely positioned manually within the hutch. Once coarsely positioned, fine alignment of the detectors will be done with the motorized stages. Once in position, the location of the detector on the LDDP relative to the sample will be reported using a laser tracking system.

The air casters for the LDDP will be activated using two manual triggers on the handle of the instrument. The air casters will then lift the base and all of the supported components a minimum of 6 mm off of the floor, allowing free movement around the enclosure.

Once the instrument has been coarsely positioned, the granite base provides a stable, low-vibration support for the stages and detector. The instrument will support detectors up to 20 kg, and the stages will provide ± 100 mm of travel both vertically and horizontally. The LDDP is shown with a detector positioned at the center of travel in Fig. 4.



Figure 4: Long Distance Detector Positioner. Design and 3D model of the LDDP instrument provided by JJ X-ray

VACUUM FLIGHT PATH ASSEMBLIES

All 3 operating configurations will require the use of a vacuum flight path assembly downstream of the sample environment. When the detector is mounted on the diffractometer, a short pipe will be mounted directly to the detector arm of the diffractometer, along with other components such as anti-scatter slits and a remotely operated filter box. In the long-distance WA-XPCS mode, a flight path assembly will be supported by the second mounting rail of the diffractometer's detector arm, and at the other end a mobile support. For Pinhole US-XPCS, a sample will be placed on the diffractometer and a flight path assembly will be supported by the diffractometer. This flight path will connect to the downstream optical components of the enclosure and will be supported by a mobile support.

Figure 5 shows an initial concept for the flight path assembly for long-distance WA-XPCS mode. This flight path will contain several removable rigid sections to allow users to place the LDDP, along with its mounted detector, at positions between 2.5 m and 4 m from the sample, across a range of 0-55 degrees horizontally.

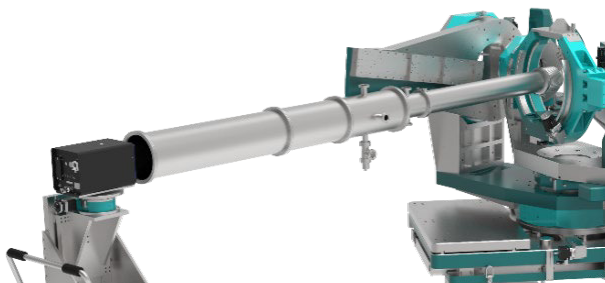


Figure 5: Removable flight path for the LDDP.

LASER TRACKER

The combination of the diffractometer and LDDP provides maximum versatility in detector positioning while preserving space in the enclosure. However, there is not a fixed spatial and angular relationship between a sample mounted in the diffractometer and a detector mounted on the LDDP. To determine this spatial and angular relationship, once the LDDP has been positioned, a laser tracker will be used to determine the location of carefully chosen fixed reflectors on the base of the diffractometer and on the LDDP. This information along with the known motion of the stages on the LDDP and the diffractometer will be used to determine the distance and angle between the sample and the detector. The yellow dots in Fig. 6 show potential locations for mounting laser reflectors. The precise configuration of the reflectors will be optimized once all the components have been installed.

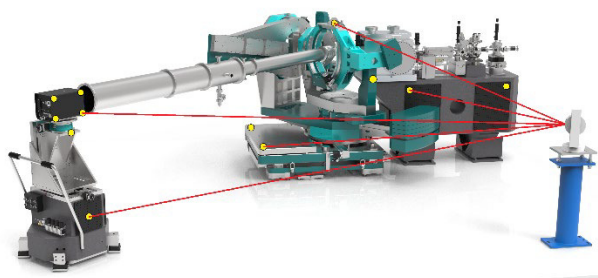


Figure 6: Conceptual schematic showing the laser tracker being used with the diffractometer and the LDDP

CONCLUSION

The APS-U will significantly enhance the coherence properties of the APS x-ray source. XPCS is one of the x-ray techniques that will most directly benefit from the 100-fold increased coherence. To fully realize these benefits, the x-ray instruments must be designed with sufficient functionality and stability to take advantage of them. The WA-XPCS instrument uses a combination of a 6-circle diffractometer, LDDP, and laser tracker to meet these requirements, while maintaining maximum versatility to adapt to the future needs of the scientific program.

ACKNOWLEDGEMENTS

The Advanced Photon Source is a U.S. Department of Energy (DOE) Office of Science User Facility operated for the DOE Office of Science by Argonne National Laboratory under Contract No. DE-AC02-06CH11357

DETERMINATION OF MAXIMUM REPETITION RATE OF A CORRUGATED-WAVEGUIDE-BASED WAKEFIELD ACCELERATOR

K. Suthar*, A. Siy¹, G. J. Waldschmidt, S. Lee, S. Sorsher,
 E. Trakhtenberg, and A. Zholents,
 Advanced Photon Source, Argonne National Laboratory, Lemont, USA
¹also at University of Wisconsin, Madison, USA

Abstract

Beam-driven wakefield accelerators hold great promise toward reducing the size of contemporary accelerators. One possibility under study at Argonne National Laboratory is the use of a miniature corrugated waveguide for generation of the wakefield. The effect of electromagnetic heating by the electron beam traveling on its centerline is investigated applying the steady-state thermal analysis coupled with computational fluid dynamics, and structural mechanics. A design of the accelerator module suitable for acceleration of electrons with an energy gain up to 100 MeV m^{-1} is considered. A heat load on the waveguide inner surface with corrugations is calculated using a conservative assumption for the copper electrical conductivity at a high frequency of the electromagnetic field. It is shown that the von Mises stress caused by thermal expansion grows with the increased bunch repetition rate and reaches a yield level in a most stressed location at the bunch repetition rate of 16.5 kHz . Other effects associated with the waveguide heating, such as waveguide expansion and contraction, are quantified.

INTRODUCTION

A miniature accelerator employing a copper cylindrical corrugated waveguide is being designed at Argonne National Laboratory to produce Čerenkov radiation at 180 GHz using a high charge electron bunch traveling longitudinally on the centerline of the waveguide. The radiation field accelerates a low-charge electron bunch traveling behind with an energy gain of $\sim 100 \text{ MeV m}^{-1}$ [1]. The electromagnetic (EM) wave of Čerenkov radiation propagates downstream of the waveguide with a slower group velocity than the beam velocity. Interacting with corrugations, it excites surface currents responsible for the waveguide heating. As shown in Fig. 1, the waveguide is embedded into a "bow-tie"-shaped copper structure with four water cooling channels, although the optimal location of these channels and thermal conductivity from the corrugated surface to water is severely limited by external constraints. The heat load deposition gradually increases along the 0.5 m length of the waveguide and produces a temperature gradient that leads to progressively higher thermal expansion in the downstream direction. The stress from the differential expansion can lead to material tensile-yield failure, surface cracking, arcing, and beam loss. Therefore, determination of the acceptable bunch repetition rate and the ultimate performance of the accelerator are directly related to

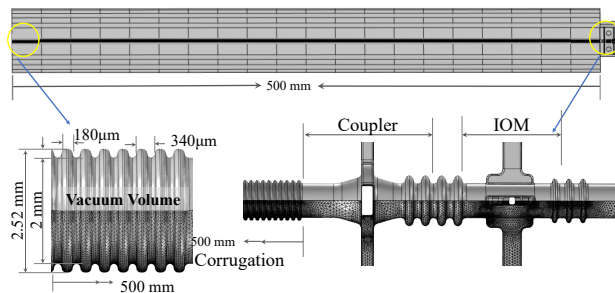


Figure 1: The corrugated waveguide and transition section showing surface mesh.

the thermal management of the average heat load deposited by the electron beam on the corrugations in a steady state operation. Quantitative analysis of the differential dimensional changes is critical for understanding of the operating conditions, and we are investigating the limits based on heat transfer, cooling, and mechanical integrity of the structure applying fully coupled multiphysics finite element analysis while the EM design [2] and prototype fabrication efforts [3] are still developing.

MULTIPHYSICS FORMULATION

Multiphysics calculations were performed with CST Microwave Studio[®] [4] and COMSOL Multiphysics[®] software [5]. Modeling electromagnetic heating with computational fluid dynamics (CFD) and solid mechanics in the corrugated waveguide follow the scheme shown in Fig. 2a, and are summarized in the following steps:

- Solve the electromagnetic problem in CST studio[®] to find the electromagnetic fields and calculate the electromagnetic surface losses on the wall.
- Apply thermal loads induced by the electromagnetic fields in the heat transfer module to perform the calculation for the temperature rise.
- Apply the flow condition in the CFD, then define the temperature field as a coupling parameter to couple both physics.
- Define the boundary conditions for the Structural Mechanics module, then create a coupling parameter that couples the temperature field of Structure Mechanics for thermal expansion.
- Have the coupled solution compute the temperature field as a fully coupled equation between the heat transfer and the CFD modules, and use it as input for the

* suthar@anl.gov

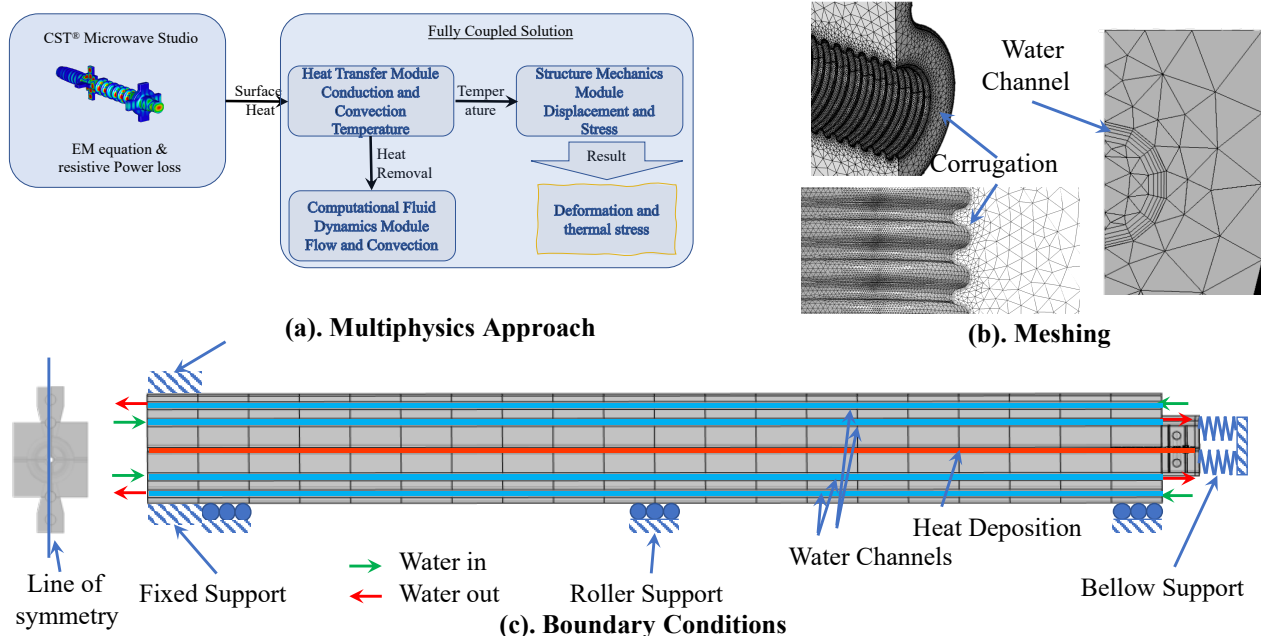


Figure 2: Information on the finite element formulation: (a) fully coupled approach of solving three physics, (b) surface meshes utilized in the study, and (c) boundary conditions used in this study.

thermal and mechanical analysis, provided that the influence of the deformation on the temperature field is negligible.

The Geometry

The corrugated waveguide geometry is shown in Fig. 1. The length of the corrugated waveguide is 0.5 m and the length of the transition section (TS) between adjacent waveguides is 25 mm. The dimension of corrugation is shown in the figure. To reduce the number of mesh elements and speed up calculations, we analyze the corrugated section only for the last 25 mm that is exposed to the highest heat load from the Čerenkov electromagnetic wave generated by the electron bunch. The RF wave is removed in the TS using the electromagnetic coupler, while a small-amplitude signal informing about the beam offset in the corrugated waveguide passes the coupler and a notch filter and is taken by the integrated offset monitor (IOM). The structure has a fourfold symmetry, and thus analyzing half of the volume is sufficient.

Materials

The copper properties that were used in the calculation are listed in Table 1. Note that the value of electrical conductivity was intentionally degraded by a factor of 2.5. This value was used to perform conservative calculations since at the time of writing we do not know either the surface roughness of the corrugations or the actual conductivity of an electroformed copper.

Table 1: Material Specifications

Parameter	Value	Units
Thermal Conductivity	400	W/(m K)
Electrical Conductivity	2.3×10^7	S/m
Expansion Coeff.	17×10^{-6}	1/K
Specific Heat	385	J/(kg K)
Modulus of Elasticity	190	GPa
Poisson's Ratio	0.35	

Meshing and Boundary Conditions

Meshing can be seen in Fig. 1 and Fig. 2. The mesh consists of 2,856,122 elements with an average quality of 70%. All the boundaries with allied electromagnetic heat load conditions were meshed at least three layers deep within approximately 25 μm . Figure 2c shows the boundary conditions for all the physics.

Heat Transfer

The electromagnetic field calculation was performed with CST Microwave Studio[®] using an electron bunch charge of 10 nC.

The heat load caused by surface currents excited by the electromagnetic wave of Čerenkov radiation was scaled linearly with the bunch repetition rate. Table 2 lists all the values for the heat load that are being absorbed on the surfaces of the corrugated waveguide and on the transition section. The corrugated and transition sections are painted with red in Fig. 2c. The natural convective heat transfer boundary condition was used for the outer surface of the device with the heat transfer coefficient of $2 \text{ W m}^{-2} \text{ K}^{-1}$. The water in-

Content from this work may be used under the terms of the CC BY 3.0 licence (© 2021). Any distribution of this work must maintain attribution to the author(s), title of the work, publisher, and DOI

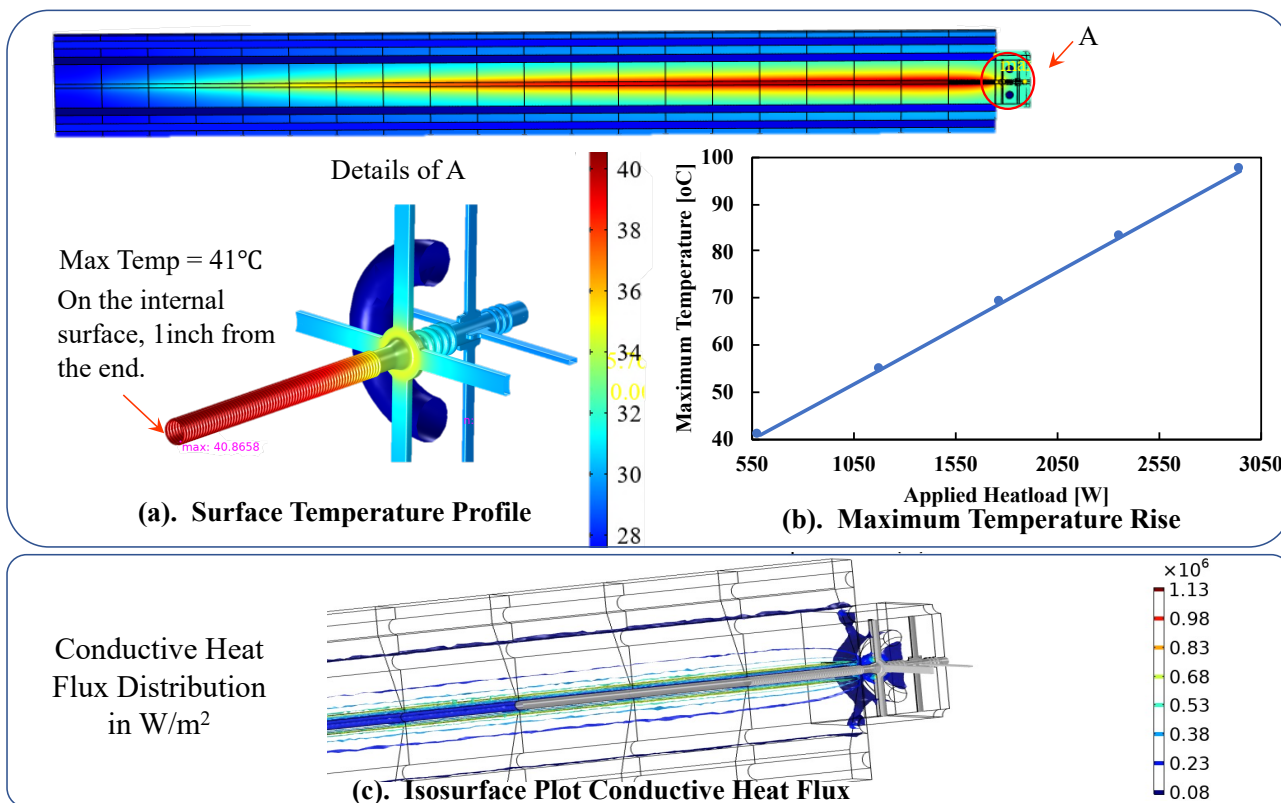


Figure 3: Results of the multiphysics simulation showing (a) surface temperature profile, (b) parametric study of applied heat load, and (c) isosurface plot of conducive heat flux in the volume.

Table 2: Heat Load from CST Microwave Studio® at 10 kHz Bunch Repetition Rate

Geometry	Value	Remark
Corrugated waveguide	589 W	Increases linearly from 0.03 W/cm at the beginning to 39.75 W/cm at the end of the waveguide.
Coupler IOM	21.81 W 1.2 W	

let temperature was 25.6 °C. The ambient temperature was 22 °C.

Computational Fluid Dynamics

Four water channels, two channels per side, are provided to extract the heat from the structure, as seen in Fig. 2c. The water flow direction in the closest water channels is in the e-beam travel direction, which is from left to right towards the transition section. The outer water channels flow from right to left. The heat transfer between fluid flow and the structure is done by providing a coupling parameter that calculates the heat removal by forced convective heat transfer in the CFD module of COMSOL Multiphysics®. The isothermal heat transfer condition is assumed, and therefore

the coupling between computational fluid dynamics and heat transfer modules is one-way.

Solid Mechanics

All the boundary conditions are shown in Fig. 2c. The left ends of the corrugated waveguide are fixed and the structure is allowed to roll on the horizontal plane and to grow in the vertical plane. A spring foundation boundary condition is used on the right side of the transition section, since the end is connected with a bellows with a spring constant of 80 N/mm.

RESULTS

The simulation was performed at varying heat load conditions. These conditions represent the bunch repetition rate from 10 kHz to 50 kHz in increments of 10 kHz. All the plots and images in Fig. 3 show the results of the calculations for the 10 kHz case, which deposits about 600 W of heat on the walls of the waveguide. The top image in Fig. 3a shows the temperature profile of the corrugated waveguide (A) sectioned at the center. The details of 'A' show the temperature distribution on the corrugation and transition section. The graph in Fig. 3b shows the maximum temperature upon application of the various heat loads. The graph is linear because we assume constant thermal and electrical conductivity values. The isosurface plot in Fig. 3c shows a map of the conducive heat flux in the critical region of this section.

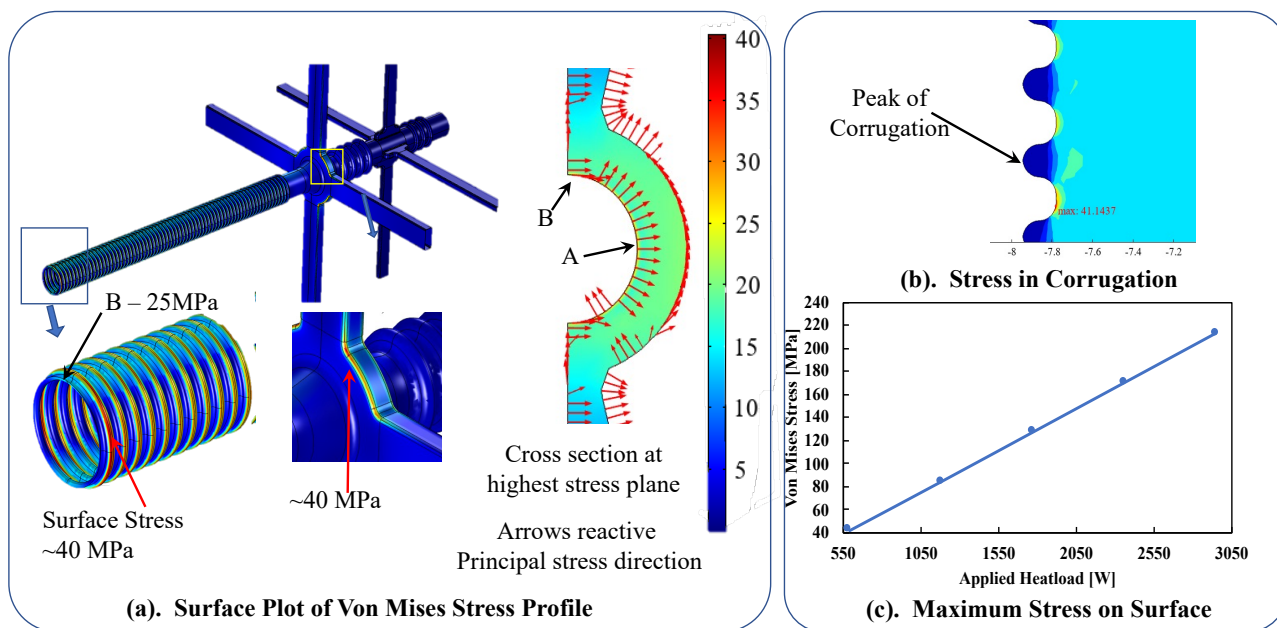


Figure 4: Results of multiphysics simulation.

Table 3: Maximum Displacement Based on the Applied Heat Load

Heat Load	Displacement
590 W	29.29 μm
1180 W	61.93 μm
1770 W	94.59 μm
2360 W	127.26 μm
2950 W	159.92 μm

The temperature rise in copper has a direct correlation with the conductive heat flux. It can be seen that the conductive heat flux value reduces near the end and towards the transition section, which represents a high rate of cooling due to a conduction cooling operation.

Figures 4a, b, and c represent the von Mises stress in the structure, while the maximum displacement at the extreme right tip of the structure is listed in Table 3. Figure 4b shows the maximum stress occurring in the trough region, which is 41 MPa, while the peak region is experiencing a lower stress. The 2D image in Fig. 4a shows the stress at the cross section is the maximum stress in the structure. The image with arrows on the surface is showing the directions for the derived principal stresses on the cross section. The outer surface near the thinnest section of the part undergoes tensile stresses, which are also higher, as shown in the images of surface stress on the right side of Fig. 4a, marked by point A. At point A, the part is being stretched, and the stresses are in the tensile regime. At point B, the stresses are lower than point A because the section thickness is higher. Figure 4c shows the maximum stress produced on the surface for the applied heat load.

Simulation
Thermal

DISCUSSION

The temperature rise for the 600 W case is about 15 °C above the room temperature, which is not a considerable temperature change in copper. However, the stress level at the corrugation is higher than in the bulk since corrugations can be viewed as a series of thin rings attached to the linearly expanding structure. Moreover, stresses due to thermal expansion in the high-aspect-ratio structures increase monotonically [6], and our structure has a high aspect ratio. The average temperature rise over the entire volume is about 6 °C, which leads to an average stress of 11 MPa when calculated analytically. The simulation shows similar numbers in the bulk, while a higher stress level is seen at the corrugation. The maximum value of the von Mises stress calculated for a 10 kHz bunch repetition rate is 41 MPa. The same calculations show that the yield stress is reached at 1 kW of heat load, which corresponds to a 16.5 kHz bunch repetition rate. The zone with the maximum stress is only 10 μm deep, which is an indication of the tensile stress criteria on the surface. The maximum linear expansion is 29.3 μm , and the pitch of the corrugated structure is 340 μm . There are 1470 corrugations in the 0.5-meter-long structure. By distributing the thermal expansion linearly over this number of corrugations, the change in pitch will be less than 100 nm.

SUMMARY

The miniature beam-driven wakefield accelerator based on the corrugated waveguide has been considered where the electromagnetic heat load has been deposited in a linearly increasing manner in the downstream direction of the corrugated waveguide, and thus the expansion has also increased linearly toward the transition section between the neighboring waveguides. The multiphysics model has been

created to calculate the expansion in the long thin structure of the corrugated waveguide and related von Mises stress caused by the structure heating up from the electron beam propagating along its axis. The calculations have helped to develop an understanding of how to support the structure with a fixed support, a roller support, and a bellows support to minimize the stress.

The investigation has also helped define safe operating conditions when the maximum stress on the heat-affected zone is less than the yield strength of the material. Based on the finite element analysis study, it was inferred that for an electron beam with a bunch charge of 10 nC, the bunch repetition rate can safely be at 15 kHz.

ACKNOWLEDGMENT

We thank our colleagues, W. Jansma, A. Nassiri, B. Popovic, and J. Xu for useful discussions. This research used resources of the Advanced Photon Source, a U.S. Department of Energy (DOE) Office of Science User Facility and is based on work supported by Laboratory Directed Research and Development (LDRD) funding from Argonne National Laboratory, provided by the Director, Office of Science, of the U.S. DOE under Contract No. DE-AC02-06CH11357.

REFERENCES

- [1] A. Zholents *et al.*, “A conceptual design of a compact wake-field accelerator for a high repetition rate multi user x-ray free-electron laser facility,” in *Proc. IPAC’18*, Vancouver, BC, Canada, Jun. 2018, pp. 1266–1268. doi:10.18429/JACoW-IPAC2018-TUPMF010
- [2] G. Waldschmidt *et al.*, “Design and test plan for a prototype corrugated waveguide,” in *Proc. IPAC’18*, Vancouver, BC, Canada, Jun. 2018, pp. 1550–1552. doi:10.18429/JACoW-IPAC2018-TUPML009
- [3] K. Suthar *et al.*, “Investigation of various fabrication methods to produce a 180GHz corrugated waveguide structure in 2mm-diameter 0.5m-long copper tube for the compact wakefield accelerator for FEL facility,” in *Proc. NAPAC’19*, Lansing, MI, USA, Oct. 2019, pp. 286–289. doi:10.18429/JACoW-NAPAC2019-MOPL023
- [4] Dassault Systems, *CST, Microwave Studio*, 2020.
- [5] Comsol Multiphysics, *COMSOL Multiphysics*, 2020, <https://www.comsol.com>
- [6] Y.-L. Shen, “Modeling of thermal stresses in metal interconnects: Effects of line aspect ratio,” *J. Appl. Phys.*, vol. 82, no. 4, pp. 1578–1581, 1997. doi:10.1063/1.365944

A FAMILY OF HIGH-STABILITY GRANITE STAGES FOR SYNCHROTRON APPLICATIONS*

C.A. Preissner[†], S.J. Bean, M. Erdmann

Advanced Photon Source, Argonne National Laboratory, Lemont, IL 60439, USA

M. Bergeret, J.R. Nasiatka

Advanced Light Source, Lawrence Berkeley National Laboratory, Berkeley, CA 94720, USA

Abstract

Engineers at the APS have developed a granite, air-bearing stage concept that provides many millimeters of motion range and nanometer-level vibrational stability. This technique was first conceptualized and used on the Velociprobe x-ray microscope [1, 2]. The success of that design spurred adaption of the approach to over 90 devices, including many new instruments at the APS [3] and high performing instruments at other synchrotrons [4]. This paper details the design concept, some performance measurements, and new developments allowing for a six-degree-of-freedom device.

BACKGROUND

The stability needs of multi-bend achromat (MBA) synchrotrons [5] mean that both the accelerator and beam line equipment require more stable platforms as compared to those of the previous generation of synchrotrons. At facilities like the APS-U, new and more precise x-ray beam position monitors are required for the front ends and numerous fine-focusing (tens of nm or better) instruments are being deployed. Each of these requires multiple axes to align the equipment to the beam.

Many of these axes are simply to position or align the instrument and are not moved during a measurement or moved only for alignment. Conventional rolling element bearings are readily available in many forms and easily integrated into designs and make these motions easy to implement. However, there is a price to pay when using these rolling-element bearings: compliance.

Engineers at the APS were frustrated that the bearings necessary to allow for a practical and easy to use instrument also amplified floor vibration and reduced performance potential. Granite air bearing staging systems can offer advantages over conventional rolling-element bearing staging systems, including a) higher stiffness, b) lower thermal expansion, c) slow thermal changes/drift, and d) low angular position errors. While planar air bearings were in common usage, air bearing vertical stages required a novel wedge design [2] to realize a design in which there is no cantilevered load. This paper provides insight into basic aspects of the granite stage design, some measured performance, illustration of some examples, and new developments.

* This research used resources of the Advanced Photon Source, a U.S. Department of Energy (DOE) Office of Science User Facility at Argonne National Laboratory and is based on research supported by the U.S. DOE Office of Science-Basic Energy Sciences, under Contract No. DE-AC02-06CH11357.

[†] preissner@anl.gov

DESIGN CONSIDERATIONS

The basic principles of the Velociprobe-style air bearing stages are to integrate orifice-balanced air bearings [6] into granite blocks (Fig. 1), flow air to create a stiff film for movement, and vent the bearings when not moving to provide a stiff structure. All current systems are designed as positioning systems, meaning they are moved into position and then the air bearings are vented. Figure 1 shows the geometry of a typical granite block with integrated air bearings.

The integration of the bearing into the granite takes advantage of both the favorable granite thermal properties ($\sim 4 \times 10^{-6}$ m/m/ $^{\circ}$ C thermal expansion coefficient) and the high level of flatness that can be achieved [7]. Normally “flat-on-flat” contacts should be avoided, as surfaces are not exactly flat. However, the high level of flatness achievable with granite enables a stiff “flat-on-flat” type of contact when the bearings are vented. The “fly height” (air film thickness) is controlled by the size of the orifice located upstream of the bearing surface. The target film thickness is between seven and ten microns, and the APS has developed a spreadsheet to estimate the orifice size necessary to achieve this fly height. Alternatively, fly height can be determined during assembly by measuring the fly height and changing orifice size to achieve the desired fly height.

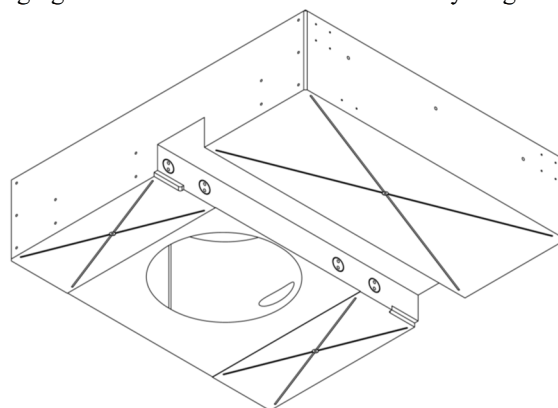


Figure 1: Picture of a typical granite block with three integrated, orifice balanced, air bearings. The orifices are located at the center of the “Xs”.

Stiffness of a vented granite air bearing is over 20 times that of the stiffest configuration of rolling-element bearings. Figure 2 shows a comparison of various rolling element bearings to a flat-on-flat contact typical of granite. Hertzian contact stiffness as described in Puttock [8] is compared to the AE/L stiffness of granite, with reference

dimensions (length, width, and area) of about 6.4 mm. In practical air bearing designs the stiffness difference is likely much greater due to the large area. APS experience shows that the vented blocks behave as a monolith from the vibration standpoint.

Geometry and friction play key roles in both the kinematics of the stage and the static stability. Figure 3 shows the basic layout for an independent, three-axis system. Constraints are provided to the horizontal block by mechanical or air bearings resulting in two in-plane degrees of freedom. The granite-to-granite contact provides constraints for rotations about the X and Z axes and it is important that some compliance or a flexure is provided between the block and the horizontal constraints such that the block is not overconstrained. In addition, the horizontal block can be used to provide small rotations (a few degrees) about the Y axis if the proper actuation and constraints are incorporated.

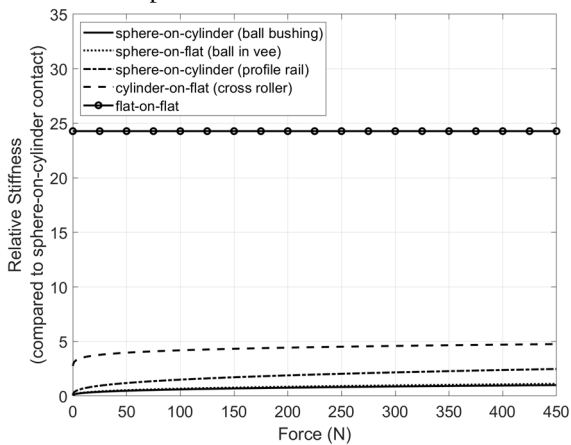


Figure 2: Plot showing the relative stiffness of various rolling element bearing types compared to a flat-on-flat type of contact. For similar reference dimension (6.4 mm), the flat-on-flat contact is approximately 25 times stiffer. In a practical application this difference can be even larger due to the large extent of the area contact.

The Y axis motion is provided by driving the bottom wedge (driving wedge) under a properly constrained top wedge (follower wedge). The kinematics and resulting forces are determined by the wedge angle, α .

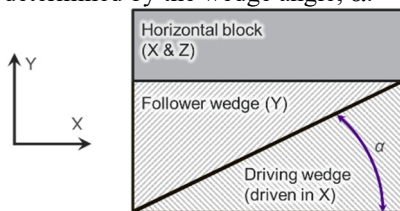


Figure 3: Diagram showing the basic structure of a three-axis system. The driving wedge (bottom) is moved in the X direction to cause a Y motion from the follower wedge (top). The wedge angle is denoted by α .

The expression $Y = X * \tan \alpha$ relates the vertical motion to the wedge angle and driving motion, including the friction and thrust forces. The friction force is what ensures the system is statically stable when the air bearings are vented,

while the thrust force is relevant for sizing the driving mechanism and needs to be known to prevent back driving.

A smaller wedge angle reduces the thrust force, increases the friction force, and increases the amount of X travel required for a given amount of Y travel. Figure 4 shows the resultant forces for a pair of wedges.

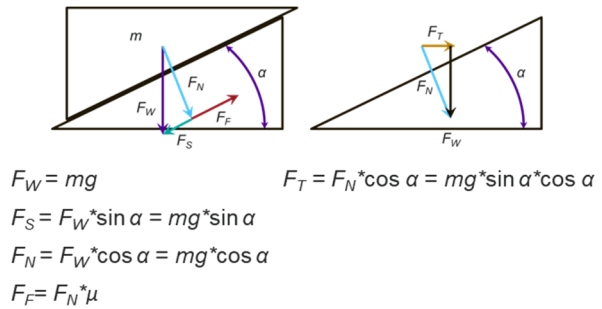


Figure 4: Wedge force diagram.

Figure 5 shows the relation of these forces and wedge angle. About 20 mm of Y travel is possible with a 7.5-degree wedge angle and 151 mm of driving wedge travel. The support for the driving wedge needs to be long enough to support the air bearings of the driving wedge, plus the motion range. This requirement places a practical limit on the Y (vertical) travel range of the air-bearing wedge stage. Though the APS has found 20-25 mm of travel to meet most needs.

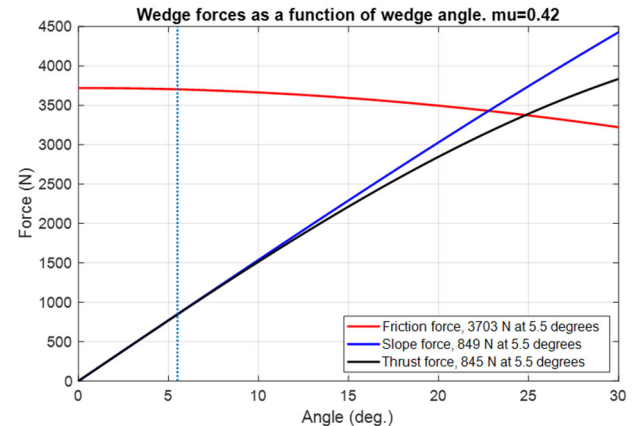


Figure 5: Chart showing how the vertical axis friction, slope (force parallel to wedge surface), and thrust forces change as a function of wedge angle. The vertical line is at the design point of 5.5 degrees for the APS-U PtychoProbe stage. The coefficient of friction (μ) has been measured.

Key to both the good static performance and achieving low fly height is the granite flatness. Fortunately, granite finishing is a well-known and common practice. Granite pieces of approximately 700 mm by 800 mm have been shown with autocollimator measurements to have flatness of around 2 microns, exceeding the tolerance of an “AA” grade surface plate [7].

PERFORMANCE

The vibrational performance is likely the main reason for selecting a granite air bearing stage for a particular application. Air bearing granite stages have demonstrated over

a 100 times reduction in relative vibration level as compared to a similar instrument using stages with all rolling element bearings. Figure 6 shows the measured relative vibration on the APS Velociprobe granite stage system.

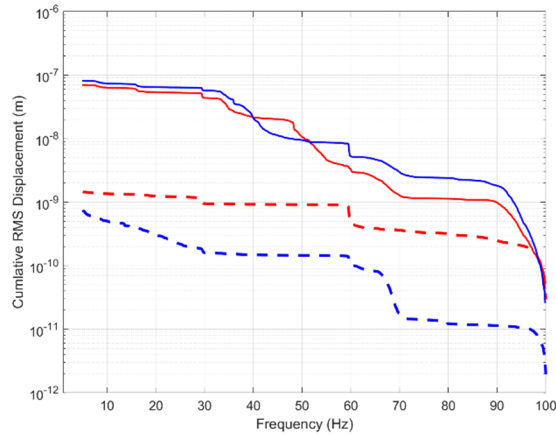


Figure 6: Chart showing comparing the relative vibration between the optic and sample mounting points for a granite stage system (dashed) and a conventional stage system (solid). Blue curves are for vertical vibration and red for the horizontal directions. The measurements show the granite stage system has nanometer level relative vibration whereas the conventional system is in the 70 to 80 nm range.

The angular errors that are present when the stage system is move are another important aspect of performance. For the example system shown in Fig. 3, the angular errors about the X and Z axes have the main contribution from the flatness of the granite (when the components are properly constrained). The angular errors about the Y axes have the main contribution from the bearings that guide blocks on their trajectories. These bearings can be either rolling element or air bearings. Air bearing guides will provide the lowest errors about the Y axis.

The angular errors are better than typical rolling element stage system and Fig. 7 shows angular errors as measured on the Velociprobe. Note: this system was not designed with particular consideration to minimize such errors.

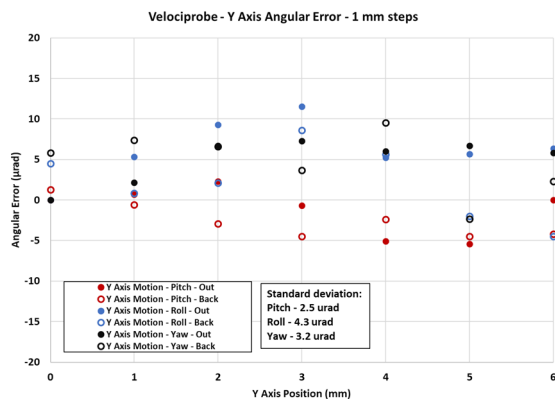


Figure 7: Chart showing angular errors in the pitch (rotZ), roll (rotX), and yaw (rotY) directions, as measured on the Velociprobe.

RECENT EXAMPLES AND NEW DEVELOPMENTS

Recent developments have reduced the volume for a given number of axes by combining multiple degrees of freedom into one block (horizontal motion of top wedge and in-plane rotations, used in many APS-U designs). Engineers at the ALS have improved the angular error performance (Fig. 8). APS engineers recently applied for a patent to realize six degrees of freedom by adding pitch and roll (Fig. 9) [9].

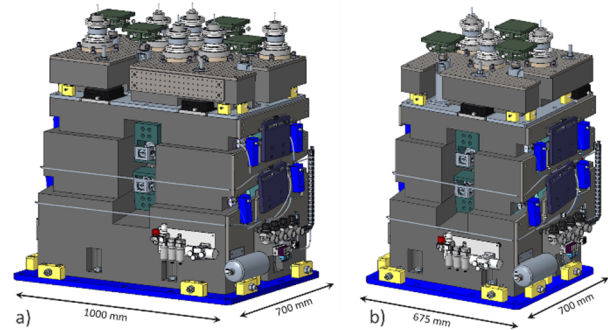


Figure 8: Image showing the a) ALS dual mirror, and b), single mirror granite positioning systems. Each uses commercial off-the-shelf, porous-media air bearings for lateral guiding.

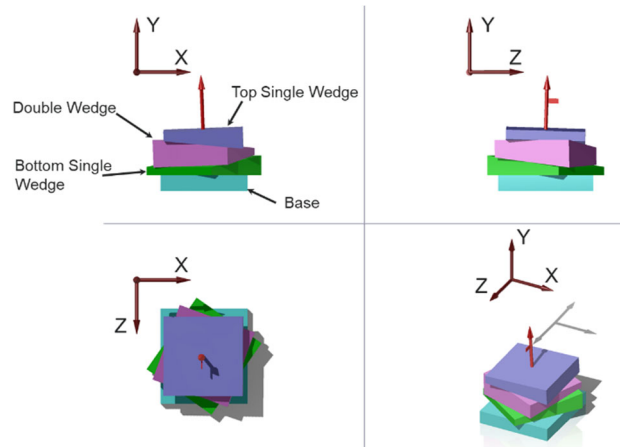


Figure 9: A new design that can provide small pitch and roll rotations through the addition of a orthogonal double width and by rotating the blocks about the Y axis. The motions are coupled, and this arrangement is best used for small rotations of a few tens of mrad.

CONCLUSION

Granite stage systems offer nanometer level vibrations and low angular errors. New developments offer small but useful rotations. They can be a good choice for sensitive instruments and vertical travel ranges of a few tens of mm.

ACKNOWLEDGEMENTS

The authors would like to acknowledge the useful discussions and insights of Dennis Ethen and Derek Hoium of Starrett Tru-Stone.

REFERENCES

- [1] J. Deng *et al.*, “The Velociprobe: An ultrafast hard X-ray nanoprobe for high-resolution ptychographic imaging,” *Rev. Sci. Instrum.* vol. 90, p. 083701, 2019.
 doi:10.1063/1.5103173
- [2] C. Preissner *et al.*, “Method and apparatus for implementing ultra-high stability long-vertical travel stage,” US Patent and Trademark Office 10,393,242, August 27, 2019.
- [3] S. Bean *et al.*, “A New Ultra-Stable Variable Projection Microscope for the APS Upgrade of 32-ID”, presented at the 11th Int. Conf. on Mechanical Engineering Design of Synchrotron Radiation Equipment and Instrumentation (MEDSI2020), Chicago, IL, USA, virtual conference, July 2021, paper TUPC15, this conference.
- [4] R. R. Geraldès *et al.*, “Granite Benches for Sirius X-ray Optical Systems”, in *Proc. 10th Mechanical Engineering Design of Synchrotron Radiation Equipment and Instrumentation Int. Conf. (MEDSI'18)*, Paris, France, Jun. 2018, pp. 361-364.
 doi:10.18429/JACoW-MEDSI2018-THPH12
- [5] Z. Liu *et al.*, “Validation of APS-U Magnet Support Design Analysis and Prediction”, presented at the 11th Int. Conf. on Mechanical Engineering Design of Synchrotron Radiation Equipment and Instrumentation (MEDSI2020), Chicago, IL, USA, virtual conference, July 2021, paper MOPC16, this conference.
- [6] Newway Technical Report 1, <https://www.newwayairbearings.com/technical-report/technical-report-1-orifice-vs-porous-media-air-bearings/>.
- [7] *GGG-P-463C, Amendment 1, Federal Specification Plate, Surface, (Granite)*. National Bureau of Standards Publications, June 1977.
- [8] M. J. Puttock *et al.*, “Elastic Compression of Spheres and Cylinders at Point and Line Contact,” Commonwealth Scientific and Industrial Research Organization, Melbourne, Australia, National Standards Technical Paper No. 25, 1969.
- [9] C. Preissner *et al.*, “Method and apparatus for implementing ultra-high stability stages with combined degrees of freedom for multiple axes of motion,” USPTO Application SN 17/034 September 28, 2020.

A NEW TRAVELING INTERFEROMETRIC SCHEME FOR THE APS UPGRADE OF THE 2-ID BIONANOPROBE*

S. Bean, S. Chen, T. Graber[†], C. Jacobsen, B. Lai, E. Maxey,
T. Mooney, C. Preissner, X. Shi, D. Shu, J. Tan, M. Wojcik

Advanced Photon Source, Argonne National Laboratory, Lemont, IL 60439, USA

[†] Deceased April 29, 2021

Abstract

The Advanced Photon Source (APS) at Argonne National Laboratory (ANL) is being upgraded to a multi-bend achromat (MBA) lattice storage ring which will increase brightness and coherent flux by several orders of magnitude. As part of this upgrade a total of 15 beamlines were selected to be enhanced to take advantage of the new source – these are designated as “Enhanced Beamlines”. Among these is the enhancement to 2-ID, which includes an upgrade and move of the existing Bionanoprobe (BNP) from 9-ID [1]. This instrument will become the second generation Bionanoprobe II (BNP-II) with intent of studying cryogenic samples with sub-10 nm resolution. This upgrade requires a high performing metrology configuration and design to achieve the desired spatial resolution while adapting to the various constraints of the instrument. The cryogenic sample environment and detection constraints offer significant challenges for implementing a metrology scheme. In this paper we report on the new traveling interferometer configuration proposed for BNP-II.

INTRODUCTION

The unique challenge for implementing metrology for BNP-II is the cryogenic sample environment. The desired instrument resolution lends to a design that measures positions as close to the actual cryogenic sample as is feasible. This must be accomplished for a sample that translates in X/Y/Z directions and rotates around a vertical (Y) axis.

Recent developments at Swiss Light Source have resulted robust metrology solutions for rotating samples such as passive anti rotation and tracking interferometer designs [2-4]. These schemes were considered for BNP-II. Implementation would come with a unique set of challenges for BNP-II give the space limitations in the XZ plane, and the desire to measure a reference object which is at cryogenic temperatures.

Our design incorporates a new traveling interferometer concept for the sample as shown in Figure 1. A traveling interferometer platform tracks a cryogenic cylindrical reference in the horizontal plane and is decoupled from the other degrees of freedom (DOF) of the sample stage stack. A set of stationary global interferometers measure

information both from the reference and from the traveling platform.

It is worth note that the desired instrument resolution is pushing the limits on off-the-shelf interferometer hardware. Periodic error is considered for the design but is not discussed further [5].

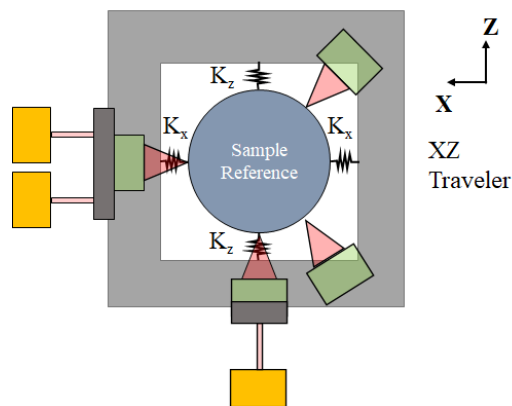


Figure 1: The coupled traveling interferometer concept. The traveling XZ traveler support is coupled to the sample reference on the X and Z degrees of freedom, while decoupled in the other degrees of freedom. Focused traveling interferometers (green) and global stationary interferometers (gold) are depicted.

SCANNING & METROLOGY METHODOLOGY

The following numbered items represent the most critical and complex set of requirements of the metrology strategies for BNP-II:

1. The metrology system must provide position information below 2 nm in order to achieve a 10 nm fluorescence resolution for the instrument.
2. The cryogenic sample will be continuously scanned while the optics are stationary during measurement.
3. The metrology scheme must be able to measure re-positioning of the sample through translations and one main vertical rotation axis.
4. The sample metrology reference optic and the sample should be intimately coupled.
5. The metrology must incorporate relative measurements between the optic and sample positions for both positioning and scanning.
6. The metrology should be non-intrusive to the nearby XZ (horizontal) plane of the sample to allow for signal collection, beam-conditioning optics, and thermal shielding.

* This research used resources of the Advanced Photon Source, a U.S. Department of Energy (DOE) Office of Science User Facility at Argonne National Laboratory and is based on research supported by the U.S. DOE Office of Science-Basic Energy Sciences, under Contract No. DE-AC02-06CH11357.

METROLOGY REFERENCE DESIGN

A cylindrical metrology reference is selected for this configuration as shown in Figure 2. The radial and top surface are to be made to optically acceptable form and surface finish. The resultant metrology surfaces of the reference must be characterized, as they will be needed for position controls corrections.

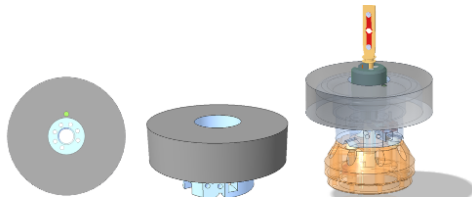


Figure 2: The sample optical reference top and isometric view (left). Sample mount design (right) including from bottom up the warm kinematic interface, cryogenic reference, and sample loading interface.

TRAVELING CONFIGURATION

The proposed sample scanning stack configuration is shown in Figure 3. A vertical fast scanning axis is implemented above the traveler mechanics (TM). All other degrees of freedom are below the TM, including the slow scanning XZ stage.

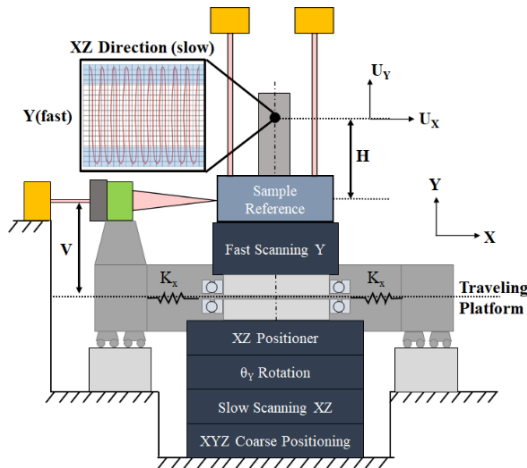


Figure 3: Schematic showing how the configuration of the interferometers, traveling platform (TP), traveling mechanics (TM), and sample stages can be configured in order to have the focused interferometers track the XZ position of the reference while also allowing for uncoupled fast vertical scanning to occur. The fly scan strategy is depicted for the sample. The fast direction is vertical (Y), while the slow direction is in an arbitrary direction in the XZ plane. The traveling platform is supported by an external planar XZ bearing.

BNP-II METROLOGY CONFIGURATION

The proposed metrology configuration (see Figure 4) consists of 16 interferometers situated in a strategic way to measure all the information required to know the relative position of the optic and sample. A summary of what

interferometers are measuring which DOF is shown in Table 1.

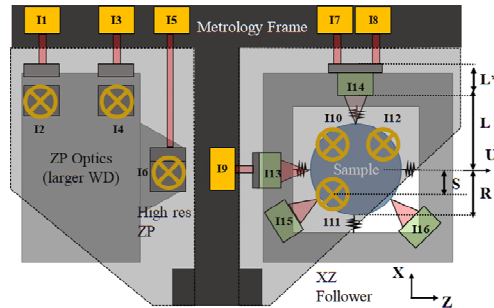


Figure 4: Schematic showing complete metrology configuration for relative sample and optic measurement. Gold indicates nonmoving measurements with respect to the global metrology frame. An “X” indicates the measurement is from above to the respective reference surface. Green indicates a traveling interferometer. The shape of the interferometer beam is either collimated (straight) or focused (angled). Z is the beam direction.

Table 1: Table showing which interferometers are measuring which DOF of the optic and sample.

Measured Degrees of Freedom of Interferometers			
Interferometer/s	Measured (Or Calculated*) Degrees of Freedom	Measurement From	Metrology Head Type
I1 & I3	Coarse Optic X, θ_y	Reference Frame	Collimated
I2 & I4	Coarse Optic Y, θ_x	Reference Frame	Collimated
I5	High Res. Optic X	Reference Frame	Collimated
I6	High Res. Optic Y	Reference Frame	Collimated
I7 & I8	Sample Follower X, θ_y	Reference Frame	Collimated
I9	Sample Follower Z	Reference Frame	Collimated
I10 & I11 & I12	Sample Y, θ_x , θ_z	Reference Frame	Collimated
I13	Sample Z	Sample Follower	Focused
I14	Sample X	Sample Follower	Focused
I15 & I16*	N/A, For Form Characterization	Sample Follower	Focused

REFERENCE ERROR ANALYSIS

Some geometric first order errors are considered between the reference optic and the interferometers. This includes the traveler X and Z interferometers (I13, I14), along with the global Y interferometers (I10, I11, I12). Table 2 is a summary of the parasitic error motion of the reference, the corresponding interferometer change and actual sample motion.

Table 2: Table showing the optic errors and the corresponding geometric changes in metrology and sample position. A “/” indicates the respective equations for the x or z direction.

Optic Error Motion	Change in Traveling Interferometer (T), Global Interferometer (G)	Actual Sample Change (U)
$\delta x/z$	$T_{x/z} = \delta x/z$ $T_{z/x} = R - \sqrt{R^2 - \delta x/z^2}$	$U_{x/z} = \delta x/z$
$\delta \theta_{x/z}$	$T_{z/x} = R \left(1 - \frac{1}{\cos(\delta \theta_{x/z})} \right) \approx 0$ $G_{y1} = (S)\delta \theta_{x/z}$ $G_{y2} = -(S)\delta \theta_{x/z}$ $G_{y3} = -(S)\delta \theta_{x/z}$	$U_{z/x} = (H)\delta \theta_{x/z}$ $U_y = (H) \frac{\delta \theta_{x/z}^2}{4}$ $U_{\theta_{x/z}} = \delta \theta_{x/z}$
$\delta \theta_y$	Blind	$U_{\theta_y} = \delta \theta_y$

The following conclusions are made:

1. The X & Z interferometers don't discern actual sample displacements U_X and U_Z caused by angular errors of the optic.
2. U_X and U_Z changes caused by angular errors must be calculated; they are not measured directly.
3. The X and Z measurements are coupled.

The first two conclusions are a result of not measuring the reference at the work point, which some designed metrology schemes have taken care to implement [6]. The last conclusion is discussed next.

XZ COUPLED EQUATIONS

The measurement coupling of the X and Z reference DOF are depicted in Figure 5. When calculating the true δx and δz change of the optic with respect to obtained signals, the following relationships can be derived:

$$\begin{aligned} \text{INT1} &= \delta x + R - \sqrt{R^2 - \delta z^2} \\ \text{INT2} &= \delta z + R - \sqrt{R^2 - \delta x^2} \end{aligned}$$

This system of equations can be solved iteratively. To determine the total change of the actual sample position in the XZ plane, the result is added to any additional XZ changes from the global Y interferometers. However, if the radius term R is much larger than the errors, these interferometers then give a direct measurement of the reference X and Z.

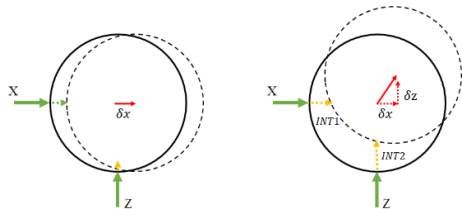


Figure 5: Schematic showing X error of the fast-scanning optic (left), and a combined error of the optic (right).

TRAVELER ERROR ANALYSIS

As was done for the reference, a geometric error study was done for the traveler and is summarized in Table 3.

Table 3. Table showing the traveler errors and the corresponding geometric changes in metrology and sample position. A “/” indicates the respective direction equation and terms.

Traveler Error Motion	Change in Traveling Interferometer (T), Global Interferometer (G)	Actual Sample Change (U)
$\delta x/z$	$\begin{aligned} T_{x/z} &= \delta x/z \\ T_{z/x} &= R - \sqrt{R^2 - \delta x/z^2} \\ G_{x/z} &= -\delta x/z \end{aligned}$	None
$\delta \theta_{x/z}$	$\begin{aligned} T_{z/x} &= (L - V \delta \theta_{x/z} - R) \left(\sqrt{\delta \theta_{x/z}^2 + 1} - 1 \right) \\ T_{x/z} &= R - \sqrt{R^2 - V \delta \theta_{x/z}^2} \\ G_{z/x} &= V \delta \theta_{x/z} - \delta \theta_{x/z}^2 (L + L') \end{aligned}$	None
$\delta \theta_y$	$G_{x1} = -G_{x2}$	None

The following conclusions are made:

1. The X & Z traveler interferometers see similar coupling as if the reference has moved, however now

there is no sample motion. This is to be compensated by the global interferometer change.

2. The sum of the global and traveler interferometer response from angular traveler changes is not zero. This cannot be compensated by measurements unless more opposing interferometers are utilized.

Based on the error analysis of Table 3, and given a set of characteristic lengths for a feasible design, 50 μrad change of the traveler leads to about 0.1 nm error in a measurement. As the traveler rotates, the global and traveling interferometers respond in an opposite manner, but do not completely cancel, thus leading to this small sensitivity. This amount of error and sensitivity should be accounted for in the error budget when guiding mechanics for the follower are being chosen.

TRAVELER RESONANCE CONSIDERATIONS

Assuming the traveler planar coupling stiffnesses is much lower than typical stage bearings, the twice repeated eigenvalue for two directions of Figure 1 is given as

$$\omega = \sqrt{2K/m}, \text{ where } K = K_X = K_Z$$

where m is the mass of the traveler platform. The traveler mass must be chosen appropriately with respect to the stiffness coupling in the XZ plane versus the desired scanning frequency of the instrument to avoid resonance.

PROPOSED DESIGN CONCEPT

The design concept for the traveling interferometer scheme is shown in Figure 6. The central stack as seen in the exploded view is then supported by the other DOF below as shown in Figure 3.

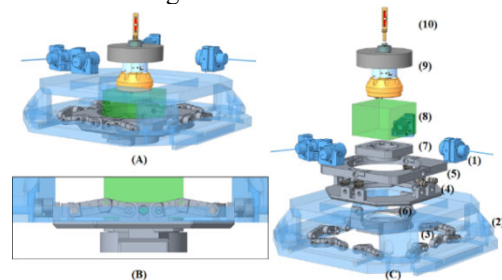


Figure 6: A schematic showing the design concept for the traveling interferometer. A- overview, B- front view of vertical compliant link interface, C- exploded view showing 1- traveling interferometer, 2- traveling frame, 3- vertical compliant links, 4/5/6- tip tilt mechanism with buried radial bearing set, 7- radial bearing preload and stage interface plate, 8- scanning Y stage space claim, 9- sample reference, 10- sample mount.

CONCLUSIONS

A new metrology configuration is proposed for BNP-II to measure a cryogenic reference. The first analysis indicates there is potential to achieve the performance goals of this instrument. Important design considerations were discussed. The design and control strategies will be further refined and completed.

REFERENCES

- [1] S. Chen *et al.*, “The Bionanoprobe: Hard X-ray fluorescence nanoprobe with cryogenic capabilities,” *J. Synchrotron Radiat.*, vol. 21, pp. 66-75, 2014.
10.1107/S1600577513029676
- [2] M. Holler, J. Raabe., “Error motion compensating tracking interferometer for the position measurement of objects with rotational degree of freedom,” *Opt. Eng.*, vol. 54, no. 5, p. 054101, May 2015.
<https://doi.org/10.1117/1.OE.54.5.054101>
- [3] M. Holler, M. Odstrcil, M. Guizar-Sicairos *et al.*, “Three-dimensional imaging of integrated circuits with macro- to nanoscale zoom,” *Nat. Electron.* vol. 2, pp. 464–470, 2019.
<https://doi.org/10.1038/s41928-019-0309-z>
- [4] M. Holler, J. Raabe, A. Diaz, M. Guizar-Sicairos, C. Quitmann, A. Menzel, and O. Bunk, “An instrument for 3D x-ray nano-imaging,” *Rev. Sci. Instrum.*, vol. 83, p. 073703, 2012, <https://doi.org/10.1063/1.4737624>
- [5] K. Turner, F. Quacquarelli, P.F. Braun, C. Savio, and K. Karrai, “Fiber-based distance sensing interferometry,” *Appl. Opt.*, vol. 54, pp. 3051-3063, 2015.
10.1364/AO.54.003051
- [6] F. Villar and L. Ducotté, “L8–Introduction to Precision Positioning Systems,” presented at ESRF MEDSI School 2, Grenoble, France, 2019, unpublished.

ALIGNMENT STRATEGIES AND FIRST RESULTS ON SIRIUS BEAMLINES

G. Rovigatti[†], H. Geraissate, R. Leão, CNPEM, Campinas, Brazil

Abstract

The new Brazilian Synchrotron Light Source had its first friendly users late in 2019. During 2020, the first experimental stations were aligned and had the first beam successfully at the sample. The reference network of points used for the storage ring alignment was connected to an external network located in the experimental hall. Following this step, it was possible to extend these references to the hutches environment, where the beamlines components are installed. During the alignment of the first beamlines, a sequence of common tasks was performed, from the bluelining of the hutches footprints, to the components fine alignment. The position and orientation deviation of the main components will be presented for the Manacá, Catteretê, Ema, and Carnaúba beamlines. Two specific measurement strategies used for aligning special components will also be presented: (1) an indirect fiducialization procedure developed for most of the mirrors and their mechanisms using a mix of coordinate measuring machine and articulated measuring arm measurements, and (2) a multi-station setup arranged for the alignment of a 30 meters long detector carriage, using a mix of laser tracker, physical artifacts, and a rotary laser alignment system used as a straightness reference.

INTRODUCTION

Sirius, the 4th generation Brazilian synchrotron light source is designed to accommodate 38 beamlines. The initial phase comprises 14 beamlines to be delivered until 2022 [1]. By the end of 2020, Manacá, Catteretê, Ema and Carnaúba concluded their installation and alignment phase and started their commissioning with friendly users.

All beamlines of Sirius have many critical requirements to work properly, such as stability and temperature. Alignment is one of these requirements, and its importance begins at the installation phase, guiding the positioning of big components (e.g. hutches and girders); continues at the commissioning, supporting the scientists in making the beam reach the sample position and remains essential over time, when installing new components, verifying deformations, etc.

This work describes how the beamlines alignment was managed and details particular cases where metrological methodologies were developed.

REFERENCE NETWORK

Alignment is a critical requirement to the well-being of a synchrotron accelerator. To reach the designed tolerances, not only a reliable equipment is necessary but also a metrological reference network needs to be created.

The main reference was created inside the radiation shielding (RS) of the storage ring (SR). Approximately 1220 SMR nests were distributed on the floor, walls and ceiling. Outside the tunnel, a secondary network was created for the Experimental Hall (EH). This one is referenced to the primary network and has approximately 730 points, at walls, floor, and columns. Also, tertiary networks were created for the hutches and long beamlines.

The strategy used to create the networks was a classical laser tracker (LT) survey, with several stations along the volume measuring the points of the network with redundancy. The stations followed a “zig zag” pattern and different heights were used for the instruments [2]. All LTs used were from the Leica AT400 family. Also, levelling campaigns were done inside the accelerators tunnel, at the EH and long beamlines. The equipment used was the optical level Leica NA2. Radius measurements were done from the central pillar of the Sirius building to inside the RS, to bring more robustness to the network [3].

A normal connection between networks would be done by a simple overlapping of common points between the environments. But, as the RS is fully enclosed, there is no way to do this between the Sirius primary and secondary networks. The only free lines of sight from inside to outside the RS are holes with $\varnothing 150$ mm and 1 m length. So, the link was done using a reciprocal connection technique, using two LTs measuring each other and fitting spheres that constructs the rotation center of the instrument. With mathematical manipulations of the centers created, the located LT from inside the RS will reference the second instrument at the EH [3-5].

After each network is calculated, they are adjusted in space by means of least square transformations. The SR network is adjusted with respect to the last epoch and become the reference for the subsequent ones. The Hall network is then adjusted to the SR, preserving its level and using the common points for the other degrees of freedom; and the tertiary networks are adjusted to the Hall's following the same strategy, except for the hutches networks, which inherits the same level as their parent network.

Through the adjustment steps, the network uncertainty propagation is done with a Python based script, developed in-house, using Monte Carlo simulations of the possible transformation matrix between two networks, which considers the individual uncertainty value for each point on the networks [6]. It creates point-clouds for each network, calculates the different transformations possibilities and apply these transformations to the network being adjusted. As expected, the uncertainty results are influenced by which coordinate system is being used. A study was made to evaluate how it propagates from a source point within the

[†] gustavo.rovigatti@cnpem.br

accelerator (an insertion device in this case) to the end of the longest beamline (Carnaúba), as shown in Fig. 1.

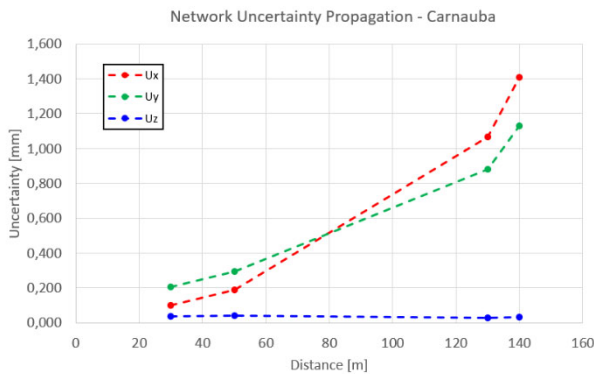


Figure 1: Uncertainty propagation for the Carnaúba beamline.

It is important to mention that these values are for the points in the network with respect to the beamline source, while the uncertainty for relative alignment of adjacent components are much smaller (in the order of a few dozen micrometers).

BEAMLINE INSTALLATION

From the point of view of metrology and alignment, all the beamlines follow a same sequence of tasks, beginning with data preparation and compatibilization of CAD designs with the geometric entities within the software SpatialAnalyzer™ (SA) from New River Kinematics.

The second step consists of blue lining the perimeter of the hutches and making as-built measurements of slabs and RS walls (interfaces of hutches and equipment with the building). This is necessary because all the parts of hutches are designed and manufactured to avoid gaps, according to as-built data. For the components, a study of shims is done for each pedestal of the beamline. Then, all drilling marks for bolts are done.

The next task is related to externalize references of the components, a procedure known as fiducialization. There are a lot of critical pieces in a component, and sometimes its main aspects are inaccessible for the LT because there is no position to put the station and have a good line of sight. Or, for example, that component cannot stay open during its positioning, because of vacuum and cleanliness demands. The solution to this problem is to relate accessible parts of the component to your functional characteristics, because when installing inside the hutches, almost any position of station will be able to see the external references and align the component.

It may be very simple for some components (collimators and shutters), but also challenging for others (mirrors, monochromators, slits etc.). Almost all of them needs to be fiducialized before their installation.

Following the fiducialization phase, the component must be installed and pre-positioned inside the hutch, which is done together with the installation team and beamline staff. Using a LT located at the reference network of that beamline, a pre-alignment of the component is done, achieving

tolerances that will allow the vacuum assembly and commissioning, which may take days depending on the component. Finally, the components final alignment must be done also using a LT, achieving the designed tolerances.

CASE STUDIES

Mirrors Indirect Fiducialization

A novel technique of indirect fiducialization was developed for the Sirius mirrors. The method consists in matching geometries constructed from measured points in two acquisition setups. Firstly, the mirror substrate and optical axis/face are measured in a high precision CMM. Secondly, the mechanics that support the mirror is assembled inside its vacuum chamber and measured with an Articulated Measuring Arm. In this process, the assembly layouts that define the mirror position on its mechanism (Fig. 2) are measured and used to define the same geometries measured on the substrate. Four fiducial references outside the vacuum chamber are also measured. Finally, the coincident geometries measured on the substrate and on the mechanics are matched using least square transformations in SA, resulting in the mirror functional axis represented by the four external fiducial points.

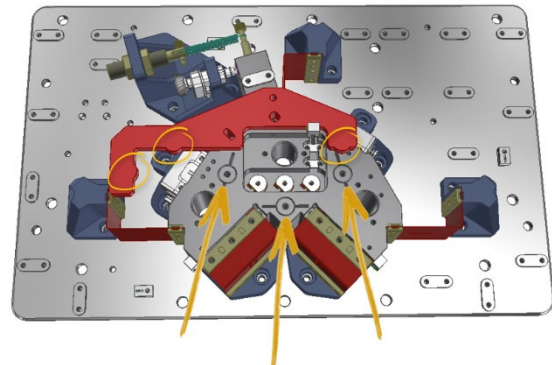


Figure 2: Mirror assembly layout. The yellow circles and arrows show the contact points between mirror and mechanism.

The Articulated measuring arm used (7 axis ROMER by Hexagon) have a basic volumetric accuracy of approximately $\pm 35 \mu m$. But it is an equipment that also depends on other factors, such as operator experience and relative position between the Arm and the measured part. To quantify the task-specific uncertainty related to each different mirror system, the mechanism measurement process was repeated five times. The repeatability was then evaluated, and the average coordinates of the fiducial references are used during the mirror fine alignment in the beamline. The estimated uncertainty for the fiducialization of a mirror for the Cateretê beamline is shown as an example in Table 1.

Table 1: Cateretê M1 Fiducialization Repeatability in mm and mrad.

Repeatability				
	Tx	Ty	Tz	Mag
StdDev	0.026	0.038	0.016	0.049
	Rx	Ry	Rz	
StdDev	0.1328	0.3189	0.2869	

Detectors Tunnel for the CDI Beamline

Cateretê beamline is one of the longest of Sirius. It is focused on using the coherent X-ray scattering and diffraction technique [7]. Its detector is installed over a carriage that moves longitudinally over a 30 meters long rail, inside a vacuum chamber.

This rail was installed and positioned by the AVS team (manufacturer) in partnership with the Sirius Metrology team. After completing the installation by the manufacturer, an acceptance test was done, aiming to validate the straightness and trajectory orientation of the carriage. The specification was to keep the vertical and horizontal straightness within a diameter of 1 mm along the whole longitudinal movement, requisite called Disc of Confusion (DoC).

Two setups (Fig. 3) involving LT were planned to be realized in this experiment, including a reference measurement using a laser alignment system (L-743 Ultra-Precision Triple Scan) from the manufacturer Hamar Laser Instruments, which has a good accuracy of 0.0013 mm/m with an operational range of 30.5 m in radius.

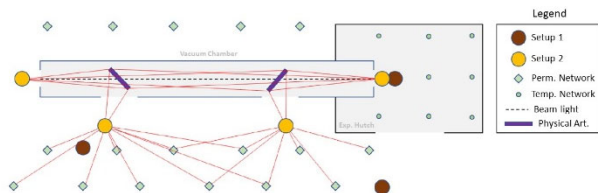


Figure 3: Setup schematics.

The first setup was a classical approach. It consisted in using two LT stations for measuring the permanent network and creating a temporary one. Then, a third station was located in the created temporary network inside the experimental hutch. This station measured the DoC, acquiring points every 1 m.

The second setup proposed a novel configuration. Two LT and two physical artifacts (PA) were used [8]. The LTs were positioned at the tunnel ends and doing a collaborative measurement of the points. The LTs location was made in two steps. First, two stations measured the permanent network and the PAs positioned inside the tunnel. Then, the second step was the location of the stations positioned at the tunnel ends, using the PAs previously located as a reference. Finally, the DoC was measured by both stations, acquiring points every 1 m.

The data analysis confirms that the combination of the measurements of LTs could decrease the measurement

uncertainty and maintain it for the whole trajectory, which would normally increase with distance.

Also, using the PAs inside the measured volume increased the reliability and allowed a good location and orientation of the instruments. The comparison between the three DoCs (metric combining uncertainty, orientation, and trajectory) can be seen at Fig. 4.

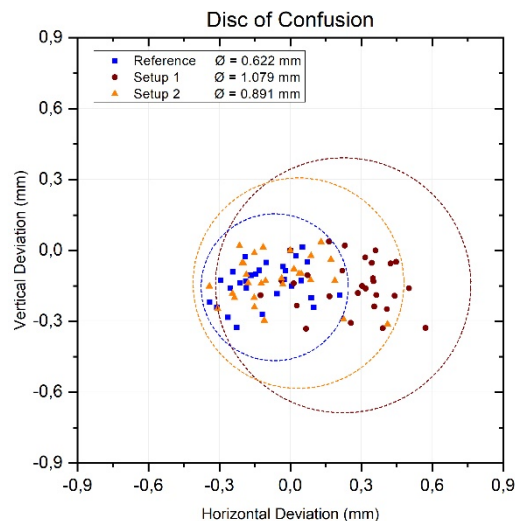


Figure 4: Disc of confusion of the acceptance test. It represents the minimum circumscribed circle for each data set and considers the setup estimated uncertainty.

ALIGNMENT RESULTS

Some of the Sirius beamlines entered commissioning phase at late 2019. The installation and alignment process were completed, and the first tests could be started.

Table 2 shows the compiled final alignment results for components of the 4 beamlines described in the introduction section. An average of the main coincident components results was done, since each one has its own tolerance.

Table 2: Alignment results of the 4 beamlines of the study in mm and mrad.

Comp.	X	Y	Z	Rx	Ry	Rz
Mirrors	-0.01	0.01	1.11	0.04	0.03	0.02
Collimators	0.04	-0.06	-0.19	0.23	-0.11	0.28
DVFs	0.03	-0.08	2.16	1.04	2.81	0.06
Shutters	0.05	-0.06	-0.13	0.05	0.09	0.13

CONCLUSIONS

Besides the alignment results, the feedback from the operators of the beamlines is good, showing that the alignment process done was successful. This shows that the strategies described along this paper were adequate and may continue to be used for the next beamlines.

REFERENCES

- [1] R. Picoreti, H. Westfahl, “Sirius facility update”, *Synchrotron Radiation News*, vol. 34, no. 1-3, pp. 12-13, 2021. doi:10.1080/08940886.2021.1902713
- [2] R. J. Leao, C. R. Baldo, M. L. C. C. Reis, and J. L. A. Trabanco, “Engineering survey planning for the alignment of a particle accelerator: part ii. design of a reference network and measurement strategy”, *Meas. Sci. Technol.*, vol. 29, no. 3, p. 034007, 2018. doi:10.1088/1361-6501/aa9dc3
- [3] H. Geraissate, G. Rovigatti, and R. J. Leão, “Establishing a metrological reference network of points for the alignment of Sirius”, presented at IPAC’21, Campinas, Brazil, May 2021, paper TUPAB310, to be published.
- [4] Y. Gao *et al.*, “Laser tracker orientation in confined space using on-board targets”, *Meas. Sci. Technol.*, vol. 27, no 8, p. 085010, 2016. doi:10.1088/0957-0233/27/8/085010
- [5] G. Rovigatti, “Validação de conexão recíproca entre Laser Trackers usando a técnica de calotas esféricas”, Undergraduate thesis, Centro Universitário Salesiano de São Paulo, Campinas, Brazil, 2020.
- [6] C. E. Papadopoulos, and H. Yeung, “Uncertainty estimation and Monte Carlo simulation method”, *Flow Meas. Instrum.*, vol. 12, no. 4, pp. 291–298, 2001. doi:10.1016/S0955-5986(01)00015-2
- [7] H. Westfahl *et al.*, “X-ray microscopy at Sirius, the new Brazilian synchrotron light source”, *Microsc. Microanal.*, vol. 24, no S2, pp. 176–179, 2018. doi:10.1017/S1431927618013235
- [8] D. L. Passuelo, H. Geraissate, G. Rovigatti, M. C. Oliveira, R. J. Leão, “Preliminary evaluation of physical artifacts to perform laser tracker relocations in confined environments”, in *Proc. Metrologia 2019*, Florianópolis, Brazil, Nov. 2019, ISBN 978-65-990471-0-7.

THERMAL CONTACT CONDUCTANCE IN A TYPICAL SILICON CRYSTAL ASSEMBLY FOUND IN PARTICLE ACCELERATORS

P. Navarro, Diamond Light Source Ltd., Didcot, England

Abstract

Every mirror at Diamond Light Source (the UK's Particle Accelerator) has been installed with the premise of clamping the cooling copper manifolds as lightly as possible to minimize distortion. The problem with this approach is that the Thermal Contact Conductance (TCC) depends on the applied pressure among other factors. The assembly is usually a symmetric stack of Copper - Indium Foil - Silicon Crystal - Indium Foil - Copper. Variables that interest the most are those that are easily adjustable in the set-up assembly (number of clamps, pressure applied and cooling water flow rate) PT100 temperature sensors have been used along the surface of the crystal and along the surface of the copper manifolds. Custom PCB units have been created for this project to act as a mean of collecting data and Matlab has been used to plot the temperature measurements vs. time. Another challenge is the creation of an accurate model in Ansys that matches reality up to a good compromise where the data that is being recorded from the sensors matches Ansys results within reason.

INTRODUCTION

The set-up (Fig. 1) of a typical Silicon Crystal assembly is comprised of a symmetric stack of Copper - Indium Foil - Silicon Crystal - Indium Foil - Copper.

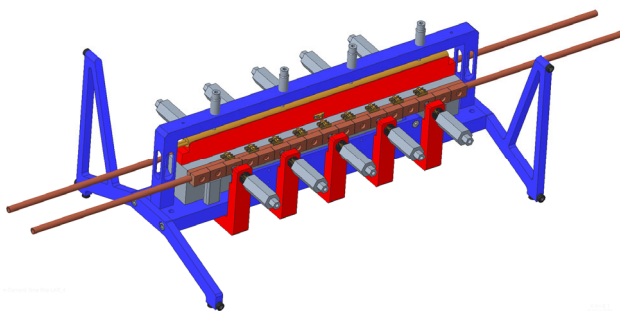


Figure 1: 3D model for the experimental assembly.

A cartridge heater embedded in an aluminium block and located at the top surface of the crystal mimics the input power of the beam that bounces off the silicon mirrors in a particle accelerator. An industrial chiller is used for cooling down the water flowing through the copper manifolds. Temperature is read by PT100 sensors along the surface of the Crystal and at the other side of the interface (along the surface of the copper manifolds) so the drop in temperature across the interface is known. The PT100 sensors have been glued on both surfaces. Custom adjustable spring clamps with a fine thread (0.75mm pitch) along the crystal control the amount of force applied to the interface. Strips of Indium Foil (100µm thick) have been used between the silicon crystal and copper manifolds to cope with surface's irregularities like roughness, waviness and flatness. Spring

pushers at the top, screwed into an arch and exerting a force on to the heater to make sure that a good contact among the parts is achieved. A thin layer of oil has been added at the interface between the aluminium block and the silicon crystal to improve the TCC at that interface. The silicon crystal is sat on three sprung stainless-steel balls at the bottom and up against two more at the back. A 4mm insulating layer of Calcium-Magnesium Silicate covers the cartridge heater and aluminium block make sure that most of the power goes into the crystal (Fig. 2).

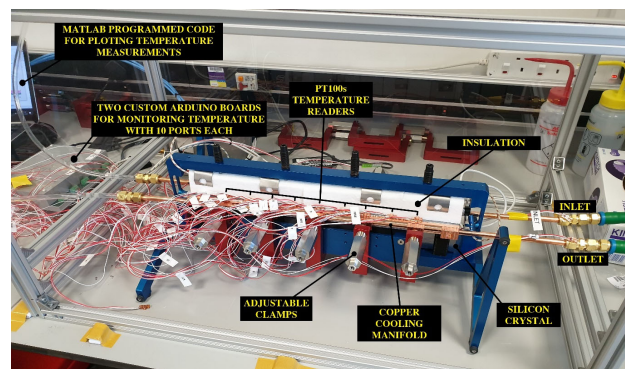


Figure 2: Experimental assembly set-up.

The TCC between two components defines how much heat energy flows through the interface per unit of area and unit of time. The bigger the TCC, the better thermal contact among the parts and thus, more heat flows through the interface. At the microscopic level, only a few discrete points are actually in contact [1]. The TCC depends on many factors [2] (Fig. 3).

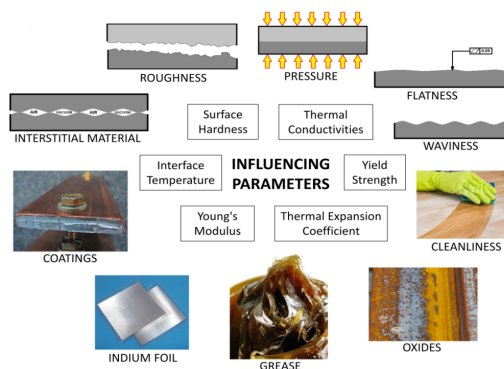


Figure 3: Variables of thermal contact conductance.

ANALYSIS

The following studies have been performed in this project:

- Comparison between a perfect TCC vs actual value (Fig. 4 and Fig. 5).
- Temperature comparison using different Power Inputs (100W, 150W & 200W).

Content from this work may be used under the terms of the CC BY 3.0 licence (© 2021). Any distribution of this work must maintain attribution to the author(s), title of the work, publisher, and DOI

- Temperature comparison using different fluids (Fig. 6) at the interface between the cartridge heater and the aluminium block and between the latter and the silicon crystal (Oil, Thermal Paste and Bear Surfaces).
- Effect of pump speed (Fig. 7) on the temperatures (Pump speed 3[2l/min] and 5[20l/min]).
- Measurement of the temperature Drop across 7mm of the top surface of the silicon crystal.
- Temperature measurement at the front surface of the silicon crystal near the copper manifold.
- Temperature measurement along the length of the Cartridge Heater.
- Effect of the insulation with different Input Power (100W, 150W & 200W).
- Effect of clamping pressure (Fig. 8) on the TCC (45, 60, 75, 90N).
- Temperature comparison between Ansys and measurements (Fig. 9).
- Analysis of the Thermal Contact Conductance for different clamping forces and input powers (Fig. 10).
- Calculation of power loss by convection and radiation in every case.

An ideal scenario is checked for comparison where all the contacts are set to Program Controlled (Perfect TCC). This is very unrealistic but interesting nevertheless as it highlights the importance of adding the thermal contact conductance in the simulations in order to get accurate results. In addition, Heat Transfer Coefficients (HTC) for most surfaces have been manually calculated using the appropriate correlations and fed in to Ansys.

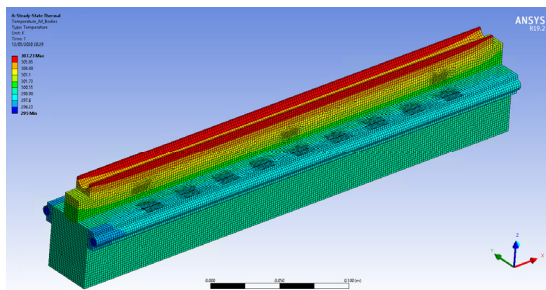


Figure 4: Temperature distribution with perfect TCC.

As we can see the temperature distribution is not realistic as the maximum temperature (307K) is way below that of the PT100s sensor readings (358.5K) On the other hand, by using a TCC at the interfaces, the results are very close to reality.

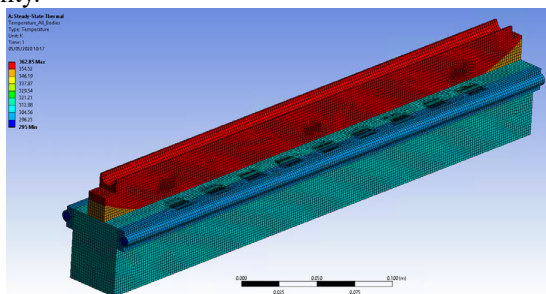


Figure 5: Temperature distribution with actual TCC.

To find out the Thermal Contact Conductance in Ansys, a Response Surface Optimization is used to create iteration analyses based on the temperature measurements from the actual experiment test. To create this iteration analysis the TCC needs to be set as a parameter. Ansys Mechanical doesn't have an automatic way to make the TCC a parameter but to get around this problem an APDL Command (Ansys Parametric Design Language) can be used [3].

The following charts show some of the results from the measurements.

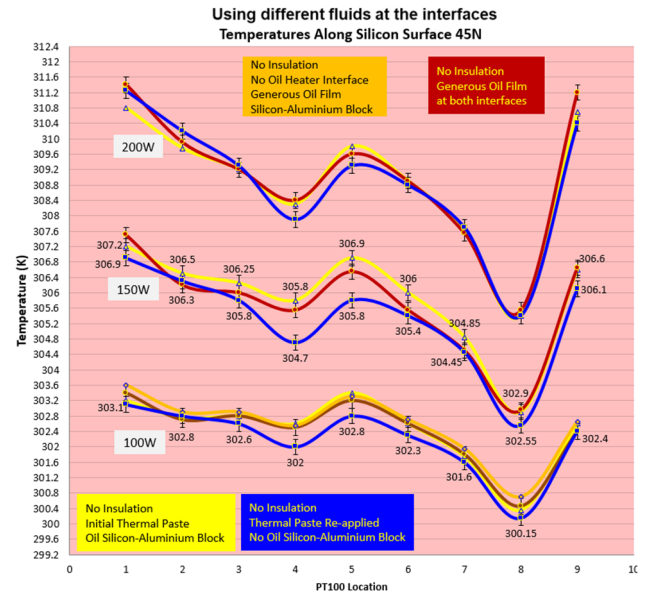


Figure 6: Temperature along the Si top surface using different fluids at the interfaces.

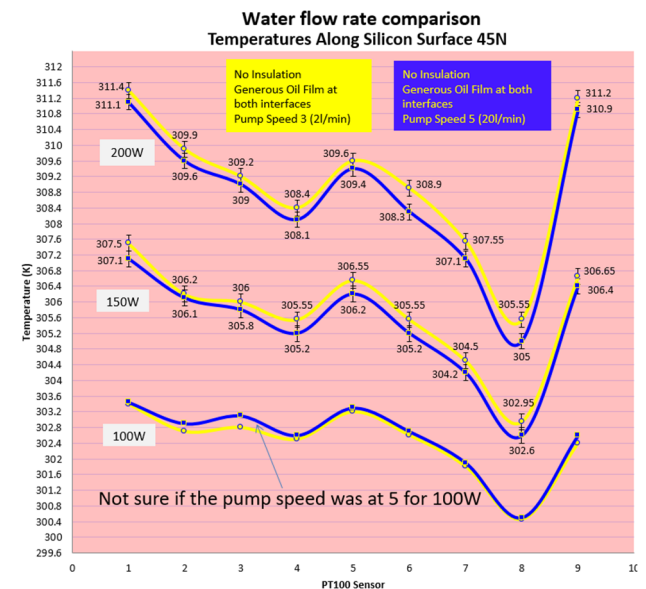


Figure 7: Temperature along the Si top surface using different cooling water flow rates.

All data has been taken using 3 different input powers (100W, 150 and 200W) as can be noted in the charts.

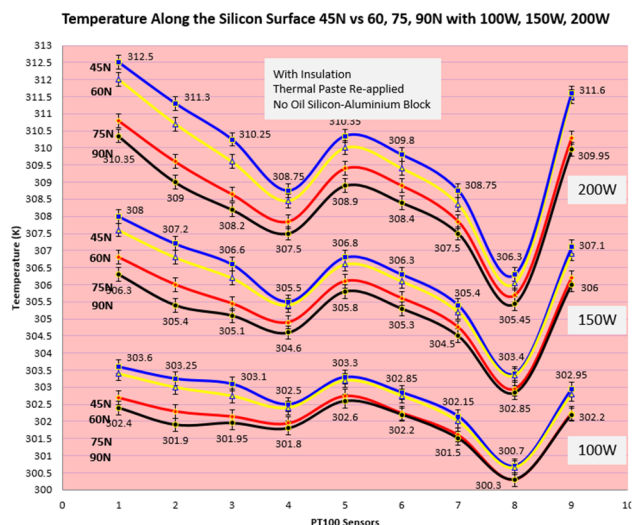


Figure 8: Temperature along the Si top surface using different clamping forces for the copper manifolds.

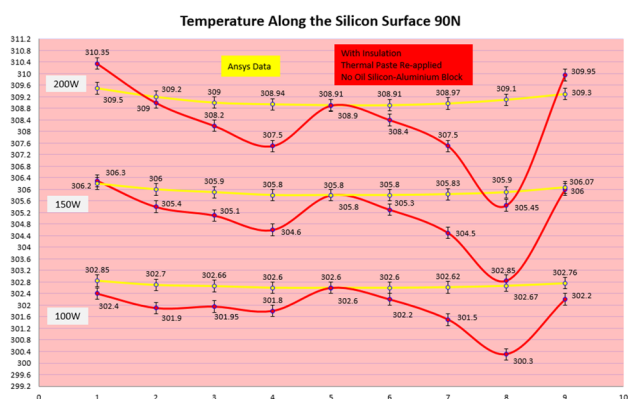


Figure 9: Temperature along the Si top surface compared with Ansys results.

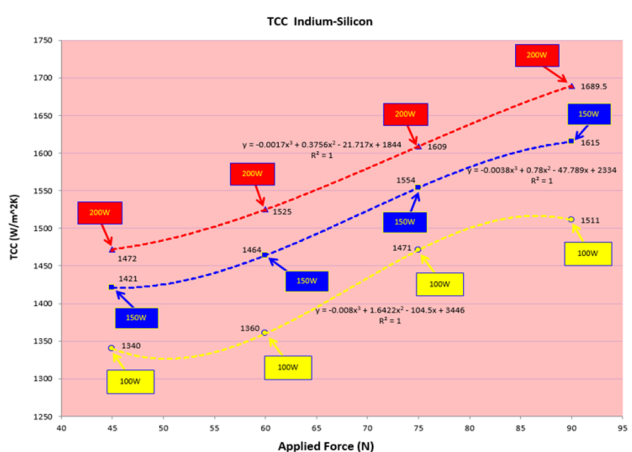


Figure 10: Thermal Contact Conductance vs applied Force.

CONCLUSION

Finding the Thermal Contact Conductance has proven to be challenging as there are many influencing parameters that affect this coefficient. Furthermore, real experiments show that reality is far from the ideal world of computer simulation despite of creating an FEA as close to reality as

possible. Nevertheless, it has been proven that calculating convection and radiation losses was worthy as they play a role in the temperatures and thus on the accuracy of the TCC. In addition, the Ansys simulation calculates the TCC assuming that the clamping force among the parts is evenly distributed over the mating area which has been proven not to be the case in this assembly due to the distortion of the copper manifolds. This highlights the importance of challenging the results regardless of whether we agree or not with them at a first glance and do not blindly trust the simulation.

Vacuum brazing of the copper cooling manifolds play a big role in the flatness of the mating face with the Indium Foil that is up against the Silicon Crystal. This is a typical process in many assemblies that are used under high vacuums environments and it completely distorts the copper blocks. Therefore, it is recommended to get the parts machined afterwards to make sure that distortion is minimized. This may explain the odd behaviour of sensor number 8 as the copper may be distorted in several planes which could produce a very good TCC at discrete locations.

The increase in clamping pressure shows an improvement in the TCC about 13.5% in all cases when comparing the extremes (from 45N to 90N) as well as a reduction of the overall temperatures (up to 2 degrees in some cases).

The increase in water cooling flow rate (pump speed 3[2l/min] to 5[20l/min]) shows a drop in temperature along the Silicon crystal top face up to 0.6 degrees in some cases but with an average of 0.3-0.4 in most readings. Which offers the possibility of reducing the pump speed to get the benefits of low vibration and sharper images without being too detrimental on the Silicon bulk temperature.

The interstitial fluid between the cartridge heater and the Aluminium Block and between the Aluminium Block and the Silicon Crystal doesn't seem to play a big role in the temperatures of the Silicon Crystal as the maximum change is about 1.1 degrees in some locations but with an average of 0.5 degrees in most cases.

The insulation of the cartridge heater and the aluminium block show an average change in temperature up to 1.2 degrees for the 200W analyses whereas for 150W the change is about 1 degree and only about 0.5 degrees for analyses with lower input power like 100W. Therefore, depending on the input power the losses due to convection may be neglected.

Ansys Response Surface Optimization (RSO) has proven to be a great tool for finding the TCC when comparing hundreds of scenarios automatically and allows the user to easily check the influence of the parameters by using the sensitivity analysis tool in the RSO. To lastly iterate accordingly after the best candidates have been found to get the most accurate values.

In addition, a number of hand calculations have been performed to compare them to the Ansys results which show a good agreement among. Furthermore, the energy balance check has been carried out in every analysis as a sanity check.

REFERENCES

- [1] A. Bejan, A.D. Kraus, *Heat Transfer Handbook, Volume 1*, John Wiley & Sons, 2003, p. 1479,
https://books.google.com/books?hl=en&lr=&id=d4cgNG_IUq8C&pgis=1
- [2] D. Gilmore, *Spacecraft Thermal Control Handbook. Volume 1, Fundamental Technologies*, Aerospace Press, 2002,
<http://app.knovel.com/hot-link/toc/id:kpSTCHVFT2/spacecraft-thermal-control>
- [3] Making Thermal Contact Conductance a Parameter in ANSYS Mechanical 18.0 and Earlier with an APDL Command Object,
<https://www.padtinc.com/blog/ansys-mechanical-contact-conductance-apdl/>

HEAT LOAD SIMULATION OF OPTIC MATERIALS AT EUROPEAN XFEL

F. Yang*, D. La Civita†, M. Vannoni, H. Sinn
European XFEL GmbH, Schenefeld, Germany

Abstract

In the beam transport system at European XFEL, the optic components which have direct contact with the beam, e. g. mirror, absorber and beam shutter, etc., could get up to 10kW heat load on a sub-mm spot in 0.6 ms. Therefore, the thermo-mechanical performance of these optic components is playing an important role in the safety operation of the facility, restricting the maximum allowed beam power delivered to each experiment station. In this contribution, using finite element simulation tools, a parametric study about coupled thermo-mechanical behavior of some general used materials, e. g. CVD diamond and B₄C. is presented. Based on the design of several devices which are already in operation at European XFEL [1], a generalized model for setting up the damage threshold of these materials is established, with respect to the corresponding beam parameters. These simulation results can be referred as design and operation benchmark for the optic elements in the beamlines.

INTRODUCTION

Heat load simulation has been a main subject during the design and operation phases for the beamline instruments [2]. In this contribution, only the components that have the function of power absorbing are briefly presented, the heat load on the reflecting elements like mirrors have been discussed in detail in other publications, e.g. [3,4]. Considering the X-Ray laser beam as equivalent heat load, the numerical model to simulate the interaction of the beam with matters using the numerical tools (including FEM and FVM codes based on continuum mechanics formulations) could be complex. In Fig. 1, some of the multiphysical phenomena involved in the simulation models are listed. The corresponding numerical methods, e.g. the level set, elastoplastic model [5] and deformed geometry or moving mesh are required for the multiphysics simulations, to study the damage process after the damage threshold are reached.

But to set up a damage threshold in the scope of engineering design, the multiphysics model is not essential. A standard patch test model will be presented in the following sections.

GENERALIZED MODELS FOR SETTING UP DAMAGE THRESHOLD

According to the material tests for the current used optic materials at European XFEL, e.g. beam stop and upgraded frontends (see Fig. 2 and 3), CVD diamond and B₄C

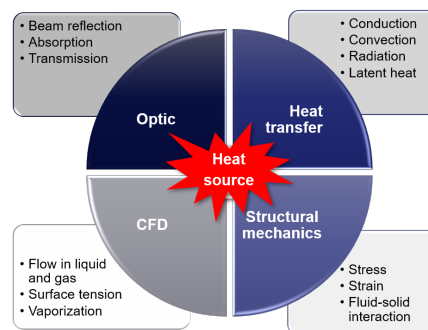


Figure 1: Physical phenomena involved.

are chosen with priority as optic components to absorb the beam power. A generalized simulation model is defined in Fig. 4. Only a quarter of the model is simulated due to symmetry of the boundary conditions in ANSYS and COMSOL, and the results with single pulse/train has been compared consistently with the analytical solutions, see [6, 7]. In ANSYS, nonlinear coupled-field elements, PLANE223 and SOLID226 are used by implement APDL code in workbench to simulate the coupled thermo-mechanical behaviors directly.

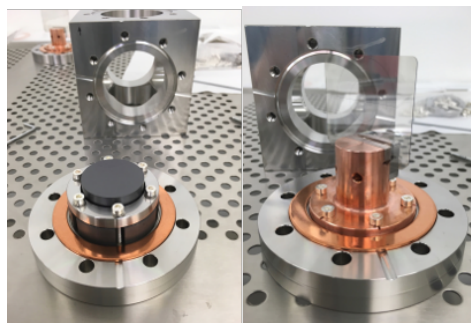


Figure 2: Beam stop.

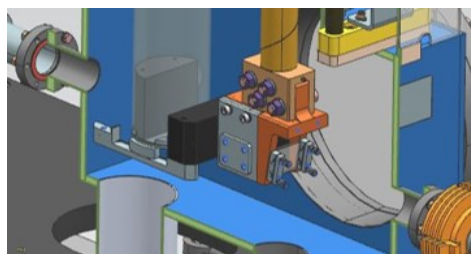


Figure 3: Upgraded frontend.

To improve the precision and reliability of the simulation results, With the support of IKTS Fraunhofer Institute, the temperature dependent diffusivity was measured for various B₄C samples, see Fig. 5. For the material param-

* fan.yang@xfel.eu
† daniele.lacivita@xfel.eu

Content from this work may be used under the terms of the CC BY 3.0 licence (© 2021). Any distribution of this work must maintain attribution to the author(s), title of the work, publisher, and DOI



Figure 4: left: CVD diamond model, right: B₄C

ter of CVD diamond samples in various lattice directions, the Young's modulus and Poisson's ratio were measured at Helmut-Schmidt University, see Fig. 6. According to the current measurements, the Young's modulus from the measured sample is 20% higher than the values from material library.

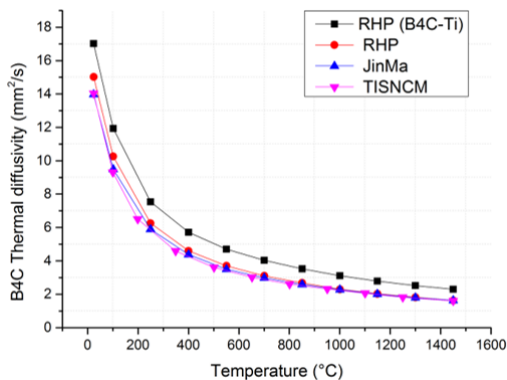


Figure 5: Temperature dependent diffusivity.

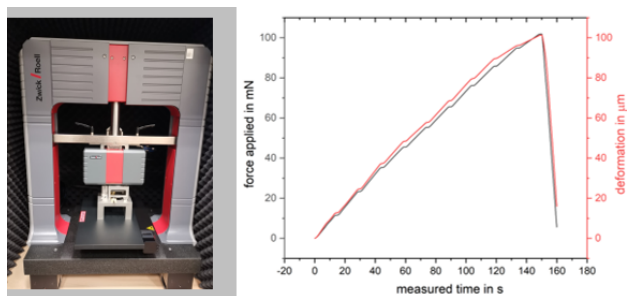


Figure 6: Nanoindenter measurement with loading cycle.

B₄C

The simulation results show that stress, strain and temperature fields should be considered as damage threshold for the engineering design, see [7, 8]. Taking one type of beam stop as an example, the maximum allowed pulses/train with respect to photon energy is shown in Fig. 7.

CVD Diamond

For a generalized data analysis that could take more variables into account, e.g. photon energy-beam size-temperature, or photon energy-pulse number/train-stress, a 3D plot figure with plane mapping is shown in Fig. 8. As an example, using the maximum permissible temperature of 1200 °C as the criterion [9], the design threshold with respect to photon energy and pulse dimension can be derived from the 3D plot with a plane 1200 °C.

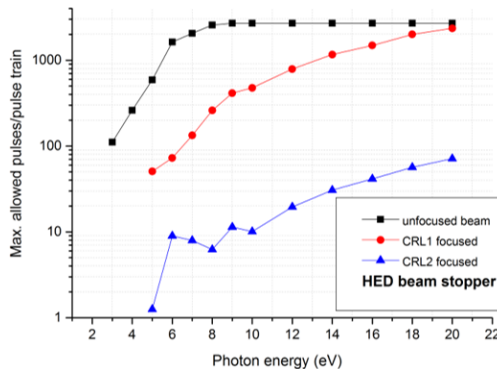


Figure 7: Max. allowed pulses/train.

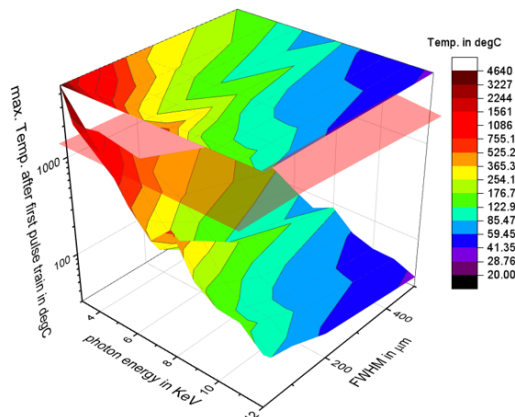


Figure 8: Photon energy-pulse dimension-max. transient temperature.

Similar 3D figures have been plotted with respect to other beam parameters and other materials as well. Due to the page limit, only one more plot is shown below, see Fig. 9.

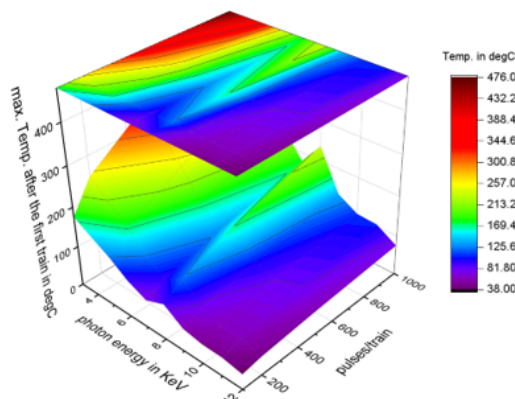


Figure 9: Photon energy-pulse numbers/train-max. transient temperature.

BEAM INTERACTION WITH GAS

Besides solid materials, there are also demand of numerical simulation in terms of beam interaction with gas, e.g. for soft X-ray gas attenuators, to estimate the beam transmission with respect to various beam parameters. Because of the ultra-short time duration of 150 fs each pulse and high repetition rate of 2.5 MHz, a density depression was observed

during experiments in various beam conditions, see the previous theoretical and numerical study in [10, 11]. Using a constant FEL pulse energy of 4 mJ, pressure of 0.0375 Torr in the N₂ gas attenuator chamber, a multiphysical model including thermal effect and the gas flow were simulated, see Fig. 10. In Fig. 11 and Fig. 12, the bleaching effect can be observed.

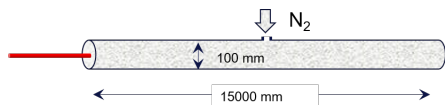


Figure 10: Gas attenuator model in COMSOL.

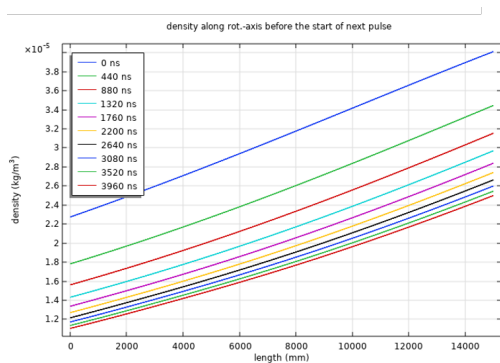


Figure 11: Density distribution along the beam direction.

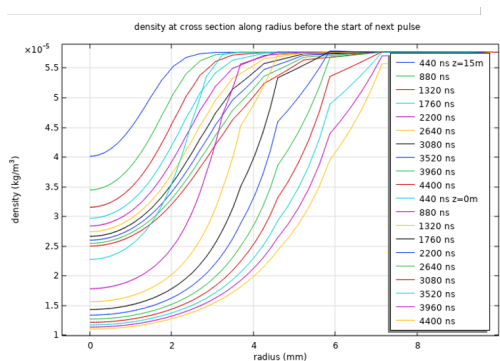


Figure 12: Density distribution in the radial direction.

CONCLUSION

In this contribution, an overview of heat load simulation to set up a standard damage threshold in the scope of engineering design is introduced briefly. As examples, part of the simulation results with respect to various beam parameters for B₄C, CVD diamond are presented. In the scope of material study, the multiphysical and multiscale phenomena should be considered in the simulations. For the future works, new materials could be investigated to improve the thermo-mechanical performance of the instruments, e.g. titanium doped B₄C or diamond-copper composite (RHP-Technology GmbH). Another plan in the future is to implement digital twin model to the facility. By coupling the measured data from the installed sensors and experimental

data systematically, the precision and functionality of the simulation results can be improved adaptively.

ACKNOWLEDGEMENTS

Experimental methods and results of the bleaching effect of gas attenuator will be published later by J. Gruenert, J. Liu, R. Villanueva, F. Yang, Th. Maltezopoulos, T. Mazza, B. van Kuiken, and L. Mercadier soon.

Measurement for the CVD diamond in various lattice directions is collaborated with L. Samoylova (optic group at EuXFEL) R. Diguov (TISNCM Institute) and M. Linke (Helmut-Schmidt University).

All the collaborations above are very much acknowledged.

REFERENCES

- [1] Th. Tschentscher *et al.*, “Photon Beam Transport and Scientific Instruments at the European XFEL”, *Appl. Sci.*, vol. 7, no. 6, p. 592, 2017. doi: 10.3390/app7060592
- [2] H. Sinn *et al.*, “The SASE1 X-ray beam transport system”, *J. Synchrotron Rad.*, vol. 26, pp. 692-699, 2019. doi:10.1107/S1600577519003461
- [3] Zh.X. Qu, “Photo-Thermo-Mechanical Analysis and Control for High-brightness and High-repetition-rate X-ray Optics”, Dissertation, 2020. <https://escholarship.org/uc/item/9jq7d245>
- [4] L. Zhang, D. Cocco, *et al.*, “Optimizing X-ray mirror thermal performance using matched profile cooling”, *J. Synchrotron Rad.*, vol. 22, no. 5, pp. 1170–1181, 2015. doi:10.1107/S1600577515013090
- [5] J.C. Simo and R.L. Taylor, *Consistent Tangent Operators for Rate-Independent Elasto-Plasticity*, *Comput. Methods Appl. Mech. Eng.*, vol. 48, no. 1, pp. 101-118, 1985. doi: 10.1016/0045-7825(85)90070-2
- [6] H. Sinn, “Heat load estimates for XFEL beamline optics”, HASYLAB Annual Report, 2008. http://hasyweb.desy.de/science/annual_reports/2007_report/part1/contrib/30/22200.pdf
- [7] D.D. Ryutov, “Thermal stresses in the reflective x-ray optics for the Linac Coherent Light Source”, *Rev. Sci. Instrum.*, vol. 74, no. 8, pp. 3722-3725, 2003. doi:10.1063/1.1590747
- [8] I. Jiménez, D.G.J. Sutherland, *et al.*, “Photoemission and x-ray-absorption study of boron carbide and its surface thermal stability”, *Phys. Rev. B*, vol. 57, pp. 13167–13174, 1998. doi: 10.1103/PhysRevB.57.13167
- [9] M. Seal, “Graphitization of Diamond”, *Nature*, vol. 185, pp. 522–523, 1960. doi:10.1038/18522a0
- [10] Y. Feng, J. Krzywinski, *et al.*, “Filamentation effect in a gas attenuator for high-repetition-rate X-ray FELs”, *J. Synchrotron Rad.*, vol. 23, pp. 21-28, 2016. doi:10.1107/S1600577515018408
- [11] A.M. Ortega, Y. Dabin, *et al.*, “Study of Energy Transfer Mechanism for a Synchrotron X-ray Gas Absorber with COMSOL Multiphysics”, in *Proceedings of COMSOL Conference in Grenoble*, 2015. https://www.comsol.com/paper/download/289181/martínortega_paper.pdf

INNOVATIVE AND BIOLOGICALLY INSPIRED PETRA IV GIRDER DESIGN*

S. Andresen[†], Alfred Wegener Institute Helmholtz Center for Polar and Marine
 Research (AWI), Bremerhaven, Germany

N. Meyners, D. Thoden, Deutsches Elektronen-Synchrotron (DESY), Hamburg, Germany

Abstract

DESY (Deutsches Elektronen Synchrotron) is currently expanding the PETRA III storage ring X-ray radiation source to a high-resolution 3D X-ray microscope providing all length scales from the atom to millimeters. This PETRA IV project involves an optimization of the girder magnet assemblies to reduce the impact of ambient vibrations on the particle beam. For this purpose, an innovative and biologically inspired girder structure has been developed. Beforehand, a large parametric study analyzed the impact of different loading and boundary conditions on the eigenfrequencies of a magnet-girder assembly. Subsequently, the girder design process was generated, which combined topology optimizations with biologically inspired structures (e.g., complex Voronoi combs, hierarchical structures, and smooth connections) and cross section optimizations using genetic algorithms to obtain a girder magnet assembly with high eigenfrequencies, a high stiffness, and reduced weight. The girder was successfully manufactured from gray cast iron and first vibration experiments have been conducted to validate the simulations.

INTRODUCTION

Biomimetics is a scientific discipline that deals systematically with the technical implementation and application of constructions, processes, and development principles of biological systems. Biological models are not copied, but investigated, understood, and applied to technical problems [1,2].

Natural structures are often complex and show good mechanical properties. They are highly optimized during the process of evolution and usually fulfil different functions.

In particular, aquatic plankton organisms with silicate cell covers (such as diatoms and radiolaria) have developed an extremely high diversity of irregular structures that show efficient lightweight design principles. Aside from the high stiffness and strength observed in these lightweight structures [3,4], diatom shells are expected to also protect the inner cell against vibrational load cases.

In different studies, irregular biologically inspired structures were analyzed regarding their natural vibrations. Irregular honeycomb and lattice structures show significantly higher eigenfrequencies compared to regular structures [5,6]. In addition, pre-deforming structures according to mode shapes, which can be observed in diatom shells [7], strongly raises the eigenfrequencies [8].

* Work financed by the Alfred Wegener Institute and the Deutsches Elektronen-Synchrotron.

[†] simone.andresen@awi.de

In a case study, biologically inspired structures and optimization techniques were applied to a PETRA IV girder. The PETRA IV project at DESY aims at upgrading the currently running synchrotron radiation facility PETRA III. For more information about this project it is referred to [9,10]. Generally, a high particle beam stability is essential to obtain a low-emittance and diffraction limited storage ring [11]. Magnet-girder assemblies play an important role, because they have to prevent that amplified ground vibrations reach the particle beam.

The objective of the here presented study was to design an innovative, bio-inspired PETRA IV girder.

MATERIAL AND METHOD

The applied girder design process was based on seven steps:

Definition of the Boundary Conditions

Figure 1 shows the considered boundary conditions. The girder was equipped with eight magnets and connected at three locations to three pedestals.

The overall design objectives were the maximization of the 1st magnet-girder eigenfrequency, the minimization of the static deformation due to gravity, and the minimization of the girder mass.

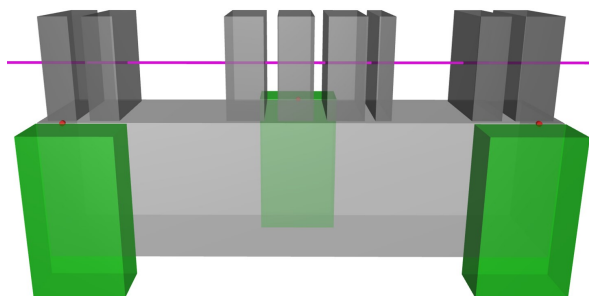


Figure 1: Model assembly including the girder design space (light gray), the magnets (dark gray), the pedestals (green), and the connection of the design space to the pedestals using beams (red). The position of the vacuum chamber is demonstrated in magenta.

Topology Optimization

A topology optimization was conducted to reveal an optimum material distribution. Thus, during the optimization process, material was removed from the design space shown in Fig. 1.

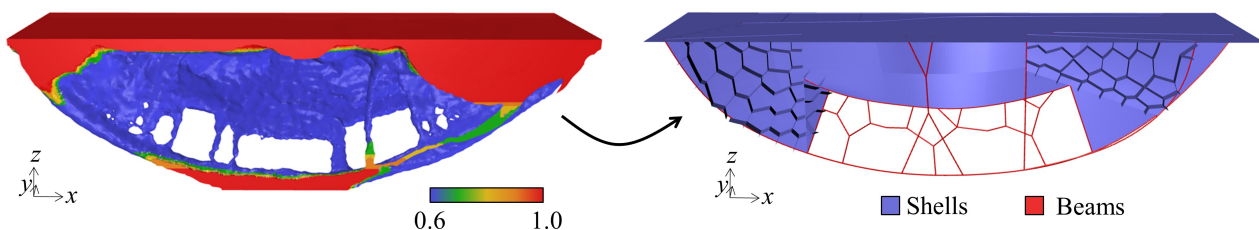


Figure 2: Topology optimization result (left), in which the coloring represents the artificial element density, and the abstracted beam-shell model (right).

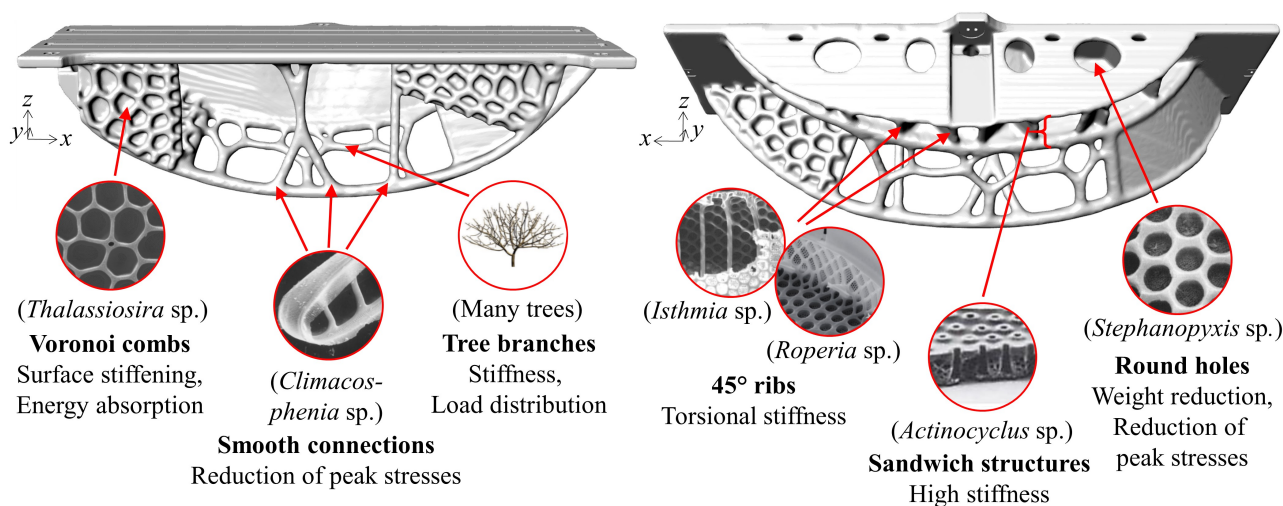


Figure 3: Front view (left) and rear view (right) of the final biologically inspired girder structure. The different structural elements inspired by nature are explained.

Parametric Beam-Shell Model

The structure resulting from the topology optimization was abstracted into a beam-shell model. This included the replacement of strut- and beam-like parts by lines (beams). Surface-like parts were abstracted as surfaces (shells) or – in the case of rather thick surfaces – as sandwich structures. The result of this step was a parametric beam-shell model.

Cross Section Optimization

In a large evolutionary strategic optimization, the thickness values and cross section diameters of all shells and beams were varied in order to obtain an optimum parameter combination. In this optimization procedure, the principles of biological evolution were applied to the present technical problem including accidents (mutation, cross over) and the proximate election strategies (selection). In several iterations, many parameter combinations were analyzed. The structure showing the highest 1st eigenfrequency and a tolerable maximum static deformation and mass was chosen as the optimum girder structure.

Final Girder Structure

The optimum beam-shell model was converted into a volume model that was meshed and numerically analyzed regarding its eigenfrequencies.

Simulation

Structural Statics And Dynamics

Manufacturing

The designed girder was manufactured using casting technology in connection with 3D printed sand molds. Grey cast iron (EN-GJL-250) was utilized. The interface surfaces to the magnets and pedestals were machined afterwards.

Vibration Measurement

The eigenfrequencies of the free and unloaded, manufactured girder were measured in an impact test. The girder was hit at the middle front of the upper girder surface. Eight accelerometers fixed to the upper girder surface recorded the girder movement. The power spectral density of the upper girder surface was plotted and the measured eigenfrequencies were compared to those obtained in the simulations.

RESULTS

The topology optimization result was a continuous structure that reminded of a bridge. It was composed of arch-like and surface-like structures as well as several interconnections. Figure 2 shows the topology optimization result and the abstraction into a beam-shell model, which contained multiple beams and shells.

The subsequent cross section optimization using the evolutionary strategy revealed an optimum dimension of each strut and shell leading to the final bio-inspired girder structure displayed in Fig. 3. It is based on different structural

elements inspired by, in particular, aquatic plankton organisms.

In Fig. 4, the manufactured girder is positioned on three pedestals. Springs were located between the girder and the bases. This set-up was used for the impact testing.



Figure 4: Front view of the manufactured bio-inspired girder connected via springs to the three pedestals.

Figure 5 shows the PSD (power spectral density) obtained for the eight accelerometers. The measured and numerically obtained eigenfrequencies were compared among each other (Table 1).

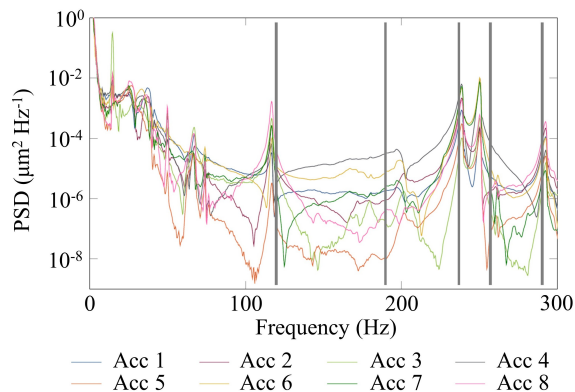


Figure 5: Power spectral density (logarithmic scale) obtained for the eight accelerometers (Acc.). The vertical gray lines illustrate the numerically obtained eigenfrequencies.

Table 1: Comparison of the Measured and the Numerically Obtained Eigenfrequencies of the Bio-inspired Girder Design

	Simulation	Measurement
f_1	119.6 Hz	116.6 Hz
f_2	189.8 Hz	199.7 Hz
f_3	236.8 Hz	238.7 Hz
f_4	257.1 Hz	250.2 Hz
f_5	290.4 Hz	292.5 Hz

DISCUSSION

The high potential of applying biologically inspired structures and optimization techniques to girder design processes has been demonstrated.

A development process for a girder structure of the synchrotron radiation facility PETRA IV has been generated. It resulted in an innovative girder design that combined different biologically inspired structural elements. The numerically obtained eigenfrequencies were validated by performing eigenfrequency measurements on the manufactured girder structure. In addition, the high conformity of the measured and simulated eigenfrequency values indicated a successful manufacturing process despite of the high complexity of the structure.

Future changes in the specifications can be implemented in the development process to obtain adapted girder structures.

CONCLUSION

In this case study, a girder design process was generated with the objective to design an innovative and biologically inspired girder structure. The successful manufacturing of the designed girder and the subsequent vibration measurements allowed a validation of the numerically obtained results.

REFERENCES

- [1] W. Nachtigall, *Bionik. Grundlagen und Beispiele für Ingenieure und Naturwissenschaftler*, 2nd ed., Berlin, Heidelberg, Germany: Springer, 2002.
- [2] G. Pohl and W. Nachtigall, *Biomimetics for Architecture & Design. Nature – Analogies – Technology*, Switzerland: Springer International Publishing Switzerland, 2015.
- [3] C.E. Hamm, R. Merkel, O. Springer, P. Jurkojc, C. Maier, K. Prechtel, and V. Smetacek, “Architecture and material properties of diatom shells provide effective mechanical protection”, *Nature*, vol. 421.6925, pp. 841–843, 2003. doi: 10.1038/nature01416
- [4] C.E. Hamm, “The evolution of advanced mechanical defenses and potential technological applications of diatom shells”, *Journal of Nanoscience and Nanotechnology*, vol. 5.1, pp. 108–119, 2005. doi: 10.1166/jnn.2005.023.
- [5] S. Andresen, A. Bäger, and C. Hamm, “Eigenfrequency maximisation by using irregular lattice structures”, *Journal of Sound and Vibration*, vol. 465, p. 115027, 2020. doi: 10.1016/j.jsv.2019.115027
- [6] S. Andresen, “Impact of Bio-inspired Structural Irregularities on Plate Eigenfrequencies”, in *Proceedings of the 14th International Conference on Vibration Problems, Lecture Notes in Mechanical Engineering*, Ed. by E.J. Sapountzakis, M. Banerjee, P. Biswas, and E. Inan, Singapore: Springer, pp. 1117–1125, 2021. doi: 10.1007/978-981-15-8049-9_71
- [7] A. Gutiérrez, R. Gordon, and L.P. Dávila, “Deformation modes and structural response of diatom frustules”, *Journal of Materials Science and Engineering with Advanced Technology*, vol. 15, pp. 105–134, 2017. doi: 10.18642/jmseat_7100121810
- [8] S. Andresen, L.M. Lottes, S.K. Linnemann, and R. Kienzler, “Shape adaptation of beams (1D) and plates (2D) to maximise eigenfrequencies”, *Advances in Mechanical Engineering*, vol. 12, no. 11, pp. 1–18. doi: 10.1177/1687814020971903

- [9] I.V. Agapov, R. Bacher, M. Bieler, R. Bospflug, R. Brinkmann, Y.-C. Chae, *et al.*, “Status of the PETRA IV project”, in *Proc. IPAC’19*, Melbourne, Australia, pp. 1404–1407, 2019. doi:10.18429/JACoW-IPAC2019-TUPGW011
- [10] C.G. Schroer, R. Röhlsberger, E. Weckert, R. Wanzenberg, I. Agapov, R. Brinkmann, and W. Leemans, “PETRA IV. Upgrade of PETRA III to the Ultimate 3D X-ray Microscope”, Conceptual Design Report, Deutsches Elektronen-Synchrotron, A Research Center of the Helmholtz Association, 2019. doi:10.3204/PUBDB-2019-03613.
- [11] L. Zhang, “Beam stability consideration for low emittance storage ring”, Presentation at the *Workshop on Ambient Ground Motion and Vibration Suppression for Low Emittance Storage Rings (GM 2017)*, Beijing, China. 2017.

List of Authors

Bold papercodes indicate primary authors; ~~crossed-out~~ papercodes indicate 'no submission'

— A —

Abiven, Y.-M.	TUPB01 , WEPB11
Adamian, A.	WEPA08
Adamson, L.W.S.	WEPA14
Afshar, N.	TUPA18
Åhnberg, K.	MOOA02
Al Shehab, M.M.	WEPA10
Al-Dmour, E.	MOOA02
Al-Najdawi, M.A.	WEPA10
Alloza, D.	WEPA07
Altissimo, M.	WEPA10
Álvarez, J.M.	WEPA11
Amann, P.N.	WEPB15
Andresen, S.	THOB03
Anliker, E.A.	MOPB09 , MOPB10 , MOPB11
Antipov, S.P.	MOPC03
Anton, J.W.J.	TUOA01 , TUOA02 , TUPC09 , TUPC10 , WEPC10
Arab, N.B.	WEPA08
Assell, D.	MOPC12
Assoufid, L.	TUOA01 , TUOA02 , TUPC10
Auckett, J.E.	TUPA16
Avellar, G.C.	MOPB10 , MOPB11
Ayas, E.	TUPB05 , TUPB12

— B —

Bacescu, D.M.	WEPC12
Bado, P.	TUPB15
Baker, R.	MOOB01
Barnsley, L.	WEOB01
Barrett, R.	MOOB01
Barrière, N.	WEPA12
Bartlein, M.	WEPB15
Bassan, H.	TUOA02
Baumann, G.	TUPB13
Bavdaz, M.	WEPA12
Bean, S.J.	TUPC10 , TUPC15 , WEPB15 , WEPC13 , THOA01 , THOA02
Béchade, J.-L.	WEPB10
Bechtold, R.	WEPB07
Behdad, N.	TUPC05
Bender, T.J.	MOPC07
Bergeret, M.	THOA01
Berman, L.	WEPC12
Bernard, P.	MOOB01
Berruyer, G.	MOOB01
Beyer, M.	TUPB13
Bhamjee, M.	WEPB09
Biasci, J.C.	WEI001
Billett, B.	MOPC11 , MOPC14
Bisti, F.	MOOB02
Boiadjieva, N.A.	MOPC08
Bonnefoy, J.	MOOB01 , TUI002

Booske, J.H.	TUPC05
Borges, F.A.	MOPB08
Borland, M.	WEPB06
Botta, S.	TUOB03 , TUPB02
Boullon, R.	WEPB10
Brajuskovic, B.	MOPC11
Brandt, J.A.	TUPC06
Brendike, M.	MOOB01
Brito Neto, J.L.	MOPB03
Brumund, P.	WEPB08
Bueno, C.S.N.C.	MOPB06 , MOPB08 , TUOB01 , WEPB13 , WEPC02
Bueno, M.	TUPB11
Buisson, A.-L.	MOI002
Button, M.	WEPC04
Buxadera, J.	TUPB12

— C —

Cai, Z.	WEPB15
Calcanha, M.P.	MOPB02
Caliari, R.M.	MOPB03
Caliebe, W.A.	WEPA09
Capatina, D.	TUPC10 , WEPC13
Capovilla, L.G.	WEPB13
Carballedo, A.	WEPA12 , WEPA14
Cardenas, E.	WEPC05
Cardoso, F.H.	WEPC02
Carriere, P.R.	TUPC01
Carter, J.A.	MOPC11 , MOPC14
Carvalho, J.C.	WEPC02
Casas, J.J.	TUPB05 , TUPB12 , WEPA12 , WEPB16
Celestre, R.	MOPC03
Chaichuay, S.	TUPA10
Chang, C.F.	WEPA06 , WEPA16
Chang, C.H.	WEPA16
Chang, C.Y.	WEPA16
Chang, S.H.	WEPA16
Chen, J.X.	TUPA05 , TUPA13 , TUPA15
Chen, S.	MOPC10 , THOA02
Cherukuvada, H.	TUPA03
Chiang, L.C.	WEPA16
Chu, M.	TUPC09
Chuang, J.-Y.	WEPA03
Chumakov, A.	WEOB02
Cianciosi, F.	MOI002
Claudiano, G.V.	MOPB02 , MOPB06 , TUPC14
Clement, J.M.	WEOB03
Clement, W.	WEPA05
Clulow, A.J.	WEOB01
Clute, T.K.	WEPB06
Colldelram, C.	MOOB02 , TUPB01 , TUPB05 , TUPB12 , WEPA07 , WEPA11 ,

Content from this work may be used under the terms of the CC BY 3.0 licence (© 2021). Any distribution of this work must maintain attribution to the author(s), title of the work, publisher, and DOI

Collette, C.G.R.L. WEPA12, WEPA14, WEPB16
 TUI002
 Collon, M.J. WEPA12
 Conesa-Zamora, G. WEOB01
 Connell, S.H. WEPB09
 Corsaletti, J.C. TUPC14, WEPC07
 Corwin, T.M. MOPC12
 Crisol, A. MOOB02, WEPA14
 Crivelli, D. TUOB02
 Cudin, I. WEPA10
 Cuní, G. WEPA12

— D —

da Silva, J.L. WEPB13
 de Albuquerque, G.S. MOPB03, MOPB04, MOPB08,
 TUPC11
 De Andrade, V. TUPC10, TUPC15
 de Jonge, M.D. TUPA18
 Decker, F.-J. TUOA02
 Dehaeze, T. TUI002, WEPB08
 Deiter, C. WEPA15
 Deng, R. TUPA07
 DePaola, F.A. MOPC12
 Deriy, A. TUPC15
 Di Felice, M. WEPA05
 Diaz Moreno, B. WEPC04
 DiMarco, J. MOPC12
 Docker, P. TUPB03
 Doehrmann, R. TUOB03
 Dommach, M. WEPA05
 Donatti, M.M. WEPC02
 Donetsk, D. MOPC01
 Dong, Y.H. TUPA09
 Doom, L. MOPC12
 Doose, C.L. MOPC12, WEPB03
 Doran, D.S. WEPB05
 Downey, J.S. WEPB06
 Duarte, H.O.C. TUPC11
 Dubuisson, J.M. WEPB11
 Ducotté, L. MOOB01
 Dufresne, E.M. TUPC10, WEPC13
 Dugan, M. TUPB15

— E —

Eggenstein, F. TUPB09
 Ehinger, M. TUPB13
 Eleoterio, M.A.S. MOPB03
 Eng, C. MOPC01
 Engblom, C. WEPB11
 Erdmann, M. THOA01

— F —

Faussete, R. MOPC12
 Fenwick, M. TUPA16
 Fernández, P.S. WEPC03
 Ferreira, G.R.B. MOPB08
 Ferreira, I. WEPA12
 Fezzaa, K. TUPC15

Fiedler, S. TUPB11
 Fisher, M.V. MOPC05, WEPC13
 Fontoura, A.F.M. MOPB02
 Francisco, B.A. MOPB02, WEPC07
 Frith, M.G. MOPC04
 Fritz, D.M. MOPC08
 Fuentes, Ll. TUPB05, TUPB12
 Fung, H.S. MOOB03

— G —

Galante, D. WEPB13
 Gao, L. TUPA09
 Garich, H.M. TUPC16
 Gassner, G.L. TUOA02
 Geraissate, H. THOA03
 Geraldes, R.R. MOPB03, MOPB06, MOPB08,
 TUOB01, TUPC11, TUPC14,
 WEPB13, WEPC02, WEPC03,
 WEPC07
 Giorgetta, J.L. WEOA02, WEPB11
 Giraldo, J.C. TUPB12
 Glover, C. TUPA17
 Gluskin, E. MOI001
 Goerlitz, M. WEPA09
 Gomez, E. MOPC03
 González Fernández, J.B. WEPA14, WEPB12
 Gonzalez, H. MOOB01
 González, N. WEPA11, WEPA14
 González Romero, A. WEPB16
 Graber, T. MOPC04, TUPC10, TUPC15,
 WEPB15, THOA02
 Grabski, M.J. MOOA02
 Grubb, R. WEOB01
 Gubbels, E. MOPB13
 Guedes, L.C. WEPB13
 Guillou, R. WEPB10

— H —

Ha, T. MOOA03
 Haas, E. WEPC05
 Haeffner, D. MOPC04
 Hagge, L. WEOA01
 Hall, T.D. TUPC16
 Hamedi, H. WEOB01
 Handick, E. WEPA12
 Harder, D.A. MOPC12
 Harder, R. TUPC10
 Hashimoto, A.H. TUOA03
 Haskel, D. TUPC10
 Hasse, Q.B. MOPB09
 He, H.Y. TUPA02, TUPA05, TUPA06,
 TUPA13, TUPA15
 Heilig, R. TUPB13
 Heinis, D. WEPA12
 Hermange, H. WEPB10, WEPB11
 Hernández, F. TUPB05
 Highland, M.J. MOPC04, WEPC13
 Ho, H.C. MOOB03

Hogan, R.B. TUPA16
 Holt, M. WEPB15
 Hsu, K.H. MOOB03
 Huang, C.S. MOOB03
 Huang, D.-G. MOOB03
 Huang, Z. TUOA02
 Huber, N. TUPB08
 Hüning, M. WEOA01
 Hulbert, S. MOPC01, WEPB12
 Hunault, M.O.J.Y. WEPB10

— I —

Iglesias, J. TUPB05, TUPB12
 Inman, M.E. TUPC16
 Iori, G. WEPA10, WEPB09
 Ivanyushenkov, Y. MOPB09
 Izzo, S.J. WEPB03

— J —

Jacobsen, C. THOA02
 Jain, A.K. MOPC12, WEPB03, WEPB07
 Jane, E.R. WEPA14
 Jansma, W.G. MOPC16, TUOA02, WEPB03,
 WEPB04, WEPB05, WEPB07
 Jasionowski, K. TUPC10
 Jaski, M.S. WEPB06
 Jaski, Y. MOPC01, THCL01
 Jensen Jr., D.P. TUPC07
 Jensen, B. WEOB01
 Jiang, Z. TUPC09
 Jing, X.P. TUPA12
 jonquères, N. WEPB10
 Juanhuix, J. WEPA11, WEPA14
 Junqueira Leão, R. THOA03
 Just, D.M. WEOA03

— K —

Kakizaki, D.Y. TUPC14
 Kamma-Lorger, C.S. WEOB01
 Kang, L. TUPA05, TUPA06, TUPA13,
 TUPA15
 Kaprolat, A. WEPA10, WEPB09
 Kasa, M. MOPB09
 Ke, Z.Y. TUPA06
 Kearney, S.P. MOPC10, TUOA01, TUOA02,
 TUPC10
 Kelly, J.H. TUOB02
 Kewish, C.M. TUPA18
 Khan, A.A. MOPC05, TUPC02, TUPC10
 Khan, F. TUOB02
 Kikuchi, T. TUOA03, TUPA01
 Kim, K.-J. TUOA02
 Kimpton, J.A. TUPA16
 Kitel, M. WEPA15
 Klinkhiew, S. TUPA10
 Knopp, J.J. MOPC05, WEPB06
 Kofukuda, L.M. MOPB02, MOPB04, MOPB08,
 WEPB13, WEPB02, WEPB03

Kohlstrunk, N. WEPA05
 Kolodziej, T. WEPA10
 Kolwicz-Chodak, L. TUPB11
 Kontogiorgos, G.N. MOPB06, WEPB13
 Krumrey, M. WEPA12
 Kuan, C.K. MOOB03

— L —

La Civita, D. WEPA05, THOB02
 Lai, B. MOPC10, TUPC10, THOA02
 Lai, W.Y. MOOB03
 Lau, M. TUPB13
 Lauberton, R. WEPB10
 Lausi, A. WEPA10
 Lee, R. WEPA16
 Lee, S.H. TUPB06, TUPC05, WEPB04,
 WEPB05, THIO02
 Lena, F.R. MOPB02, MOPB06, TUOB01,
 TUPC14, WEPB13, WEPB02

Leontowich, A.F.G. WEPB04
 Lerch, J.E. MOPB01, MOPB10, MOPB11
 Lestrade, A. WEOA02
 Leterme, D. WEPB10
 Li, C.H. TUPA14
 Li, M. TUPA09
 Li, X. WEPB01
 Liang, H. TUPA04, TUPA08
 Liao, B.Y. WEPA16
 Lin, C.J. MOOB03
 Lin, G.P. TUPA12
 Lindberg, R.R. TUOA02
 Lippi, R. TUPA16
 List, B. WEOA01
 Liu, C.Y. WEPA06, WEPA16
 Liu, D.X. TUPC16
 Liu, F. TUPA07
 Liu, J. WEPB06
 Liu, J. MOPC01
 Liu, J.M. TUPA02
 Liu, L. TUPA06, TUPA13, TUPA15
 Liu, L. TUPA05
 Liu, R.H. TUPA05, TUPA13, TUPA02,
 TUPA06, TUPA15
 Liu, W. TUPC10
 Liu, Y. TUPA07
 Liu, Z. MOPC16, WEPB07, WEPB09
 Llonch, M.L. MOOB02
 Lu, A.Z. TUPA12
 Lu, X. TUPC16
 Lu, Y.S. TUPA04
 Luiz, S.A.L. MOPB03, MOPB04, MOPB06,
 TUOB01, WEPB13

— M —

Male, A. TUOB02
 Mandin, P. WEPB10
 Mao, N. TUPA07
 Marcos, J. WEPA12

Marcus, G.	TU0A02
Marion, P.	TUPB01
Martins dos Santos, L.	MOPB04
Mary, A.	WE0A02
Mase, K.	TU0A03, TUPA01
Maser, J.	MOPC10, TUPC10
Mashrafi, S.T.	TU0A01, TU0A02, TUPC10
Masuda, Y.	TUPA01
Mateos, L.	MOPB05
Matichard, F.	TUI001
Matilla, O.	WEPA12
Matus, J.	TUPC15
Maxey, E.R.	TH0A02
Mazonowicz, A.P.	WE0B01
Mazzoli, C.	MOPC01
McDonald, S.A.	WEPB12
McElderry, A.	MOPC11, MOPC14
McMahon, B.J.	TUPA16
Meneau, F.	MOPB02
Menut, D.	WEPB10, WEPB11
Meyer, J.	TUPB11
Meyners, N.	TH0B03
Micolon, F.	WEPA13
Miller, D.	WE0A01
Mistri, G.K.	TUPC10, TUPC08
Miyazawa, T.	TU0A03
Mokoena, T.F.	WEPB09
Molas, B.	M00B02
Monge, R.	M00B02
Monk, B.L.	WEPC01
Mooney, T.	MOPC10, TH0A02
Moradi, V.	WEPA08
Moraes, M.A.L.	MOPB03, MOPB08, TUPC11
Moreno, G.B.Z.L.	MOPB02, MOPB06, MOPB08, TU0B01, WEPB13
Mountford, B.	TUPA17, TUPA18
Mueller, P.	WEPA12
Mulvany, O.K.	MOPC11, MOPC14
Muñoz Pequeño, C.	WE0B03
Musardo, M.	MOPC12

— N —

Nakayama, Y.	TUPA01
Narayanan, S.	TUPC09, TUPC10, WEPC13
Nasiatka, J.R.	TH0A01
Navrotsky, G.	TUPC01
Neckel, I.T.	WEPB13, WEPC03
Nicolás, J.	M00B02, WEPA07, WEPA11, WEPA12, WEPA14
Nie, X.J.	TUPA05, TUPA13, TUPA06, TUPA15
Nikitina, L.	M00B02
Ning, C.J.	TUPA05, TUPA06, TUPA13, TUPA15
Nudell, J.	MOPC16, WEPB07
Nuhn, H.-D.	TU0A02
Nygaard, K.	WEPB12

— O —

Ocko, B.	WEPC12
Ohno, S.	TU0A03, TUPA01
Olea, G.	TUPB08
Oliver, T.	MOPC15
Ono, M.	TUPA01
Ozawa, K.	TUPA01

— P —

Parise, R.L.	TUPC14
Pereira, E.O.	TU0B01
Perez, C.A.	WEPB13
Perissinotto, L.S.	WEPC02
Perna, A.V.	MOPB03, TUPC11
Perng, S.Y.	M00B03
Petersen, P.-O.	WE0A01
Piccino Neto, A.C.	WEPB13
Pinto, A.C.	MOPB06, WEPB13
Piragibe, E.	WEPC02
Pocock, B.A.	TUPA17
Podobedov, B.	MOPC01
Pongampai, S.	TUPA10
Pont, M.	TUPB12
Popovic, B.K.	TUPB06
Porsa, S.	TUPA16
Power, J.G.	TUPC16
Pradervand, C.	WE0A03
Pradhan, P.	WEPC10
Preissner, C.A.	MOPC16, TUPC02, TUPC10, TUPC15, WEPB07, TH0A01, TH0A02
Pruvost, J.B.P.	WEPB10
Punset, M.	TUPB12

— Q —

Qian, J.	TU0A01
Qiao, Z.	TU0A01
Qiu, J.	TUPA12
Quispe, M.	M00B02, TUPB05, TUPB12, WEPB16

— R —

Rabedeau, T.	MOPC08
Ramanathan, M.	MOPC04, TUPC10
Rebuffi, L.	TUPC10
Reininger, R.	TUPC10
Reyes-Herrera, J.	WEPA10, WEPB17
Režende, J.H.	MOPB02, MOPB04
Ribó, L.	M00B02
Ribó, L.R.M.	WEPA07, WEPA14
Ristau, U.	TUPB11
Robert, Y.	WEPB10
Rocha e Silva, D.V.	MOPB08
Rodrigues, G.L.M.P.	MOPB02, MOPB06
Roslund, L.K.	WEPB12
Roth, S.	WE0B02
Roth, T.	M00B01, MOPC03
Rovigatti de Oliveira, G.R.	TH0A03

Roy, C.J.	WEOB01
Rubeck, J.R.	WEOB02
Ruget, C.	WEPA14
Ruijl, T.A.M.	THI001
— S —	
Said, A.A.	TUPB15
Saliba, J.G.	MOPB10
Samardzic-Boban, V.I.	WEOB01
Sanchez del Rio, M.	WEPB17
Sanchez Navarro, P.	THOB01
Sandy, A.	WEPC13
Sanfelici, L.	MOPB02
Sato, C.	WEPB13, WEPC02
Sato, Y.	TUOA03, TUPA01
Saveri Silva, M.	MOPB02, MOPB04, TUPC11, TUPC14
Schlutig, S.	WEPB10
Schmidt, O.A.	MOPC04, MOPC07, TUPC10
Schulz, J.	WEPA15
Schwartzkopf, M.	WEOB02
Schwarz, L.	TUPB09
Schweizer, M.	TUPB13
Scott, D.S.	TUPC16
Sebdaoui, M.	WEPB11
Semeraro, M.	TUPA18
Shao, J.	TUPC16
Sharma, S.K.	MOPB15, MOPC12, MOPC13
Shen, X.	WEPB01
Sheng, W.F.	TUPA04, TUPA08, TUPA09
Sherrell, D.A.	WEPC15
Shi, H.	TUPA08
Shi, X.	TUOA01, TUOA02, TUPC10, THOA02
Shiroyanagi, Y.	MOPB09
Shu, D.	MOPC10, TUOA01, TUOA02, TUPC09, TUPC10, TUPC15, WEPB15, WEPC10, THOA02
Shvyd'ko, Yu.	TUOA02, WEPC10
Šics, I.	WEPA07, WEPA11
Silva, M.H.S.	MOPB08
Silva, M.S.	MOPB03, WEPC07
Sinn, H.	WEPA05, THOB02
Sirna, A.P.	WEPC05
Sittisard, K.	TUPA10
Siy, A.E.	TUPB06, TUPB15, TUPC05, WEPB04, WEPB05, THI002
Snyder, S.T.	TUPC16
Solari, P.L.	WEPB10, WEPB11
Song, H.	TUPA02
Sorsher, S.	TUPB06, TUPB07, TUPC05, WEPB04, WEPB05, THI002
Sosin, M.	WEPA13
Sotero, A.P.S.	MOPB04, WEPB13
Souza, M.S.	MOPB06, TUPC11, TUPC14
Spataro, C.J.	MOPC13
Srichan, S.	TUPA10

Strzalka, J.	TUPC09
Suthar, A.K.	TUPC08
Suthar, K.J.	TUPB06, TUPB07, TUPB15, TUPC01, TUPC05, TUPC08, WEPB04, WEPB05, THI002
Suthar, S.K.	TUPC08
Swanson, R.R.	MOPC11
Szubert, M.E.	MOPB10, MOPB11
Sánchez, A.	WEPA12
— T —	
Tafforeau, P.	MOI002
Tallarida, M.	MOOB02
Tan, J.	THOA02
Tan, T.-F.	TUOA02
Tanabe, T.	MOPC12
Tardieu, P.	MOOB01
Tavakoli, K.	WEOA02
Taylor, E.J.	TUPC16
Teixeira, V.C.	WEPB13
Thevenau, P.	WEOB03
Thoden, D.	THOB03
Tian, S.K.	TUPA13
Tischler, J.Z.	TUPC10
Tolentino, H.C.N.	MOPB02, MOPB04, MOPB08, TUOB01, WEPB13, WEPC02, WEPC03
Tonin, Y.R.	TUOB01
Toter, W.F.	MOPC07, TUOA02
Trakhtenberg, E.	TUPB06, TUPB07, TUPC05, WEPB04, WEPB05, THI002
Tseng, T.C.	MOOB03
— U —	
Utke, O.	TUPA10
— V —	
Vacanti, G.	WEPA12
Valenza, P.	WEPB10
Valls Vidal, N.	WEPA12
Van Vaerenbergh, P.	MOI002, WEOB03, WEPA10, WEPB09
Vannoni, M.	WEPA05, THOB02
Venkatesan, S.	WEOB01
Viefhaus, J.	TUPB09
Volin, K.J.	WEPB07
Volpe, L.M.	MOPB02, MOPB04, MOPB06, MOPB08, TUPC14, WEPC07
— W —	
Wakefield, K.J.	TUPC10, WEPC13
Waldschmidt, G.J.	TUPB06, TUPC05, WEPB04, WEPB05, THI002
Walko, D.	TUPC10
Wang, A.X.	TUPA05, TUPA13
Wang, A.X.	TUPA06, TUPA15
Wang, G.Y.	TUPA05, TUPA13, TUPA06
Wang, G.Y.	TUPA02, TUPA15
Wang, H.	TUPA14

Wang, H. **WEI002**
 Wang, H.R. ~~TUPA09~~
 Wang, H.S. **M00B03**
 Wang, J. **TUPC09, TUPC10**
 Wang, Z. ~~TUPA07~~
 Wang, Z.H. **TUPA14**
 Weber, J. ~~TUPB13~~
 Weir, N.R. **M0PB13**
 White, M. **TU0A02, TUPC08**
 Wienands, U. **WEPB06**
 Wilendorf, W.H. **TU0B01, WEPB13, WEPC02, WEPC03**
 Wiljes, P. ~~TU0B03, TUPB10~~
 Winarski, R. **M0PC04**
 Wojcik, W. **TH0A02**
 Wysokinski, T.W. **WEPC04**

— X —

Xing, Y.L. **TUPA12**
 Xu, G. **TUPA12**
 Xu, Z.G. **TUPA12**

— Y —

Yakovenko, A.A. **WEPC01**
 Yamanaka, M. **TU0A03**
 Yan, F. **TUPA12**
 Yang, F. **WEPA05, TH0B02**
 Yang, F.G. **TUPA09**
 Yang, Y.M. **TUPA08**
 Yin, Z. **WEPC12**

Yoshikawa, I. **TUPA01**
 Yoshioka, K. **TUPA01**
 Yu, J.B. **TUPA05, TUPA13, TUPA15**
 Yu, Y.J. **TUPA05, TUPA06, TUPA13, TUPA15**

— Z —

Zeeb, J. **TUPB08**
 Zeschke, T. ~~TUPB09~~
 Zhang, J.S. **TUPA06, TUPA05, TUPA13, TUPA15**
 Zhang, L. ~~TUPA07~~
 Zhang, X. **TUPC10**
 Zhang, X.W. ~~TUPA09~~
 Zhang, Y.S. **TUPA12**
 Zhang, Z. **TUPA04**
 Zhao, L.Q. **TUPA05**
 Zheng, L.R. **TUPA08**
 Zholents, A. **TUPB06, TUPB07, TUPB15, TUPC01, TUPC05, WEPB04, WEPB05, THI002**
 Zhou, N.C. **TUPA12**
 Zhu, D. **TU0A02**
 Zhu, D.H. **TUPA05, TUPA06, TUPA13, TUPA15**
 Zhu, W. ~~TUPA07~~
 Ziegler, R. **WEPC13**
 Zilli, V.B. **M0PB06, M0PB08**
 Zwarich, R. **WEPB01**

Institutes List

ALBA-CELLS Synchrotron

Cerdanyola del Vallès, Spain

- Alloza, D.
- Álvarez, J.M.
- Ayas, E.
- Bisti, F.
- Carballado, A.
- Casas, J.J.
- Colldelram, C.
- Crisol, A.
- Cuní, G.
- Fuentes, Ll.
- Giraldo, J.C.
- González, N.
- Heinis, D.
- Iglesias, J.
- Juanhuix, J.
- Llonch, M.L.
- Marcos, J.
- Matilla, O.
- Molas, B.
- Monge, R.
- Nicolás, J.
- Nikitina, L.
- Pont, M.
- Quispe, M.
- Ribó, L.
- Ribó, L.R.M.
- Ruget, C.
- Šics, I.
- SÁñchez, A.
- Tallarida, M.
- Valls Vidal, N.

Alfred-Wegener-Institut

Bremerhaven, Germany

- Andresen, S.

ANL

Lemont, Illinois, USA

- Amann, P.N.
- Anliker, E.A.
- Anton, J.W.J.
- Assoufid, L.
- Avellar, G.C.
- Bartlein, M.
- Bean, S.J.
- Bechtold, R.
- Bender, T.J.
- Billett, B.
- Borland, M.
- Brajuskovic, B.
- Cai, Z.
- Capatina, D.
- Carter, J.A.
- Chen, S.
- Chu, M.
- Clute, T.K.
- De Andrade, V.

- Deriy, A.
- Doose, C.L.
- Doran, D.S.
- Downey, J.S.
- Dufresne, E.M.
- Erdmann, M.
- Fezzaa, K.
- Fisher, M.V.
- Frith, M.G.
- Gluskin, E.
- Graber, T.
- Gubbels, E.
- Haeffner, D.
- Harder, R.
- Haskel, D.
- Hasse, Q.B.
- Highland, M.J.
- Holt, M.
- Ivanyushenkov, Y.
- Izzo, S.J.
- Jacobsen, C.
- Jain, A.K.
- Jansma, W.G.
- Jasionowski, K.
- Jaski, M.S.
- Jaski, Y.
- Jensen Jr., D.P.
- Jiang, Z.
- Kasa, M.
- Kearney, S.P.
- Khan, A.A.
- Kim, K.-J.
- Knopp, J.J.
- Lai, B.
- Lee, S.H.
- Lerch, J.E.
- Lindberg, R.R.
- Liu, J.
- Liu, W.
- Liu, Z.
- Lu, X.
- Maser, J.
- Mashrafi, S.T.
- Matus, J.
- Maxey, E.R.
- McElderry, A.
- Mistri, G.K.
- Monk, B.L.
- Mooney, T.
- Mulvany, O.K.
- Narayanan, S.
- Navrotski, G.
- Nudell, J.
- Popovic, B.K.
- Power, J.G.
- Pradhan, P.
- Preissner, C.A.
- Qian, J.
- Qiao, Z.

- Ramanathan, M.
- Rebuffi, L.
- Reininger, R.
- Saliba, J.G.
- Sandy, A.
- Schmidt, O.A.
- Scott, D.S.
- Shao, J.
- Sherrell, D.A.
- Shi, X.
- Shiroyanagi, Y.
- Shu, D.
- Shvyd'ko, Yu.
- Sorsher, S.
- Strzalka, J.
- Suthar, K.J.
- Swanson, R.R.
- Szubert, M.E.
- Tan, J.
- Tischler, J.Z.
- Toter, W.F.
- Trakhtenberg, E.
- Volin, K.J.
- Wakefield, K.J.
- Waldschmidt, G.J.
- Walko, D.
- Wang, J.
- Weir, N.R.
- White, M.
- Wienands, U.
- Winarski, R.
- Wojcik, W.
- Yakovenko, A.A.
- Zhang, X.
- Zholents, A.
- Ziegler, R.

ANSTO

Menai, New South Wales, Australia

- Conesa-Zamora, G.
- de Jonge, M.D.
- Grubb, R.
- Hamedi, H.
- Jensen, B.
- Kamma-Lorger, C.S.
- Samardzic-Boban, V.I.

AS - ANSTO

Clayton, Australia

- Afshar, N.
- Auckett, J.E.
- Barnsley, L.
- Cherukuvada, H.
- Clulow, A.J.
- Fenwick, M.
- Hogan, R.B.
- Kewish, C.M.
- Kimpton, J.A.
- Lippi, R.
- Mazonowicz, A.P.
- McMahon, B.J.
- Pocock, B.A.

- Porsa, S.
- Roy, C.J.
- Semeraro, M.
- Venkatesan, S.

ASCo

Clayton, Victoria, Australia

- Adamson, L.W.S.
- Glover, C.
- Mountford, B.

BNL

Upton, New York, USA

- Bacescu, D.M.
- Berman, L.
- Corwin, T.M.
- DePaola, F.A.
- Doom, L.
- Eng, C.
- Faussette, R.
- Haas, E.
- Harder, D.A.
- Hulbert, S.
- Mazzoli, C.
- Musardo, M.
- Ocko, B.
- Podobedov, B.
- Sharma, S.K.
- Spataro, C.J.
- Tanabe, T.
- Yin, Z.

CEA, DES-IRESNE-DEC, Université Paris-Saclay

Saint-Paul-Lez-Durance, France

- Schlutig, S.
- Valenza, P.

CEA, DES-ISAS-DM2S, Université Paris-Saclay

Gif-sur-Yvette, France

- Boullon, R.
- jonquères, N.
- Lauberton, R.
- Leterme, D.
- Mandin, P.
- Robert, Y.

CEA, DES-ISAS-DMN, Paris-Saclay University

Gif-sur-Yvette, France

- Béchade, J-L.
- Guillou, R.

CEEDI

Beijing, People's Republic of China

- Lu, A.Z.
- Xing, Y.L.
- Xu, Z.G.
- Zhang, Y.S.

CERN

Meyrin, Switzerland

- Micolon, F.
- Sosin, M.

CLS

Saskatoon, Saskatchewan, Canada

- Button, M.
- Diaz Moreno, B.
- Leontowich, A.F.G.
- Li, X.
- Shen, X.
- Wysokinski, T.W.
- Zwarich, R.

CNPEM

Campinas, SP, Brazil

- Martins dos Santos, L.
- Režende, J.H.

Cosine Measurement Systems

Warmond, The Netherlands

- Barrière, N.
- Collon, M.J.
- Vacanti, G.

DESY

Hamburg, Germany

- Botta, S.
- Caliebe, W.A.
- Chumakov, A.
- Clement, W.
- Doehrmann, R.
- Goerlitz, M.
- Hagge, L.
- Hüning, M.
- List, B.
- Meyners, N.
- Miller, D.
- Petersen, P.-O.
- Roth, S.
- Rubeck, J.R.
- Schwartzkopf, M.
- Thoden, D.
- Wiljes, P.

DLS

Oxfordshire, United Kingdom

- Crivelli, D.
- Docker, P.
- Kelly, J.H.
- Khan, F.
- Male, A.
- Sanchez Navarro, P.

DNCS

Dongguan, People's Republic of China

- Liu, J.M.

Elettra-Sincrotrone Trieste S.C.p.A.

Basovizza, Italy

- Altissimo, M.
- Cudin, I.

EMBL

Hamburg, Germany

- Bueno, M.
- Fiedler, S.
- Kolwicz-Chodak, L.
- Meyer, J.
- Ristau, U.

Enrico Fermi Institute, University of Chicago

Chicago, Illinois, USA

- Brandt, J.A.

ESA-ESTEC

Noordwijk, The Netherlands

- Bavdaz, M.
- Ferreira, I.

ESEIAAT

Terrassa, Spain

- González Romero, A.
- Hernández, F.

ESRF

Grenoble, France

- Baker, R.
- Barrett, R.
- Bernard, P.
- Berruyer, G.
- Biasci, J.C.
- Bonnefoy, J.
- Brendike, M.
- Brumund, P.
- Buisson, A.-L.
- Celestre, R.
- Cianciosi, F.
- Clement, J.M.
- Dehaeze, T.
- Ducotté, L.
- Gonzalez, H.
- Kaprolat, A.
- Marion, P.
- Mokoena, T.F.
- Muñoz Pequeño, C.
- Reyes-Herrera, J.
- Roth, T.
- Sanchez del Rio, M.
- Tafforeau, P.
- Tardieu, P.
- Thevenau, P.
- Van Vaerenbergh, P.

Euclid TechLabs

Solon, Ohio, USA

- Antipov, S.P.
- Gomez, E.

EuXFEL

Schenefeld, Germany

- Deiter, C.
- Di Felice, M.
- Dommach, M.
- Kitel, M.
- Kohlstrunk, N.
- La Civita, D.
- Schulz, J.
- Sinn, H.
- Vannoni, M.
- Yang, F.

Faraday Technology, Inc.

Clayton, Ohio, USA

- Garich, H.M.
- Hall, T.D.
- Inman, M.E.
- Liu, D.X.
- Snyder, S.T.
- Taylor, E.J.

Fermilab

Batavia, Illinois, USA

- Assell, D.
- DiMarco, J.

FMB Oxford

Oxford, United Kingdom

- Jane, E.R.
- Mateos, L.

HBH Microwave GmbH

Stutensee, Germany

- Baumann, G.
- Beyer, M.
- Heilig, R.
- Weber, J.

HUBER Diffractionstechnik GmbH&Co.KG

Rimsting, Germany

- Huber, N.
- Olea, G.
- Zeeb, J.

HZB

Berlin, Germany

- Eggenstein, F.
- Schwarz, L.
- Viefhaus, J.
- Zeschke, T.

IHEP

Beijing, People's Republic of China

- Dong, Y.H.
- Gao, L.
- He, H.Y.
- Jing, X.P.
- Kang, L.
- Li, C.H.
- Li, M.
- Liang, H.
- Lin, G.P.
- Liu, L.
- Liu, R.H.
- Lu, Y.S.
- Nie, X.J.
- Qiu, J.
- Sheng, W.F.
- Shi, H.
- Song, H.
- Tian, S.K.
- Wang, A.X.
- Wang, H.R.
- Wang, H.
- Wang, Z.H.

- Xu, G.
- Yan, F.
- Yang, F.G.
- Yang, Y.M.
- Zhang, J.S.
- Zhang, X.W.
- Zhang, Z.
- Zhao, L.Q.
- Zheng, L.R.
- Zhou, N.C.

IHEP CSNS

Guangdong Province, People's Republic of China

- Chen, J.X.
- He, H.Y.
- Ke, Z.Y.
- Liu, L.
- Liu, R.H.
- Nie, X.J.
- Ning, C.J.
- Wang, A.X.
- Wang, G.Y.
- Yu, J.B.
- Yu, Y.J.
- Zhang, J.S.
- Zhu, D.H.

ILSF

Tehran, Iran

- Moradi, V.

Institute of High Energy Physics, CAS

Guangdong, People's Republic of China

- Wang, G.Y.

KEK

Tsukuba, Japan

- Kikuchi, T.
- Mase, K.

LBNL

Berkeley, California, USA

- Bergeret, M.
- Matichard, F.
- Nasiatka, J.R.
- Oliver, T.

LNLS

Campinas, Brazil

- Borges, F.A.
- Brito Neto, J.L.
- Bueno, C.S.N.C.
- Calcanha, M.P.
- Caliari, R.M.
- Capovilla, L.G.
- Cardoso, F.H.
- Carvalho, J.C.
- Claudiano, G.V.
- Corsaletti, J.C.
- da Silva, J.L.
- de Albuquerque, G.S.
- Donatti, M.M.
- Duarte, H.O.C.
- Eleoterio, M.A.S.

- Ferreira, G.R.B.
- Fontoura, A.F.M.
- Francisco, B.A.
- Galante, D.
- Geraissate, H.
- Geraldes, R.R.
- Guedes, L.C.
- Junqueira Leão, R.
- Kakizaki, D.Y.
- Kofukuda, L.M.
- Kontogiorgos, G.N.
- Lena, F.R.
- Luiz, S.A.L.
- Meneau, F.
- Moraes, M.A.L.
- Moreno, G.B.Z.L.
- Neckel, I.T.
- Parise, R.L.
- Pereira, E.O.
- Perez, C.A.
- Perissinotto, L.S.
- Perna, A.V.
- Piccino Neto, A.C.
- Pinto, A.C.
- Piragibe, E.
- Rocha e Silva, D.V.
- Rodrigues, G.L.M.P.
- Rovigatti de Oliveira, G.R.
- Sanfelici, L.
- Sato, C.
- Saveri Silva, M.
- Silva, M.H.S.
- Silva, M.S.
- Sotero, A.P.S.
- Souza, M.S.
- Teixeira, V.C.
- Tolentino, H.C.N.
- Tonin, Y.R.
- Volpe, L.M.
- Wilendorf, W.H.
- Zilli, V.B.

MAX IV Laboratory, Lund University

Lund, Sweden

- Al-Dmour, E.
- González Fernández, J.B.
- Grabski, M.J.
- McDonald, S.A.
- Nygard, K.
- Roslund, L.K.
- Åhnberg, K.

MI-Partners

Eindhoven, The Netherlands

- Ruijl, T.A.M.

MSB

Naperville, Illinois, USA

- Mistri, G.K.

NIMS

Tsukuba, Ibaraki, Japan

- Hashimoto, A.H.
- Yamanaka, M.

Northern Illinois University

DeKalb, Illinois, USA

- Lu, X.

NSRC SOLARIS

Kraków, Poland

- Kolodziej, T.

NSRRC

Hsinchu, Taiwan

- Chang, C.F.
- Chang, C.H.
- Chang, C.Y.
- Chang, S.H.
- Chiang, L.C.
- Chuang, J.-Y.
- Fung, H.S.
- Ho, H.C.
- Hsu, K.H.
- Huang, C.S.
- Huang, D.-G.
- Kuan, C.K.
- Lai, W.Y.
- Lee, R.
- Liao, B.Y.
- Lin, C.J.
- Liu, C.Y.
- Perng, S.Y.
- Tseng, T.C.
- Wang, H.S.

NVHS

Naperville, Illinois, USA

- Suthar, A.K.
- Suthar, S.K.

NYIT

Old Westbury, New York, USA

- Cardenas, E.

PAL

Pohang, Republic of Korea

- Ha, T.

PML

Liège, Belgium

- Dehaeze, T.

PPRC

Tehran, Iran

- Adamian, A.
- Arab, N.B.

PSI

Villigen PSI, Switzerland

- Just, D.M.
- Pradervand, C.

PTB

Berlin, Germany

- Handick, E.
- Krumrey, M.
- Mueller, P.

RadiaBeam

Santa Monica, California, USA

- Carriere, P.R.

SARI-CAS

Pudong, Shanghai, People's Republic of China

- Deng, R.
- Mao, N.
- Zhang, L.
- Zhu, W.

SBU

Stony Brook, New York, USA

- Sirna, A.P.

SESAME

Allan, Jordan

- Al Shehab, M.M.
- Al-Najdawi, M.A.
- Iori, G.
- Lausi, A.

Shanghai Institute of Optics and Fine Mechanics

Shanghai, People's Republic of China

- Liu, Y.

ShanghaiTech University

Shanghai, People's Republic of China

- Liu, F.
- Wang, Z.

SLAC

Menlo Park, California, USA

- Bassan, H.
- Boiadjieva, N.A.
- Decker, F.-J.
- Fritz, D.M.
- Gassner, G.L.
- Huang, Z.
- Marcus, G.
- Nuhn, H.-D.
- Rabedeau, T.
- Tan, T.-F.
- Wang, H.
- Zhu, D.

SLRI

Nakhon Ratchasima, Thailand

- Chaichuay, S.
- Klinkhieo, S.
- Pongampai, S.
- Sittisard, K.
- Srichan, S.

Sokendai, The Graduate University for Advanced Studies

Tsukuba, Japan

- Mase, K.
- Miyazawa, T.

SOLEIL

Gif-sur-Yvette, France

- Abiven, Y.-M.
- Dubuisson, J.M.

- Engblom, C.
- Giorgetta, J.L.
- Hermange, H.
- Hunault, M.O.J.Y.
- Lestrade, A.
- Mary, A.
- Menut, D.
- Pruvost, J.B.P.
- Sebdaoui, M.
- Solari, P.L.
- Tavakoli, K.

Stony Brook University

Stony Brook, New York, USA

- Donetski, D.
- Liu, J.

Synchrotron Light Research Institute (SLRI)

Muang District, Thailand

- Utke, O.

Technical University of Catalonia, The Biomaterials, Biomechanics and Tissue Engineering

Barcelona, Spain

- Buxadera, J.
- Punset, M.

TIT

Tokyo, Japan

- Ozawa, K.

Tokyo University of Science

Noda, Japan

- Masuda, Y.
- Nakayama, Y.

Translume, Inc.

Ann Arbor, Michigan, USA

- Bado, P.
- Dugan, M.
- Said, A.A.

TRUMPF Huettinger

Freiburg, Germany

- Ehinger, M.
- Lau, M.
- Schweizer, M.

ULB

Bruxelles, Belgium

- Collette, C.G.R.L.

UNICAMP

Campinas, São Paulo, Brazil

- Fernández, P.S.

University of Johannesburg

Johannesburg, South Africa

- Bhamjee, M.
- Connell, S.H.

University of Tokyo

Kashiwa, Japan

- Ono, M.
- Yoshikawa, I.
- Yoshioka, K.

UW-Madison

Madison, Wisconsin, USA

- Behdad, N.
- Booske, J.H.
- Siy, A.E.

UW-Madison/PD

Madison, Wisconsin, USA

- Siy, A.E.

Yokohama National University

Yokohama, Japan

- Ohno, S.

**Yokohama National University, Graduate School of
Engineering Science**

Yokohama, Japan

- Sato, Y.

Attendees



Last Name	First Name	Affiliation
Abrams	Jay	Argonne National Laboratory
Adam	Madison	Canadian Light Source
Adamson	Luke	ANSTO - Australian Synchrotron
Afzali Far	Behrouz	MAX IV Laboratory-Lund University
Åhnberg	Karl	MAX IV Laboratory
Al-Dmour	Eshraq	MAX IV Laboratory-Lund University
AL-Najdawi	Mohammad	MAX IV Laboratory
Álvarez	José María	ALBA Synchrotron Light Source
Alves	Filipe	Synchrotron SOLEIL
Amann	Paul	Argonne National Laboratory
Andresen	Simone	Alfred Wegener Institute
Anliker	Ethan	Argonne National Laboratory
Ansaldi	Gabriele	European XFEL
Antipov	Sergey	Euclid Techlabs
Antipova	Olga	Argonne National Laboratory
Anton	Jayson	Argonne National Laboratory
Antonelli	Stephen	Brookhaven National Laboratory
Aran	Emily	Argonne National Laboratory
Arcuri	Marychris	Sydor Technologies
Armenta	Rebecca	SLAC National Accelerator Laboratory
Avellar	Grace	Argonne National Laboratory
Bacescu	Daniel	Brookhaven National Laboratory
Bado	Philippe	Translume Inc.
Bailey	Frankie	Diamond Light Source Ltd
Baker	Nick	Diamond Light Source Ltd
Baker	Robert	ESRF
Ballesta	Jerome	SYMETRIE
Barbier	Charlotte	ORNL
Barkway	Gordon	Canadian Light Source
Basar	Alper	University of Minnesota
Basi Reddy	Sree	Argonne National Laboratory
Batista Zilli	Vinicius	Brazilian Synchrotron Light Laboratory - LNLS
Bean	Sunil	Argonne National Laboratory
Benda	Erika	Argonne National Laboratory
Bender	Timothy	Argonne National Laboratory
Bennett	Marvin	Columbia University
Berlioux	Anthony	Synchrotron SOLEIL
Bernhard	Andrew	Argonne National Laboratory
Beyer	Kevin	Argonne National Laboratory
Biasci	Jean-Claude	ESRF
Bienert	Hilmar	DESY - Deutsches Elektronen-Synchrotron

Content from this work may be used under the terms of the CC BY 3.0 licence (© 2021). Any distribution of this work must maintain attribution to the author(s), title of the work, publisher, and DOI

MEDSI2020 Attendees

Last Name	First Name	Affiliation
Biller	Regina	DESY - Deutsches Elektronen-Synchrotron
Biskin	Özkan	DESY - Deutsches Elektronen-Synchrotron
Bjermo	Anders	MAX IV Laboratory
Boiadjieva	Nina	SLAC National Accelerator Laboratory
Boin	Nadia	FMB Oxford
Bongiovanni	Stefano	CINEL Strumenti Scientifici Srl
Botta	Stephan	DESY - Deutsches Elektronen-Synchrotron
Brady	Amanda	Leybold
Brandt	John	The University of Chicago
Brumund	Philipp	ESRF
Bueno	Cassiano	CNPEM/LNLS
Bueno	Moises	EMBL Hamburg
BUISSON	Anne-Lise	ESRF
Burgess	Terrance	Argonne National Laboratory
Burt	Martin	Diamond Light Source Ltd
Butler	David	Diamond Light Source Ltd
Cacho-Nerin	Fernando	AVS Added Value Solutions
Cameli	Patricia	Argonne National Laboratory
Campo	Eva	University of Maryland
Canjura	Hector	Argonne National Laboratory
Capatina	Dana	Argonne National Laboratory
Capostagno	Daniel	TRUMPF Huettinger
Carballedo	Antonio	ALBA Synchrotron Light Source
Cardenas	Edwin	New York Institute of Technology
Carlsson	Tommy	MAX IV Laboratory
Carr	Matt	Diamond Light Source Ltd
Carriere	Shawn	Canadian Light Source
Carvelli	Jeremy	Argonne National Laboratory
Casas	Joan	ALBA Synchrotron Light Source
Cease	Herman	Argonne National Laboratory
Celmer	Lynnean	Argonne National Laboratory
Chang	Chia-Feng	National Synchrotron Radiation Research Center
Chang	Chao Yu	NSRRC
Chang	C-Y	NSRRC
Charalambous	Harry	Argonne National Laboratory
Chen	Si	Argonne National Laboratory
Chen	June_Rong	NSRRC
Cheng	Charles	Northwestern University
Cheng	Tony	SLAC National Accelerator Laboratory
Cheng	Xianchao	SLAC National Accelerator Laboratory
Cherukuvada	Hima	ANSTO - Australian Synchrotron
Chisman	Liam	Diamond Light Source Ltd
Chithirai-Pandi	Muthuraj	Diamond Light Source Ltd

Content from this work may be used under the terms of the CC BY 3.0 licence (© 2021). Any distribution of this work must maintain attribution to the author(s), title of the work, publisher, and DOI

MEDSI2020 Attendees

Last Name	First Name	Affiliation
Choi	William	SLAC National Accelerator Laboratory
Chuang	Jyun-Yan	NSRRC
Cianciosi	Filippo	ESRF
Coburn	Scott	Brookhaven National Laboratory
Colldelram	Carles	ALBA Synchrotron Light Source
Collins	Jeff	Argonne National Laboratory
Collins	Kevin	Diamond Light Source Ltd
Comnesso	John	Prior Scientific/Queensgate
Connolly	John	Argonne National Laboratory
Connolly	Brian	PI - PHYSIK INSTRUMENTE LP
Cravedi	Amy	PI - PHYSIK INSTRUMENTE LP
Crisol	Alejandro	ALBA Synchrotron Light Source
Crivelli	Davide	Diamond Light Source Ltd
Croatto	Sandy	DESY - Deutsches Elektronen-Synchrotron
Cunrath	Aymeric	IRELEC
Cuzco	Henry	Argonne National Laboratory
Danielyan	Vahe	Diamond Light Source Ltd
Davis	Benjamin	Argonne National Laboratory
Day	Alan	Diamond Light Source Ltd
de Oliveira Caiafa Duarte	Henrique	CNPEM/LNLS
de Vink	David	Swinburne University of Technology
de Zubiaurre Wagner	Antonio	DESY - Deutsches Elektronen-Synchrotron
Defavari	Rafael	Brazilian Center for Research in Energy and Materials
Defever	Jim	SLAC National Accelerator Laboratory
Dehaeze	Thomas	ESRF
Deiter	Carsten	European XFEL
Delitz	Jan Torben	European XFEL
Den Hartog	Patric	Argonne National Laboratory
Diaz	Luis	Argonne National Laboratory
Diete	Wolfgang	AXILON AG
Dill	Frank Uwe	DESY - Deutsches Elektronen-Synchrotron
Divitcos	Jim	ANSTO - Australian Synchrotron
Docker	Peter	Diamond Light Source Ltd
Döhrmann	Ralph	DESY - Deutsches Elektronen-Synchrotron
Dommach	Martin	European XFEL
Doran	Scott	Argonne National Laboratory
Ducotte	Ludovic	ESRF
Duget	Anne	SYMETRIE
Dymoke-Bradshaw	James	Diamond Light Source Ltd
Eastman	Debbie	SAES Group
Ederer	Katrin	DESY - Deutsches Elektronen-Synchrotron
Ehnes	Anita	Research Center of the Helmholtz Association

Content from this work may be used under the terms of the CC BY 3.0 licence (© 2021). Any distribution of this work must maintain attribution to the author(s), title of the work, publisher, and DOI

MEDSI2020 Attendees

Last Name	First Name	Affiliation
Elahibakhsh	Yahya	Lamar University
Endo	Katsumi	Toyama Co., Ltd.
Eng	Christopher	Brookhaven National Laboratory
Eyberger	Cathy	Argonne National Laboratory
Eybert	Laurent	ESRF
Fairley	Andrew	Diamond Light Source Ltd
Felcsuti	Gabor	MAX IV Laboratory-Lund University
Fiedler	Stefan	European Molecular Biology Laboratory (EMBL)
Fisher	Mike	Argonne National Laboratory
Foley	Virginia	Zygo Corporation
Forcat	Silvia	MAX IV Laboratory
Föse	Manon	DESY - Deutsches Elektronen-Synchrotron
Francisco	Bárbara	CNPEM
Frank	Ben	FMB Oxford
Frankenberger	Paul	European XFEL
Friedrich	Bertram	European XFEL
Frith	Matt	Argonne National Laboratory
Frommherz	Ulrich	Paul Scherrer Institute
Fry	Luke	Diamond Light Source Ltd
Fudala	Krzysztof	Argonne National Laboratory
Fuentes	Lluïsa	ALBA Synchrotron Light Source
Gaddam	Sriyothi	Argonne National Laboratory
Galbierz	Vanessa	DESY - Deutsches Elektronen-Synchrotron
García	José Ramón	ALBA Synchrotron Light Source
Gehrmann	Thomas	EMBL Hamburg
Geraldes	Renan	Eindhoven University of Technology
Giessel	Tatjana	BESTEC GmbH
Giesteira	Filipe	DESY - Deutsches Elektronen-Synchrotron
Giorgetta	Jean-Luc	Synchrotron SOLEIL
Giraldo	Juan Carlos	Consorti C.E.E. Lab Llum Sincrotró
Glamann	Nicole	KIT/IBPT
Glettig	Wayne	Paul Scherrer Institute
Gluskin	Efim	Argonne National Laboratory
Goerlitz	Marcel	DESY Hamburg
Golebiowski	Marek	Argonne National Laboratory
Gomez	Diana	Carnegie Mellon University
González	Nahikari	ALBA Synchrotron Light Source
Gonzalez Fernandez	Joaquin B.	MAX IV Laboratory
González Romero	Andrea	Universitat Politècnica de Catalunya - UPC ESEIAAT
Gorin	James	Canadian Light Source
Grabski	Marek	MAX IV Laboratory-Lund University
Grenville	David	Diamond Light Source Ltd
Griffin	Emily	ANSTO - Australian Synchrotron

Content from this work may be used under the terms of the CC BY 3.0 licence (© 2021). Any distribution of this work must maintain attribution to the author(s), title of the work, publisher, and DOI

MEDSI2020 Attendees

Last Name	First Name	Affiliation
Grimmer	John	Argonne National Laboratory
Gutschmidt	Sven	Data One GmbH
Ha	Taekyun	Pohang Accelerator Laboratory
Haas	Edwin	Brookhaven National Laboratory
Haghighat	Vahid	MAX IV Laboratory-Lund University
Hamill	Alan	Huber Difraktionstechnik GmbH & Co. KG
Hammerschmidt	Rainer	BESTEC GmbH
Hammond	Nigel	Diamond Light Source Ltd
Hanuska	Steven	Argonne National Laboratory
Hardy	Russell	UHV Design Ltd
Harnik	Stan	Argonne National Laboratory
Hauser	Jakob	DESY - Deutsches Elektronen-Synchrotron
He	Huayan	Institute of High Energy Physics, CAS
He	Ping	Institute of High Energy Physics, CAS
Henning	Robert	The University of Chicago
Hernández	Francesc	Universitat Politècnica de Catalunya - UPC ESEIAAT
Hetzel	Charles	Brookhaven National Laboratory
Hillegass	Brian	Leybold
Hillenberg	Jake	Allied Metals Corporation
Hillman	Michael	Diamond Light Source Ltd
Hodbod	Stephen	Diamond Light Source Ltd
Holmes	Benjamin	Allectra
Huber	Norman	Huber Difraktionstechnik GmbH & Co. KG
Hulbert	Steven	Brookhaven National Laboratory
Humbert	Christine	IRELEC
Hutcheson	Will	Lawrence Berkeley National Laboratory
Iori	Gianluca	SESAME
Iriarte	Silvia	AVS Added Value Solutions
Izzo	Scott	Argonne National Laboratory
Jaje	Kelly	Argonne National Laboratory
Jane	Elliot	FMB Oxford
Jansma	William	Argonne National Laboratory
Jaski	Yifei	Argonne National Laboratory
Jensen	Don	Argonne National Laboratory
Jim Rank	Jim Rank	Brookhaven National Laboratory
Johns	Evan	Northwestern University
Just	David	Paul Scherrer Institute
Karas	Constantine	Argonne National Laboratory
Kary	Dana	Canadian Light Source
Kearney	Steven	Argonne National Laboratory
Khan	Altaf	Argonne National Laboratory
Khan	Fariha	Diamond Light Source Ltd
Knopp	Jonathan	Argonne National Laboratory

Content from this work may be used under the terms of the CC BY 3.0 licence (© 2021). Any distribution of this work must maintain attribution to the author(s), title of the work, publisher, and DOI

MEDSI2020 Attendees

Last Name	First Name	Affiliation
Kohlstrunk	Nicole	European XFEL
Koldrack	Normann	DESY - Deutsches Elektronen-Synchrotron
Kolwicz-Chodak	Liliana	EMBL Hamburg
La Civita	Daniele	European XFEL
La Fleche	Kyle	Lawrence Berkeley National Laboratory
Ladrera	Jon	ALBA Synchrotron Light Source
Lai	Barry	Argonne National Laboratory
LaLonde	Luke	Argonne National Laboratory
Le Jollec	Antoine	Synchrotron SOLEIL
Lee	Soonhong	Argonne National Laboratory
Lena	Francesco	LNL
Lerch	Jason	Argonne National Laboratory
Li	Elen	Canadian Light Source
Liang	Hao	Institute of High Energy Physics, CAS
Lienhard	Lukas	Brookhaven National Laboratory
List	Benno	DESY - Deutsches Elektronen-Synchrotron
Littlewood	Robert	Sydor Technologies
Liu	Jie	Argonne National Laboratory
Liu	Zunping	Argonne National Laboratory
Liu	Xia	Diamond Light Source Ltd
Liu	Ao	Euclid Techlabs
Liu	Danny	Faraday Technology, Inc.
Liu	Renhong	Institute of High Energy Physics, CAS
Liu	Fang	ShanghaiTech University
Llonch	Marta	ALBA Synchrotron Light Source
Lomperski	Mark	DESY - Deutsches Elektronen-Synchrotron
Lucas	Michael	Brookhaven National Laboratory
Luis Mateos	Luis Mateos	FMB Oxford
Maccallini	Enrico	SAES Group
Macdonell	Sarah	Diamond Light Source Ltd
Male	Andrew	Diamond Light Source Ltd
Malmgren	Magnus	MAX IV Laboratory
Mandin	Paul	CEA
Marion	Philippe	ESRF
Martin	Ben	Sydor Technologies
Mase	Kazuhiko	High Energy Accelerator Research Organization (KEK)
Mashrafi	Sheikh	Argonne National Laboratory
Massey	Adrian	ANSTO - Australian Synchrotron
Matichard	Fabrice	Lawrence Berkeley National Laboratory
Matus	Janusz	Argonne National Laboratory
Maxey	Evan	Argonne National Laboratory
McElderry	Austin	Argonne National Laboratory
McFall	Matthew	University of Saskatchewan (Canadian Lightsource)

Content from this work may be used under the terms of the CC BY 3.0 licence (© 2021). Any distribution of this work must maintain attribution to the author(s), title of the work, publisher, and DOI

MEDSI2020 Attendees

Last Name	First Name	Affiliation
McGhee	Christine	Argonne National Laboratory
McGuire	Ann	SLAC National Accelerator Laboratory
McMahon	Ben	ANSTO - Australian Synchrotron
Meissner	Daniel	DESY - Deutsches Elektronen-Synchrotron
Mejia Ramos	Eduardo	Argonne National Laboratory
Mendes da Rocha	Thiago	CNPEM
Menut	Denis	Synchrotron SOLEIL
Meyners	Norbert	DESY - Deutsches Elektronen-Synchrotron
Micolon	Frederic	CERN
Miguel	Jorge	SmarAct Inc.
Milas	Mirko	MAX IV Laboratory-Lund University
Milongo	Chadrack	Conseils national de la jeunesse
Mistri	Gayatri	Argonne National Laboratory
Mokoena	Fortune	University of Johannesburg
Monge	Raquel	ALBA Synchrotron Light Source
Monk	Bryan	University of Illinois at Urbana-Champaign
Moradi	Vahid	Azad University (Tehran Central)
Moreno	Gabriel	CNPEM
Morey	Callan	ANSTO - Australian Synchrotron
Morton	Peter	Applied Diamond, Inc.
Mountford	Brad	ANSTO - Australian Synchrotron
MOYNE	Alban	ESRF
Mulvany	Oliver	Argonne National Laboratory
Munoz Pequeno	Carlos	ESRF
Murri	Cameron	Vacuum Volume, LLC
Musardo	Marco	Brookhaven National Laboratory
Nagy	Marcell	Diamond Light Source Ltd
Nasiatka	Jamie	Lawrence Berkeley National Laboratory
Navarro	Pablo	Diamond Light Source Ltd
Navrotski	Gary	Argonne National Laboratory
Nie	Xiaojun	Institute of High Energy Physics, CAS
Nikitin	Yury	ALBA Synchrotron Light Source
Nikitina	Liudmila	ALBA Synchrotron Light Source
Nudell	Jeremy	Argonne National Laboratory
O'Connell	Scott	Anderson Dahlen - Applied Vacuum Division
O'Connell	Kelly	University of Notre Dame
O'Dowd	Frank	SLAC National Accelerator Laboratory
Ohashi	Haruhiko	JASRI/SPring-8
Olea	Gheorghe	Huber Difraktionstechnik GmbH & Co. KG
Oliver	Thomas	Lawrence Berkeley National Laboratory
O'Neill	Maria	Argonne National Laboratory
Oprondek	Samuel	Argonne National Laboratory
Ostrom	Walker	University of Saskatchewan

Content from this work may be used under the terms of the CC BY 3.0 licence (© 2021). Any distribution of this work must maintain attribution to the author(s), title of the work, publisher, and DOI

MEDSI2020 Attendees

Last Name	First Name	Affiliation
Peli	Mario	Allectra
Peña	Gabriel	ALBA Synchrotron Light Source
Perna	Alain	CNPEM/LNLS
Petersen	Per-Ole	DESY - Deutsches Elektronen-Synchrotron
Pile	Geoff	Argonne National Laboratory
Plambeck	Nils	DESY Hamburg
Planas Carbonell	Marc	European XFEL
Platzer	Roland	DESY - Deutsches Elektronen-Synchrotron
Plueckthun	Mark	Allied Metals Corporation
Pocock	Benjamin	ANSTO - Australian Synchrotron
Pocock	Robert	Diamond Light Source Ltd
Porsa	Sina	ANSTO - Australian Synchrotron
Powell	Eric	Lawrence Berkeley National Laboratory
Power	Maria	N/A
Pradervand	Claude	Paul Scherrer Institute
Preissner	Curt	Argonne National Laboratory
Prieto	Montserrat	ALBA Synchrotron Light Source
Prigent	Pascale	Synchrotron SOLEIL
Proskey	Michael	The University of Chicago
Qiao	Zhi	Argonne National Laboratory
Quispe	Marcos	ALBA Synchrotron Light Source
Raabe	Jana	DESY - Deutsches Elektronen-Synchrotron
Raby	Alison	Prior Scientific/Queensgate
Randall	Jon	FMB Oxford
Rasmussen	Olaf	DESY - Deutsches Elektronen-Synchrotron
Reuter	Florian	REUTER TECHNOLOGIE GmbH
Reuter	Karl-Heinz	REUTER TECHNOLOGIE GmbH
Reuther	David	DESY Hamburg
Reyes Herrera	Juan	ESRF
Ribó	Llibert	ALBA Synchrotron Light Source
Richaud	Raphael	IRELEC
Rider	Kate	Allectra
Rod	Eric	Argonne National Laboratory
Röh	Jan Torben	DESY - Deutsches Elektronen-Synchrotron
Roschka	Michael	FMB Berlin & FMB Oxford
Rovigatti de Oliveira	Gustavo	CNPEM/LNLS
Rubeck	Jan	DESY - Deutsches Elektronen-Synchrotron
Ruett	Uta	Argonne National Laboratory
Ruijl	Theo	MI-Partners
Rustighini	Giorgio	Diamond Light Source Ltd
Sandy	Alec	Argonne National Laboratory
Sanfelici	Lucas	Brazilian Synchrotron Light Laboratory - LNLS
Saveri Silva	Marlon	LNLS

MEDSI2020 Attendees

Last Name	First Name	Affiliation
Schaa	Volker RW	GSI, Darmstadt, Germany
Schmidt	Oliver	Argonne National Laboratory
Schmidt	Andreas	European XFEL
Schneider	Sandra	DESY Hamburg
Schneider	Ronald	MI-Partners
Schott	Steffen	Karlsruher Institut für Technologie (KIT)
Schwark	Iris	DESY Hamburg
Schwarz	Lisa	Helmholtz-Zentrum Berlin
Scolari	Simone Maria	MAX IV Laboratory
Scott	Stewart	Diamond Light Source Ltd
Semeraro	Michela	ANSTO - Australian Synchrotron
Sharma	Sushil	Brookhaven National Laboratory
Shea	Tim	AVS Added Value Solutions
Sheng	Weifan	Institute of High Energy Physics, CAS
Sherrell	Darren	Argonne National Laboratory
Shu	Deming	Argonne National Laboratory
Siegel	Zack	The University of Chicago
Siemers	Dirk Jan	Helmholtz-Zentrum Hereon
Signorato	Riccardo	CINEL Strumenti Scientifici Srl
Sinkovits	Theo	SAES Rial Vacuum
Sirna	Amanda	Stony Brook University
Smart	Moises Enrique	SLAC National Accelerator Laboratory
Sorsher	Simon	Argonne National Laboratory
Spreizer	Steven	Argonne National Laboratory
Spreizer	Steven	Rensselaer Polytechnic Institute
Srichan	Supawan	Synchrotron Light Research Institute - SLRI
Stasic	Damir	Argonne National Laboratory
Stillwell	Benjamin	The University of Chicago
Streiffer	Stephen	Argonne National Laboratory
Sullivan	Joe	Argonne National Laboratory
Sun	Chengjun	Argonne National Laboratory
Suthar	Kamlesh	Argonne National Laboratory
Suzuki	Hiroya	Toyama Co., Ltd.
Swetin	Eugene	Argonne National Laboratory
Szubert	Megan	Argonne National Laboratory
Tabeling	Joseph	Applied Diamond, Inc.
Takahashi	Sunao	RIKEN/SPring-8
Tan	Joanna	Argonne National Laboratory
TANG	Shanzhi	Institute of High Energy Physics, CAS
Tavakoli	Keihan	Synchrotron SOLEIL
Tendron	Brian	SYMETRIE
Thielen	Niklas	DESY - Deutsches Elektronen-Synchrotron
Thoden	Daniel	DESY - Deutsches Elektronen-Synchrotron

MEDSI2020 Attendees

Last Name	First Name	Affiliation
Thwaites	Richard	Diamond Light Source Ltd
Tiessen	Jens	DESY - Deutsches Elektronen-Synchrotron
Tizzano	Walter	Diamond Light Source Ltd
Tocci	Joseph	Lawrence Berkeley National Laboratory
Tong	Yajun	ShanghaiTech University
Trakhtenberg	Emil	Argonne National laboratory
Trapp	Antje	European XFEL
Trutmann	Daniel	Paul Scherrer Institute
Tseng	Tse-Chuan	NSRRC
Utke	Oliver	Synchrotron Light Research Institute - SLRI
Van Every	Eric	AVS Added Value Solutions
Van Vaerenbergh	pierre	ESRF
Vanni	Constance	Argonne National Laboratory
Vardanyan	Vahagn	DESY - Deutsches Elektronen-Synchrotron
Venkatesan	Sudharshan	ANSTO - Australian Synchrotron
Vilcins-Czvitkovits	Silke	DESY - Deutsches Elektronen-Synchrotron
Villanueva	Raúl	European XFEL
Villar	François	ESRF
Volin	Kenneth	Argonne National Laboratory
Volpe	Lucas	LNLS
Wakefield	Kevin	Argonne National Laboratory
Waldschmidt	Geoff	Argonne National Laboratory
Walker	Karen	Argonne National Laboratory
Wang	Zihao	Institute of High Energy Physics, CAS
Wang	Xinyu	Paul Scherrer Institute
Wang	Hengzi	SLAC National Accelerator Laboratory
Waterstradt	Timm	AXILON AG
Wayman	Heath	Argonne National Laboratory
Weigel	James	Argonne National Laboratory
Weir	Nicholas	Argonne National Laboratory
Welzenbach	Undine	AXILON AG
Wendt	Mario	DESY - Deutsches Elektronen-Synchrotron
white	marion	Argonne National Laboratory
White	Marion	Argonne National Laboratory
Wiechecki	Jaroslav	National Synchrotron Radiation Centre Solaris
Wiemerslage	Greg	Argonne National Laboratory
Wiesener	Paul	DESY - Deutsches Elektronen-Synchrotron
Wilendorf	Willian Henrique	Brazilian Synchrotron Light Laboratory - LNLS
Wiljes	Patrik	DESY - Deutsches Elektronen-Synchrotron
Willis	David	UT-Battelle
Witek	Konrad	The Ohio State University
Wolford	Chasen	Argonne National Laboratory
Wuenschel	Mark	European XFEL

Content from this work may be used under the terms of the CC BY 3.0 licence (© 2021). Any distribution of this work must maintain attribution to the author(s), title of the work, publisher, and DOI

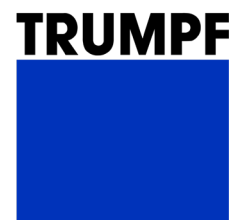
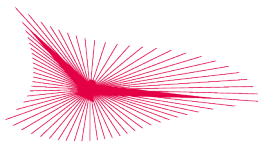
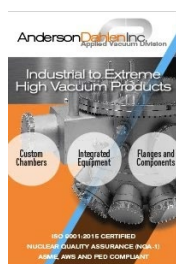
MEDSI2020 Attendees

Last Name	First Name	Affiliation
Wulfsberg	Steven	SAES Group
Wurm	Maximilian	Paul Scherrer Institute
Wysokinski	Tomasz	Canadian Light Source
Xu	Shenglan	Argonne National Laboratory
Yakovenko	Andrey	Argonne National Laboratory
Yan	Fang	Institute of High Energy Physics, CAS
Yang	Fan	European XFEL
Yang	Fugui	Institute of High Energy Physics, CAS
Yu	Jiebing	Institute of High Energy Physics, CAS
Yu	Tony	The University of Chicago
Zhang	Lin	SLAC National Accelerator Laboratory
Zhiltsov	Vitalii	Diamond Light Source Ltd
Zholents	Alexander	Argonne National Laboratory
Zhou	Keyu	MAX IV Laboratory-Lund University



INDUSTRIAL EXHIBITORS/SPONSORS

We were grateful to have 22 industrial exhibitors/sponsors who sponsored the MEDSI2020 virtual conference. They put up a lively exhibition on the MEDSI2020 Whova virtual conference platform with product information, many photos, and videos, and some of them had live-streamed events. Not only did they sponsor us financially, most importantly, their participation made the conference complete. We would like to acknowledge all of our sponsors here. The detailed description of the companies is based on the information entered by the companies on the MEDSI2020 Whova platform.



Details for Exhibitors/Sponsors



Allectra

Description: Allectra is a leading manufacturer and supplier of High Vacuum and UHV components including custom items.

The company was founded in 2002 by two physicist entrepreneurs to bring a new approach to manufacturing high technology components to the scientific instruments market. In the last nineteen years Allectra has seen widespread adoption of its proprietary technology across multiple scientific disciplines. Some of our components have been adopted as a standard by synchrotrons worldwide.

Electrical feedthrough range includes Sub-D and Co-axial types alongside cables and accessories, also viewports and hardware. Allectra has three facilities with scientific and engineering capabilities, one in the UK and two in Germany, and ships worldwide.

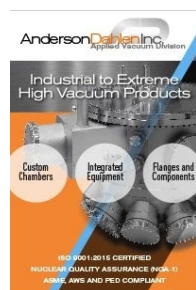
Address: Meridian House, Bluebell Business Estate, Sheffield Park, East Sussex, TN22 3HQ, UK

Phone: 44 (0)1825 721900

Contact person: Kate Rider

Contact email: k.rider@allectra.com

Website: <http://www.allectra.com>



Anderson Dahlen - Applied Vacuum Division

Description: The Applied Vacuum Division of Anderson Dahlen delivers total vacuum solutions including chambers and assemblies, flanges and components, as well as custom integrated equipment. We fabricate custom

chambers and assemblies from rough and high vacuum (HV) for industrial processes to ultra-high (UHV) and extreme-high vacuum (XHV) for critical scientific study. Our engineering and manufacturing resources will help take your requirements from initial concepts, to fully engineered designs, to completed and tested products ready for use. We utilize SOLIDWORKS® 3D design and advanced analysis software, enabling expert review of critical tolerances, port alignment, chamber wall deformations, weld stresses, and other features. We can also assist you with design considerations to meet safety and mechanical concerns, including ratings for ASME/PED pressure and cryogenic requirements. Throughout the build process, extreme cleanliness and attention to finish quality are paramount. All welded assemblies are 100% helium leak tested. We have Certified Welding Inspectors® (CWI) to review critical weld joints. Final dimensional inspection utilizes our Coordinate Measuring Machine (CMM). Applied Vacuum is ISO 9001:2015 Certified, Nuclear Quality Assurance (NQA-1) Certified, ASME, AWS, and PED Compliant.

Address: 6850 Sunwood Dr NW Ramsey MN 55303

Phone: 781-299-0657

Contact person: Scott O'Connell

Contact email: ocos@andersondahlen.com

Website: <https://andersondahlen.com/applied-vacuum-division>



Applied Diamond, Inc.

Description: Applied Diamond supplies products made from single crystal and polycrystalline diamond, including highly transparent windows, ultra high thermal conductivity high spreaders and beam monitoring products. We have expertise in diamond polishing for smooth surfaces, metallization for bonding and mounting of windows to flanges.

Our beam monitoring products range from fluorescent screens to instrumented diamond pixel detectors. We can mount large windows to

UHV flanges, including water cooled flanges for high temperature applications. Diamond's high thermal conductivity and radiation hardness make for effective products in the high power and white beam applications.

Applied Diamond also fabricates a refractive x-ray lens for optics applications.

We make standalone diamond as thin as 20 um and can provide filters mounted on Silicon as thin as 300 nm. We can customize a stack of filters ranging in thicknesses from 1 um to 700 um thick, enabling a beam to use the diamond thickness appropriate for the experimental conditions.

Our single crystal diamond is available in both optical grade and high purity electronic grade. We offer SC plates as thin a 20 um and as thick 1 mm with sizes as large as 8 mm square."

Address: 3825 Lancaster Pike, Wilmington, DE 19805

Phone: 1-302-999-1132

Contact person: Peter Morton

Contact email: pete@ddk.com

Website: <http://www.usapplieddiamond.com>



added value solutions

AVS Added Value Solutions

Description: AVS is proud to be one of the world's leading companies in the design and development of custom-made equipment for large science and research infrastructure across the globe.

The core activity of AVS is the development, design, manufacture, assemble and delivery of custom instrumentation and equipment for large scientific facilities, supplied under ISO 9001 EN 9100. AVS has specific skills and extensive experience in the development of precision motion systems, micromechanisms and optomechanics, operating under harsh conditions of vacuum (UHV), temperature (cryogenics as well as high temperatures) and high magnetic fields.

AVS designs and develops specific equipment for synchrotrons. AVS has developed and supplied tailored accelerator and storage ring components (Linac transport elements and diagnostics as well as ID's), as well as beamline elements including beam transport, X-ray optics, filters, slits, diagnostics, sample environments

and positioning systems, as well as high-end SAXS flight tubes.

AVS is the proud supplier of the ESRF-UBS storage ring girders. Our extensive expertise and long tradition of high-load, high-precision structures makes us the ideal partner for your next challenging project.

Address: 126 Ridge Rd, Lansing, NY 14882

Phone: 1-607-533-3531

Contact person: Eric Van Every

Contact email: eric.vanevery@a-v-s.us

Website: <https://www.a-v-s.es/>



Description: AXILON is your industrial partner in the international synchrotron, accelerator & photon community. Based on the extensive and long-term experience of our dedicated experts, we serve our customers with excellent and efficient solutions for complete beamlines, beamline components, monochromators, cryo coolers, mirror systems, experimental stations, X-ray microscopes and other special engineering and manufacturing solutions.

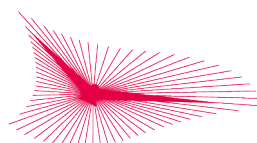
Address: Robert-Bosch-Str. 1b; 50354 Huerth; Germany

Phone: +49 221 165324 00

Contact person: Wolfgang Diete

Contact email: wolfgang.diete@axilon.de

Website: <http://www.axilon.de>



BESTEC

BESTEC GmbH

Description: Bestec GmbH develops, builds and installs customer specific ultrahigh vacuum systems (UHV systems) with focus on two application areas:

- Optical instruments for photon energies from the infrared to the hard X-ray range.
- Fully automated deposition systems for production and optimization of functional layer systems."

Address: Am Studio 2b, 12489 Berlin, Germany

Phone: +49 30 6774376

Contact person: Rainer Hammerschmidt

Contact email: rainer.hammerschmidt@bestec.de

Website: <http://www.bestec.de>



CINEL STRUMENTI SCIENTIFICI SRL

Description: CINEL Strumenti Scientifici (<http://www.cinel.com>) is an established supplier of components and integrated systems for synchrotron, XFEL light sources and particle accelerators. We provide innovative and tailored solutions into integrated UHV systems, complete beamlines, beamline components (mirror systems, monochromators, etc.). Our combination of in-house expertise in precision design and engineering, metrology, assembly and integration, vacuum and, last but not least, our precision manufacturing capabilities allowing us to produce every single part of our instruments, make CINEL the right partner to realize challenging and state-of-the-art instruments for your beamlines.

Address: Viale dell'Artigianato 14, 35010, Vigonza (PD), Italy

Contact person: Riccardo Signorato

Contact email: riccardo.signorato@cinel.com

Website: <http://www.cinel.com>



Huber Diffractionstechnik GmbH & Co. KG

Description: Huber is a leading supplier for high precision positioning systems and equipment for X-ray- and Neutron scattering.

For more than 50 years, Huber is designing and manufacturing equipment for X-ray laboratories, synchrotron and neutron facilities, ranging from a large variety of standard stages to highly complex multi-axes systems for micro- and nano-positioning.

Huber's products can be custom-tailored for specific requirements to suit all applications, no matter if used in vacuum environment, exposed to high radiation or operated in high magnetic fields."

Address: HUBER Diffractionstechnik GmbH & Co. KG Sommerstrasse 4 D-83253 Rimsting, Germany

Contact person: Alan Hamill

Contact email: ahamill@xhuberusa.com

Website: <http://www.xhuber.com>



IRELEC

Description: Since 1985, IRELEC has been designing and producing high performance opto-mechanical equipment, biomedical robotic systems and precision instrumentation, enhancing the innovation capabilities and operational efficiency of its customers' applications in the scientific and biomedical fields.

Located in a highly dynamic European research and innovation area, IRELEC brings together multi-disciplinary expertise in reliable high technology, easy-to-use and finely tunable equipment for the maximum benefit of a worldwide user community."

Address: 20 Rue du tour de l'eau, 38400 St Martin d'Hères, FRANCE

Phone: +33 4 76 44 12 96

Contact person: Christine Humbert

Contact email: chumbert@irelec-alcen.com

Website: <http://www.irelec-alcen.com>



Leybold

Description: As a pioneer of vacuum technology for over 170 years, Leybold offers a wide range of vacuum components, standardized and fully customized vacuum solutions, and many after-market services. With the most extensive worldwide sales and after-sales network in the vacuum technology industry, Leybold ranks among the top leaders in its specific business segments - Process Industry, Information Technology, Analytical Processes, and Research & Development.

Address: 6005 Enterprise Drive, Export, PA 15632

Phone: +1 800.764.5369

Contact person: Brian Hillegass

Contact email: brian.hillegass@leybold.com

Website: <https://www.leybold.com/us/en>



MI-Partners B.V.

Description: "MI-Partners is a high-end engineering company specialized in custom design and realization of accurate and highly dynamic systems such as sample manipulators, nano-end stations and monochromators (DCM). Core competences are: system architecture, dynamics, thermal (cryo) design and calculations, predictive modeling and metrology.

We have a proven track-record in the development of next generation high-end stages and custom developed manipulators that meet their requirements for various synchrotrons. Together with our customers, we translate the scientific requirements into mechatronic specifications and a feasible concept. We define error budgets to predict the performance in an early stage based on thermal, dynamic and metrology models. We are used to work on high-risk development projects and know how to manage these innovative projects in a controlled manner. We have a flexible and customer oriented approach and are very open to discuss your mechatronic challenges. Please contact us!

Address: Habraken 1199, 5507TB Veldhoven

Phone: +31 614751371

Contact person: Ronald Schneider

Contact email: R.Schneider@MI-Partners.nl

Website: <http://www.MI-Partners.nl>

PI

PI - PHYSIK

INSTRUMENTE LP

Description: PI manufactures world-class precision motion and automation systems for industry and research, including high performance positioning and alignment systems for beamline instrumentation. PI products include air bearings, 6-Axis hexapods, piezo actuators / motors and high performance motion controllers. PI has design and service centers at locations in North America, Europe, and Asia. Founded 50 years ago and employing 1300+ people with global support, PI's customers are leaders in high-tech industry and research fields including photonics, life-sciences, semiconductors, astronomy, aerospace and basic research.

Address: 16 Albert Street, Auburn, MA 01501

Phone: 1-508-832-3456

Contact person: Amy Cravedi

Contact email: amyc@pi-usa.us

Website: <http://www.pi-usa.us>

queensgate

a brand of **PRIOR**

Prior

Scientific/Queensgate

Description: Queensgate offers an extensive product line of UHV compatible sensors, piezo actuators, and piezo stages. Whether standard or custom, our systems typically deliver decades of reliable performance.

What distinguishes Queensgate?

- Performance: Experts in high speed, high precision applications.
- Enhanced control technology: A tool kit to deliver the best performance for the application.
- Reliability: Trouble free installation in beamlines with over decades of use. True plug and play electronics.
- Experience: Over 40 years of delivering performance-critical components.
- Design: Material selection and FEA design to meet the demands of synchrotron applications
- Custom solutions: Over 70% of our products are custom made

Address: 80 Reservoir Park Drive, Rockland, MA 02370

Phone: 1-781-878-8442

Contact person: John Commesso

Contact email: jcommesso@prior.com

Website: <https://www.nanopositioning.com>



REUTER TECHNOLOGIE GmbH

Description: REUTER TECHNOLOGIE is specialized in customized solutions for liquid cooling in vacuum. We design and manufacture cooling blocks, cooling plates and specific assemblies made of copper and stainless steel for sophisticated thermal applications in vacuum. Starting with the constructive support of your engineering team, through a precise modern production with qualified joining technologies such as high vacuum brazing, up to qualified tests and inspection procedures.

Contact person: Florian Reuter

Contact email: f.reuter@reuter-technologie.de

Website: <http://www.precision-brazing.com>



SAES Group

Description: The SAES CapaciTorr and NEX Torr pumps continue to be the benchmark compact and powerful UHV/XHV pumps. The recently developed ZAO alloy has allowed for extending the operational pressure of NEG's to the 1e-7 Torr range with CapaciTorr HV and NEX Torr HV pumps as well as for developing the CapaciTorr Z and NexTorr Z pumps that deliver up to 50 % more pumping speed in the same package as the existing CapaciTorr and NEX Torr pumps. The ZAO alloy also exhibits an improved mechanical stability, allowing ZAO-based pumps to be used in the cleanest applications without a risk of particle contamination. Recently, Jefferson Lab has started retrofitting the warm sections between SRF cavities of CEBAF with ZAO-based CapaciTorr HV200 pumps since they are cleaner and provide a better background than ion pumps. The standard NEX Torr pumps are now being implemented in cold waveguides because of their outstanding hydrogen performance..

Contact person: Steven Wulfsberg

Contact email: steven.wulfsberg@saesgroupusa.com

Website: <https://www.saesgroup.com>



SmarAct Inc.

Description: SmarAct develops and produces piezo-based, high-accuracy positioning and measuring systems for industrial and research applications in the micro and nanometer scale. Comprehensive positioner systems with numerous degrees of freedom and parallel kinematics, microscopy stages and laser interferometers can be assembled to custom-built, complete robotic systems, and work under extreme conditions, e.g., ultrahigh vacuum, cryogenic temperatures, and non-magnetic materials.

Address: 2140 Shattuck Ave, STE 302, CA 94704

Phone: 1-415-766-9006

Contact person: Jorge Miguel

Contact email: miguel@smaract.com

Website: <http://www.smaract.com>



COMPLEX MEASUREMENTS—CRITICAL RESULTS

Sydor Technologies

Description: Sydor Technologies is a global provider of advanced x-ray detectors and diagnostic instrumentation for the energy, research, and defense industries. We manufacture complex measurement solutions for the world's most advanced applications. Our products are customized to each user's requirements. Our hard and soft x-ray detectors are engineered to provide the best sensitivity, across the widest dynamic range, and are optimized for use at modern and up-and-coming light sources. Our x-ray Diamond Beam Position Monitors (DBPM) are available in a variety of packages for use in ambient to UHV environments. X-ray streak cameras and framing cameras are available to accompany our line of gated imagers and visible streak cameras. Established in 2004, Sydor Technologies is headquartered in Rochester, NY and now supplies systems and support in over 33 countries. For more information, please visit www.SydorTechnologies.com

Address: 78 Schuyler Baldwin Dr. Fairport, NY 14450, USA

Phone: 1-585-278-1168

Contact person: Marychris Arcuri

Contact email: marketing@sydortechnologies.com

Website: <http://www.sydortechnologies.com>



SYMETRIE

Description: SYMETRIE specializes in hexapods, which are 6DOF parallel kinematics systems that bring accuracy, stability and stiffness. SYMETRIE was created in 2001 by two engineers of LNE, the French National Laboratory of Metrology (equivalent to NIST).

The precision positioning hexapods of SYMETRIE are particularly adapted for the specific needs of synchrotrons. They can position components such as samples, mirrors or vacuum chambers with high precision.

SYMETRIE provides a range of standard products and also offers highly customized systems with specific geometry or additional axes.

Software comes with several interesting features, such as virtual pivot point configuration and workspace limits. The hexapod control system can be integrated into a third-party environment (EPICS, TANGO, Labview...).

SYMETRIE hexapods are already used at APS, the Australian Synchrotron, DLS, Elettra, ESRF, IHEP, LBL, LNLS, MAX-lab, PAL, PSI, RRCAT, SLAC, SOLEIL, and SSRF.

Address: 10 allée Charles Babbage, 30000 Nîmes, France

Phone: +33 466294388

Contact person: Anne Duget

Contact email: anne.duget@symetrie.fr

Website: <https://www.symetrie.fr>

TOYAMA TOYAMA Co., Ltd.

Description: Toyama, are regarded as one of the excellent suppliers of whole beamline packages comprising major systems such as grating or double crystal monochromators, mirror chambers, high heat load slits and masks, and also smaller components such as beam diagnostics and beam shutters.

Toyama has rich experience and capability to design and build such hardware components in its own plant located near Tokyo in Japan. We have system integration technologies covering FEA simulation, optical design, vacuum engineering and control systems and software.

Full and precise inspection and testing of equipment can be performed in our special clean rooms in Toyama's plant with many high-precision measurement tools such as laser trackers, laser interferometers, triaxial vibration testing and so on. We have used our clean rooms with fine temperature control and

vibration-free circumstances for many important projects from worldwide customers.

Finally, we proudly announce that we have constructed our new factory and headquarters together with our R&D center. The new factory and headquarters are located at approximately 70 km southwest of Tokyo, where we have a very beautiful view of our world natural treasure of "Mt. Fuji".

Address: Toyama Co., Ltd. 3816-1 Kishi, Yamakita-machi, Ashigarakami-gun Kanagawa, 258-0112, JAPAN

Phone: +81-46-579-1411

Contact person: Hiroya Suzuki

Contact email: h-suzuki@toyama-jp.com

Website: <http://www.toyama-en.com>

TRUMPF



TRUMPF Huettinger

Description: TRUMPF Hüttinger is a leading global manufacturer of process power supplies for plasma applications, induction heating, and CO2 laser excitation. TRUMPF Hüttinger has been part of the TRUMPF Group since 1990.

Address: 4000 Burton Drive, Santa Clara, CA 95054

Phone: 1-408-568-9908

Contact person: Daniel Capostagno

Contact email: daniel.capostagno@trumpf.com

Website: https://www.trumpf.com/en_INT/products/powerelectronics/



UHV Design Ltd

Description: UHV Design Ltd. specializes in the design, manufacture and supply of high-quality, low maintenance, manipulation and heating/cooling solutions for vacuum applications.

Solutions include: magnetically coupled rotary motion drives; sample transfer solutions; 5-axis sample manipulators with heating and LN2/LHe cooling; high uniformity heating stages for 1"-8" diameter wafers. Products are sold and supported globally via an extensive distribution network to customers worldwide."

Address: Judges House, Lewes Road,
Laughton, East Sussex England, BN8
6BN

Phone: +44 1323 811188

Contact person: Russell Hardy

Contact email: R.Hardy@uhvdesign.com

Website: <https://www.uhvdesign.com/>



Zygo Corporation

Description: For 50 years, Zygo Corporation designs and manufactures noncontact measuring instruments and systems, providing productivity and yield improvement. ZYGO provides a wide range of inspection, surface analysis, and precision displacement measurement solutions, as well as precision optics, optical design, and opto-mechanical assembly.

Contact person: Virginia Foley

Contact email: Virginia.Foley@ametec.com

Website: <http://www.zygo.com>